

REPORT DOCUMENTATION PAGE**Form Approved**
OMB No. 0704-0188

Public reporting burden for this collection of information is estimated to average 1 hour per response, including the time for reviewing instructions, searching data sources, gathering and maintaining the data needed, and completing and reviewing the collection of information. Send comments regarding this burden estimate or any other aspect of this collection of information, including suggestions for reducing this burden to Washington Headquarters Service, Directorate for Information Operations and Reports, 1215 Jefferson Davis Highway, Suite 1204, Arlington, VA 22202-4302, and to the Office of Management and Budget, Paperwork Reduction Project (0704-0188) Washington, DC 20503.

PLEASE DO NOT RETURN YOUR FORM TO THE ABOVE ADDRESS.**1. REPORT DATE** 07/31/2012**2. REPORT TYPE**

Final Technical Report

3. DATES COVERED (From - To)

01-MAY-09 to 31-JUL-12

4. TITLE AND SUBTITLE

Investigation of ELF Signals Associated with Mine Warfare: A University of Idaho and Acoustic Research Detachment Collaboration, Phase Three

5a. CONTRACT NUMBER**5b. GRANT NUMBER** N00014-09-1-0923**5c. PROGRAM ELEMENT NUMBER****6. AUTHOR(S)**

Young, Jeffrey L.; and Wagner, Christopher L.

5d. PROJECT NUMBER

11PR06807-00

5e. TASK NUMBER**5f. WORK UNIT NUMBER****7. PERFORMING ORGANIZATION NAME(S) AND ADDRESS(ES)**University of Idaho, Office of Sponsored Programs
Morrill Hall Room 414
PO Box 443020
Moscow, ID 83844-3020**8. PERFORMING ORGANIZATION
REPORT NUMBER****9. SPONSORING/MONITORING AGENCY NAME(S) AND ADDRESS(ES)**Office of Naval Research
1107 NE 45th Street
Suite 350
Seattle, WA 98105-4631**10. SPONSOR/MONITOR'S ACRONYM(S)**
ONR**11. SPONSORING/MONITORING
AGENCY REPORT NUMBER**
PR# 11PR06807-00**12. DISTRIBUTION AVAILABILITY STATEMENT**

Unlimited

13. SUPPLEMENTARY NOTES**14. ABSTRACT**

Described herein are the key findings and results associated with the project entitled "Investigation of ELF Signals Associated with Mine Warfare, A University of Idaho and Acoustic Research Detachment Collaboration, Phase Three." Phase Three is a continuation of the Phase One and Two efforts under the same title.

The questions that are being asked in this investigation are: 1) once an ELF signal is generated, how far will it propagate and still be detectable and 2) how can such signals be modeled, excited and measured? To this end, the scenario considered is one in which an ELF source of the electric or magnetic kind is located in or above water, such as a lake or ocean. This source stimulates an ELF signal that is free to propagate in the water and air, and is reflected by various material interfaces, say between the water and air, or between the water and the floor. For purposes of experimental demonstration the investigation focuses on the scenario of ELF sources and signals in the context of Lake Pend Oreille, where the Acoustic Research Detachment (ARD, Bayview, Idaho) is located and entrusted with the necessary assets to perform validation measurements.

The research program was designed with two major thrusts: Modeling and experimentation. The modeling thrust was coordinated and executed by the University of Idaho (UI), Moscow, Idaho; the experimentation thrust was coordinated and executed by ARD. This report focuses primarily on the modeling thrust. A separate report from ARD has been issued that addresses the experimentation thrust.

INSTRUCTIONS FOR COMPLETING SF 298

15. SUBJECT TERMS

Extremely low frequency signals, electromagnetic wave propagation, numerical modeling, experimental measurements

16. SECURITY CLASSIFICATION OF:a. REPORT
Ub. ABSTRACT
Uc. THIS PAGE
U17. LIMITATION OF
ABSTRACT
UU18. NUMBER
OF PAGES
100319a. NAME OF RESPONSIBLE PERSON
Jeffrey L. Young19b. TELEPHONE NUMBER (Include area code)
208-885-6829

Final Report

**Investigation of ELF Signals Associated with Mine Warfare: A University of
Idaho and Acoustic Research Detachment Collaboration, Phase Three**

By

Jeffrey L. Young and Christopher L. Wagner

Primary Contact:

Jeffrey L. Young
Electrical and Computer Engineering
University of Idaho
Moscow, ID 83844-1023
208-885-6829
jyoung@uidaho.edu

July 2012

Supporting Information:

Contract Number: N00014-09-1-0923

Original Contract Period: August 1, 2009 through July 31, 2010

Extended Contract Period: August 1, 2010 through July 31, 2012

FY08 Funded Amount: \$787,014.00

Introduction

Described herein are the key findings and results associated with the project entitled “Investigation of ELF Signals Associated with Mine Warfare, A University of Idaho and Acoustic Research Detachment Collaboration, Phase Three.” Phase Three is a continuation of the Phase One and Two efforts under the same title. The scope, objectives and outcomes of Phase Three are similar to those described in the reports and proposals of Phase One and Two. Some of the following text is also found in the Phase One and Two reports.

Extremely low frequency (ELF) electromagnetic signals are used by enemy combatants to detect and, subsequently, to incapacitate, by means of surface and subsurface mines, naval vessels. This program is of high importance to the Navy – particularly since ELF signals are one of the primary signature emissions of the Navy’s proposed electric ship fleet.

The questions that are being asked in this investigation are: 1) once an ELF signal is generated, how far will it propagate and still be detectable and 2) how can such signals be modeled, excited and measured? To this end, the scenario considered is one in which an ELF source of the electric or magnetic kind is located in or above water, such as a lake or ocean. This source stimulates an ELF signal that is free to propagate in the water and air, and is reflected by various material interfaces, say between the water and air, or between the water and the floor. For purposes of experimental demonstration the investigation focuses on the scenario of ELF sources and signals in the context of Lake Pend Oreille, where the Acoustic Research Detachment (ARD, Bayview, Idaho) is located and entrusted with the necessary assets to perform validation measurements.

The research program was designed with two major thrusts: Modeling and experimentation. The modeling thrust was coordinated and executed by the University of Idaho (UI), Moscow, Idaho; the experimentation thrust was coordinated and executed by ARD. This report focuses primarily on the modeling thrust. A separate report from ARD has been issued that addresses the experimentation thrust (See Appendix A.)

Both students and faculty of the University of Idaho were involved in the project. Phase Three team members include:

Prof. Jeffrey L. Young, Lead PI:

- Prof. Dennis Sullivan
- Dr. Christopher L. Wagner, Research Engineer, FDTD code development
- Mr. Robert Rebich, MSEE RA, Quasi-static code development

- Mr. Christopher Johnson, MSEE RA, Data analysis and code development
- Mr. Das Butherus, MSEE RA, Data analysis and code development
- Mr. Chenchen “Jimmy” Li, BSEE RA, Topographical data translation
- Ms. Neelima Dahal, BSEE RA, Data analysis
- Mr. Markus Geiger, BSEE RA, Data analysis

Contents

Introduction.....	2
ELF Modeling.....	4
Sommerfeld Full-Wave (SFW) Method	4
Finite Difference, Time-Domain Method (FDTD).....	5
Low Frequency Diffusion Problem	6
High Frequency Structural Simulator (HFSS)	6
Maxwell.....	6
Quasi-Static Method.....	6
Lake Parameters and Discretization	7
Electric and Magnetic Sources	9
Reciprocity and Moving Sources	10
Experimental Data Post-Processing	10
UI Experimental Support.....	11
Results and Validation.....	11
Data Comparisons: Simulation Methods vs Sommerfeld Full-Wave Method	11
Data Comparisons: Simulation vs. Experimentation	15
Data Comparisons: Phase Two Test near “TMH Range” (Run 1003).....	15
Data Comparisons: Phase Three Test near Idlewilde Bay (Run 304.02)	19
Data Comparisons: Overall Trends in Simulation Performance	25

Attached Appendices:

- Appendix A: Test Reports
- Appendix B: Scenario Reports
- Appendix C: Publications
- Appendix D: Theses
- Appendix E: Auxiliary Documents
- Appendix F: Finite-Difference Time-Domain User’s Manual

ELF Modeling

The activities pursued during Phase Three continued those pursued during Phases One and Two, with particular emphasis on the refinement and validation of the numerical models. Portions of the following text summarize the modeling effort undertaken by the University of Idaho and are also found in the Phase One and Two reports. Some of that text has been updated to reflect new knowledge gained since the Phase One and Two reports were issued. In subsequent sections unique results and findings associated with Phase Three activities will be presented.

Modeling of ELF electromagnetic signals in water environments can be accomplished either by means of direct, analytical solution of Maxwell's equations or by numerical solutions of the same. The former is attractive for purposes of gaining insights into the physical mechanisms that hinder or aid the propagation of ELF signals. The disadvantage is found in the number of simplifying assumptions that are made to bring about a closed-form solution. A numerical solution has no such simplifying assumptions, but does suffer from discretization errors. In principle it can model all of the physical and geometrical features of the domain of consideration. The price paid for doing so, however, is the required time and the CPU/memory resources needed to accomplish the task. Data visualization and management are other issues that need to be addressed when working with large data sets produced by numerical solvers. The positive and negative tradeoffs between these two approaches (i.e. analytical vs. numerical) suggest that no one method is superior. For that reason the UI team adopted a diverse strategy that encompasses many different approaches in order to assure a positive outcome and to provide deliverable modeling methodologies.

The five principle techniques or tools that were considered during the Phase One, Two and Three efforts were the a) Sommerfeld Full-Wave (SFW) method, b) Finite-difference, time-domain method (FDTD), c) High Frequency Structural Simulator (HFSS), finite-element code, d) Maxwell code and e) quasi-static method (QES). A summary of these methods is provided next. Detailed technical information on the SFW, FDTD and quasi-static methods are provided in the Phase Two Final Report.

Sommerfeld Full-Wave (SFW) Method

The SFW method is an analytical approach that assumes that all interfaces (say between water and air, or between water and floor) are planar and infinitely extended. This assumption is reasonably valid for the water-air interface, particularly in open water regions where the source is located near the surface. For the littoral zones, the method may fail, particularly when electric sources are used to excite the ELF signals.

By assuming that the interfaces are flat, a closed-form solution can be devised that is cast in terms of Fourier-Bessel integrals. These integrals can be evaluated numerically and rapidly in a matter of seconds on any desktop machine. Even with the potential deficiency of treating all interfaces as planar, the SFW method is attractive as a validation tool for the other numerical modeling approaches. For example, the team used the SFW method to validate the data produced by the FDTD or HFSS methods when these numerical methods considered the same layered media problem statement. A discussion of this validation outcome is provided in an ensuing section entitled “*Data Comparisons: Simulation Methods vs Sommerfeld Full-Wave Method*,” see Appendix B for detailed information. The SFW method is also attractive in quantifying the up-over-down effect. This effect is associated with a low signal loss path through the air and a high signal loss path up and down through the water. If the path through the water is short, then the up-over-down signal loss can be low relative to a direct path between a source and sensor in the water. Professor Robert Olsen of Washington State University (WSU) was the lead investigator of the up-over-down effect during Phase Two; see the Phase Two Final Report for more information.

Finite Difference, Time-Domain Method (FDTD)

The FDTD method is a numerical approach that discretizes Maxwell’s equations in their fundamental form using a staggered grid and leap-frog integrator. This method has been fully vetted in the open literature and has been established as a robust way of obtaining accurate simulation data. In principle, the FDTD method accounts for all material interfaces and inhomogeneities by assigning permittivity, permeability and conductivity values to each cell in the simulation domain. Curvilinear boundaries are approximated by straight line, stair-stepped boundaries. For geometrical features that are significantly less than a wavelength, such stair-stepping causes no appreciable errors in the computed data. Note that the domain of interest at Lake Pend Oreille does not exceed 8 km on a side; the lake floor at its deepest point is about 335 m. Assuming an operating frequency of 100 Hz and a water conductivity of 0.01 S/m, we note that the corresponding skin depth is 503 m and the wavelength is 3.162 km; for air, the wavelength is 3,000 km. Thus the domain spans a fraction of a wavelength in air but about 2.5 wavelengths (or 15.9 skin depths) in water. The significant disparity between these two relative sizes potentially introduces computational complexities. One area of concern is the proper design of an absorbing boundary condition (ABC) or perfectly matched layer (PML) that will allow an open physical domain to be truncated into a finite computational domain. Placement of this ABC/PML in terms of wavelengths is critical if non-spurious reflections are to be avoided. Significant time and effort was expended to figure out a way to design an optimal PML. The outcome of this effort is described in the paper by Wagner and Young, “FDTD numerical tests of the convolutional-PML at extremely low frequencies,” *IEEE Antennas and Wireless Propagation Letters*, vol. 8, pp. 1398-1401, 2009. This paper is found in

Appendix C, p. C11. A user's manual for the UI developed FDTD code is found in Appendix F. FDTD code is available upon request.

Low Frequency Diffusion Problem

The propagation of electromagnetic signals in the ELF band in water is a diffusive process. Analysis of the problem shows that time domain simulation times grow rapidly for low enough frequencies. This effect has been seen with FDTD simulations, as a lack of convergence to expected results, in which case more time steps must be taken to allow the diffusion processes to occur. For ELF simulations with FDTD, it is important to perform convergence testing to ensure the best results from the FDTD calculations.

High Frequency Structural Simulator (HFSS)

HFSS is a commercially available electromagnetic, finite-element, frequency-domain, numerical solver that has been designed by Ansys for antenna and microwave circuit applications. One question that was asked in this investigation was whether such a tool could be used to predict the electromagnetic propagation characteristics of an ELF signal in a highly conductive environment. In Phase One and Two, the answer to this question was inconclusive due to source modeling issues. During Phase Three, the answer was conclusive – HFSS is a viable tool if appropriately used and configured. More information regarding HFSS can be found in Appendix D under the thesis title “Modeling extremely low frequency electromagnetic signals for naval applications;” see p. D199.

Maxwell

Maxwell is also a commercial code developed by Ansys. However, unlike HFSS it is a static solver for either electric or magnetic fields. Since ELF waves are static-like in the vicinity of the source, questions that have been raised by the team are these: 1) At what distance are the fields more static-like rather than wave-like and 2) can ELF waves be modeled by a static solver in some region about the source. Answers to these questions can be found in Appendix D under the thesis title “Sensor orientation, reciprocity and software evaluation in the context of extremely low frequency applications;” see p. D108.

Quasi-Static Method

A custom quasi-static method was also considered given that ELF signals are

quasi-static in the vicinity of the source. By definition, the quasi-static method does not consider any wavelike mechanisms in Maxwell's equations; it assumes that the field lines are the same as the static field, but oscillating. This is accomplished by neglecting magnetic displacement currents for electric sources. By doing so, simple solutions can be constructed that correlate well with other more advanced solutions, like HFSS and FDTD. See the thesis "Multiple-layered quasi-electrostatic model development for extremely low frequencies" in Appendix D, p. D2.

Lake Parameters and Discretization

Unlike the December 2008 experiments in which the experiments were conducted in an open area of the lake, the domain for the March and September 2010 experiments encompass significant geometrical features above and below water. This was purposefully chosen to be so in order to exercise the limits of the various numerical and analytical models. That is, we would expect the ELF signals in the open area to be far easier to model than those in a more cluttered environment due to the changes in the material parameters and geometrical features of the environment. Hence, we wanted the most severe environment possible to see if the models would fail to produce the correct data.

The FDTD and HFSS numerical methods require a precise understanding of the electrical and geometrical features of the Lake. The domain of interest considered in Phase Three is the area known as Idlewild Bay and is shown below. The domain is about 6 km by 7 km on a side and represents the general area where actual experiments were performed in March and September 2010 using both electric and magnetic sources. (See Appendix A for more information regarding these experiments.)



The terrain elevation data (relative to sea level) along with their corresponding coordinates (in varying forms) were extracted from three sources: a data set from insideidaho.org, an AUTOCAD file of Lake Pend Oreille Contours from the Idaho Geological Survey, and data points taken manually from a provisional map of Lake Pend Oreille. The coordinates of each data point were converted into meters northing and easting in Idaho West State Plane; any elevation data in feet were converted to meter – thus, all three data sets conform to the same system. All three data sets were compiled together (minor adjustments were made to eliminate conflict between the data sets). Interpolation of elevation data at all points along two vectors (in x and y direction that define the area to interpolate) was accomplished using the 'griddata' function in Matlab. This created a matrix height field that defines the elevation and depth of the terrain or Lake at each point in 1m intervals. The matrix height field was then used as an input file for the various numerical solvers, i.e. FDTD, HFSS or Maxwell.

The height field, if used with HFSS or Maxwell, needs to be converted into a solid model. The first step is to extract data from the height field into x,y,z coordinates. Then in AutoCAD the command '3dmesh' is used to create a mesh that is up to 255x255 cells in dimension from those coordinates. Since the height field is 6240x7520 cells in size, the data is down-sampled so that it will be within the bounds of '3dmesh'. After meshing, an AutoCAD script, 'M2S-2007.lsp' is used to convert the mesh into a solid figure. This solid figure is then exported as an ACIS .sat file (which is supported by HFSS). However, the mesh on the surface of the solid is too refined and uniform for HFSS to use efficiently in data computation. Therefore, an additional remeshing step is necessary via the mesh tool Cubit. By combining all the surfaces of the original mesh into one composite surface, the composite surface is then meshed

using one of Cubit's meshing schemes. Unfortunately, Cubit cannot imprint the new mesh onto the original AutoCAD solid; the new mesh must be converted into a solid itself. The mesh is exported into an .inp file and then re-imported into Cubit, which removes the AutoCAD solid and leaves only the Cubit mesh. The mesh is then converted into a solid within Cubit and is exported back into an ACIS .sat format. Clearly, this is an involved process, but a necessary one when using HFSS or Maxwell. More information regarding this process is found in Appendix D, p. 199 entitled "Modeling extremely low frequency electromagnetic signals for naval applications."

In addition to precise geometrical data, the various solvers also require precise knowledge of the conductivity of the lake and the mud at the bottom of the lake. The UI team used a value of 0.01 S/m for the water and 0.012 S/m for the mud in the deep part of the lake; see Appendix E for more information on how these values were measured. For shallow portions of the lake, the floor was considered more rock-like and value of 0.0012 S/m was used. As for the value of the dielectric permittivity of the lake, this was not deemed essential, since displacement currents in the lake are virtually insignificant relative to the conduction currents. A value of 81 was used for the relative permittivity.

It should be noted that a major shortcoming of the modeling effort has nothing to do with the modeling methodology, but with the lack of information about the environment to be modeled. For example, we treat the problem statement as if the environment is only comprised of three homogeneous substances: water, air and mud. Clearly, this is not so. The lake bottom, which we call mud, is actually an inhomogeneous substance of rock and silt that is saturated by water. The land, which is called mud, is an inhomogeneous substance of rock, dirt, trees and structures. Only the water and air are homogeneous for which numbers like permittivity and conductivity are known. Hence, errors between experimental data and simulation data can be attributed to the lack of knowledge of the environment and certain guesses about the quantification of the environment.

Electric and Magnetic Sources

Two kinds of electric sources were used in the March and September 2010 experiments: 1) a 4 meter, 2 Ampere (max) electric source placed on a boat hull that skimmed the surface of the water and 2) a 15 meter, 3 Ampere (max) portable electric source that was lowered from 15 meters in the water to the lake floor (i.e. about 152 meters). Additionally, a 3.6 meter by 3.6 meter, 12 turn, 20 Ampere magnetic source was also used to stimulate ELF signals; this source was rigidly placed on the shore at Farragut State Park. For both electric and magnetic sources, the ELF signals were measured using a portable electromagnetic array (PEMA) that was lowered into the water at depths ranging from 15 m to 152 m. Source and sensor locations associated with the March 2010 experiment are shown below. Similar set-ups were used in the

September 2010 experiment; see Appendix A for precise information regarding the location of the sensors and sources.



Reciprocity and Moving Sources

Simulations typically place a source at some fixed location and record the electromagnetic field in any region of interest. This modeling procedure is not appropriate for the case of ELF boat sources, as the source is moving. Numerical simulations essentially require the source to be fixed, which suggests that a moving source could be simulated as a sequence of many fixed-location sources along the path of the boat. And, for each location, a computationally long simulation is required. When the boat path covers some kilometer scale distance, the number of simulations required would be computationally prohibitive. We solve this problem by employing the principle of Lorentz Reciprocity.

To employ reciprocity in the simulations we assume point sources to establish reactions between sources and fields at the experiment and simulation source and sensor locations. The reciprocity reaction relations are projections of a source current onto a field and vice versa. The projection operation is a scalar operation, so in order to obtain vector fields we require one simulation per field component. Six simulations are then required to calculate the vector electric and magnetic fields. See Appendix F for a detailed description of the method under the publication title “Roving sources, simulation and reciprocity,” p. C64.

Experimental Data Post-Processing

Once the experimental data was collected it was transferred to the University of Idaho in binary format for processing – particularly, to extract the desired frequency domain signals from the time-domain data. The first step was to pre-process the measured

data into a standard format and to scale the data using appropriate scaling factors, as provided by ARD. Next data sets were selected and transformed into the frequency domain using fast Fourier Transform (FFT) methods. The FFT data reveal the time-harmonic signal strength of each electromagnetic field component relative to the coordinate system of the experiment. To compare these data with simulation data, coordinate transformations are performed on the experimental data using GPS sensor data. The processing of the data is not completely automatic given random noise spikes and discontinuities in the data streams. The following theses provide detailed information regarding the post-processing of data: “Modeling extremely low frequency electromagnetic signals for naval applications” and “Sensor orientation, reciprocity and software evaluation in the context of extremely low frequency applications.” See Appendix D for reprints of these theses.

UI Experimental Support

The UI provided support to ARD by developing data acquisition software and hardware to monitor the signals produced by the ELF sources and GPS location of the same. Details of this support is found in Appendix D, p. D199 under the thesis title “Modeling extremely low frequency electromagnetic signals for naval applications”

Results and Validation

We now discuss simulation and experimental results and the validation thereof. There are two methods by which validation is achieved. First, the Sommerfeld Full Wave (SFW) solution, which is an exact solution that has been validated by data available in the open literature, is used as a benchmark for the other ELF methods (e.g. quasi-static, HFSS, Maxwell, FDTD). By comparing all solutions to the SFW solution we assured ourselves that we have consistency between solutions for a problem whose solution is known exactly. Moreover, since the SFW solution is validated by additional data in the open literature, we also assure ourselves that the solutions are correct. Second, experimental and simulation results are compared, showing the ability of the simulations to predict the measured fields. In the following sections, excerpts of the validation and experimental calculations are presented; see Appendix B for the entire suite of comparisons.

Data Comparisons: Simulation Methods vs Sommerfeld Full-Wave Method

As noted previously, the Sommerfeld Full-Wave (SFW) Method, being an exact solution of Maxwell's equations, can be used to benchmark the accuracy of the various methods employed in this project. Three-layer geometry was chosen for the canonical test problems, as it is similar to the deep-lake experiments of Phase Two. The layer geometry is shown in Figure 1.

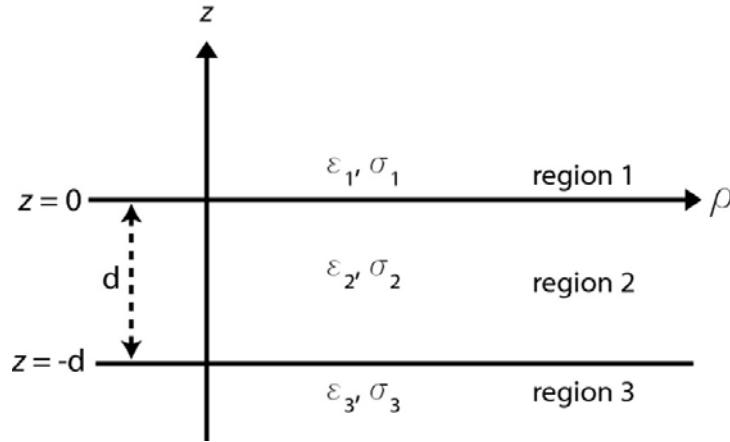


Figure 1: Three layer geometry of the canonical problem. Region one is air, region two is water, and region three is mud. Regions one and three are infinite half-spaces, region two is 180 meters thick. The FDTD and HFSS methods use finite thicknesses for regions one and three.

Comparison problems were calculated for each of the four source types (HED, VED, HMD, VMD) with the source and sensor in either air or water, giving sixteen test cases. The complex components of the fields were compared in each case. Only four of the sixteen source and sensor cases are configurations similar to experimental runs. The sensor is always in water in the experiment.

The plots shown in Figures 2-5 show some results for the case of a VMD source in air and an observation point in water (a case similar to several experimental Phase Two and Three runs). The full report for this calculation can be found in Appendix B, page B119. The x component of the electric field is shown in Figures 2 and 3. The real and imaginary parts of the components agree well for SFW, FDTD and HFSS methods. The QES method does not calculate results for magnetic sources. The z -component of the electric field is zero; the various methods compute different small values for zero components. The very good agreement of the exact Sommerfeld solutions and the FDTD and HFSS simulation methods provides a validation of the simulation codes and methodology.

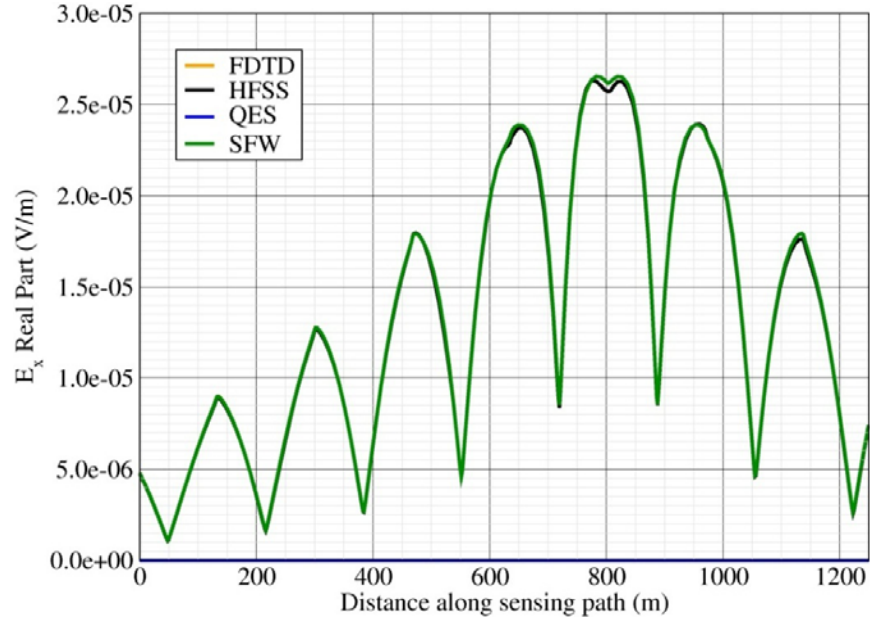


Figure 2: Real part of the x component of the electric field for a three layer problem with a VMD source. Observation is in water at a depth of about 10.1 meters.

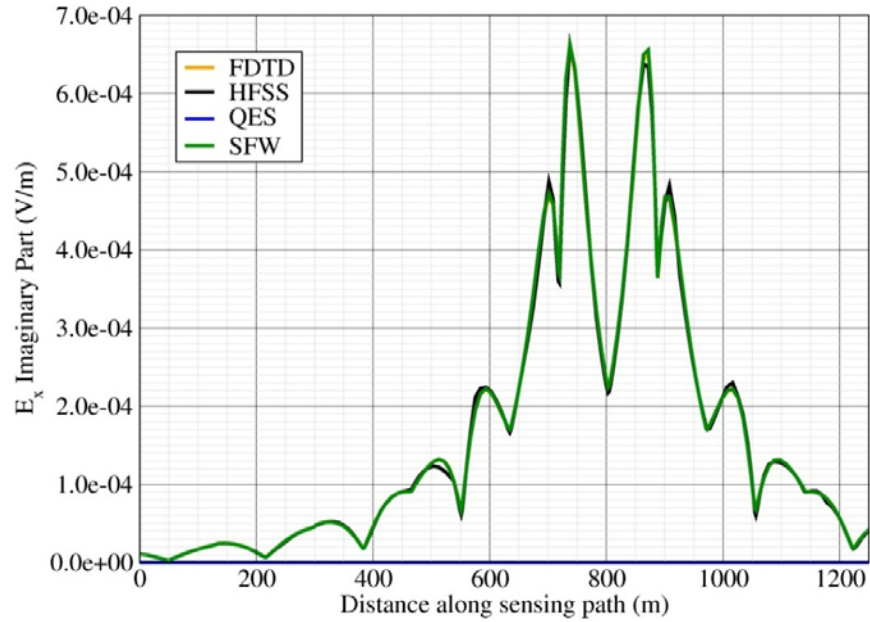


Figure 3: Imaginary part of the x component of the electric field for the VMD three layer problem.

The magnetic fields are shown in Figures 4-5. Again we see that the methods agree well for all the field components. The cases where there are small differences between a method and Sommerfeld are usually due to poor mesh shape or grid size, which can be improved at a cost of increased calculation time.

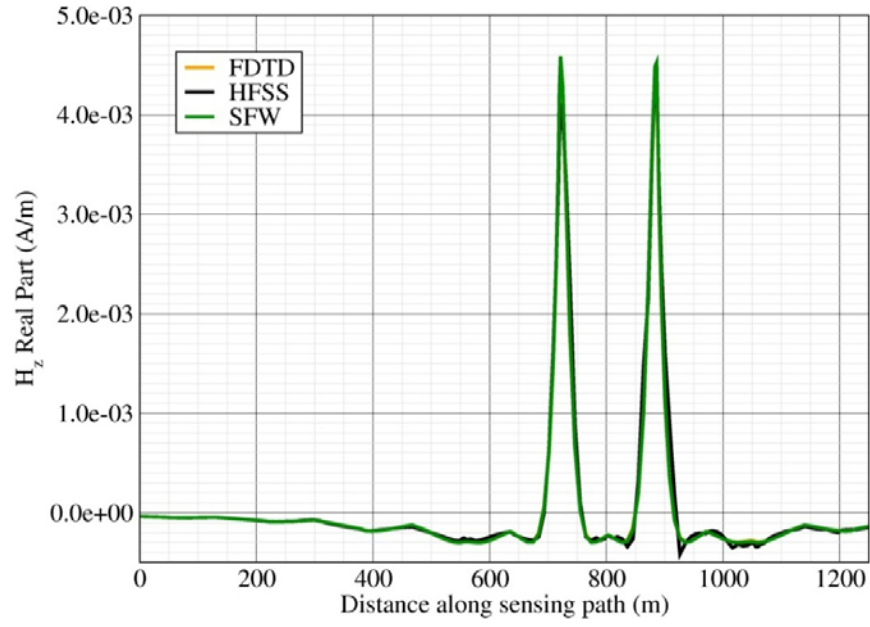


Figure 4: Real part of the z component of the magnetic field for the VMD three layer problem.

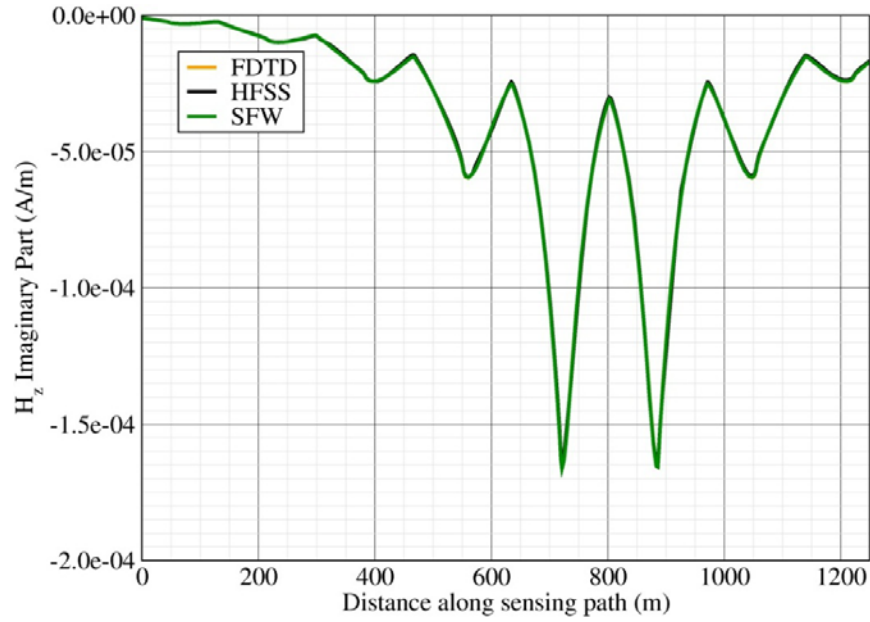


Figure 5: Imaginary part of the z component of the magnetic field for the VMD three layer problem.

Data Comparisons: Simulation vs. Experimentation

The plots on the following pages show selected comparisons between data as obtained from experimentation and simulation. Experimental run numbers are shown in the figure captions. The cases shown are typical of the better results.

Data Comparisons: Phase Two Test near “TMH Range” (Run 1003)

Phase Two experiments possess a simple geometry that is well-approximated by planar media, so it is expected that the simulations can produce good results. The full report on run 1003 is in Appendix B, page B178. The source boat passes by the EMA on a path shown in Figure 6. Figures 7-13 show the electric and magnetic field components excited by a 10 Hz vertical magnetic dipole on the bow of a small boat. The electric field z -component is at the noise floor and is not shown. In this experiment the Lake is deep, with a relatively flat bottom, so the problem is very much like the three-layer canonical problem. In general, the agreement between experiment and simulation is very good for the Phase Two tests, particularly for the 10 and 100 Hz cases. Discrepancies between data sets are more prevalent for the 1 kHz case. We attribute some of these discrepancies to the complicated rigging of the Electromagnetic Sensor Array (EMA) from the Target Model Hauldown (TMH). This complexity adds ambiguity to the position and orientation of the EMA. Even small position (few meter) and orientation (10 degrees) ambiguities can significantly alter the details of the calculated and observed fields.

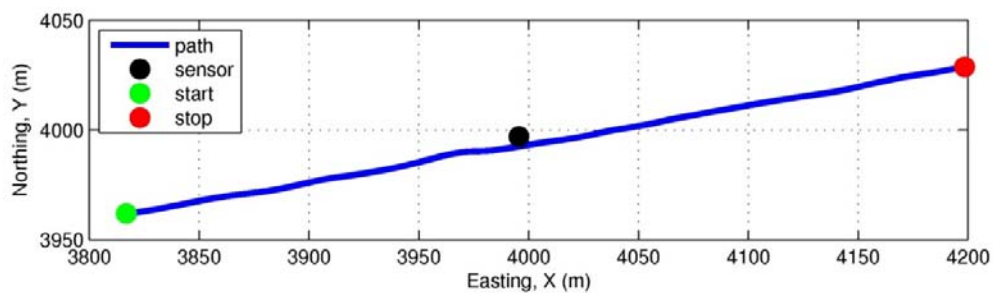


Figure 6: Path of the source boat as it passes by the EMA for run 1003. The coordinate system origin is at the south-west corner of the map used for simulation. In this coordinate system the TMH coordinate is near 4000,4000.

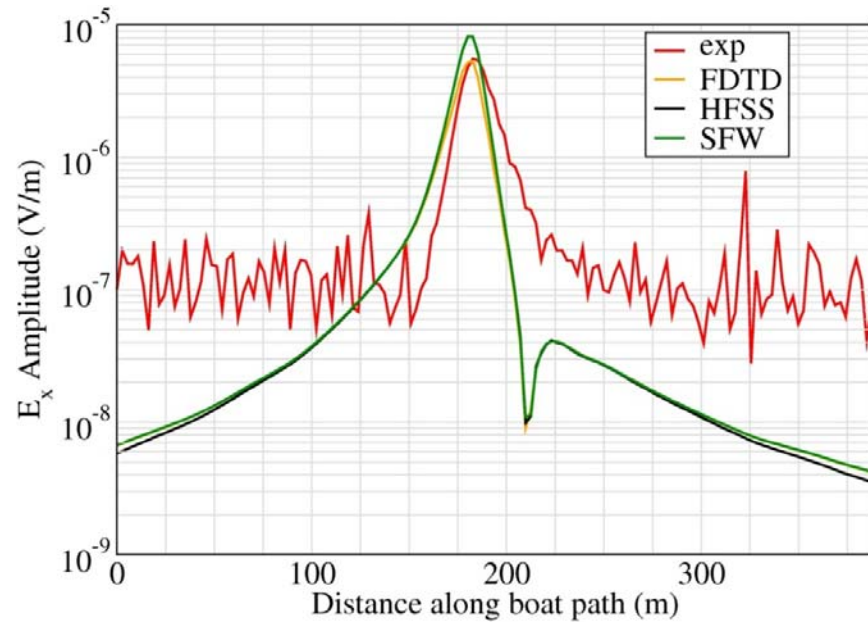


Figure 7: x component of the electric field for VMD source in experimental run 1003 conducted on December 6, 2008. The EMA is about 8.2 meters deep.

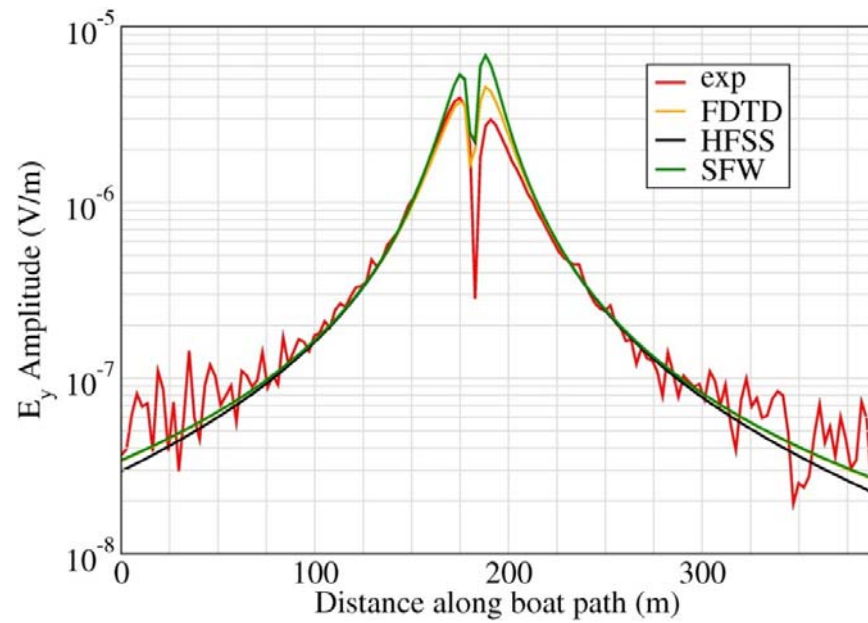


Figure 8: Magnitude of the y component of the electric field for run 1003.

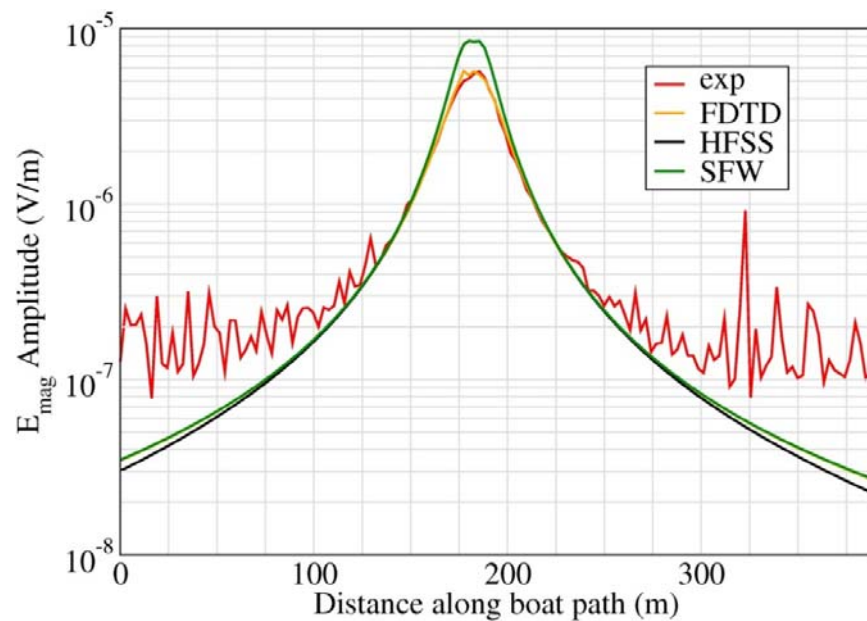


Figure 9: Magnitude of the electric field for run 1003.

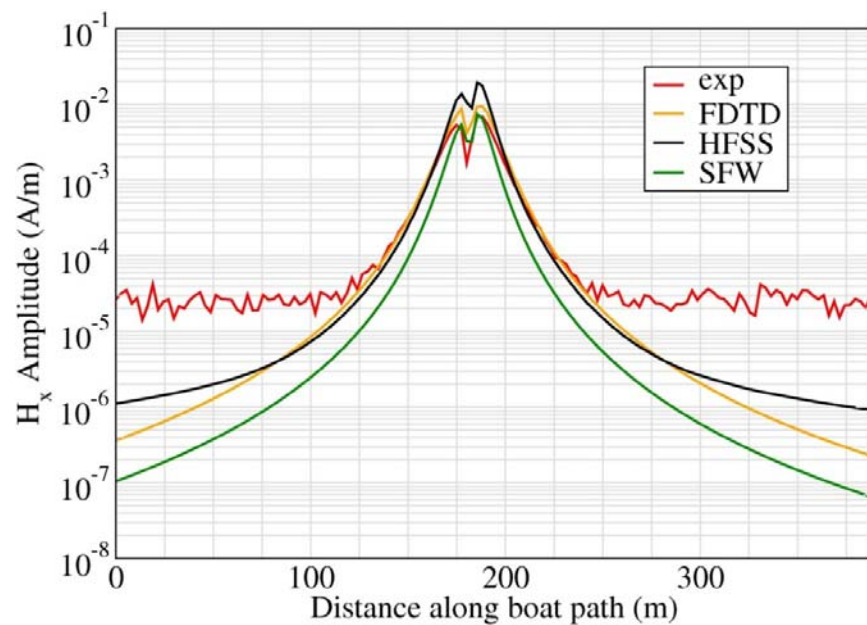


Figure 10: x component of the magnetic field for run 1003.

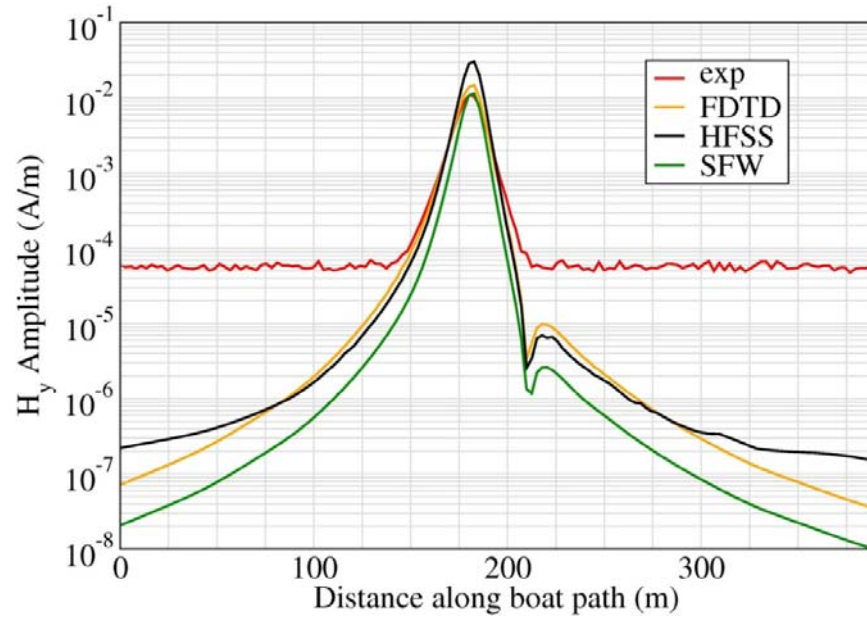


Figure 11: y component of the magnetic field for run 1003.

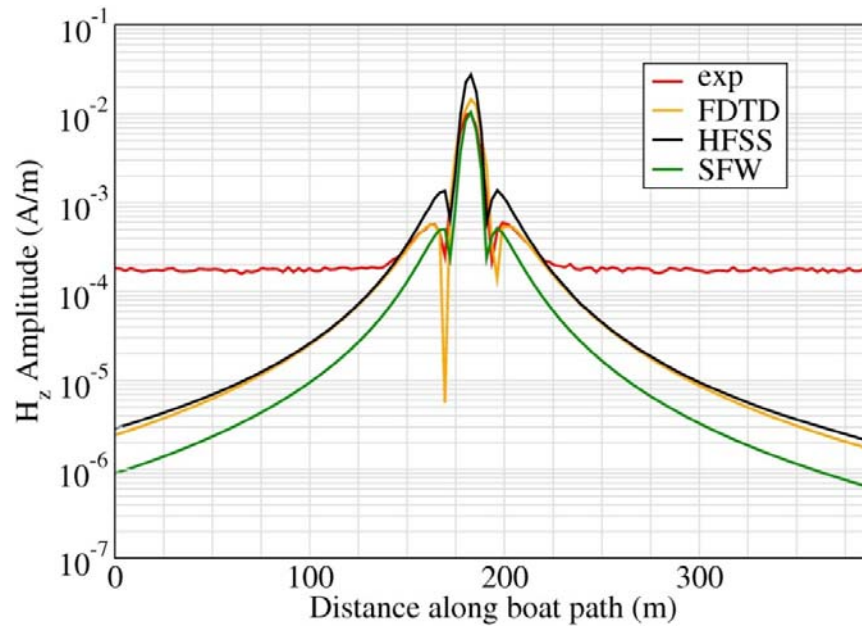


Figure 12: z component of the magnetic field for run 1003. Note small shift in the null positions between experiment and simulations.

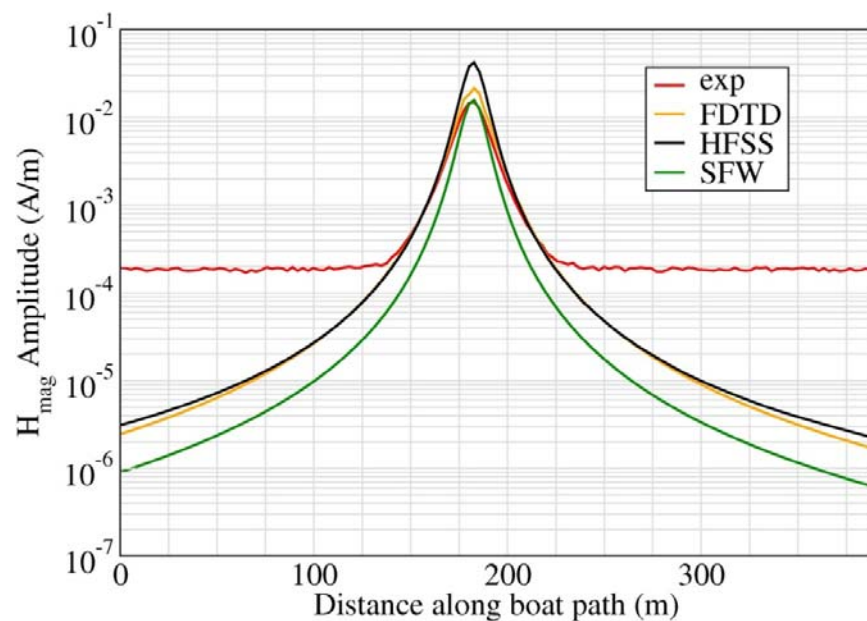


Figure 13: Magnitude of the magnetic field for run 1003.

Data Comparisons: Phase Three Test near Idlewilde Bay (Run 304.02)

An example of a Phase Three experiment using a 100 Hz Horizontal Electric Dipole (HED) is now discussed. The full report for run 304.02 is presented in Appendix B, page B274. The Portable Electromagnetic Array (PEMA) sensor is near the shoreline.

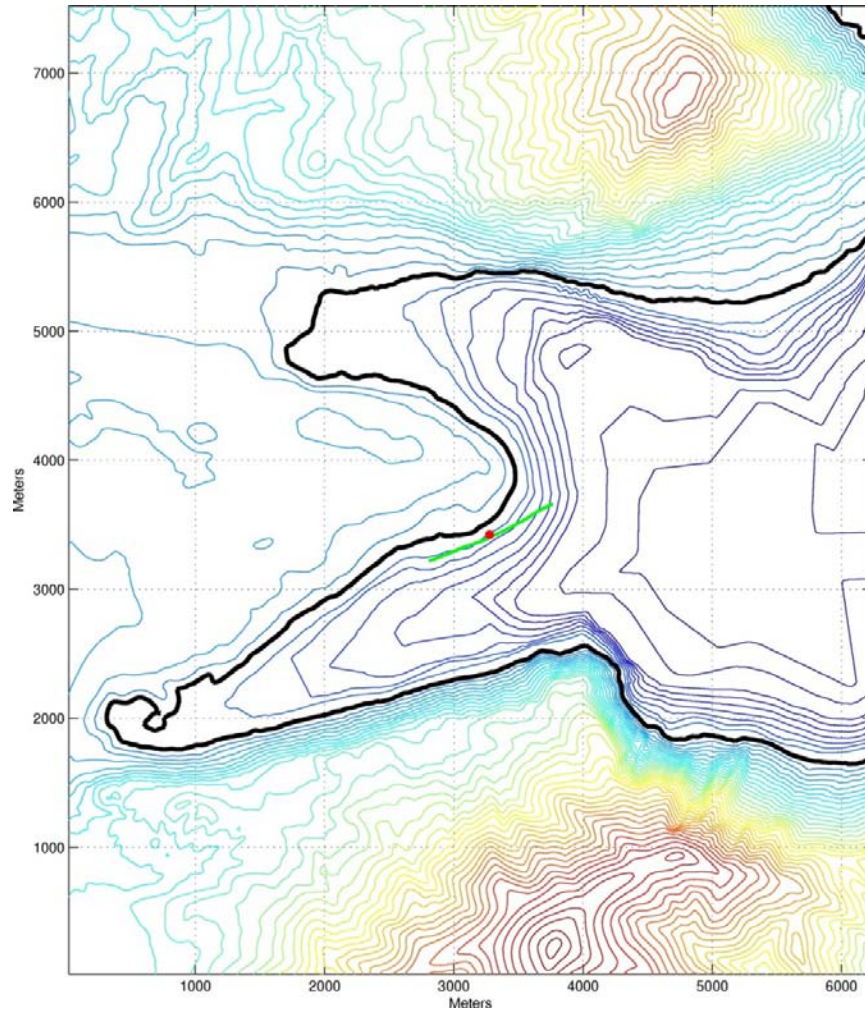


Figure 14: Path of the boat past the PEMA sensor array. The coordinate system origin is the map origin used as the simulation space. The boat starts at the upper right end of the green path and moves by the PEMA (red dot). Contour interval is 25 meters. Topographic data is a 20 meter spacing height-field, similar to that used in FDTD simulations.

Figures 15-22 show the electric and magnetic field components excited by a 100 Hz electric dipole formed with copper plates on the hull of a small boat. Data is shown as a function of distance along the path of the boat, which is shown in Figure 14. The source depth is about 0.6 meters. The depth of the PEMA is about 14.9 meters. This data is for run 304.02 conducted on September 14, 2010.

The electric fields, shown in Figures 15-18 are about right, except for the z component which is excessively large. The x and y components dominate the field, so the simulation magnitude in Figure 18 is close to experiment in amplitude and shape.

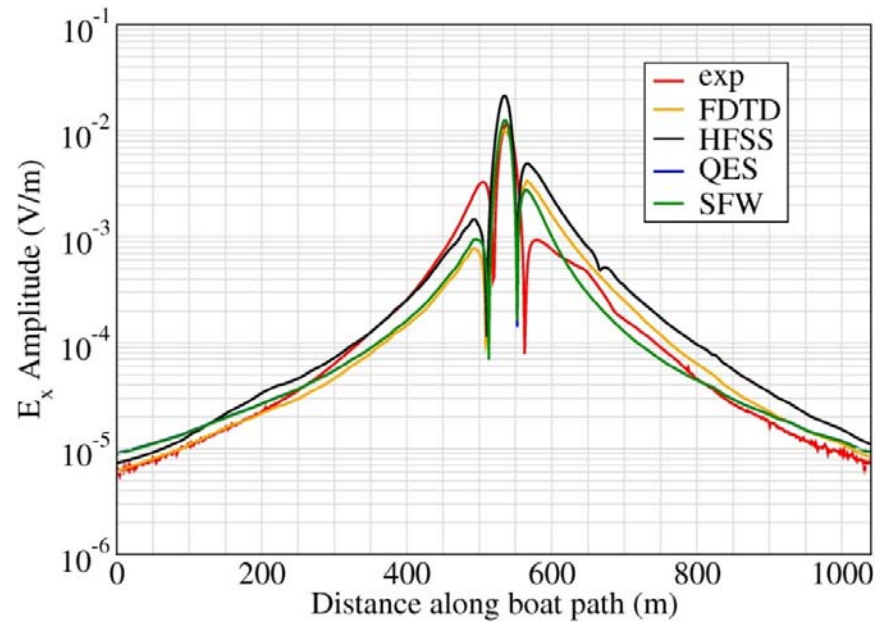


Figure 15: x component of the electric field for run 304.02. Note null position shifts between experiment and simulations.

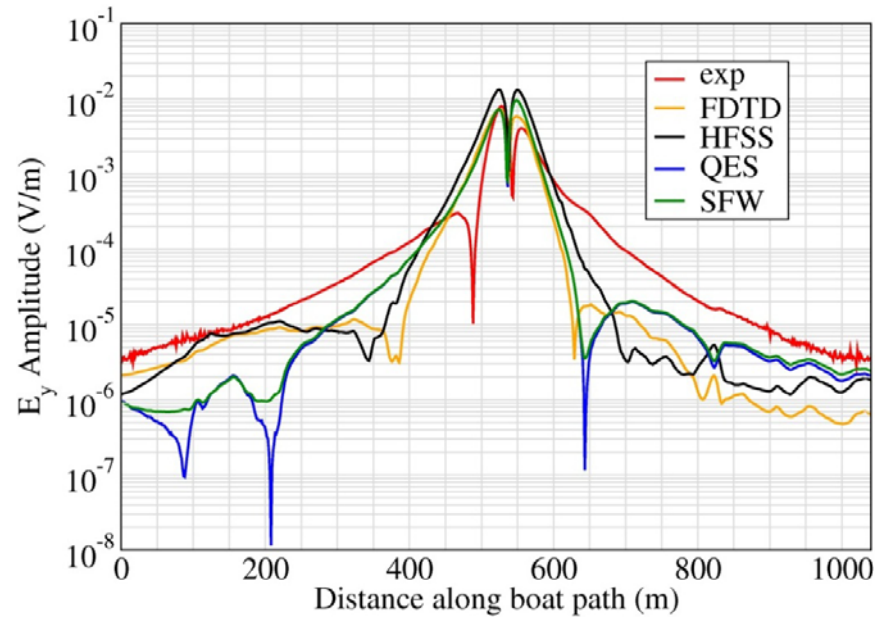


Figure 16: y component of the electric field for run 304.02.

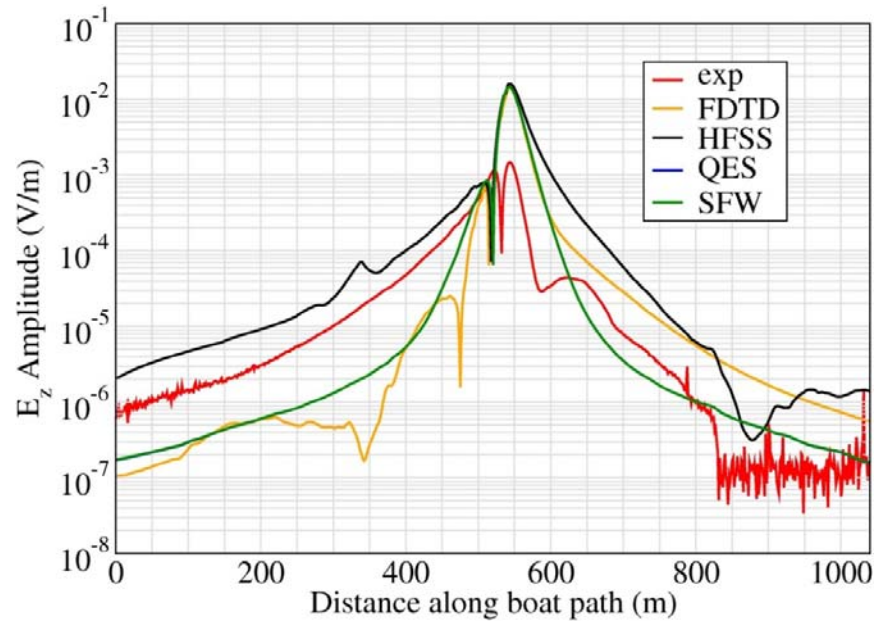


Figure 17: z component of the electric field for run 304.02. Simulations significantly exceed the amplitude of the experimental result for this component.

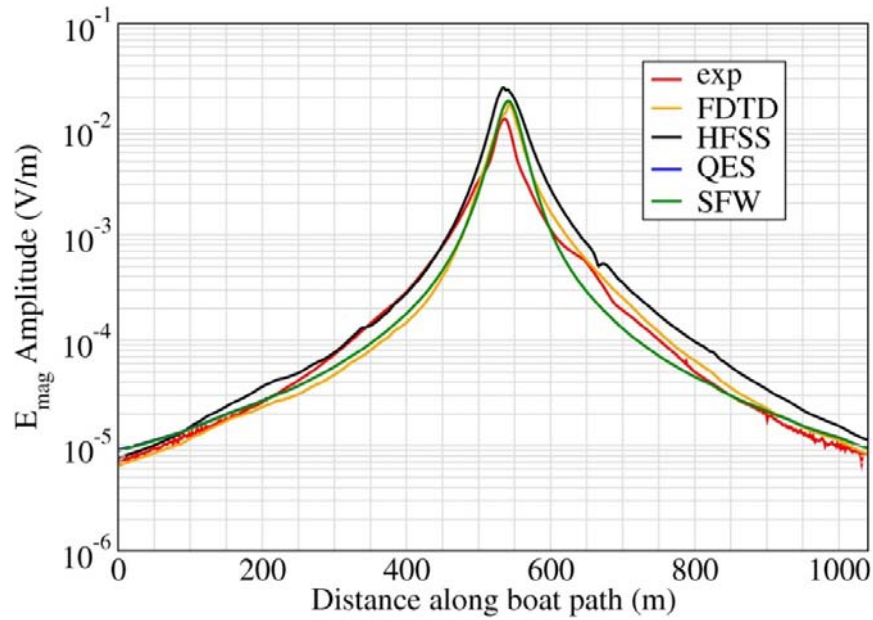


Figure 18: Electric field magnitude for run 304.02.

The magnetic fields are shown in Figures 19-22. The magnetic fields are not predicted as well as the electric fields, although the magnitude is about right. The

material parameters of the shore and lake bottom are important parameters of the calculations and are not well known.

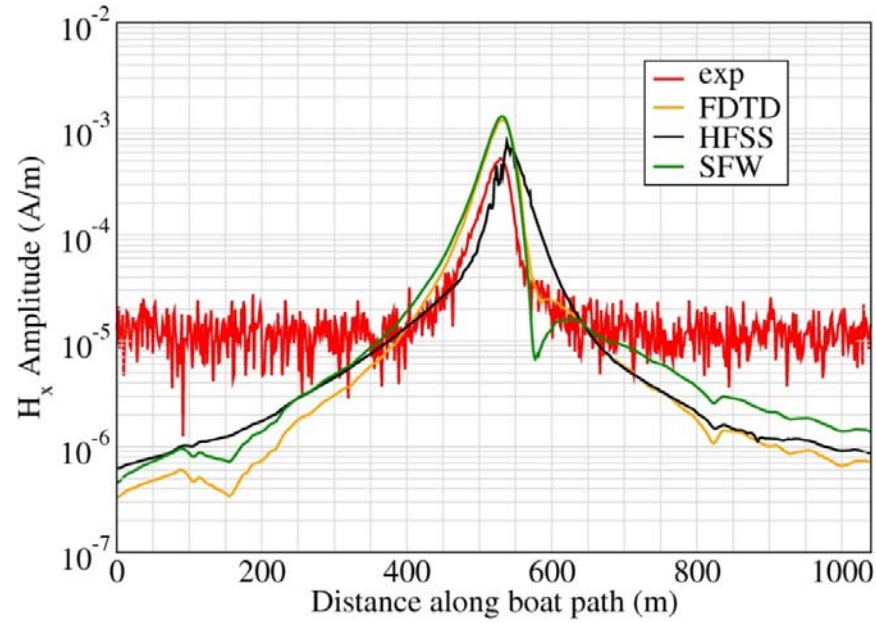


Figure 19: x component of the magnetic field for run 304.02.

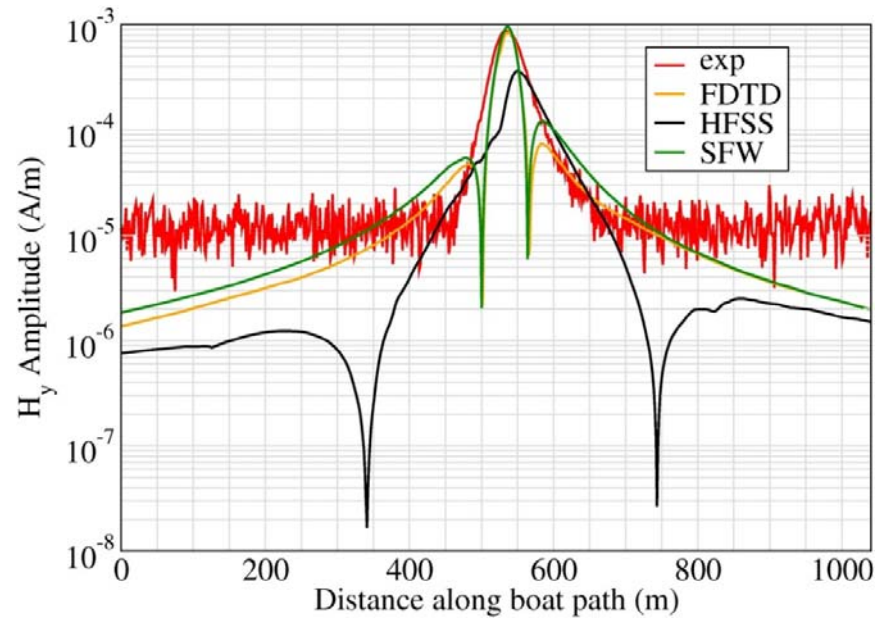


Figure 20: y component of the magnetic field for run 304.02. FDTD and SFW predict the peak value of the experimental data, but not the overall shape.

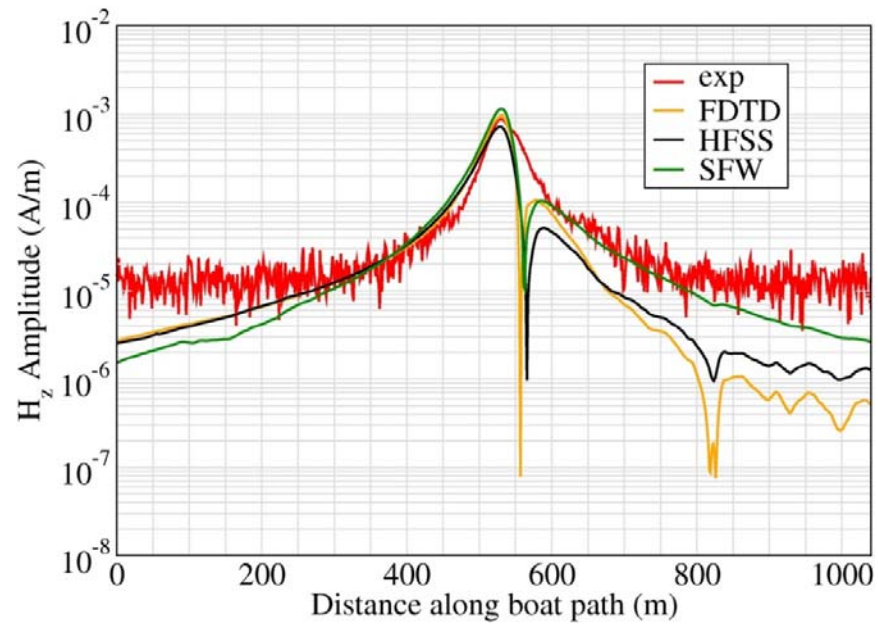


Figure 21: z component of the magnetic field for run 304.02.

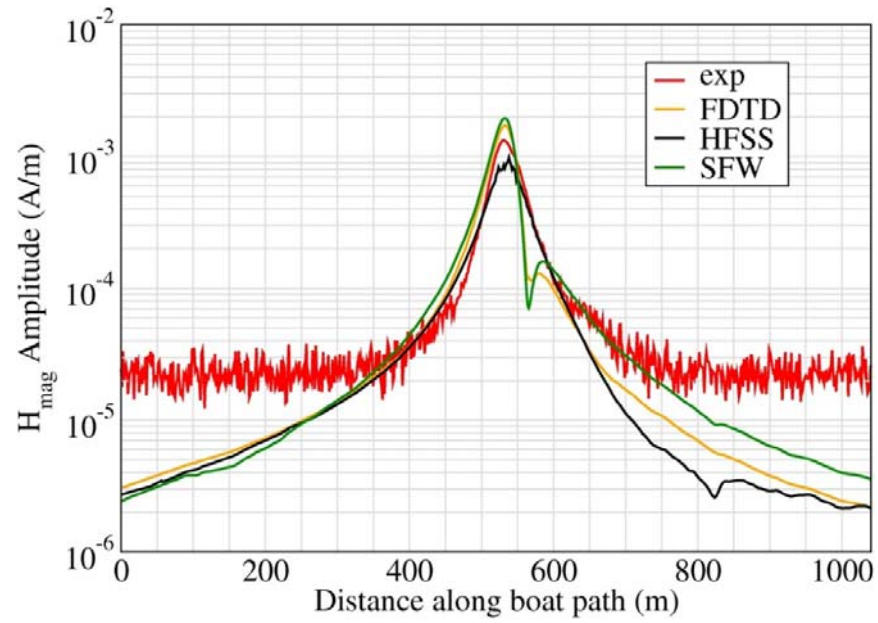


Figure 22: Magnitude of the electric field for run 304.02.

Data Comparisons: Overall Trends in Simulation Performance

It is simpler to judge the data quality associated with horizontal moving sources (i.e. sources on a boat, whether that source is HED or VMD) verses data associated with sources that move up and down along some vertical column. The larger datasets of the former allow direct observation of trends and overall plot shapes. Vertical column observation experiments have few data points (less than 10), and so observation of trends and overall data shapes are more difficult to ascertain. Some of the boat run experiments have field components that have the same shape as simulation, but with small shifts in position. For example, see E_x in Figure 15, which shows the nulls shifted a few meters between the simulations and experiment. This shift, however, is not observable for vertical column data experiments due to the dearth of experimental data. Through detailed studies we determined that the position of the minima is very sensitive to the exact geometry of the source and sensors. Small changes in the positions and orientations of the source and sensor can significantly shift the minima. While recorded GPS coordinates are very accurate, there are uncertainties in translating the GPS antenna positions to the exact locations of the source and sensor.

For unknown reasons the simulations produced poorer data agreement with experiment at 1 kHz compared to 10 Hz. The diffusive nature of EM fields in water was expected to cause calculation problems for the FDTD method, but even the FDTD method had better correlation to experiment at 10 Hz compared to 1 kHz. The magnitude of the electric field tends to be well predicted by all the methods at all frequencies. The z component of the electric field was the most problematic electric component at all frequencies. Vertical column experiments typically had poor results for the magnetic field with electric sources, and poor results for the electric fields with magnetic sources. For moving sources (on a small boat), lower frequency signals tended to produce better correlation. Electric source experiments had more difficulty with predicting magnetic fields, and vice versa. The Phase Two experiments in open deep water had better correlation with predictions than the Phase Three experiments in shallow water near shore. Unknown land and bottom material parameters are thought to be a major problem in this latter case. If the constitutive composition of the shore is not known precisely in the vicinity of the shore, then there is no expectation that the model will predict the experimental outcome. That is, the simulations cannot produce reliable data when unreliable information about the problem space is used.

Appendix A: Test Reports

To validate the ELF simulation codes against real-world scenarios, one experiment was conducted during Phase Two and two experiments were conducted during Phase Three, both by the Acoustic Research Detachment. These reports are attached. A preliminary experiment called the Cal-Source Experiment was conducted during Phase One in March 2008. The data from that experiment were not used as validation data since the purpose of that experiment was to work through the logistics of doing ELF-type experiments. That is, one could call the Cal Source Experiment a “dry-run” prototype experiment.

Attached Reports:

- Steve Frommer, Frank Jurenka and Vikie Pfeifer, “ELF Phase II Test Report,” July 30, 2009.
- Frank Jurenka, Chris Burgy and Vickie Pfeifer, “ELF Phase III Test 1 (March 5 – 11, 2010) Test Record,” July 15, 2010.
- Frank Jurenka, Don Pugsley, Stephanie Ferrone and Vickie Pfeifer, “ELF Phase III Test 2 (September 11 – 17, 2010) Test Record,” December 8, 2010.



ELF PHASE II Test Report

**Steve Frommer, NSWCCD 7510
Frank Jurenka, NSWCCD 7260
Vickie Pfeifer, NTI**

July 30, 2009

TABLE OF CONTENTS

1. PROJECT TEST ABSTRACT.....	4
1.1. OVERVIEW	4
1.2. OBJECTIVES	4
2. TEST RISK ANALYSIS	4
3. TEST ORGANIZATION MATRIX.....	5
4. TEST SCENARIO.....	5
4.1. TEST SITE	5
4.2. COORDINATE SYSTEM.....	7
4.3. LAKE ENVIRONMENTAL PARAMETERS	8
4.4. GPS SYSTEM	8
4.5. TRANSMITTERS.....	10
4.5.1. Calibrated Magnetic Source.....	10
4.5.2. Calibrated Electric Source.....	12
4.5.3. Electric Transmitter	12
4.5.4. Electric Transmitter Drive and Control	13
4.6. RUN PLAN	14
4.6.1. Noise Measurements	15
4.6.2. Calibrated Source Runs	15
4.6.3. ELF Runs	16
4.6.4. Additional Measurements.....	16
5. EM SENSORS AND ARRAY	17
5.1. EM RECEIVER ARRAY	17
5.1.1. Magnetometers	18
5.1.2. Electric Field Sensors	19
6. DATA ACQUISITION AND PROCESSING	21
7. DATA REPORTING REQUIREMENTS	22
8. TEST SITE OPERATIONS	22
8.1. OPERATIONS TEAM AND POC	22
APPENDIX 1. TEST RUN RECORD	24
NOISE RUNS	24
MAGNETIC SOURCE CALIBRATION VERIFICATION RUNS	26
ELECTRIC SOURCE CALIBRATION VERIFICATION RUNS.....	27
ELECTRIC SOURCE RUNS – 4 M.....	28
ELECTRIC SOURCE RUNS – 40 M TOWED, SOUTH.....	29
ELECTRIC SOURCE RUNS – 40 M TOWED, WEST	30
ELECTRIC SOURCE RUNS – 40 M TOWED, EAST	31
ELECTRIC SOURCE RUNS – 40 M TOWED, MISCELLANEOUS.....	31
ELECTRIC SOURCE RUNS – 40 M TOWED, ARRAY AT BOTTOM.....	32
ISMS BACKGROUND NOISE RUNS	33

TABLE OF FIGURES

Figure 1. Lake Pend Oreille.....	6
Figure 2. EM Array and Outpost Pier.....	6
Figure 3. Coordinate System	7
Figure 4. GPS Base Station and Rover Set-Up	9
Figure 5. Calibrated Magnetic Source	10
Figure 6. Calibrated Source Boat.....	11
Figure 7. Magnetic Source Drive and Control	11
Figure 8. Calibrated Electric Source Electrode	12
Figure 9. Electric Transmitter	13
Figure 10. Electric Transmitter Drive and Control.....	14
Figure 11. Receiving Sensor Array	18
Figure 12. EM Receiving Array Layout.....	19
Figure 13. Receiving Array Magnetometer (Billingsley TFM-100G4SS).....	19
Figure 14. EM array potential cell pair	20
Figure 15. Receiving Array Ag/Ag/Cl Potential Cell.....	21
Figure 16. ROC GPS/EMA Configuration	22

1. PROJECT TEST ABSTRACT

1.1. OVERVIEW

Efforts to understand, measure, and model the propagation of underwater Extremely Low Frequency (ELF) signals is important in the evaluation of Navy vessels' susceptibility to detection systems and mines. This is especially significant in light of the Navy's desire to build an all electric ship.

1.2. OBJECTIVES

The objectives of the testing were to:

- Research analytical theories to better understand the propagation, scattering, refraction, and reflection of ELF fields.
- Develop an experimental test-bed for the complete characterization and prediction of ELF signals in shallow and deep water environments.
- Develop numerical simulation tools for predicting EM propagation in environments with variable conductiveness and geometrical features.

ELF testing was successfully conducted at the Acoustic Research Detachment (ARD) of the Naval Surface Warfare Center Carderock Division (NSWCCD), located on Lake Pend Oreille in Bayview, Idaho from December 6 to December 12, 2008. This test was conducted during Phase II of a 3-year project that is a collaborative effort between University of Idaho (UI), NSWCCD, and the ARD.

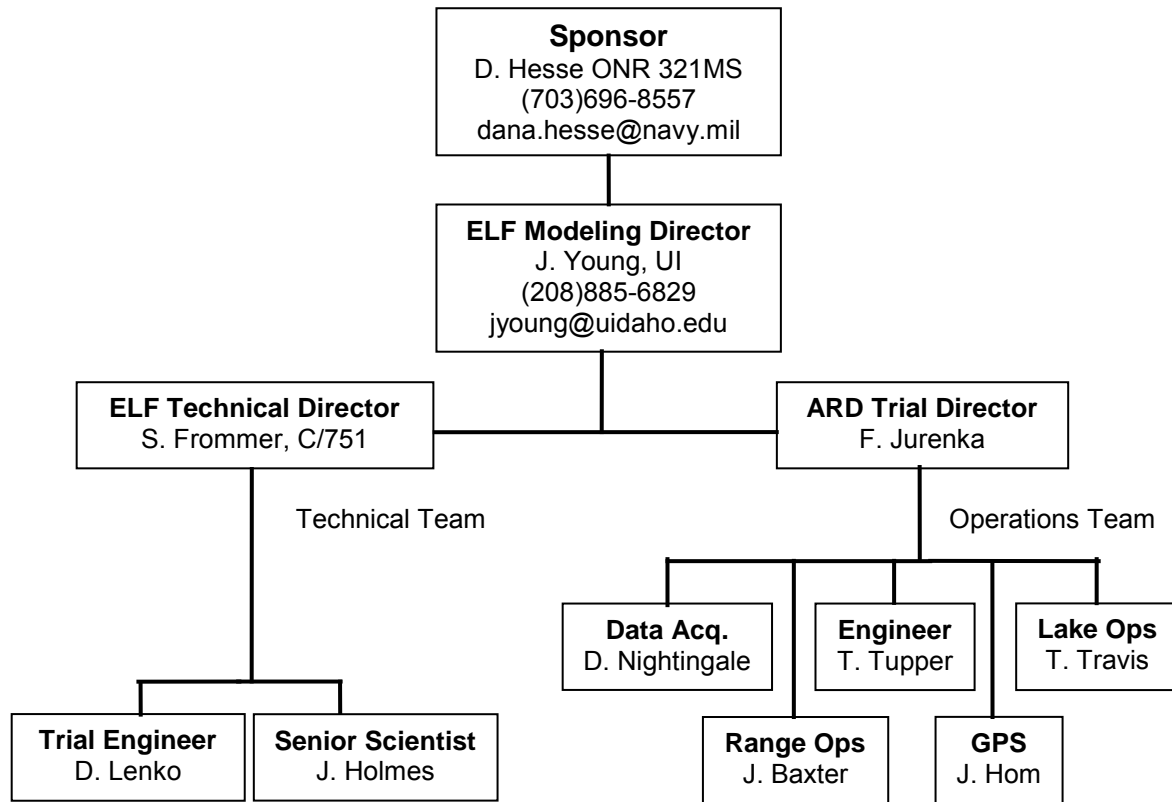
2. TEST RISK ANALYSIS

The following risk was addressed:

- Weather
 - Winds can have a detrimental effect on the test outcomes
 - December is typically a windy month
 - Contingency time was built into the schedule to accommodate weather-related delays.

Testing was accomplished over 5 days. Some minor weather-related delays occurred.

3. TEST ORGANIZATION MATRIX



4. TEST SCENARIO

4.1. TEST SITE

The test was conducted at the ARD, located on Lake Pend Oreille in Bayview, Idaho from December 6 to December 12, 2008. The facility is uniquely capable of conducting the ELF propagation tests due to its uniform and stable water conductivity throughout the water column.

The ELF tests were performed at the Intermediate Scale Measurement System (ISMS) site as shown in Figure 1. The test range and array orientation are shown in Figure 2.

ELF Phase II Test Report

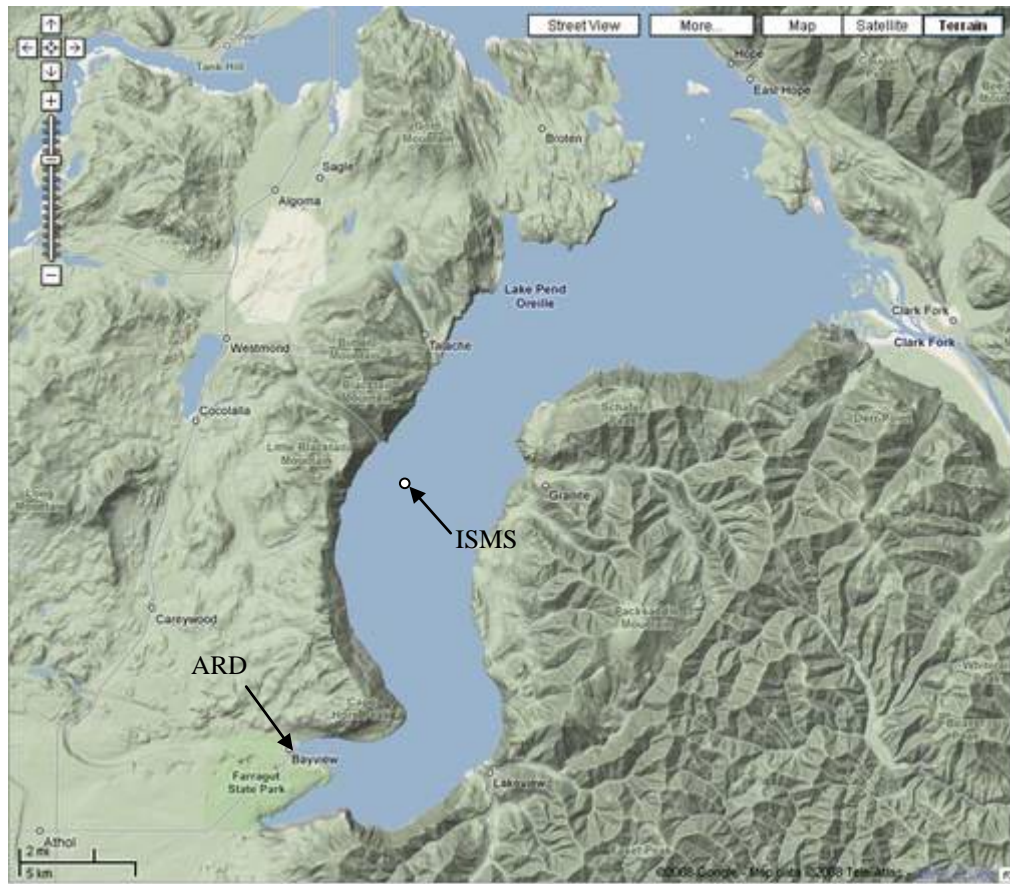


Figure 1. Lake Pend Oreille

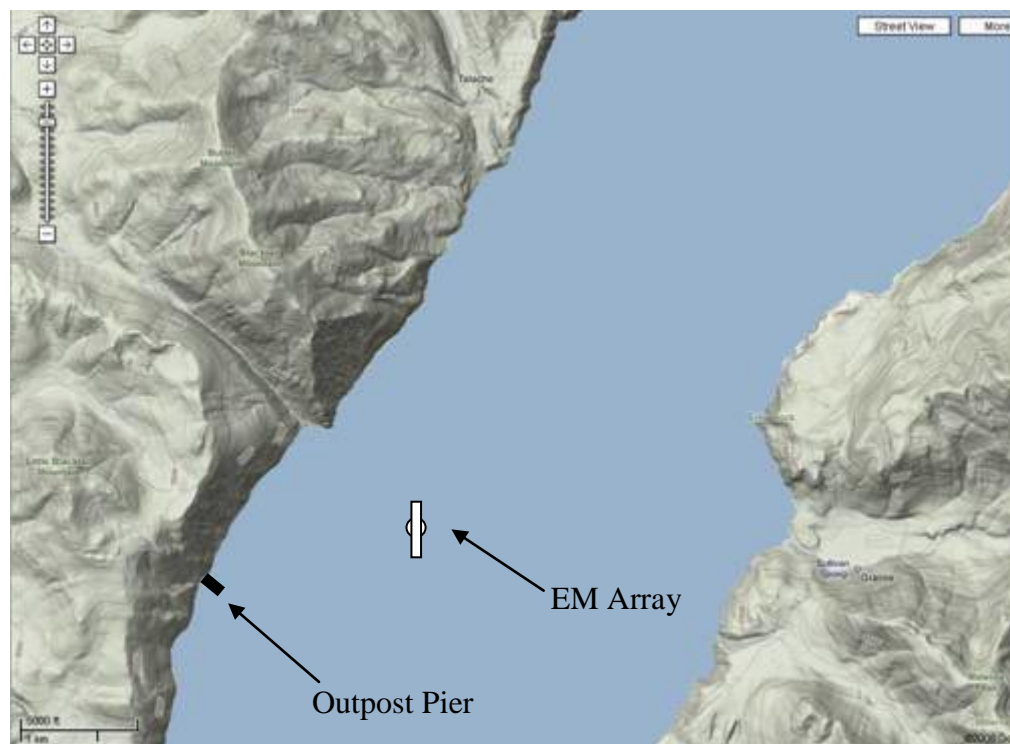


Figure 2. EM Array and Outpost Pier

4.2. COORDINATE SYSTEM

The origin of the rectilinear coordinate system that was used for this experiment and the data analysis was horizontally located at the Target Model Hauldown (TMH) and vertically located 2048 ft above mean sea level. The positive x axis was directed east (wrt to true north); the positive y axis was directed true north; and the positive z axis was directed up. A sketch of the coordinate system is shown in Figure 3. The TMH has the following coordinates:

Latitude: N 48° 05' 17.8493'' 48.0882914722°
 Longitude: W 116° 29' 03.6498'' -116.484347167°

Northing: 713844.61 m (wrt State Plane Idaho West)
 Easting: 745296.46 m (wrt State Plane Idaho West)

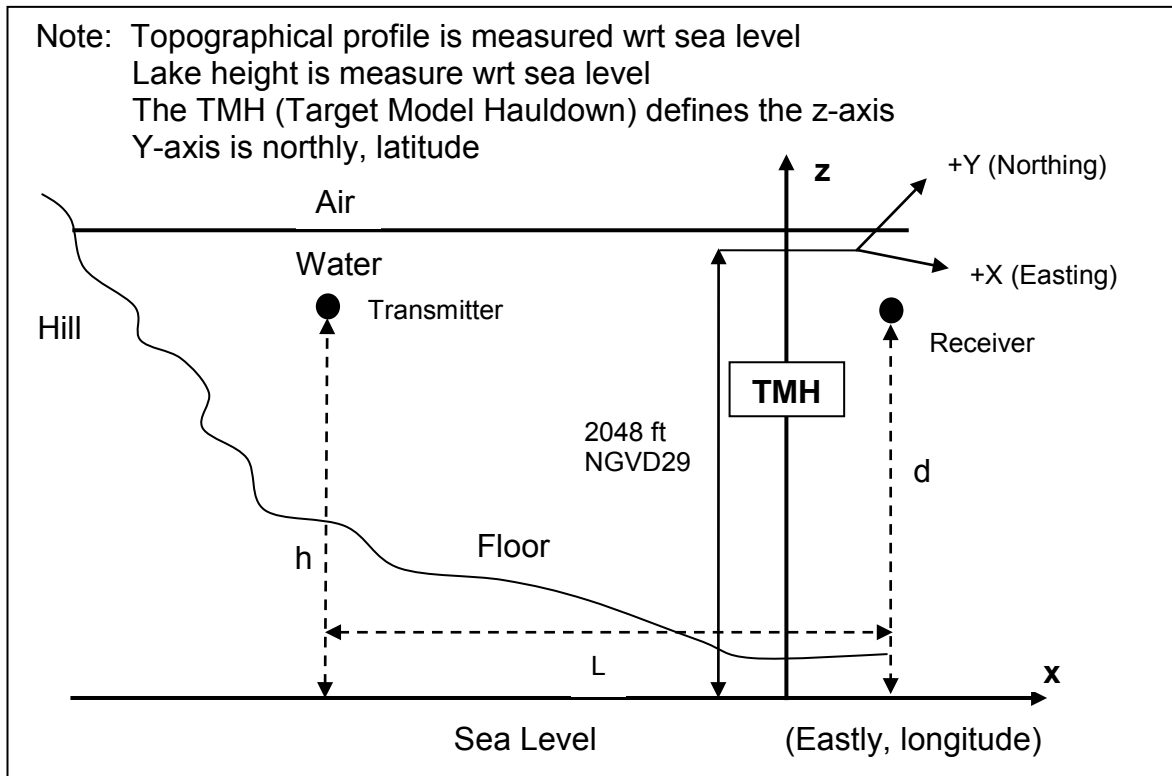


Figure 3. Coordinate System

4.3. LAKE ENVIRONMENTAL PARAMETERS

The lake was formed by glaciers cutting through the mountains resulting in steep sides forming a 'V' made of bedrock. Over time the bottom of the 'V' filled with silt resulting in a present day flat bottom of approximately 1100 ft. depth.

The conductivity of the lake water is a consistent 0.018 S/m throughout the water column. A sample of lake bottom muck from an anchor resulted in a measured conductivity of 0.012 S/m. The conductivity of the bedrock is unknown. The depth of the silt is estimated to be hundreds of feet.

4.4. GPS SYSTEM

The differential GPS system consisted of a base station antenna located on the outpost pier (N 48.08100726 deg, W 116.52802104 deg) and radio links to send corrections to the two GPS rover antennas. Figure 4 shows the GPS base station and rover set-up. During the electric source tests the GPS rover antennas were mounted to the calibrated source boat as described later in the report and shown in Figure 6.

ELF Phase II Test Report

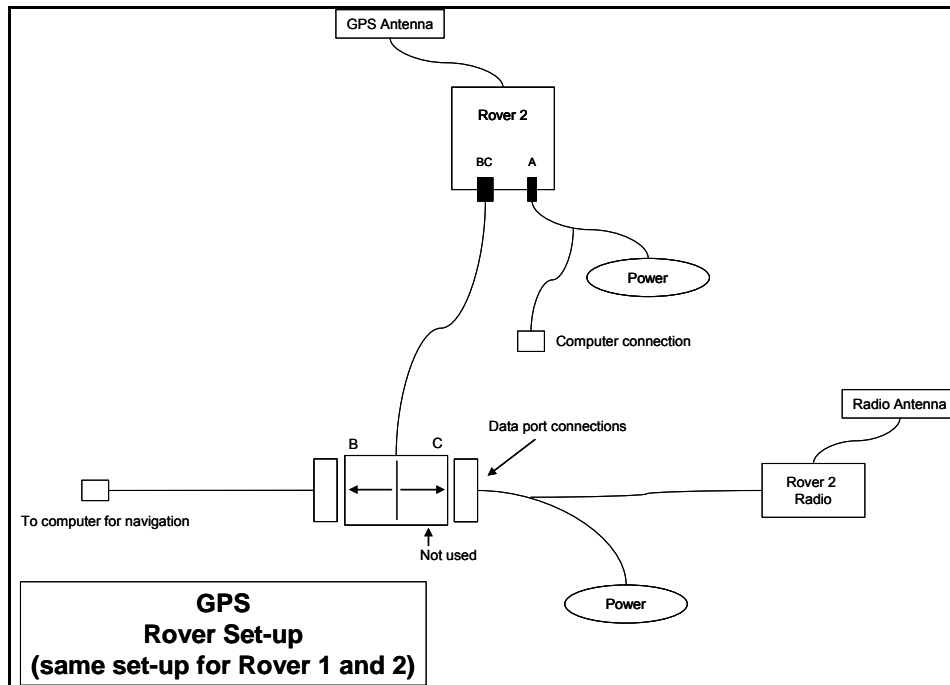
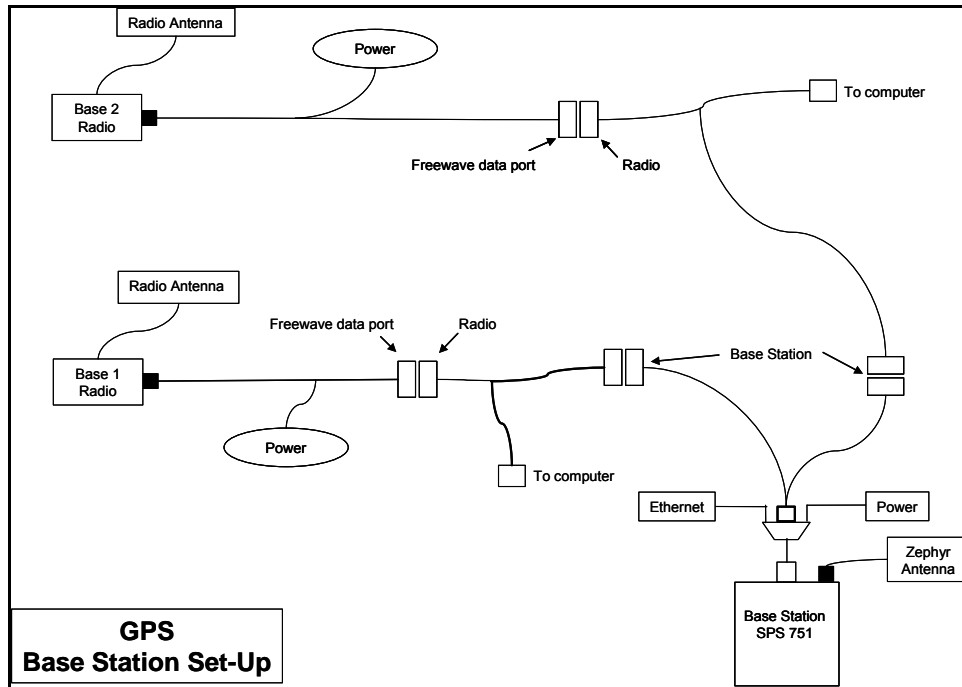


Figure 4. GPS Base Station and Rover Set-Up

4.5. TRANSMITTERS

After installation of the EM array and prior to execution of the ELF runs, a series of calibrated source runs were executed. The calibrated source runs verified that the entire process (source levels, sensors, data acquisition, GPS, etc) was operating as expected. Calibrated source runs were executed with a magnetic source and an electric source as described below. The ELF propagation runs included the use of electric transmitters as described below.

4.5.1. Calibrated Magnetic Source

The calibrated magnetic source consists of a horizontal coil approximately 43" in diameter with 10 turns and a maximum current of 20 amps. The maximum vertical moment that can be produced is 190 A-m^2 . The coil is mounted to the front deck of a 24' fiberglass boat as shown in Figure 5. The location of the source relative to the GPS antennae is shown in Figure 6.



Figure 5. Calibrated Magnetic Source

ELF Phase II Test Report

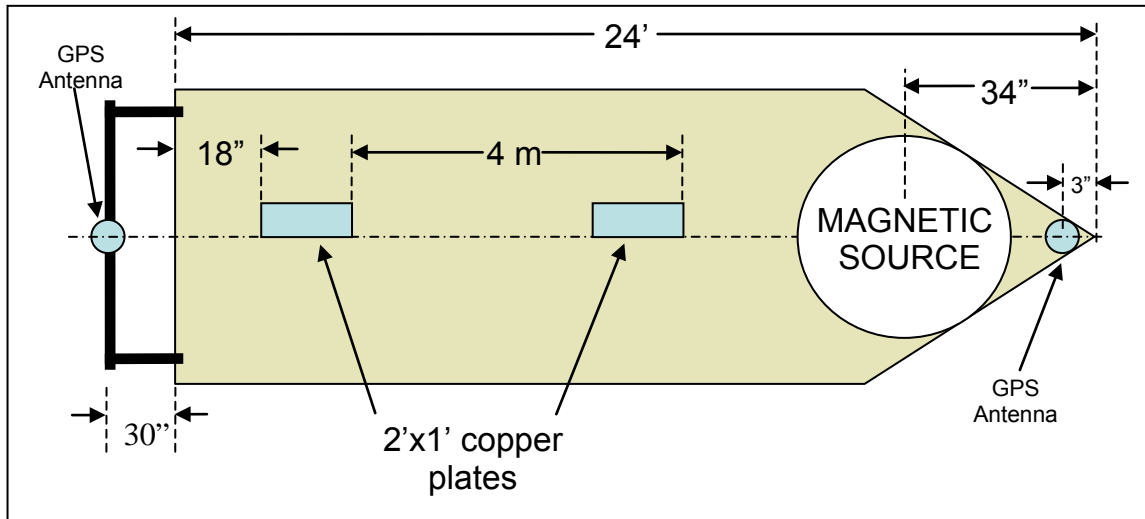


Figure 6. Calibrated Source Boat

The magnetic source was driven by a BOP 20/20M linear amplifier controlled by a function generator as shown in Figure 7. Shunt values were monitored and recorded by onboard personnel to ensure that the desired current was being driven to the source. Measurements of the driven current were GPS time-stamped for correlation to the measured fields at the receiver array.

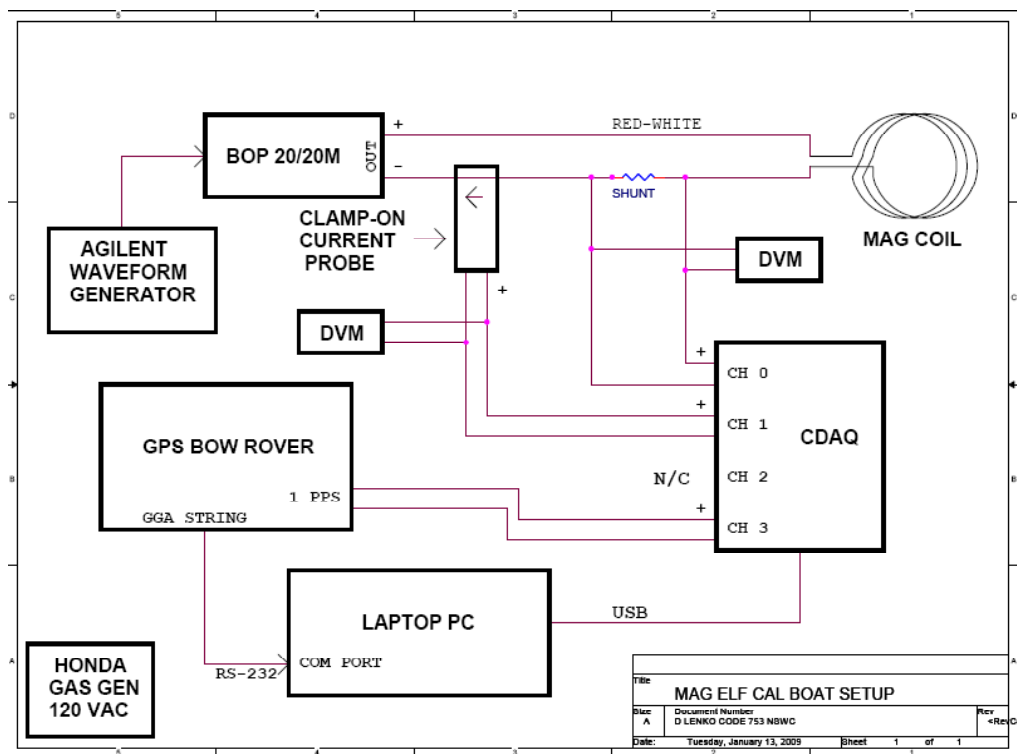


Figure 7. Magnetic Source Drive and Control

4.5.2. Calibrated Electric Source

The calibrated electric source consists of two 2 ft by 1 ft copper electrodes separated by 4 m on-center, mounted to the bottom of a fiberglass boat. A photo of a single electrode is shown in Figure 8. The locations of the electrodes relative to the GPS antennae are as shown in Figure 6.



Figure 8. Calibrated Electric Source Electrode

4.5.3. Electric Transmitter

The electric transmitter consisted of a pair of copper electrodes separated by specified distance driven by a Techtron LVC 5050 linear amplifier. The primary electric transmitter has a 40 A-m dipole moment created by a 40 m (the actual separation during testing was 42.6 m) electrode separation driven with 1 A. The low conductivity of the lake water made it prohibitive to drive more current, therefore it was necessary to have a long baseline transmitter with low current. The transmitter was towed behind the fiberglass calibrated source boat on a skiff and was capable of transmitting from any desired location at any horizontal orientation. The 40 m separation was maintained by a slight forward movement of the boat keeping tension on the line towing one electrode. The other electrode was mounted on the bottom of the boat. A picture of the boat and electric transmitter is shown in Figure 9.

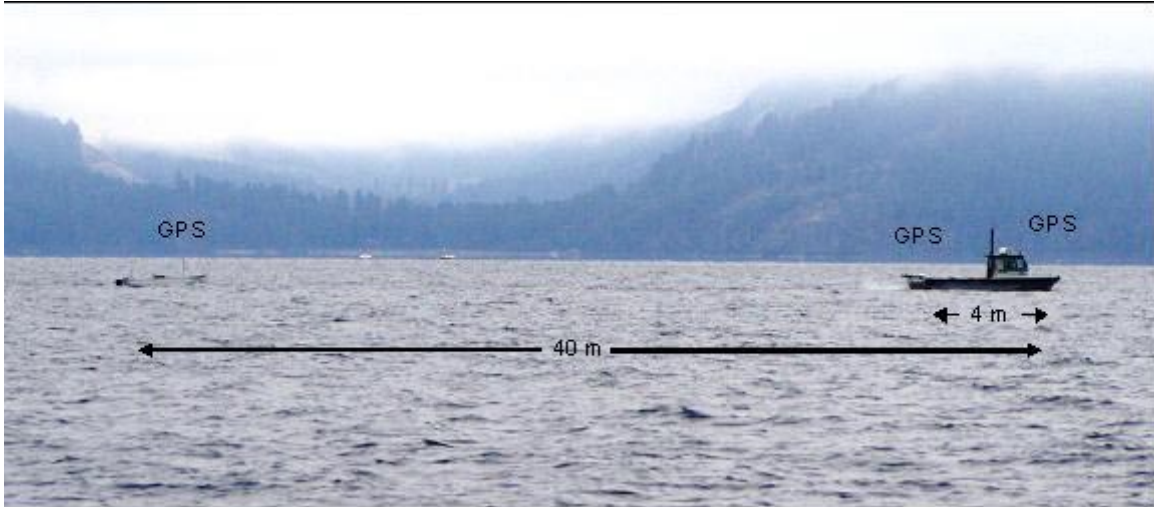


Figure 9. Electric Transmitter

The orientation of the electric dipole moment was determined from two GPS receivers. One mounted on the towing boat and one mounted on the towed skiff. It was assumed that the direction of the dipole moment was the same as the heading determined from the two GPS receivers.

A shorter baseline electric moment was used for measurements closer to the receiver. For modeling purposes it is desired to have the distance from the transmitter to receiver be at least 10 times the electrode separation. This permits the models to treat the transmitter as a point dipole, instead of modeling the detailed geometry of the transmitter. The shorter baseline (4 m) dipole was formed by using the two electrodes attached to the bottom of the boat. The orientation of the 4m electric dipole moment was determined from the two GPS receivers mounted on the boat. The 4 m dipole was also used during the system calibration process at the beginning of the experiment.

4.5.4. Electric Transmitter Drive and Control

The electric transmitters were driven by a Techron LVC 5050 linear amplifier controlled by a function generator as shown in Figure 10. Shunt values were monitored and recorded by onboard personnel to ensure that the desired current was being driven to the source. Measurements of the driven current

were GPS time-stamped for correlation to the measured fields at the receiver array.

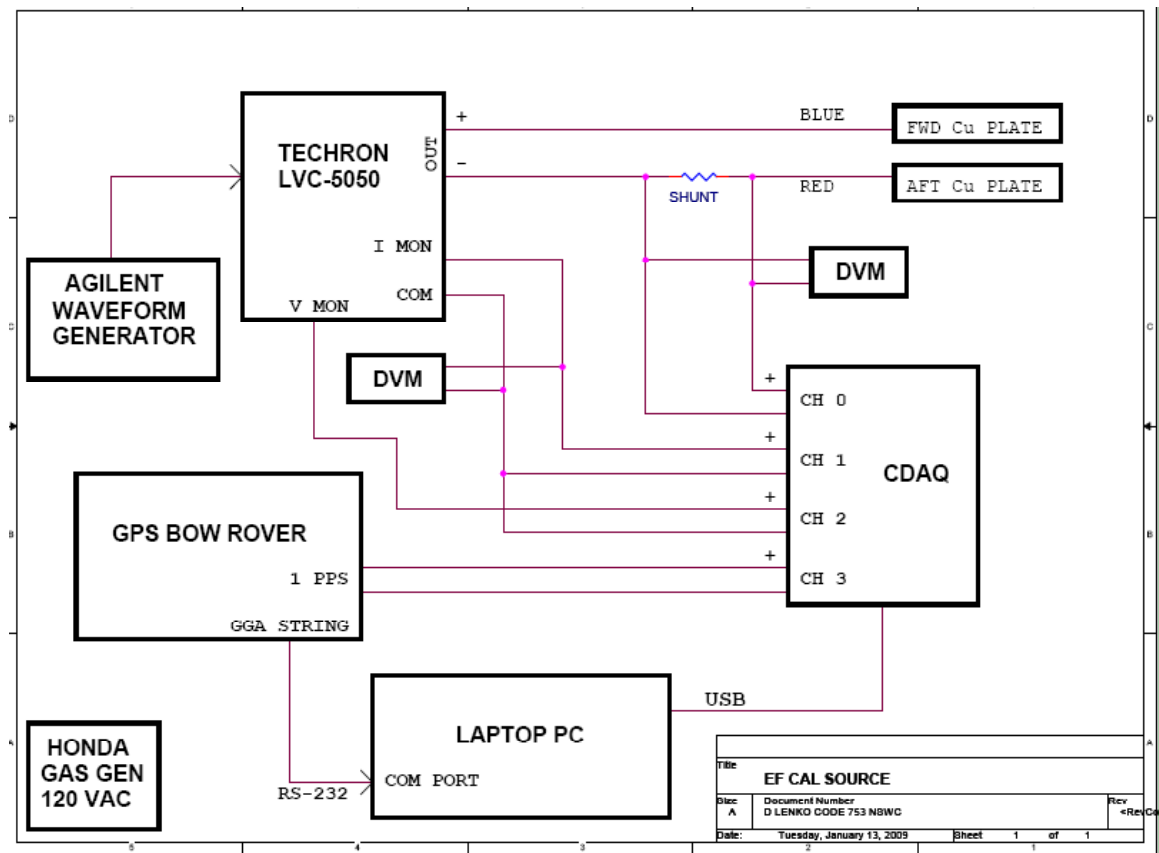


Figure 10. Electric Transmitter Drive and Control

4.6. RUN PLAN

The run plan included noise measurements, calibrated source runs to verify proper operation of the entire system, the ELF runs designed to exercise the models, and additional measurements of existing ISMS equipment. General descriptions of the various runs are given below and the actual test run record can be found in Appendix 1. The following is a summary of data taken during the test:

- **Electric (134 measurements)**
 - 4 A-m
 - Horizontal, surface
 - Frequencies: DC, 10,100,1000 Hz
 - EMA depth 27 ft, distances 0-10,000 ft

- 40 A-m
 - Horizontal, surface
 - Frequencies: 10, 100, 1000 Hz
 - EMA depth 27 ft: deep water and near shore, distances 1000-10,000 ft
 - EMA depth 968 ft: deep water, near shore, over array, distances 2000 ft and near Maiden Rock on western shore
- Vertical, surface
 - Frequencies: 1, 10, 100, 1000 Hz
 - EMA depth 968 ft: deep water, near shore, over array, distances 2000 ft and near Maiden Rock on western shore
- **Magnetic (13 measurements)**
 - 190 A-m²
 - Vertical, surface
 - Frequencies: DC, 10 Hz
 - EMA depth 27 ft, distances 0-20 ft

4.6.1. Noise Measurements

Noise measurements lasting at least 2 minutes each were collected at the beginning and end of each test day. No sources were energized during data collection and the measurements were used to quantify the environmental and system noise.

4.6.2. Calibrated Source Runs

Magnetic and electric calibrated sources were used to verify proper operation of the entire system:

1. location and orientation of the receiver array
2. scale factors of data acquisition channels
3. location and orientation of source
4. operation of transmitter equip

Runs were made near and over the array with source parameters that were expected to result in EM fields that can be predicted by analytical models that are not reliant on topography.

4.6.3. ELF Runs

The ELF runs consisted of a series of measurements to be used to exercise the numerical models developed by UI. They included measurements with the electric transmitter energized at various locations on the lake. Much of the data was collected with the EM array located 27 ft below the lake surface, but a set of data was collected with the EM array 30 m above the lake bottom (968 ft below the lake surface), the deepest that the EM array can be lowered.

4.6.3.1. Electric Source

Several series of runs were made with the array 27 ft below the lake surface. The first series of runs with the electric dipole moment directed N/S were executed at increasing distances south of the EM array. At short distances the 4 m baseline hull-mounted electrodes were used and the 40 (42.6 actual) m baseline towed electrode was used at greater distances. At each location the source was driven with approximately 1 A (except the shortest distances) over a frequency range of 10 to 1000 Hz. Data collection occurred for at least 30 seconds. A second series of runs was executed as described above except that the source moved to the west of the array toward the shoreline. The above two series were repeated with the source moment directed E/W. Additional miscellaneous runs were made as defined in Appendix 1.

Measurements were made with the EM array lowered to 30 m above the lake bottom in an effort to test the down-over-up propagation path. To reduce the vertical propagation distance through the water to the lake bottom the electric source was located near the shore for these runs. Also, a series of runs were conducted at this array depth with the electric source in a vertical configuration.

4.6.4. Additional Measurements

The following additional measurements were made to assist in providing comparisons for similar future experiments.

1. EM field levels of the NFTA while transmitting a broadband continuous waveform at maximum power output level.

2. EM field levels of the ESP when operating the main and standby generators and the ESP crane.

5. EM SENSORS AND ARRAY

5.1. EM RECEIVER ARRAY

The receiving array is made up of ten triaxial fluxgate magnetometers and 11 electric potential cells distributed in two dimensions on a 'T' shaped support structure. The EM array was suspended from the High Resolution Array (HRA) as shown in Figure 11. The HRA was suspended from the Target Model Hauldown (TMH) located at the center of the Near Field Receive Array (NFRA). The EM array was oriented North-South and mounted on the east end of the HRA (perpendicular to the HRA). After installation, the center of the EM array was measured at N 48.088273 deg, W 116.484302 deg, and an orientation heading of 350/170 degrees.

An attempt was made initially to orient the EM array in an East-West position. Array stability issues resulted from this orientation, so the array was re-positioned in the North-South orientation.

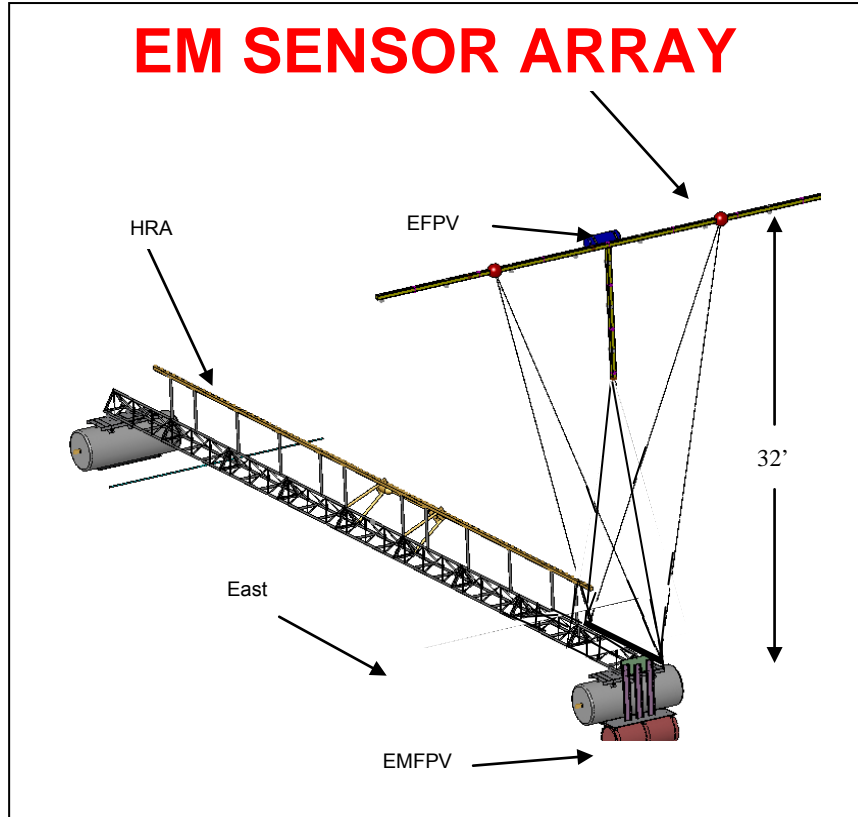


Figure 11. Receiving Sensor Array

5.1.1. Magnetometers

The layout of the EM receive array is shown in Figure 12. Each of the magnetometers measures the magnetic field in three orthogonal directions. For the long range measurements that were made during this test the ten magnetometers essentially represent redundant data. A photograph of the magnetometer is shown in Figure 13.

ELF Phase II Test Report

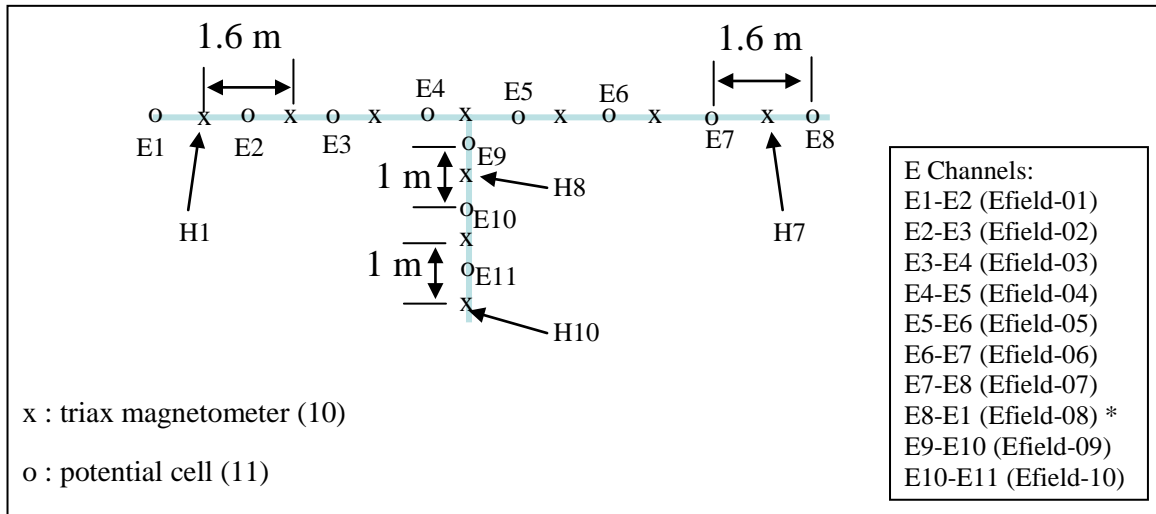


Figure 12. EM Receiving Array Layout



Figure 13. Receiving Array Magnetometer (Billingsley TFM-100G4SS)

5.1.2. Electric Field Sensors

The electric field was measured by recording the difference in electrical potential between two cells separated by a given distance in a particular direction. Each cell location consists of a pair of cells with differing electrochemistry (Figure 14). The Ag/Ag-Cl cells are used for most of the measurements, while the titanium is only used for the long baseline horizontal measurements and the center (E4-E5) horizontal measurement. An exploded

view of the Ag/Ag-Cl is shown in Figure 15. Measurements between cells E9-E10 and E10-E11 (each separated by 1 m) result in the vertical electric field (z direction). Potential differences between each neighboring pair of cells (each separated by 1.6 m) result in seven essentially redundant measurements of the electric field in one horizontal direction (x or y direction, depending on orientation of the array). A measurement of the potential difference between cells E8-E1 is also made, resulting in a horizontal electric field measurement across a baseline of 11.2 m. Platinum cells E4 and E5 were reconfigured to provide a measurement of the horizontal electric field in the E/W direction while the array was installed N/S.

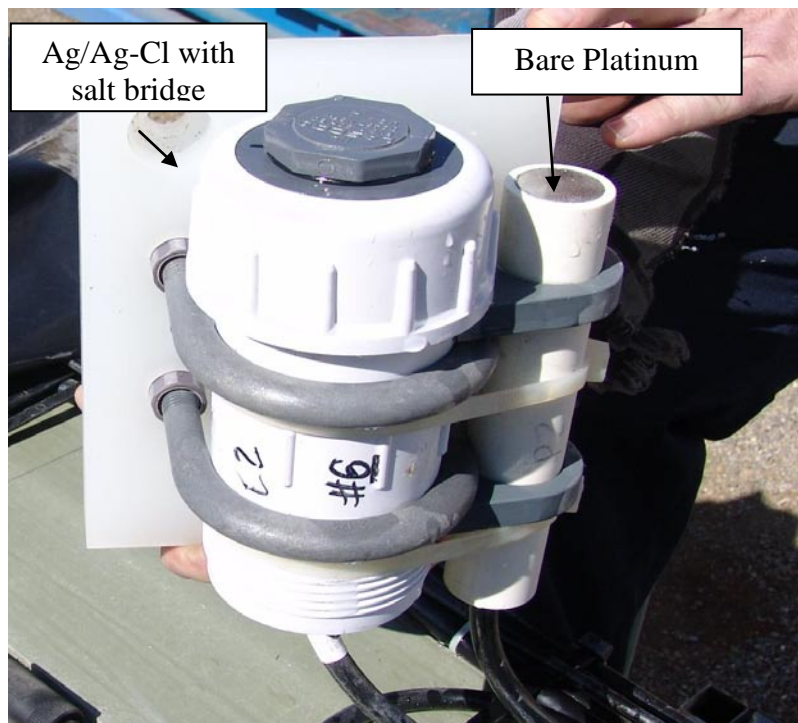


Figure 14. EM array potential cell pair



Figure 15. Receiving Array Ag/Ag/Cl Potential Cell

The EM receiving array was suspended 150 ft above the TMH. The vertical position of the TMH can be adjusted from the lake floor to the lake surface, so the EM array can be adjusted from 150 ft above the lake floor to the surface.

6. DATA ACQUISITION AND PROCESSING

The receiving array data acquisition system was comprised of National Instruments equipment located in a pressure vessel mounted to the array structure. The 40 channels of data (30 magnetic field and 10 electric field) were recorded on 24 bit A/Ds at a sample rate of 6000 samples per second. The sampled data was time stamped using a GPS clock. The data was transmitted back to the ROC via a fiber optic cable where it was written to files on a hard drive as shown in Figure 16. NSWCCD performed quick-look calculations during operations to ensure the quality and integrity of the data.

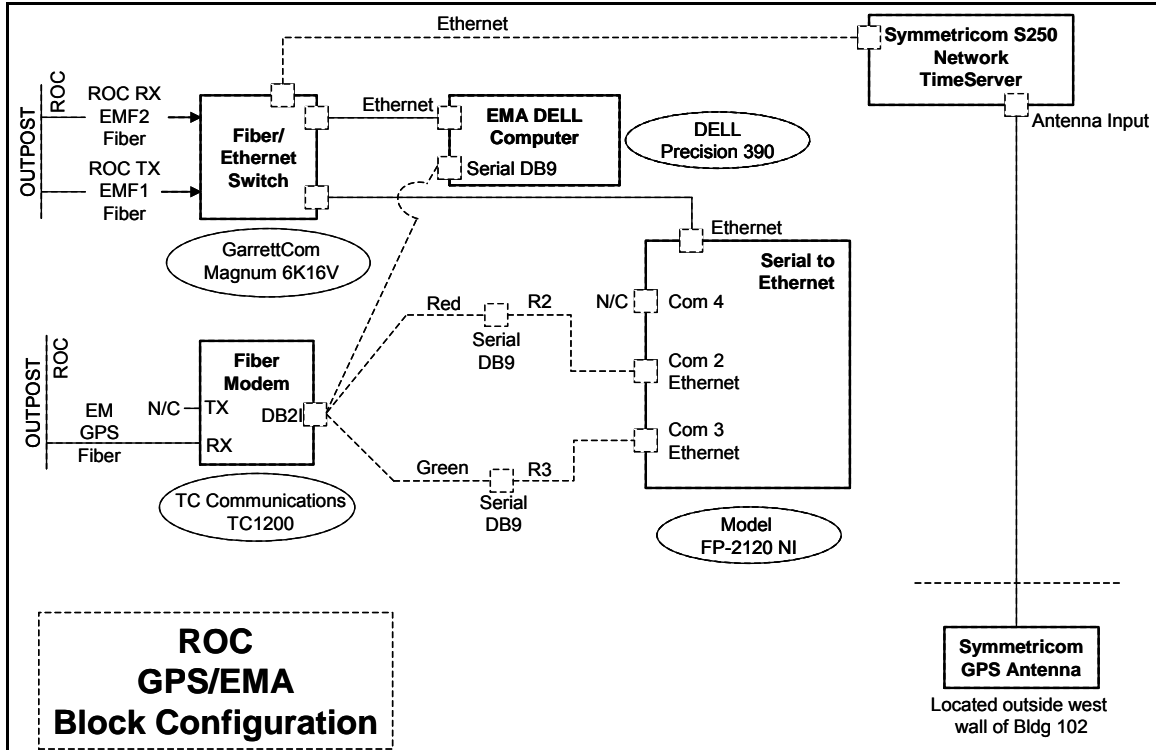


Figure 16. ROC GPS/EMA Configuration

7. DATA REPORTING REQUIREMENTS

Data reporting requirements were the responsibility of NSWCCD and UI. NSWCCD ensured the integrity of the data acquired during the tests and validated the data at Carderock before sending to UI for further analysis and modeling.

8. TEST SITE OPERATIONS

8.1. OPERATIONS TEAM AND POC

Personnel assignments were as listed in Table 1. The personnel listed in Table 1 were assigned the senior level responsibility for their task areas.

ELF Phase II Test Report

Table 1 Personnel Assignments

Program Test POC	Alan Griffiths
Test Director	Frank Jurenka
Technical Director	Steve Frommer
Trial Measurements/Engineer	Dan Lenko
ROC Data Acquisition	Duane Nightingale
Mechanical Engineer	Tom Tupper
Lake Operations	Tony Travis
Range Support	Jim Baxter
GPS	Jeanne Hom

The Test Director was responsible for the overall safe conduct of the test, the execution of the test plan, and called Comex and Finex. The Test Director ensured proper coordination and execution of all ARD efforts. The Technical Director was responsible for technical issues, checking the quality of data being collected, and making judgment calls regarding technical changes to the run plan.

APPENDIX 1. TEST RUN RECORD

NOISE RUNS

ELF Phase II Run Record - Noise Runs – Day 1														
Day 1, 12/6/2008, Underway with source boat @ 0900, return 1730. Record data from 200 yds before CPA (over EMA) to 200 yds after CPA Repeat runs will append a letter to the Run # (0101A, 0101B, etc)														
Run #	Comex Local	CPA Time	CPA Loc (from Boat)	Finex Local	Range Range	Range Depth (ft)	Source Type	Area (m ²)	Current (amps)	Freq (Hz)	Heading (° true)	Offset (ft)	Comments	Notes
0101	0930				EMA	36	None						Noise Run - 120 sec	
0102	0933				EMA	36	None						Noise Run - 120 sec	
0103	0936				EMA	36	None						Noise Run - 120 sec	
0104	0939				EMA	36	None						Noise Run - 120 sec	
0104A	1042				EMA	27	None						Noise Run - 120 sec	Ambient after height adjustment
0104B	1046 30				EMA	27	None						Noise Run - 120 sec	Ambient after height adjustment
0105	1057 55	1059 05	S of center	1100 23	EMA	27	None				80	0	25' Boat Speed - 5 knots	5.1 kts
0106	1104 08	1105 23	Center	1106 44	EMA	27	None				260	0	25' Boat Speed - 5 knots	5.1 kts
0107	1152 34	1153 46	S of center	1202 00	EMA	27	None				80	20 S	25' Boat Speed - 5 knots	5.2 kts
0108	1200 02	1201 19	S of center	1202 00	EMA	27	None				260	20 S	25' Boat Speed - 5 knots	5.1 kts
0108A	1207 17	1208 43	South	1210 05	EMA	27	None				80	20 S	25' Boat Speed - 5 knots	4.7 kts
0111	1114 57	1116 14	Little East	1117 15	EMA	27	None				170	0	25' Boat Speed - 5 knots	A little E, 5.1 kts
0112	1121 18	1122 16	East	1123 24	EMA	27	None				350	0	25' Boat Speed - 5 knots	5.2 kts
0113	1132 43	1133 58	50' East	1135 00	EMA	27	None				170	20 E	25' Boat Speed - 5 knots	
0114	1145 29	1146 27	East	114746	EMA	27	None				350	20 E	25' Boat Speed - 5 knots	
0121	1704 00			1706 00	EMA	27	None						Noise Run - 120 sec	
0122	1707 00			1709 00	EMA	27	None						Noise Run - 120 sec	
0123	1710 00			1712 00	EMA	27	None						Noise Run - 120 sec	
0124	1714 00			1716 00	EMA	27	None						Noise Run - 120 sec	
*Measured EMA depth using underwater camera. 36' depth matches LMS. Depth for runs 0101-1014.														
*Raised winch 9 teeth. Conducted mechanical measurement. 27' depth, repeated measurement (accurate). Depth for Run 0104A and following runs.														
*EMA Orientation, 350/170 degrees true.														

ELF Phase II Run Record – Noise Runs – Day 2														
Day 2, 12/8/2008														
Run #	Comex Local	CPA Time	CPA Loc (ft from Boat)	Finex Local	Range Range	Range Depth (ft)	Source Type	Length (m)	Current (amps)	Freq (Hz)	Heading (° true)	Offset (ft)	Duration (sec)	Comments
0201	0953 52				EMA	27	None						2 m 0 s	Noise run
0202	0957 00				EMA	27	None						2 m 0 s	Noise run
0211	1453 00			1455 00	EMA	27	None						2m 0s	Noise run
0212	1455 30			1504 10	EMA	27	None						2m 0s	Noise run
*EMA Orientation, 350/170 degrees true.														

ELF Phase II Test Report

ELF Phase II Run Plan - Noise Runs – Day 3

Day 3, 12/9/2008 Wind in AM. Tested towing of skiff in AM. Proceeded to range @ 1030.

Run #	Comex Local	CPA Time	CPA Loc (ft from Boat)	Finex Local	Range	Range Depth (ft)	Source Type	Length (m)	Current (amps)	Freq (Hz)	Heading (° true)	Offset (ft)	Duration (sec)	Comments
0301	1121 00			1129 23	EMA	27	None						8m 23s	Noise Run
0311	1642 00				EMA	27	None						8m 0s	Noise Run

*EMA Orientation, 350/170 degrees true.

ELF Phase II Run Record – Noise Runs – Day 4

Day 4, 12/10/2008

Run #	Comex Local	Finex Local	Range	Range Depth (ft)	Source Type	Length (m)	Current (amps)	Freq (Hz)	Heading (° true)	Offset (ft)	Duration (sec)	Comments
0401			EMA	27	None						8m 0s	Noise run
0411	1713 15		EMA	27	None						2m 0s	Noise run

*EMA Orientation, 350/170 degrees true.

ELF Phase II Run Record - Noise Runs – Day 5

Day 5, 12/11/2008

Run #	Comex Local	Finex Local	Range	Range Depth (ft)	Source					Offset (ft)	Duration (sec)	Comments
					Type	Length (m)	Current (amps)	Freq (Hz)	Heading (° true)			
0501	0852 20	0902 30	EMA	27	None						10m 10s	Noise run
0511	1653 40		EMA	968	None						8m 0s	Noise run

*EMA Orientation, 350/170 degrees true.

MAGNETIC SOURCE CALIBRATION VERIFICATION RUNS

ELF Phase II Run Record – Cal Source Verification – Magnetic

Day 1, 12/6/2008

Record data from 200 yds before CPA (over EMA) to 200 yds after CPA

Repeat runs will append a letter to the Run # (1001A, 1001B, etc)

Run #	Comex Local	CPA Time	CPA Loc (from Boat)	Finex Local	Range Range	Range Depth (ft)	Source Type	Area (m ²)	Current (amps)	Freq (Hz)	Heading (° true)	Offset (ft)	Comments	Notes
1001	1310 20	1311 38	Center	1313 08	EMA	27	Mag-boat	9.5	20	DC	80	0	Verify location of array and proper operation of GPS	4.9 kts
1002	1317 36	1318 47	Center	1320 00	EMA	27	Mag-boat	9.5	20	DC	260	0		5.4 kts
1003	1528 20	1529 35		1532 20	EMA	27	Mag-boat	9.5	20	10	80	20 S		20 ft S, 5.2 kts
1004	1537 59	1539 14		1544 11	EMA	27	Mag-boat	9.5	20	10	260	20 S		15 ft S, 5.1 kts
1005	1544 27	1545 45		1548 06	EMA	27	Mag-boat	9.5	20	10	80	20 N		20 ft S, 5.3 kts
1006	1551 09	1552 26		1554 08	EMA	27	Mag-boat	9.5	20	10	260	20 N		26 ft N, 5.1 kts
1007	1335 26	1336 42		1337 49	EMA	27	Mag-boat	9.5	20	DC	170	0		2 ft ?, 5.2 kts
1008	1345 00	1346 00		1347 17	EMA	27	Mag-boat	9.5	20	DC	350	0		1.5 ft W, 5.2 kts
1015	1506 43			1511 54	EMA	27	Mag-boat	9.5	20	10	80	0	Verify EM array magnetic measurement capability	1 ft. S, 5.1 kts
1016	1518 43			1522 54	EMA	27	Mag-boat	9.5	20	10	260	0		5.1 kts
1021	1600 33			1603 42	EMA	27	Mag-boat	9.5	20	10	170	0		2.5 ft E, 5.1 kts
1022	1605 50				EMA	27	Mag-boat	9.5	20	10	350	0		Abort, Source on boat lost power
1022A	1610 00				EMA	27	Mag-boat	9.5	20	10	350	0		Abort, boat course failure
1022B	1613 51			1616 45	EMA	27	Mag-boat	9.5	20	10	350	0		3 ft. W, 5.1 kts

*EMA Orientation, 350/170 degrees true.

ELECTRIC SOURCE CALIBRATION VERIFICATION RUNS

ELF Phase II Run Record – Cal Source Verification – Electric

Day 2, 12/8/2008, Underway 0930

Record data from 200 yds before CPA (over EMA) to 200 yds after CPA

Run #	Comex Local	CPA Time	CPA Loc (ft from Boat)	Finex Local	Range	Range Depth (ft)	Source Type	Length (m)	Current (amps)	Freq (Hz)	Heading (° true)	Offset (ft)	Comments	Notes
1101	1019 53	1021 04	3 N	1022 04	EMA	27	Elec-Hull	4	0.25	DC	80	0	Verify location of array and proper operation of GPS	5.9 kts
1102	1025 00	1026 08	1.5 S	1027 21	EMA	27	Elec-Hull	4	0.25	DC	260	0		5.3 kts
1103	1031 45	1033 01	11 S	1034 22	EMA	27	Elec-Hull	4	-0.125	DC	80	10 S		5.0 kts
1104	1040 15	1041 35	8 S	1044 18	EMA	27	Elec-Hull	4	-0.125	DC	260	8 S		4.9 kts
1105	1046 22	1047 33	8.5 N	1048 58	EMA	27	Elec-Hull	4	-0.125	DC	80	8 N		5.3 kts
1106	1051 26	1052 43	6.5 N	1054 05	EMA	27	Elec-Hull	4	-0.125	DC	260	8 N		4.8 kts
1107	1059 37		0 N	1102 01	EMA	27	Elec-Hull	4	-0.125	DC	170	0		5.0 kts
1109	1109 21	1110 42	18 E	1111 53	EMA	27	Elec-Hull	4	-0.125	DC	170	20 E		5.0 kts
1110	1104 38	1105 38	7.5 E	1106 59	EMA	27	Elec-Hull	4	-0.125	DC	350	10 E		5.2 kts
1115	1633 40	1634 24	2 N	1636 46	EMA	27	Elec-Hull	4	0.25	10	80	0	Verify EM array AC measurement capability	(Day 1) 5.3 kts
1116	1641 09	1642 18	1 N	1644 46	EMA	27	Elec-Hull	4	0.125	10	260	0		(Day 1) 5.3 kts
1117	1141 45	1142 46	1 N	1144 03	EMA	27	Elec-Hull	4	0.125	100	80	0		5.4 kts
1118	1145 54	1147 19	1 N	1148 41	EMA	27	Elec-Hull	4	0.125	100	260	0		4.7 kts
1119	1238 34	1239 38	0 N	1240 40	EMA	27	Elec-Hull	4	0.125	1000	80	0		6.3 kts
1120	1242 33	1243 47	1 S	1244 56	EMA	27	Elec-Hull	4	0.125	1000	260	0		5.6 kts
1121	1121 44	1122 58	9 S	1124 14	EMA	27	Elec-Hull	4	0.125	3	80	10 S		5.2 kts
1122	1126 00	1127 21	9 S	1128 53	EMA	27	Elec-Hull	4	0.125	3	260	8 S		4.7 kts
1123	1130 15	1131 30	8 N	1133 08	EMA	27	Elec-Hull	4	0.125	3	80	8 N		5.3 kts
1124	1134 42	1136 09	9 N	1137 05	EMA	27	Elec-Hull	4	0.125	3	260	8 N		4.8 kts
1127	1252 11	1253 44	13 E	1301 35	EMA	27	Elec-Hull	4	1.2	1000	170	0	Start N of EMA, head S until signal is gone	5.8 kts, 4600' S Finex. At 1315 a boat headed W of EMA to ESP
1128	1309 23	1311 09	4 W	1319 00	EMA	27	Elec-Hull	4	1.2	100	170	0	Start N of EMA, head S until signal is gone	5.4 kts, 3500' S Finex, LSV 25' boat W of range
1129	1326 11	1327 35	3 W	1335 30	EMA	27	Elec-Hull	4	1.2	10	170	0	Start N of EMA, head S until signal is gone	5.1 kts, 4200' S Finex

*EMA Orientation, 350/170 degrees true.

ELF Phase II Test Report

ELECTRIC SOURCE RUNS – 4 M

ELF Phase II Run Record - Electric Source – 4 m														
Day 3, 12/9/2008, Underway with source boat @ 1030. Record data from 200 yds before CPA (over EMA) to 200 yds after CPA														
Run #	Comex	CPA Time	CPA Loc (ft from Boat)	Finex	Range	Range Depth (ft)	Source					Offset (ft)	Duration (sec)	Comments
	Local			Local			Type	Length (m)	Current (amps)	Freq (Hz)	Heading (° true)			
2004	1347 47			1349 15	EMA	27	Elec - hull	4	1.2	10	260	250 S	88	(Day 2) From -200' to -500' Northing, stationary test, 3 kts
2019	1206 57	1209 10	499 S	1211 25	EMA	27	Elec - hull	4	1.1	100	260	500 S	4m 28s	2.0 kts
2020	1214 50	1216 22	502 S	1218 21	EMA	27	Elec - hull	4	1.1	100	80	500 S	3m 31s	2.7 kts
2021	1223 55	1225 46	300 S	1227 56	EMA	27	Elec - towed	4	1.1	100	260	300 S	4m 1s	2.2 kts
2022	1230 43	1232 00	302 S	1233 53	EMA	27	Elec - towed	4	1.1	100	80	300 S	3m 10s	2.8 kts
2023	1238 15	1240 34	1000 S	1242 33	EMA	27	Elec - towed	4	1.1	100	260	1000 S	4m 18s	2.2 kts
2024	1244 43	1244 45	1002 S	1247 48	EMA	27	Elec - towed	4	1.1	100	80	1000 S	3m 5s	2.7 kts
2051	1408 29			1411 20	EMA	27	Elec - hull	4	1.2	10	260	250 S	2m 51s	(Day 2) 2.5 kts. AESD_DAQ stopped just before CPA, restarted. Run covers ~6 min w/~20 sec gap after 2 min
2052	1416 37			1422 59	EMA	27	Elec - hull	4	1.2	10	170	0 to 2000 S	6m 22s	(Day 2) 3 kts. Start at EMA, S slow as possible w/constant heading.
2053	1427 56	1431 34		1433 12	EMA	27	Elec - hull	4	1.2	10	260	1000 S	5m 16s	(Day 2) 1.5 kts. Source athwartships to EMA at 1000'
2054	1437 09	1438 11		1440 00	EMA	27	Elec - hull	4	1.2	10	80	400 S	2m 51s	(Day 2) 405' S, 3 kts. Source athwartships to EMA at 1000'
Day 5, 12/11/2008														
5001	0923 28	0924 32	17 W	0925 25	EMA	27	Elec - hull	4	1.25	DC	350	17 W	1m 57s	Positioning run, 1.1 kts
5002	0926 57	0928 02	21 E	0929 02	EMA	27	Elec - hull	4	1.25	DC	170	21 E	2m 5s	Positioning run, 1.5 kts
5003	0935 50	0936 05	8 S	0936 36	EMA	27	Elec - hull	4	1.25	DC	80	8 S	46s	Positioning run, 2.8 kts
5004	0938 06	0938 07	8 N	0938 37	EMA	27	Elec - hull	4	1.25	DC	260	8 N	31s	started late
5005	0940 03	0940 25	8 N	0941 01	EMA	27	Elec - hull	4	1.25	DC	80	8 N	58s	Positioning run
*EMA Orientation, 350/170 degrees true. *Skiff is positive terminal.														

ELF Phase II Test Report

ELECTRIC SOURCE RUNS – 40 M TOWED, SOUTH

ELF Phase II Run Record – Electric Source – Towed – South														
Day 3, 12/9/2008														
Adjust distances as necessary based on Runs 3005-3006														
25' Boat speed – as slow as possible while maintaining orientation														
Run #	Comex	CPA Time	CPA Loc (ft from Boat)	Finex	Range	Range Depth	Source					Offset	Duration	Comments
	Local			Local			Type	Length (m)	Current (amps)	Freq (Hz)	Heading (° true)			
3005	1457 20			1513 28	EMA	27	Elec-Towed	42.6	1.2	100	170	3000 S to 11000 S	16m 8s	Headed south of EMA until signal was gone. 3.8 kts
3006	1515 51	1545 11		1547 22	EMA	27	Elec-Towed	42.6	1.25	1000	350	11000 S (start)	31m 31s	Started south of EMA and headed north, 3.7 kts
3042	1336 32	1338 50	1510 S	1341 37	EMA	27	Elec-Towed	42.6	1.2	100	260	1500 S	5m 5s	1.6 kts
3044	1348 06	1349 50	1999 S	1352 02	EMA	27	Elec-Towed	42.6	1.2	100	80	2000 S	3m 56s	3.3 kts
3046	1408 25	1440 27	3000 S	1413 12	EMA	27	Elec-Towed	42.6	1.2	100	260	3000 S	4m 47s	2.8 kts
*EMA Orientation, 350/170 degrees true.														
*Skiff is positive terminal.														

ELF Phase II Test Report

ELECTRIC SOURCE RUNS – 40 M TOWED, WEST

ELF Phase II Run Record - Electric Source - Towed - West												
Day 4, 12/10/2008, underway @ 0845 Adjust distances as necessary based on Runs 3005-3006 25' Boat speed - as slow as possible while maintaining orientation												
Run #	Comex	Finex	Range	Range Depth (ft)	Source					Offset (ft)	Duration (sec)	Comments
	Local	Local			Type	Length (m)	Current (amps)	Freq (Hz)	Heading (° true)			
4990	1007 10		EMA	27	Elec - towed	42.6	1.25	DC	260	0	2m 54s	Checking set-up. ESP generator operating.
4014	1035 06	1037 06	EMA	27	Elec - towed	42.6	1.25	100	170	2000 W	120s	2.3 kts
4020	1057 02	1059 55	EMA	27	Elec - towed	42.6	1.25	10	170	6000 W	2m 53s	5997 ft W, 2.3 kts
4914	1043 39	1047 16	EMA	27	Elec - towed	42.6	1.25	10	350	2000 W	3m 37s	2001 ft W, 2.3 kts
4034	1025 50	1027 56	EMA	27	Elec - towed	42.6	1.25	100	350	2000 W	2m 6s	1.1 kts
4040	1103 23	1106 15	EMA	27	Elec - towed	42.6	1.25	100	350	6000 W	2m 52s	6001 ft W, 2.2 kts
4054	1018 09	1020 16	EMA	27	Elec - towed	42.6	1.25	1000	~170	2000 W	2m 7s	1.6 kts
4060	1108 37	1111 19	EMA	27	Elec - towed	42.6	1.25	1000	~170	6000 W	2m 42s	5995 ft W, 2.2 kts
4901	1138 21	1141 22	EMA	27	Elec - towed	42.6	1.25	10	~90	Source skiff tied with ~160 ft of line to inboard ISMS hauldown float offshore of Outpost. Source boat pointed towards EMA providing tension and positioning for moored source system. ~9500 ft. from EMA. 3m 1s.		
4902	1144 23	1147 39	EMA	27	Elec - towed	42.6	1.25	100	~90	Configuration same as above. 3m 16s duration.		
4903	1148 33	1151 25	EMA	27	Elec - towed	42.6	1.25	1000	~90	Configuration same as above. 2m 52s duration.		
4904	1156 34	115934	EMA	27	Elec - towed	42.6	1.25	10	~90	Configuration same as above. 3m 0s duration.		
4905	1205 34	1208 34	EMA	27	Elec - towed	42.6	1.25	10	~180	Source skiff tied, with ~160 ft of line to inboard ISMS hauldown float offshore of the Outpost. Source boat pointed south approximately orthogonal to Horizontal-East orientation. 25' boat providing tension and positioning for moored source system. ~9500 ft. from the EMA. 3m 0s duration.		
4906	1210 44	1213 44	EMA	27	Elec - towed	42.6	1.25	100	~180	Configuration same as above. 3m 0s duration.		
4907	1221 28	1224 28	EMA	27	Elec - towed	42.6	1.25	1000	~180	Configuration same as above. 3m 0s duration.		
4908	1226 40	1229 40	EMA	27	Elec - towed	42.6	1.25	10	~180	Repeat of 4905 (more stable orientation). Configuration same as above. 3m 0s duration.		
4909	1401 00	1403 00	EMA	27	Elec - towed	42.6	1.25	10	48	Towed source ~300-400 yds from W shore, S of Maiden Rock, due W of TMH. 48° true. 2.0 kts.		
4910	1404 45	1406 30	EMA	27	Elec - towed	42.6	1.25	100	48	Same as above, further NE.		
4911	1407 10	1409 10	EMA	27	Elec - towed	42.6	1.25	1000	48	Same as above, further NE.		
4912	1415 47	1417 47	EMA	27	Elec - towed	42.6	1.25	1000	45	Same as above, NE of Maiden Rock. 2.1 kts. Limited GPS A & B data		
4913	1418 45	1421 07	EMA	27	Elec - towed	42.6	1.25	100	58	Same as above, further NE of Maiden Rock. Limited GPS A & B data.		
4915	1422 30	1424 30	EMA	27	Elec - towed	42.6	1.25	10	45	Same as above, further NE of Maiden Rock. No GPS B data.		
4916	1431 46	1434 12	EMA	27	Elec - towed	42.6	1.25	10	170	NE of Maiden Rock, ~5500 ft from EMA, heading S towards EMA. 2.4 kts. Limited GPS A&B data		
4917	1435 00	1437 15	EMA	27	Elec - towed	42.6	1.25	1000	170	Heading south towards the EMA. 5500' from EMA. 2.3 kts.		
4918	1443 46	1445 46	EMA	27	Elec - towed	42.6	1.25	1000	170	~2500 ft. from the EMA, heading south towards the EMA. 2.3 kts.		
4919	1446 22	1448 22	EMA	27	Elec - towed	42.6	1.25	100	170	~2500 ft. from the EMA, heading south towards the EMA. 2.3 kts.		
4920	1448 50	1450 50	EMA	27	Elec - towed	42.6	1.25	10	170	~2500 ft. from the EMA, heading south towards the EMA. 2.3 kts.		
*EMA Orientation, 350/170 degrees true. *Skiff is positive terminal.												

ELF Phase II Test Report

ELECTRIC SOURCE RUNS – 40 M TOWED, EAST

ELF Phase II Run Record - Electric Source - Towed - East												
Day 4, 12/10/2008, underway @ 0845. 25' Boat speed - as slow as possible while maintaining orientation												
Run #	Comex	Finex	Range	Range Depth (ft)	Source					Offset (ft)	Duration (sec)	Comments
	Local	Local			Type	Length (m)	Current (amps)	Freq (Hz)	Heading (° true)			
4923	1517 45	1523 58	EMA	27	Elec-towed	42.6	1.25	10	350°	10,000 E	6m 13s	2.3 kts, compare to inboard buoy
4924	1524 14	1526 38	EMA	27	Elec-towed	42.6	1.25	100	350°	10,000 E	2m 24s	2.3 kts, compare to inboard buoy
4925	1527 04	1529 07	EMA	27	Elec-towed	42.6	1.25	1000	350°	10,000 E	2m 24s	2.2 kts, compare to inboard buoy
4926	1534 34	1536 34	EMA	27	Elec-towed	42.6	1.25	1000	260°	9000 E	2m 0s	2.3 kts, compare to inboard buoy
4927	1537 00	1539 00	EMA	27	Elec-towed	42.6	1.25	100	260°	9000 E	2m 0s	Heading West, closing towards the EMA, 2.4 kts, compare to inboard buoy
4928	1539 30	1541 30	EMA	27	Elec-towed	42.6	1.25	10	260°	9000 E	2m 0s	Heading West, closing towards the EMA, 2.4 kts, compare to inboard buoy, very little signal
4929	1546 09	1548 09	EMA	27	Elec-towed	42.6	1.25	10	260°	4615 E	2m 0s	2.4 kts
4930	1548 40	1550 40	EMA	27	Elec-towed	42.6	1.25	100	260°	4615 E	2m 0s	2.3 kts
4931	1551 05	155105	EMA	27	Elec-towed	42.6	1.25	1000	260°	4615 E	2m 0s	2.3 kts
4932	1600 52	1602 52	EMA	27	Elec-towed	42.6	1.25	1000	260°	2500 E	2m 0s	2.3 kts
4933	1603 16	1605 01	EMA	27	Elec-towed	42.6	1.25	100	260°	2000 E	1m 45s	2.3 kts
4934	1605 22	1607 22	EMA	27	Elec-towed	42.6	1.25	10	260°	1600 E	2m 0s	2.3 kts, finished at 900'
*EMA Orientation, 350/170 degrees true. *Skiff is positive terminal.												

ELECTRIC SOURCE RUNS – 40 M TOWED, MISCELLANEOUS

ELF Phase II Run Record - Electric Source - Towed - Misc.												
Day 4, 12/10/2008 Adjust distances as necessary based on Runs 3005-3006 25' Boat speed - as slow as possible while maintaining orientation												
Run #	Comex	Finex	Range	Range Depth (ft)	Source					Offset (ft)	Duration (sec)	Comments
	Local	Local			Type	Length (m)	Current (amps)	Freq (Hz)	Heading (° true)			
4921	1459 30	1501 49	EMA	27	Elec-towed	42.6	0.83	10 Sq	170°	1750 S	2m 19s	Heading away from EMA, 2.3 kts
4922	1502 21	1504 21	EMA	27	Elec-towed	42.6	0.83	75 Sq	170°	1500 S	2m 0s	Heading away from EMA, 2.3 kts
4935	1612 08	1614 02	EMA	27	Elec-towed	42.6	1.25	1	170°	1750 S	1m 54s	2.3 kts
4936	1618 17	1620 45	EMA	27	Elec-towed	42.6	1.25	1	260°	2000 S, 200 E	2m 28s	2.4 kts, channel 36 had almost no signal. Other long E sensors had signal.
*EMA Orientation, 350/170 degrees true. *Skiff is positive terminal.												

ELF Phase II Test Report

ELECTRIC SOURCE RUNS – 40 M TOWED, ARRAY AT BOTTOM

ELF Phase II Run Record - Electric Source - Towed - Array at Bottom												
Day 5, 12/11/2008												
25' Boat speed - as slow as possible while maintaining orientation												
Run #	Comex	Finex	Range	Range Depth	Source					Offset	Duration	Comments
	Local	Local			Type	Length	Current	Freq	Heading			
				(ft)		(m)	(amps)	(Hz)	(° true)	(ft)	(sec)	
011	1044 05	1046 11	EMA	968	Elec-towed	42.6	1.25	10	170	150 S	2m 6s	Comex 200' from EMA.
5012	1046 36	1048 00	EMA	968	Elec-towed	42.6	1.25	100	170	1000 S	1m 24s	Continuing South from 5011, 3 kts.
5013	1048 22	1050 15	EMA	968	Elec-towed	42.6	1.25	1000	170	1750 S	1m 53s	Continuing South, Finex 1750' S.
5014	1056 15	1058 40	EMA	968	Elec-towed	42.6	1.25	10	170	5000 S	2m 25s	2.9 kts, fishing boat making E/W passes close to EMA.
5015	1059 20	1101 24	EMA	968	Elec-towed	42.6	1.25	100	170	6100 S	2m 4s	Continuing South from 5014, 1.9 kts
5016	1102 28	1104 33	EMA	968	Elec-towed	42.6	1.25	1000	170	6500 S	2m 5s	Continuing South, no 1 kHz signal, very little signal on DAQ FFT
5017	1112 46	1114 46	EMA	968	Elec-towed	42.6	1.25	10	260	5000 S, 300 E	2m 0s	Comex 300' before CPA to EMA.
5018	1115 29	1117 32	EMA	968	Elec-towed	42.6	1.25	100	260	5000 S, 700 W	2m 3s	Continuing West from 5017.
5019	1118 01	1120 02	EMA	968	Elec-towed	42.6	1.25	1000	260	5000 S, 1200 W	2m 1s	Continuing West
5020	1129 18	113118	EMA	968	Elec-towed	42.6	1.25	10	80	2000 S, 1000 W	2m 0s	Comex 1000' before CPA to EMA.
5021	1131 51	1133 57	EMA	968	Elec-towed	42.6	1.25	100	80	2000 S, 650 W	2m 6s	Continuing East from 5020.
5022	1134 31	113632	EMA	968	Elec-towed	42.6	1.25	1000	80	2000 S, 100 W	2m 1s	Continuing East, Comex 100' before CPA
5023	1240 28	1242 36	EMA	968	Elec-towed	42.6	1.25	10	170	500 S, 5000 W	2m 8s	Comex ~500 ft South of CPA, 2.9 kts.
5024	1243 00	1245 15	EMA	968	Elec-towed	42.6	1.25	100	170	5000 W	2m 15s	Continuing South from 5023.
5025	1246 01	1248 04	EMA	968	Elec-towed	42.6	1.25	1000	170	5000 W	2m 3s	Continuing South.
5026	1306 06	1308 22	EMA	968	Elec-towed	42.6	1.25	10	180		2m 16s	Parallel to west shore.
5027	1309 52	131154	EMA	968	Elec-towed	42.6	1.25	100	180		2m 2s	Parallel to west shore, 2.9 kts
5028	1312 39	1314 50	EMA	968	Elec-towed	42.6	1.25	1000	211		2m 11s	Parallel to west shore, ~200 ft S of Outpost Pier, 3.0 kts.
5029	1319 28	1321 35	EMA	968	Elec-towed	42.6	1.25	10	211		2m 7s	200' off shore, parallel to west shore, 3.0 kts.
5030	1321 59	1323 47	EMA	968	Elec-towed	42.6	1.25	100	20		1m 48s	200' off shore, parallel to west shore, 3.0 kts.
5031	1324 15	1326 15	EMA	968	Elec-towed	42.6	1.25	1000	24		2m 0s	200' off shore, parallel to west shore, 3.0 kts.
5032	1350 00	1352 00	EMA	968	Elec-towed	42.6	1.25	10	38		2m 0s	Parallel to W shore ~500 ft S of Maiden Rock, ~200 ft offshore, 3.0 kts.
5033	1352 30	1354 30	EMA	968	Elec-towed	42.6	1.25	100	62		2m 0s	Parallel to W shore N of Outpost next to Maiden Rock beach, 3.0 kts.
5034	1354 50	1357 50	EMA	968	Elec-towed	42.6	1.25	1000	71 - 56		3m 0s	Parallel to W shore N of Outpost next to Maiden Rock beach, 3.0 kts.
5035	1410 48	1412 48	EMA	968	Elec-towed	42.6	1.25	10	80	5000 W	2m 0s	Heading towards EMA, 2.8 kts.
5036	1413 21	1415 25	EMA	968	Elec-towed	42.6	1.25	100	80		2m 4s	Heading towards EMA, 2.7 kts.
5037	1415 45	1417 52	EMA	968	Elec-towed	42.6	1.25	1000	80	3500 W	2m 7s	Heading towards EMA, 3.0 kts.
5038	1420 13	1422 20	EMA	968	Elec-towed	42.6	1.25	10	80	2000 W	2m 7s	Heading towards EMA, 3.0 kts.
5039	1422 46	1424 48	EMA	968	Elec-towed	42.6	1.25	100	80		2m 2s	Heading towards EMA, 3.0 kts.
5040	1425 19	1427 15	EMA	968	Elec-towed	42.6	1.25	1000	80	300 W	1m 56s	3.0 kts.
5041	1429 18	1431 18	EMA	968	Elec-towed	42.6	1.25	10	125		2m 0s	SE of EMA, heading away

ELF Phase II Test Report

ELF Phase II Run Record - Electric Source - Towed - Array at Bottom

Day 5, 12/11/2008

25' Boat speed - as slow as possible while maintaining orientation

Run #	Comex	Finex	Range	Range Depth (ft)	Source					Offset (ft)	Duration (sec)	Comments
					Type	Length (m)	Current (amps)	Freq (Hz)	Heading (° true)			
5042	1431 50	1433 50	EMA	968	Elec-towed	42.6	1.25	100	125		2m 0s	Continuing SE, 2.9 kts.
5043	1434 20	1436 20	EMA	968	Elec-towed	42.6	1.25	1000	125		2m 0s	Continuing SE, 2.9 kts.
5044	1437 06	1439 10	EMA	968	Elec-towed	42.6	1.25	1	125		2m 4s	Continuing SE, 3.0 kts.
5045	1452 26	1454 26	EMA	968	Elec-towed	42.6	1.25	10 Sq	350	2000 S	2m 0s	Inbound to EMA, 3.5 kts.
5046	1454 56	1456 56	EMA	968	Elec-towed	42.6	1.25	75 Sq	350	700 S	2m 0s	Inbound to EMA, 3.3 kts, spectral & acoustic lines at 290 Hz
5051	1531 15	1533 12	EMA	968	Vertical Plate	29	1.2	1		17 N	1m 57s	Drifting over the EMA
5052	1533 30	1535 30	EMA	968	Vertical Plate	29	1.2	10			2m 0s	Drifting over the EMA.
5053	1536 08	1538 08	EMA	968	Vertical Plate	29	1.2	100			2m 0s	Drifting over the EMA.
5054	1538 40	1540 40	EMA	968	Vertical Plate	29	1.25	1000			2m 0s	Drifting over the EMA.
5055	1546 57	1548 56	EMA	968	Vertical Plate	29	1.2	1		2000 W	1m 59s	
5056	1549 15	1551 09	EMA	968	Vertical Plate	29	1.2	10		2000 W	1m 54s	
5057	1551 30	1553 32	EMA	968	Vertical Plate	29	1.2	100		2000 W	2m 2s	
5058	1554 00	1556 00	EMA	968	Vertical Plate	29	1.2	1000		2000 W	2m 0s	
5059	1607 30	1609 30	EMA	968	Vertical Plate	29	1.2	10			2m 0s	N of the Outpost, just off Maiden Rock.
5060	1610 03	1612 05	EMA	968	Vertical Plate	29	1.2	100			2m 2s	N of the Outpost, just south of Maiden Rock.
5061	1613 00	1615 00	EMA	968	Vertical Plate	29	1.2	1000			2m 0s	N of the Outpost, just south of Maiden Rock.
5062	1615 50	1616 55	EMA	968	Vertical Plate	29	1.2	75 Sq			1m 5s	N of the Outpost, just south of Maiden Rock. No signal.
5063	1618 03	1620 03	EMA	968	Vertical Plate	29	1.2	10 Sq			2m 0s	N of the Outpost, just south of Maiden Rock. No signal.

*EMA Orientation, 355/175 degrees true.

*Skiff is positive terminal.

* Vertical plate is 29 m below the surface.

ISMS BACKGROUND NOISE RUNS

ELF Phase II Run Record - ISMS Background Noise

Run #	Range	Duration	Condition	Date Completed
9002	EMA	2m 20s	EM field levels of the NFTA while transmitting a broadband continuous waveform at maximum power output level (ST2-6 projector, waveform "bbc_50_1k.wfm")	12/11/08 @ 0945 40
9004	EMA	2m 0s	EM field levels of the ESP when operating the main generator and crane	12/10/08 @ 0919 00
9005	EMA	2m 6s	EM field levels of the ESP when operating the main generator	12/10/08 @ 1258 00
9006	EMA	2m 0s	EM field levels of the ESP when operating the standby generator	12/10/08 @ 1640 00

*EMA Orientation, 350/170 degrees true.

*EMA Depth Run #9002, 27 ft.

*EMA moved to 968 ft. depth after Run #9002.

**ELF PHASE III TEST 1
(March 5 – 11, 2010)
Test Record**

**Compiled by:
Frank Jurenka, NSWCCD 7260
Chris Burgy, NSWCCD 7510
Vickie Pfeifer, NTI**

July 15, 2010

TABLE OF CONTENTS

1. PROJECT TEST ABSTRACT.....	4
1.1. OVERVIEW	4
1.2. OBJECTIVES	4
1.3. RESPONSIBILITIES	4
1.4. PROJECT PHASES	4
2. TEST RISK ANALYSIS	5
3. OPERATIONAL SAFETY	6
4. WEIGHT HANDLING.....	6
5. ENVIRONMENTAL/HAZMAT	7
6. TEST ORGANIZATION MATRIX.....	7
7. TEST SCENARIO.....	7
7.1. TEST SITE	7
7.2. LAKE ENVIRONMENTAL PARAMETERS	11
7.3. GPS SYSTEM	11
7.4. MAGNETIC AND ELECTRIC SOURCES	14
7.4.1. Calibrated Electric Source.....	14
7.4.2. Portable Electric Source.....	16
7.4.2.1. <i>Electric Source Drive and Control</i>	18
7.4.3. Magnetic Source	19
7.4.3.1. <i>Magnetic Source Drive and Control</i>	22
7.5. PORTABLE ELECTRO-MAGNETIC MEASUREMENT ARRAY (PEMA).....	23
7.6. DATA ACQUISITION	28
8. TEST SITE OPERATIONS.....	32
8.1. OPERATIONS TEAM.....	32
8.2. MOORING PLAN.....	32
8.3. OPERATING PROCEDURES.....	35
8.4. EMERGENCY PROCEDURES.....	36
9. TEST RUN PLAN EXECUTION	36
9.1. NOISE MEASUREMENTS.....	36
9.2. CALIBRATED SOURCE RUNS	37
9.3. ELF RUNS.....	37
9.3.1. Electric Source Runs.....	37
9.3.2. Magnetic Source Runs.....	38
9.4. DATA REPORTING.....	39
APPENDIX A: UI DATA ESTIMATES	A-1
APPENDIX B: TEST RUN RECORD	B-1
APPENDIX C: PORTABLE EM ARRAY TECHNICAL SPECIFICATIONS	C-1
APPENDIX D: SENSOR PRE-TESTS AT CARDEROCK.....	D-1
APPENDIX E: SENSOR CALIBRATION TILT DATA (IN MESF).....	E-1
APPENDIX F: MAGNETIC, TILT AND PRESSURE DATA.....	F-1
APPENDIX G: ARD TRIP REPORT	G-1

LIST OF FIGURES

Figure 1	Lake Pend Oreille	8
Figure 2	Topographical Map of Test Area.....	9
Figure 3	Source and Sensor Locations.....	10
Figure 4	GPS System Diagram.....	12
Figure 5	GPS Antennas on Barges.....	13
Figure 6	GPS Equipment Set-up on Sensor Barge.....	14
Figure 7	Calibrated Source Boat.....	15
Figure 8	Calibrated Electric Source Electrode	15
Figure 9	Calibrated Electric Source System Diagram	16
Figure 10	Portable Electric Source	17
Figure 11	60' Barge Layout (E-Source)	18
Figure 12	Electric Source System Diagram	19
Figure 13	Magnetic Source	20
Figure 14	Magnetic Source at Shore Location	20
Figure 15	Magnetic Source GPS Layout - Horizontal	21
Figure 16	Magnetic Source GPS Layout – Vertical.....	22
Figure 17	Magnetic Source System Diagram	23
Figure 18	Portable EM Array Drawing	24
Figure 19	Wiring Diagram – Sensor Pigtail to Connector Cable	24
Figure 20	Wiring Diagram – Sensor Underwater E-field Cable.....	25
Figure 21	Portable EM Array Tilt Test in MESF	26
Figure 22	Portable EM Array Deployment	27
Figure 23	Scow (Sensor Barge) Layout	28
Figure 24	Sensor and Data Acquisition System Diagram	30
Figure 25	45' Mooring Barge	33
Figure 26	60' E-Source Barge Moored	34
Figure 27	Sensor Barge Moored at Location 6	35

LIST OF TABLES

Table 1	GPS Output.....	14
Table 2	CDAQ PEMA Channel Assignments.....	29
Table 3	Personnel Assignments	32
Table 4	ARD Base Radio Call Signs.....	36

1. PROJECT TEST ABSTRACT

1.1. OVERVIEW

Efforts to understand, measure, and model the propagation of underwater Extremely Low Frequency (ELF) signals is important in the evaluation of Navy vessels' susceptibility to detection systems and mines. This is especially significant in light of the Navy's desire to build an all electric ship.

1.2. OBJECTIVES

The overall objectives of the ELF testing are to:

- Research analytical theories to better understand the propagation, scattering, refraction, and reflection of ELF fields.
- Develop an experimental test-bed for the complete characterization and prediction of ELF signals in shallow and deep water environments.
- Develop numerical simulation tools for predicting EM propagation in environments with variable conductiveness and geometric features.

Appendix A provides magnetic and electric field estimates from the University of Idaho (UI) models for parameters similar to those of this test phase.

1.3. RESPONSIBILITIES

This project was a collaborative effort between UI, the Naval Surface Warfare Center Carderock Division (NSWCCD), and the Acoustic Research Detachment (ARD). UI was responsible for modeling and simulation, Carderock was responsible for experiment design and data acquisition, and the ARD was responsible for developing, assembling, and deploying test apparatus onto the lake. Conducting the prescribed experiments was a collaborative responsibility.

1.4. PROJECT PHASES

The ELF project was a three phase project. During Phase I, the following was accomplished:

- Cal source runs executed (3/08) and data delivered to UI
- Initial data set acquired during AESD testing

- Initial numerical model development

During Phase II, the following was accomplished:

- Lake topography delivered to UI
- Testing completed with towed electric source (12/08)
- Verification of test data and delivery to UI (1/09)

During Phase III testing the following was accomplished:

- A portable electric source (e-source) was deployed on the lake at varying depths and orientations.
- A magnetic source (m-source) was deployed on-shore at Farragut State Park in vertical and horizontal orientations.
- Measurements of the generated electric and magnetic fields at several points and depths using a portable measurement array (PEMA) and a portable data acquisition system.
- Verification of test data and delivery to UI (3/10)

2. TEST RISK ANALYSIS

Operational Risk Management (ORM) was performed prior to and during all test operations. The following risks were addressed:

- Weather
 - Winds and storms can have a detrimental effect on the test outcomes
 - Weather in March can be windy and stormy.
 - Contingency time is built into the schedule to accommodate weather-related delays
 - Run plan can be modified as necessary
- PEMA, portable e-source running aground/hitting bottom
 - Depth sounders, GPS location information, and orientation information allowed for precise knowledge of location/depth of equipment
 - Detailed deployment procedures were developed for PEMA and

the e-source (ELF-OP-001, “ELF Portable E-Source Array and Electromagnetic Sensor Deployment Procedure”).

- Deployment platforms were secured by bottom mounted moorings in areas where grounding may be an issue (ELF-OP-002, “Mooring Procedure”).

It was the responsibility of all personnel to practice ORM during test operations. Additional risks may have been identified as conditions changed during test operations.

3. OPERATIONAL SAFETY

ORM principles and processes were adhered to during all test operations.

All personnel followed safety instructions detailed in ARDINST 5100.4B “Operation of Watercraft on Lake Pend Oreille” and ARDINST 5100.5 “ARD Safety Rules Handbook”. Life jackets were worn by all personnel during boat/barge transfers to the test area and during operations on barges and boats when outside of lab/control areas.

The ARD Trial Director briefed the customer field party and ARD operating crews on safety requirements and specific test safety concerns prior to initial underway operations. Requirements and concerns included, but were not limited to, crane operations safety requirements, wearing PFDs while working around the waterfront and on-board vessels, specific test related operations, and operations protocol.

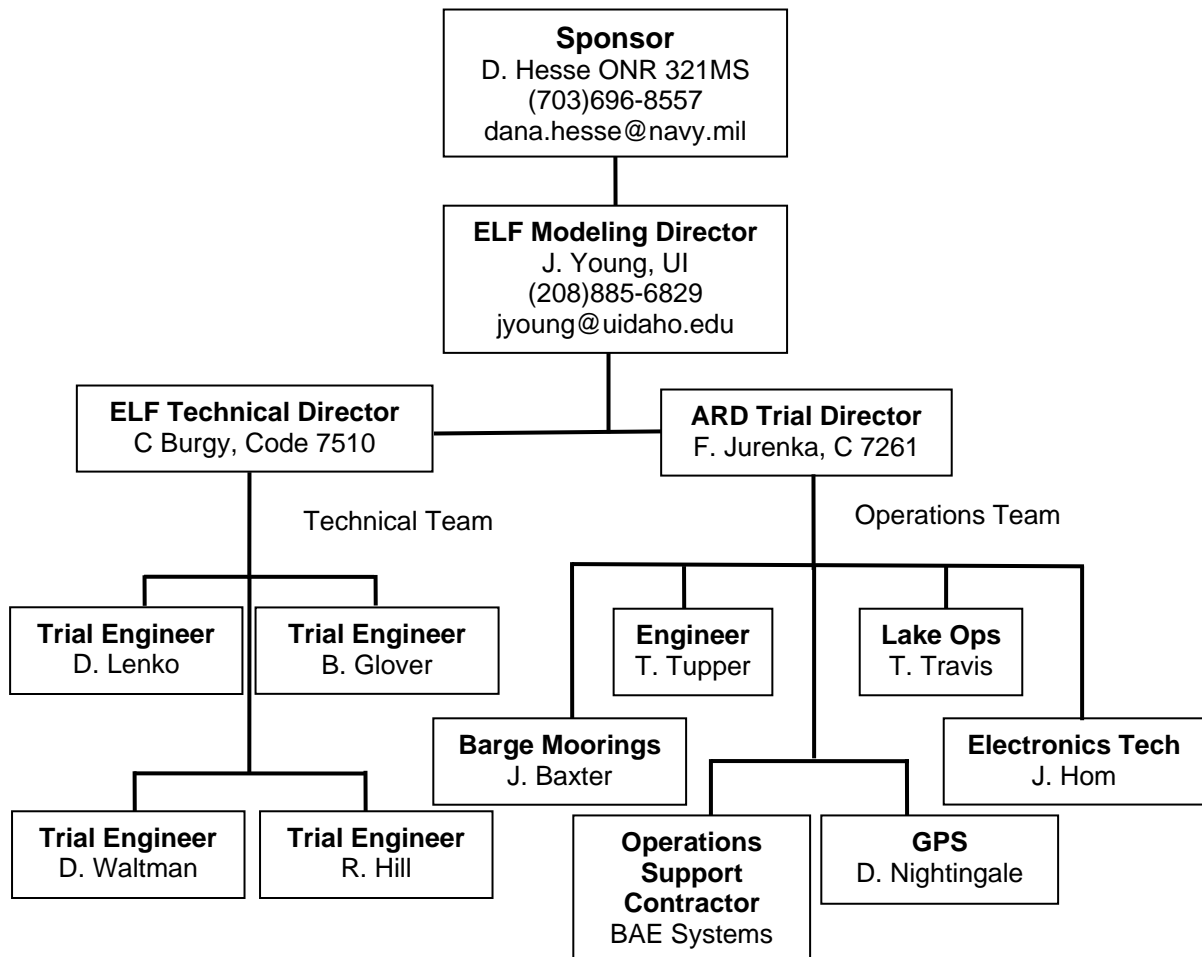
4. WEIGHT HANDLING

The ARD provided certified weight handling equipment as required. All weight handling operations were in accordance with NAVFAC P-307.

5. ENVIRONMENTAL/HAZMAT

An internal Environmental Scoping Questionnaire was completed in accordance with local ARD instructions which indicated that this testing falls under the ARD's current scope of operations.

6. TEST ORGANIZATION MATRIX



7. TEST SCENARIO

7.1. TEST SITE

The tests were conducted at the ARD located on Lake Pend Oreille in Bayview, Idaho during March 5 – 11, 2010. Lake Pend Oreille is uniquely suited

for conducting the ELF propagation tests due to its uniform and stable water conductivity throughout the water column.

The ELF tests were performed at various locations in Idlewild Bay in the southern portion of Lake Pend Oreille, as shown in Figure 1, using a portable measurement array and data acquisition system, a portable electric source, and a magnetic source located on-shore at Farragut State Park. This location was chosen due to the interesting bathymetric features in the area. The shallow bay provides more complex ELF propagation paths than the deep water in the middle of the lake. Figure 2 shows the topographic and bathymetric features in the test area. Figure 3 shows the locations of the sources and the measurement array.

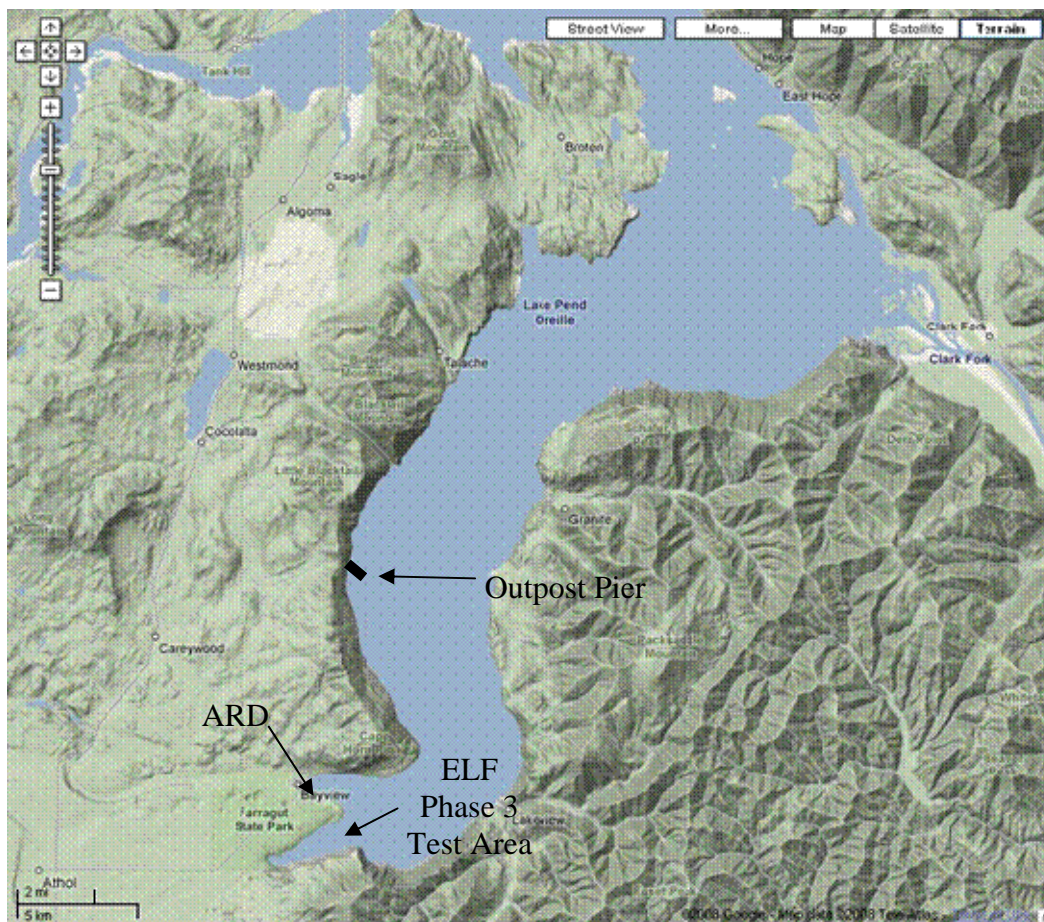


Figure 1 Lake Pend Oreille

ELF Phase III Test 1 Test Record

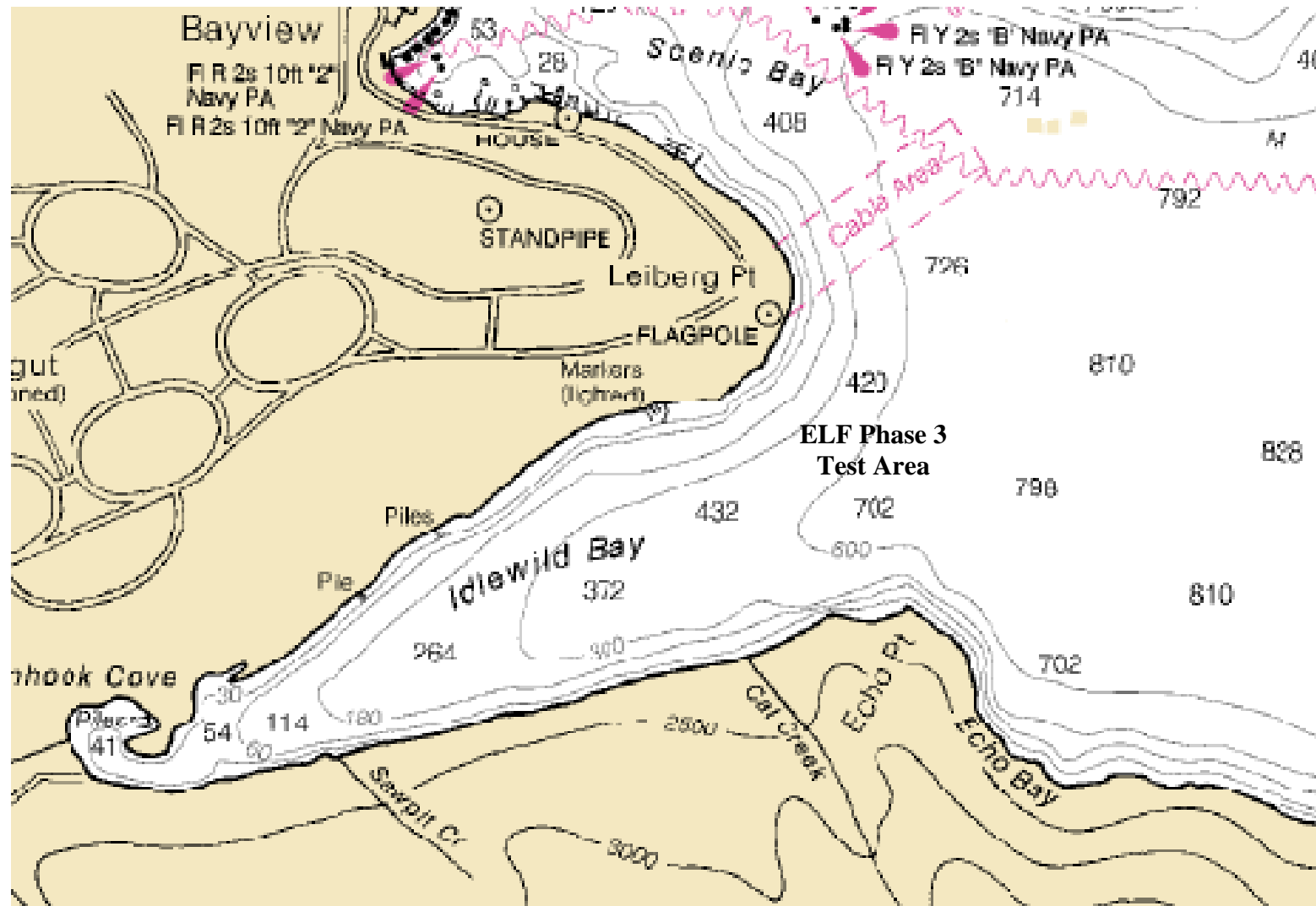


Figure 2 Topographical Map of Test Area

ELF Phase III Test 1 Test Record

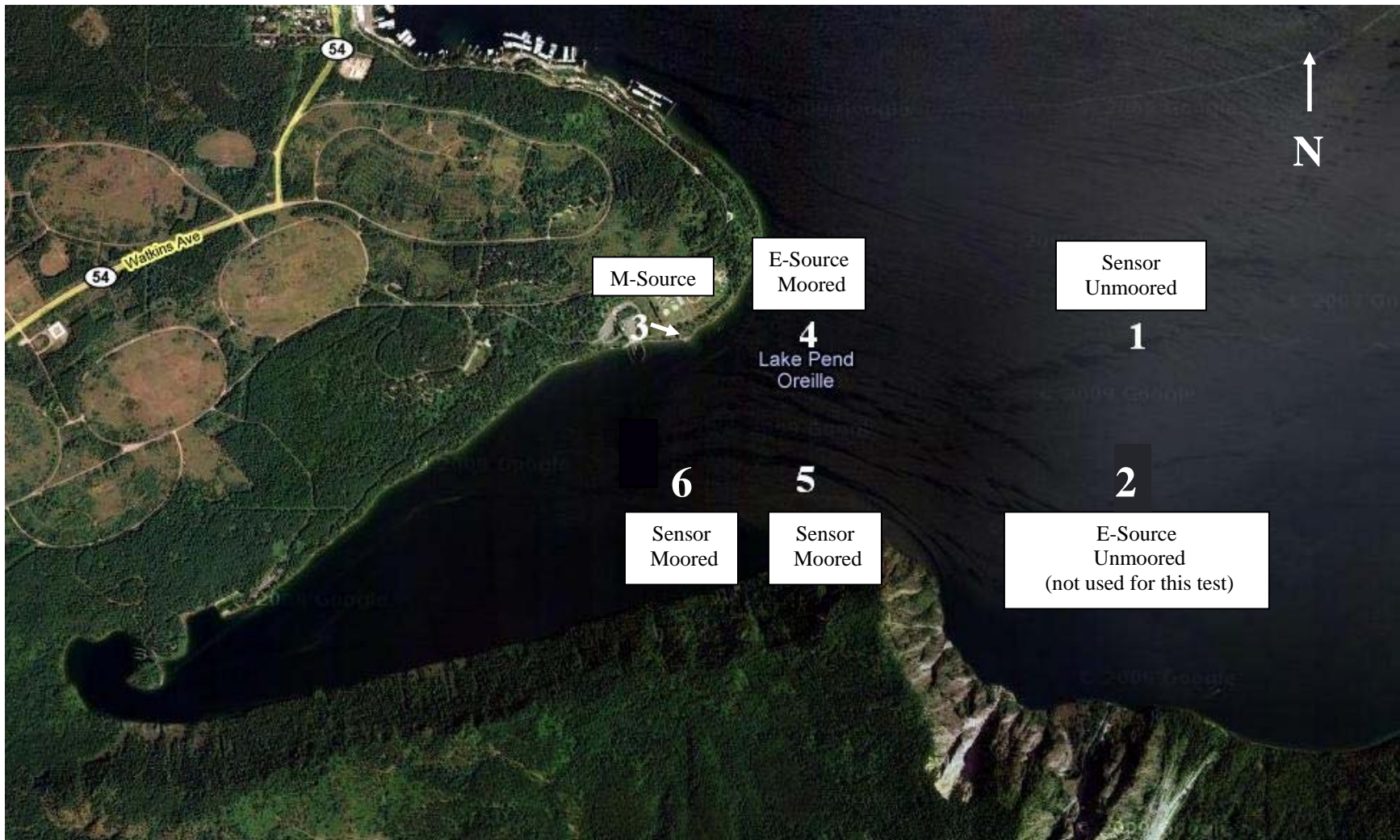


Figure 3 Source and Sensor Locations

The numbers in Figure 3 correspond to the following locations:

1. Sensor Barge (unmoored)
 - a. Lat: 47° 57.9' N
 - b. Long: 116° 31.3' W
2. Electric Source Barge (unmoored, not used for this test)
 - a. Lat: 47° 57.6' N
 - b. Long: 116° 31.3' W
3. Magnetic Source (on-shore)
 - a. Lat: 47° 57.892' N
 - b. Long: 116° 32.549' W
4. Electric Source Barge (moored)
 - a. Lat: 47° 57.9' N
 - b. Long: 116° 32.0' W
5. Sensor Barge (moored)
 - a. Lat: 47° 57.7' N
 - b. Long: 116° 31.9' W
6. Sensor Barge (moored)
 - a. Lat: 47° 57.5' N
 - b. Long: 116° 32.5' W

7.2. LAKE ENVIRONMENTAL PARAMETERS

The lake was formed by glaciers cutting through the mountains resulting in steep sides forming a 'V' made of bedrock. Over time the bottom of the 'V' filled with silt resulting in a present day flat bottom of approximately 1100 ft.

The conductivity of the lake water is a consistent 0.018 S/m throughout the water column. A sample of lake bottom muck from an anchor resulted in a measured conductivity of 0.012 S/m. The conductivity of the bedrock is unknown. The depth of the silt is estimated to be hundreds of feet.

7.3. GPS SYSTEM

A Global Positioning System (GPS) was used to locate and to determine orientation of the e-source barge, the m-source, and the barge. ELF testing required that high accuracy (RTK) positioning of the sources and the sensor be measured. The GPS system consisted of a base station located at the Outpost (N 48.08100726 deg, W 116.52802104 deg), radio links and repeaters to send

corrections to the GPS rover antennas, and two GPS rovers each equipped with two antennas.

During calibration tests, one GPS rover with dual antennas was mounted on the 25' fiberglass source boat. During the electric source tests, one GPS rover with dual antennas was mounted to the electric source barge (60' Barge). During the magnetic source tests, one GPS rover with dual antennas was used to locate the magnetic source (on-shore). During all tests, one GPS rover with dual antennas was mounted to the sensor barge (Scow). A block diagram of the GPS system for the source and the sensor barge is shown in Figure 4.

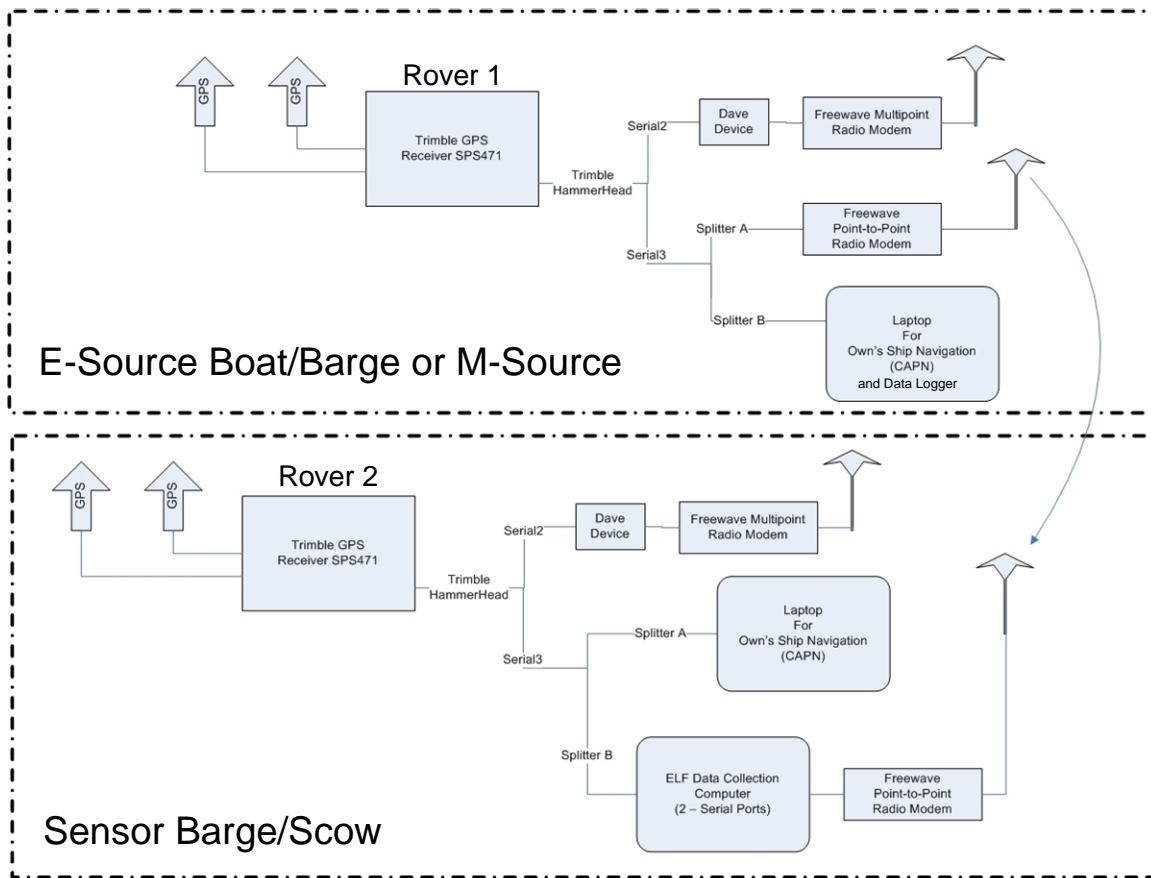


Figure 4 GPS System Diagram

Rover 1 was used to locate the source being used: calibration, e-source, or m-source. Rover 2 was always used on the sensor barge. Figure 5 depicts the layout of the source/sensor in relation to the position and heading antennas on the barges.

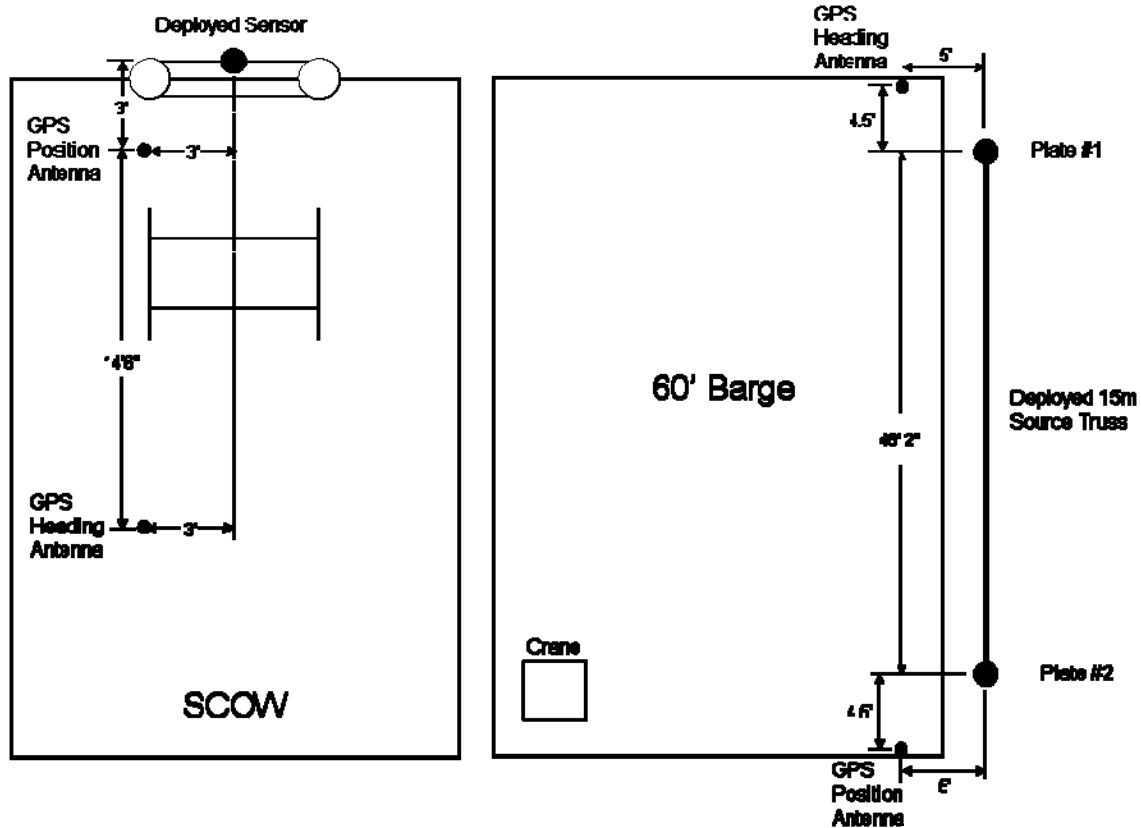


Figure 5 GPS Antennas on Barges

The source boat/barge and the sensor barge were configured with two radio modems. The first modem (Multipoint Mode) was used to communicate with the base station at the Outpost and receive CMR corrections (necessary for RTK accuracy). The second modem (Point-to-Point Mode) communicated directly with the other barge/source platform. The source boat/barge was configured to send its GPS position to the sensor barge. Hence, the sensor barge tracked both its real-time GPS position and also the position of the source boat/barge. Figure 6 is a picture of the GPS equipment as it was configured on the sensor barge.



Figure 6 GPS Equipment Set-up on Sensor Barge

The Outpost also received GPS data from each boat/barge and stored it on the GPS server at the ISMS Range Operations Center (ROC). Three NEMA sentences were output by each GPS system; GGA, RMC, and HDT. An example of this output is shown in Table 1.

Table 1 GPS Output

NEMA OUTPUT SENTENCES for ELF GPS Receivers	
\$GPGGA,203324.00,4758.34570360,N,11632.31337203,W,4,07,1.4,646.937,M,-16.880,M,4.0,0000*79	
\$GPHDT,154.064,T*37	
\$GPRMC,203324.00,A,4758.34570360,N,11632.31337203,W,27.208,152.686,080110,15.5349,E,D*1D	

7.4. MAGNETIC AND ELECTRIC SOURCES

7.4.1. Calibrated Electric Source

The calibrated electric source consisted of two, 2' by 1', copper electrodes mounted to the bottom of a 25' fiberglass boat with a 4m separation. The

locations of the electrodes relative to the GPS antennae are as shown in Figure 7. A photo of a single electrode is shown in Figure 8.

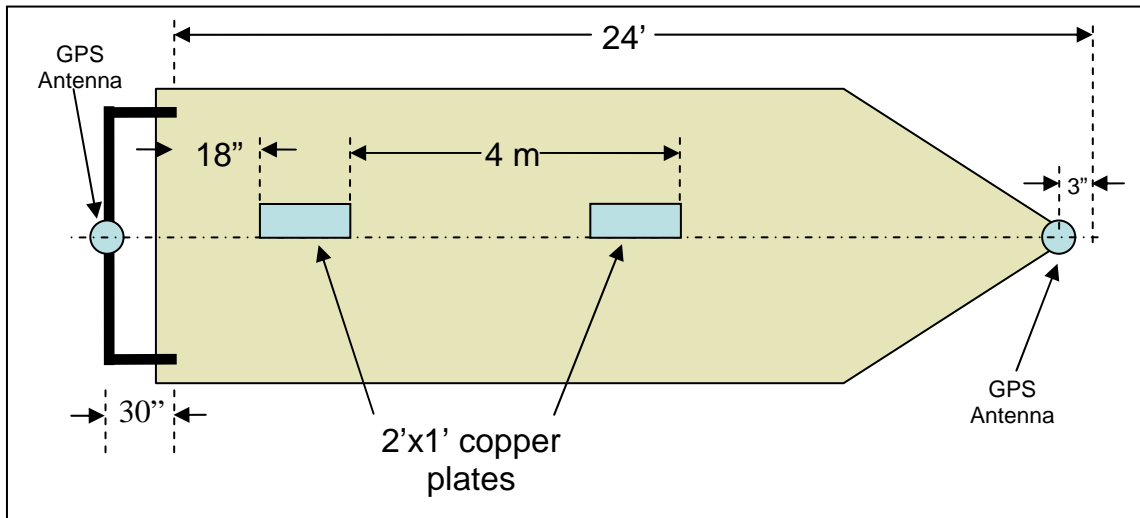


Figure 7 Calibrated Source Boat



Figure 8 Calibrated Electric Source Electrode

With the boat at rest, the angle (athwart ships) from horizontal of the forward plate was 35 degrees and the angle from horizontal of the aft plate was 18 degrees. The plates were within 2 degrees of horizontal in the fore/aft direction. Both plates are on the port side of the boat just outboard of the keel.

ELF Phase III Test 1 Test Record

orientation up to a depth of 500'. E-source deployment was in accordance with ELF-OP-001, "ELF Portable E-Source Array and Electromagnetic Sensor Deployment Procedure". Figure 10 shows the details of the portable e-source.

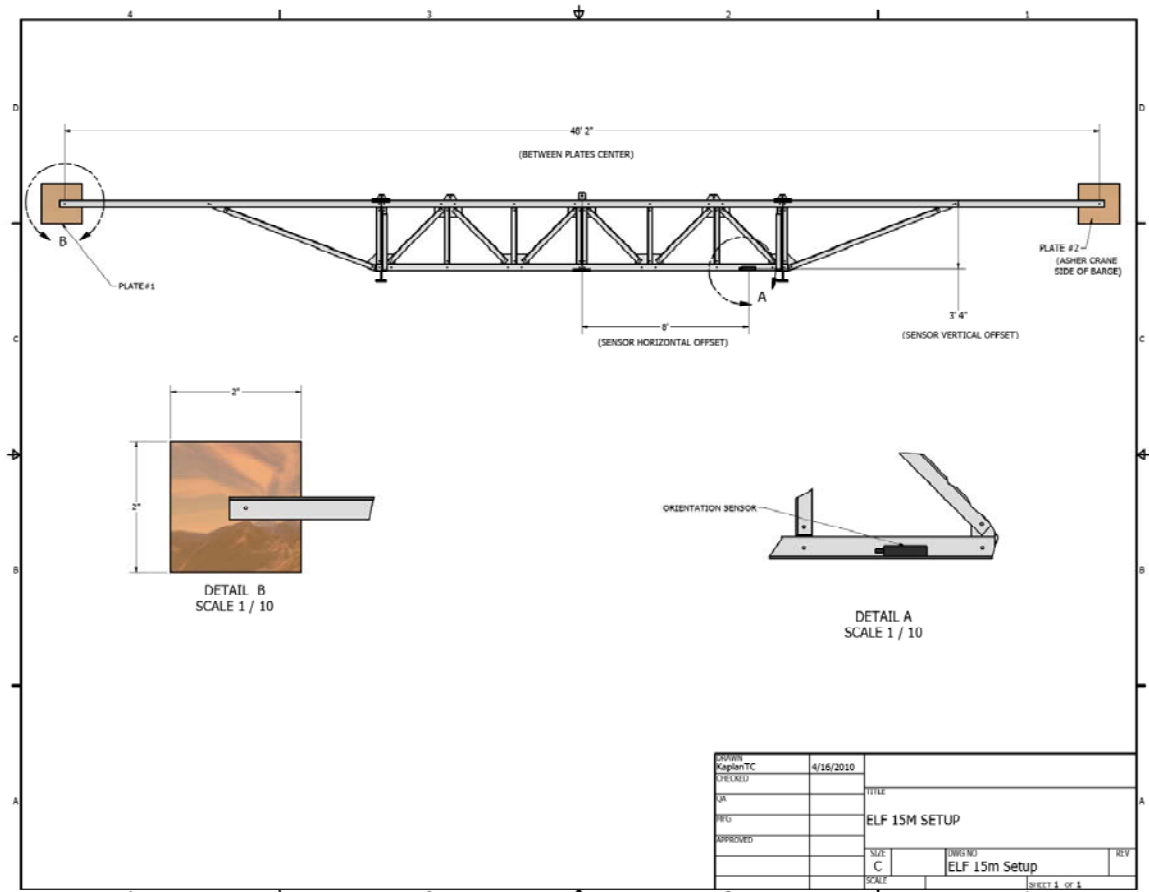


Figure 10 Portable Electric Source

The orientation of the electric dipole moment was determined from the dual channel GPS receiver mounted to the deployment barge and the orientation package mounted on the electric source truss.

The layout of the 60' Barge for the e-source is shown in Figure 11.



Figure 11 60' Barge Layout (E-Source)

7.4.2.1. Electric Source Drive and Control

The electric source was driven by a Techron LVC 5050 linear amplifier controlled by a function generator as shown in Figure 12. Shunt values were monitored and recorded by onboard personnel to ensure that the desired current was being driven to the source.

A National Instruments data logging system was used to record current, waveform, GPS messages, and information from the orientation package on the source. Measurements were GPS time-stamped for correlation to the measurements at the portable measurement array.

ELF Phase III Test 1 Test Record

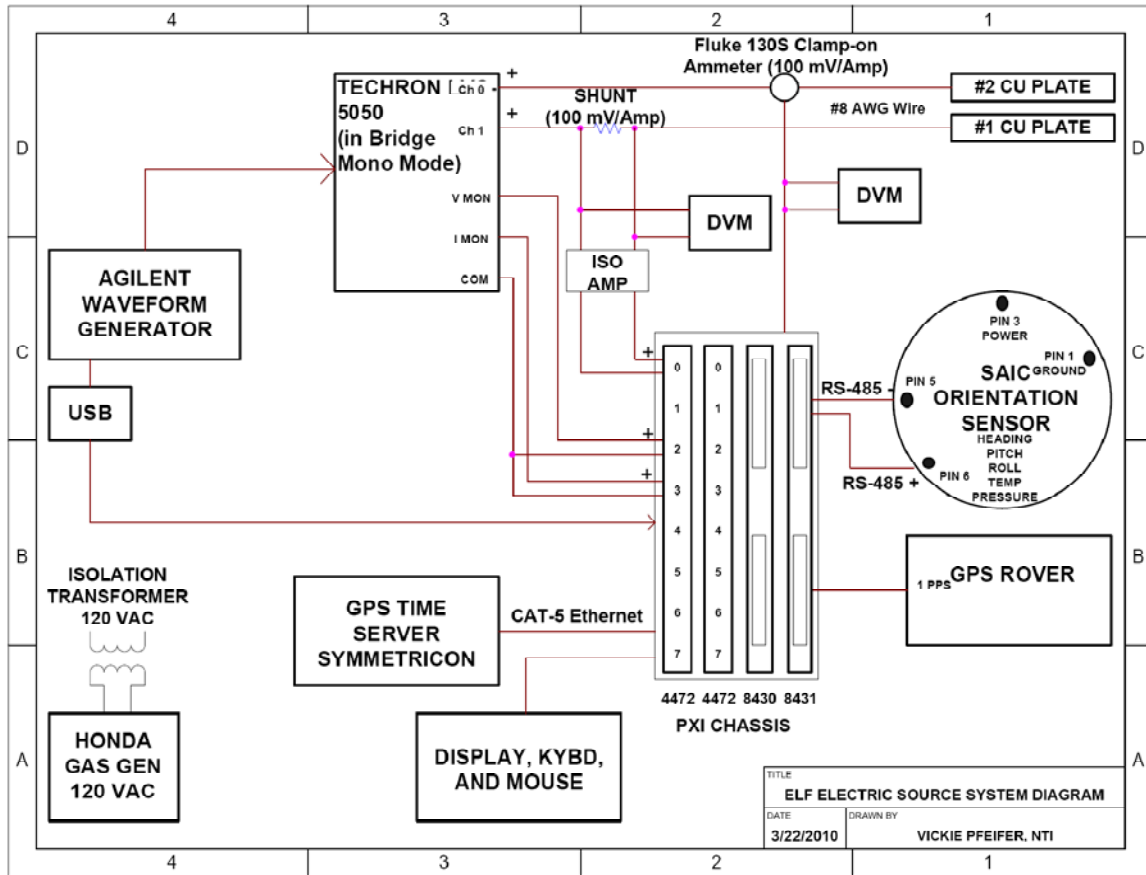


Figure 12 Electric Source System Diagram

7.4.3. Magnetic Source

The magnetic source was located on-shore at Farragut State Park (Location 3 on Figure 3, just east of the Eagle Boat Launch). The source was oriented both horizontally and vertically. A description of the horizontal and vertical orientations of the magnetic source can be found in Appendix B, “Test Run Record”, page B-23. The magnetic source was a ~2400 amp-m² coil on a 12' x 12' wooden frame. It had 12 turns and used ~15 amps of current. To reduce inductance, the turns were concentric and three 10 microfarad capacitors were added (two in series, one in parallel). A picture of the magnetic source is shown in Figure 13.

ELF Phase III Test 1 Test Record



Figure 13 Magnetic Source

A picture of the magnetic source at the shore location is shown in Figure 14.



Figure 14 Magnetic Source at Shore Location

Figures 15 and 16 depict the layout of the GPS antenna(s) in relation to the magnetic source for the horizontal and vertical dipole orientations.

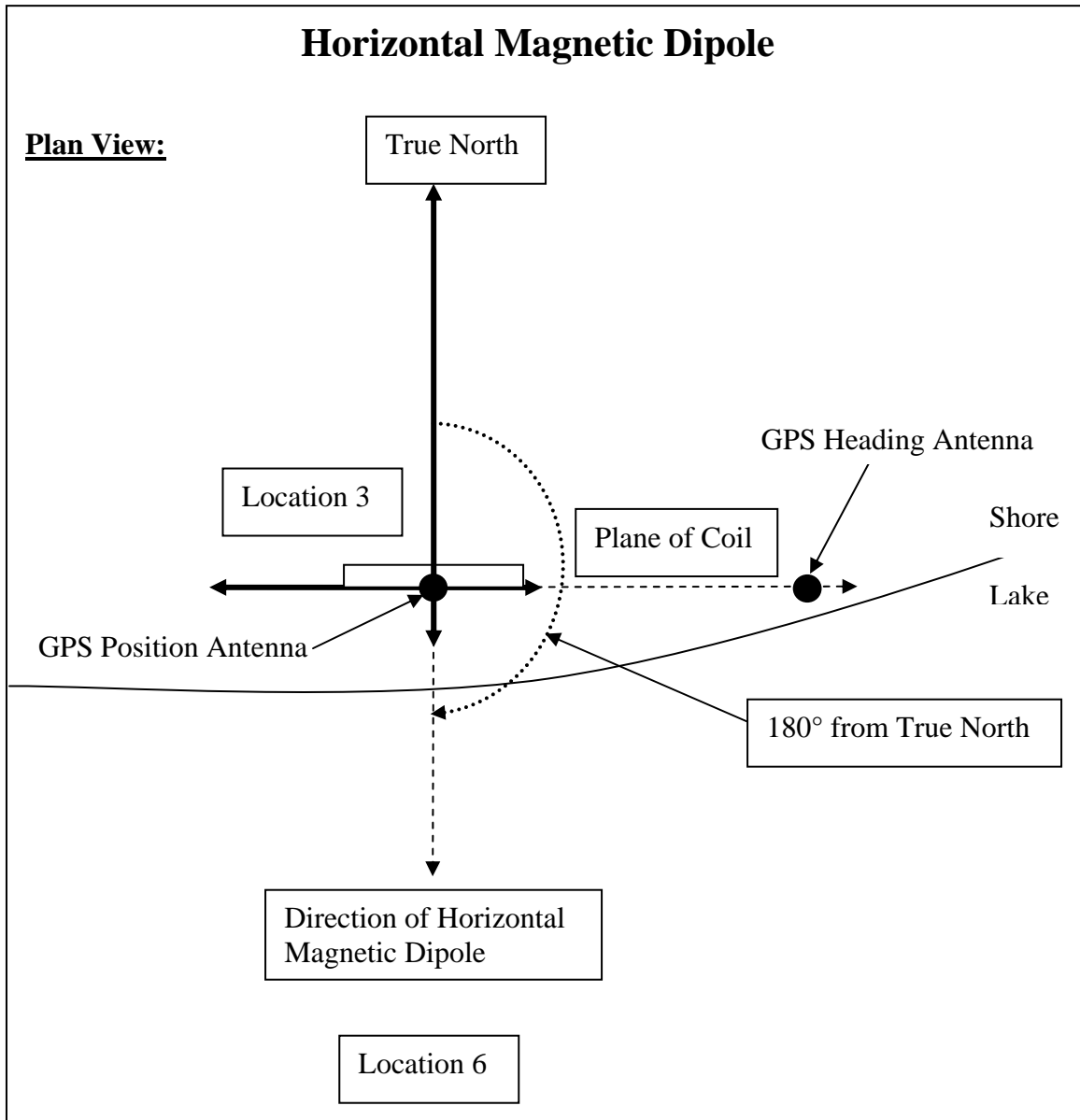


Figure 15 Magnetic Source GPS Layout - Horizontal

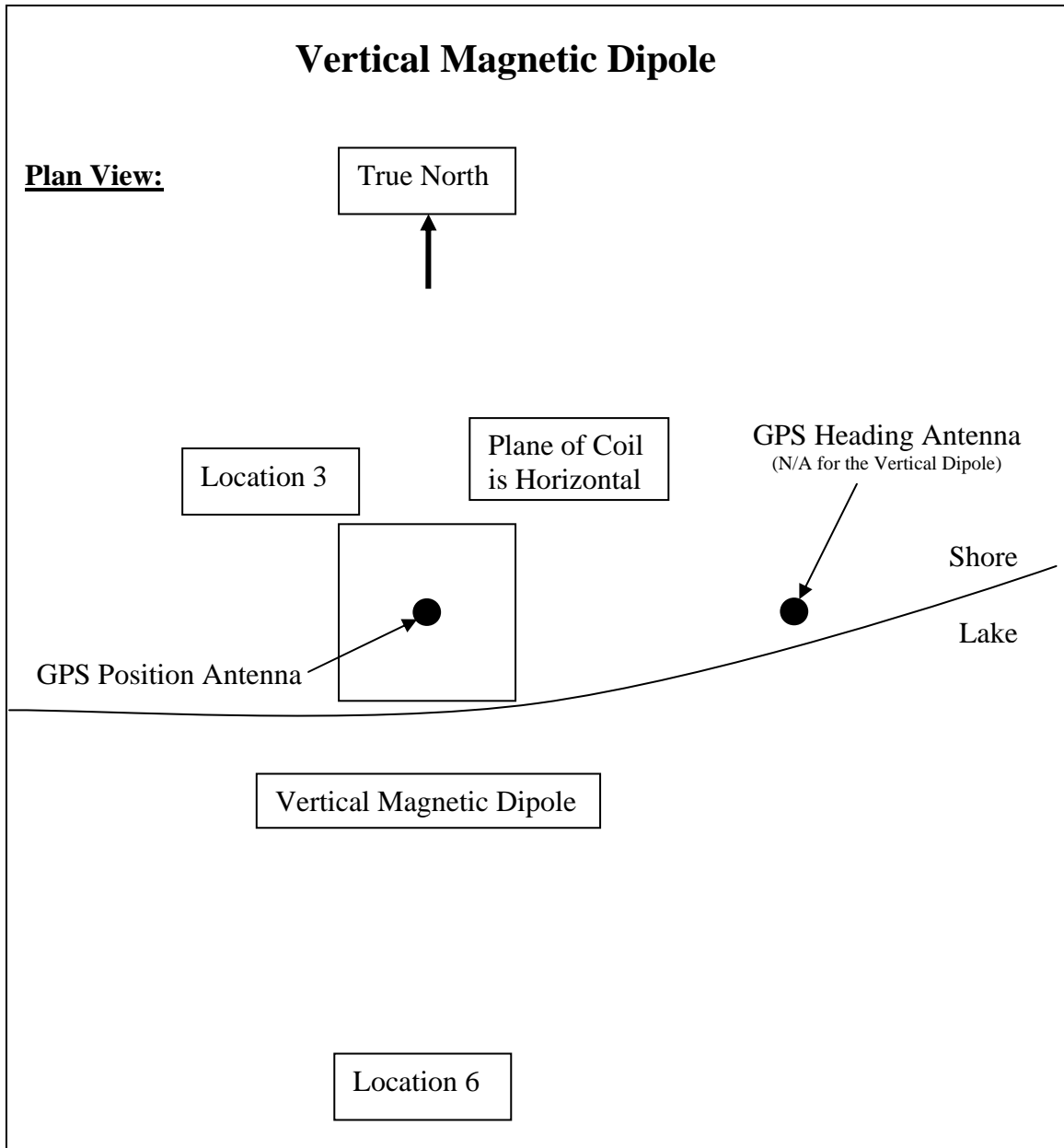


Figure 16 Magnetic Source GPS Layout – Vertical

7.4.3.1. Magnetic Source Drive and Control

The magnetic source was driven by a Kepco 20-20 Bipolar Amplifier for frequencies up to 120 Hz and a Techron LVC-5050 Amplifier for frequencies up to 1 kHz. The Code 75 CDAQ system was used to record current, waveform, and GPS information. Figure 17 shows a system diagram for the magnetic source.

ELF Phase III Test 1 Test Record

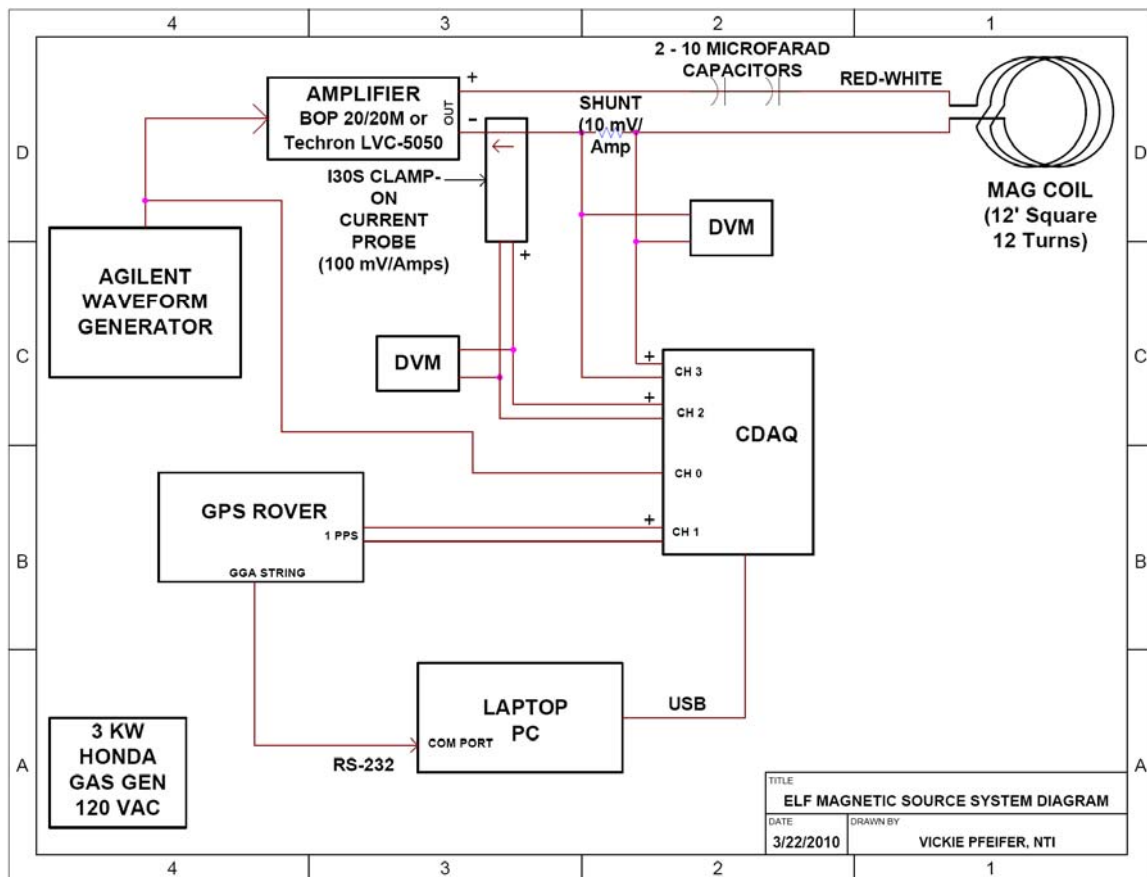


Figure 17 Magnetic Source System Diagram

7.5. PORTABLE ELECTRO-MAGNETIC MEASUREMENT ARRAY (PEMA)

The portable measurement array consisted of tri-axial magnetic and electric field sensors. Figure 18 is an arrangement drawing of the sensor. The technical specifications for the sensor are detailed in Appendix C.

Figure 18 Portable EM Array Drawing



ELF Phase III Test 1 Test Record

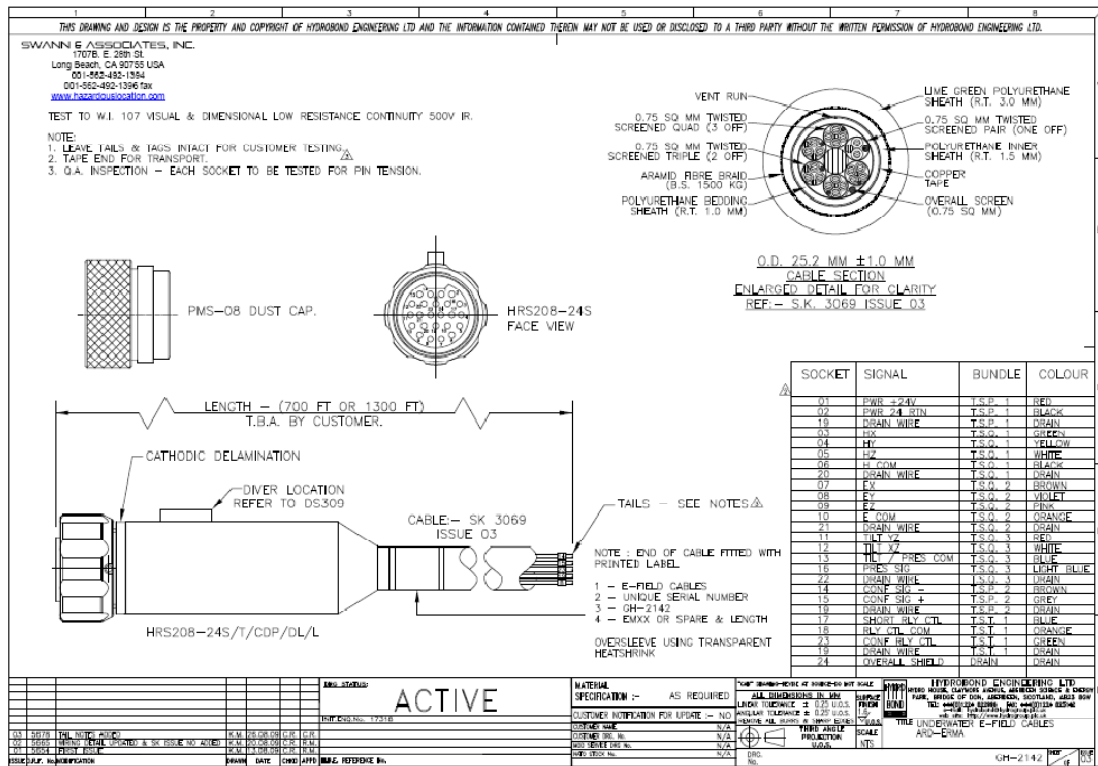


Figure 20 Wiring Diagram – Sensor Underwater E-field Cable

Tilt and depth sensors were incorporated into the unit. Results of tilt testing on the sensor at Carderock are detailed in Appendix D. Prior to deployment, calibration tilt measurements were conducted in the MESF at the ARD (see Figure 21). The results of the measurements are listed in Appendix E.

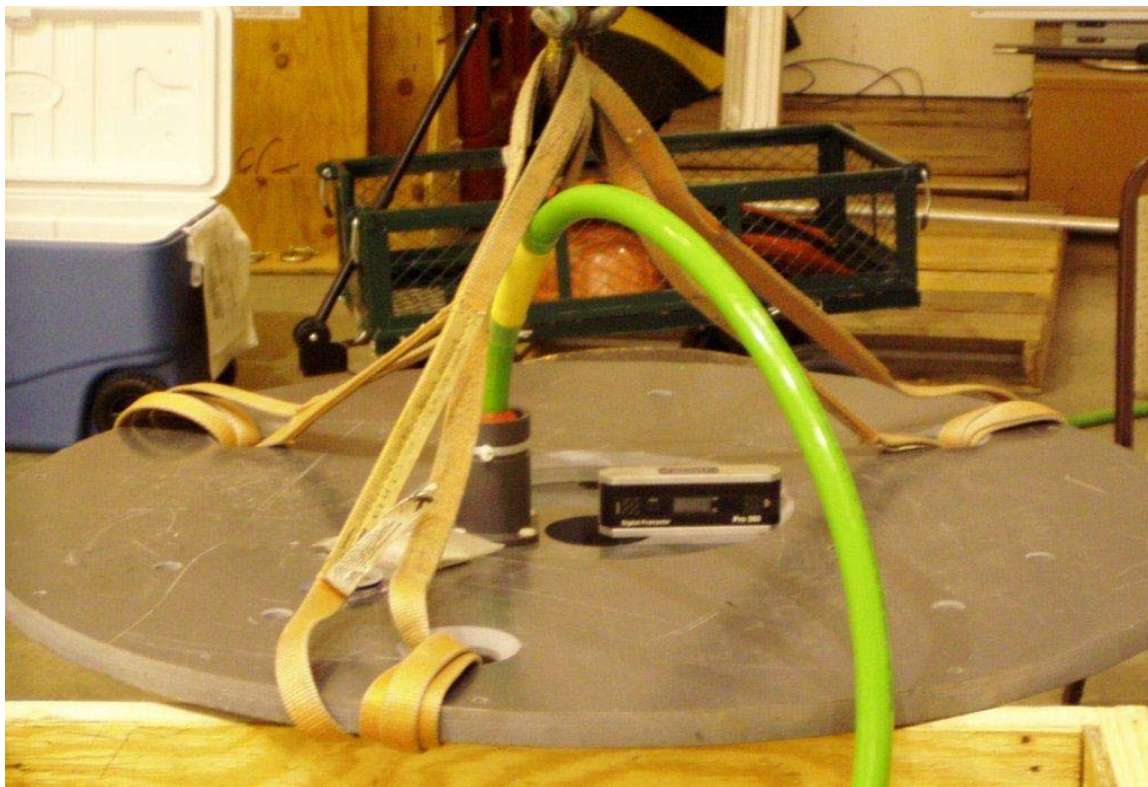


Figure 21 Portable EM Array Tilt Test in MESF

The array was deployed from the Scow (a self-propelled barge) and rigged to be suspended in the water at various depths up to 500'. The sensor was deployed upside down for all tests as shown in the Figure 22 pictures.

ELF Phase III Test 1 Test Record

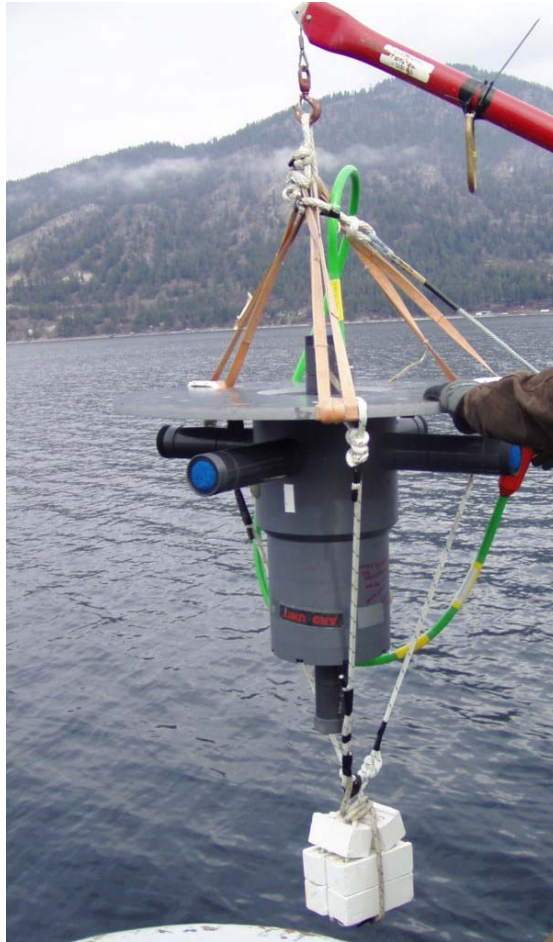


Figure 22 Portable EM Array Deployment

A dual channel GPS rover unit with two antennas was located on the barge to record position and heading as shown in Figure 5. The layout of the Scow (sensor barge) is shown in Figure 23.

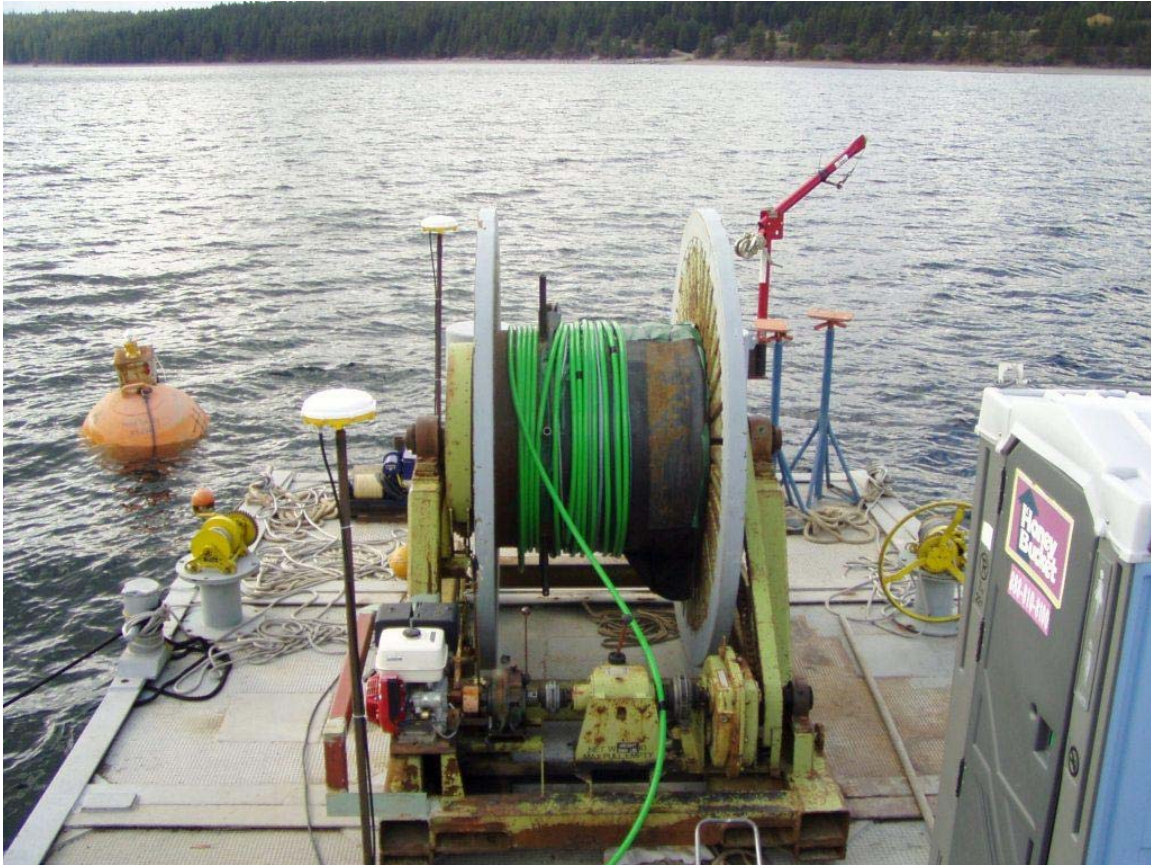


Figure 23 Scow (Sensor Barge) Layout

7.6. DATA ACQUISITION

The portable measurement array (PEMA) data acquisition system was comprised of National Instruments equipment located on the 28' Almar boat tied alongside the Scow. Analog data lines were cabled to the data acquisition system on the surface, so no pressure vessel was required. Data channel assignments used during the tests are listed in Table 2.

ELF Phase III Test 1 Test Record

Table 2 CDAQ PEMA Channel Assignments

Channel	Measurements
0	H_x
1	H_y (-y)
2	H_z (-z)
3	E_x
4	E_y (-y)
5	E_z (-z)
6	T_{x-z} (within x-z plane)
7	T_{y-z} (within y-z plane)
8	Pressure
9	1PPS
10	High Gain EG&G PARC Model 113 Pre-Amp (magnetic source only)
11	Empty
12	Empty
13	Empty
14	Empty
15	Empty

Figure 24 is a system diagram for the sensor and the data acquisition system.

ELF Phase III Test 1 Test Record

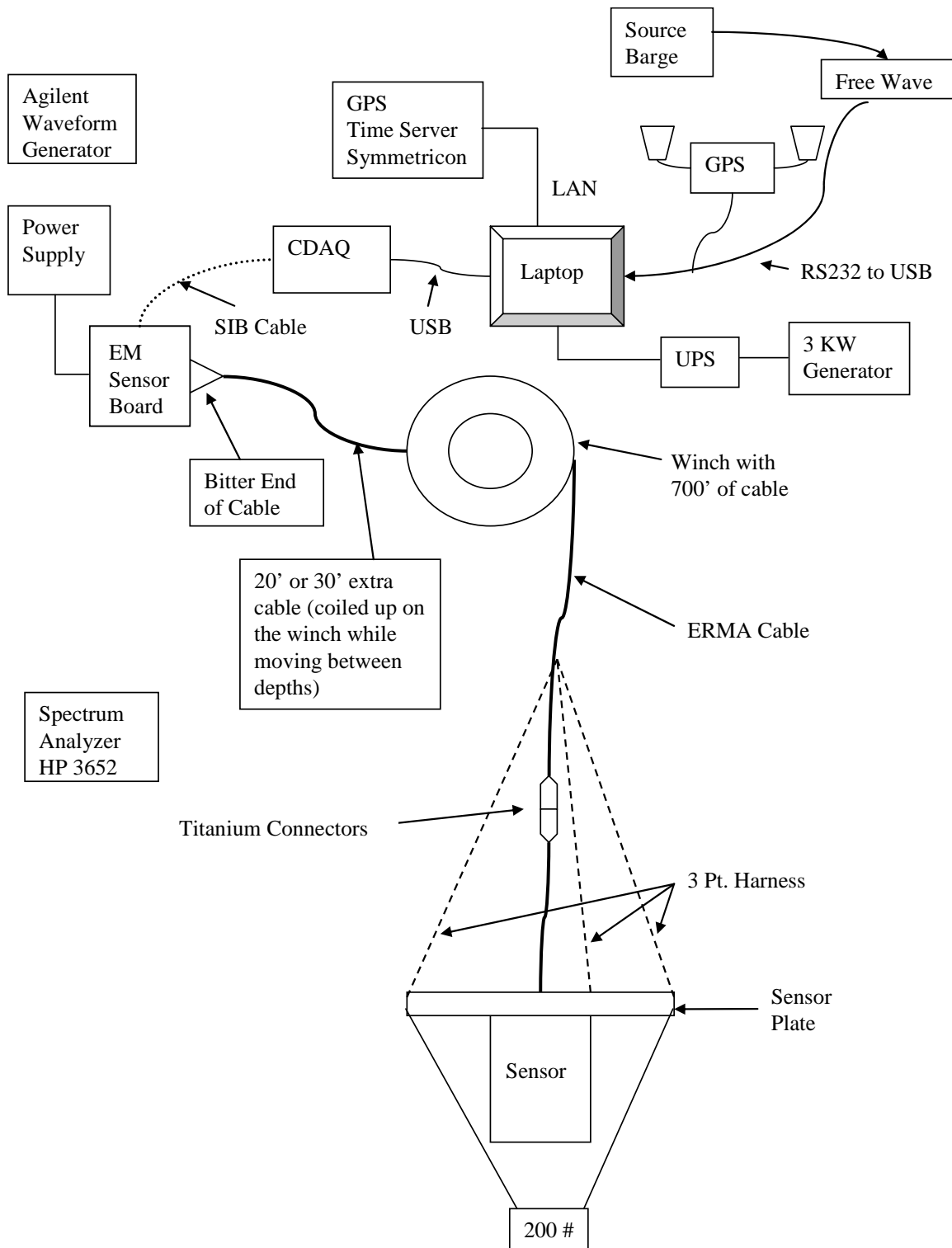


Figure 24 Sensor and Data Acquisition System Diagram

ELF Phase III Test 1 Test Record

The channel conversion factors for the data acquisition system were as follows:

- E-F gain factor – 10 mVolts input on the electrode arm pair (1 meter separation) yields 10 volts into A/D.
- Magnetometer scale factor – 100,000 nT field yields 10 Volts into A/D
- Pressure sensor (when it functioned correctly for the first half of test) – 0 Volts = 0 psi (gage), 5 volts = 500 psi or 1150 feet (gage).
- Tilt sensor – 35 mV per degree, nominal 2.5 V = zero tilt.

The gain was set at 1000 for the two magnetic runs when one magnetic axis channel (x) was amplified (run numbers 0407 and 4303 in Appendix B) and recorded on Channel 10 of the CDAQ. The gain was set at 100 for the other magnetic runs where the electric axes channels were amplified individually (marked by x, y, or z after the run number in the run tables for the magnetic tests in Appendix B) and recorded on Channel 10 of the CDAQ.

The sampling rate was 6.25 KHz. The number of samples per data file is listed below:

- 03-05-10 (Day 1): 2000 samples per ELFBIN file
- 03-08-10 (Day 2): 5000 samples per ELFBIN file
- 03-09-10 (Day 3): 5000 samples per ELFBIN file
- 03-10-10 (Day 4): 2000 samples per ELFBIN file
- 03-11-10 (Day 5): 5000 samples per ELFBIN file

GPS messages from up to 4 locations were recorded:

- Source platform rover (2 antenna) – sent to sensor platform via radio link
- Sensor platform rover (2 antenna)
- RTK corrections received from base station on Outpost Pier

8. TEST SITE OPERATIONS

8.1. OPERATIONS TEAM

Personnel assignments are listed in Table 3. The personnel listed in Table 3 were assigned the senior level responsibility for their task areas.

Table 3 Personnel Assignments

Program Test POC	Alan Griffitts
ELF Technical Director (C/7510)	Chris Burgy
ELF Trial Engineers (C/7510)	Dan Lenko, Brian Glover, Don Waltman, Rafael Hill
ARD Test Director	Frank Jurenka
ARD Mechanical Engineer	Tom Tupper
ARD Lake Operations	Tony Travis
ARD Barge Moorings	Jim Baxter
ARD GPS	Duane Nightingale
ARD Electronics Technician	Jeanne Hom
Operations Support Contractor	Toby Kaplan, Lead Engineer

The ARD Test Director was responsible for the overall safe conduct of the test and the execution of the test plan. The ARD Test Director ensured proper coordination and execution of all ARD efforts. The ELF Technical Director was responsible for technical issues, checking the quality of data being collected, and making judgment calls regarding technical changes to the run plan.

8.2. MOORING PLAN

Temporary moors were set up prior to testing. Mooring was in accordance with ELF-OP-002, "Mooring Procedure".

A 45' barge was moored at the e-source site (Location 4 on Figure 3) as shown in Figure 25. The 60' e-source barge docked up to the mooring barge (see Figure 26). This allowed the e-source barge to change orientation as required in the test run plan. This was a "soft" moor so weather conditions were monitored during testing.

ELF Phase III Test 1 Test Record



Figure 25 45' Mooring Barge



Figure 26 60' E-Source Barge Moored

Mooring anchors were pre-positioned at the sensor sites (Locations 5 and 6 on Figure 3). There were two anchors at each site for mooring the sensor barge. Pictures of the sensor barge moored at Location 6 are shown in Figure 27.

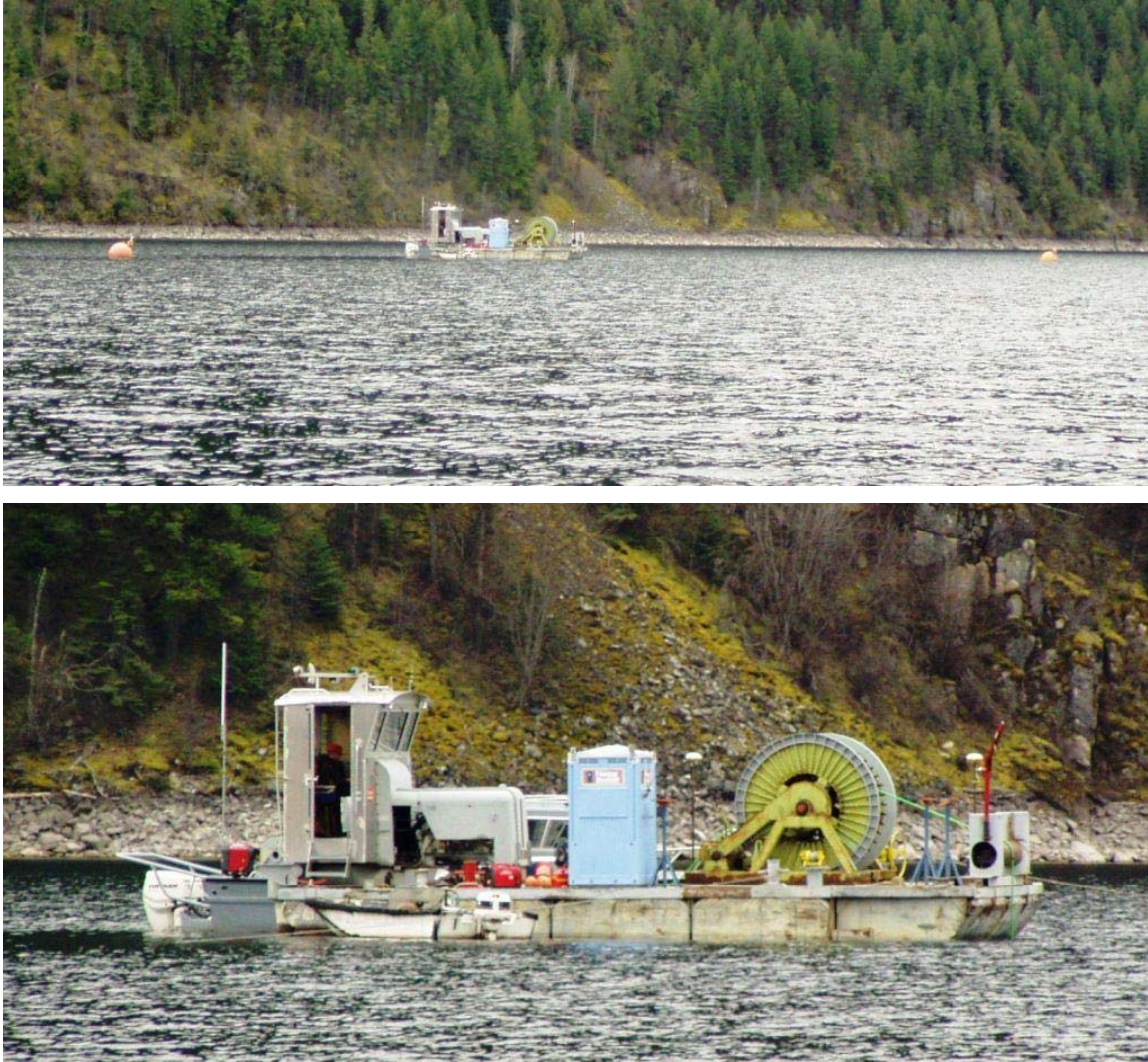


Figure 27 Sensor Barge Moored at Location 6

8.3. OPERATING PROCEDURES

Mooring of the PEMA and e-source barges were in accordance with ELF-OP-002, "Mooring Procedure". PEMA and portable e-source deployments were in accordance with ELF-OP-001, "ELF Portable E-Source Array and Electromagnetic Sensor Deployment Procedure".

Table 4 lists the ARD base radio call signs that were used for this test.

Table 4 ARD Base Radio Call Signs

Description	Function	Call Sign
28' Almar	EM Sensor Measurement	A-21
25' Whaler	4 M E-source and M-source	A-32
60' Barge	Portable E-source Deployment and Data Logging	A-67
Scow	EM Sensor Deployment and Positioning	A-29
ISMS Tug	60' Barge Transit and Positioning	A-14
ISMS ROC	GPS Data Collection (back-up)	A-44

8.4. EMERGENCY PROCEDURES

All personnel followed safety and emergency procedures detailed in ARDINST 5100.4B, "Operation of Watercraft on Lake Pend Oreille" and ARDINST 5100.5 "ARD Safety Rules Handbook".

9. TEST RUN PLAN EXECUTION

The run plan included noise measurements, calibrated electric source runs to verify proper operation of the entire system, and the ELF runs designed to exercise the models. A total of 233 measurements were taken over five days of testing. General descriptions of the various runs are given below and the executed run plan can be found in Appendix B. Appendix F contains the hand recorded magnetic, tilt, and pressure data logs from the sensor during the tests. Appendix G is the trip report generated by Carderock after the conclusion of the test.

9.1. NOISE MEASUREMENTS

Noise measurements were collected at the beginning, end, and during each test day. No sources were energized during data collection and the measurements were used to quantify the environmental and system noise. Noise measurements were taken with the sensor at each test depth (50', 250', and 500', or ~40' from the bottom of the lake) at the location of that day's testing. 22 noise measurements were taken over the five days of testing.

9.2. CALIBRATED SOURCE RUNS

Calibrated source runs were conducted on Day 1. The portable measurement array (sensor) was unmoored near Location 1. The 25' boat cal-source runs were made near the array with source parameters that were expected to result in EM fields that can be predicted by analytical models that are not reliant on topography. These tests verified that the entire process (source levels, sensors, data acquisition, GPS, etc.) was operating as expected.

1. Conducted a noise run with source boat on a N/S heading at 100' offset location (source not energized)
2. Source energized for sensor calibration
 - a. Verified location of sensor and proper GPS operation
 - b. N/S and E/W headings at various offsets
 - c. Frequency sweep (DC, 1 Hz, 10 Hz, 100 Hz, 1000 Hz)
 - d. 26 measurements

For the calibration runs, the sensor barge was unmoored near Location 1 and the sensor was deployed at depths of 50' and 410'.

9.3. ELF RUNS

The ELF runs consisted of an extensive series of measurements to be used to exercise the numerical models developed by UI. They included measurements with the portable electric source at Location 4, at depths up to 500', and with the magnetic source (horizontally and vertically) at the on-shore location at Farragut State Park (Location 3). The run plan contained both transverse and longitudinal orientations for the e-source. The data was collected with the portable measurement array deployed at Locations 1, 5, and 6 and depths up to 500'.

9.3.1. Electric Source Runs

The electric source runs occurred in various configurations as follows:

1. (Day 2, Day 4) Sensor barge moored at Location 6. E-source barge moored at Location 4.

ELF Phase III Test 1 Test Record

- a. Multiple source and sensor depths: 50', 250', 500' (or 40' from the bottom of the lake).
 - b. ~2.5 amp source current
 - c. Frequency sweep (DC, 10 Hz, 100 Hz, 1000 Hz)
 - d. N/S and E/W source orientations
 - e. Source tilted 30° for 4 measurements
 - f. 68 measurements
2. (Day 3) Sensor barge moored at Location 5. E-source barge moored at Location 4.
 - a. Multiple source and sensor depths: 50', 250', 500' (or 40' from the bottom of the lake).
 - b. ~2.5 amp source current
 - c. Frequency sweep (DC, 10 Hz, 100 Hz, 1000 Hz)
 - d. N/S and E/W source orientations
 - e. 73 measurements
3. (Day 4) Sensor barge unmoored near Location 1. E-source barge moored at Location 4.
 - a. Multiple source depths: 50', 250', 500' or 40' from the bottom.
 - b. Sensor depth: 500'
 - c. ~2.5 amp source current
 - d. Frequency sweep (DC, 10 Hz, 100 Hz, 1000 Hz)
 - e. N/S source orientations
 - f. 12 measurements

9.3.2. Magnetic Source Runs

1. (Day 5) Sensor barge moored at Location 6. M-source at Location 3.
 - a. Sensor depths: 50', 250'
 - b. Frequency: 100 Hz, 1000 Hz
 - c. Vertical and horizontal source orientations
 - d. 27 measurements

2. (Day 5) Sensor barge moored at Location 6 and then motoring toward Location 3. M-source at Location 3.
 - a. Sensor depth 7' above the water surface.
 - b. 1000 Hz
 - c. Vertical source orientation
 - d. 2 measurements

9.4. DATA REPORTING

Data reporting was the responsibility of Carderock and UI. Carderock performed a quick look analysis of the data during testing and released the data to UI at the end of the test period. All data were unclassified.

APPENDIX A: UI DATA ESTIMATES

The following tables contain the data for the four cases of interest: vertical magnetic dipole, horizontal magnetic dipole (facing sensor), horizontal electric dipole (parallel) and horizontal electric dipole (perpendicular). The data were obtained through simulations using the WSU analytical solution that treats the floor, water and air as a parallel, three layered medium. All sources are regarded as Hertzian dipole point sources. For each of the four source configurations mentioned above, four separate numerical experiments were conducted; sensor depth @ -150m at 100Hz, sensor depth @ -150m at 1000Hz, sensor depth @ -75m at 100Hz, sensor depth @ -75m at 1000Hz.

The values for $|E|$ and $|B|$ represent the total magnitudes of that respected field for distances of 650m and 965m radially outward from the source. The values of $|E|$ are in uV/m and the values for $|B|$ are in nT. The source strength for the magnetic sources was $2500 \text{ A}\cdot\text{m}^2$ and $45 \text{ A}\cdot\text{m}$ for the electric sources. Data values highlighted in blue correspond to field values that exceed the minimum specifications of 1 uV/m and 1 nT.

VERTICAL MAGNETIC DIPOLE

(WSU formulation using the VMD_inwater source @ $z = 0$, $2500 \text{ A}\cdot\text{m}^2$)

100Hz (sensor @ -150m)

	<u>650m</u>	<u>965m</u>
$ E $	0.243303	0.08256
$ B $	0.001248	0.00038

100Hz (sensor @ -75m)

	<u>650m</u>	<u>965m</u>
$ E $	0.26374	0.086781
$ B $	0.00128	0.000109

1000Hz (sensor @ -150m)

	<u>650m</u>	<u>965m</u>
$ E $	0.192149	0.019608
$ B $	0.000295	4.43E-05

1000Hz (sensor @ -75m)

	<u>650m</u>	<u>965m</u>
$ E $	0.253709	0.040254
$ B $	0.000444	7.93E-05

note:

$$|E| = \text{abs}(\sqrt{E_{\text{phi}}^2}) \quad \text{uV/m}$$

$$|B| = |u \cdot H| = \text{abs}(u \cdot \sqrt{H_{\text{rho}}^2 + H_z^2}) \quad \text{nT}$$

ELF Phase III Test 1 Test Record

HORIZONTAL MAGNETIC DIPOLE (facing sensor)

(WSU formulation using the HMD_inwater source @ z = 0, 2500 A*m^2)

100Hz (sensor @ -150m)

	650m	965m
E	0.257572	0.125369
B	0.001429	0.000597

100Hz (sensor @ -75m)

	650m	965m
E	0.333433	0.148744
B	0.001759	0.000721

1000Hz (sensor @ -150m)

	650m	965m
E	0.663989	0.166589
B	0.001178	0.000328

1000Hz (sensor @ -75m)

	650m	965m
E	1.122396	0.314052
B	0.002066	0.000603

note:

$$|E| = \text{abs}(\sqrt{E_x^2 + E_y^2 + E_z^2}) \quad \text{Uv/m}$$

$$|B| = |u \cdot H| = \text{abs}(u \cdot \sqrt{H_x^2 + H_y^2 + H_z^2}) \quad \text{Nt}$$

HORIZONTAL ELECTRIC DIPOLE (parallel to sensor)

(WSU formulation using the HED_inwater source @ z = -15, 45 A*m)

100Hz (sensor @ -150m)

	650m	965m
E	1.862854	0.43682
B	0.00265	0.001491

100Hz (sensor @ -75m)

	650m	965m
E	1.989009	0.442724
B	0.004896	0.00205

1000Hz (sensor @ -150m)

	650m	965m
E	0.345377	0.113212
B	0.000886	0.000209

1000Hz (sensor @ -75m)

	650m	965m
E	0.660227	0.210945
B	0.001419	0.000394

note:

$$|E| = \text{abs}(\sqrt{E_x^2 + E_y^2 + E_z^2}) \quad \text{uV/m}$$

$$|B| = |u \cdot H| = \text{abs}(u \cdot \sqrt{H_x^2 + H_y^2 + H_z^2}) \quad \text{nT}$$

HORIZONTAL ELECTRIC DIPOLE (perpendicular to sensor)

(WSU formulation using the HED_inwater source @ z = -15, 45 A*m)

100Hz (sensor @ -150m)

	<u>650m</u>	<u>965m</u>
E	2.318099	0.81593
B	0.010526	0.003774

100Hz (sensor @ -75m)

	<u>650m</u>	<u>965m</u>
E	2.521253	0.883139
B	0.011816	0.004359

1000Hz (sensor @ -150m)

	<u>650m</u>	<u>965m</u>
E	0.784554	0.222697
B	0.00156	0.000432

1000Hz (sensor @ -75m)

	<u>650m</u>	<u>965m</u>
E	1.390705	0.421061
B	0.002781	0.000799

note:

$$|E| = \text{abs}(\sqrt{E_x^2 + E_y^2 + E_z^2}) \quad \text{uV/m}$$

$$|B| = |u \cdot H| = \text{abs}(u \cdot \sqrt{H_x^2 + H_y^2 + H_z^2}) \quad \text{nT}$$

APPENDIX B: TEST RUN RECORD

DAY 1 – MARCH 5, 2010

Sensor unmoored near Location 1, drifting to the west. 25' source boat speed ~ 5 knots										
ELF Phase III Run Plan - Noise Runs										
Run #	Comex (Local Time)	Sensor	Sensor Depth (ft)	Source Type	Length (m)	Current (amps)	Freq (Hz)	Heading (degrees true)	Offset (ft)	Comments
0101	1118-1119	PEMA	50	None						Noise Run - 120 s
0102	1119-1120	PEMA	50	None						Noise Run - 120 s
0103	1120-1122	PEMA	50	None						Noise Run - 120 s
0104	1127-1129	PEMA	50	Elect - Hull	4	2	100	?		Source boat moored to scow, square and sine wave
0105	1151-1152	PEMA	50	Elect - Hull	4	1.8	100	?		Source boat moored to scow, sine wave, z channel clipping
0106	1159-1201	PEMA	50	None		Background	Background	?	100 West	Source boat CPA 100 ft.
0107	1203-1204	PEMA	50	Elect - Hull	4	1.7	10	?	100 West	Source boat CPA 100 ft.
0110	1206-1207	PEMA	50	Elect - Hull	4	1.7	100	?	100 West	Source boat CPA 100 ft. Water depth, 782 ft.

Notes:

Headings and offsets are approximate, verify using GPS data.

0855 Underway from the ARD

0930 At ELF1 location

1130 Sensor in water (50')

Day 1 measurements - 34

A/D Channels:

0 – V_{mon}

1 – I_{mon}

2 – Clamp on

3 – Shunt IV/IOA

Clamp on + current direction out to terminal (plate) 2

ELF Phase III Test 1 Test Record

Sensor unmoored near Location 1, drifting to the west. 25' source boat speed ~ 5 knots										
ELF Phase III Run Plan - Boat Calibration - Electric										
Run #	Comex (Local Time)	Sensor	Sensor Depth/ Water Depth (ft)	Source Type	Length (m)	Current (amps)	Freq (Hz)	Heading (degrees true)	Offset (ft)	Comments
1001	1218-1224	PEMA	50/760	Elect - Hull	4	1	DC	125	20 NE	Sensor Barge heading, 45°.
1002	1223-1225	PEMA	50/741	Elect - Hull	4	1	DC	303	10 NE	Sensor Barge heading, 38°.
1005	1228:45-1231	PEMA	50/700	Elect - Hull	4	1	DC	125	100 NE	Sensor Barge heading, 31°
1006	1233-1236	PEMA	50/670	Elect - Hull	4	1	DC	305	100 NE	Sensor Barge heading, 27°
1007	1335-1337	PEMA	50/839	Elect - Hull	4	1	DC	205	10 West	Sensor Barge heading, 3°
1008	1341-1344	PEMA	50/834	Elect - Hull	4	1	DC	?	10 East	Sensor Barge heading, 15°
1011	1351-1354	PEMA	50/826	Elect - Hull	4	1	DC	180	200 NE	Sensor Barge heading, 115°
1012	1356-1359	PEMA	50/823	Elect - Hull	4	1	DC	007	200 East	Sensor Barge heading, 137°

Notes:

Headings and offsets are approximate, verify using GPS data.
Relocated back near Location #1 after Run #1006.

ELF Phase III Test 1 Test Record

Sensor unmoored near Location 1, drifting towards the west.
25' source boat speed ~ 5 knots.

ELF Phase III Run Plan - Boat Calibration - Electric

Run #	Comex (Local Time)	Sensor	Sensor Depth/ Water Depth (ft)	Source Type	Length (m)	Current (amps)	Freq (Hz)	Heading (degrees true)	Offset (ft)	Comments
1101	1413-1415	PEMA	50/813	Elect - Hull	4	1	1	61	15 SE	Sensor Barge heading, 183°
1102	1406-1408	PEMA	50/820	Elect - Hull	4	1	1	235	10 SE	Sensor Barge heading, 137°
1103	1428-1431	PEMA	50/800	Elect - Hull	4	1	10	97	30 South	Sensor Barge heading, 203°
1104	1423-1425	PEMA	50/800	Elect - Hull	4	1	10	275	200 South	Sensor Barge heading, 191°
1105	1443-1445	PEMA	50/785	Elect - Hull	4	1	100	103	50 South	Sensor Barge heading, 183°
1106	1435-1438	PEMA	50790	Elect - Hull	4	1	100	287	20 South	Sensor Barge heading, 200°
1107	1451-1453	PEMA	50/780	Elect - Hull	4	1	1000	92	20 South	Sensor Barge heading, 172°
1108	1447-1449	PEMA	50780	Elect - Hull	4	1	1000	275	10 South	Sensor Barge heading, 184°

Notes:

Headings and offsets are approximate, verify using GPS data.

ELF Phase III Test 1 Test Record

Sensor unmoored near Location 1, drifting to the west.
25' boat speed ~ 5 knots.

ELF Phase III Run Plan - Boat Calibration - Electric

Run #	Comex (Local Time)	Sensor	Sensor Depth/ Water Depth (ft)	Source Type	Length (m)	Current (amps)	Freq (Hz)	Heading (degrees true)	Offset (ft)	Comments
1201	1514-1517	PEMA	410/774	Elect - Hull	4	1	1	222	10 East	Sensor Barge heading, 157°
1202	1519-1521	PEMA	410/776	Elect - Hull	4	1	1	048	10 East	Sensor Barge heading, 155°
1203	1522-1524	PEMA	410/777	Elect - Hull	4	1	10	222	10 East	Sensor Barge heading, 157°
1204	1524-1527	PEMA	410/777	Elect - Hull	4	1	10	050	50 East	Sensor Barge heading, 158°
1205	1528-1530	PEMA	410/777	Elect - Hull	4	1	100	234	10 East	Sensor Barge heading, 160°
1206	1532-1534	PEMA	410/777	Elect - Hull	4	1	100	065	25 East	Sensor Barge heading, 159°
1207	1535-1537	PEMA	410/774	Elect - Hull	4	1	1000	251	15 East	Sensor Barge heading, 162°
1208	1538-1540	PEMA	410/774	Elect - Hull	4	1	1000	073	50 East	Sensor Barge heading, 159°

Notes:

Locations, headings, and offsets are approximate, verify using GPS data.

Sensor unmoored near Location 1, drifting to the west.

ELF Phase III Run Plan - Noise Runs

Run #	Comex (Local Time)	Sensor	Sensor Depth (ft)	Source Type	Length (m)	Current (amps)	Freq (Hz)	Heading (degrees true)	Offset (ft)	Comments
0114	1540-1542	PEMA	50	None						Noise Run
0115	1542-1543	PEMA	50	None						Noise Run

ELF Phase III Test 1 Test Record

DAY 2 – MARCH 8, 2010

Sensor moored at Location 6. E-source barge moored at Location 4.										
ELF Phase III Run Plan - Noise Runs										
Run #	Comex (Local Time)	Sensor	Sensor Depth (ft)	Source Type	Orientation (degrees true)	Source Depth (ft)	Current (amps)	Freq (Hz)	Sensor/ Source Location	Comments
0204	1232-1234	PEMA	465	None					6/4	Noise Run - with source barge
0205	1214-1216	PEMA	250	None					6/4	Noise Run - with source barge
0206	1058-1060	PEMA	50	None					6/4	Noise Run - with source barge

Notes:

0745 Scow underway
 0830 60'Barge underway
 0900-1045 Setting up and troubleshooting
 1645 Sensor recovered
 1650 Source recovered
 Day 2 Measurements - 32

ELF Phase III Test 1 Test Record

Sensor moored at Location 6. E-source barge moored at Location 4.										
ELF Phase III Run Plan – Electric Source										
Run #	Comex (Local Time)	Sensor	Sensor Depth (ft)	Source Type 15m	Orientation (degrees true)	Source Depth (ft)	Current (amps)	Freq (Hz)	Sensor/ Source Location	Comments
2302	1437-1439	PEMA	465	Elect – truss	84	400	3	10	6/4	2.173 A _{rms}
2303	1440-1441	PEMA	465	Elect - truss	86	400	3	100	6/4	2.217 A _{rms}
2304	1443-1444	PEMA	465	Elect - truss	87	400	3	1000	6/4	2.184 A _{rms}
2305	1416	PEMA	465	Elect - truss	87	250	3	DC	6/4	3.22 A _{pk}
2306	1342-1344	PEMA	465	Elect - truss	87	250	3	10	6/4	2.16 A _{rms}
2306A	1349	PEMA	465	Elect - truss	87	250	3	10	6/4	2.161 A _{rms}
2307	1356-1358	PEMA	465	Elect - truss	92	250	3	100	6/4	
2308	1358-1400	PEMA	465	Elect - truss	90	250	3	1000	6/4	
2309	1244-1245	PEMA	465	Elect - truss	92	50	3	DC	6/4	Possible radio spikes in data.
2310	1248-1250	PEMA	465	Elect - truss	80	50	3	10	6/4	2.137 A _{rms} Possible radio spikes in data.
2311	1315-1317	PEMA	465	Elect - truss	80	50	3	100	6/4	2.22 A _{rms} Possible radio spikes in data.
2312	1320-1322	PEMA	465	Elect - truss	92	50	3	1000	6/4	2.18 A _{rms} Possible radio spikes in data.

Notes:

60' barge on north side of 45' barge. Long side to long side.

Truss deployed off north side of 60' barge.

Electrode 2 – Channel 1 output terminal

Electrode 1 – Channel 2 output terminal

@ 1000 Hz Iso Amp reads 4 A, not 3 A

Fluke 85 Clamp-on

Verify headings and locations using GPS and Orientation Sensor data.

ELF Phase III Test 1 Test Record

Sensor moored at Location 6.

E-source barge moored at Location 4.

ELF Phase III Run Plan – Electric Source

Run #	Comex (Local Time)	Sensor	Sensor Depth (ft)	Source Type 15m	Orientation (degrees true)	Source Depth (ft)	Current (amps)	Freq (Hz)	Sensor/ Source Location	Comments
2402	1547-1548	PEMA	240	Elect - truss	88	50	3	10	6/4	
2403	1545-1546	PEMA	240	Elect - truss	84	50	3	100	6/4	2.214 A _{rms}
2404	1543-1544	PEMA	240	Elect - truss	85	50	3	1000	6/4	2.179 A _{rms}
2406	1524-1526	PEMA	240	Elect - truss	92	250	3	10	6/4	2.160 A _{rms}
2407	1526-1528	PEMA	240	Elect - truss	83	250	3	100	6/4	2.209 A _{rms}
2408	1528-1530	PEMA	240	Elect - truss	88	250	3	1000	6/4	2.174 A _{rms}
2410	1510-1512	PEMA	240	Elect - truss	93	400	3	10	6/4	2.169 A _{rms}
2411	1506-1508	PEMA	240	Elect - truss	89	400	3	100	6/4	2.21 A _{rms}
2412	1504-1506	PEMA	240	Elect - truss	88	400	3	1000	6/4	2.181 A _{rms}

Notes:

60' barge on north side of 45' barge. Long side to long side.

Truss deployed off north side of 60' barge.

Verify headings and locations using GPS and Orientation Sensor data.

ELF Phase III Test 1 Test Record

Sensor moored at Location 6. E-source barge moored at Location 4.										
ELF Phase III Run Plan – Electric Source										
Run #	Comex (Local Time)	Sensor	Sensor Depth (ft)	Source Type 15m	Orientation (degrees true)	Source Depth (ft)	Current (amps)	Freq (Hz)	Sensor/ Source Location	Comments
2506	1628-1630	PEMA	50	Elect - truss	86	250	3	10	6/4	2.142 A _{rms}
2507	1626-1628	PEMA	50	Elect - truss	90	250	3	100	6/4	2.190 A _{rms}
2508	1624-1626	PEMA	50	Elect - truss	90	250	3	1000	6/4	2.158 A _{rms}
2510	1604-1606	PEMA	50	Elect - truss	87	50	3	10	6/4	2.168 A _{rms}
2511	1606-1608	PEMA	50	Elect - truss	90	50	3	100	6/4	2.210 A _{rms}
2512	1608-1610	PEMA	50	Elect - truss	88	50	3	1000	6/4	2.174 A _{rms}
2512A	1614-1616	PEMA	50	Elect - truss	90	50	3	1000	6/4	2.174 A _{rms}

Sensor moored at Location 6. E-source barge moored at Location 4.										
ELF Phase III Run Plan - Noise Runs										
Run #	Comex (Local Time)	Sensor	Sensor Depth (ft)	Source Type	Orientation (degrees true)	Source Depth (ft)	Current (amps)	Freq (Hz)	Sensor/ Source Location	Comments
0207	1630-1631	PEMA	50	None					6/4	Noise Run

Notes:

60' barge on north side of 45' barge. Long side to long side.

Truss deployed off north side of 60' barge.

Verify headings and locations using GPS and Orientation Sensor data.

ELF Phase III Test 1 Test Record

DAY 3 – MARCH 9, 2010

Sensor moored at Location 5. E-source barge moored at Location 4.										
ELF Phase III Run Plan - Noise Runs										
Run #	Comex (Local Time)	Sensor	Sensor Depth (ft)	Source Type	Orientation (degrees true)	Source Depth (ft)	Current (amps)	Freq (Hz)	Sensor/ Source Location	Comments
0304	1237-1238	PEMA	492	None					5/4	Noise Run - with source barge
0305	1129-1131	PEMA	250	None					5/4	Noise Run - with source barge Sensor Barge heading, 275°
0306	0934-0936	PEMA	50	None					5/4	Noise Run - with source barge Sensor Barge heading, 280°
0307	1703-1704	PEMA	50	None					5/4	Noise Run - with source barge

Notes:

0745 Scow underway
 0815 60' Barge underway
 0845 Scow moored
 0915 Sensor deployed
 0940 Truss deployed
 1330 Relocating 60' Barge for 160° heading
 1415 60' Barge reoriented
 1720 Scow unmoored
 1730 60' Barge unmoored
 Verify headings and locations using GPS data.
 Day 3 Measurements - 77

ELF Phase III Test 1 Test Record

Sensor moored at Location 5. E-source barge moored at Location 4.										
ELF Phase III Run Plan – Electric Source										
Run #	Comex (Local Time)	Sensor	Sensor Depth (ft)	Source Type 15m	Orientation (degrees true)	Source Depth (ft)	Current (amps)	Freq (Hz)	Sensor/ Source Location	Comments
3001	163119-163240	PEMA	50	Elect - truss	341	50	3	DC	5/4	2.54 A _{pk} Sensor Barge heading, 280°
3002	162910-163040	PEMA	50	Elect - truss	335	50	3	10	5/4	2.20 A _{rms} Sensor Barge heading, 286°
3003	162635-162840	PEMA	50	Elect - truss	340	50	3	100	5/4	2.25 A _{rms} Sensor Barge heading, 300°
3004	162406-162558	PEMA	50	Elect - truss	337	50	3	1000	5/4	2.2207 A _{rms} Sensor Barge heading, 293°
3005	169035-164210	PEMA	50	Elect - truss	336	250	3	DC	5/4	2.54 A _{pk} Sensor Barge heading, 295°
3006	164247-164416	PEMA	50	Elect - truss	336	250	3	10	5/4	2.213 A _{rms} Sensor Barge heading, 290°
3007	164440-164610	PEMA	50	Elect - truss	336	250	3	100	5/4	2.258 A _{rms} Sensor Barge heading, 285°
3008	164640-164810	PEMA	50	Elect - truss	333	250	3	1000	5/4	2.215 A _{rms} Sensor Barge heading, 280°
3009	170109-170231	PEMA	50	Elect - truss	340	400	3	DC	5/4	2.53 A _{pk} Sensor Barge heading, 280°
3010	165900-170030	PEMA	50	Elect - truss	338	400	3	10	5/4	2.22 A _{rms} Sensor Barge heading, 279°
3011	165713-165840	PEMA	50	Elect - truss	335	400	3	100	5/4	2.26 A _{rms} Sensor Barge heading, 276°
3012	165455-165640	PEMA	50	Elect - truss	338	400	3	1000	5/4	2.22 A _{rms} Sensor Barge heading, 284°

Notes:

Iso Amp on shunt wrong values @ 1 KHz. True for all 1000 Hz measurements
 Verify headings and locations using GPS and Orientation Sensor data.
 30 sec delay for source on with DC input.

ELF Phase III Test 1 Test Record

Sensor moored at Location 5. E-source barge moored at Location 4.										
ELF Phase III Run Plan – Electric Source										
Run #	Comex (Local Time)	Sensor	Sensor Depth (ft)	Source Type 15m	Orientation (degrees true)	Source Depth (ft)	Current (amps)	Freq (Hz)	Sensor/ Source Location	Comments
3101	152910-153030	PEMA	250	Elect - truss	337	400	2.5	DC	5/4	2.53 A _{pk}
3102	153137-153310	PEMA	250	Elect - truss	344	400	3	10	5/4	2.22 A _{rms}
3103	153350-153520	PEMA	250	Elect - truss	339	400	3	100	5/4	2.268 A _{rms}
3104	153600-153730	PEMA	250	Elect - truss	340	400	3	1000	5/4	2.227 A _{rms} Sensor Barge heading, 277°
3105	155125-155315	PEMA	250	Elect - truss	336	250	2.5	DC	5/4	2.54 A _{pk} Sensor Barge heading, 291°
3106	154915-155045	PEMA	250	Elect - truss	377	250	3	10	5/4	2.212 A _{rms} Sensor Barge heading, 290°
3107	154705-154845	PEMA	250	Elect - truss	339	250	3	100	5/4	2.26 A _{rms} Sensor Barge heading, 284°
3108	154513-154644	PEMA	250	Elect - truss	333	250	3	1000	5/4	2.22 A _{rms}
3109	160150-160320	PEMA	250	Elect - truss	339	50	2.5	DC	5/4	2.56 A _{pk} Sensor Barge heading, 295°
3110	160415-160530	PEMA	250	Elect - truss	345	50	3	10	5/4	2.225 A _{rms} Sensor Barge heading, 283°
3111	160622-160700	PEMA	250	Elect - truss	339	50	3	100	5/4	2.27 A _{rms} Sensor Barge heading, 287°
3112	160820-160940	PEMA	250	Elect - truss	339	50	3	1000	5/4	2.23 A _{rms}

Notes:

Verify headings and locations using GPS and Orientation Sensor data.
30 sec delay for source on with DC input.

ELF Phase III Test 1 Test Record

Sensor moored at Location 5.

E-source barge moored at Location 4.

ELF Phase III Run Plan – Electric Source

Run #	Comex (Local Time)	Sensor	Sensor Depth (ft)	Source Type 15m	Orientation (degrees true)	Source Depth (ft)	Current (amps)	Freq (Hz)	Sensor/ Source Location	Comments
3201	142100-142296	PEMA	492	Elect - truss	344	50	2.5	DC	5/4	2.54 A _{pk} Sensor Barge heading, 268°
3202	143030-	PEMA	492	Elect - truss	342	50	3	10	5/4	2.20 A _{rms} Sensor Barge heading, 271°
3203	143255-143405	PEMA	492	Elect - truss	341	50	3	100	5/4	2.25 A _{rms}
3204	143533-143700	PEMA	492	Elect - truss	342	50	3	1000	5/4	2.21 A _{rms} Sensor Barge heading, 262°
3205	145247-145422	PEMA	492	Elect - truss	340	250	2.5	DC	5/4	2.54 A _{pk}
3206	145000-145135	PEMA	492	Elect - truss	344	250	3	10	5/4	2.20 A _{rms}
3207	144757-144730	PEMA	492	Elect - truss	342	250	3	100	5/4	2.25 A _{rms}
3208	144537-144710	PEMA	492	Elect - truss	342	250	3	1000	5/4	2.20 A _{rms}
3209	150245-150414	PEMA	492	Elect - truss	342	400	3	DC	5/4	2.54 A _{pk}
3210	150500-150630	PEMA	492	Elect - truss	343	400	3	10	5/4	2.22 A _{rms}
3211	150700-150830	PEMA	492	Elect - truss	343	400	3	100	5/4	2.267 A _{rms}
3212	150900-151033	PEMA	492	Elect - truss	342	400	3	1000	5/4	2.23 A _{rms}

Notes:

Transformer circuit breaker popped at end of run 3205 – 6 seconds

Verify headings and locations using GPS and Orientation Sensor data.

30 sec delay for source on with DC input.

ELF Phase III Test 1 Test Record

Sensor moored at Location 5. E-source barge moored at Location 4.										
ELF Phase III Run Plan – Electric Source										
Run #	Comex (Local Time)	Sensor	Sensor Depth (ft)	Source Type 15m	Orientation (degrees true)	Source Depth (ft)	Current (amps)	Freq (Hz)	Sensor/ Source Location	Comments
3301	131646-131834	PEMA	492	Elect - truss	82	500 or 40 ft from bottom	2.5	DC	5/4	2.55 A _{pk}
3302	131920-132105	PEMA	492	Elect - truss	84	500 or 40 ft from bottom	3	10	5/4	2.22 A _{rms} Sensor Barge heading, 268°
3303	132140-132258	PEMA	492	Elect - truss	83	500 or 40 ft from bottom	3	100	5/4	2.27 A _{rms} Sensor Barge heading, 273°
3304	132340-132518	PEMA	492	Elect - truss	80	500 or 40 ft from bottom	3	1000	5/4	2.23 A _{rms} Sensor Barge heading, 286°
3305	130731-130900	PEMA	492	Elect - truss	81	250	2.5	DC	5/4	2.54 A _{pk}
3306	130500-130630	PEMA	492	Elect - truss	81	250	3	10	5/4	2.165 A _{rms}
3307	130250-130430	PEMA	492	Elect - truss	82	250	3	100	5/4	2.21 A _{rms}
3308	130000-130150	PEMA	492	Elect - truss	80	250	3	1000	5/4	2.226 A _{rms}
3309	1240-124136	PEMA	492	Elect - truss	82	50	2.5	DC	5/4	2.54 A _{pk} Sensor Barge heading, 281°
3310	1242-124344	PEMA	492	Elect - truss	81	50	3	10	5/4	2.207 A _{rms}
3311	124420-124547	PEMA	492	Elect - truss	80	50	3	100	5/4	2.25 A _{rms}
3312	124635-124810	PEMA	492	Elect - truss	81	50	3	1000	5/4	2.22 A _{rms}

Notes:

60' barge on north side of 45' barge. Long side to long side.

Truss deployed off north side of 60' barge.

Verify headings and locations using GPS and Orientation Sensor data.

30 sec delay for source on with DC input.

Iso Amp: 1) spikes, 2) @1000 Hz ~4V vs 3V, must have frequency dependent transfer function

ELF Phase III Test 1 Test Record

Sensor moored at Location 5.

E-source barge moored at Location 4.

ELF Phase III Run Plan – Electric Source

Run #	Comex (Local Time)	Sensor	Sensor Depth (ft)	Source Type 15m	Orientation (degrees true)	Source Depth (ft)	Current (amps)	Freq (Hz)	Sensor/ Source Location	Comments
3401	1222-1223	PEMA	250	Elect - truss	82	50	2.5	DC	5/4	2.53 A _{pk}
3402	1219-1221	PEMA	250	Elect - truss	80	50	3	10	5/4	2.22 A _{rms}
3403	1217-1219	PEMA	250	Elect - truss	82	50	3	100	5/4	2.267 A _{rms}
3404	1214-1216	PEMA	250	Elect - truss	83	50	3	1000	5/4	2.27 A _{rms} Sensor Barge heading, 284°
3405	1151-1153	PEMA	250	Elect - truss	77	250	2.5	DC	5/4	2.53 A _{pk} Sensor Barge heading, 271°
3406	1153-1155	PEMA	250	Elect - truss	80	250	3	10	5/4	2.213 A _{rms} Sensor Barge heading, 265°
3407	1156-1158	PEMA	250	Elect - truss	78	250	3	100	5/4	2.26 A _{rms} Sensor Barge heading, 270°
3408	1159-1201	PEMA	250	Elect - truss	80	250	3	1000	5/4	File fault. 221.5 A _{rms}
3408A	1204-1205	PEMA	250	Elect - truss	81	250	3	1000	5/4	2.22 A _{rms} Sensor Barge heading, 277°
3409	1140-1142	PEMA	250	Elect - truss	81	400	2.5	DC	5/4	2.54 A _{pk}
3410	1137-1139	PEMA	250	Elect - truss	82	400	3	10	5/4	2.22 A _{rms} Sensor Barge heading, 295°
3411	1135-1137	PEMA	250	Elect - truss	81	400	3	100	5/4	2.27 A _{rms}
3412	1133-1134	PEMA	250	Elect - truss	83	400	3	1000	5/4	2.227 A _{rms} Sensor Barge heading, 283°

Notes:

60' barge on north side of 45' barge. Long side to long side.

Truss deployed off north side of 60' barge.

Verify headings and locations using GPS and Orientation Sensor data.

30 sec delay for source on with DC input.

ELF Phase III Test 1 Test Record

Sensor moored at Location 5.

E-source barge moored at Location 4.

ELF Phase III Run Plan – Electric Source

Run #	Comex (Local Time)	Sensor	Sensor Depth (ft)	Source Type 15m	Orientation (degrees true)	Source Depth (ft)	Current (amps)	Freq (Hz)	Sensor/ Source Location	Comments
3501	1106-1108	PEMA	50	Elect - truss	82	400	2.5	DC	5/4	2.54 Vdc Sensor Barge heading, 285°
3502	1109-1110	PEMA	50	Elect - truss	80	400	3	10	5/4	2.20 A _{rms} Sensor Barge heading, 285°
3503	1111-1112	PEMA	50	Elect - truss	80	400	3	100	5/4	2.25 A _{rms}
3504	1113-1114	PEMA	50	Elect - truss	80	400	3	1000	5/4	2.21 A _{rms} Sensor Barge heading, 294°
3505	1047-1048	PEMA	50	Elect - truss	78	250	2.5	DC	5/4	2.54 A _{pk} Sensor Barge heading, 283°
3506	1044-1046	PEMA	50	Elect - truss	80	250	3	10	5/4	2.21 A _{rms} Sensor Barge heading, 281°
3507	1042-1043	PEMA	50	Elect - truss	82	250	3	100	5/4	2.26 A _{rms}
3508	1040-1041	PEMA	50	Elect - truss	80	250	3	1000	5/4	2.22 A _{rms} Sensor Barge heading, 294°
3509	1019-1021	PEMA	50	Elect - truss	80	50	2.5	DC	5/4	2.52 A _{pk} Sensor Barge heading, 287°
3510	1024-1025	PEMA	50	Elect - truss	81	50	3	10	5/4	2.19 A _{rms} Sensor Barge heading, 286°
3511	1026-1028	PEMA	50	Elect - truss	78	50	3	100	5/4	2.24 A _{rms} Sensor Barge heading, 288°
3512	1028-1030	PEMA	50	Elect - truss	80	50	3	1000	5/4	2.20 A _{rms} Sensor Barge heading, 284°

Notes:

Verify headings and locations using GPS and Orientation Sensor data.

30 sec delay for source on with DC input.

ELF Phase III Test 1 Test Record

DAY 4 – MARCH 10, 2010

Sensor moored at Location 6. E-source barge moored at Location 4.										
ELF Phase III Run Plan - Noise Runs										
Run #	Comex (Local Time)	Sensor	Sensor Depth (ft)	Source Type	Orientation (degrees true)	Source Depth (ft)	Current (amps)	Freq (Hz)	Sensor/ Source Location	Comments
0210	0948-094930	PEMA	45	None					6/4	Noise Run - with source barge
0211	1200-1201	PEMA	253	None					6/4	Noise Run - with source barge
0212	121840-122020	PEMA	473	None					6/4	Noise Run - with source barge
0213	1332-1333	PEMA	473	None					6/4	Noise Run - with source barge

Notes:

0740 Scow underway
0750 60' Barge underway
1545 Finished testing
1630 Back at base

Day 4 measurements - 58

ELF Phase III Test 1 Test Record

Sensor moored at Location 6.

E-source barge moored at Location 4.

ELF Phase III Run Plan – Electric Source

Run #	Comex (Local Time)	Sensor	Sensor Depth (ft)	Source Type 15m	Orientation (degrees true)	Source Depth (ft)	Current (amps)	Freq (Hz)	Sensor/ Source Location	Comments
2001	0959-100030	PEMA	45	Elect - truss	312	50	2.5	DC	6/4	2.5 A _{pk} Sensor Barge heading, 344°
2002	100150-100330	PEMA	45	Elect - truss	311	50	3	10	6/4	2.21 A _{rms} Sensor Barge heading, 351°
2003	100415-100545	PEMA	45	Elect - truss	312	50	3	100	6/4	2.26 A _{rms} Sensor Barge heading, 347°
2004	100620-100800	PEMA	45	Elect - truss	311	50	3	1000	6/4	2.23 A _{rms} Sensor Barge heading, 346°
2005	102425-102603	PEMA	45	Elect - truss	312	250	2.5	DC	6/4	2.52 A _{pk} Sensor Barge heading, 335°
2006	102210-100245-	PEMA	45	Elect - truss	312	250	3	10	6/4	2.21 A _{rms} Sensor Barge heading, 336°
2007	102000-102130	PEMA	45	Elect - truss	312	250	3	100	6/4	2.26 A _{rms} Sensor Barge heading, 333°
2008	101715-101920	PEMA	45	Elect - truss	308	250	3	1000	6/4	2.22 A _{rms} Sensor Barge heading, 345°
2009	103715-103900	PEMA	45	Elect - truss	318	432	3	DC	6/4	2.53 A _{pk} , 173 V Sensor Barge heading, 349°
2010	103945-104115	PEMA	45	Elect - truss	316	432	3	10	6/4	2.22 A _{rms} Sensor Barge heading, 358°
2011	104150-104325	PEMA	45	Elect - truss	314	432	3	100	6/4	2.265 A _{rms} Sensor Barge heading, 360°
2012	104400-104530	PEMA	45	Elect - truss	313	432	3	1000	6/4	2.238 A _{rms} Sensor Barge heading, 358°

Notes:

Ideal orientation is an angle from a line between truss and sensor and truss axis of 90°, i.e., truss heading of 315°.

60' barge on north side of 45' barge. Short side of 60' barge to long side of 45' barge.

Truss deployed off west side of 60' barge.

Verify headings and locations using GPS and Orientation Sensor data.

1000 Hz Iso Amp reads 4 V vice 3 V

30 sec delay for source on with DC input.

ELF Phase III Test 1 Test Record

Sensor moored at Location 6. E-source barge moored at Location 4.										
ELF Phase III Run Plan – Electric Source										
Run #	Comex (Local Time)	Sensor	Sensor Depth (ft)	Source Type 15m	Orientation (degrees true)	Source Depth (ft)	Current (amps)	Freq (Hz)	Sensor/Source Location	Comments
2101	111315-111450	PEMA	253	Elect - truss	322	432	3	DC	6/4	2.53 A _{pk} , 173 V DC
2102	111100-111235	PEMA	253	Elect - truss	322	432	3	10	6/4	2.22 A _{rms} , 153 V _{rms} Sensor Barge heading, 003°
2103	110710-110858	PEMA	253	Elect - truss	320	432	3	100	6/4	2.27 A _{rms} Sensor Barge heading, 009°
2104	110430-110630	PEMA	253	Elect - truss	320	432	3	1000	6/4	2.24 A _{rms} Sensor Barge heading, 004°
2105	112430-112610	PEMA	253	Elect - truss	316	248	3	DC	6/4	2.53 A _{pk} Sensor Barge heading, 009°
2106A	113100-113235	PEMA	253	Elect - truss	323	248	3	10	6/4	2.19 A _{rms} Sensor Barge heading, 011°
2107	112710-112835	PEMA	253	Elect - truss	317	248	3	100	6/4	2.24 A _{rms} Sensor Barge heading, 007°
2108	113330-113500	PEMA	253	Elect - truss	322	248	3	1000	6/4	2.20 A _{rms} Sensor Barge heading, 009°
2109	114829-115040	PEMA	253	Elect - truss	316	49	3	DC	6/4	2.52 A _{pk} Sensor Barge heading, 007°
2110	115140-115330	PEMA	253	Elect - truss	318	49	3	10	6/4	2.20 A _{rms}
2111	115425-115600	PEMA	253	Elect - truss	312	49	3	100	6/4	2.24 A _{rms}
2112	115625-115800	PEMA	253	Elect - truss	313	49	3	1000	6/4	2.206 A _{rms}

Notes:

60' barge on north side of 45' barge. Short side of 60' barge to long side of 45' barge.

Truss deployed off west side of 60' barge.

Verify headings and position using GPS and Orientation Sensor data.

30 sec delay for source on with DC input.

ELF Phase III Test 1 Test Record

Sensor moored at Location 6.
E-source barge moored at Location 4.

ELF Phase III Run Plan – Electric Source

Run #	Comex (Local Time)	Sensor	Sensor Depth (ft)	Source Type 15m	Orientation (degrees true)	Source Depth (ft)	Current (amps)	Freq (Hz)	Sensor/ Source Location	Comments
2201	122137-122320	PEMA	473	Elect - truss	314	49	2.5	DC	6/4	2.54 A _{pk} , 173 VDC Sensor Barge heading, 015°
2202	122400-122535	PEMA	473	Elect - truss	317	49	3	10	6/4	2.2 A _{rms} , 217 VAC _{pk}
2203	122600-122750	PEMA	473	Elect - truss	322	49	3	100	6/4	2.246 A _{rms} Sensor Barge heading, 012°
2204	122820-122950	PEMA	473	Elect - truss	321	49	3	1000	6/4	2.2 A _{rms} Sensor Barge heading, 015°
2205	123955-124200	PEMA	473	Elect - truss	320	249	3	DC	6/4	2.51 A _{pk} Sensor Barge heading, 013
2206	124320-124454	PEMA	473	Elect - truss	318	249	3	10	6/4	219.6 A _{rms} Sensor Barge heading, 014°
2207	124535-124705	PEMA	473	Elect - truss	313	249	3	100	6/4	Sensor Barge heading, 358°
2208	124740-124920	PEMA	473	Elect - truss	318	249	3	1000	6/4	2.203 A _{rms} Sensor Barge heading, 359°
2209	132300-132441	PEMA	473	Elect - truss	316	429	3	DC	6/4	2.52 A _{pk} , 172 VDC Sensor Barge heading, 014°
2210	132515-132650	PEMA	473	Elect - truss	317	429	3	10	6/4	2.21 A _{rms} Sensor Barge heading, 006°
2211	132733-132907	PEMA	473	Elect - truss	316	429	3	100	6/4	2.26 A _{rms} Sensor Barge heading, 358°
2212	132930-133105	PEMA	473	Elect - truss	319	429	3	1000	6/4	2.22 A _{rms}
2213*	130322-130517	PEMA	473	Elect - truss	316	250	3	DC	6/4	2.5 A _{pk} Sensor Barge heading, 010°
2214*	130115-130250	PEMA	473	Elect - truss	314	250	3	10	6/4	2.184 A _{rms} Sensor Barge heading, 007°
2215*	125847-130000	PEMA	473	Elect - truss	318	250	3	100	6/4	2.234 A _{rms} Sensor Barge heading, 015°
2216*	125616-125805	PEMA	473	Elect - truss	318	250	3	1000	6/4	2.20 A _{rms}

Notes: 60' barge on north side of 45' barge. Short side of 60' barge to long side of 45' barge.

Truss deployed off west side of 60' barge.

Verify headings and position using GPS and Orientation Sensor data.

*Runs 2213-2216: 30° tilt on source. East end low. West end high.

For DC, Electrode #2 is (+).

30 sec delay for source on with DC input.

ELF Phase III Test 1 Test Record

Sensor unmoored near Location 1. E-source barge moored at Location 4.										
ELF Phase III Run Plan - Noise Runs										
Run #	Comex (Local Time)	Sensor	Sensor Depth (ft)	Source Type	Orientation (degrees true)	Source Depth (ft)	Current (amps)	Freq (Hz)	Sensor/ Source Location	Comments
0504	145315-145445	PEMA	500	None					1/4	Noise Run - with source barge

Notes:
Verify position using GPS data.

ELF Phase III Test 1 Test Record

Sensor unmoored near Location 1.
E-source barge moored at Location 4.

ELF Phase III Run Plan – Electric Source										
Run #	Comex (Local Time)	Sensor	Sensor Depth (ft)	Source Type 15m	Orientation (degrees true)	Source Depth (ft)	Current (amps)	Freq (Hz)	Sensor/ Source Location	Comments
5201	153830-154005	PEMA	500	Elect - truss	160	50	3	DC	1/4	159.8°, 2.52 A _{pk} Sensor Barge heading, 223°
5202	153620-153750	PEMA	500	Elect - truss	154	50	3	10	1/4	2.22 A _{rms} Sensor Barge heading, 216°
5203	153415-153550	PEMA	500	Elect - truss	156	50	3	100	1/4	2.27 A _{rms} Sensor Barge heading, 228°
5204	153215-153350	PEMA	500	Elect - truss	164	50	3	1000	1/4	2.227 A _{rms} Sensor Barge heading, 231°
5205	151615-151750	PEMA	500	Elect - truss	166	250	3	DC	1/4	2.52 A _{pk} Sensor Barge heading, 245°
5206	1518201-151955	PEMA	500	Elect - truss	170	250	3	10	1/4	2.21 A _{rms} Sensor Barge heading, 249°
5207	152023-152200	PEMA	500	Elect - truss	173	250	3	100	1/4	2.26 A _{rms} Sensor Barge heading, 241°
5208	152225-152404	PEMA	500	Elect - truss	162	250	3	1000	1/4	2.22 A _{rms} Sensor Barge heading, 241°
5209	150612-150750	PEMA	500	Elect - truss	153	429	3	DC	1/4	2.54 A _{pk} Sensor Barge heading, 240°
5210	150357-150535	PEMA	500	Elect - truss	158	429	3	10	1/4	2.22 A _{rms} Sensor Barge heading, 216°
5211	150200-150335	PEMA	500	Elect - truss	163	429	3	100	1/4	2.27 A _{rms} Sensor Barge heading, 198°
5212	150000-150136	PEMA	500	Elect - truss	161	429	3	1000	1/4	2.235 A _{rms} Sensor Barge heading, 205°

Notes:

60' barge on north side of 45' barge. Short side of 60' barge to long side of 45' barge.

Truss deployed off east side of 60' barge.

Verify headings and locations using GPS and Orientation Sensor data.

30 sec delay for source on with DC input.

ELF Phase III Test 1 Test Record

Sensor unmoored near Location 1.										
ELF Phase III Run Plan - Noise Runs										
Run #	Comex (Local Time)	Sensor	Sensor Depth (ft)	Source Type	Orientation (degrees true)	Source Depth (ft)	Current (amps)	Freq (Hz)	Sensor/ Source Location	Comments
0509	1540-154130	PEMA	500	None					1/	Noise Run - with source barge

Notes:
Verify location using GPS data.

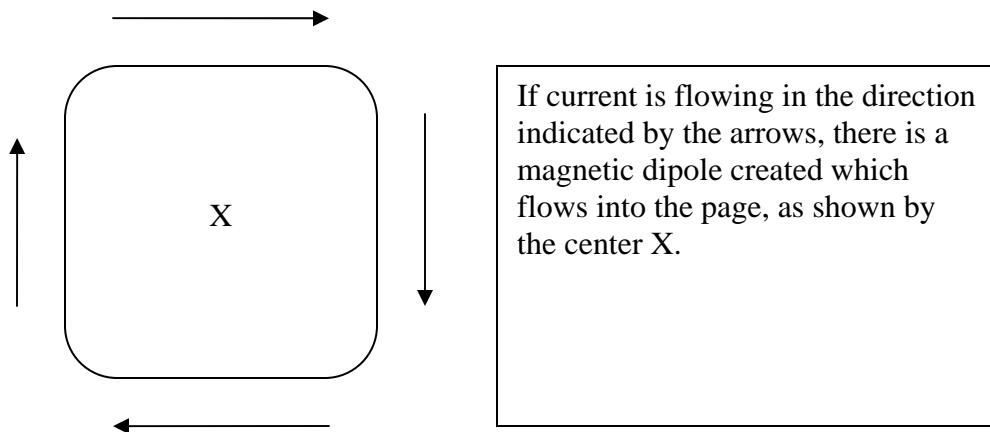
DAY 5 – MARCH 11, 2010

Magnetic Source Orientation Clarification

“Vertical Orientation”:

The “Vertically Oriented” magnetic source is defined as when the plane of the coil loop is laid flat/parallel to the ground. Thus, the coil will create a vertically oriented magnetic dipole (located at the center of the coil structure).

The direction of the vertical magnetic dipole (into the ground or into the air) is not specified in the run plan, but should probably be recorded for later analysis. That direction is determined based on the right-hand rule as follows:

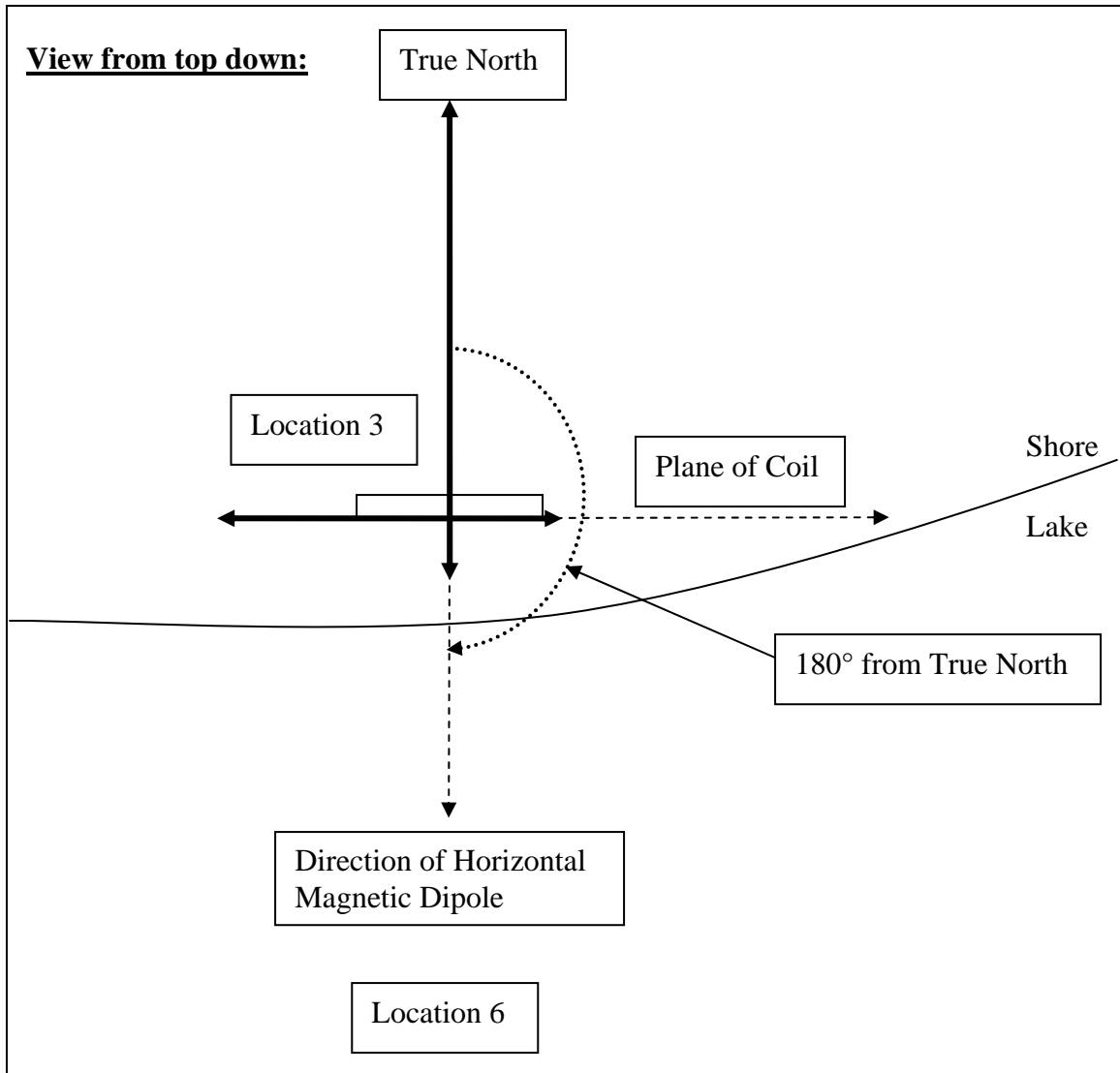


Black wire on top of coil.
Blue wire on bottom of coil.

“Horizontal Orientation”:

The “Horizontally Oriented” magnetic source is defined as when the structure is propped up, with the plane of the coil forming a right angle with the ground. Furthermore, the resulting horizontally oriented magnetic dipole (which will face in the direction perpendicular to the plane of the coil) should be oriented so that it faces to 180 Degrees from true North. The figure below shows the intended direction of the magnetic dipole, with respect to True North. The coil is to be set up at location 3 as shown:

ELF Phase III Test 1 Test Record



ELF Phase III Test 1 Test Record

Sensor moored at Location 6.										
ELF Phase III Run Plan - Noise Runs										
Run #	Comex (Local Time)	Sensor	Sensor Depth (ft)	Source Type	Orientation (degrees true)	Source Depth (ft)	Current (amps)	Freq (Hz)	Sensor/ Source Location	Comments
0407	104748-104928	PEMA	53	None					6/	Noise Run 1000 gain on magnetic x-axis (Channel 10)
0408	132600-132728	PEMA	246	None					6/	Noise Run

Notes:

1000 Magnet set up.

Magnetic Source Location: N 47° 57.89198', W 116° 32.54915'

Verify Sensor Barge location using GPS data.

Day 5 measurements - 32

ELF Phase III Test 1 Test Record

Sensor moored at Location 6. Mag-source at Location 3.										
ELF Phase III Run Plan – Magnetic Source										
Run #	Comex (Local Time)	Sensor	Sensor Depth (ft)	Source Type	Orientation (degrees true)	Source Depth (ft)	Current (amps)	Freq (Hz)	Sensor/ Source Location	Comments
4207z	132130-132235	PEMA	246	Mag – horiz.	180		20	100	6/3	12.34 A _{rms} , -70 dB 100 gain on electric z-axis (Channel 10)
4208x	131513-131620	PEMA	246	Mag – horiz.	180		20	1000	6/3	15.04 A _{rms} , -24 dB Sensor Barge heading, 301° 100 gain on electric x-axis (Channel 10)
4211x	125030-125115	PEMA	53	Mag – horiz.	180		20	100	6/3	12.4 A _{rms} , -64 dB 100 gain on electric x-axis (Channel 10)
4212z	125706-125810	PEMA	53	Mag – horiz.	180		20	1000	6/3	15.0 A _{rms} , -38 dB Sensor Barge heading, 280° 100 gain on electric z-axis (Channel 10)
4211y	125230-125340	PEMA	53	Mag – horiz.	180		20	100	6/3	-60 dB 100 gain on electric y-axis (Channel 10)
4211z	125430-125530	PEMA	53	Mag – horiz.	180		20	100	6/3	-49 dB Sensor Barge heading, 289° 100 gain on electric z-axis (Channel 10)
4212y	125900-	PEMA	53	Mag – horiz.	180		20	1000	6/3	-28 dB Sensor Barge heading, 293° 100 gain on electric y-axis (Channel 10)
4212x	130030-130131	PEMA	53	Mag – horiz.	180		20	1000	6/3	-24 db Sensor Barge heading, 291° 100 gain on electric x-axis (Channel 10)
4208y	131710-131810	PEMA	246	Mag – horiz.	180		20	1000	6/3	-50 dB Sensor Barge heading, 304° 100 gain on electric y-axis (Channel 10)
4208z	131834-131955	PEMA	246	Mag – horiz.	180		20	1000	6/3	-50 dB Sensor Barge heading, 305° 100 gain on electric z-axis (Channel 10)
4207y	132300-132400	PEMA	246	Mag – horiz.	180		20	100	6/3	-63 dB Sensor Barge heading, 291° 100 gain on electric y-axis (Channel 10)
4207x	132435-132550	PEMA	246	Mag – horiz.	180		20	100	6/3	-59 dB Sensor Barge heading, 294° 100 gain on electric x-axis (Channel 10)

Notes:

Magnetic Source Location: N 47° 57.89198', W 116° 32.54915'

Verify Sensor Barge location using GPS data.

dB level read off spectrum analyzer on Sensor Barge.

ELF Phase III Test 1 Test Record

Sensor moored at Location 6. Mag-source at Location 3.										
ELF Phase III Run Plan – Magnetic Source										
Run #	Comex (Local Time)	Sensor	Sensor Depth (ft)	Source Type	Orientation (degrees true)	Source Depth (ft)	Current (amps)	Freq (Hz)	Sensor/ Source Location	Comments
4303	105500-105700	PEMA (324°)	53	Mag - vert.	vertical		18	100	6/3	18 A _{pk} , 12.35 A _{rms} 1000 gain on magnetic x-axis (Channel 10) Sensor Barge heading, 321°
4304	1156-1158	PEMA	53	Mag - vert.	vertical		20	1000	6/3	Ey=-32dB, 15 A _{rms}
4307x	133325-133455	PEMA	246	Mag - vert.	vertical		20	100	6/3	12.4 A _{rms} , -65 dB Sensor Barge heading, 307° 100 gain on electric x-axis (Channel 10)
4308z	133911-134011	PEMA	246	Mag - vert.	vertical		20	1000	6/3	15.0 A _{rms} , -41 dB Sensor Barge heading, 296° 100 gain on electric z-axis (Channel 10)
4303A		PEMA	53	Mag - vert.	vertical		20	100	6/3	17.5 A _{pk}
4304x	121202-121315	PEMA	53	Mag - vert.	vertical		20	1000	6/3	-40dB Sensor Barge heading, 336° 100 gain on electric x-axis (Channel 10)
4304y	121402-121530	PEMA	53	Mag - vert.	vertical		20	1000	6/3	-32 dB Sensor Barge heading, 338° 100 gain on electric y-axis (Channel 10)
4304z	121556-121725	PEMA	53	Mag - vert.	vertical		20	1000	6/3	-40 dB Sensor Barge heading, 339° 100 gain on electric z-axis (Channel 10)
4303z	122145-122255	PEMA	53	Mag - vert.	vertical		20	100	6/3	-49 dB 100 gain on electric z-axis (Channel 10)
4303y	122325-122425	PEMA	53	Mag - vert.	vertical		20	100	6/3	-55 dB 100 gain on electric y-axis (Channel 10)
4303x	122500-122600	PEMA	53	Mag - vert.	vertical		20	100	6/3	-60 dB 100 gain on electric x-axis (Channel 10)
4307y	133520-133625	PEMA	246	Mag - vert.	vertical		20	100	6/3	-64 dB 100 gain on electric y-axis (Channel 10)
4307z	133645-133748	PEMA	246	Mag - vert.	vertical		20	100	6/3	-75 dB Sensor Barge heading, 277° 100 gain on electric z-axis (Channel 10)
4308y	134100-134205	PEMA	246	Mag - vert.	vertical		20	1000	6/3	-33 dB 100 gain on electric y-axis (Channel 10)
4308x	134226-134330	PEMA	246	Mag - vert.	vertical		20	1000	6/3	-50 dB 100 gain on electric x-axis (Channel 10)

Notes:

Magnetic Source Location: N 47° 57.89198', W 116° 32.54915'

Verify Sensor Barge location using GPS data.

dB level read off spectrum analyzer on Sensor Barge.

ELF Phase III Test 1 Test Record

Sensor moored at Location 6. Mag-source at Location 3.										
ELF Phase III Run Plan - Noise Runs										
Run #	Comex (Local Time)	Sensor	Sensor Depth (ft)	Source Type	Orientation (degrees true)	Source Depth (ft)	Current (amps)	Freq (Hz)	Sensor/ Source Location	Comments
0401	141720-141720	PEMA	-7 (7' above water level)	None					6/	Noise Run Sensor in air on barge. Sensor Barge heading, 289°

Sensor moored at Location 6 then motoring towards Location 3. Mag-source at Location 3.										
ELF Phase III Run Plan – Magnetic Source										
Run #	Comex (Local Time)	Sensor	Sensor Depth (ft)	Source Type	Orientation (degrees true)	Source Depth (ft)	Current (amps)	Freq (Hz)	Sensor/ Source Location	Comments
4004	142140-142319	PEMA	-7 (7' above water level)	Mag - vert.	vertical		20	1000	6/3	Sensor Barge moored at Location 6. Radio interference before 142210. 15 A _{rms}
4008	143730-144700	PEMA	-7 (7' above water level)	Mag - vert.	vertical		20	1000	/3	Sensor Barge driving from Location #6 towards #3. 15 A _{rms}

Notes:

Magnetic Source Location: N 47° 57.89198', W 116° 32.54915'

Verify Sensor Barge location and heading using GPS data.

APPENDIX C: PORTABLE EM ARRAY TECHNICAL SPECIFICATIONS

MAGNETIC SENSOR

- Magnetic Sensor Location
 - Shall be located within a 6" radius of the geometric center of the electric field antenna
- Magnetic Sensor Type:
 - Shall be a three-axis second harmonic fluxgate with "+" indications for North, East, and Down. Measurements shall be expressed as nanoTesla (nT)
- Bandwidth
 - Measurement and recording shall have a pass band response between 0 Hz and 3000 Hz. Roll-off of gain to -3 dB is allowable at upper limit of pass band.
 - Gain within pass band shall be level within 99-101% of correct value outside of roll-off corner effects.
- Dynamic Range and resolution
 - Shall measure absolute magnetic field within the range of +/- 100,000 nT on each axis.
 - Shall digitize field with a word length of 24 bits
 - Shall reliably record changes in magnetic field 0.1 nT and greater
 - Desirable to have a flat (uniformly distributed) noise floor below the 200 picoTesla RMS level from DC to 3000 Hz
- Observed noise after processing
 - The peak to peak noise after low-pass filtering data to DC-25 Hz shall not exceed +/- 0.5 nT (1.0 nT PkPk) when observed over a ten second period.
- Alignment
 - Sensor axes shall be manufactured mutually perpendicular within +/- 0.5 degree
 - Sensor shall be installed with axes aligned to magnetic north coordinate system within +/- 0.5 degree
 - A two-axis horizontal tilt sensor (east/west and north/south) shall be fitted to detect sensor motion after installation

ELECTRIC FIELD SENSOR

- Electric Sensor Location
 - Triaxial dipole antenna shall be centered on the defined sensor location
- Electric Sensor Type
 - The electric sensor shall be a three-axis dipole antenna sensing electric field with “+” indications for North, East, and Down (if the sensor is deployed right side up. For this test, the sensor was deployed upside down). Measurements shall be expressed as Volts/meter.
 - Dipole antenna length shall be one meter in all directions
 - Or: Dipole length shall be 1 meter in the North and East directions, with shorter, off-center dipole allowable in the down direction
- Bandwidth
 - Electric measurement and recording system as installed shall have a pass band response between 0.001 Hz and 3000 Hz. Roll-off of gain to – 3 dB is allowable at both lower and upper limit of pass band.
 - Gain within pass band shall be level within 99-101% of correct value outside of roll-off corner effects.
- Dynamic Range
 - Shall measure absolute electric field within the range of +/- 10,000 uV/M on each axis.
 - Shall digitize field with a word length of 24 bits
 - Shall reliably record changes in electric field 0.5 uV/M and greater.
 - Desirable to have a flat (uniformly distributed) noise floor below the 200 nV/M RMS level from 0.001 to 3000 Hz
- Observed noise after processing
 - The peak to peak noise of acquired data after low-pass filtering data to 0.1 Hz and below shall not exceed +/- 2.0 uV/M (4.0 uV/M PkPk) when observed over a 100 second period.
- Alignment
 - Sensor axes shall be manufactured mutually perpendicular within +/- 0.5 degree
 - Sensor shall be installed with axes aligned to magnetic north coordinate system within +/- 0.5 degree
 - A two-axis horizontal tilt sensor (east/west and north/south) shall be fitted to detect sensor motion after installation
- Confidence Test
 - Each sensor shall be equipped with remotely controlled local electric dipole transmitter to produce an observable output from each axis of the sensor

APPENDIX D: SENSOR PRE-TESTS AT CARDEROCK

SENSOR CHECK OUT REPORT

Check Out of ARD Sensor in High Bay of bld. 80

January 13, 2010

From: Niel Alam

To: Chris Burgy, Dan Lenko, Henry Larion, Donald Waltman, Dana Hesse, Scott Turner, John Ramboz

Report:

All,

ARD Sensor was checked out and tested with proper procedure. The checking of the ARD was completed on, January 11, 2010. Testing and checking includes;

Dry testing

- 1) Tilt test (check the tilt sensor inside the pod and record the voltage value with the corresponding degree as a reference).
- 2) Record Voltage Input (VI) Characteristic and the corresponding current draw
- 3) Leak Test (Nitrogen fill)
- 4) Polarity & Voltage GAIN check on each axis of the ARD sensor(record for 1min)
- 5) Check the orientation of the Magnetometer

Wet testing (putting the pod sensor in the water with its electrode arms in placed)

- 1) Noise Run (record for 1min)
- 2) Shorting electrode Ex, Ey, Ez & save a Run test (record for 1min)
- 3) Confidence electrode input test (record for 1 min)
- 4) Check polarity of Ex, Ey, Ez using external signal w/ Platinum Electrodes
- 5) Rotate Sensor to confirm the right orientation of the magnetometer
- 6) Check Oscillation of Mag and Tilt signal.

Just a reminder:

The plan for this pod sensor is to suspend it up side down when installing this ARD sensor in the lake of Idaho. In that case, the ARD sensor was therefore also put in an up side down position when doing the check out in the High Bay of bld. 80. When doing the tilt test and all the rest of the check outs, the white band, which is commonly marked on the positive (+) X-Axis of the sensor pod, is still pointed to the NORTH direction after it was placed up side down. Attached is the result of the tilt test. Be aware that when the ARD sensor is tilted along X-Axis, the corresponding voltage value will show up on the Y-Axis tilt screen and vise versa when Y-Axis is tilted. One easy fix is to switch those X-Z and Y-Z tilt sensor wires coming into the channels

ELF Phase III Test 1 Test Record

of the acquisition program or just alter it in the program. This is just a minor change that can be left alone and no switching of wire is needed as long as the user is aware of what is going on. Don Waltman has a hard copy of this tilt data. For the E-field reading, there will be no difference or switching of polarity in the acquisition program is not needed since AC signal has no polarities regardless of how the sensor is oriented. However, it is different in the case of the magnetic field reading. The polarities of the Y-axis and Z-axis magnetic field must be flipped. Albeit the ARD is placed up side down, the positive (+) X-axis of the pod (white band) is still pointed to the NORTH therefore no switching of polarities along X-axis is needed. Again, only the tilt sensor inside the pod was mounted up side down and not the magnetometer.

Other check out results turned out fine and no problem or any weird signal generated while doing each test. There are couples of things that might be noticeable. Base on Niel and Don Waltman observation when doing the water testing, the e-field moment in fresh water (less conductor) is higher than the sea water. In addition, a 0.1Hz with 1Vp-p sine wave input signal in sea water and 0.1Hz with 80mVp-p sine wave in fresh water will almost generate a similar output result when “checking the electrode signal using the external tripod electrode in the water” Test was done. Moreover, Don Waltman observed that as the frequency increases from 0.1Hz to 100Hz, the amplitude of the output signal increases somehow.

ELF Phase III Test 1 Test Record

SENSOR CHECK OUT DATA

Sensor #	ARD UNIT S/N 40			<div>Additional Notes</div> <div>Voltage on chassis with green cable: 33.55VDC Voltage before green cable: 55.37V DC</div> <div>ARD POD will be suspended for testing POD for the TILT TEST is up side down</div>
Electrode Arms	Arm #			
X (north)	132A			
X (south)	132B			
Y (east)	133A			
Y (west)	133B			
Z (top)	134A			
Z (bottom)	134B			
VI Characteristics				
Input Voltage (V)	Current Draw	(milliAmp)		
20	0.4		<div>Dry test</div> <div>Tilt Sensor Test<div>Done</div></div> <div>Record VI charact<div>Done</div></div> <div>Wet Testing</div> <div>Noise Run (1 min)<div>Done</div></div> <div>Shorting electrode Ex, Ey, Ez and save a Run<div>Done</div></div> <div>Check polarity of Ex, Ey, Ez with external signal w/ Platinum Electrodes<div>Done</div></div> <div>Confidence check<div>Done</div></div> <div>Rotate sensor X(N) (no problems)<div>Done</div></div> <div>Check Oscillation of Mag & Tilt signal (no problems)<div>Done</div></div>	
21	0.39			
22	0.37			
23	0.35			
24	0.34			
25	0.33			
26	0.32			
27	0.3			
28	0.29			
29	0.29			
30	0.28			
31	0.29			
Shorting of Electrodes				
Axes	Initial Voltage/Before	After Shorting		
EX	0.023	0.025		
EY	0.007	0.005		
EZ	-0.026	0.015		
Confidence Electrode Check Input 1Vpp @ 0.1, 1, 10, 100Hz square and sine wave				
Peak Voltage for X, Y, Z	Max (V)	Min (V)		
EX	10.64	-10.76		
EY	10.57	-10.7		
EZ	10.64	-10.7		
Rotate Sensor	HX	HY	HZ	
White band to Northwest (new sensors)	check	check	check	

ELF Phase III Test 1 Test Record

Checks After Re-wired by EG&G			
Calibrated Input signal	Output Signal		
1 mV AC	EX	EY	EZ
positive peak	0.99	0.98	1
negative peak	-1.01	-1.02	-1
9.7656Hz & 10mV AC Sine Wave using spectrum Analyzer Output in V AC RMS			
7.101mV RMS input	7.28	7.287	7.438
Ambient Magnetic Field X-North pointing Northwest and Y pointing Northeast			
Hx	1.279		
Hy	1.29		
Hz	2.47		

SENSOR TILT TEST DATA AND ORIENTATION

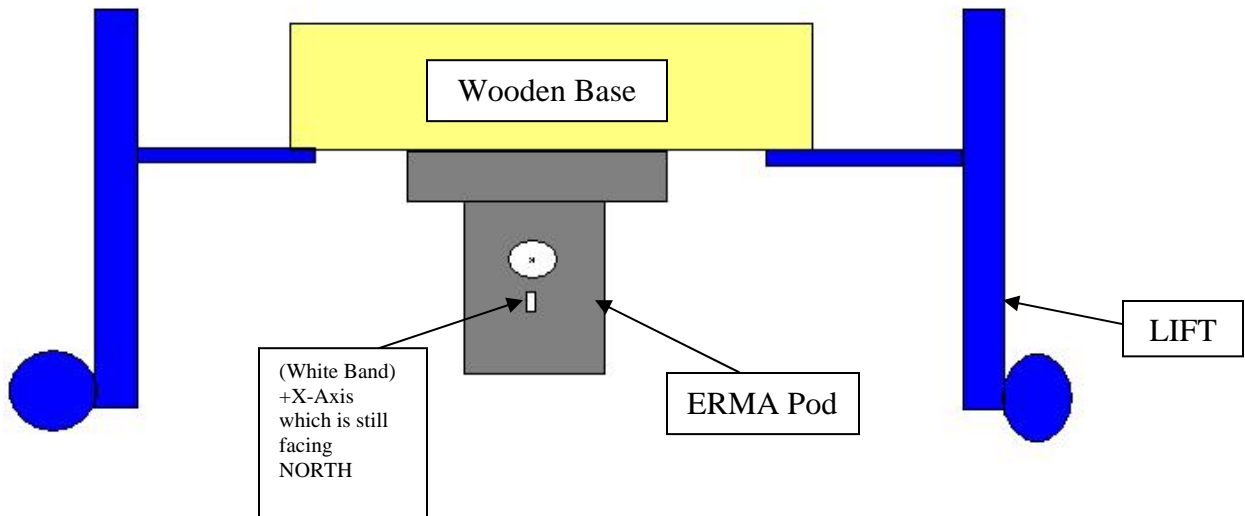
ARD Tilt Data for S/N 040	
Accelerometer/ Crossbow tilt sensor	
<i>NOTE: This is the tilt Data when you tilt the POD along the Y-Axis</i>	
<i>The corresponding result below is for the (-) Negative Y-Axis or when you tilt the Sensor POD towards WEST reference to white band when POD is up_side_down it is shown on the x-axis screen. Just FYI so you can be aware of</i>	
Angle in Degree	Corresponding Voltage
0°	2.492
0.5°	2.505
1.0°	2.527
1.5°	2.543
2°	2.559
2.5°	2.578
3°	2.595
3.5°	2.61
4°	2.629
4.5°	2.647
5°	2.663
6°	2.699
7°	2.731
8°	2.768
9°	2.802
10°	2.835
11°	2.87
12°	2.905
13°	2.939
14°	2.976
15°	3.008

ARD Tilt Data for S/N 040	
Accelerometer/ Crossbow tilt sensor	
<i>NOTE: This is the tilt Data when you tilt the POD along the Y-Axis</i>	
<i>The corresponding result below is for the (+) Positive Y-Axis or when you tilt the Sensor POD towards EAST reference to white band when POD is up_side_down it is shown on the x-axis screen. Just FYI so you can be aware of</i>	
Angle in Degree	Corresponding Voltage
0°	2.49
0.5°	2.474
1.0°	2.448
1.5°	2.43
2°	2.413
2.5°	2.397
3°	2.377
3.5°	2.362
4°	2.345
4.5°	2.33
5°	2.313
6°	2.275
7°	2.241
8°	2.204
9°	2.171
10°	2.137
11°	2.072
12°	2.055
13°	2.037
14°	2.004
15°	1.971

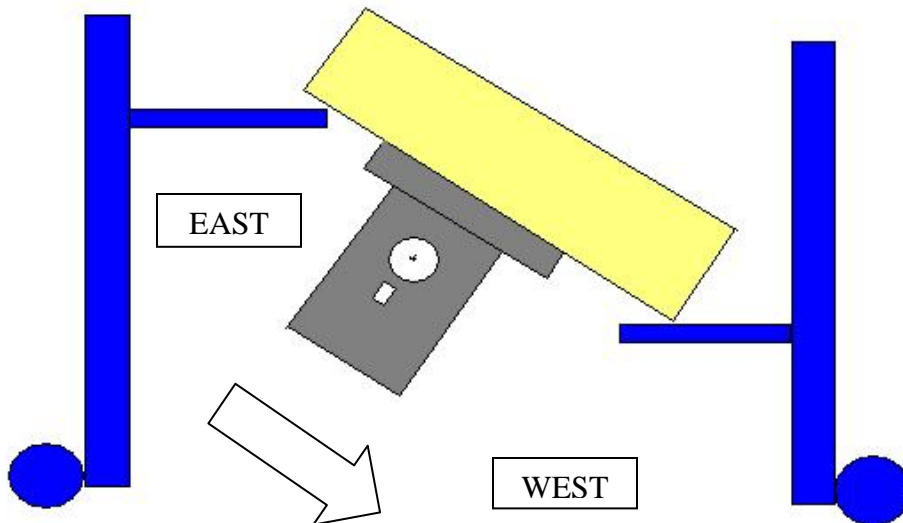
ARD Tilt Data for S/N 040	
Accelerometer/ Crossbow tilt sensor	
<i>NOTE: This is the tilt Data when you tilt the POD along the X-Axis</i>	
<i>The corresponding result below is for the (-) Negative X-Axis or when you tilt the Sensor POD towards NORTH reference to white band when POD is up_side_down it is shown on the y-axis screen. Just FYI so you can be aware of</i>	
Angle in Degree	Corresponding Voltage
0°	2.554
0.5°	2.534
1.0°	2.518
1.5°	2.502
2°	2.483
2.5°	2.467
3°	2.45
3.5°	2.433
4°	2.418
4.5°	2.398
5°	2.381
6°	2.348
7°	2.314
8°	2.277
9°	2.245
10°	2.211
11°	2.176
12°	2.141
13°	2.105
14°	2.072
15°	2.04
25°	1.715

ARD Tilt Data for S/N 040	
Accelerometer/ Crossbow tilt sensor	
<i>NOTE: This is the tilt Data when you tilt the POD along the X-Axis</i>	
<i>The corresponding result below is for the (+) Positive X-Axis or when you tilt the Sensor POD towards SOUTH reference to white band when POD is up_side_down it is shown on the y-axis screen. Just FYI so you can be aware of</i>	
Angle in Degree	Corresponding Voltage
0°	2.556
0.5°	2.57
1.0°	2.592
1.5°	2.607
2°	2.625
2.5°	2.64
3°	2.661
3.5°	2.677
4°	2.694
4.5°	2.711
5°	2.728
6°	2.763
7°	2.798
8°	2.832
9°	2.869
10°	2.9
11°	2.935
12°	2.967
13°	3
14°	3.038
15°	3.07
24°	3.346

Initial position of Tilt test

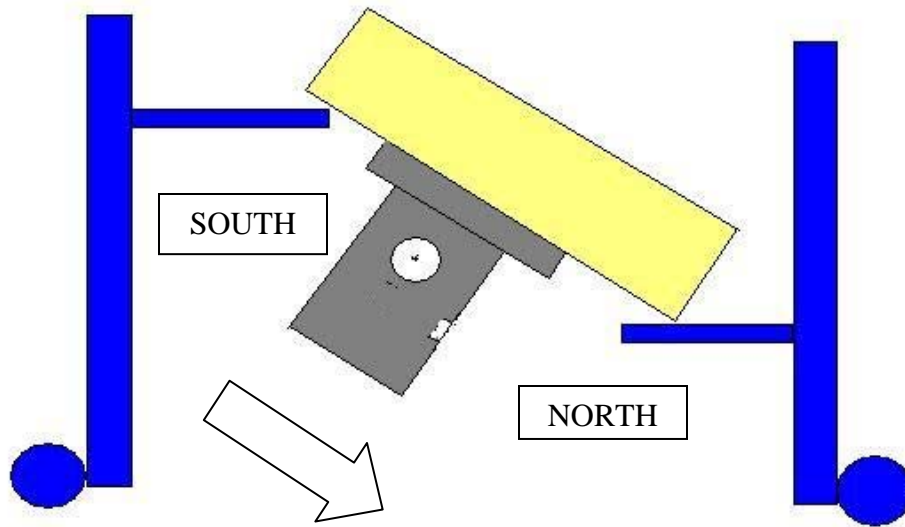


This is the picture when I mean “Sensor Pod tilted towards WEST”



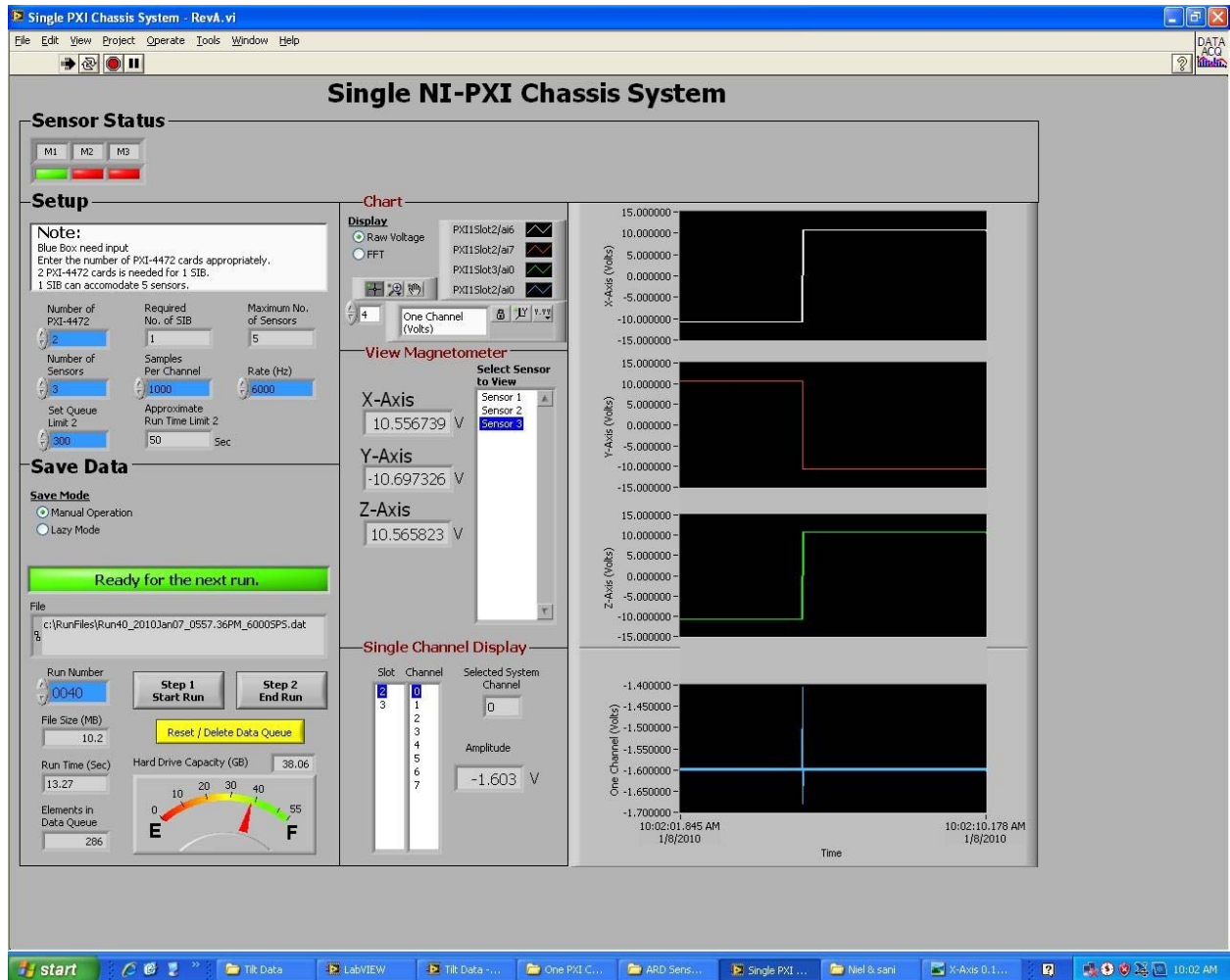
Note: It is tilted towards WEST since the white band which is NORTH is facing you

This is the picture when I mean “Sensor Pod tilted towards NORTH”



ELF Phase III Test 1 Test Record

CONFIDENCE TEST PICTURE



APPENDIX E: SENSOR CALIBRATION TILT DATA (IN MESF)

EAST-WEST AXIS Sensor Tilt Data For S/N 040 Accelerometer/Crossbow Tilt Sensor			
Angle in Degree	Corresponding Voltage	UP (West)	DOWN (West)
0°	2.49	2.4986	2.4970
0.5°	2.474	2.4804	2.5141
1.0°	2.448	2.4638	2.5344
1.5°	2.43	2.4426	2.5500
2°	2.413	2.4248	2.5689
2.5°	2.397	2.4096	2.5837
3°	2.377	2.3909	2.6038
3.5°	2.362	2.3758	2.6173
4°	2.345	2.3566	2.6350
4.5°	2.33	2.3380	2.6522
5°	2.313	2.23221	2.6721
6°	2.275	2.2889	2.7098
7°	2.241	2.2528	2.7432
8°	2.204	2.2174	2.7738
9°	2.171	2.1868	2.8090
10°	2.137	2.1511	2.8429
11°	2.072	2.1150	2.8800
12°	2.055	2.0812	2.9141
13°	2.037	2.0482	2.9480
14°	2.004	2.0150	2.9820
15°	1.971	1.9811	3.0180
26°	1.641		

Note:

This is the tilt data when you tilt the POD along the Y-axis.

The corresponding result below is for the (+) Positive Y-axis or when you tilt the Sensor POD towards EAST reference to white band when POD is upside down.

It is shown on the X-axis screen.

DVM 5380

Sensor is deployed upside-down.

Axis direction assumed East/West when viewed from top.

ELF Phase III Test 1 Test Record

NORTH-SOUTH AXIS Sensor Tilt Data For S/N 040 Accelerometer/Crossbow Tilt Sensor			
Angle in Degree	Corresponding Voltage	+X UP	+X DOWN
0°	2.556	2.5631	2.5636
0.5°	2.57	2.5810	2.5470
1.0°	2.592	2.5990	2.5301
1.5°	2.607	2.6155	2.5136
2°	2.625	2.6347	2.4971
2.5°	2.64	2.6530	2.4760
3°	2.661	2.6696	2.4601
3.5°	2.677	2.6863	2.4444
4°	2.694	2.7058	2.4246
4.5°	2.711	2.7213	2.4068
5°	2.728	2.7381	2.3885
6°	2.763	2.7712	2.3540
7°	2.798	2.8072	2.3209
8°	2.832	2.8432	2.2898
9°	2.869	2.8760	2.2528
10°	2.9	2.9100	2.2197
11°	2.935	2.9444	2.1872
12°	2.967	2.9812	2.1484
13°	3	3.0164	2.1155
14°	3.038	3.0468	2.0813
15°	3.07	3.0810	2.0509
26°	3.346		

Notes:

This is the tilt data when you tilt the POD along the Y-axis.

The corresponding result below is for the (+) Positive Y-axis or when you tilt the Sensor POD towards SOUTH reference to white band when POD is upside down.

It is shown on the X-axis screen.

DVM 5380

Sensor is deployed upside-down.

Axis direction assumed North/South when viewed from top.

Switched wires xz and yz.

APPENDIX F: MAGNETIC, TILT AND PRESSURE DATA

DAY 1 – MARCH 5, 2010

Run #	Mag x (V)	Mag y (V)	Mag z (V)	Tilt x (V)	Tilt y (V)	Pressure (V)	Angle of Scow (deg)	Comments:
0106	-1.19	-1.26	-5.24	2.62	2.56	.23(.227)		
0107	-1.41	-1.07	-5.23	2.62	2.56	.23(.227)		
0110	-1.34	-1.16	-5.24	2.62	2.56	.23(.227)		
1001	-1.44	-1.06	-5.24	2.62	2.57	.23(.227)		
1002	-1.4	-1.09	-5.24	2.62	2.57	.23(.227)		
1005	-1.57	-0.91	-5.23	2.62	2.57	.23(.227)		
1006	-1.65	-0.8	-5.23	2.62	2.56	.23(.227)		
1007	-1.63	-0.8	-5.22	2.63	2.57	.23(.227)		
1008	-1.18	-1.29	-5.26	2.62	2.57	.23(.227)		
1011	1.24	-0.96	-5.3	2.62	2.57	.23(.227)		
1012	1.59	-0.34	-5.3	2.62	2.57	.23(.227)		
1102	1.68	0.33	-5.28	2.62	2.57	.23(.227)		
1101	0.89	1.68	-5.2	2.62	2.57	.23(.227)		
1104	0.4	1.94	-5.18	2.62	2.57	.23(.227)	192	
1103	0.3	1.97	-5.16	2.63	2.57	.23(.227)	196	
1106	0.6	2.01	-5.16	2.63	2.57	.23(.227)	201	
1105	0.54	1.88	-5.18	2.64	2.58	.23(.227)	188	
1108	0.63	1.85	-5.18	2.63	2.57	.23(.227)	183	
1107	0.79	1.75	-5.19	2.62	2.57	.23(.227)		
1201	-1.57	-0.89	-5.2	2.63	2.57	1.86(1.855)	135	
1202	-1.57	-0.9	-5.21	2.62	2.57	1.86(1.855)	136	
1203	-1.46	-1.09	-5.22	2.62	2.57	1.86(1.855)	156	
1204	-1.6	-0.86	-5.2	2.63	2.57	1.86(1.855)	158	
1205	-1.61	-0.83	-5.2	2.63	2.57	1.86(1.855)		
1206	-1.66	-0.77	-5.2	2.63	2.57	1.86(1.855)	159	
1207	-1.68	-0.74	-5.2	2.63	2.57	1.86(1.855)	160	
1208	-1.7	-0.69	-5.2	2.63	2.57	1.86(1.855)		
0114	-1.7	-0.7	-5.2	2.63	2.57	1.86(1.855)	161	

Notes:

For Day 1: (Mag x, Mag y, Mag z)

90 deg = (.75, -1.36, -5.31)

107 deg = (1.1, -1.1, -5.31)

180 deg = (.89, 1.65, -5.20)

Angle of Scow approximate, verify using GPS data.

ELF Phase III Test 1 Test Record

DAY 2 – MARCH 8, 2010

Run #	Mag x (V)	Mag y (V)	Mag z (V)	Tilt x (V)	Tilt y (V)	Pressure (V)	Angle of Scow (deg)	Comments:
0206	n/a	n/a	n/a	n/a	n/a	in negatives		
0205	n/a	n/a	n/a	2.59	2.55	0.03		
0204	-1.08	-1.14	-5.21	2.59	2.54	1.20(1.204)		
2309	0.8	-1.65	-5.22	2.6	2.54	1.20(1.204)		
2310	0.3	-1.7	-5.24	2.59	2.54	1.20(1.204)		flickered during run
2311	-1.01	-1.48	-5.23	2.59	2.54	1.20(1.204)		
2312	-0.96	-1.43	-5.23	2.59	2.54	1.20(1.204)		
2306	1.3	-0.85	-5.24	2.59	2.54	1.20(1.204)		
2306A	-0.6	-1.64	-5.24	2.59	2.54	1.20(1.204)		
2307	1.08	-1.47	-5.25	2.59	2.54	1.20(1.204)		
2308	1.75	-0.59	-5.25	2.59	2.54	1.20(1.204)		
2305	-1.2	-1.07	-5.21	2.59	2.54	1.20(1.204)		
2302	1	-1.51	-5.25	2.59	2.54	1.20(1.204)		
2303	-0.01	-1.69	-5.25	2.59	2.54	1.20(1.204)		
2304	0.28	-1.65	-5.25	2.59	2.54	1.20(1.204)		
2412	-0.65	1.88	-5.17	2.6	2.54	0.17		250 feet
2411	-1.65	0.74	-5.18	2.6	2.54	0.17		
2410	-1.31	1.61	-5.16	2.6	2.54	0.17		
2406	-1.16	1.63	-5.16	2.6	2.54	0.17		
2407	-0.13	1.93	-5.2	2.6	2.54	0.17		
2408	-1.05	1.64	-5.16	2.6	2.54	0.17		
2404	-1.84	0.61	-5.17	2.6	2.54	0.17		
2403	-1.3	1.56	-5.17	2.6	2.54	0.17		
2402	-1.84	0.37	-5.17	2.6	2.54	0.17		
2510	-1.57	-0.17	-4.48	2.53	2.52	-0.789		radio static
2511	-0.42	0.98	-5.27	2.53	2.52	-0.789		
2512A	-1.5	1.15	-5.25	2.53	2.52	-0.789		
2508	-1.25	1.25	-5.26	2.53	2.52	-0.789		
2507	-1.5	1.1	-5.26	2.53	2.52	-0.789		
2506	-0.8	1.67	-5.24	2.53	2.52	-0.789		
0207	-0.5	1.81	-5.23	2.53	2.52	-0.789		

ELF Phase III Test 1 Test Record

DAY 3 – MARCH 9, 2010

Run #	Mag x (V)	Mag y (V)	Mag z (V)	Tilt x (V)	Tilt y (V)	Pressure (V)	Angle of Scow (deg)	Comments:
0306	0.65	1.83	-5.21	2.54	2.51	-0.71		
3509	0.63	1.78	-5.2	2.54	2.51	-0.71		
3510	0.68	1.77	-5.2	2.54	2.52	-0.71		
3511	0.57	1.81	-5.2	2.54	2.52	-0.71		
3512	1	1.67	-5.2	2.54	2.52	-0.71		
3508	0.63	1.8	-5.2	2.54	2.51	-0.71	293	
3507	0.73	1.75	-5.2	2.54	2.51	-0.71	285	
3506	1.01	0.166	-5.2	2.54	2.51	-0.71	277	
3505	0.96	1.66	-5.2	2.54	2.51	-0.71	284	
3501	1.05	1.78	-5.2	2.54	2.51	-0.71		
3502	0.7	1.79	-5.2	2.54	2.51	-0.71	285	
3503	0.9	1.68	-5.2	2.54	2.51	-0.71		
3504	0.55	1.82	-5.2	2.54	2.52	-0.71	297	
0305	-1.29	1.2	-5.21	2.56	2.52	0.24		
3412	-1.14	1.5	-5.2	2.56	2.52	0.24		
3411	-0.61	1.81	-5.19	2.56	2.52	0.24	283	
3410	-1.77	0.2	-5.2	2.56	2.53	0.24	295	
3404	-1.75	0.44	-5.21	2.56	2.53	0.24		
3405	-1.76	-0.16	-5.22	2.56	2.52	0.24		
3406	-1.77	0.4	-5.21	2.56	2.53	0.24		
3407	-1.33	1.29	-5.2	2.56	2.53	0.24		
3408	-1.66	0.72	-5.21	2.56	2.52	0.24	274	
3408A	-1.6	0.85	-5.21	2.56	2.52	0.24	270	
3404	-1.78	0.07	-5.22	2.56	2.52	0.24		
3403	-1.68	0.67	-5.21	2.56	2.53	0.24		
3402	-1.77	0.28	-5.22	2.56	2.53	0.24		
3401	-1.78	0.18	-5.22	2.56	2.53	0.24		
0304	-1.28	1.42	-5.19	2.56	2.53	1.36		492 feet
3309	-1.35	1.26	-5.2	2.57	2.53	1.36		
3310	-1.38	1.21	-5.2	2.57	2.53	1.36		
3311	-1.65	0.77	-5.2	2.57	2.53	1.36		
3312	-1.66	0.82	-5.2	2.57	2.53	1.36		
3308	-1.78	-0.05	-5.22	2.56	2.53	1.36		
3307	-1.74	-0.28	-5.22	2.56	2.53	1.36		
3306	-1.79	0.19	-5.21	2.57	2.53	1.36		
3305	-1.7	-0.32	-5.22	2.57	2.53	1.36		
3301	-1.24	-1.25	-5.23	2.57	2.53	1.36		
3302	-0.95	-1.44	-5.24	2.57	2.53	1.36		
3303	-1.7	-1.35	-5.24	2.57	2.53	1.36		
3304	-0.29	-1.69	-5.24	2.57	2.53	1.36		
3201	1.33	-1.2	-5.23	2.57	2.53	1.36		
3202	0.08	-1.73	-5.24	2.57	2.53	1.36	273	
3203	-0.16	-1.72	-5.24	2.55	2.53	1.36		
3204	0.71	-1.51	-5.23	2.58	2.54	1.36	262	

ELF Phase III Test 1 Test Record

Run #	Mag x (V)	Mag y (V)	Mag z (V)	Tilt x (V)	Tilt y (V)	Pressure (V)	Angle of Scow (deg)	Comments:
3208	1.65	0.89	-5.2	2.57	2.53	1.36		
3207	1.83	0.45	-5.2	2.57	2.54	1.36	265	
3206	1.83	-0.13	-5.2	2.57	2.54	1.36		
3205	1.73	-0.53	-5.22	2.57	2.53	1.36		
3209	1.57	-0.99	-5.22	2.57	2.54	1.36		
3210	1.39	1.2	-5.2	2.57	2.53	1.36		
3211	1.04	1.69	-5.18	2.57	2.54	1.36		
3212	1.67	0.7	-5.2	2.57	2.54	1.36		
3101	-1.77	0.45	-5.2	2.57	2.52	0.226	268	
3102	-1.65	-0.79	-5.22	2.57	2.53	0.226		
3103	-1.62	1.15	-5.2	2.57	2.53	0.226		
3104	-1.41	1.21	-5.2	2.57	2.53	0.226		
3108	-1.02	1.62	-5.19	2.57	2.53	0.226	280	
3107	-1.42	1.27	-5.19	2.57	2.53	0.226		
3106	-1.52	1.17	-5.19	2.57	2.53	0.226	290	
3105	-1.07	1.56	-5.19	2.57	2.53	0.226		
3109	-1.67	-0.61	-5.2	2.58	2.53	0.226	294	
3110	-1.52	0.92	-5.2	2.58	2.53	0.226		
3111	-1.81	0.3	-5.2	2.58	2.53	0.226	290	
3112	-1.56	0.9	-5.2	2.57	2.53	0.226		
3004	1.48	1.23	-5.18	2.51	2.51	-0.709	290	
3003	1.41	1.41	-5.18	2.52	2.52	-0.709		
3002	1.76	0.9	-5.17	2.52	2.52	-0.709	285	
3001	1.85	0.75	-5.17	2.52	2.52	-0.709		
3005	1.84	0.71	-5.17	2.52	2.52	-0.709	293	
3006	1.74	0.94	-5.17	2.52	2.52	-0.709		
3007	1.82	0.77	-5.17	2.52	2.52	-0.709	284	
3008	1.65	1.2	-5.18	2.52	2.52	-0.709		
3012	1.75	0.94	-5.17	2.52	2.52	-0.709	284	
3011	1.93	0.45	-5.17	2.52	2.52	-0.709		
3010	1.9	0.57	-5.17	2.52	2.52	-0.709		
3009	1.9	0.55	-5.17	2.52	2.52	-0.709	282	
0307	1.8	0.8	-5.17	2.52	2.52	-0.709		

ELF Phase III Test 1 Test Record

DAY 4 – MARCH 10, 2010

Run #	Mag x (V)	Mag y (V)	Mag z (V)	Tilt x (V)	Tilt y (V)	Pressure (V)	Angle of Scow (deg)	Comments:
0210	0.4	1.89	-5.2	2.59	2.54	6.967		Pressure in air ~7.00 (which is incorrect)
0211	-1.53	-0.87	-5.21	2.58	2.53	6.967		45 feet deep
2001	0.2	1.92	-5.2	2.59	2.53	6.967	384	
2002	0.14	1.93	-5.2	2.58	2.53	6.967		
2003	0.2	1.92	-5.2	2.58	2.53	6.967		
2004	0.32	1.9	-5.2	2.58	2.53	6.967		
2008	0.3	1.9	-5.2	2.58	2.53	6.967		
2007	0.65	1.8	-5.2	2.58	2.53	6.967		
2006	0.6	1.82	-5.2	2.58	2.53	6.967	336	
2005	0.67	1.78	-5.21	2.58	2.53	6.967		
2009	0.2	1.92	-5.2	2.58	2.53	6.967	349	
2010	0.04	1.93	-5.2	2.58	2.53	6.967		
2011	0.03	1.92	-5.2	2.58	2.53	6.967		
2012	-0.04	1.92	-5.2	2.58	2.53	6.967	0	
2104	-1.33	-1.12	-5.22	2.58	2.53	6.967		
2103	-0.79	-1.54	-5.23	2.58	2.53	6.967		
2102	-1.35	-1.1	-5.22	2.58	2.53	6.967		
2101	-1.19	-1.27	-5.22	2.58	2.53	6.967		
2105	-1.5	-0.98	-5.21	2.58	2.53	6.967		
2107	-1.4	-1.04	-5.21	2.58	2.53	6.967		100 Hz for this run
2106A	-1.43	-1.07	-5.22	2.58	2.53	6.967		
2108	-1.5	-0.98	-5.22	2.58	2.53	6.967		
2109	-1.68	-0.58	-5.21	2.58	2.53	6.967		
2110	-1.5	-1	-5.22	2.58	2.53	6.967		
2111	-1.55	-0.97	-5.22	2.58	2.53	6.967		
2112	-1.46	-1.03	-5.22	2.58	2.53	6.967		
0212	1.31	1.32	-5.2	2.59	2.535	6.97		
2201	1.57	0.98	-5.21	2.59	2.535	6.97		
2202	0.72	1.79	-5.18	2.59	2.535	6.97		
2203	1.2	1.44	-5.2	2.59	2.535	6.97		
2204	1.02	1.61	-5.19	2.59	2.535	6.97		
2205	0.71	1.79	-5.18	2.59	2.535	6.97		
2206	0.24	1.92	-5.17	2.59	2.535	6.97	14	
2207	1.25	1.36	-5.2	2.59	2.535	6.97	351	
2208	0.6	1.83	-5.18	2.59	2.535	6.97	0	
2216	-0.54	1.87	-5.17	2.59	2.535	6.97		
2215	-0.66	1.84	-5.17	2.59	2.535	6.97		
2214	-0.81	1.78	-5.17	2.59	2.535	6.97		
2213	-0.46	1.88	-5.17	2.59	2.535	6.97		
2209	-1.04	1.62	-5.17	2.59	2.535	6.97	15	
2210	-0.62	1.86	-5.17	2.59	2.535	6.97		
2211	-0.59	1.85	-5.17	2.59	2.535	6.97	358	
2212	-0.78	1.79	-5.17	2.59	2.535	6.97		

ELF Phase III Test 1 Test Record

Run #	Mag x (V)	Mag y (V)	Mag z (V)	Tilt x (V)	Tilt y (V)	Pressure (V)	Angle of Scow (deg)	Comments:
0213	-1.38	1.36	-5.17	2.59	2.535	6.97		
0504	-0.93	1.6	-5.21	2.56	2.52	6.97		Moved to location 5 (496 feet)
5212	-1.36	-1.14	-5.24	2.56	2.52	6.97		
5211	-0.54	-1.65	-5.24	2.56	2.52	6.97		
5210	0.3	-1.74	-5.24	2.56	2.51	6.97		
5209	0.39	-1.72	-5.24	2.56	2.51	6.97		
5205	-1.04	-1.43	-5.24	2.56	2.52	6.97		
5206	-0.99	-1.42	-5.24	2.57	2.51	6.97		
5207	-1.11	-1.3	-5.23	2.57	2.51	6.97		
5208	-1.24	-1.22	-5.24	2.57	2.52	6.97		
5204	-0.4	-1.69	-5.23	2.57	2.52	6.97		
5203	-1.11	-1.37	-5.24	2.57	2.52	6.97		
5202	0.43	-1.7	-5.23	2.56	2.52	6.97		
5201	0.6	-1.67	-5.23	2.56	2.52	6.97		
0509	1.2	-1.38	-5.22	2.55	2.51	6.97		

ELF Phase III Test 1 Test Record

DAY 5 – MARCH 11, 2010

Run #	Mag x (V)	Mag y (V)	Mag z (V)	Tilt x (V)	Tilt y (V)	Pressure (V)	Angle of Scow (deg)	Comments:
0407	1.73	-0.46	-5.23	2.58	2.51	6.97		
4303	1.75	-0.38	-5.23	2.58	2.51	6.97		
4304x	1.8	0.21	-5.24	2.59	2.51	6.97		
4304y	1.79	0.28	-5.24	2.59	2.51	6.97		
4304z	1.78	0.3	-5.24	2.59	2.52	6.97		
4303z	1.78	-0.22	-5.24	2.59	2.52	6.97		
4303y	1.75	-0.34	-5.24	2.59	2.52	6.97		
4303x	1.8	0.14	-5.24	2.59	2.52	6.97		
4211x	1.78	-0.19	-5.24	2.59	2.52	6.97		
4211y	1.61	-0.72	-5.24	2.59	2.52	6.97		
4211z	1.4	-1.12	-5.24	2.58	2.52	6.97		
4212z	1.07	-1.4	-5.24	2.59	2.52	6.97		
4212y	0.69	-1.6	-5.24	2.59	2.52	6.97		
4212x	1.2	-1.23	-5.24	2.59	2.52	6.97		
4208x	0.66	1.74	-5.2	2.58	2.52	6.98		246 feet
4208y	0.54	1.78	-5.2	2.59	2.52	6.98		
4208z	0.55	1.82	-5.2	2.58	2.52	6.98		
4207z	0.4	1.8	-5.19	2.59	2.52	6.98		started moving a lot
4207y	0.5	1.7	-5.2	2.59	2.52	6.98		
4207x	1.58	0.9	-5.2	2.59	2.51	6.98		
0408	0.99	1.56	-5.2	2.59	2.52	6.98		
4307x	0.5	1.85	-5.19	2.58	2.52	6.97		
4307y	-0.4	1.79	-5.19	2.58	2.52	6.975		
4307z	1.73	0.52	-5.22	2.58	2.52	6.975		
4308z	1.8	-0.02	-5.22	2.59	2.51	6.975		
4308y	1.75	0.23	-5.22	2.58	2.52	6.975		
4308x	1.32	1.32	-5.2	2.58	2.52	6.975		
0401	-1.39	-0.95	-2.68	2.59	2.53	7.16		7 feet in the air
4009	-1.56	-1.23	-2.64	2.6	2.5	7.17		
4008	-1.4	-2.44	-2.61	2.6	2.51	7.19		

APPENDIX G: ARD TRIP REPORT

ARD Trip Report

By: Rafael Hill

Dates: March 1 - 13, 2010

Purpose: Code 75 personnel provided support to NSWCCD's Acoustic Research Detachment (ARD) for the Extremely Low Frequency Electric Phase III Trial.

Personnel: Dan Lenko was primarily responsible for setup, testing and operation of electrical equipment.

Chris Burgy was primarily responsible for overall project implementation and data retrieval.

Rafael Hill was responsible for test setup and technical support.

Daily Log: First three days were spent setting up and troubleshooting the equipment.
The final six days were spent measuring and checking data.

Objectives: To obtain data that will exercise and improve the current University of Idaho analytical models.

Pre-Test:

The test plan called for four separate platforms to be used over the course of the trial. Thus, the first days were spent collecting equipment onto the deployment barges, as well as the cal-source boat. Code 75 and University of Idaho personnel also used the initial days to test software. The equipment was divided between the platforms, including: a calibration source boat, a sensor boat, a sensor barge (scow), and an electric field barge. The Acoustic Research Detachment had most of the GPS equipment set up before Code 75 personnel arrived. The remaining issues included: the recording of GPS data in the required format, troubleshooting unexpected sensor readouts, and the overall deployment of the sensor.

ELF Phase III Test 1 Test Record

Before arrival, it had been assumed that adding lead weights to the top of the sensor plate (the plastic plate the sensor was mounted to) would be sufficient to stabilize the sensor. However, after more careful inspection, Code 75 personnel determined that the center of buoyancy was somewhere in the middle of the sensor with the center of mass above that point. After determining that adding weights to the top plate would only partially solve the problem, with the sensor still inclined to flip over if it started to tilt, it was decided that ARD would have to develop a system to deploy the sensor a different way. Additionally, the lead weights had to be deployed low enough to stabilize the sensor and avoid effecting the sensor readings (being too close to the bottom electric arm), while also fitting the requirements of deployment from the sensor barge.

The solution which Code 75 and ARD personnel decided on utilized 200 pounds of lead weights suspended from a tripod sling attached to the sensor plate. This worked extremely well from a stability standpoint, as seen in the sensor data. It is unknown if having the lead so close to the bottom electric sensor arm (within 2 feet) had any real effect on the readings. To minimize effects, the lead blocks were coated with paint to avoid having exposed metals close to the sensor arm. The ERMA sensor used in the test resembles the one pictured below, but was deployed in an inverted state:



Code 75 discovered even more deployment issues when they realized that the bottom arm of the sensor would have had to be “burped” at the beginning of each deployment to function correctly. To accomplish this, the sensor would have to tilt enough to fill the bottom arm with

ELF Phase III Test 1 Test Record

water (while deployed), or the arm would have to be pre-filled and then the cap removed when the arm was partially submerged (during deployment). Due to difficulties surrounding the deployment of the lead weights with the sensor, Code 75 personnel chose the second option. Accordingly, ARD personnel used a small boat to maneuver close to the semi-deployed sensor, and unscrewed the cap while submerged under a few inches of water.

This was the first time Code 75 had created software for the new GPS system from ARD in which two base-station antennas were used, with the combined output of one position, and their relative heading. Previous systems used two rover antennas to get the position of the bow and stern of a platform and then the heading was manually calculated. However, due to coding errors, the acquisition systems deployed by Code 75 could not record the information from the multiple GPS systems. This proved irrelevant, as ARD had set up the GPS systems to individually report back to the Remote Operations Center.

During the previous shakedown trip, the orientation sensor for the electric source truss did not function properly when rotated in certain directions. ARD provided new orientation sensors for this test, and the University of Idaho and Code 75 confirmed proper functionality before testing began.

Testing:



The testing was divided into five days of tests. One day was done with the cal-source boat, three with the E-source truss, and one with the magnetic source coil. One of the main concerns going into testing was the possibility of inclement weather. The biggest weather

concern was wind, as the induced chop would affect deploying the source/sensor and possibly have altered readings. Additionally, as some locations were unmoored, windy days would add unnecessary risk in deployment. Despite the expectations of Code 75, there were only brief spurts of wind and rain, and for the most part the weather was not a factor.

The first day consisted of 28 runs, with the sensor barge unmoored at location 1 (see map above). Each “run” consisted of recording Data for two minutes. While unmoored it had a tendency to drift and rotate. This made it difficult to drive the calibration boat past the sensor at a precise angle and distance from the sensor. Code 75 observed the data recorder during and after the runs to ensure the acquisition software was working properly.

The second day consisted of 31 runs, with the sensor moored at location 6, in which the lake was less than 450 feet deep, with the E-source moored at location 4. The day was the first with both the sensor and E-source truss deployed, and due to time constraints involved with the deployment learning curve, all runs were completed with the E-source in one orientation (day four finished the second orientation originally planned for this day). Two gas-powered generators ceased to function on the E-source barge during the day, which ARD subsequently replaced.

The third day consisted of 77 runs. The sensor was moored at location 5 with the E-source moored at location 4. This day we were able to achieve three different depths for the sensor and E-source each, two orientations for the E-source, and four different frequencies at each depth and orientation (DC, 10, 100, and 1000 Hz).

The fourth day we completed 58 runs, completing the second orientation from day two. The University of Idaho requested a couple of runs with the E-source slanted upward (where one plate was deeper than the other), and those were taken as well. The second half of the day placed the sensor barge unmoored at location 1 and the E-source moored at location 4. Code 75 took measurements in one E-source orientation, with the electric dipole facing perpendicular to the sensor.

The fifth and final day we completed 30 runs with the magnetic source coil beached at location 3 and the sensor barge moored at location 6. The University of Idaho determined that these runs may be more difficult to observe and record because the signal strength was not much greater than the noise during all runs. Code 75 was able to see the analog signal on the spectrum analyzer, but it was not determined whether this signal would be seen after passing through the

ELF Phase III Test 1 Test Record

A-D converter. To aid the analysts in the future, the subsequent runs were broken up into components in which a signal amplifier was used to boost the signal for the x, y, and then z axes.

For each day the acquisition system, along with the GPS, recorded: the locations of the sensor, the sensor measurement channels, the location of each source, the signal produced from each source, and orientation of each barge. Code 75 also recorded (manually) the rotation/direction of the sensor, its tilt, and pressure from the EM sensor interface board; as well as the depth of the sensor according to markers installed by ARD. These manual recordings proved useful as the built-in depth sensor ceased to function correctly after the first day.

As of yet, the Code 75, U of I, and ARD personnel involved consider the trial a success. Many of the issues, such as sensor deployment and the recording of GPS strings, were identified and corrected during the pre-test. Lowering and raising the sensor and E-source was not a problem and the data acquired appeared to be what was expected. Dealing with the sensor and the sensor arms were at times cumbersome but they did not cause any problems in the end. In the future there were a few things that could be improved upon such as: testing out Code 75's GPS software beforehand, having reliable generators, and exploring different depth-sensor options. Code 75 and ARD will now await the results and all three parties will reconvene to decide whether an upcoming test is viable to further exercise the University of Idaho's model.

**ELF PHASE III TEST 2
(September 11 – 17, 2010)
Test Record**

**Compiled by:
Frank Jurenka, NSWCCD 7260
Don Pugsley, NSWCCD 7530
Stephanie Ferrone, NSWCCD 7530
Vickie Pfeifer, NSWCCD 7260**

December 8, 2010

TABLE OF CONTENTS

1. PROJECT TEST ABSTRACT.....	4
1.1. OVERVIEW	4
1.2. OBJECTIVES	4
1.3. RESPONSIBILITIES	4
1.4. PROJECT PHASES	4
2. TEST RISK ANALYSIS	5
3. OPERATIONAL SAFETY	7
4. WEIGHT HANDLING.....	8
5. ENVIRONMENTAL/HAZMAT	8
6. TEST ORGANIZATION MATRIX.....	9
7. TEST SCENARIO.....	9
7.1. TEST SITE	9
7.2. LAKE ENVIRONMENTAL PARAMETERS	13
7.3. GLOBAL POSITIONING SYSTEM.....	14
7.4. ELECTRIC AND MAGNETIC SOURCES	17
7.4.1. 4-M Electric Source	18
7.4.2. Portable Electric Source.....	19
7.4.2.1. <i>Electric Source Drive and Control</i>	22
7.4.3. Magnetic Source	24
7.4.3.1. <i>Magnetic Source Drive and Control</i>	27
7.5. PORTABLE MEASUREMENT ARRAY (PEMA)	29
7.6. DATA ACQUISITION	31
8. TEST SITE OPERATIONS	35
8.1. OPERATIONS TEAM.....	35
8.2. MOORING PLAN.....	35
8.3. OPERATING PROCEDURES.....	38
8.4. EMERGENCY PROCEDURES.....	38
9. TEST RUN PLAN EXECUTION	38
9.1. NOISE MEASUREMENTS	39
9.2. SYSTEM CHECK-OUT RUNS	39
9.3. ELF RUNS.....	39
9.3.1. Magnetic Source Runs	40
9.3.2. 4-M Electric Source Boat Runs	41
9.3.3. Electric Source Runs.....	42
9.4. DATA REPORTING.....	44
REFERENCES	44
APPENDIX A: PORTABLE EM SENSOR TECHNICAL SPECIFICATIONS....	A-1
APPENDIX B: TEST RUN RECORD	B-1

LIST OF FIGURES

Figure 1	Lake Pend Oreille	10
Figure 2	Topographical Map of Test Area.....	11
Figure 3	Source and Sensor Locations.....	12
Figure 4	GPS Diagram.....	15
Figure 5	GPS Antennas on Barges.....	16
Figure 6	GPS Equipment Set-up on Sensor Barge.....	17
Figure 7	4-M Electric Source Boat	18
Figure 8	4-M Electric Source Electrode	18
Figure 9	4-M Electric Source System Diagram	19
Figure 10	Portable Electric Source	20
Figure 11	60' Barge Layout (E-Source)	21
Figure 12	E-Source Deployment from 60' Barge	21
Figure 13	Electric Source System Diagram	22
Figure 14	E-Source Drive and Control System Set-Up	23
Figure 15	NI Data Logging System for E-Source	24
Figure 16	Magnetic Source	25
Figure 17	Magnetic Source GPS Layout - Horizontal	26
Figure 18	Magnetic Source GPS Layout – Vertical.....	27
Figure 19	Magnetic Source System Diagram	28
Figure 20	M-Source Drive and Control System Set-Up	29
Figure 21	PEMA Deployment	30
Figure 22	Scow (Sensor Barge) Layout	31
Figure 23	Sensor and Data Acquisition System Diagram	33
Figure 24	Sensor Control and Data Acquisition	34
Figure 25	45' Mooring Barge	36
Figure 26	60' E-Source Barge Moored to 45' Barge	36
Figure 27	Sensor Barge Moored at Location 8	37
Figure 28	M-Source, Source Control Boat, and Moored Sensor Barge	41
Figure 29	4-M Source Boat Passing by Sensor Barge Moored at Location 7	42
Figure 30	Sensor Barge and E-Source Barge Moored in Test Configuration	43

LIST OF TABLES

Table 1	ELF Phase 3 Test 2 ORM Analysis.....	6
Table 2	GPS Output.....	17
Table 3	CDAQ PEMA Channel Assignments.....	32
Table 4	Personnel Assignments	35
Table 5	ARD Base Radio Call Signs.....	38

1. PROJECT TEST ABSTRACT

1.1. OVERVIEW

Efforts to understand, measure, and model the propagation of underwater Extremely Low Frequency (ELF) signals is important in the evaluation of Navy vessels' susceptibility to detection systems and mines. This is especially significant in light of the Navy's desire to build an all electric ship.

1.2. OBJECTIVES

The overall objectives of the ELF testing are to:

- Research analytical theories to better understand the propagation, scattering, refraction, and reflection of ELF fields.
- Develop an experimental test-bed for the complete characterization and prediction of ELF signals in shallow and deep water environments.
- Develop numerical simulation tools for predicting EM propagation in environments with variable conductivity and geometric features.

1.3. RESPONSIBILITIES

This project was a collaborative effort between the University of Idaho (UI), the Naval Surface Warfare Center Carderock Division (NSWCCD), and the Acoustic Research Detachment (ARD). UI was responsible for modeling and simulation, Carderock was responsible for experiment design and data acquisition, and the ARD was responsible for developing, assembling, and deploying test apparatus onto the lake. Conducting the prescribed experiments was a collaborative responsibility.

1.4. PROJECT PHASES

The ELF project was a three phase project. During Phase I, the following was accomplished:

- Cal source runs executed (3/08) and data delivered to UI
- Initial data set acquired during AESD testing
- Initial numerical model development

ELF Phase III Test 2 Test Record

During Phase II, the following was accomplished:

- Lake topography delivered to UI
- Testing completed with towed electric source (12/08)
- Verification of test data and delivery to UI (1/09)

Two tests were conducted during Phase III. The first test occurred in March 2010 and the second test occurred in September 2010. During Phase III testing the following was accomplished:

- A portable electric source (E-source) was deployed on the lake at varying depths and orientations
- A magnetic source (M-source) was deployed on, and next to, shore at Farragut State Park in vertical and horizontal orientations
- A 4-m hull mounted electric source was deployed at varying distances and orientations from the portable measurement array (PEMA)
- Measurements of the generated electric and magnetic fields at many locations and depths using PEMA and a portable data acquisition system
- Verification of test data and delivery to UI (3/10, 9/10)

This report documents the ELF Phase III Test 2 that was conducted September 11–17, 2010.

2. TEST RISK ANALYSIS

An Operational Risk Management (ORM) analysis was performed prior to test operations (9/2/2010). Table 1 details the risks that were addressed.

ELF Phase III Test 2 Test Record

Table 1 ELF Phase 3 Test 2 ORM Analysis

Operational Analysis	Potential Hazards	Risk Control Options
Outfitting 45', 60' Barges with winches, power packs, equipment, sources	Dropped equipment, overloading equipment, injury	Safety observer for crane ops. Follow P-307, ARD INSTR 11262, and Daily Work Sheet instructions. Designated rigger in charge, crane operator, and signalman. Tag line on loads.
Installing Anchors for Scow, 45' Barge	Equipment damage, injury	Surveyed locations with GPS and depth finder to determine proper scope. Follow mooring procedure (ELF OP 003). Safety/procedure pre-brief conducted with crews prior to operations. Check safety shackles/cotter pins, ensure proper rigging.
Weather	Loss of equipment, injury	Obtain weather forecast from multiple sources prior to starting operations. Monitor weather during operations. Cancel operations should the weather conditions deteriorate to the point that personnel injury or equipment damage is imminent. In severe weather conditions, all personnel are to wear PFD's when on deck. Limit for E-source truss lift is 20 mph.
Mooring barges to anchor lines	Personnel Injury, Equipment Damage	A-frame and scow offset during mooring operation. Props rotated in board. Follow mooring procedure (ELF OP 003). Safety/procedure pre-brief conducted with crews prior to operations.
E-Source Truss Deployment (Asher Crane Ops)	Equipment damage, injury	Safety observer for crane ops. Follow P-307 ARD INSTR 11262, and Daily Work Sheet instructions. Designated rigger in charge, crane operator, and signalman. Two tag lines on truss. Complex lift procedure developed for this lift as part of deployment procedure (ELF OP 001). Depth of truss will be no less than 40' from the lake bottom. Lines are marked with depth. Depth sensor on truss monitored during real-time. Fish finder/depth sounder on barge to monitor truss depth simultaneously with water depth. Safety/procedure pre-brief conducted with crews prior to operations.
EM Sensor Deployment from the Scow	Equipment damage, injury	Follow EM sensor deployment procedure (ELF OP 002). Safety/procedure pre-brief conducted with crews prior to operations. Use two davits during deployment to avoid working under the load from a small boat. Depth of sensor will be no less than 40' from the lake bottom.
M Source Deployment	Equipment damage to tug, injury	Follow M-source deployment procedure (ELF OP 004). Safety/procedure pre-brief conducted with crews prior to operations. Use small tug to mobilize source and transit to location next to shore. Use weighted frame and clamps for vertical orientation. 25' boat tied up adjacent to floats.

ELF Phase III Test 2 Test Record

Operational Analysis	Potential Hazards	Risk Control Options
Test Conduct - Raising & Lowering E-source and EM Sensor	Equipment damage, injury	Depth of truss and sensor will be no less than 40' from the lake bottom. Lines are marked with depth. Depth sensor on truss monitored during real-time. Fish finder/depth sounder on barges to monitor truss and sensor depth simultaneously with water depth. Testing coordinated by test director. Safety/procedure pre-brief conducted with crews prior to operations. Use slip ring which allows real time pitch and depth of truss.
Powering E-source in water	Electrical Shock	Establish a minimum distance between E-source truss and barge before power up. Isolation of the generator from the barge deck. Personnel barrier around generator. Caution tape. Tag out E-source power source until at appropriate depth.
Buoys moored for ~ 1 week	Boating hazard, damage to buoy or boats	Lighted buoys. Testing to occur after Labor Day for reduced boat traffic.
Location 8 surface positioning line	Surface boating hazard	Chase boat ready to intercept public boats. Line will only be there when barges are staffed. Caution tape sections at 20' sections of line. Day time testing only.

It was the responsibility of all personnel to practice ORM during test operations. Additional risks may have been identified and mitigated as conditions changed during test operations.

3. OPERATIONAL SAFETY

ORM principles and processes were adhered to during all test operations.

All personnel followed safety instructions detailed in ARDINST 5100.4B "Operation of Watercraft on Lake Pend Oreille" and ARDINST 5100.5 "ARD Safety Rules Handbook". Life jackets were worn by all personnel during boat/barge transfers to the test area and during operations on barges and boats when outside of lab/control areas.

The ARD Trial Director and the Lake Operations Project Engineer briefed the customer field party and ARD operating crews on safety requirements and specific test safety concerns prior to initial underway operations. Requirements and concerns included, but were not limited to, crane operations safety

requirements, wearing PFDs while working around the waterfront and on-board vessels, electrical safety, specific test related operations, and operations protocol.

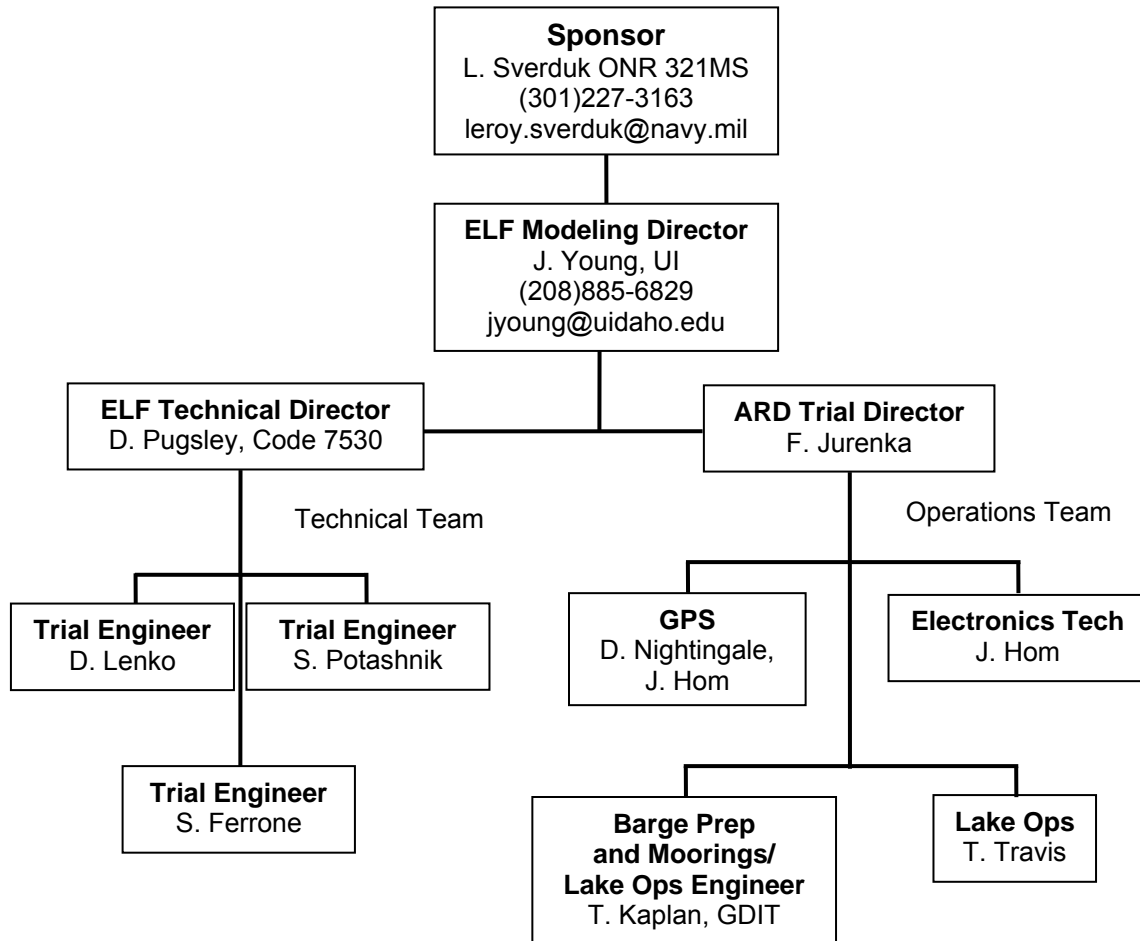
4. WEIGHT HANDLING

The ARD provided certified weight handling equipment as required. All weight handling operations were in accordance with NAVFAC P-307 and the ARD Weight Handling Instruction (ARDINSTR 11262A).

5. ENVIRONMENTAL/HAZMAT

An internal Environmental Scoping Questionnaire was completed in accordance with local ARD instructions which indicated that this testing falls under the ARD's current scope of operations.

6. TEST ORGANIZATION MATRIX



7. TEST SCENARIO

7.1. TEST SITE

The tests were conducted at the ARD located on Lake Pend Oreille in Bayview, Idaho during September 11 – 17, 2010. Lake Pend Oreille is uniquely suited for conducting the ELF propagation tests due to its uniform and stable water conductivity throughout the water column.

The ELF tests were performed at various locations in Idlewild Bay in the southern portion of Lake Pend Oreille, as shown in Figure 1, using a portable

ELF Phase III Test 2 Test Record

measurement array and data acquisition system, a portable electric source, a 4-m electric source boat, and a portable magnetic source located near the shore at Farragut State Park. This location was chosen due to the interesting bathymetric features in the area. The shallow bay provides more complex ELF propagation paths than the deep water in the middle of the lake. Figure 2 shows the topographic and bathymetric features in the test area. Figure 3 shows the locations of the sources and the measurement array.

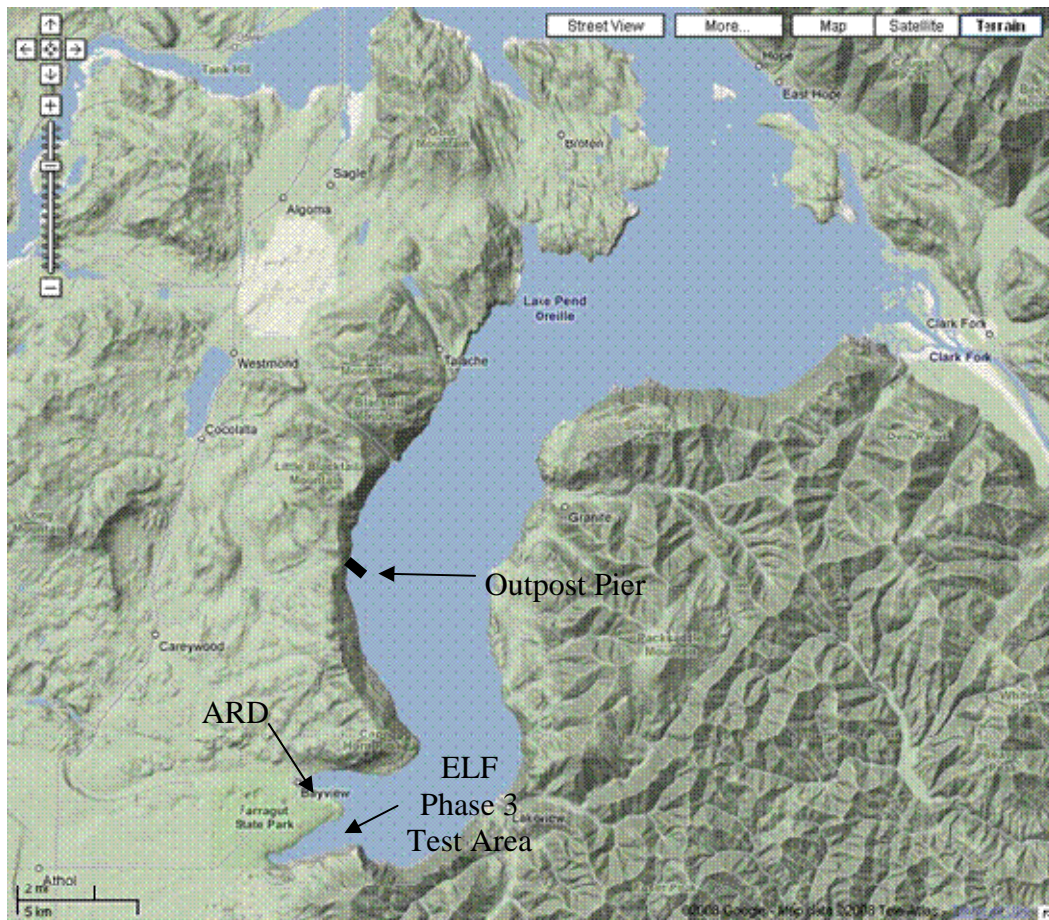


Figure 1 Lake Pend Oreille

ELF Phase III Test 2 Test Record

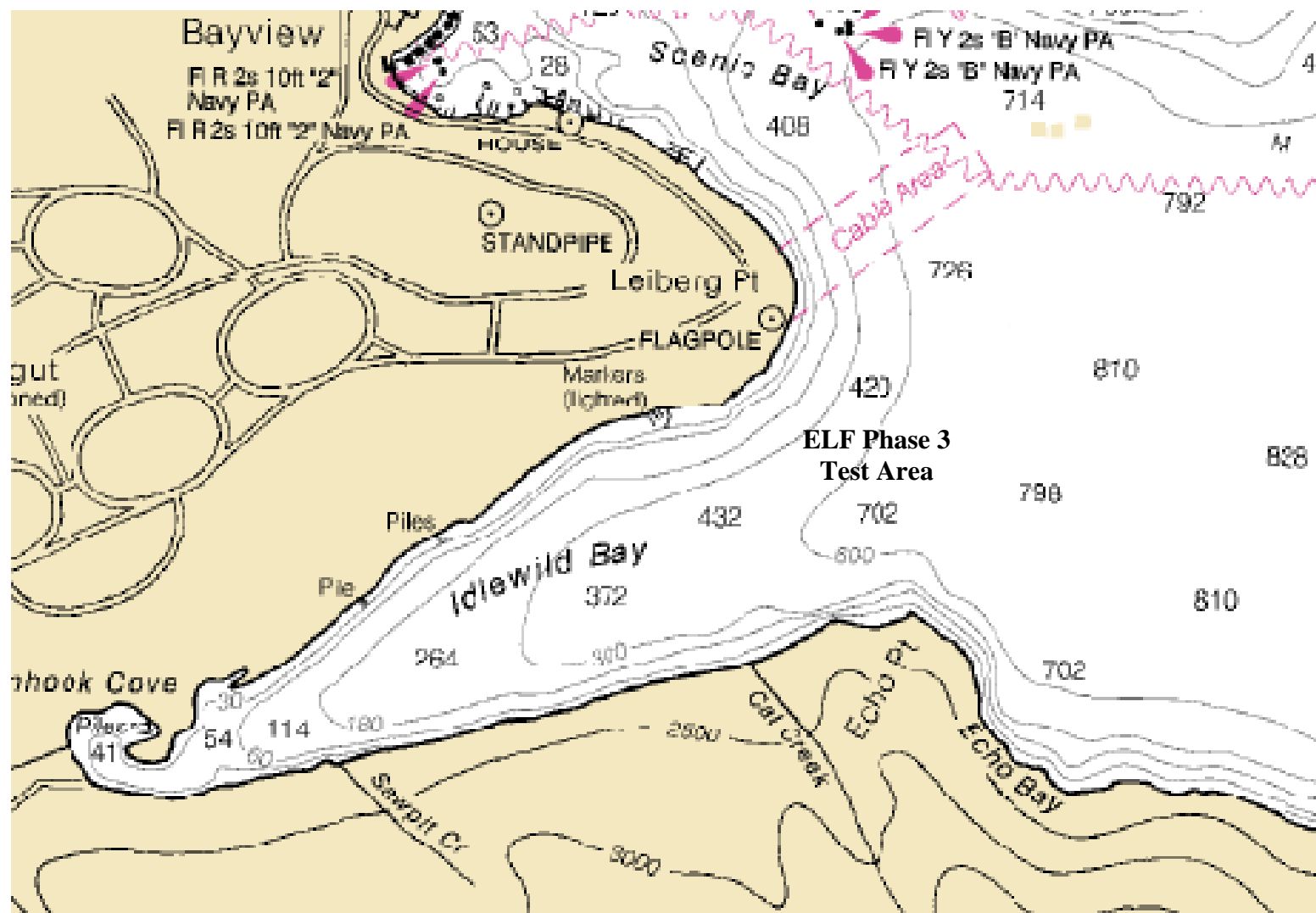


Figure 2 Topographical Map of Test Area

ELF Phase III Test 2 Test Record

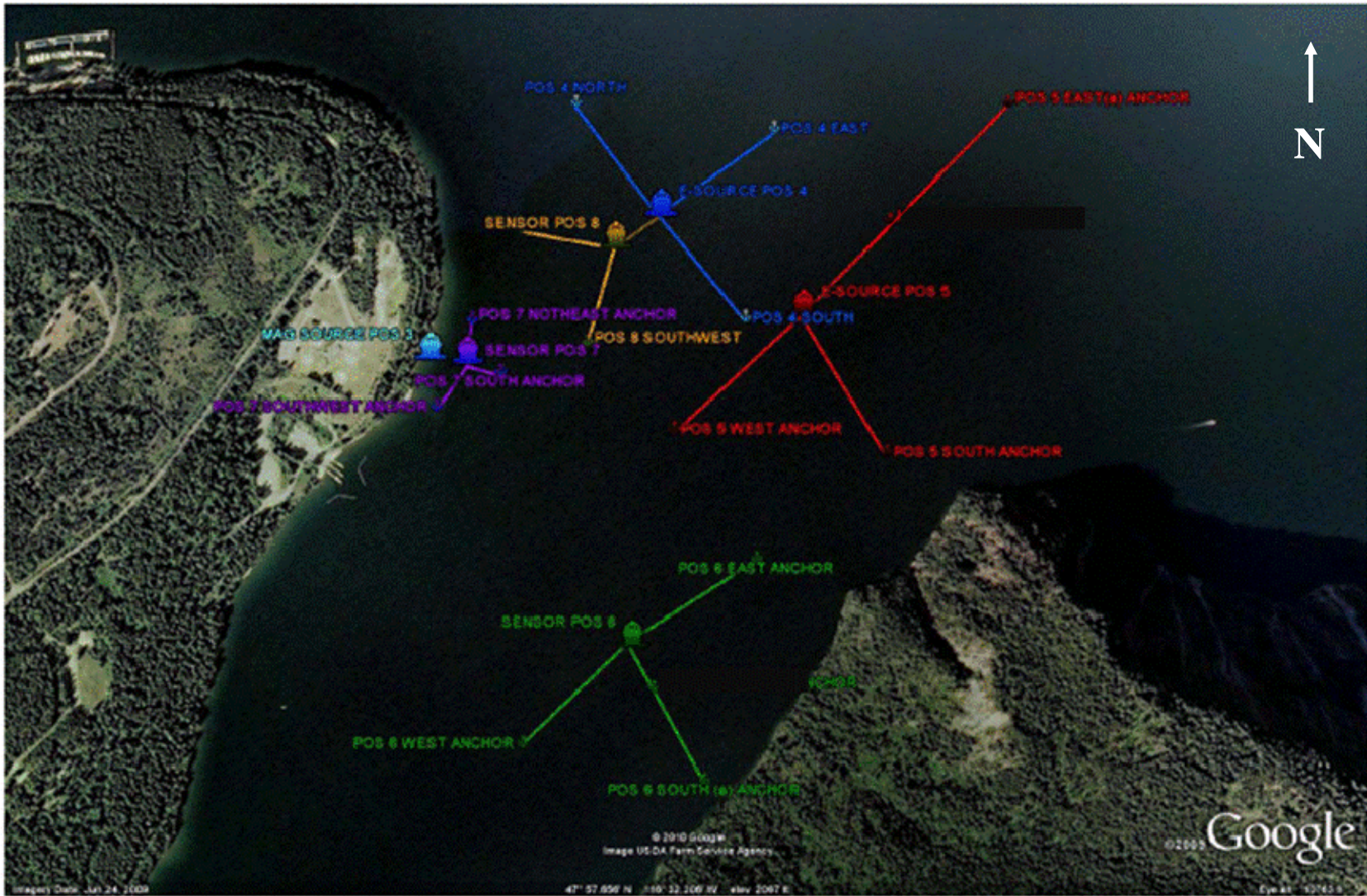


Figure 3 Source and Sensor Locations

The numbers in Figure 3 correspond to the following locations:

3. Magnetic Source (next to shore)
Lat: N 47° 57.940'
Long: W 116° 32.488'
4. Electric Source Barge (moored)
Lat: N 47° 57.90'
Long: W 116° 31.98'
Depth: 515'
5. Sensor Barge (unmoored, general location), used for system check-out
Lat: N 47° 58'
Long: W 116° 32'
6. Sensor Barge (moored)
Lat: N 47° 57.47'
Long: W 116° 32.53'
Depth: 510'
7. Sensor Barge (moored)
Lat: N 47° 57.906'
Long: W 116° 32.439'
Depth: 62'
8. Sensor Barge (moored)
Lat: N 47° 57.919'
Long: W 116° 32.095'
Depth: 340'

7.2. LAKE ENVIRONMENTAL PARAMETERS

The lake was formed by glaciers cutting through the mountains resulting in steep sides forming a 'V' made of bedrock. Over time the bottom of the 'V' filled with silt resulting in a present day flat bottom of approximately 1100 ft. in the deepest portion of the lake.

The conductivity of the lake water is a consistent 0.018 S/m throughout the water column. A sample of lake bottom muck from an anchor resulted in a measured conductivity of 0.012 S/m. The conductivity of the bedrock is unknown. The depth of the silt is estimated to be hundreds of feet.

7.3. GLOBAL POSITIONING SYSTEM

A Global Positioning System (GPS) was used to locate and to determine orientation of the 4-m electric source boat, the E-Source Barge, the M-Source, and the Sensor Barge. ELF testing required that high accuracy (RTK) positioning of the sources and the sensor be measured. The GPS system consisted of a base station located at the Outpost (N 48.08100726 deg, W 116.52802104 deg), radio links and repeaters to send corrections to the GPS rover antennas, and two GPS rovers each equipped with two antennas.

During the 4-m electric source boat tests, one GPS rover with dual antennas was mounted on the 25' fiberglass source boat. During the portable electric source tests, one GPS rover with dual antennas was mounted to the electric Source Barge (60' Barge). During the magnetic source tests, one GPS rover with dual antennas was used to locate the magnetic source (next to shore). During all tests, one GPS rover with dual antennas was mounted to the sensor barge (Scow). A block diagram of the GPS system for the sources and the Sensor Barge is shown in Figure 4.

ELF Phase III Test 2 Test Record

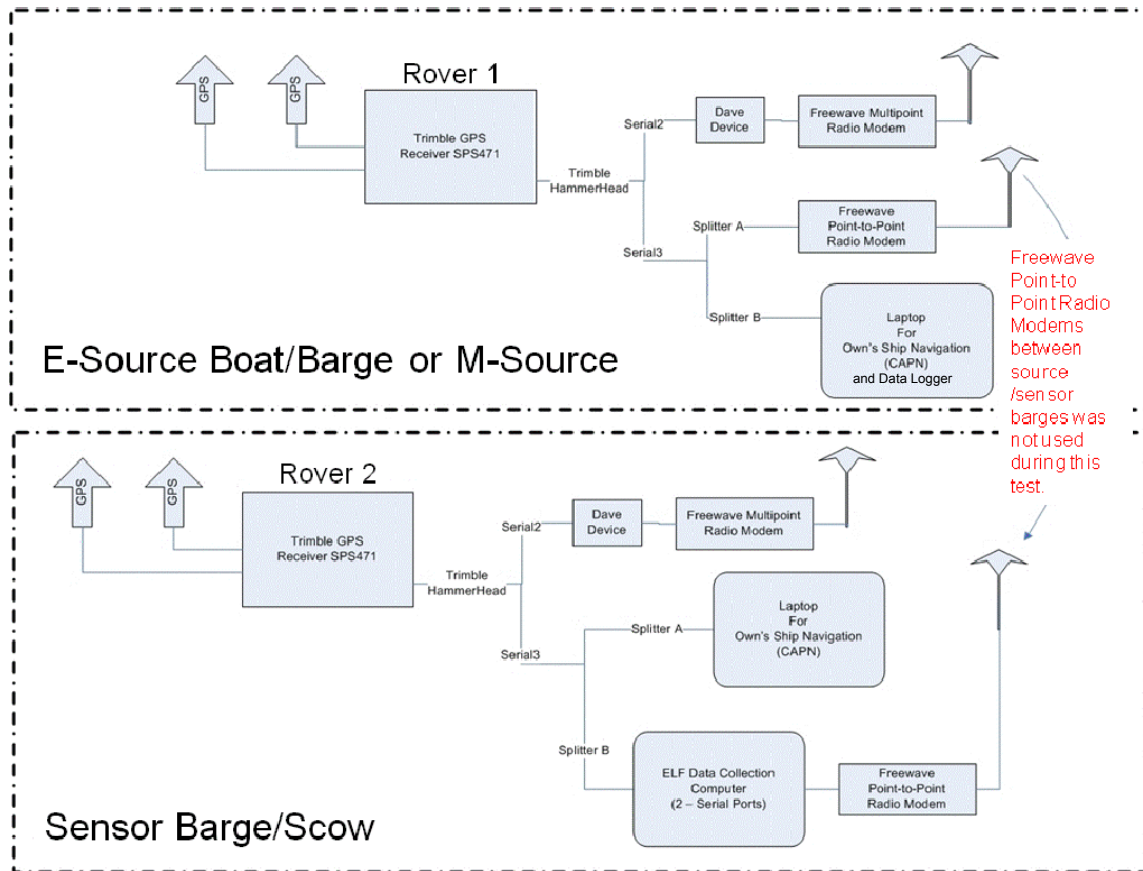


Figure 4 GPS Diagram

Rover 1 was used to locate the source being used: 4-m source boat, portable electric source, or magnetic source. Rover 2 was always used on the Sensor Barge. Figure 5 depicts the layout of the source/sensor in relation to the position and heading antennas on the barges.

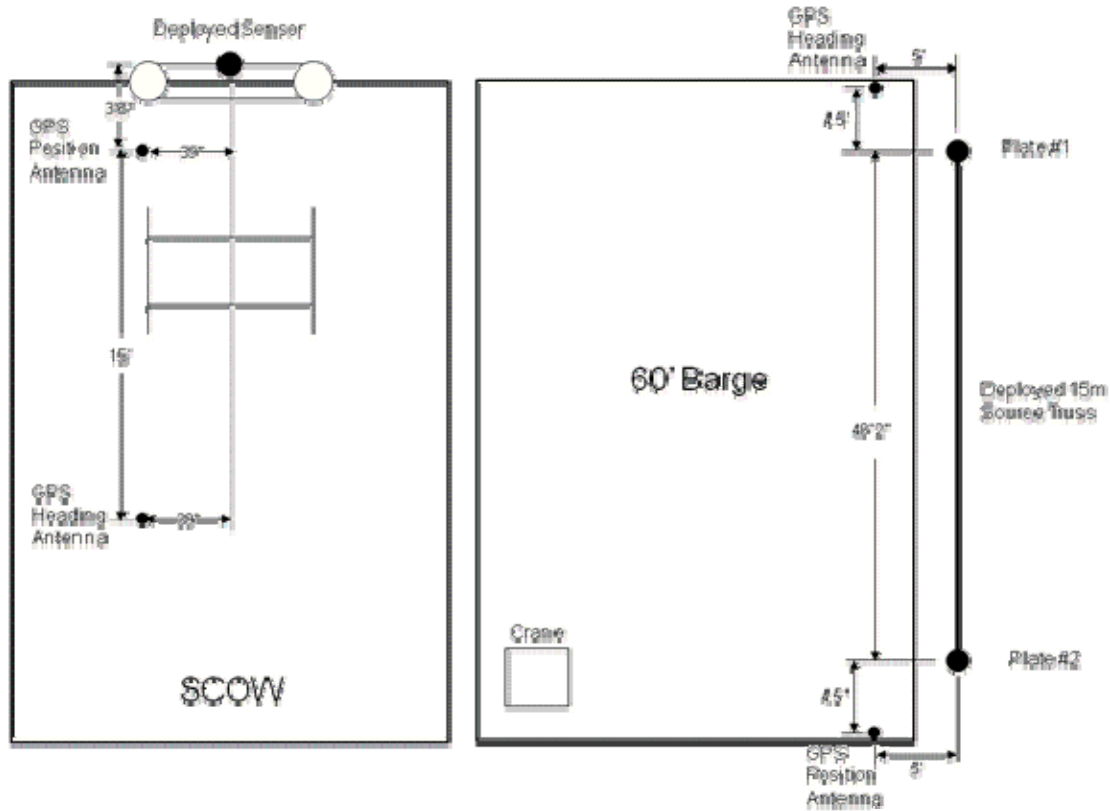


Figure 5 GPS Antennas on Barges

The source boat/barge and the Sensor Barge were configured with one radio modem. The modem (Multipoint Mode) was used to communicate with the base station at the Outpost and receive CMR corrections (necessary for RTK accuracy). The configuration of the GPS antennas on the magnetic source is shown in Figures 17 and 18 (Section 7.4.3 Magnetic Source). Figure 6 is a picture of the GPS equipment as it was configured on the Sensor Barge.



Figure 6 GPS Equipment Set-up on Sensor Barge

The Outpost also received GPS data from each boat/barge and stored it on the GPS server at the ISMS Range Operations Center (ROC). Three NEMA sentences were output by each GPS system; GGA, RMC, and HDT. An example of this output is shown in Table 2.

Table 2 GPS Output

NEMA OUTPUT SENTENCES for ELF GPS Receivers	
\$GPGGA,203324.00,4758.34570360,N,11632.31337203,W,4,07,1.4,646.937,M,-16.880,M,4.0,0000*79	
\$GPHDT,154.064,T*37	
\$GPRMC,203324.00,A,4758.34570360,N,11632.31337203,W,27.208,152.686,080110,15.5349,E,D*1D	

7.4. ELECTRIC AND MAGNETIC SOURCES

The ELF propagation measurements included the use of magnetic and electric sources as described below.

7.4.1. 4-M Electric Source

During this test, the 4-m electric source was used as a platform to obtain experimental data and to verify the test set up. The 4-m electric source consisted of two, 2' by 1', copper electrodes mounted to the bottom of a 25' fiberglass boat with a 4 m separation. The locations of the electrodes relative to the GPS antennae are as shown in Figure 7. A photo of a single electrode is shown in Figure 8.

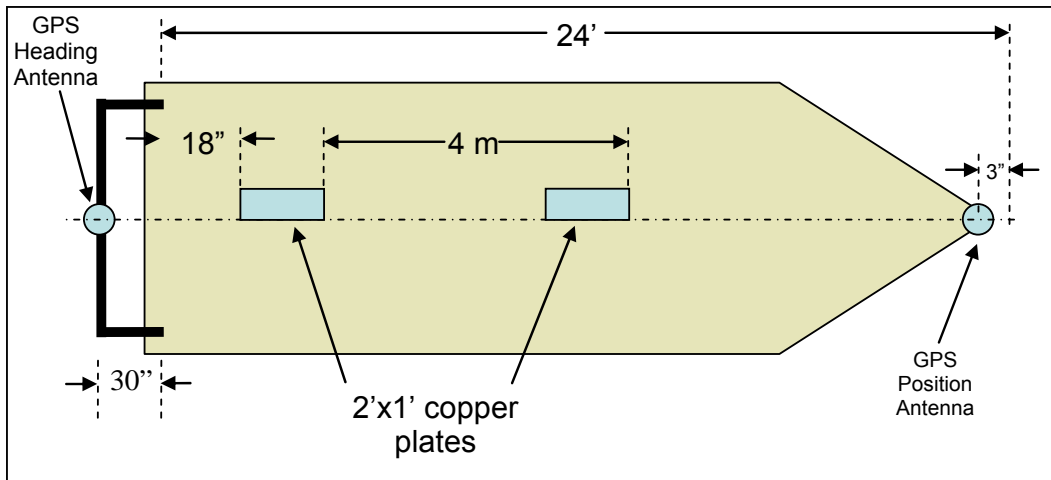


Figure 7 4-M Electric Source Boat



Figure 8 4-M Electric Source Electrode

With the boat at rest, the angle (athwart ships) from horizontal of the forward plate was 35 degrees and the angle from horizontal of the aft plate was 18 degrees. The plates were within 2 degrees of horizontal in the fore/aft direction. Both plates were on the port side of the boat just outboard of the keel.

The Code 75 CDAQ system was used to record current, waveform, and GPS information. Figure 9 shows a system diagram for the 4-m electric source on the 25' boat.

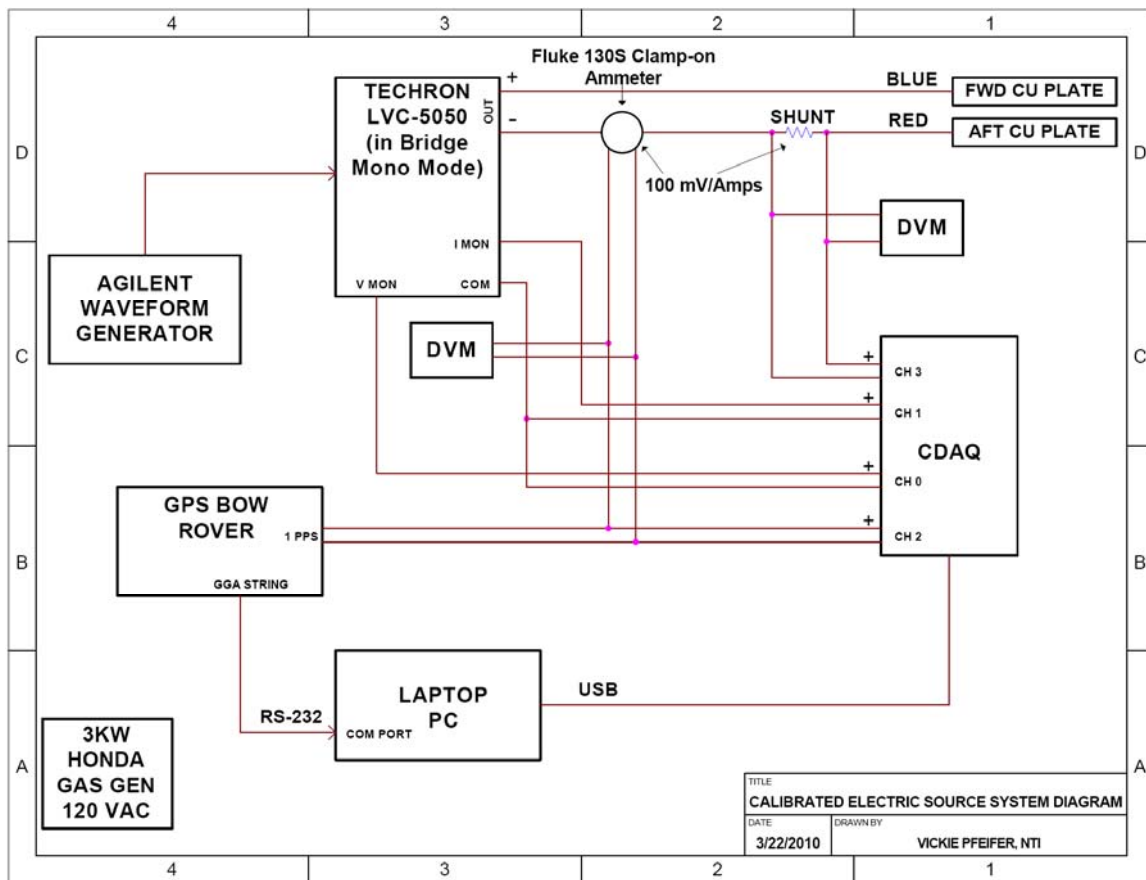


Figure 9 4-M Electric Source System Diagram

7.4.2. Portable Electric Source

The portable electric source (transmitter) consisted of a pair of copper electrodes separated by ~15 m and driven by a Techron LVC 5050 linear amplifier. The surface area of each electrode was 8 ft². The primary electric transmitter had a ~38 A-m dipole moment created by a 15 m electrode

separation driven with 2.5 amps. The low conductivity of the lake water made it prohibitive to drive more current, therefore it was necessary to have a long baseline transmitter with low current. The E-source was deployed from the 60' Barge and was capable of transmitting from any desired location at any horizontal orientation up to a depth of 500'. E-source deployment was in accordance with ELF-OP-001, "ELF Portable E-Source Truss Deployment" (Reference 1). Figure 10 shows the details of the portable E-source.

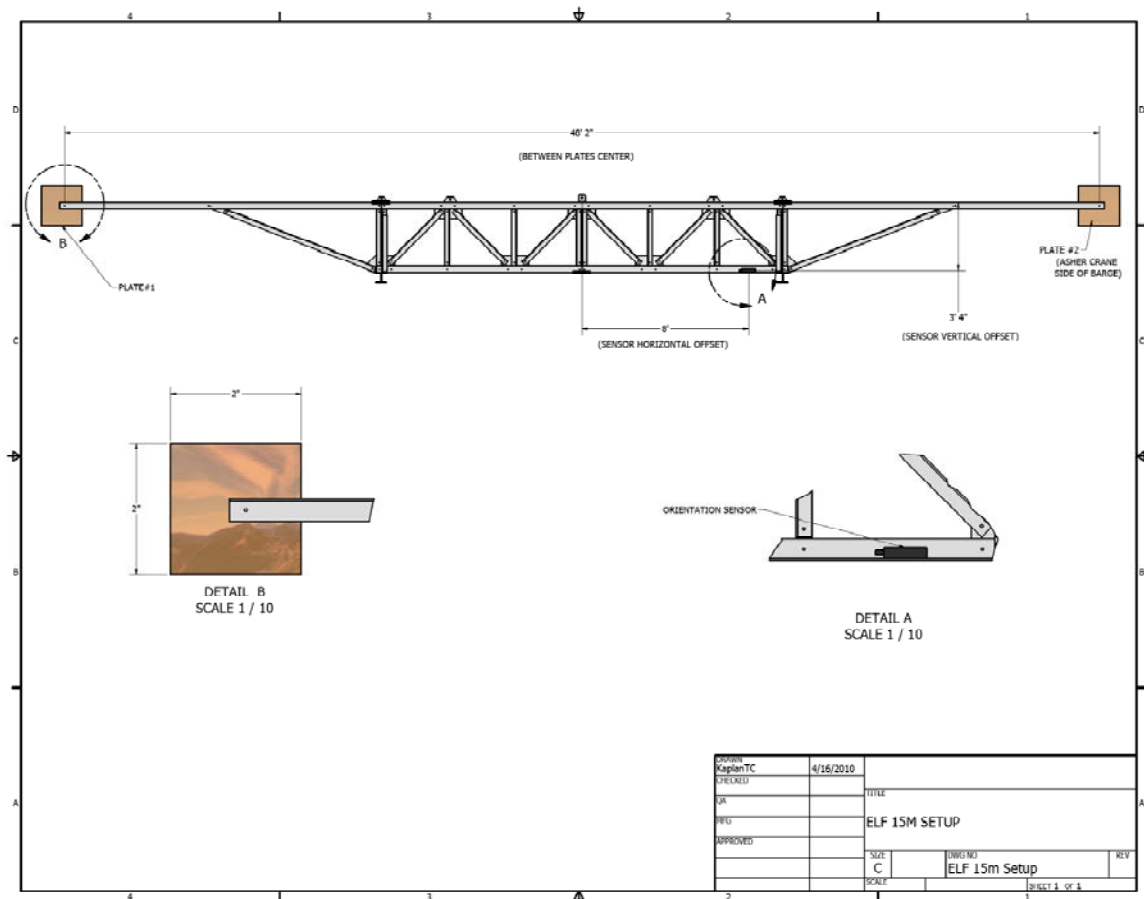


Figure 10 Portable Electric Source

The orientation of the electric dipole moment was determined from the dual channel GPS receiver mounted to the deployment barge and the orientation package mounted on the electric source.

The layout of the 60' Barge for the E-source is shown in Figure 11 and a picture of deploying the E-source truss is shown in Figure 12.

ELF Phase III Test 2 Test Record



Figure 11 60' Barge Layout (E-Source)



Figure 12 E-Source Deployment from 60' Barge

7.4.2.1. Electric Source Drive and Control

The electric source was driven by a Techron LVC 5050 linear amplifier controlled by a function generator as shown in Figure 13. Shunt values were monitored and recorded by onboard personnel to ensure that the desired current was being driven to the source.

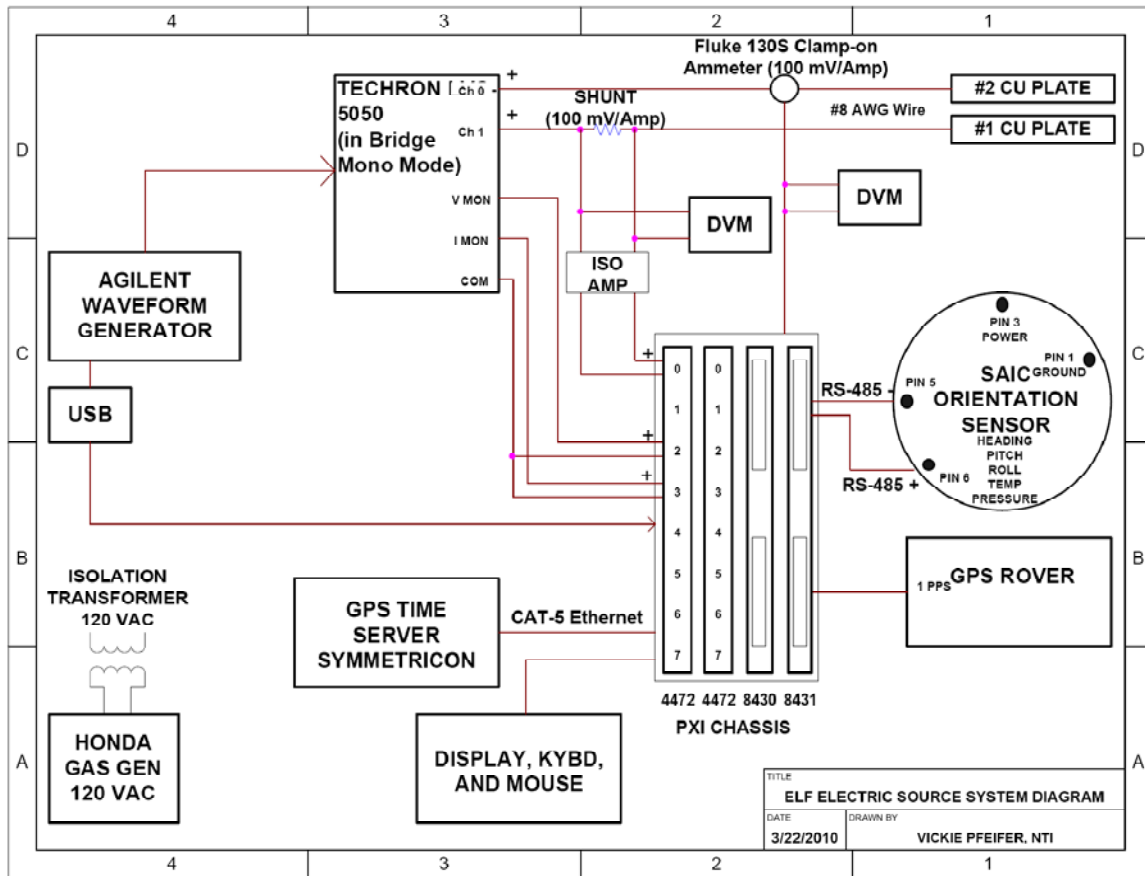


Figure 13 Electric Source System Diagram

Figure 14 is a picture of the E-source drive and control system set-up on the Source Barge.

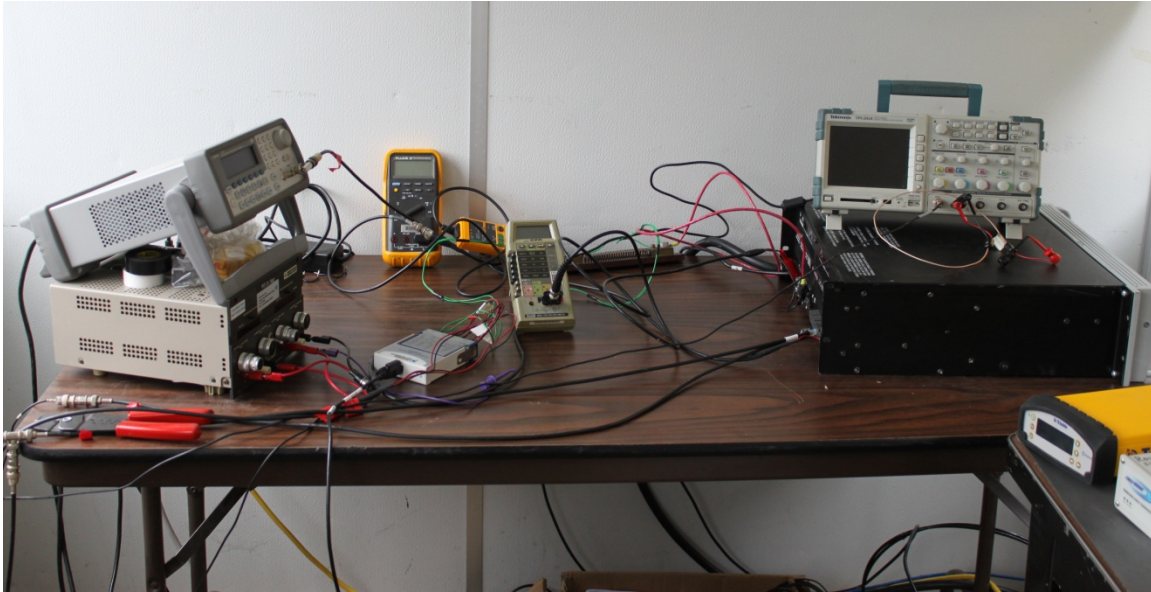


Figure 14 E-Source Drive and Control System Set-Up

A National Instruments data logging system was used to record current, waveform, GPS messages, and information from the orientation package on the source. Figure 15 is a picture of the data logging system. Measurements were GPS time-stamped for correlation to the measurements at the portable measurement array.



Figure 15 NI Data Logging System for E-Source

7.4.3. Magnetic Source

The magnetic source was located next to shore at Farragut State Park (Location 3 on Figure 3, just east of the Eagle Boat Launch). The source was mounted on plastic dock sections. The source was oriented both horizontally and vertically. A description of the horizontal and vertical orientations of the magnetic source can be found in Appendix B, “Test Run Record,” Page B-5. The magnetic source was deployed in accordance with ELF-OP-004 ELF Magnetic Source Deployment Procedure (Reference 4). The magnetic source was a ~ 2400 amp-m² coil on a 12' x 12' wooden frame. It had 12 turns and used ~ 15 amps of current. To reduce inductance, the turns were concentric and three 10 microfarad capacitors were added (two in series, one in parallel). A picture of the magnetic source is shown in Figure 16.



Figure 16 Magnetic Source

Figures 17 and 18 depict the layout of the GPS antennae in relation to the magnetic source for the horizontal and vertical dipole orientations.

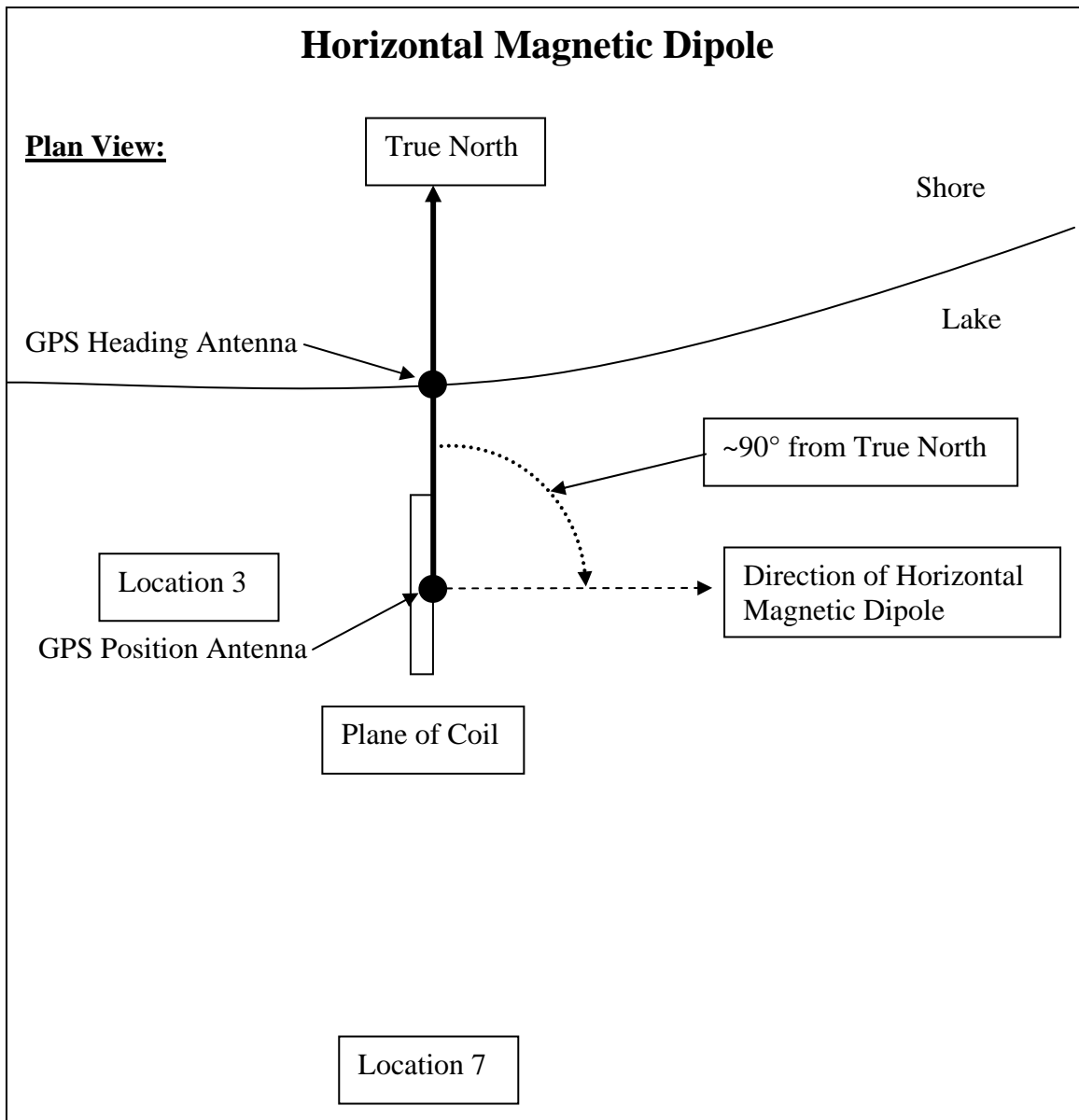


Figure 17 Magnetic Source GPS Layout - Horizontal

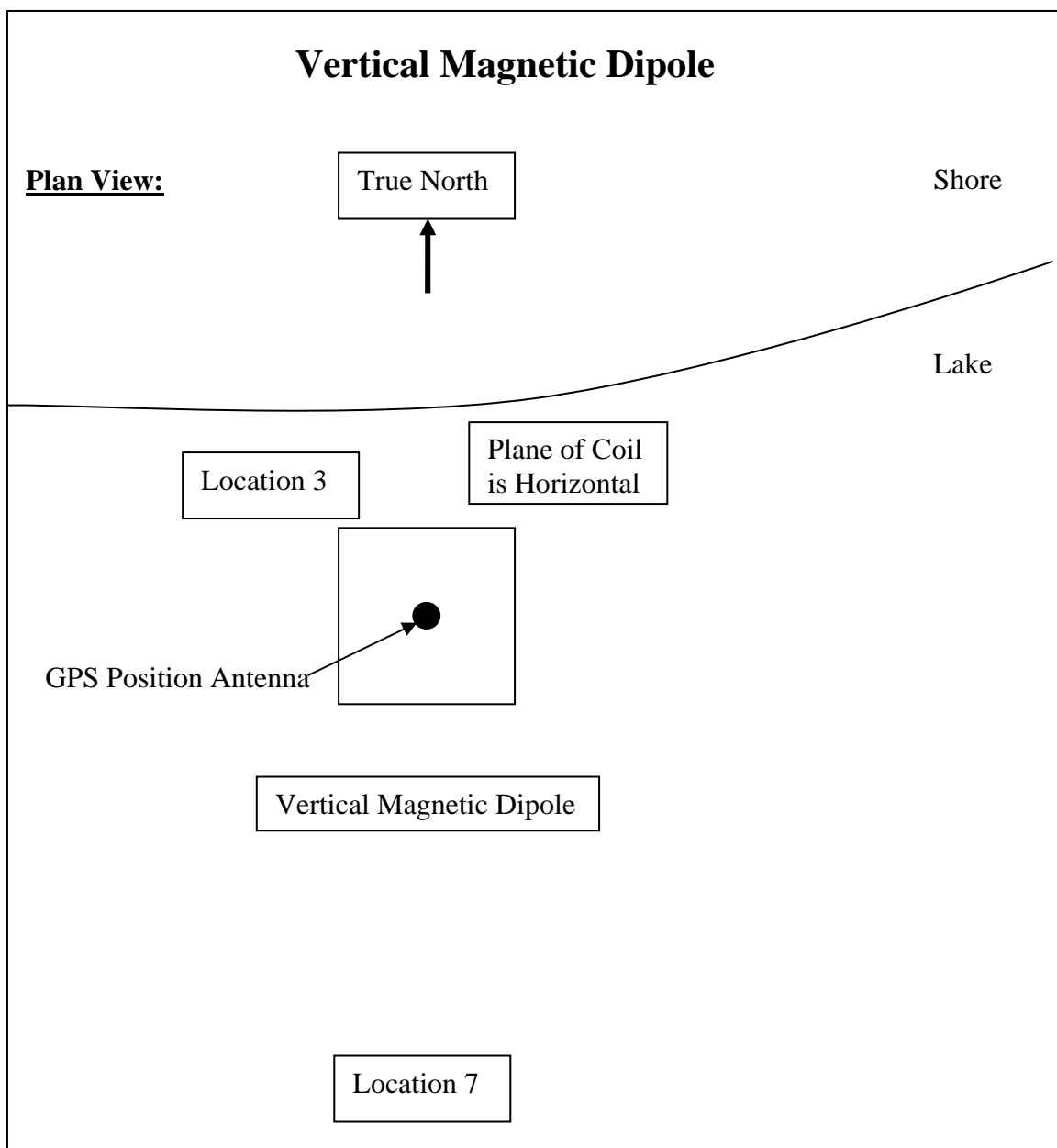


Figure 18 Magnetic Source GPS Layout – Vertical

7.4.3.1. Magnetic Source Drive and Control

The magnetic source was driven by a Kepco 20-20 Bipolar Amplifier for frequencies up to 120 Hz and a Techtron LVC-5050 Amplifier for frequencies up to 1 kHz. The Code 75 CDAQ system was used to record current, waveform, and GPS information. Figure 19 shows a system diagram for the magnetic source.

ELF Phase III Test 2 Test Record

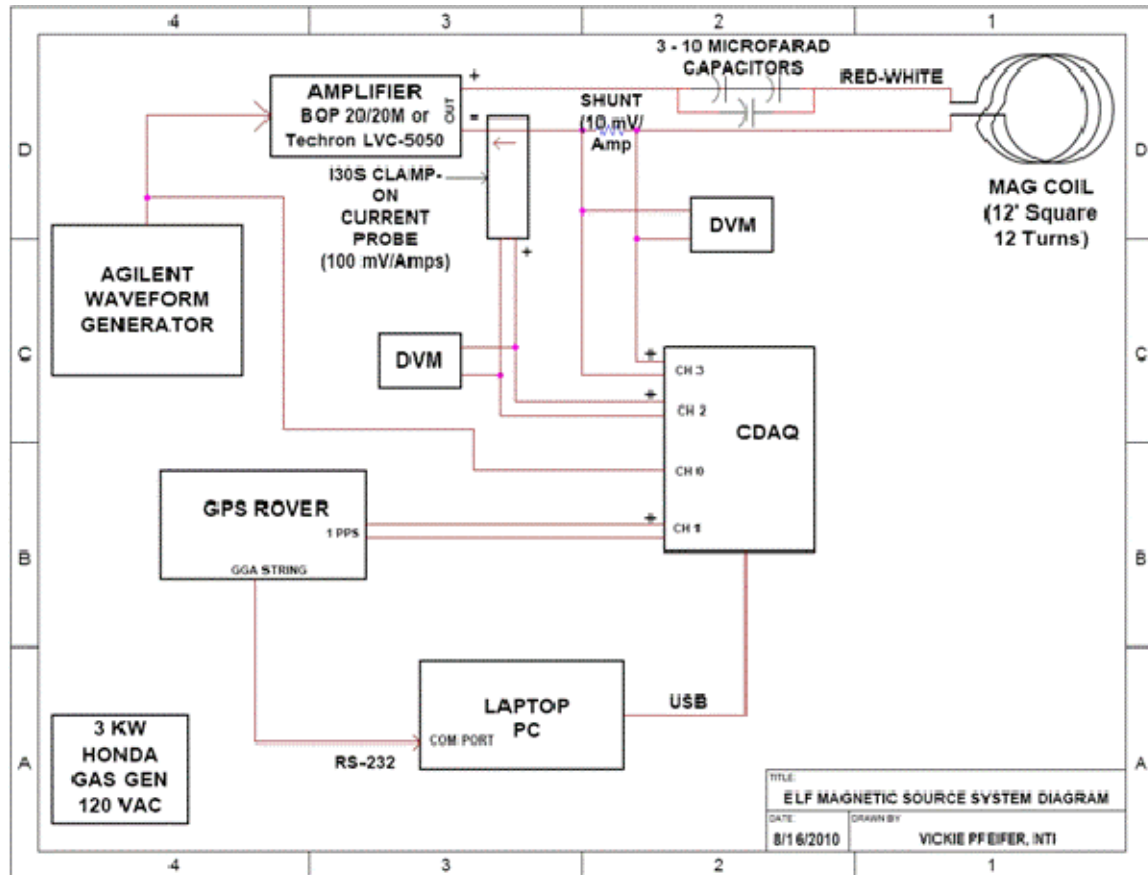


Figure 19 Magnetic Source System Diagram

Figure 20 is a picture of the system installed in the 25' Boat and the operator.



Figure 20 M-Source Drive and Control System Set-Up

7.5. PORTABLE MEASUREMENT ARRAY (PEMA)

The portable measurement array consisted of tri-axial magnetic and electric field sensors. Tilt and depth sensors were incorporated into the unit. The array was deployed from the Scow (a self-propelled barge) and rigged to be suspended in the water at various depths up to 500'. Deployment of the sensor was in accordance with ELF-OP-002 "ELF Portable EM Array Deployment Procedure" (Reference 2). The sensor was deployed upside down for all tests as shown in the Figure 21 pictures. The technical specifications for the sensor are detailed in Appendix A.

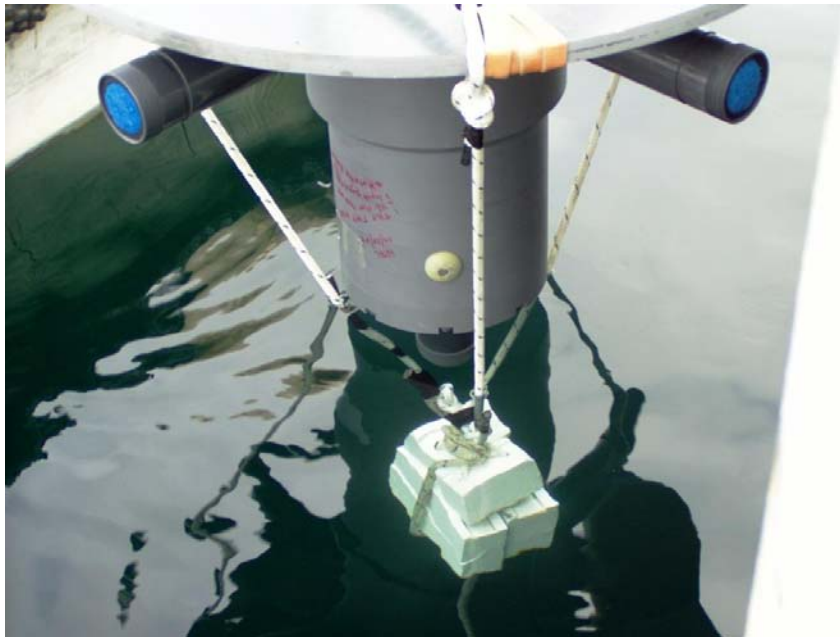


Figure 21 PEMA Deployment

A dual channel GPS rover unit with two antennas was located on the barge to record position and heading as shown in Figure 5. The layout of the Sensor Barge and Boat (Scow and 28' Almar) is shown in Figure 22.



Figure 22 Scow (Sensor Barge) Layout

7.6. DATA ACQUISITION

The portable measurement array (PEMA) data acquisition system was comprised of National Instruments equipment located on the 28' Almar boat tied alongside the Scow. Analog data lines were cabled to the data acquisition system on the surface, so no pressure vessel was required. Data channel assignments used during the tests are listed in Table 3.

Table 3 CDAQ PEMA Channel Assignments

Channel	Measurements
0	H_x
1	$H_y (-y)$
2	$H_z (-z)$
3	E_x
4	$E_y (-y)$
5	$E_z (-z)$
6	T_{x-z} (within x-z plane)
7	T_{y-z} (within y-z plane)
8	Pressure
9	1PPS
10	High Gain EG&G PARC Model 113 Pre-Amp (magnetic source only)
11	Empty
12	Empty
13	Empty
14	Empty
15	Empty

Figure 23 is a system diagram for the sensor and the data acquisition system and Figure 24 is pictures of the set-up on the boat.

ELF Phase III Test 2 Test Record

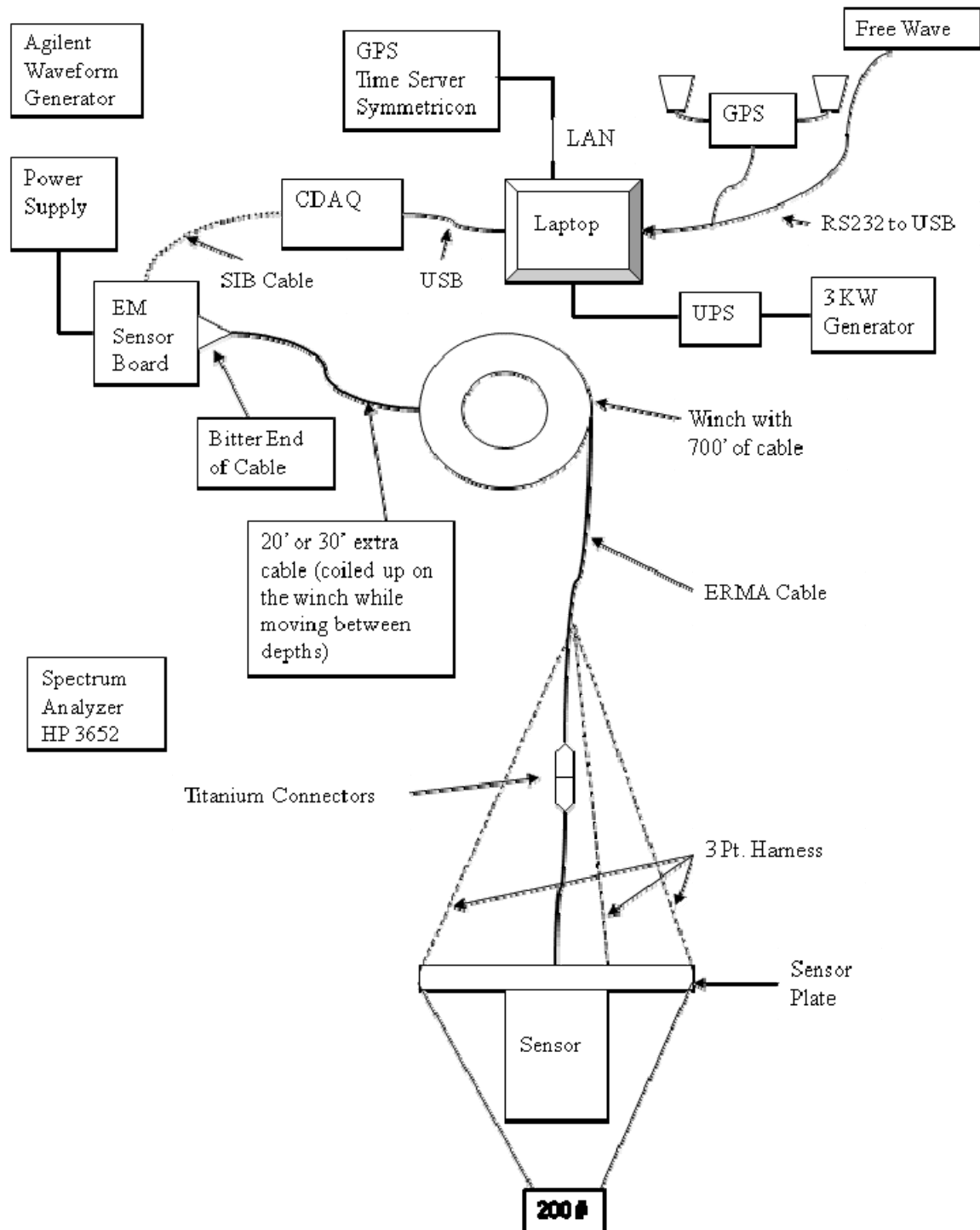


Figure 23 Sensor and Data Acquisition System Diagram

ELF Phase III Test 2 Test Record

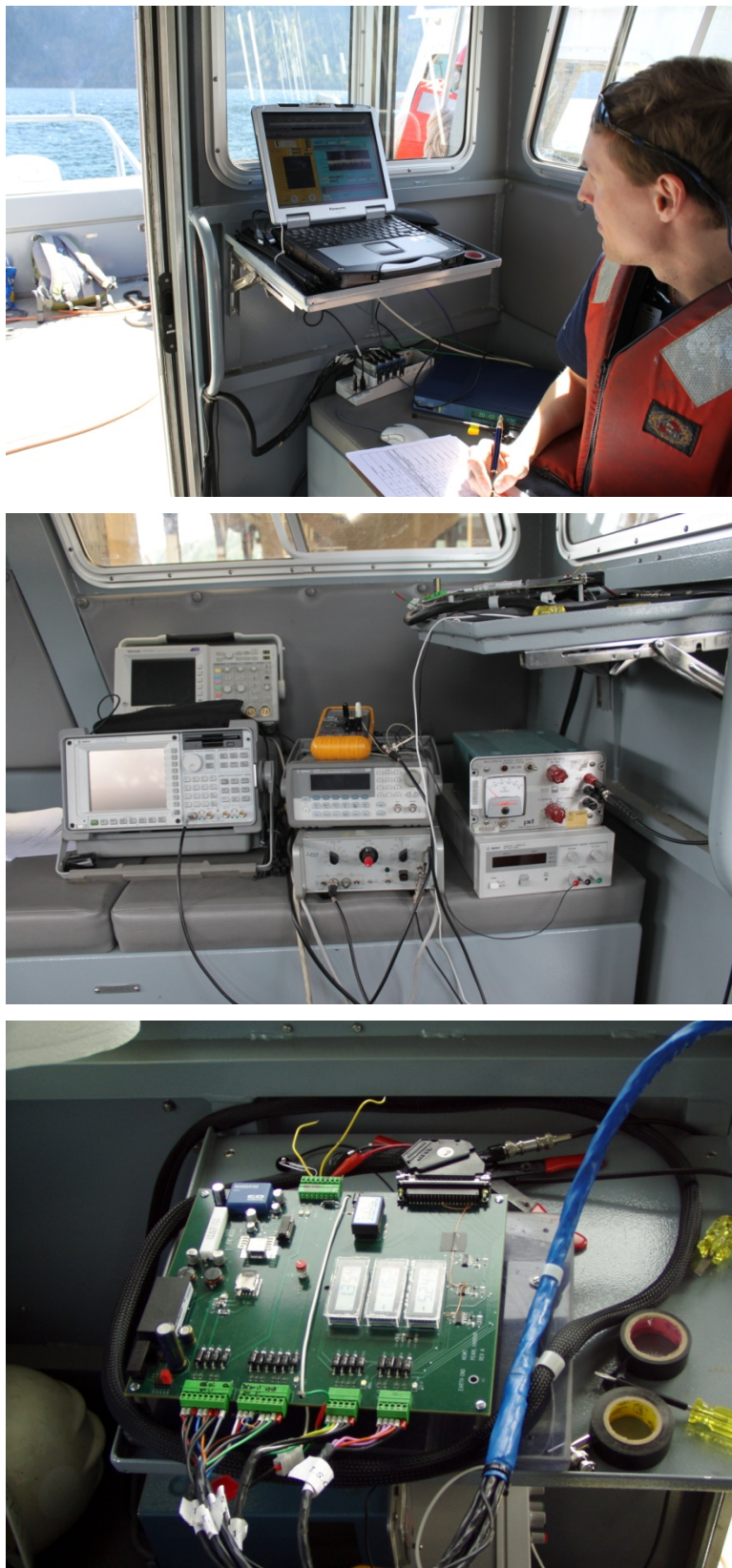


Figure 24 Sensor Control and Data Acquisition

8. TEST SITE OPERATIONS

8.1. OPERATIONS TEAM

Personnel assignments are listed in Table 4. The personnel listed in Table 4 were assigned the senior level responsibility for their task areas.

Table 4 Personnel Assignments

Program Test POC	Alan Griffiths
ELF Technical Director (C/7530)	Don Pugsley
ELF Trial Engineers (C/7510, 7530)	Dan Lenko, Steve Potashnik, Stephanie Ferrone
ARD Test Director	Frank Jurenka
ARD Lake Ops Engineer/Barge Prep and Mooring	Toby Kaplan (GDIT)
ARD Lake Operations	Tony Travis
ARD GPS	Duane Nightingale, Jeanne Hom
ARD Electronics Technician	Jeanne Hom

The ARD Test Director was responsible for the overall safe conduct of the test and the execution of the test plan. The ARD Test Director ensured proper coordination and execution of all ARD efforts. The ELF Technical Director was responsible for technical issues, checking the quality of data being collected, and making judgment calls regarding technical changes to the run plan.

8.2. MOORING PLAN

Temporary moors were set up prior to testing. Mooring was in accordance with ELF-OP-003, "Anchoring and Mooring Procedure" (Reference 3). 3-point anchoring configurations were used to minimize the rotation of the E-source truss and the sensor.

A 45' barge was moored at the E-source site (Location 4 on Figure 3) as shown in Figure 25. The 60' E-Source Barge docked up to the mooring barge (see Figure 26). This allowed the E-Source Barge to change orientation as required in the test run plan.



Figure 25 45' Mooring Barge



Figure 26 60' E-Source Barge Moored to 45' Barge

Mooring anchors were pre-positioned at the sensor sites (Locations 6, 7, and 8 on Figure 3). There were three anchors at each site for mooring the Sensor Barge. Pictures of the Sensor Barge moored at Location 8 are shown in Figure 27.



Figure 27 Sensor Barge Moored at Location 8

8.3. OPERATING PROCEDURES

Portable E-source deployments were in accordance with ELF-OP-001 ELF Portable E-Source Truss Deployment Procedure (Reference 1).

Portable measurement array (PEMA) deployments were in accordance with ELF-OP-002 ELF Portable EM Array Deployment Procedure (Reference 2).

Anchoring and mooring of the PEMA and E-Source Barges were in accordance with ELF-OP-003 Anchoring and Mooring Procedure (Reference 3).

The magnetic source deployment was in accordance with ELF-OP-004 ELF Magnetic Source Deployment Procedure (Reference 4).

Table 5 lists the ARD base radio call signs that were used for this test.

Table 5 ARD Base Radio Call Signs

Description	Function	Call Sign
28' Almar	EM Sensor Measurement	A-21
25' Whaler	4 M E-source and M-source	A-32
60' Barge	Portable E-Source Deployment and Data Logging	A-67
Scow	EM Sensor Deployment and Positioning	A-29
ISMS Tug	60' Barge Transit and Positioning	A-14
ISMS ROC	GPS Data Collection (back-up)	A-44
A-Frame Barge	Scow Anchoring	A-15

8.4. EMERGENCY PROCEDURES

All personnel followed safety and emergency procedures detailed in ARDINST 5100.4B, "Operation of Watercraft on Lake Pend Oreille" and ARDINST 5100.5 "ARD Safety Rules Handbook".

9. TEST RUN PLAN EXECUTION

The run plan included noise measurements and the ELF measurements designed to exercise the models. A total of 249 measurements were taken over six days of testing. General descriptions of the various runs are given below and the executed run plan can be found in Appendix B.

9.1. NOISE MEASUREMENTS

Noise measurements were collected at the beginning, end, and/or during each test day. No sources were energized during data collection and the measurements were used to quantify the environmental and system noise. Noise measurements were taken with the sensor at test depths at the location of that day's testing.

9.2.SYSTEM CHECK-OUT RUNS

System check-out runs were conducted on Day 1. The portable measurement array (sensor) was unmoored at Location 5. The 25' 4-m electric source boat ran in various configurations as described in the test run tables (Appendix B, Day 1) These tests verified that the entire process (source levels, sensors, data acquisition, GPS, etc.) was operating as expected.

1. Sensor depths of 50', 250', and 500'
2. Various headings and offsets
3. Frequency sweep (DC, 300 Hz, 1000 Hz)
4. 15 source measurements
5. 5 noise measurements

9.3. ELF RUNS

The ELF runs consisted of an extensive series of measurements to be used to exercise the numerical models developed by UI. They included measurements with the portable electric source at Location 4, at depths up to 500', with the magnetic source (horizontally and vertically) at the on-shore location at Farragut State Park (Location 3), and with the 4-m electric source boat at various headings and offsets. The run plan contained both transverse and longitudinal orientations for the E-source. The data was collected with the portable measurement array deployed at Locations 6, 7, and 8 and at depths up to 500'.

9.3.1. Magnetic Source Runs

1. (Day 2) Sensor Barge moored at Location 7. M-source at Location 3.
 - a. Sensor depth: 10', 20', 30', 40', and 50'
 - b. Frequency: 81 Hz, 1000 Hz
 - c. Vertical and horizontal dipole orientation
 - d. 12 source measurements
 - e. 5 noise measurements
2. (Day 3) Sensor Barge moored at Location 7. M-source at Location 3.
 - a. Sensor depth: 10', 20', 30', 40', and 50'
 - b. Frequency: 81 Hz, 1000 Hz
 - c. Horizontal dipole orientation
 - d. 10 source measurements
 - e. 6 noise measurements

Figure 29 shows the M-Source, Source Control Boat, and moored Sensor Barge test configuration.



Figure 28 M-Source, Source Control Boat, and Moored Sensor Barge

9.3.2. 4-M Electric Source Boat Runs

1. (Day 3) Sensor Barge moored at Location 7. 4-m electric source boat traveling at various headings and offsets near location 7.
 - a. Sensor depth: 40', 50'
 - b. Frequency: 10 Hz, 100 Hz, 1000 Hz
 - c. Various headings and offsets.
 - d. 15 source measurements

Figure 29 shows the 4-m Source Boat passing by the Sensor Barge moored at Location 7 during a run.



Figure 29 4-M Source Boat Passing by Sensor Barge Moored at Location 7

9.3.3. Electric Source Runs

The electric source runs occurred in various configurations as follows:

1. (Day 4) Sensor Barge moored at Location 8. E-Source Barge moored at Location 4.
 - a. Sensor depth: 50' and 40' from the bottom of the lake.
 - b. Source depth: 50', 100', 150', 200', 250', 300', 350', 400' and 40' from the bottom of the lake.
 - c. ~3 amp source current
 - d. Frequency: 10 Hz, 100 Hz, 1000 Hz
 - e. Source orientation: ~180 degrees (true)
 - f. 54 source measurements
 - g. 2 noise measurements

2. (Day 5) Sensor Barge moored at Location 8. E-Source Barge moored at Location 4.
 - a. Sensor depth: 50' and 40' from the bottom of the lake.
 - b. Source depth: 50', 100', 150', 200', 250', 300', 350', 400' and 40' from the bottom of the lake.
 - c. ~3 amp source current
 - d. Frequency: 10 Hz, 100 Hz, 1000 Hz
 - e. Source orientation: 90 degrees (true)
 - f. 66 source measurements
 - g. 3 noise measurements

Figure 30 shows the Sensor Barge and E-Source Barge moored in the test configuration.



Figure 30 Sensor Barge and E-Source Barge Moored in Test Configuration

3. (Day 6) Sensor Barge moored at Location 6. E-Source Barge moored at Location 4.
 - a. Sensor depth: 50' and 250'
 - b. Source depth: 50', 100', 150', 200', 250', 300', 350', 400', and 40' from the bottom of the lake.
 - c. ~3 amp source current
 - d. Frequency: 10 Hz, 100 Hz, 1000 Hz
 - e. Source orientation: ~350 and ~75 degrees (true)
 - f. 54 source measurements
 - g. 2 noise measurements

9.4. DATA REPORTING

Data reporting was the responsibility of Carderock and UI. Carderock performed a quick look analysis of the data during testing and released the data to UI at the end of the test period. All data were unclassified.

REFERENCES

Reference 1: ELF-OP-001 ELF Portable E-Source Truss Deployment Procedure

Reference 2: ELF-OP-002 ELF Portable EM Array Deployment Procedure

Reference 3: ELF-OP-003 Anchoring and Mooring Procedure

Reference 4: ELF-OP-004 ELF Magnetic Source Deployment Procedure

APPENDIX A: PORTABLE EM SENSOR TECHNICAL SPECIFICATIONS

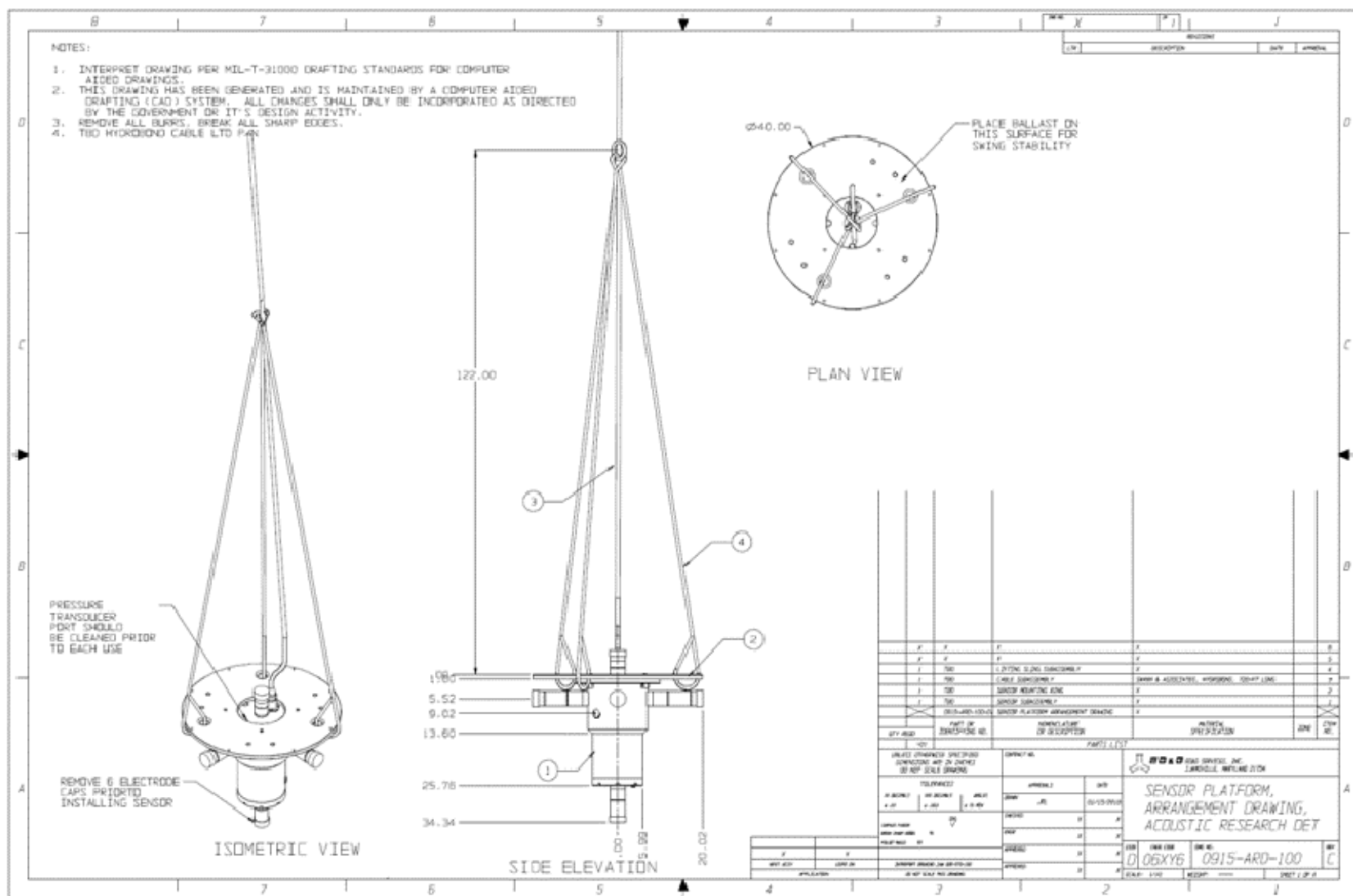
MAGNETIC SENSOR

- Magnetic Sensor Location
 - Shall be located within a 6" radius of the geometric center of the electric field antenna
- Magnetic Sensor Type:
 - Shall be a three-axis second harmonic fluxgate with "+" indications for North, East, and Down
 - Measurements shall be expressed as nanoTesla (nT)
- Bandwidth
 - Measurement and recording shall have a pass band response between 0 Hz and 3000 Hz
 - Roll-off of gain to -3 dB is allowable at upper limit of pass band
 - Gain within pass band shall be level within 99-101% of correct value outside of roll-off corner effects
- Dynamic Range and resolution
 - Shall measure absolute magnetic field within the range of +/- 100,000 nT on each axis
 - Shall digitize field with a word length of 24 bits
 - Shall reliably record changes in magnetic field 0.1 nT and greater
 - Desirable to have a flat (uniformly distributed) noise floor below the 200 picoTesla RMS level from DC to 3000 Hz
- Observed noise after processing
 - The peak to peak noise after low-pass filtering data to DC-25 Hz shall not exceed +/- 0.5 nT (1.0 nT PkPk) when observed over a ten second period
- Alignment
 - Sensor axes shall be manufactured mutually perpendicular within +/- 0.5 degree
 - Sensor shall be installed with axes aligned to magnetic north coordinate system within +/- 0.5 degree
 - A two-axis horizontal tilt sensor (east/west and north/south) shall be fitted to detect sensor motion after installation

ELECTRIC FIELD SENSOR

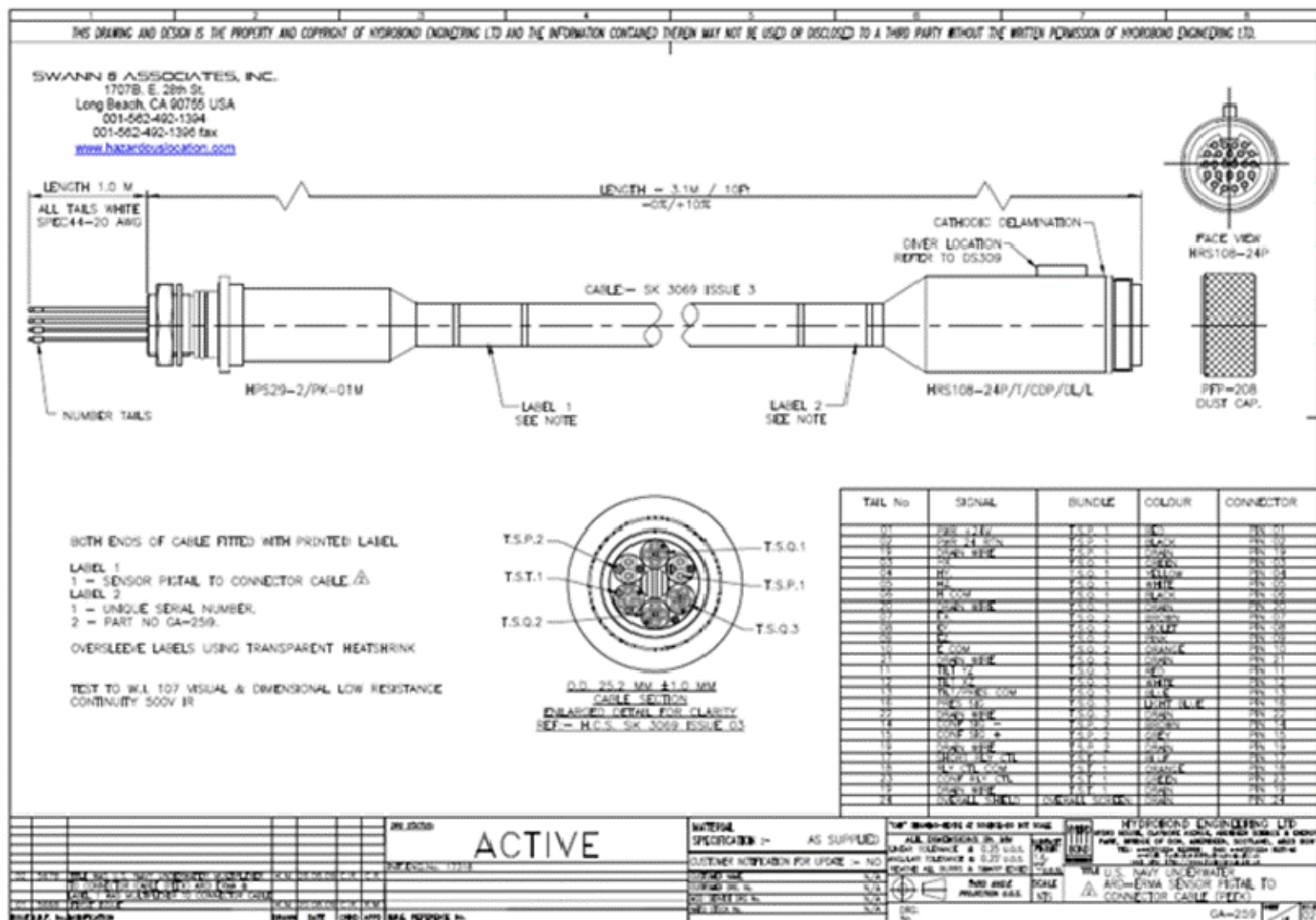
- Electric Sensor Location
 - Triaxial dipole antenna shall be centered on the defined sensor location
- Electric Sensor Type
 - The electric sensor shall be a three-axis dipole antenna sensing electric field with “+” indications for North, East, and Down
 - Measurements shall be expressed as Volts/meter
 - Dipole antenna length shall be one meter in all directions
 - Or: Dipole length shall be one meter in the North and East directions, with shorter, off-center dipole allowable in the down direction
- Bandwidth
 - Electric measurement and recording system as installed shall have a pass band response between 0.001 Hz and 3000 Hz
 - Roll-off of gain to -3 dB is allowable at both lower and upper limit of pass band
 - Gain within pass band shall be level within 99-101% of correct value outside of roll-off corner effects
- Dynamic Range
 - Shall measure absolute electric field within the range of +/- 10,000 uV/M on each axis
 - Shall digitize field with a word length of 24 bits
 - Shall reliably record changes in electric field 0.5 uV/M and greater
 - Desirable to have a flat (uniformly distributed) noise floor below the 200 nV/M RMS level from 0.001 to 3000 Hz
- Observed noise after processing
 - The peak to peak noise of acquired data after low-pass filtering data to 0.1 Hz and below shall not exceed +/- 2.0 uV/M (4.0 uV/M PkPk) when observed over a 100 second period
- Alignment
 - Sensor axes shall be manufactured mutually perpendicular within +/- 0.5 degree
 - Sensor shall be installed with axes aligned to magnetic north coordinate system within +/- 0.5 degree
 - A two-axis horizontal tilt sensor (east/west and north/south) shall be fitted to detect sensor motion after installation
- Confidence Test
 - Each sensor shall be equipped with remotely controlled local electric dipole transmitter to produce an observable output from each axis of the sensor

ELF Phase III Test 2 Test Record



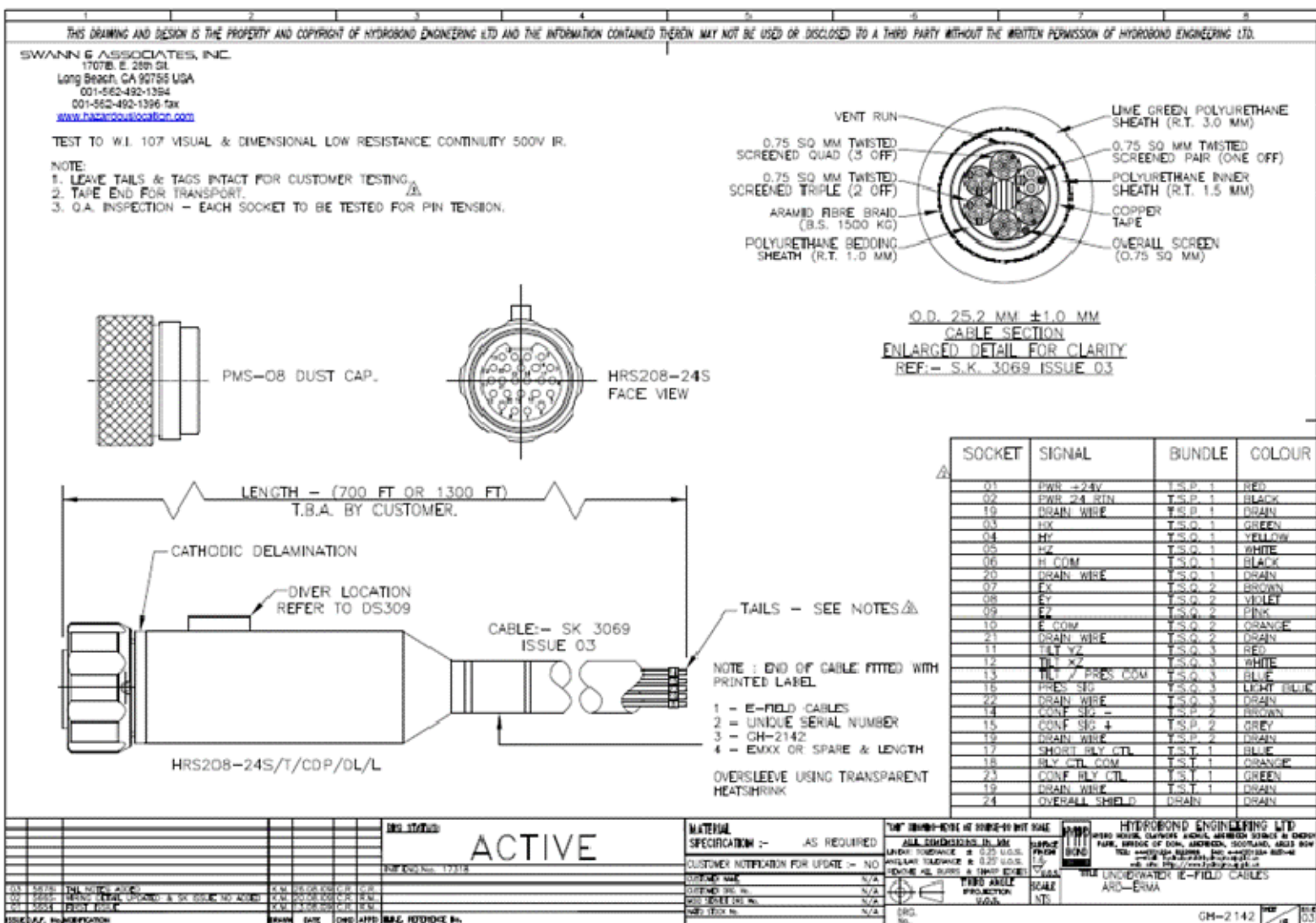
Portable EM Array Drawing

ELF Phase III Test 2 Test Record



Wiring Diagram – Sensor Pigtail to Connector Cable

ELF Phase III Test 2 Test Record



Wiring Diagram – Sensor Underwater E-field Cable

ELF Phase III Test 2 Test Record

APPENDIX B: TEST RUN RECORD

DAY 1 – SEPTEMBER 11, 2010

Checkout Runs – 4-M Electric Dipole (Boat Hull)													
Run #	Comex	Finex	CPA	Speed (knots)	Sensor Location	Sensor Depth (ft)	Source Heading (deg)	Current (100mV/Amp)	Voltage (V)	Freq (Hz)	Start Distance (ft)	CPA (ft)	Comments
1	18:46:45	18:50:31	18:49:11	~5	~5	50	137	178 mVrms	224.8	DC	500	~30	Parallel to barge; positive plate at bow
2	18:55:44	18:57:30	18:46:14	~5	~5	50	350	179 mVrms 180 mVrms		DC	500	~30	Parallel to barge
3	19:01:12	19:04:00	19:02:40	~5	~5	50	150	179 mVrms 178 mVrms		DC	500	~300	Parallel to barge
4	19:07:10	19:10:25	19:09:12	~5	~5	50	350	179 mVrms	224	DC	500	~150	Parallel to barge
5	19:32:11	19:35:32	19:33:35	~5	~5	50	234	186 mVrms		1000	500	~70-100	Perpendicular to barge; coming port to starboard; lost signal on analyzer at 19:35:45
7	19:14:17	Not noted	Not noted	~5	~5	50	~0	179 mVrms	210 VAC	1000	500	~300	Parallel to barge; sailboat interference after CPA; 8-9 mVrms on analyzer at 1kHz
8	19:21:10	19:24:15	19:22:50	~5	~5	50	355	182 mVrms 188 mVrms	223 VAC	1000	500	~150	Parallel to barge; 130 mVrms on SA at CPA
9	18:05:40	18:07:55	N/A	0	~5	50	N/A	off	off	N/A	N/A	N/A	Noise run; small boat far away on second run
10	20:15	20:17:00	N/A	0	~5	250	N/A	off	off	N/A	N/A	N/A	Noise run
11	20:22:10	20:24:50	20:23:22	~5	~5	250	70	183 mVrms 184 mVrms	226 VDC	DC	500	~30	Parallel to barge; positive electrode at bow
12	20:28:47	20:32:12	20:30:20	~5	~5	250	154	183 mVrms 184 mVrms	226 VDC	DC	500	~20	Perpendicular to barge
13	20:35:10	20:39:10	20:37:05	~5	~5	250	350	181 mVrms	226 VAC	300	500	~20	Perpendicular to barge; Par at 300/300, gain 100
15	20:44:20	20:49:00	20:46:18	~5	~5	250	90	183 mVrms 184 mVrms	224	1000	500	~15	Parallel to barge; terminated run when signal was lost; Par at 1k/1k/100
16	20:50:55	Not noted	N/A	0	~5	250	N/A	off	off	N/A	N/A	N/A	Noise run; Temp = 1.637 V
20	21:20:45	Not noted	N/A	0	~5	500	N/A	off	off	N/A	N/A	N/A	Noise run
21	21:31:10	21:34:45	21:30:51	~5	~5	500	90	182 mVrms	226	DC	500	~25	Parallel to barge
22	21:38:00	21:41:20	21:40:00	~5	~5	500	70	183 mVrms	226	DC	500	~20	Perpendicular to barge
23	21:44:00	21:48:20	21:46:38	~5	~5	500	174	191 mVrms	224 VAC	1000	500	~30	Perpendicular to barge; Par 1k/1k/500
24	21:52:15	21:56:00	21:54:00	~5	~5	500	80	191 mVrms	225 VAC	1000	500	~30	Parallel to barge; Par 1k/1k/500
25	Not noted	Not noted	N/A	0	~5	500	N/A	off	off	N/A	N/A	N/A	Noise run

Day 1 Notes:

Sensor unmoored, near Location #5.

Positive electrode at Source Boat bow.

Comex/Finex Times are UTC.

Headings, offsets, and speeds are approximate, verify using GPS data.

0850: Underway from the ARD

0950: Sensor deployed to 50'

1300: Sensor deployed to 250'

1415: Sensor deployed to 500'

Day 1 measurements: 20

ELF Phase III Test 2 Test Record

DAY 2 – SEPTEMBER 13, 2010

Day 2 - Noise Runs						
Run #	Run Length (sec)	Comex	Finex	Sensor Location	Sensor Depth (ft)	Comments
101	120	19:25:45	19:27:50	7	10	
102	120	20:07:24	20:09:40	7	20	
103	120	20:36:00	20:38:02	7	30	
104	120	21:19:50	21:21:50	7	40	
105	120	21:58:50	22:00:55	7	50	

Magnetic Source (Current Loop) Vertical Dipole												
Run #	Run Length (sec)	Comex	Finex	Sensor Location	Sensor Depth (ft)	Source Location	Current (100mV/Amp)	Frequency (Hz)	Voltage (V)	Moment Orientation (θ(deg),Φ(deg true))	Source Height (ft)	Comments
Set 100	500			7	10 - 60'	3	Max	100, 1000		(0,NA)	Ground	Source on floating dock next to shore.
100.01	500	19:52:40	20:01:30	7	10	3	1.448, 1.449 Vrms, 20Apeak	81		(0,NA)	Ground	Vertical dipole; boats passed at 195301 and 195320. Data collection on source computer interrupted several times due to error messages. Par 100/3k/200.
100.02	500	19:37:40	19:46:30	7	10	3	1.727 Vrms 24 Apeak, 24.5 App	1,000		(0,NA)	Ground	Vertical dipole; run done before run 100.01 because dipole was already set at 1000 Hz. Speedboat passed at ~1937. Wake rocked source. Par 100/3k/200
100.03	500	20:12:05	20:20:35	7	20	3	1.449 Vrms, 1.450 Vrms, 100 mV/A conversion	81		(0,NA)	Ground	Vertical dipole
100.04	500	20:24:40	20:33:10	7	20	3	1.735 Vrms	1,000		(0,NA)	Ground	Vertical dipole
100.05	500	20:55:10	21:03:30	7	30	3	1.448 Vrms 1.446 Vrms	81		(0,NA)	Ground	Vertical dipole; small boat passing between sensor & M-source at 205545. 1 stop in source data collection due to Labview error.
100.06	500	20:42:50	20:51:10	7	30	3	1.707 Vrms 1.71 Vrms 1.695 Vrms	1,000		(0,NA)	Ground	Vertical dipole; radio transmissions at 134430 and 134440
100.07	500	21:09:45	21:18:05	7	40	3	1.446 Vrms	81		(0,NA)	Ground	Vertical dipole; amp settings changed prior to run 100.07
100.08	500	21:24:10	21:32:30	7	40	3	1.720 Vrms 1.710 Vrms	1,000		(0,NA)	Ground	Vertical dipole
100.09	500	21:49:00	21:57:20	7	50	3	1.444 Vrms 1.445 Vrms	81		(0,NA)	Ground	Vertical dipole; boat passed at ~2154
100.10	500	21:36:00	21:44:25	7	50	3	1.721 Vrms 1.725 Vrms	1,000		(0,NA)	Ground	Vertical dipole; A29 boat going over to M-source during this run in order to change dipole orientation

ELF Phase III Test 2 Test Record

Magnetic Source (Current Loop) Horizontal Dipole												
Run #	Run Length (sec)	Comex	Finex	Sensor Location	Sensor Depth (ft)	Source Location	Current (100mV/Amp)	Frequency (Hz)	Voltage (V)	Moment Orientation (θ(deg),Φ(deg true))	Source Height (ft)	Comments
Set 101	500			7	10 - 60'	3	Max	100, 1000		(90,90)	Ground	Source on floating dock next to shore.
101.09	500	22:19:40	22:28:01	7	50	3	1.455 Vrms 1.452 Vrms	81		(90,92)	7	Horizontal dipole
101.10	500	22:30:45	22:39:05	7	50	3	1.734 Vrms 1.721 Vrms	1,000		(90,92)	7	Horizontal dipole

Day 2 Notes:

Magnetic Source Vertical Dipole Location 3: N 47° 57.940'
W 116° 32.488'

Magnetic Source Horizontal Dipole Location 3: N 47° 57.940'
W 116° 32.488'
Dipole Heading – 92 deg true

Sensor Barge Location 7: N 47° 57.906'
W 116° 32.439'

For exact Sensor location use GPS data and barge layout offsets.

Sensor Location water depth: 62'
Comex/Finex Times are UTC

0845: Underway from the ARD
1200: Sensor Barge moored and Sensor deployed to 10'

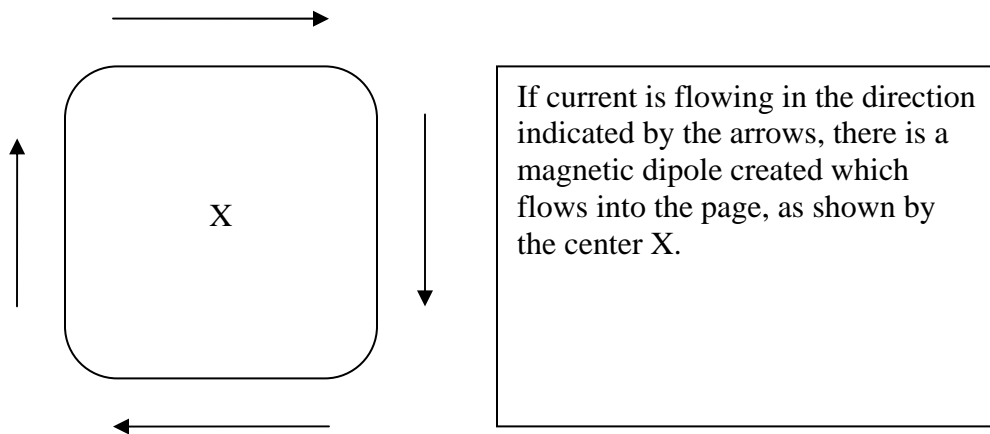
Day 2 measurements: 17

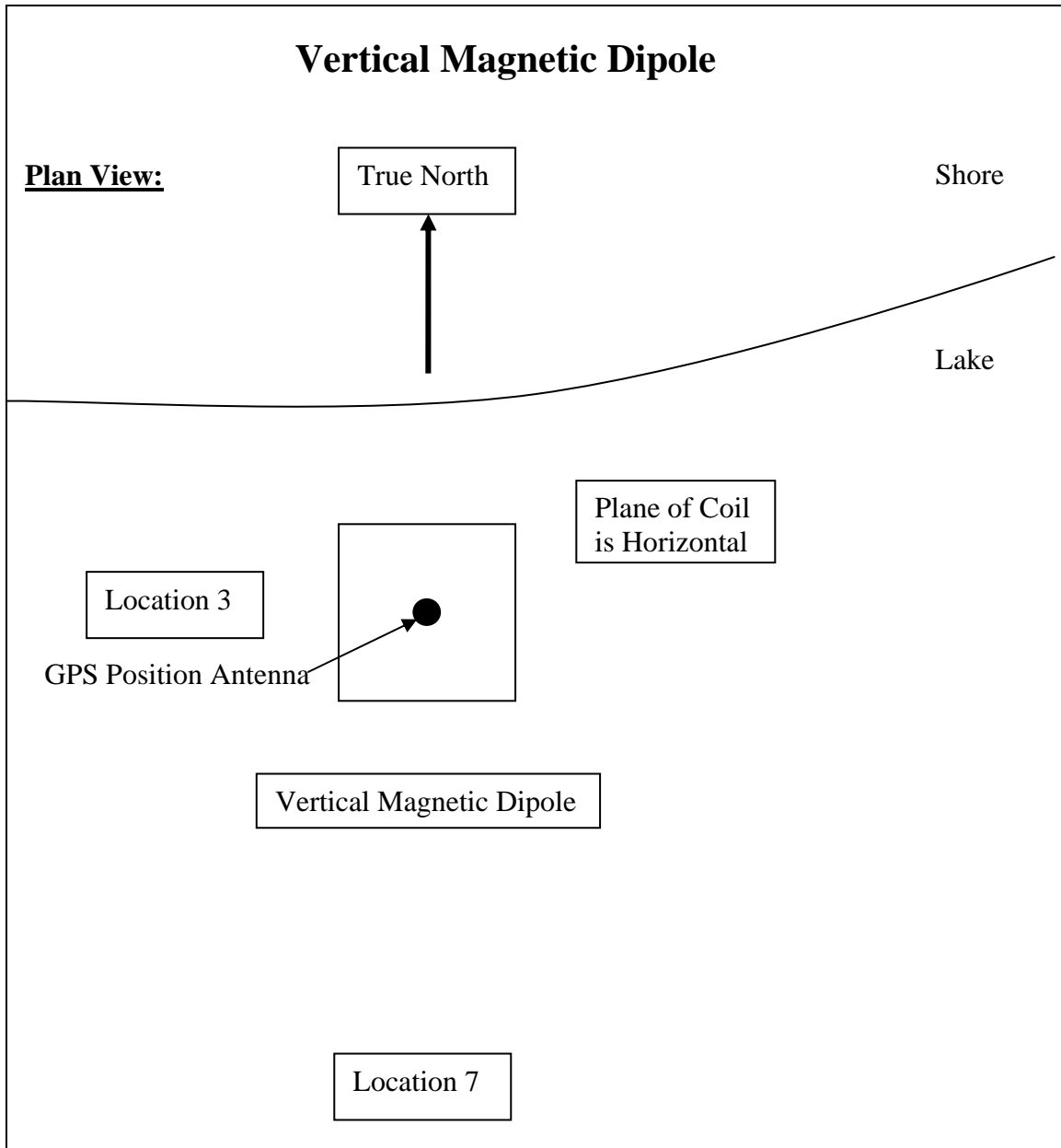
Magnetic Source Orientation Clarification

“Vertical Orientation”:

The “Vertically Oriented” magnetic source is defined as when the plane of the coil loop is laid flat/parallel to the ground. Thus, the coil will create a vertically oriented magnetic dipole (located at the center of the coil structure).

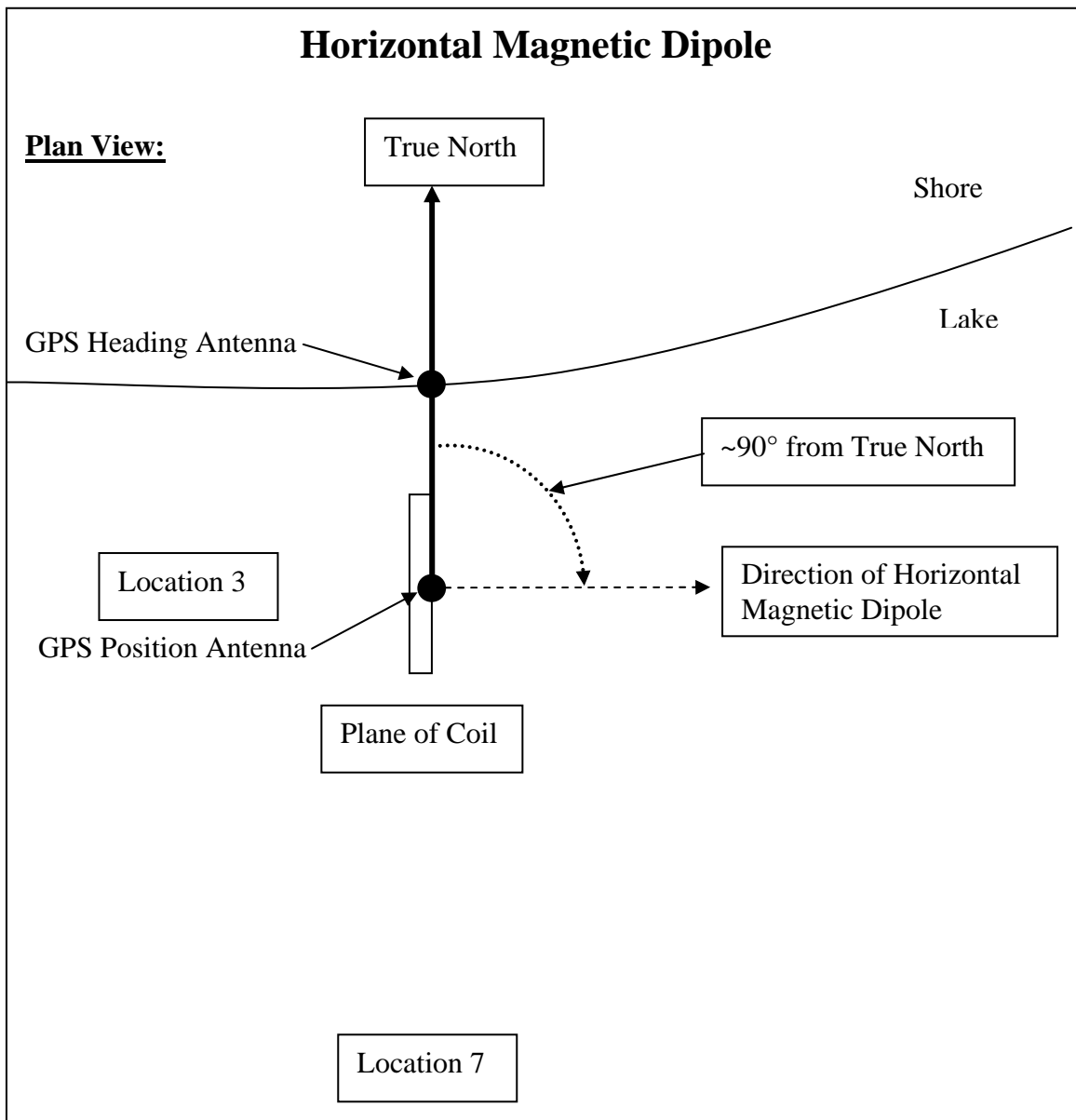
The direction of the vertical magnetic dipole (into the ground or into the air) is not specified in the run plan, but should probably be recorded for later analysis. That direction is determined based on the right-hand rule as follows:





“Horizontal Orientation”:

The “Horizontally Oriented” magnetic source is defined as when the structure is propped up, with the plane of the coil forming a right angle with the ground. Furthermore, the resulting horizontally oriented magnetic dipole (which will face in the direction perpendicular to the plane of the coil) should be oriented so that it faces to 170 Degrees from true North. The figure below shows the intended direction of the magnetic dipole, with respect to True North. The coil is to be set up at location 3 as shown:



ELF Phase III Test 2 Test Record

DAY 3 – SEPTEMBER 14, 2010

Day 3 - Noise Runs						
Run #	Run Length (sec)	Comex	Finex	Sensor Location	Sensor Depth (ft)	Comments
106	120	17:29:04	17:31:15	7	10	
107	120	18:18:10	18:20:15	7	20	
108	120	18:44:00	18:46:00	7	30	
109	120	19:09:05	19:11:05	7	40	
110	120	19:34:10	19:36:10	7	50	
111	120	00:17:44	00:19:44	7	40	Taken Tue, UTC time reads Wed

Magnetic Source (Current Loop) Horizontal Dipole												
Run #	Run Length (sec)	Comex	Finex	Sensor Location	Sensor Depth (ft)	Source Location	Current (100mV/Amp)	Frequency (Hz)	Voltage (V)	Moment Orientation (θ(deg),Φ(deg true))	Source Height (ft)	Comments
Set 101	500			7	10 - 60'	3	Max	100, 1000		(90,90)	Ground	Source on floating dock next to shore.
101.01	500	17:56:05	18:04:40	7	10	3	1.471 Vrms 1.466 Vrms	81		(90,90)	7	Horizontal dipole
101.02	500	18:07:40	18:16:30	7	10	3	1.726 Vrms	1,000		(90,90)	7	Horizontal dipole; network error on sensor computer at 181130
101.03	500	18:33:55	18:42:15	7	20	3	1.453 Vrms	81		(90,90)	7	Horizontal dipole
101.04	500	18:22:10	18:30:30	7	20	3	1.735 Vrms 1.724 Vrms	1,000		(90,90)	7	Horizontal dipole; boat passed at 182750
101.05	500	18:47:20	18:55:44	7	30	3	1.454 Vrms 1.453 Vrms	81		(90,90)	7	Horizontal dipole
101.06	500	18:58:20	19:06:40	7	30	3	1.723 Vrms 1.719 Vrms	1,000		(90,90)	7	Horizontal dipole
101.07	500	19:24:05	19:32:25	7	40	3	1.450 Vrms	81		(90,90)	7	Horizontal dipole; source boat file is an extra long file
101.08	500	19:12:50	19:21:10	7	40	3	1.722 Vrms 1.703 Vrms	1,000		(90,90)	7	Horizontal dipole
101.11	500	19:38:50	19:47:10	8	50	3	1.452 Vrms 1.450 Vrms	81		(90,90)	7	Horizontal dipole; boat passed at 193945
101.12	500	19:49:45	19:58:05	9	50	3	1.753 Vrms 1.745 Vrms	1,000		(90,90)	7	Horizontal dipole; boat moving by source 1945-1956

ELF Phase III Test 2 Test Record

4-M Electric Dipole (Boat Hull)												
Run #	Run Speed (knots)	Comex	Finex	Sensor Location	Sensor Depth (ft)	Source Heading (deg)	Current (100mV/Amp)	Frequency (Hz)	Voltage (V)	Furthest Distance from Sensor (ft)	Closest Distance from Sensor (ft)	Comments
Set 300	2.5			7	50	~270	Max	10, 100, 1000		1500	30	Parallel along shore traveling away from sensor. Skimming surface.
300.01	~3.0	23:10:37	23:17:43	7	50	~225-245	194 mVrms 197 mVrms	10	243	1500	~30	Speedboat passed sensor boat at start of data collection; source boat hit wakes ~231140
300.02	~3.0	23:29:21	23:37:40	7	40	~055-070	200 mVrms	100	240	1500	~30	Moved sensor to 40' depth prior to this run because the Sensor Barge had moved into shallower water and sensor was close to the bottom. Wind, thunder, and lightning; noise signal jumped 3 orders of magnitude with lightning strikes.
300.03	~3.0	23:39:32	23:47:09	7	40	~210-250	189 mVrms	1000		1500	~30	Rain and lightning.
Set 301	2.5			7	50	~090	Max	10, 100, 1000		1500	30	Parallel along shore traveling away from sensor. Skimming surface.
301.01	~2.5	20:39:52	20:49:57	7	50	~040-045	173 mVrms 175 mVrms	10		1500	~30	Radio transmissions at end of data; source boat moving away from barge
301.02	~2.5	20:53:47	21:03:27	7	50	~220	182 mVrms	100	218	1500	~30	Many boats passing source during this run; source moving toward barge
301.03	~2.5	21:05:50	21:12:55	7	50	~045	173 mVrms 174 mVrms	1000		1500	~30	Boat passed at 210620
Set 302	2.5			7	50	180	Max	10, 100, 1000		1500	30	Perpendicular to shore, traveling away from sensor. Skimming surface
302.01	~2.7	23:58:00	00:03:27	7	40	~135-150	192 mVrms	10		1500	~30	UTC time rolled over to Wednesday; local time still Tuesday.
302.02	~2.5	00:04:38	00:10:19	7	40	~325-335	199 mVrms	100		1500	~30	
302.03	~2.7	00:11:25	00:17:08	7	40	~140-150	190 mVrms 189 mVrms 188 mVrms	1000		1500	~30	
Set 303	2.5			7	50	~090/270	Max	10, 100, 1000		1500	300	Source boat passing between sensor and shore. Parallel to shore. Skimming surface (Note change from initial run plan)
303.01	~2.5	21:51:20	22:06:42	7	50	~230-250	195 mVrms 194 mVrms	10	241	±1500	~60	Boat passed at 215320; Source Boat stopped at 2157 because it briefly snagged the starboard mooring line. Continued run at 2200, CPA at ~2200. west heading. Late stop to source boat file.
303.02	~2.5	21:33:55	21:48:40	7	50	~050-070	200 mVrms	100		±1500	~60	CPA 21:41:41; east heading
303.03	~2.5	21:16:36	21:31:10	7	50	~240-250	173 mVrms	1000		±1500	~60	Boat at 211815; boat at 212508; CPA 21:23:28; west heading
Set 304	2.5			7	50	~090/270	Max	10, 100, 1000		1500	60	Source boat passing sensor with sensor between source boat and shore. Skimming surface (Note change from initial run plan)
304.01	~2.5	22:09:24	22:23:45	7	50	~050-060	194 mVrms	10		±1500	~60	CPA 22:17:29; east heading
304.02	~2.8	22:26:27	22:39:00	7	50	~235-250	200 mVrms	100		±1500	~60	CPA 22:32:23; west heading
304.03	~2.5	22:42:15	22:57:15	7	50	~050-070	190 mVrms 193 mVrms	1000	238	±1500	~60	CPA 22:50:48; east heading

ELF Phase III Test 2 Test Record

Day 3 Notes:

Magnetic Source Horizontal Dipole Location 3: N 47° 57.940'
W 116° 32.489'
Dipole Heading – 90 deg true

Sensor Barge Location 7: N 47° 57.906'
W 116° 32.436'

For exact Sensor and Source locations use GPS data and barge/boat layout offsets.

Sensor Location water depth: 62'

Comex/Finex Times are UTC

0745: Underway from the ARD

1015: Sensor Barge moored and Sensor deployed to 10'.

Day 3 measurements: 31

ELF Phase III Test 2 Test Record

DAY 4 – SEPTEMBER 15, 2010

Day 4 - Noise Runs						
Run #	Run Length (sec)	Comex	Finex	Sensor Location	Sensor Depth (ft)	Comments
201	120	18:29:17	18:31:20	8	50	Noise run originally at 18:22:50, had to be redone because source not secured
202	120	22:43:55	22:45:55	8	40' from bottom (300')	

Portable Electric Source (Electric Truss) Near Field Orientation 2												
Run #	Run Length (sec)	Comex	Finex	Sensor Location	Sensor Depth (ft)	Source Location	Current (100mV/Amp)	Frequency (Hz)	Voltage (V)	Moment Orientation (θ(deg), Φ(deg true))	Source Depth (ft)	Comments
Set 204	100			8	50' and 40' from bottom	4	Max	10, 100, 1000		(90, 180)	50' to 40' from bottom	Close to validate QES and Maxwell. Near field measurement.
204.01	100	18:36:15	18:37:55	8	50	4	402 mVrms	10		(90, ~180)	50	
204.02	100	18:39:20	18:41:00	8	50	4	409 mVrms	100	224.8	(90, ~180)	50	
204.03	100	18:42:15	18:43:55	8	50	4	406 mVrms	1000	222.6	(90, ~180)	50	
204.04	100	22:35:52	22:37:32	8	40' from bottom (300')	4	403 mVrms	10	223	(90, ~180)	50	Source temp = 7.4 ° degC / 45.3 ° degF
204.05	100	22:38:18	22:39:58	8	40' from bottom (300')	4	415 mVrms	100	226	(90, ~180)	50	
204.06	100	22:41:03	22:42:48	8	40' from bottom (300')	4	414 mVrms	1000	223	(90, ~180)	50	
204.07	100	18:53:52	18:55:36	8	50	4	342 mVrms	10	223	(90, ~180)	100	
204.08	100	18:56:27	18:58:16	8	50	4	358 mVrms	100	225	(90, ~180)	100	
204.09	100	19:00:55	19:02:35	8	50	4	356 mVrms	1000		(90, ~180)	100	
204.10	100	22:25:01	22:26:41	8	40' from bottom (300')	4	330 mVrms	10	228	(90, ~180)	100	Source temp = 4.2 ° degC, 4.6 ° degC; radio at 222530, 222555
204.11	100	22:27:31	22:29:14	8	40' from bottom (300')	4	348 mVrms	100	226	(90, ~180)	100	Radio at 222739
204.12	100	22:29:57	22:31:37	8	40' from bottom (300')	4	348 mVrms	1000	223	(90, ~180)	100	
204.13	100	19:09:47	19:11:33	8	50	4	325 mVrms	10	223	(90, ~180)	150	
204.14	100	19:12:25	19:14:12	8	50	4	340 mVrms	100	225	(90, ~180)	150	Radio transmissions at start of run
204.15	100	19:15:07	19:16:47	8	50	4	338 mVrms	1000	223	(90, ~180)	150	
204.16	100	22:14:00	22:15:40	8	40' from bottom (300')	4	323 mVrms	10	224	(90, ~180)	150	Source temp = 3.7 ° degC / 38.66 ° degF; Sailboat nearby during run; radio at 221432

ELF Phase III Test 2 Test Record

Portable Electric Source (Electric Truss) Near Field Orientation 2												
Run #	Run Length (sec)	Comex	Finex	Sensor Location	Sensor Depth (ft)	Source Location	Current (100mV/Amp)	Frequency (Hz)	Voltage (V)	Moment Orientation (θ(deg), Φ(deg true))	Source Depth (ft)	Comments
204.17	100	22:16:33	22:18:13	8	40' from bottom (300')	4	339 mVrms	100	226	(90, ~180)	150	
204.18	100	22:19:09	22:20:49	8	40' from bottom (300')	4	336 mVrms 335 mVrms	1000	223	(90, ~180)	150	
204.19	100	19:22:15	19:23:55	8	50	4	320 mVrms	10	223	(90, ~180)	200	Radio transmission at 192315
204.20	100	19:24:47	19:26:27	8	50	4	335 mVrms	100	225	(90, ~180)	200	
204.21	100	19:27:28	19:29:08	8	50	4	333 mVrms 332 mVrms	1000	223	(90, ~180)	200	Sailboat passed sensor boat during run
204.22	100	22:02:55	22:04:35	8	40' from bottom (300')	4	317 mVrms 318 mVrms	10	223	(90, ~180)	200	Cell phone rang and answered at end of run
204.23	100	22:05:26	22:07:06	8	40' from bottom (300')	4	335 mVrms	100	227	(90, ~180)	200	Radio at 220555
204.24	100	22:07:48	22:09:28	8	40' from bottom (300')	4	332 mVrms	1000	223	(90, ~180)	200	Source temp = 3.5 ° degC / 38.3 ° degF
204.25	100	19:34:55	19:36:35	8	50	4	318 mVrms	10	223	(90, ~180)	250	
204.26	100	19:37:20	19:39:00	8	50	4	333 mVrms 334 mVrms	100	225	(90, ~180)	250	Source temp = 3.8 degC; 3.5 degM HDG
204.27	100	19:40:09	19:41:49	8	50	4	332 mVrms	1000	225	(90, ~180)	250	
204.28	100	21:48:05	21:49:49	8	40' from bottom (300')	4	318 mVrms	10	224	(90, ~180)	250	Temp at sensor = 1.305 V / 3.3 ° degC
204.29	100	21:51:20	21:53:00	8	40' from bottom (300')	4	330 mVrms	100	225	(90, ~180)	250	300' sensor depth
204.30	100	21:53:37	21:55:17	8	40' from bottom (300')	4	330 mVrms	1000	223	(90, ~180)	250	
204.31	100	19:46:04	19:47:44	8	50	4	318 mVrms 317 mVrms	10	223	(90, ~180)	300	
204.32	100	19:48:28	19:50:08	8	50	4	332 mVrms	100	225	(90, ~180)	300	
204.33	100	19:50:59	19:52:39	8	50	4	328 mVrms	1000	223	(90, ~180)	300	
204.34	100	21:35:32	21:37:12	8	40' from bottom (300')	4	317 mVrms	10	225	(90, ~180)	300	Source temp = 3.1 ° degC / 37.58 ° degF
204.35	100	21:38:05	21:39:45	8	40' from bottom (300')	4	331 mVrms	100	226	(90, ~180)	300	
204.36	100	21:40:46	21:42:42	8	40' from bottom (300')	4	331 mVrms	1000	225	(90, ~180)	300	
204.37	100	19:57:44	19:59:24	8	50	4	316 mVrms	10	223	(90, ~180)	350	
204.38	100	20:03:20	20:05:00	8	50	4	331 mVrms	100	225	(90, ~180)	350	

ELF Phase III Test 2 Test Record

Portable Electric Source (Electric Truss) Near Field Orientation 2												
Run #	Run Length (sec)	Comex	Finex	Sensor Location	Sensor Depth (ft)	Source Location	Current (100mV/Amp)	Frequency (Hz)	Voltage (V)	Moment Orientation (θ(deg), Φ(deg true))	Source Depth (ft)	Comments
204.39	100	20:06:13	20:07:53	8	50	4	327 mVrms	1000	223	(90, ~180)	350	
204.40	100	21:22:21	21:24:01	8	40' from bottom (300')	4	317 mVrms	10	225	(90, ~180)	350	
204.41	100	21:24:46	21:26:26	8	40' from bottom (300')	4	328 mVrms	100	225	(90, ~180)	350	
204.42	100	21:27:27	21:29:07	8	40' from bottom (300')	4	328 mVrms	1000	223	(90, ~180)	350	
204.43	100	20:15:21	20:17:01	8	50	4	317 mVrms	10	224	(90, ~180)	400	
204.44	100	20:17:47	20:19:07	8	50	4	332 mVrms	100	226	(90, ~180)	400	Radio at 201803
204.45	100	20:19:50	20:21:10	8	50	4	326 mVrms	1000	223	(90, ~180)	400	Run was 20 seconds short of 100 seconds
204.46	100	21:07:12	21:08:42	8	40' from bottom (300')	4	314 mVrms	10	223	(90, ~180)	400	Source temp = 2.9 ° degC
204.47	100	21:09:27	21:11:07	8	40' from bottom (300')	4	328 mVrms	100	225	(90, ~180)	400	
204.48	100	21:12:00	21:13:40	8	40' from bottom (300')	4	330 mVrms	1000	224	(90, ~180)	400	
204.49	100	20:27:00	20:28:40	8	50	4	315 mVrms	10	223	(90, ~180)	40' from bottom (474')	Truss at 474' depth
204.50	100	20:29:22	20:31:02	8	50	4	329 mVrms	100	225	(90, ~180)	40' from bottom (474')	
204.51	100	20:31:48	20:33:28	8	50	4	325 mVrms	1000	223	(90, ~180)	40' from bottom (474')	Small boat near source at end of run
204.52	100	20:53:20	20:55:00	8	40' from bottom (300')	4	316 mVrms	10	224	(90, ~180)	40' from bottom (474')	Source temp = 2.9 ° degC; sensor at 300' depth
204.53	100	20:56:10	20:57:50	8	40' from bottom (300')	4	331 mVrms	100	226	(90, ~180)	40' from bottom (474')	
204.54	100	20:58:30	21:00:10	8	40' from bottom (300')	4	327 mVrms	1000		(90, ~180)	40' from bottom (474')	

Day 4 Notes:

Source Barge Location 4: N 47° 57.904'
W 116° 31.980'

Sensor Barge Location 8: N 47° 57.919'
W 116° 32.095'

For exact Sensor and Source locations use GPS data and barge/boat layout offsets.

Source Orientation: ~194° True
Source Location water depth: 515'
Sensor Location water depth: 340'

Comex/Finex Times are UTC

0940: Mooring E-Source Barge.
1015: Deploying E-source truss.
1100: Sensor Barge moored and Sensor deployed to 50'.

Day 4 measurements: 56

ELF Phase III Test 2 Test Record

DAY 5 – SEPTEMBER 16, 2010

Day 5 - Noise Runs						
Run #	Run Length (sec)	Comex	Finex	Sensor Location	Sensor Depth (ft)	Comments
203	120	16:42:20	16:44:20	8	50	
204	120	19:44:45	19:46:46	8	40' from bottom (300')	Sensor at 300' depth
205	120	22:11:11	22:13:11	8	50	Radio at 21:12:50 and 21:13:06

Portable Electric Source (Electric Truss) Near Field Orientation 1												
Run #	Run Length (sec)	Comex	Finex	Sensor Location	Sensor Depth (ft)	Source Location	Current (100mV/Amp)	Frequency (Hz)	Voltage (V)	Moment Orientation (θ(deg),Φ(deg true))	Source Depth (ft)	Comments
Set 203	100			8	50' and 40' from bottom	4	Max	10, 100, 1000		(90,90)	50' to 40' from bottom	Close to validate QES and Maxwell. Near field measurement.
203.01	100	16:47:44	16:49:24	8	50	4	404 mVrms	10	222	(90,~90)	50	Rained during setup. Rain was done by the time the test started but was still overcast.
203.02	100	16:50:11	16:51:51	8	50	4	419 mVrms	100	227	(90,~90)	50	
203.03	100	16:52:49	16:54:29	8	50	4	417 mVrms	1000	225	(90,~90)	50	Source temp = 13.9° C
203.04	100	21:07:25	21:09:05	8	40' from bottom (300')	4	400 mVrms	10	223	(90,~90)	50	
203.05	100	21:09:48	21:11:28	8	40' from bottom (300')	4	417 mVrms	100	225	(90,~90)	50	
203.06	100	21:12:09	21:13:49	8	40' from bottom (300')	4	416 mVrms	1000	222	(90,~90)	50	Sensor temp = 1.666 V; source temp = 6.2° C
203.07	100	16:58:24	17:00:04	8	50	4	330 mVrms	10	222	(90,~90)	100	
203.08	100	17:00:51	17:02:31	8	50	4	345 mVrms	100	225	(90,~90)	100	
203.09	100	17:03:17	17:04:57	8	50	4	347 mVrms	1000	225	(90,~90)	100	Source temp = 11.6° C
203.10	100	20:58:32	21:00:13	8	40' from bottom (300')	4	332 mVrms	10	223	(90,~90)	100	
203.11	100	21:00:55	21:02:35	8	40' from bottom (300')	4	348 mVrms	100	225	(90,~90)	100	
203.12	100	21:03:12	21:04:52	8	40' from bottom (300')	4	349 mVrms 350 mVrms	1000	224	(90,~90)	100	Source temp = 4.0° C
203.13	100	17:09:45	17:11:25	8	50	4	320 mVrms	10	222	(90,~90)	150	

ELF Phase III Test 2 Test Record

Portable Electric Source (Electric Truss) Near Field Orientation 1												
Run #	Run Length (sec)	Comex	Finex	Sensor Location	Sensor Depth (ft)	Source Location	Current (100mV/Amp)	Frequency (Hz)	Voltage (V)	Moment Orientation (θ(deg),Φ(deg true))	Source Depth (ft)	Comments
203.14	100	17:12:03	17:13:43	8	50	4	337 mVrms	100	227	(90,~90)	150	Weights came off sensor between runs 203.14 and 203.15, confirmed via tilt sensors.
203.15	100	17:14:21	17:16:05	8	50	4	336 mVrms 337 mVrms	1000	224	(90,~90)	150	Source temp = 7.5° C. Sensor not vertical.
203.16	100	20:48:57	20:50:37	8	40' from bottom (300')	4	321 mVrms	10	223	(90,~90)	150	Sensor not vertical.
203.17	100	20:51:10	20:52:50	8	40' from bottom (300')	4	335 mVrms 336 mVrms	100	225	(90,~90)	150	Sensor not vertical.
203.18	100	20:53:35	20:55:15	8	40' from bottom (300')	4	335 mVrms	1000	223	(90,~90)	150	Source temp = 3.6° C. Sensor not vertical.
203.19	100	17:19:25	17:21:10	8	50	4	317 mVrms	10	223	(90,~90)	200	Sensor not vertical.
203.20	100	17:21:47	17:23:27	8	50	4	335 mVrms	100	226	(90,~90)	200	Sensor not vertical.
203.21	100	17:24:00	17:25:40	8	50	4	333 mVrms 334 mVrms	1000	224	(90,~90)	200	Source temp = 5.5° C. Sensor not vertical.
203.22	100	20:39:00	20:40:40	8	40' from bottom (300')	4	317 mVrms 318 mVrms	10		(90,~90)	200	Sensor not vertical.
203.23	100	20:41:30	20:43:10	8	40' from bottom (300')	4	332 mVrms 333 mVrms	100	225	(90,~90)	200	Sensor not vertical.
203.24	100	20:43:45	20:45:25	8	40' from bottom (300')	4	331 mVrms	1000	223	(90,~90)	200	Source temp = 3.3° C. Sensor not vertical.
203.25	100	17:29:46	17:31:41	8	50	4	315 mVrms	10	227	(90,~90)	250	Sensor not vertical.
203.26	100	17:32:22	17:34:02	8	50	4	333 mVrms	100	227	(90,~90)	250	Sensor not vertical.
203.27	100	17:34:46	17:36:26	8	50	4	332 mVrms	1000	224	(90,~90)	250	Source temp = 4.3° C. Sensor not vertical.
203.28	100	20:29:13	20:30:53	8	40' from bottom (300')	4	316 mVrms	10	223	(90,~90)	250	Sensor not vertical.
203.29	100	20:31:38	20:33:18	8	40' from bottom (300')	4	333 mVrms 334 mVrms	100	227	(90,~90)	250	Sensor not vertical.
203.30	100	20:33:55	20:35:35	8	40' from bottom (300')	4	330 mVrms	1000	223	(90,~90)	250	Source temp = 3.3° C. Sensor not vertical.
203.31	100	17:40:03	17:41:43	8	50	4	314 mVrms	10	223	(90,~90)	300	Sensor not vertical.
203.32	100	17:42:25	17:44:05	8	50	4	329 mVrms	100	225	(90,~90)	300	Sensor not vertical.
203.33	100	17:44:39	17:46:19	8	50	4	330 mVrms	1000	225	(90,~90)	300	Source temp = 3.7° C. Sensor not vertical.

ELF Phase III Test 2 Test Record

Portable Electric Source (Electric Truss) Near Field Orientation 1												
Run #	Run Length (sec)	Comex	Finex	Sensor Location	Sensor Depth (ft)	Source Location	Current (100mV/Amp)	Frequency (Hz)	Voltage (V)	Moment Orientation (θ(deg),Φ(deg true))	Source Depth (ft)	Comments
203.34	100	20:18:34	20:20:14	8	40' from bottom (300')	4	315 mVrms	10	223	(90,~90)	300	Sensor not vertical.
203.35	100	20:21:00	20:22:40	8	40' from bottom (300')	4	330 mVrms	100	225	(90,~90)	300	Sensor not vertical.
203.36	100	20:23:35	20:25:15	8	40' from bottom (300')	4	338 mVrms 329 mVrms	1000	222	(90,~90)	300	Source temp = 3.2° C. Sensor not vertical.
203.37	100	17:49:31	17:51:11	8	50	4	314 mVrms	10	229	(90,~90)	350	Sensor not vertical.
203.38	100	17:51:53	17:53:33	8	50	4	328 mVrms 329 mVrms	100	225	(90,~90)	350	Sensor not vertical.
203.39	100	17:54:10	17:55:50	8	50	4	327 mVrms 328 mVrms	1000	223	(90,~90)	350	Source temp = 3.4° C. Sensor not vertical.
203.40	100	20:09:10	20:10:50	8	40' from bottom (300')	4	314 mVrms	10	222	(90,~90)	350	Sensor not vertical.
203.41	100	20:11:25	20:13:05	8	40' from bottom (300')	4	328 mVrms 329 mVrms	100	225	(90,~90)	350	Sensor not vertical.
203.42	100	20:13:40	20:15:20	8	40' from bottom (300')	4	330 mVrms 331 mVrms	1000	224	(90,~90)	350	Source temp = 3.1° C; Radio transmissions at 131444 and 131458. Sensor not vertical.
203.43	100	17:59:42	18:01:22	8	50	4	313 mVrms 314 mVrms	10	222	(90,~90)	400	Temp = 1.815 V. Sensor not vertical.
203.44	100	18:02:20	18:04:00	8	50	4	328 mVrms	100	225	(90,~90)	400	Sensor not vertical.
203.45	100	18:04:38	18:06:18	8	50	4	327 mVrms 328 mVrms	1000	222	(90,~90)	400	Source temp = 3.3° C. Sensor not vertical.
203.46	100	19:59:20	20:01:00	8	40' from bottom (300')	4	314 mVrms	10	223	(90,~90)	400	Sensor not vertical.
203.47	100	20:01:41	20:03:21	8	40' from bottom (300')	4	328 mVrms	100	224	(90,~90)	400	Sensor not vertical.
203.48	100	20:04:02	20:05:42	8	40' from bottom (300')	4	327 mVrms	1000	222	(90,~90)	400	Source temp = 3.1° C. Sensor not vertical.
203.49	100	18:11:19	18:12:59	8	50	4	313 mVrms	10		(90,~90)	40' from bottom (474')	Started to rain again around 181330; source at 474' depth. Sensor not vertical.
203.50	100	18:13:33	18:15:13	8	50	4	330 mVrms 331 mVrms	100	226	(90,~90)	40' from bottom (474')	Sensor not vertical.
203.51	100	18:15:52	18:17:32	8	50	4	336 mVrms 337 mVrms	1000	229	(90,~90)	40' from bottom (474')	Sensor temp = 1.820 V (3.2° C); phone call 181710 to end of run; source at 475' depth. Sensor not vertical.

ELF Phase III Test 2 Test Record

Portable Electric Source (Electric Truss) Near Field Orientation 1												
Run #	Run Length (sec)	Comex	Finex	Sensor Location	Sensor Depth (ft)	Source Location	Current (100mV/Amp)	Frequency (Hz)	Voltage (V)	Moment Orientation (θ(deg),Φ(deg true))	Source Depth (ft)	Comments
203.52	100	19:48:25	19:50:05	8	40' from bottom (300')	4	313 mVrms	10	223	(90,~90)	40' from bottom (474')	Source temp = 3.2° C; Sensor at 300' depth. Recovered sensor and installed weights before this run.
203.53	100	19:50:43	19:52:23	8	40' from bottom (300')	4	327 mVrms 328 mVrms	100	225	(90,~90)	40' from bottom (474')	
203.54	100	19:53:00	19:54:40	8	40' from bottom (300')	4	326 mVrms 327 mVrms	1000	222	(90,~90)	40' from bottom (474')	

Portable Electric Source (Electric Truss) Near Field Orientation 1												
Run #	Run Length (sec)	Comex	Finex	Sensor Location	Sensor Depth (ft)	Source Location	Current (100mV/Amp)	Frequency (Hz)	Voltage (V)	Moment Orientation (θ(deg),Φ(deg true))	Source Depth (ft)	Comments
Set 403	100			8	50'	4	Max	10, 100, 1000		(90,90)	50' to 40' from bottom	Redone versions of some of 203 set due to loss of weights for 203.14 through 203.51.
403.49	100	21:31:35	21:33:15	8	50	4	313 mVrms	10	229	(90,~90)	40' from bottom (475')	Source at 475' depth
403.50	100	21:34:05	21:35:45	8	50	4	327 mVrms	100	224	(90,~90)	40' from bottom (475')	
403.51	100	21:36:23	21:38:03	8	50	4	329 mVrms	1000	224	(90,~90)	40' from bottom (475')	Source temp = 4.3° C
403.43	100	21:42:01	21:43:41	8	50	4	313 mVrms 314 mVrms	10	222	(90,~90)	400	
403.44	100	21:44:24	21:46:04	8	50	4	328 mVrms	100	224	(90,~90)	400	
403.45	100	21:46:37	21:48:17	8	50	4	327 mVrms	1000	222	(90,~90)	400	Source temp = 3.5° C
403.37	100	21:51:20	21:53:05	8	50	4	314 mVrms	10	223	(90,~90)	350	Error at start of file.
403.38	100	21:53:44	21:55:28	8	50	4	328 mVrms 329 mVrms	100	225	(90,~90)	350	
403.39	100	21:56:17	21:57:57	8	50	4	327 mVrms 328 mVrms	1000	223	(90,~90)	350	Source temp = 3.3° C; radio transmission at 215636
403.25	100	22:03:33	22:05:13	8	50	4	316 mVrms	10	225	(90,~90)	250	
403.26	100	22:05:49	22:07:29	8	50	4	331 mVrms	100	222	(90,~90)	250	
403.27	100	22:08:04	22:09:44	8	50	4	330 mVrms	1000	223	(90,~90)	250	Sensor temp = 1.696 V; Source temp = 3.3° C

Day 5 Notes:

Source Barge Location 4: N 47° 57.899'
W 116° 31.975'

Sensor Barge Location 8: N 47° 57.919'
W 116° 32.096'

For exact Sensor and Source locations use GPS data and barge/boat layout offsets.

Source Orientation: ~102° True
Source Location water depth: 515'
Sensor Location water depth: 340'

Comex/Finex Times are UTC

0940: Mooring E-Source Barge.
1015: Deploying E-source truss.
1100: Sensor Barge moored and Sensor deployed to 50'.

Day 5 measurements: 69

ELF Phase III Test 2 Test Record

DAY 6 – SEPTEMBER 17, 2010

Day 6 - Noise Runs						
Run #	Run Length (sec)	Comex	Finex	Sensor Location	Sensor Depth (ft)	Comments
301	120	17:31:00	17:33:00	6	50	Choppy water all day Friday
302	120	20:26:10	20:28:10	6	250	

Portable Electric Source (Electric Truss) Case 2												
Run #	Run Length (sec)	Comex	Finex	Sensor Location	Sensor Depth (ft)	Source Location	Current (100mV/Amp)	Frequency (Hz)	Voltage (V)	Moment Orientation (θ(deg), Φ(deg true))	Source Depth (ft)	Comments
Set 201	100			6	50	4	Max	10, 100, 1000		(90,0)	50' to 40' from bottom	Repeat of Case 2. Get more samples.
201.01	100	18:37:48	18:39:28	6	50	4	417 mVrms	10	222	(90,~350)	50	Phone call from 183751 to end of run
201.02	100	18:40:20	18:42:00	6	50	4	428 mVrms	100	225	(90,~350)	50	
201.03	100	18:42:47	18:44:27	6	50	4	436 mVrms 437 mVrms	1000	222	(90,~350)	50	Sensor rotated 60deg in horizontal plane during run
201.04	100	18:47:26	18:49:06	6	50	4	356 mVrms 357 mVrms	10	222	(90,~350)	100	
201.05	100	18:50:03	18:51:43	6	50	4	373 mVrms	100	225	(90,~350)	100	
201.06	100	18:52:35	18:54:15	6	50	4	377 mVrms 378 mVrms	1000	222	(90,~350)	100	
201.07	100	18:57:45	18:59:25	6	50	4	329 mVrms 330 mVrms	10	223	(90,~350)	150	Sensor rotating a great deal (< ~80 °) due to motion of barge in wind.
201.08	100	19:01:28	19:03:08	6	50	4	343 mVrms 344 mVrms	100	225	(90,~350)	150	
201.09	100	19:03:49	19:05:29	6	50	4	348 mVrms 349 mVrms	1000	223	(90,~350)	150	
201.10	100	19:08:35	19:10:24	6	50	4	320 mVrms	10	222	(90,~350)	200	
201.11	100	19:11:10	19:12:50	6	50	4	336 mVrms	100	225	(90,~350)	200	
201.12	100	19:13:40	19:15:20	6	50	4	340 mVrms	1000	222	(90,~350)	200	
201.13	100	19:19:15	19:20:55	6	50	4	320 mVrms	10	224	(90,~350)	250	
201.14	100	19:21:43	19:23:23	6	50	4	336 mVrms	100	227	(90,~350)	250	
201.15	100	19:24:13	19:25:53	6	50	4	339 mVrms	1000	224	(90,~350)	250	
201.16	100	19:29:05	19:30:45	6	50	4	319 mVrms	10	224	(90,~350)	300	
201.17	100	19:31:39	19:33:19	6	50	4	333 mVrms	100	227	(90,~350)	300	
201.18	100	19:34:14	19:35:54	6	50	4	338 mVrms-	1000	224	(90,~350)	300	

ELF Phase III Test 2 Test Record

Portable Electric Source (Electric Truss) Case 2												
Run #	Run Length (sec)	Comex	Finex	Sensor Location	Sensor Depth (ft)	Source Location	Current (100mV/Amp)	Frequency (Hz)	Voltage (V)	Moment Orientation (θ(deg),Φ(deg true))	Source Depth (ft)	Comments
201.19	100	19:39:04	19:40:44	6	50	4	318 mVrms	10	224	(90,~350)	350	
201.20	100	19:41:35	19:43:15	6	50	4	332 mVrms 333 mVrms	100	227	(90,~350)	350	
201.21	100	19:44:10	19:45:50	6	50	4	342 mVrms	1000	224	(90,~350)	350	
201.22	100	19:49:45	19:51:45	6	50	4	317 mVrms 318 mVrms	10	224	(90,~350)	400	
201.23	100	19:52:31	19:54:27	6	50	4	333 mVrms	100	227	(90,~350)	400	
201.24	100	19:55:18	19:56:58	6	50	4	342 mVrms	1000	224	(90,~350)	400	
201.25	100	20:01:30	20:03:10	6	50	4	316 mVrms 317 mVrms	10	224	(90,~350)	40' from bottom (475')	Source at 475' depth
201.26	100	20:04:07	20:05:47	6	50	4	330 mVrms	100	227	(90,~350)	40' from bottom (475')	
201.27	100	20:06:35	20:08:15	6	50	4	333 mVrms	1000	222	(90,~350)	40' from bottom (475')	Sensor temp = 1.822 V / 3.1° C

Portable Electric Source (Electric Truss) Case 3												
Run #	Run Length (sec)	Comex	Finex	Sensor Location	Sensor Depth (ft)	Source Location	Current (100mV/Amp)	Frequency (Hz)	Voltage (V)	Moment Orientation (θ(deg),Φ(deg true))	Source Depth (ft)	Comments
Set 202	100			6	250	4	Max	10, 100, 1000		(90,90)	50' to 40' from bottom	Repeat of Case 3. Get more samples.
202.01	100	21:04:37	21:06:17	6	250	4	419 mVrms	10	222	(90,~75)	50	180° rotation in azimuthal angle
202.02	100	21:07:54	21:09:34	6	250	4	430 mVrms	100	225	(90,~75)	50	
202.03	100	21:10:20	21:12:00	6	250	4	434 mVrms	1000	223	(90,~75)	50	
202.04	100	21:15:00	21:16:40	6	250	4	362 mVrms 363 mVrms	10	224	(90,~75)	100	
202.05	100	21:17:37	21:19:17	6	250	4	379 mVrms	100	227	(90,~75)	100	
202.06	100	21:20:05	21:21:45	6	250	4	385 mVrms	1000	224	(90,~75)	100	
202.07	100	21:24:35	21:26:15	6	250	4	332 mVrms	10	224	(90,~75)	150	
202.08	100	21:27:08	21:28:48	6	250	4	345 mVrms	100	226	(90,~75)	150	
202.09	100	21:29:44	21:31:24	6	250	4	350 mVrms 351 mVrms	1000	224	(90,~75)	150	

ELF Phase III Test 2 Test Record

Portable Electric Source (Electric Truss) Case 3												
Run #	Run Length (sec)	Comex	Finex	Sensor Location	Sensor Depth (ft)	Source Location	Current (100mV/Amp)	Frequency (Hz)	Voltage (V)	Moment Orientation (θ(deg),Φ(deg true))	Source Depth (ft)	Comments
202.10	100	21:34:35	21:36:15	6	250	4	323 mVrms	10	224	(90,~75)	200	
202.11	100	21:37:30	21:39:10	6	250	4	337 mVrms	100	227	(90,~75)	200	
202.12	100	21:39:55	21:41:35	6	250	4	344 mVrms	1000	224	(90,~75)	200	Didn't see 1kHz line
202.13	100	21:45:48	21:47:28	6	250	4	317 mVrms 318 mVrms	10	223	(90,~75)	250	
202.14	100	21:48:16	21:49:56	6	250	4	331 mVrms 332 mVrms	100	225	(90,~75)	250	Started to rain
202.15	100	21:51:00	21:52:50	6	250	4	336 mVrms	1000	223	(90,~75)	250	Didn't see 1 kHz line from here through the end of the test run 202.xx
202.16	100	21:56:41	21:58:21	6	250	4	319 mVrms	10	224	(90,~75)	300	
202.17	100	21:59:12	22:00:52	6	250	4	333 mVrms	100	227	(90,~75)	300	
202.18	100	22:01:34	22:03:32	6	250	4	328 mVrms	1000	224	(90,~75)	300	Source off before end of run.
202.19	100	22:06:56	22:08:36	6	250	4	318 mVrms	10	224	(90,~75)	350	
202.20	100	22:09:25	22:11:05	6	250	4	333 mVrms 334 mVrms	100	227	(90,~75)	350	
202.21	100	22:11:50	22:13:30	6	250	4	327 mVrms 328 mVrms	1000	224	(90,~75)	350	
202.22	100	22:16:53	22:18:33	6	250	4	310 mVrms 311 mVrms	10	219	(90,~75)	400	
202.23	100	22:19:25	22:21:05	6	250	4	325 mVrms	100	221	(90,~75)	400	
202.24	100	22:22:05	22:23:45	6	250	4	319 mVrms 320 mVrms	1000	219	(90,~75)	400	
202.25	100	22:28:46	22:30:26	6	250	4	314 mVrms	10	223	(90,~75)	40' from bottom (475')	Source at 475' depth
202.26	100	22:31:11	22:32:51	6	250	4	328 mVrms	100	225	(90,~75)	40' from bottom (475')	
202.27	100	22:33:46	22:35:26	6	250	4	338 mVrms 339 mVrms	1000	223	(90,~75)	40' from bottom (475')	Sensor temp = 1.649 V

Day 6 Notes:

Source Barge Location 4: N 47° 57.90'
W 116° 31.99'

Sensor Barge Location 6: N 47° 57.47'
W 116° 32.53'

For exact Sensor and Source locations use GPS data and barge/boat layout offsets.

Source Orientation for Set 201: ~350° True

Source Orientation for Set 202: ~75° True

Source Location water depth: 515'

Sensor Location water depth: 510'

Comex/Finex Times are UTC

1015: Sensor Barge moored and Sensor deployed to 50'.

Day 6 measurements: 56

Appendix B: Scenario Reports

The attached documents are referred to as scenario reports. Each report is identified with a set of data for a particular experiment and corresponding simulation. There are three report classes: Complex Canonical, Experiment 2 and Experiment 4. The Complex Canonical reports are associated with the classical three layer geometry and are used to establish consistency between the various computational methods; there are no experimental data associated with these reports. Experiment 2 and Experiment 4 are associated with experiments that took place during December 6-11, 2008 and September 11-17, 2010, respectively. Another experiment was conducted during March 5-11, 2010, i.e. Experiment 3. However, the results from this experiment were inconclusive, which necessitated Experiment 4. See Appendix A for the test reports.

Canonical Complex

Experiment 1

Experiment Date: November 2, 2011

1 Discussion

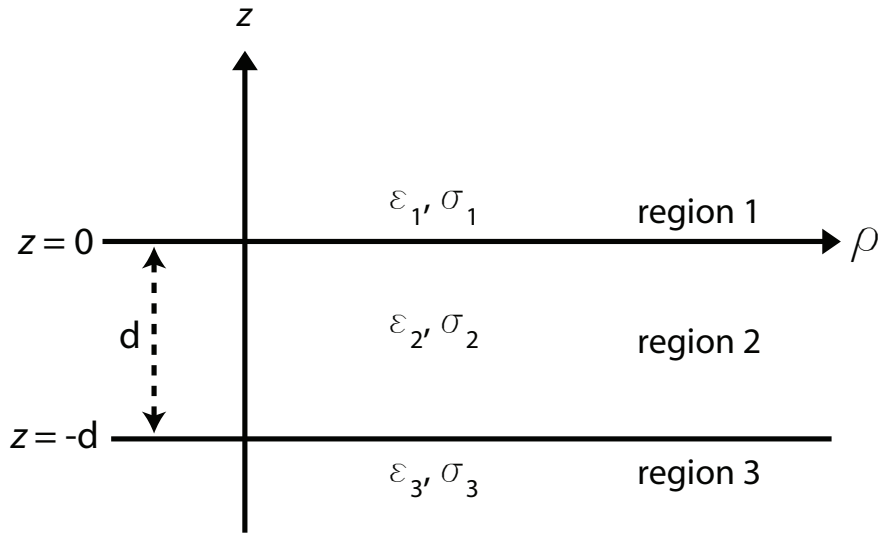


Figure 1: 3-layer topology.

Source Parameters

- Source Type: HED (Boat Hull: plates 0.6 m by 0.3 m separated by 4 m).
- Source Strength: 7.144 A-m.
- $f = 100$ Hz.

Environment

- Water thickness: $d = 180$ m
- Air: $\sigma_1 = 0$ S/m and $\epsilon_{r1} = 1$
- Water: $\sigma_2 = 0.01$ S/m and $\epsilon_{r2} = 81$
- Mud: $\sigma_3 = 0.0012$ S/m and $\epsilon_{r3} = 1$

Table 1: Simulation Details

	FDTD	HFSS	QES/SFW
Domain Size	$200 \times 200 \times 120$ cells	64747 tets	N/A
Cell Size (m)	$5 \times 5 \times 5$	N/A	N/A
Time Step (ns)	9.6	N/A	N/A
Run Time (Hrs)	6	1.77	< 1 min

Comments

- Computational time is based on actual elapsed real time. This number is highly subjective and based on how many other applications might be running at a particular time. However, the reported number is an indication of the amount of time typically needed for a particular simulation. The computer specs are: 16 CPU cores at 2.8 GHz.
- Run times for HFSS are given for a single frequency.
- QES is not applicable for magnetic fields using electric source excitation.

2 Simulation Variables

Sensor_P1(x,y,z) [m]	(-276.8760,-43.8732,-15.7470)
Sensor_P2(x,y,z) [m]	(348.3009,-39.4584,-15.7470)
Source_P1(x,y,z) [m]	(10.2560,13.7320,-8.2296)
Source_P2(x,y,z) [m]	(10.2560,13.7320,-8.2296)
Source_Plate_Separation [m]	4
Source_Size [m X m X #]	[0.6 X 0.3 X 1]
Source_Heading [deg]	0.0
Source_Voltage [V Peak]	NaN
Source_Current [A Peak]	1.786
Source_Frequency [Hz]	100

--- Extra Information ---

Source_Heading_Bounds [deg]	(N/A)
Average_Boat_Speed [m/s]	NaN
Source_Type	Electric truss (truss)
Sensor_Type	EMA
Bin_Size [sec]	1
Number_of_Datapoints	200
Lake_Origin (Easting,Northing)	NaN
Analysis_Date	26-Sep-2011

3 Boat Path

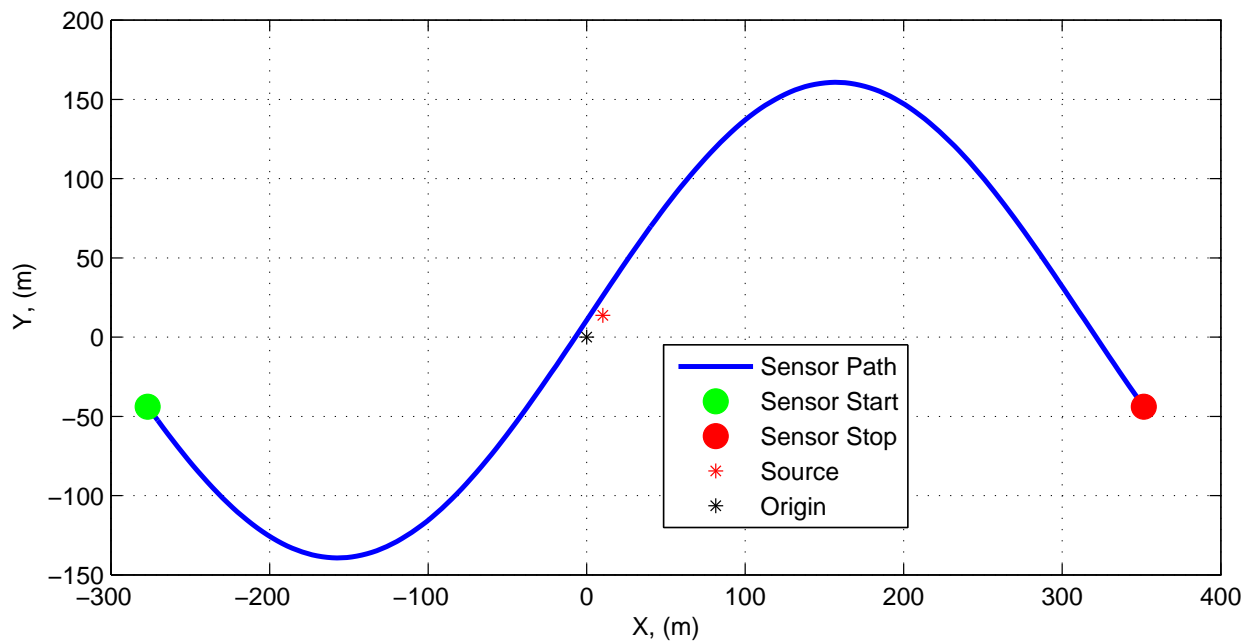


Figure 2: Source and sensor relationship.

4 Plots

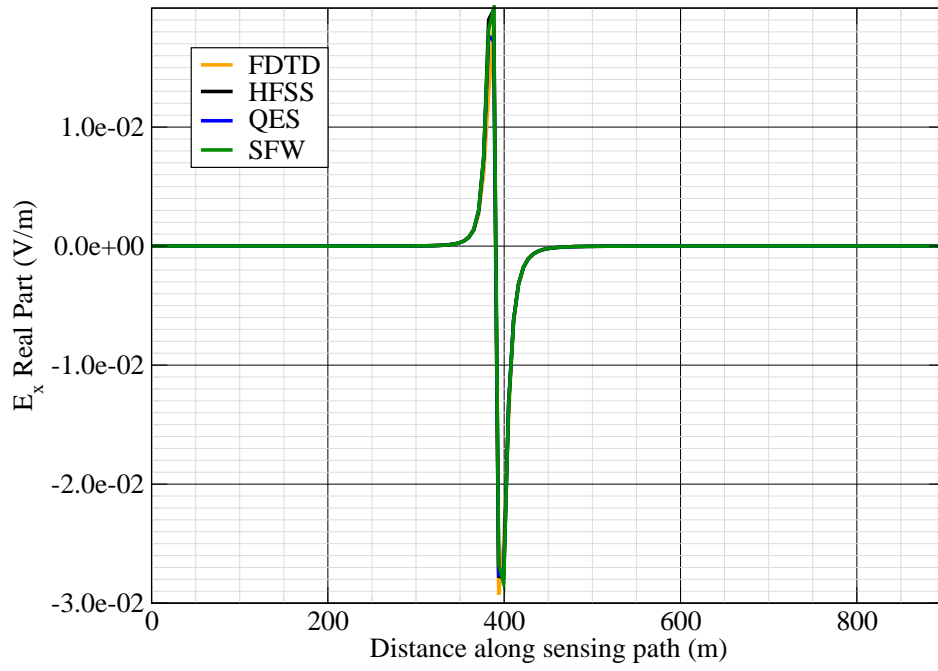


Figure 3: E_x real.

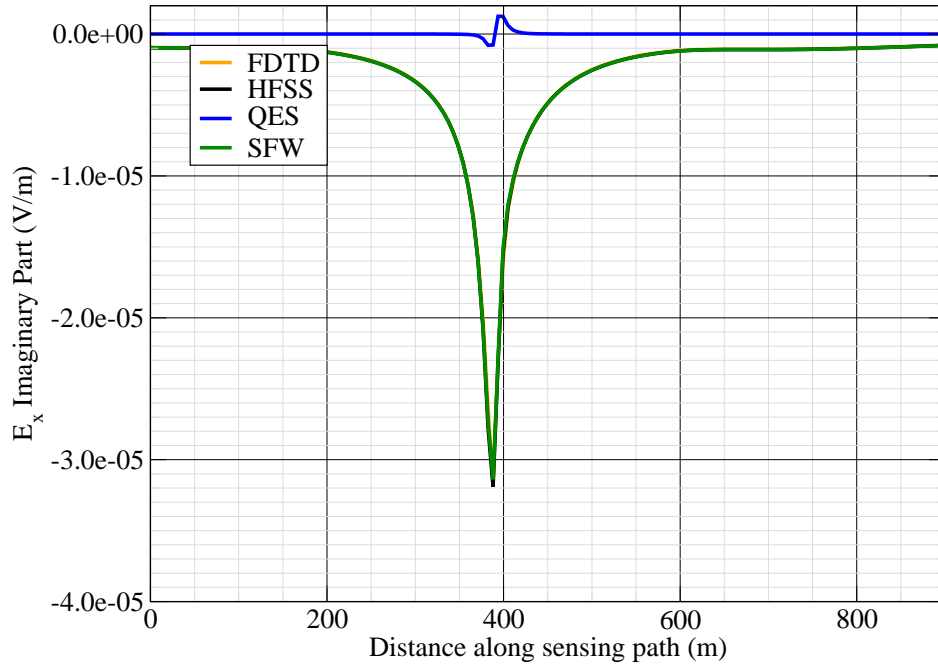


Figure 4: E_x imag.

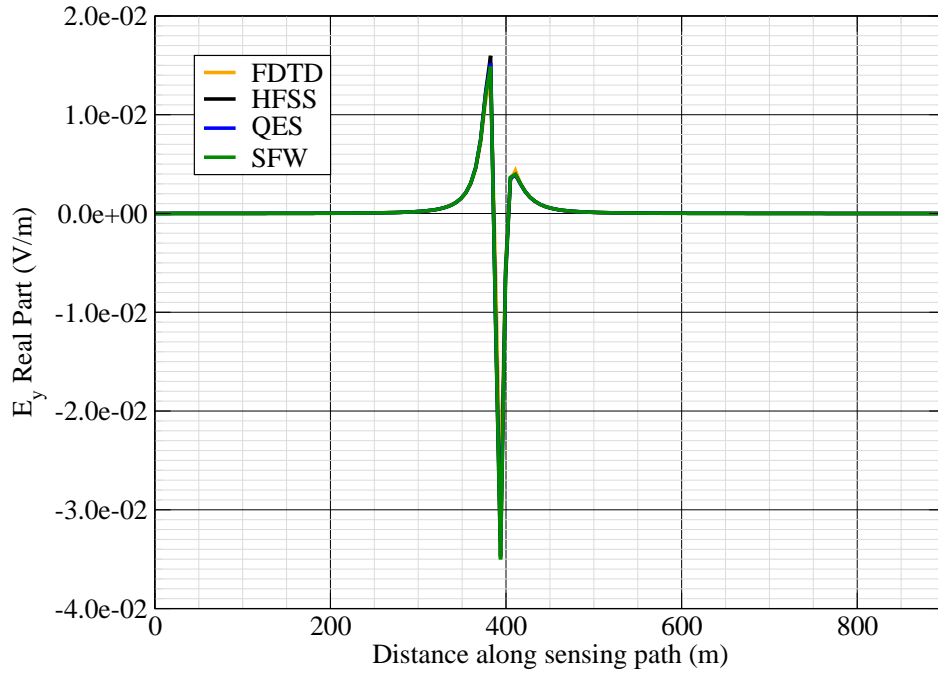


Figure 5: E_y real.

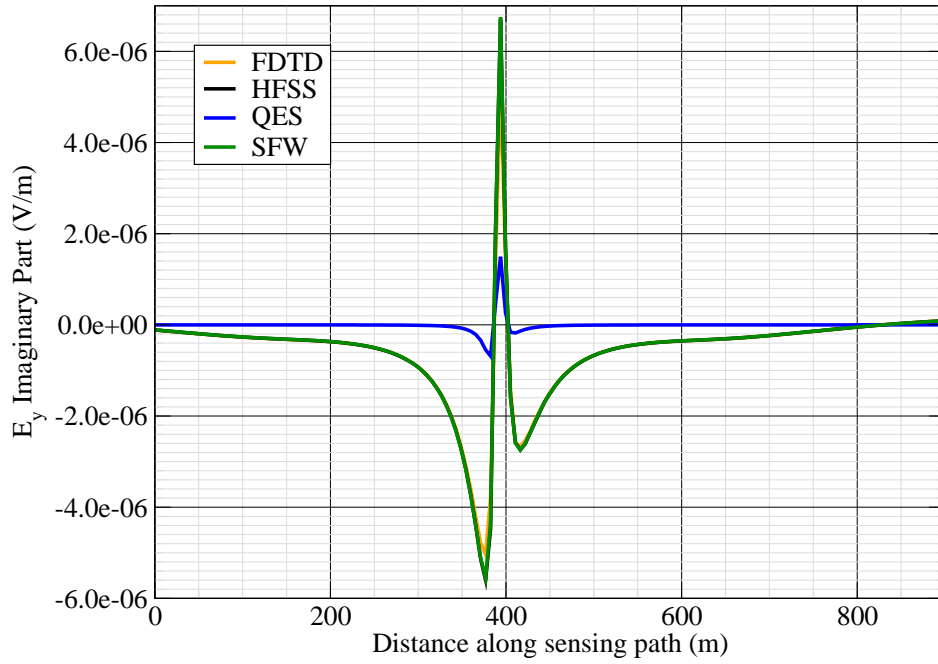


Figure 6: E_y imag.

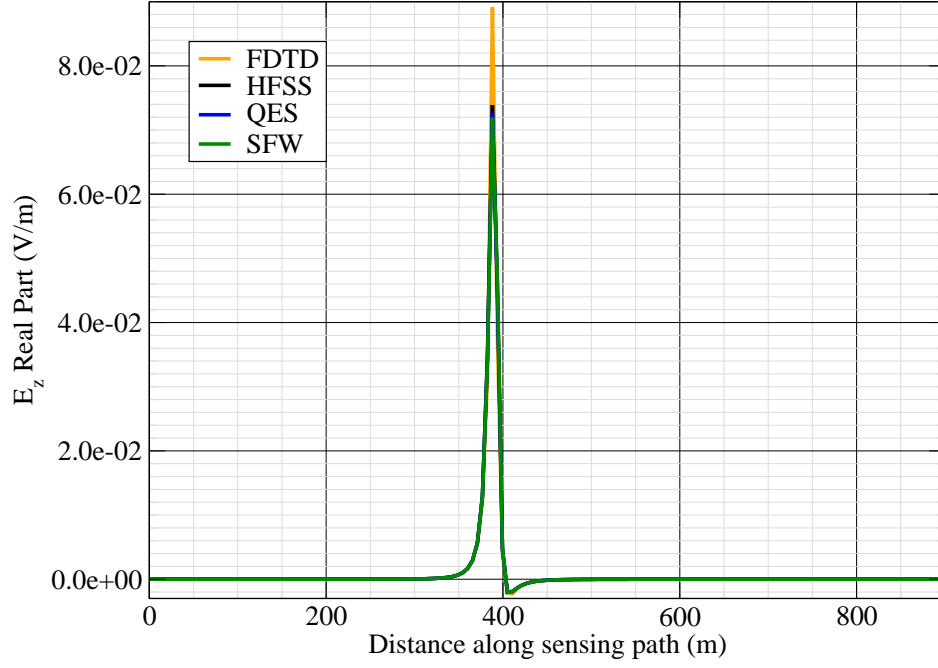


Figure 7: E_z real.

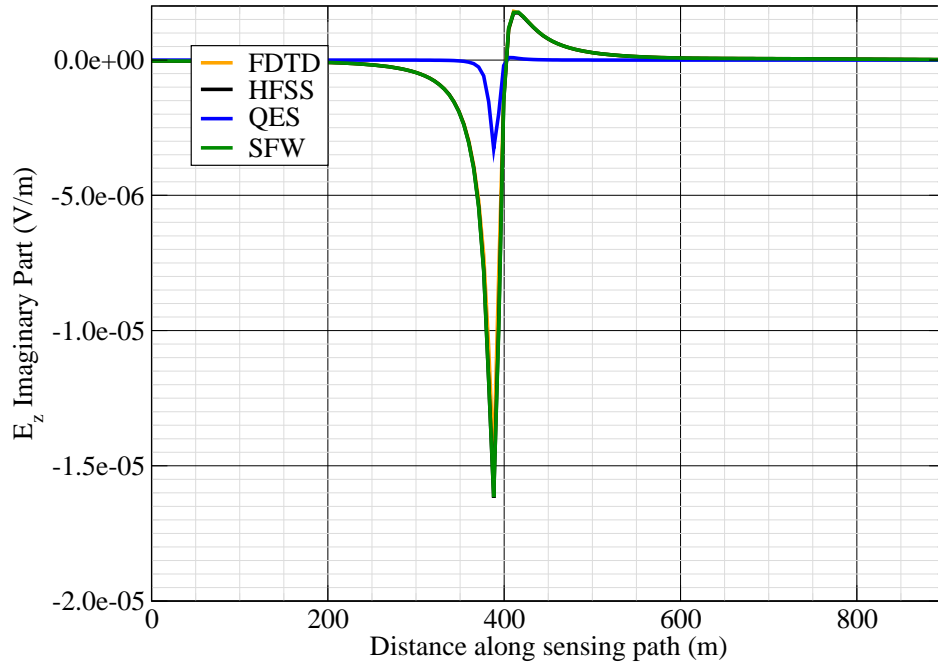


Figure 8: E_z imag.

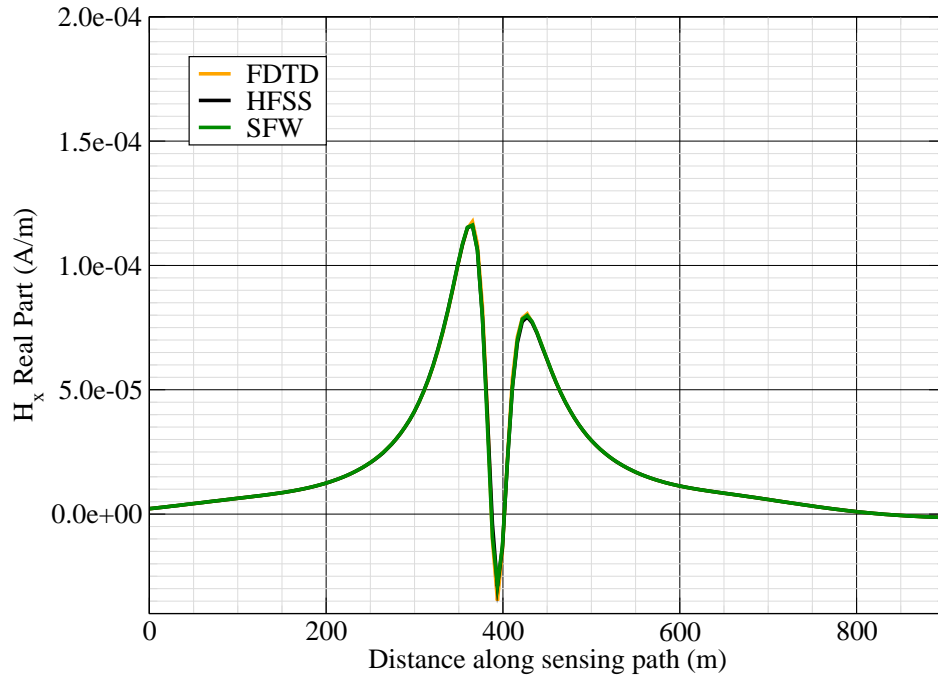


Figure 9: H_x real.

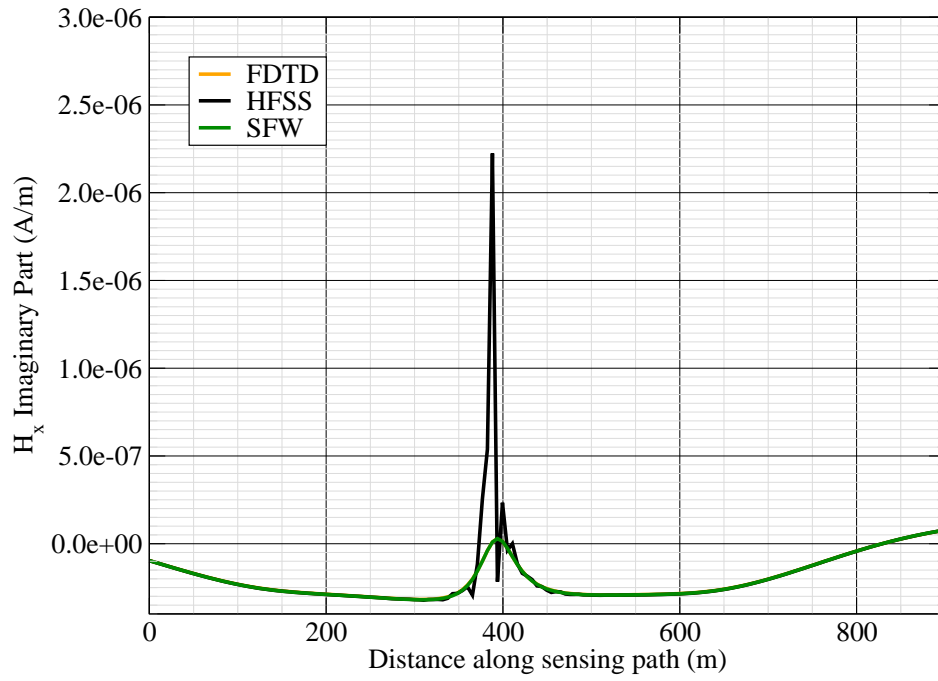


Figure 10: H_x imag.

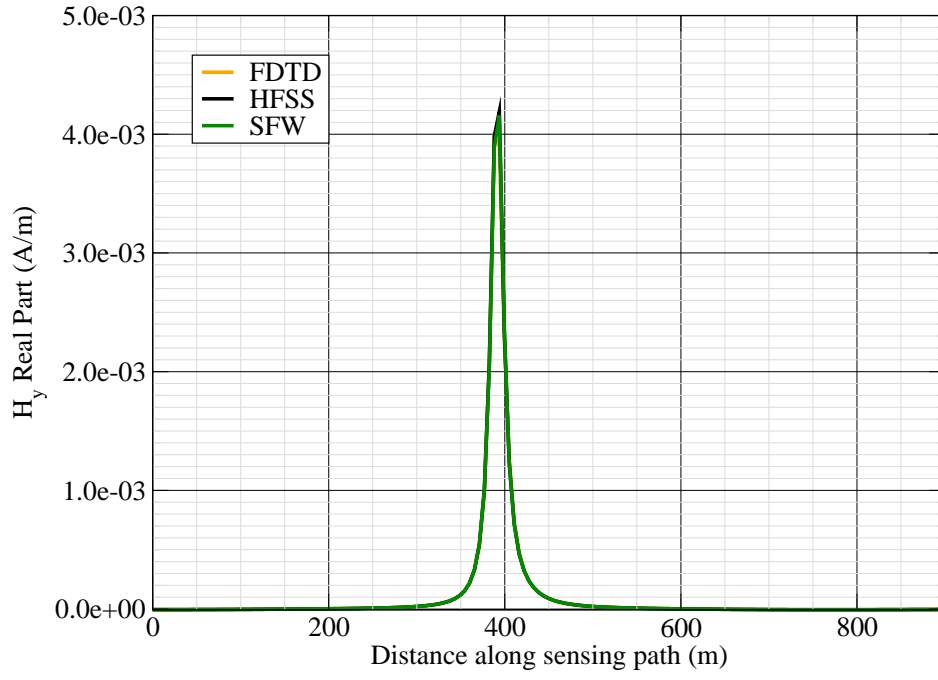


Figure 11: H_y real.

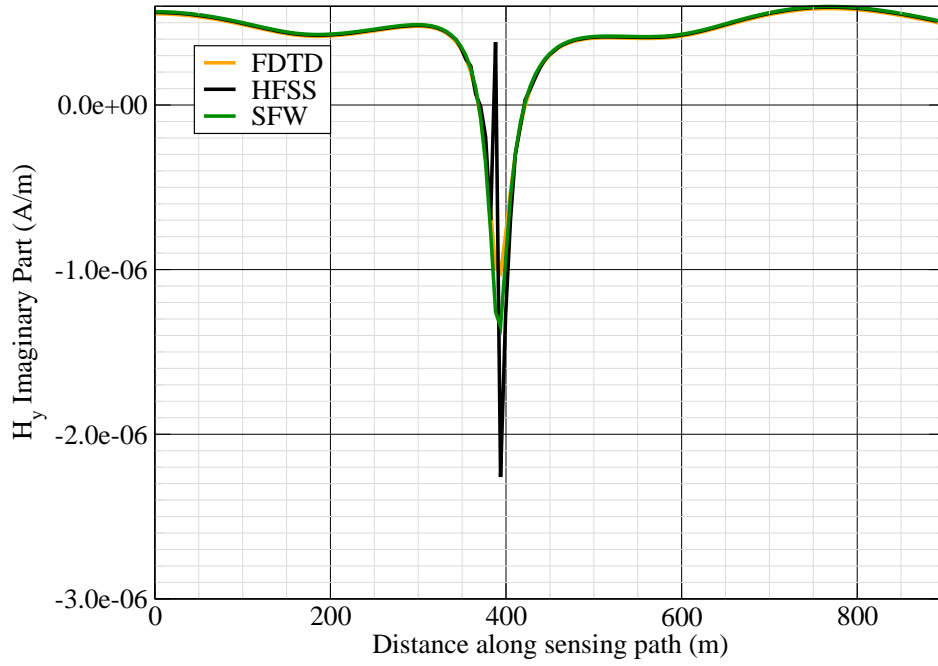


Figure 12: H_y imag.

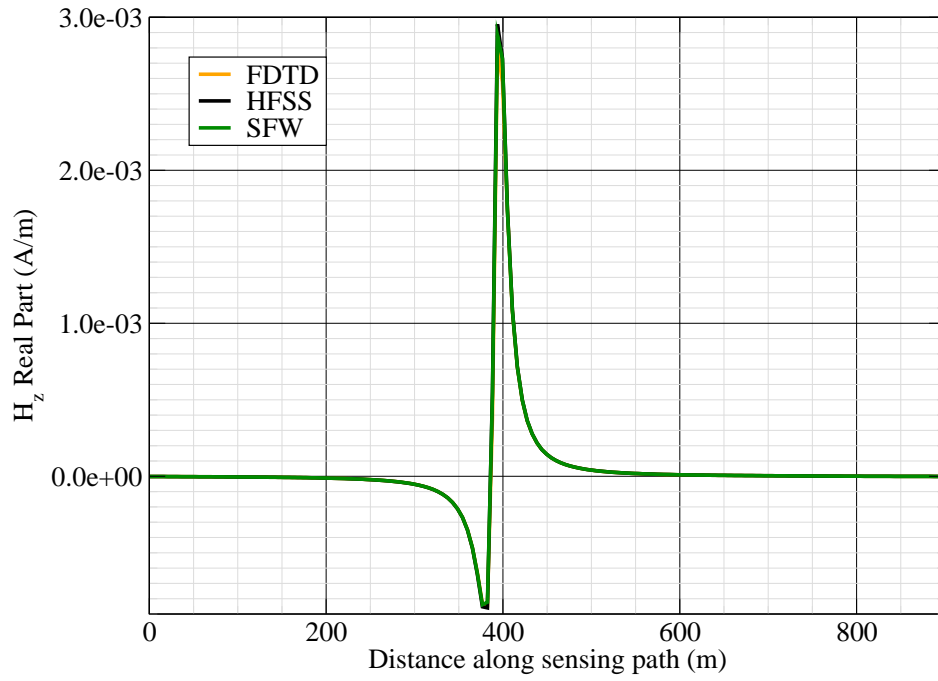


Figure 13: H_z real.

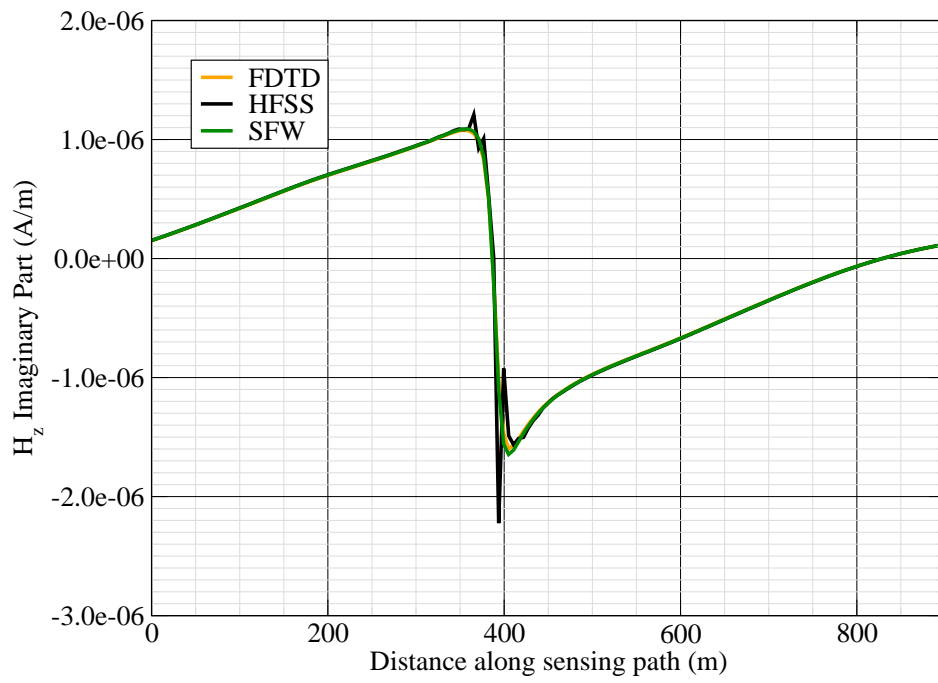


Figure 14: H_z imag.

Canonical Complex

Experiment 2

Experiment Date: November 2, 2011

1 Discussion



Figure 1: 3-layer topology.

Source Parameters

- Source Type: VED (Boat Hull: plates 0.6 m by 0.3 m separated by 4 m).
- Source Strength: 14.68 A-m.
- $f = 1000$ Hz.

Environment

- Water thickness: $d = 180$ m
- Air: $\sigma_1 = 0$ S/m and $\epsilon_{r1} = 1$
- Water: $\sigma_2 = 0.01$ S/m and $\epsilon_{r2} = 81$
- Mud: $\sigma_3 = 0.0012$ S/m and $\epsilon_{r3} = 1$

Table 1: Simulation Details

	FDTD	HFSS	QES/SFW
Domain Size	$200 \times 200 \times 120$ cells	38236 tets	N/A
Cell Size (m)	$5 \times 5 \times 5$	N/A	N/A
Time Step (ns)	9.6	N/A	N/A
Run Time (Hrs)	6	0.07	< 1 min

Comments

- Computational time is based on actual elapsed real time. This number is highly subjective and based on how many other applications might be running at a particular time. However, the reported number is an indication of the amount of time typically needed for a particular simulation. The computer specs are: 16 CPU cores at 2.8 GHz.
- Run times for HFSS are given for a single frequency.
- QES is not applicable for magnetic fields using electric source excitation.

2 Simulation Variables

Sensor_P1(x,y,z) [m]	(-200,57.1571,-10.123)
Sensor_P2(x,y,z) [m]	(114.1593,44.8169,-10.123)
Source_P1(x,y,z) [m]	(0,0,-23.343)
Source_P2(x,y,z) [m]	(0,0,-23.343)
Source_Plate_Separation [m]	4
Source_Size [m X m X #]	[0.6 X 0.3 X 1]
Source_Heading [deg]	NaN
Source_Voltage [V Peak]	NaN
Source_Current [A Peak]	3.67
Source_Frequency [Hz]	1000

--- Extra Information ---

Source_Heading_Bounds [deg]	(N/A)
Average_Boat_Speed [m/s]	NaN
Source_Type	Electric vert_truss (vert_truss)
Sensor_Type	EMA
Bin_Size [sec]	1
Number_of_Datapoints	200
Lake_Origin (Easting,Northing)	NaN
Analysis_Date	6-Oct-2011

3 Boat Path

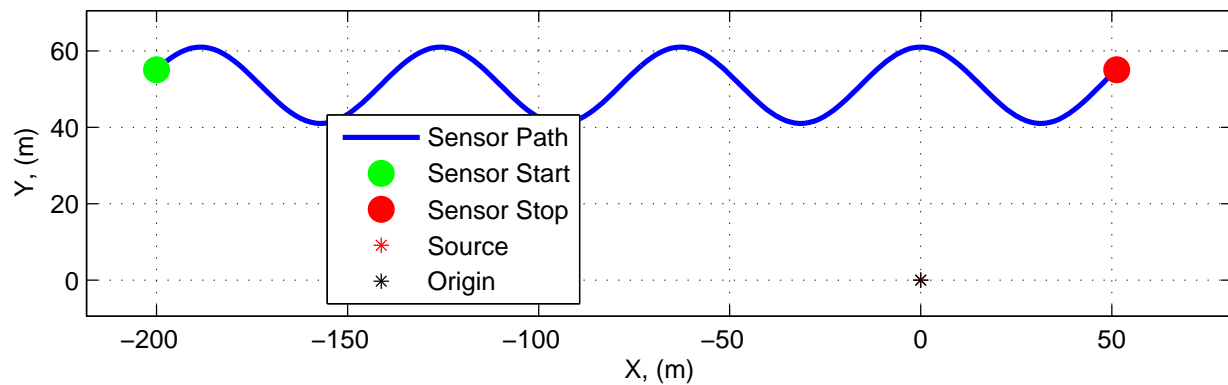


Figure 2: Source and sensor relationship.

4 Plots

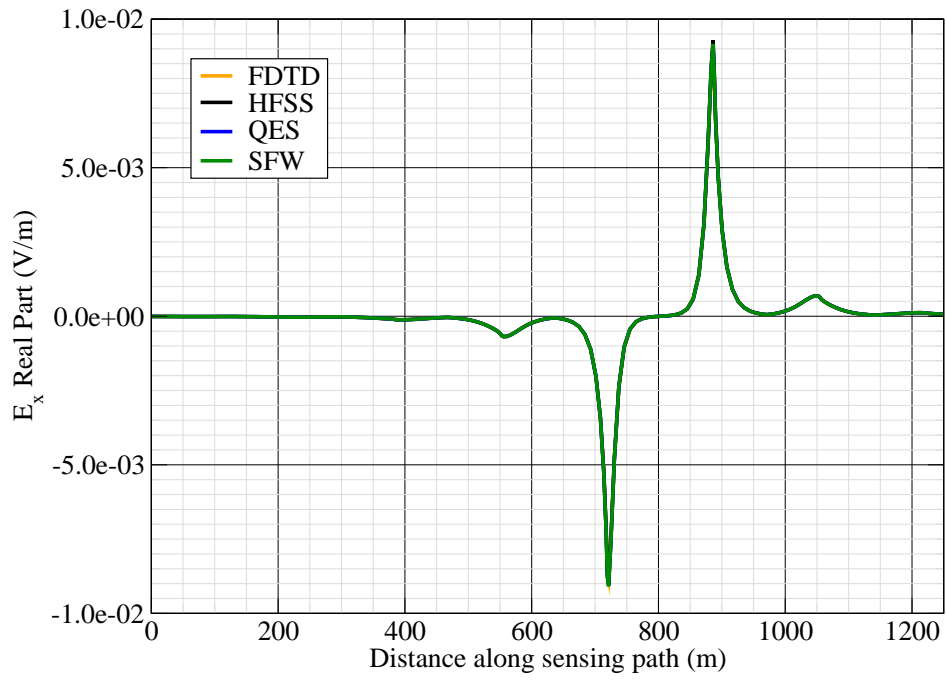


Figure 3: E_x real.

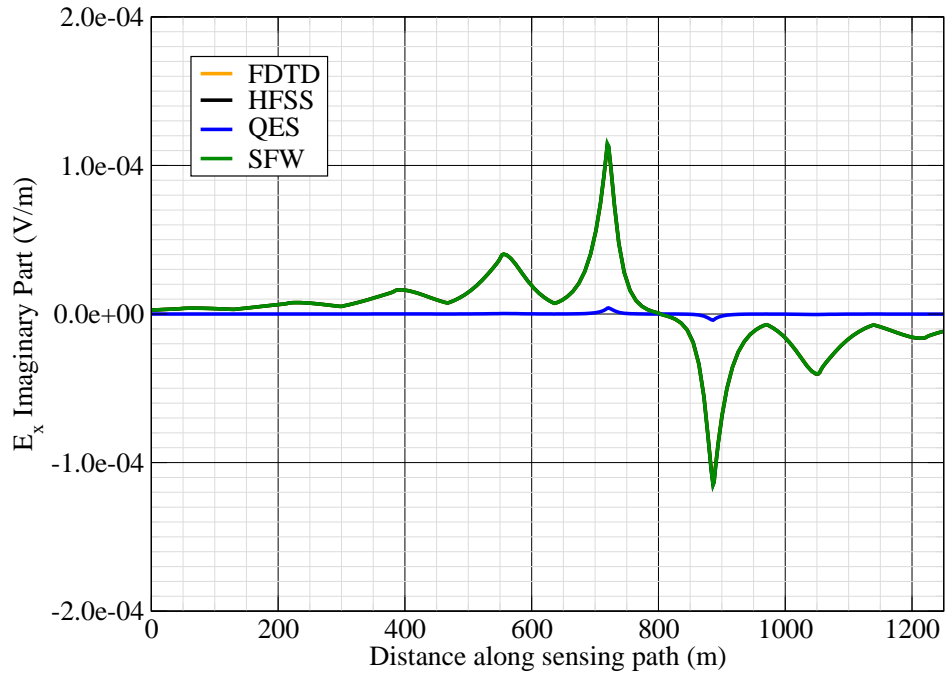


Figure 4: E_x imag.

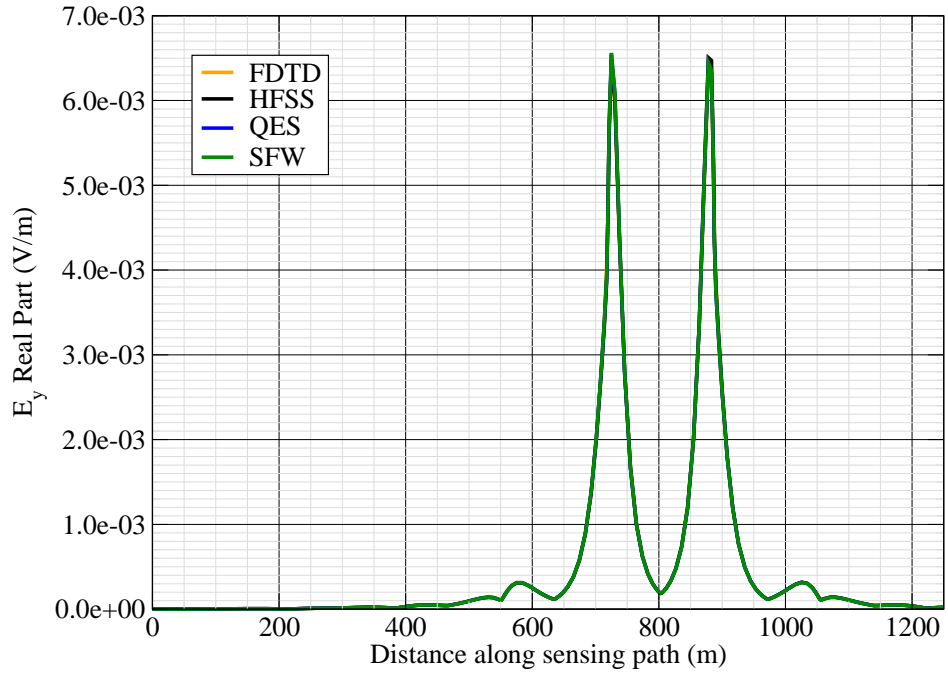


Figure 5: E_y real.

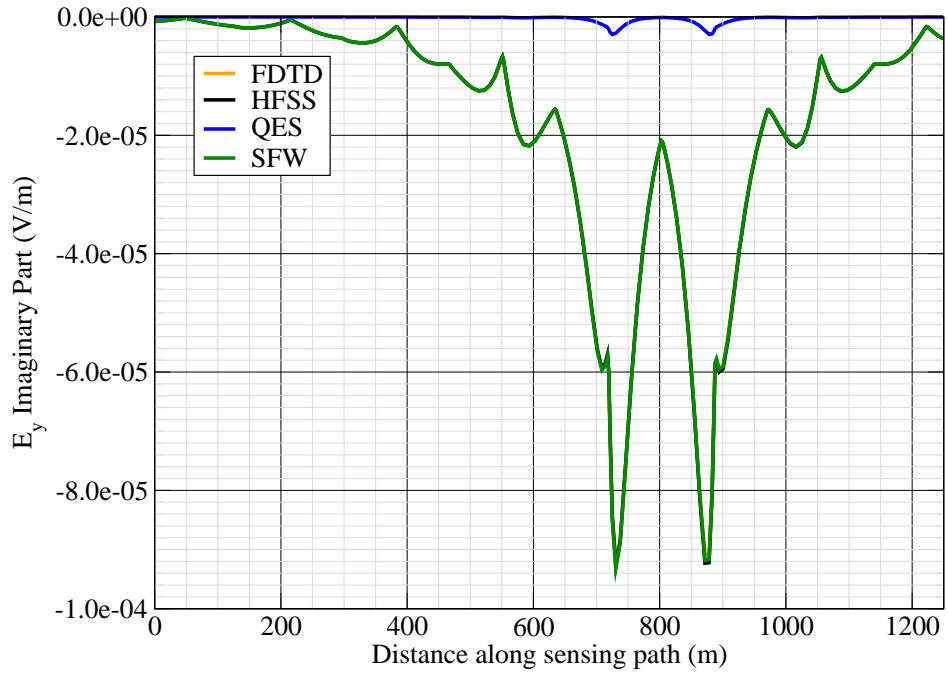


Figure 6: E_y imag.

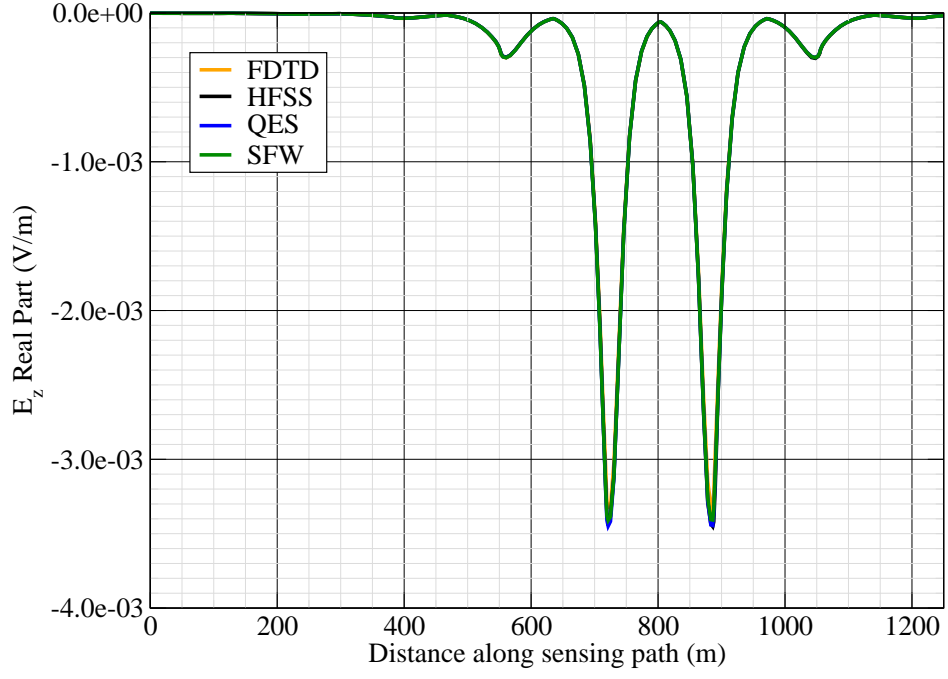


Figure 7: E_z real.

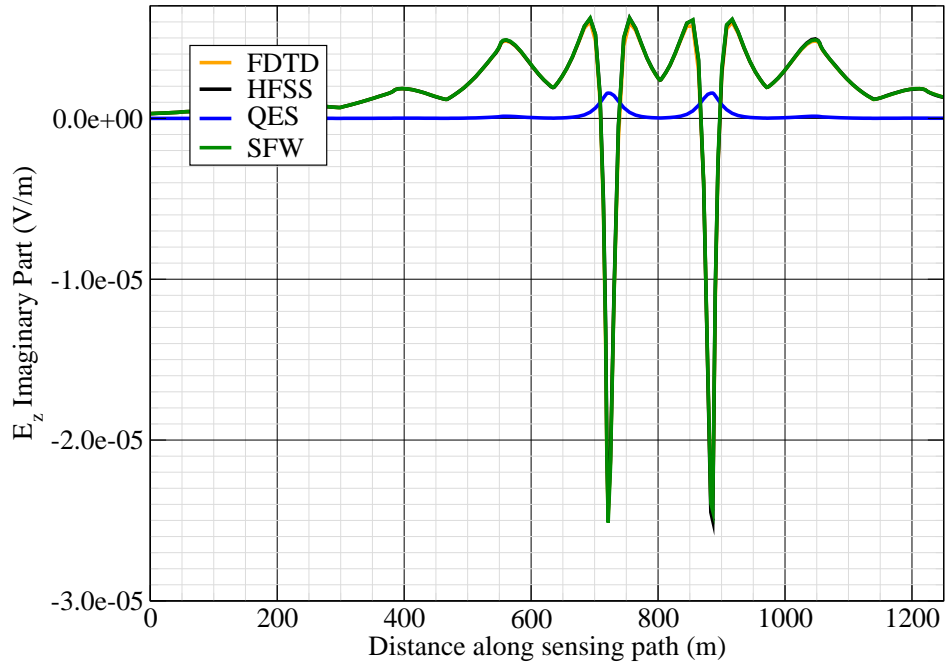


Figure 8: E_z imag.

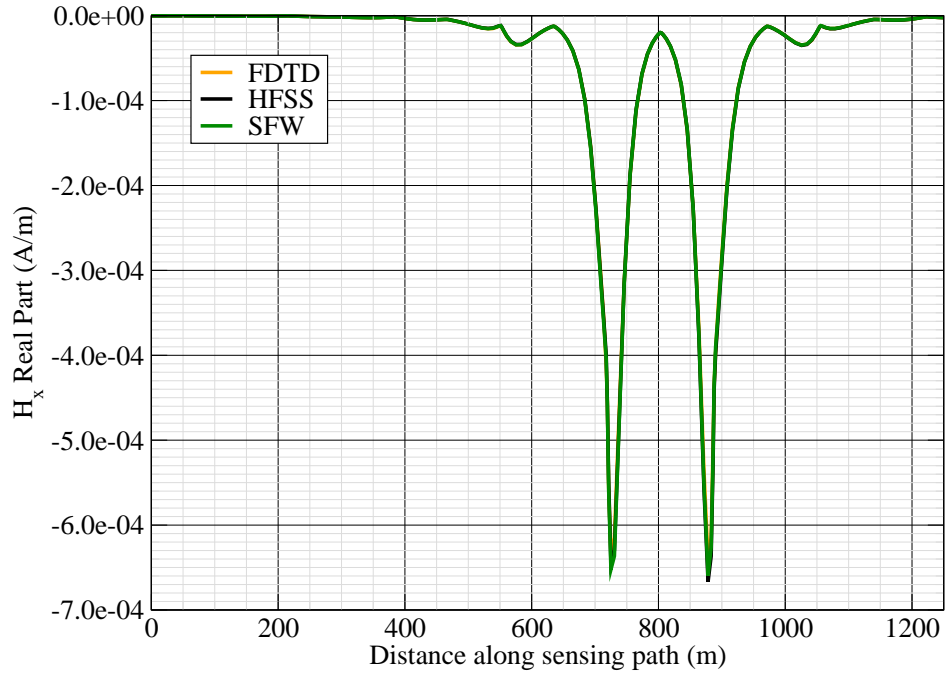


Figure 9: H_x real.

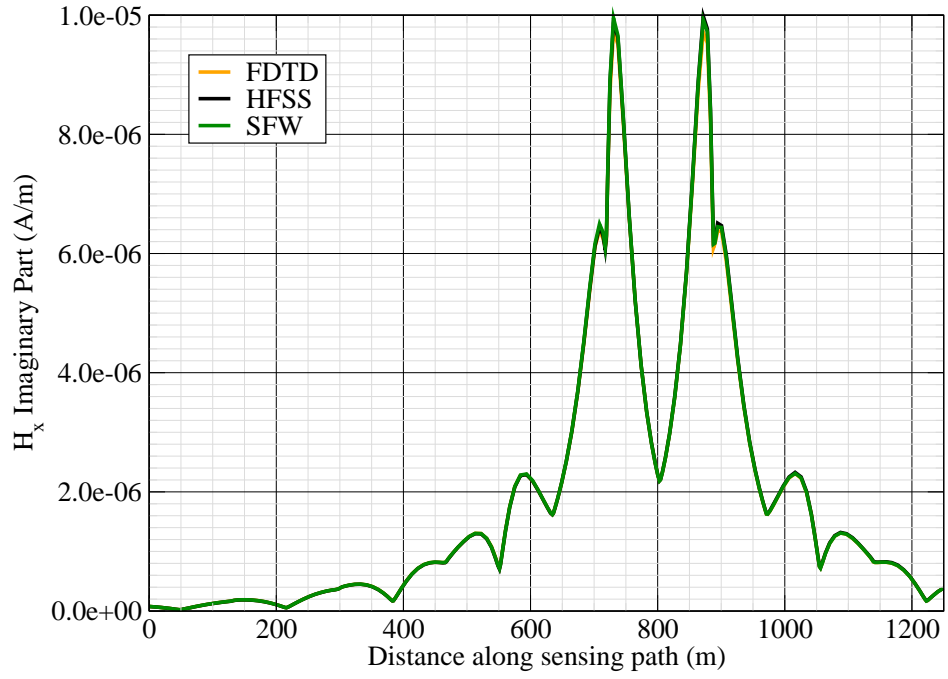


Figure 10: H_x imag.

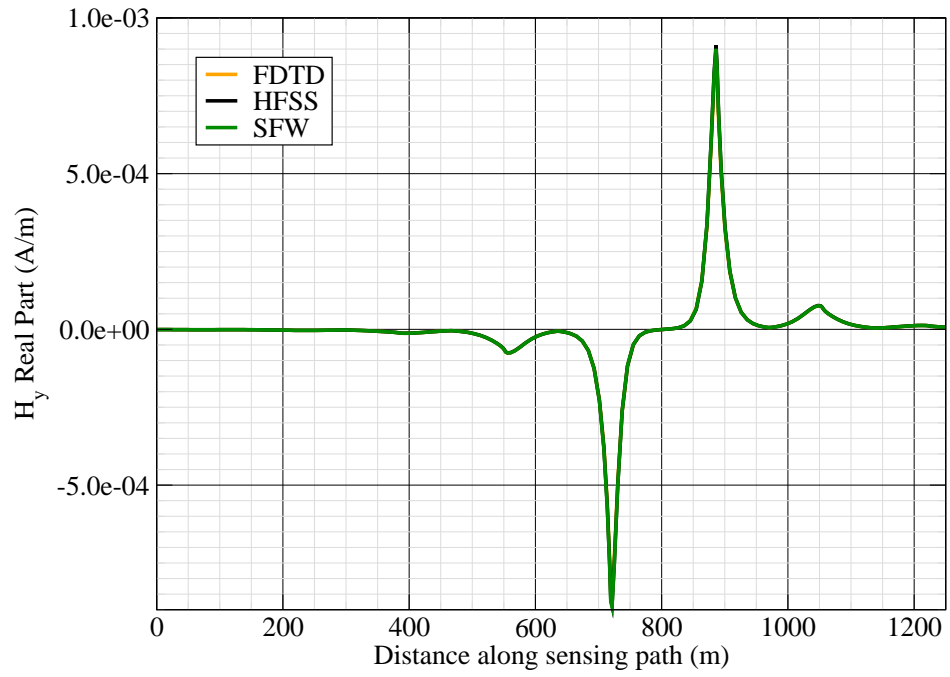


Figure 11: H_y real.

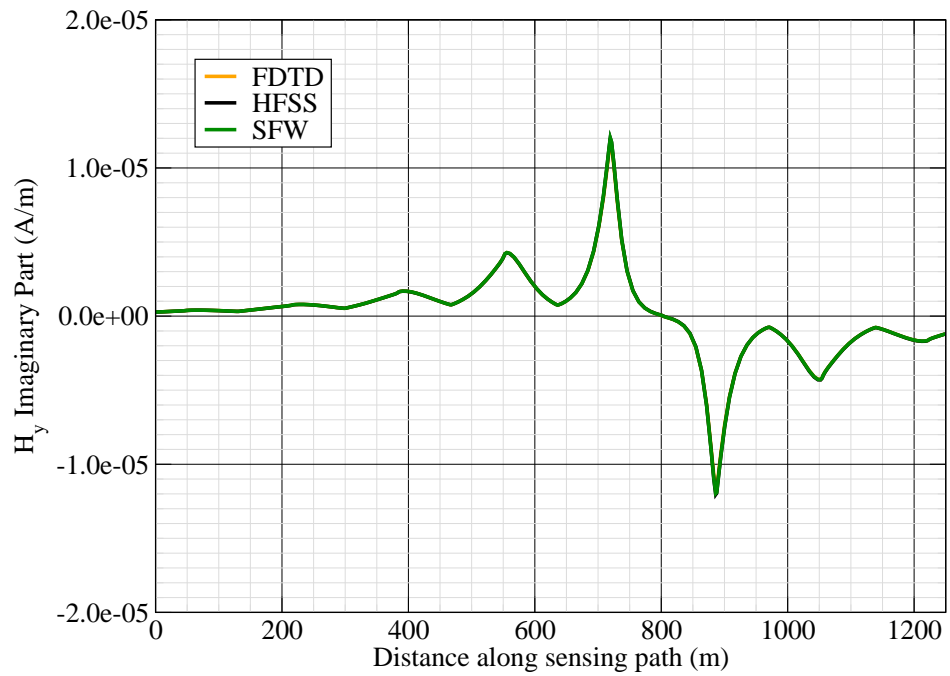


Figure 12: H_y imag.

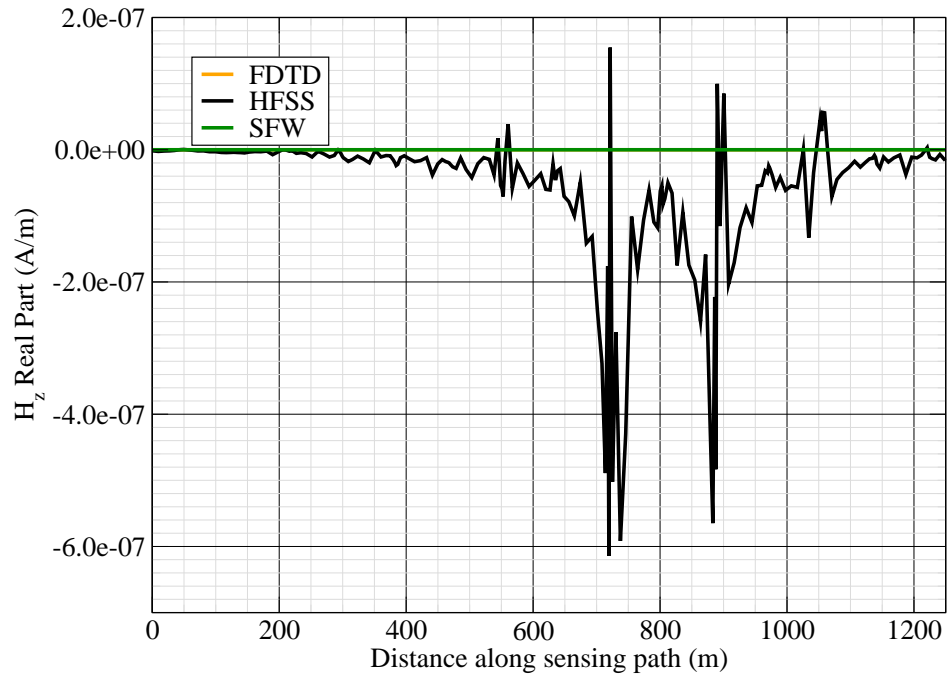


Figure 13: H_z real.

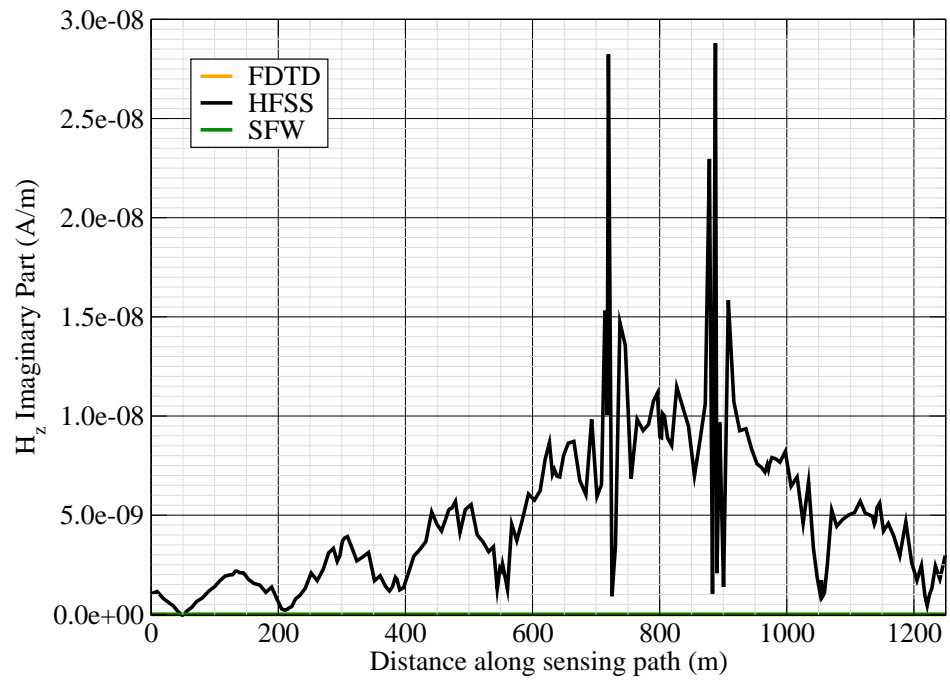


Figure 14: H_z imag.

Canonical Complex

Experiment 3

Experiment Date: November 2, 2011

1 Discussion

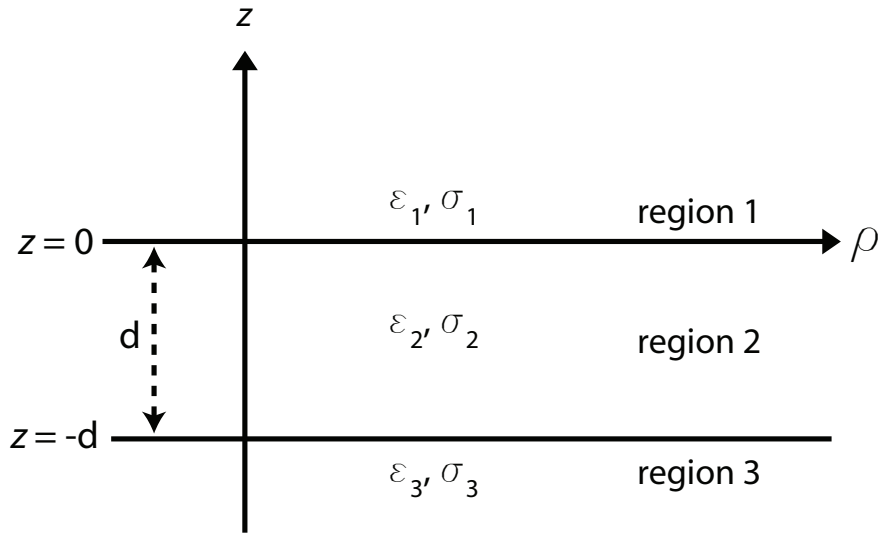


Figure 1: 3-layer topology.

Source Parameters

- Source Type: HMD (Coil: 3.66 m by 3.66 m with 12 turns).
- Source Strength: 3,683 A-m².
- f = 100 Hz.

Environment

- Water thickness: $d = 180$ m
- Air: $\sigma_1 = 0$ S/m and $\epsilon_{r1} = 1$
- Water: $\sigma_2 = 0.01$ S/m and $\epsilon_{r2} = 81$
- Mud: $\sigma_3 = 0.0012$ S/m and $\epsilon_{r3} = 1$

Table 1: Simulation Details

	FDTD	HFSS	QES/SFW
Domain Size	$400 \times 200 \times 120$ cells	16673 tets	N/A
Cell Size (m)	$5 \times 5 \times 5$	N/A	N/A
Time Step (ns)	9.6	N/A	N/A
Run Time (Hrs)	7h 50m	0.08	< 1 min

Comments

- Computational time is based on actual elapsed real time. This number is highly subjective and based on how many other applications might be running at a particular time. However, the reported number is an indication of the amount of time typically needed for a particular simulation. The computer specs are: 16 CPU cores at 2.8 GHz.
- Run times for HFSS are given for a single frequency.
- QES is not applicable for magnetic fields using electric source excitation.

2 Simulation Variables

Sensor_P1(x,y,z) [m]	(-628.3185,0,15.747)
Sensor_P2(x,y,z) [m]	(628.3185,0,15.747)
Source_P1(x,y,z) [m]	(0,0,8.2296)
Source_P2(x,y,z) [m]	(0,0,8.2296)
Source_Plate_Separation [m]	N/A
Source_Size [m X m X #]	[3.658 X 3.658 X 12]
Source_Heading [deg]	0
Source_Voltage [V Peak]	11.6294
Source_Current [A Peak]	22.9361
Source_Frequency [Hz]	100
--- Extra Information ---	
Source_Heading_Bounds [deg]	(N/A)
Average_Boat_Speed [m/s]	NaN
Source_Type	Magnetic source (portable)
Sensor_Type	PEMA
Bin_Size [sec]	1
Number_of_Datapoints	200
Lake-Origin (Easting,Northing)	NaN
Analysis_Date	7-Oct-2011

3 Boat Path

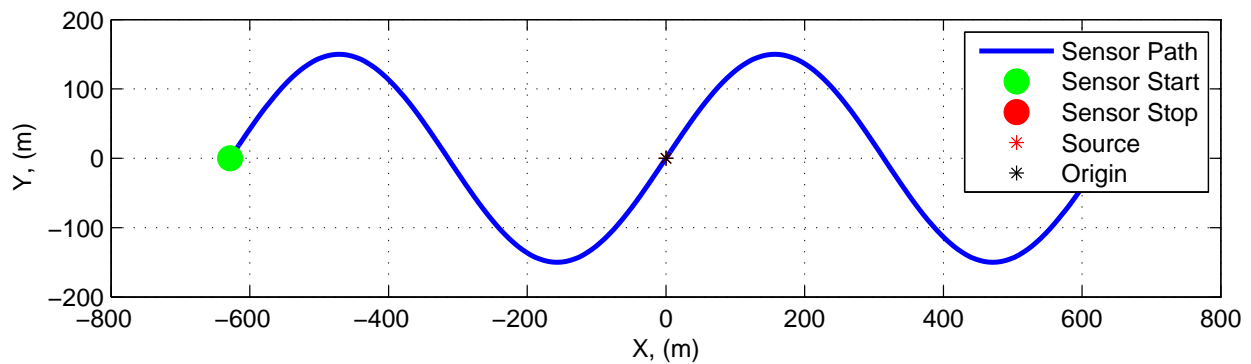


Figure 2: Source and sensor relationship.

4 Plots

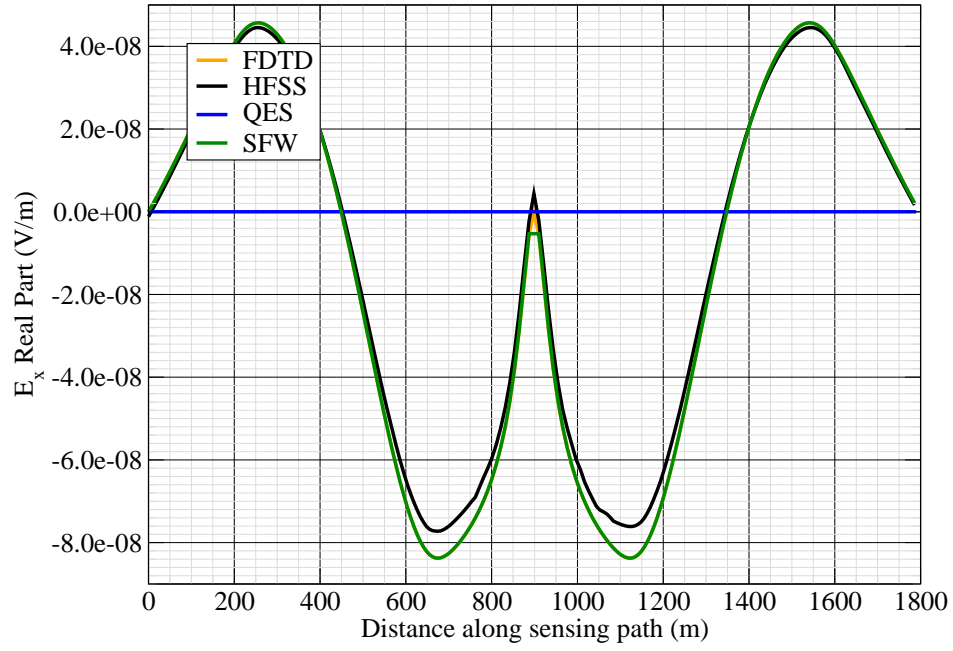


Figure 3: E_x real.

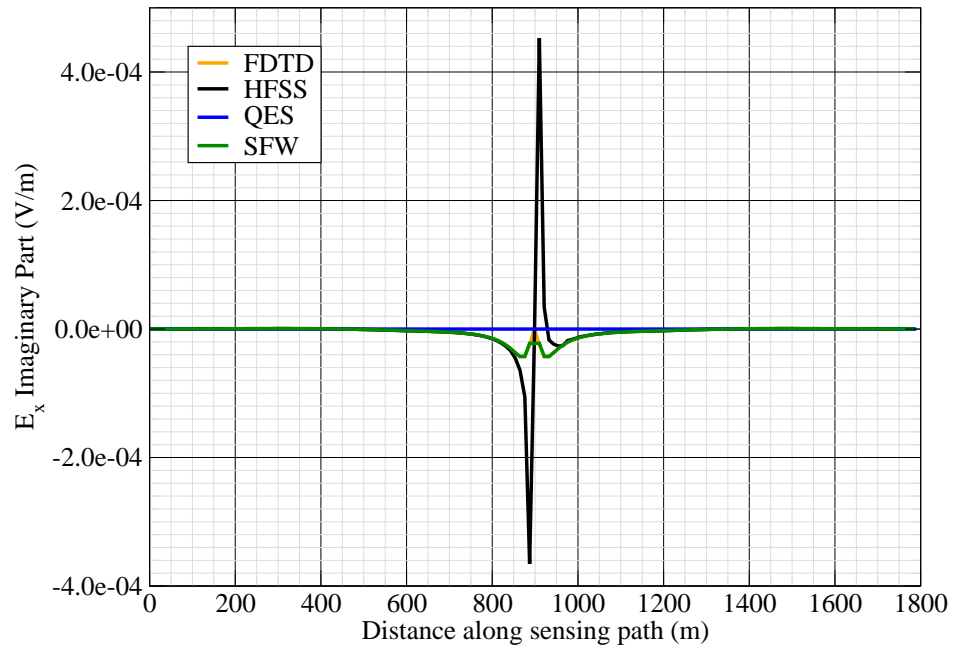


Figure 4: E_x imag.

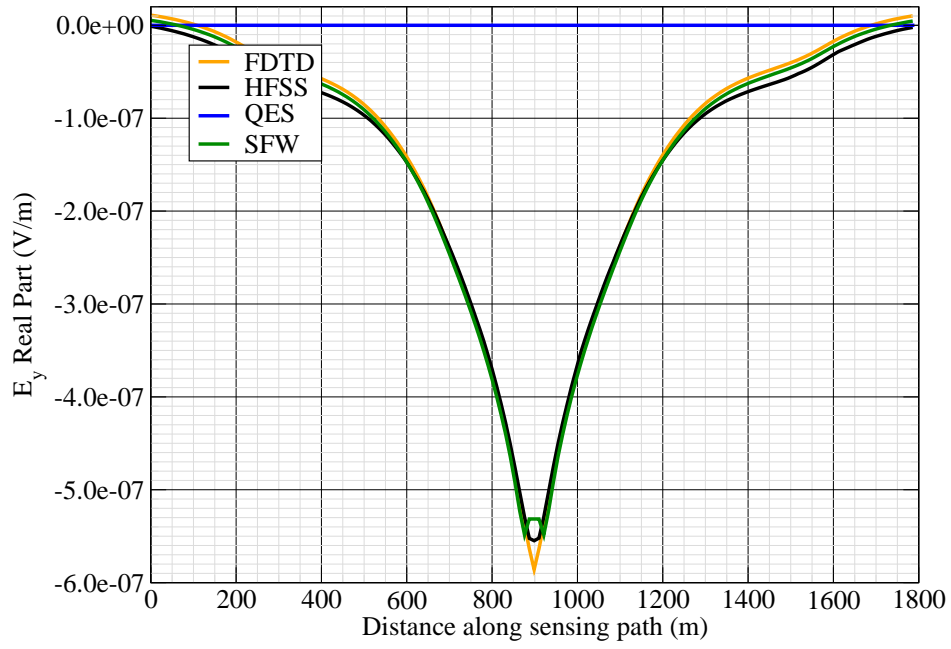


Figure 5: E_y real.

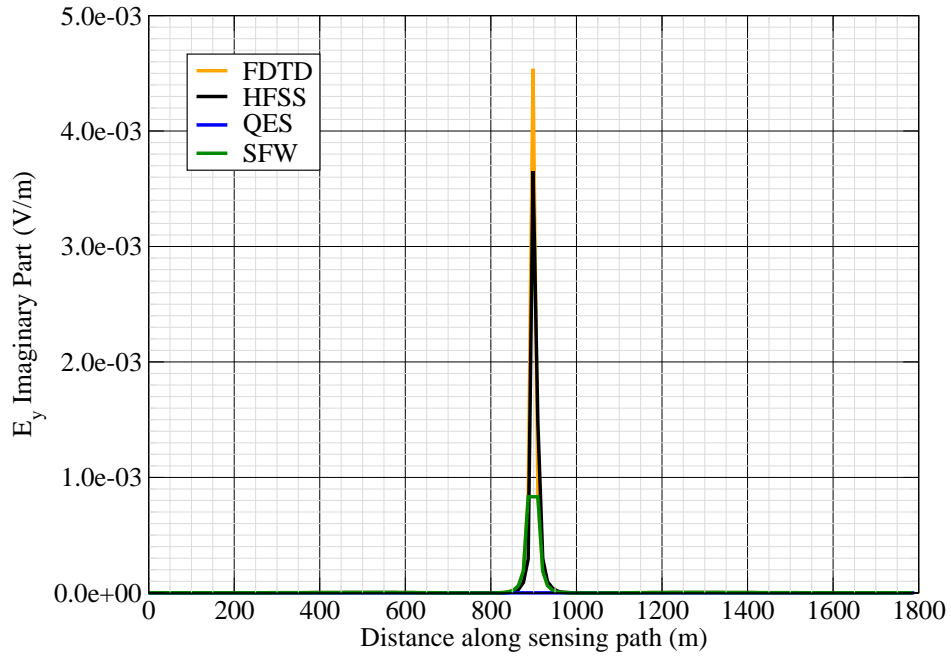


Figure 6: E_y imag.

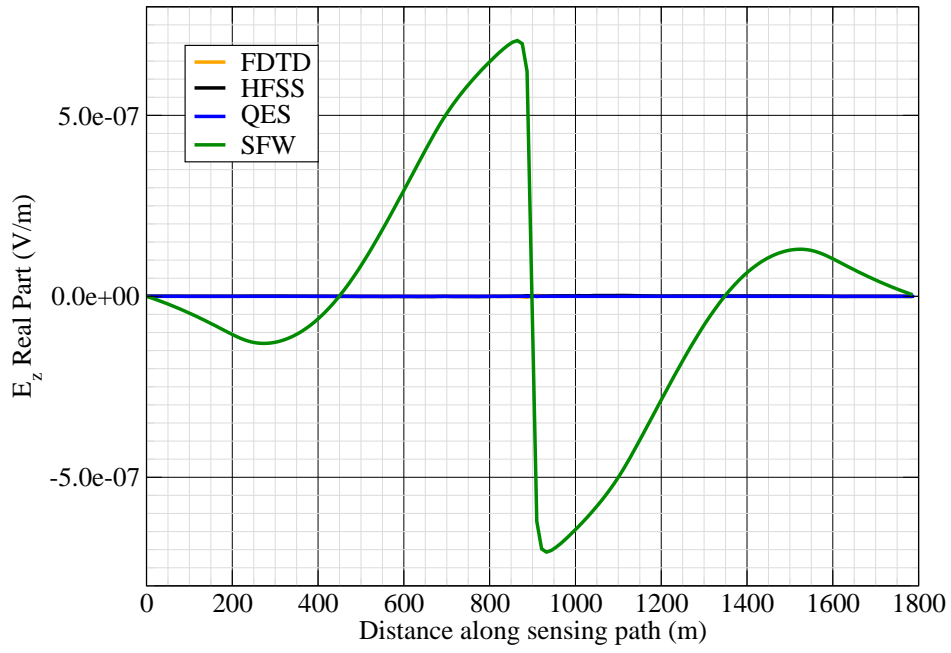


Figure 7: E_z real.

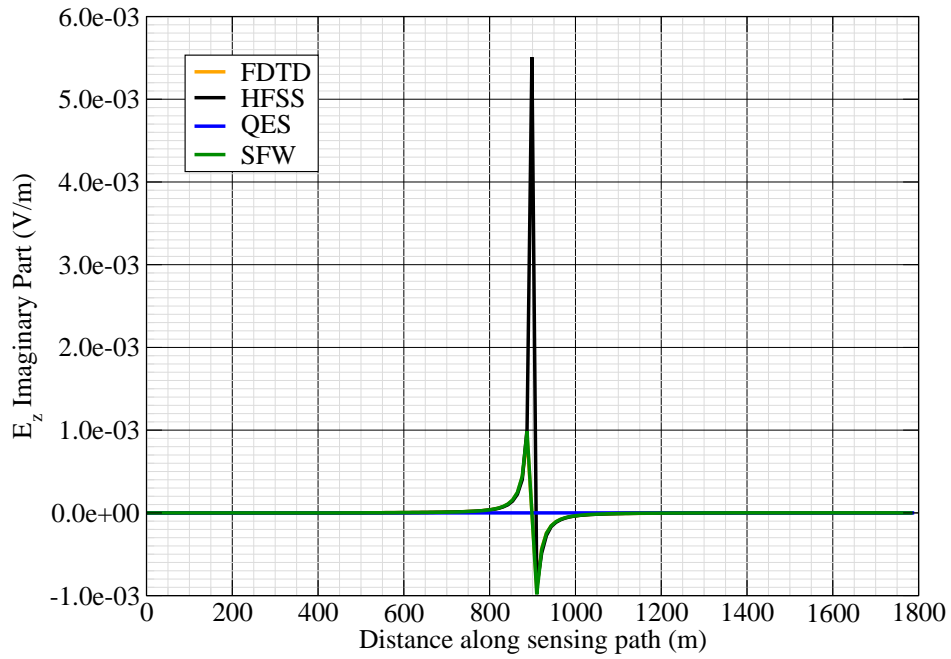


Figure 8: E_z imag.

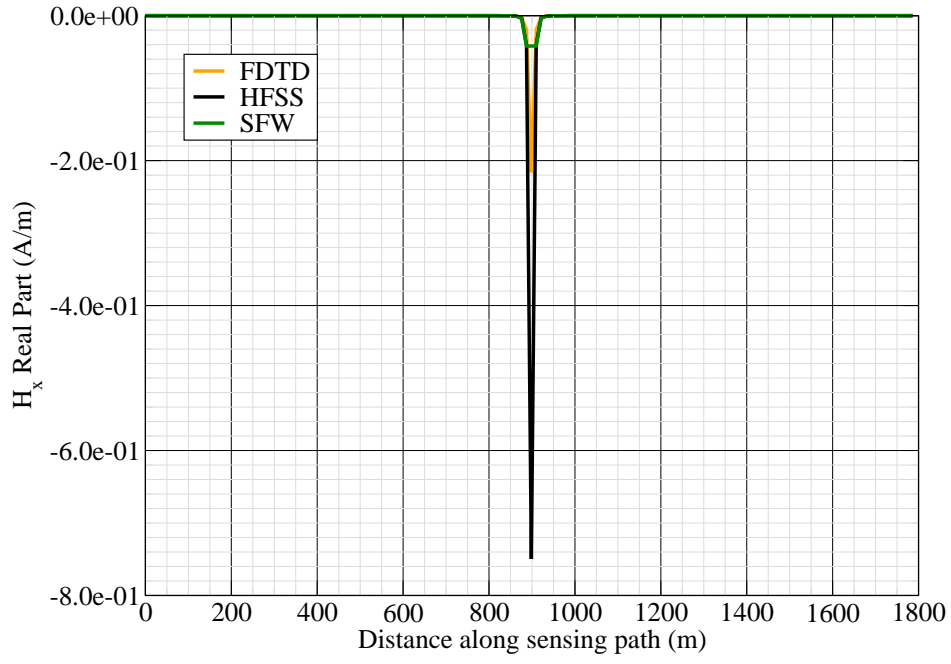


Figure 9: H_x real.

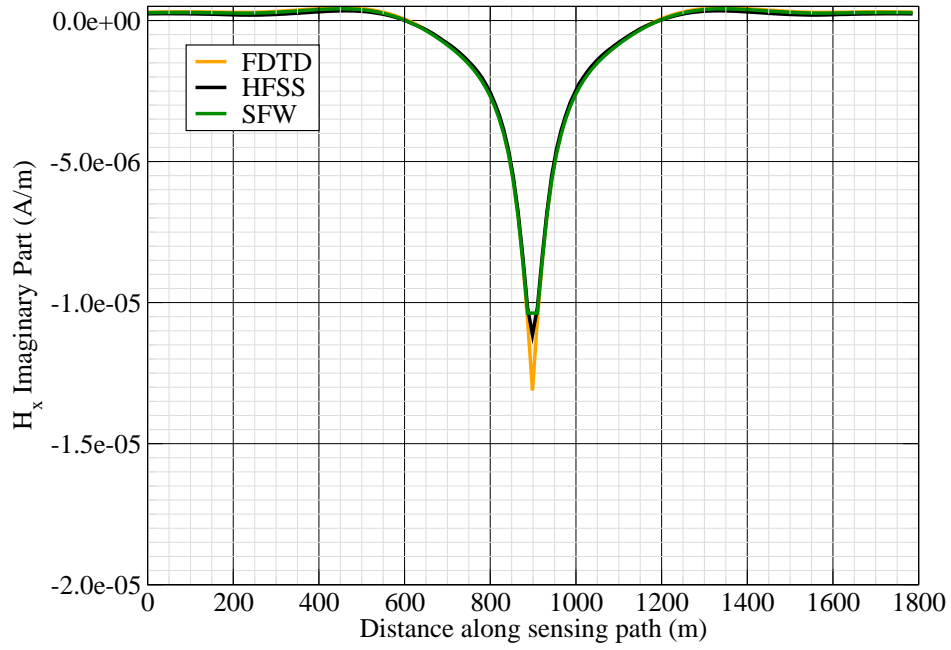


Figure 10: H_x imag.

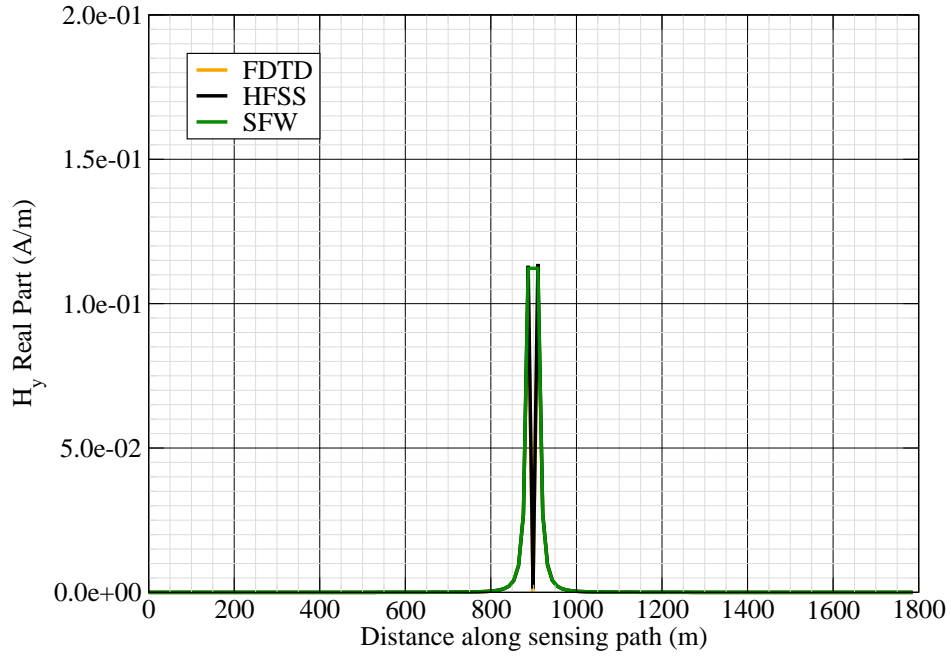


Figure 11: H_y real.

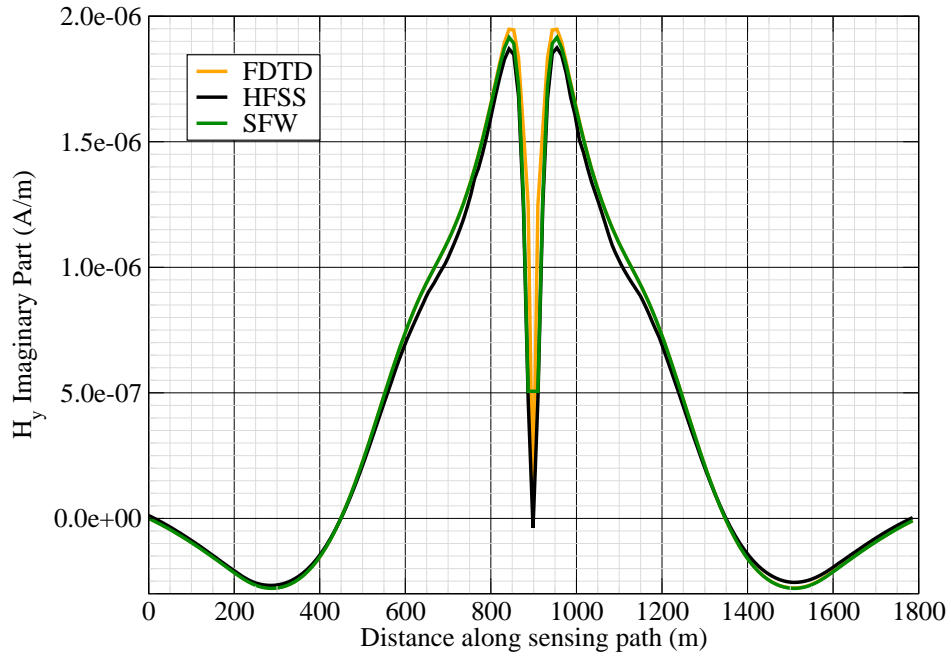


Figure 12: H_y imag.

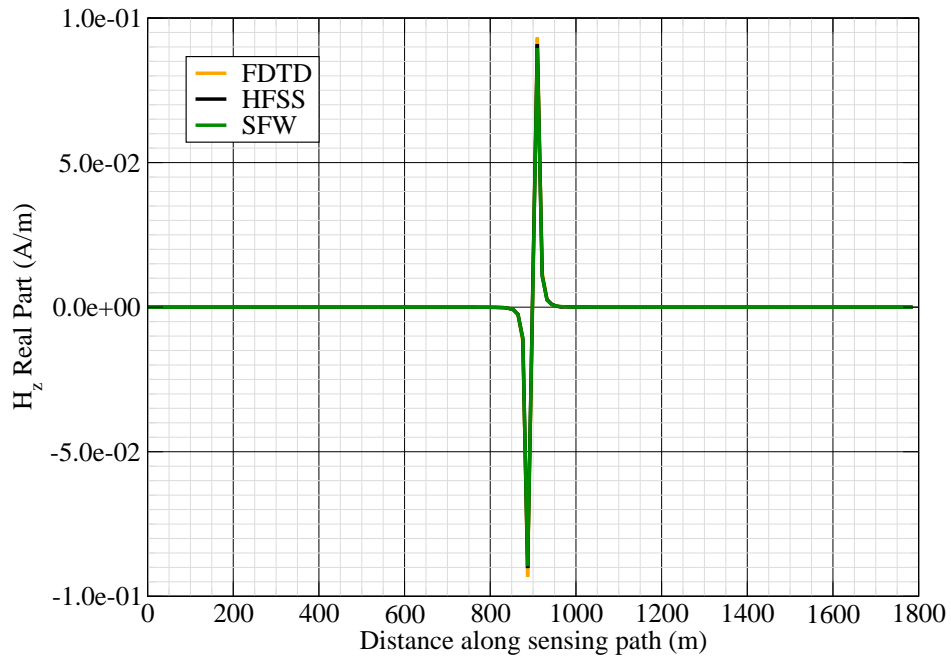


Figure 13: H_z real.

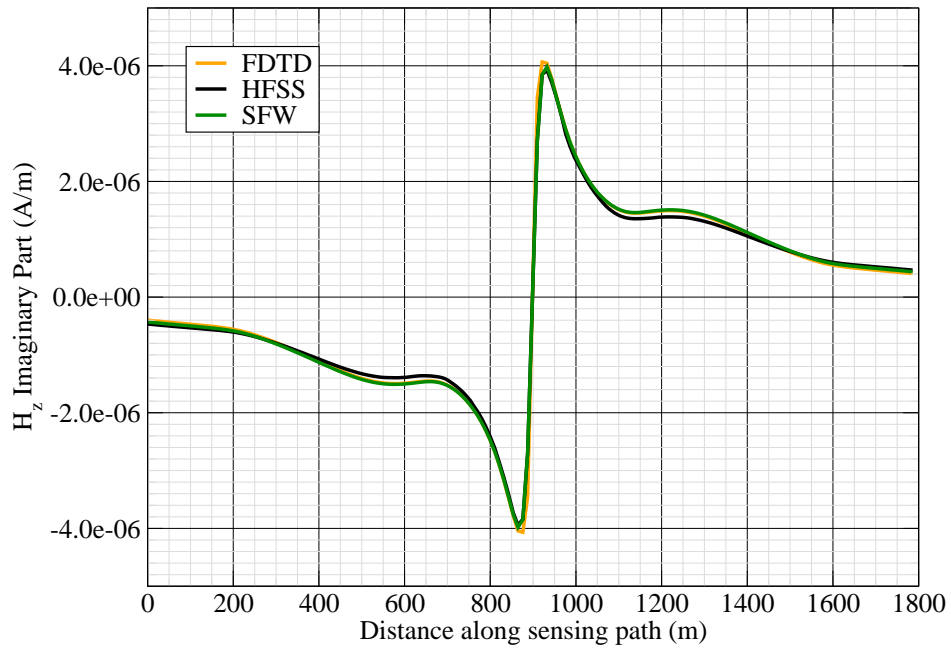


Figure 14: H_z imag.

Canonical Complex

Experiment 4

Experiment Date: November 2, 2011

1 Discussion

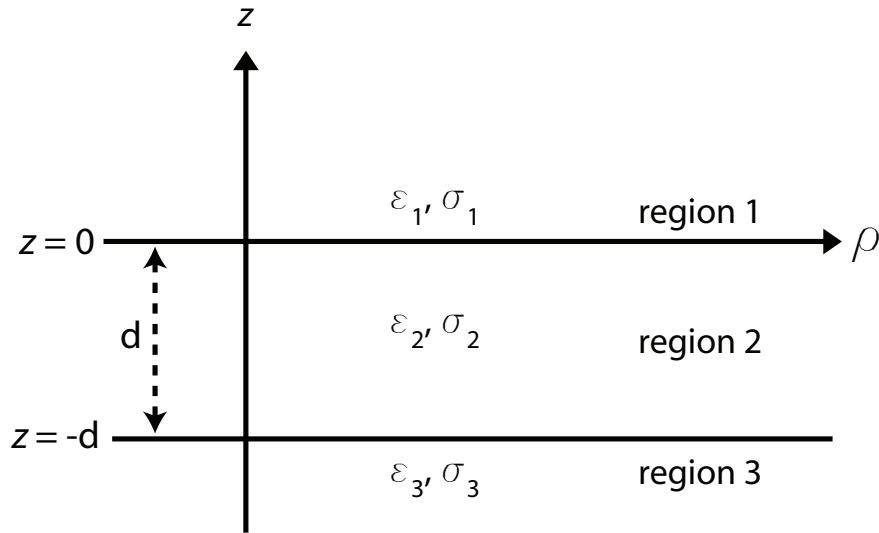


Figure 1: 3-layer topology.

Source Parameters

- Source Type: VMD (Coil: 3.66 m by 3.66 m with 12 turns).
- Source Strength: 3,683 A-m².
- $f = 70$ Hz.

Environment

- Water thickness: $d = 180$ m
- Air: $\sigma_1 = 0$ S/m and $\epsilon_{r1} = 1$
- Water: $\sigma_2 = 0.01$ S/m and $\epsilon_{r2} = 81$
- Mud: $\sigma_3 = 0.0012$ S/m and $\epsilon_{r3} = 1$

Table 1: Simulation Details

	FDTD	HFSS	QES/SFW
Domain Size	$200 \times 200 \times 120$ cells	7089 tets	N/A
Cell Size (m)	$5 \times 5 \times 5$	N/A	N/A
Time Step (ns)	9.6	N/A	N/A
Run Time (Hrs)	6	0.03	< 1 min

Comments

- Computational time is based on actual elapsed real time. This number is highly subjective and based on how many other applications might be running at a particular time. However, the reported number is an indication of the amount of time typically needed for a particular simulation. The computer specs are: 16 CPU cores at 2.8 GHz.
- Run times for HFSS are given for a single frequency.
- QES is not applicable for magnetic fields using electric source excitation.

2 Simulation Variables

Sensor_P1(x,y,z) [m]	(-200,57.1571,10.123)
Sensor_P2(x,y,z) [m]	(114.1593,44.8169,10.123)
Source_P1(x,y,z) [m]	(0,0,23.343)
Source_P2(x,y,z) [m]	(0,0,23.343)
Source_Plate_Separation [m]	N/A
Source_Size [m X m X #]	[3.658 X 3.658 X 12]
Source_Heading [deg]	NaN
Source_Voltage [V Peak]	11.6294
Source_Current [A Peak]	22.9361
Source_Frequency [Hz]	70

--- Extra Information ---

Source_Heading_Bounds [deg]	(N/A)
Average_Boat_Speed [m/s]	NaN
Source_Type	Magnetic source (portable)
Sensor_Type	EMA
Bin_Size [sec]	1
Number_of_Datapoints	200
Lake_Origin (Easting,Northing)	NaN
Analysis_Date	26-Sep-2011

3 Boat Path

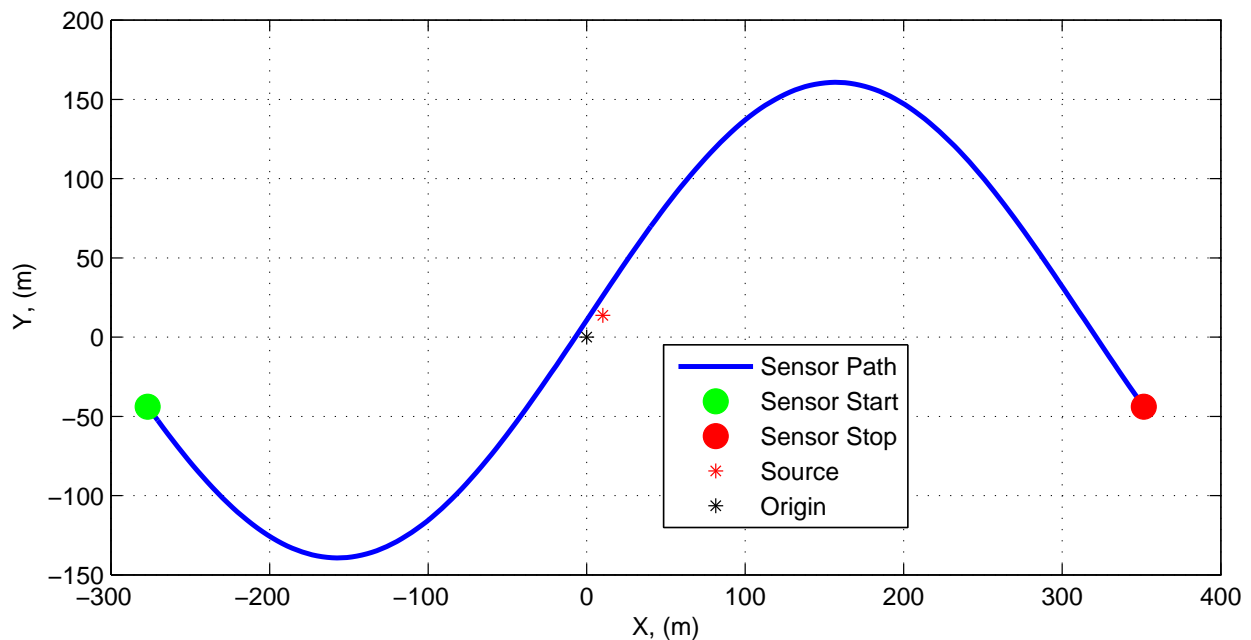


Figure 2: Source and sensor relationship.

4 Plots

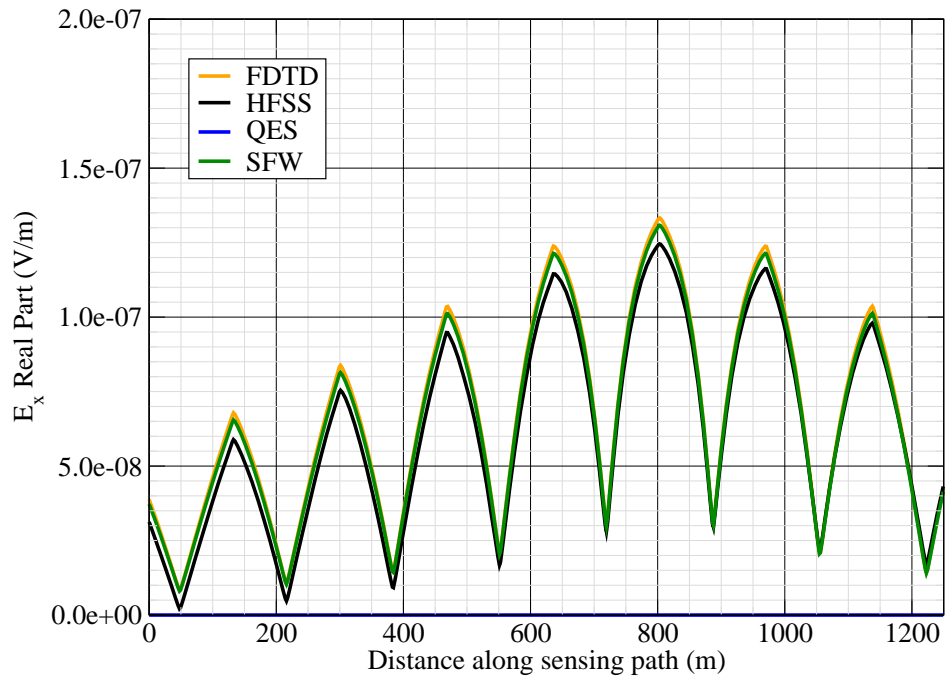


Figure 3: E_x real.

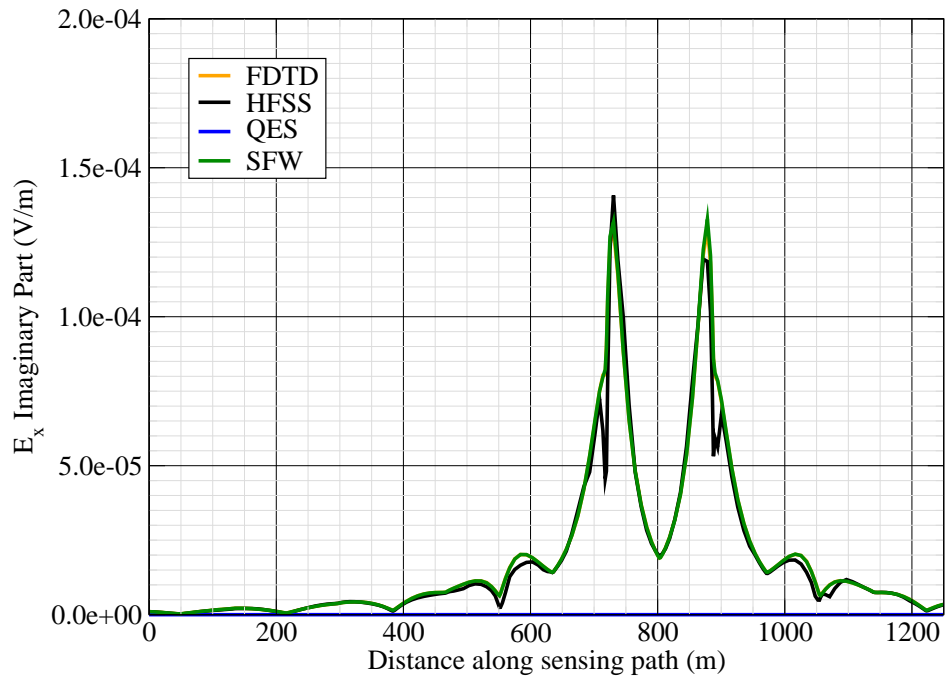


Figure 4: E_x imag.

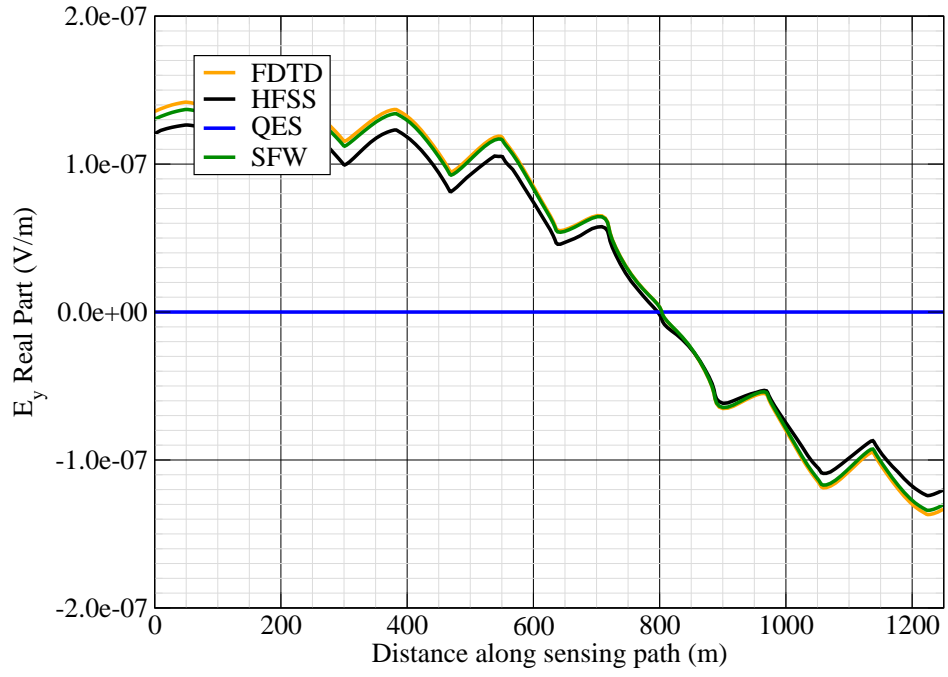


Figure 5: E_y real.

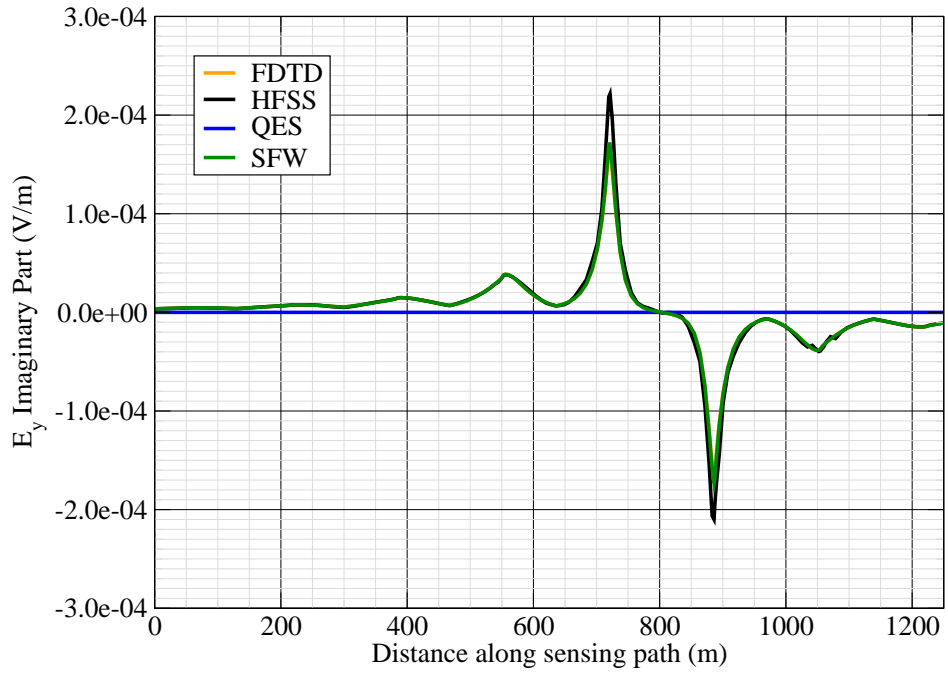


Figure 6: E_y imag.

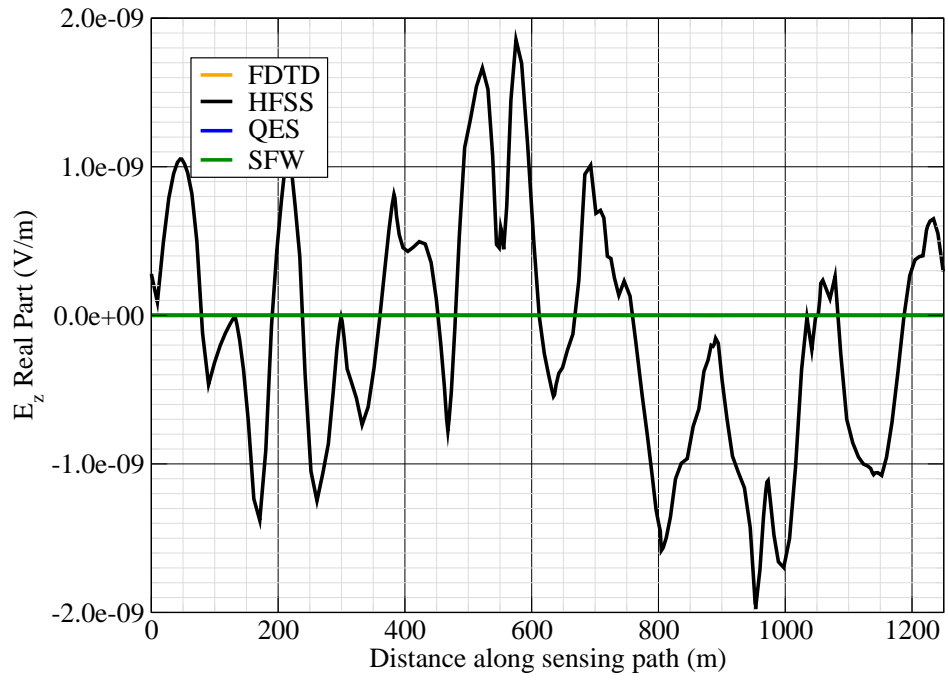


Figure 7: E_z real.

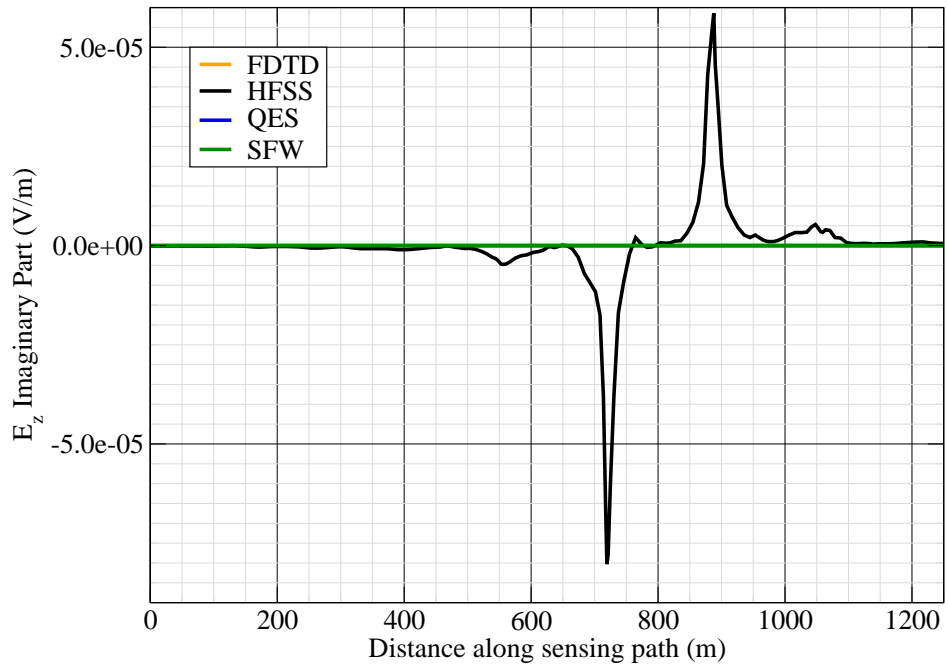


Figure 8: E_z imag.

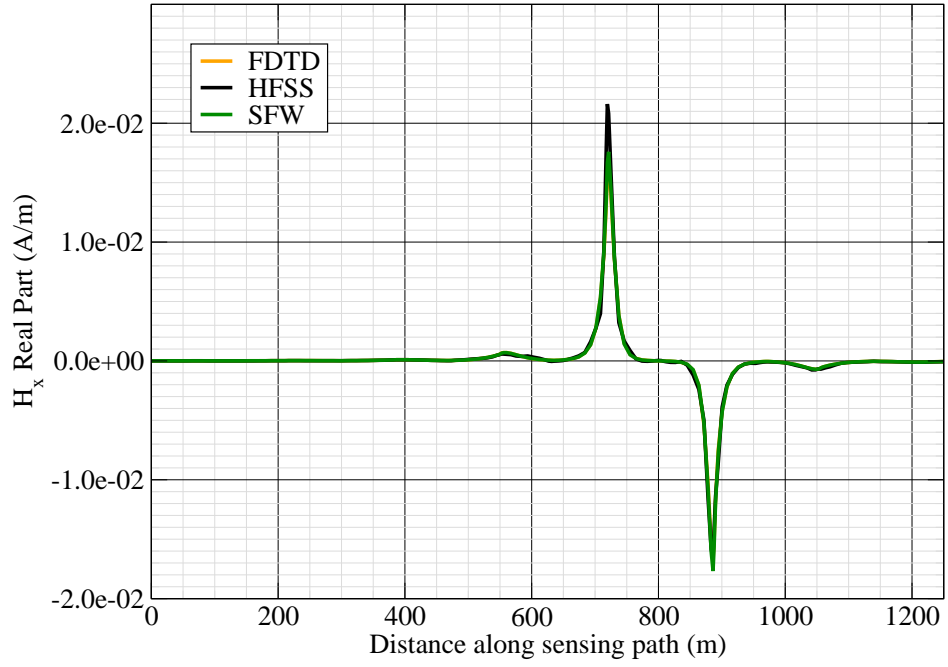


Figure 9: H_x real.

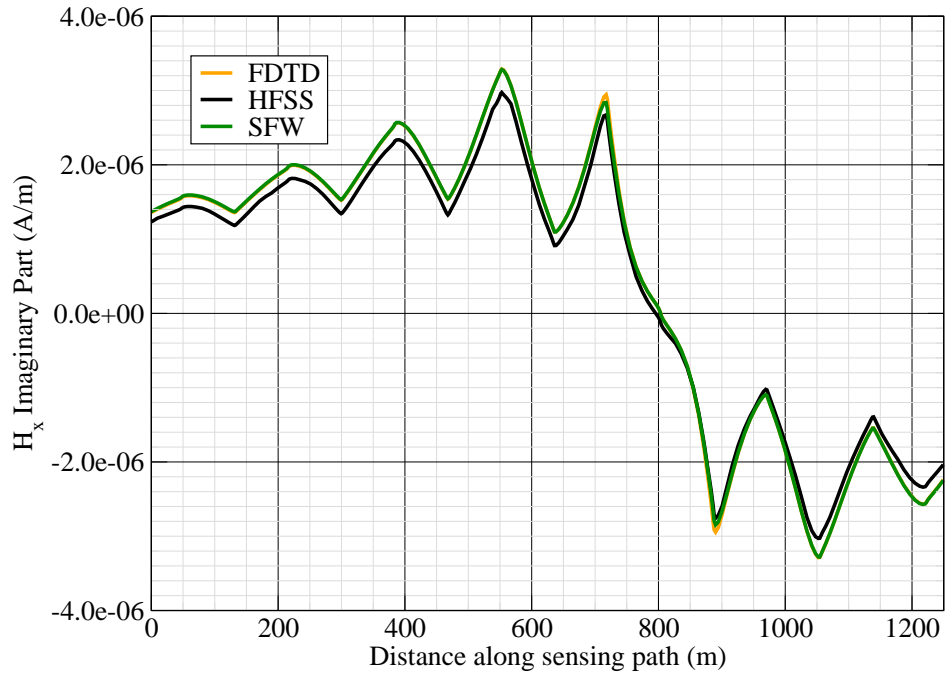


Figure 10: H_x imag.

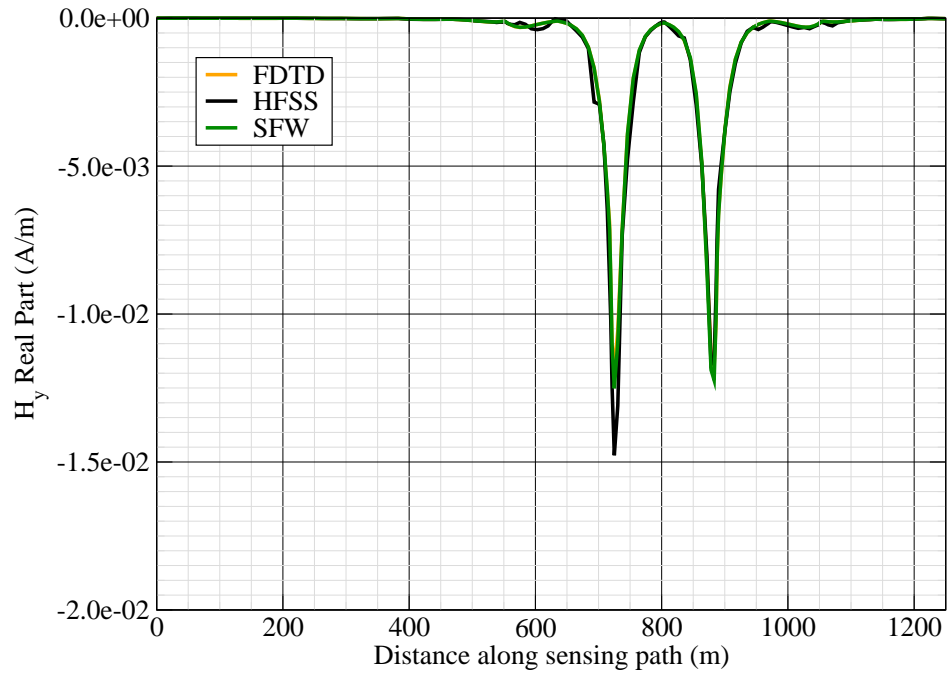


Figure 11: H_y real.

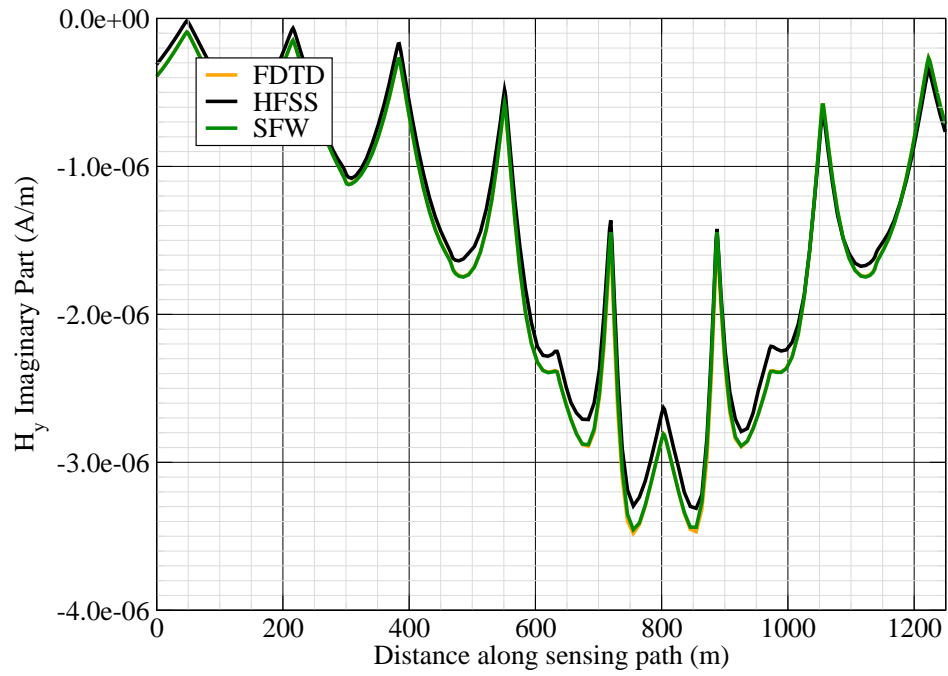


Figure 12: H_y imag.

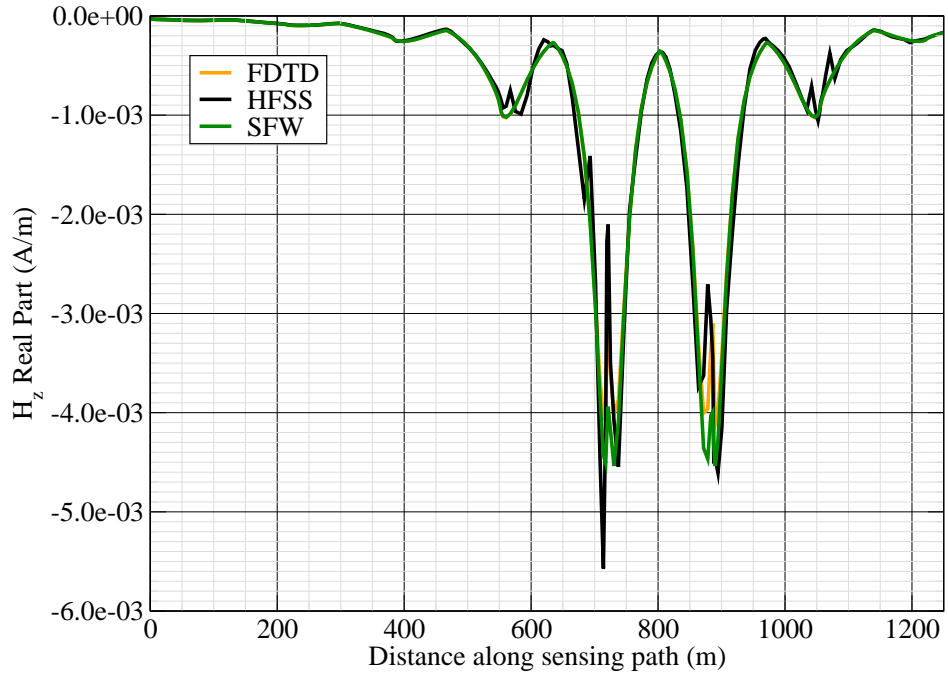


Figure 13: H_z real.

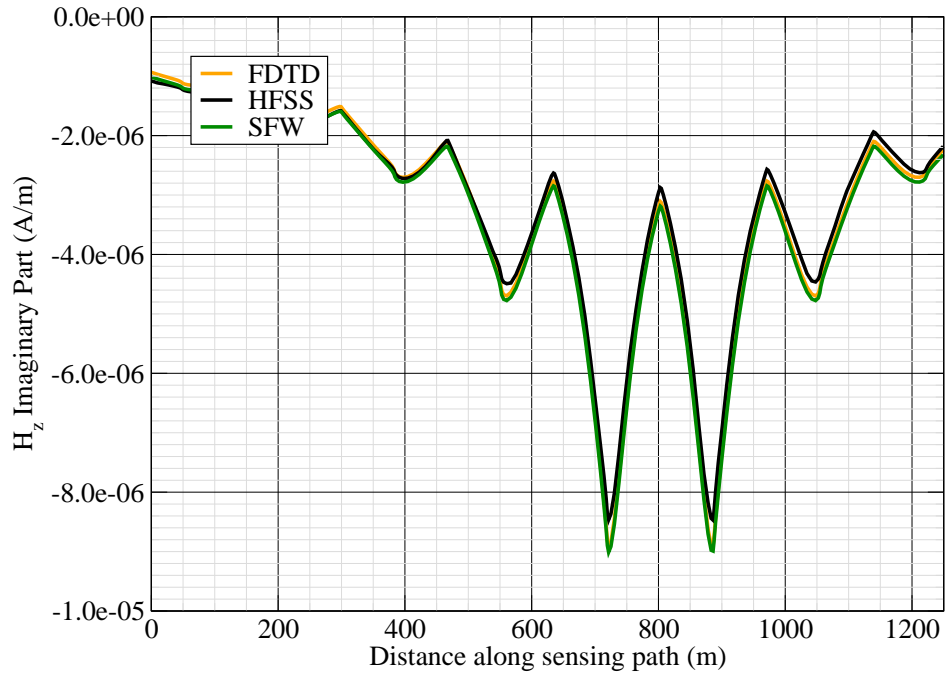


Figure 14: H_z imag.

Canonical Complex

Experiment 5

Experiment Date: November 2, 2011

1 Discussion

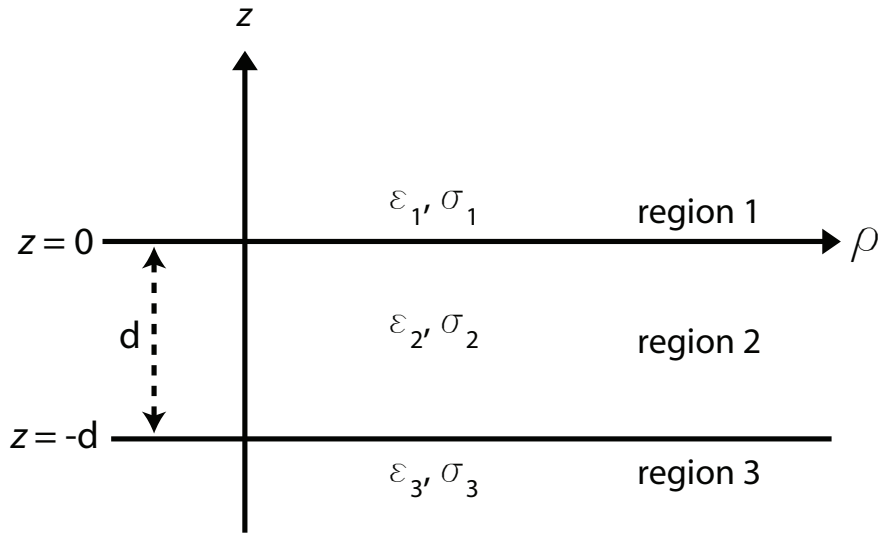


Figure 1: 3-layer topology.

Source Parameters

- Source Type: HED (Boat Hull: plates 0.6 m by 0.3 m separated by 4 m).
- Source Strength: 7.144 A-m.
- $f = 100$ Hz.

Environment

- Water thickness: $d = 180$ m
- Air: $\sigma_1 = 0$ S/m and $\epsilon_{r1} = 1$
- Water: $\sigma_2 = 0.01$ S/m and $\epsilon_{r2} = 81$
- Mud: $\sigma_3 = 0.0012$ S/m and $\epsilon_{r3} = 1$

Table 1: Simulation Details

	FDTD	HFSS	QES/SFW
Domain Size	$200 \times 200 \times 120$ cells	28752 tets	N/A
Cell Size (m)	$5 \times 5 \times 5$	N/A	N/A
Time Step (ns)	9.6	N/A	N/A
Run Time (Hrs)	6	0.05	< 1 min

Comments

- Computational time is based on actual elapsed real time. This number is highly subjective and based on how many other applications might be running at a particular time. However, the reported number is an indication of the amount of time typically needed for a particular simulation. The computer specs are: 16 CPU cores at 2.8 GHz.
- Run times for HFSS are given for a single frequency.
- QES is not applicable for magnetic fields using electric source excitation.

2 Simulation Variables

Sensor_P1(x,y,z) [m]	(-276.8760,-43.8732,50)
Sensor_P2(x,y,z) [m]	(348.3009,-39.4584,50)
Source_P1(x,y,z) [m]	(50,30,100)
Source_P2(x,y,z) [m]	(50,30,100)
Source_Plate_Separation [m]	4
Source_Size [m X m X #]	[0.6 X 0.3 X 1]
Source_Heading [deg]	45
Source_Voltage [V Peak]	NaN
Source_Current [A Peak]	1.786
Source_Frequency [Hz]	100

--- Extra Information ---

Source_Heading_Bounds [deg]	(N/A)
Average_Boat_Speed [m/s]	NaN
Source_Type	Electric truss (truss)
Sensor_Type	EMA
Bin_Size [sec]	1
Number_of_Datapoints	200
Lake_Origin (Easting,Northing)	NaN
Analysis_Date	26-Sep-2011

3 Boat Path

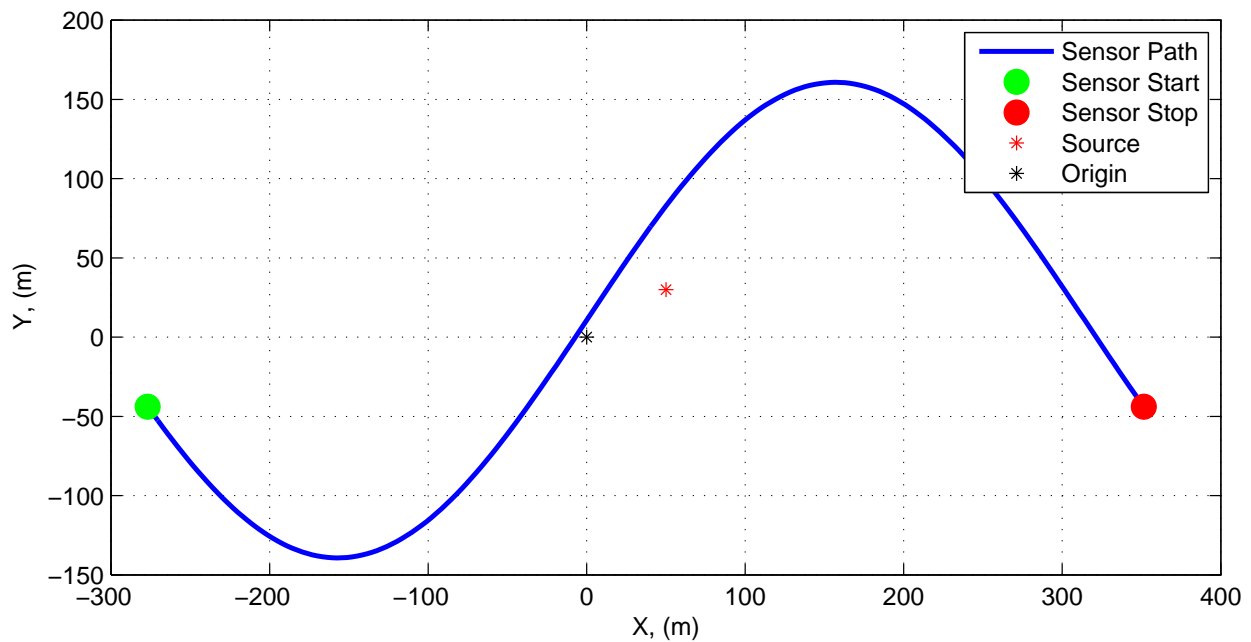


Figure 2: Source and sensor relationship.

4 Plots

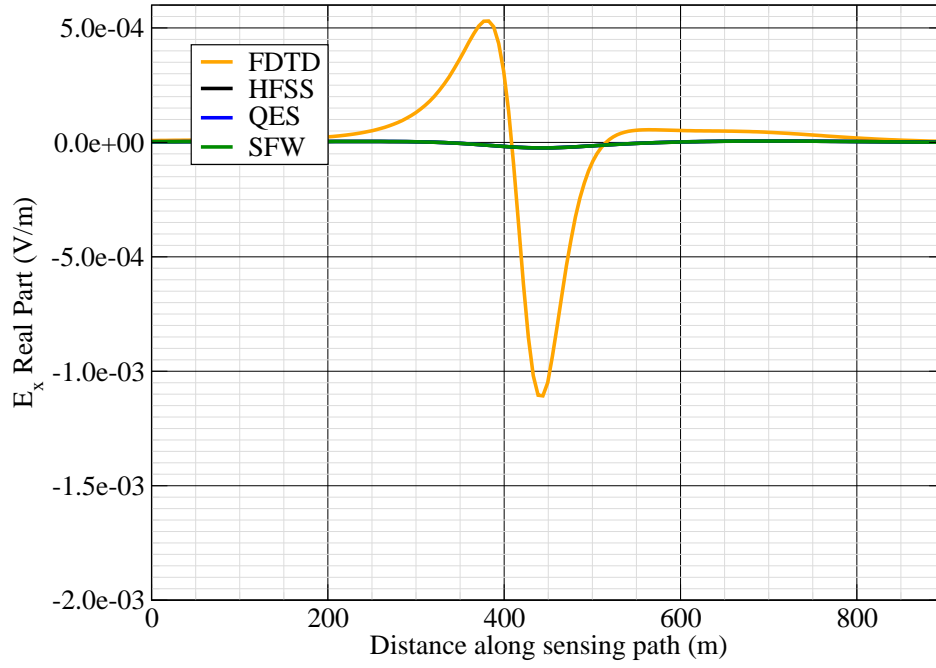


Figure 3: E_x real.

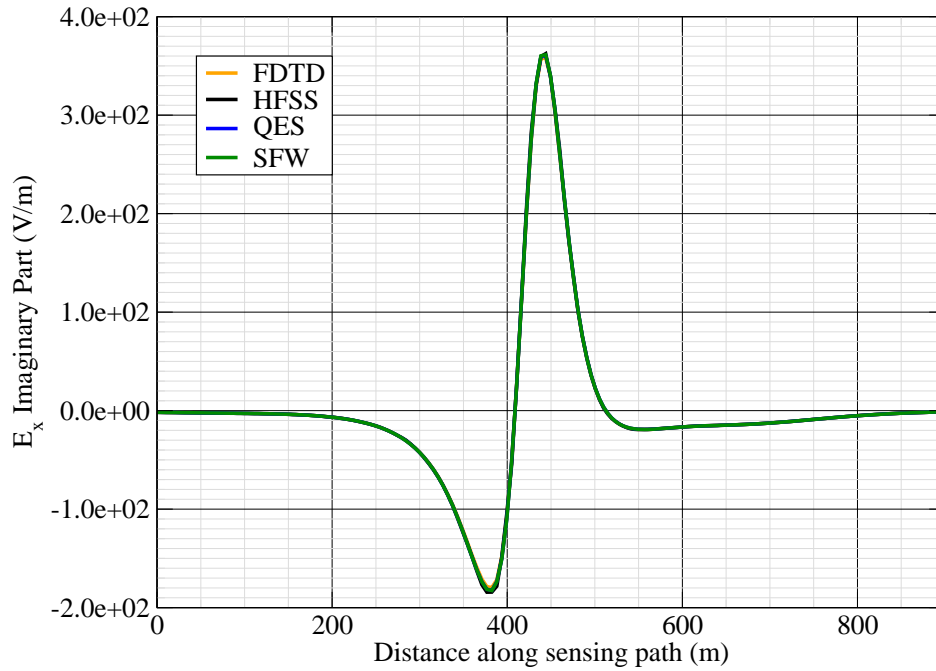


Figure 4: E_x imag.

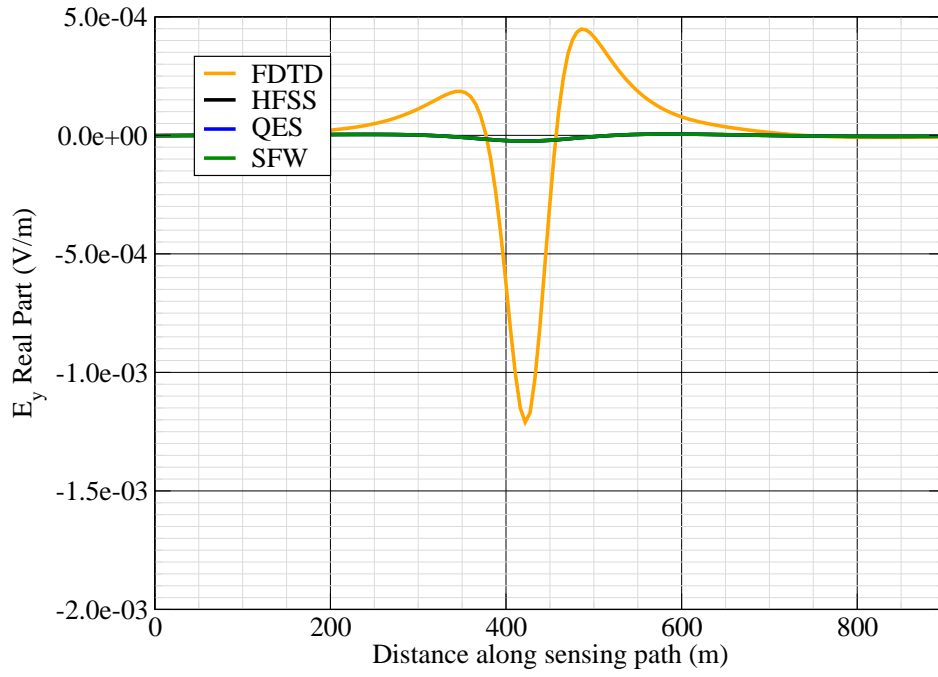


Figure 5: E_y real.

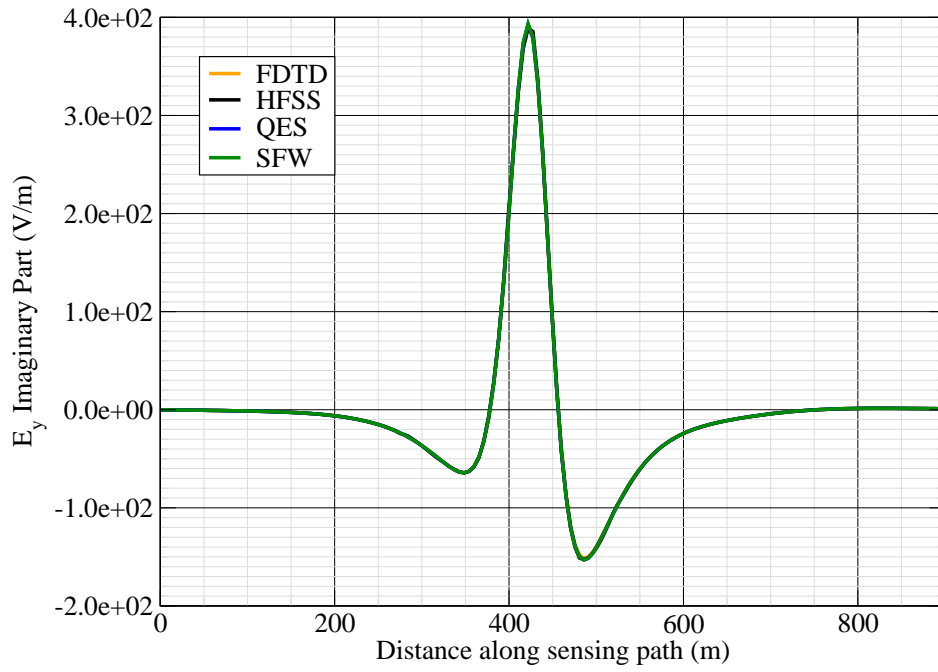


Figure 6: E_y imag.

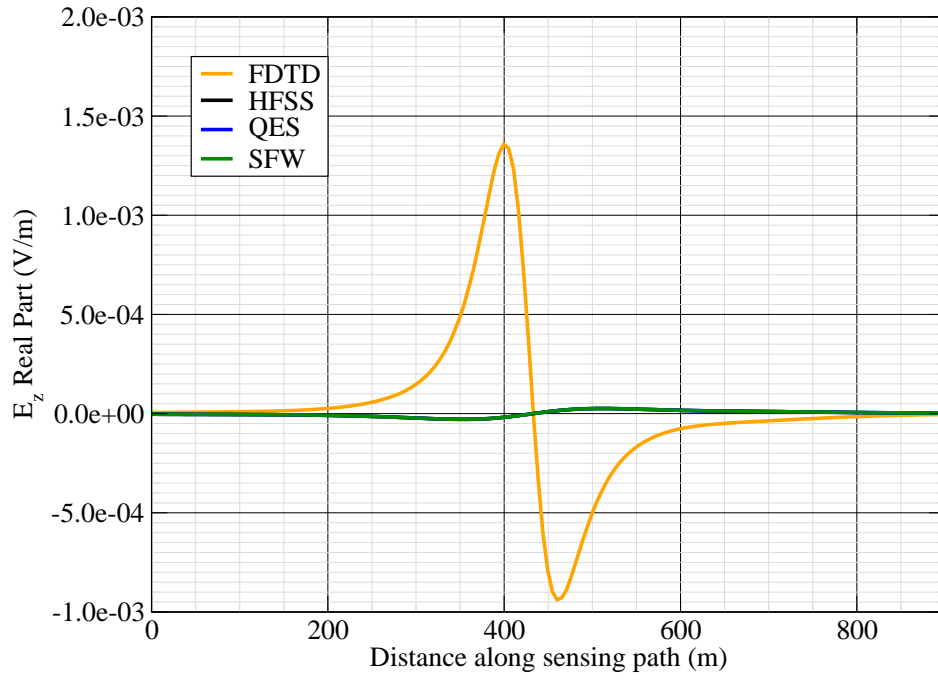


Figure 7: E_z real.

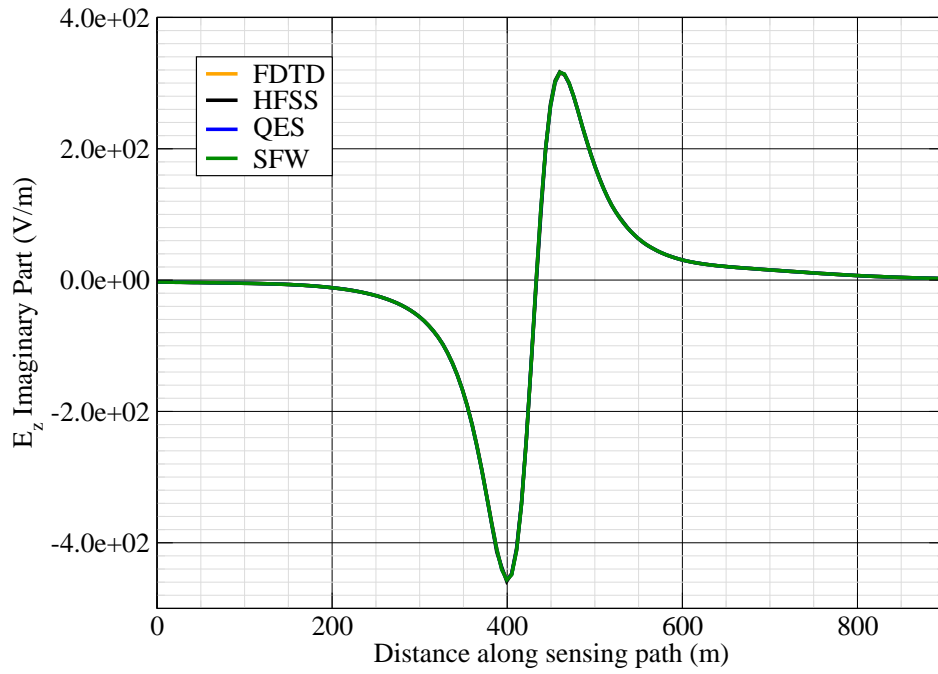


Figure 8: E_z imag.

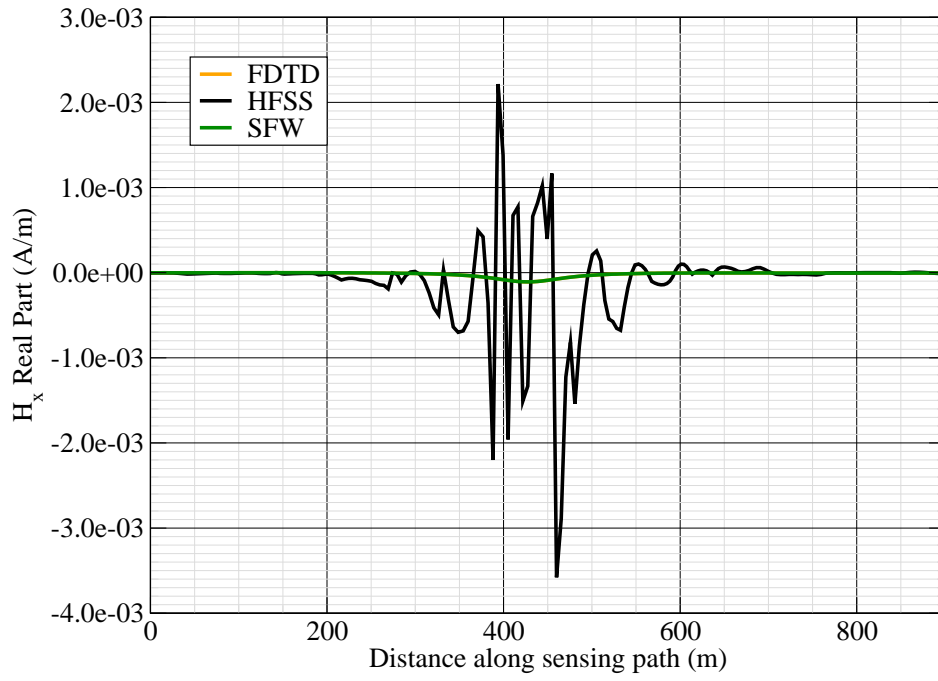


Figure 9: H_x real.

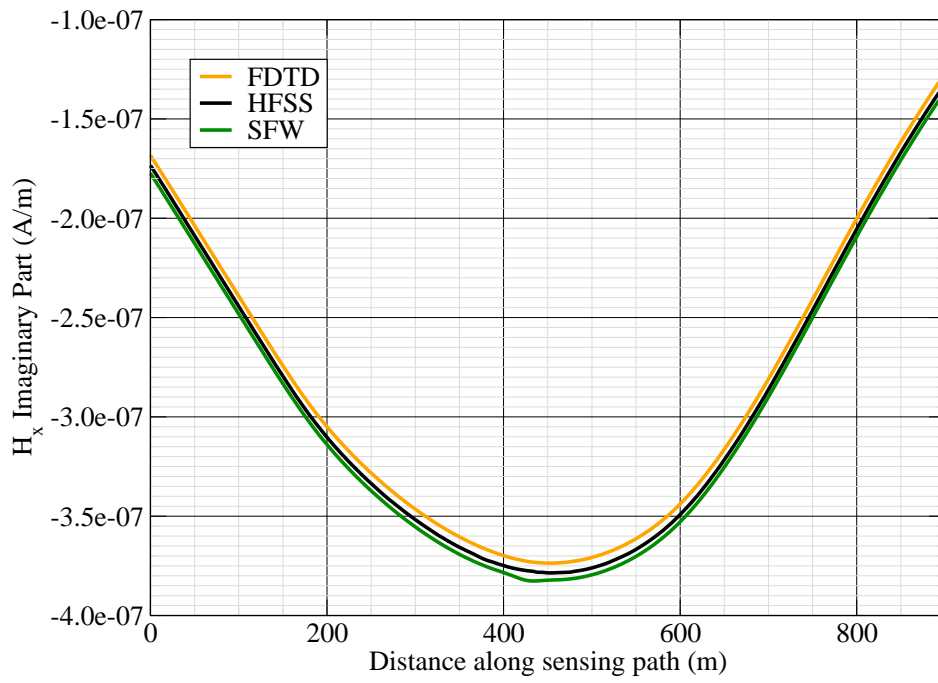


Figure 10: H_x imag.

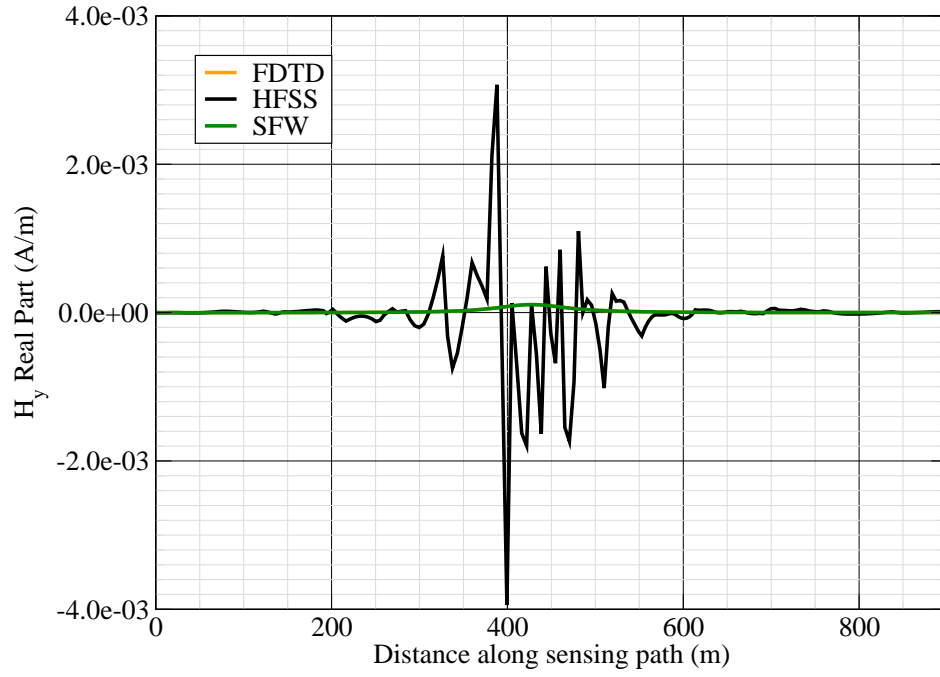


Figure 11: H_y real.

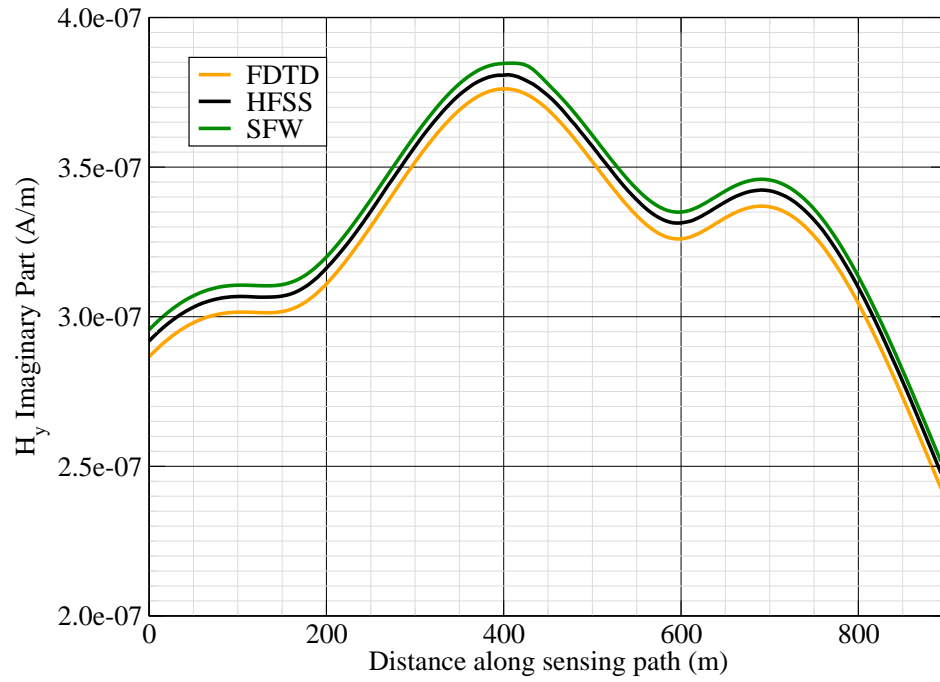


Figure 12: H_y imag.

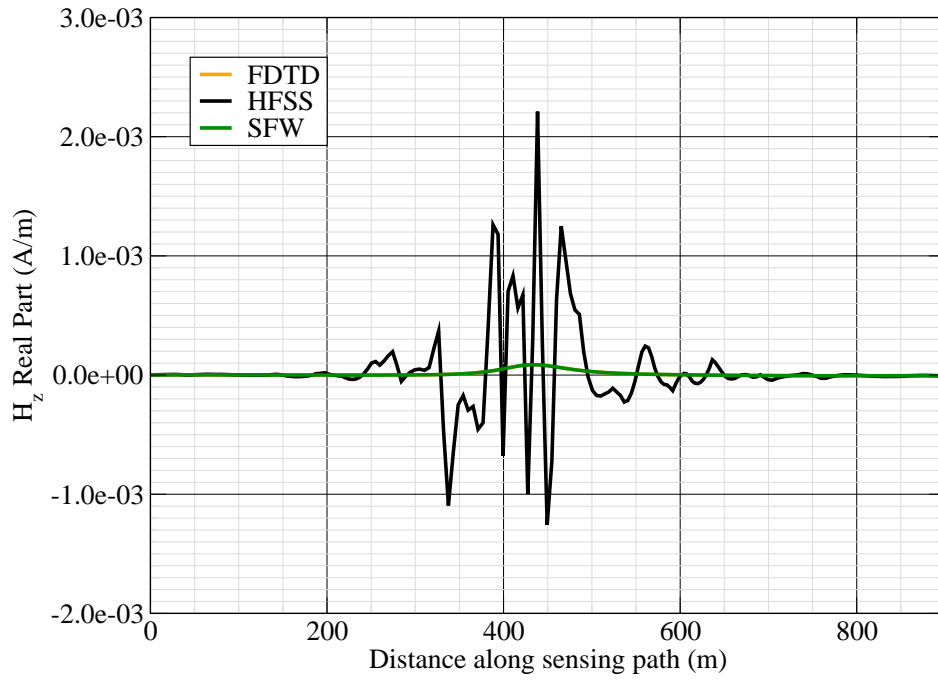


Figure 13: H_z real.

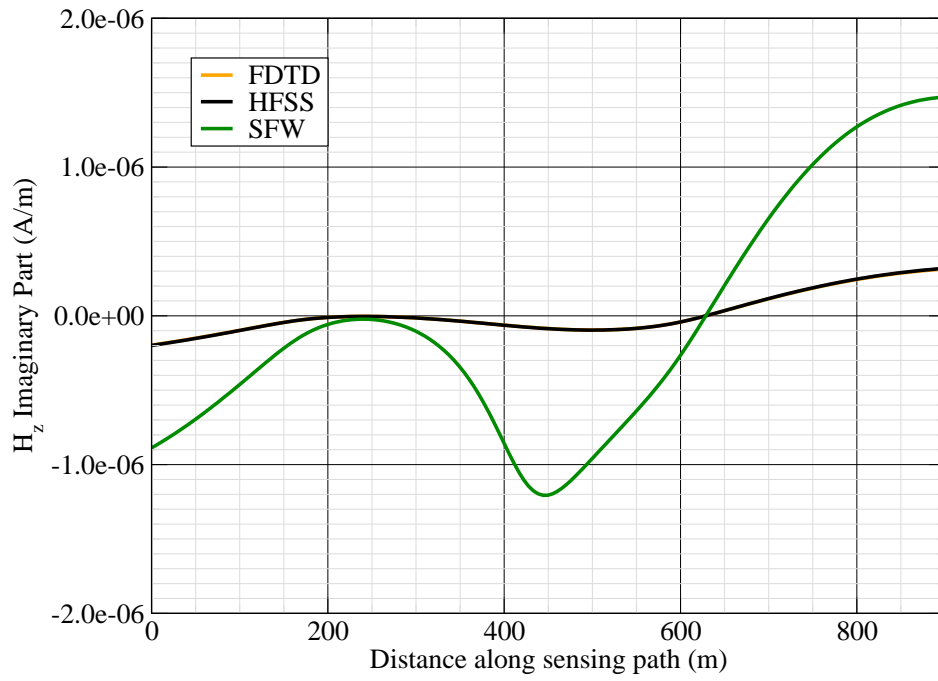


Figure 14: H_z imag.

Canonical Complex

Experiment 6

Experiment Date: November 2, 2011

1 Discussion

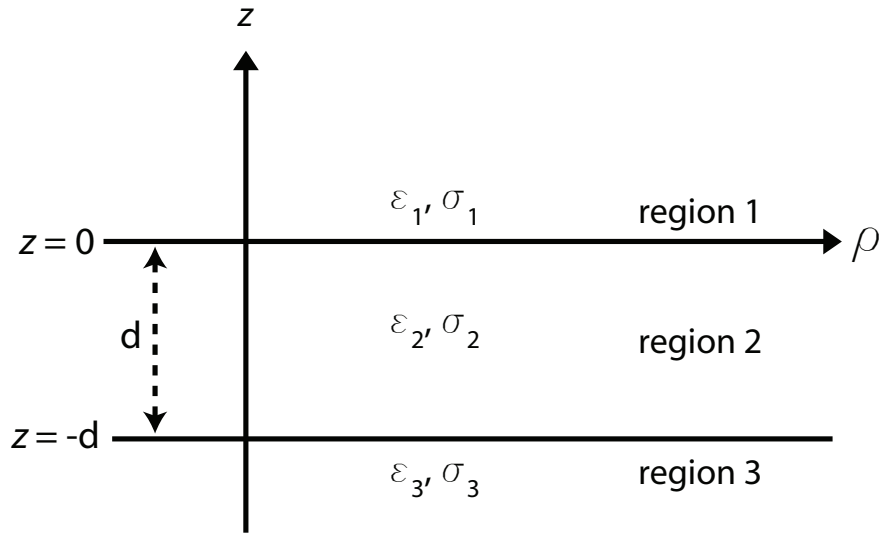


Figure 1: 3-layer topology.

Source Parameters

- Source Type: HED (Boat Hull: plates 0.6 m by 0.3 m separated by 4 m).
- Source Strength: 7.144 A-m.
- $f = 1000$ Hz.

Environment

- Water thickness: $d = 180$ m
- Air: $\sigma_1 = 0$ S/m and $\epsilon_{r1} = 1$
- Water: $\sigma_2 = 0.01$ S/m and $\epsilon_{r2} = 81$
- Mud: $\sigma_3 = 0.0012$ S/m and $\epsilon_{r3} = 1$

Table 1: Simulation Details

	FDTD	HFSS	QES/SFW
Domain Size	$200 \times 200 \times 120$ cells	36051 tets	N/A
Cell Size (m)	$5 \times 5 \times 5$	N/A	N/A
Time Step (ns)	9.6	N/A	N/A
Run Time (Hrs)	6	0.07	< 1 min

Comments

- Computational time is based on actual elapsed real time. This number is highly subjective and based on how many other applications might be running at a particular time. However, the reported number is an indication of the amount of time typically needed for a particular simulation. The computer specs are: 16 CPU cores at 2.8 GHz.
- Run times for HFSS are given for a single frequency.
- QES is not applicable for magnetic fields using electric source excitation.

2 Simulation Variables

Sensor_P1(x,y,z) [m]	(-276.8760,-43.8732,-15.7470)
Sensor_P2(x,y,z) [m]	(348.3009,-39.4584,-15.7470)
Source_P1(x,y,z) [m]	(50,30,100)
Source_P2(x,y,z) [m]	(50,30,100)
Source_Plate_Separation [m]	4
Source_Size [m X m X #]	[0.6 X 0.3 X 1]
Source_Heading [deg]	180
Source_Voltage [V Peak]	NaN
Source_Current [A Peak]	1.786
Source_Frequency [Hz]	1000

--- Extra Information ---

Source_Heading_Bounds [deg]	(N/A)
Average_Boat_Speed [m/s]	NaN
Source_Type	Electric truss (truss)
Sensor_Type	EMA
Bin_Size [sec]	1
Number_of_Datapoints	200
Lake_Origin (Easting,Northing)	NaN
Analysis_Date	26-Sep-2011

3 Boat Path

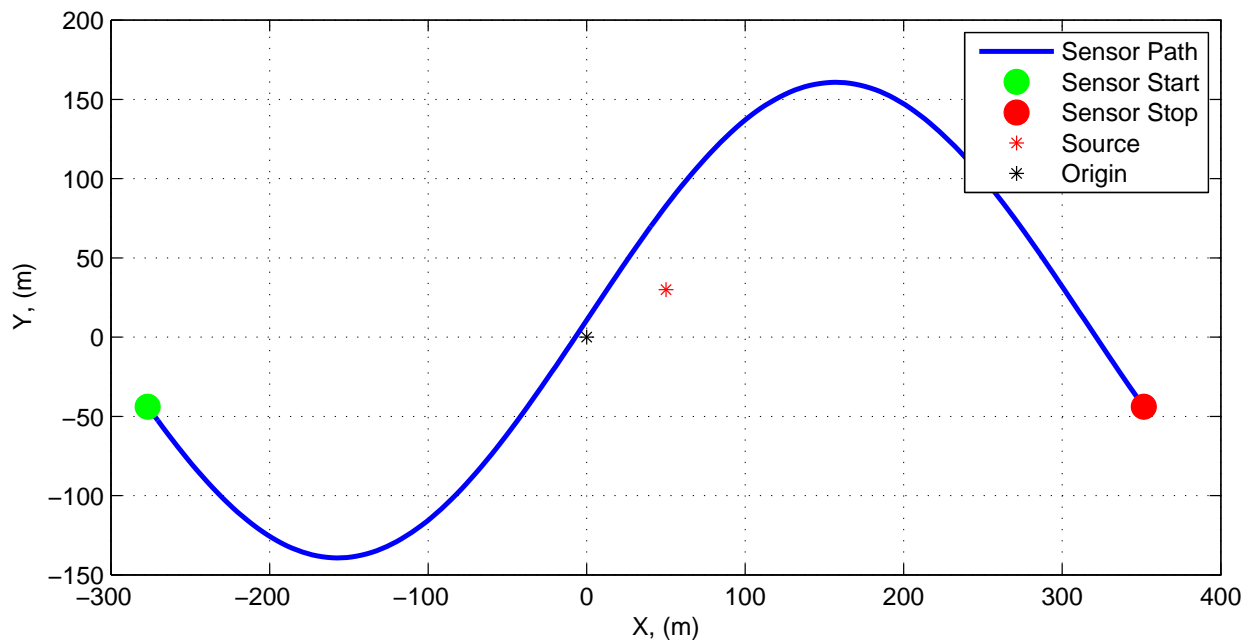


Figure 2: Source and sensor relationship.

4 Plots

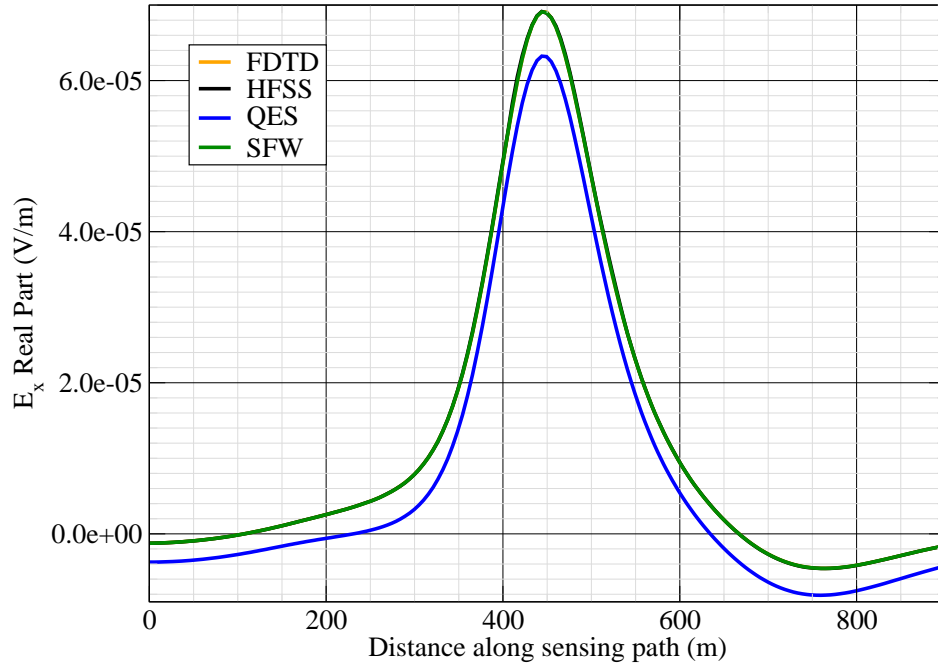


Figure 3: E_x real.

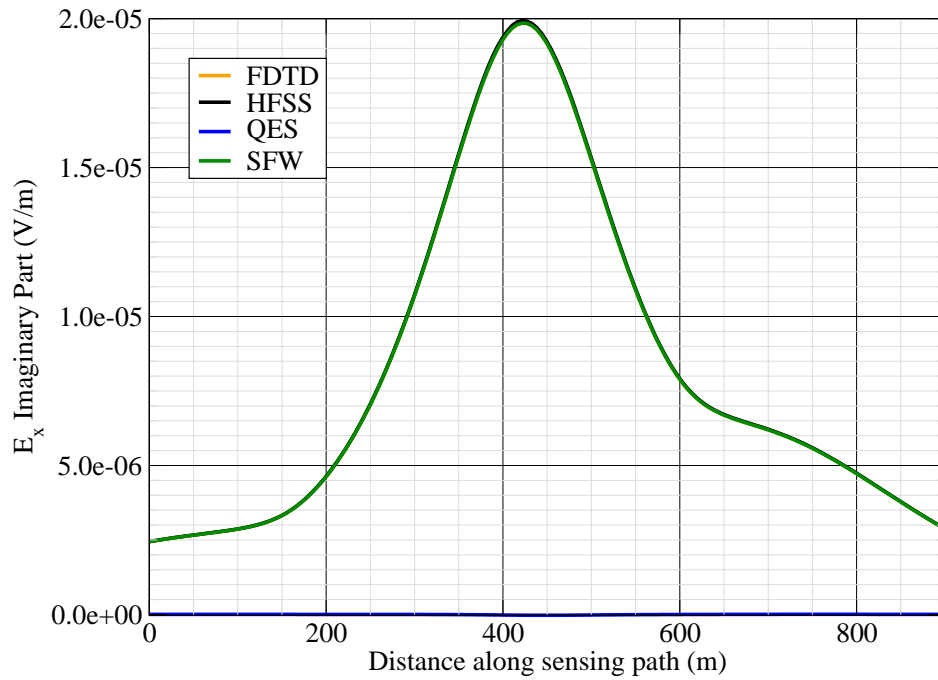


Figure 4: E_x imag.

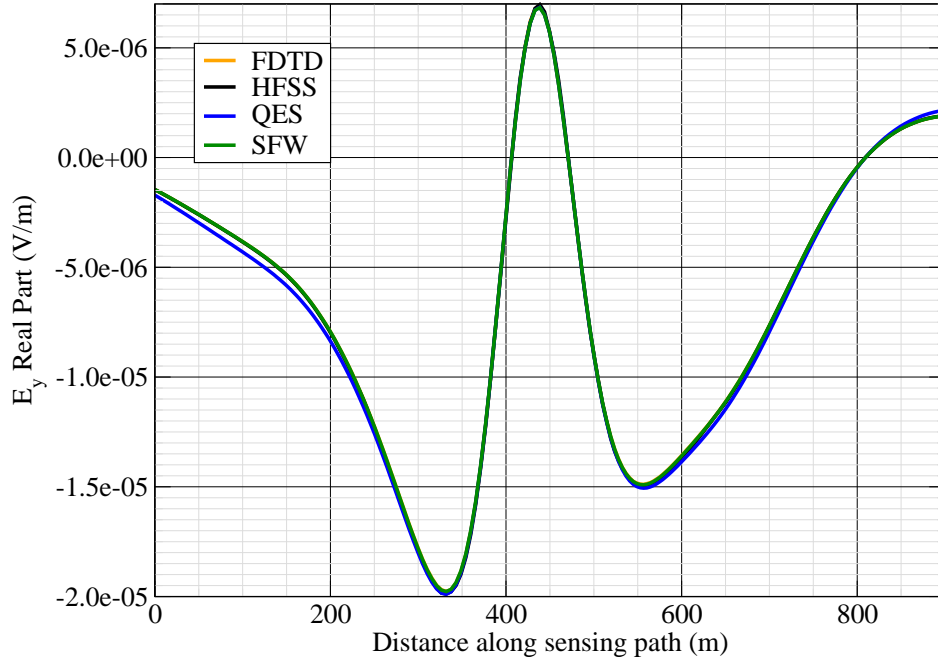


Figure 5: E_y real.

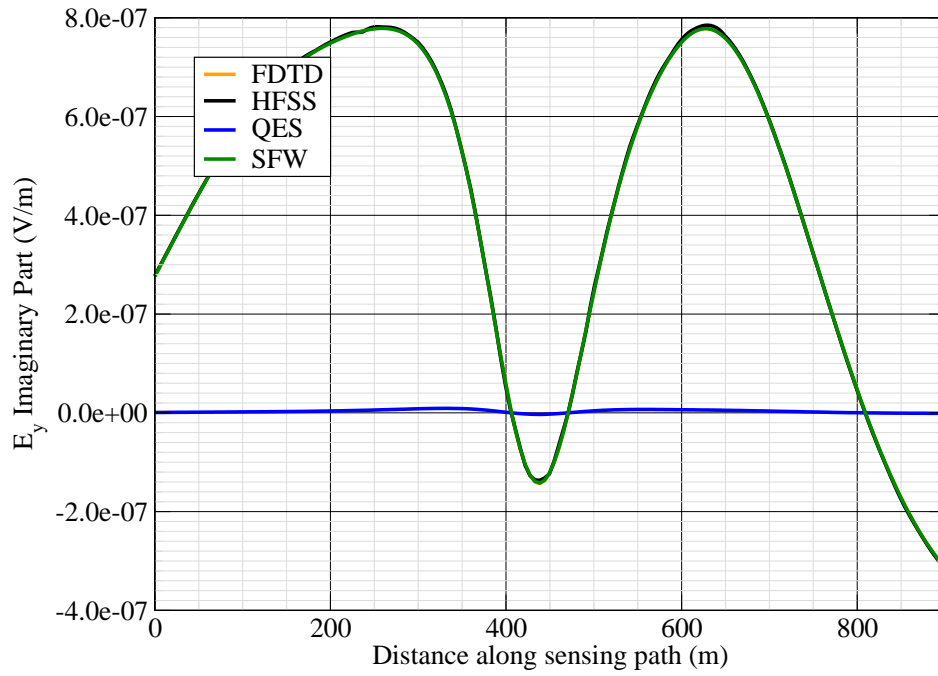


Figure 6: E_y imag.

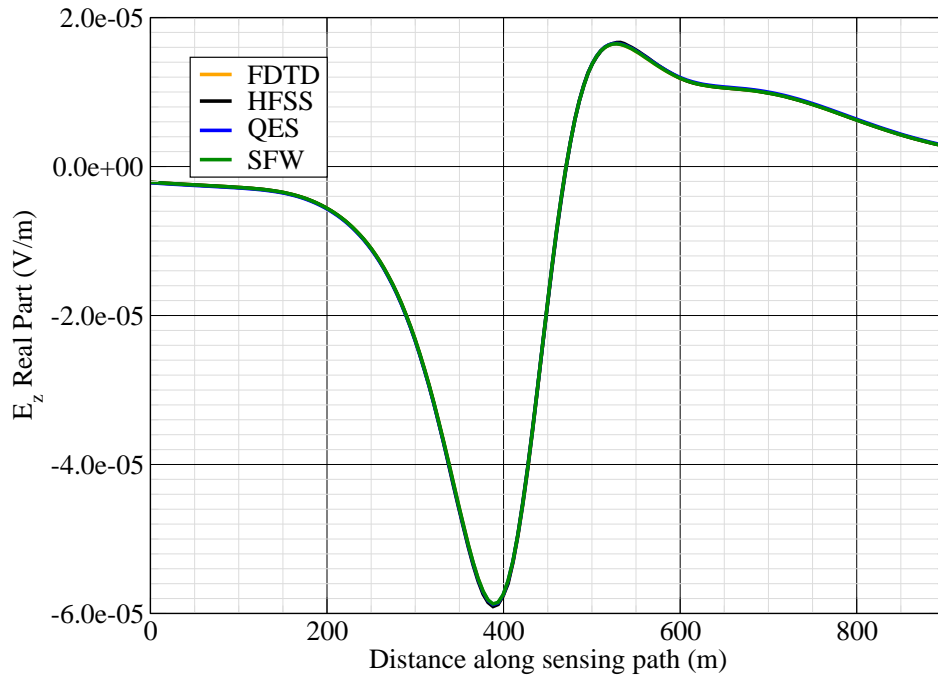


Figure 7: E_z real.

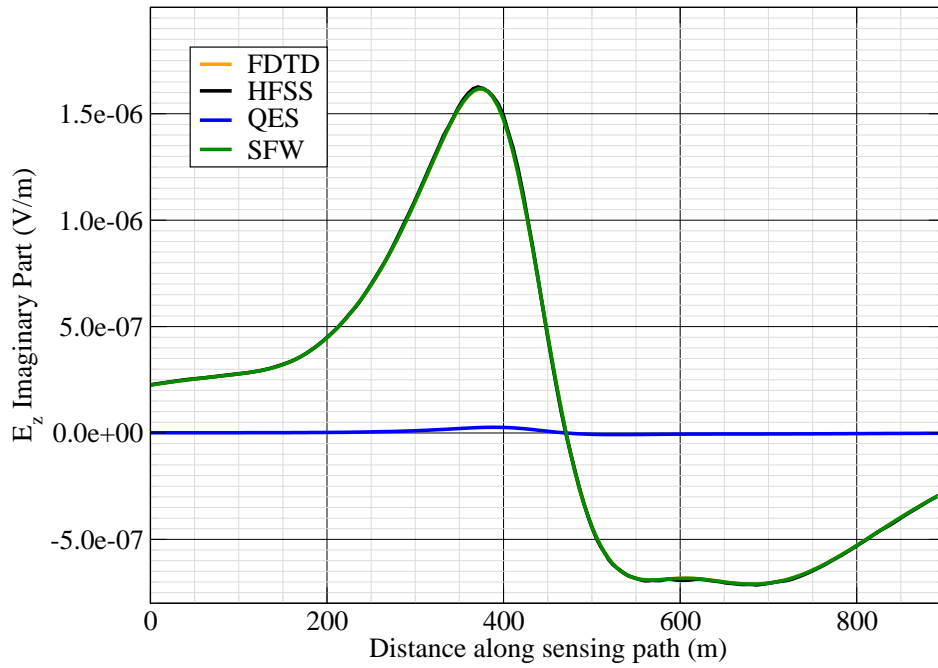


Figure 8: E_z imag.

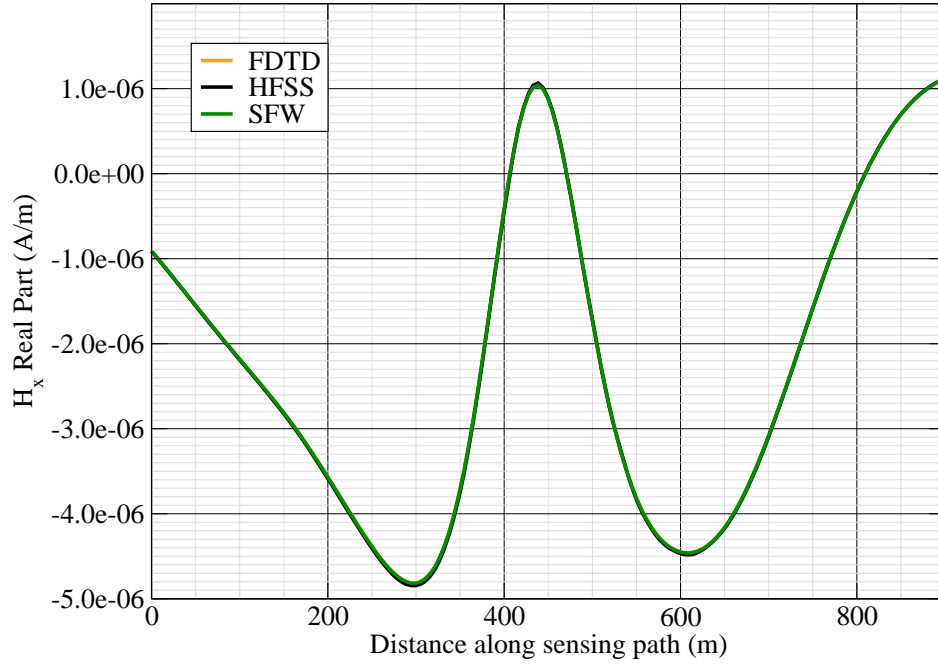


Figure 9: H_x real.

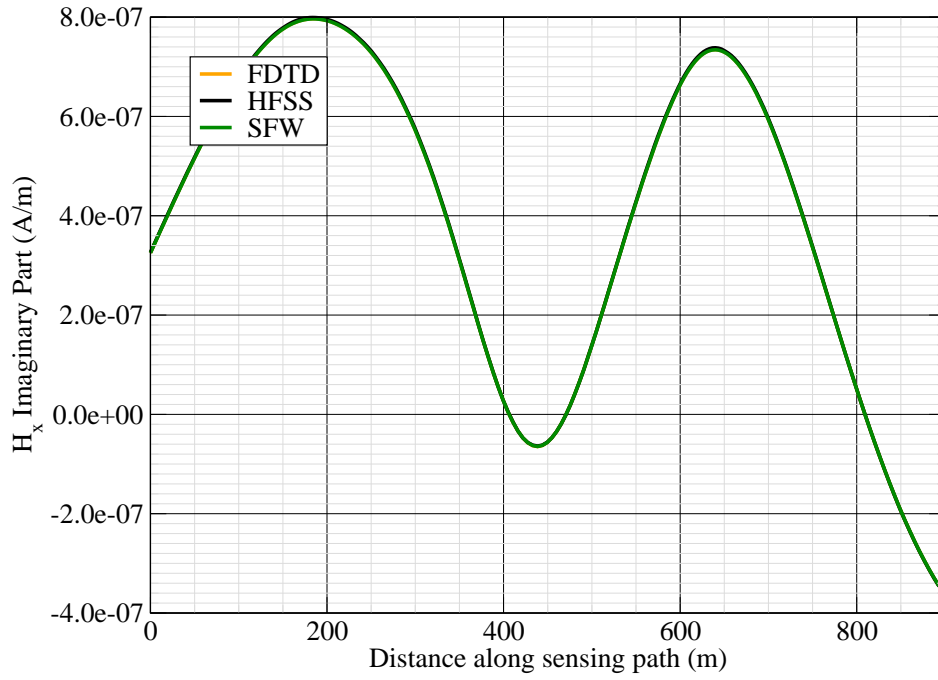


Figure 10: H_x imag.

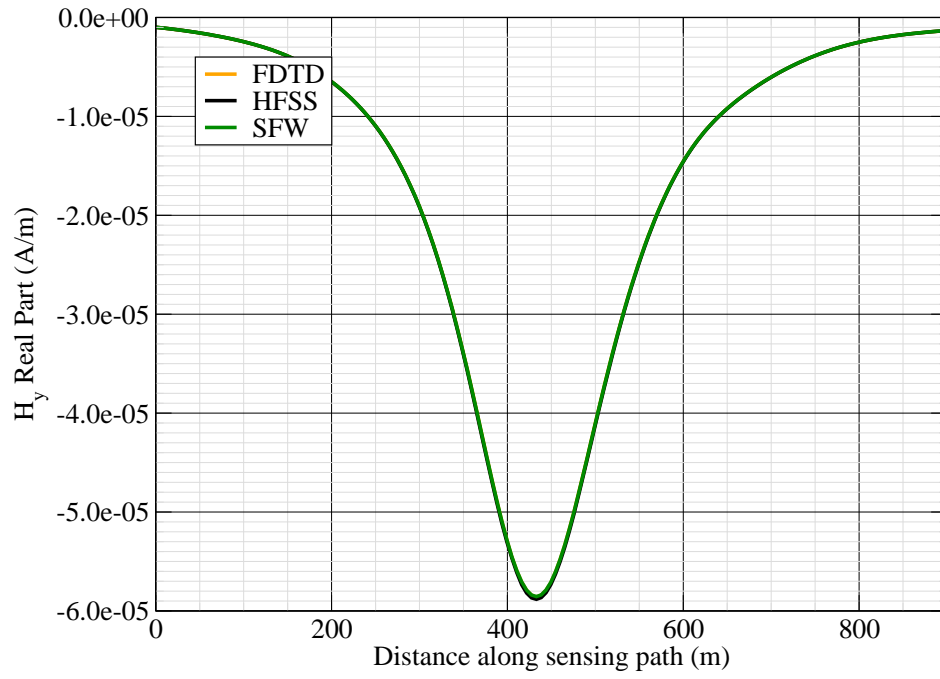


Figure 11: H_y real.

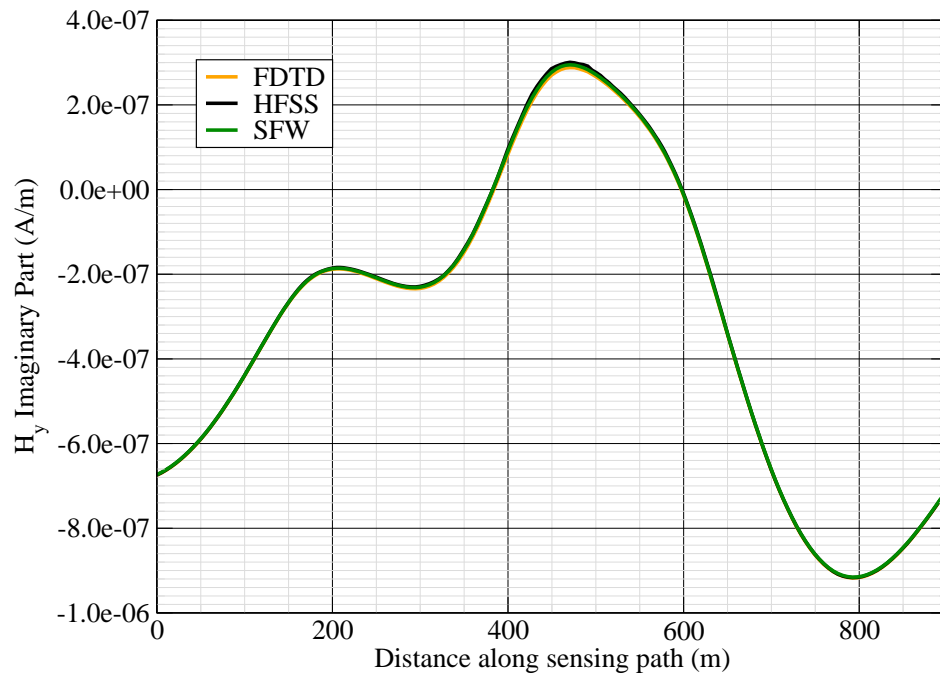


Figure 12: H_y imag.

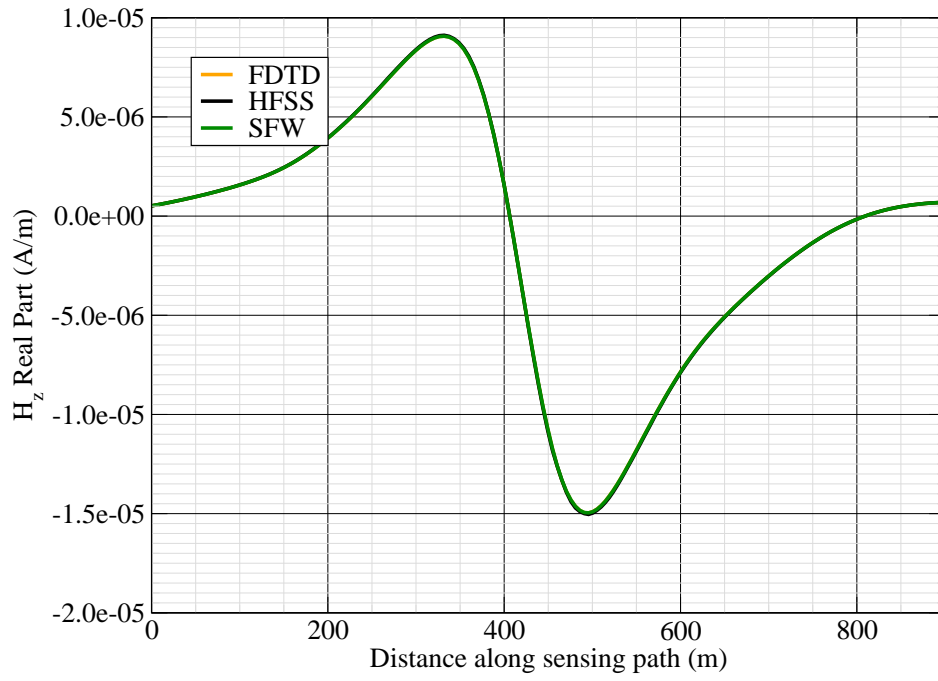


Figure 13: H_z real.

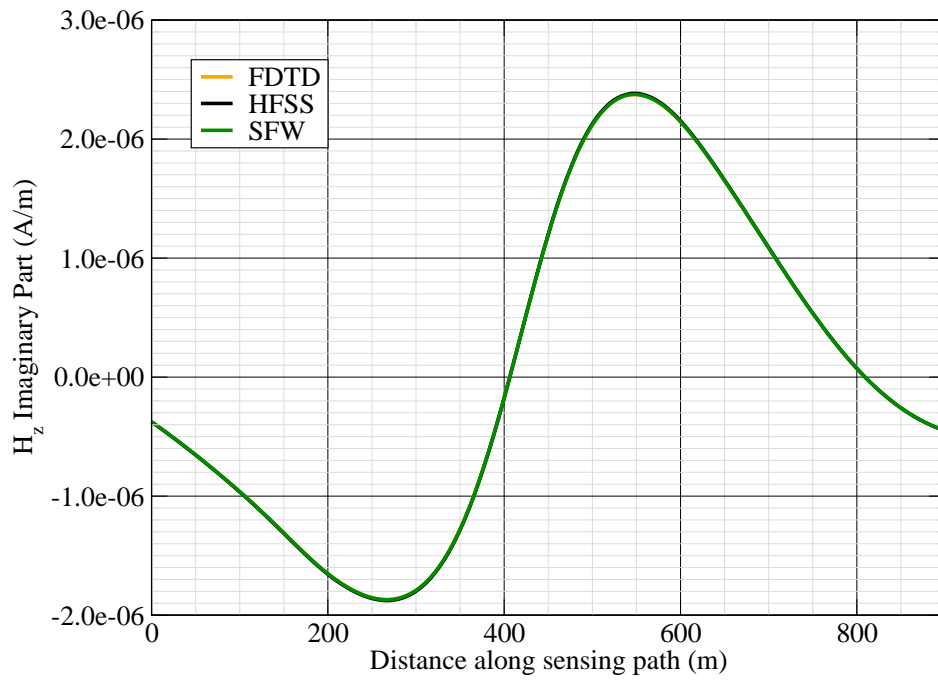


Figure 14: H_z imag.

Canonical Complex

Experiment 7

Experiment Date: November 2, 2011

1 Discussion

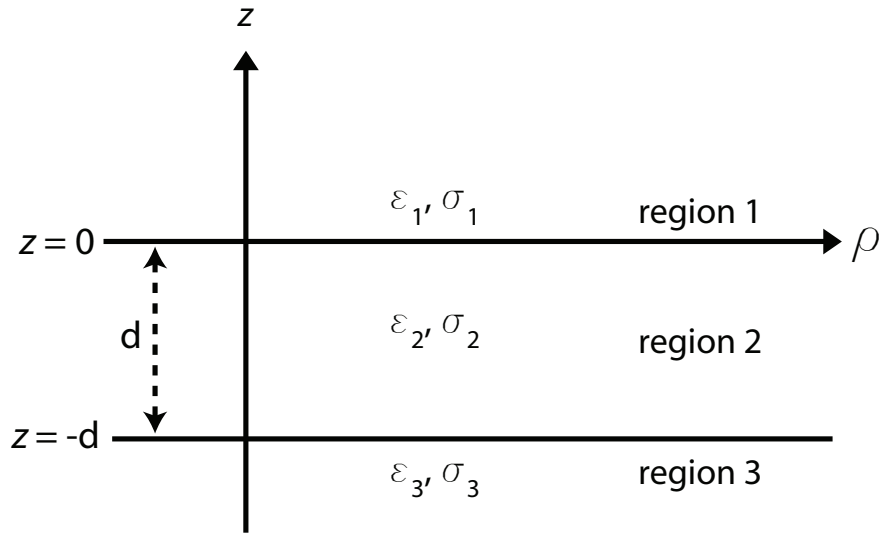


Figure 1: 3-layer topology.

Source Parameters

- Source Type: HED (Boat Hull: plates 0.6 m by 0.3 m separated by 4 m).
- Source Strength: 7.144 A-m.
- $f = 1000$ Hz.

Environment

- Water thickness: $d = 180$ m
- Air: $\sigma_1 = 0$ S/m and $\epsilon_{r1} = 1$
- Water: $\sigma_2 = 0.01$ S/m and $\epsilon_{r2} = 81$
- Mud: $\sigma_3 = 0.0012$ S/m and $\epsilon_{r3} = 1$

Table 1: Simulation Details

	FDTD	HFSS	QES/SFW
Domain Size	$200 \times 200 \times 120$ cells	28738 tets	N/A
Cell Size (m)	$5 \times 5 \times 5$	N/A	N/A
Time Step (ns)	9.6	N/A	N/A
Run Time (Hrs)	6	0.07	< 1 min

Comments

- Computational time is based on actual elapsed real time. This number is highly subjective and based on how many other applications might be running at a particular time. However, the reported number is an indication of the amount of time typically needed for a particular simulation. The computer specs are: 16 CPU cores at 2.8 GHz.
- Run times for HFSS are given for a single frequency.
- QES is not applicable for magnetic fields using electric source excitation.

2 Simulation Variables

Sensor_P1(x,y,z) [m]	(-276.8760,-43.8732,15.7470)
Sensor_P2(x,y,z) [m]	(348.3009,-39.4584,15.7470)
Source_P1(x,y,z) [m]	(50,30,-10)
Source_P2(x,y,z) [m]	(50,30,-10)
Source_Plate_Separation [m]	4
Source_Size [m X m X #]	[0.6 X 0.3 X 1]
Source_Heading [deg]	45
Source_Voltage [V Peak]	NaN
Source_Current [A Peak]	1.786
Source_Frequency [Hz]	1000

--- Extra Information ---

Source_Heading_Bounds [deg]	(N/A)
Average_Boat_Speed [m/s]	NaN
Source_Type	Electric truss (truss)
Sensor_Type	EMA
Bin_Size [sec]	1
Number_of_Datapoints	200
Lake_Origin (Easting,Northing)	NaN
Analysis_Date	26-Sep-2011

3 Boat Path

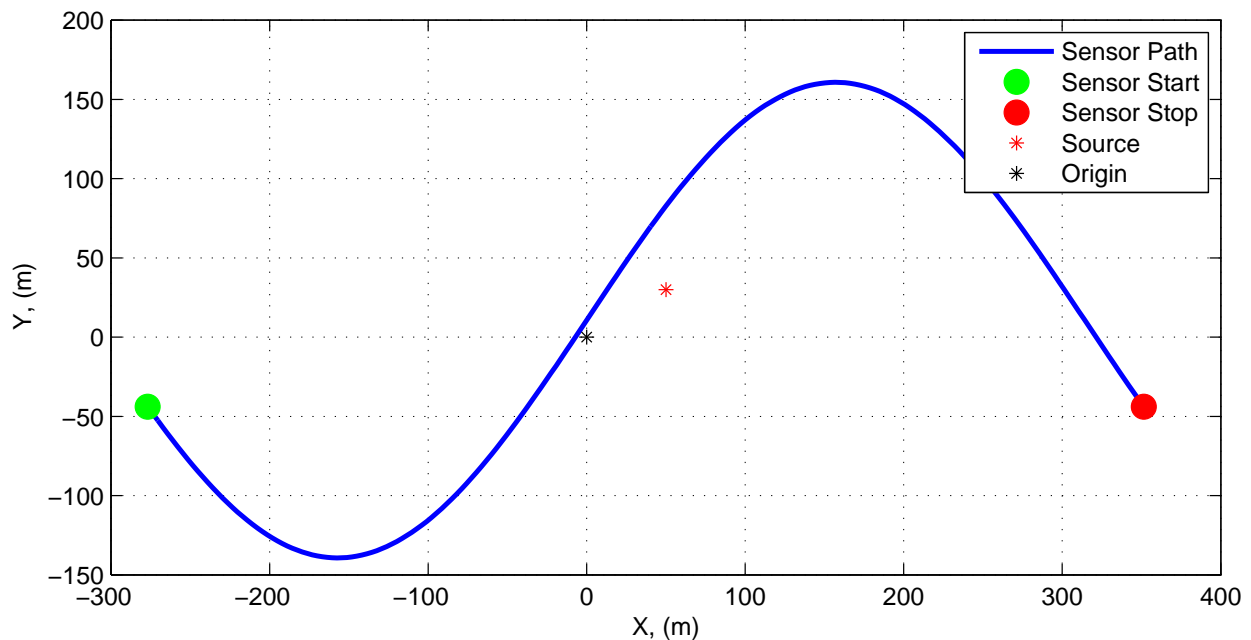


Figure 2: Source and sensor relationship.

4 Plots

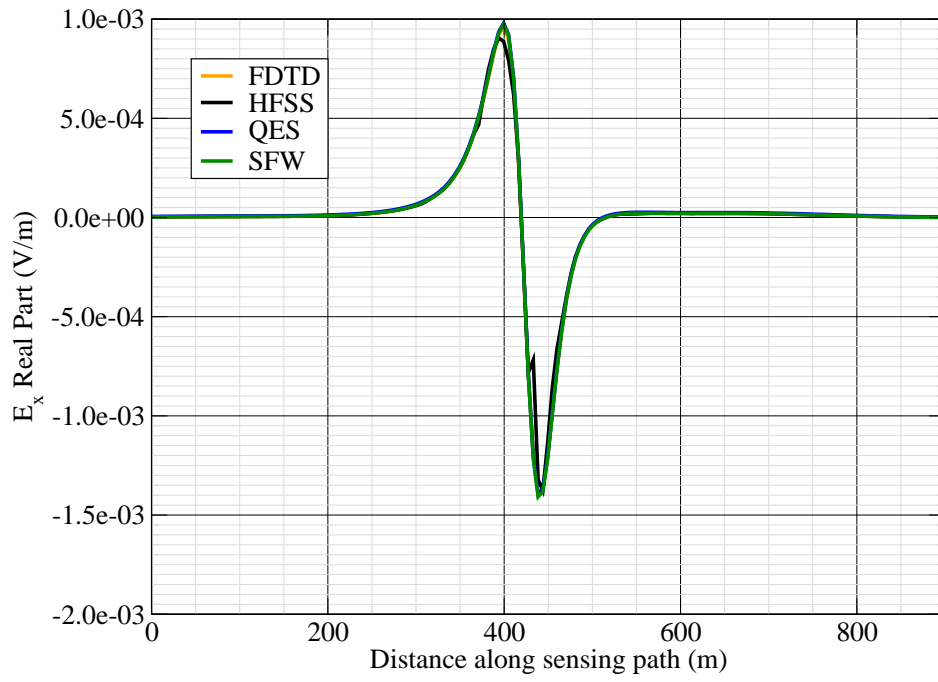


Figure 3: E_x real.

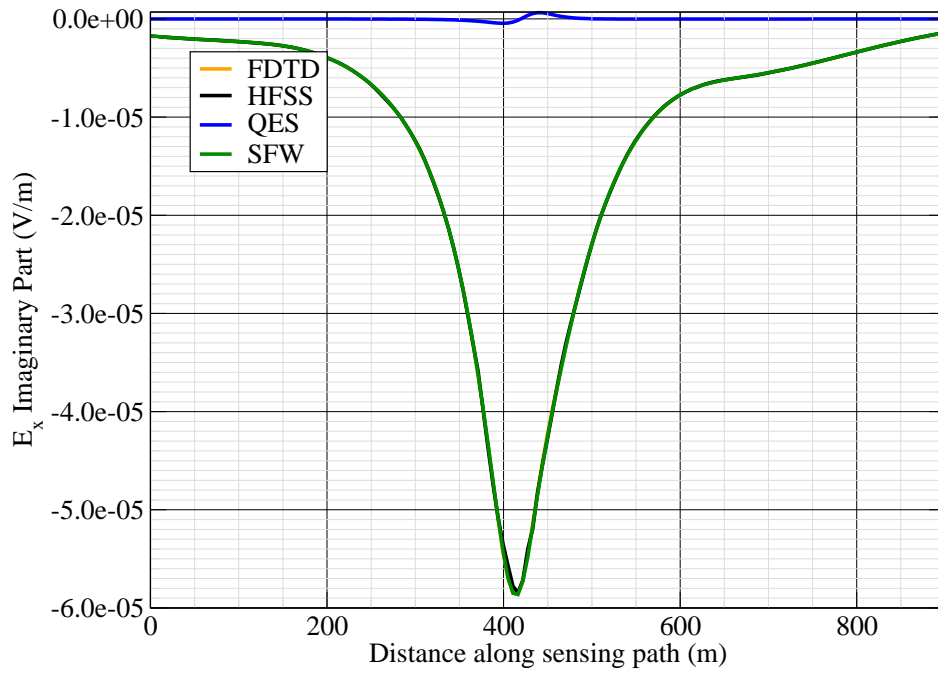


Figure 4: E_x imag.

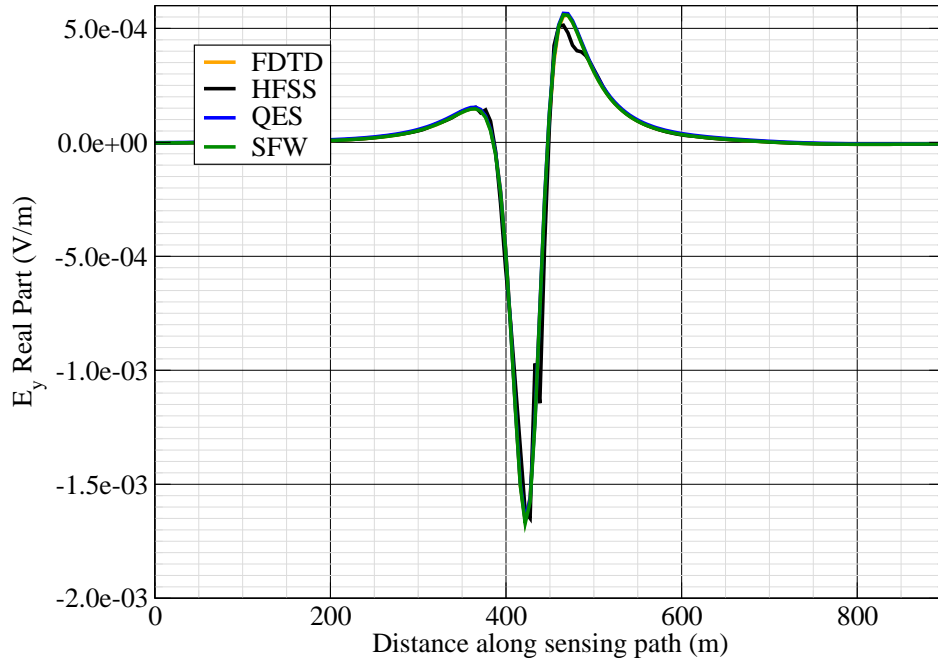


Figure 5: E_y real.

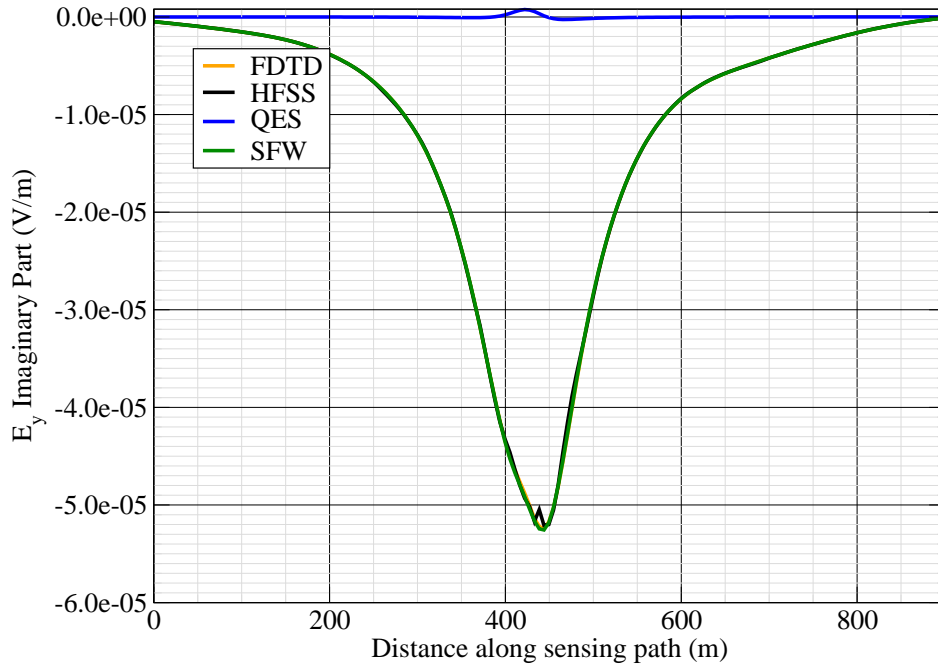


Figure 6: E_y imag.

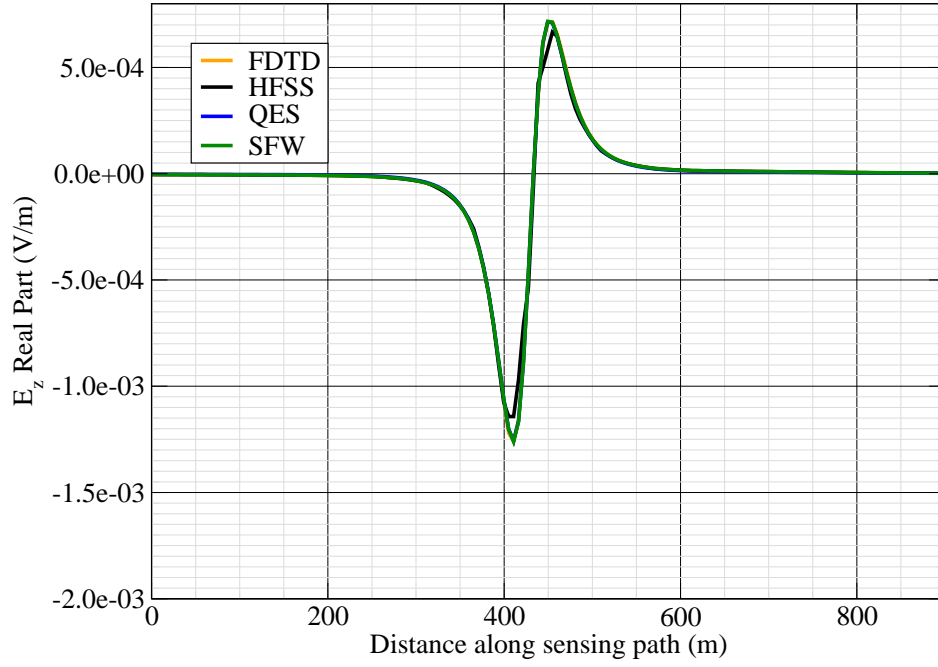


Figure 7: E_z real.

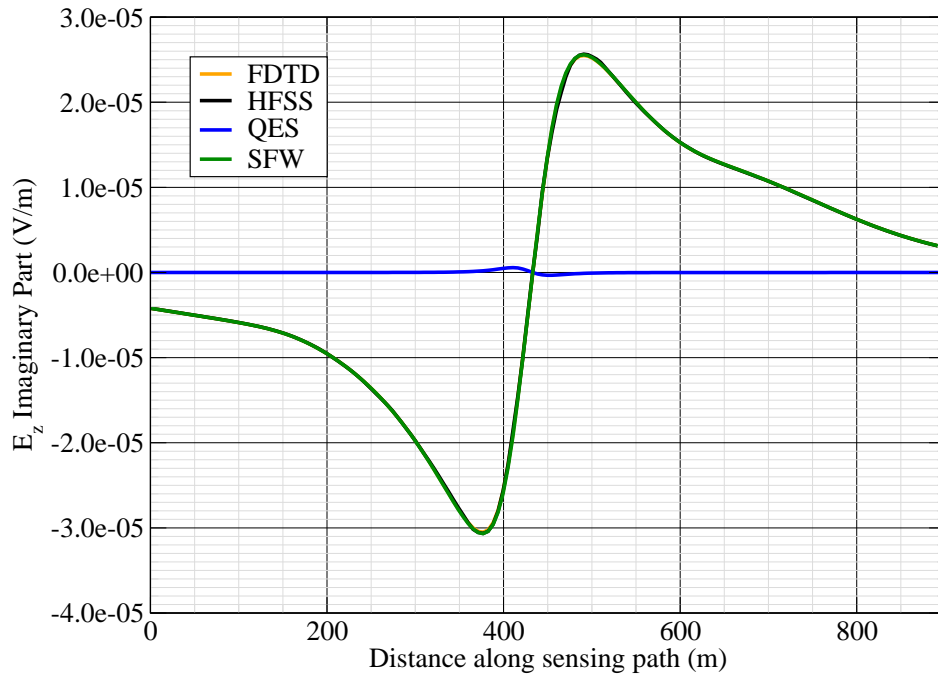


Figure 8: E_z imag.

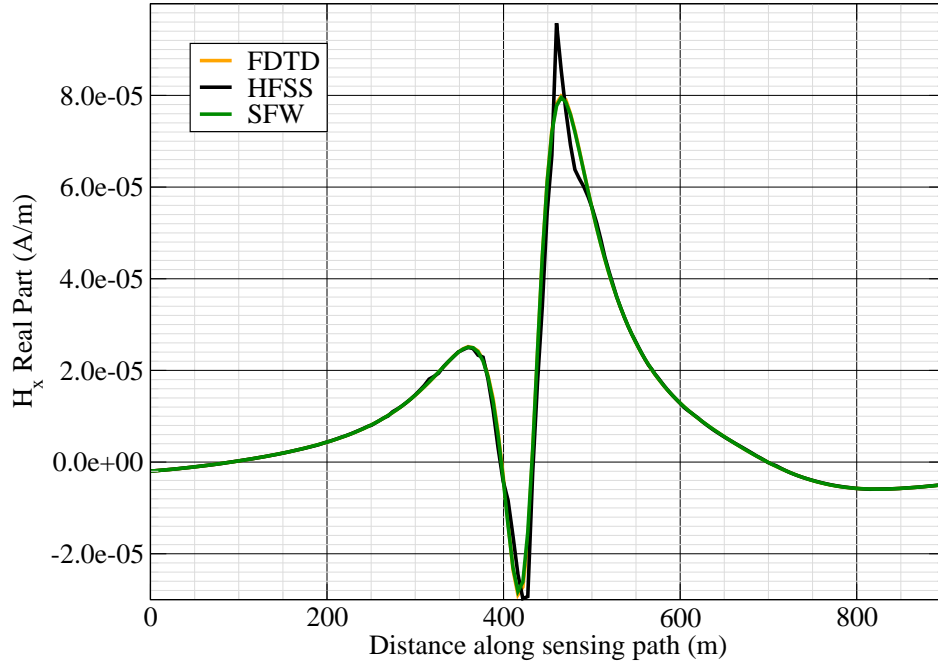


Figure 9: H_x real.

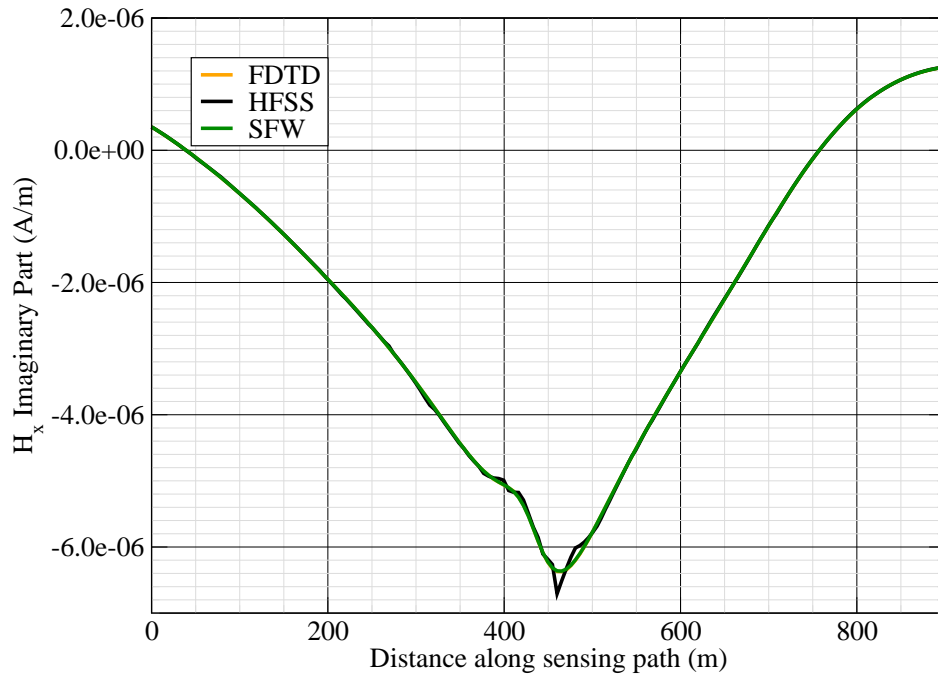


Figure 10: H_x imag.

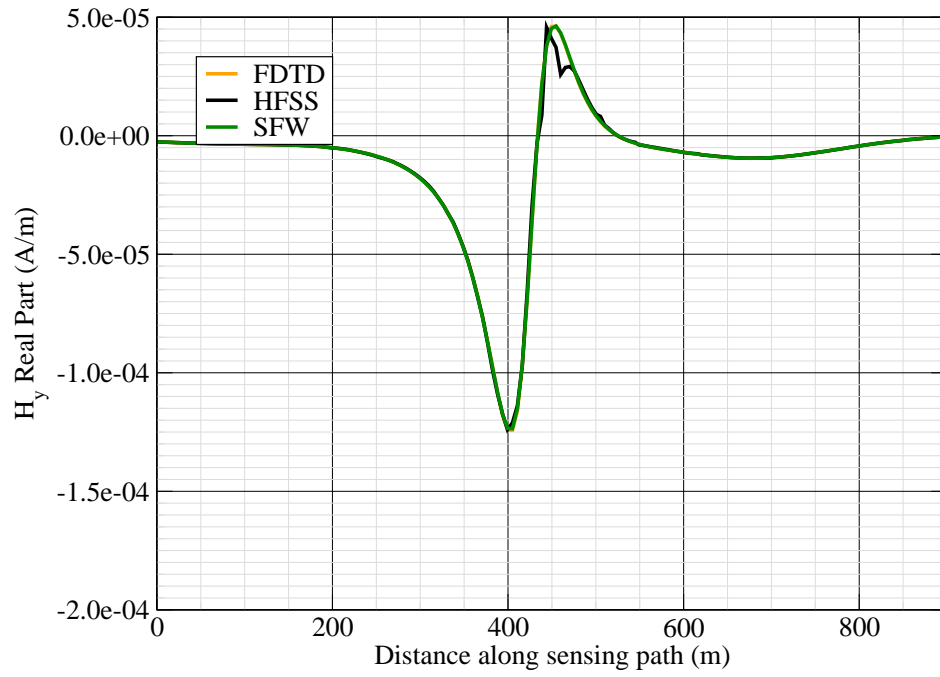


Figure 11: H_y real.

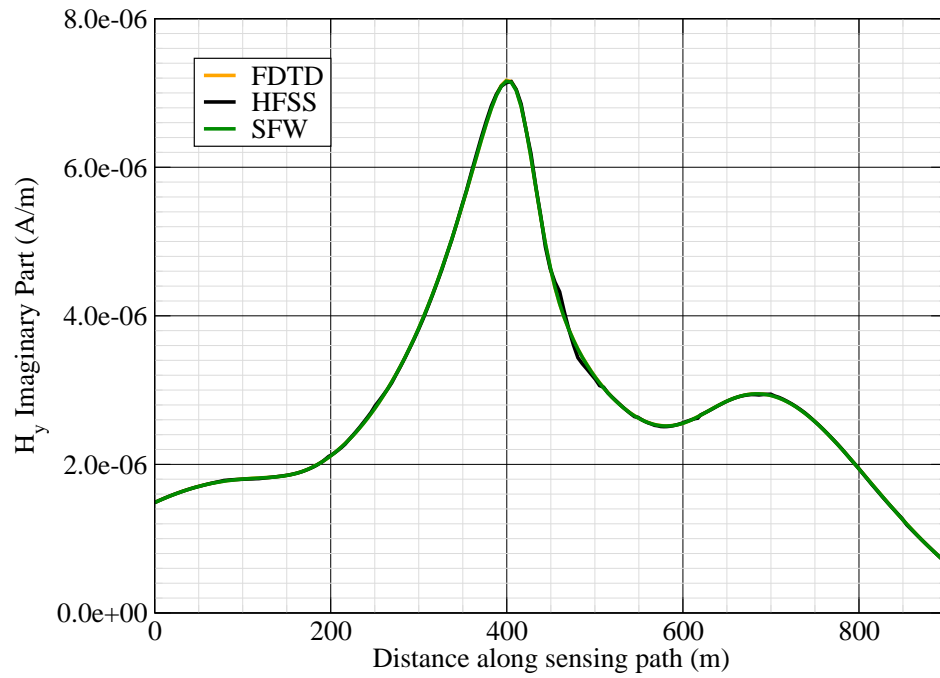


Figure 12: H_y imag.

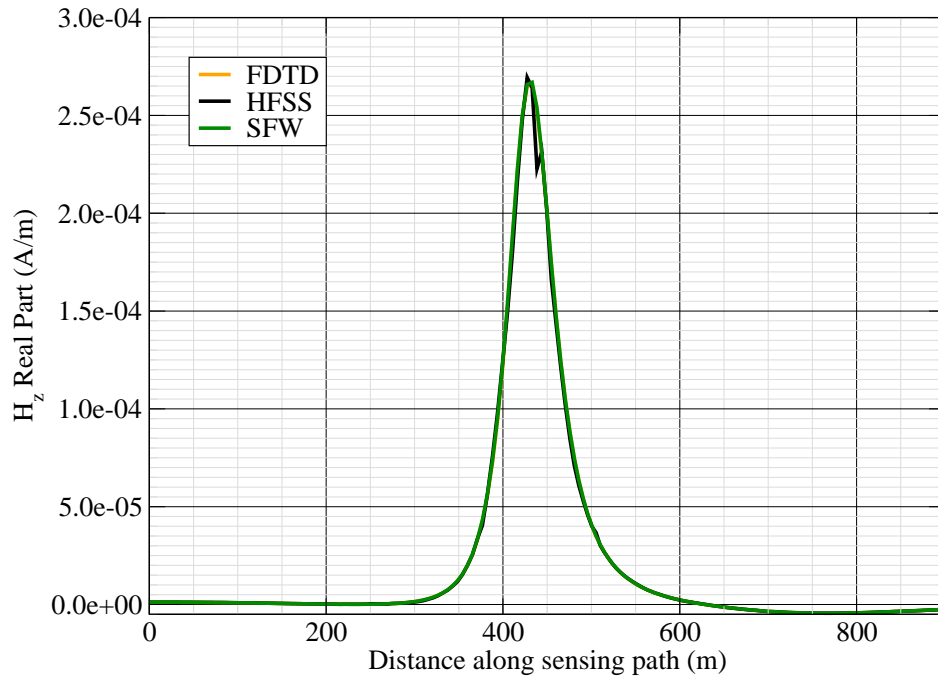


Figure 13: H_z real.

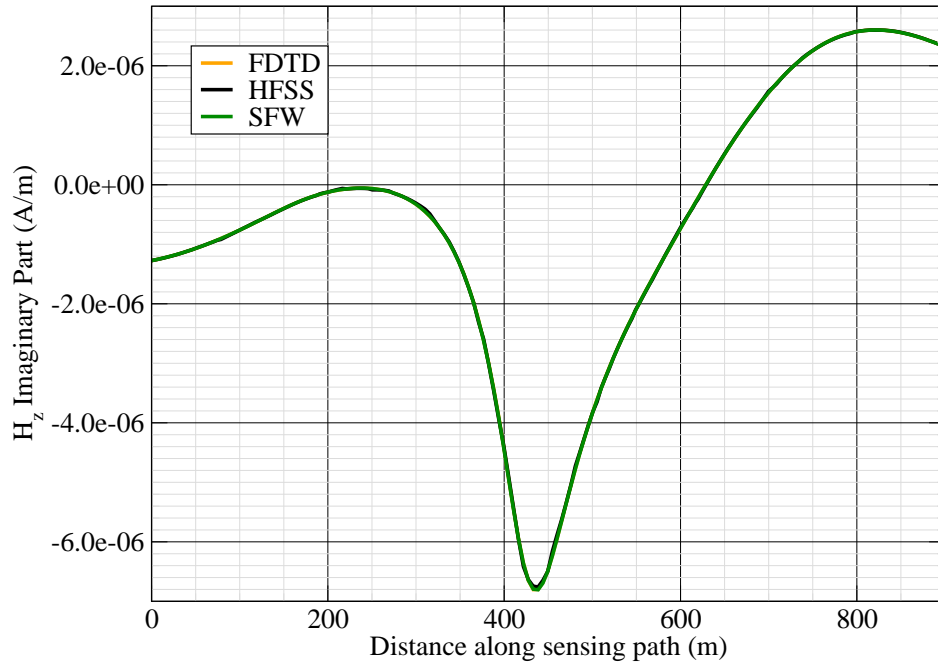


Figure 14: H_z imag.

Canonical Complex

Experiment 8

Experiment Date: November 2, 2011

1 Discussion

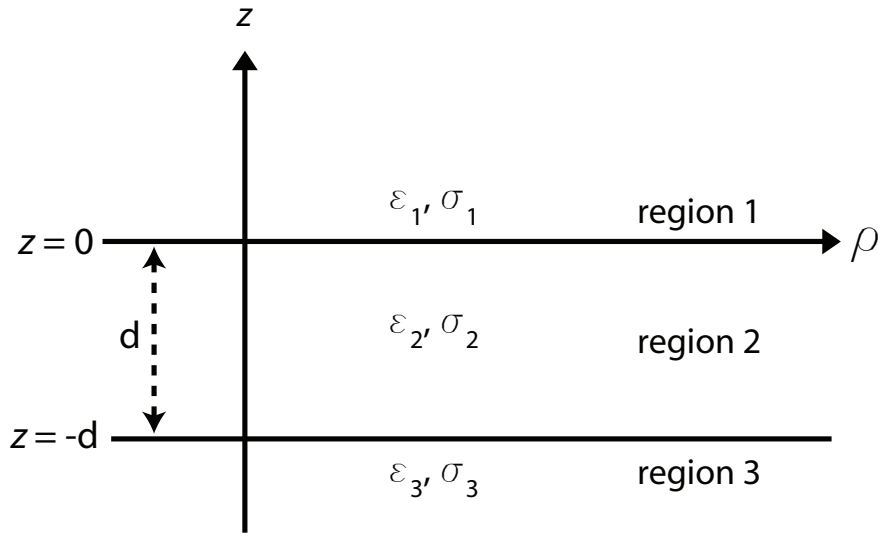


Figure 1: 3-layer topology.

Source Parameters

- Source Type: VED (Boat Hull: plates 0.6 m by 0.3 m separated by 4 m).
- Source Strength: 14.68 A-m.
- $f = 1000$ Hz.

Environment

- Water thickness: $d = 180$ m
- Air: $\sigma_1 = 0$ S/m and $\epsilon_{r1} = 1$
- Water: $\sigma_2 = 0.01$ S/m and $\epsilon_{r2} = 81$
- Mud: $\sigma_3 = 0.0012$ S/m and $\epsilon_{r3} = 1$

Table 1: Simulation Details

	FDTD	HFSS	QES/SFW
Domain Size	$200 \times 200 \times 120$ cells	54904 tets	N/A
Cell Size (m)	$5 \times 5 \times 5$	N/A	N/A
Time Step (ns)	9.6	N/A	N/A
Run Time (Hrs)	6	0.60	< 1 min

Comments

- Computational time is based on actual elapsed real time. This number is highly subjective and based on how many other applications might be running at a particular time. However, the reported number is an indication of the amount of time typically needed for a particular simulation. The computer specs are: 16 CPU cores at 2.8 GHz.
- Run times for HFSS are given for a single frequency.
- QES is not applicable for magnetic fields using electric source excitation.

2 Simulation Variables

Sensor_P1(x,y,z) [m]	(-200,57.1571,25)
Sensor_P2(x,y,z) [m]	(114.1593,44.8169,25)
Source_P1(x,y,z) [m]	(0,0,150)
Source_P2(x,y,z) [m]	(0,0,150)
Source_Plate_Separation [m]	4
Source_Size [m X m X #]	[0.6 X 0.3 X 1]
Source_Heading [deg]	NaN
Source_Voltage [V Peak]	NaN
Source_Current [A Peak]	3.67
Source_Frequency [Hz]	1000
--- Extra Information ---	
Source_Heading_Bounds [deg]	(N/A)
Average_Boat_Speed [m/s]	NaN
Source_Type	Electric vert_truss (vert_truss)
Sensor_Type	EMA
Bin_Size [sec]	1
Number_of_Datapoints	200
Lake_Origin (Easting,Northing)	NaN
Analysis_Date	6-Oct-2011

3 Boat Path

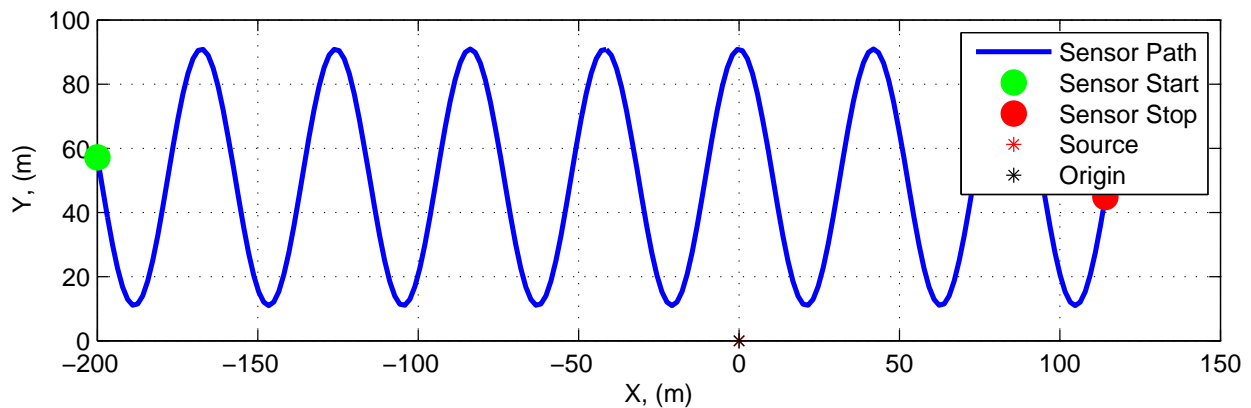


Figure 2: Source and sensor relationship.

4 Plots

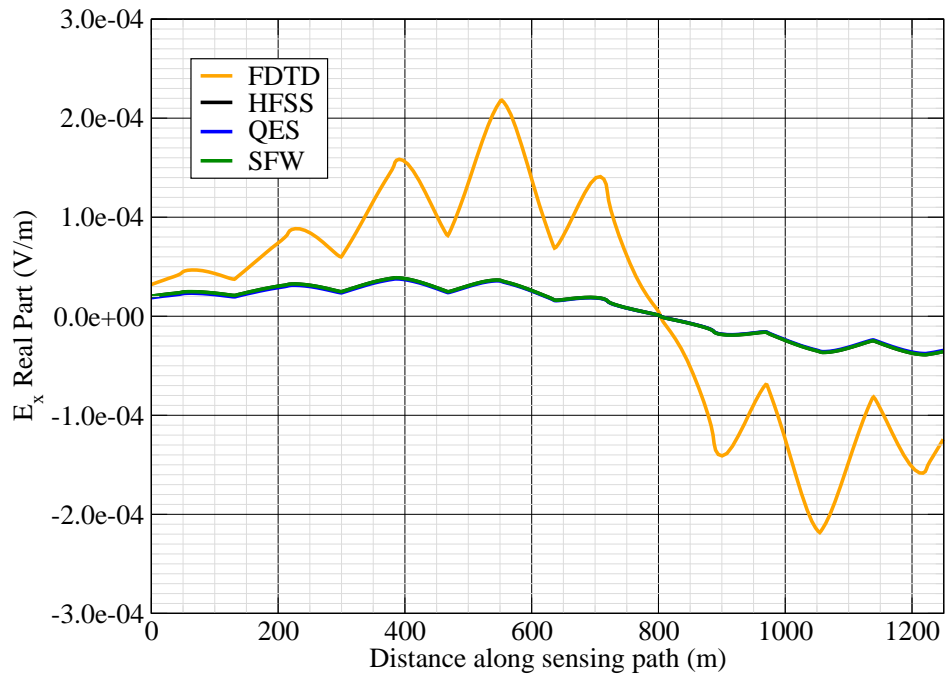


Figure 3: E_x real.

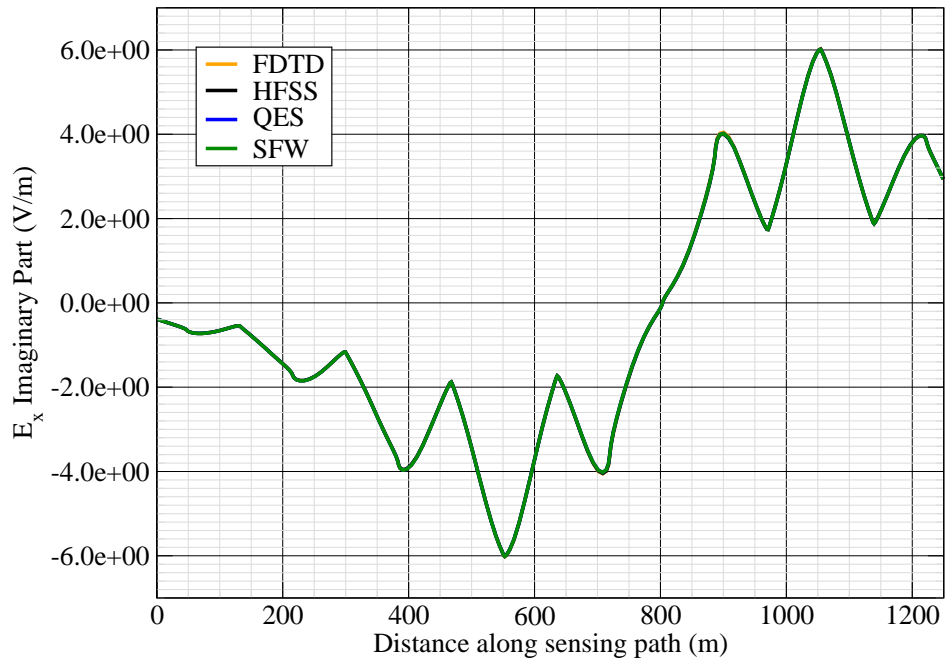


Figure 4: E_x imag.

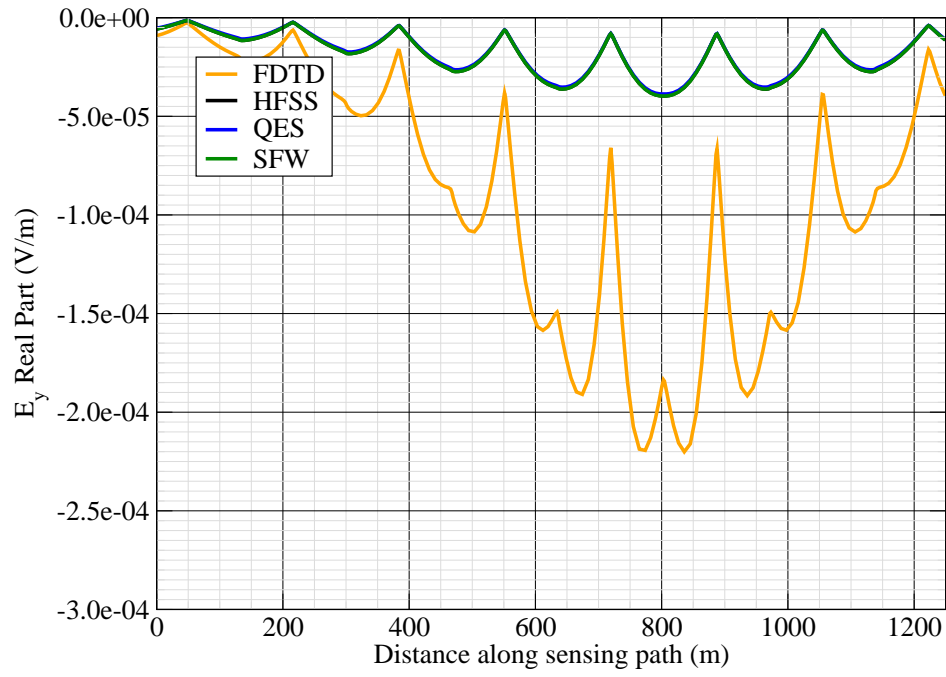


Figure 5: E_y real.

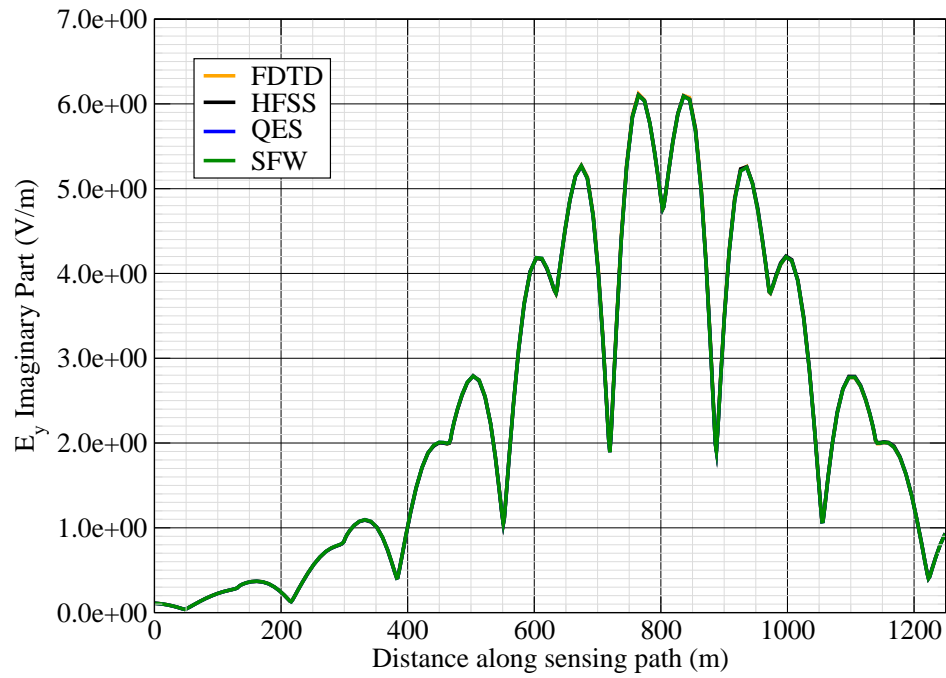


Figure 6: E_y imag.

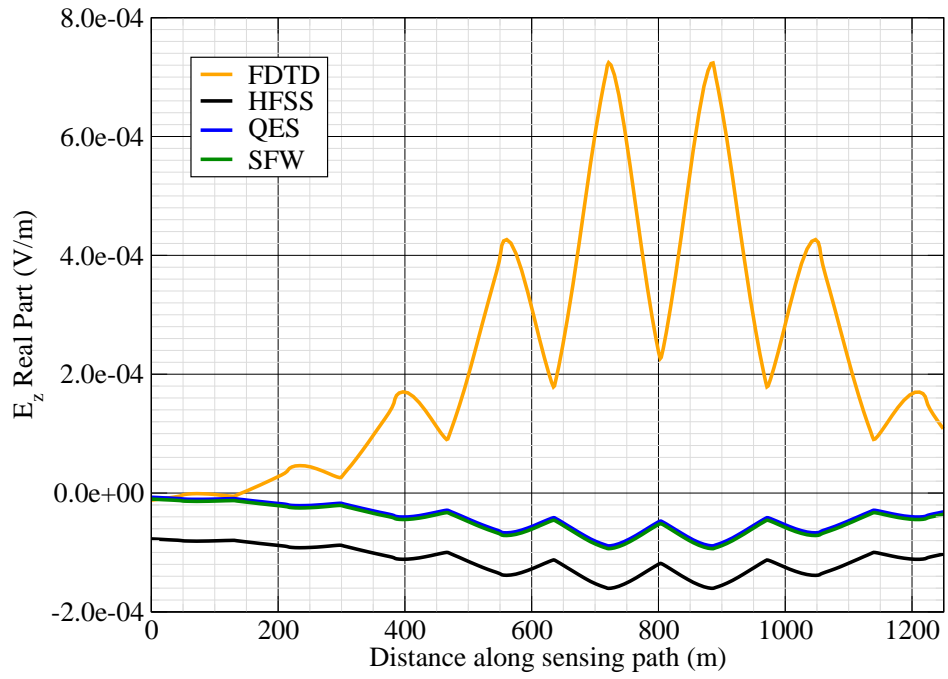


Figure 7: E_z real.

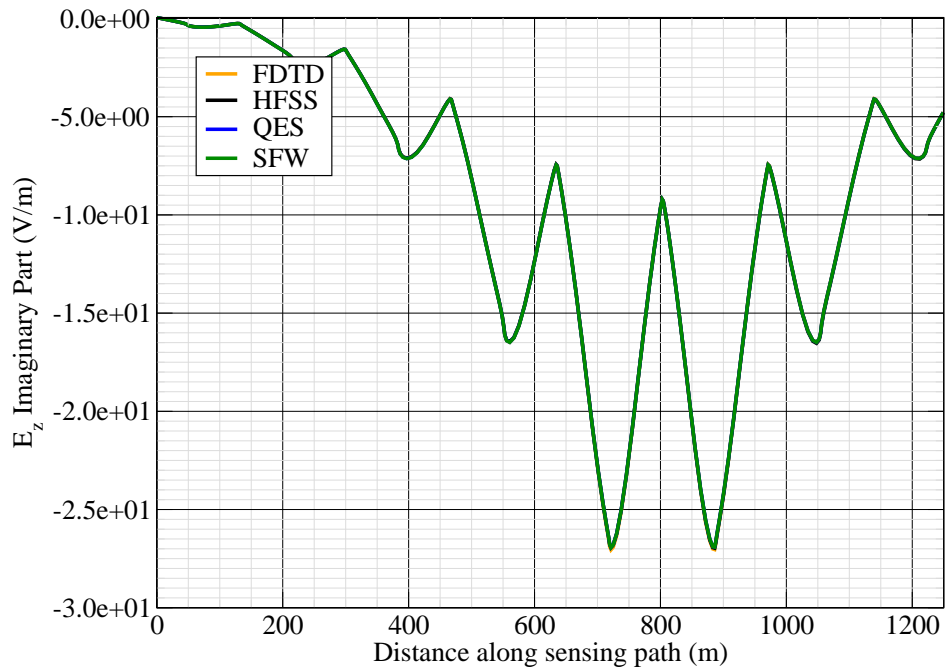


Figure 8: E_z imag.

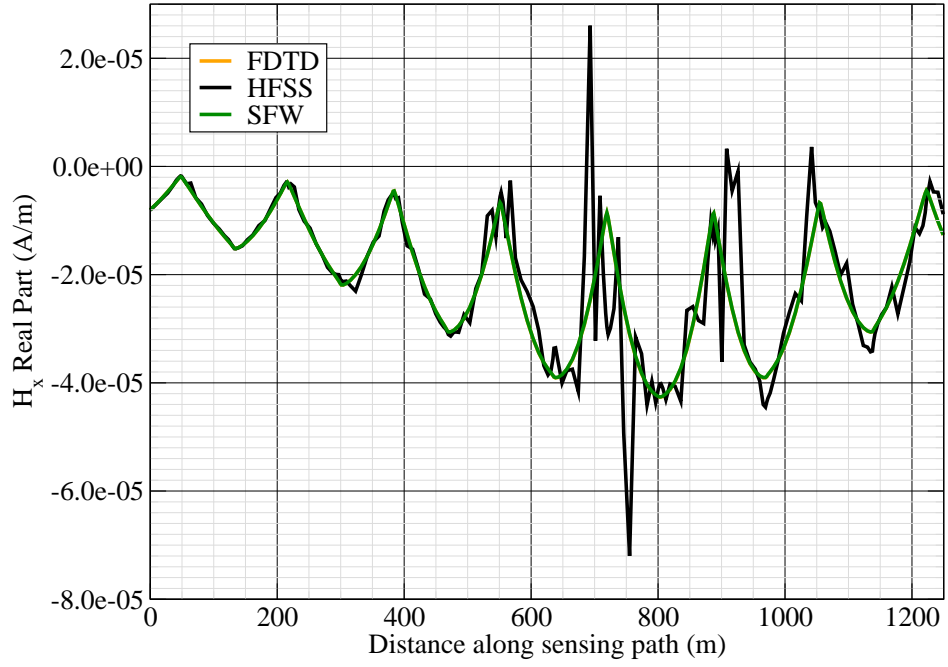


Figure 9: H_x real.

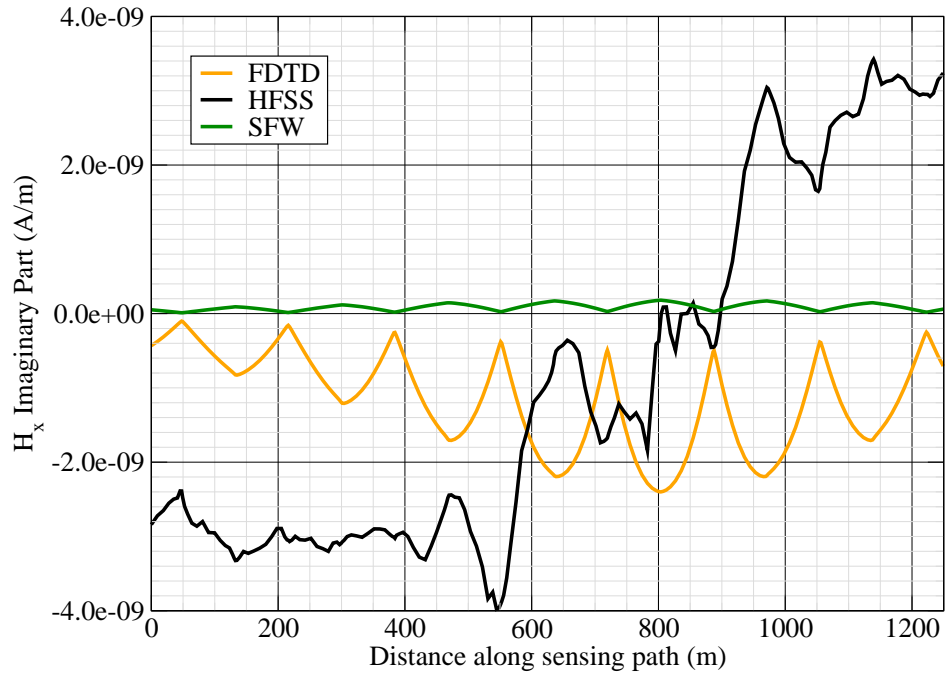


Figure 10: H_x imag.

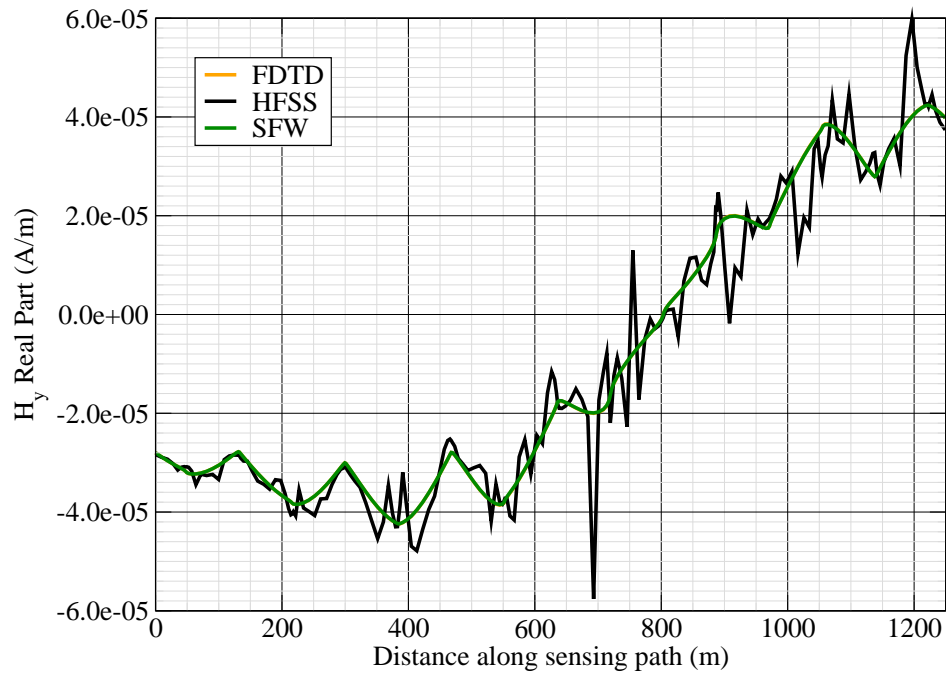


Figure 11: H_y real.

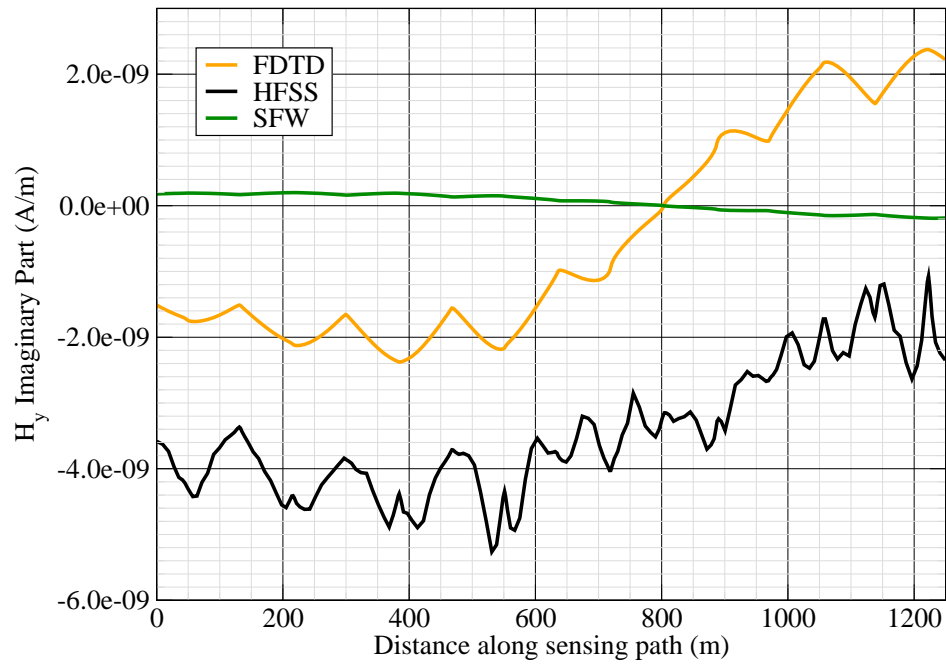


Figure 12: H_y imag.

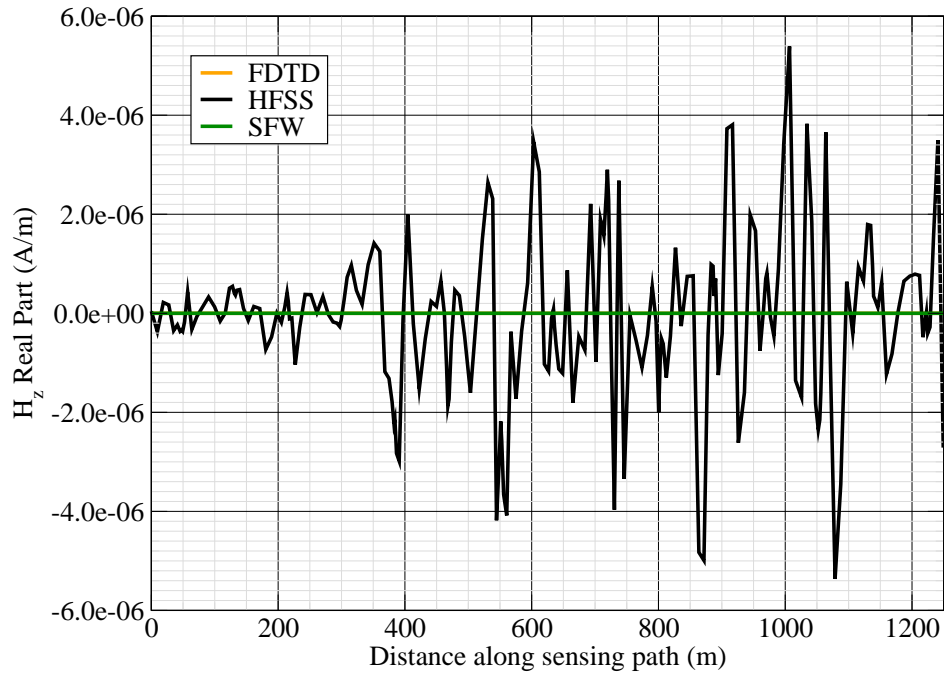


Figure 13: H_z real.

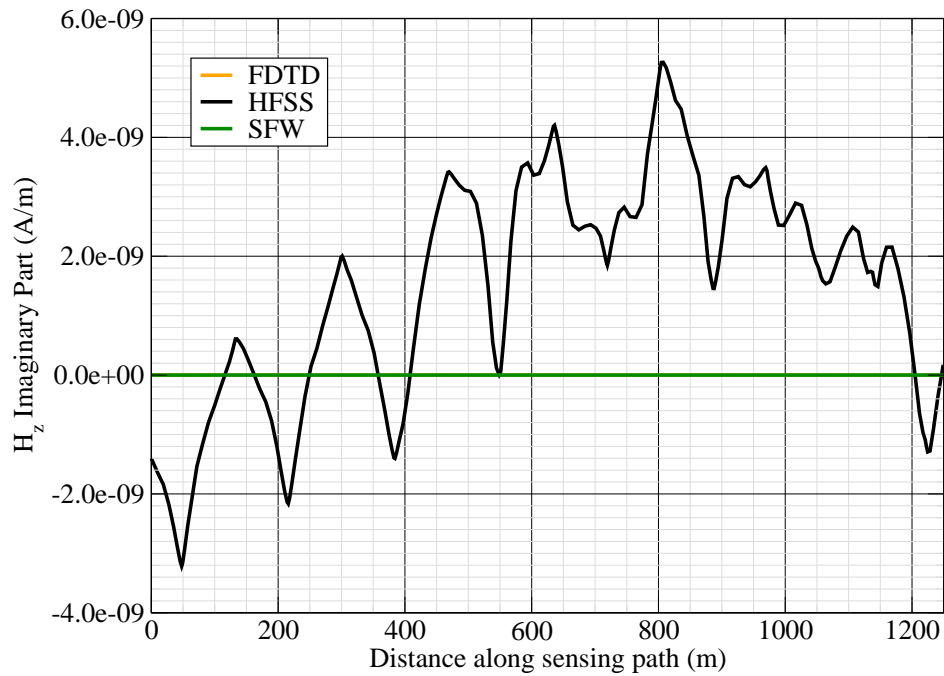


Figure 14: H_z imag.

Canonical Complex

Experiment 9

Experiment Date: November 2, 2011

1 Discussion

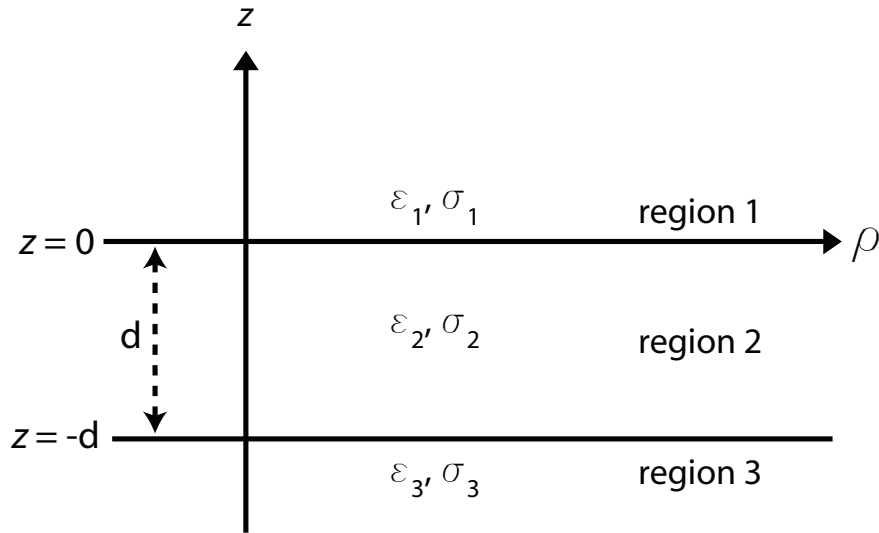


Figure 1: 3-layer topology.

Source Parameters

- Source Type: VED (Boat Hull: plates 0.6 m by 0.3 m separated by 4 m).
- Source Strength: 14.68 A-m.
- $f = 1000$ Hz.

Environment

- Water thickness: $d = 180$ m
- Air: $\sigma_1 = 0$ S/m and $\epsilon_{r1} = 1$
- Water: $\sigma_2 = 0.01$ S/m and $\epsilon_{r2} = 81$
- Mud: $\sigma_3 = 0.0012$ S/m and $\epsilon_{r3} = 1$

Table 1: Simulation Details

	FDTD	HFSS	QES/SFW
Domain Size	$200 \times 200 \times 120$ cells	38820 tets	N/A
Cell Size (m)	$5 \times 5 \times 5$	N/A	N/A
Time Step (ns)	9.6	N/A	N/A
Run Time (Hrs)	6	0.45	< 1 min

Comments

- Computational time is based on actual elapsed real time. This number is highly subjective and based on how many other applications might be running at a particular time. However, the reported number is an indication of the amount of time typically needed for a particular simulation. The computer specs are: 16 CPU cores at 2.8 GHz.
- Run times for HFSS are given for a single frequency.
- QES is not applicable for magnetic fields using electric source excitation.

2 Simulation Variables

Sensor_P1(x,y,z) [m]	(-200,57.1571,-15.7470)
Sensor_P2(x,y,z) [m]	(114.1593,44.8169,-15.7470)
Source_P1(x,y,z) [m]	(0,0,150)
Source_P2(x,y,z) [m]	(0,0,150)
Source_Plate_Separation [m]	4
Source_Size [m X m X #]	[0.6 X 0.3 X 1]
Source_Heading [deg]	NaN
Source_Voltage [V Peak]	NaN
Source_Current [A Peak]	3.67
Source_Frequency [Hz]	1000
--- Extra Information ---	
Source_Heading_Bounds [deg]	(N/A)
Average_Boat_Speed [m/s]	NaN
Source_Type	Electric vert_truss (vert_truss)
Sensor_Type	EMA
Bin_Size [sec]	1
Number_of_Datapoints	200
Lake_Origin (Easting,Northing)	NaN
Analysis_Date	6-Oct-2011

3 Boat Path

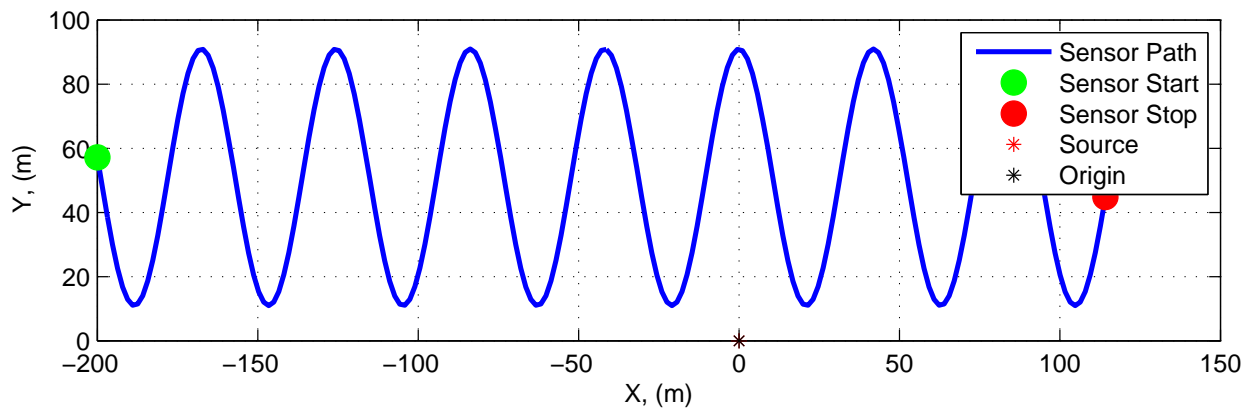


Figure 2: Source and sensor relationship.

4 Plots

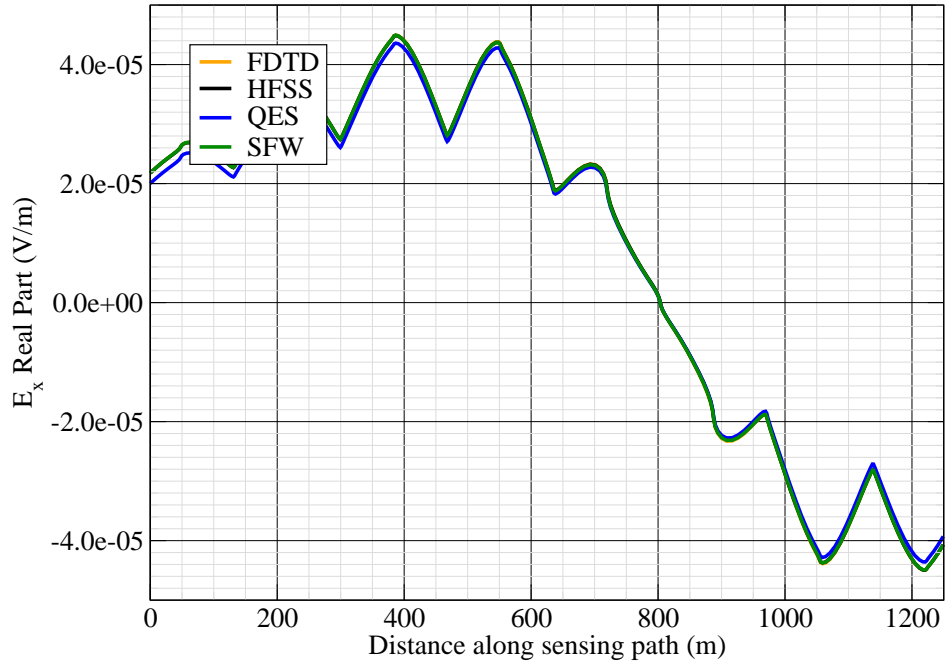


Figure 3: E_x real.

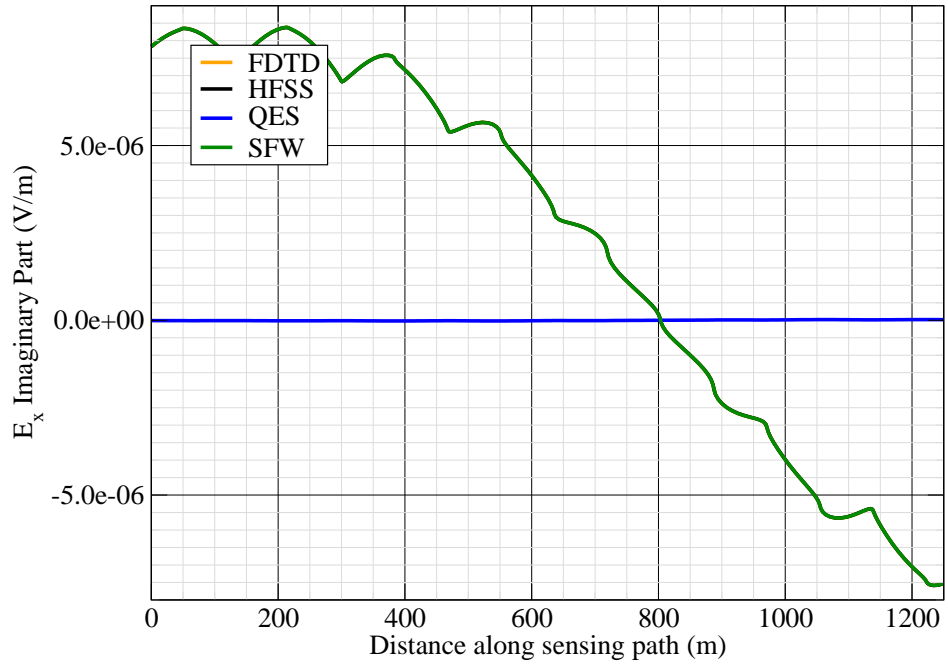


Figure 4: E_x imag.

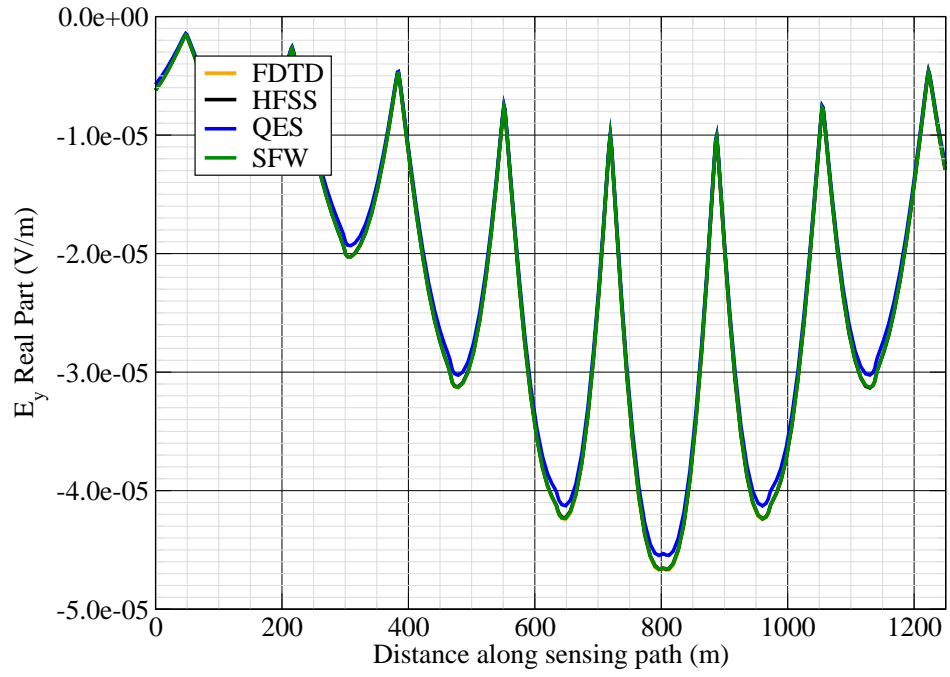


Figure 5: E_y real.

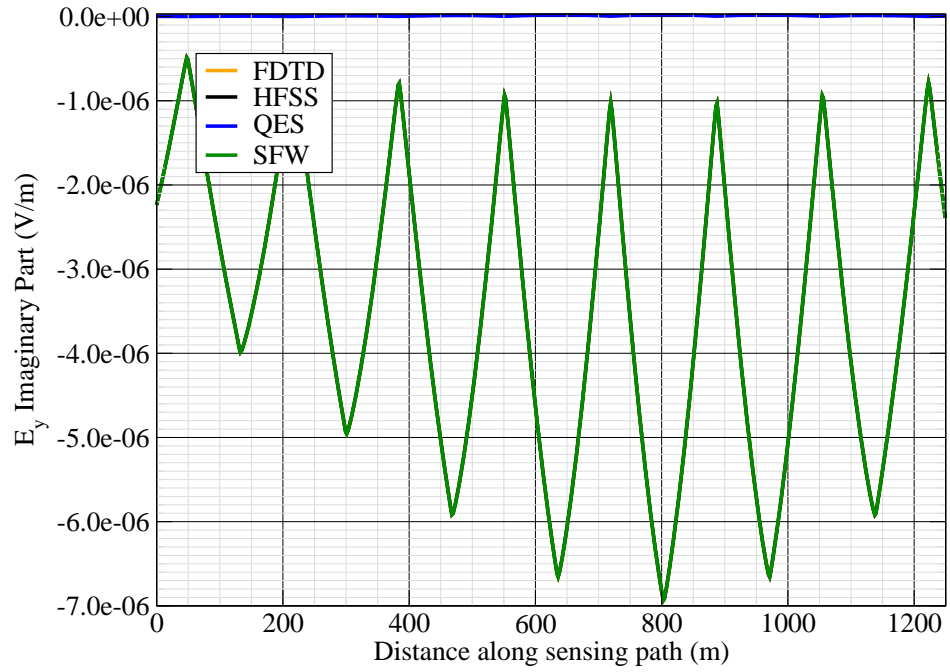


Figure 6: E_y imag.

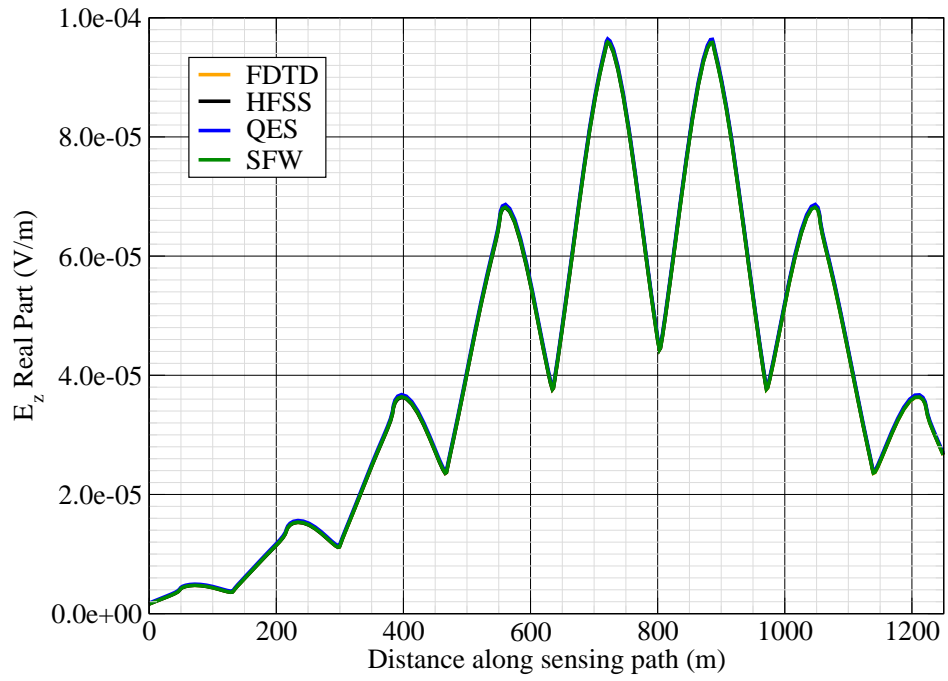


Figure 7: E_z real.

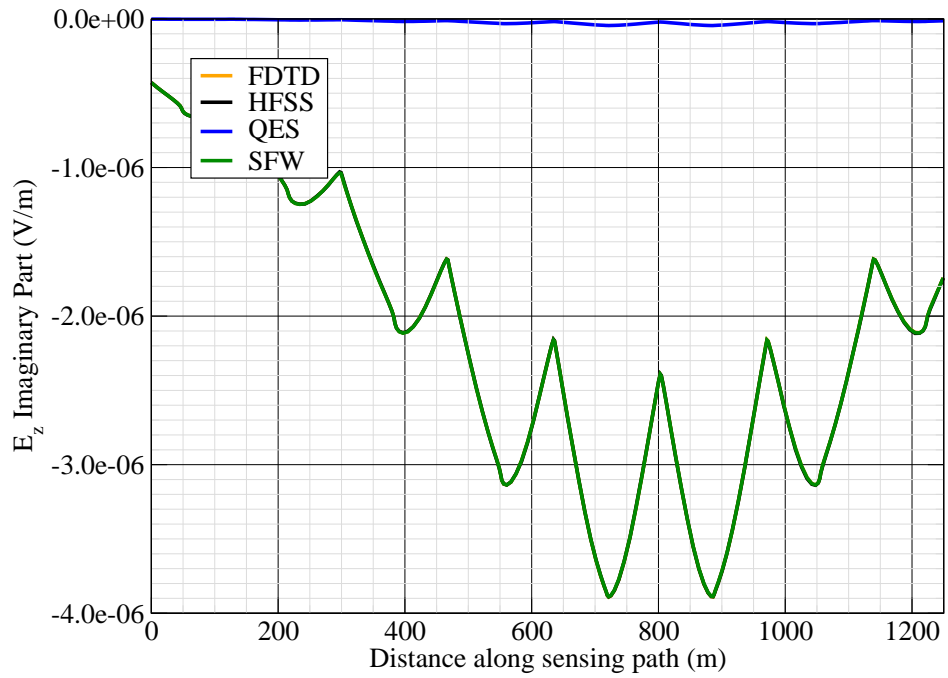


Figure 8: E_z imag.

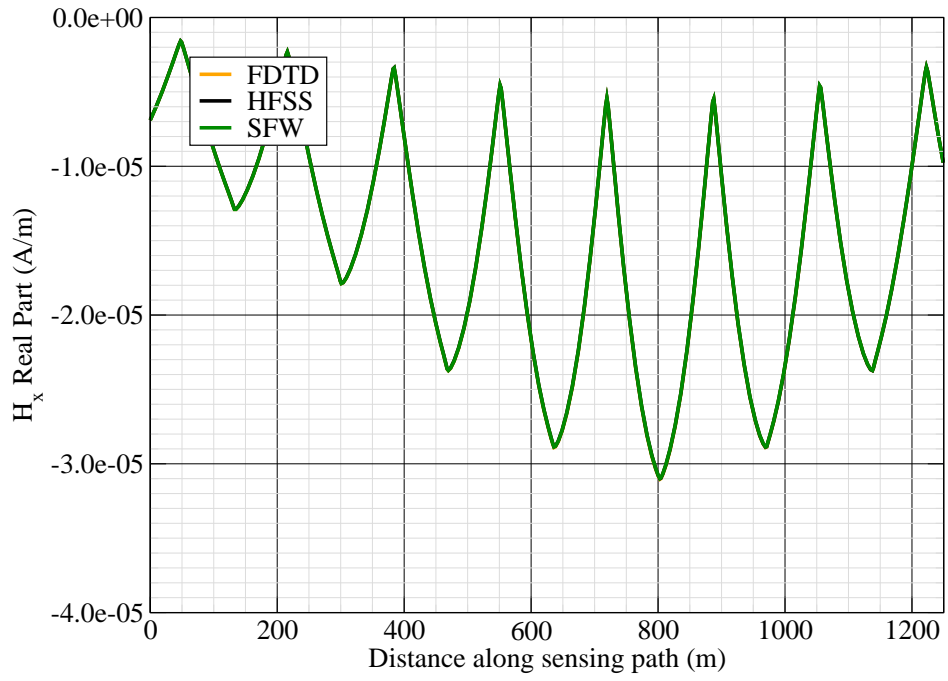


Figure 9: H_x real.

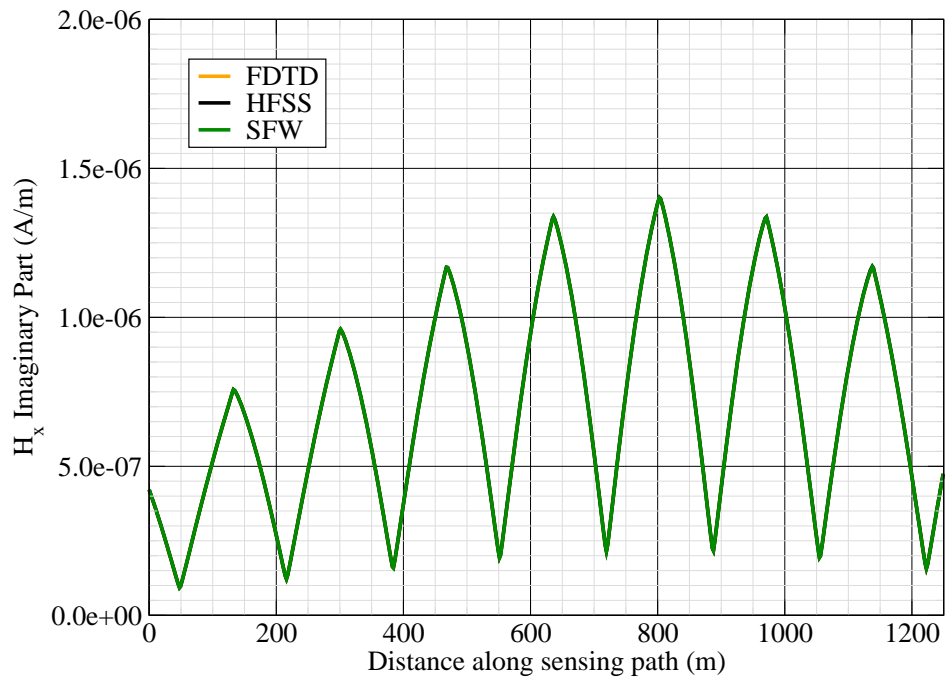


Figure 10: H_x imag.

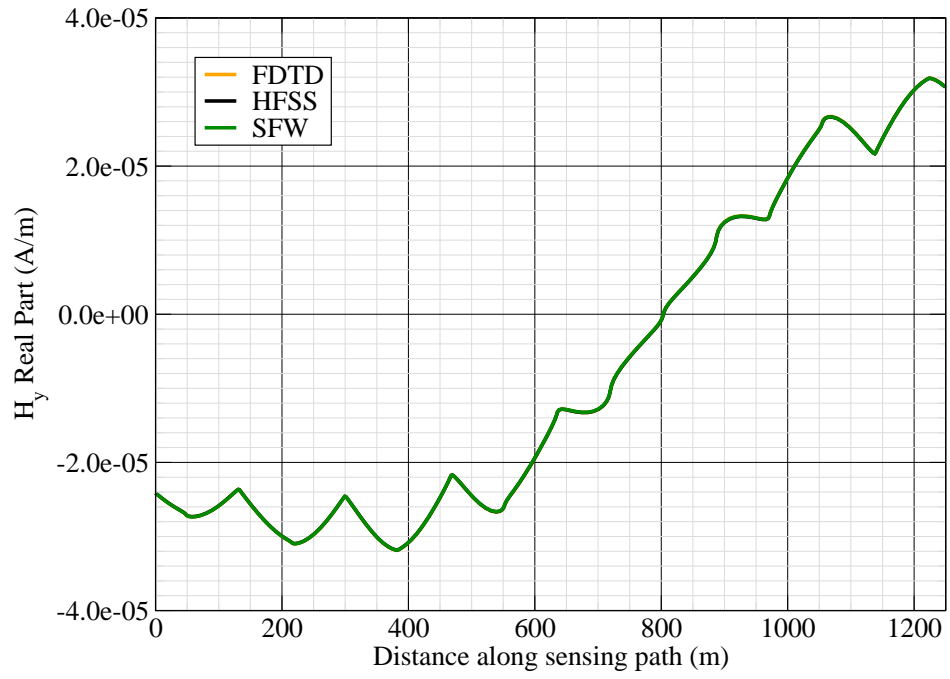


Figure 11: H_y real.

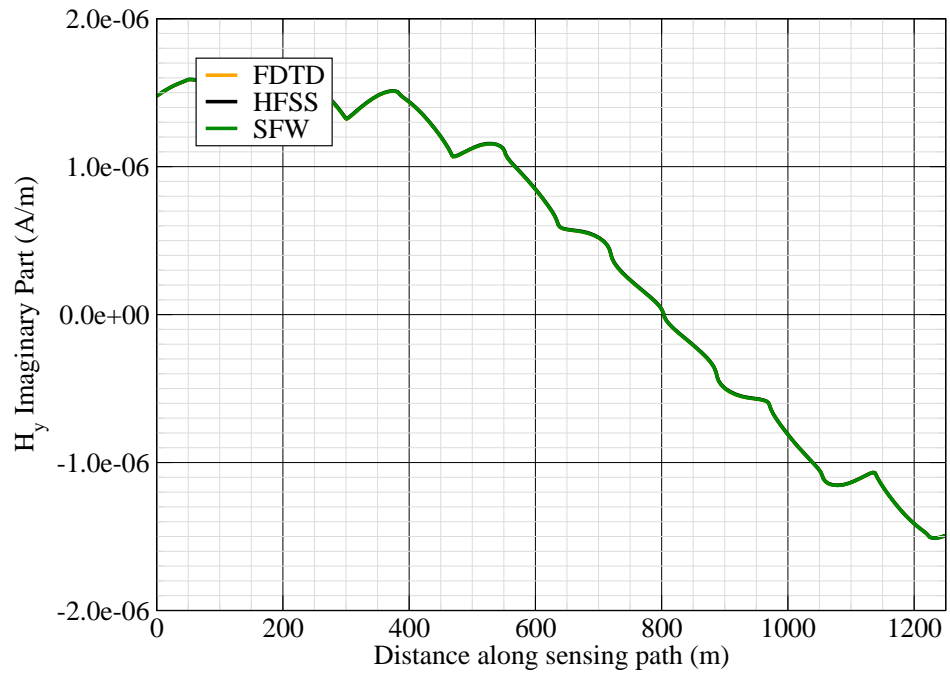


Figure 12: H_y imag.

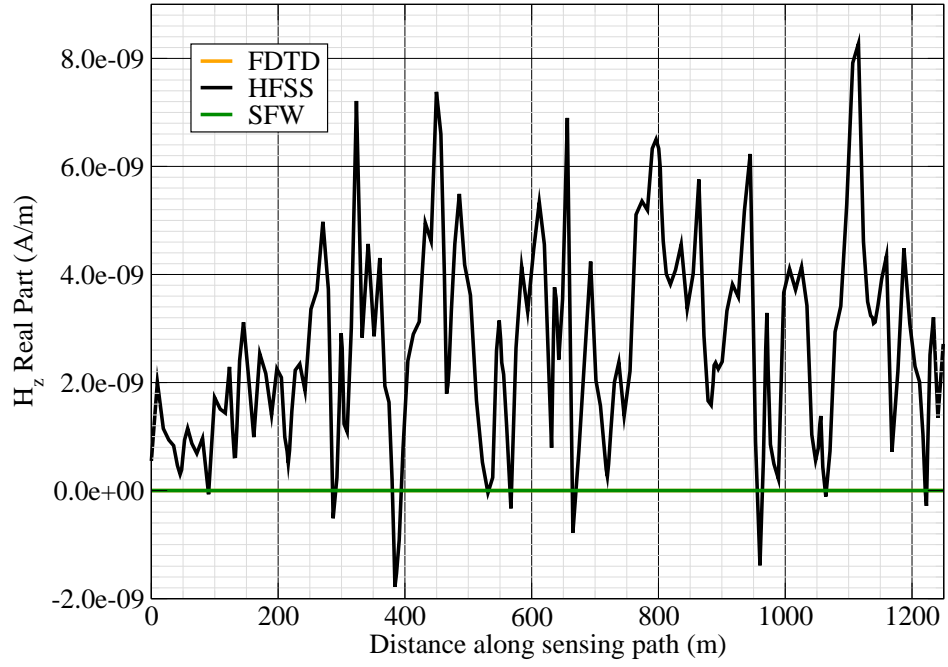


Figure 13: H_z real.

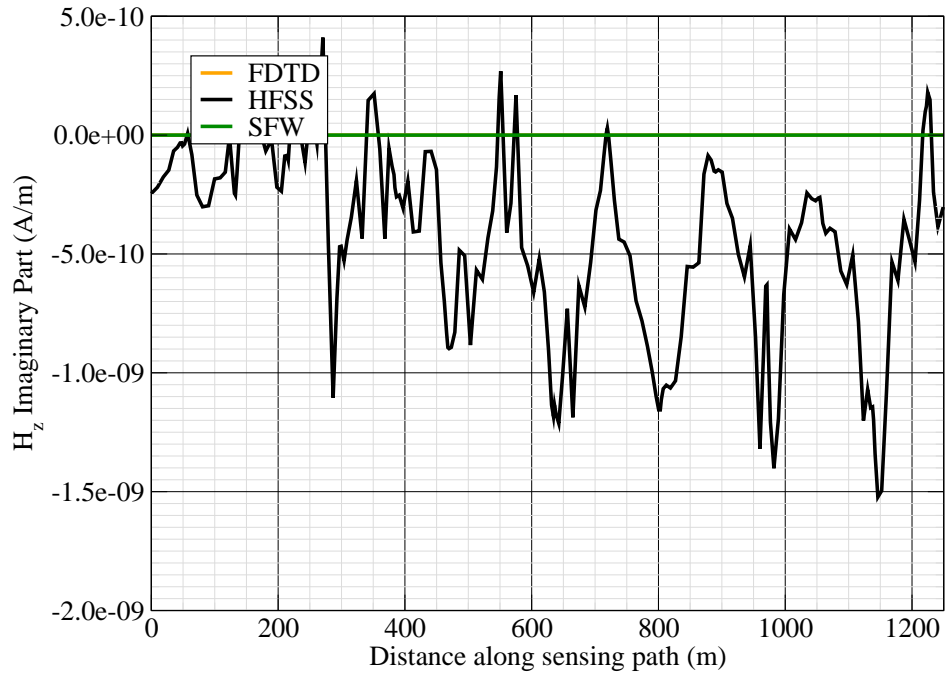


Figure 14: H_z imag.

Canonical Complex

Experiment 10

Experiment Date: November 2, 2011

1 Discussion

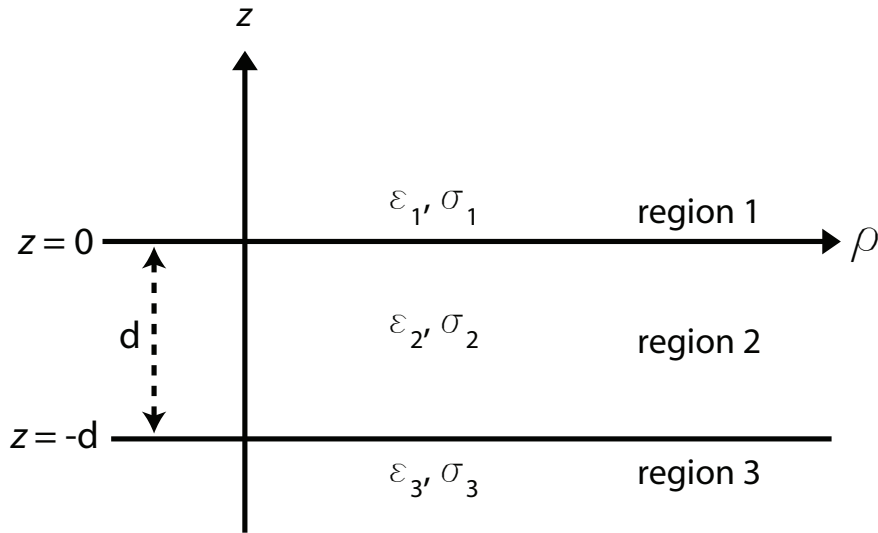


Figure 1: 3-layer topology.

Source Parameters

- Source Type: VED (plates 0.6 m by 0.3 m separated by 4 m).
- Source Strength: 14.68 A-m.
- $f = 1000$ Hz.

Environment

- Water thickness: $d = 180$ m
- Air: $\sigma_1 = 0$ S/m and $\epsilon_{r1} = 1$
- Water: $\sigma_2 = 0.01$ S/m and $\epsilon_{r2} = 81$
- Mud: $\sigma_3 = 0.0012$ S/m and $\epsilon_{r3} = 1$

Table 1: Simulation Details

	FDTD	HFSS	QES/SFW
Domain Size	$200 \times 200 \times 120$ cells	34193 tets	N/A
Cell Size (m)	$5 \times 5 \times 5$	N/A	N/A
Time Step (ns)	9.6	N/A	N/A
Run Time (Hrs)	6	0.05	< 1 min

Comments

- Computational time is based on actual elapsed real time. This number is highly subjective and based on how many other applications might be running at a particular time. However, the reported number is an indication of the amount of time typically needed for a particular simulation. The computer specs are: 16 CPU cores at 2.8 GHz.
- Run times for HFSS are given for a single frequency.
- QES is not applicable for magnetic fields using electric source excitation.

2 Simulation Variables

Sensor_P1(x,y,z) [m]	(-200,57.1571,75)
Sensor_P2(x,y,z) [m]	(114.1593,44.8169,75)
Source_P1(x,y,z) [m]	(100.5,0,-30)
Source_P2(x,y,z) [m]	(100.5,0,-30)
Source_Plate_Separation [m]	4
Source_Size [m X m X #]	[0.6 X 0.3 X 1]
Source_Heading [deg]	NaN
Source_Voltage [V Peak]	NaN
Source_Current [A Peak]	3.67
Source_Frequency [Hz]	1000
--- Extra Information ---	
Source_Heading_Bounds [deg]	(N/A)
Average_Boat_Speed [m/s]	NaN
Source_Type	Electric vert_truss (vert_truss)
Sensor_Type	EMA
Bin_Size [sec]	1
Number_of_Datapoints	200
Lake_Origin (Easting,Northing)	NaN
Analysis_Date	6-Oct-2011

3 Boat Path

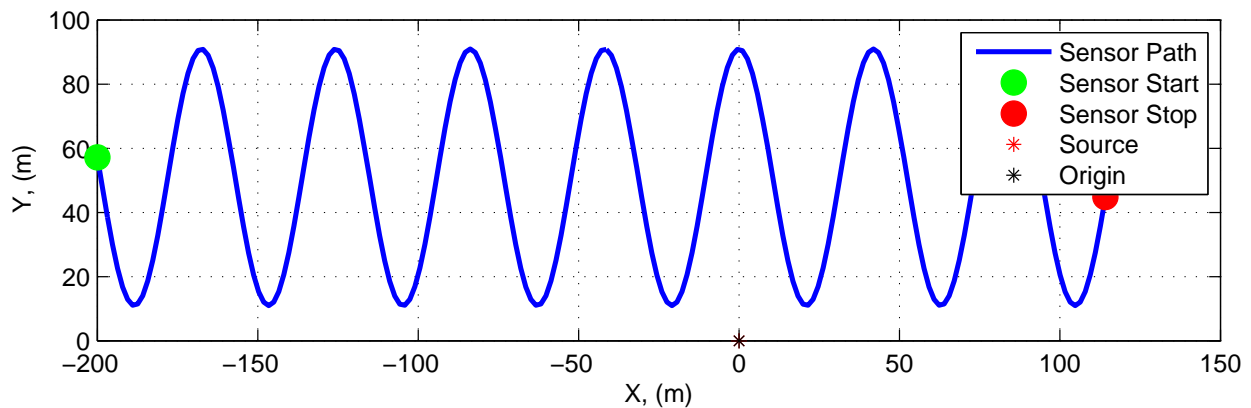


Figure 2: Source and sensor relationship.

4 Plots

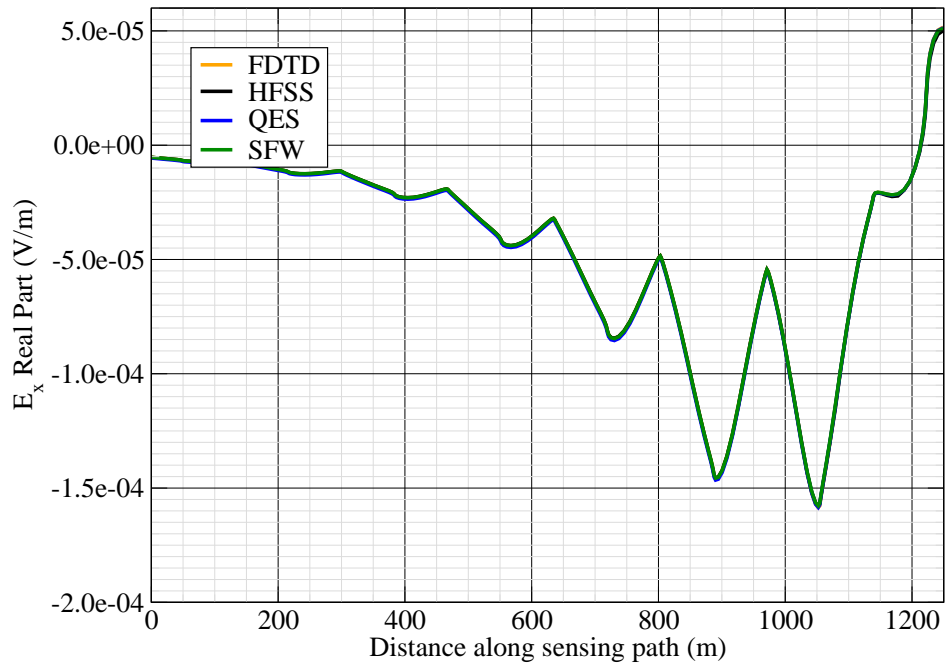


Figure 3: E_x real.

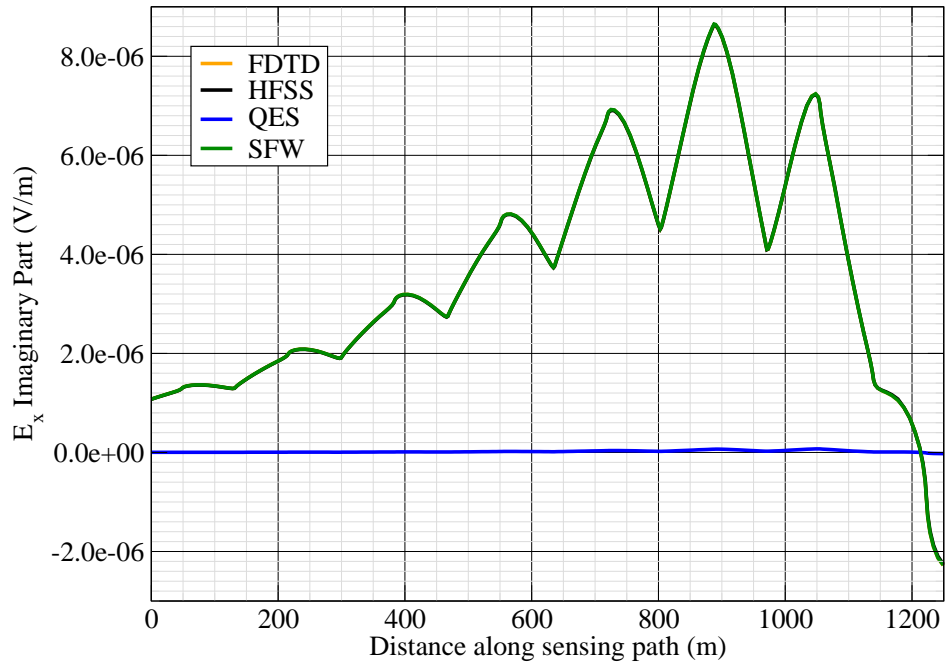


Figure 4: E_x imag.

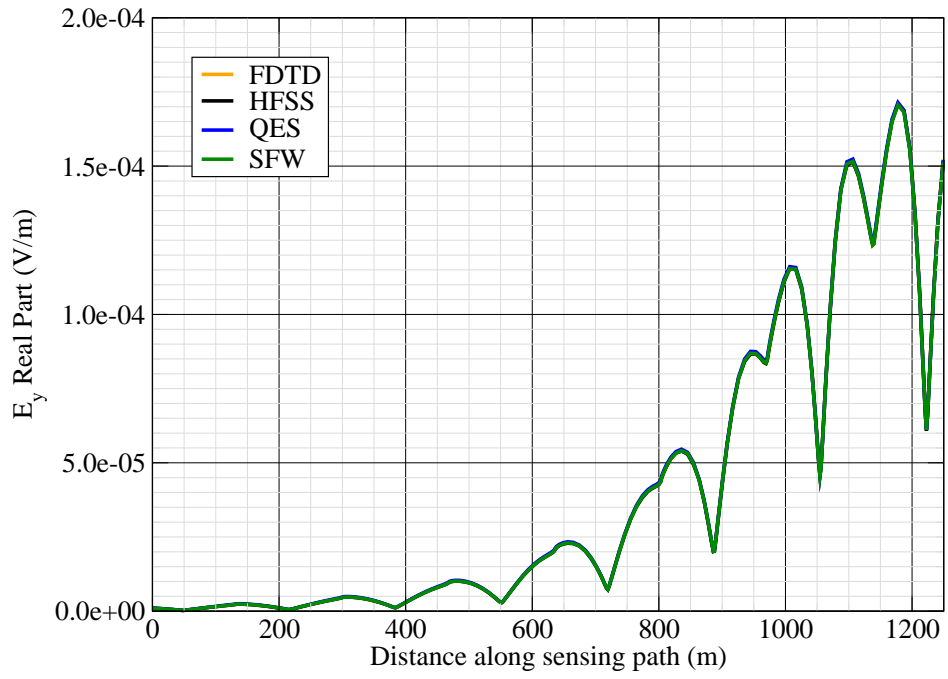


Figure 5: E_y real.

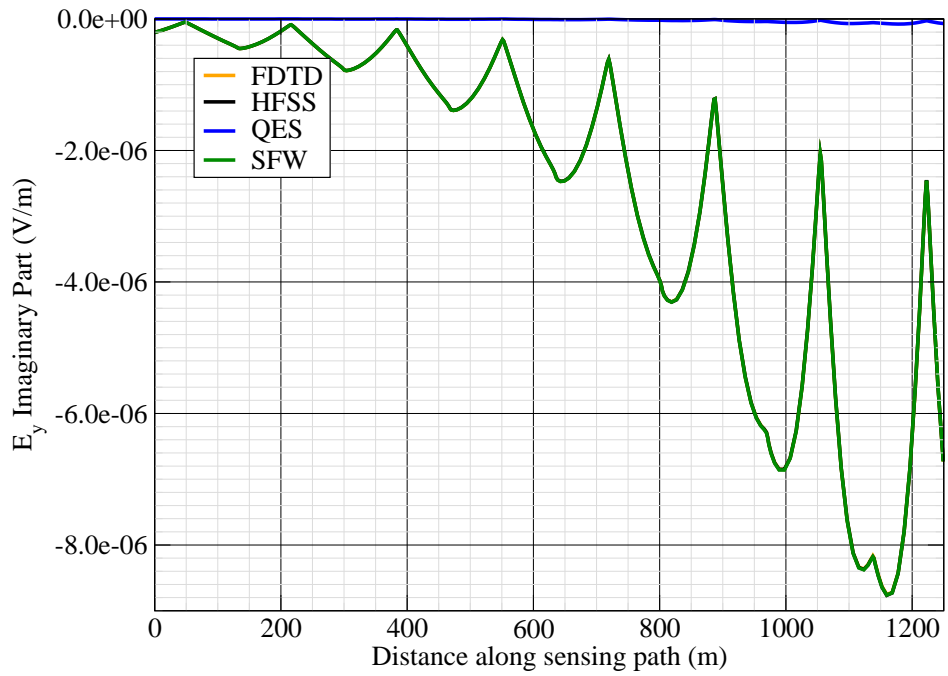


Figure 6: E_y imag.

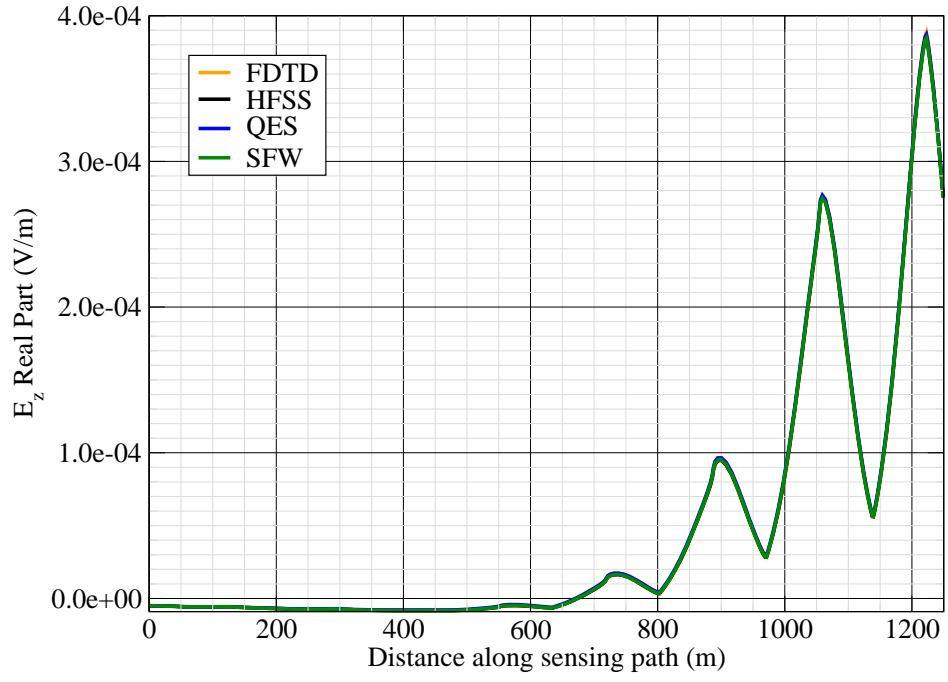


Figure 7: E_z real.

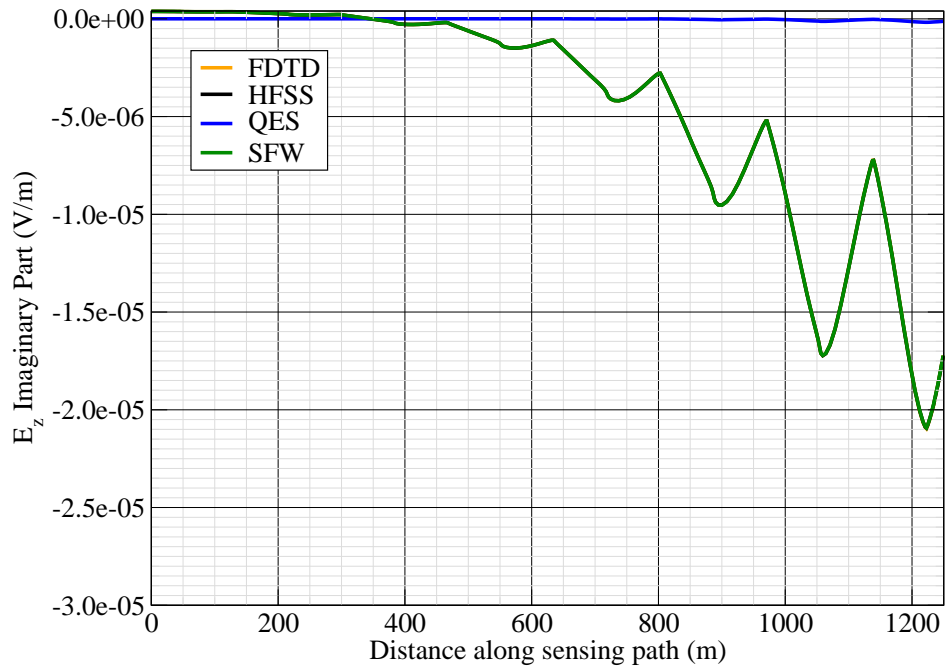


Figure 8: E_z imag.

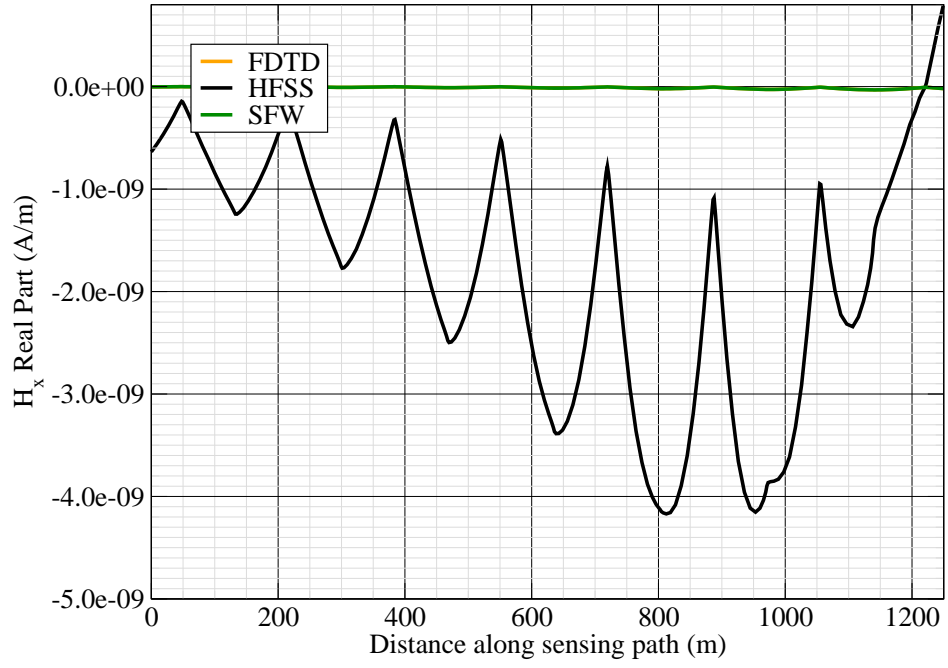


Figure 9: H_x real.

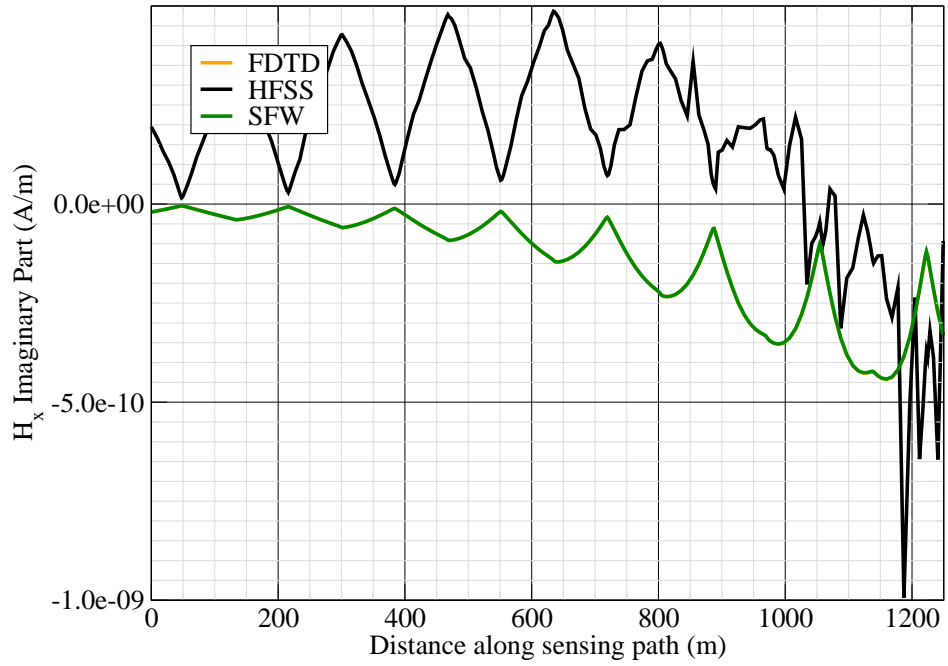


Figure 10: H_x imag.

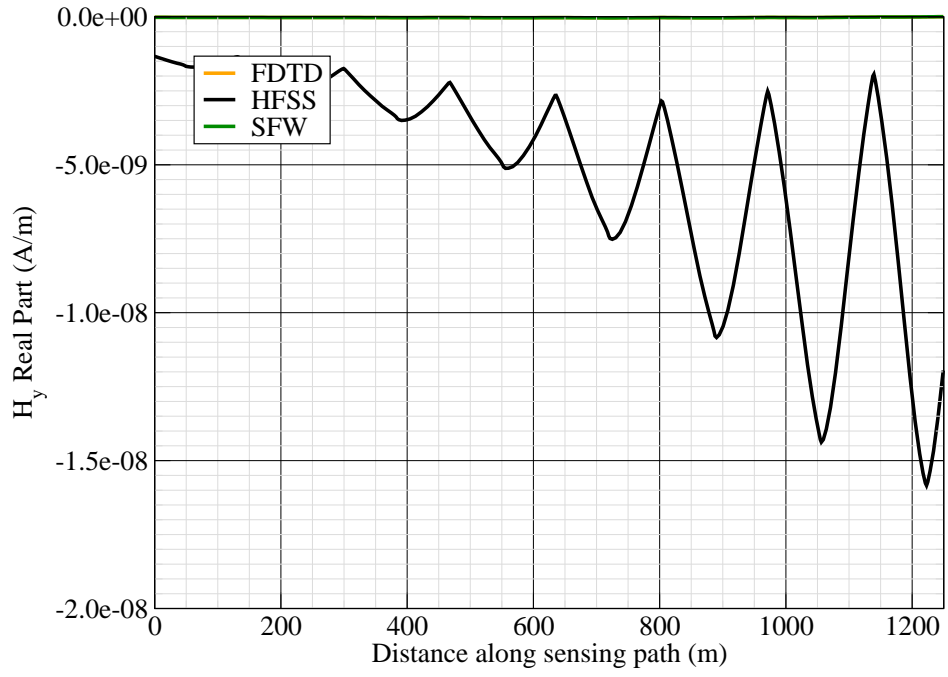


Figure 11: H_y real.

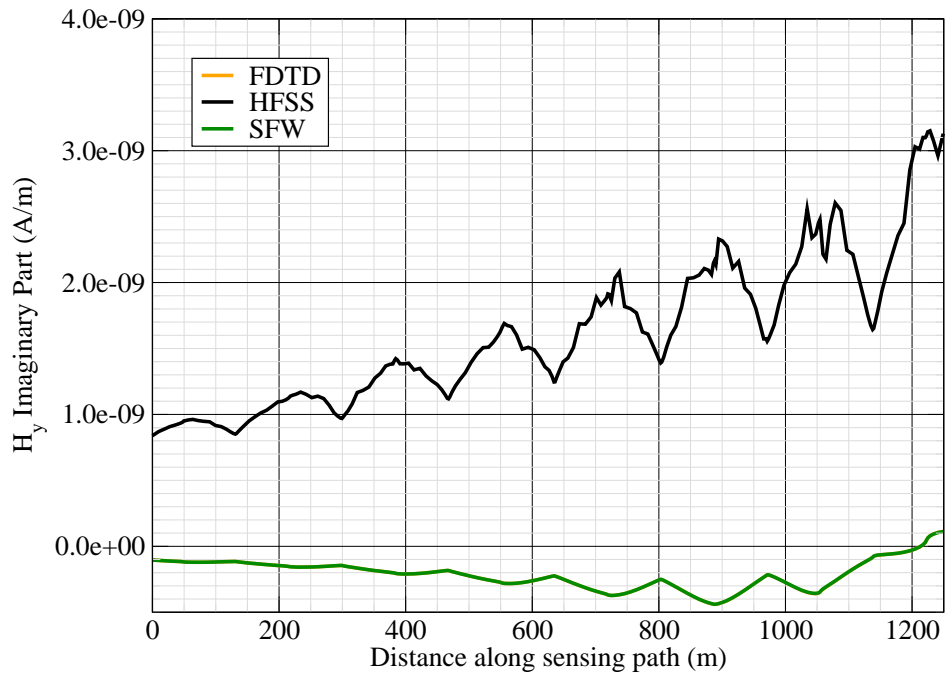


Figure 12: H_y imag.

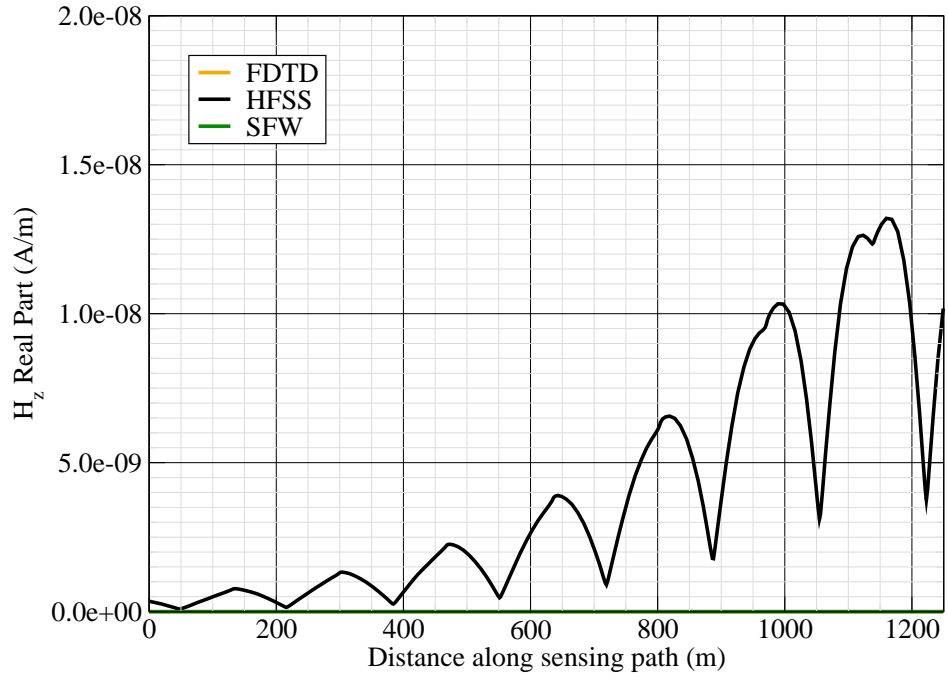


Figure 13: H_z real.

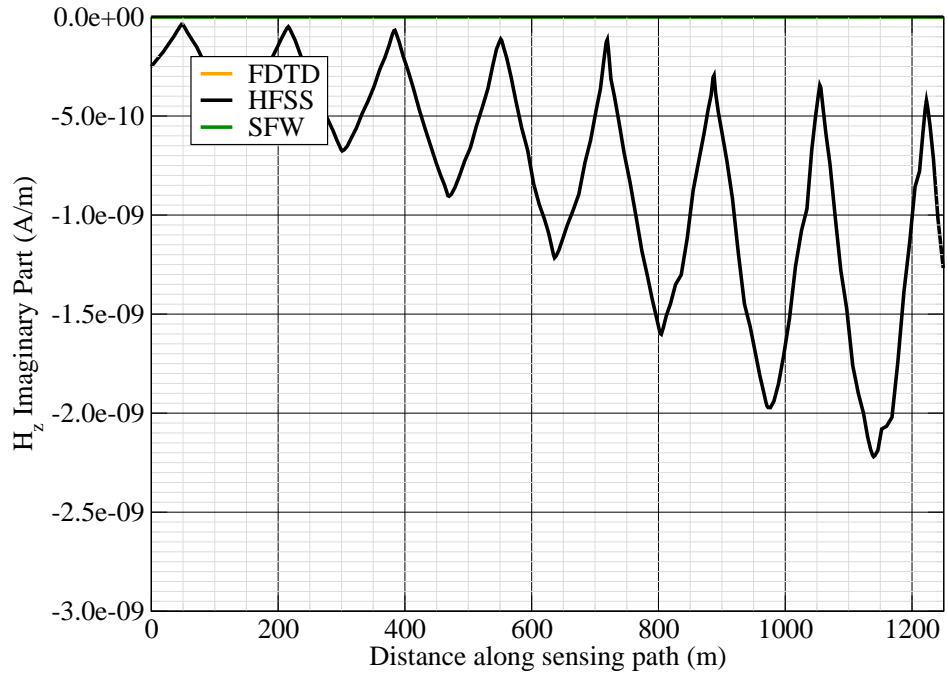


Figure 14: H_z imag.

Canonical Complex

Experiment 11

Experiment Date: November 2, 2011

1 Discussion

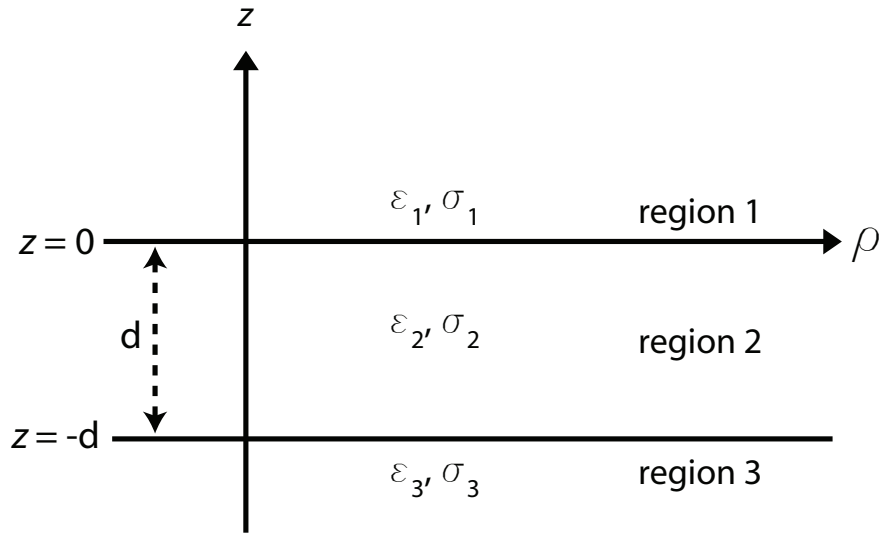


Figure 1: 3-layer topology.

Source Parameters

- Source Type: HMD (Coil: 3.66 m by 3.66 m with 12 turns).
- Source Strength: 3,683 A-m².
- f = 1000 Hz.

Environment

- Water thickness: $d = 180$ m
- Air: $\sigma_1 = 0$ S/m and $\epsilon_{r1} = 1$
- Water: $\sigma_2 = 0.01$ S/m and $\epsilon_{r2} = 81$
- Mud: $\sigma_3 = 0.0012$ S/m and $\epsilon_{r3} = 1$

Table 1: Simulation Details

	FDTD	HFSS	QES/SFW
Domain Size	$400 \times 200 \times 120$ cells	21175 tets	N/A
Cell Size (m)	$5 \times 5 \times 5$	N/A	N/A
Time Step (ns)	9.6	N/A	N/A
Run Time (Hrs)	12h 48m	0.03	< 1 min

Comments

- Computational time is based on actual elapsed real time. This number is highly subjective and based on how many other applications might be running at a particular time. However, the reported number is an indication of the amount of time typically needed for a particular simulation. The computer specs are: 16 CPU cores at 2.8 GHz.
- Run times for HFSS are given for a single frequency.
- QES is not applicable for magnetic fields using electric source excitation.

2 Simulation Variables

Sensor_P1(x,y,z) [m]	(-628.3185,0,-15.747)
Sensor_P2(x,y,z) [m]	(628.3185,0,-15.747)
Source_P1(x,y,z) [m]	(0,0,8.2296)
Source_P2(x,y,z) [m]	(0,0,8.2296)
Source_Plate_Separation [m]	N/A
Source_Size [m X m X #]	[3.658 X 3.658 X 12]
Source_Heading [deg]	45
Source_Voltage [V Peak]	11.6294
Source_Current [A Peak]	22.9361
Source_Frequency [Hz]	1000

--- Extra Information ---

Source_Heading_Bounds [deg]	(N/A)
Average_Boat_Speed [m/s]	NaN
Source_Type	Magnetic source (portable)
Sensor_Type	PEMA
Bin_Size [sec]	1
Number_of_Datapoints	200
Lake_Origin (Easting,Northing)	NaN
Analysis_Date	7-Oct-2011

3 Boat Path

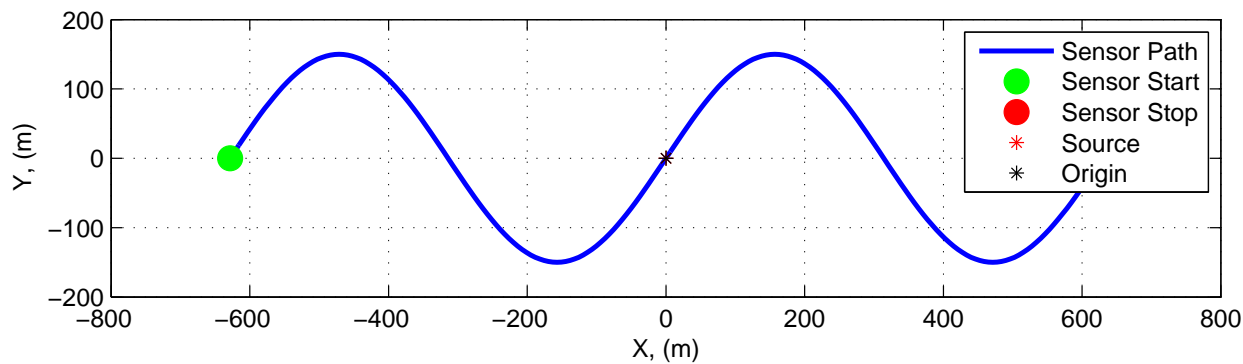


Figure 2: Source and sensor relationship.

4 Plots

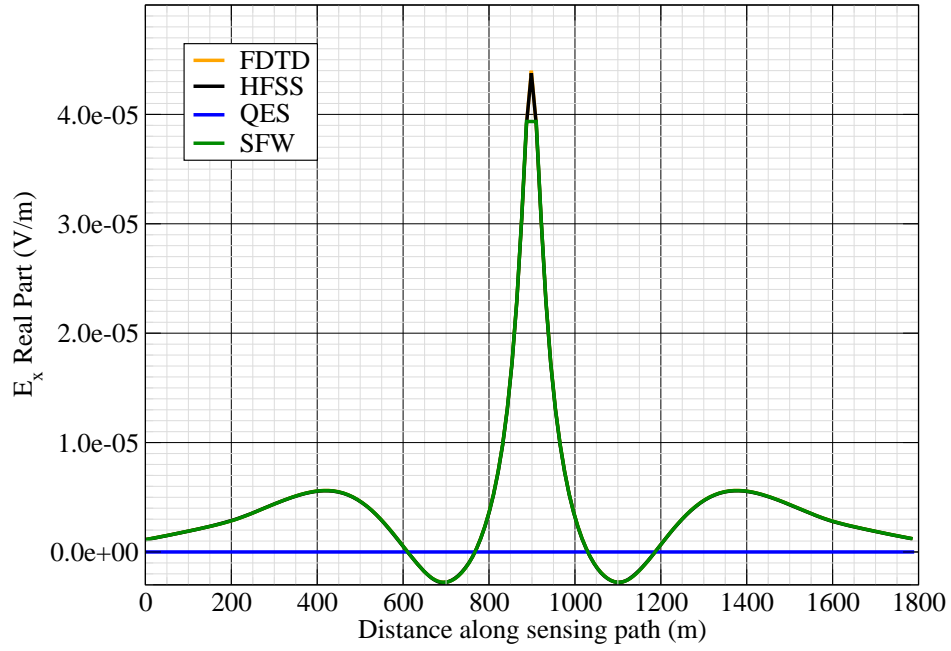


Figure 3: E_x real.

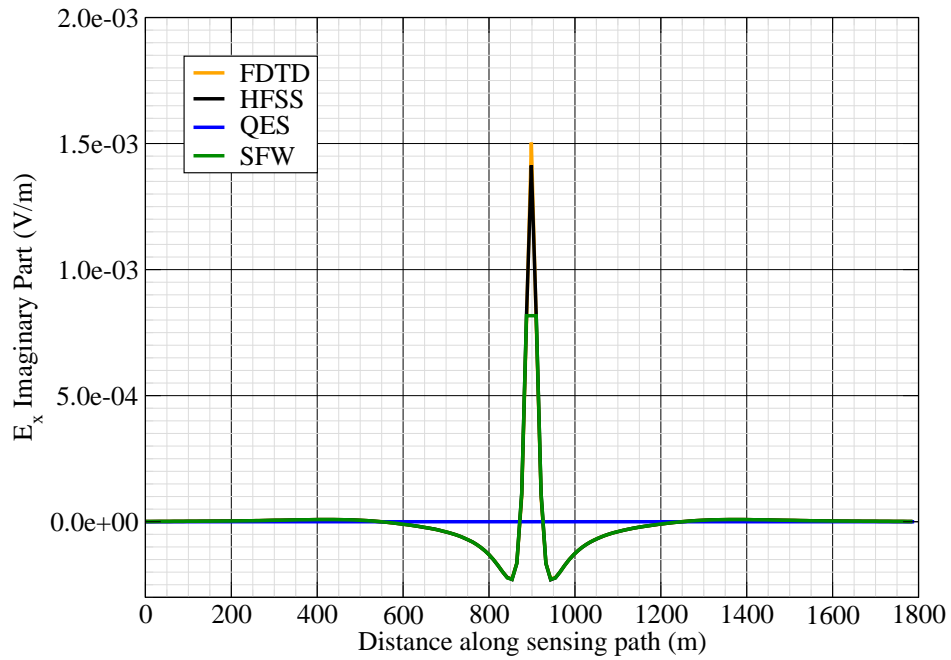


Figure 4: E_x imag.

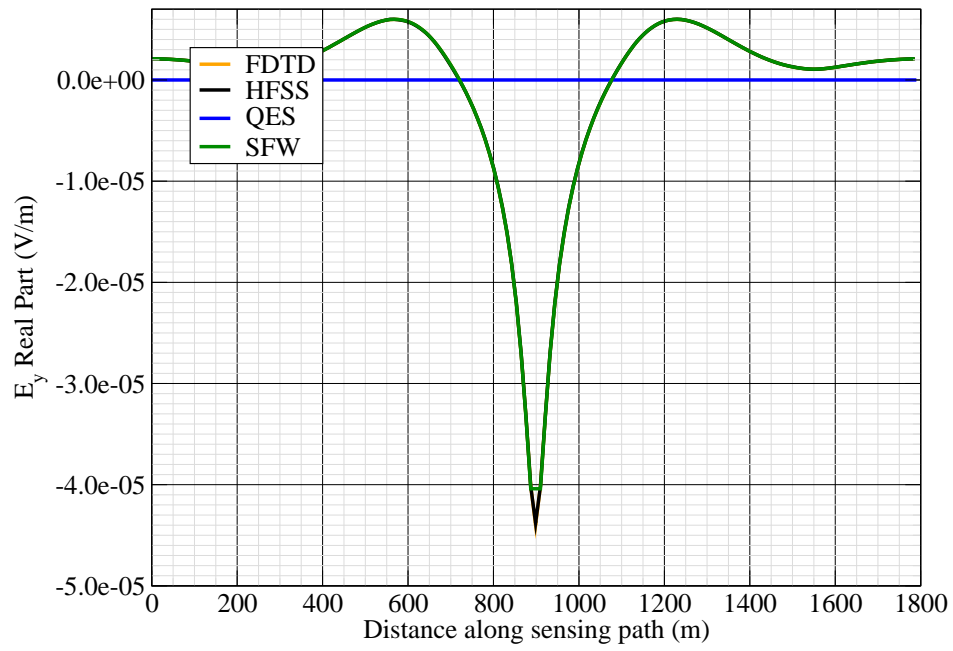


Figure 5: E_y real.

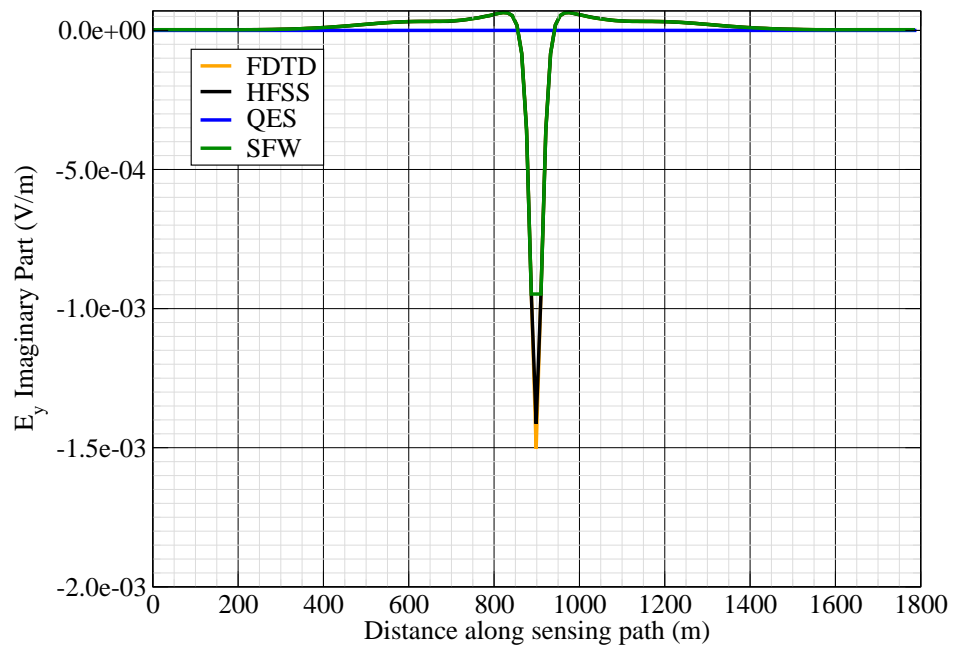


Figure 6: E_y imag.

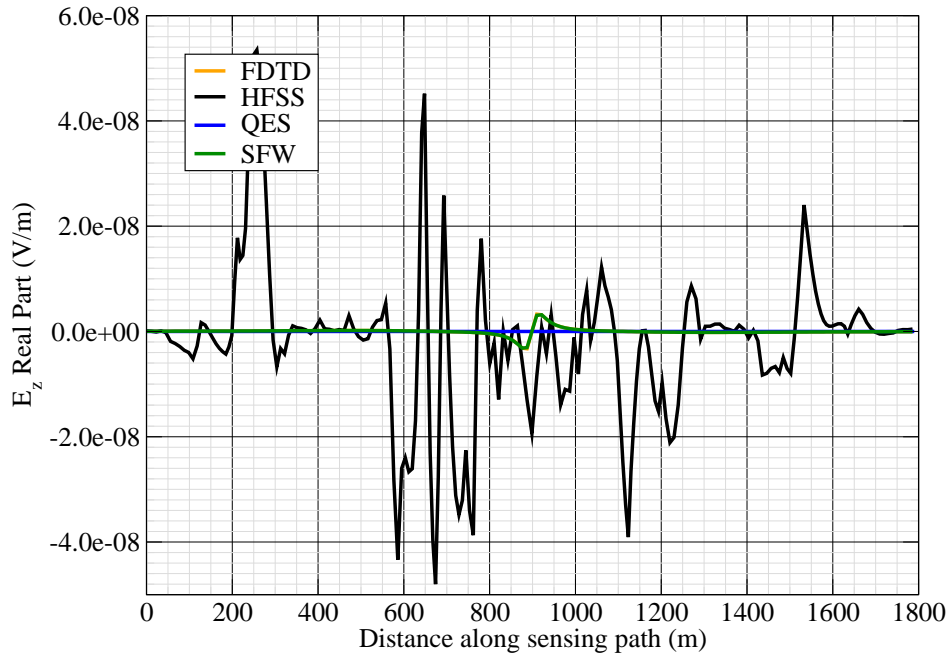


Figure 7: E_z real.

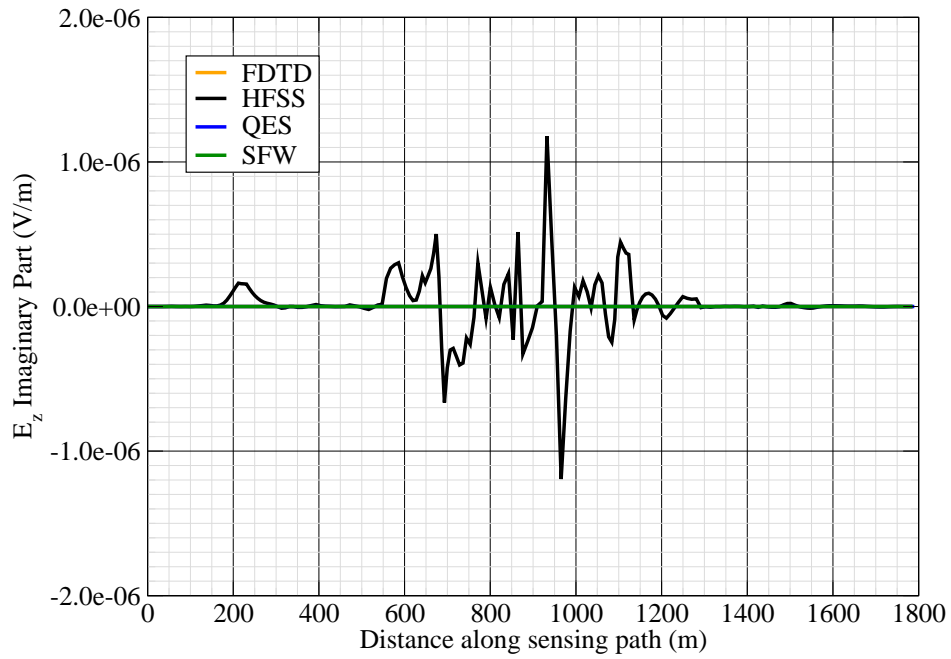


Figure 8: E_z imag.

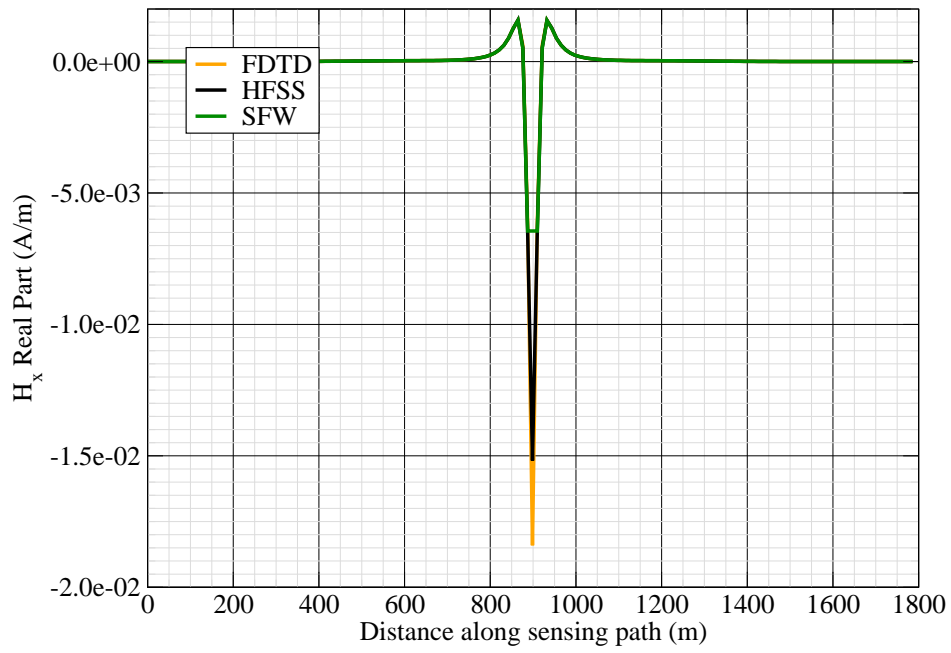


Figure 9: H_x real.

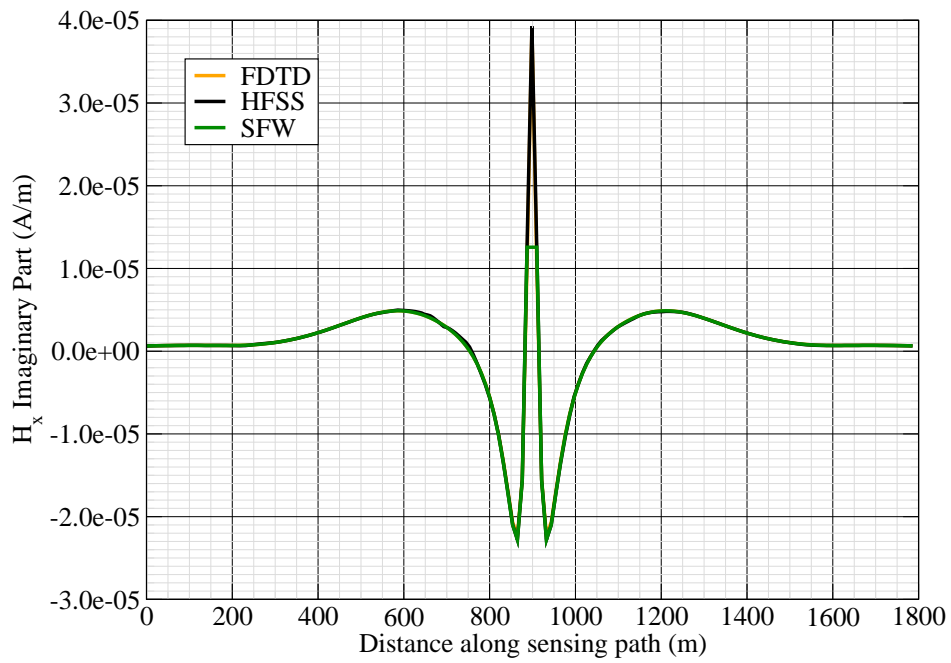


Figure 10: H_x imag.

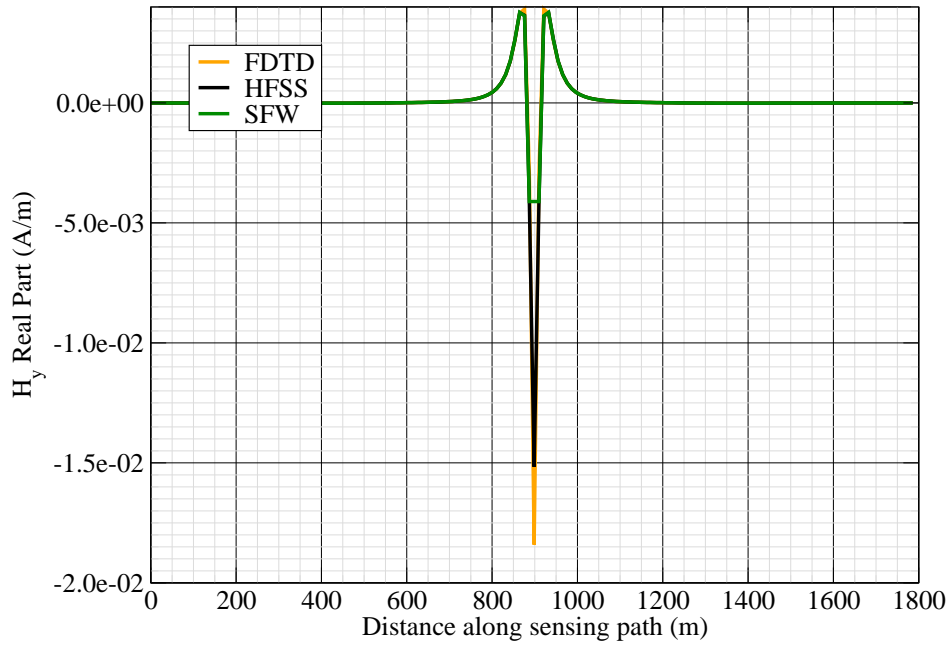


Figure 11: H_y real.

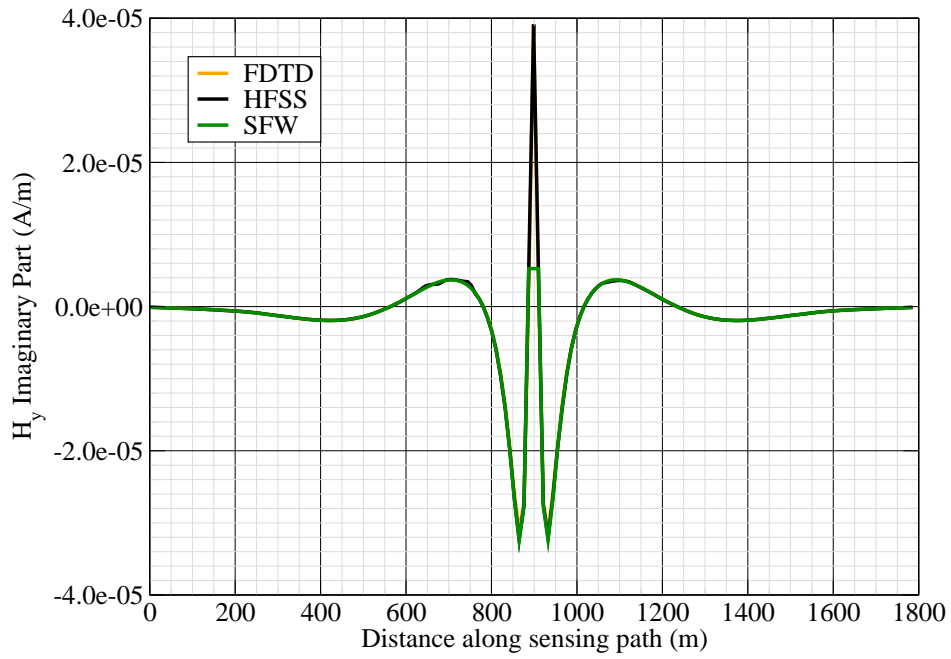


Figure 12: H_y imag.

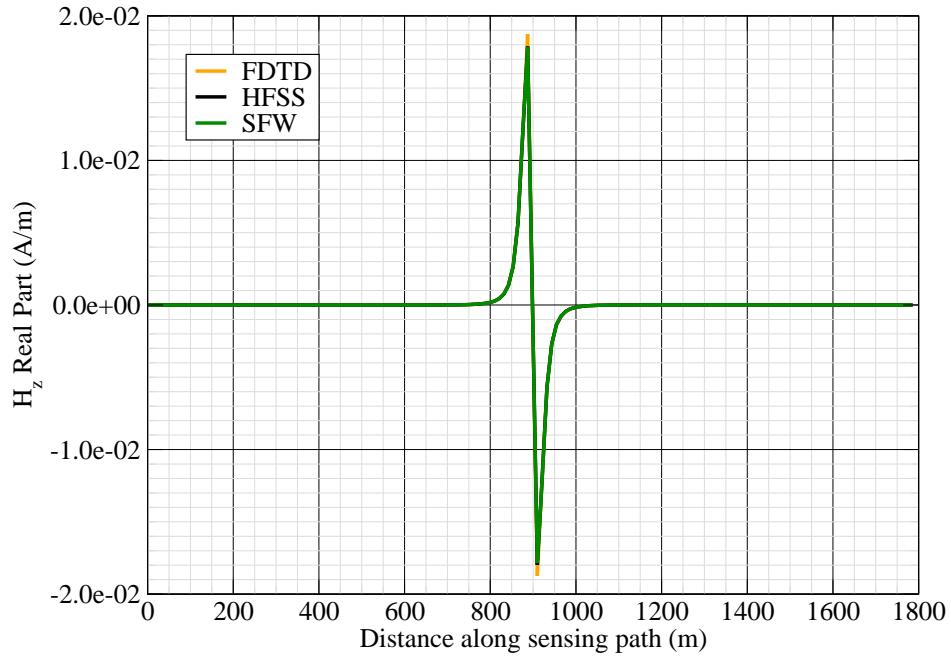


Figure 13: H_z real.

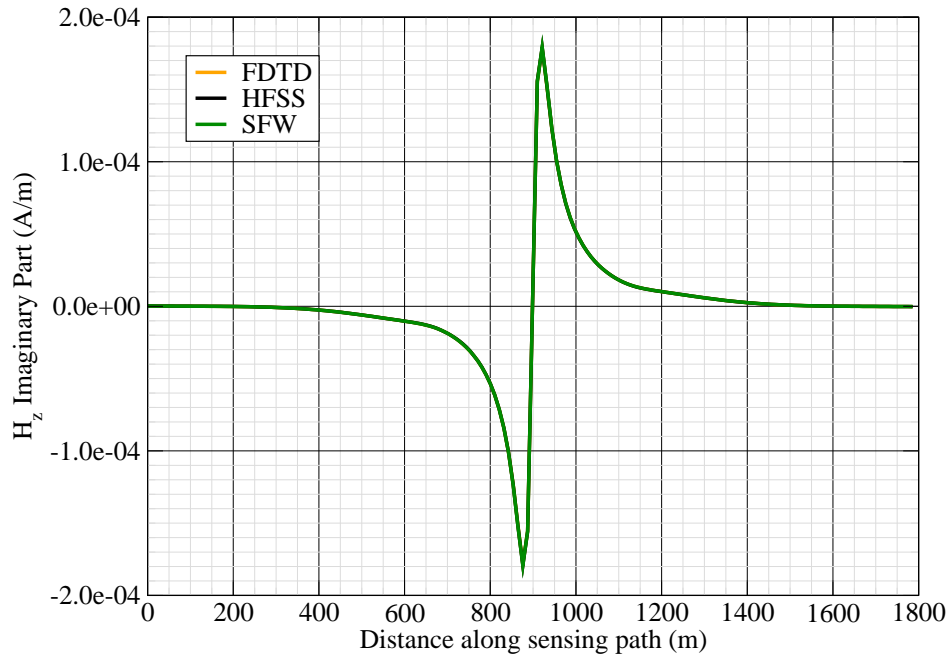


Figure 14: H_z imag.

Canonical Complex

Experiment 12

Experiment Date: November 2, 2011

1 Discussion

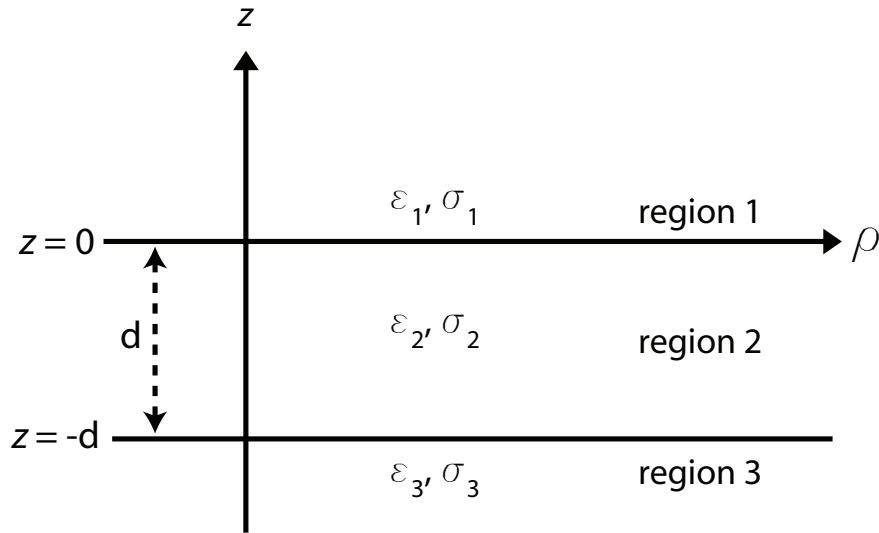


Figure 1: 3-layer topology.

Source Parameters

- Source Type: HMD (Coil: 3.66 m by 3.66 m with 12 turns).
- Source Strength: 3,683 A-m².
- f = 1000 Hz.

Environment

- Water thickness: $d = 180$ m
- Air: $\sigma_1 = 0$ S/m and $\epsilon_{r1} = 1$
- Water: $\sigma_2 = 0.01$ S/m and $\epsilon_{r2} = 81$
- Mud: $\sigma_3 = 0.0012$ S/m and $\epsilon_{r3} = 1$

Table 1: Simulation Details

	FDTD	HFSS	QES/SFW
Domain Size	$400 \times 200 \times 120$ cells	18374 tets	N/A
Cell Size (m)	$5 \times 5 \times 5$	N/A	N/A
Time Step (ns)	9.6	N/A	N/A
Run Time (Hrs)	12h 55m	0.03	< 1 min

Comments

- Computational time is based on actual elapsed real time. This number is highly subjective and based on how many other applications might be running at a particular time. However, the reported number is an indication of the amount of time typically needed for a particular simulation. The computer specs are: 16 CPU cores at 2.8 GHz.
- Run times for HFSS are given for a single frequency.
- QES is not applicable for magnetic fields using electric source excitation.

2 Simulation Variables

Sensor_P1(x,y,z) [m]	(-628.3185,0,15.747)
Sensor_P2(x,y,z) [m]	(628.3185,0,15.747)
Source_P1(x,y,z) [m]	(0,0,-8.2296)
Source_P2(x,y,z) [m]	(0,0,-8.2296)
Source_Plate_Separation [m]	N/A
Source_Size [m X m X #]	[3.658 X 3.658 X 12]
Source_Heading [deg]	45
Source_Voltage [V Peak]	11.6294
Source_Current [A Peak]	22.9361
Source_Frequency [Hz]	1000
--- Extra Information ---	
Source_Heading_Bounds [deg]	(N/A)
Average_Boat_Speed [m/s]	NaN
Source_Type	Magnetic source (portable)
Sensor_Type	PEMA
Bin_Size [sec]	1
Number_of_Datapoints	200
Lake_Origin (Easting,Northing)	NaN
Analysis_Date	7-Oct-2011

3 Boat Path

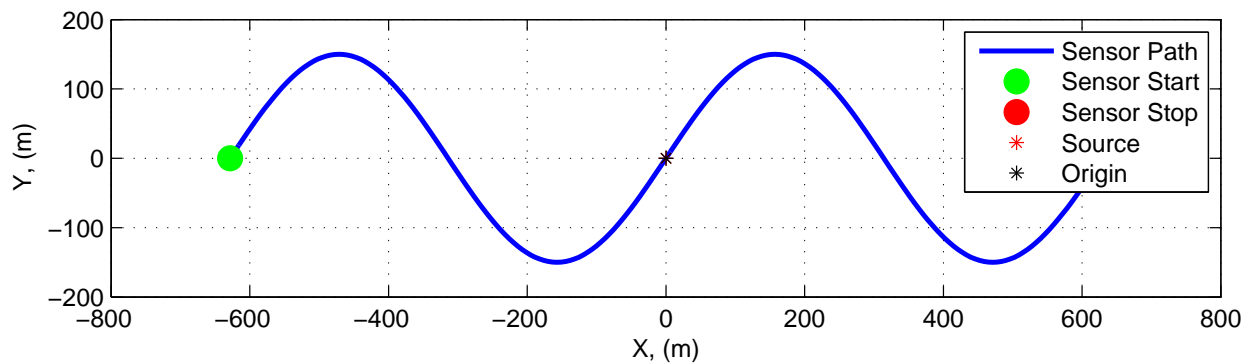


Figure 2: Source and sensor relationship.

4 Plots

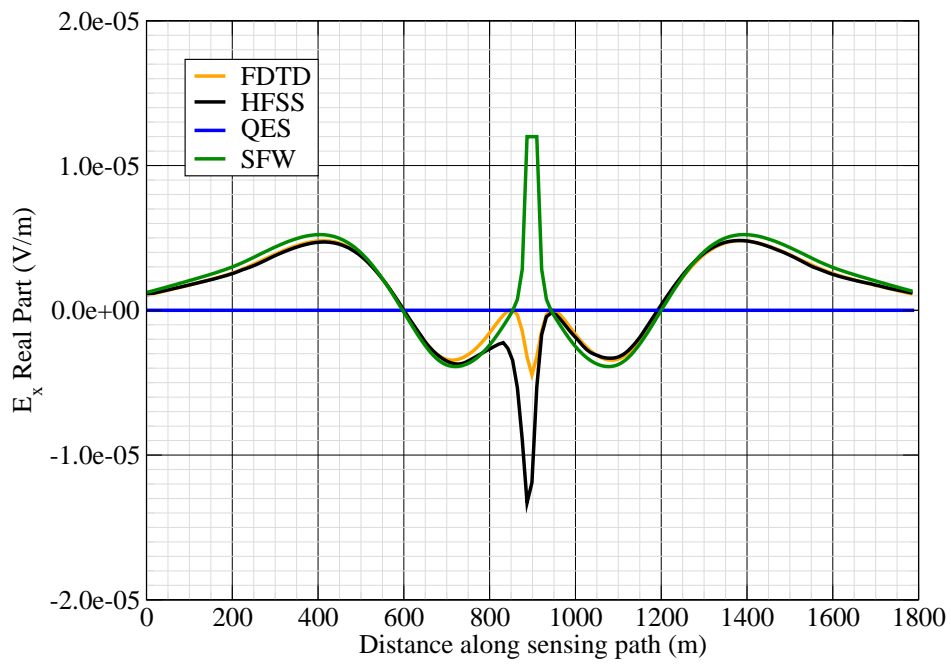


Figure 3: E_x real.

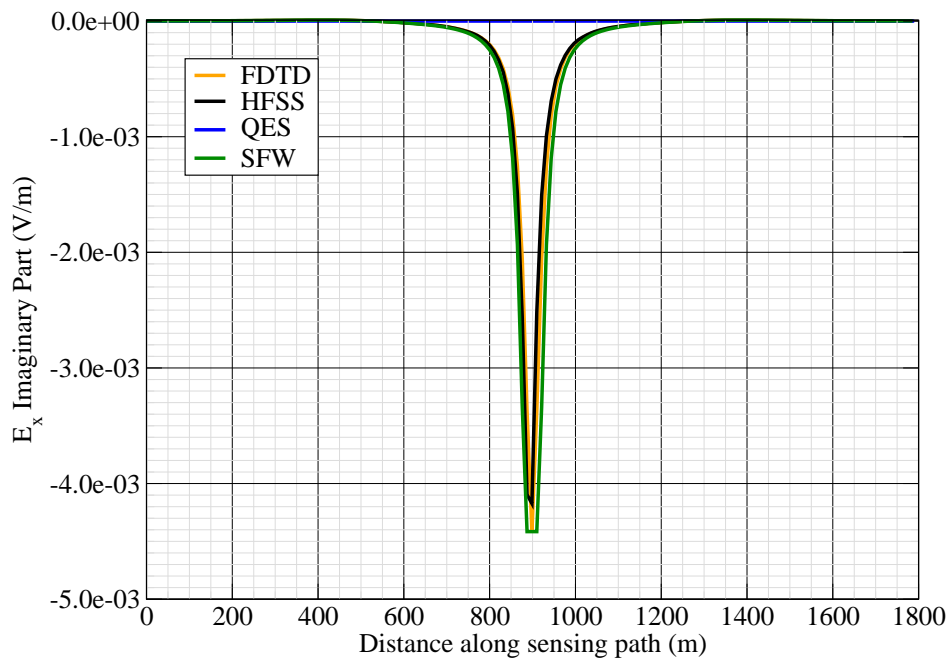


Figure 4: E_x imag.

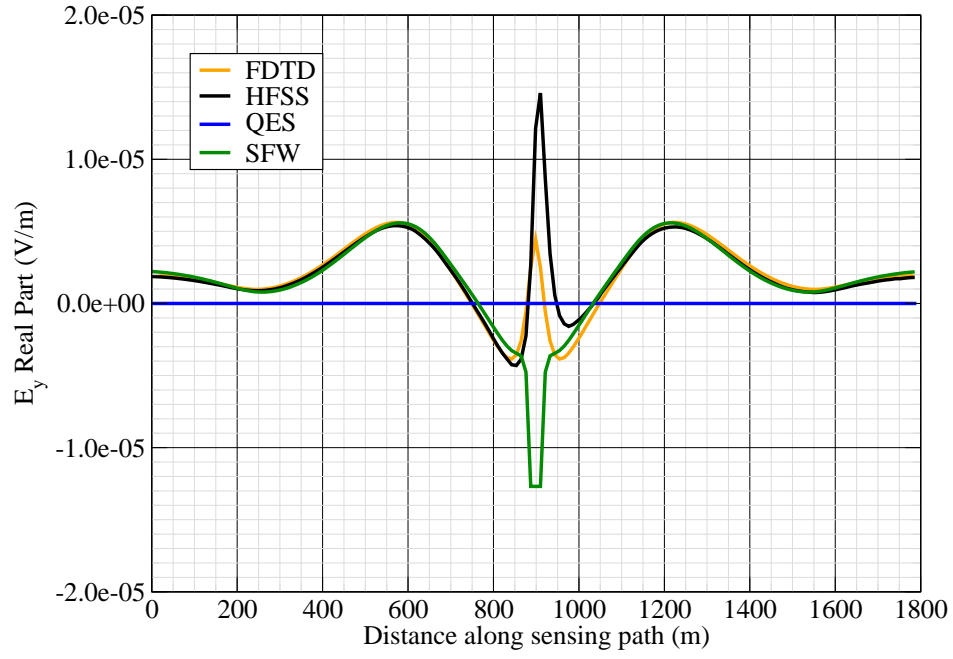


Figure 5: E_y real.

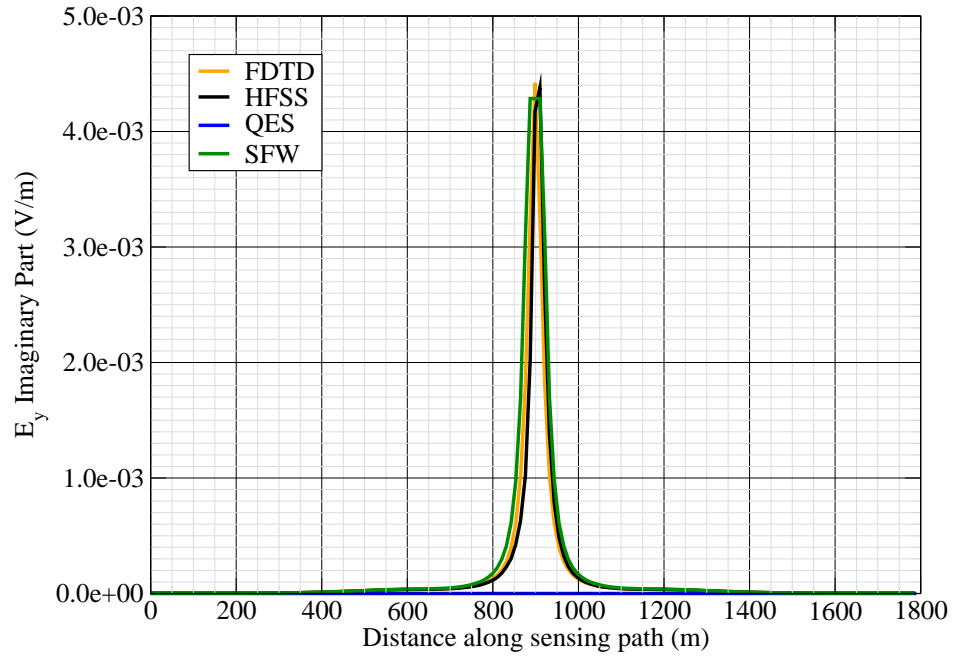


Figure 6: E_y imag.

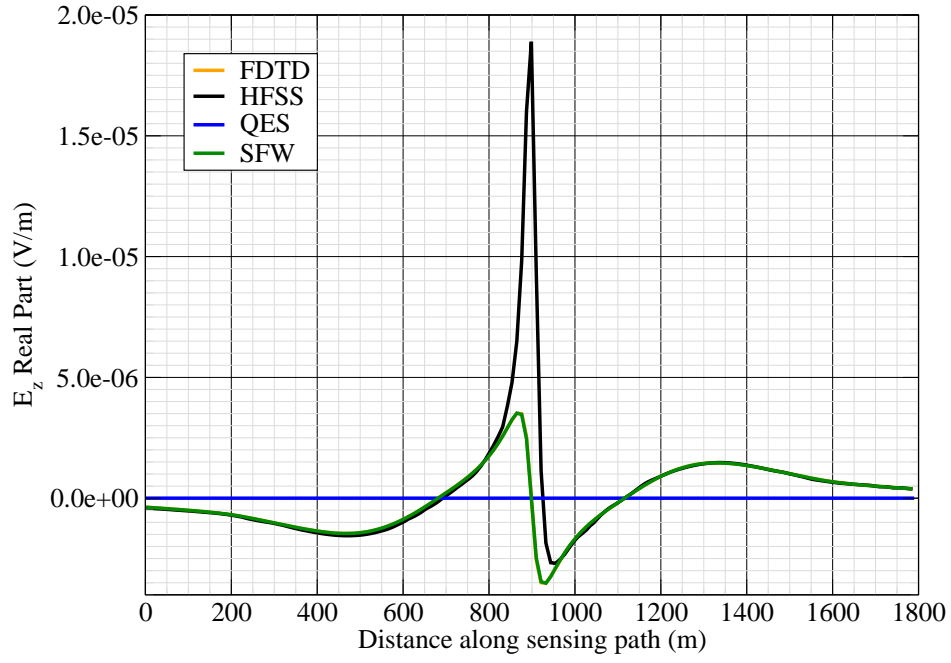


Figure 7: E_z real.

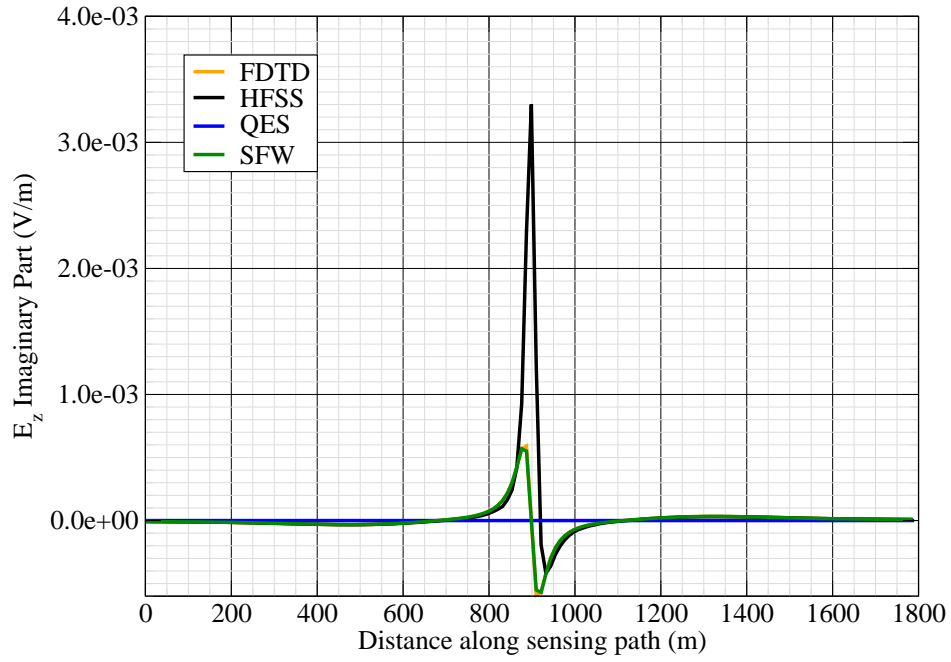


Figure 8: E_z imag.

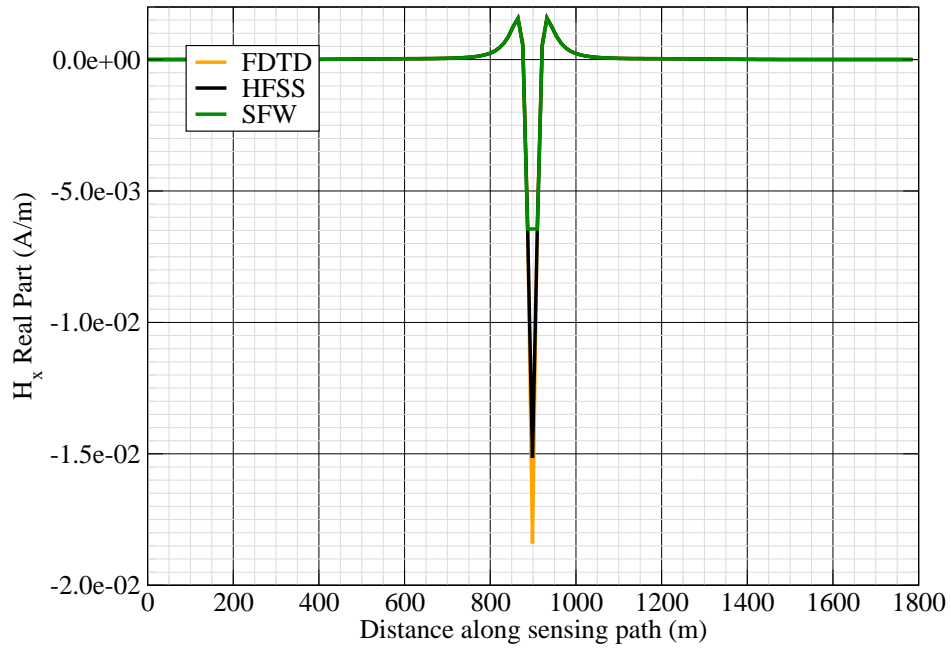


Figure 9: H_x real.

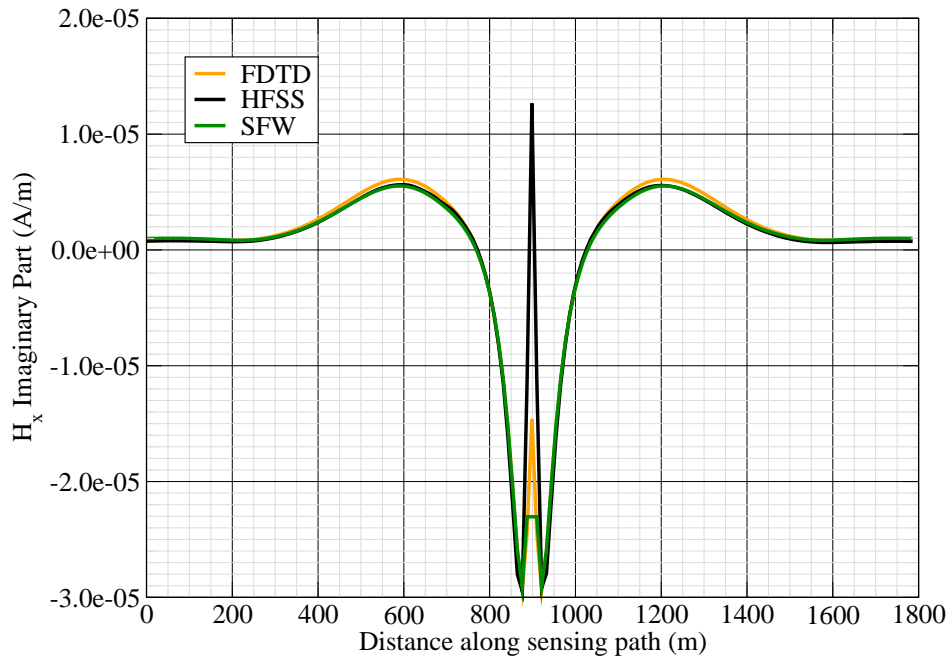


Figure 10: H_x imag.

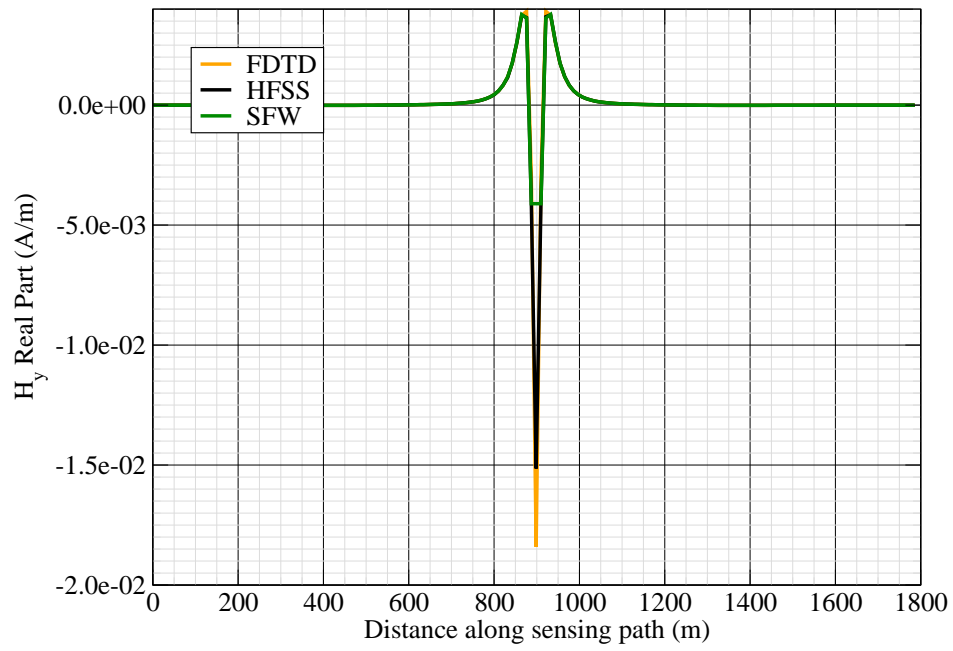


Figure 11: H_y real.

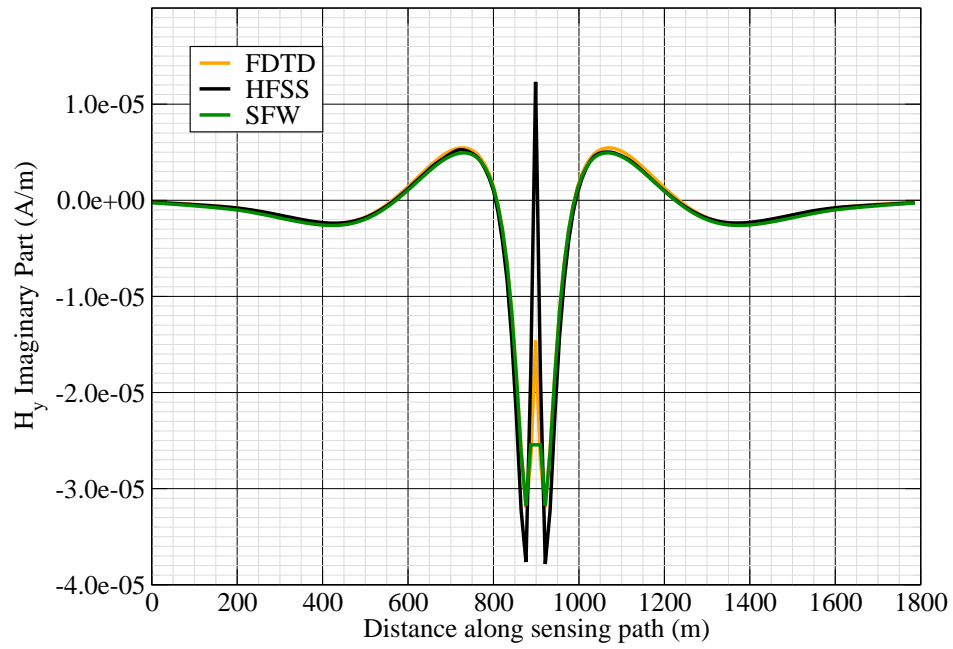


Figure 12: H_y imag.

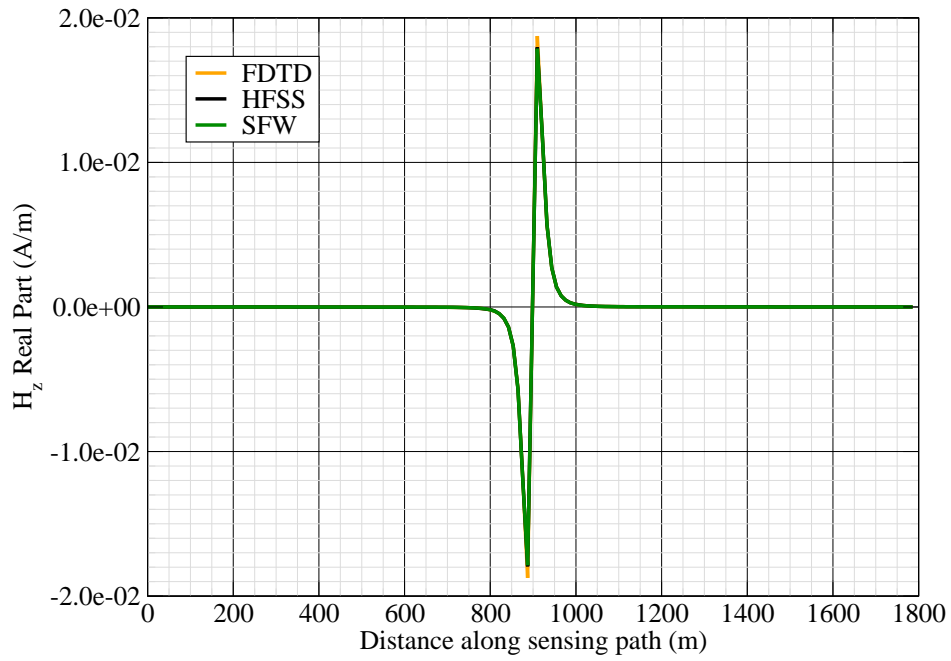


Figure 13: H_z real.

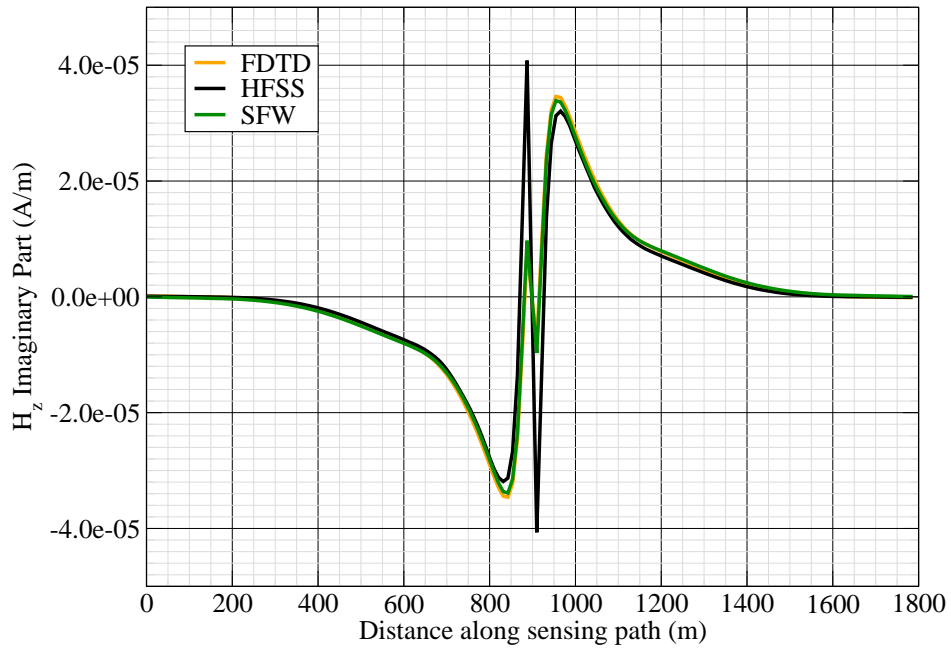


Figure 14: H_z imag.

Canonical Complex

Experiment 13

Experiment Date: November 2, 2011

1 Discussion

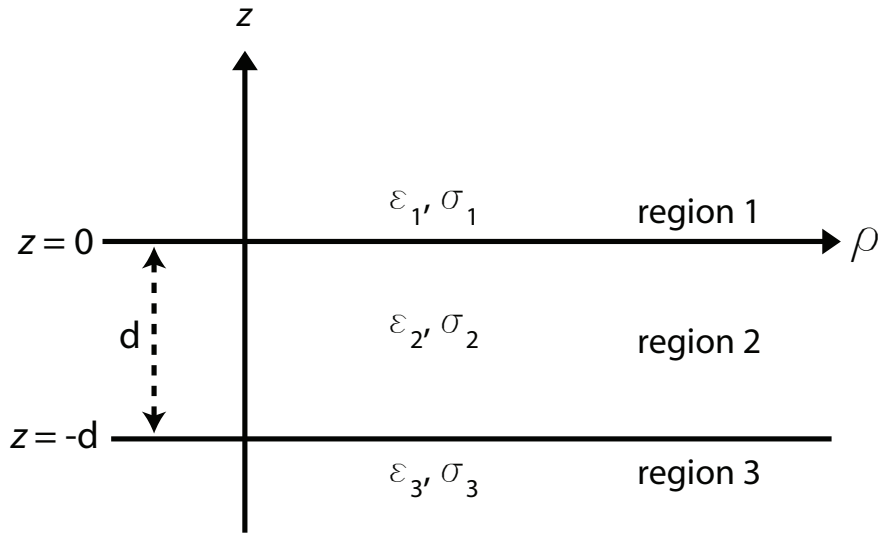


Figure 1: 3-layer topology.

Source Parameters

- Source Type: HMD (Coil: 3.66 m by 3.66 m with 12 turns).
- Source Strength: 3,683 A-m².
- f = 1000 Hz.

Environment

- Water thickness: $d = 180$ m
- Air: $\sigma_1 = 0$ S/m and $\epsilon_{r1} = 1$
- Water: $\sigma_2 = 0.01$ S/m and $\epsilon_{r2} = 81$
- Mud: $\sigma_3 = 0.0012$ S/m and $\epsilon_{r3} = 1$

Table 1: Simulation Details

	FDTD	HFSS	QES/SFW
Domain Size	$400 \times 200 \times 120$ cells	29189 tets	N/A
Cell Size (m)	$5 \times 5 \times 5$	N/A	N/A
Time Step (ns)	9.6	N/A	N/A
Run Time (Hrs)	13h 5m	0.05	< 1 min

Comments

- Computational time is based on actual elapsed real time. This number is highly subjective and based on how many other applications might be running at a particular time. However, the reported number is an indication of the amount of time typically needed for a particular simulation. The computer specs are: 16 CPU cores at 2.8 GHz.
- Run times for HFSS are given for a single frequency.
- QES is not applicable for magnetic fields using electric source excitation.

2 Simulation Variables

Sensor_P1(x,y,z) [m]	(-628.3185,0,-15.747)
Sensor_P2(x,y,z) [m]	(628.3185,0,-15.747)
Source_P1(x,y,z) [m]	(100.5,57,-8.2296)
Source_P2(x,y,z) [m]	(100.5,57,-8.2296)
Source_Plate_Separation [m]	N/A
Source_Size [m X m X #]	[3.658 X 3.658 X 12]
Source_Heading [deg]	180
Source_Voltage [V Peak]	11.6294
Source_Current [A Peak]	22.9361
Source_Frequency [Hz]	1000
--- Extra Information ---	
Source_Heading_Bounds [deg]	(N/A)
Average_Boat_Speed [m/s]	NaN
Source_Type	Magnetic source (portable)
Sensor_Type	PEMA
Bin_Size [sec]	1
Number_of_Datapoints	200
Lake-Origin (Easting,Northing)	NaN
Analysis_Date	7-Oct-2011

3 Boat Path

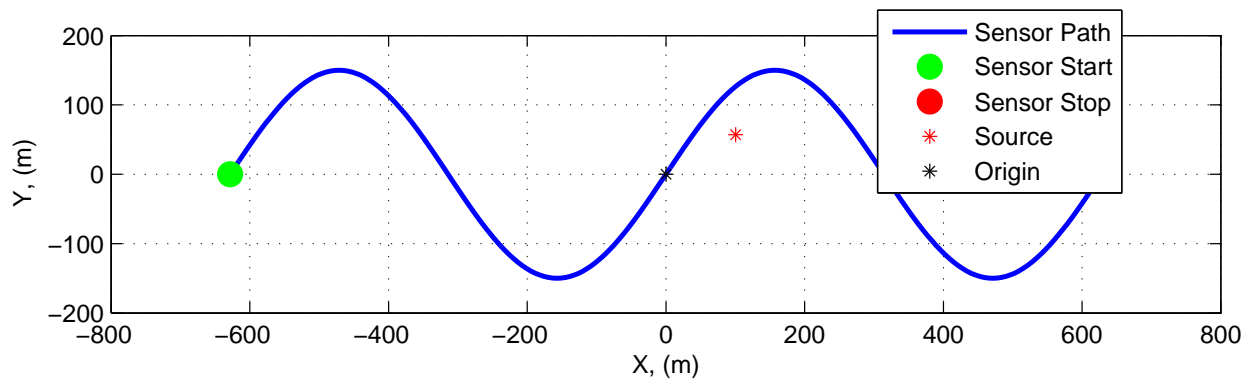


Figure 2: Source and sensor relationship.

4 Plots

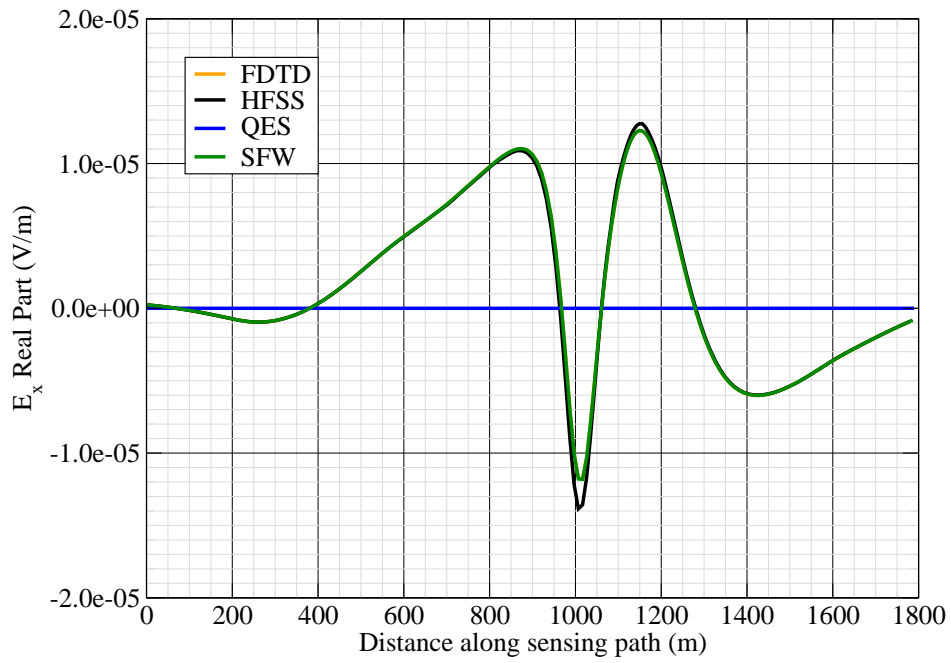


Figure 3: E_x real.

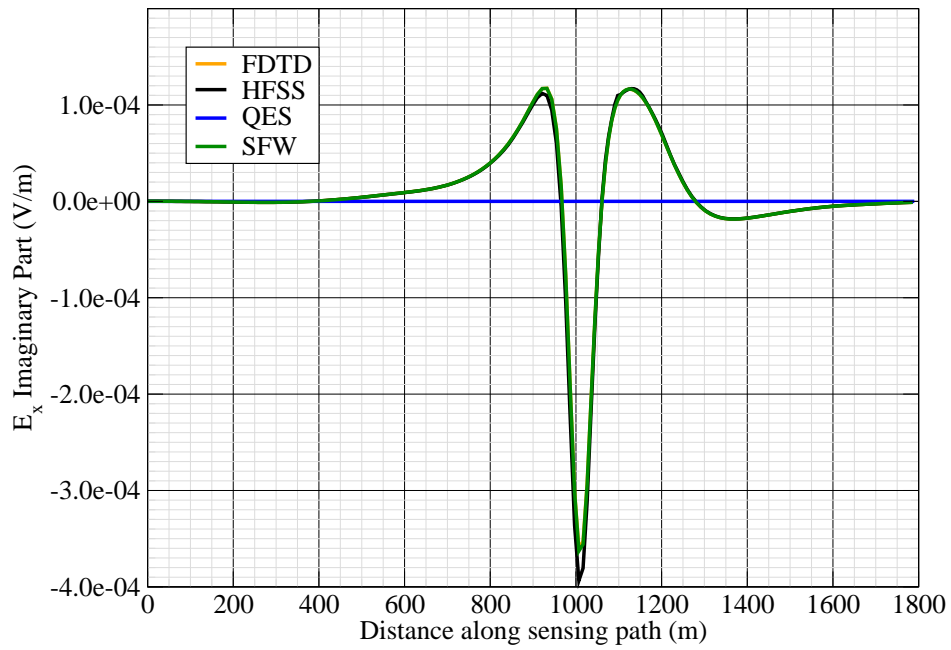


Figure 4: E_x imag.

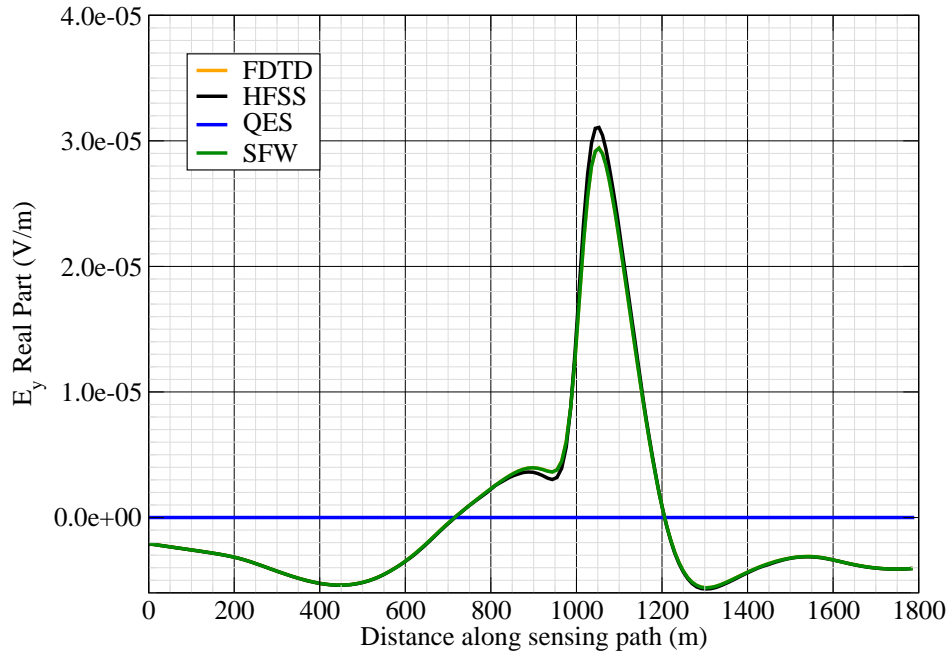


Figure 5: E_y real.

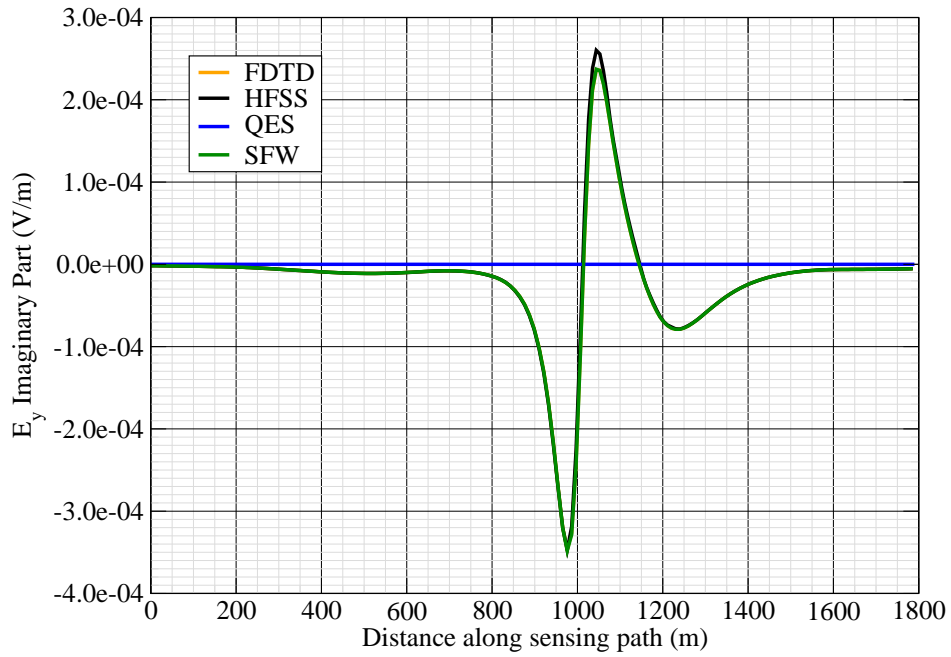


Figure 6: E_y imag.

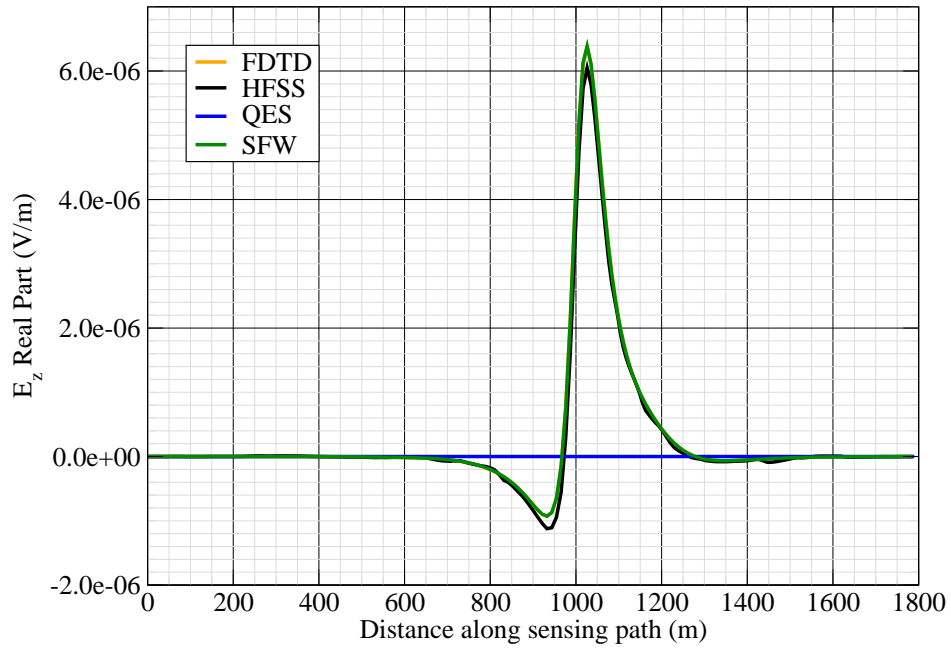


Figure 7: E_z real.

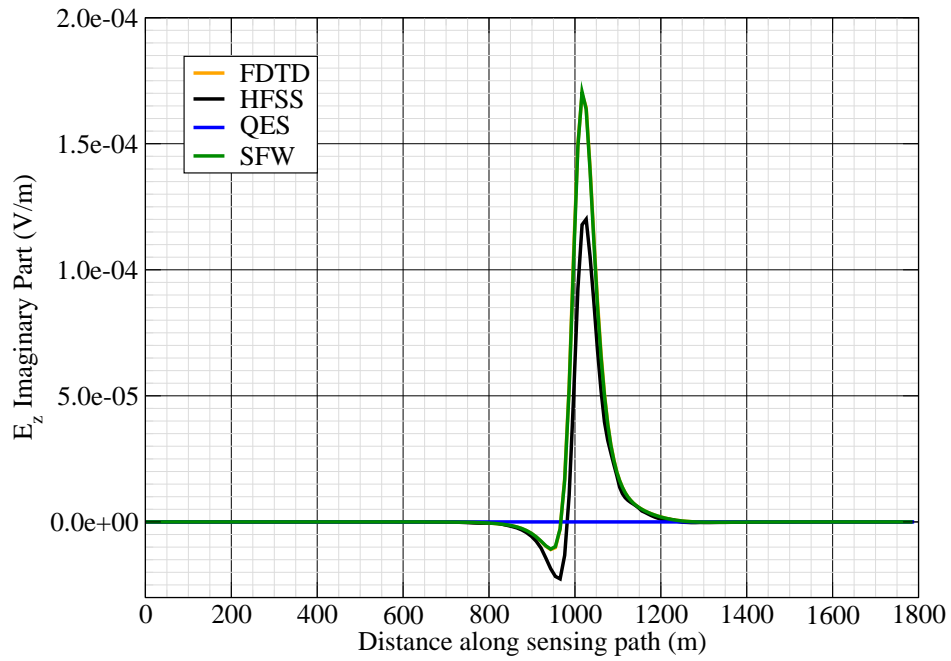


Figure 8: E_z imag.

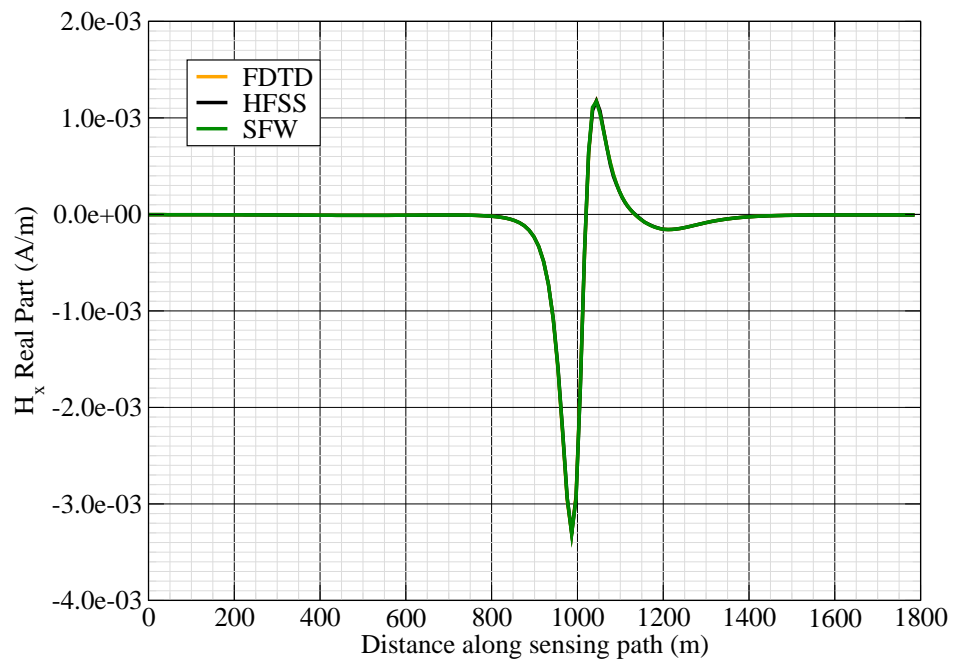


Figure 9: H_x real.

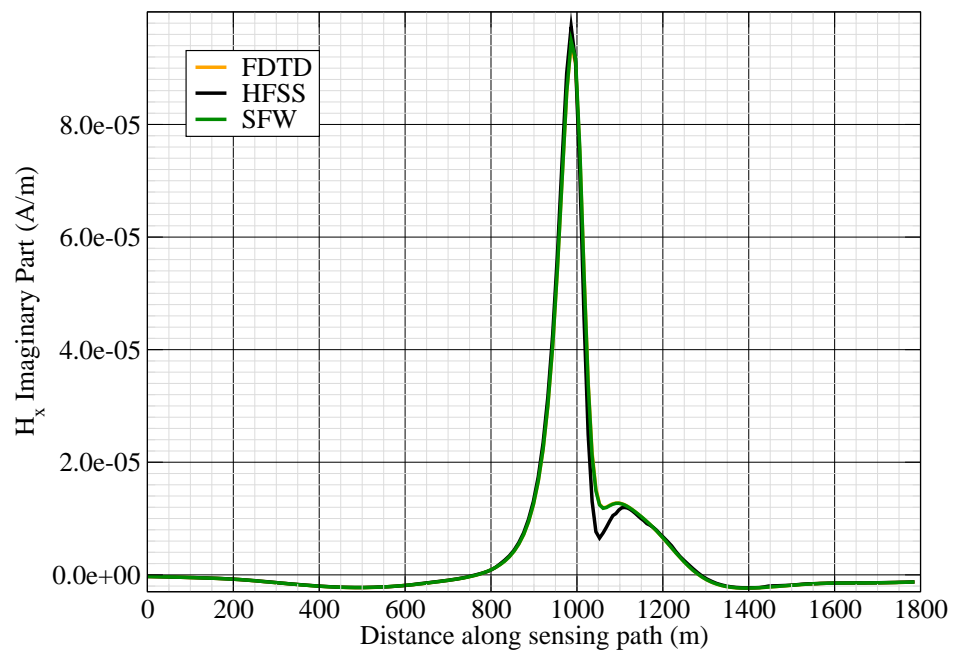


Figure 10: H_x imag.

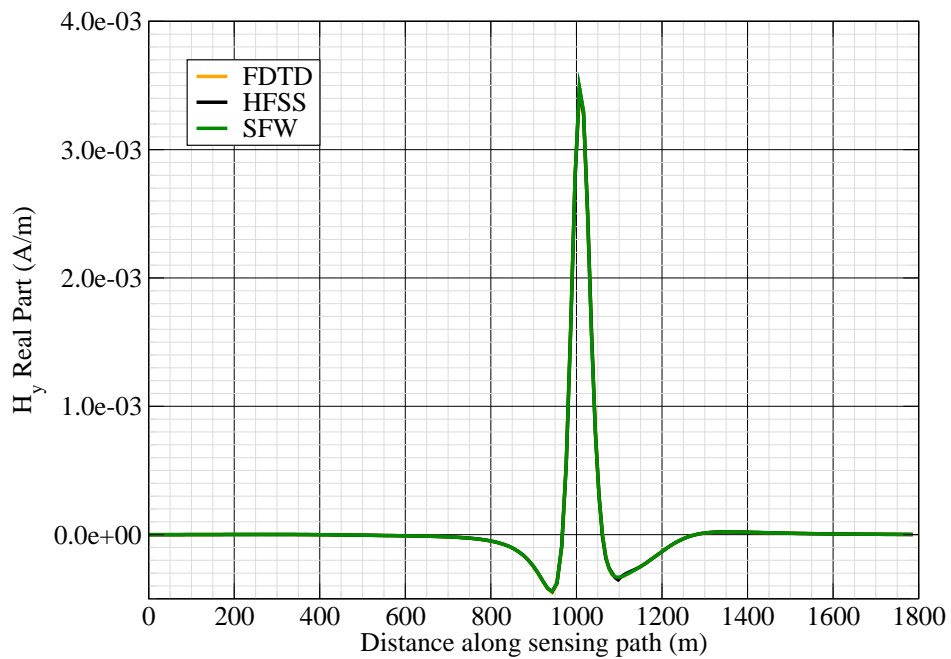


Figure 11: H_y real.

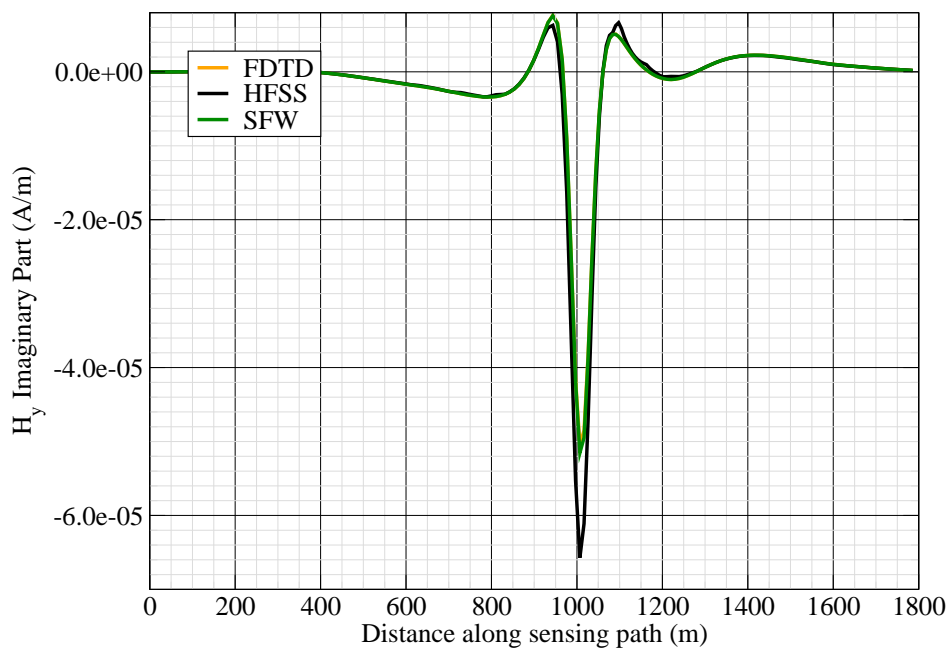


Figure 12: H_y imag.

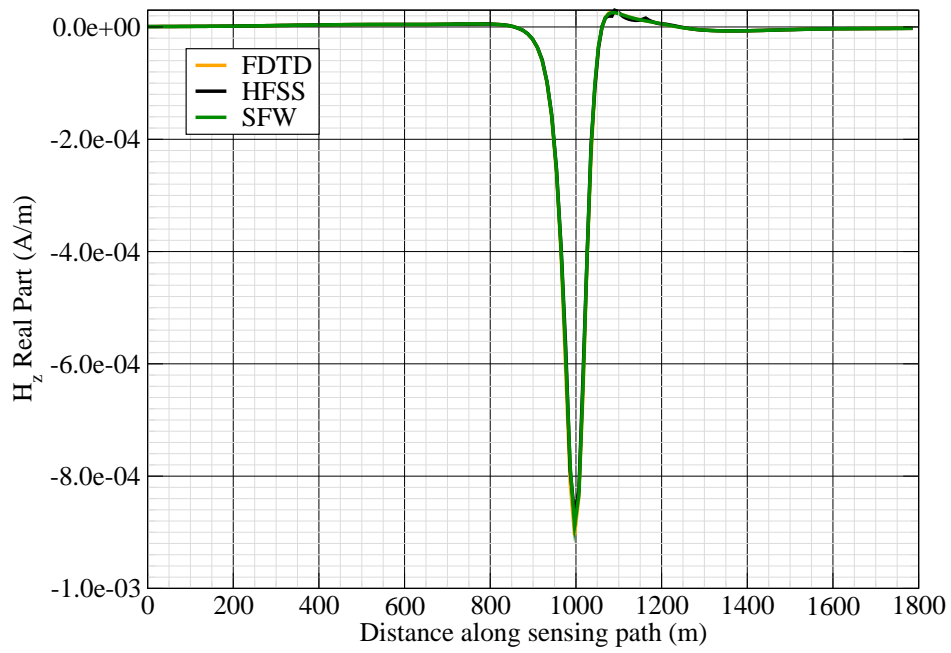


Figure 13: H_z real.

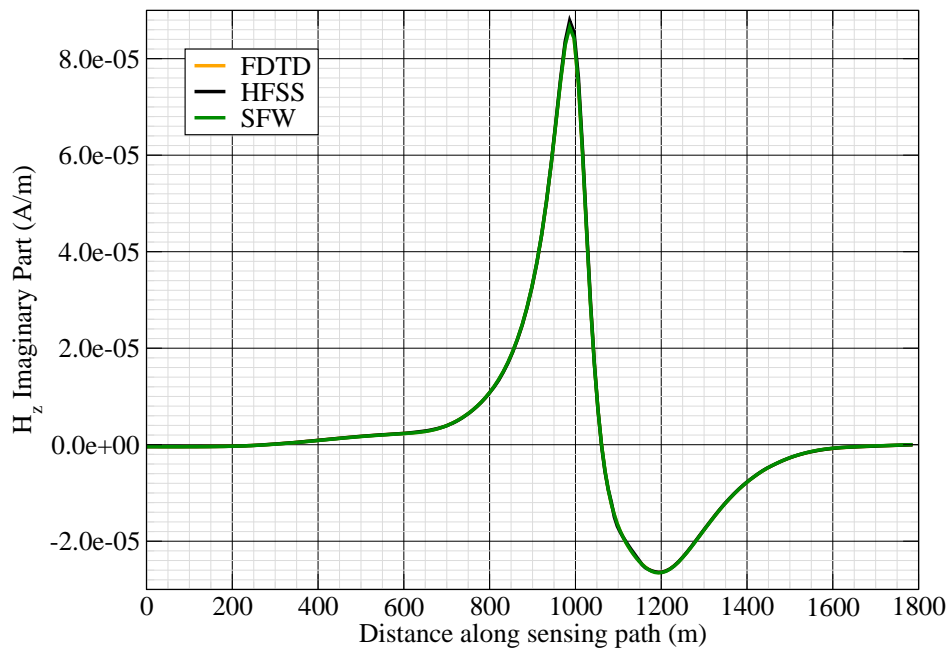


Figure 14: H_z imag.

Canonical Complex

Experiment 14

Experiment Date: November 2, 2011

1 Discussion

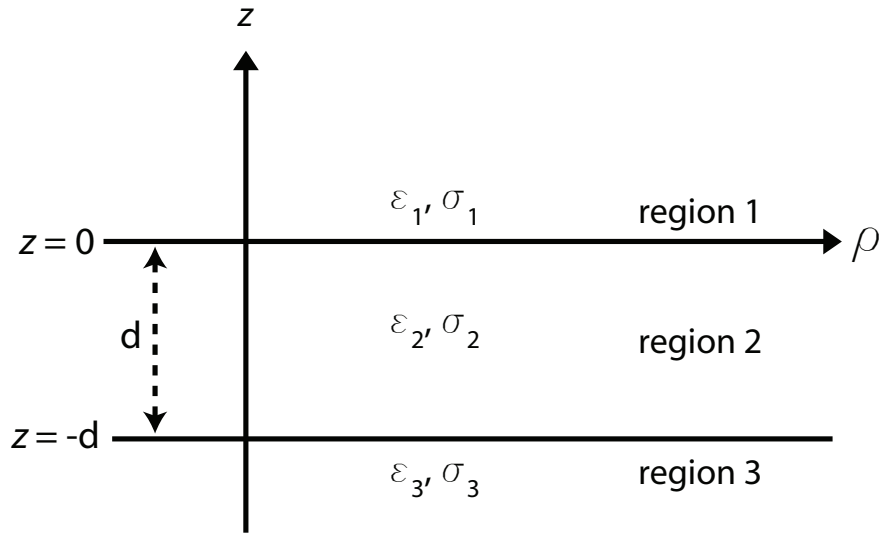


Figure 1: 3-layer topology.

Source Parameters

- Source Type: VMD (Coil: 3.66 m by 3.66 m with 12 turns).
- Source Strength: 3,683 A-m².
- f = 1000 Hz.

Environment

- Water thickness: $d = 180$ m
- Air: $\sigma_1 = 0$ S/m and $\epsilon_{r1} = 1$
- Water: $\sigma_2 = 0.01$ S/m and $\epsilon_{r2} = 81$
- Mud: $\sigma_3 = 0.0012$ S/m and $\epsilon_{r3} = 1$

Table 1: Simulation Details

	FDTD	HFSS	QES/SFW
Domain Size	$200 \times 200 \times 120$ cells	5919 tets	N/A
Cell Size (m)	$5 \times 5 \times 5$	N/A	N/A
Time Step (ns)	9.6	N/A	N/A
Run Time (Hrs)	6	0.02	< 1 min

Comments

- Computational time is based on actual elapsed real time. This number is highly subjective and based on how many other applications might be running at a particular time. However, the reported number is an indication of the amount of time typically needed for a particular simulation. The computer specs are: 16 CPU cores at 2.8 GHz.
- Run times for HFSS are given for a single frequency.
- QES is not applicable for magnetic fields using electric source excitation.

2 Simulation Variables

Sensor_P1(x,y,z) [m]	(-200,57.1571,-10.123)
Sensor_P2(x,y,z) [m]	(114.1593,44.8169,-10.123)
Source_P1(x,y,z) [m]	(0,0,23.343)
Source_P2(x,y,z) [m]	(0,0,23.343)
Source_Plate_Separation [m]	N/A
Source_Size [m X m X #]	[3.658 X 3.658 X 12]
Source_Heading [deg]	NaN
Source_Voltage [V Peak]	11.6294
Source_Current [A Peak]	22.9361
Source_Frequency [Hz]	1000

--- Extra Information ---

Source_Heading_Bounds [deg]	(N/A)
Average_Boat_Speed [m/s]	NaN
Source_Type	Magnetic source (portable)
Sensor_Type	EMA
Bin_Size [sec]	1
Number_of_Datapoints	200
Lake_Origin (Easting,Northing)	NaN
Analysis_Date	26-Sep-2011

3 Boat Path

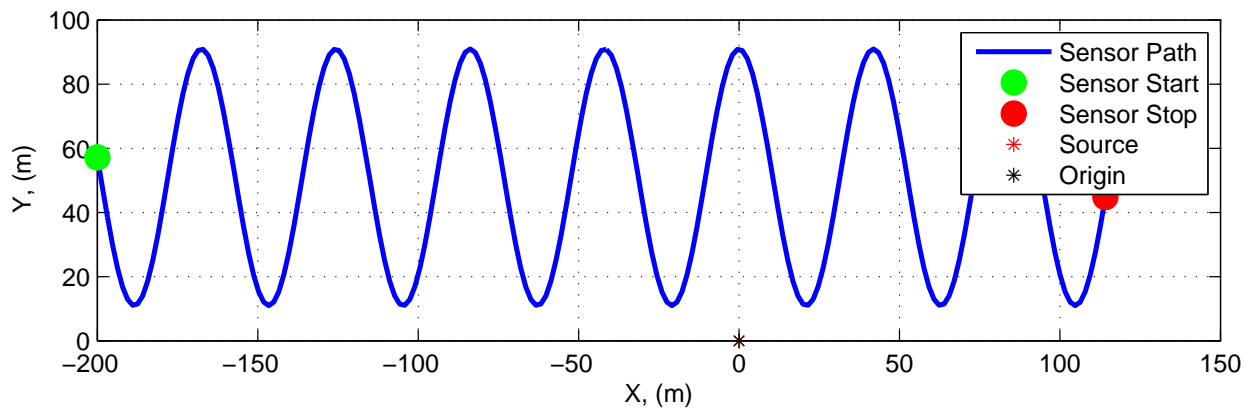


Figure 2: Source and sensor relationship.

4 Plots

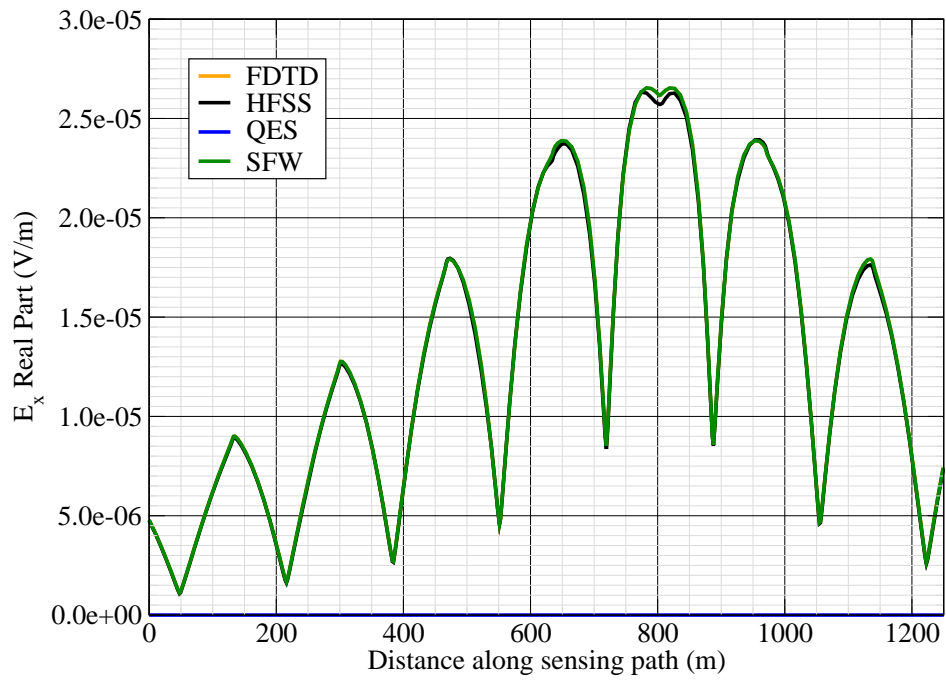


Figure 3: E_x real.

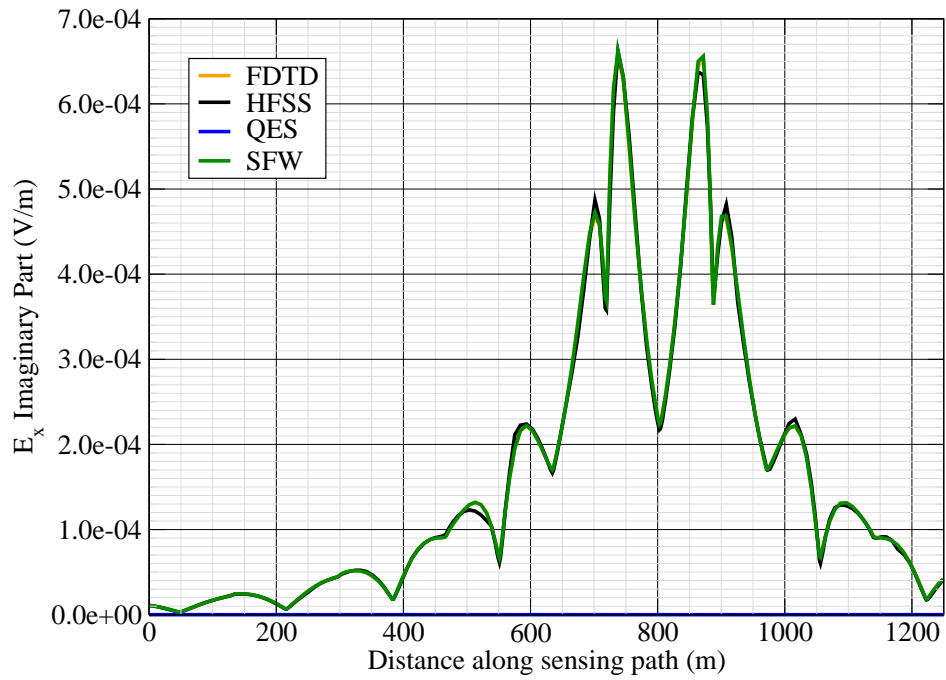


Figure 4: E_x imag.

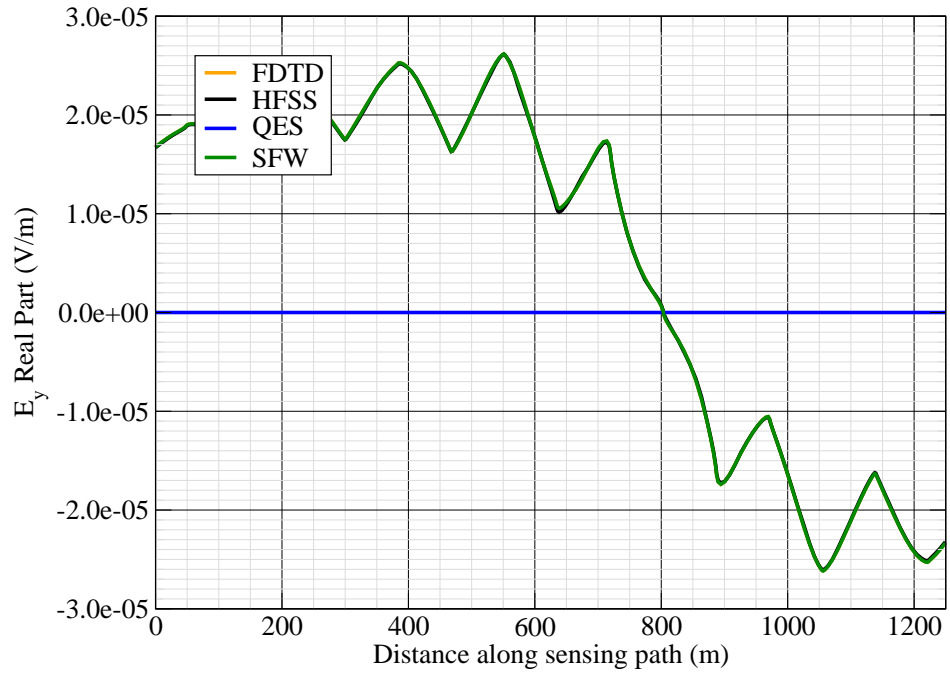


Figure 5: E_y real.

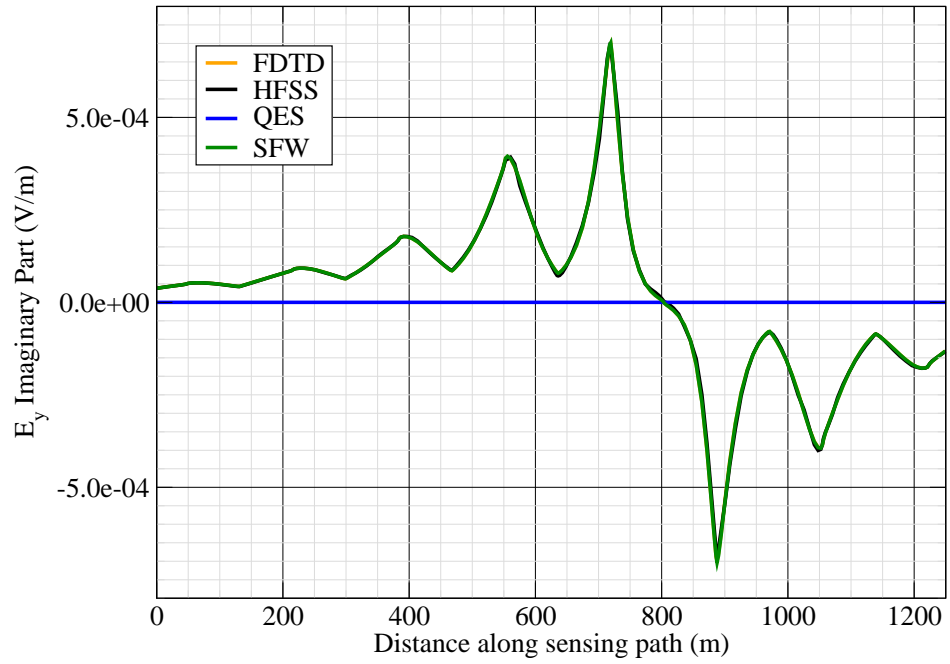


Figure 6: E_y imag.

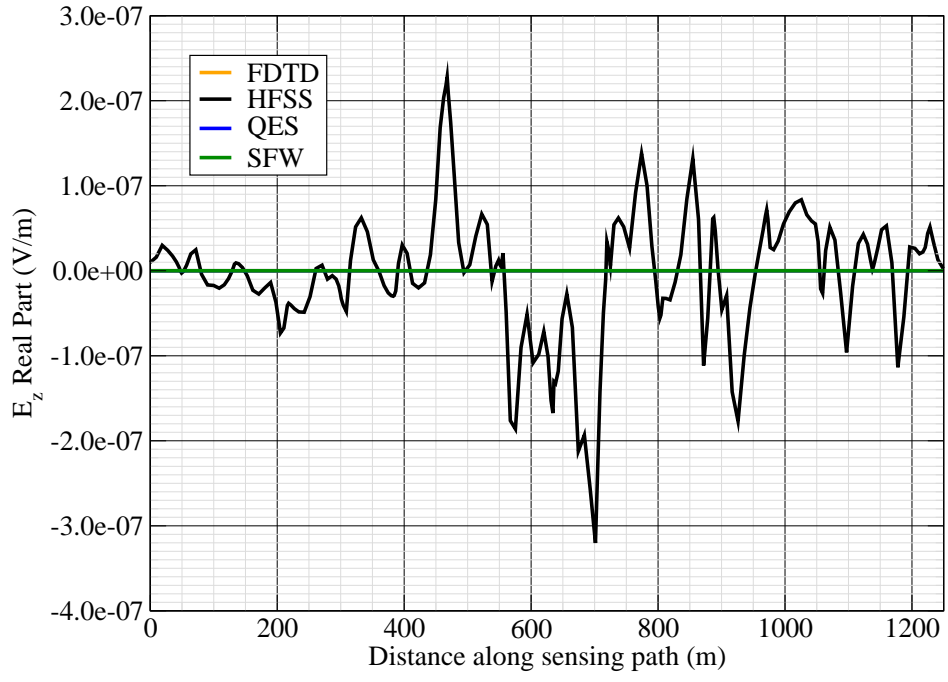


Figure 7: E_z real.

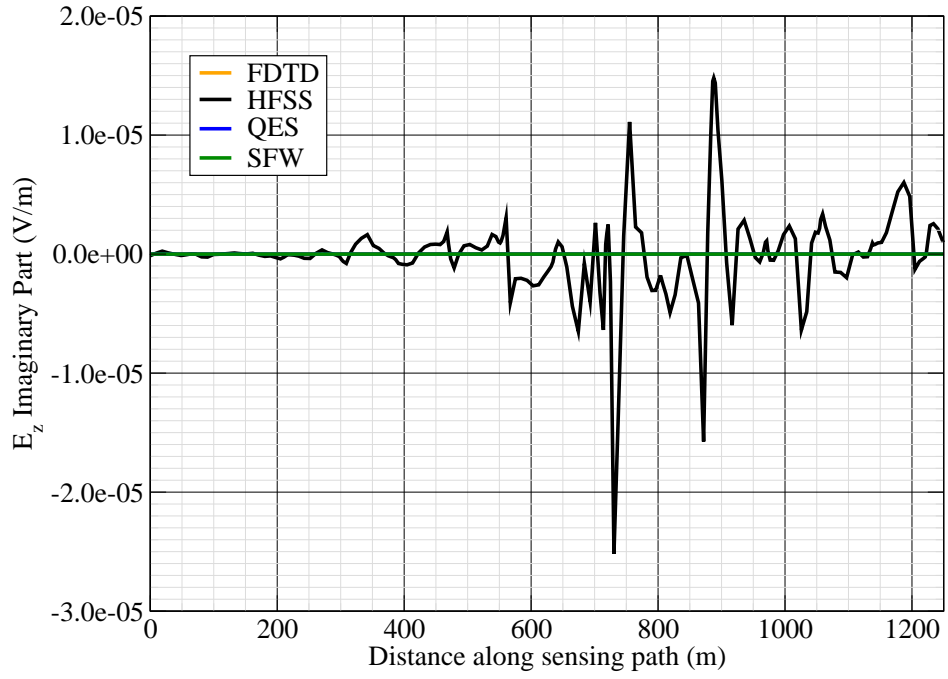


Figure 8: E_z imag.

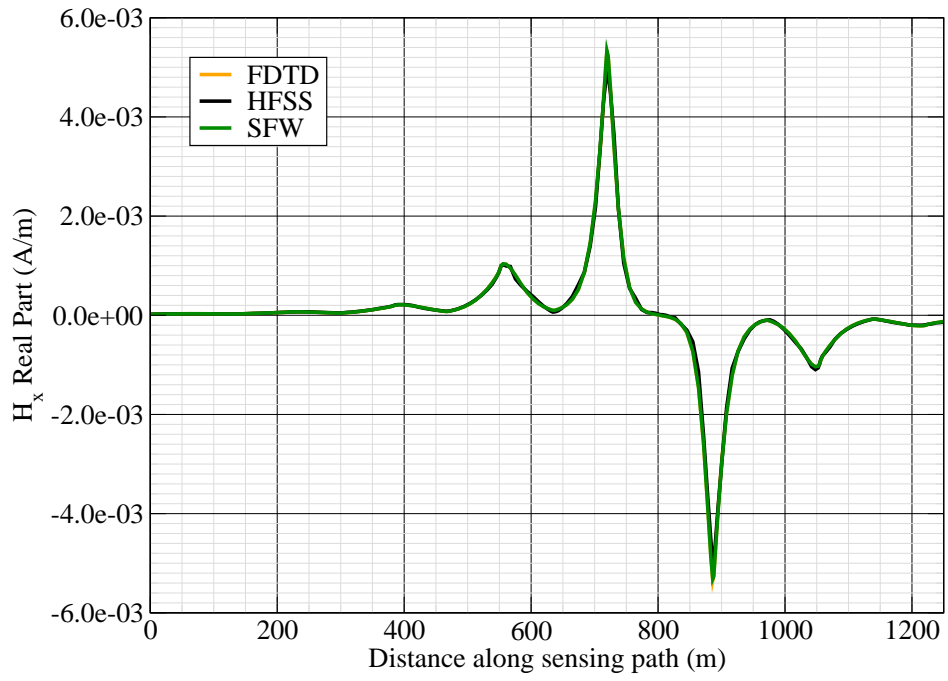


Figure 9: H_x real.

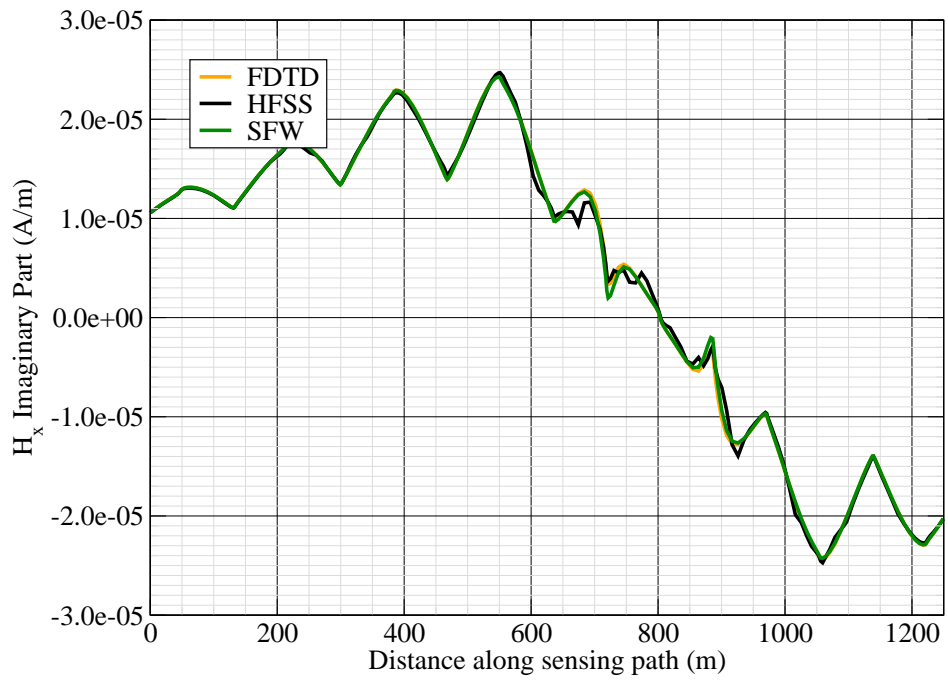


Figure 10: H_x imag.

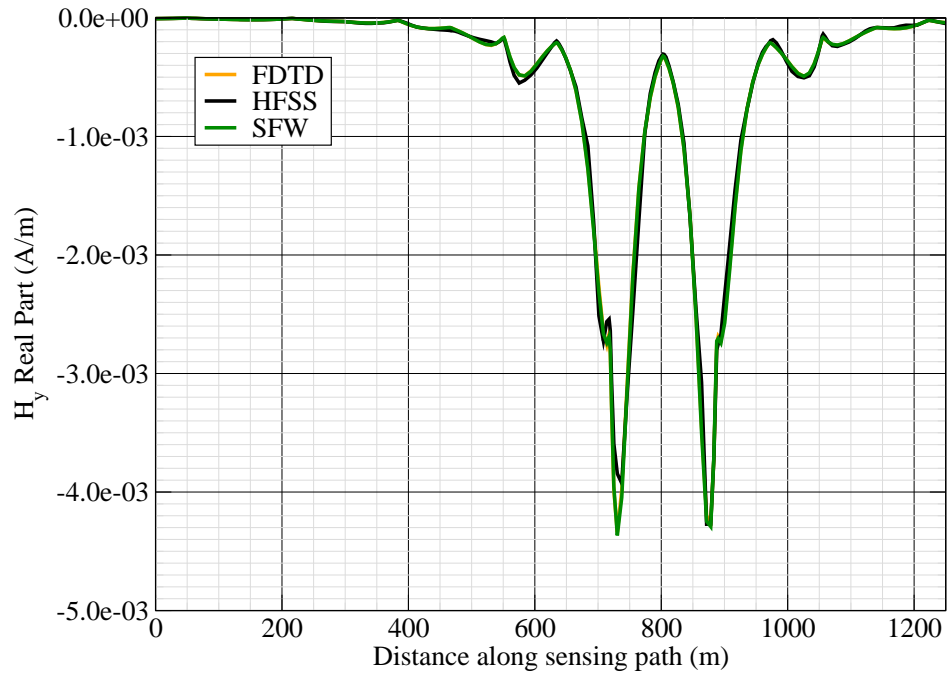


Figure 11: H_y real.

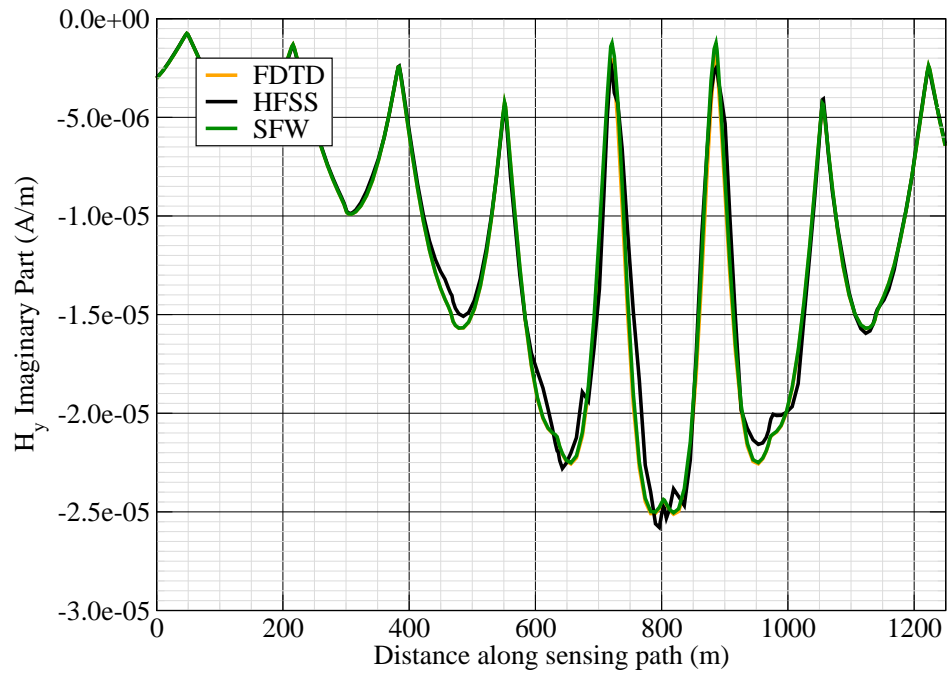


Figure 12: H_y imag.

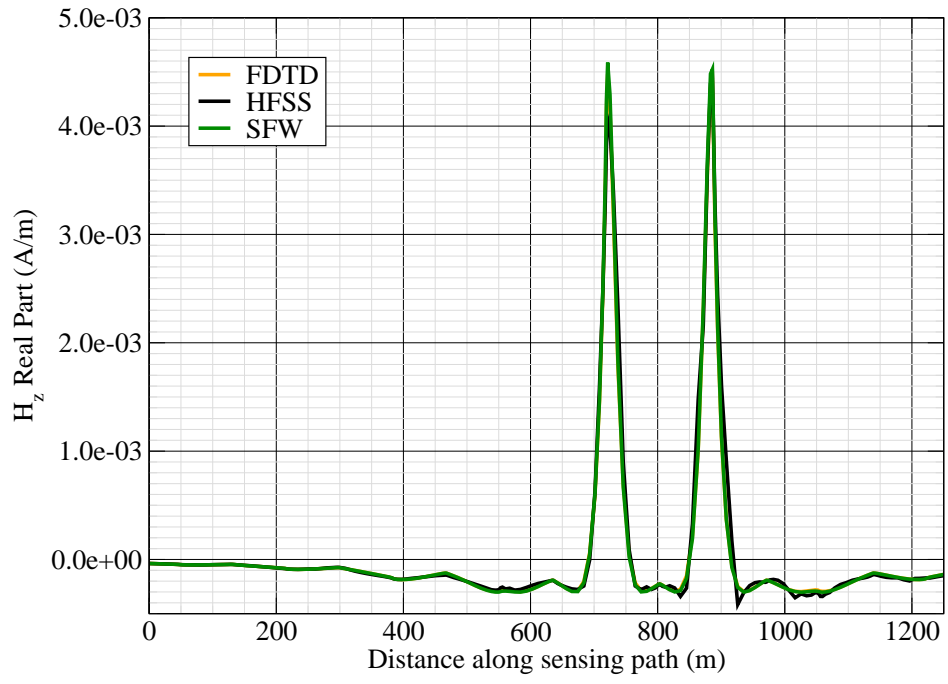


Figure 13: H_z real.

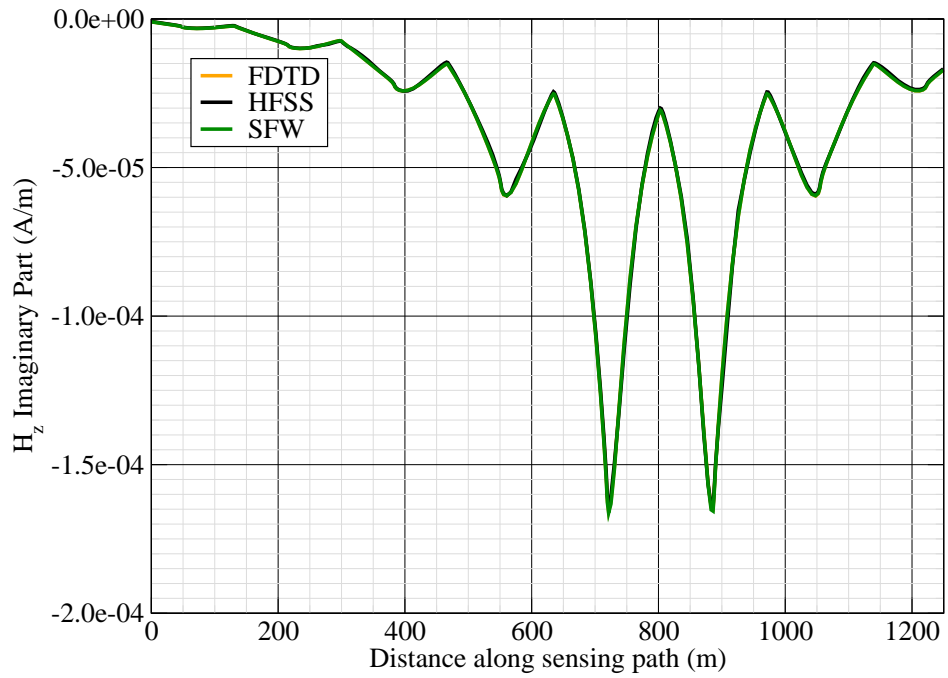


Figure 14: H_z imag.

Canonical Complex

Experiment 15

Experiment Date: November 2, 2011

1 Discussion

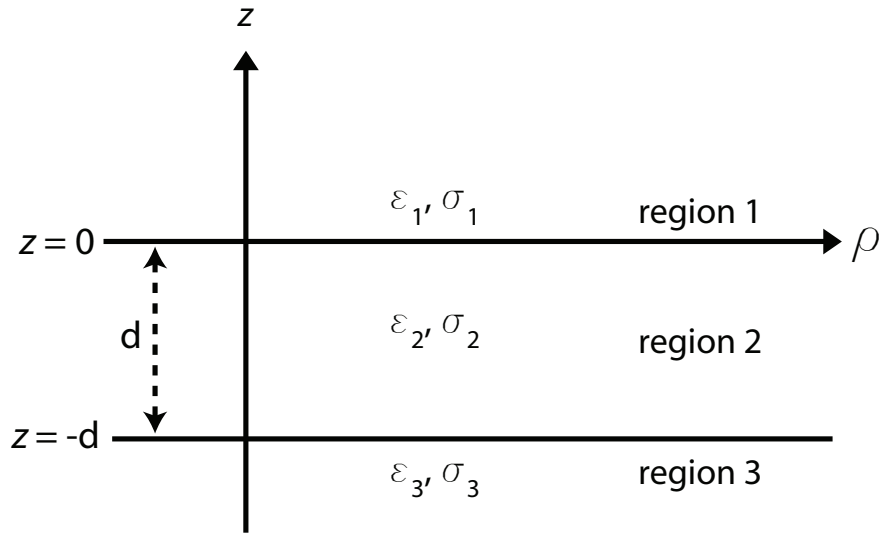


Figure 1: 3-layer topology.

Source Parameters

- Source Type: VMD (Coil: 3.66 m by 3.66 m with 12 turns).
- Source Strength: 3,683 A-m².
- f = 1000 Hz.

Environment

- Water thickness: $d = 180$ m
- Air: $\sigma_1 = 0$ S/m and $\epsilon_{r1} = 1$
- Water: $\sigma_2 = 0.01$ S/m and $\epsilon_{r2} = 81$
- Mud: $\sigma_3 = 0.0012$ S/m and $\epsilon_{r3} = 1$

Table 1: Simulation Details

	FDTD	HFSS	QES/SFW
Domain Size	$200 \times 200 \times 120$ cells	6878 tets	N/A
Cell Size (m)	$5 \times 5 \times 5$	N/A	N/A
Time Step (ns)	9.6	N/A	N/A
Run Time (Hrs)	6	0.02	< 1 min

Comments

- Computational time is based on actual elapsed real time. This number is highly subjective and based on how many other applications might be running at a particular time. However, the reported number is an indication of the amount of time typically needed for a particular simulation. The computer specs are: 16 CPU cores at 2.8 GHz.
- Run times for HFSS are given for a single frequency.
- QES is not applicable for magnetic fields using electric source excitation.

2 Simulation Variables

Sensor_P1(x,y,z) [m]	(-200,57.1571,10.123)
Sensor_P2(x,y,z) [m]	(114.1593,44.8169,10.123)
Source_P1(x,y,z) [m]	(0,57,-83.343)
Source_P2(x,y,z) [m]	(0,57,-83.343)
Source_Plate_Separation [m]	N/A
Source_Size [m X m X #]	[3.658 X 3.658 X 12]
Source_Heading [deg]	NaN
Source_Voltage [V Peak]	11.6294
Source_Current [A Peak]	22.9361
Source_Frequency [Hz]	1000

--- Extra Information ---

Source_Heading_Bounds [deg]	(N/A)
Average_Boat_Speed [m/s]	NaN
Source_Type	Magnetic source (portable)
Sensor_Type	EMA
Bin_Size [sec]	1
Number_of_Datapoints	200
Lake_Origin (Easting,Northing)	NaN
Analysis_Date	26-Sep-2011

3 Boat Path

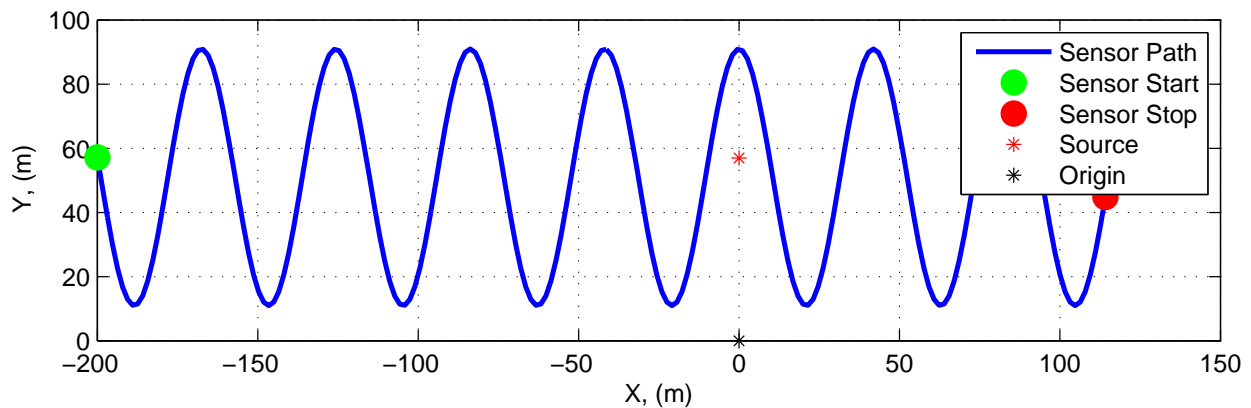


Figure 2: Source and sensor relationship.

4 Plots

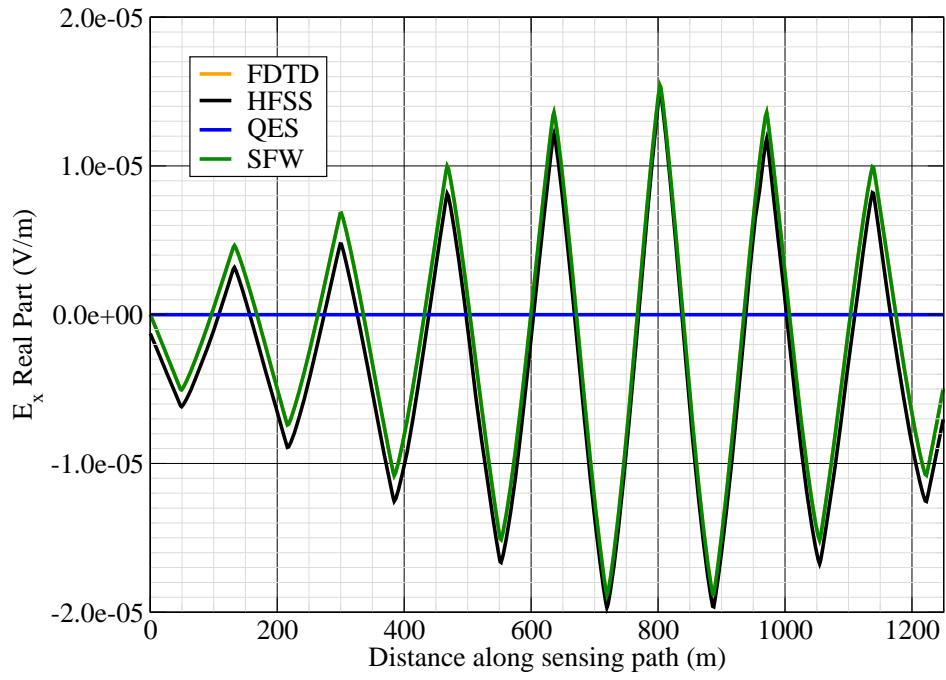


Figure 3: E_x real.

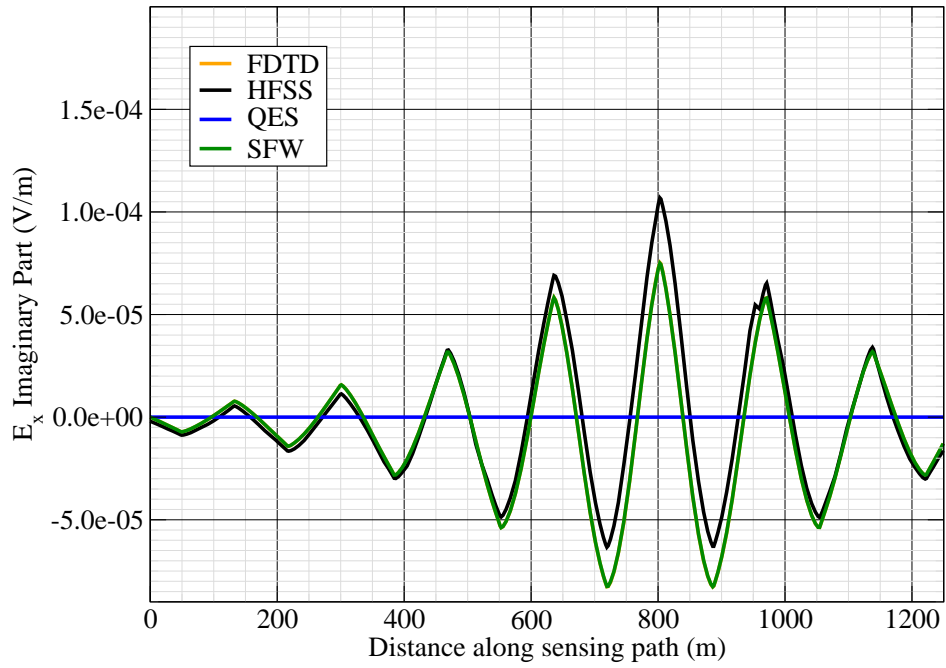


Figure 4: E_x imag.

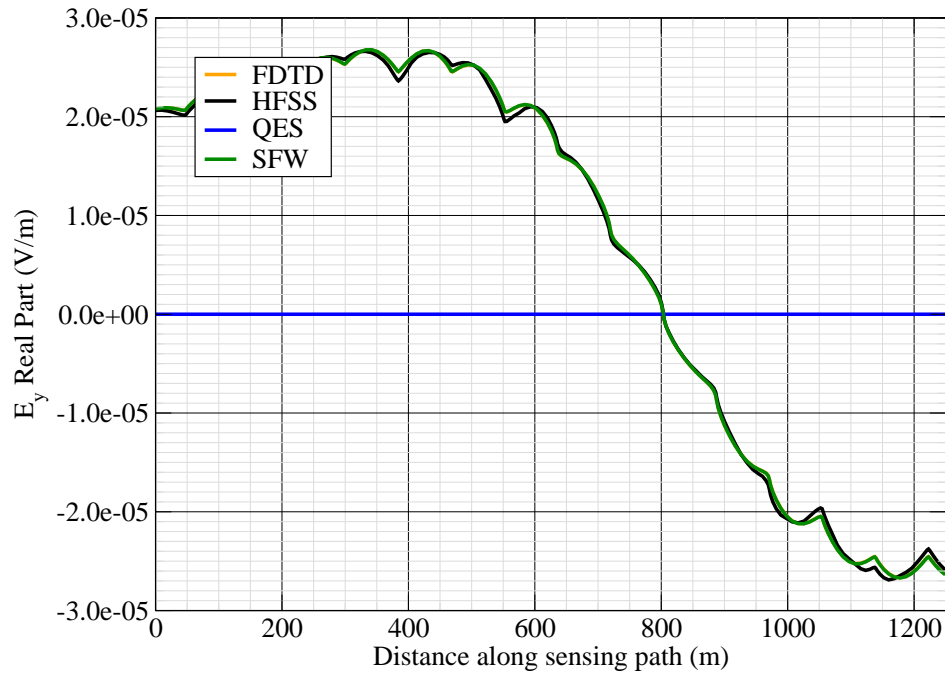


Figure 5: E_y real.

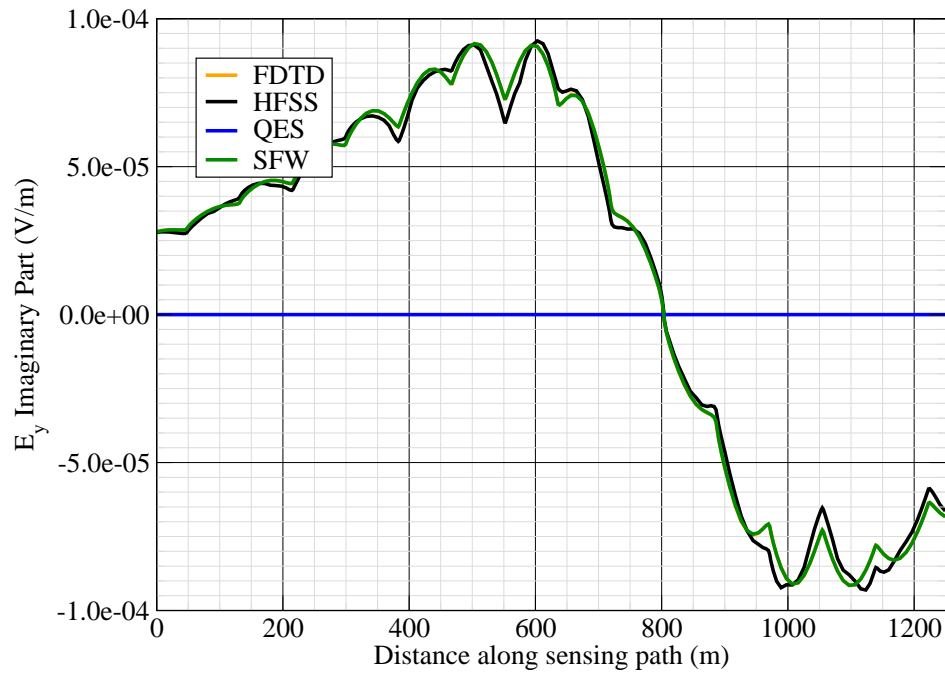


Figure 6: E_y imag.

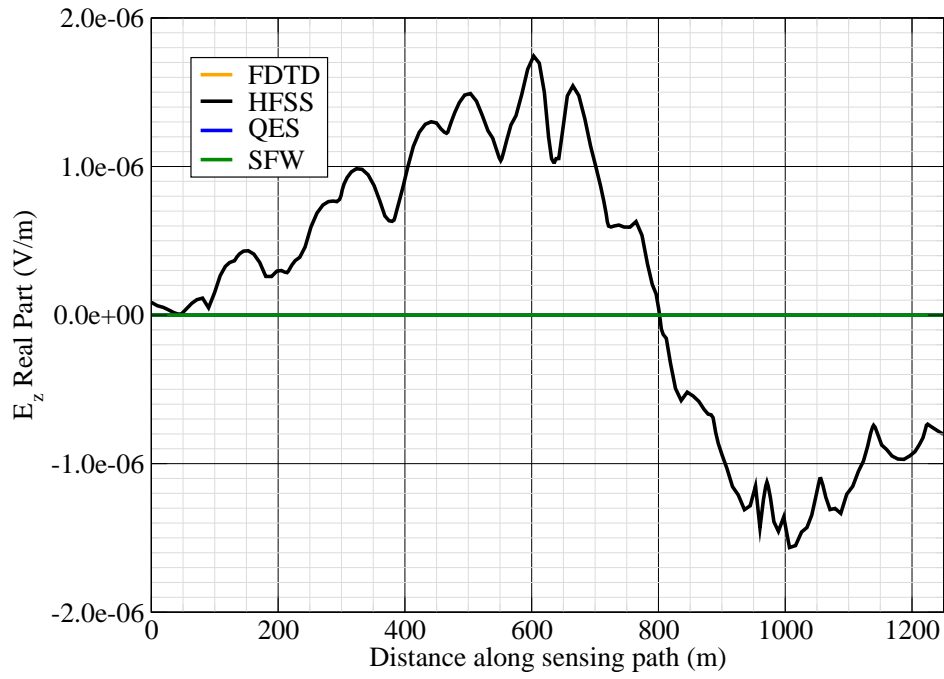


Figure 7: E_z real.

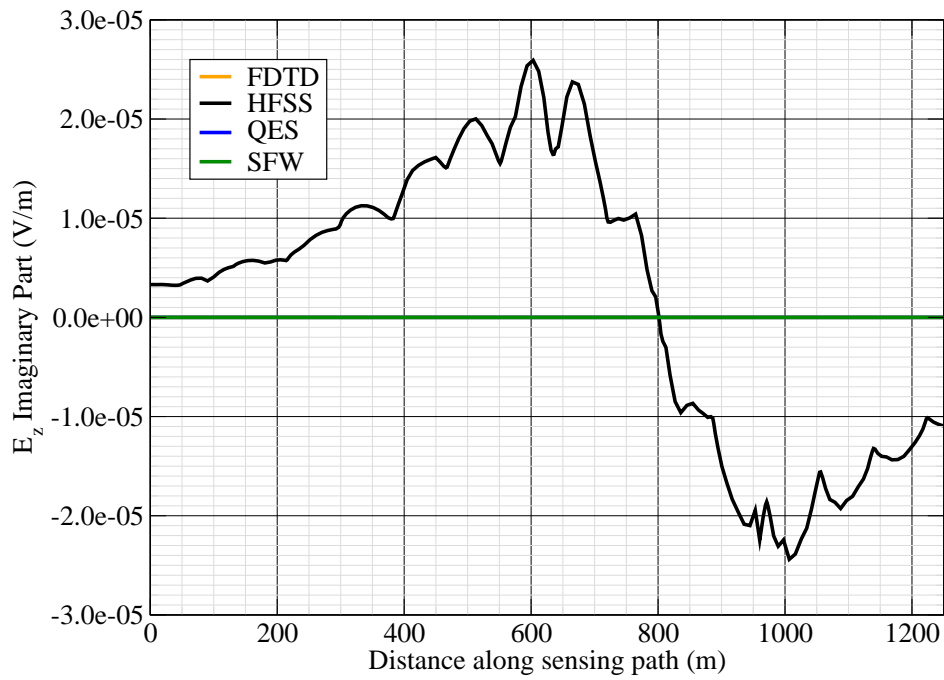


Figure 8: E_z imag.

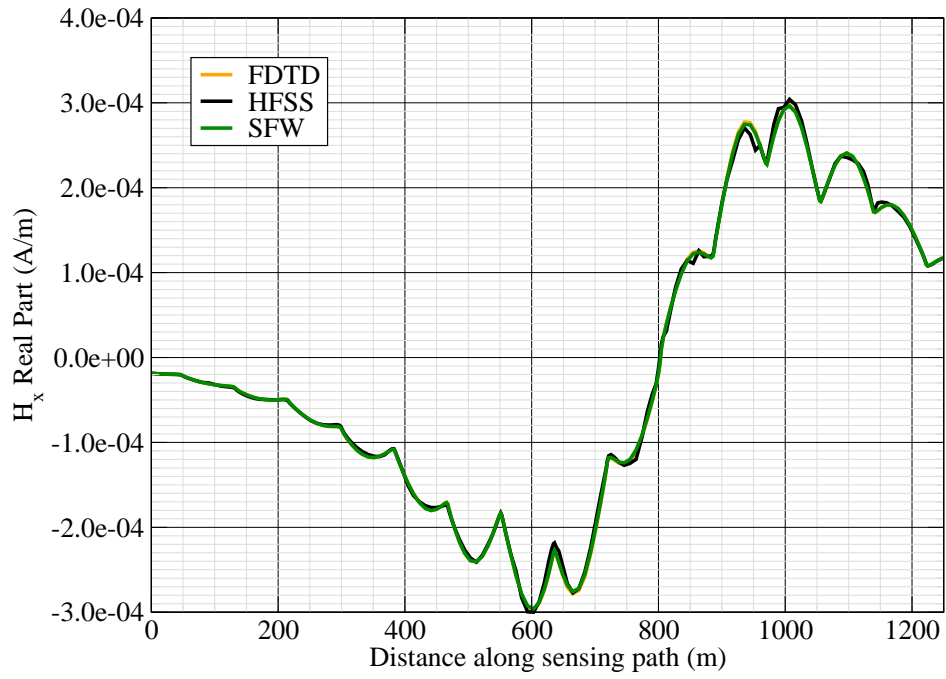


Figure 9: H_x real.

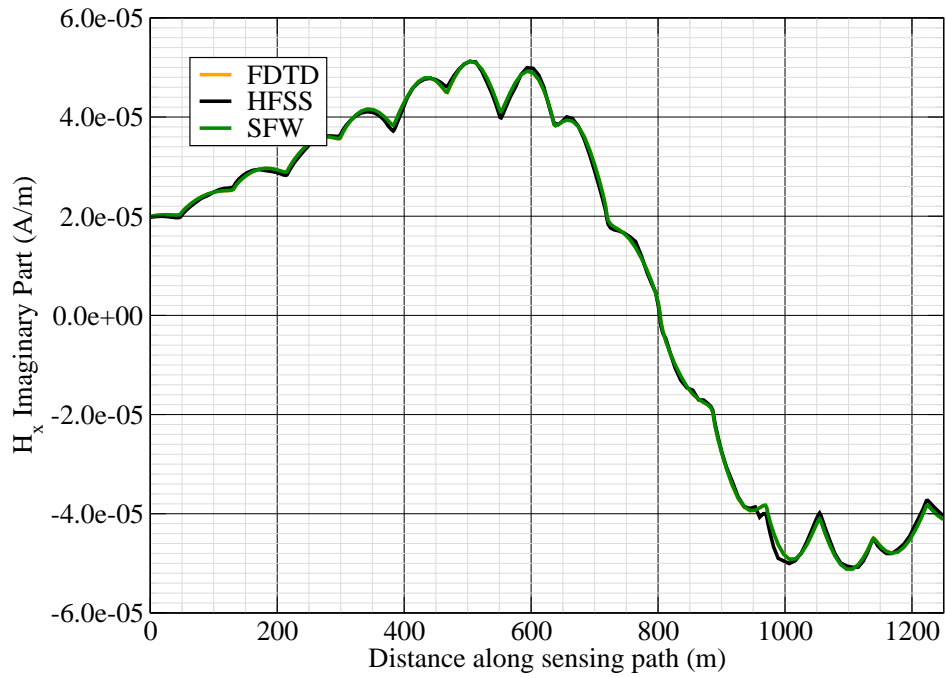


Figure 10: H_x imag.

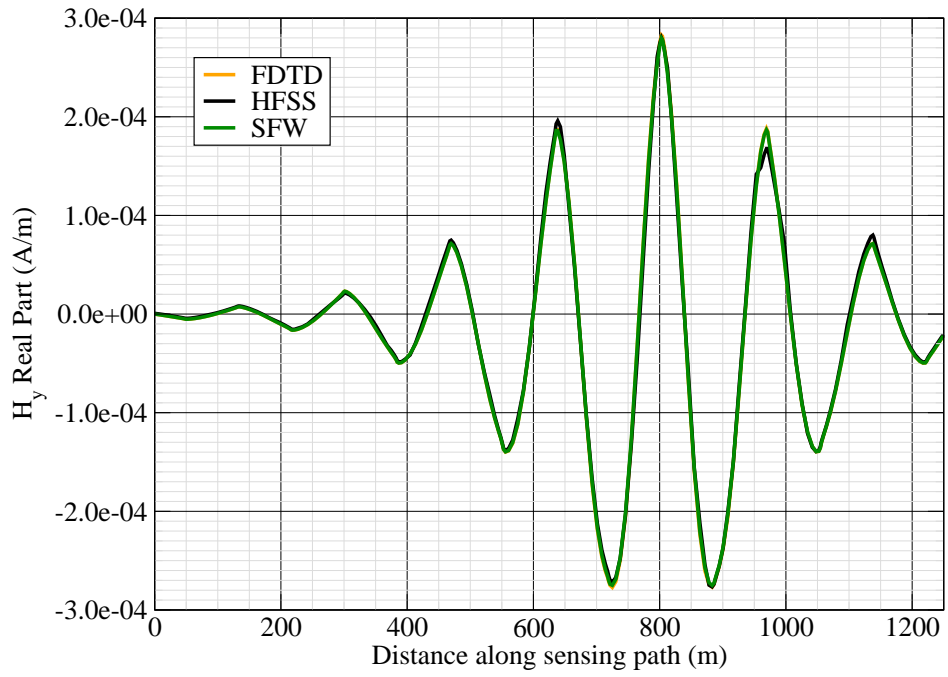


Figure 11: H_y real.

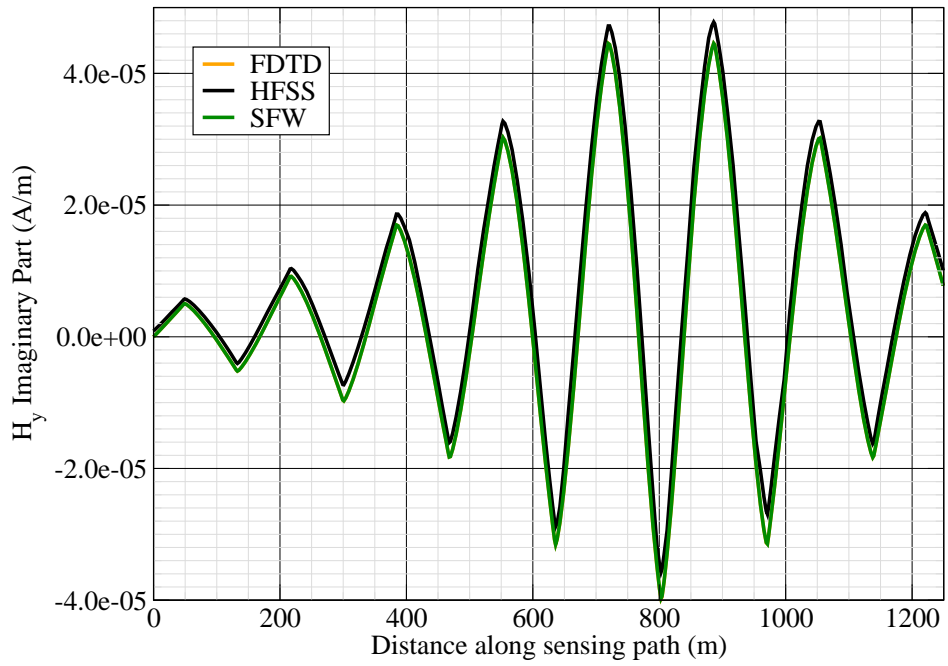


Figure 12: H_y imag.

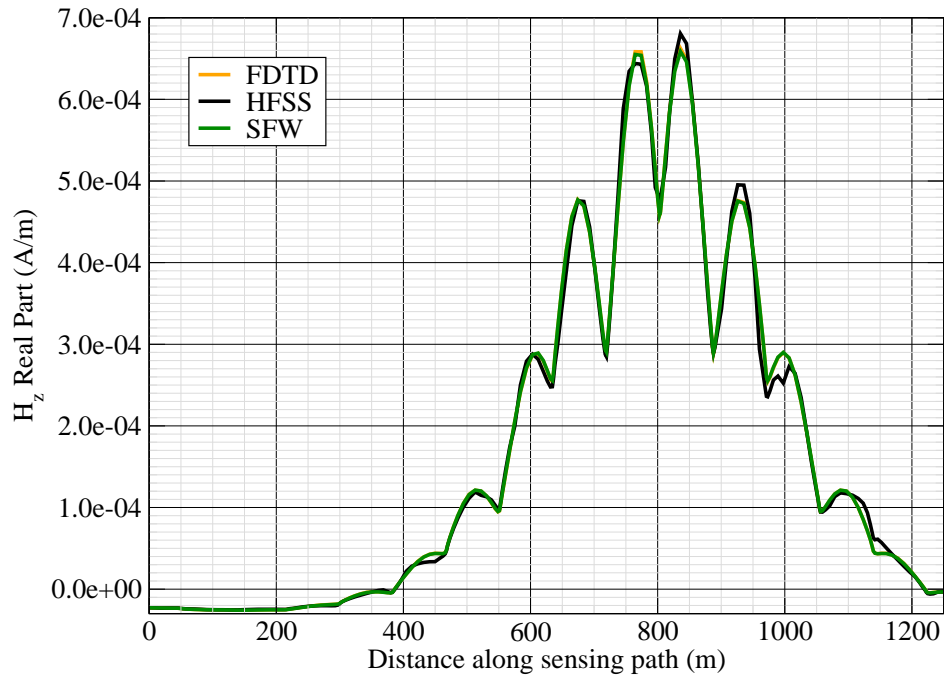


Figure 13: H_z real.

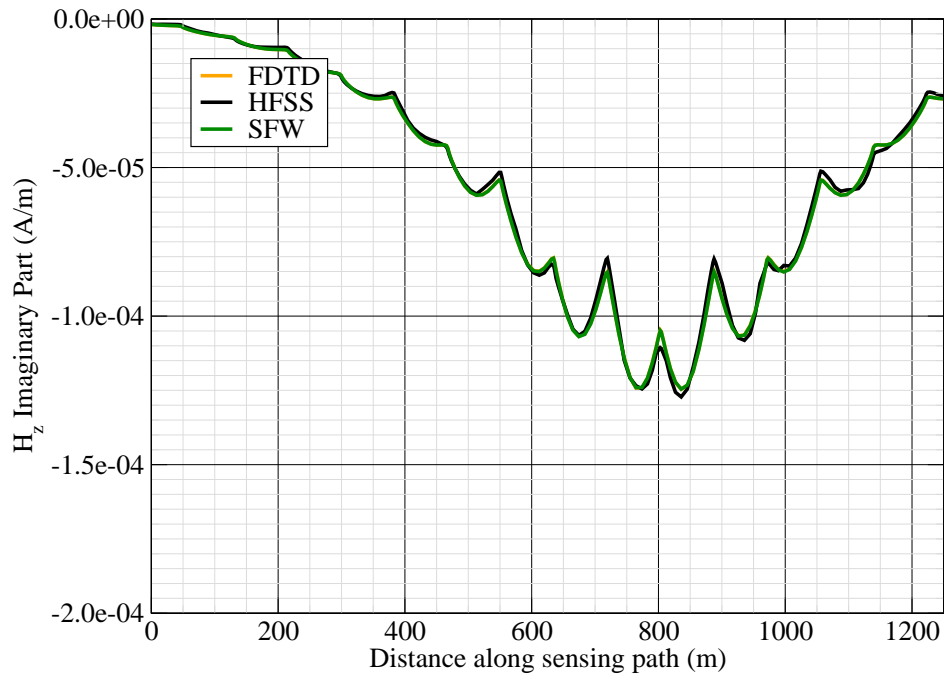


Figure 14: H_z imag.

Canonical Complex

Experiment 16

Experiment Date: November 2, 2011

1 Discussion

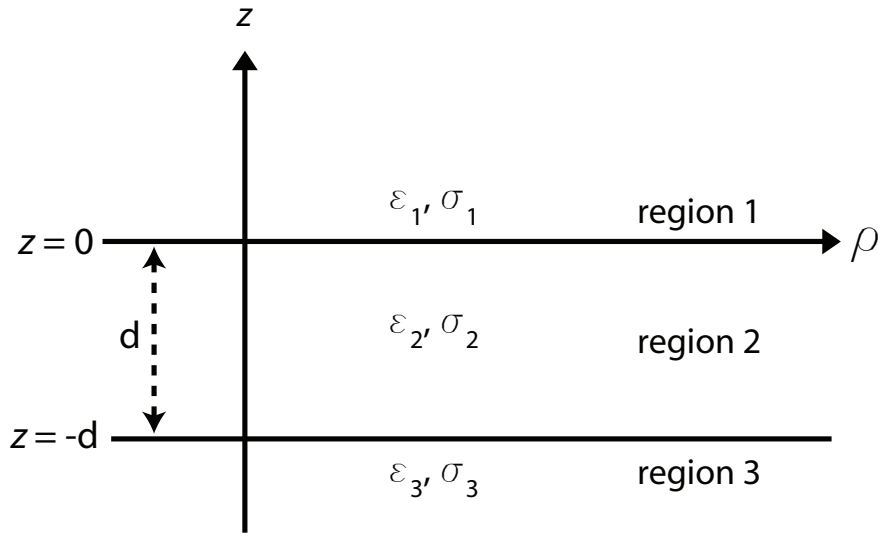


Figure 1: 3-layer topology.

Source Parameters

- Source Type: VMD (Coil: 3.66 m by 3.66 m with 12 turns).
- Source Strength: 3,683 A-m².
- f = 1000 Hz.

Environment

- Water thickness: $d = 180$ m
- Air: $\sigma_1 = 0$ S/m and $\epsilon_{r1} = 1$
- Water: $\sigma_2 = 0.01$ S/m and $\epsilon_{r2} = 81$
- Mud: $\sigma_3 = 0.0012$ S/m and $\epsilon_{r3} = 1$

Table 1: Simulation Details

	FDTD	HFSS	QES/SFW
Domain Size	$200 \times 200 \times 120$ cells	7918 tets	N/A
Cell Size (m)	$5 \times 5 \times 5$	N/A	N/A
Time Step (ns)	9.6	N/A	N/A
Run Time (Hrs)	6	0.02	< 1 min

Comments

- Computational time is based on actual elapsed real time. This number is highly subjective and based on how many other applications might be running at a particular time. However, the reported number is an indication of the amount of time typically needed for a particular simulation. The computer specs are: 16 CPU cores at 2.8 GHz.
- Run times for HFSS are given for a single frequency.
- QES is not applicable for magnetic fields using electric source excitation.

2 Simulation Variables

Sensor_P1(x,y,z) [m]	(-200,57.1571,-10.123)
Sensor_P2(x,y,z) [m]	(114.1593,44.8169,-10.123)
Source_P1(x,y,z) [m]	(3,13,-23.343)
Source_P2(x,y,z) [m]	(3,13,-23.343)
Source_Plate_Separation [m]	N/A
Source_Size [m X m X #]	[3.658 X 3.658 X 12]
Source_Heading [deg]	NaN
Source_Voltage [V Peak]	11.6294
Source_Current [A Peak]	22.9361
Source_Frequency [Hz]	1000

--- Extra Information ---

Source_Heading_Bounds [deg]	(N/A)
Average_Boat_Speed [m/s]	NaN
Source_Type	Magnetic source (portable)
Sensor_Type	EMA
Bin_Size [sec]	1
Number_of_Datapoints	200
Lake_Origin (Easting,Northing)	NaN
Analysis_Date	26-Sep-2011

3 Boat Path

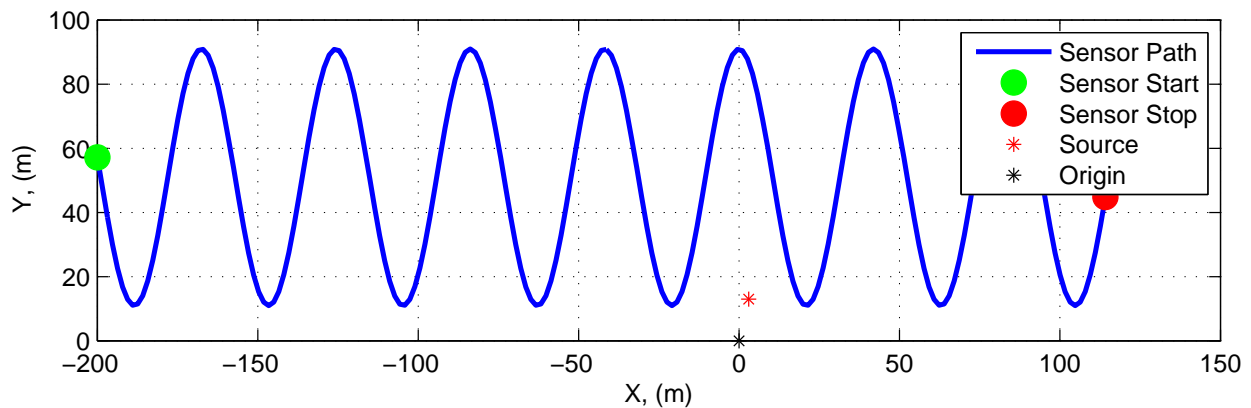


Figure 2: Source and sensor relationship.

4 Plots

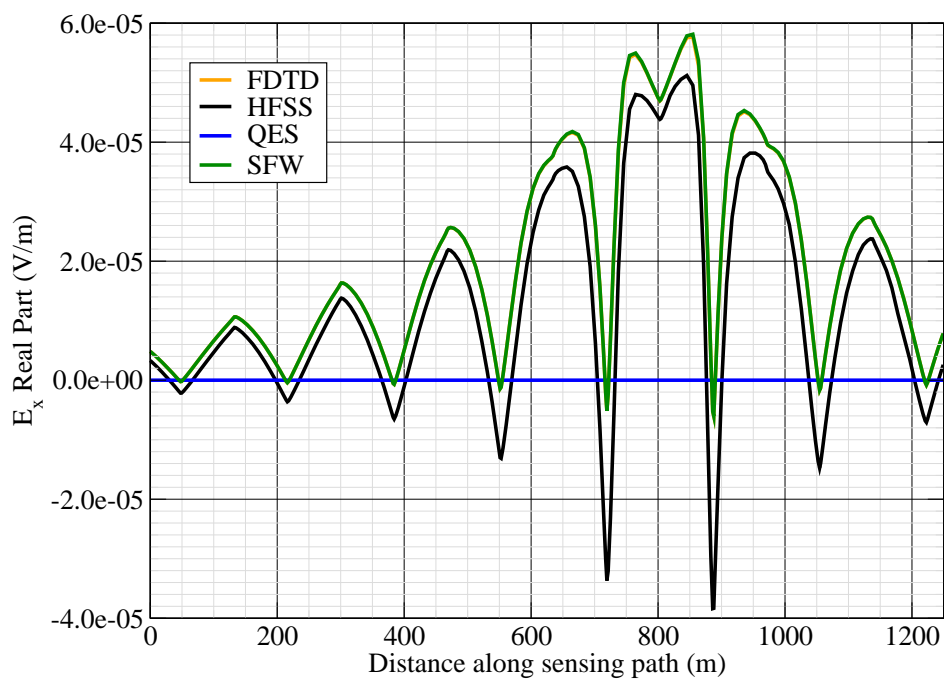


Figure 3: E_x real.

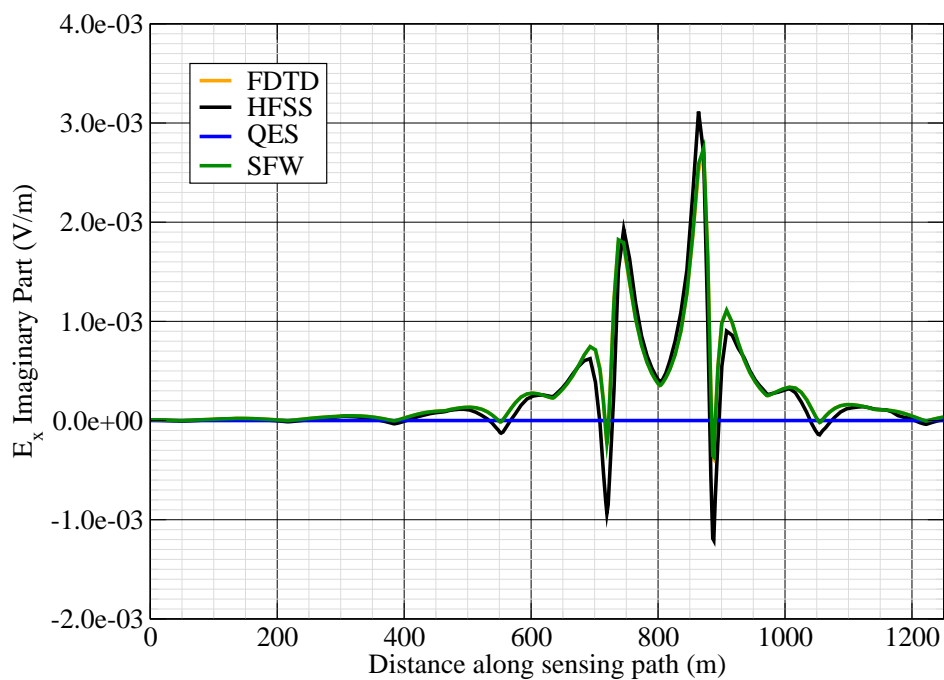


Figure 4: E_x imag.

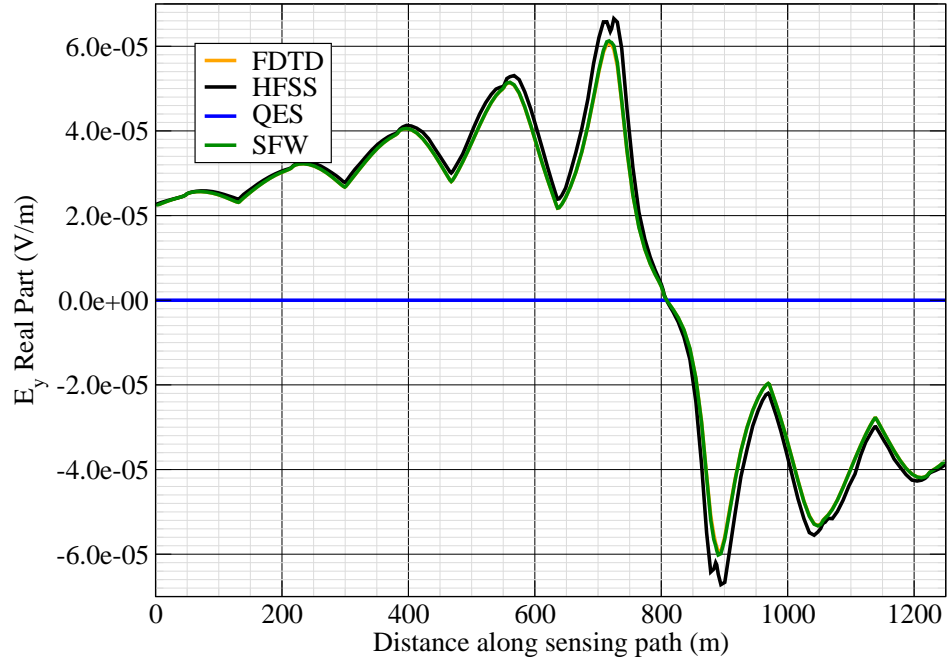


Figure 5: E_y real.

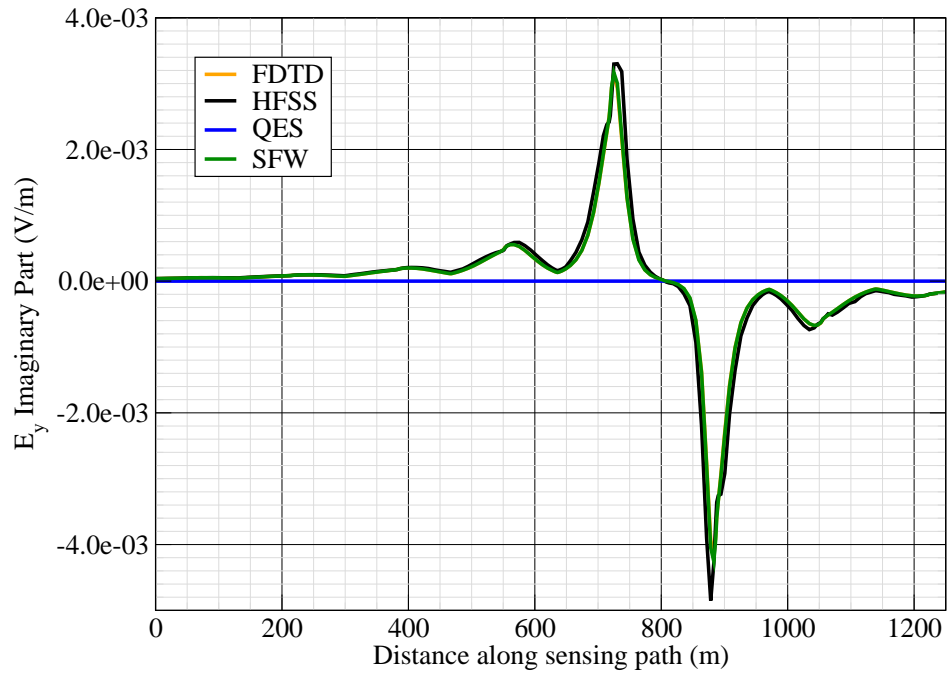


Figure 6: E_y imag.

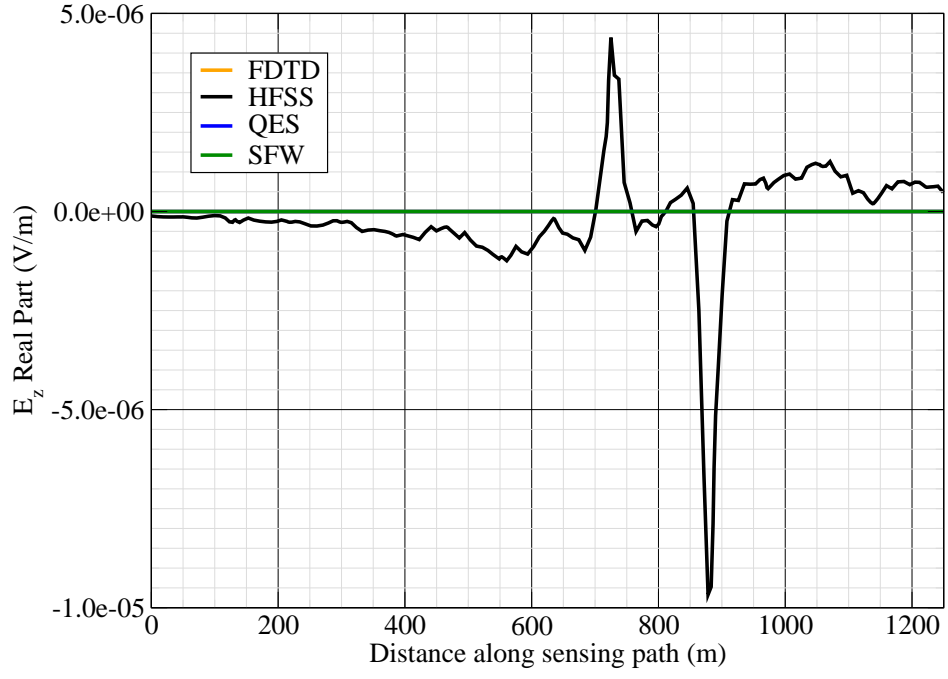


Figure 7: E_z real.

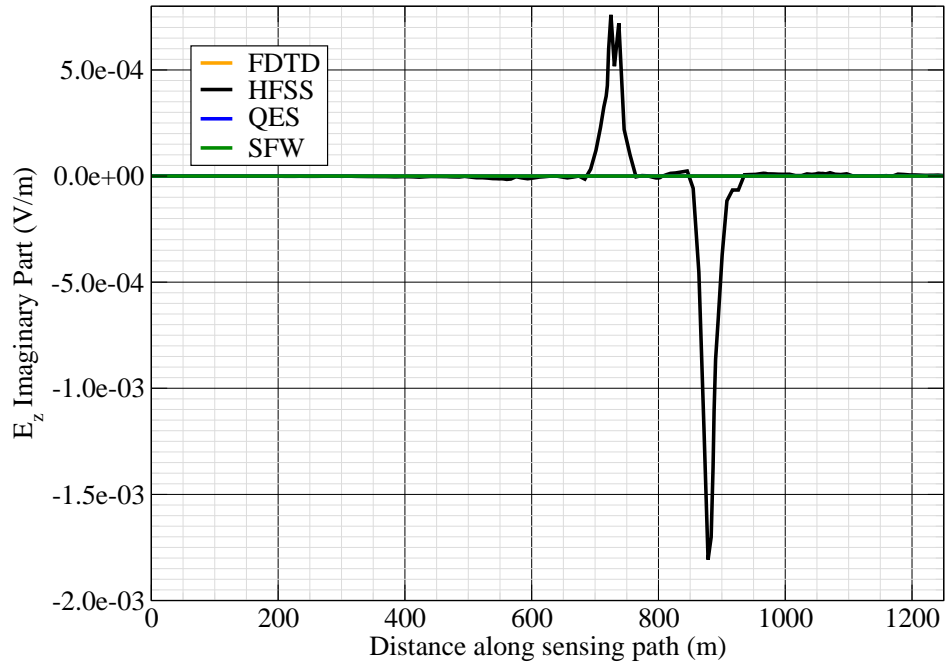


Figure 8: E_z imag.

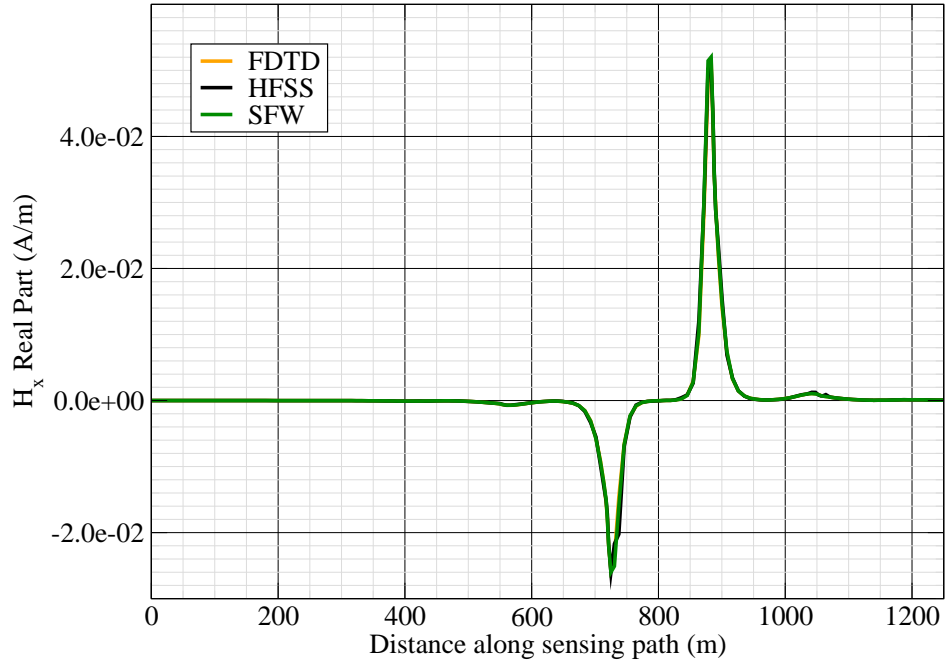


Figure 9: H_x real.

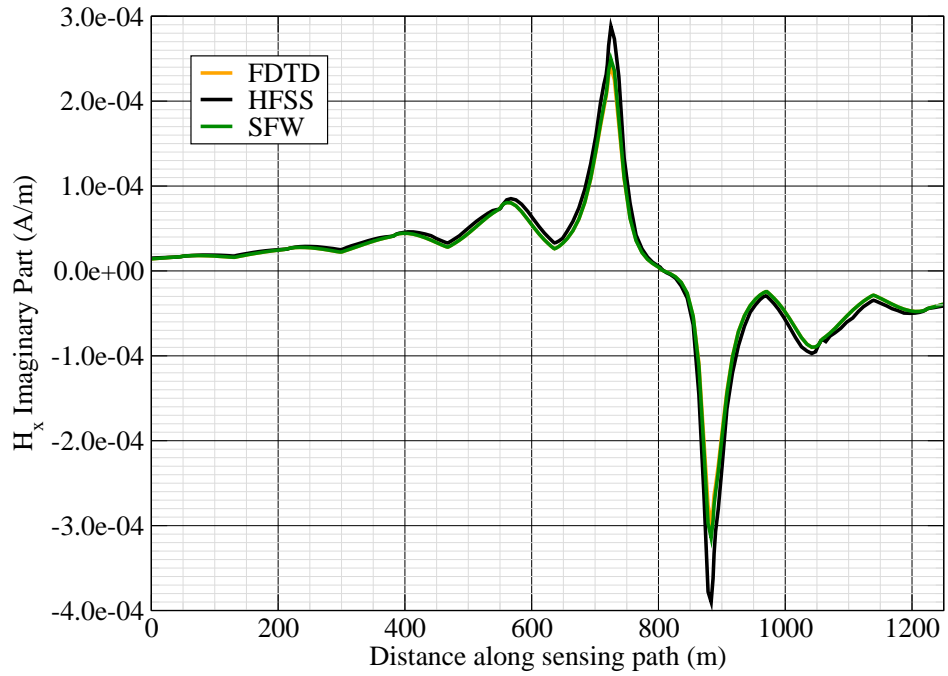


Figure 10: H_x imag.

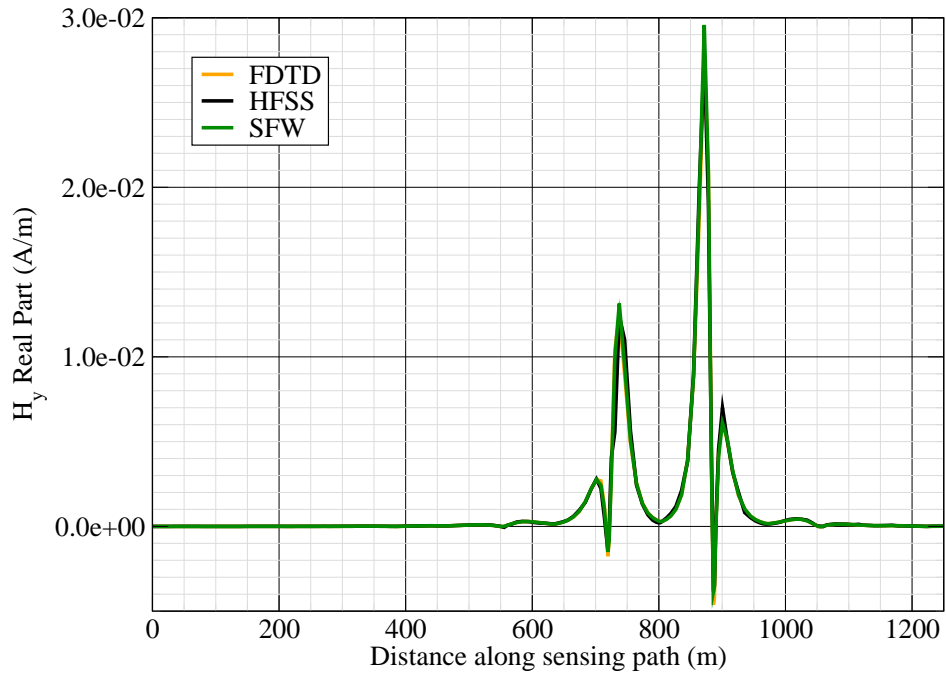


Figure 11: H_y real.

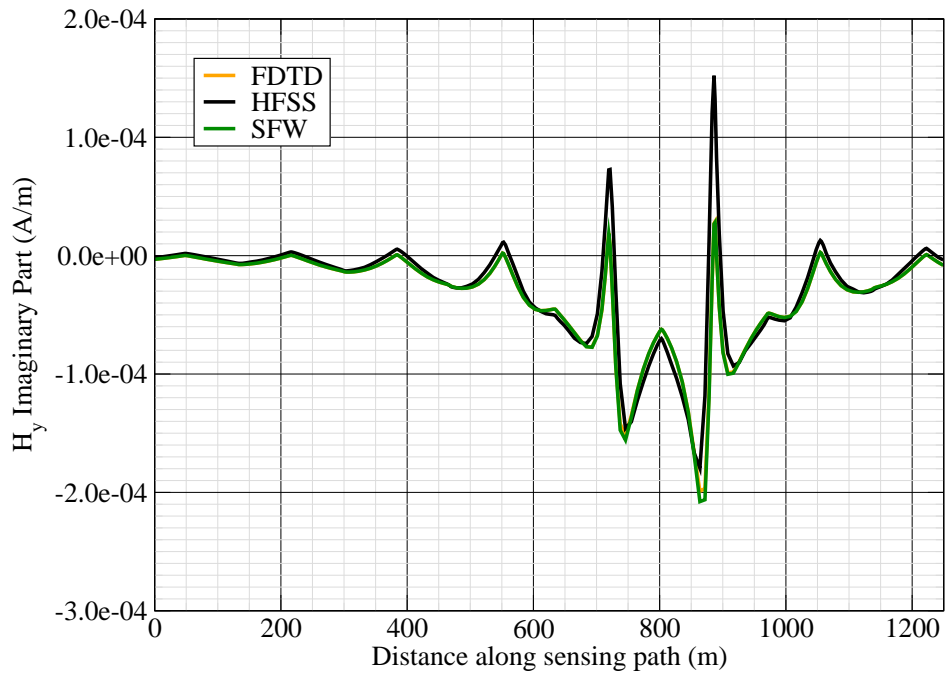


Figure 12: H_y imag.

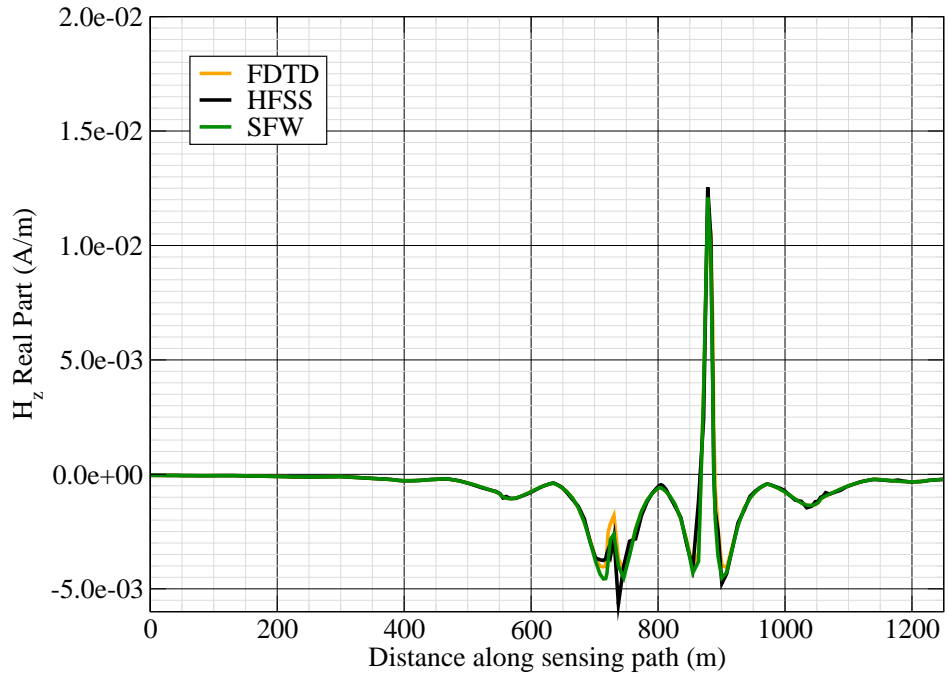


Figure 13: H_z real.

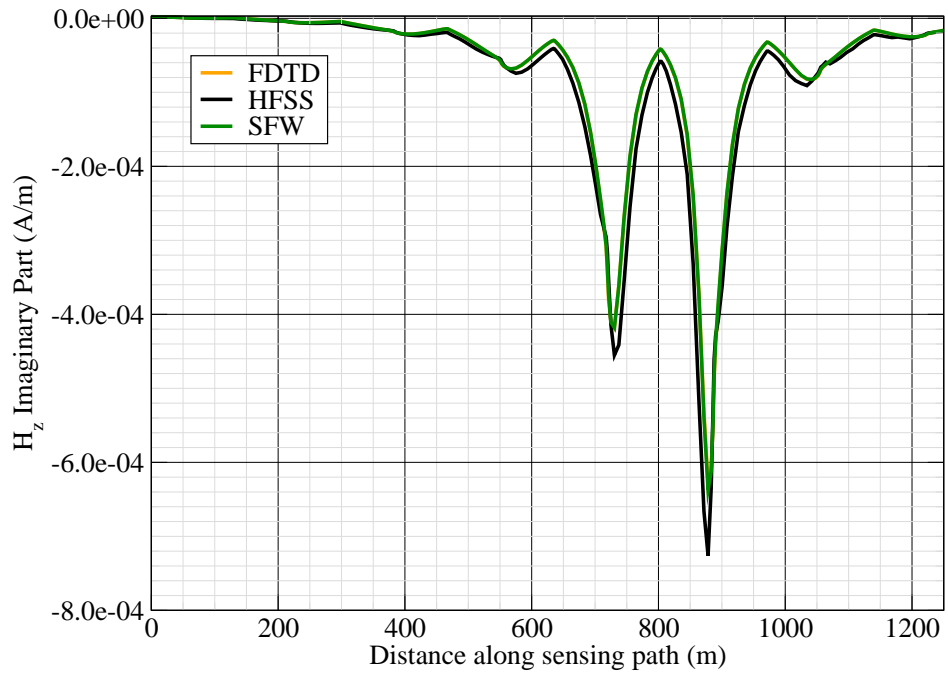


Figure 14: H_z imag.

Experiment 2

Runs 1119

Experiment Date: 12/08/2008

1 Discussion

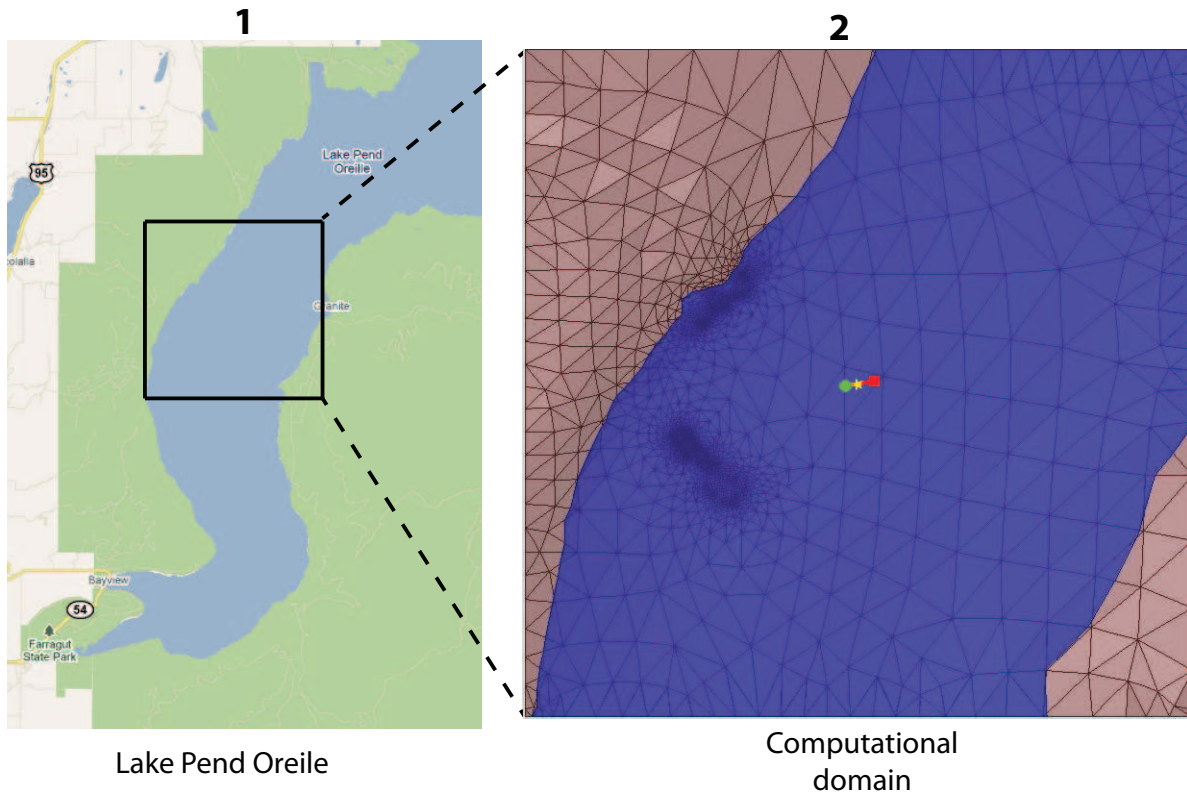


Figure 1: Sensor and source locations; see test report. Sensor is represented by the yellow star; source start and end points represented by green circle and red square.

Source Parameters

- Source Type: HED (Boat Hull: plates 0.61 m by 0.305 m separated by 4 m).
- Source Strength: 0.55 A-m.
- $f = 1000$ Hz.

Environment

- Air: $\sigma = 0$ S/m and $\epsilon_r = 1$
- Water: $\sigma = 0.01$ S/m and $\epsilon_r = 81$
- Mud: $\sigma = 0.0012$ S/m and $\epsilon_r = 1$

Table 1: Simulation Details

	FDTD	HFSS	QES/SFW
Domain Size	200 X 200 X 120 cells	88,148 tets	N/A
Cell Size (m)	5 X 5 X 5	N/A	N/A
Time Step (ns)	9.6	N/A	N/A
Run Time (Hrs)	36	3.65	0.01
Water Depth (m)	N/A	N/A	300
Effective Source Area (m)	N/A	l = 0.61 w = 0.61	r = 0.058

Comments

- To implement reciprocity, three simulations per vector field are required for a total of six simulations. Run times correspond to the time required to conduct all six simulations.
- Computational time is based on actual elapsed real time. This number is highly subjective and based on how many other applications might be running at a particular time. However, the reported number is an indication of the amount of time typically needed for a particular simulation. The computer specs are: 16 CPU cores at 2.8 GHz.
- Run times for HFSS are given for a single frequency.
- QES is not applicable for magnetic fields using electric source excitation.

2 Simulation Variables

Sensor_P1(x,y,z) [m]	(3995.5266,3997.0031,-8.2296)
Sensor_P2(x,y,z) [m]	(3995.5266,3997.0031,-8.2296)
Source_P1(x,y,z) [m]	(3844.3005,3973.5101,0)
Source_P2(x,y,z) [m]	(4186.8534,4031.6213,0)
Source_Plate_Separation [m]	4
Source_Size [m X m X #]	[0.610 X 0.305 X 1]
Source_Heading [deg]	8.2669
Source_Voltage [V Peak]	19.2997
Source_Current [A Peak]	0.13731
Source_Frequency [Hz]	1000

--- Extra Information ---

Source_Heading_Bounds [deg]	(N/A)
Average_Boat_Speed [m/s]	3.2472
Source_Type	Electric boat hull (boat hull)
Sensor_Type	EMA
Bin_Size [sec]	1
Number_of_Datapoints	108
Lake_Origin (Easting,Northing)	(741304.279,709845.52)
Analysis_Date	Exp2_ScenSa_28-Jul-2011

3 Boat Path

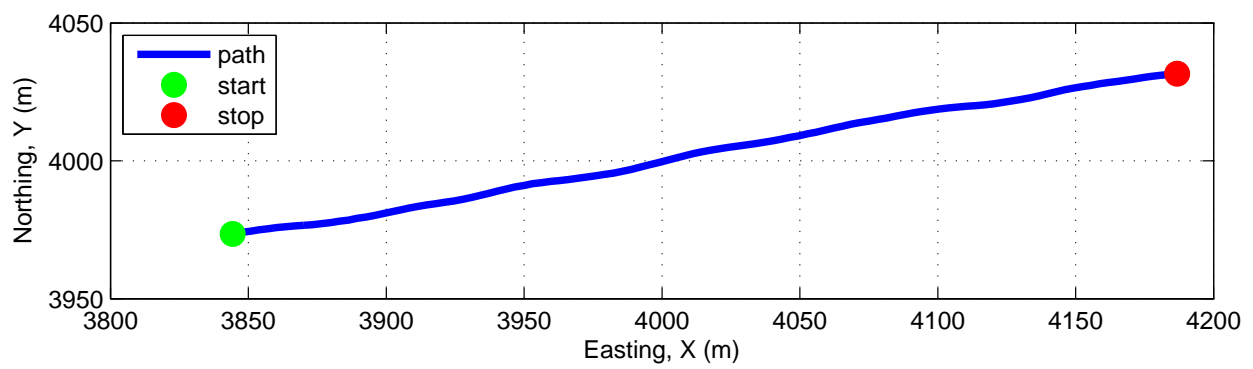
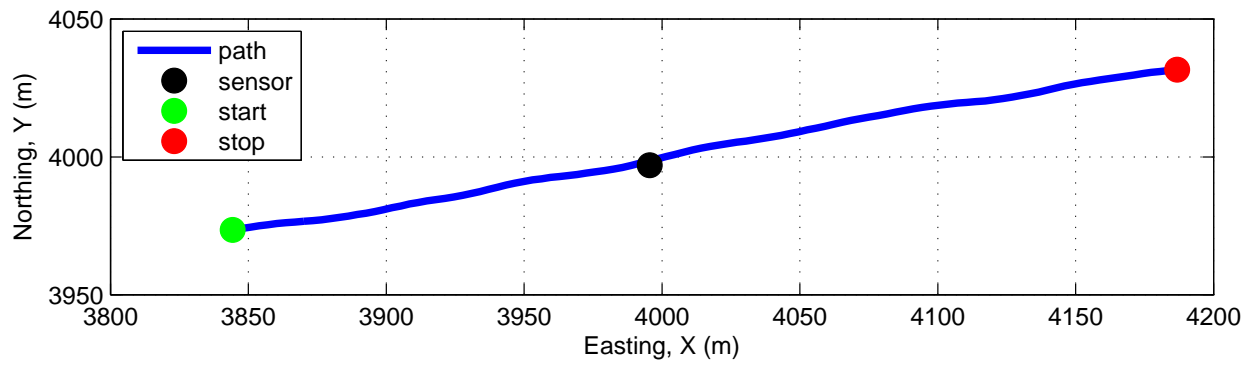


Figure 2: Source and sensor relationship.

4 Plots

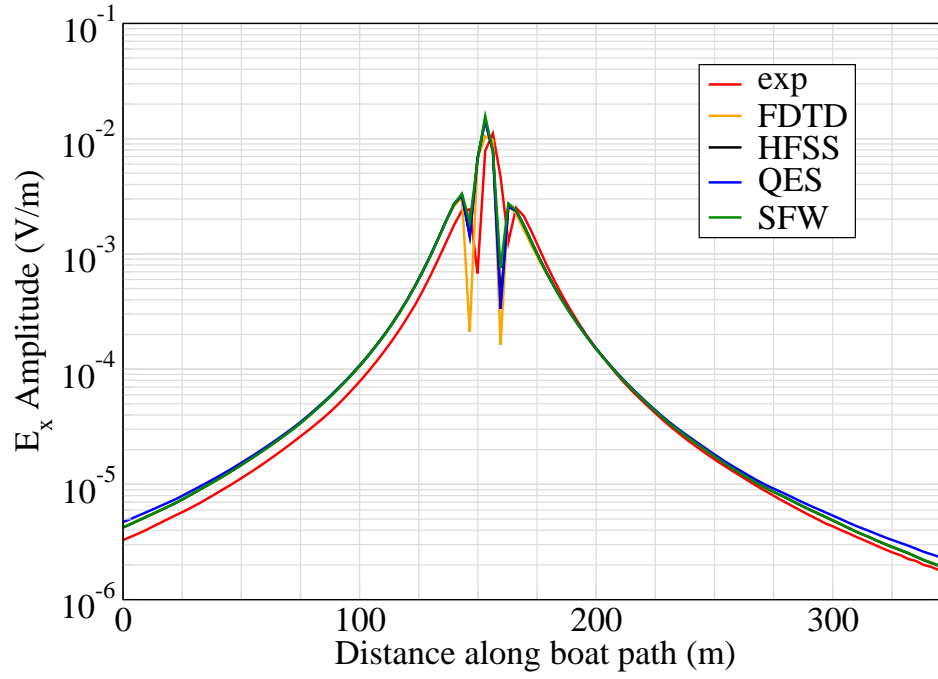


Figure 3: E_x .

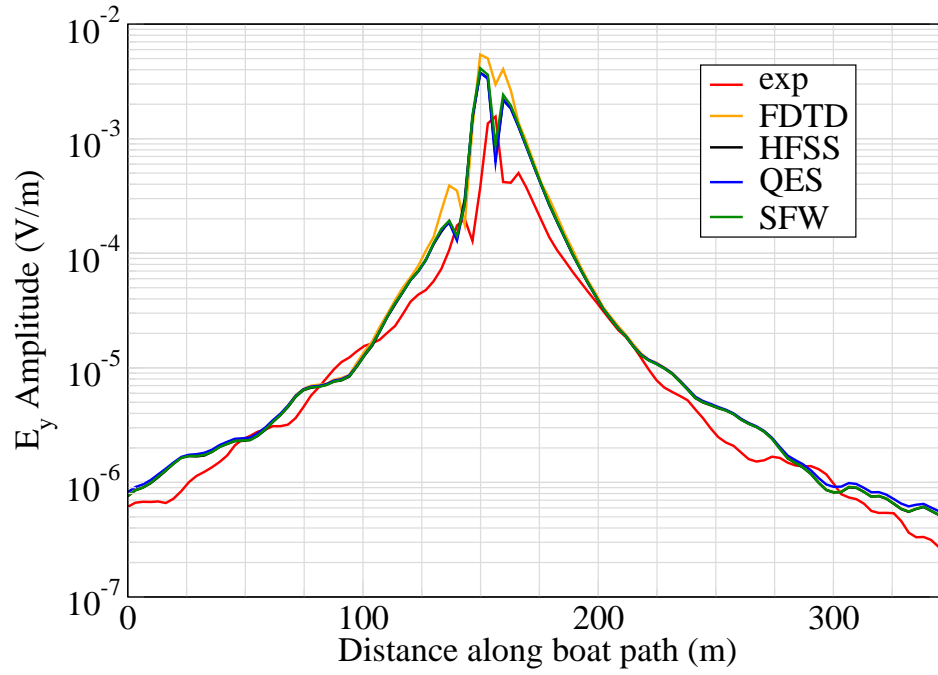


Figure 4: E_y .

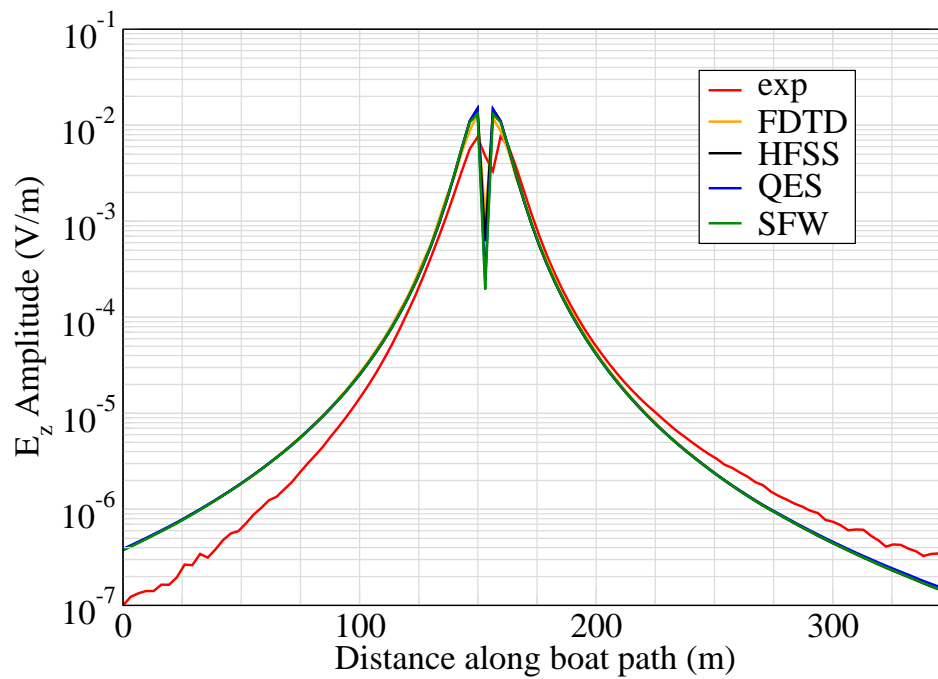


Figure 5: E_z .

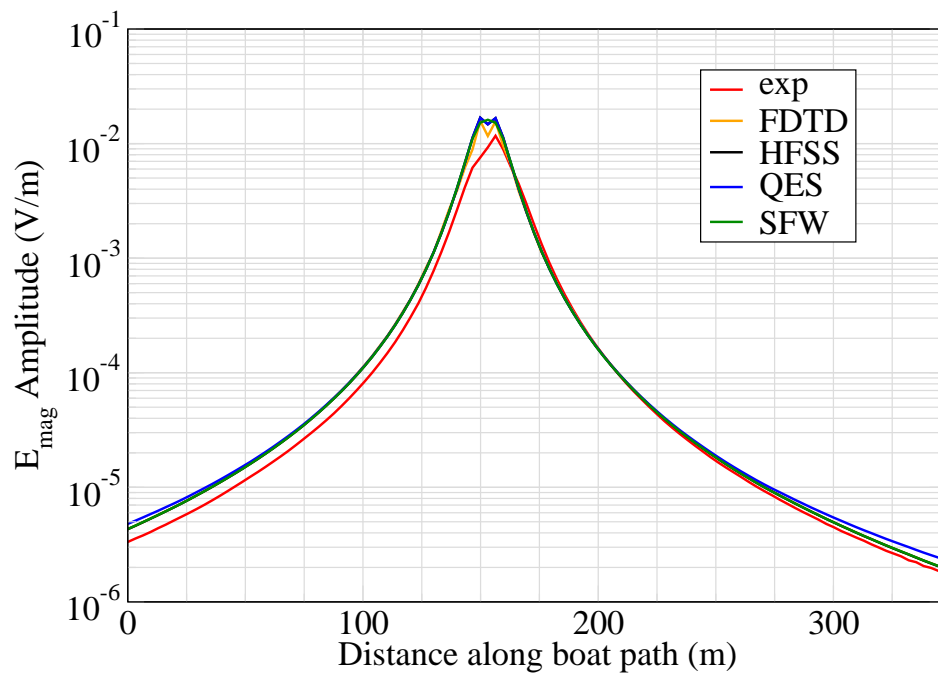


Figure 6: E_{mag} .

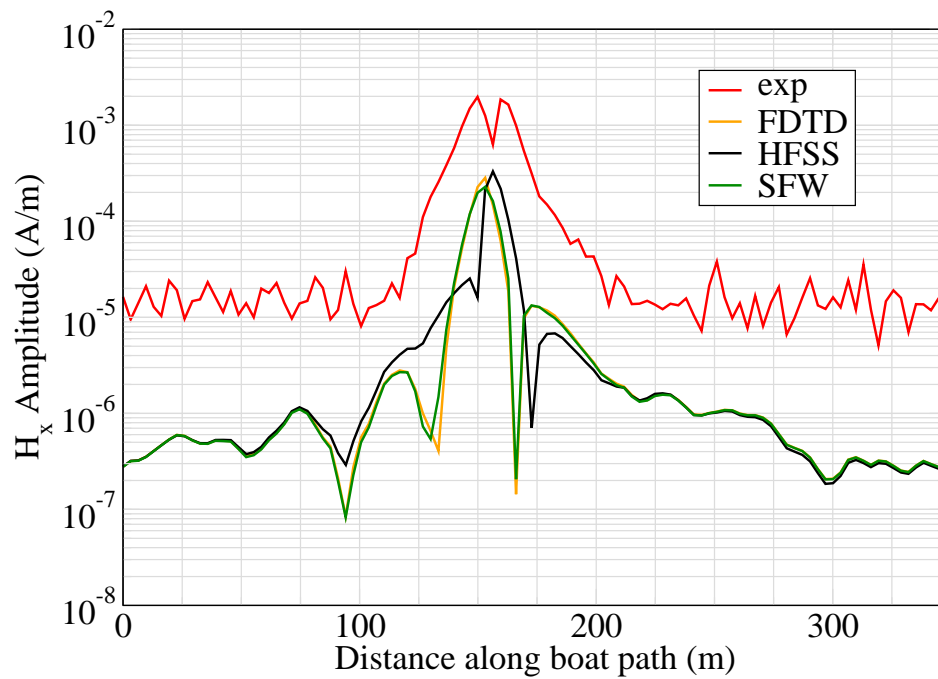


Figure 7: H_x .

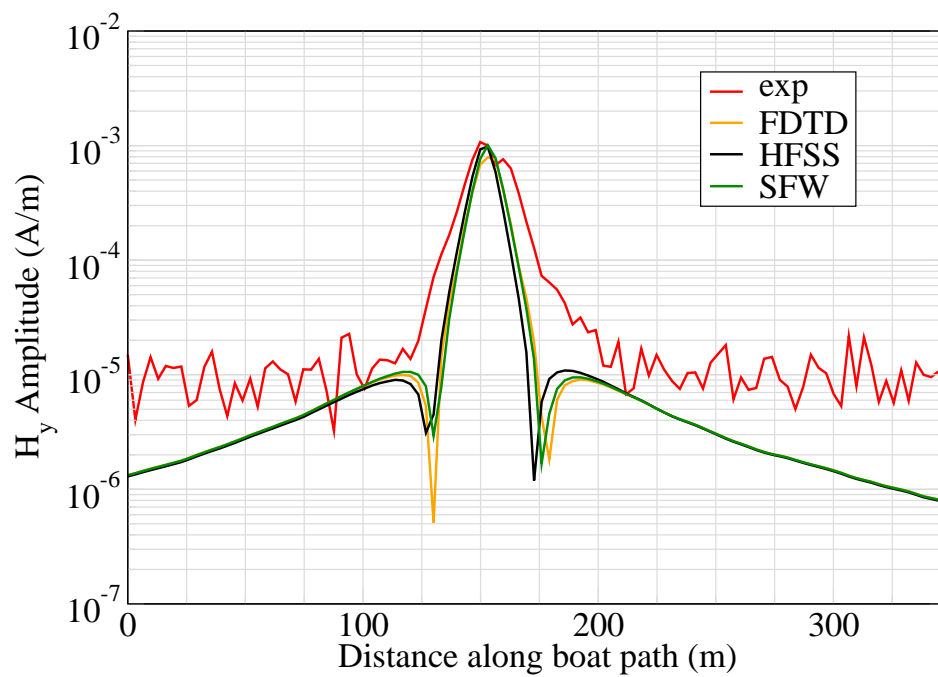


Figure 8: H_y .

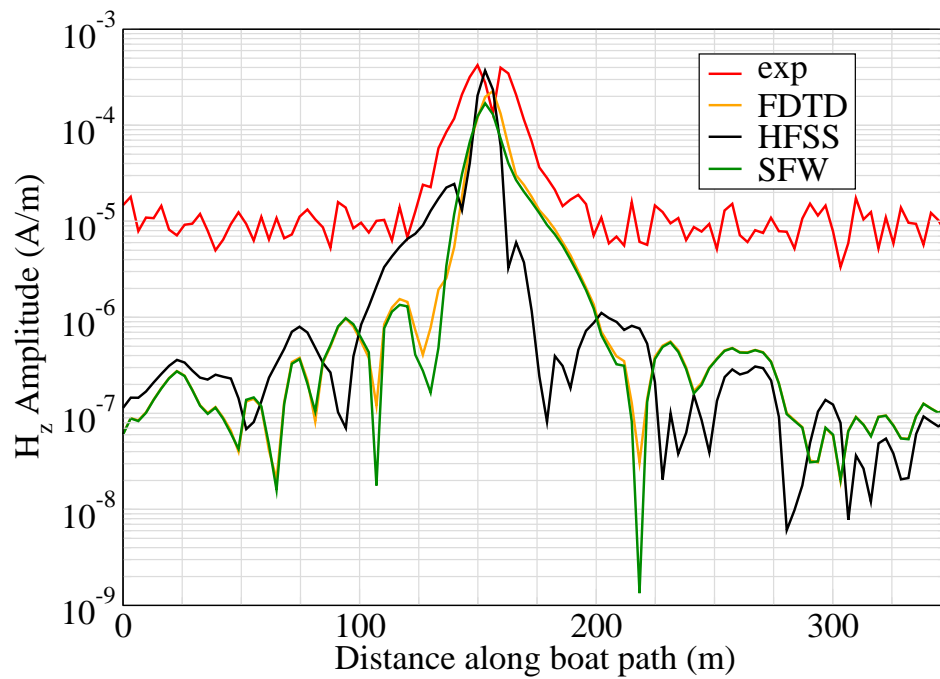


Figure 9: H_z .

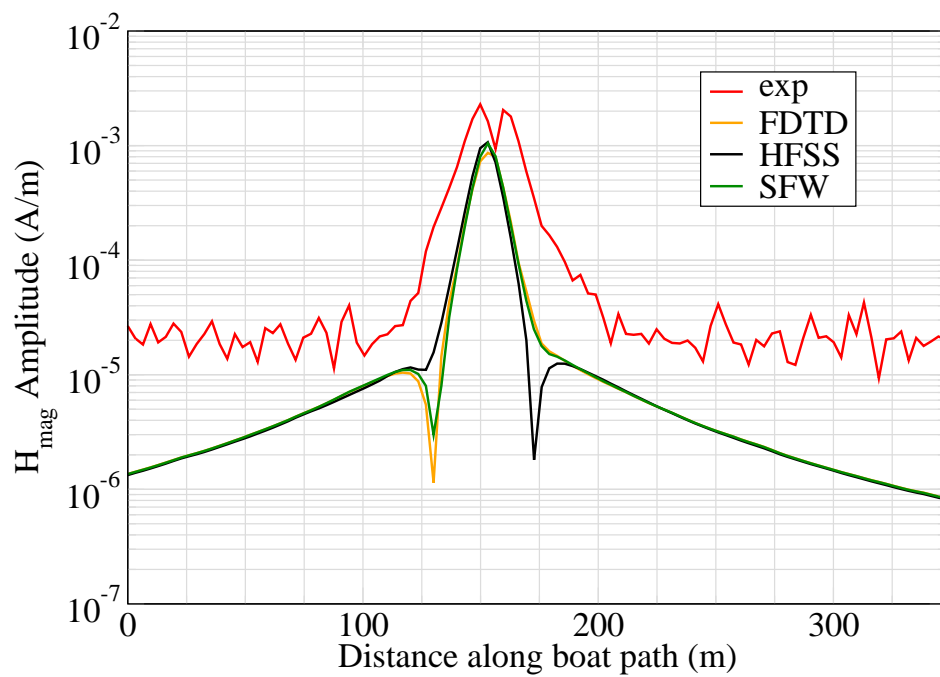


Figure 10: H_{mag} .

Experiment 2

Runs 1120

Experiment Date: 12/11/2008

1 Discussion

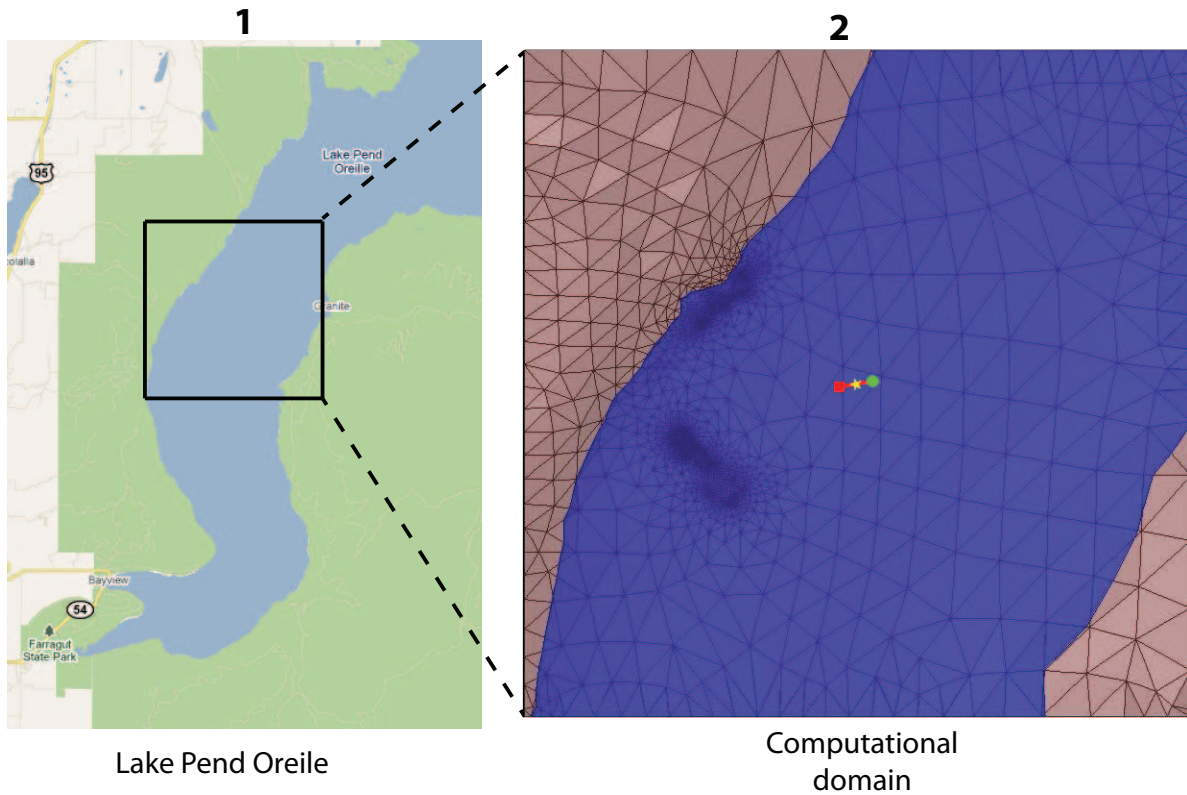


Figure 1: Sensor and source locations; see test report. Sensor is represented by the yellow star; source start and end points represented by green circle and red square.

Source Parameters

- Source Type: HED (Boat Hull: plates 0.61 m by 0.305 m separated by 4 m).
- Source Strength: 0.55 A-m.
- $f = 1000$ Hz.

Environment

- Air: $\sigma = 0$ S/m and $\epsilon_r = 1$
- Water: $\sigma = 0.01$ S/m and $\epsilon_r = 81$
- Mud: $\sigma = 0.0012$ S/m and $\epsilon_r = 1$

Table 1: Simulation Details

	FDTD	HFSS	QES/SFW
Domain Size	200 X 200 X 160 cells	133,013 tets	N/A
Cell Size (m)	5 X 5 X 5	N/A	N/A
Time Step (ns)	9.6	N/A	N/A
Run Time (Hrs)	44.8	?	0.01
Water Depth (m)	N/A	N/A	300
Effective Source Area (m)	N/A	l = 0.61 w = 0.61	r = 0.058

Comments

- To implement reciprocity, three simulations per vector field are required for a total of six simulations. Run times correspond to the time required to conduct all six simulations.
- Computational time is based on actual elapsed real time. This number is highly subjective and based on how many other applications might be running at a particular time. However, the reported number is an indication of the amount of time typically needed for a particular simulation. The computer specs are: 16 CPU cores at 2.8 GHz.
- Run times for HFSS are given for a single frequency.
- QES is not applicable for magnetic fields using electric source excitation.

2 Simulation Variables

Sensor_P1(x,y,z) [m]	(3995.5266,3997.0031,-8.2296)
Sensor_P2(x,y,z) [m]	(3995.5266,3997.0031,-8.2296)
Source_P1(x,y,z) [m]	(4200.2248,4037.7094,0)
Source_P2(x,y,z) [m]	(3801.7565,3963.3218,0)
Source_Plate_Separation [m]	4
Source_Size [m X m X #]	[0.610 X 0.305 X 1]
Source_Heading [deg]	191.1532
Source_Voltage [V Peak]	19.1957
Source_Current [A Peak]	0.13705
Source_Frequency [Hz]	1000

--- Extra Information ---

Source_Heading_Bounds [deg]	(N/A)
Average_Boat_Speed [m/s]	2.8748
Source_Type	Electric boat hull (boat hull)
Sensor_Type	EMA
Bin_Size [sec]	1
Number_of_Datapoints	142
Lake_Origin (Easting,Northing)	(741304.279,709845.52)
Analysis_Date	Exp2_ScenSC_28-Jul-2011

3 Boat Path

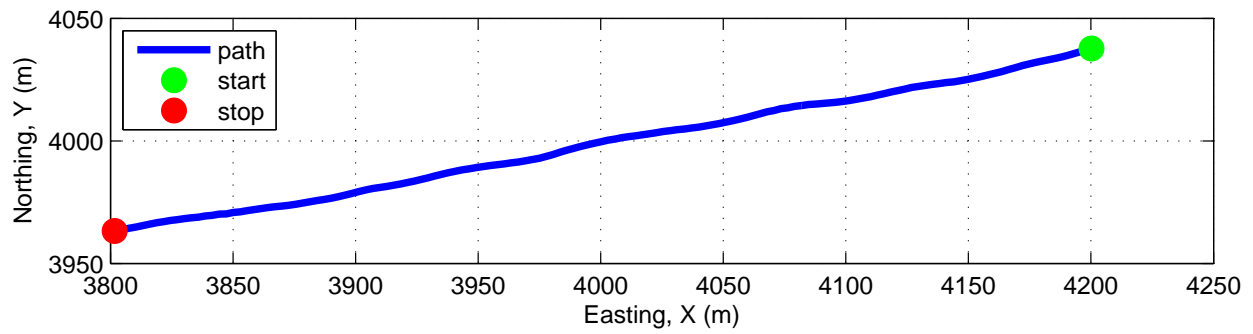
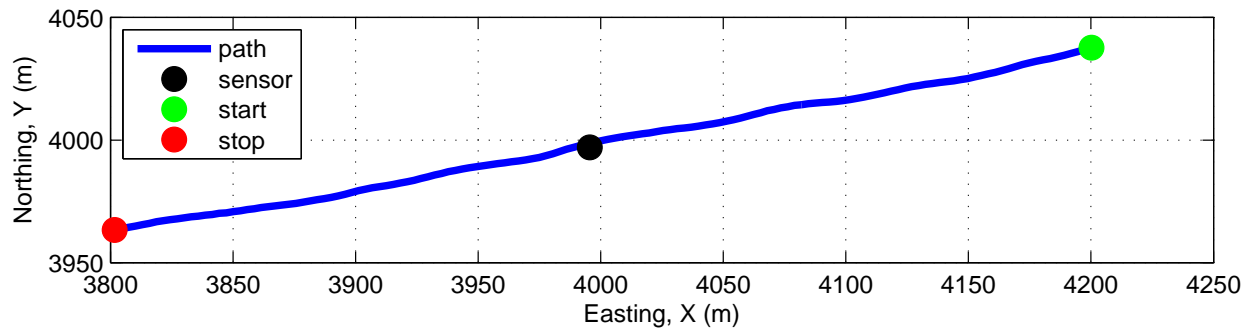


Figure 2: Source and sensor relationship.

4 Plots

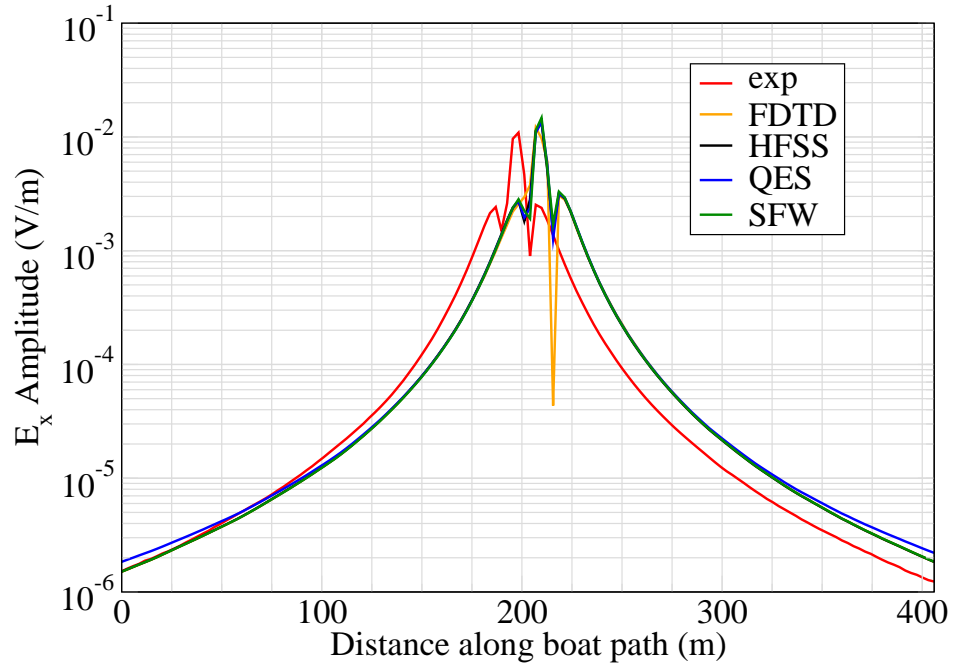


Figure 3: E_x .

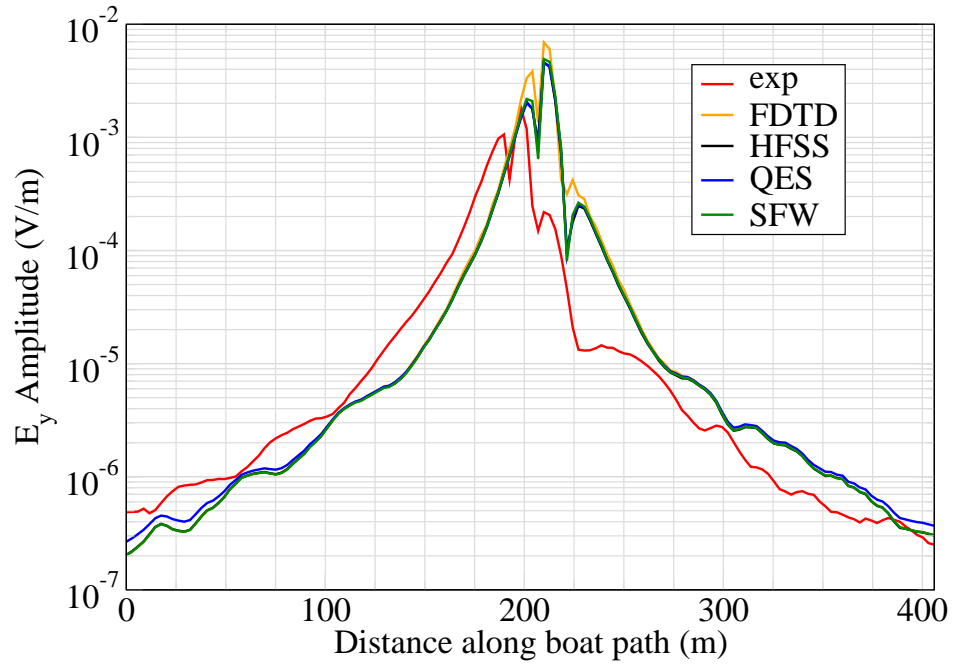


Figure 4: E_y .

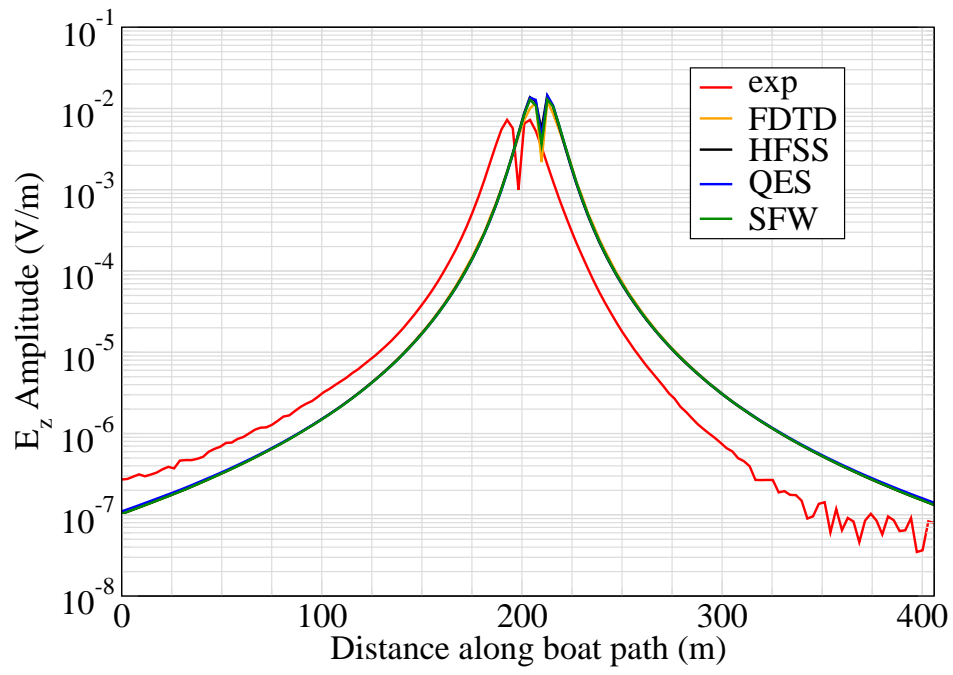


Figure 5: E_z .

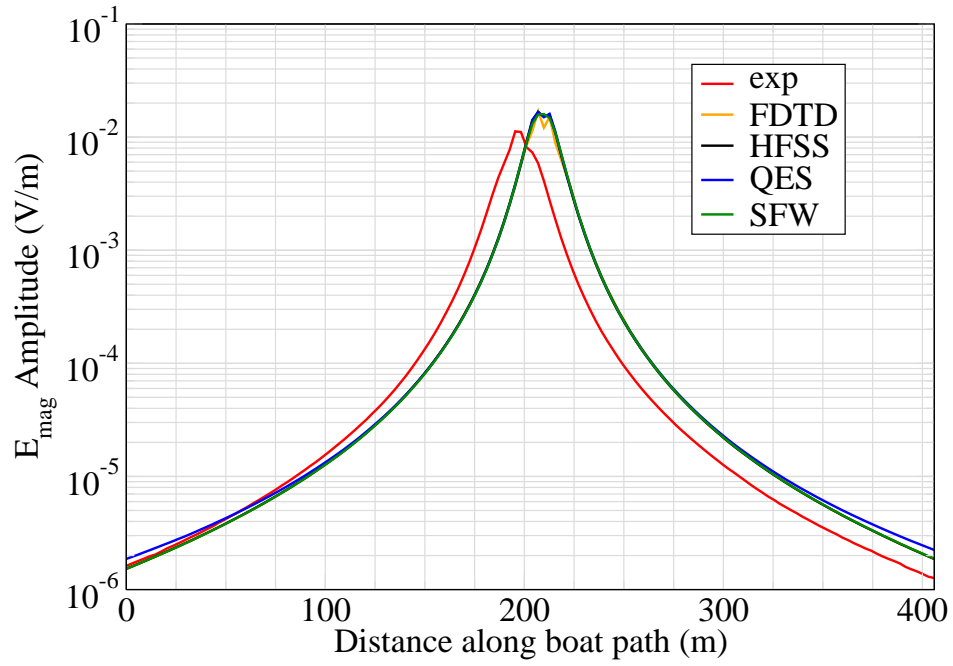


Figure 6: E_{mag} .

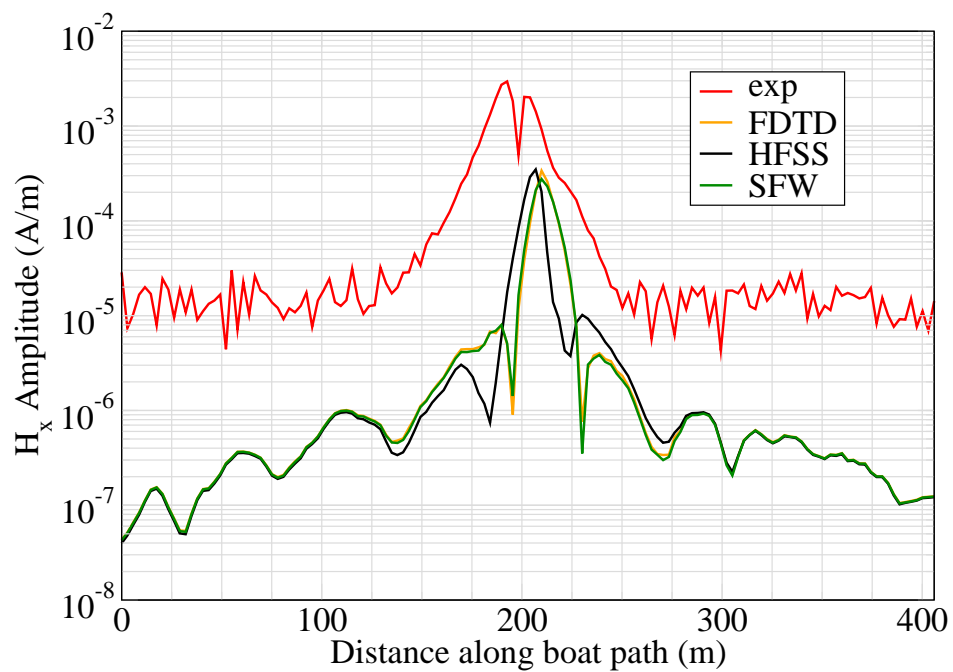


Figure 7: H_x .

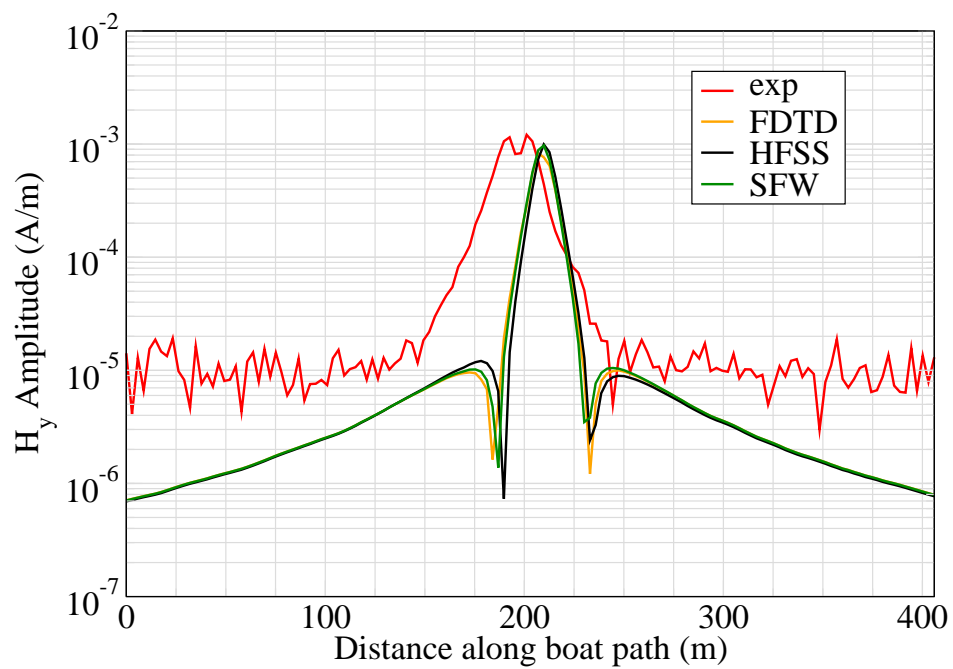


Figure 8: H_y .

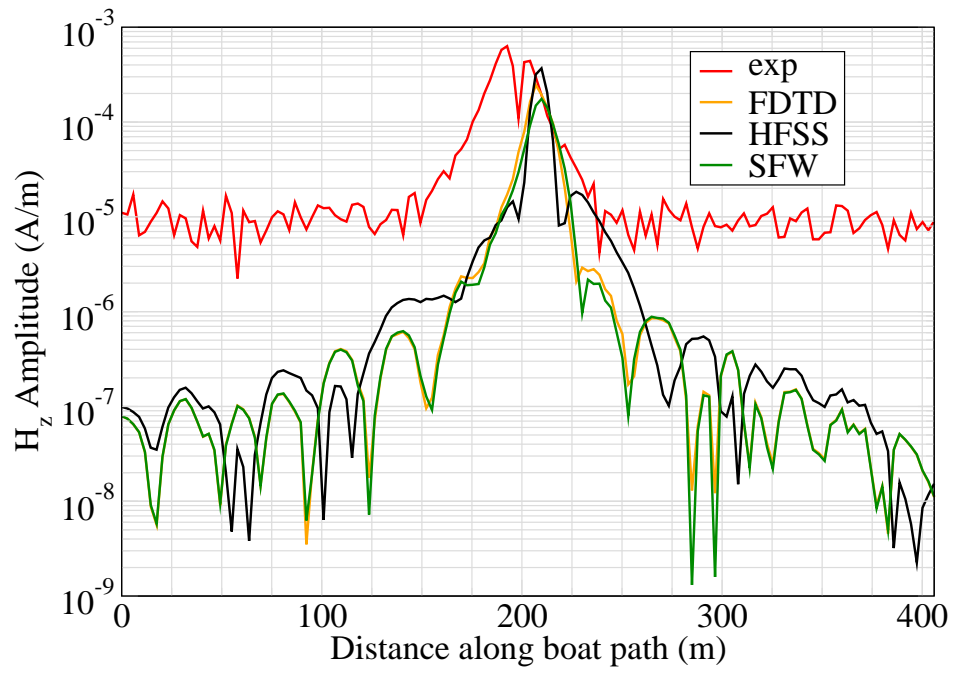


Figure 9: H_z .

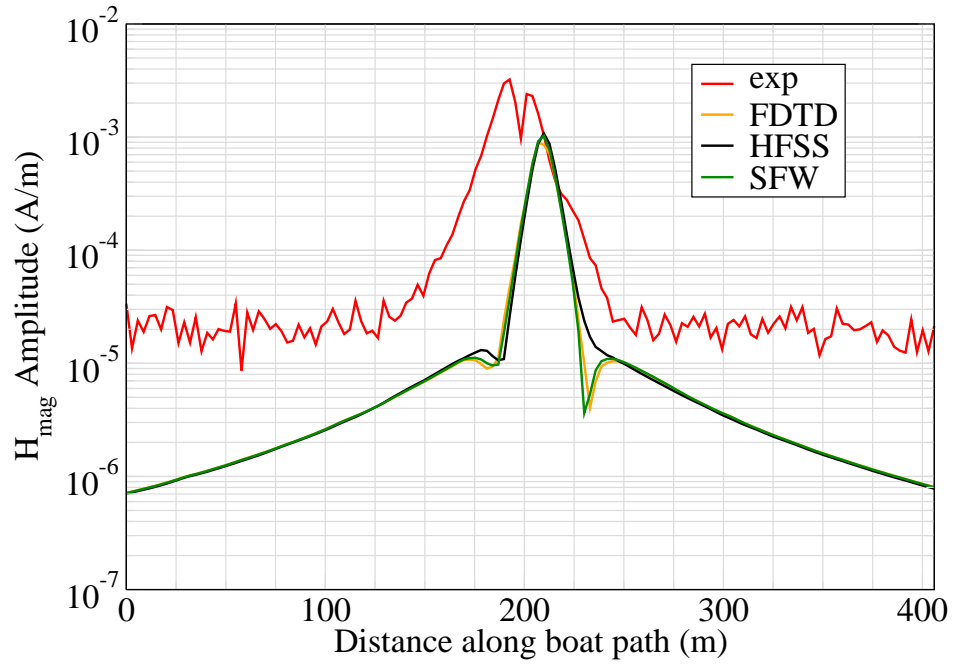


Figure 10: H_{mag} .

Experiment 2

Runs 2021

Experiment Date: 12/09/2008

1 Discussion

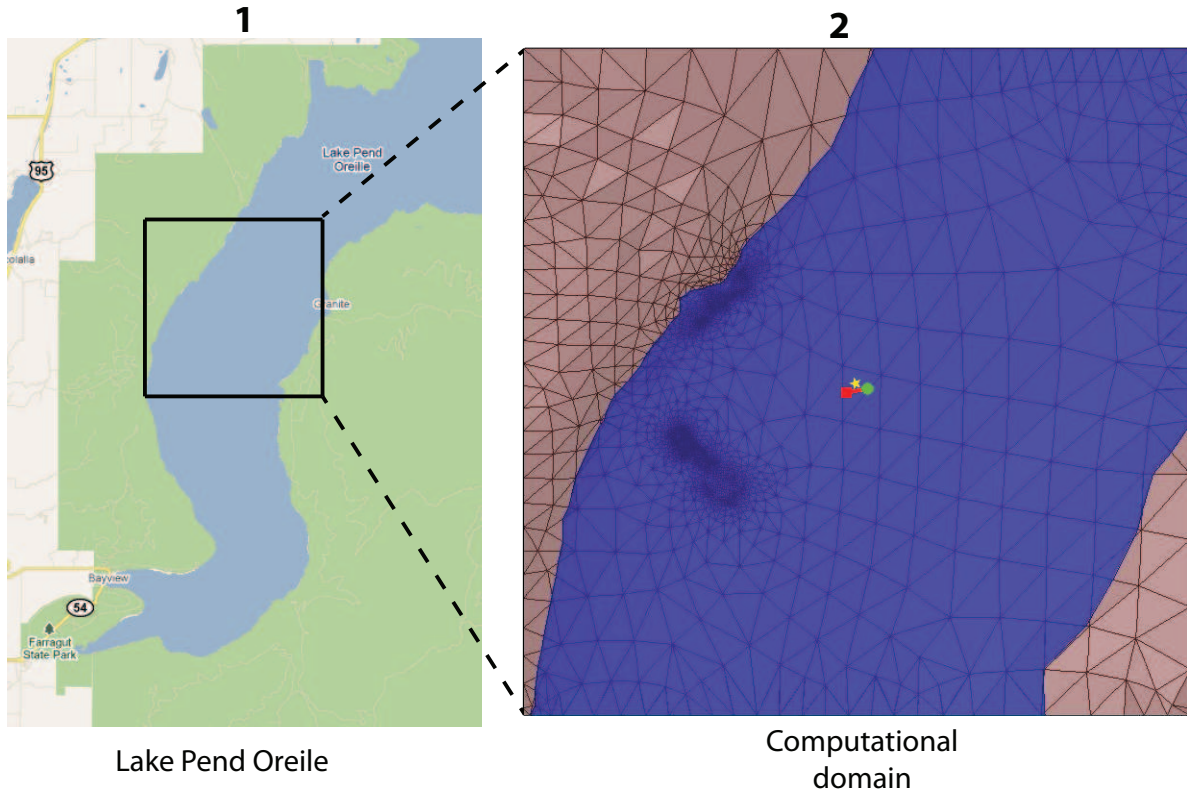


Figure 1: Sensor and source locations; see test report. Sensor is represented by the yellow star; source start and end points represented by green circle and red square.

Source Parameters

- Source Type: HED (Boat Hull: plates 0.61 m by 0.305 m separated by 4 m).
- Source Strength: 4.78 A-m.
- $f = 100$ Hz.

Environment

- Air: $\sigma = 0$ S/m and $\epsilon_r = 1$
- Water: $\sigma = 0.01$ S/m and $\epsilon_r = 81$
- Mud: $\sigma = 0.0012$ S/m and $\epsilon_r = 1$

Table 1: Simulation Details

	FDTD	HFSS	QES/SFW
Domain Size	200 X 200 X 120 cells	108,390 tets	N/A
Cell Size (m)	5 X 5 X 5	N/A	N/A
Time Step (ns)	9/6	N/A	N/A
Run Time (Hrs)	36	2.95	0.01
Water Depth (m)	N/A	N/A	300
Effective Source Area (m)	N/A	l = 0.61 w = 0.61	r = 0.058

Comments

- To implement reciprocity, three simulations per vector field are required for a total of six simulations. Run times correspond to the time required to conduct all six simulations.
- Computational time is based on actual elapsed real time. This number is highly subjective and based on how many other applications might be running at a particular time. However, the reported number is an indication of the amount of time typically needed for a particular simulation. The computer specs are: 16 CPU cores at 2.8 GHz.
- Run times for HFSS are given for a single frequency.
- QES is not applicable for magnetic fields using electric source excitation.

2 Simulation Variables

Sensor_P1(x,y,z) [m]	(3995.5266,3997.0031,-8.2296)
Sensor_P2(x,y,z) [m]	(3995.5266,3997.0031,-8.2296)
Source_P1(x,y,z) [m]	(4145.7196,3932.398,0)
Source_P2(x,y,z) [m]	(3893.3837,3889.5264,0)
Source_Plate_Separation [m]	4
Source_Size [m X m X #]	[0.610 X 0.305 X 1]
Source_Heading [deg]	192.785
Source_Voltage [V Peak]	176.9048
Source_Current [A Peak]	1.1949
Source_Frequency [Hz]	100

--- Extra Information ---

Source_Heading_Bounds [deg]	(N/A)
Average_Boat_Speed [m/s]	1.0892
Source_Type	Electric boat hull (boat hull)
Sensor_Type	EMA
Bin_Size [sec]	1
Number_of_Datapoints	236
Lake_Origin (Easting,Northing)	(741304.279,709845.52)
Analysis_Date	Exp2_ScenSE_28-Jul-2011

3 Boat Path

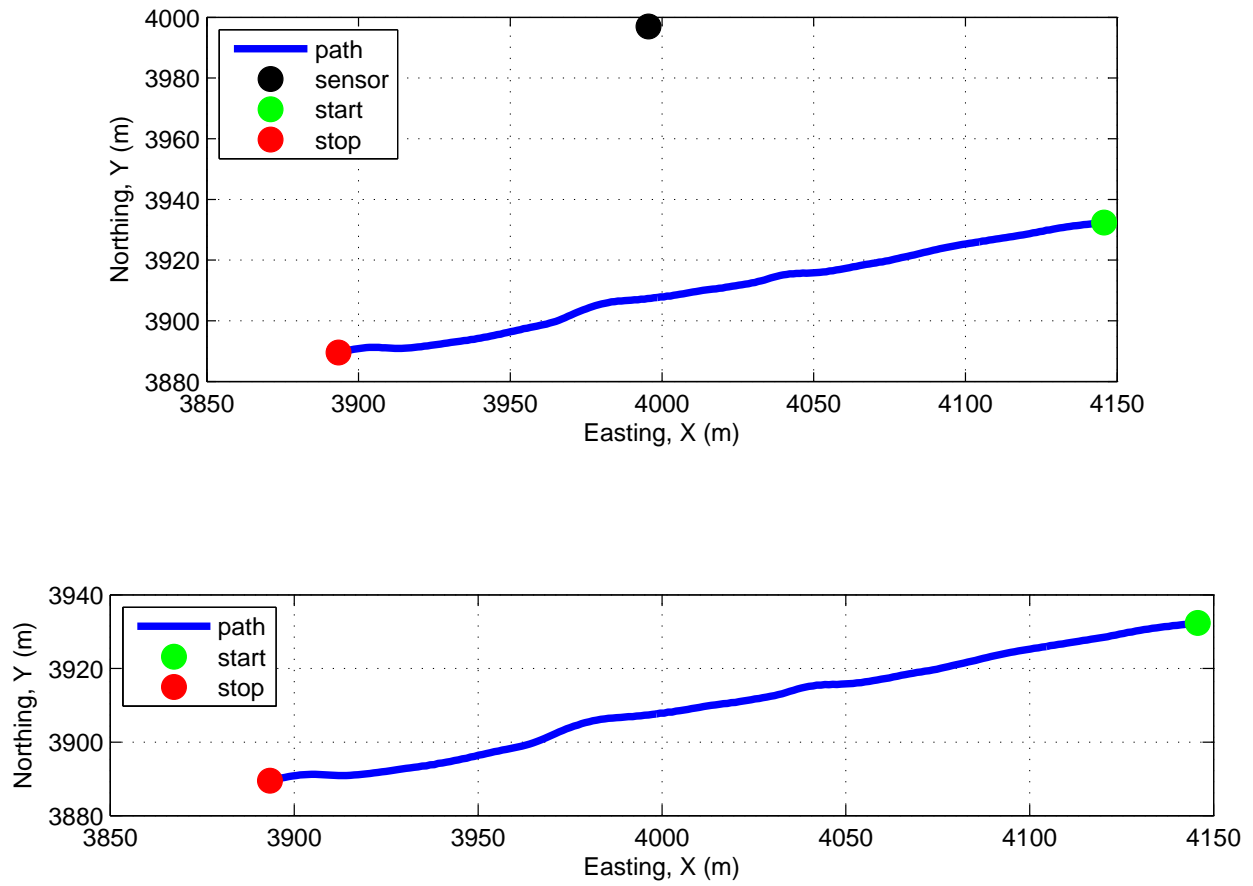


Figure 2: Source and sensor relationship.

4 Plots

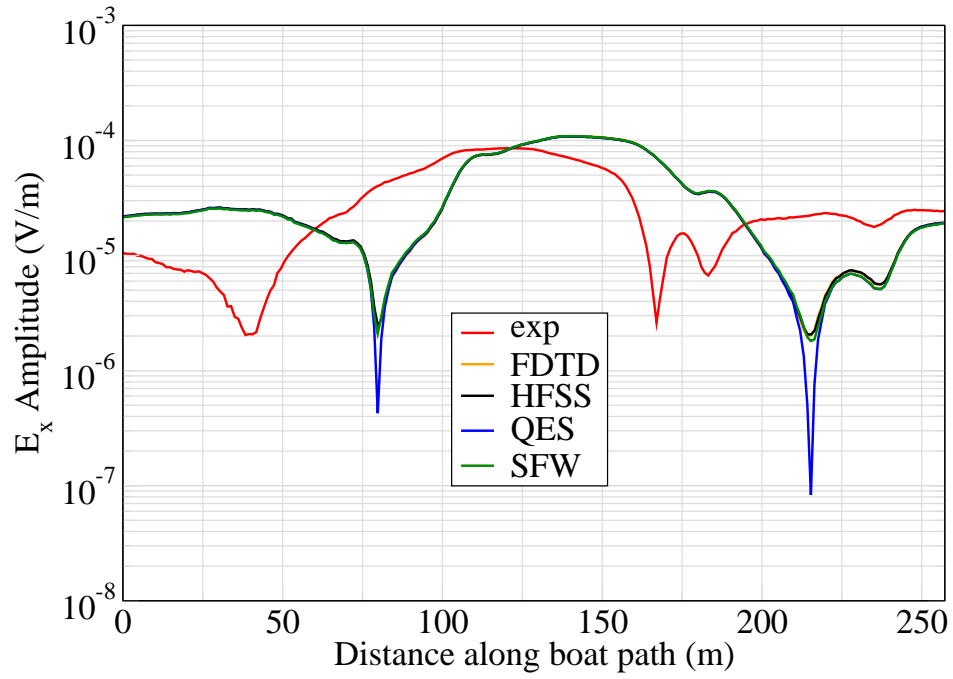


Figure 3: E_x .

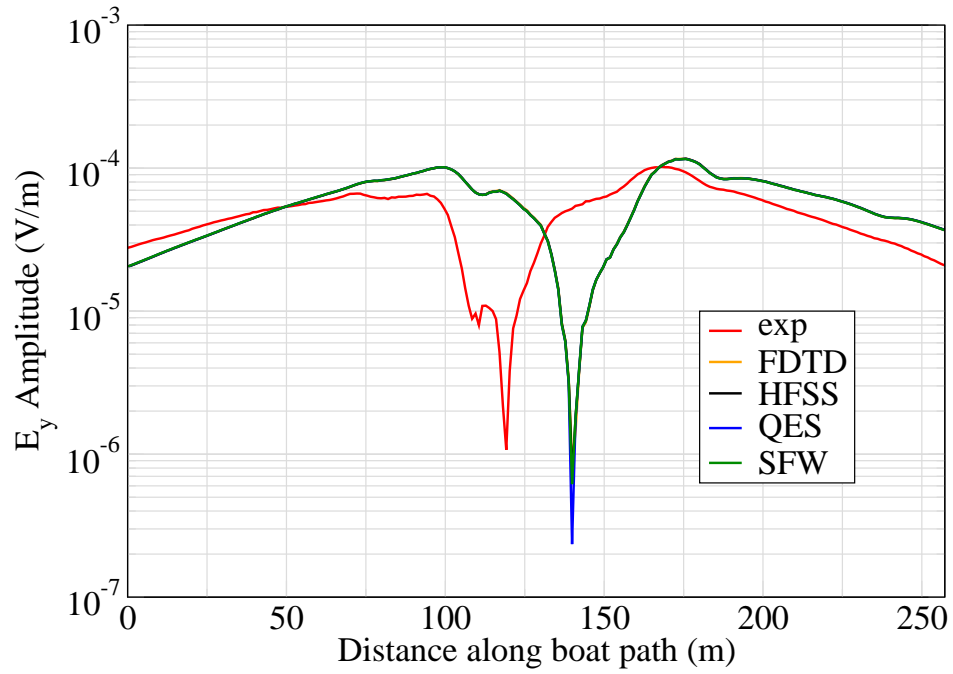


Figure 4: E_y .

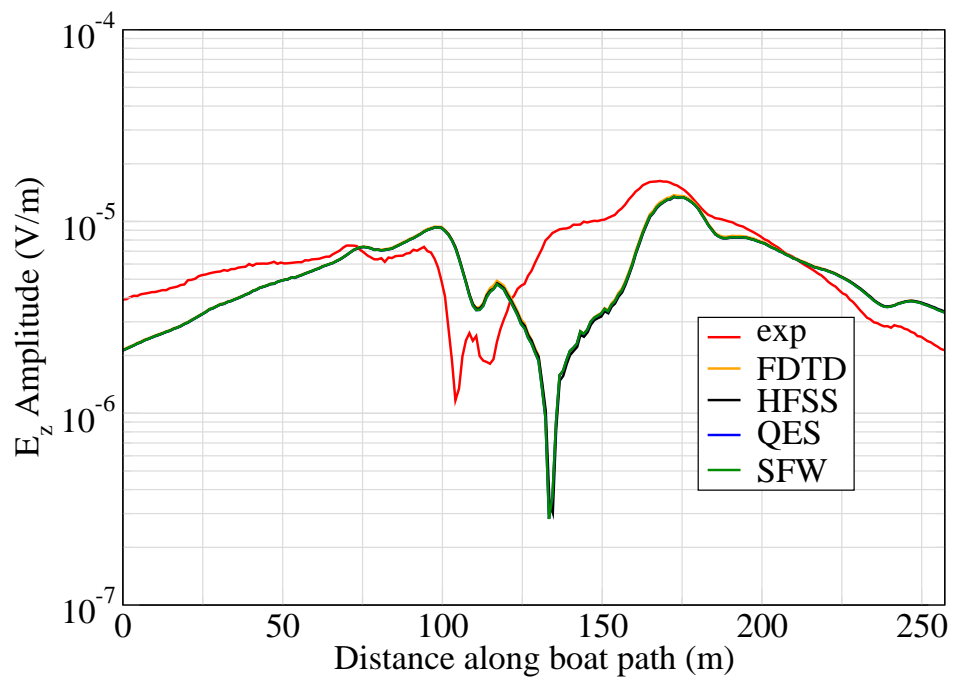


Figure 5: E_z .

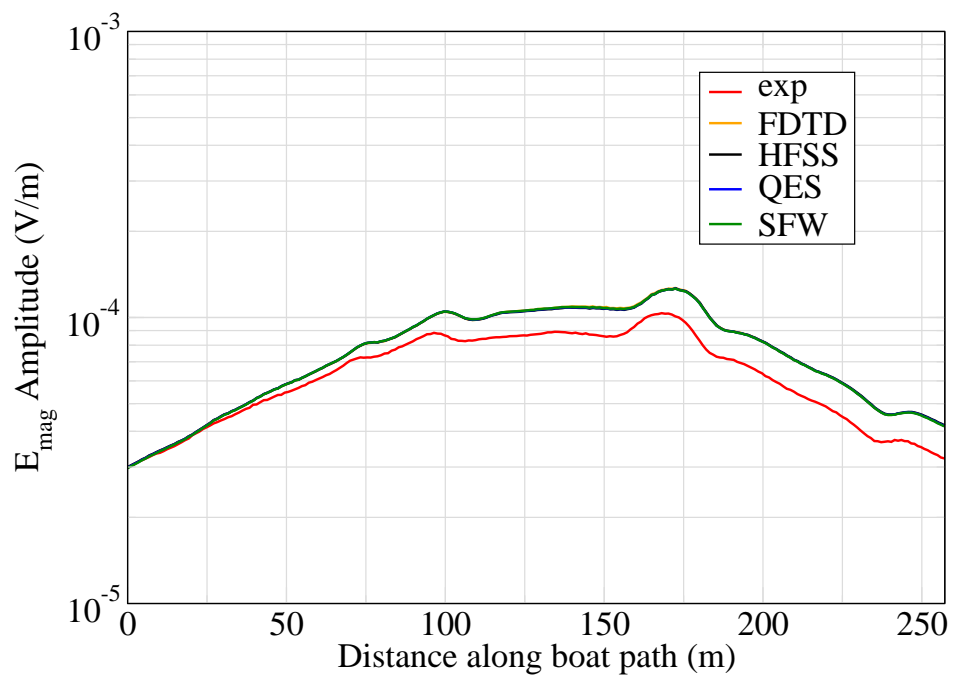


Figure 6: E_{mag} .

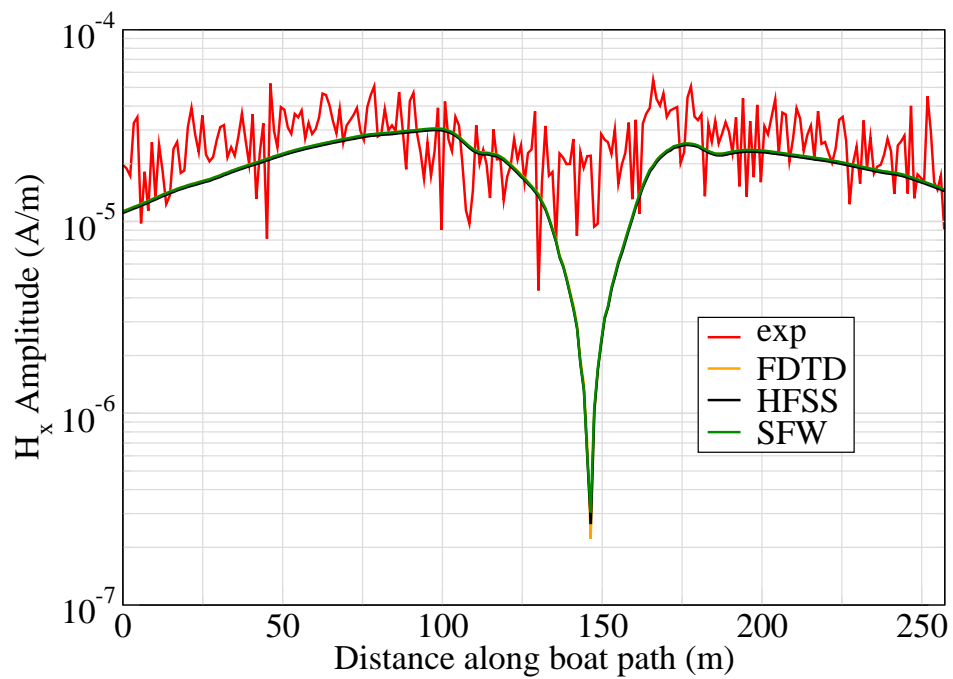


Figure 7: H_x .

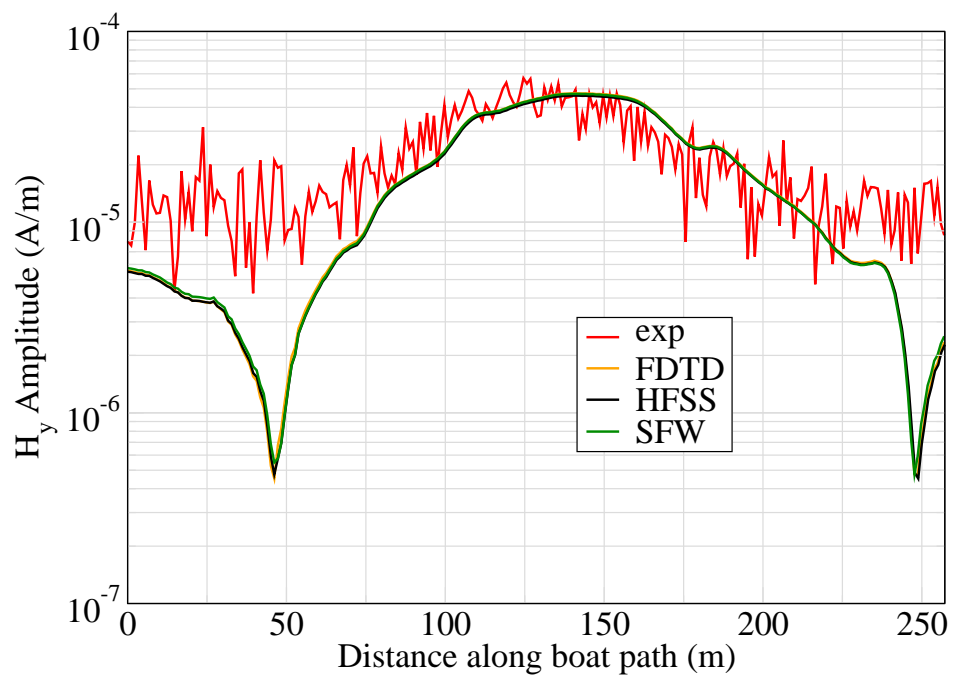


Figure 8: H_y .

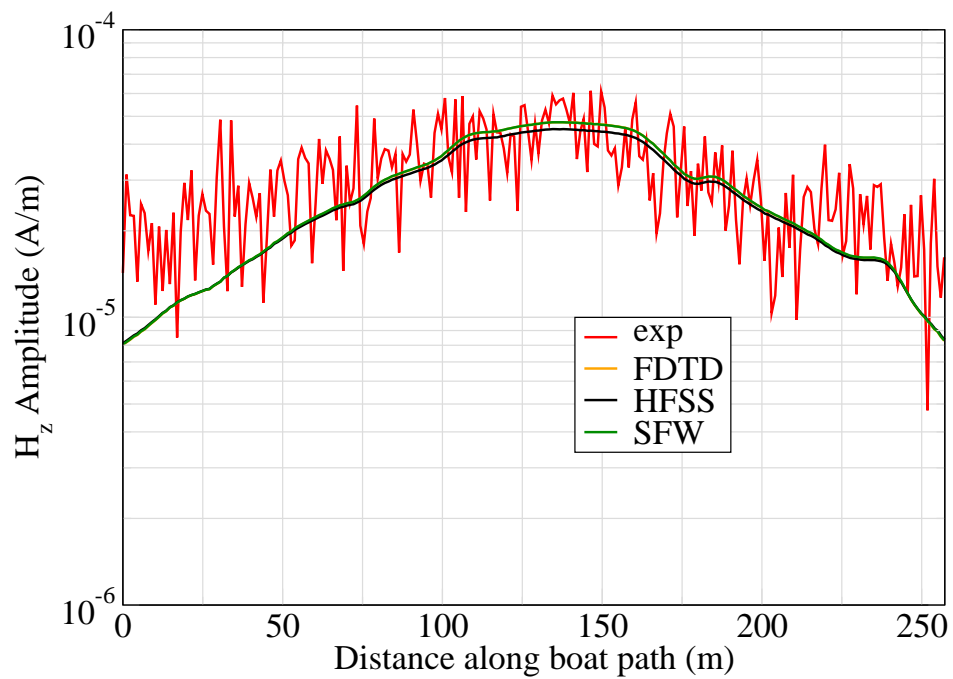


Figure 9: H_z .

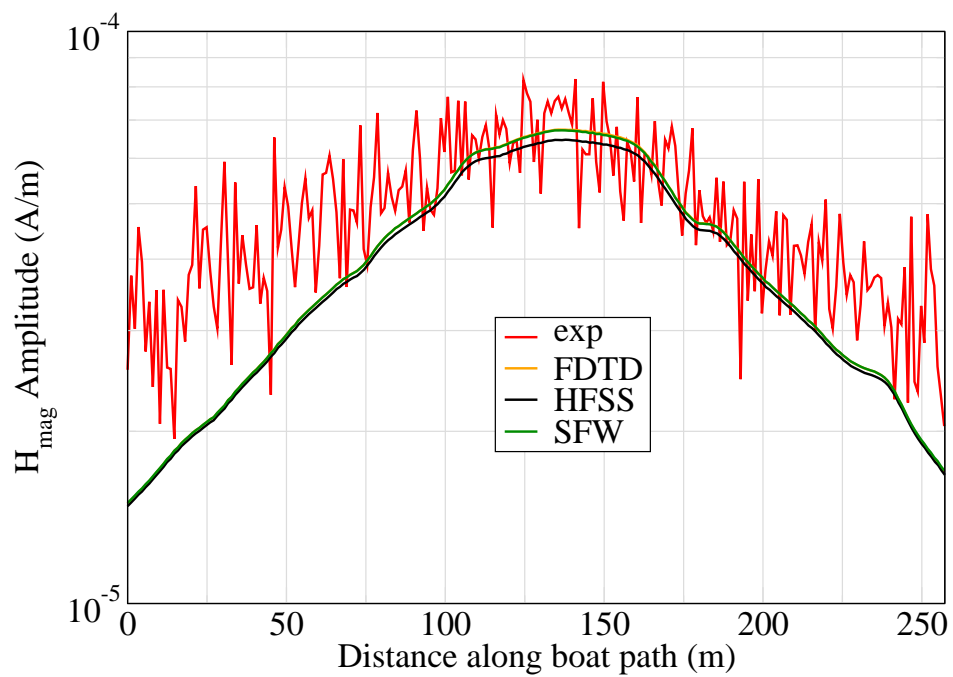


Figure 10: H_{mag} .

Experiment 2

Runs 2023

Experiment Date: 12/09/2008

1 Discussion

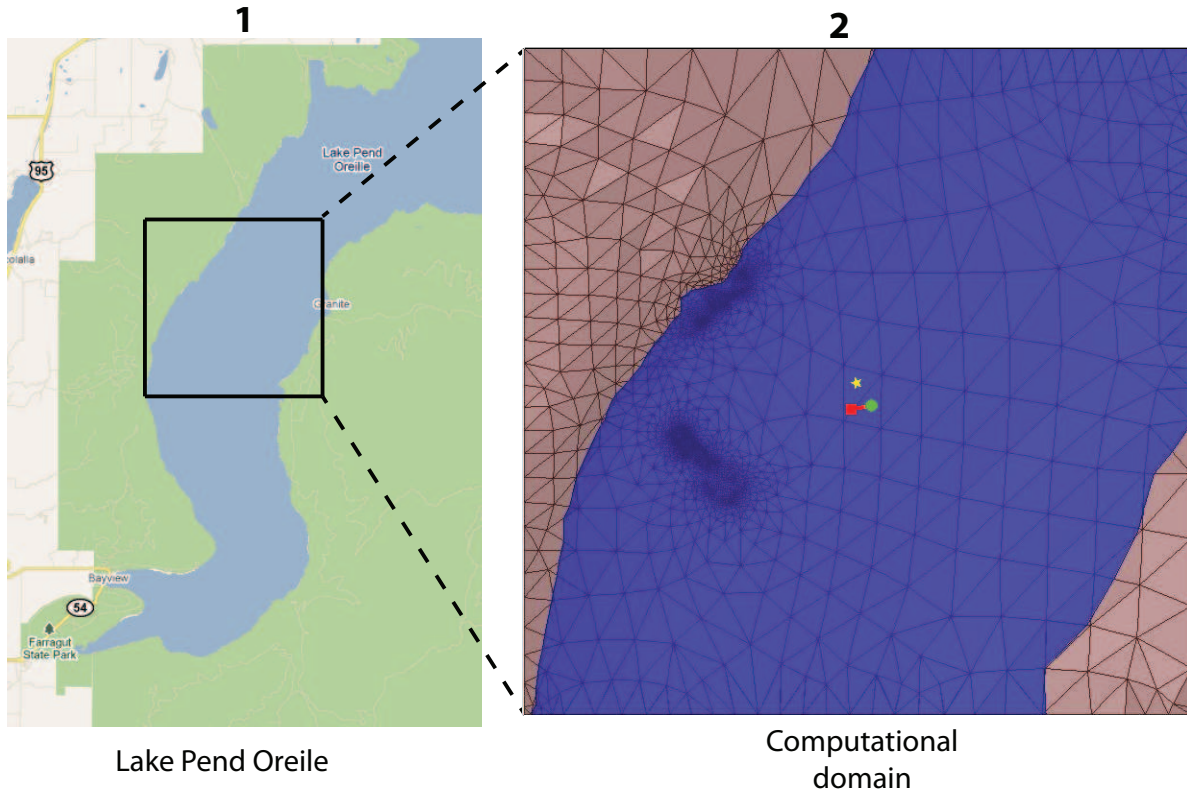


Figure 1: Sensor and source locations; see test report. Sensor is represented by the yellow star; source start and end points represented by green circle and red square.

Source Parameters

- Source Type: HED (Boat Hull: plates 0.61 m by 0.305 m separated by 4 m).
- Source Strength: 4.78 A-m.
- $f = 100$ Hz.

Environment

- Air: $\sigma = 0$ S/m and $\epsilon_r = 1$
- Water: $\sigma = 0.01$ S/m and $\epsilon_r = 81$
- Mud: $\sigma = 0.0012$ S/m and $\epsilon_r = 1$

Table 1: Simulation Details

	FDTD	HFSS	QES/SFW
Domain Size	200 X 200 X 120 cells	127,728 tets	N/A
Cell Size (m)	5 X 5 X 5	N/A	N/A
Time Step (ns)	9.6	N/A	N/A
Run Time (Hrs)	36	3.9	0.01
Water Depth (m)	N/A	N/A	300
Effective Source Area (m)	N/A	l = 0.61 w = 0.61	r = 0.058

Comments

- To implement reciprocity, three simulations per vector field are required for a total of six simulations. Run times correspond to the time required to conduct all six simulations.
- Computational time is based on actual elapsed real time. This number is highly subjective and based on how many other applications might be running at a particular time. However, the reported number is an indication of the amount of time typically needed for a particular simulation. The computer specs are: 16 CPU cores at 2.8 GHz.
- Run times for HFSS are given for a single frequency.
- QES is not applicable for magnetic fields using electric source excitation.

2 Simulation Variables

Sensor_P1(x,y,z) [m]	(3995.5266,3997.0031,-8.2296)
Sensor_P2(x,y,z) [m]	(3995.5266,3997.0031,-8.2296)
Source_P1(x,y,z) [m]	(4174.6948,3721.7698,0)
Source_P2(x,y,z) [m]	(3937.4748,3679.7185,0)
Source_Plate_Separation [m]	4
Source_Size [m X m X #]	[0.610 X 0.305 X 1]
Source_Heading [deg]	192.7306
Source_Voltage [V Peak]	176.8045
Source_Current [A Peak]	1.1943
Source_Frequency [Hz]	100

--- Extra Information ---

Source_Heading_Bounds [deg]	(N/A)
Average_Boat_Speed [m/s]	1.1051
Source_Type	Electric boat hull (boat hull)
Sensor_Type	EMA
Bin_Size [sec]	1
Number_of_Datapoints	219
Lake_Origin (Easting,Northing)	(741304.279,709845.52)
Analysis_Date	Exp2_ScenSF_28-Jul-2011

3 Boat Path

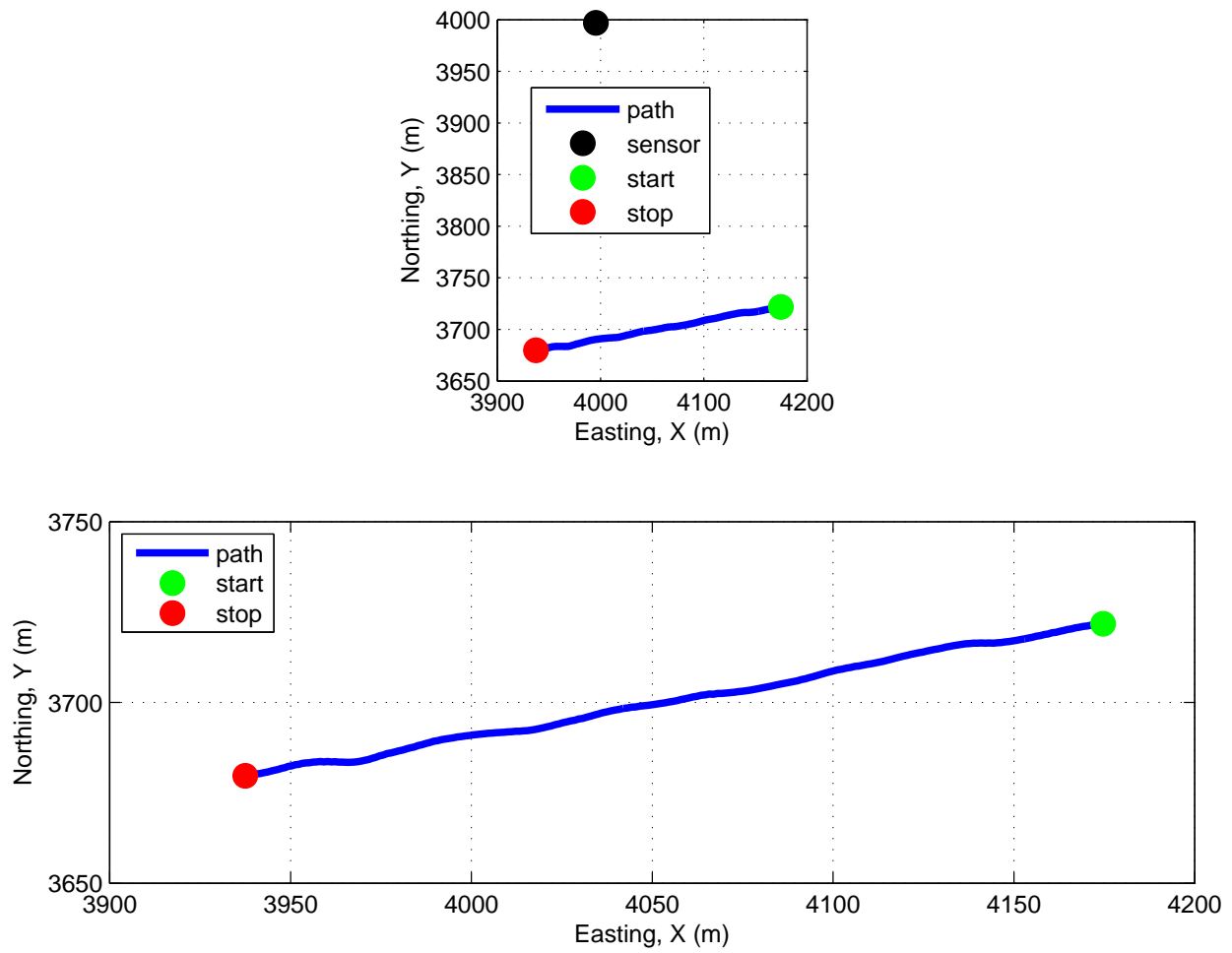


Figure 2: Source and sensor relationship.

4 Plots

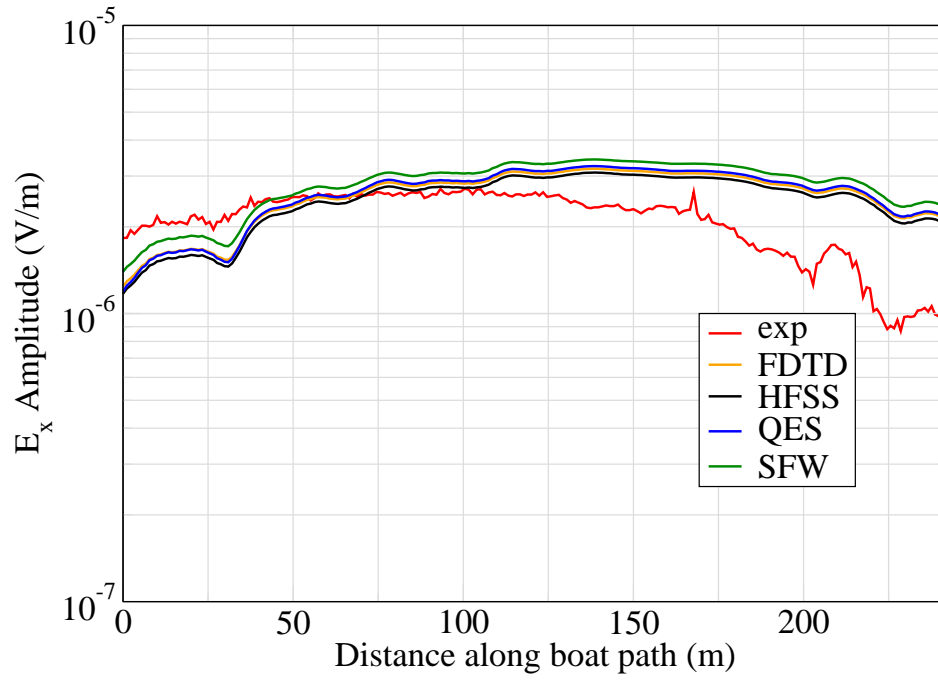


Figure 3: E_x .

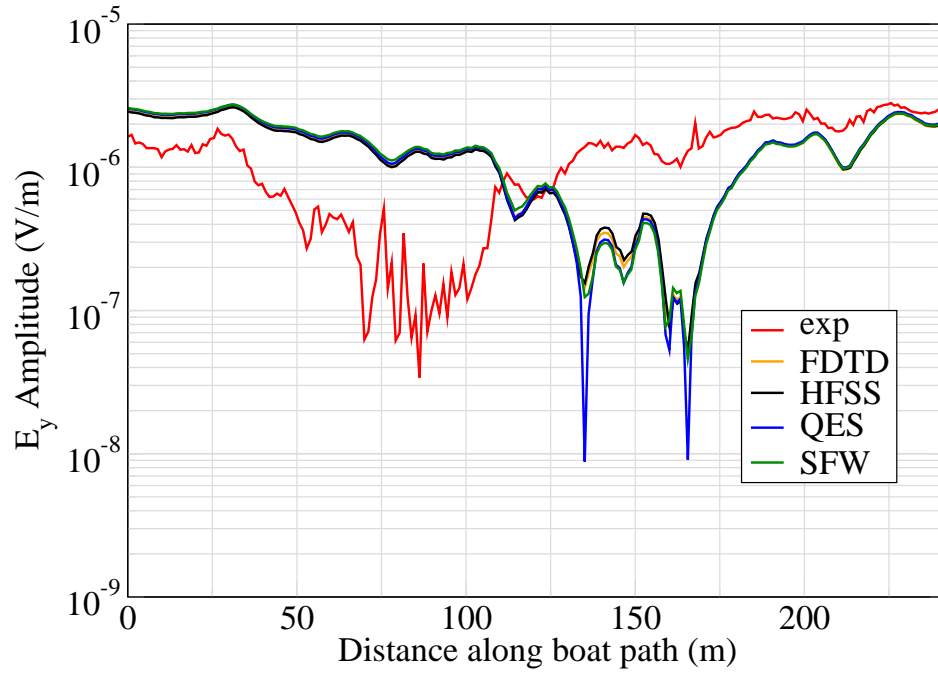


Figure 4: E_y .

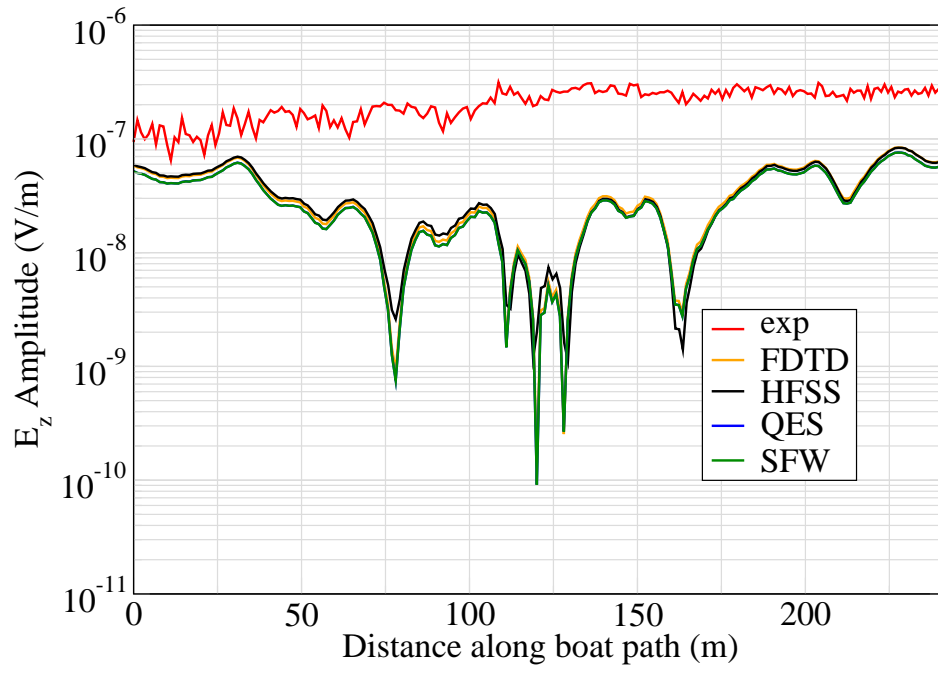


Figure 5: E_z .

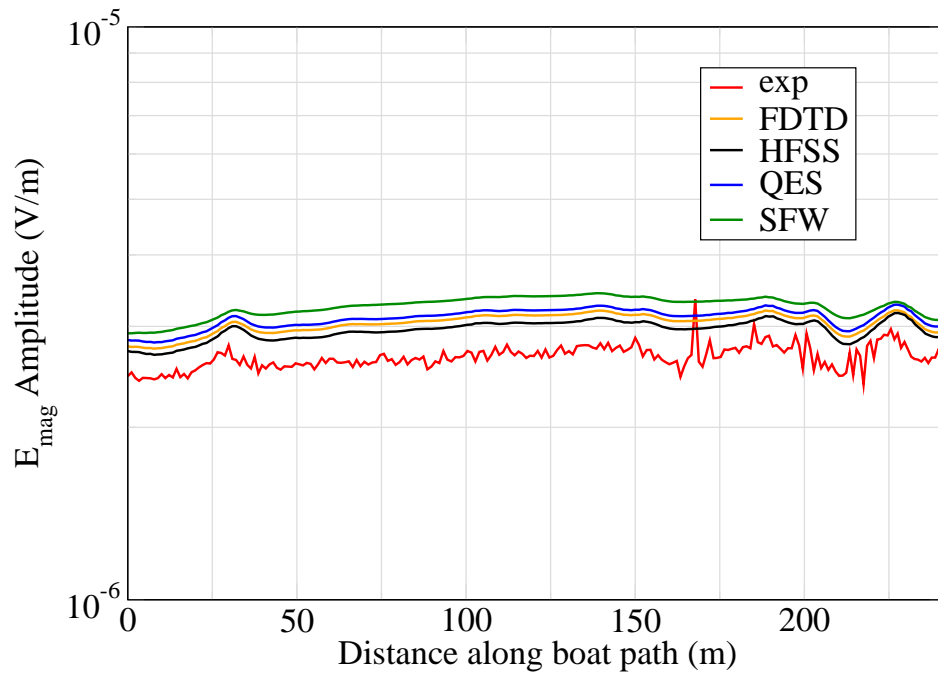


Figure 6: E_{mag} .

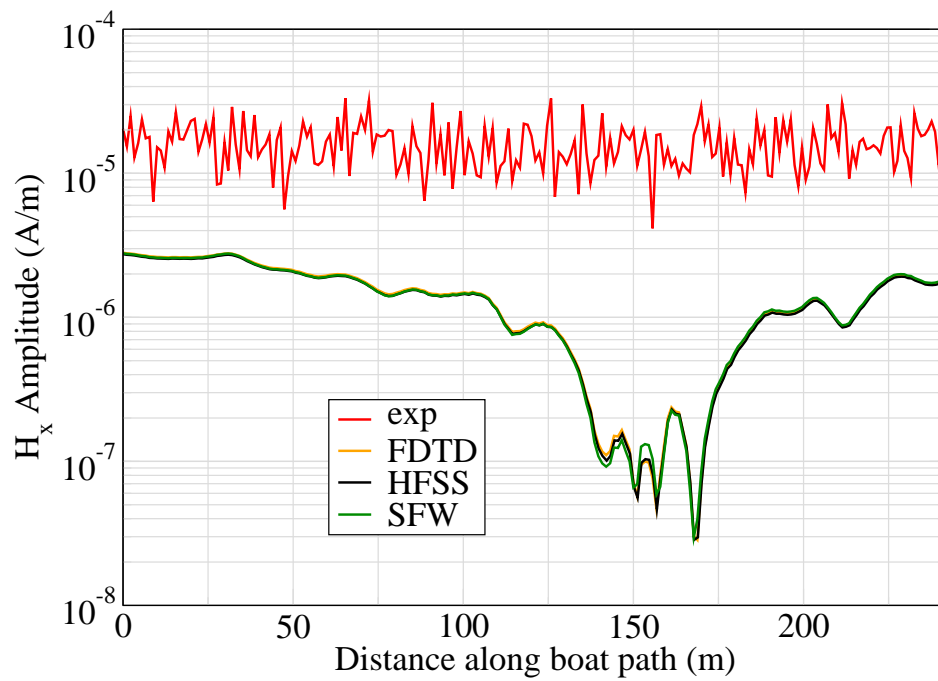


Figure 7: H_x .

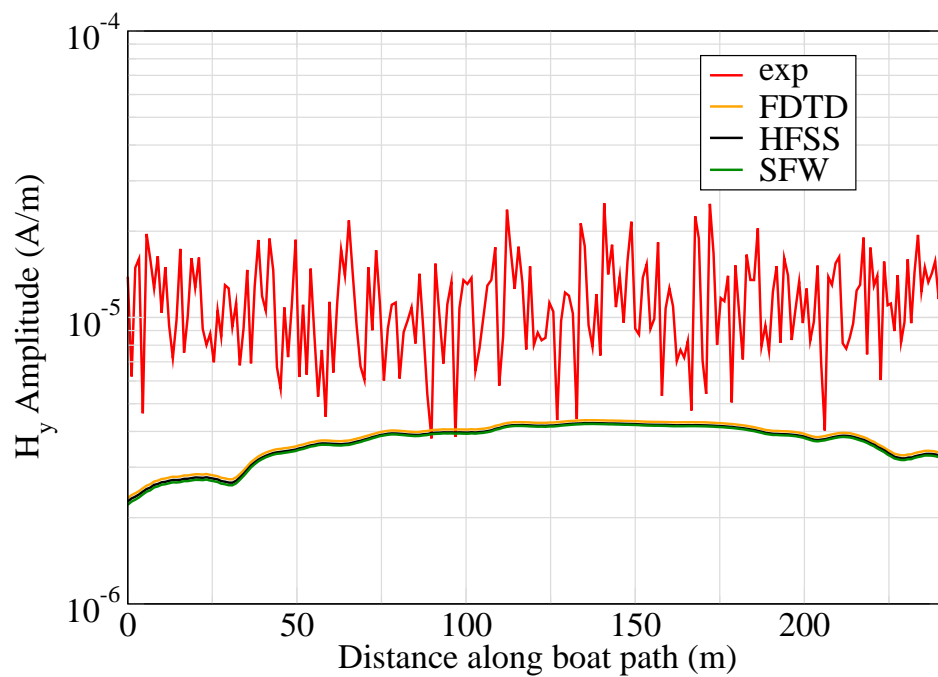


Figure 8: H_y .

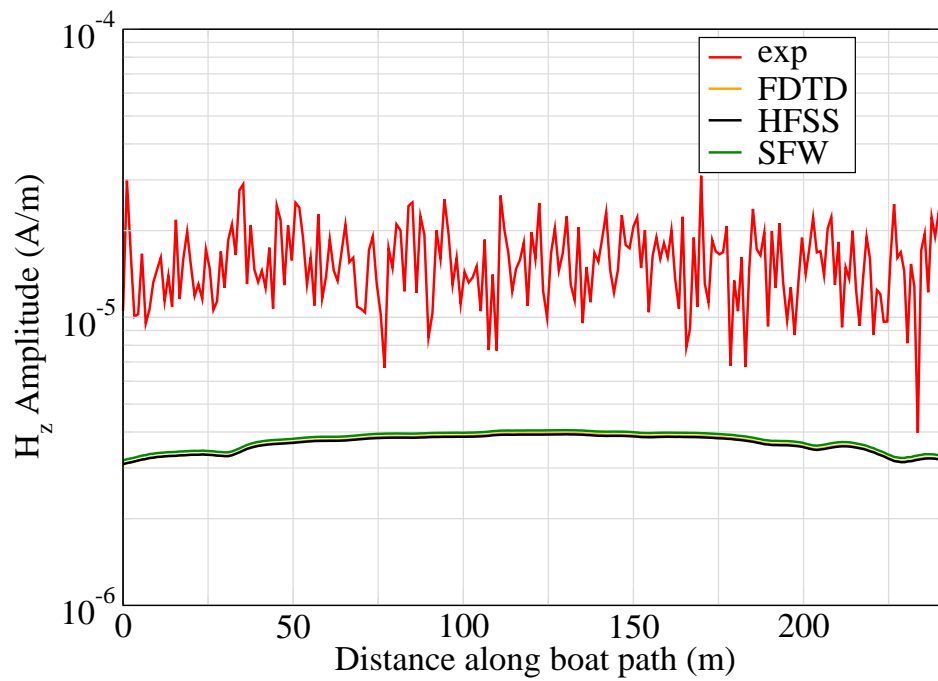


Figure 9: H_z .

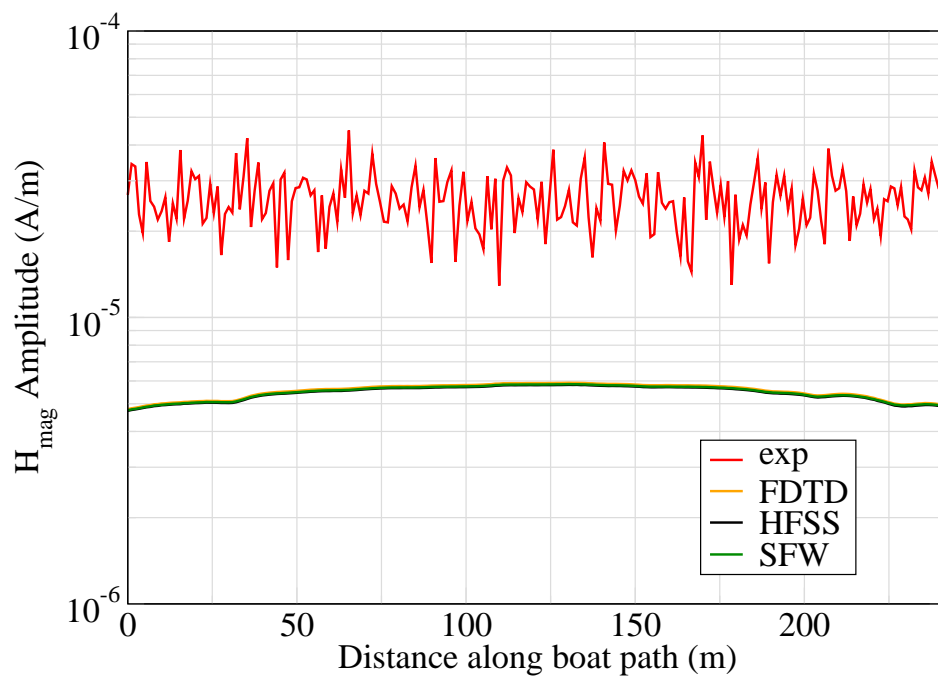


Figure 10: H_{mag} .

Experiment 2

Runs 1003

Experiment Date: 12/06/2008

1 Discussion

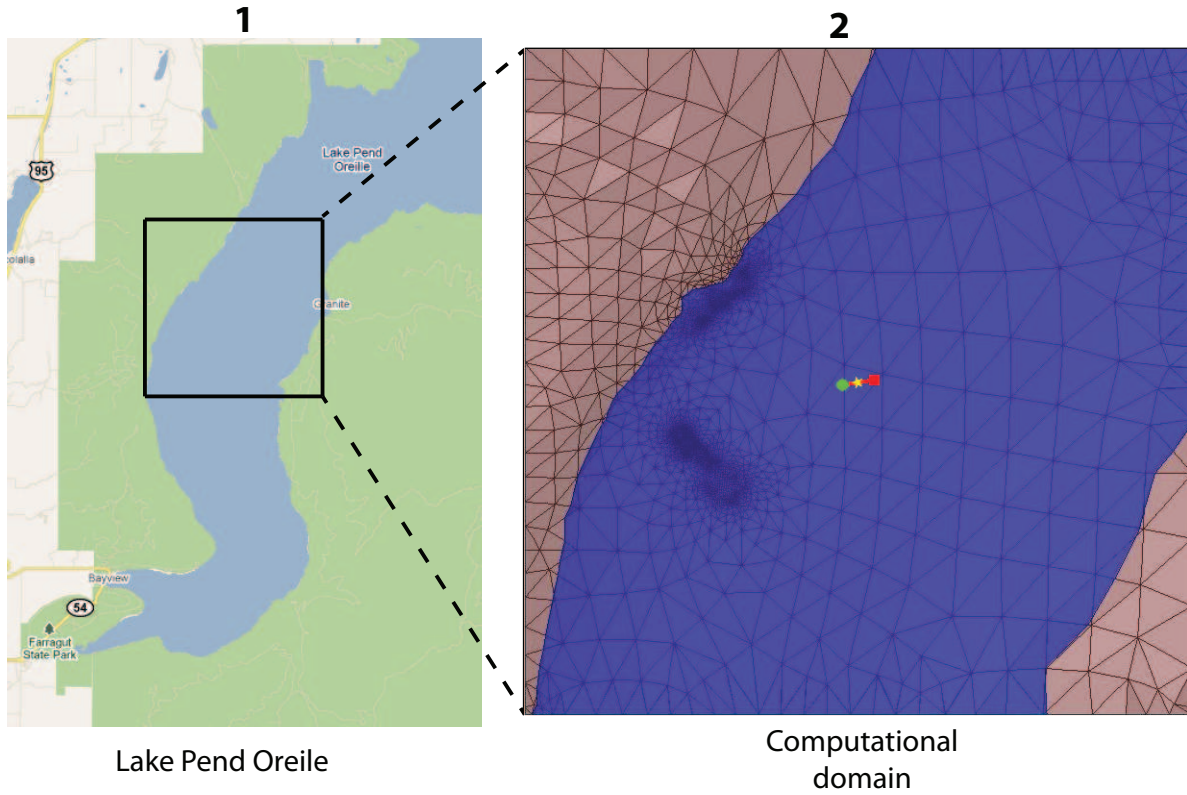


Figure 1: Sensor and source locations; see test report. Sensor is represented by the yellow star; source start and end points represented by green circle and red square.

Source Parameters

- Source Type: VMD (Mag Boat: $r = 0.657$ m with 7 turns).
- Source Strength: 184.31 A-m^2 .
- $f = 10 \text{ Hz}$.

Environment

- Air: $\sigma = 0$ S/m and $\epsilon_r = 1$
- Water: $\sigma = 0.01$ S/m and $\epsilon_r = 81$
- Mud: $\sigma = 0.0012$ S/m and $\epsilon_r = 1$

Table 1: Simulation Details

	FDTD	HFSS	QES/SFW
Domain Size	200 X 200 X 160 cells	136,732 tets	N/A
Cell Size (m)	5 X 5 X 5	N/A	N/A
Time Step (ns)	9.6	N/A	N/A
Run Time (Hrs)	35.9	3.45	0.01
Water Depth (m)	N/A	N/A	300
Effective Source Area (m)	N/A	l = 0.3 w = 0.3	r = 0.058

Comments

- To implement reciprocity, three simulations per vector field are required for a total of six simulations. Run times correspond to the time required to conduct all six simulations.
- Computational time is based on actual elapsed real time. This number is highly subjective and based on how many other applications might be running at a particular time. However, the reported number is an indication of the amount of time typically needed for a particular simulation. The computer specs are: 16 CPU cores at 2.8 GHz.
- Run times for HFSS are given for a single frequency.
- QES is not applicable for electric or magnetic fields using magnetic source excitation.

2 Simulation Variables

Sensor_P1(x,y,z) [m]	(3995.5266,3997.0031,-8.2296)
Sensor_P2(x,y,z) [m]	(3995.5266,3997.0031,-8.2296)
Source_P1(x,y,z) [m]	(3816.8133,3961.9401,0)
Source_P2(x,y,z) [m]	(4198.4621,4028.7317,0)
Source_Plate_Separation [m]	N/A
Source_Size [r X #]	[.657 X 7]
Source_Heading [deg]	NaN
Source_Voltage [V Peak]	NaN
Source_Current [A Peak]	19.4164
Source_Frequency [Hz]	10

--- Extra Information ---

Source_Heading_Bounds [deg]	(N/A)
Average_Boat_Speed [m/s]	2.6906
Source_Type	Magnetic source (boat)
Sensor_Type	EMA
Bin_Size [sec]	1
Number_of_Datapoints	145
Lake_Origin (Easting,Northing)	(741304.279,709845.52)
Analysis_Date	Exp2_ScenSH_29-Jul-2011

3 Boat Path

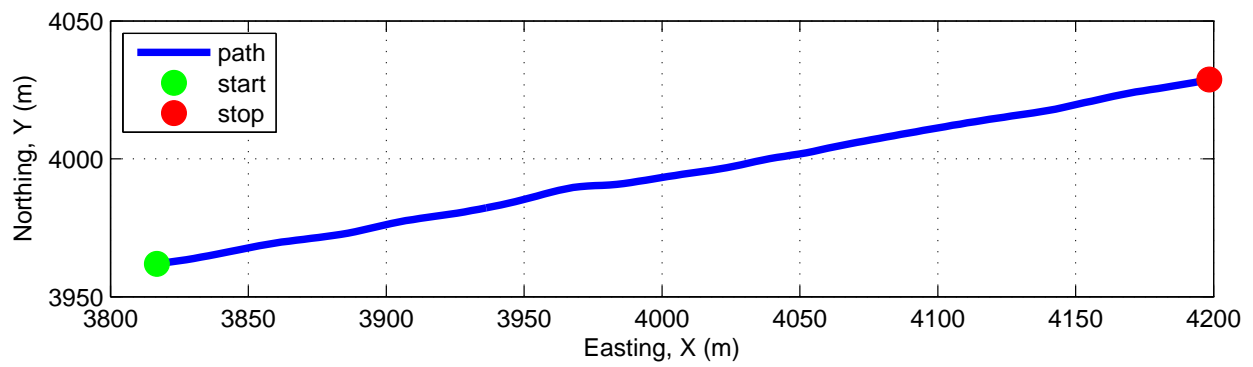
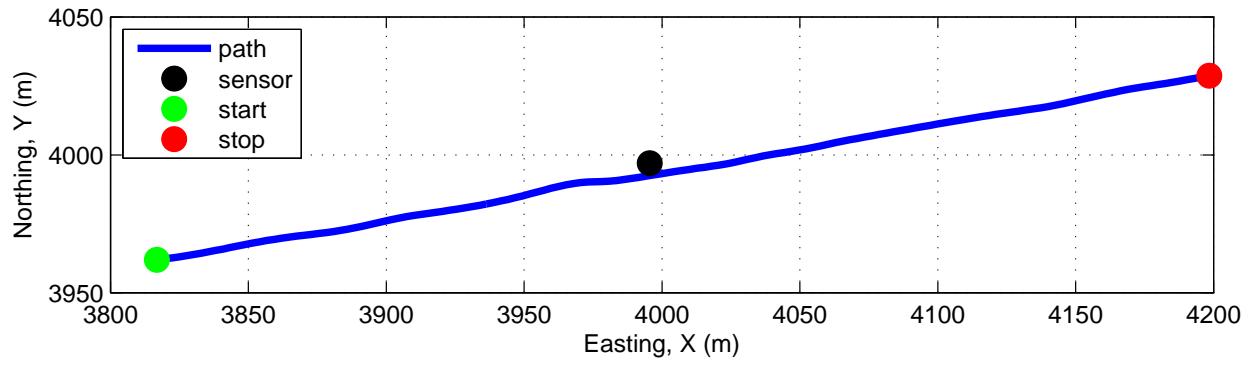


Figure 2: Source and sensor relationship.

4 Plots

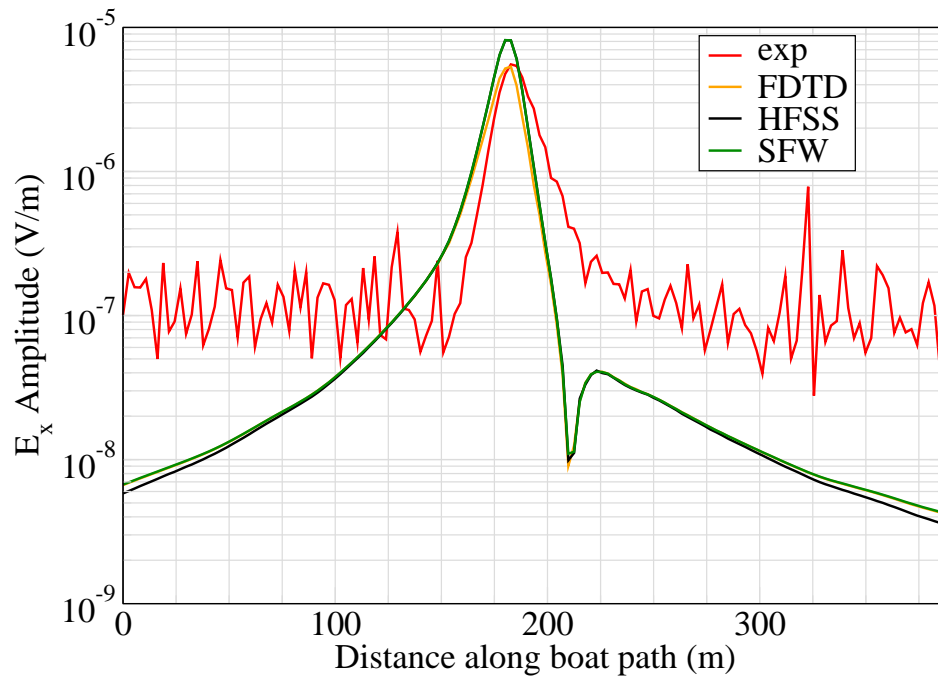


Figure 3: E_x .

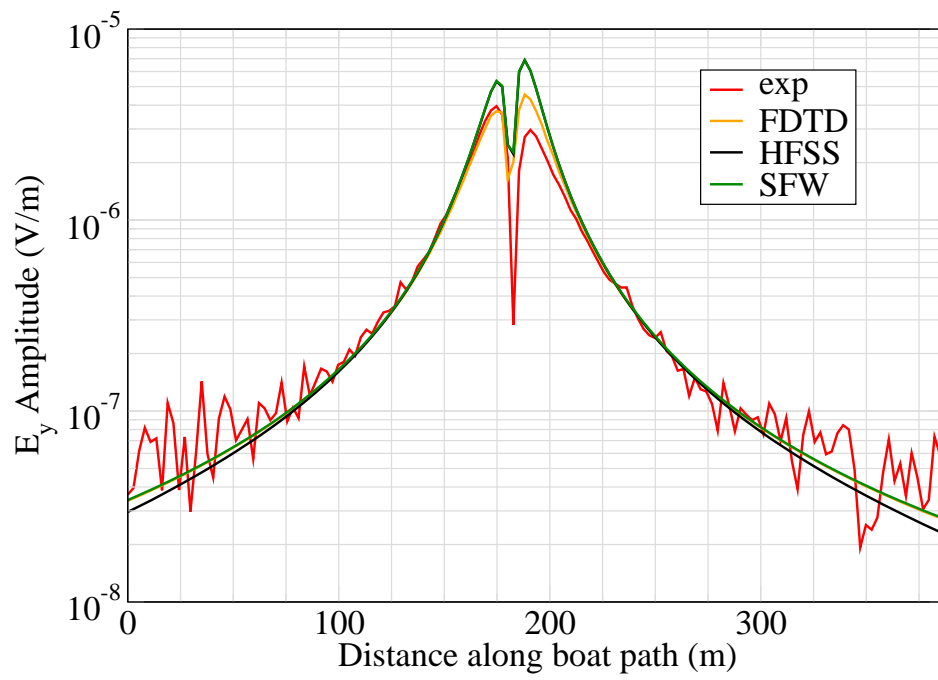


Figure 4: E_y .

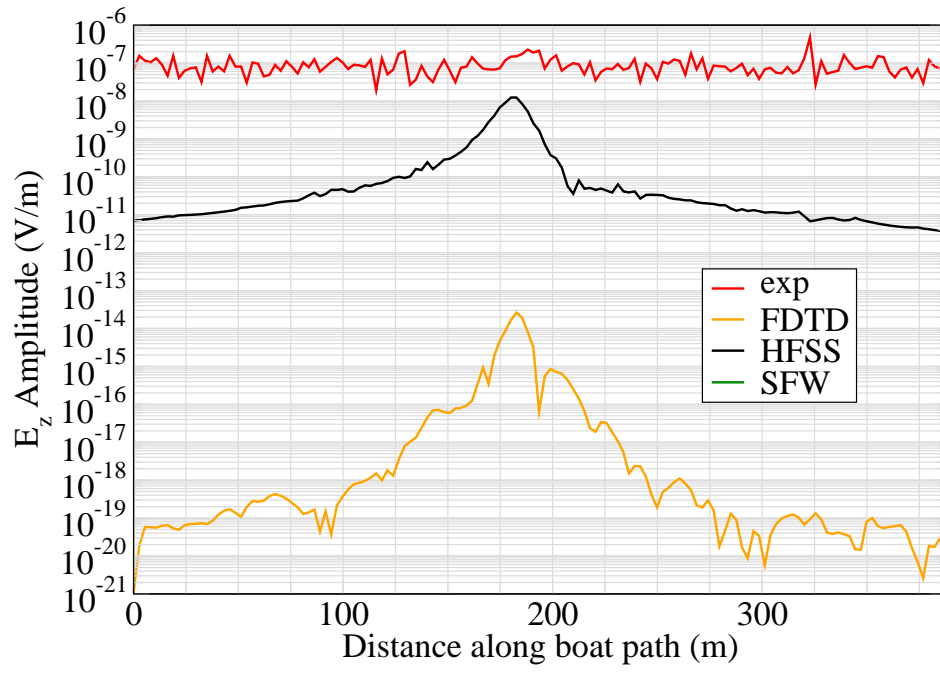


Figure 5: E_z .

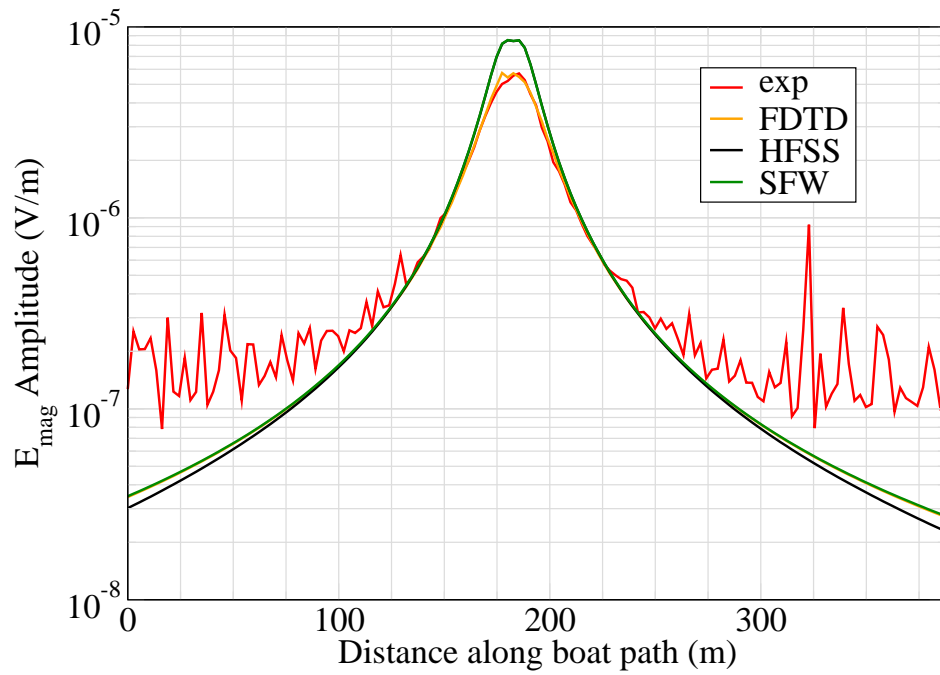


Figure 6: E_{mag} .

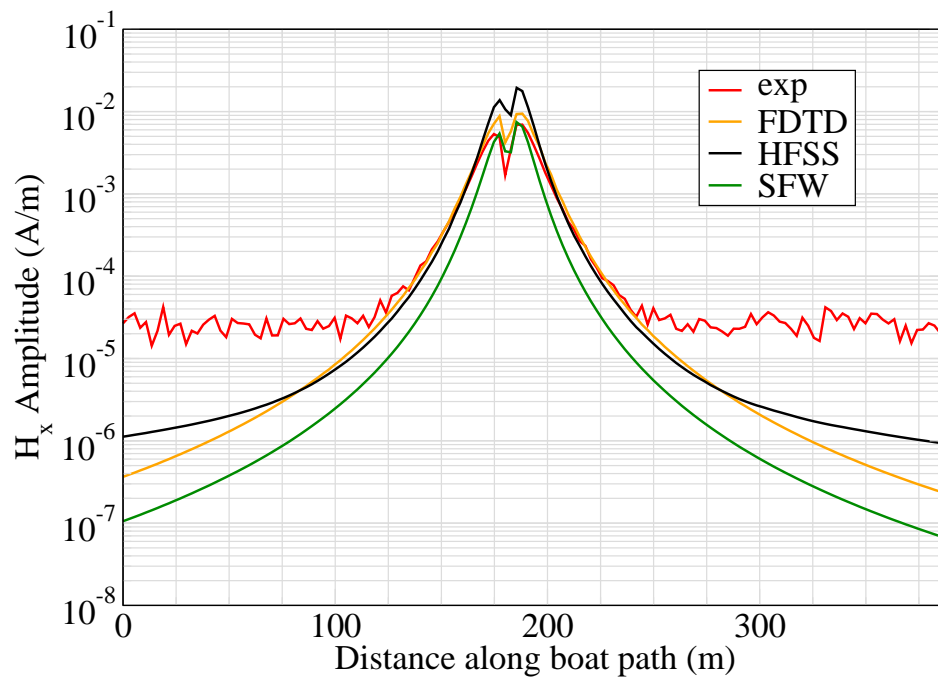


Figure 7: H_x .

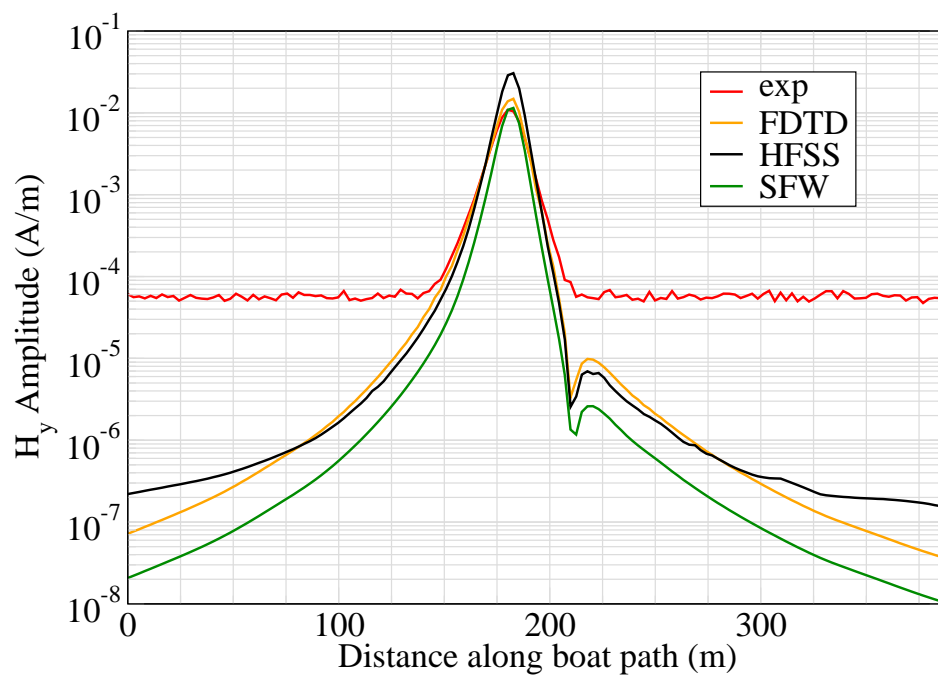


Figure 8: H_y .

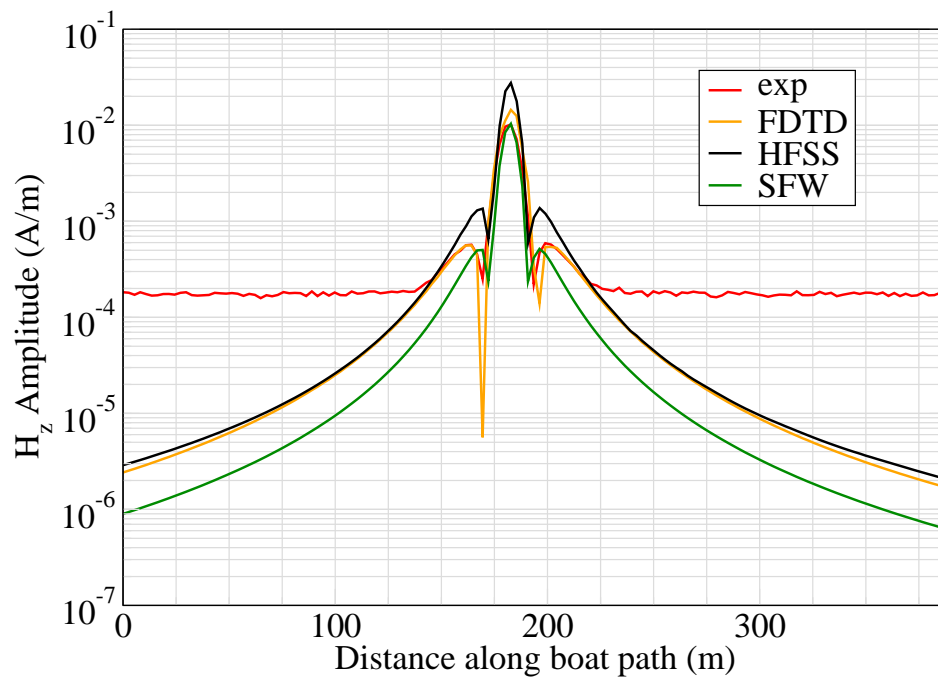


Figure 9: H_z .

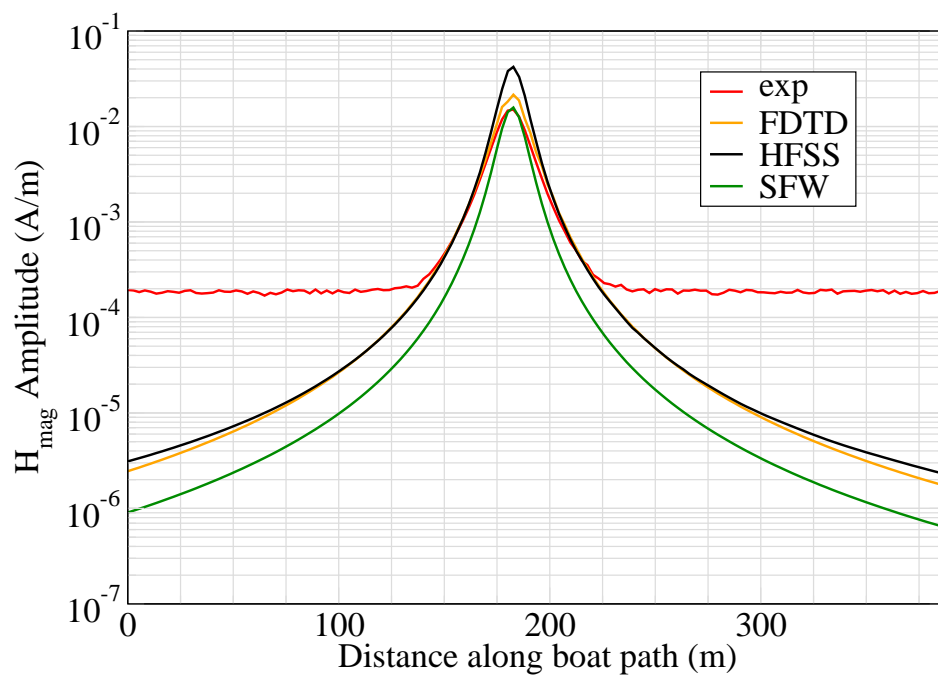


Figure 10: H_{mag} .

Experiment 2

Runs 1004

Experiment Date: 12/06/2008

1 Discussion

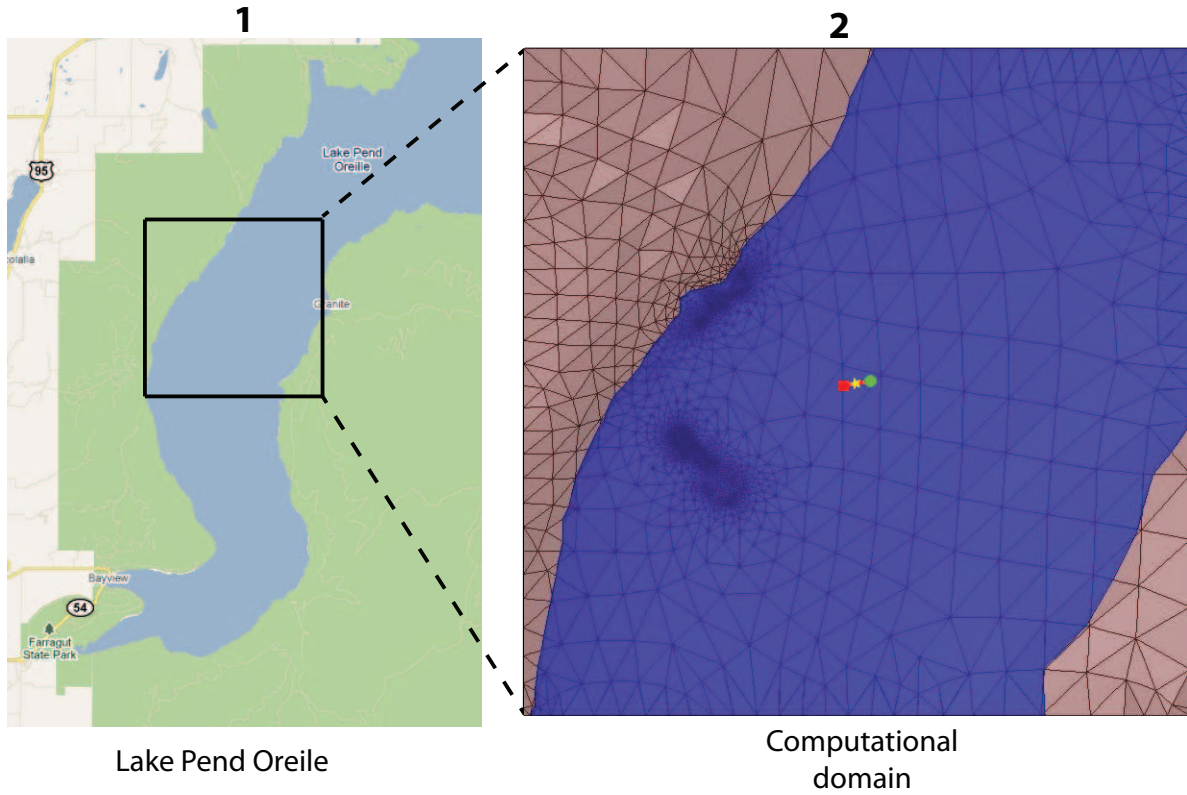


Figure 1: Sensor and source locations; see test report. Sensor is represented by the yellow star; source start and end points represented by green circle and red square.

Source Parameters

- Source Type: VMD (Mag Boat: $r = 0.657$ m with 7 turns).
- Source Strength: 184.56 A-m^2 .
- $f = 10 \text{ Hz}$.

Environment

- Air: $\sigma = 0$ S/m and $\epsilon_r = 1$
- Water: $\sigma = 0.01$ S/m and $\epsilon_r = 81$
- Mud: $\sigma = 0.0012$ S/m and $\epsilon_r = 1$

Table 1: Simulation Details

	FDTD	HFSS	QES/SFW
Domain Size	200 X 200 X 160 cells	118,939 tets	N/A
Cell Size (m)	5 X 5 X 5	N/A	N/A
Time Step (ns)	9.6	N/A	N/A
Run Time (Hrs)	35.5	2.2	0.01
Water Depth (m)	N/A	N/A	300
Effective Source Area (m)	N/A	l = 0.3 w = 0.3	r = 0.058

Comments

- To implement reciprocity, three simulations per vector field are required for a total of six simulations. Run times correspond to the time required to conduct all six simulations.
- Computational time is based on actual elapsed real time. This number is highly subjective and based on how many other applications might be running at a particular time. However, the reported number is an indication of the amount of time typically needed for a particular simulation. The computer specs are: 16 CPU cores at 2.8 GHz.
- Run times for HFSS are given for a single frequency.
- QES is not applicable for electric or magnetic fields using magnetic source excitation.

2 Simulation Variables

Sensor_P1(x,y,z) [m]	(3995.5266,3997.0031,-8.2296)
Sensor_P2(x,y,z) [m]	(3995.5266,3997.0031,-8.2296)
Source_P1(x,y,z) [m]	(4178.7075,4025.0748,0)
Source_P2(x,y,z) [m]	(3847.0563,3965.8837,0)
Source_Plate_Separation [m]	N/A
Source_Size [r X #]	[.657 X 7]
Source_Heading [deg]	NaN
Source_Voltage [V Peak]	NaN
Source_Current [A Peak]	19.4425
Source_Frequency [Hz]	10

--- Extra Information ---

Source_Heading_Bounds [deg]	(N/A)
Average_Boat_Speed [m/s]	2.632
Source_Type	Magnetic source (boat)
Sensor_Type	EMA
Bin_Size [sec]	1
Number_of_Datapoints	129
Lake-Origin (Easting,Northing)	(741304.279,709845.52)
Analysis_Date	Exp2_ScenSI_29-Jul-2011

3 Boat Path

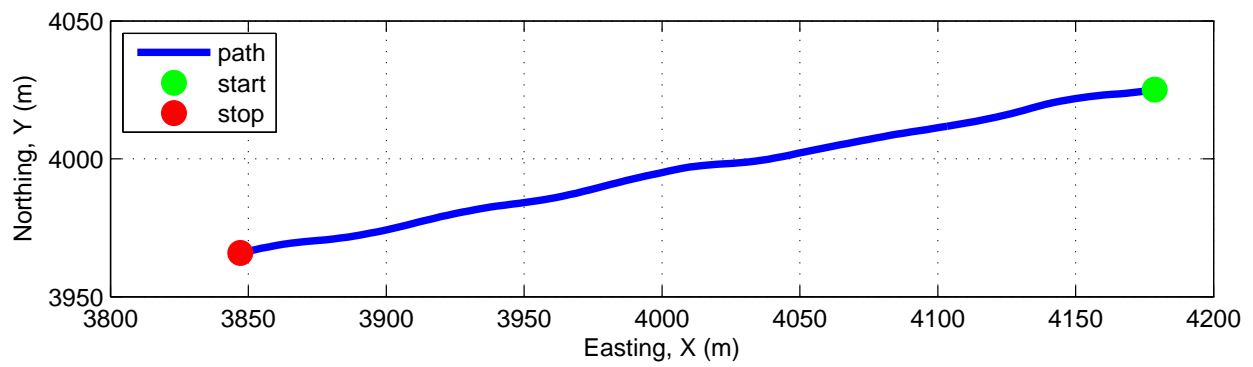
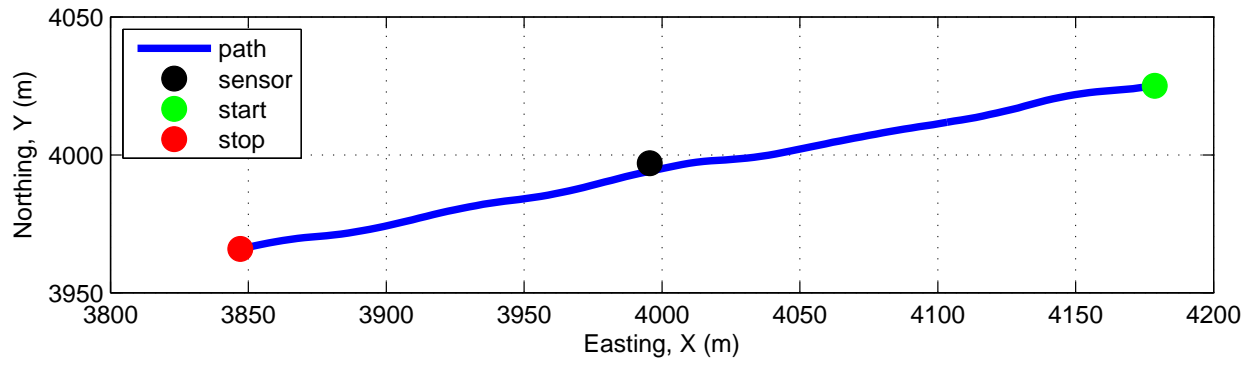


Figure 2: Source and sensor relationship.

4 Plots

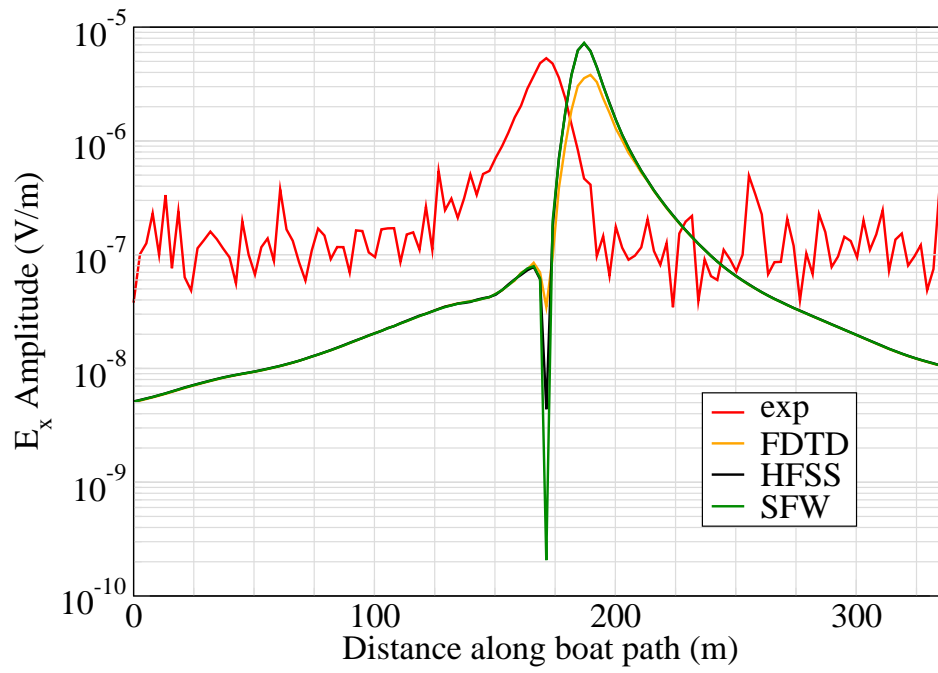


Figure 3: E_x .

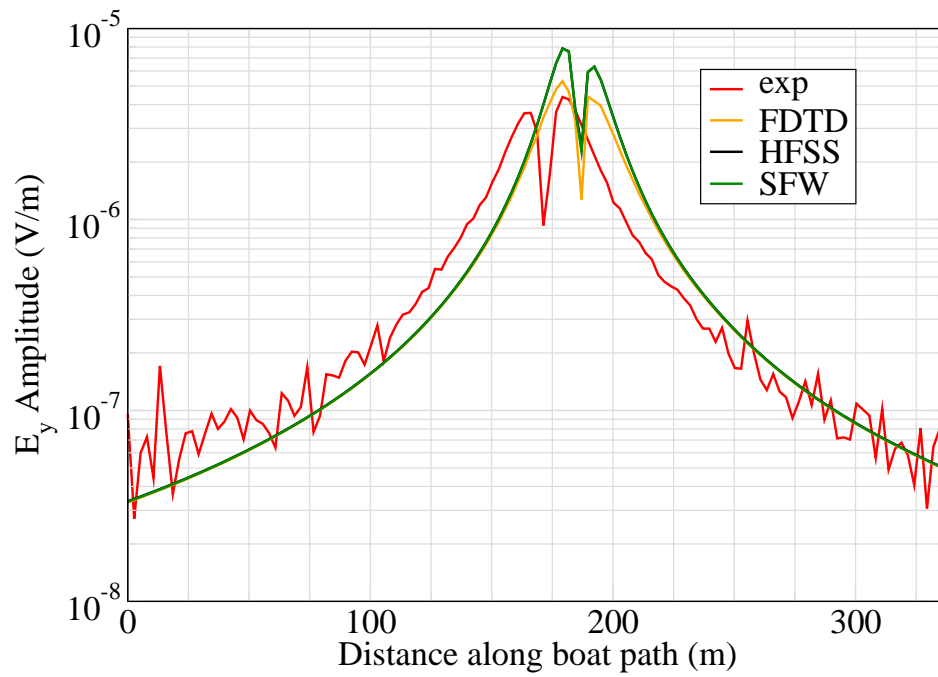


Figure 4: E_y .

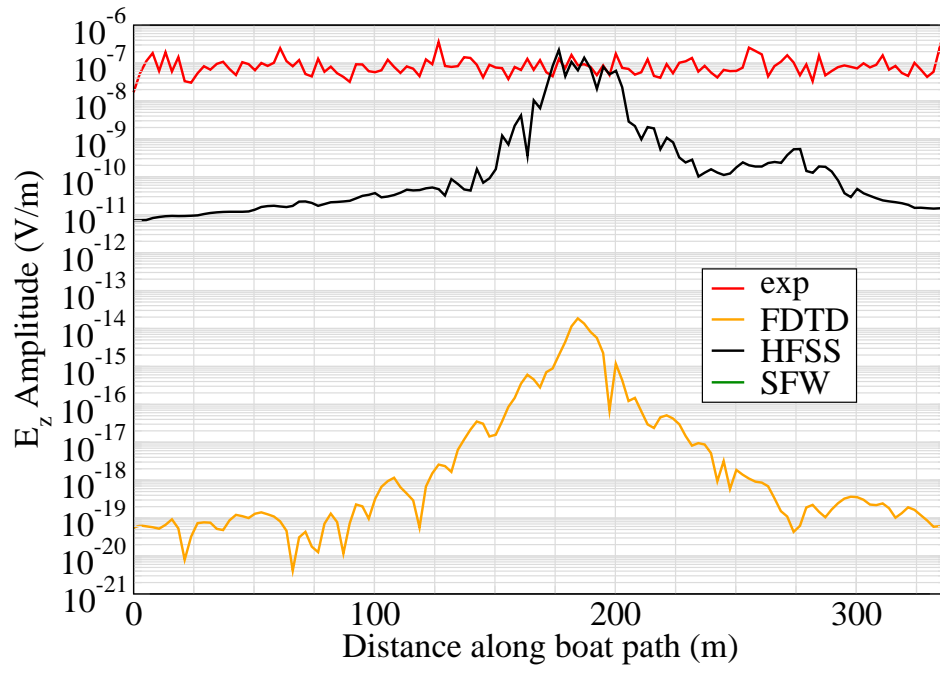


Figure 5: E_z .

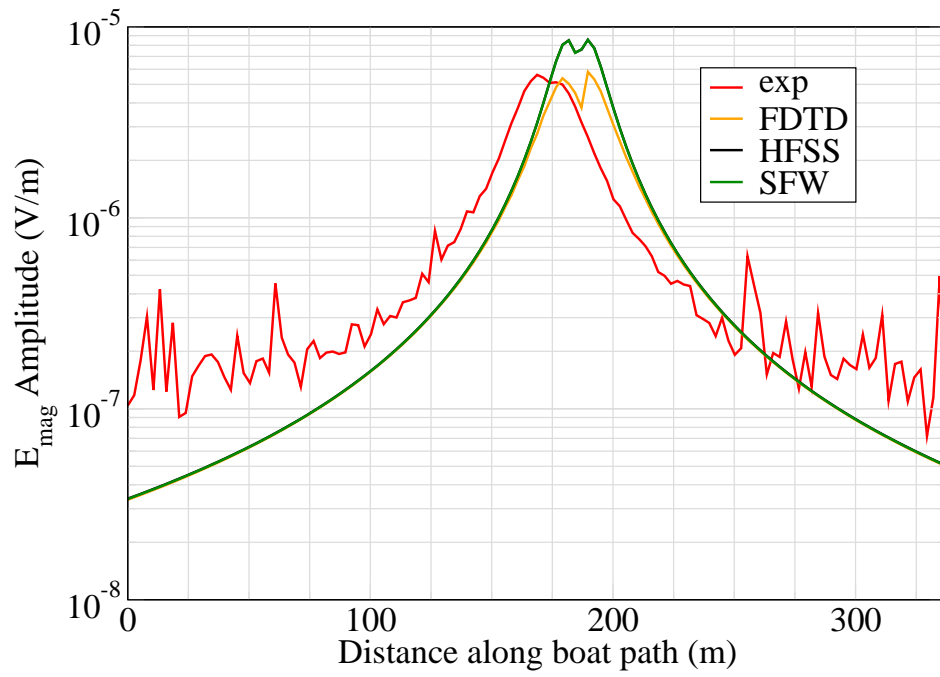


Figure 6: E_{mag} .

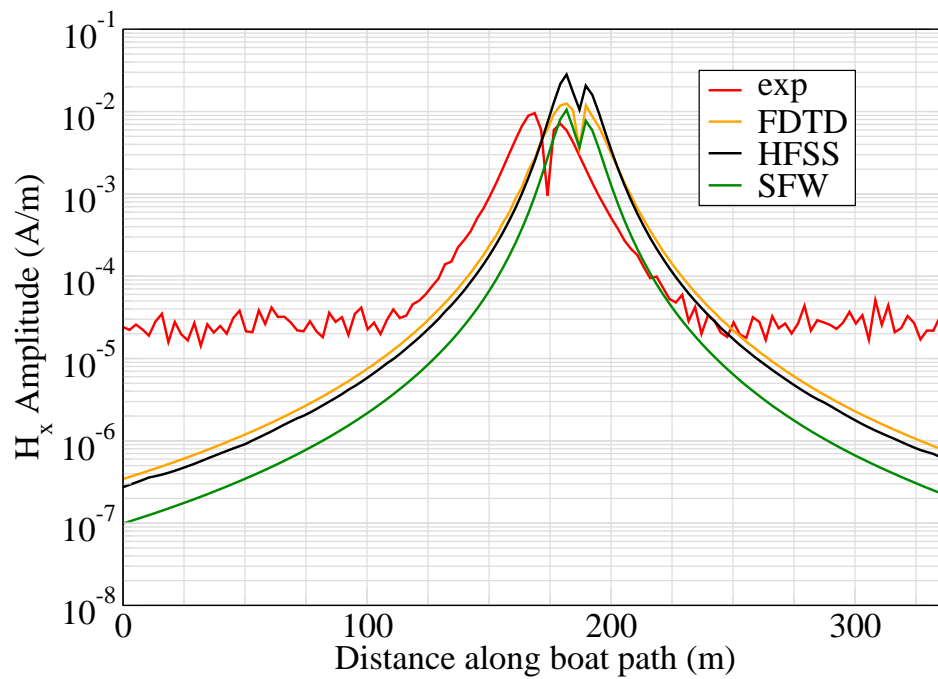


Figure 7: H_x .

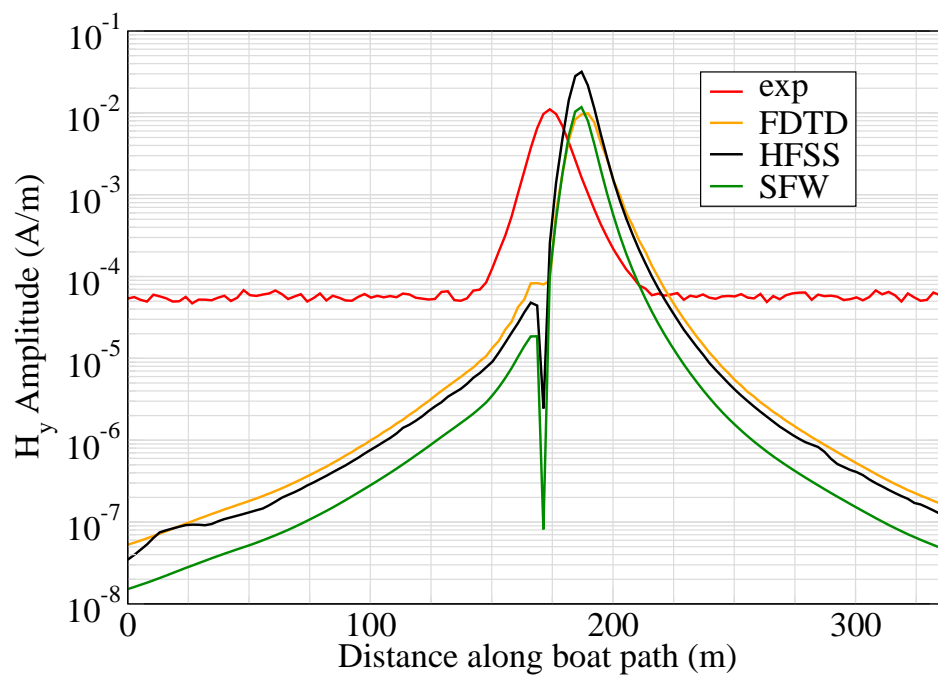


Figure 8: H_y .

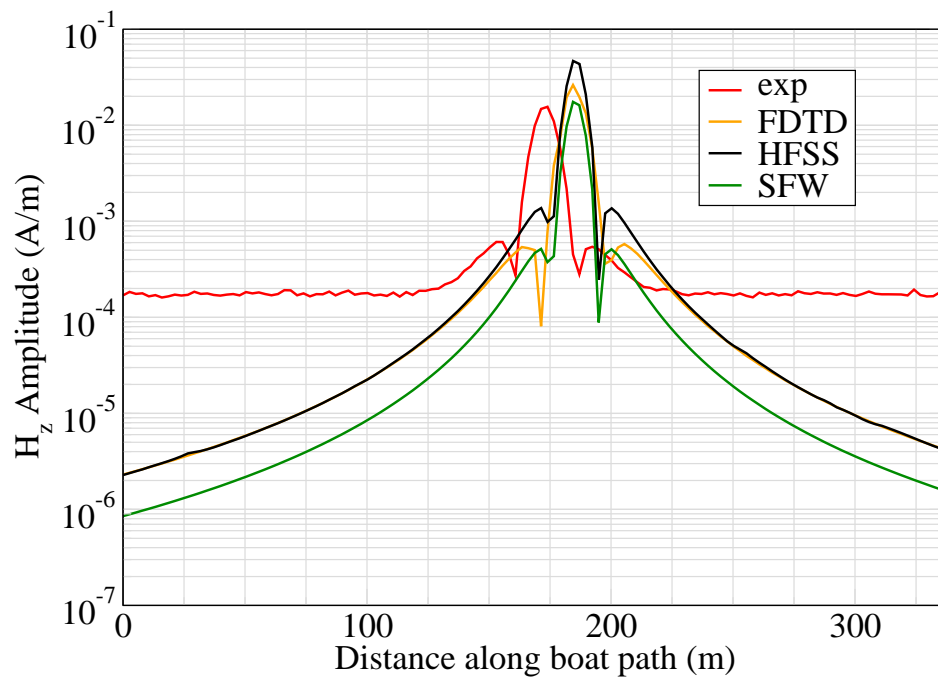


Figure 9: H_z .

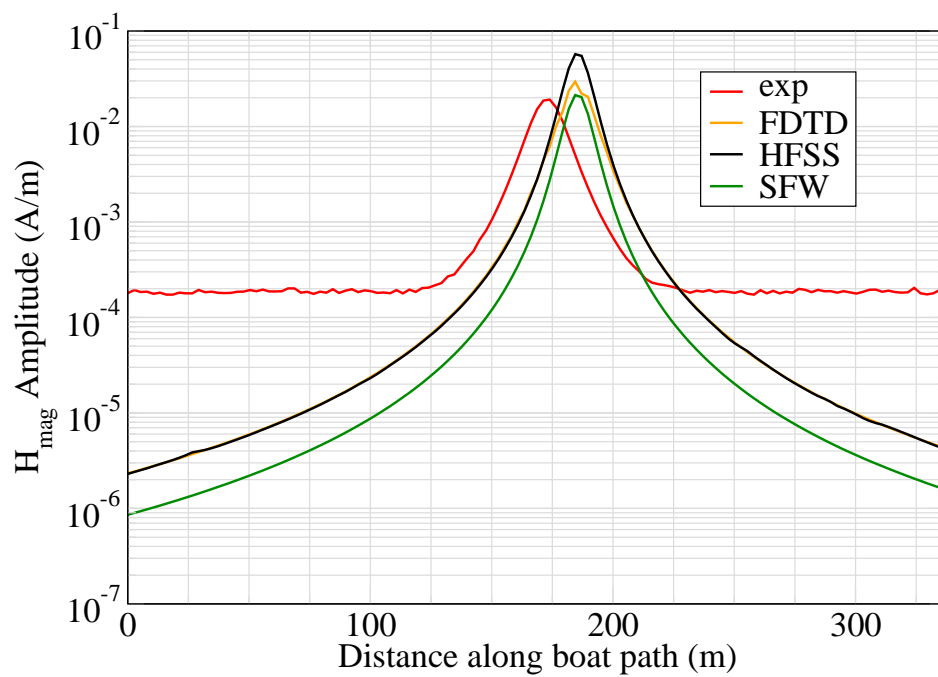


Figure 10: H_{mag} .

Experiment 2

Runs 1016

Experiment Date: 12/06/2008

1 Discussion

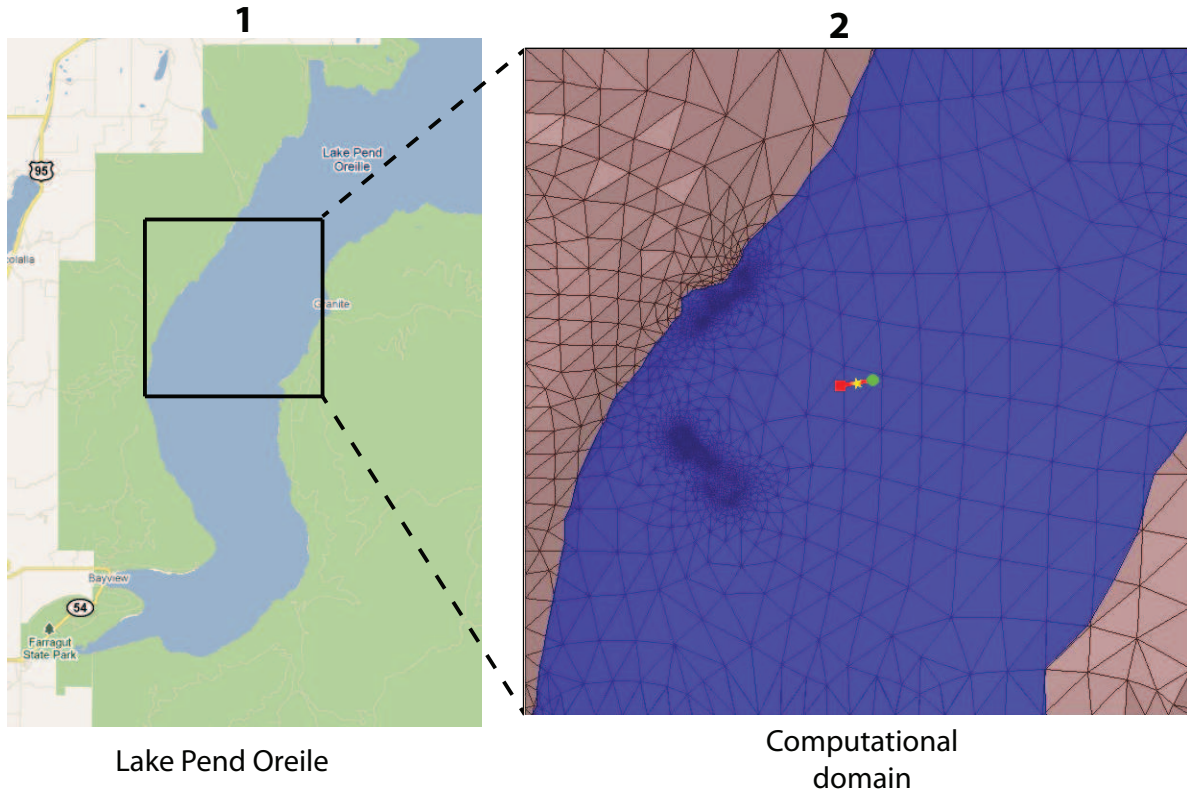


Figure 1: Sensor and source locations; see test report. Sensor is represented by the yellow star; source start and end points represented by green circle and red square.

Source Parameters

- Source Type: VMD (Mag Boat: $r = 0.657$ m with 7 turns).
- Source Strength: 184.46 A-m^2 .
- $f = 10 \text{ Hz}$.

Environment

- Air: $\sigma = 0$ S/m and $\epsilon_r = 1$
- Water: $\sigma = 0.01$ S/m and $\epsilon_r = 81$
- Mud: $\sigma = 0.0012$ S/m and $\epsilon_r = 1$

Table 1: Simulation Details

	FDTD	HFSS	QES/SFW
Domain Size	200 X 200 X 160 cells	114,442 tets	N/A
Cell Size (m)	5 X 5 X 5	N/A	N/A
Time Step (ns)	9.6	N/A	N/A
Run Time (Hrs)	35.5	1.96	0.01
Water Depth (m)	N/A	N/A	300
Effective Source Area (m)	N/A	l = 0.3 w = 0.3	r = 0.058

Comments

- To implement reciprocity, three simulations per vector field are required for a total of six simulations. Run times correspond to the time required to conduct all six simulations.
- Computational time is based on actual elapsed real time. This number is highly subjective and based on how many other applications might be running at a particular time. However, the reported number is an indication of the amount of time typically needed for a particular simulation. The computer specs are: 16 CPU cores at 2.8 GHz.
- Run times for HFSS are given for a single frequency.
- QES is not applicable for electric or magnetic fields using magnetic source excitation.

2 Simulation Variables

Sensor_P1(x,y,z) [m]	(3995.5266,3997.0031,-8.2296)
Sensor_P2(x,y,z) [m]	(3995.5266,3997.0031,-8.2296)
Source_P1(x,y,z) [m]	(4186.2517,4032.4742,0)
Source_P2(x,y,z) [m]	(3795.5354,3961.721,0)
Source_Plate_Separation [m]	N/A
Source_Size [r X #]	[.657 X 7]
Source_Heading [deg]	NaN
Source_Voltage [V Peak]	NaN
Source_Current [A Peak]	19.4327
Source_Frequency [Hz]	10

--- Extra Information ---

Source_Heading_Bounds [deg]	(N/A)
Average_Boat_Speed [m/s]	2.6296
Source_Type	Magnetic source (boat)
Sensor_Type	EMA
Bin_Size [sec]	1
Number_of_Datapoints	152
Lake_Origin (Easting,Northing)	(741304.279,709845.52)
Analysis_Date	Exp2_ScenSJ_29-Jul-2011

3 Boat Path

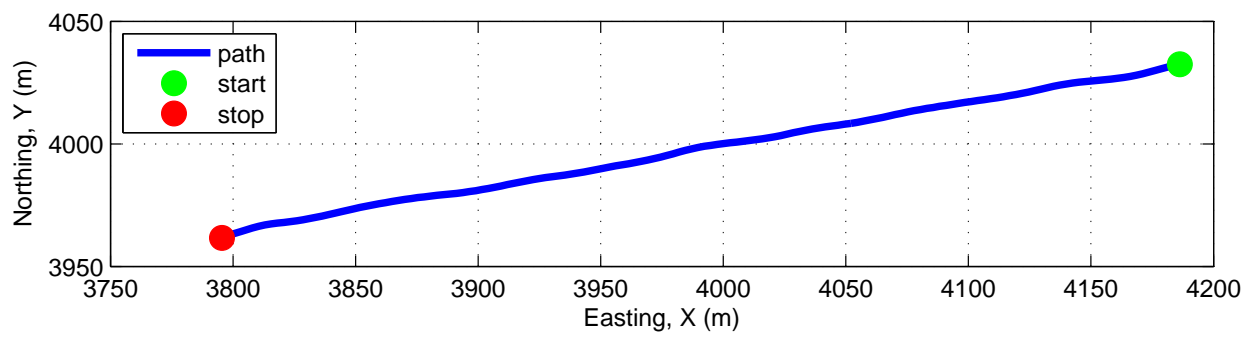
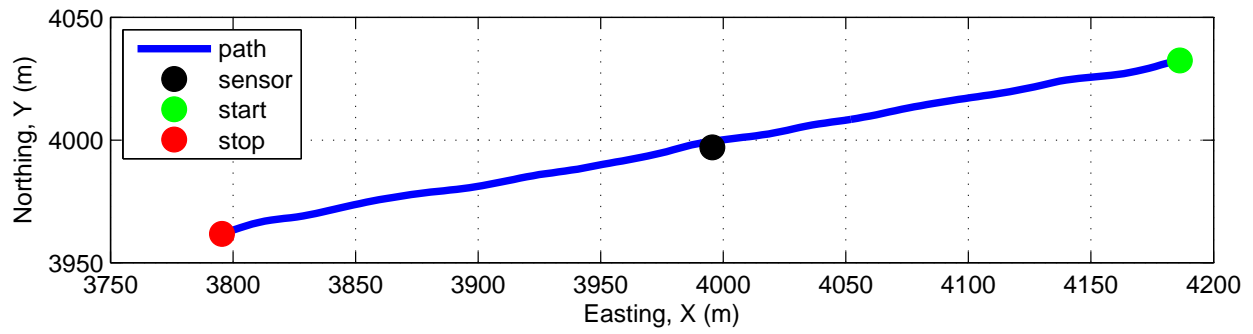


Figure 2: Source and sensor relationship.

4 Plots

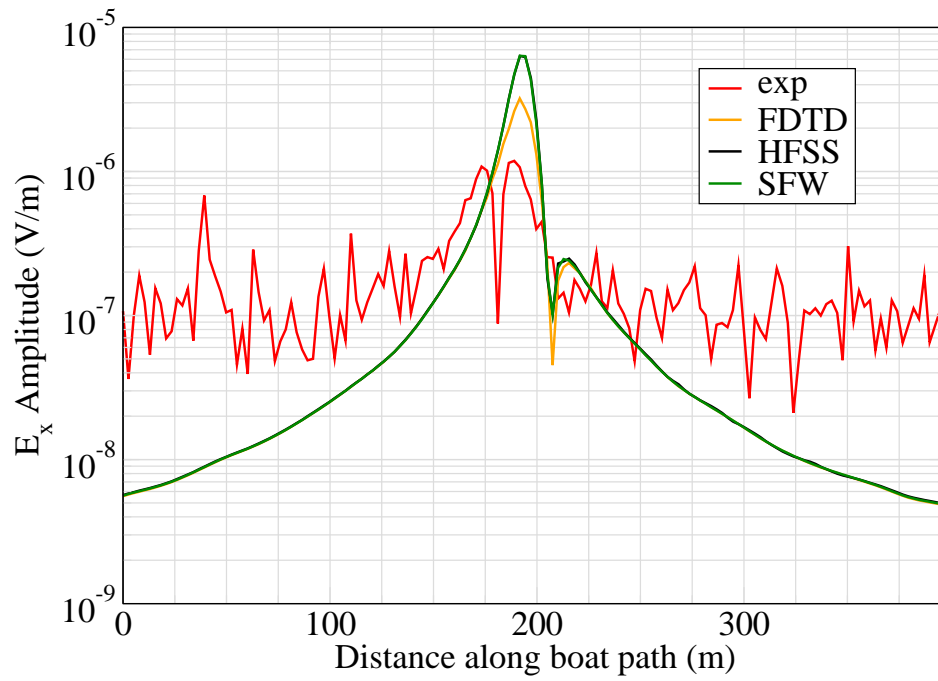


Figure 3: E_x .

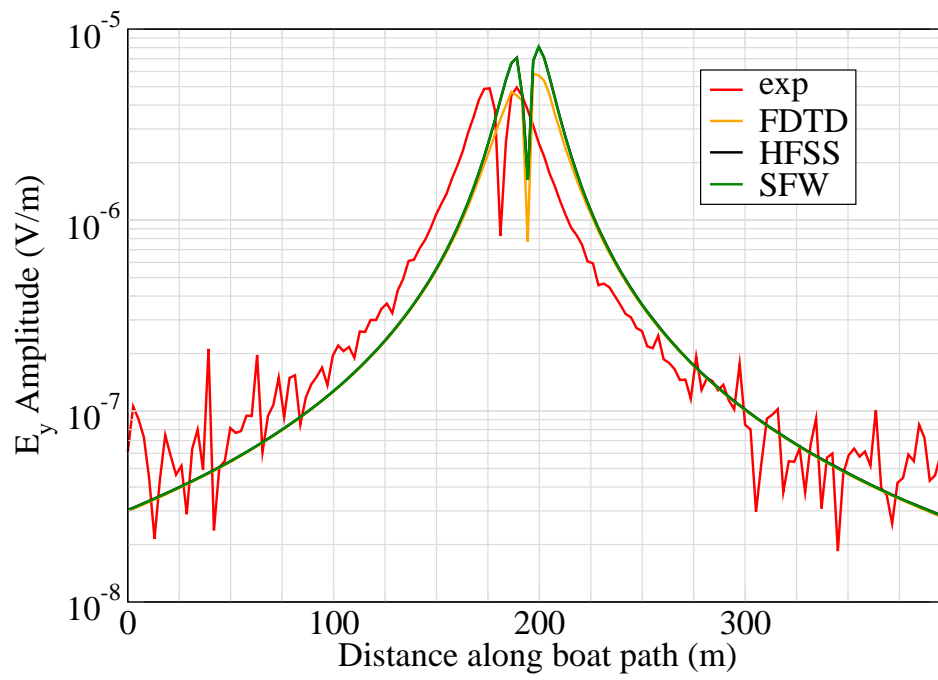


Figure 4: E_y .

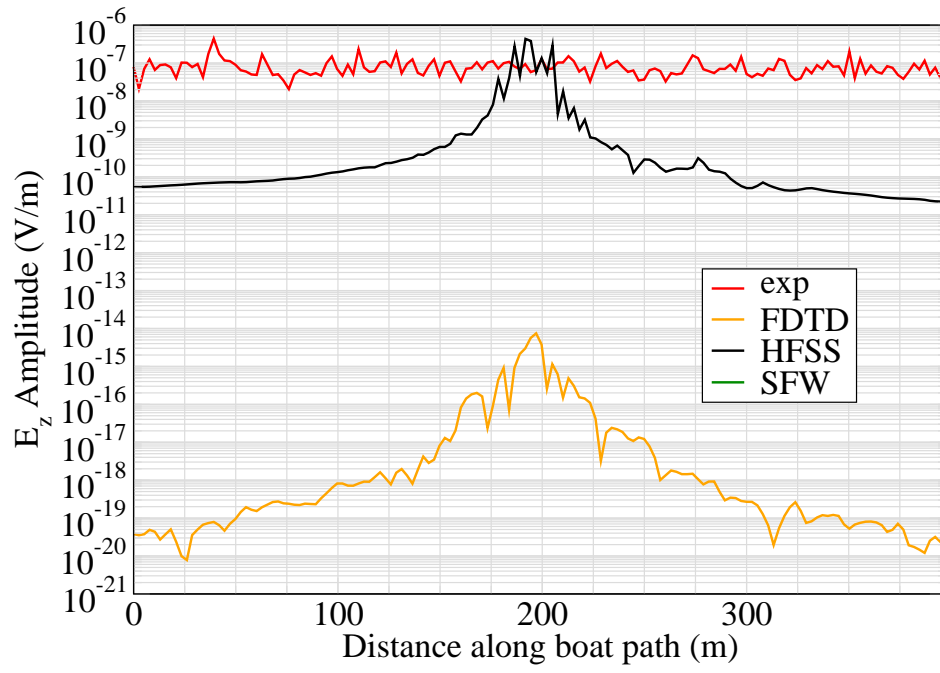


Figure 5: E_z .

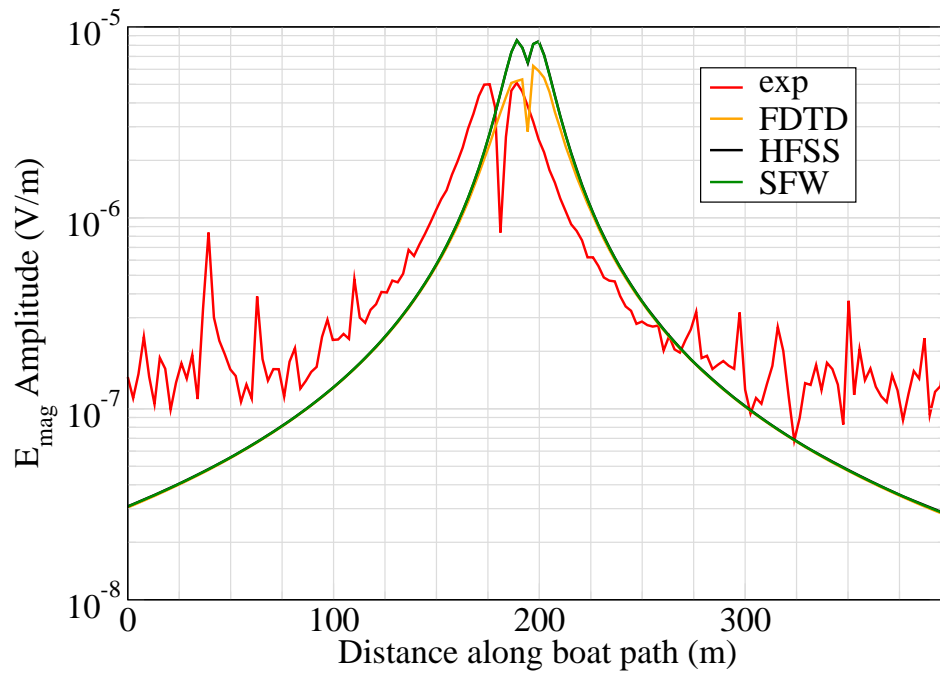


Figure 6: E_{mag} .

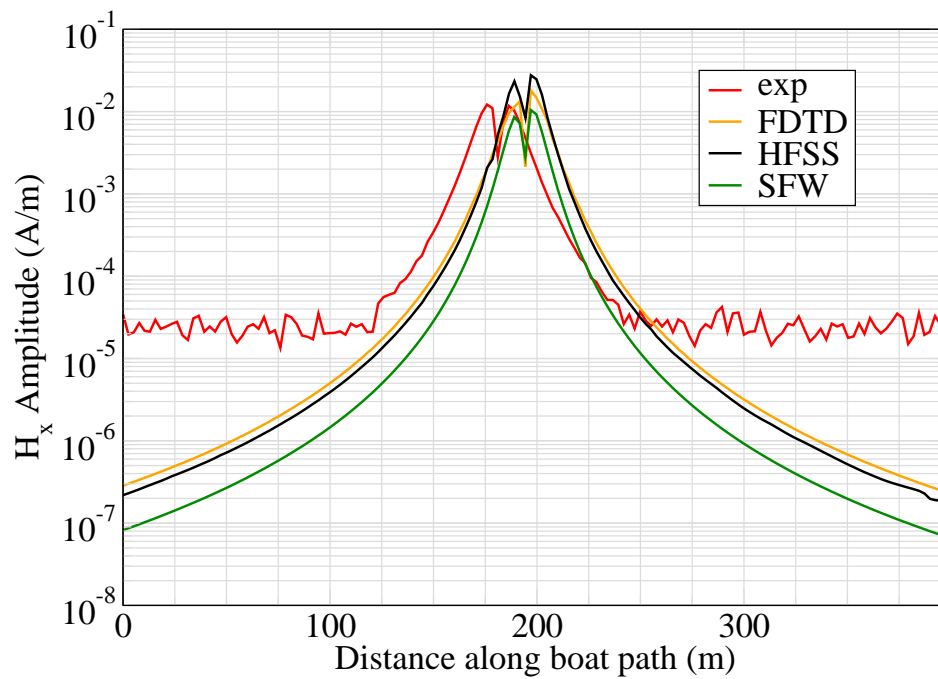


Figure 7: H_x .

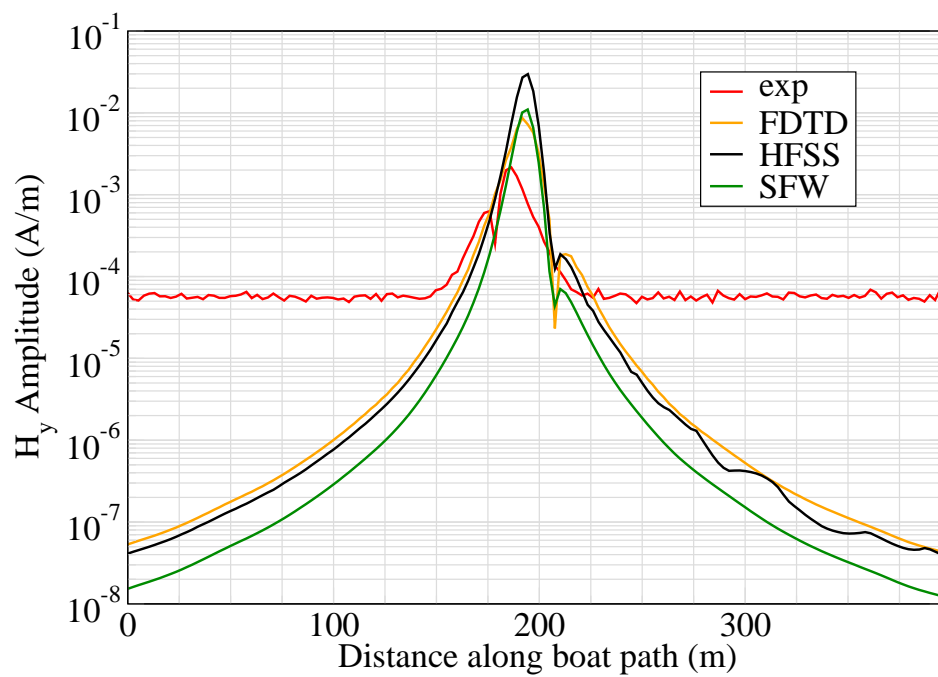


Figure 8: H_y .

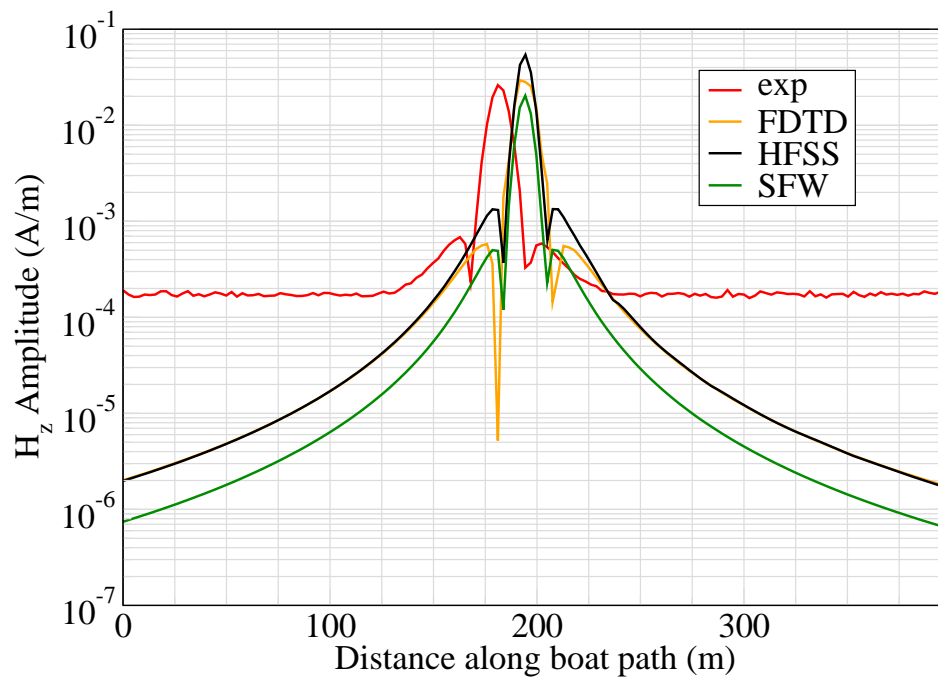


Figure 9: H_z .

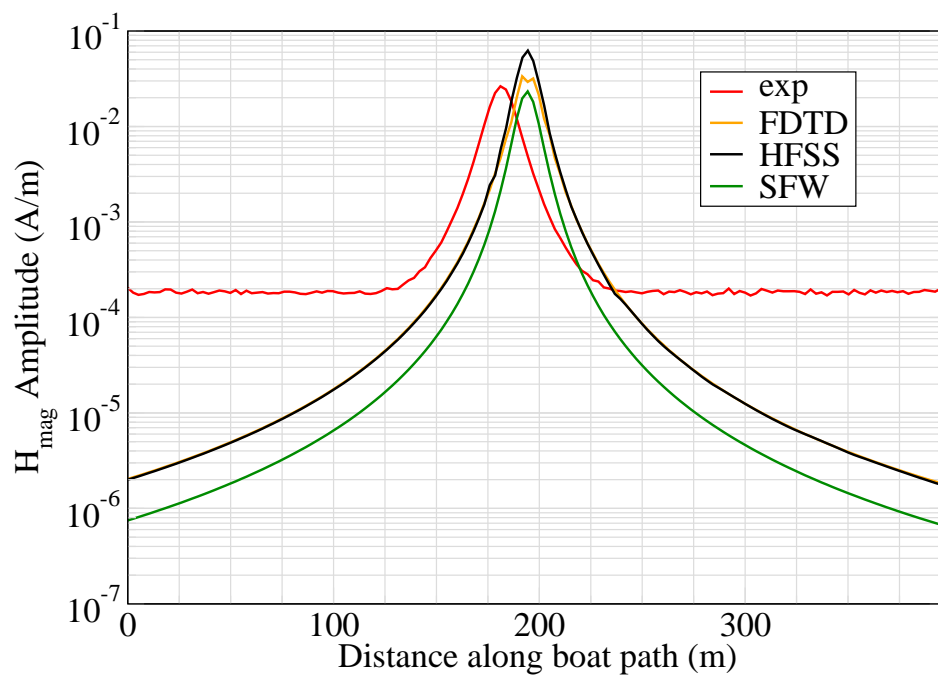


Figure 10: H_{mag} .

Experiment 2

Runs 5013

Experiment Date: 12/11/2008

1 Discussion

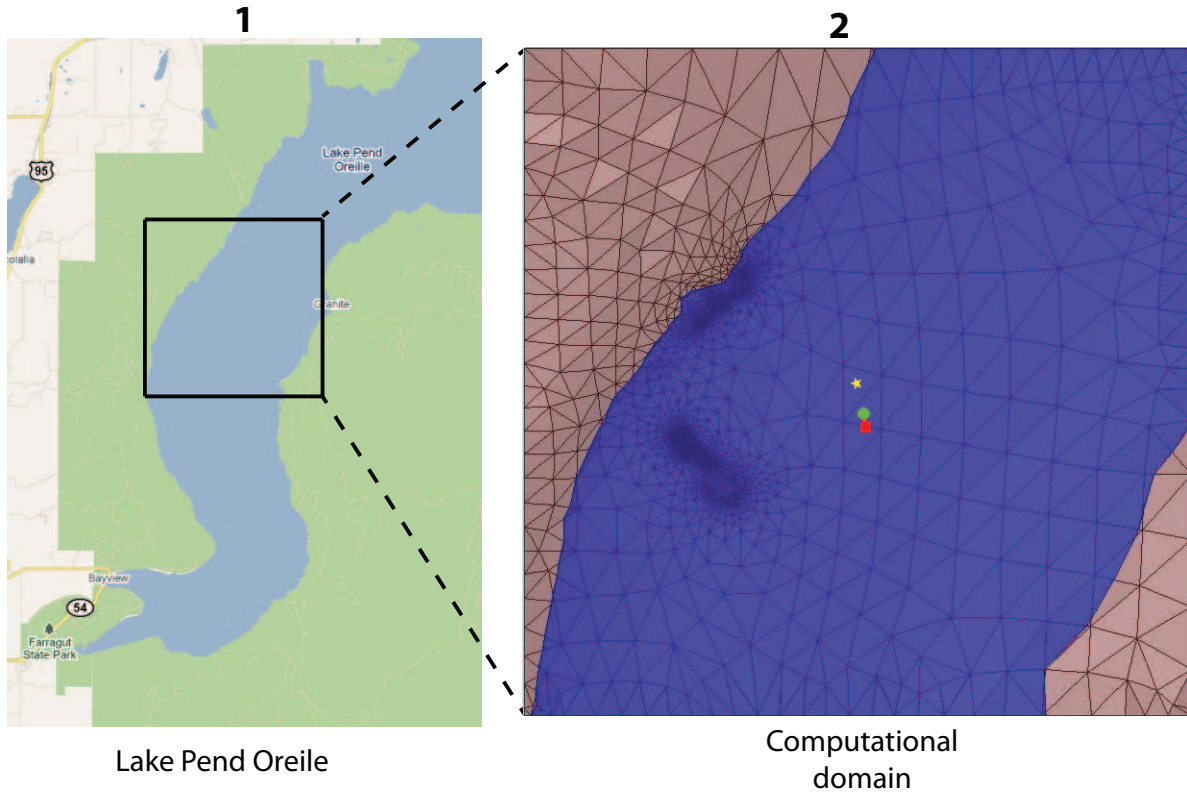


Figure 1: Sensor and source locations; see test report. Sensor is represented by the yellow star; source start and end points represented by green circle and red square.

Source Parameters

- Source Type: HED (Boat Skiff: 40 m separation).
- Source Strength: 51.6 A-m.
- $f = 1000$ Hz.

Environment

- Air: $\sigma = 0$ S/m and $\epsilon_r = 1$
- Water: $\sigma = 0.01$ S/m and $\epsilon_r = 81$
- Mud: $\sigma = 0.0012$ S/m and $\epsilon_r = 1$

Table 1: Simulation Details

	FDTD	HFSS	QES/SFW
Domain Size	200 X 200 X 160 cells	133,013 tets	N/A
Cell Size (m)	5 X 5 X 5	N/A	N/A
Time Step (ns)	9.6	N/A	N/A
Run Time (Hrs)	44.8	4	0.01
Water Depth (m)	N/A	N/A	300
Effective Source Area (m)	N/A	l = 0.61 w = 0.61	r = 0.058

Comments

- To implement reciprocity, three simulations per vector field are required for a total of six simulations. Run times correspond to the time required to conduct all six simulations.
- Computational time is based on actual elapsed real time. This number is highly subjective and based on how many other applications might be running at a particular time. However, the reported number is an indication of the amount of time typically needed for a particular simulation. The computer specs are: 16 CPU cores at 2.8 GHz.
- Run times for HFSS are given for a single frequency.
- QES is not applicable for magnetic fields using electric source excitation.

2 Simulation Variables

Sensor_P1(x,y,z) [m]	(3995.5266,3997.0031,-295.0464)
Sensor_P2(x,y,z) [m]	(3995.5266,3997.0031,-295.0464)
Source_P1(x,y,z) [m]	(4070.9632,3652.3622,0)
Source_P2(x,y,z) [m]	(4102.0278,3497.1462,0)
Source_Plate_Separation [m]	42.462
Source_Size [m X m X #]	[0.610 X 0.305 X 1]
Source_Heading [deg]	278.8294
Source_Voltage [V Peak]	164.5634
Source_Current [A Peak]	1.29
Source_Frequency [Hz]	1000

--- Extra Information ---

Source_Heading_Bounds [deg]	(N/A)
Average_Boat_Speed [m/s]	1.5076
Source_Type	Electric boat skiff (boat skiff)
Sensor_Type	EMA
Bin_Size [sec]	1
Number_of_Datapoints	106
Lake_Origin (Easting,Northing)	(741304.279,709845.52)
Analysis_Date	Exp2_ScenSN_28-Jul-2011

3 Boat Path

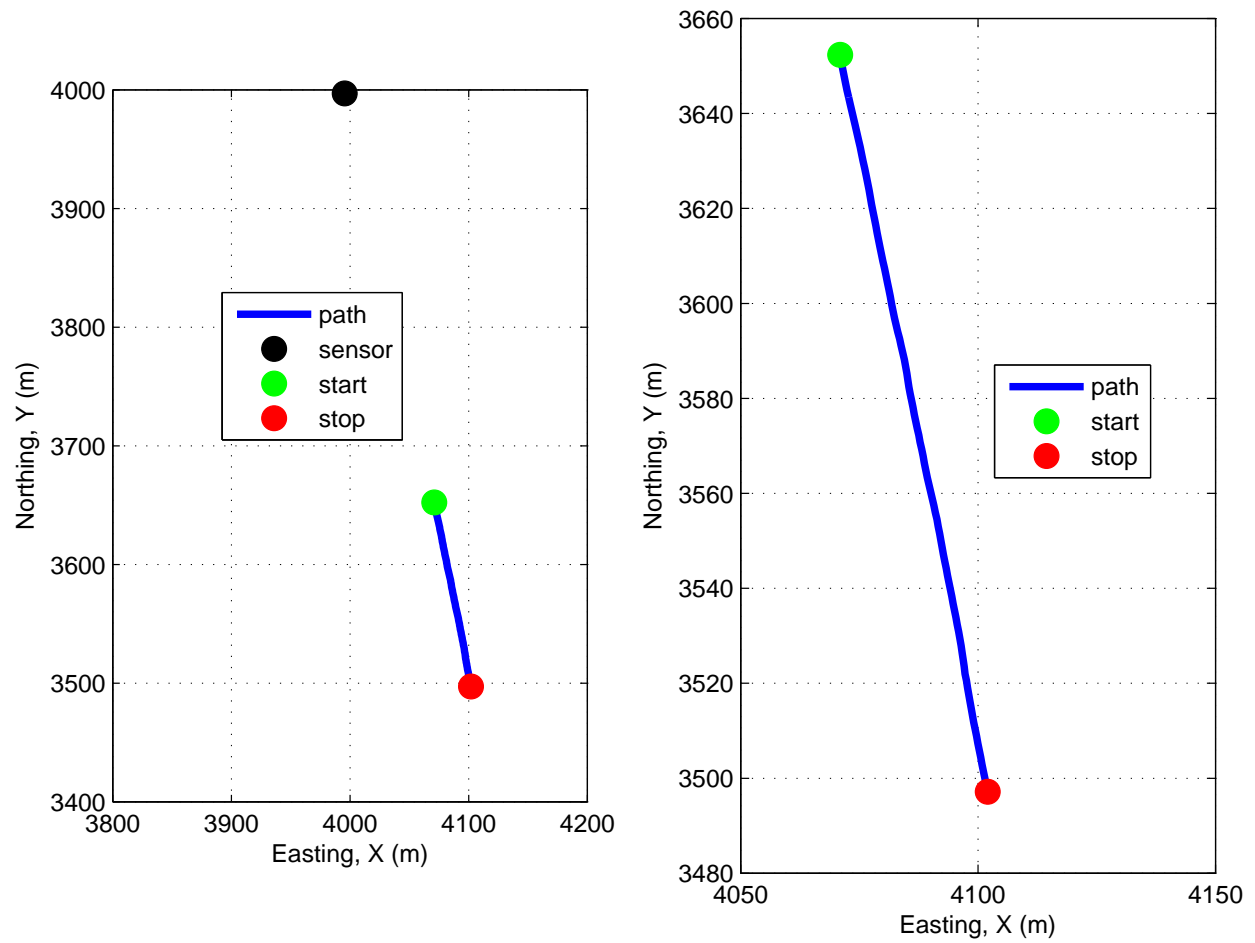


Figure 2: Source and sensor relationship.

4 Plots

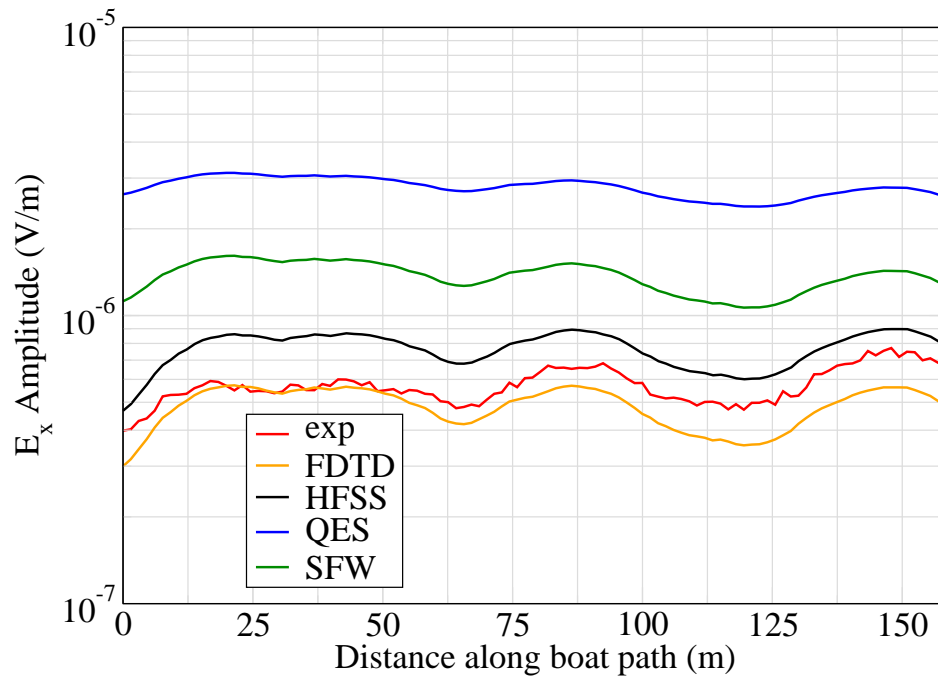


Figure 3: E_x .

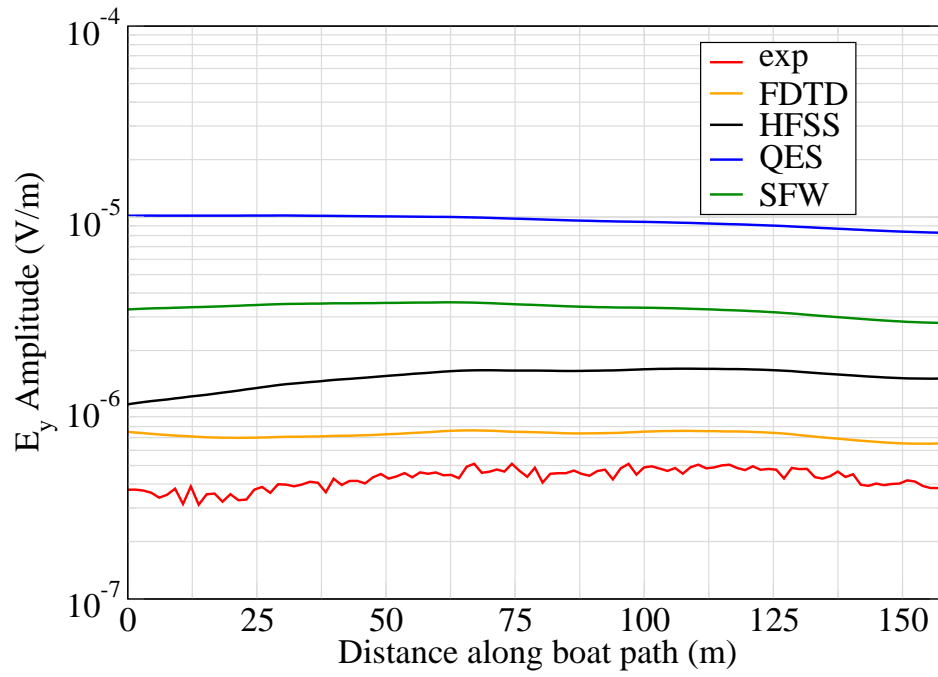


Figure 4: E_y .

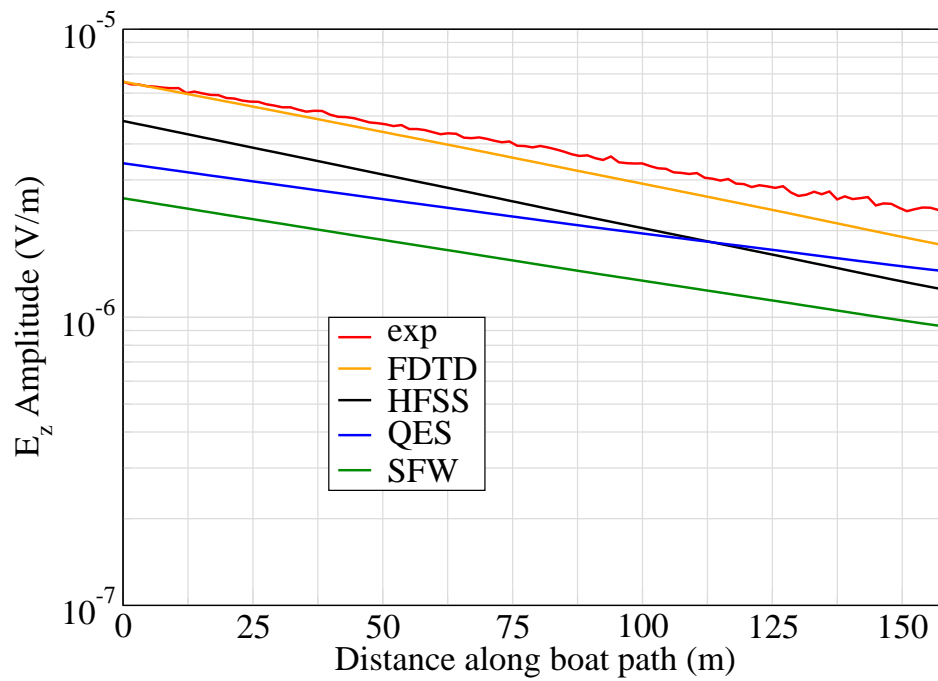


Figure 5: E_z .

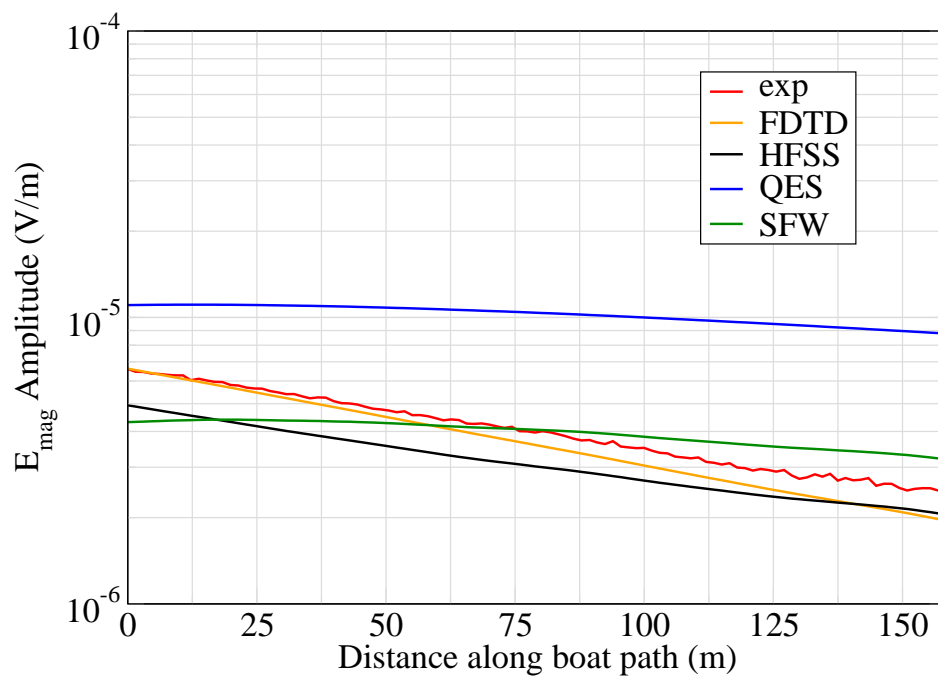


Figure 6: E_{mag} .

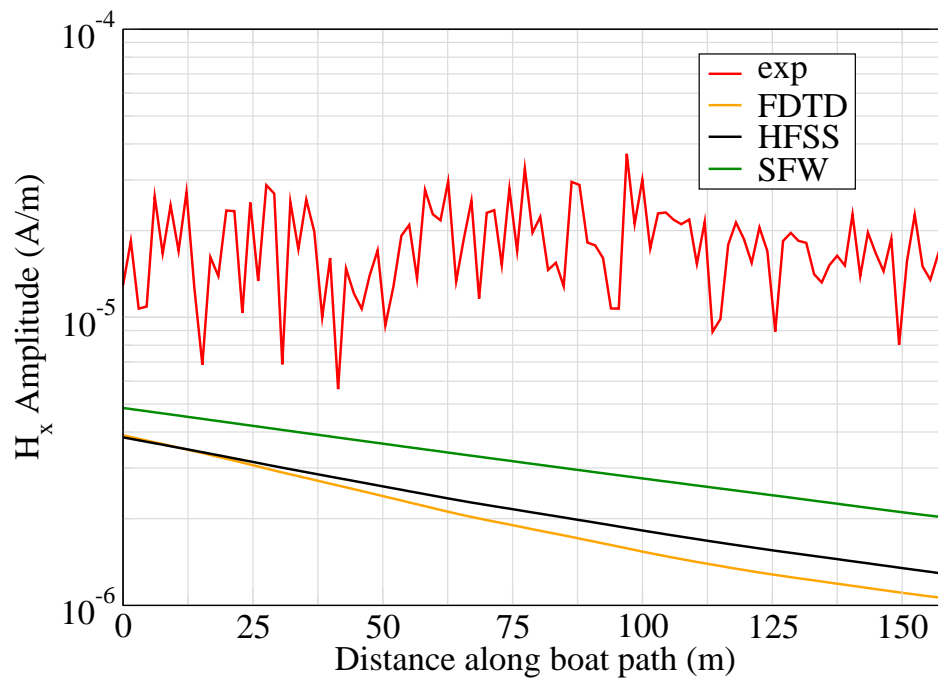


Figure 7: H_x .

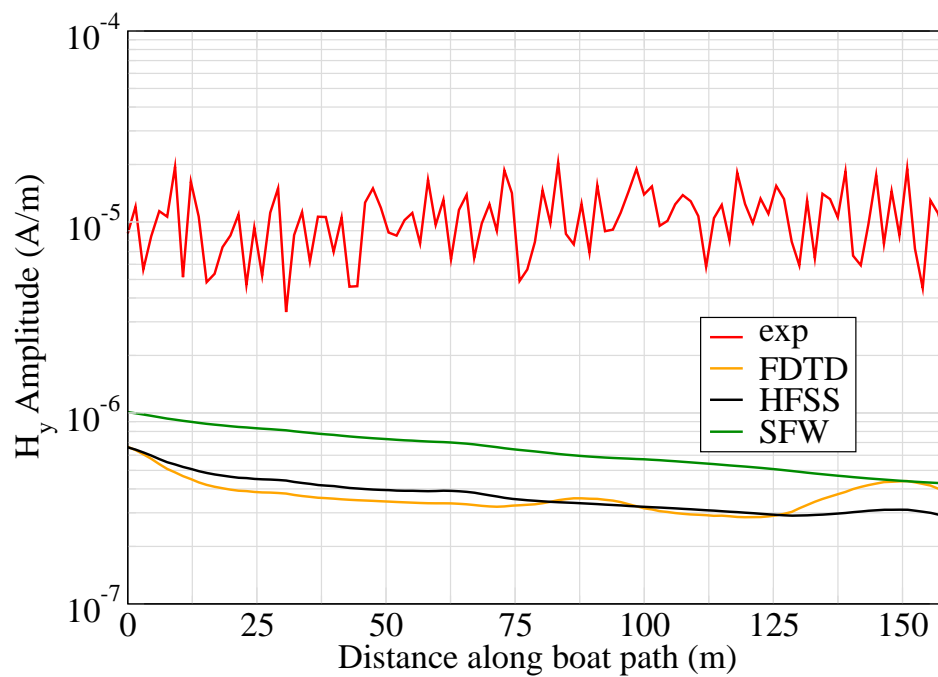


Figure 8: H_y .

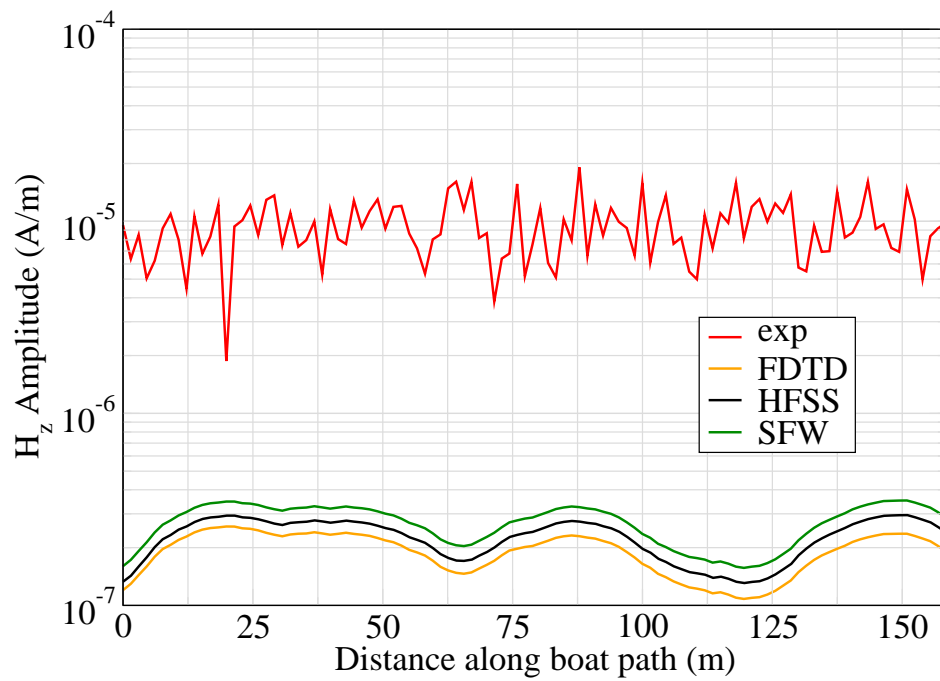


Figure 9: H_z .

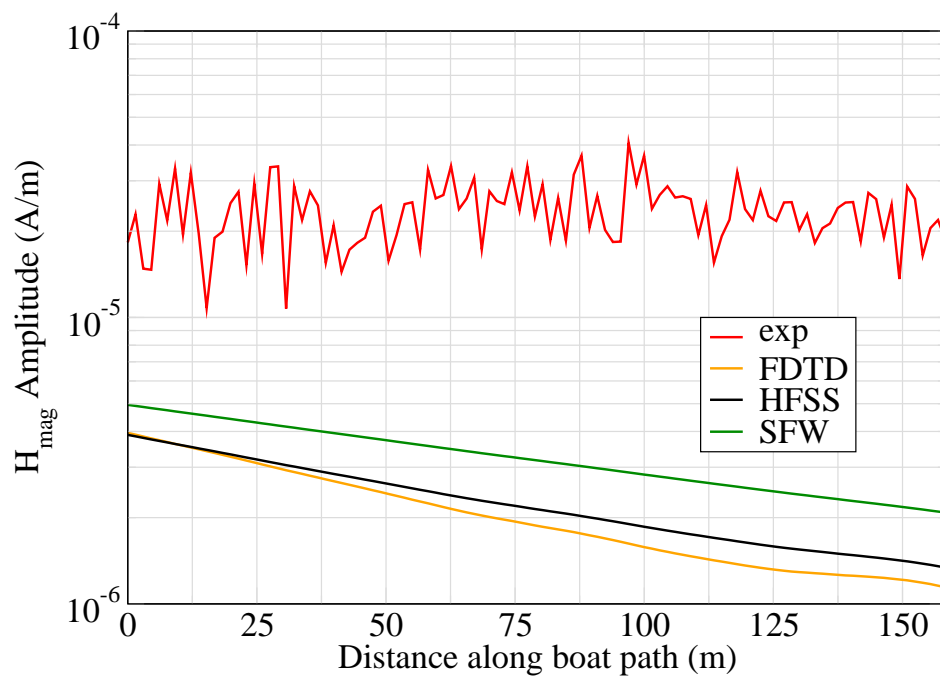


Figure 10: H_{mag} .

Experiment 2

Runs 5011

Experiment Date: 12/11/2008

1 Discussion

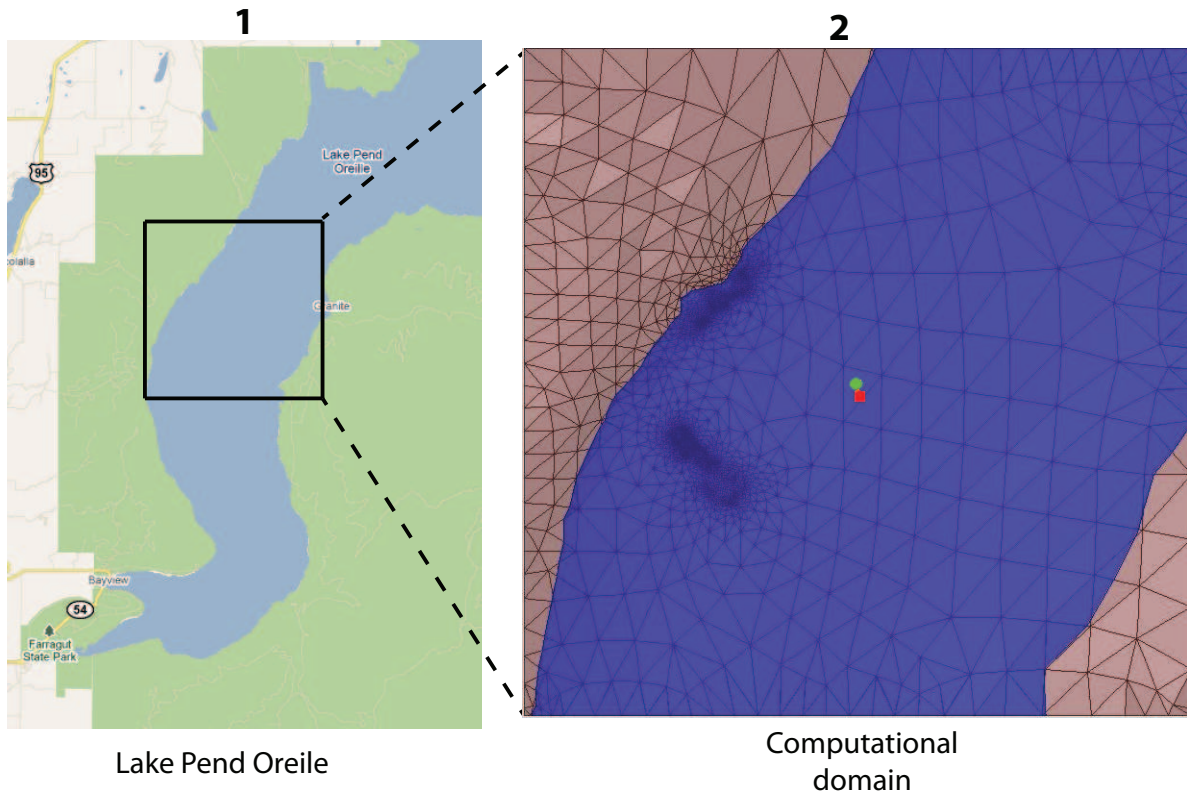


Figure 1: Sensor and source locations; see test report. Sensor is represented by the yellow star; source start and end points represented by green circle and red square.

Source Parameters

- Source Type: HED (Boat Skiff: 40 m separation).
- Source Strength: 52.67 A-m.
- $f = 10$ Hz.

Environment

- Air: $\sigma = 0$ S/m and $\epsilon_r = 1$
- Water: $\sigma = 0.01$ S/m and $\epsilon_r = 81$
- Mud: $\sigma = 0.0012$ S/m and $\epsilon_r = 1$

Table 1: Simulation Details

	FDTD	HFSS	QES/SFW
Domain Size	200 X 200 X 160 cells	128,316 tets	N/A
Cell Size (m)	5 X 5 X 5	N/A	N/A
Time Step (ns)	9.6	N/A	N/A
Run Time (Hrs)	44.8	2	0.01
Water Depth (m)	N/A	N/A	300
Effective Source Area (m)	N/A	$l = 0.61$ $w = 0.61$	$r = 0.058$

Comments

- To implement reciprocity, three simulations per vector field are required for a total of six simulations. Run times correspond to the time required to conduct all six simulations.
- Computational time is based on actual elapsed real time. This number is highly subjective and based on how many other applications might be running at a particular time. However, the reported number is an indication of the amount of time typically needed for a particular simulation. The computer specs are: 16 CPU cores at 2.8 GHz.
- Run times for HFSS are given for a single frequency.
- QES is not applicable for magnetic fields using electric source excitation.

2 Simulation Variables

Sensor_P1(x,y,z) [m]	(3995.5266,3997.0031,-295.0464)
Sensor_P2(x,y,z) [m]	(3995.5266,3997.0031,-295.0464)
Source_P1(x,y,z) [m]	(3994.1926,4020.5085,0)
Source_P2(x,y,z) [m]	(4030.1141,3859.7088,0)
Source_Plate_Separation [m]	42.462
Source_Size [m X m X #]	[0.610 X 0.305 X 1]
Source_Heading [deg]	280.9727
Source_Voltage [V Peak]	167.6549
Source_Current [A Peak]	1.3067
Source_Frequency [Hz]	10

--- Extra Information ---

Source_Heading_Bounds [deg]	(N/A)
Average_Boat_Speed [m/s]	1.3963
Source_Type	Electric boat skiff (boat skiff)
Sensor_Type	EMA
Bin_Size [sec]	1
Number_of_Datapoints	119
Lake_Origin (Easting,Northing)	(741304.279,709845.52)
Analysis_Date	Exp2_ScenS0_28-Jul-2011

3 Boat Path

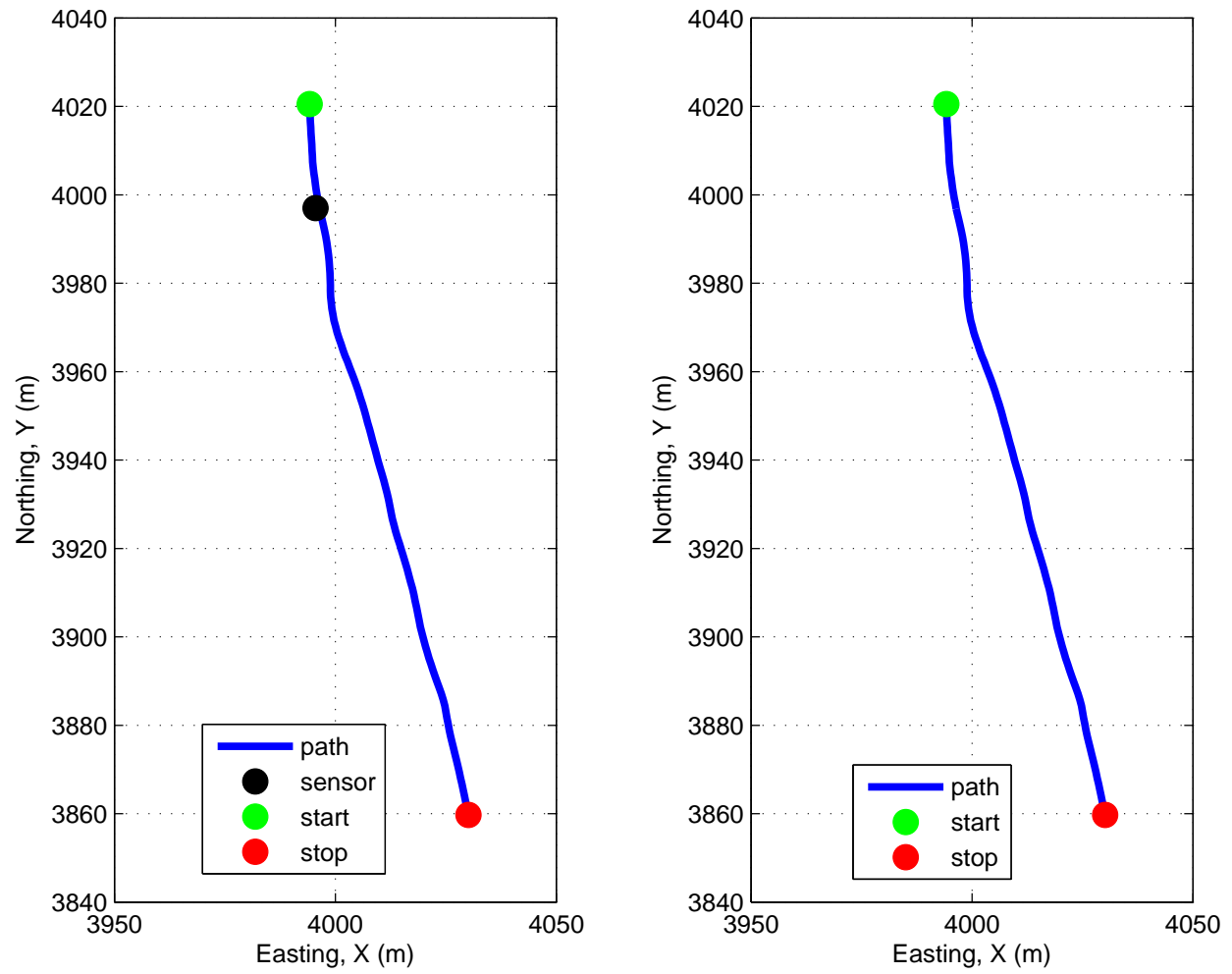


Figure 2: Source and sensor relationship.

4 Plots

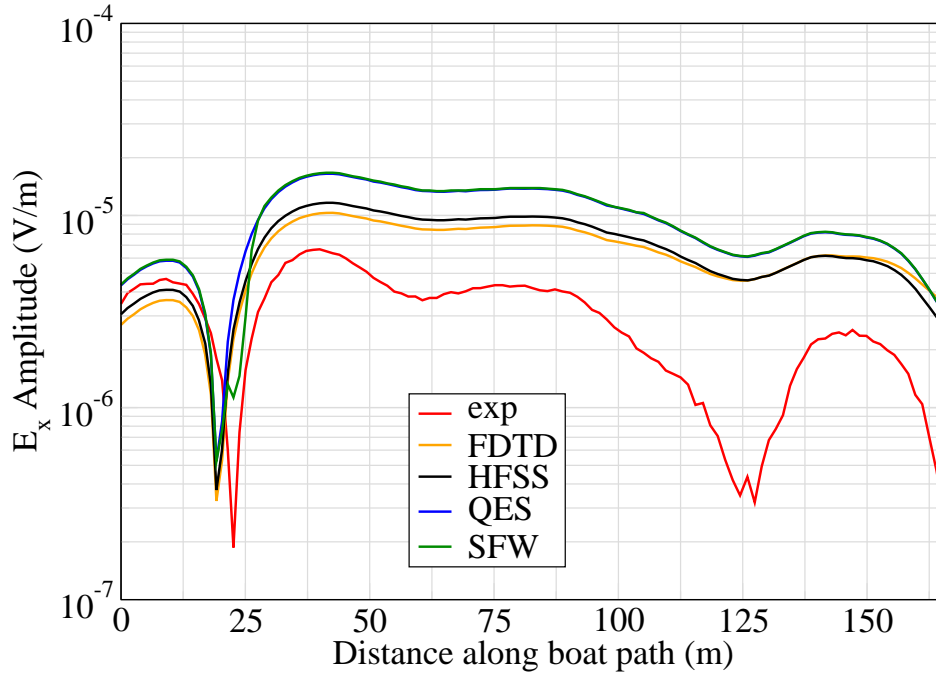


Figure 3: E_x .

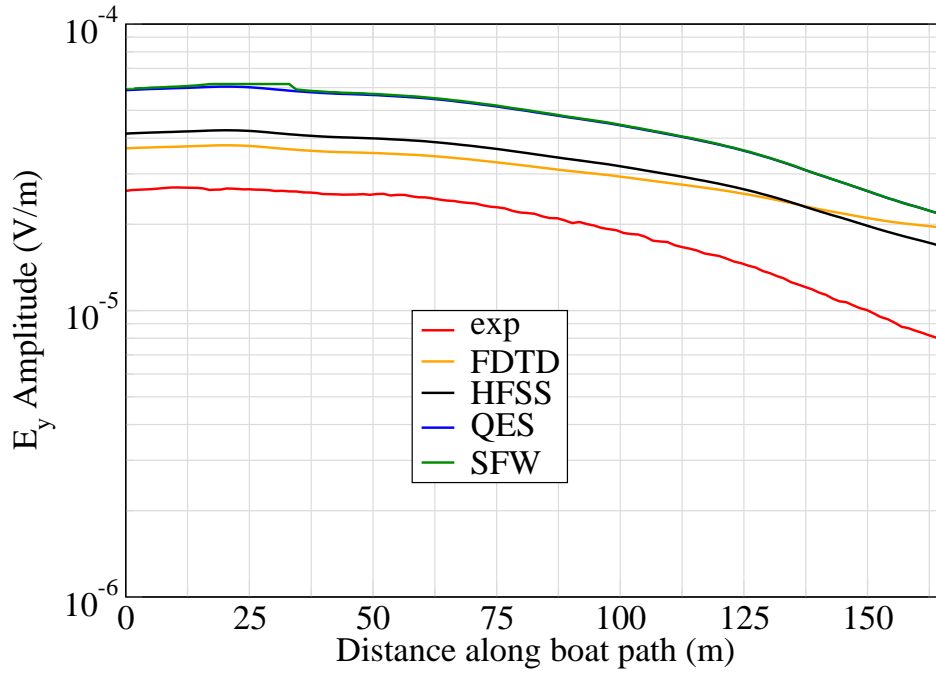


Figure 4: E_y .

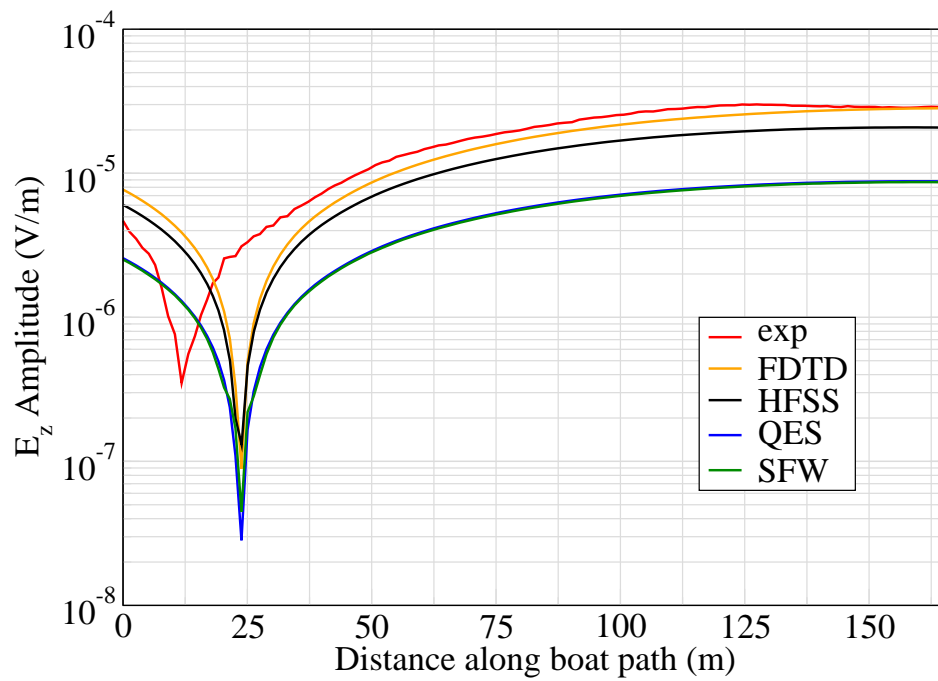


Figure 5: E_z .

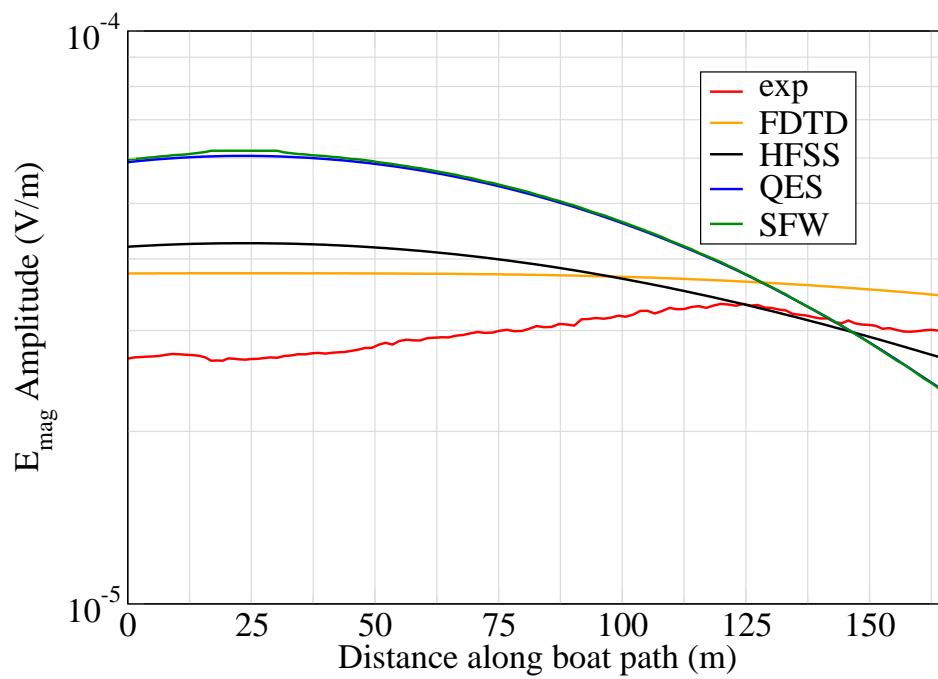


Figure 6: E_{mag} .

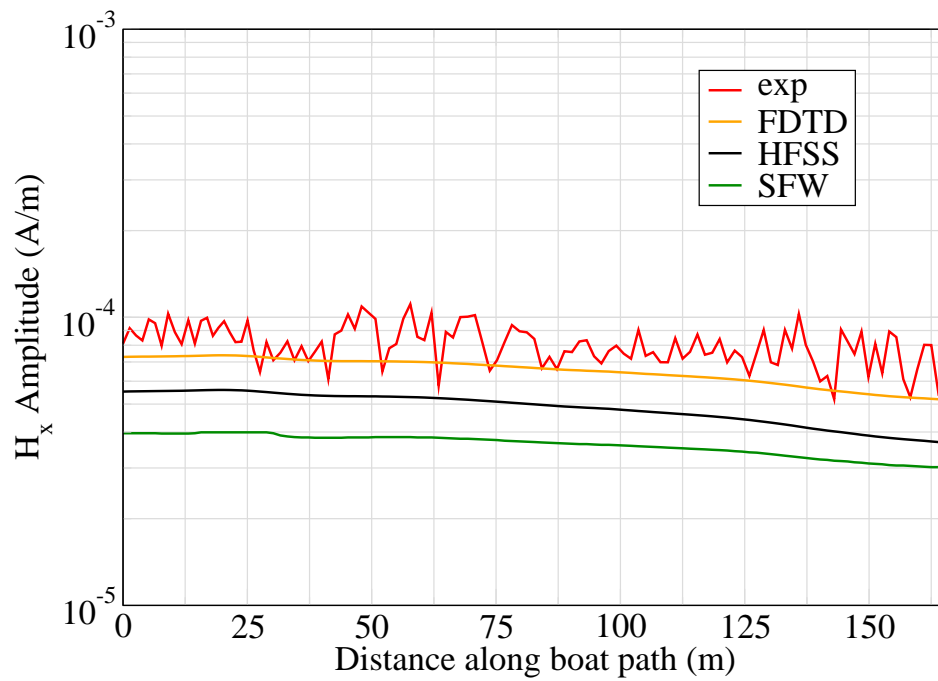


Figure 7: H_x .

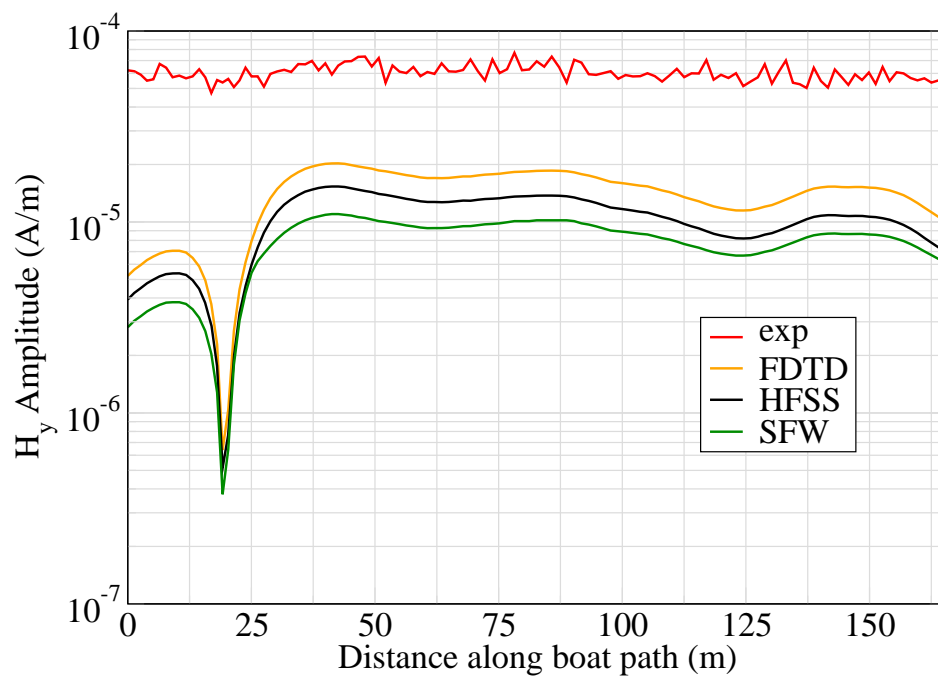


Figure 8: H_y .

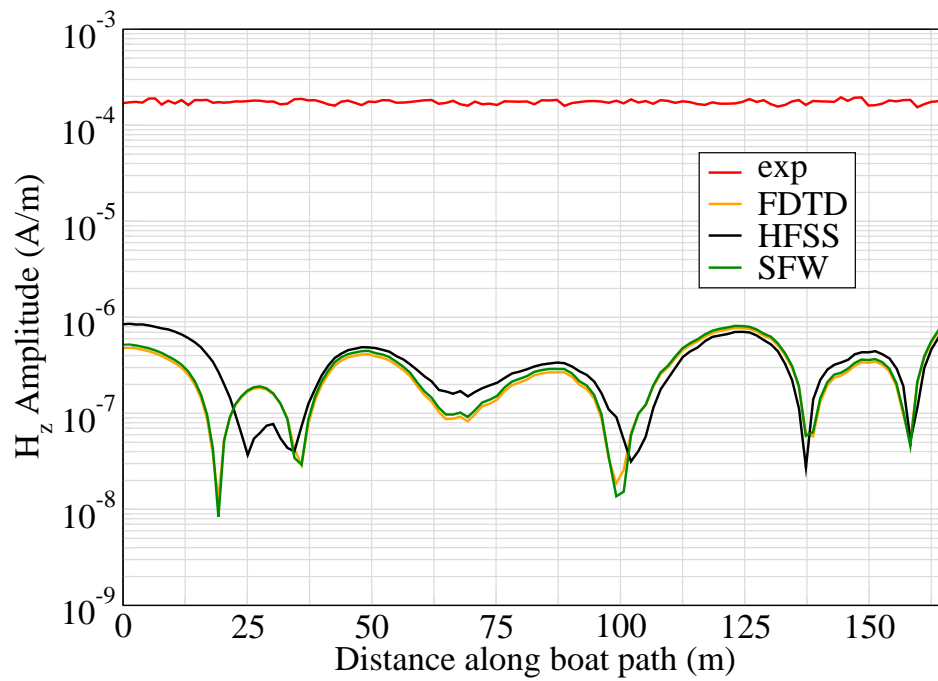


Figure 9: H_z .

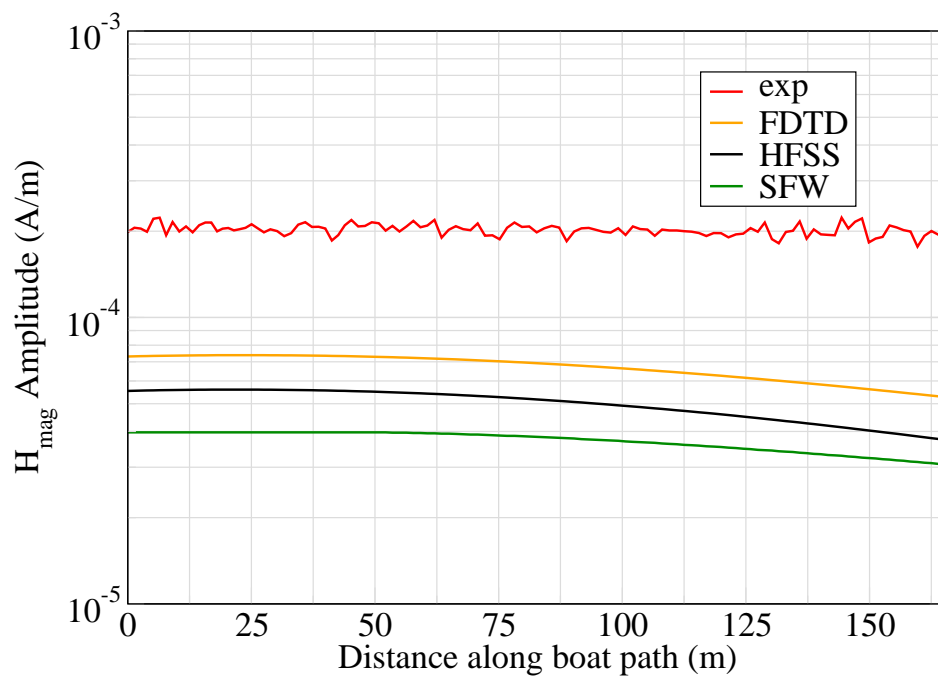


Figure 10: H_{mag} .

Experiment 2

Runs 5012

Experiment Date: 12/11/2008

1 Discussion

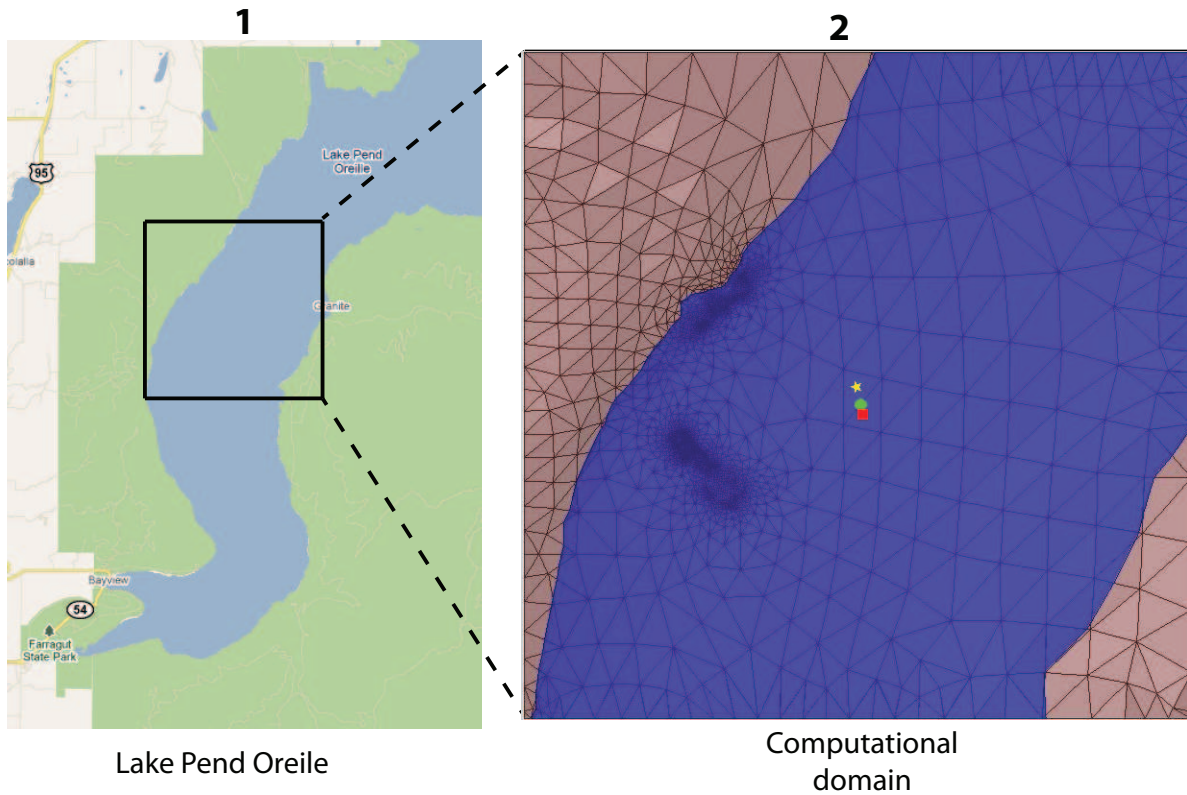


Figure 1: Sensor and source locations; see test report. Sensor is represented by the yellow star; source start and end points represented by green circle and red square.

Source Parameters

- Source Type: HED (Boat Skiff: 40 m separation).
- Source Strength: 52.24 A-m.
- $f = 100$ Hz.

Environment

- Air: $\sigma = 0$ S/m and $\epsilon_r = 1$
- Water: $\sigma = 0.01$ S/m and $\epsilon_r = 81$
- Mud: $\sigma = 0.0012$ S/m and $\epsilon_r = 1$

Table 1: Simulation Details

	FDTD	HFSS	QES/SFW
Domain Size	200 X 200 X 160 cells	137,361 tets	N/A
Cell Size (m)	5 X 5 X 5	N/A	N/A
Time Step (ns)	9.6	N/A	N/A
Run Time (Hrs)	44.8	2.05	0.01
Water Depth (m)	N/A	N/A	300
Effective Source Area (m)	N/A	l = 0.61 w = 0.61	r = 0.058

Comments

- To implement reciprocity, three simulations per vector field are required for a total of six simulations. Run times correspond to the time required to conduct all six simulations.
- Computational time is based on actual elapsed real time. This number is highly subjective and based on how many other applications might be running at a particular time. However, the reported number is an indication of the amount of time typically needed for a particular simulation. The computer specs are: 16 CPU cores at 2.8 GHz.
- Run times for HFSS are given for a single frequency.
- QES is not applicable for magnetic fields using electric source excitation.

2 Simulation Variables

Sensor_P1(x,y,z) [m]	(3995.5266,3997.0031,-295.0464)
Sensor_P2(x,y,z) [m]	(3995.5266,3997.0031,-295.0464)
Source_P1(x,y,z) [m]	(4039.642,3809.4308,0)
Source_P2(x,y,z) [m]	(4062.4623,3691.1794,0)
Source_Plate_Separation [m]	42.462
Source_Size [m X m X #]	[0.610 X 0.305 X 1]
Source_Heading [deg]	279.7249
Source_Voltage [V Peak]	167.5937
Source_Current [A Peak]	1.3061
Source_Frequency [Hz]	100

--- Extra Information ---

Source_Heading_Bounds [deg]	(N/A)
Average_Boat_Speed [m/s]	1.5245
Source_Type	Electric boat skiff (boat skiff)
Sensor_Type	EMA
Bin_Size [sec]	1
Number_of_Datapoints	80
Lake_Origin (Easting,Northing)	(741304.279,709845.52)
Analysis_Date	Exp2_ScenSP_28-Jul-2011

3 Boat Path

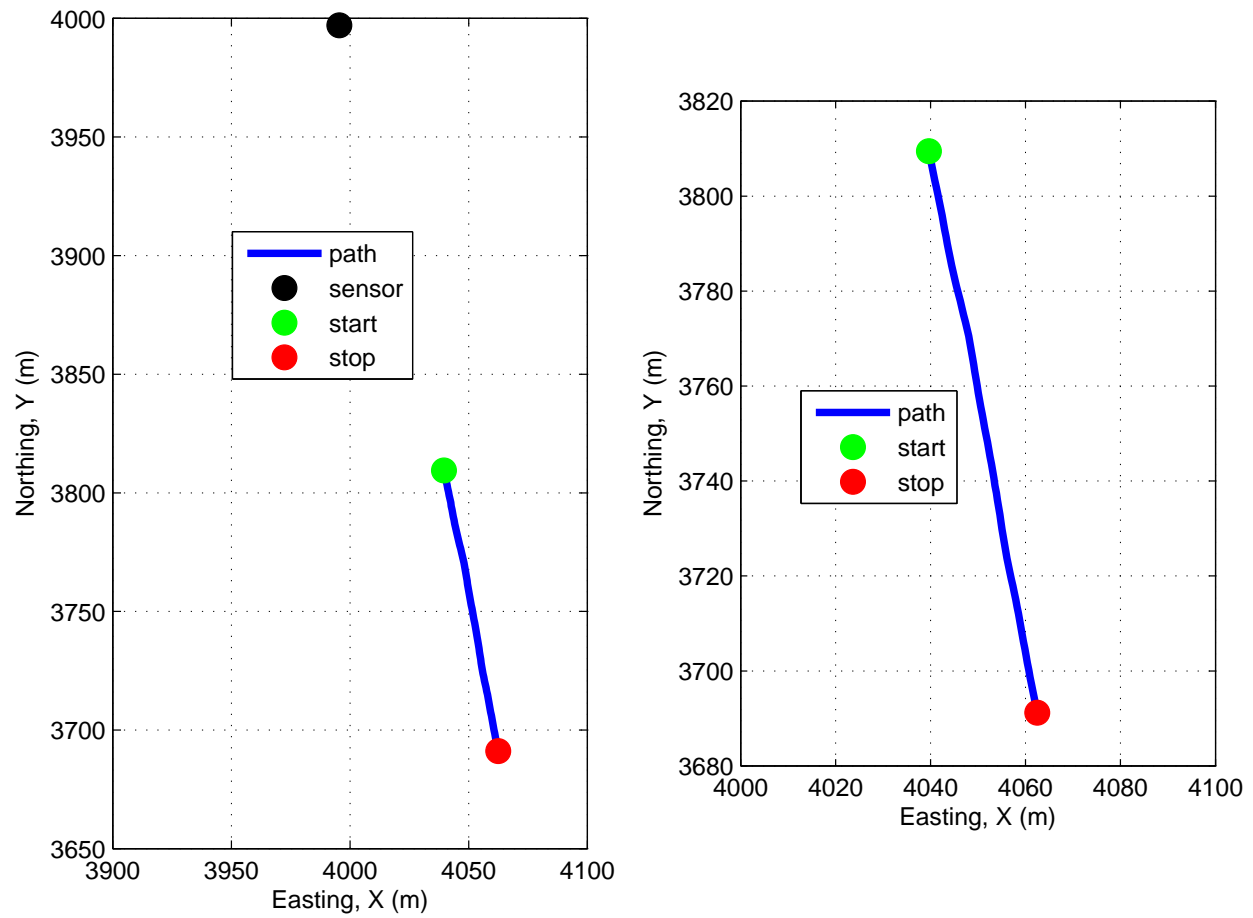


Figure 2: Source and sensor relationship.

4 Plots

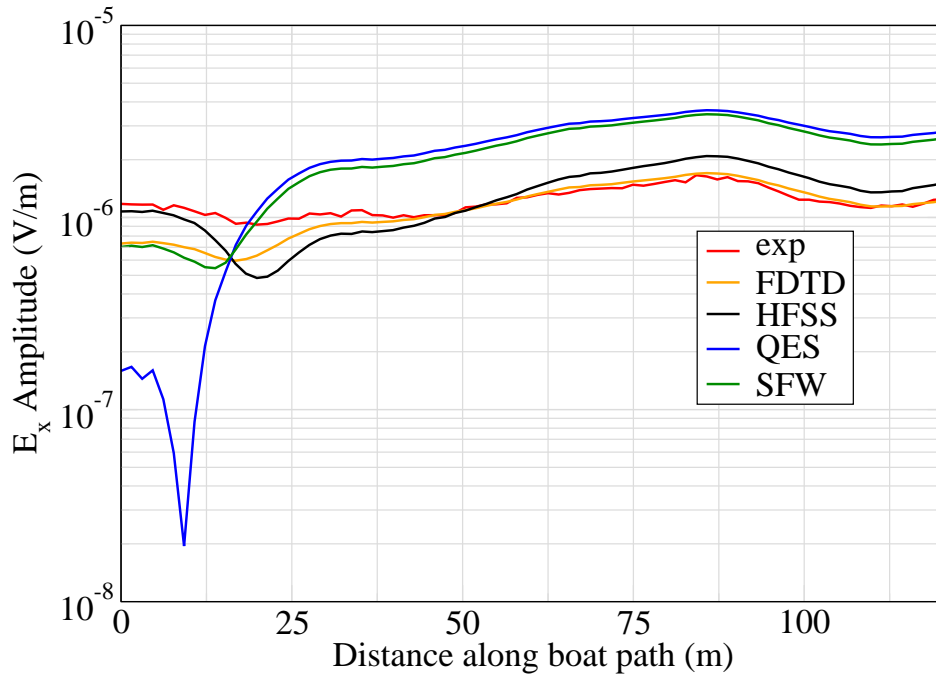


Figure 3: E_x .

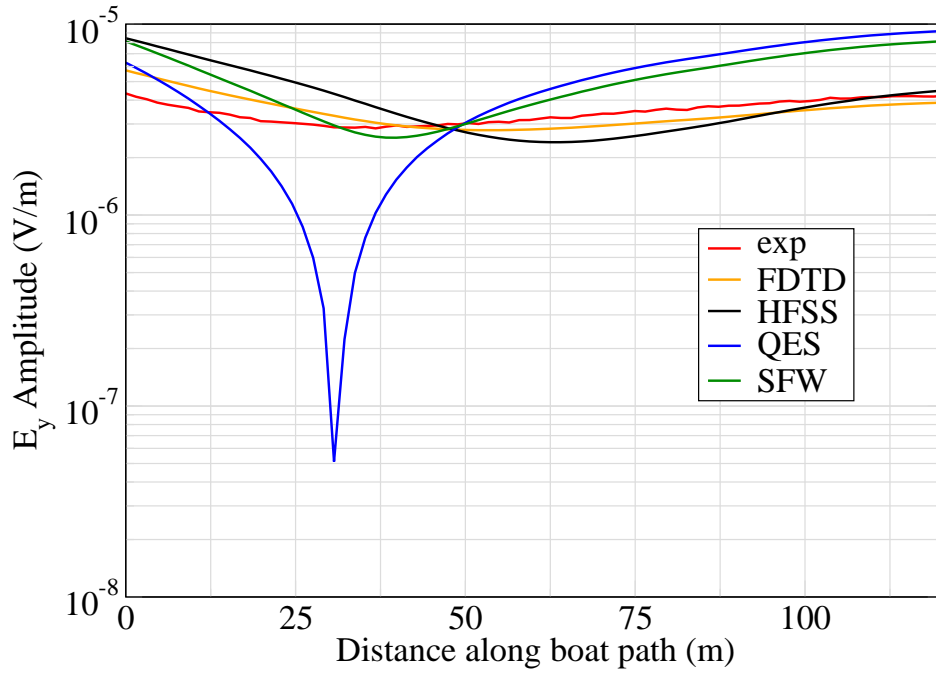


Figure 4: E_y .

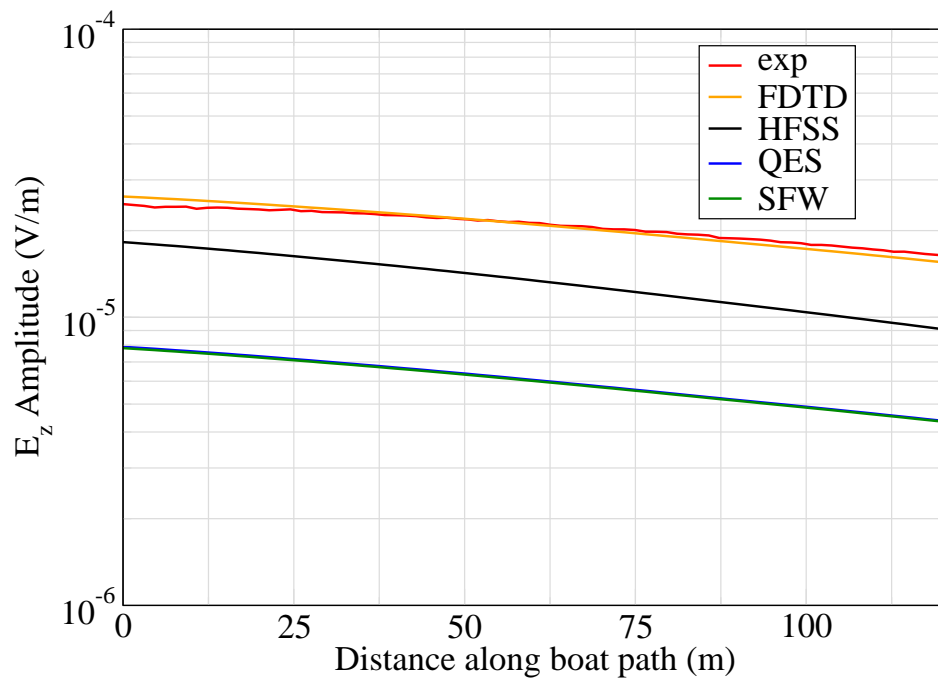


Figure 5: E_z .

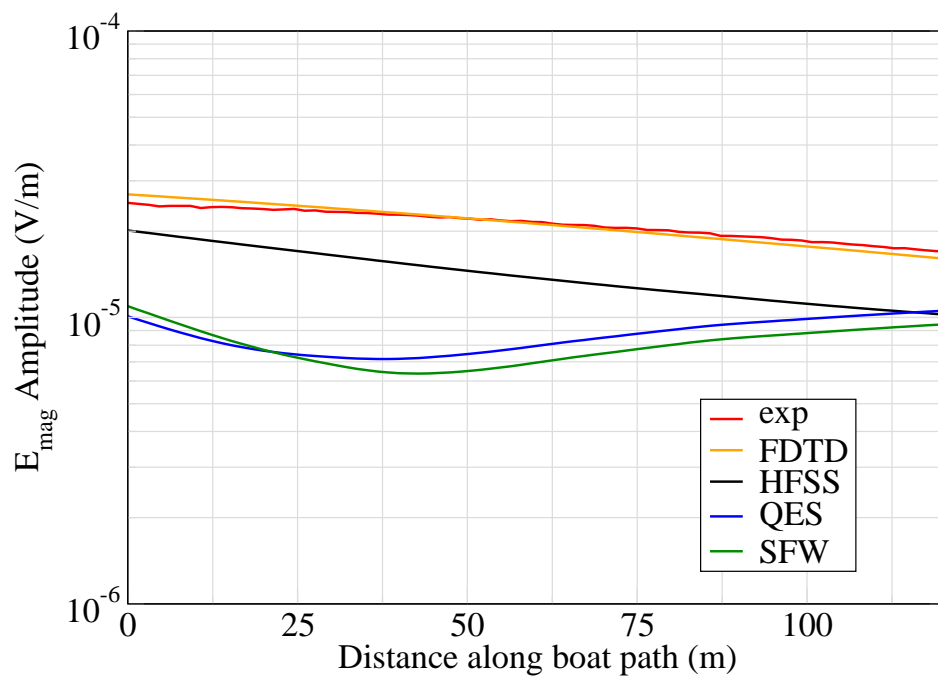


Figure 6: E_{mag} .

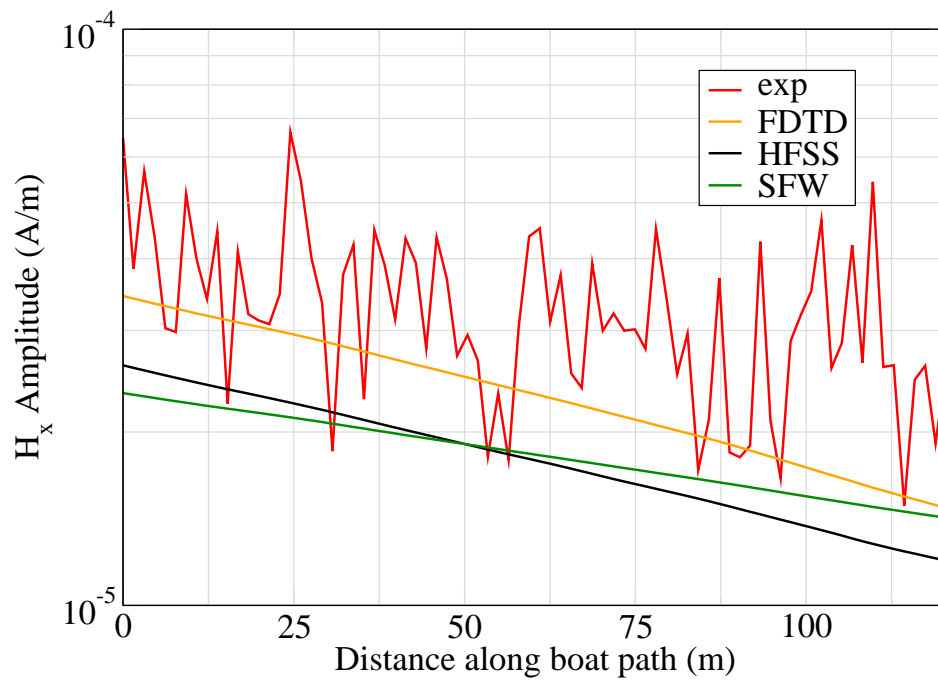


Figure 7: H_x .

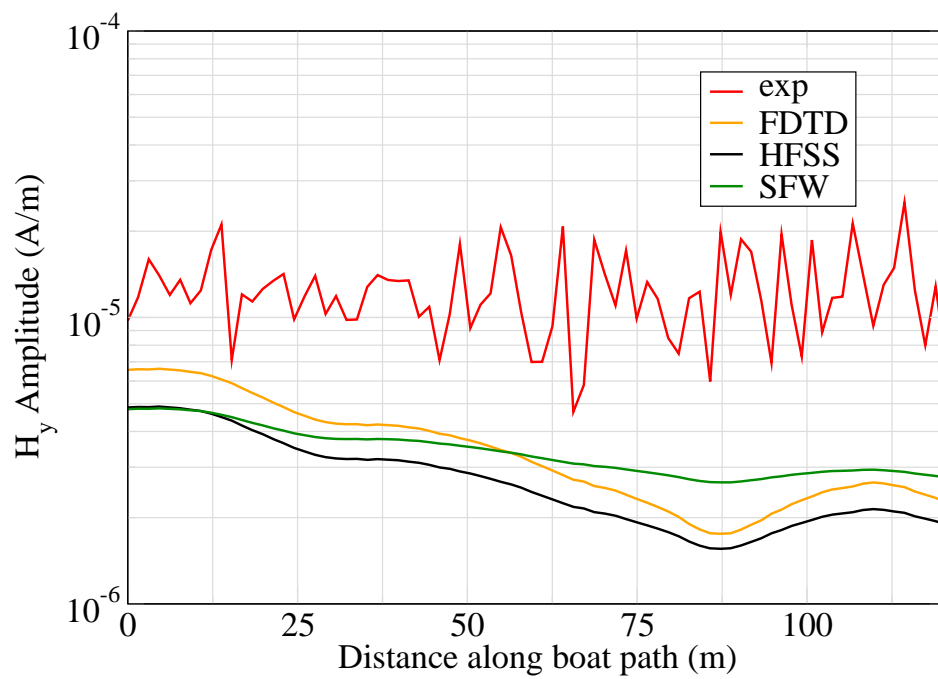


Figure 8: H_y .

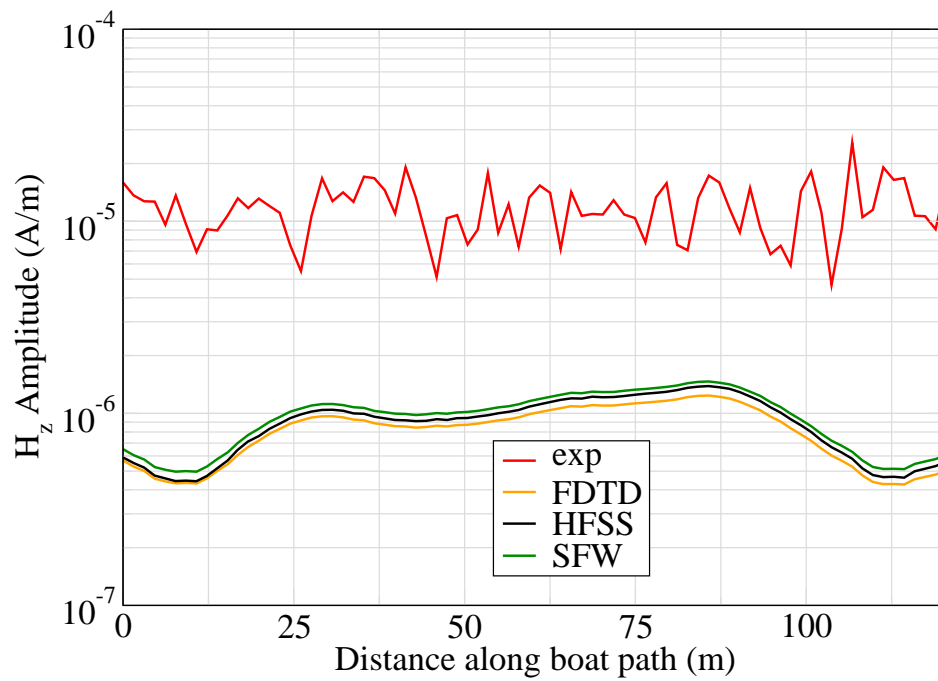


Figure 9: H_z .

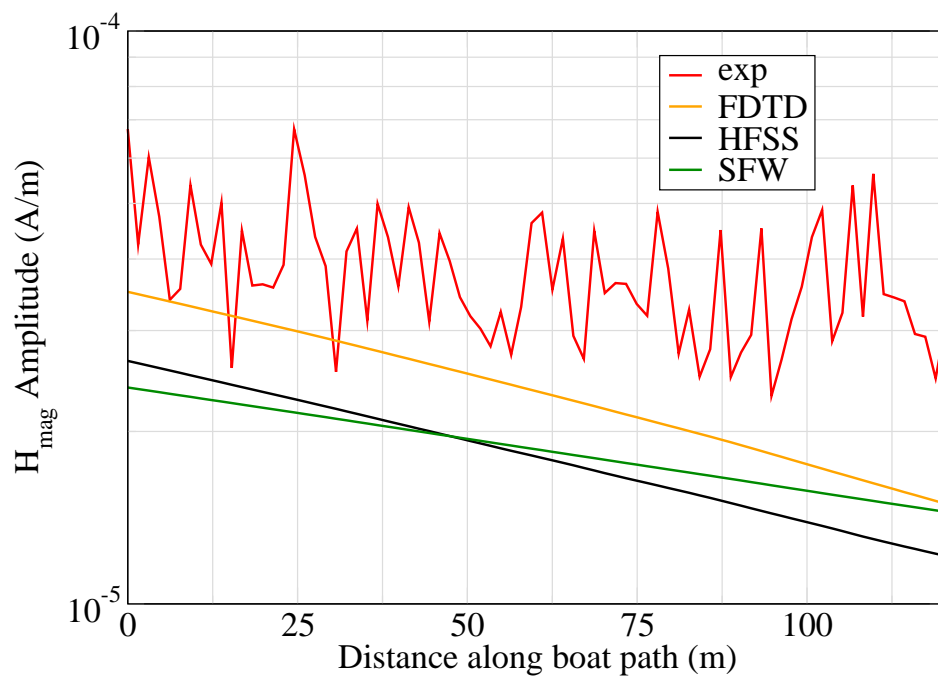


Figure 10: H_{mag} .

Experiment 4

Runs 100.01, 100.03, 100.05, 100.07 and 100.09

Experiment Date: 9/13/2010

1 Discussion

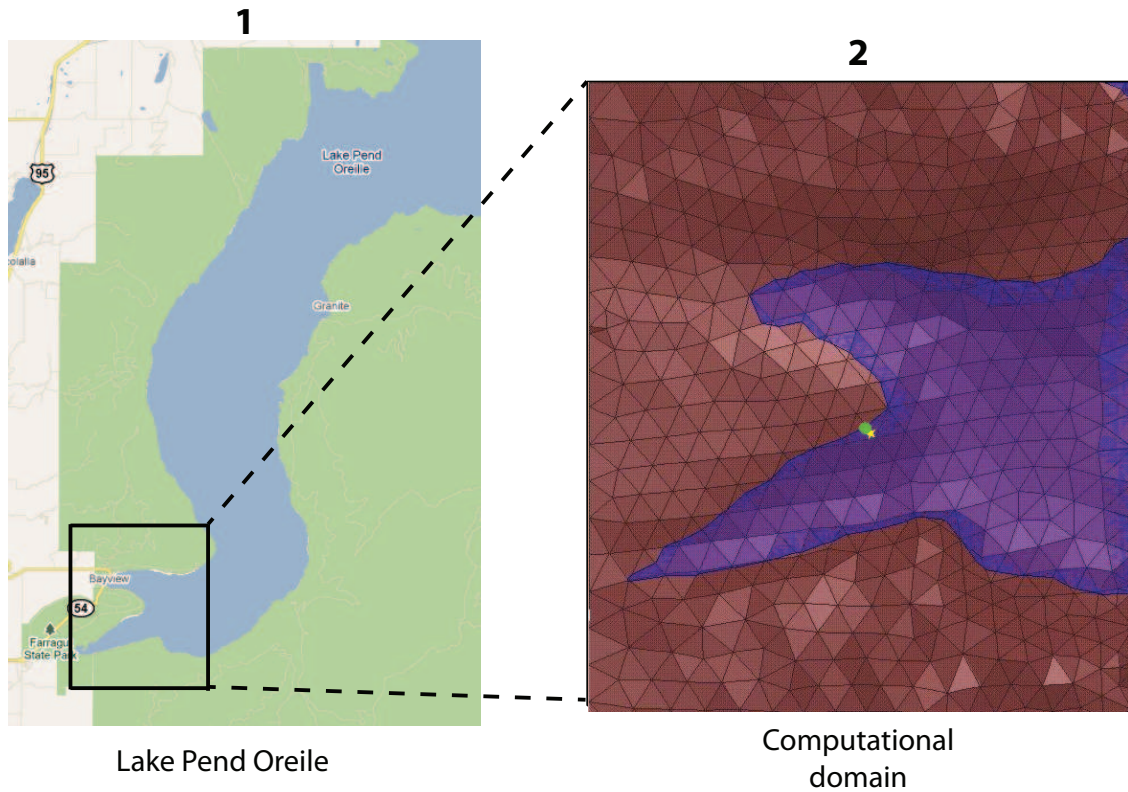


Figure 1: Sensor and source locations; see test report. Sensor is represented by the yellow star; source start and end points represented by green circle and red square.

Source Parameters

- Source Type: VMD (Coil: 3.66 m by 3.66 m with 12 turns).
- Source Strength: 3, 273.94 A-m².
- $f = 81$ Hz.

Environment

- Air: $\sigma = 0$ S/m and $\epsilon_r = 1$
- Water: $\sigma = 0.01$ S/m and $\epsilon_r = 81$
- Mud: $\sigma = 0.0012$ S/m and $\epsilon_r = 1$

Table 1: Simulation Details

	FDTD	HFSS	QES/SFW
Domain Size	200 X 200 X 120 cells	44,432 tets	N/A
Cell Size (m)	10 X 10 X 5	N/A	N/A
Time Step (ns)	13.6	N/A	N/A
Run Time (Hrs)	6.5	0.68	0.01
Water Depth (m)	N/A	N/A	18
Effective Source Area (m)	N/A	l = 3.66 w = 3.66	r = 3.66

Comments

- To implement reciprocity, three simulations per vector field are required for a total of six simulations. Run times correspond to the time required to conduct all six simulations.
- Computational time is based on actual elapsed real time. This number is highly subjective and based on how many other applications might be running at a particular time. However, the reported number is an indication of the amount of time typically needed for a particular simulation. The computer specs are: 16 CPU cores at 2.8 GHz.
- Run times for HFSS are given for a single frequency.
- QES is not applicable for electric or magnetic fields using magnetic source excitation.

2 Simulation Variables

Sensor_P1(x,y,z) [m]	(3225.7824,3496.9161,-3.1129)
Sensor_P2(x,y,z) [m]	(3225.7824,3496.9161,-15.2517)
Source_P1(x,y,z) [m]	(3164.9716,3561.9188,0)
Source_P2(x,y,z) [m]	(3164.9716,3561.9188,0)
Source_Plate_Separation [m]	N/A
Source_Size [m X m X #]	[3.658 X 3.658 X 12]
Source_Heading [deg]	NaN
Source_Voltage [V Peak]	19.7454
Source_Current [A Peak]	20.3891
Source_Frequency [Hz]	81

--- Extra Information ---

Source_Heading_Bounds [deg]	(N/A)
Average_Boat_Speed [m/s]	NaN
Source_Type	Magnetic source (portable)
Sensor_Type	PEMA
Bin_Size [sec]	[159,494,284,482,379]
Number_of_Datapoints	5
Lake_Origin (Easting,Northing)	(737736.502,696691.143)
Analysis_Date	Exp4_ScenSA_28-Jul-2011

3 Source and sensor locations

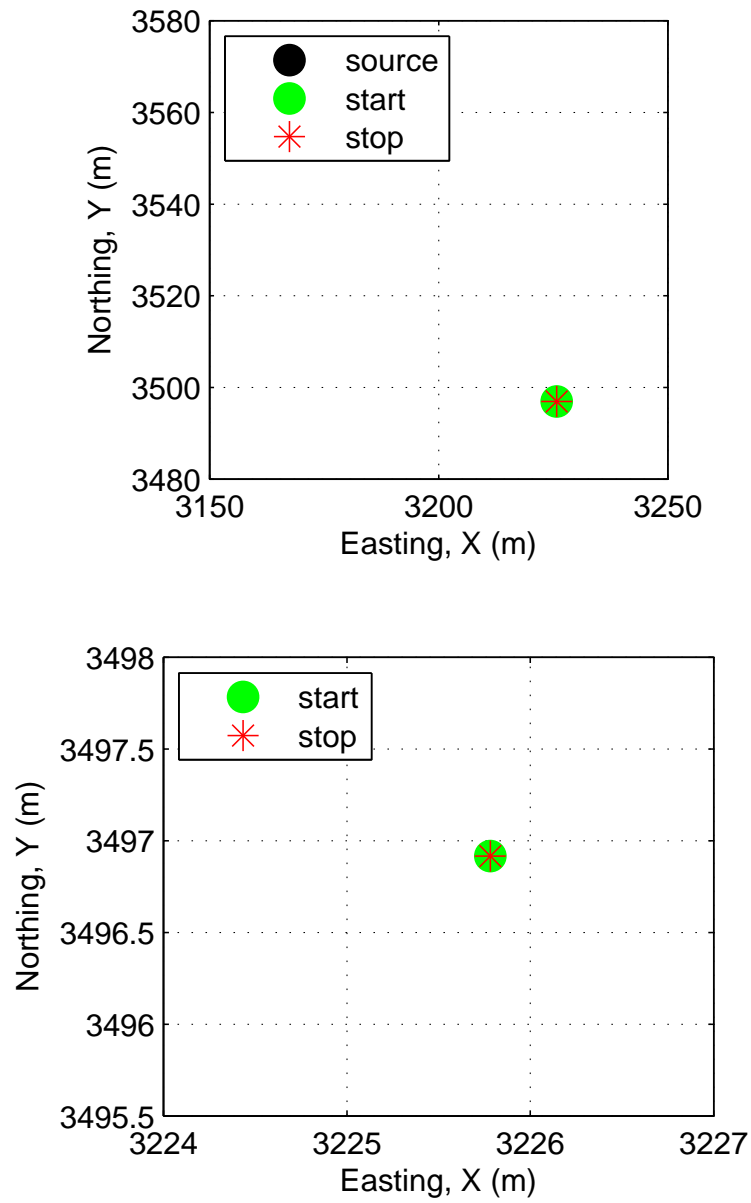


Figure 2: Source and sensor relationship.

4 Plots

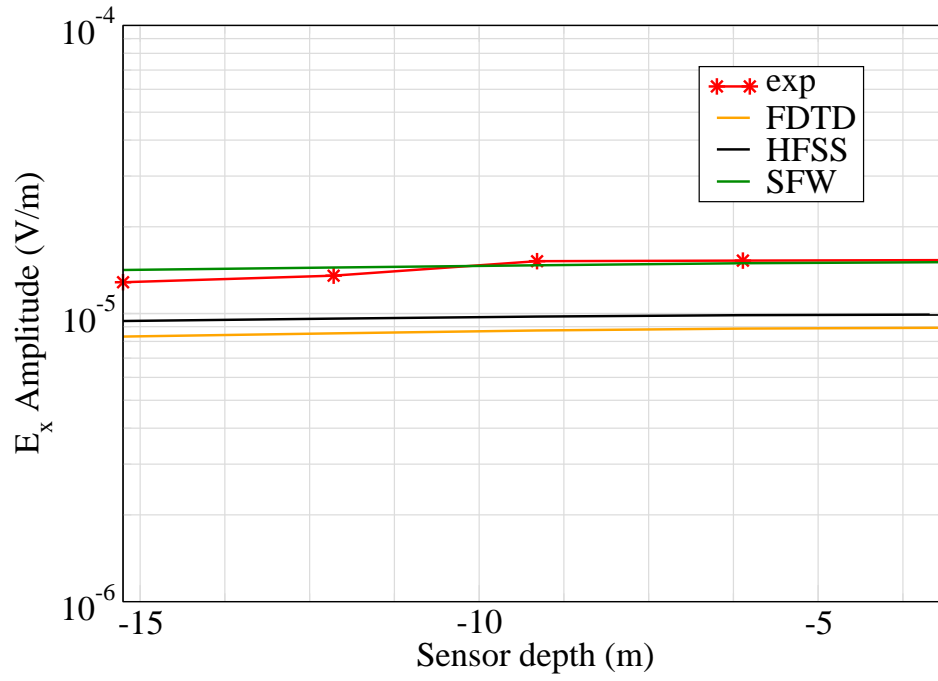


Figure 3: E_x .

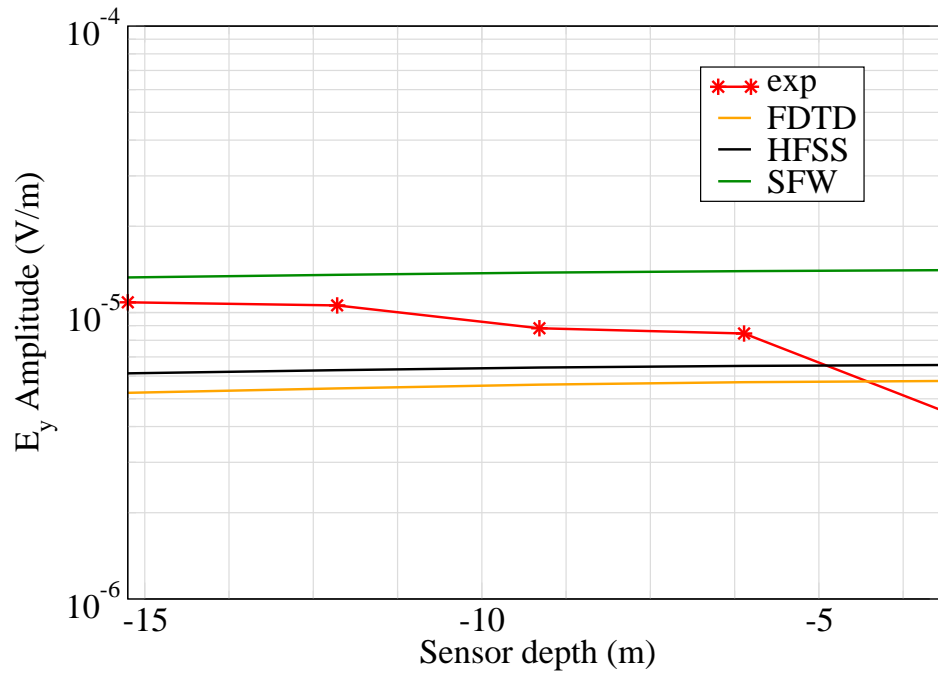


Figure 4: E_y .

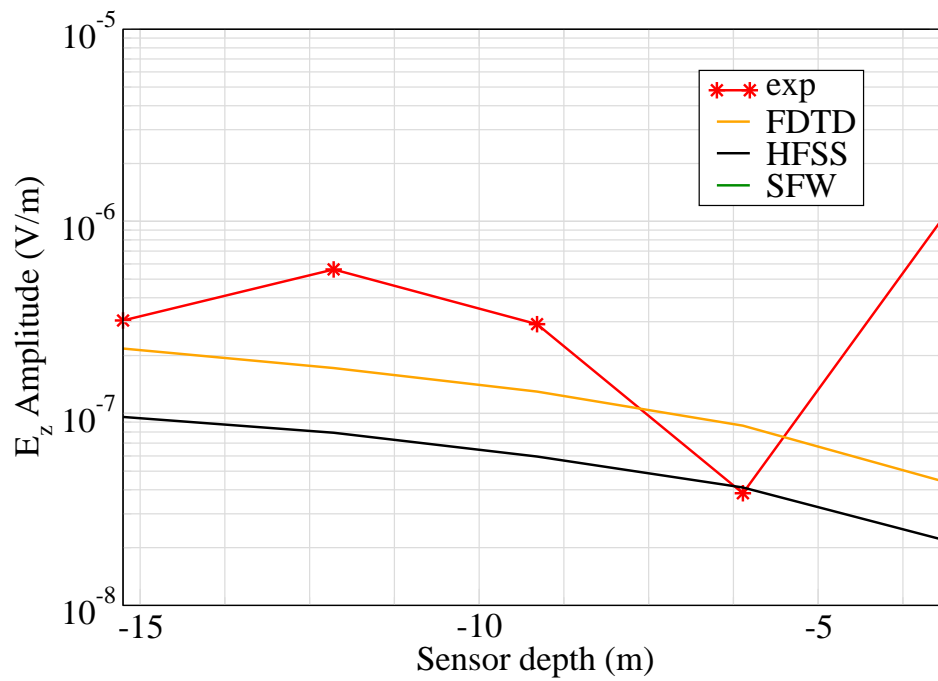


Figure 5: E_z .

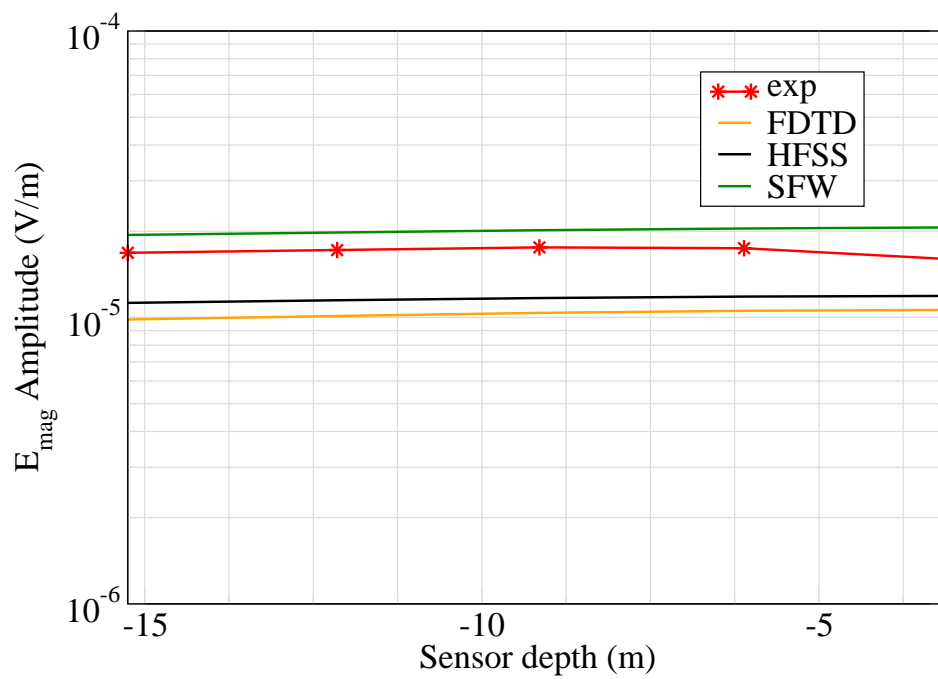


Figure 6: E_{mag} .

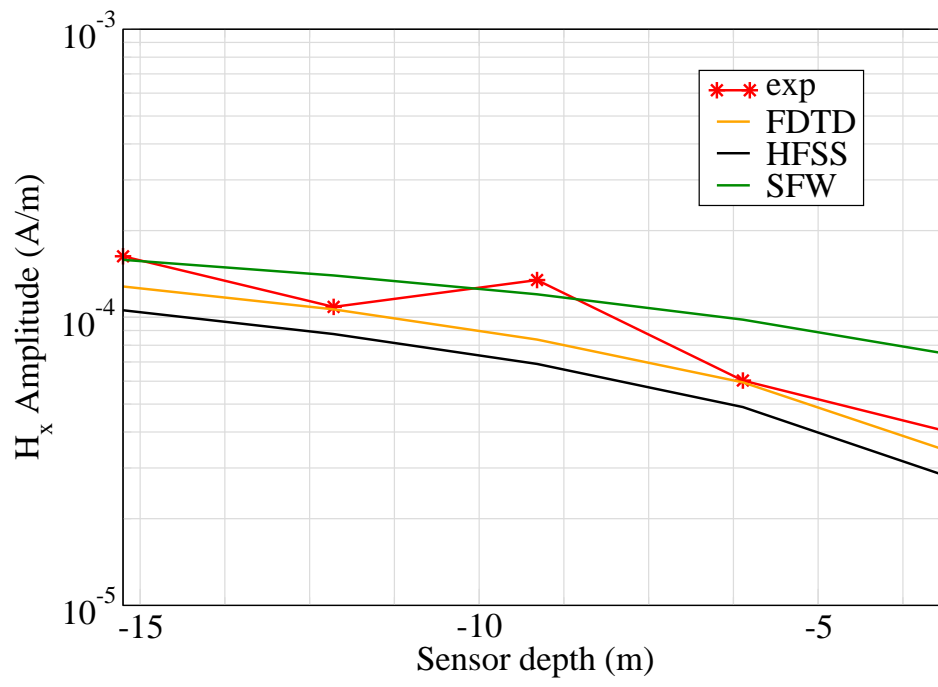


Figure 7: H_x .

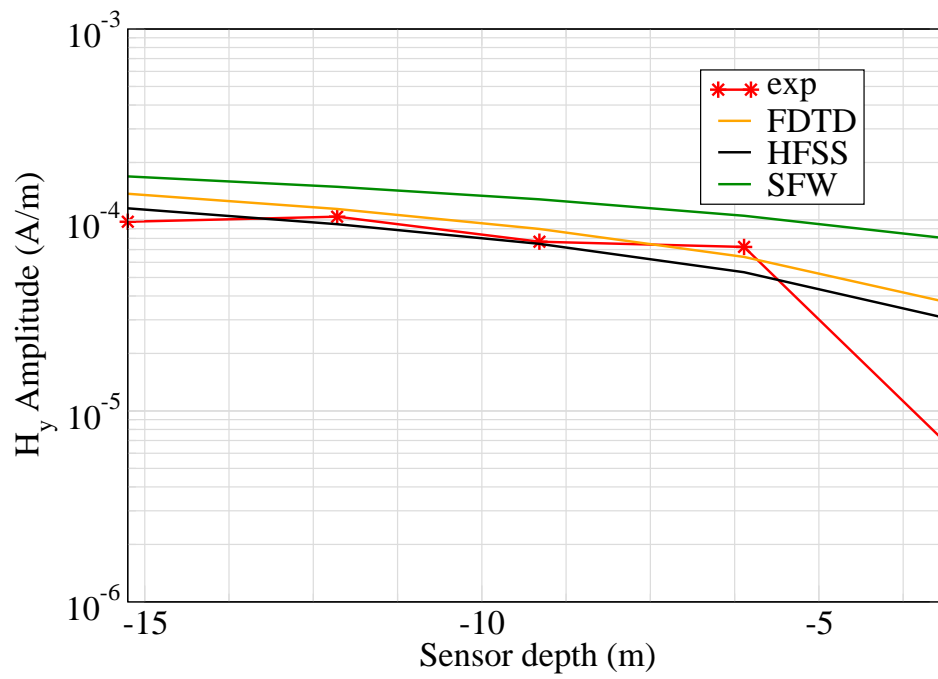


Figure 8: H_y .

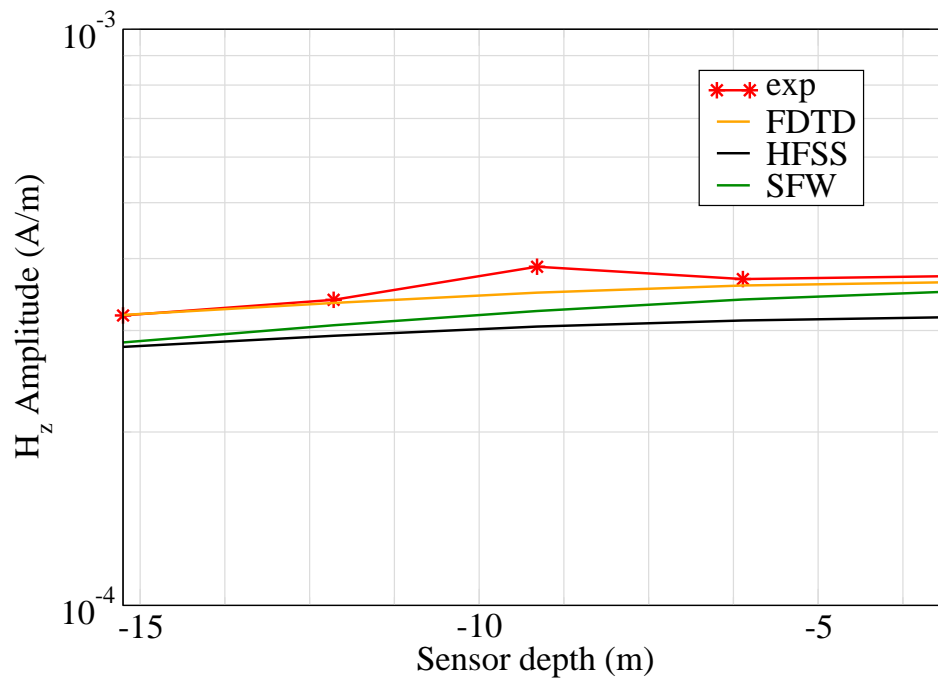


Figure 9: H_z .

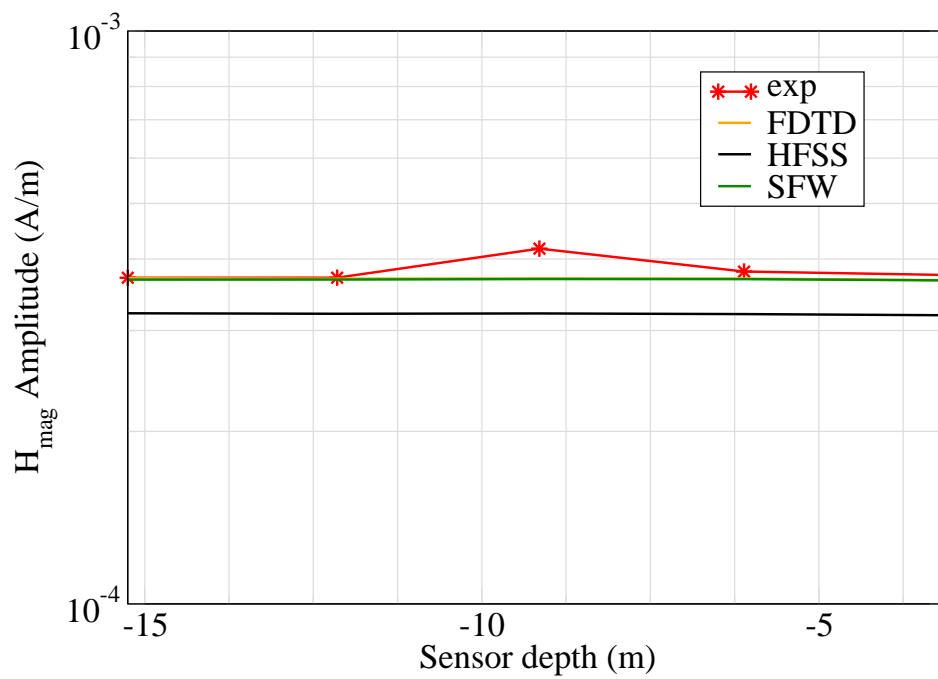


Figure 10: H_{mag} .

Experiment 4

Runs 101.02, 101.04, 101.06, 101.08 and 101.12

Experiment Date: 9/14/2010

1 Discussion

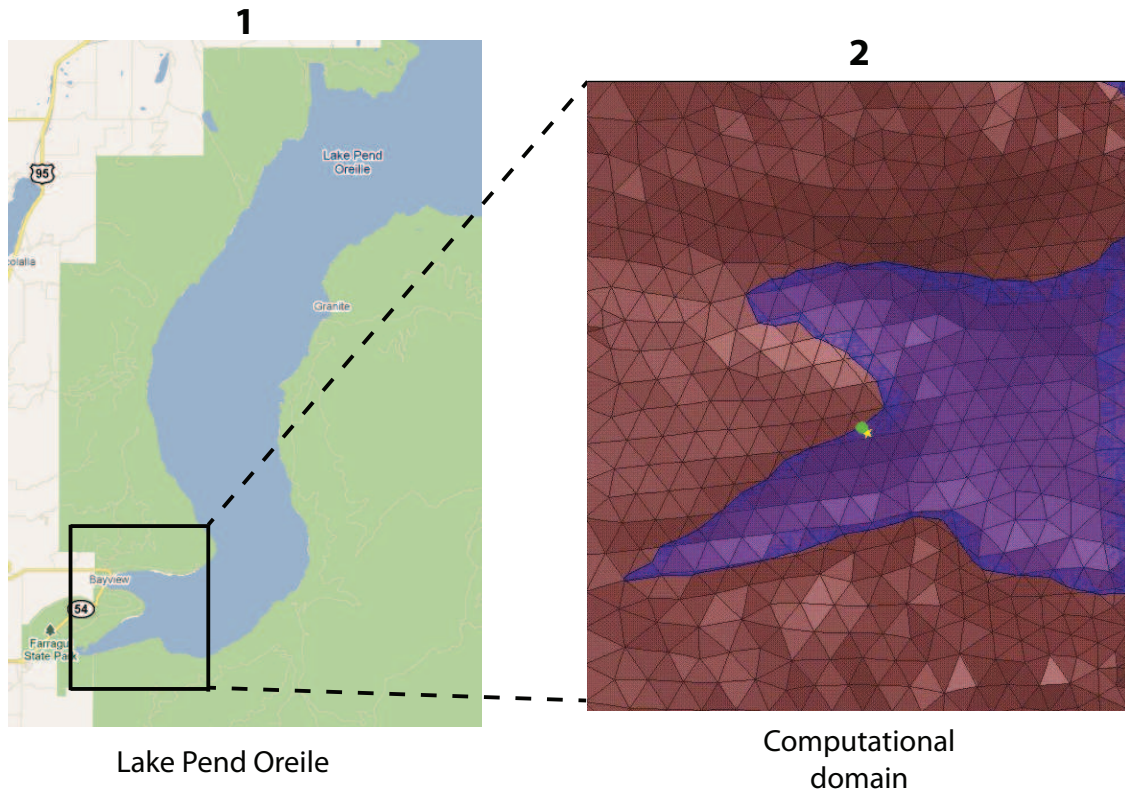


Figure 1: Sensor and source locations; see test report. Sensor is represented by the yellow star; source start and end points represented by green circle and red square.

Source Parameters

- Source Type: HMD (Coil: 3.66 m by 3.66 m with 12 turns).
- Source Strength: 3,683 A-m².
- $f = 1000$ Hz.

Environment

- Air: $\sigma = 0$ S/m and $\epsilon_r = 1$
- Water: $\sigma = 0.01$ S/m and $\epsilon_r = 81$
- Mud: $\sigma = 0.0012$ S/m and $\epsilon_r = 1$

Table 1: Simulation Details

	FDTD	HFSS	QES/SFW
Domain Size	400 X 400 X 120 cells	42,842 tets	N/A
Cell Size (m)	5 X 5 X 5	N/A	N/A
Time Step (ns)	9.6	N/A	N/A
Run Time (Hrs)	41.6	0.38	0.01
Water Depth (m)	N/A	N/A	18
Effective Source Area (m)	N/A	l = 3.66 w = 3.66	r = 3.66

Comments

- To implement reciprocity, three simulations per vector field are required for a total of six simulations. Run times correspond to the time required to conduct all six simulations.
- Computational time is based on actual elapsed real time. This number is highly subjective and based on how many other applications might be running at a particular time. However, the reported number is an indication of the amount of time typically needed for a particular simulation. The computer specs are: 16 CPU cores at 2.8 GHz.
- Run times for HFSS are given for a single frequency.
- QES is not applicable for electric or magnetic fields using magnetic source excitation.

2 Simulation Variables

Sensor_P1(x,y,z) [m]	(3227.3149,3496.6303,-3.4423)
Sensor_P2(x,y,z) [m]	(3227.3440,3496.6300,-15.0648)
Source_P1(x,y,z) [m]	(3163.7271,3561.9316,0)
Source_P2(x,y,z) [m]	(3163.7271,3561.9316,0)
Source_Plate_Separation [m]	N/A
Source_Size [m X m X #]	[3.658 X 3.658 X 12]
Source_Heading [deg]	0
Source_Voltage [V Peak]	11.6294
Source_Current [A Peak]	22.9361
Source_Frequency [Hz]	1000

--- Extra Information ---

Source_Heading_Bounds [deg]	(N/A)
Average_Boat_Speed [m/s]	NaN
Source_Type	Magnetic source (portable)
Sensor_Type	PEMA
Bin_Size [sec]	[317,486,385,484,481]
Number_of_Datapoints	5
Lake_Origin (Easting,Northing)	(737736.502,696691.143)
Analysis_Date	Exp4_ScenSB_28-Jul-2011

3 Source and sensor locations

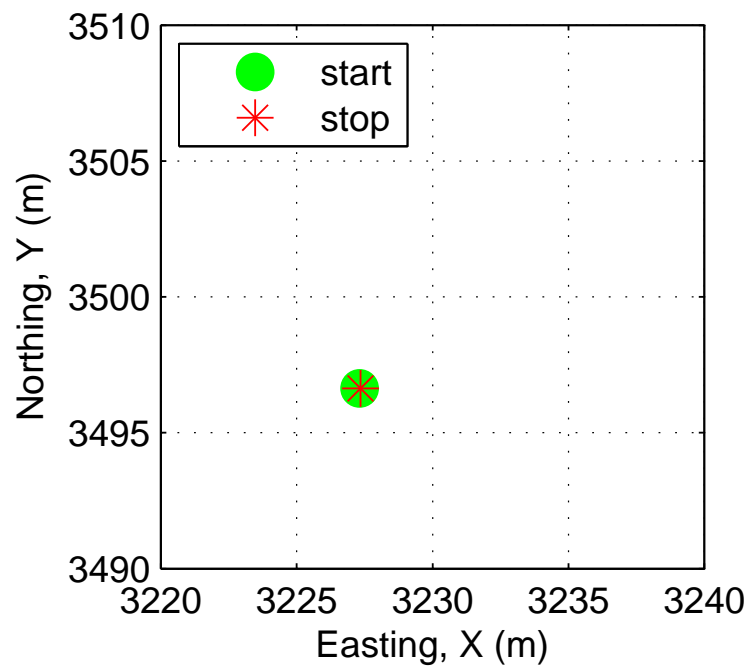
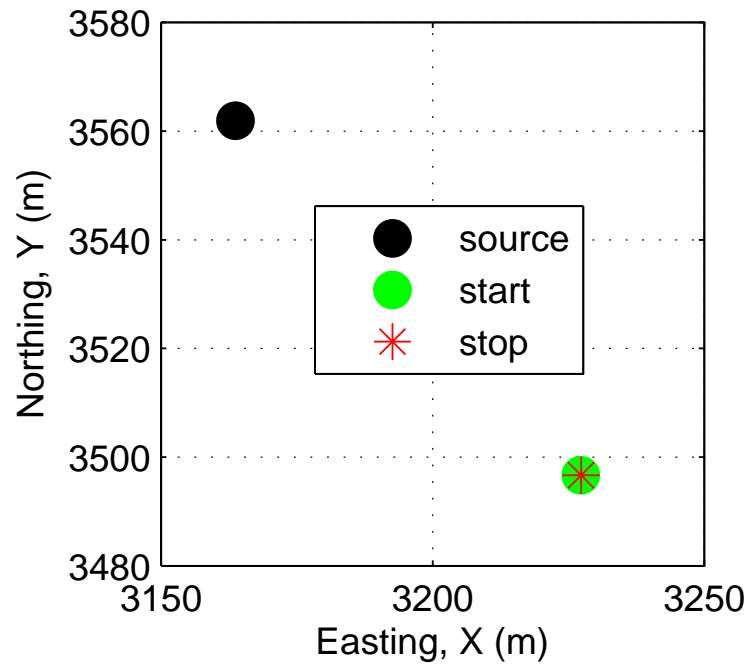


Figure 2: Source and sensor relationship.

4 Plots

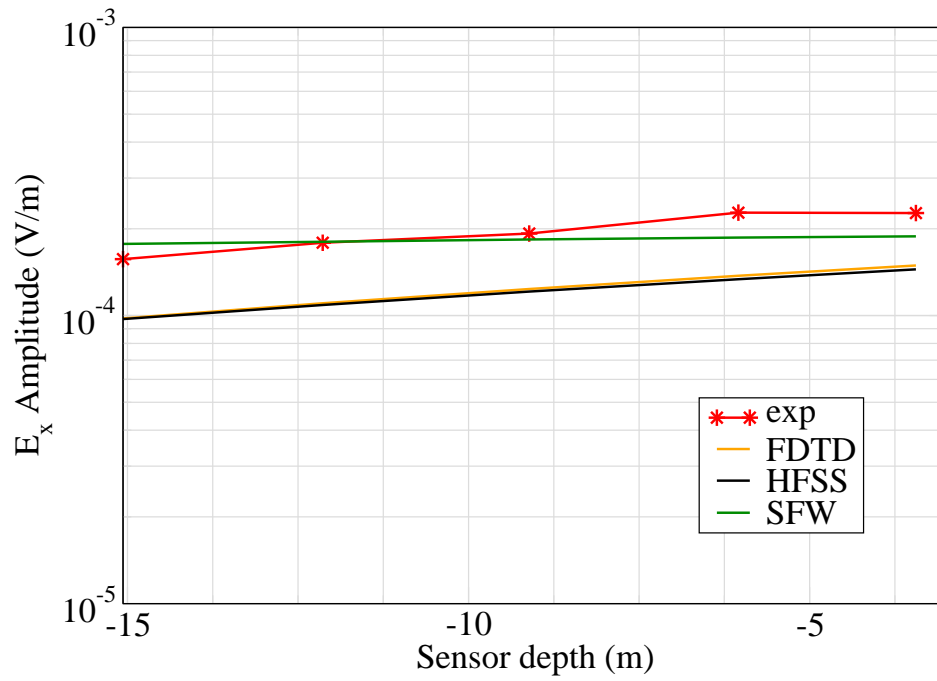


Figure 3: E_x .

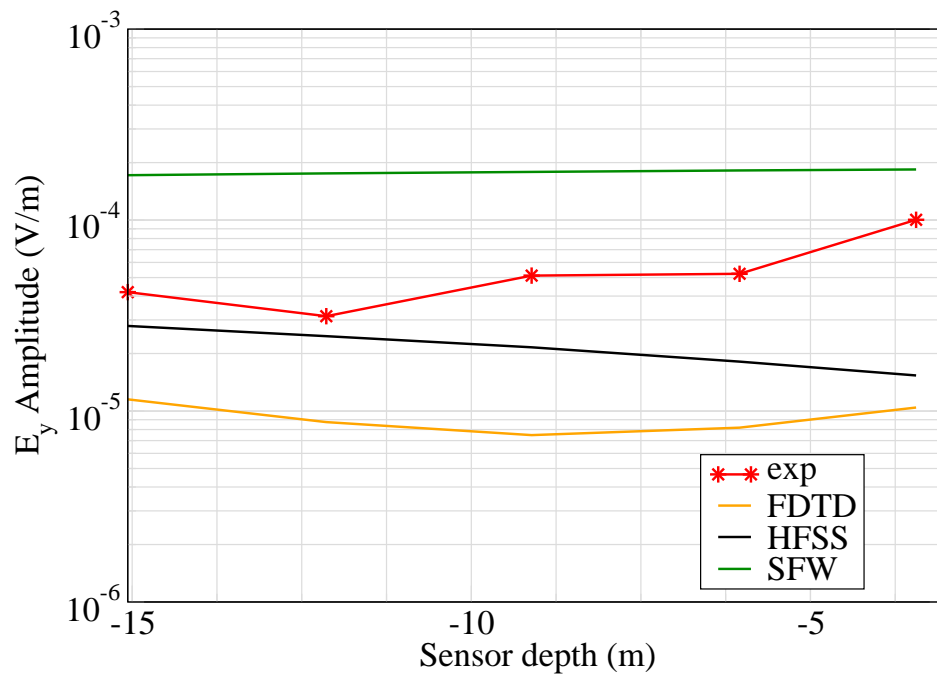


Figure 4: E_y .

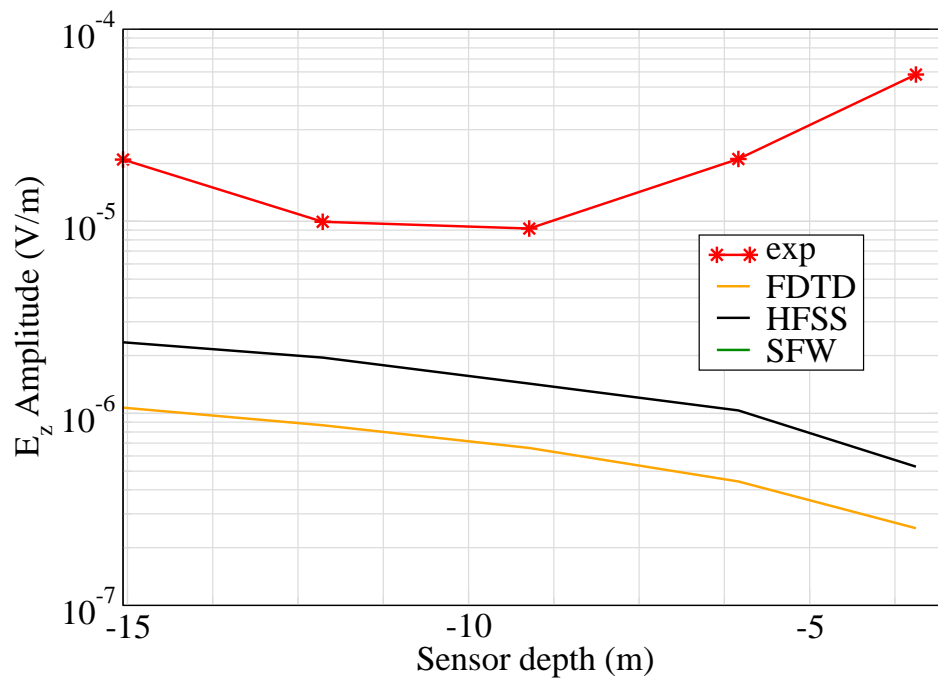


Figure 5: E_z .

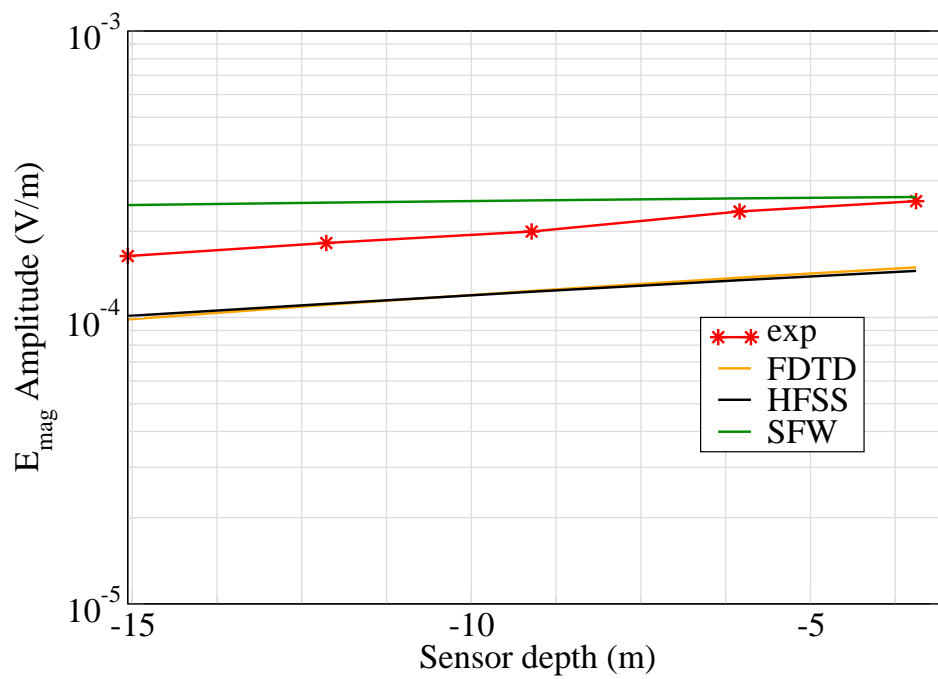


Figure 6: E_{mag} .

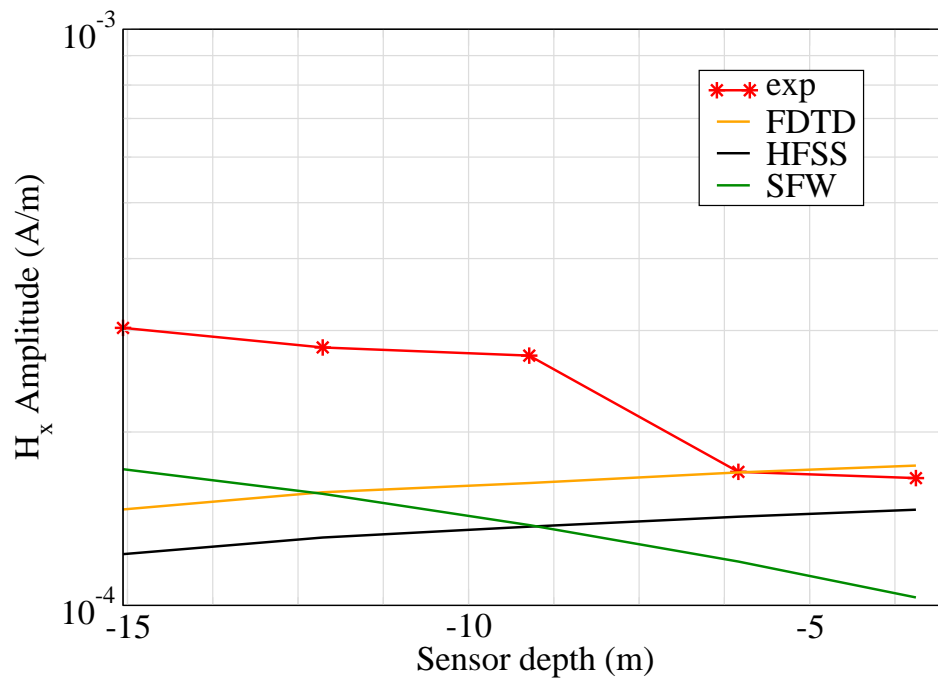


Figure 7: H_x .

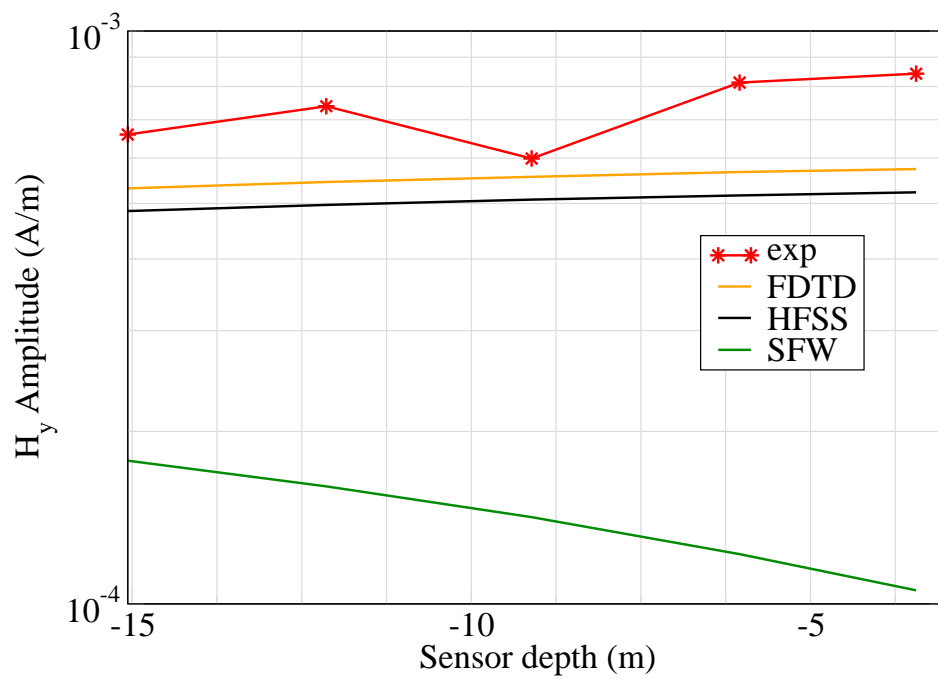


Figure 8: H_y .

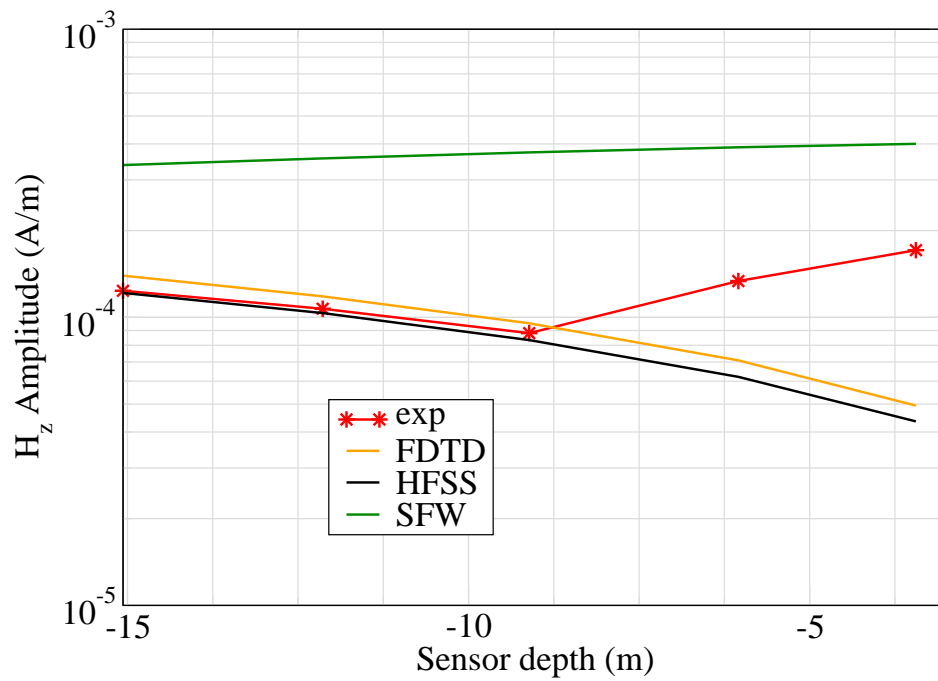


Figure 9: H_z .

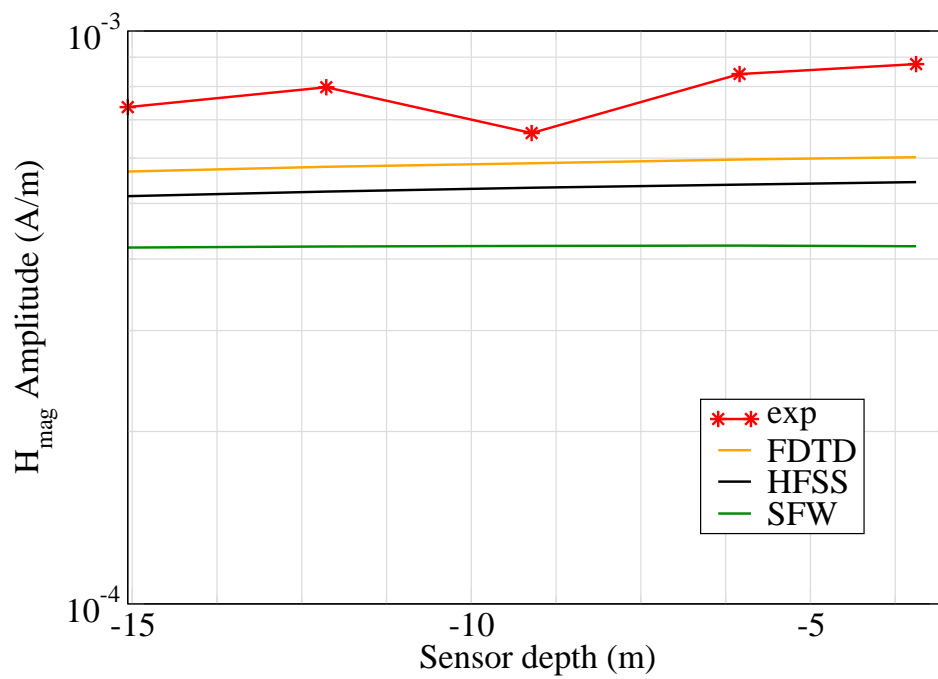


Figure 10: H_{mag} .

Experiment 4

Runs 303.01

Experiment Date: 9/14/2010

1 Discussion

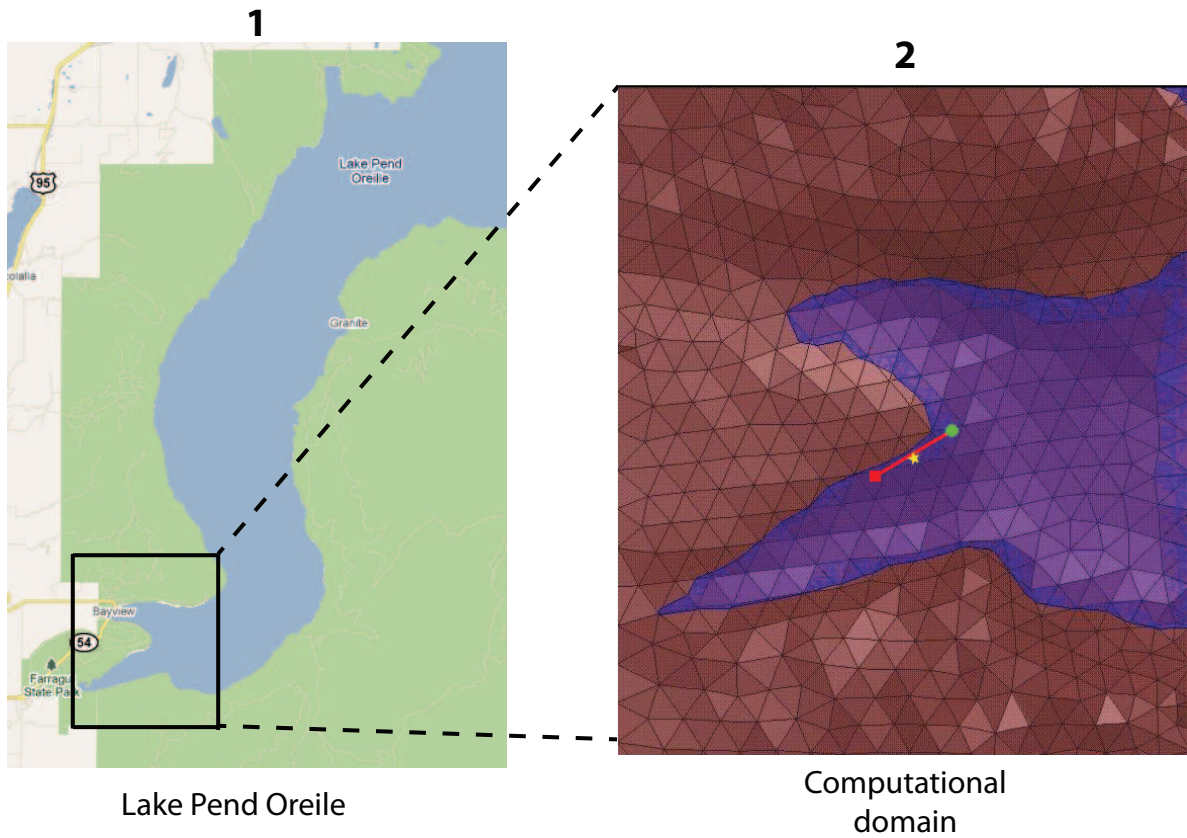


Figure 1: Sensor and source locations; see test report. Sensor is represented by the yellow star; source start and end points represented by green circle and red square.

Source Parameters

- Source Type: HED (Boat Hull: plates 0.61 m by 0.305 m separated by 4 m).
- Source Strength: 11.45 A-m.

- $f = 10$ Hz.

Environment

- Air: $\sigma = 0$ S/m and $\epsilon_r = 1$
- Water: $\sigma = 0.01$ S/m and $\epsilon_r = 81$
- Mud: $\sigma = 0.0012$ S/m and $\epsilon_r = 1$

Table 1: Simulation Details

	FDTD	HFSS	QES/SFW
Domain Size	200 X 200 X 120 cells	150,601 tets	N/A
Cell Size (m)	10 X 10 X 5	N/A	N/A
Time Step (ns)	13.6	N/A	N/A
Run Time (Hrs)	41	5.9	0.01
Water Depth (m)	N/A	N/A	50
Effective Source Area (m)	N/A	$l = 0.61$ $w = 0.61$	$r = 0.058$

Comments

- To implement reciprocity, three simulations per vector field are required for a total of six simulations. Run times correspond to the time required to conduct all six simulations.
- Computational time is based on actual elapsed real time. This number is highly subjective and based on how many other applications might be running at a particular time. However, the reported number is an indication of the amount of time typically needed for a particular simulation. The computer specs are: 16 CPU cores at 2.8 GHz.
- Run times for HFSS are given for a single frequency.
- QES is not applicable for magnetic fields using electric source excitation.

2 Simulation Variables

Sensor_P1(x,y,z) [m]	(3227.8273,3496.9224,-15.0274)
Sensor_P2(x,y,z) [m]	(3227.146,3503.0099,-15.0274)
Source_P1(x,y,z) [m]	(3637.7133,3813.5575,0)
Source_P2(x,y,z) [m]	(2809.4904,3311.0364,0)
Source_Plate_Separation [m]	4
Source_Size [m X m X #]	[0.610 X 0.305 X 1]
Source_Heading [deg]	209.8543
Source_Voltage [V Peak]	338.186
Source_Current [A Peak]	2.8631
Source_Frequency [Hz]	10

--- Extra Information ---

Source_Heading_Bounds [deg]	(N/A)
Average_Boat_Speed [m/s]	1.0812
Source_Type	Electric boat hull (boat hull)
Sensor_Type	PEMA
Bin_Size [sec]	1
Number_of_Datapoints	896
Lake_Origin (Easting,Northing)	(737736.502,696691.143)
Analysis_Date	Exp4_ScenSF_28-Jul-2011

3 Boat Path

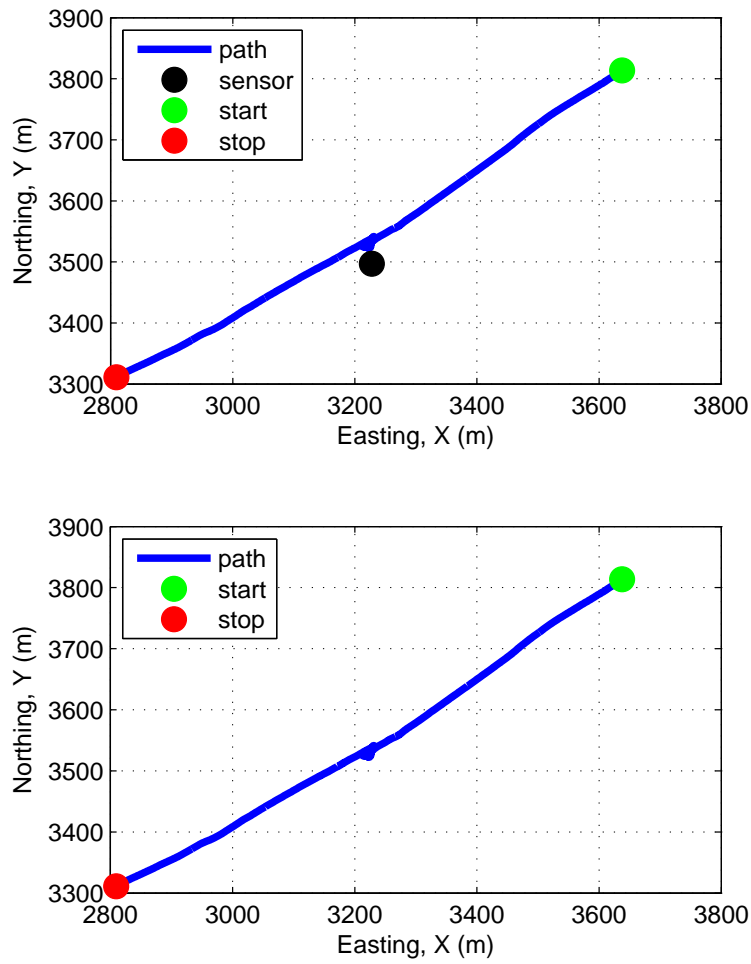


Figure 2: Source and sensor relationship.

4 Plots

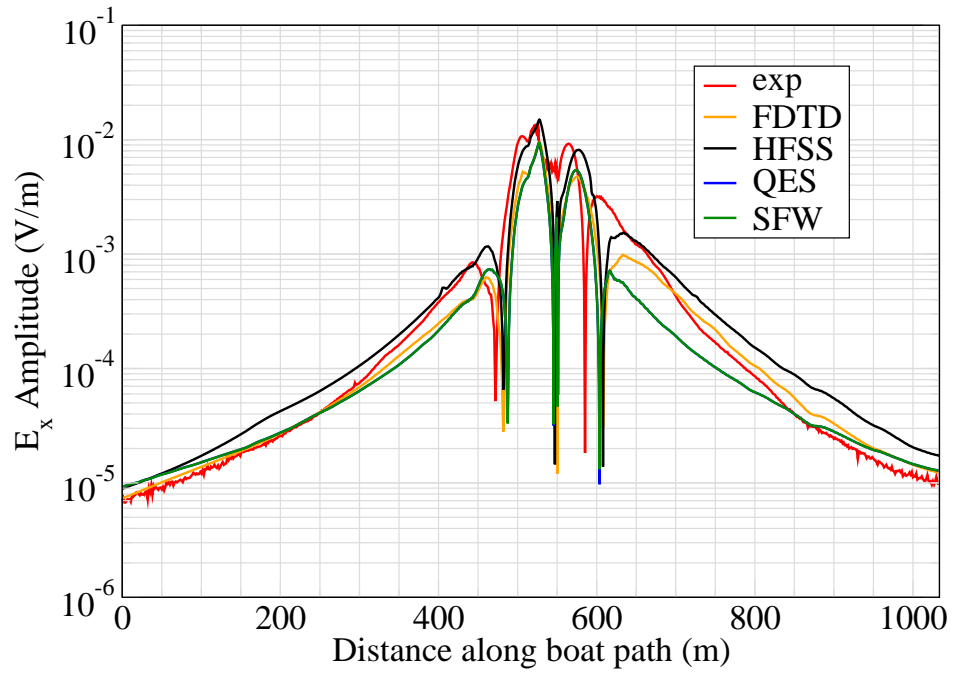


Figure 3: E_x .

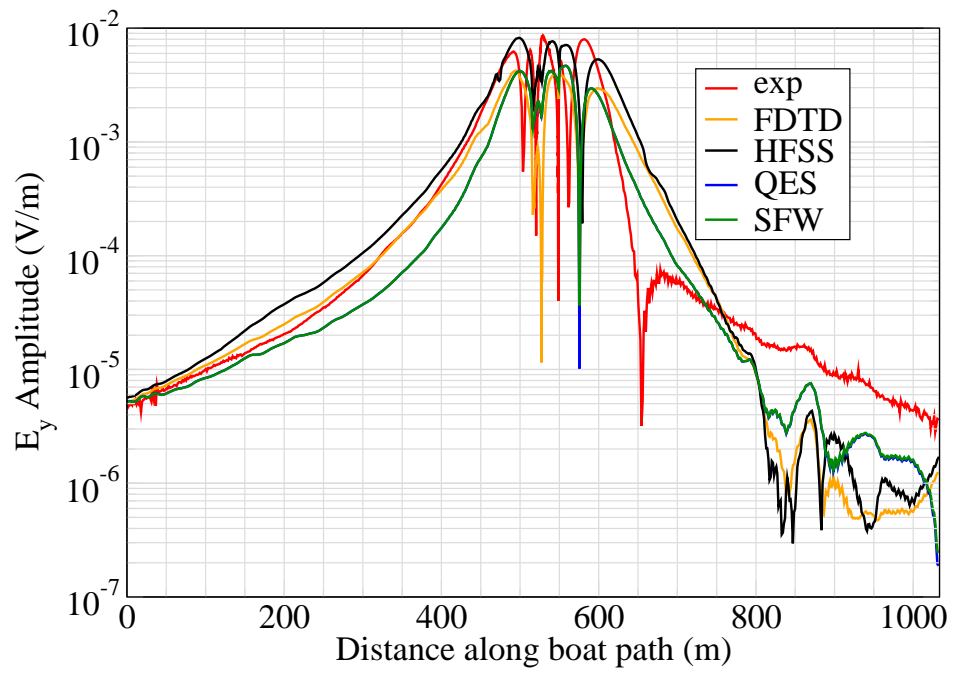


Figure 4: E_y .

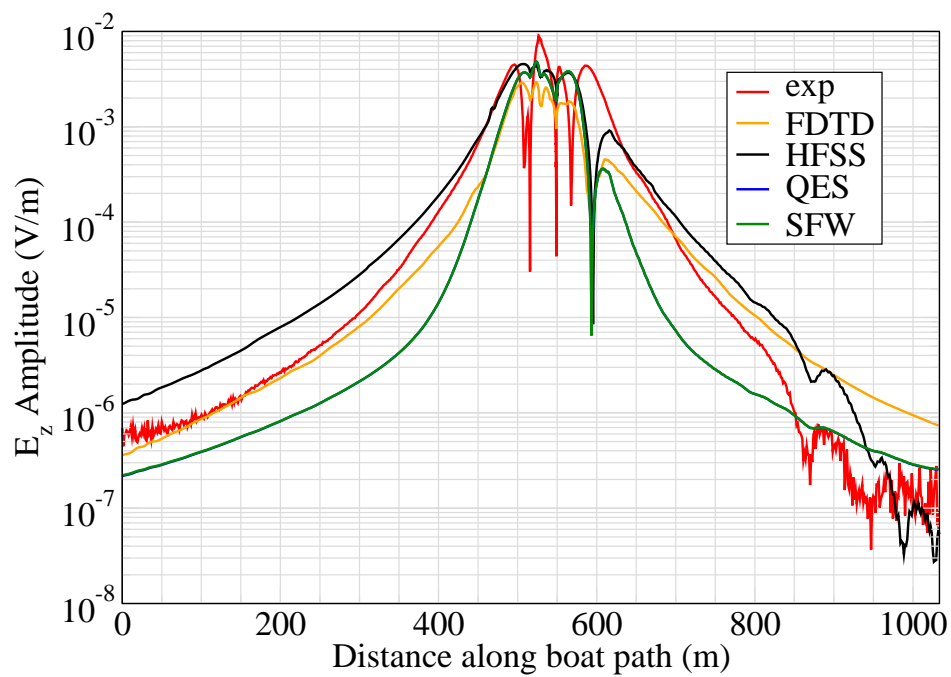


Figure 5: E_z .

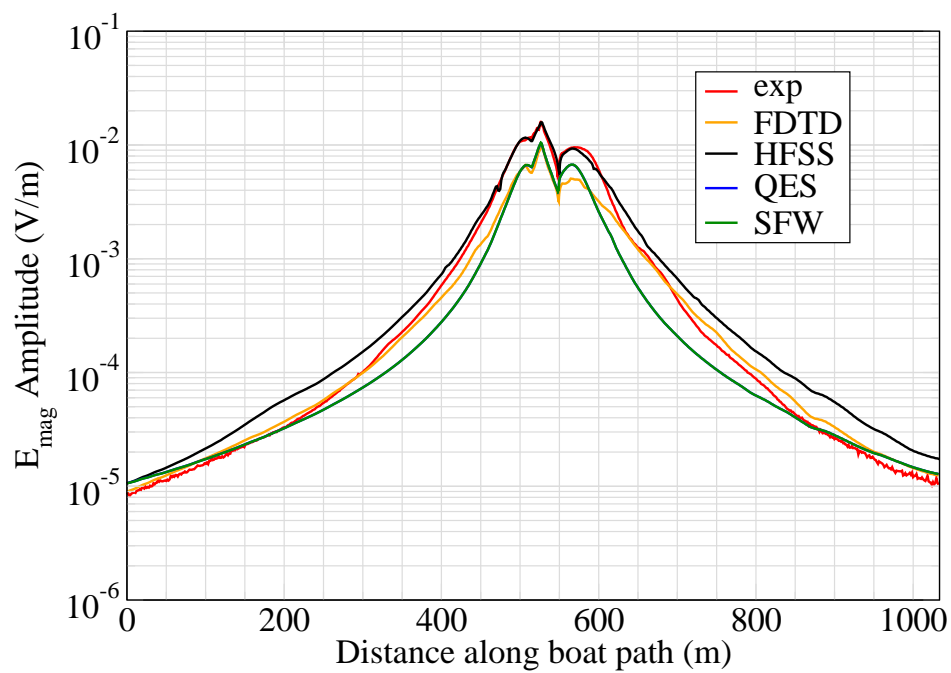


Figure 6: E_{mag} .

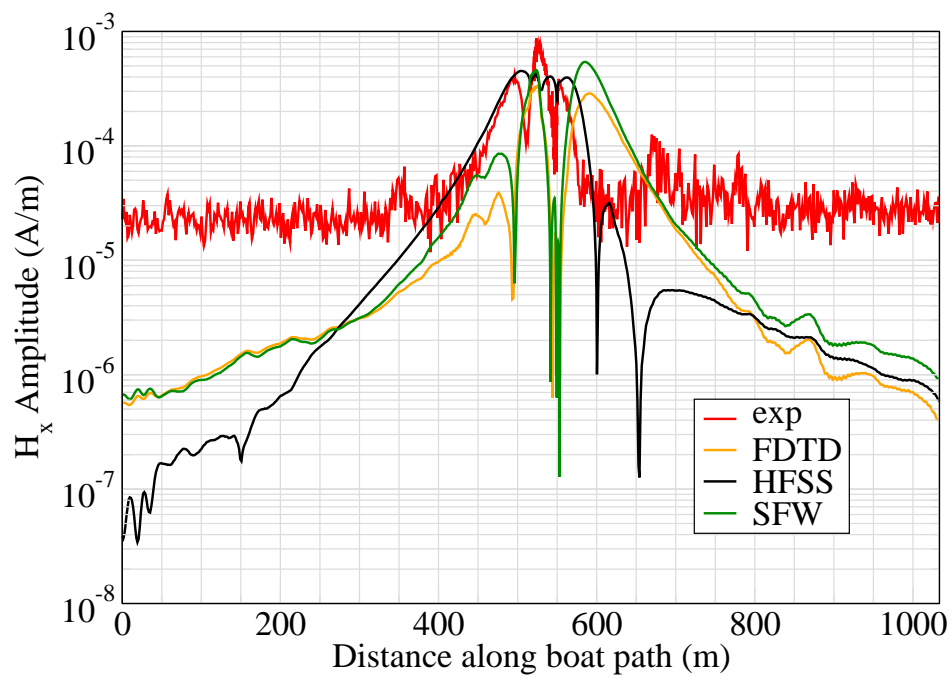


Figure 7: H_x .

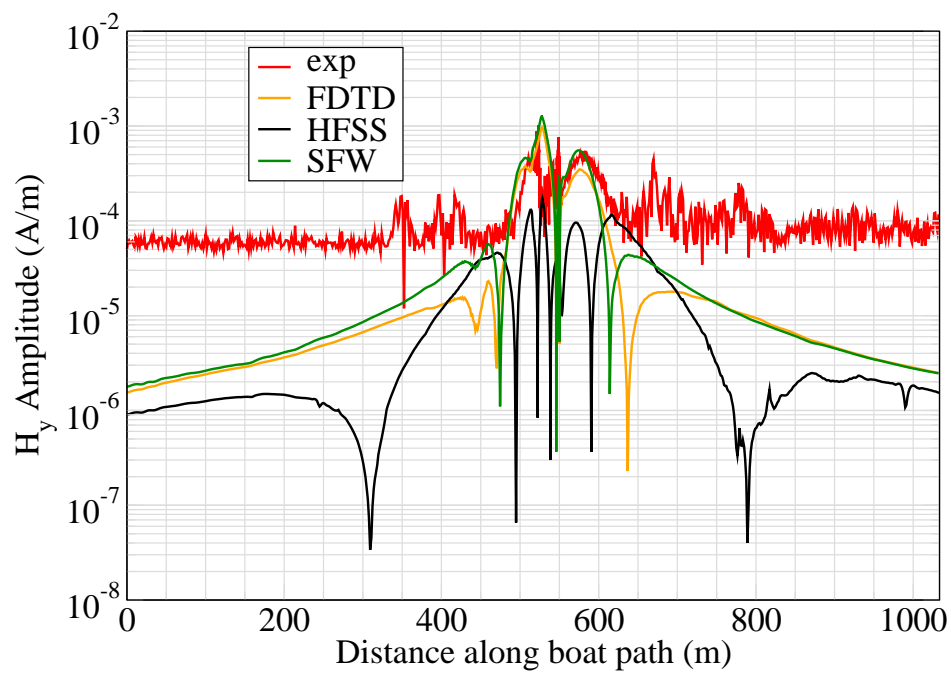


Figure 8: H_y .

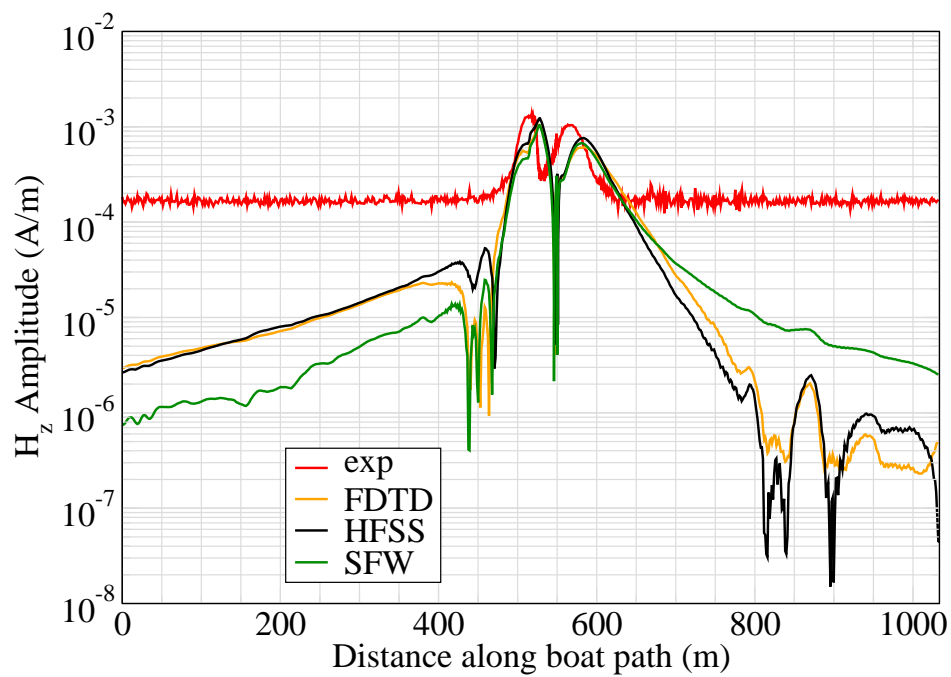


Figure 9: H_z .

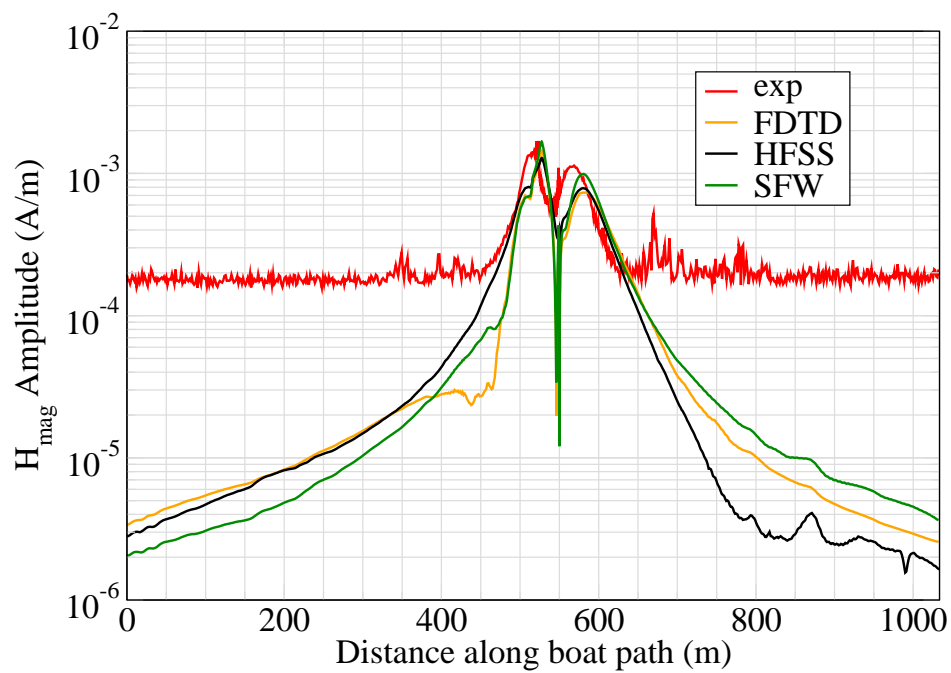


Figure 10: H_{mag} .

Experiment 4

Runs 303.02

Experiment Date: 9/14/2010

1 Discussion

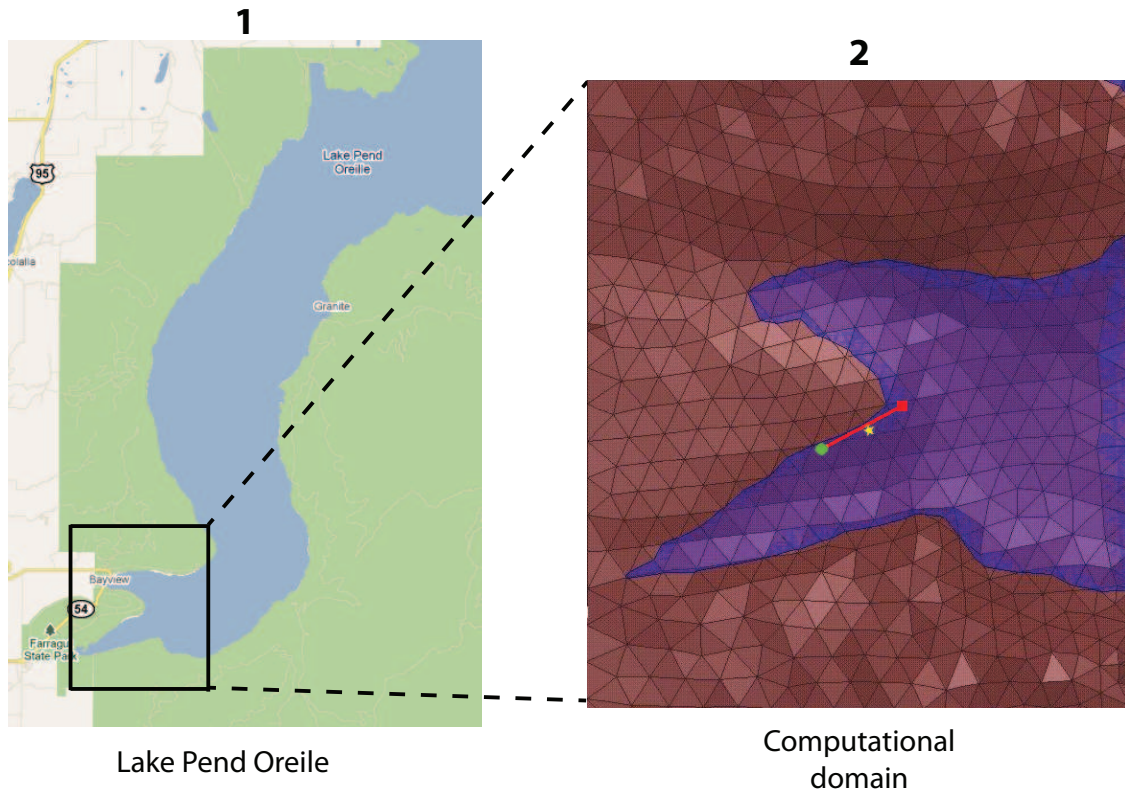


Figure 1: Sensor and source locations; see test report. Sensor is represented by the yellow star; source start and end points represented by green circle and red square.

Source Parameters

- Source Type: HED (Boat Hull: plates 0.61 m by 0.305 m separated by 4 m).
- Source Strength: 11.33 A-m.
- $f = 100$ Hz.

Environment

- Air: $\sigma = 0$ S/m and $\epsilon_r = 1$
- Water: $\sigma = 0.01$ S/m and $\epsilon_r = 81$
- Mud: $\sigma = 0.0012$ S/m and $\epsilon_r = 1$

Table 1: Simulation Details

	FDTD	HFSS	QES/SFW
Domain Size	200 X 200 X 120 cells	122,349 tets	N/A
Cell Size (m)	10 X 10 X 5	N/A	N/A
Time Step (ns)	13.6	N/A	N/A
Run Time (Hrs)	36.8	1.7	0.01
Water Depth (m)	N/A	N/A	50
Effective Source Area (m)	N/A	$l = 0.61$ $w = 0.61$	$r = 0.058$

Comments

- To implement reciprocity, three simulations per vector field are required for a total of six simulations. Run times correspond to the time required to conduct all six simulations.
- Computational time is based on actual elapsed real time. This number is highly subjective and based on how many other applications might be running at a particular time. However, the reported number is an indication of the amount of time typically needed for a particular simulation. The computer specs are: 16 CPU cores at 2.8 GHz.
- Run times for HFSS are given for a single frequency.
- QES is not applicable for magnetic fields using electric source excitation.

2 Simulation Variables

Sensor_P1(x,y,z) [m]	(3227.2165,3496.5763,-15.1186)
Sensor_P2(x,y,z) [m]	(3227.1574,3496.6058,-15.1186)
Source_P1(x,y,z) [m]	(2683.9602,3290.6226,0)
Source_P2(x,y,z) [m]	(3597.5918,3776.3651,0)
Source_Plate_Separation [m]	4
Source_Size [m X m X #]	[0.610 X 0.305 X 1]
Source_Heading [deg]	27.9619
Source_Voltage [V Peak]	334.2295
Source_Current [A Peak]	2.8314
Source_Frequency [Hz]	100

--- Extra Information ---

Source_Heading_Bounds [deg]	(N/A)
Average_Boat_Speed [m/s]	1.2046
Source_Type	Electric boat hull (boat hull)
Sensor_Type	PEMA
Bin_Size [sec]	1
Number_of_Datapoints	859
Lake_Origin (Easting,Northing)	(737736.502,696691.143)
Analysis_Date	Exp4_ScenSG_28-Jul-2011

3 Boat Path

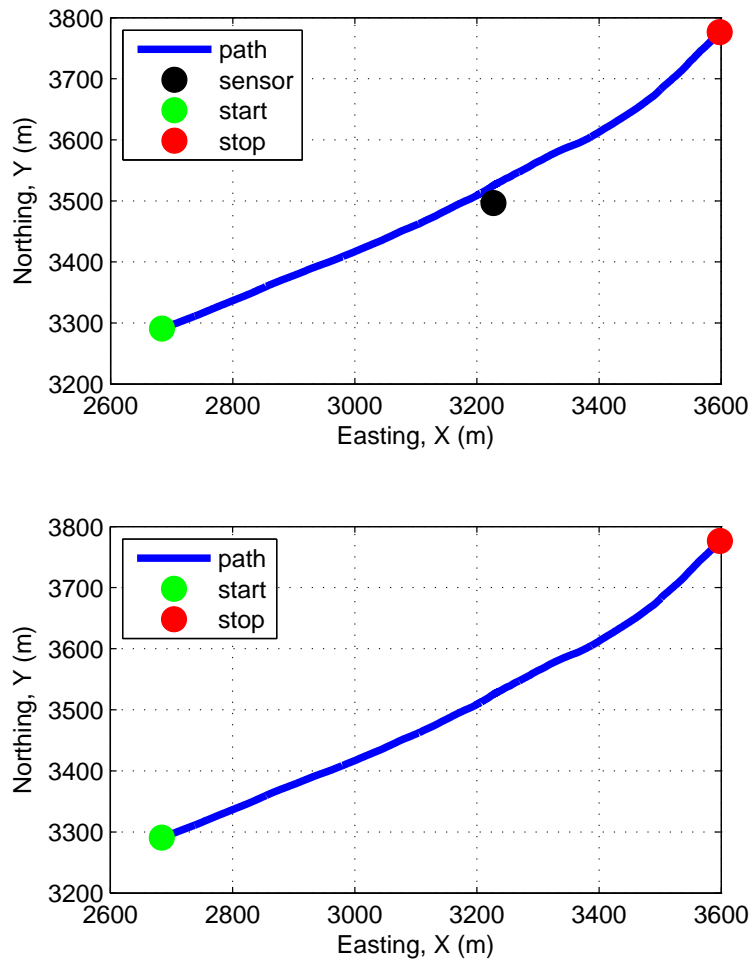


Figure 2: Source and sensor relationship.

4 Plots

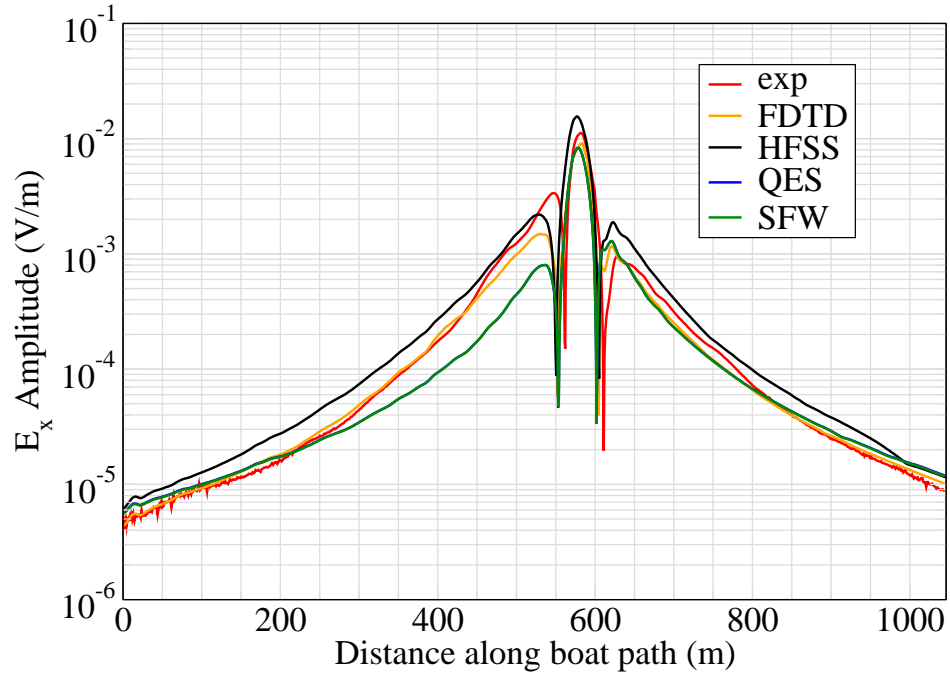


Figure 3: E_x .

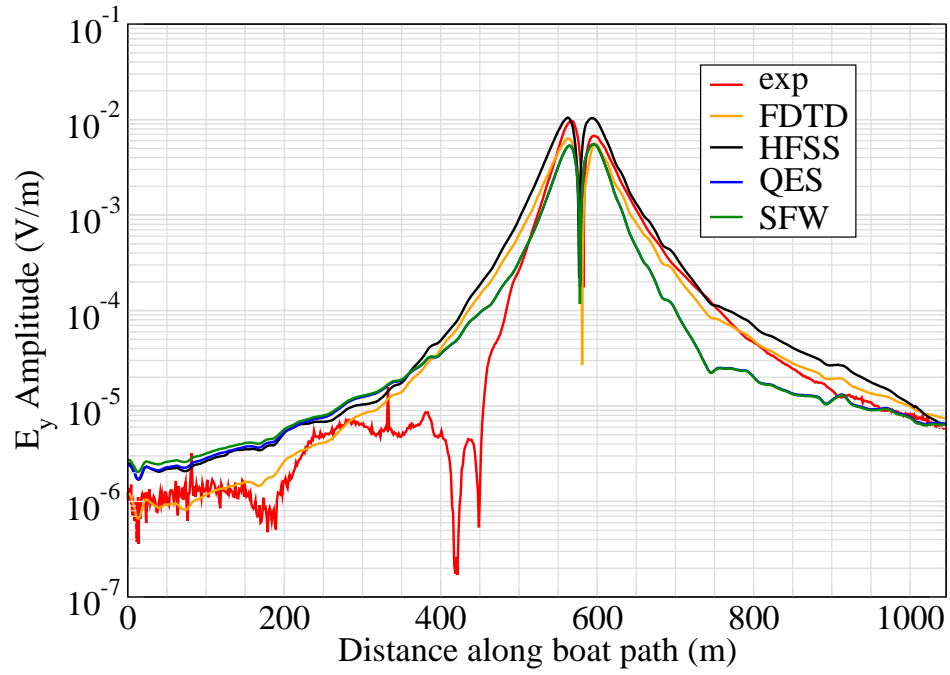


Figure 4: E_y .

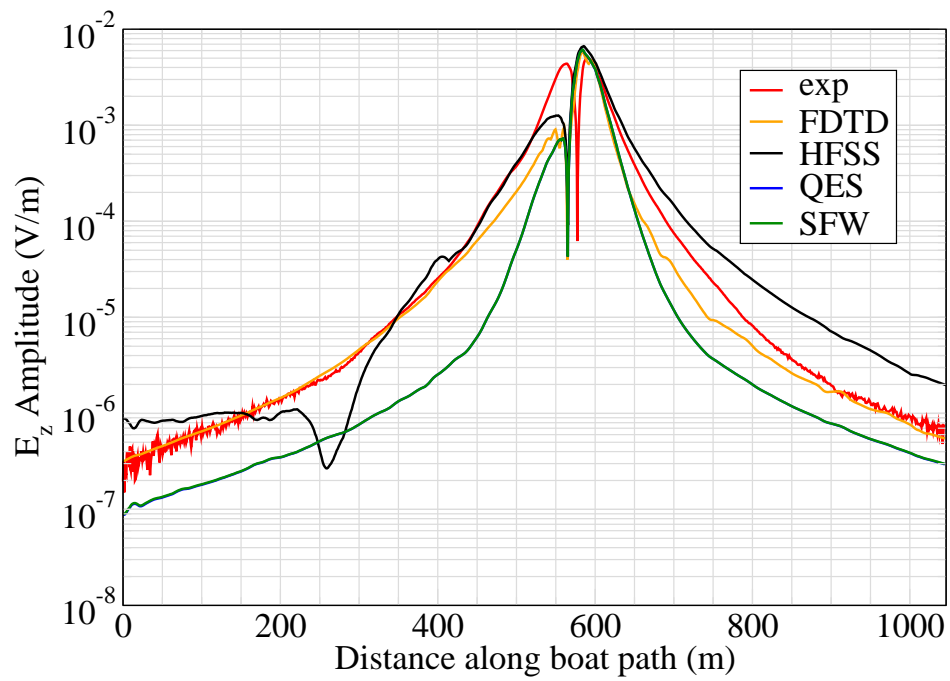


Figure 5: E_z .

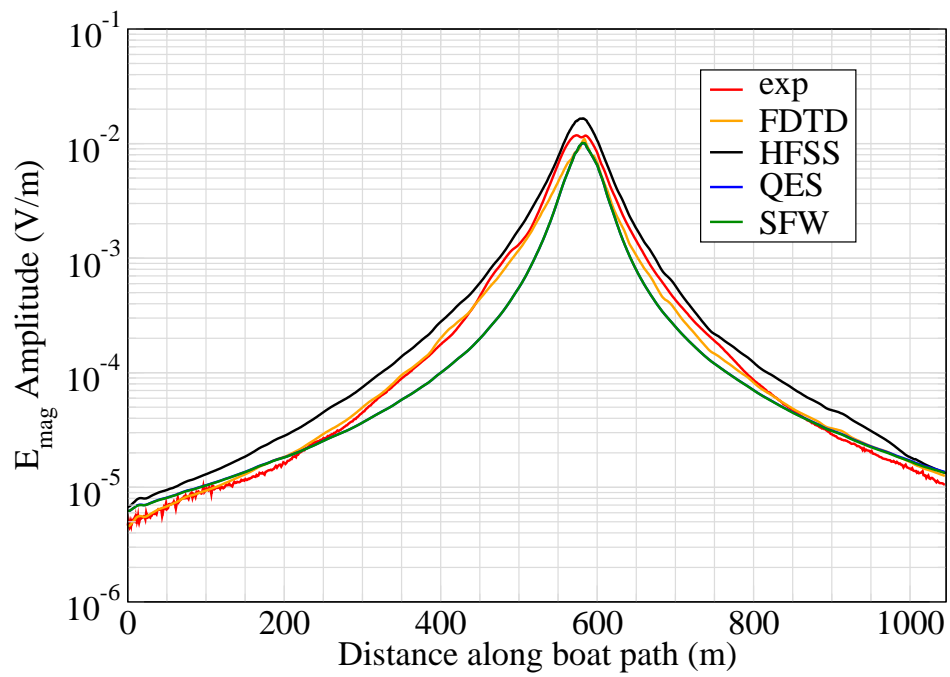


Figure 6: E_{mag} .

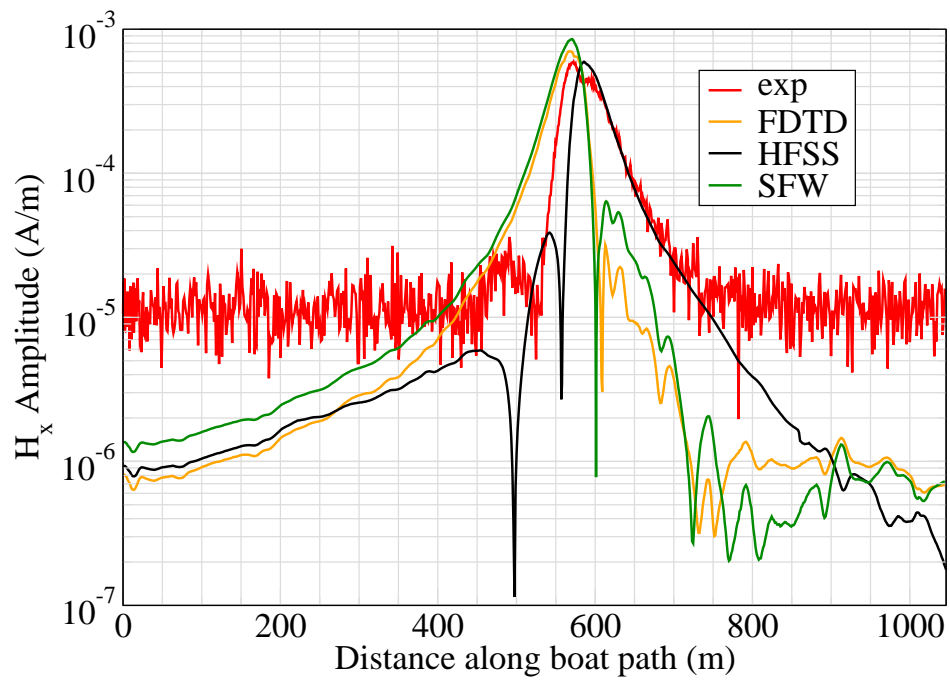


Figure 7: H_x .

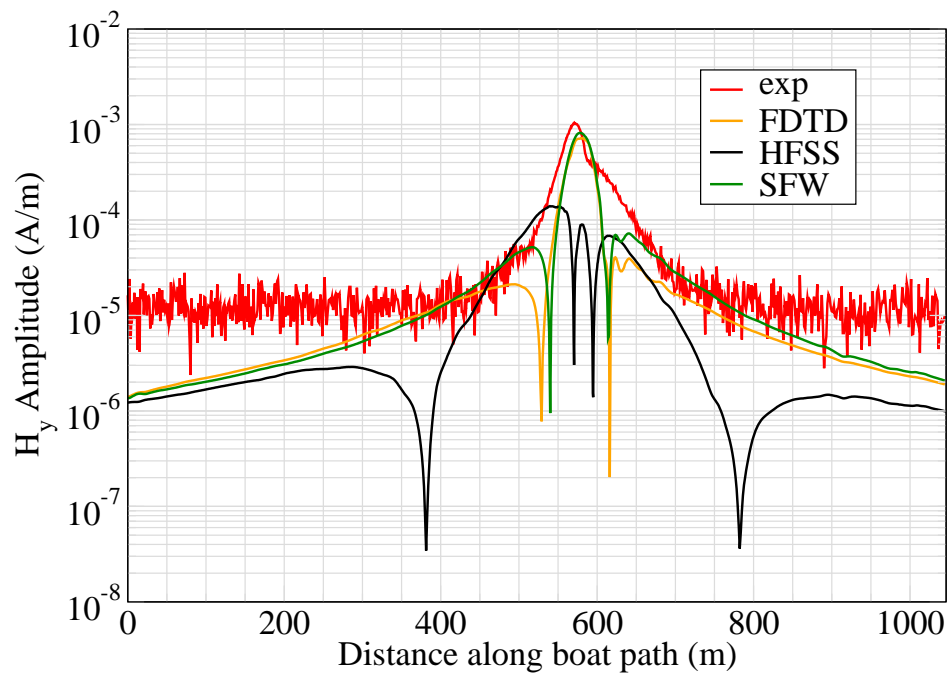


Figure 8: H_y .

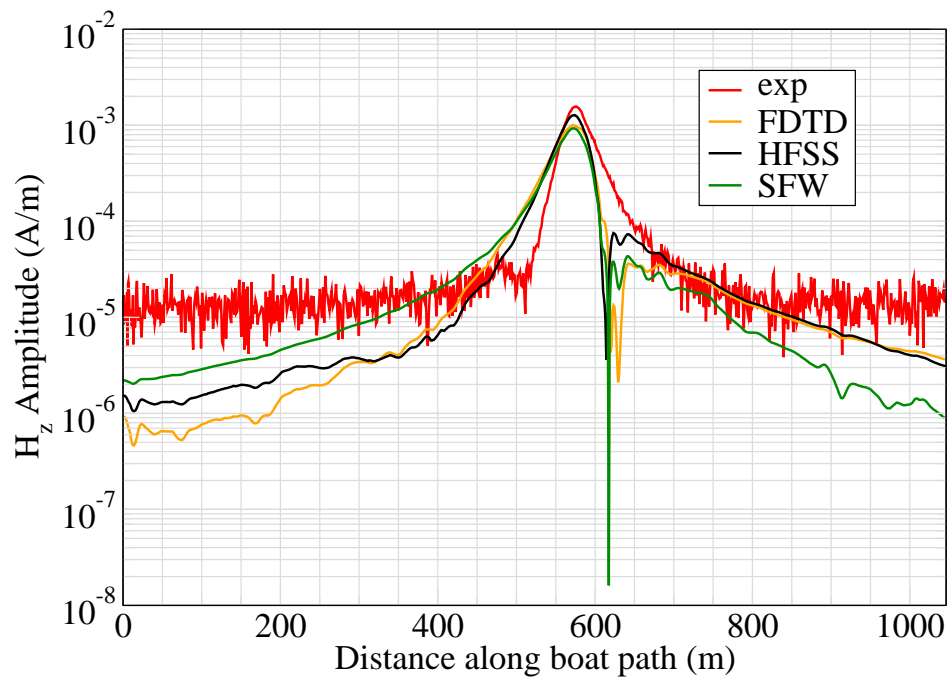


Figure 9: H_z .

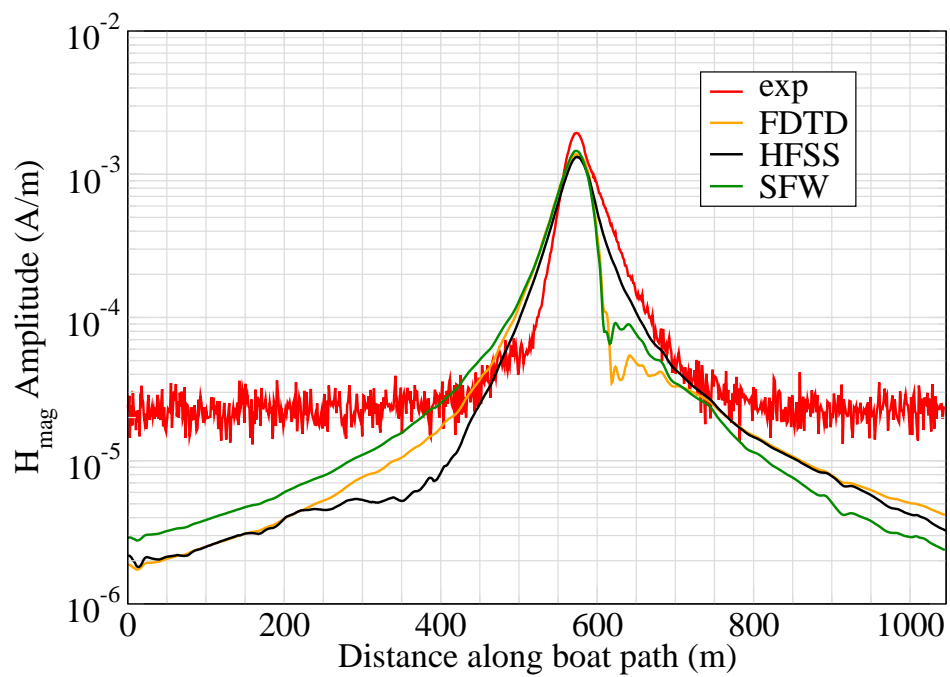


Figure 10: H_{mag} .

Experiment 4

Runs 303.03

Experiment Date: 9/14/2010

1 Discussion

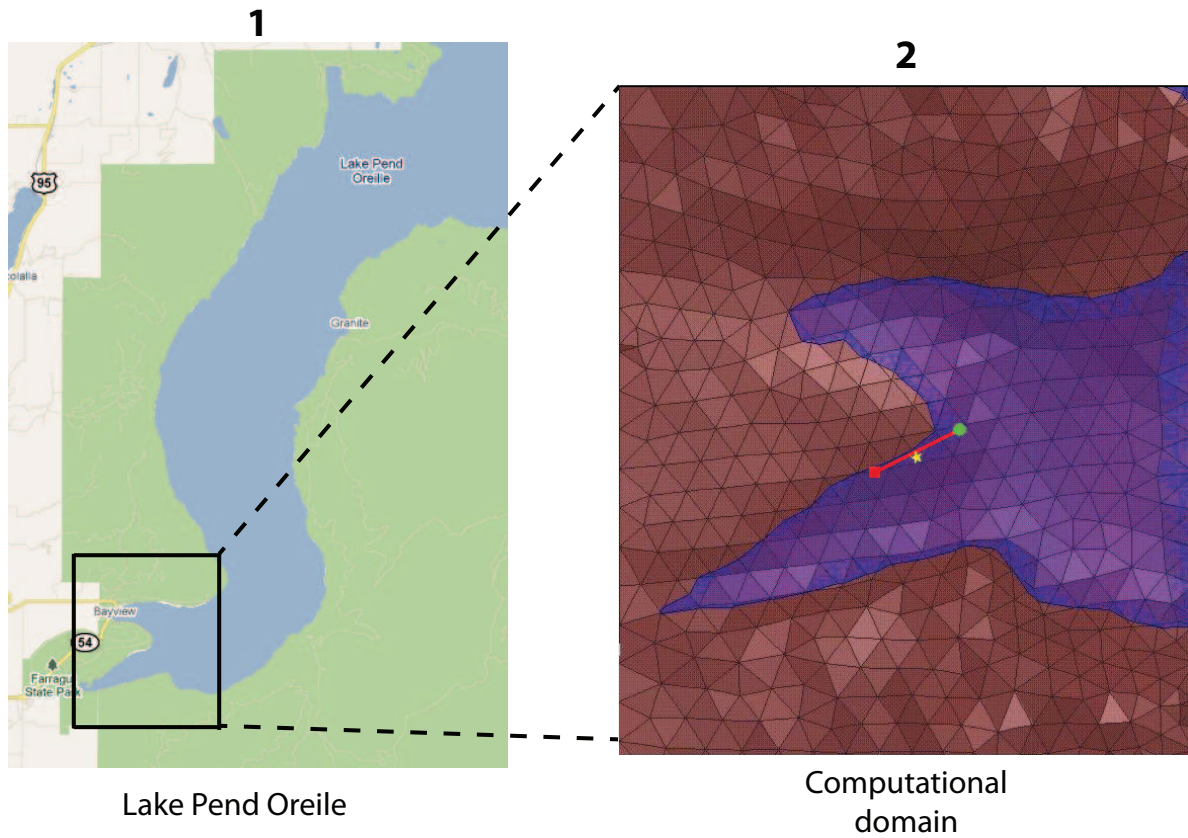


Figure 1: Sensor and source locations; see test report. Sensor is represented by the yellow star; source start and end points represented by green circle and red square.

Source Parameters

- Source Type: HED (Boat Hull: plates 0.61 m by 0.305 m separated by 4 m).
- Source Strength: 9.94 A-m.

- $f = 1000$ Hz.

Environment

- Air: $\sigma = 0$ S/m and $\epsilon_r = 1$
- Water: $\sigma = 0.01$ S/m and $\epsilon_r = 81$
- Mud: $\sigma = 0.0012$ S/m and $\epsilon_r = 1$

Table 1: Simulation Details

	FDTD	HFSS	QES/SFW
Domain Size	200 X 200 X 120 cells	143,176 tets	N/A
Cell Size (m)	10 X 10 X 5	N/A	N/A
Time Step (ns)	13.6	N/A	N/A
Run Time (Hrs)	36.8	2.23	0.01
Water Depth (m)	N/A	N/A	50
Effective Source Area (m)	N/A	$l = 0.61$ $w = 0.61$	$r = 0.058$

Comments

- To implement reciprocity, three simulations per vector field are required for a total of six simulations. Run times correspond to the time required to conduct all six simulations.
- Computational time is based on actual elapsed real time. This number is highly subjective and based on how many other applications might be running at a particular time. However, the reported number is an indication of the amount of time typically needed for a particular simulation. The computer specs are: 16 CPU cores at 2.8 GHz.
- Run times for HFSS are given for a single frequency.
- QES is not applicable for magnetic fields using electric source excitation.

2 Simulation Variables

Sensor_P1(x,y,z) [m]	(3227.1737,3496.7800,-15.1136)
Sensor_P2(x,y,z) [m]	(3227.3540,3496.8702,-15.1136)
Source_P1(x,y,z) [m]	(3697.5974,3808.104,0)
Source_P2(x,y,z) [m]	(2774.6131,3345.7356,0)
Source_Plate_Separation [m]	4
Source_Size [m X m X #]	[0.610 X 0.305 X 1]
Source_Heading [deg]	206.5494
Source_Voltage [V Peak]	297.453
Source_Current [A Peak]	2.4845
Source_Frequency [Hz]	1000

--- Extra Information ---

Source_Heading_Bounds [deg]	(N/A)
Average_Boat_Speed [m/s]	1.2202
Source_Type	Electric boat hull (boat hull)
Sensor_Type	PEMA
Bin_Size [sec]	1
Number_of_Datapoints	847
Lake_Origin (Easting,Northing)	(737736.502,696691.143)
Analysis_Date	Exp4_ScenSH_28-Jul-2011

3 Boat Path

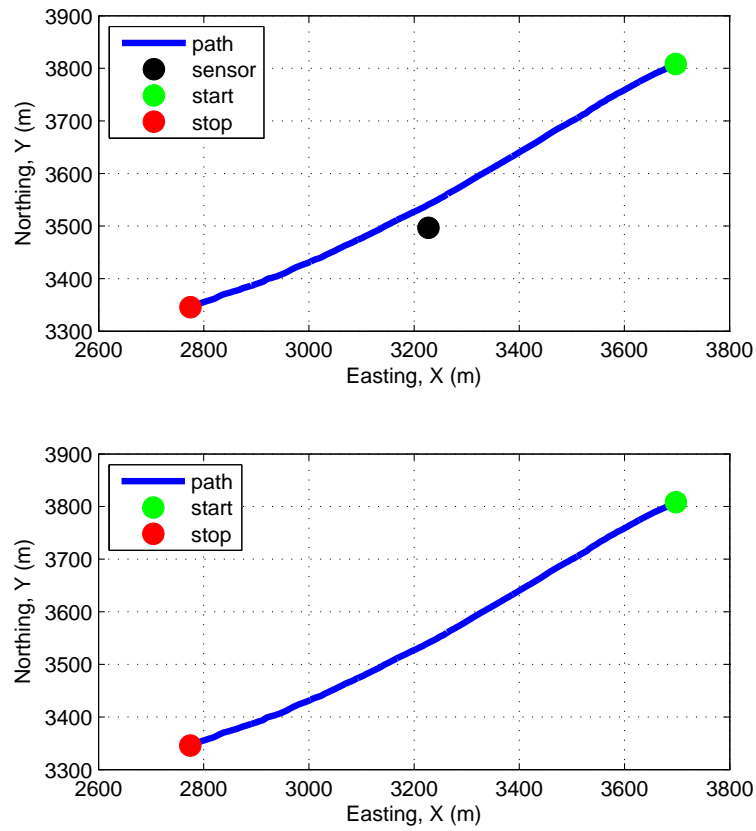


Figure 2: Source and sensor relationship.

4 Plots

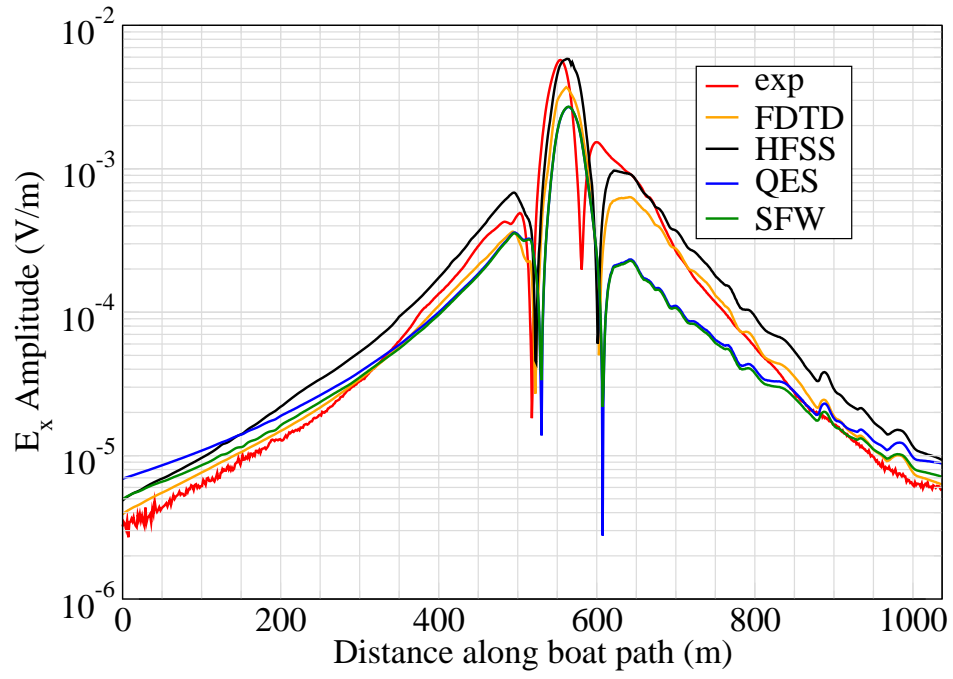


Figure 3: E_x .

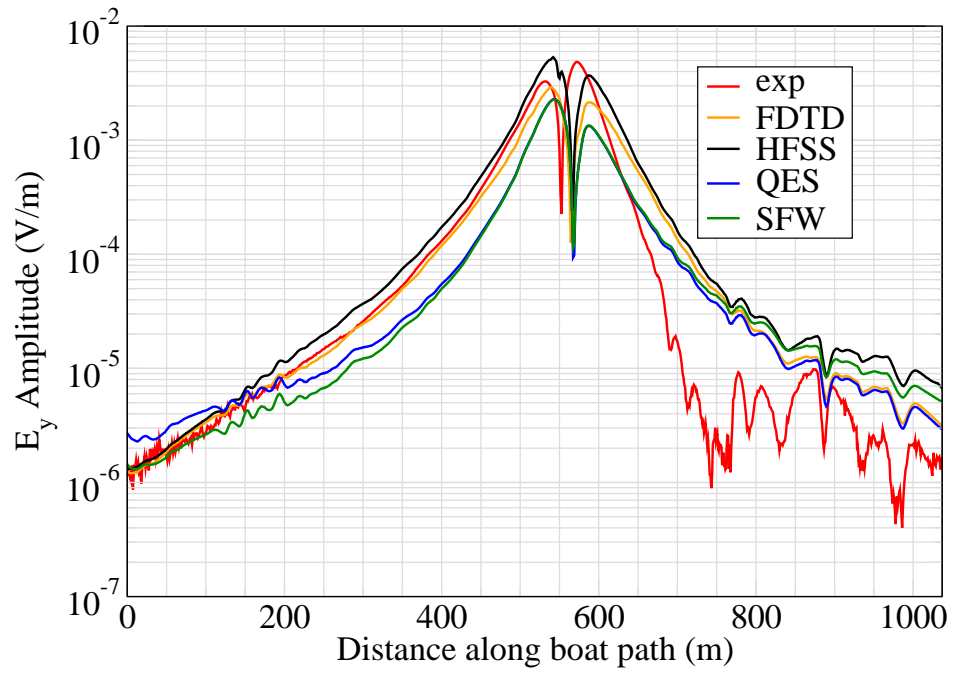


Figure 4: E_y .

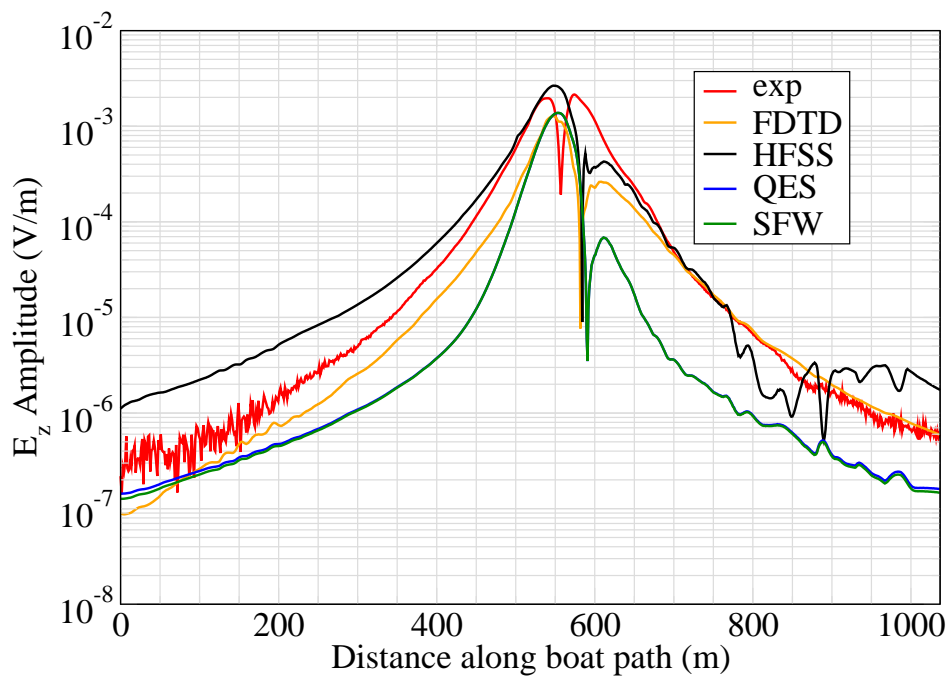


Figure 5: E_z .

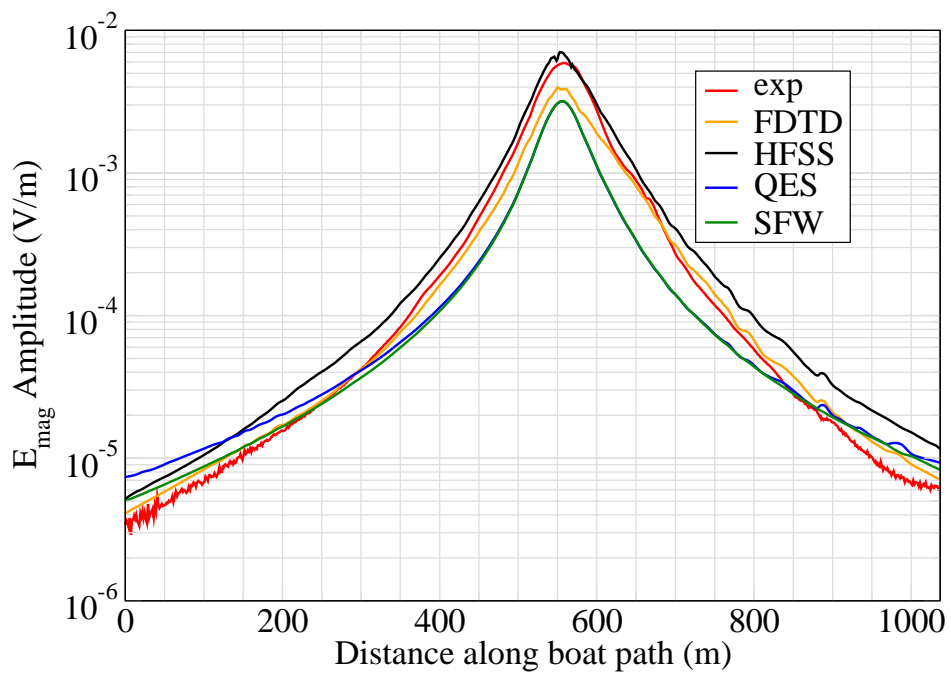


Figure 6: E_{mag} .

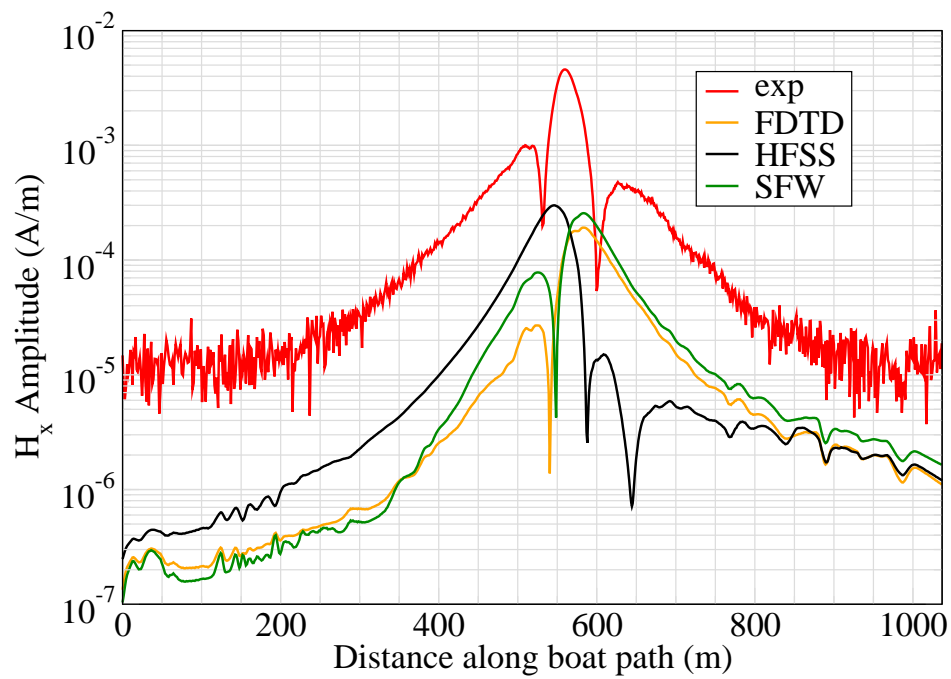


Figure 7: H_x .

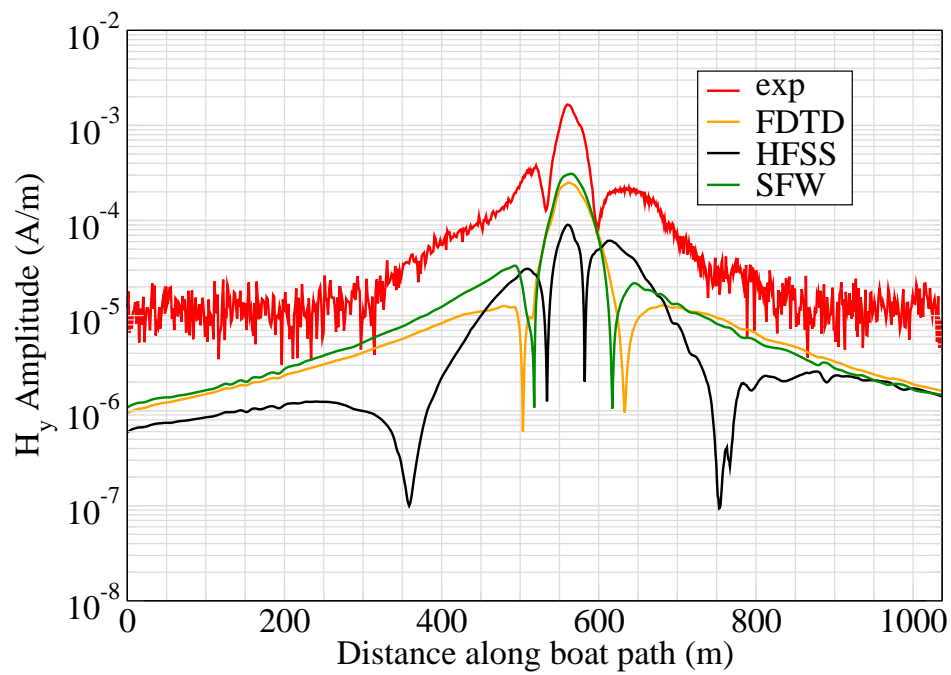


Figure 8: H_y .

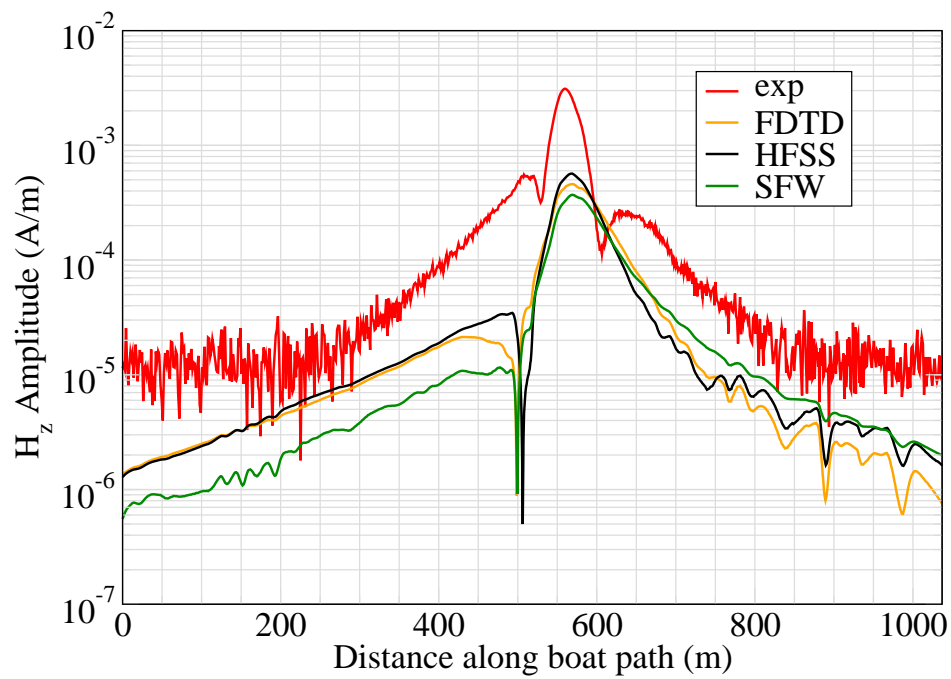


Figure 9: H_z .

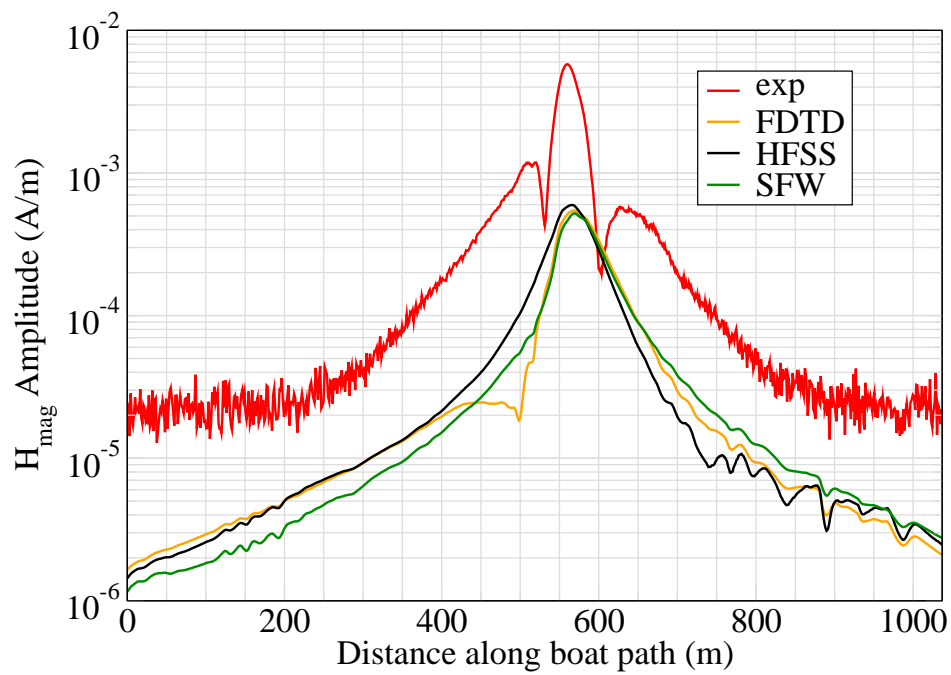


Figure 10: H_{mag} .

Experiment 4

Runs 304.01

Experiment Date: 9/14/2010

1 Discussion

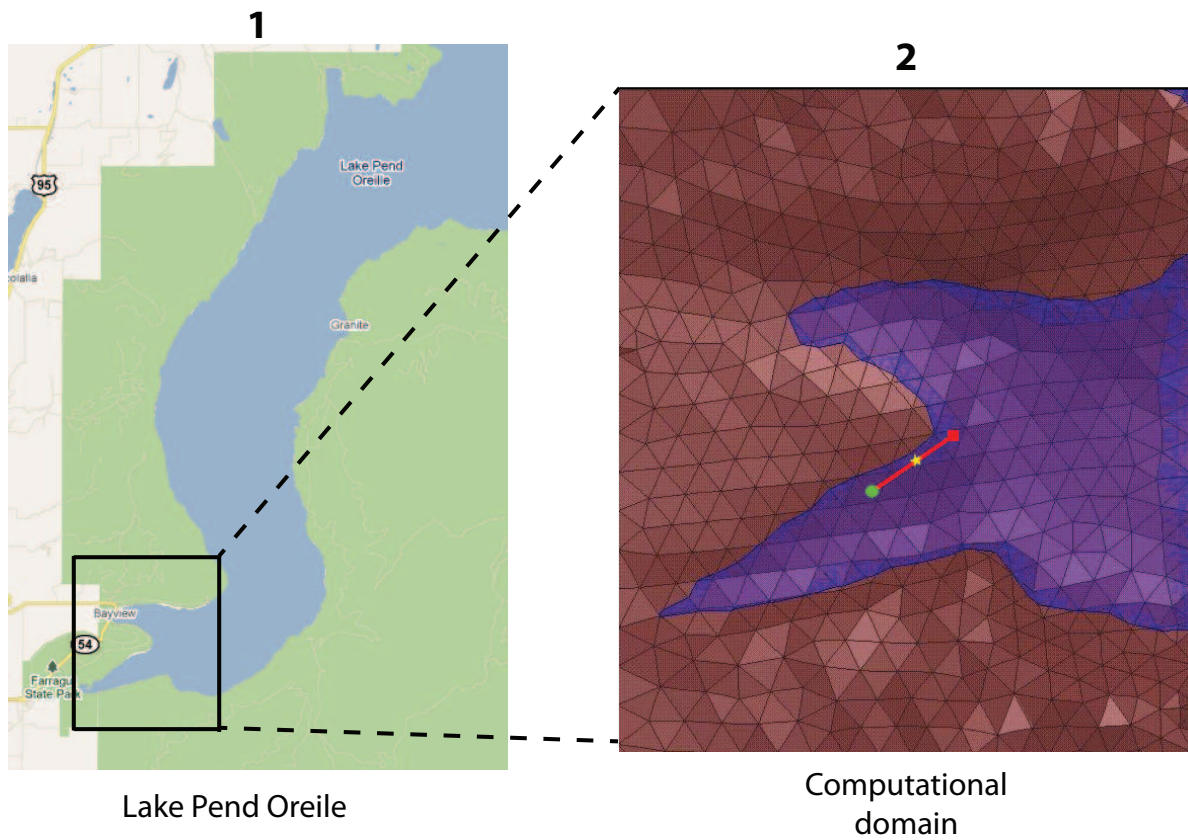


Figure 1: Sensor and source locations; see test report. Sensor is represented by the yellow star; source start and end points represented by green circle and red square.

Source Parameters

- Source Type: HED (Boat Hull: plates 0.61 m by 0.305 m separated by 4 m).
- Source Strength: 11.44 A-m.

- $f = 10$ Hz.

Environment

- Air: $\sigma = 0$ S/m and $\epsilon_r = 1$
- Water: $\sigma = 0.01$ S/m and $\epsilon_r = 81$
- Mud: $\sigma = 0.0012$ S/m and $\epsilon_r = 1$

Table 1: Simulation Details

	FDTD	HFSS	QES/SFW
Domain Size	200 X 200 X 120 cells	123,152 tets	N/A
Cell Size (m)	10 X 10 X 5	N/A	N/A
Time Step (ns)	13.6	N/A	N/A
Run Time (Hrs)	40.8	2.33	0.01
Water Depth (m)	N/A	N/A	50
Effective Source Area (m)	N/A	$l = 0.61$ $w = 0.61$	$r = 0.058$

Comments

- To implement reciprocity, three simulations per vector field are required for a total of six simulations. Run times correspond to the time required to conduct all six simulations.
- Computational time is based on actual elapsed real time. This number is highly subjective and based on how many other applications might be running at a particular time. However, the reported number is an indication of the amount of time typically needed for a particular simulation. The computer specs are: 16 CPU cores at 2.8 GHz.
- Run times for HFSS are given for a single frequency.
- QES is not applicable for magnetic fields using electric source excitation.

2 Simulation Variables

Sensor_P1(x,y,z) [m]	(3227.1709,3503.0624,-14.907)
Sensor_P2(x,y,z) [m]	(3227.1721,3503.0462,-14.907)
Source_P1(x,y,z) [m]	(2752.8222,3166.6059,0)
Source_P2(x,y,z) [m]	(3621.7607,3773.6475,0)
Source_Plate_Separation [m]	4
Source_Size [m X m X #]	[0.610 X 0.305 X 1]
Source_Heading [deg]	46.112
Source_Voltage [V Peak]	338.0723
Source_Current [A Peak]	2.8603
Source_Frequency [Hz]	10

--- Extra Information ---

Source_Heading_Bounds [deg]	(N/A)
Average_Boat_Speed [m/s]	1.2755
Source_Type	Electric boat hull (boat hull)
Sensor_Type	PEMA
Bin_Size [sec]	1
Number_of_Datapoints	832
Lake_Origin (Easting,Northing)	(737736.502,696691.143)
Analysis_Date	Exp4_ScenSI_29-Jul-2011

3 Boat Path

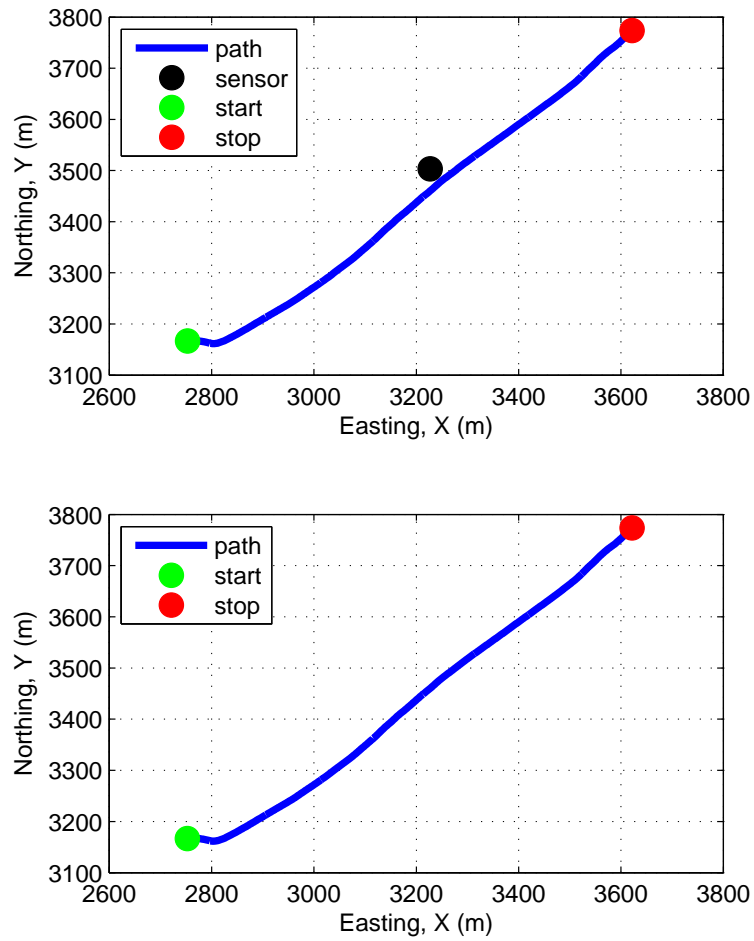


Figure 2: Source and sensor relationship.

4 Plots

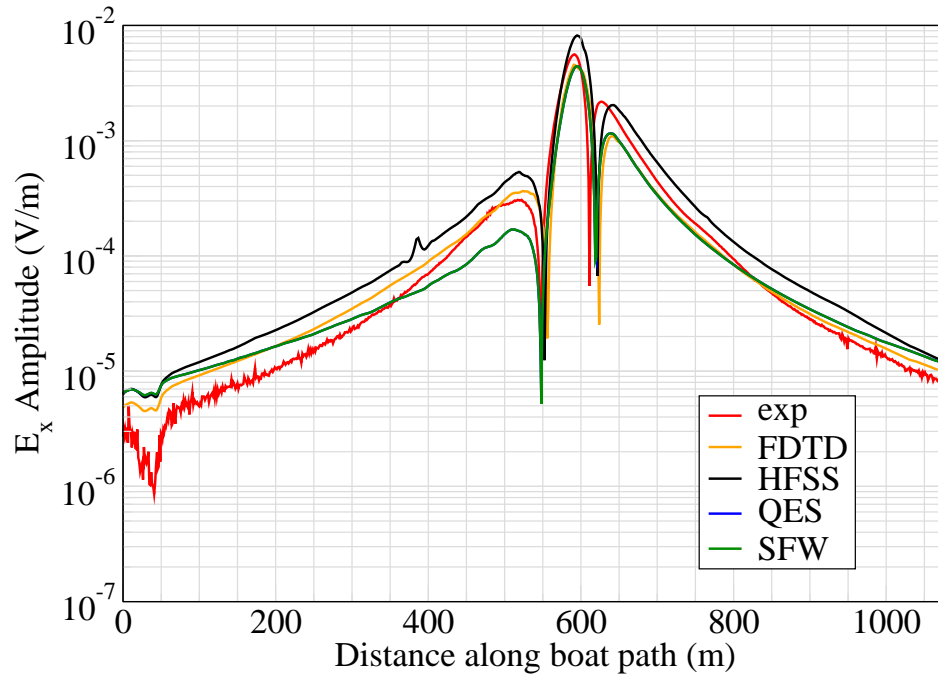


Figure 3: E_x .

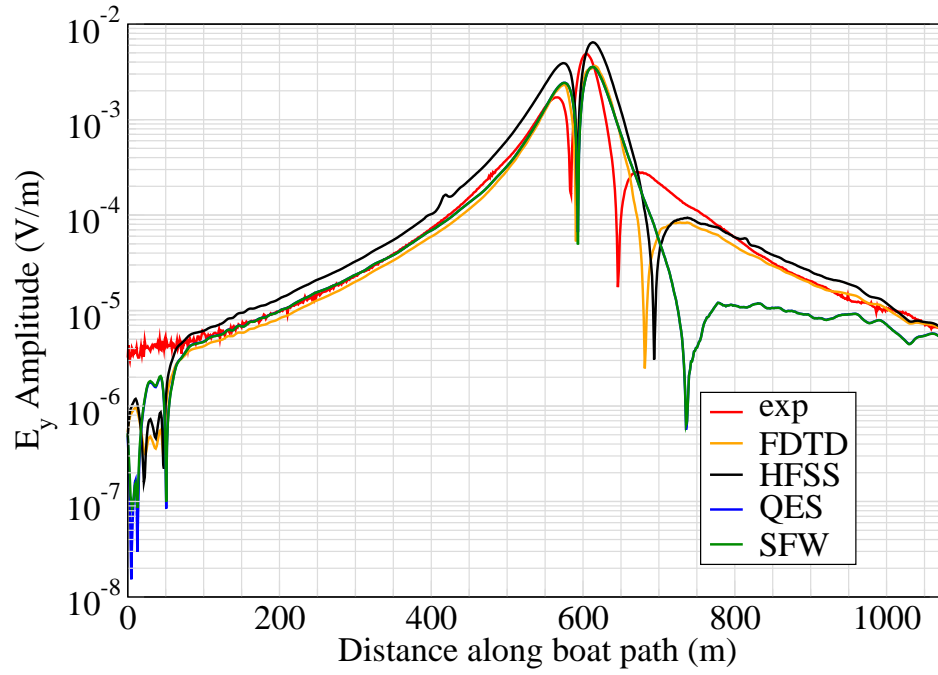


Figure 4: E_y .

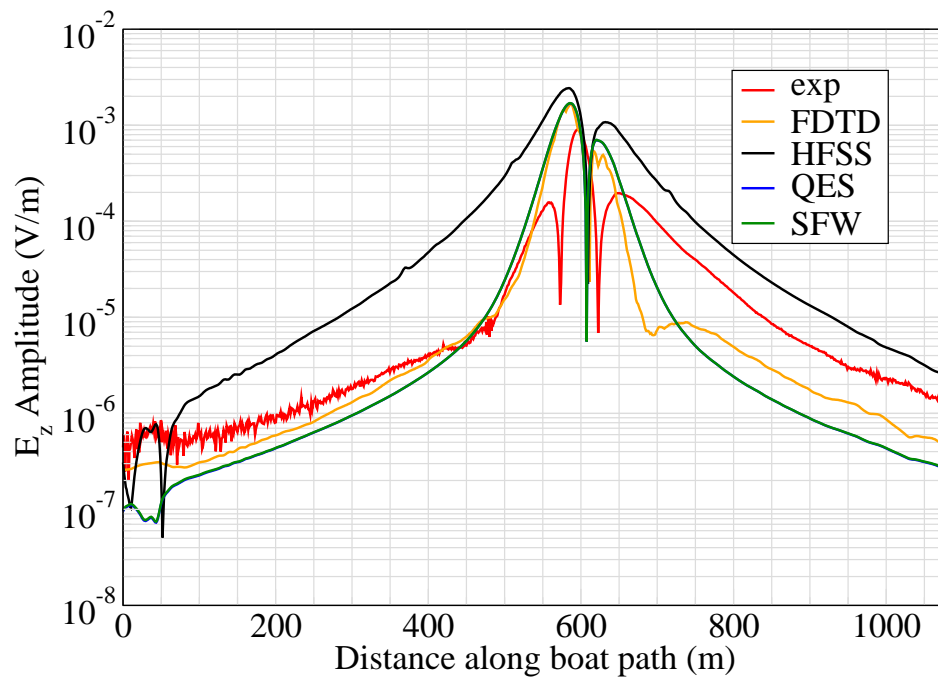


Figure 5: E_z .

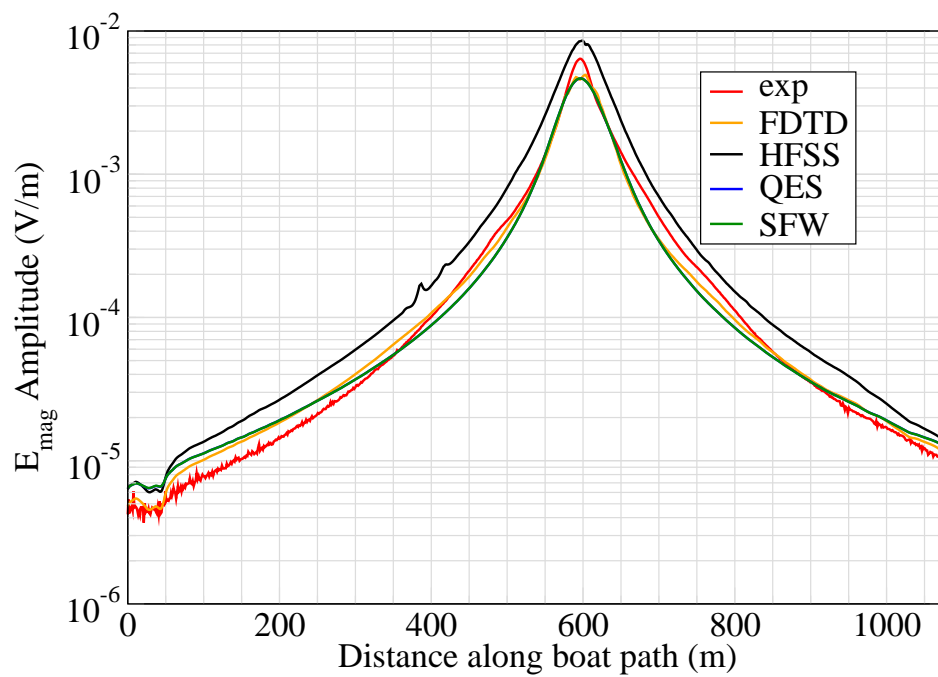


Figure 6: E_{mag} .

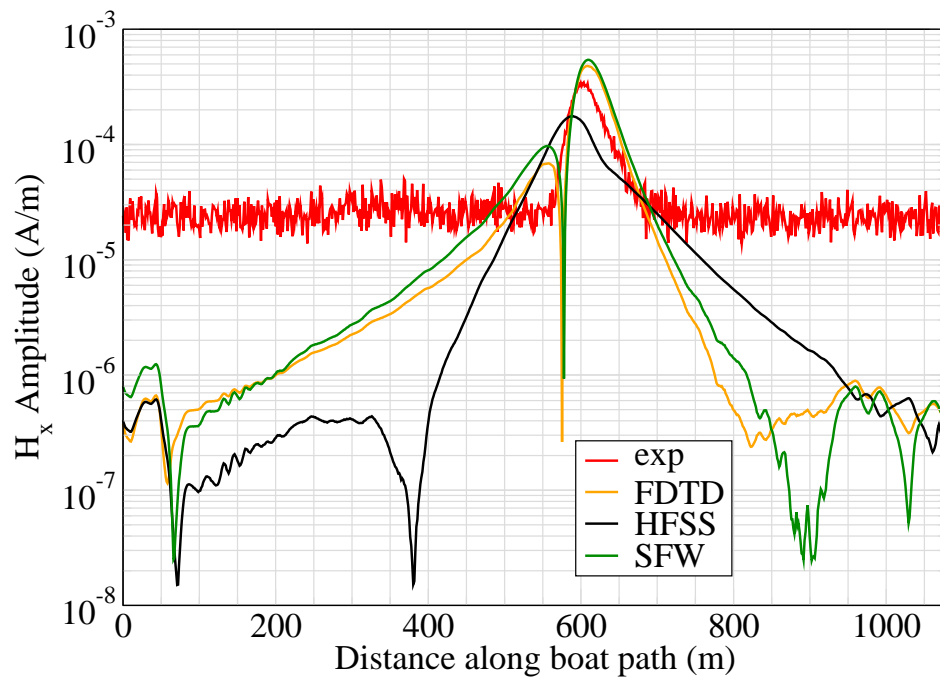


Figure 7: H_x .

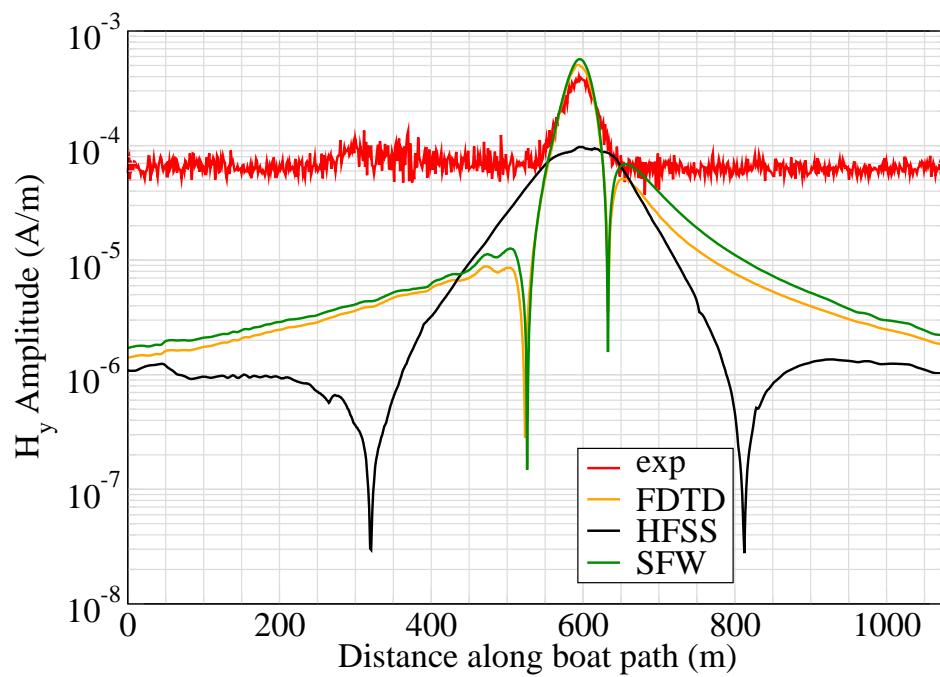


Figure 8: H_y .

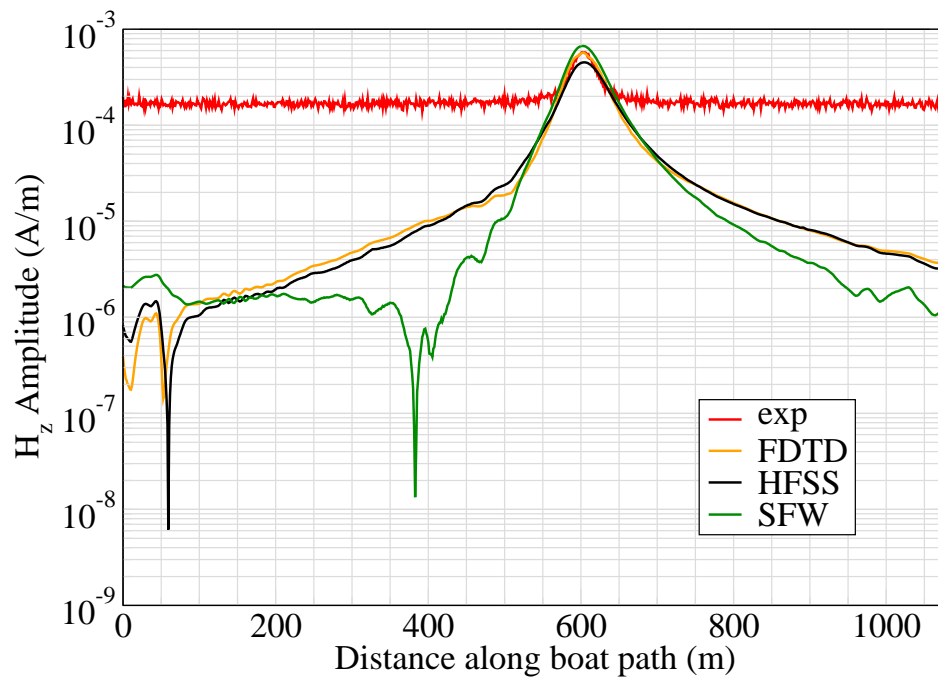


Figure 9: H_z .

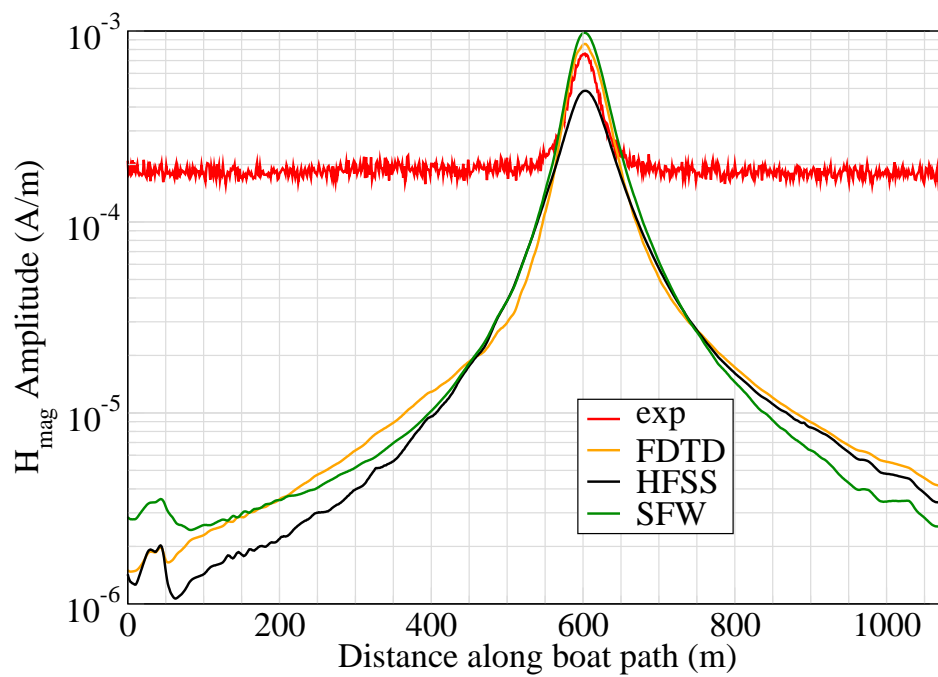


Figure 10: H_{mag} .

Experiment 4

Runs 304.02

Experiment Date: 9/14/2010

1 Discussion

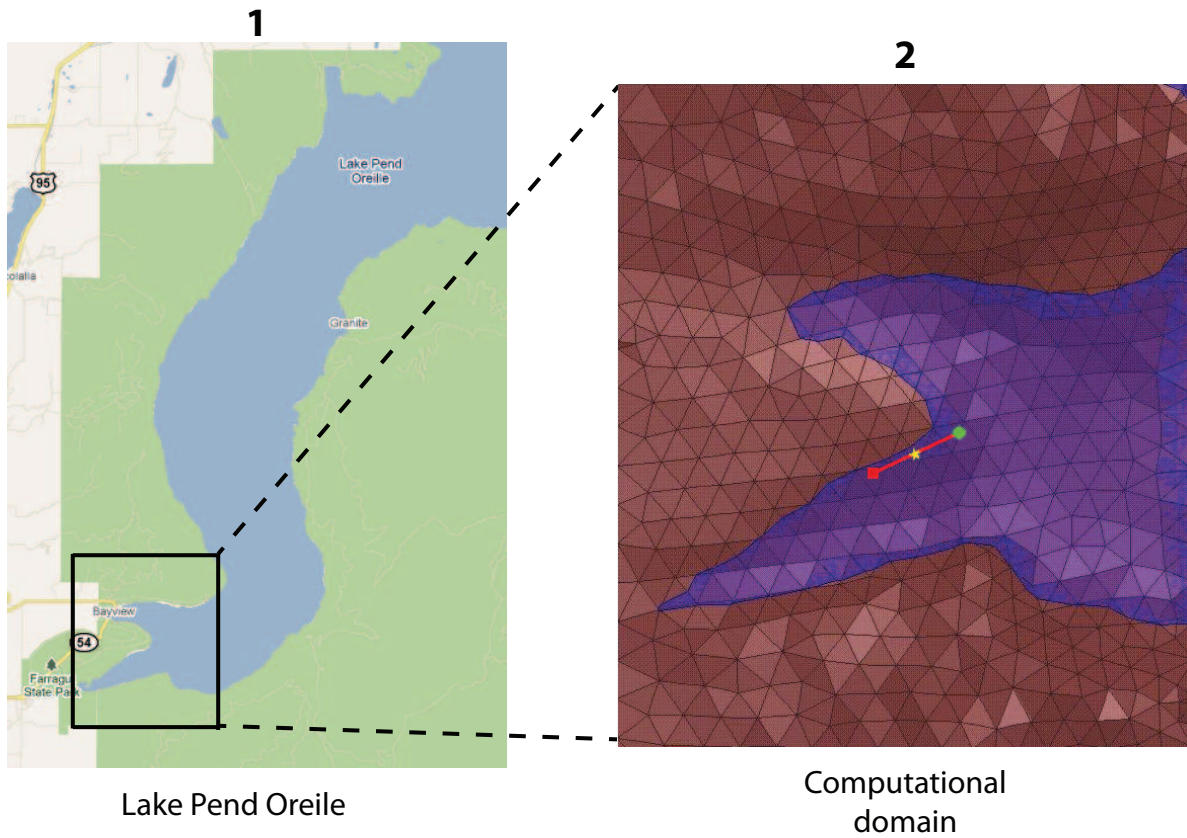


Figure 1: Sensor and source locations; see test report. Sensor is represented by the yellow star; source start and end points represented by green circle and red square.

Source Parameters

- Source Type: HED (Boat Hull: plates 0.61 m by 0.305 m separated by 4 m).
- Source Strength: 11.34 A-m.

- $f = 100$ Hz.

Environment

- Air: $\sigma = 0$ S/m and $\epsilon_r = 1$
- Water: $\sigma = 0.01$ S/m and $\epsilon_r = 81$
- Mud: $\sigma = 0.0012$ S/m and $\epsilon_r = 1$

Table 1: Simulation Details

	FDTD	HFSS	QES/SFW
Domain Size	200 X 200 X 120 cells	117,377 tets	N/A
Cell Size (m)	10 X 10 X 5	N/A	N/A
Time Step (ns)	13.6	N/A	N/A
Run Time (Hrs)	41.1	2.6	0.01
Water Depth (m)	N/A	N/A	50
Effective Source Area (m)	N/A	$l = 0.61$ $w = 0.61$	$r = 0.058$

Comments

- To implement reciprocity, three simulations per vector field are required for a total of six simulations. Run times correspond to the time required to conduct all six simulations.
- Computational time is based on actual elapsed real time. This number is highly subjective and based on how many other applications might be running at a particular time. However, the reported number is an indication of the amount of time typically needed for a particular simulation. The computer specs are: 16 CPU cores at 2.8 GHz.
- Run times for HFSS are given for a single frequency.
- QES is not applicable for magnetic fields using electric source excitation.

2 Simulation Variables

Sensor_P1(x,y,z) [m]	(3227.1638,3503.1073,-14.9068)
Sensor_P2(x,y,z) [m]	(3227.2029,3503.1619,-14.9068)
Source_P1(x,y,z) [m]	(3708.2955,3739.6298,0)
Source_P2(x,y,z) [m]	(2767.5991,3303.3463,0)
Source_Plate_Separation [m]	4
Source_Size [m X m X #]	[0.610 X 0.305 X 1]
Source_Heading [deg]	204.2386
Source_Voltage [V Peak]	334.7352
Source_Current [A Peak]	2.8343
Source_Frequency [Hz]	100

--- Extra Information ---

Source_Heading_Bounds [deg]	(N/A)
Average_Boat_Speed [m/s]	1.4342
Source_Type	Electric boat hull (boat hull)
Sensor_Type	PEMA
Bin_Size [sec]	1
Number_of_Datapoints	724
Lake_Origin (Easting,Northing)	(737736.502,696691.143)
Analysis_Date	Exp4_ScenSJ_29-Jul-2011

3 Boat Path

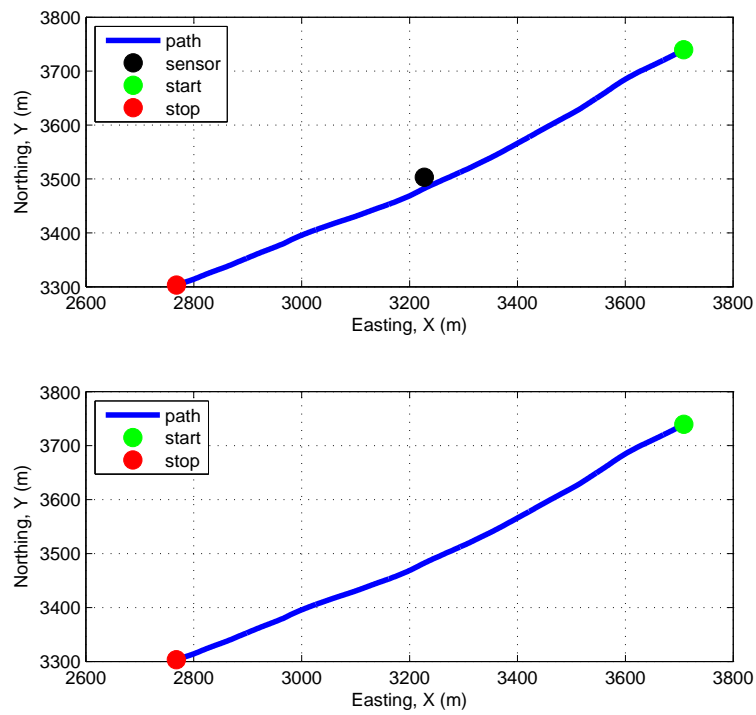


Figure 2: Source and sensor relationship.

4 Plots

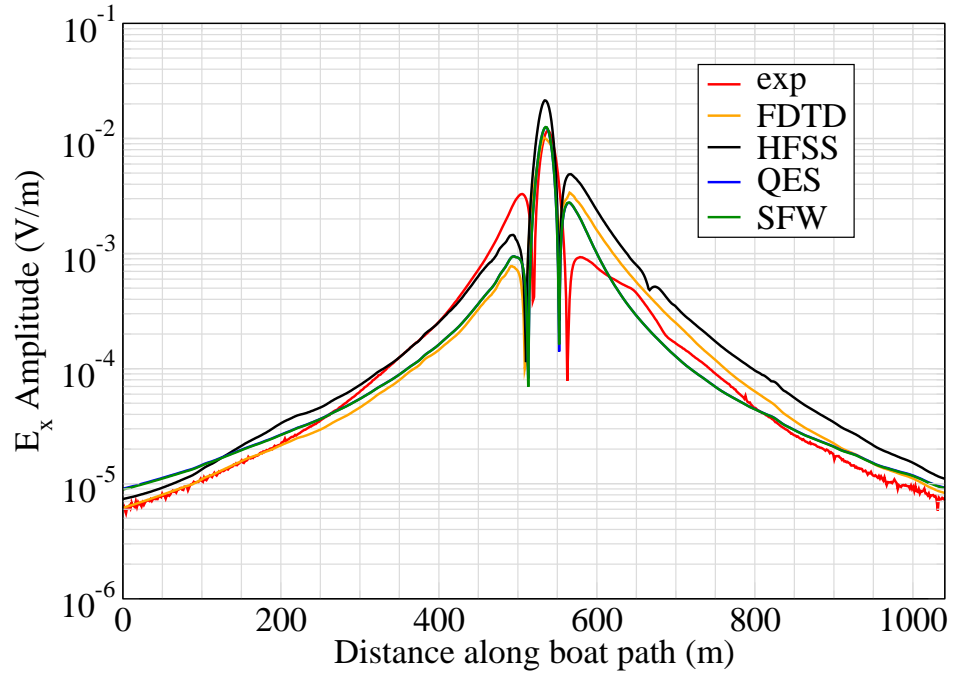


Figure 3: E_x .

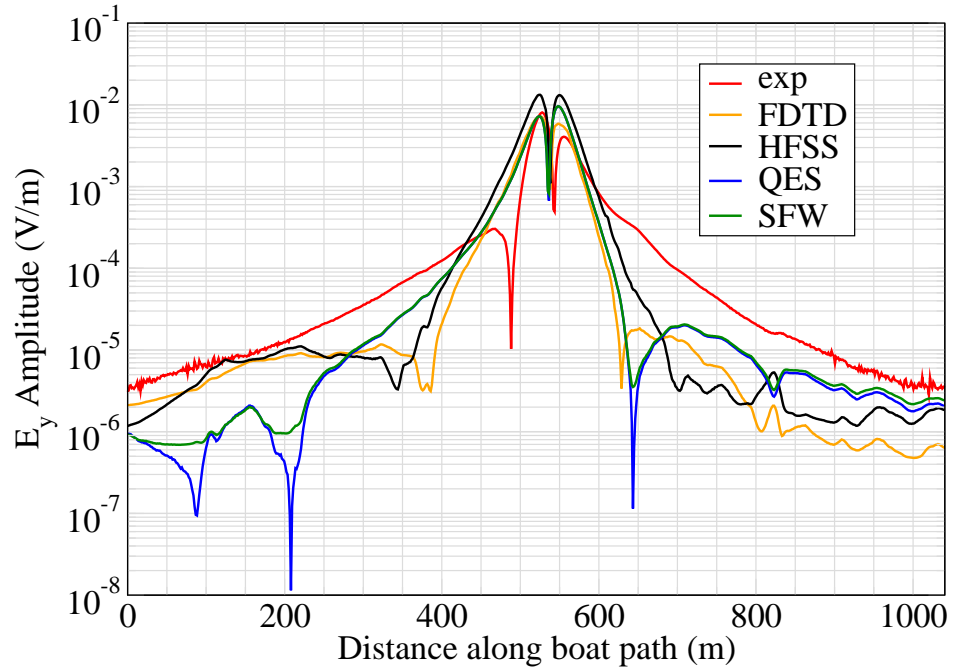


Figure 4: E_y .

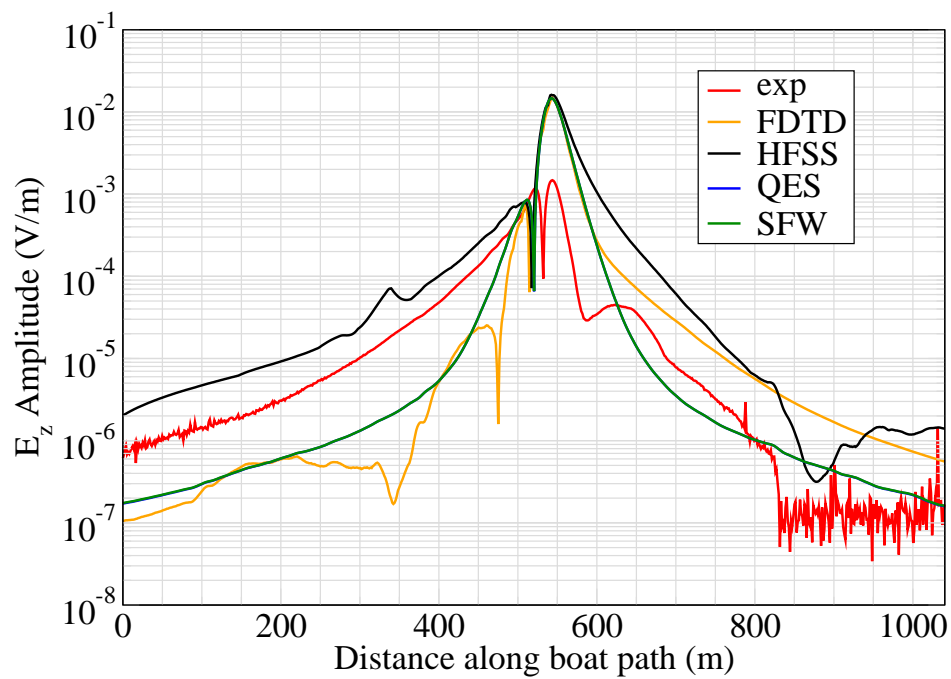


Figure 5: E_z .

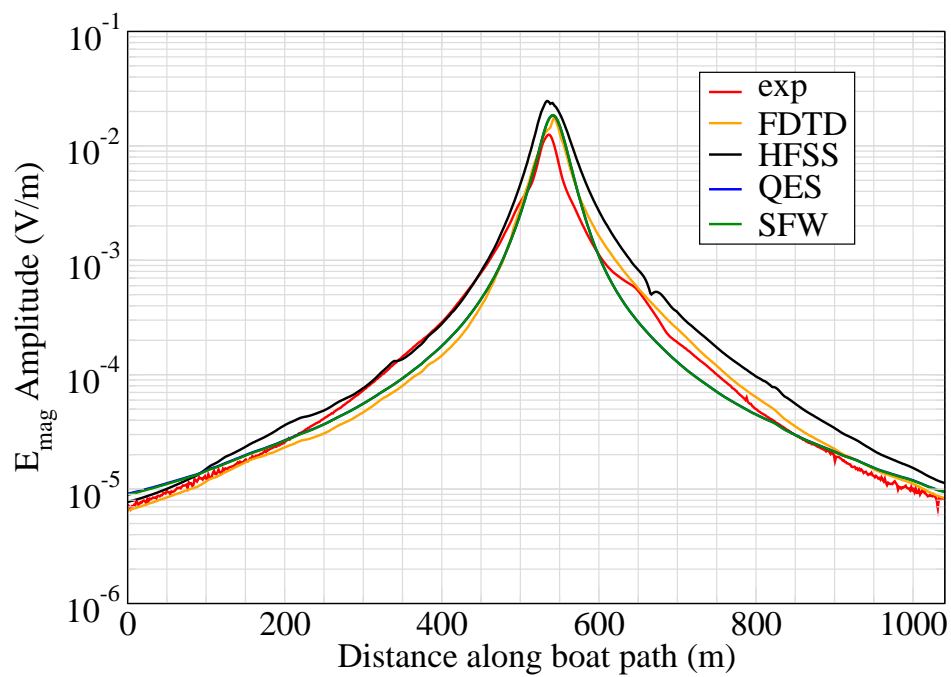


Figure 6: E_{mag} .

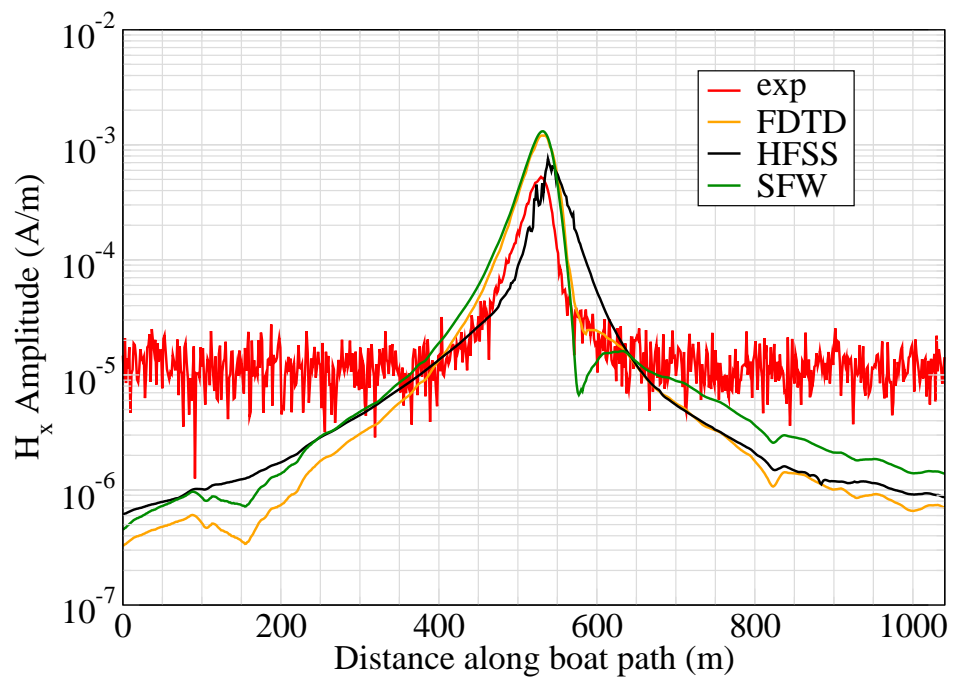


Figure 7: H_x .

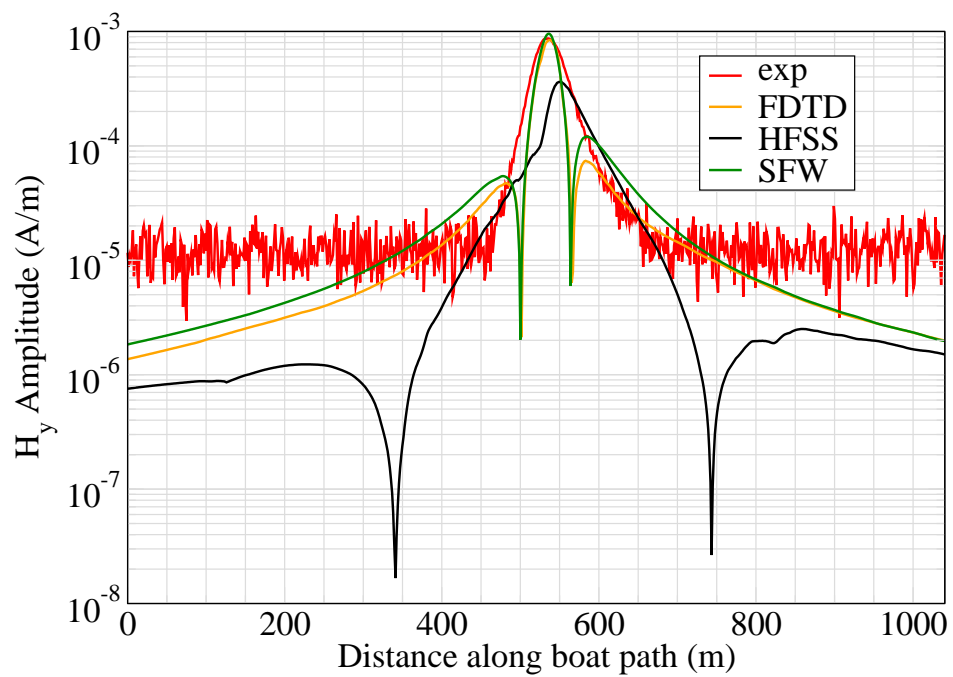


Figure 8: H_y .

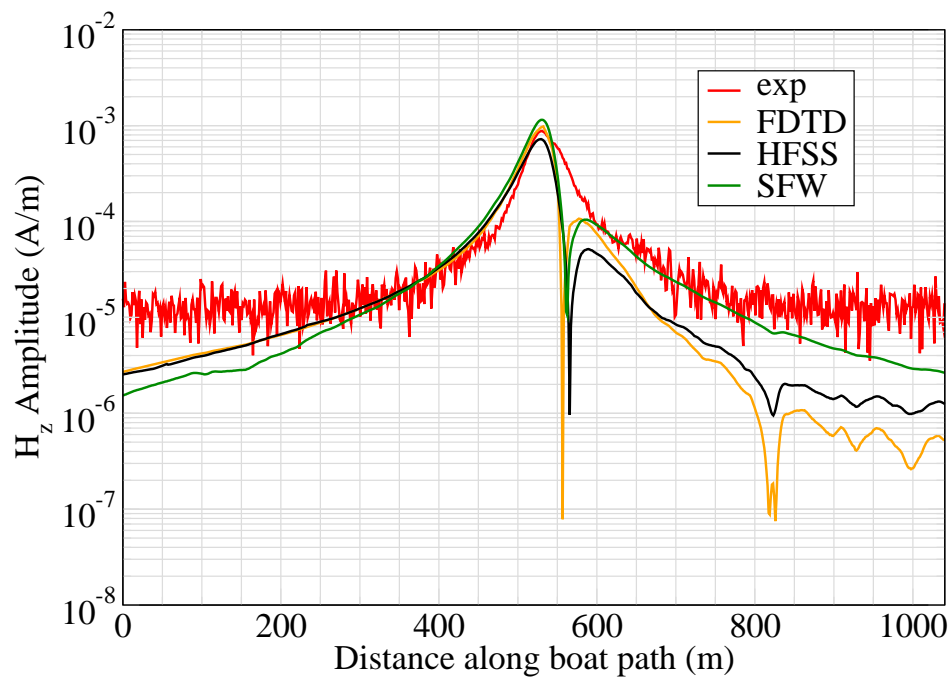


Figure 9: H_z .

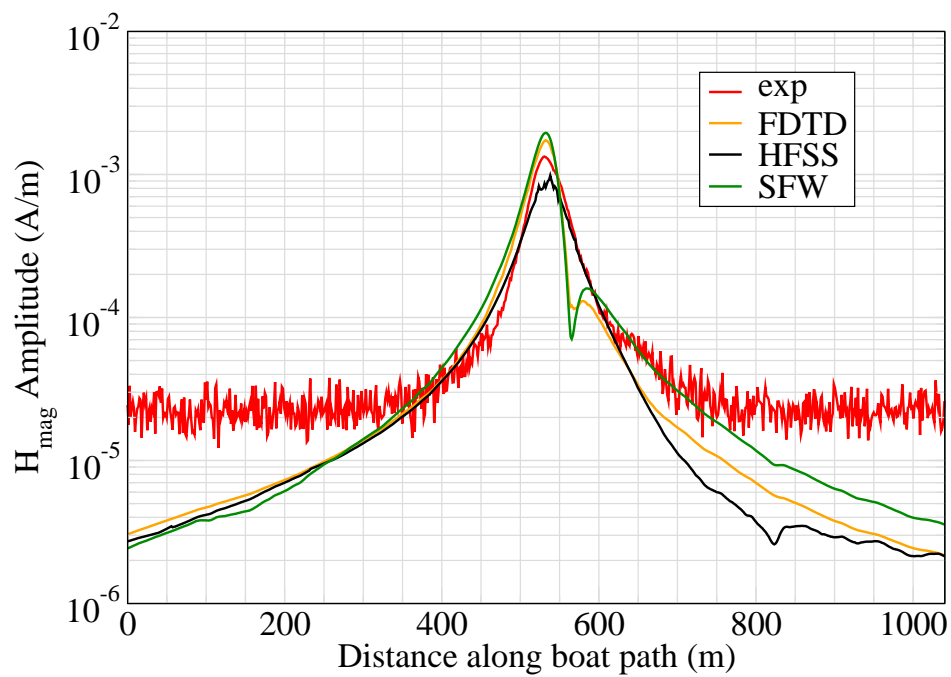


Figure 10: H_{mag} .

Experiment 4

Runs 304.03

Experiment Date: 9/14/2010

1 Discussion

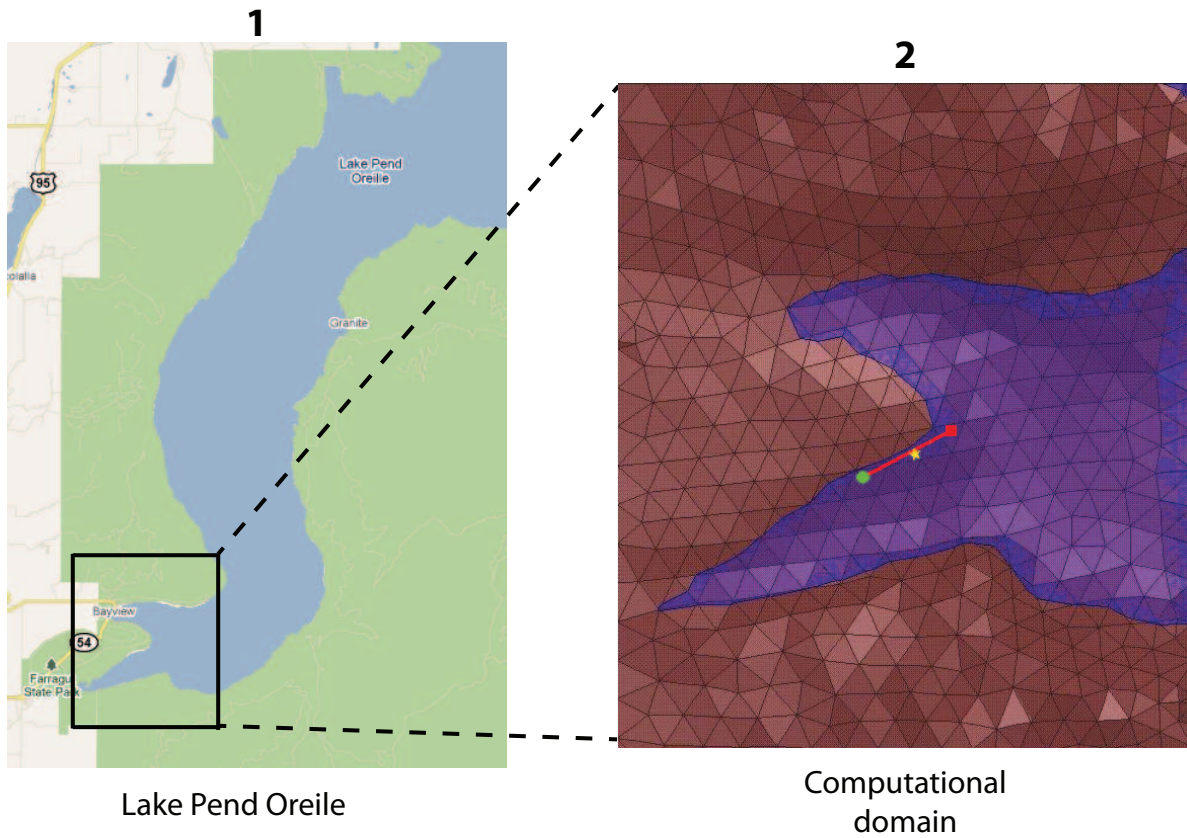


Figure 1: Sensor and source locations; see test report. Sensor is represented by the yellow star; source start and end points represented by green circle and red square.

Source Parameters

- Source Type: HED (Boat Hull: plates 0.61 m by 0.305 m separated by 4 m).
- Source Strength: 11.04 A-m.

- $f = 1000$ Hz.

Environment

- Air: $\sigma = 0$ S/m and $\epsilon_r = 1$
- Water: $\sigma = 0.01$ S/m and $\epsilon_r = 81$
- Mud: $\sigma = 0.0012$ S/m and $\epsilon_r = 1$

Table 1: Simulation Details

	FDTD	HFSS	QES/SFW
Domain Size	200 X 200 X 120 cells	104,021 tets	N/A
Cell Size (m)	10 X 10 X 5	N/A	N/A
Time Step (ns)	13.6	N/A	N/A
Run Time (Hrs)	41.2	1.9	0.01
Water Depth (m)	N/A	N/A	50
Effective Source Area (m)	N/A	$l = 0.61$ $w = 0.61$	$r = 0.058$

Comments

- To implement reciprocity, three simulations per vector field are required for a total of six simulations. Run times correspond to the time required to conduct all six simulations.
- Computational time is based on actual elapsed real time. This number is highly subjective and based on how many other applications might be running at a particular time. However, the reported number is an indication of the amount of time typically needed for a particular simulation. The computer specs are: 16 CPU cores at 2.8 GHz.
- Run times for HFSS are given for a single frequency.
- QES is not applicable for magnetic fields using electric source excitation.

2 Simulation Variables

Sensor_P1(x,y,z) [m]	(3227.2101,3503.1366,-14.9064)
Sensor_P2(x,y,z) [m]	(3227.1726,3503.1414,-14.9064)
Source_P1(x,y,z) [m]	(2654.1587,3257.2949,0)
Source_P2(x,y,z) [m]	(3605.6881,3763.7102,0)
Source_Plate_Separation [m]	4
Source_Size [m X m X #]	[0.610 X 0.305 X 1]
Source_Heading [deg]	27.691
Source_Voltage [V Peak]	331.1612
Source_Current [A Peak]	2.7602
Source_Frequency [Hz]	1000

--- Extra Information ---

Source_Heading_Bounds [deg]	(N/A)
Average_Boat_Speed [m/s]	1.2461
Source_Type	Electric boat hull (boat hull)
Sensor_Type	PEMA
Bin_Size [sec]	1
Number_of_Datapoints	866
Lake_Origin (Easting,Northing)	(737736.502,696691.143)
Analysis_Date	Exp4_ScenSK_28-Jul-2011

3 Boat Path

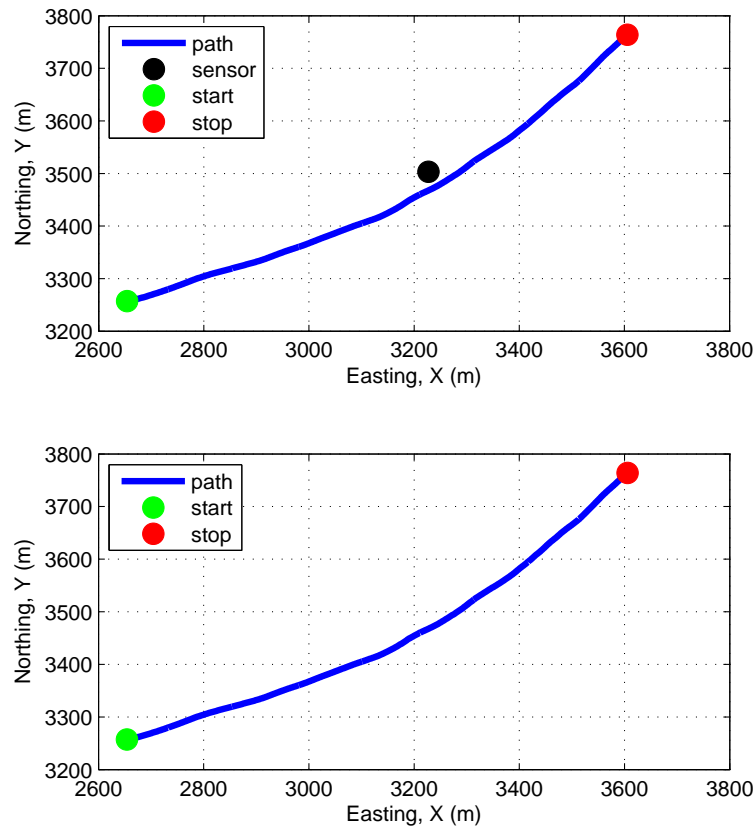


Figure 2: Source and sensor relationship.

4 Plots

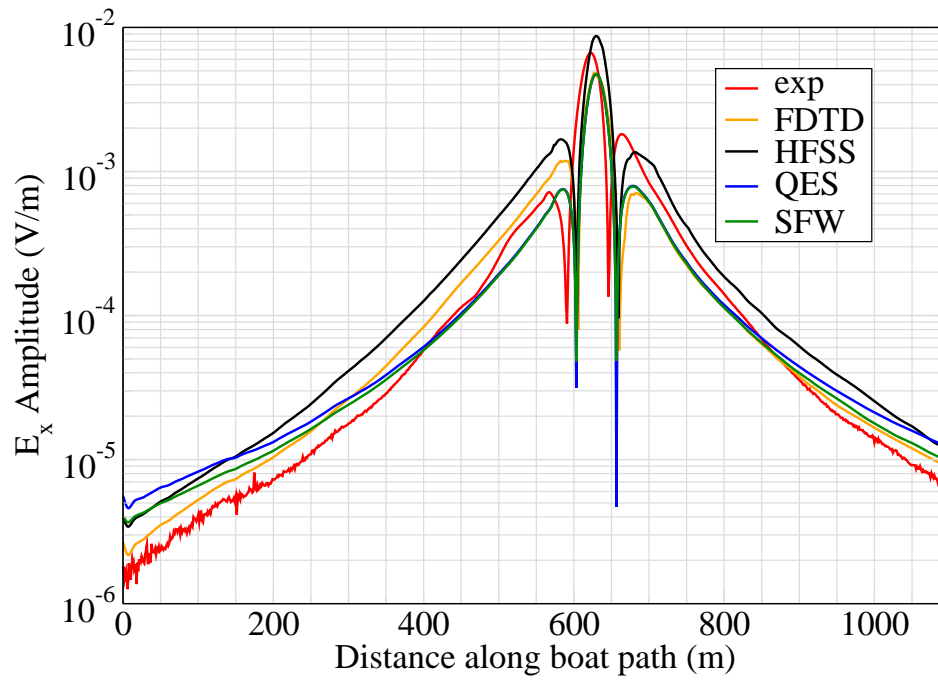


Figure 3: E_x .

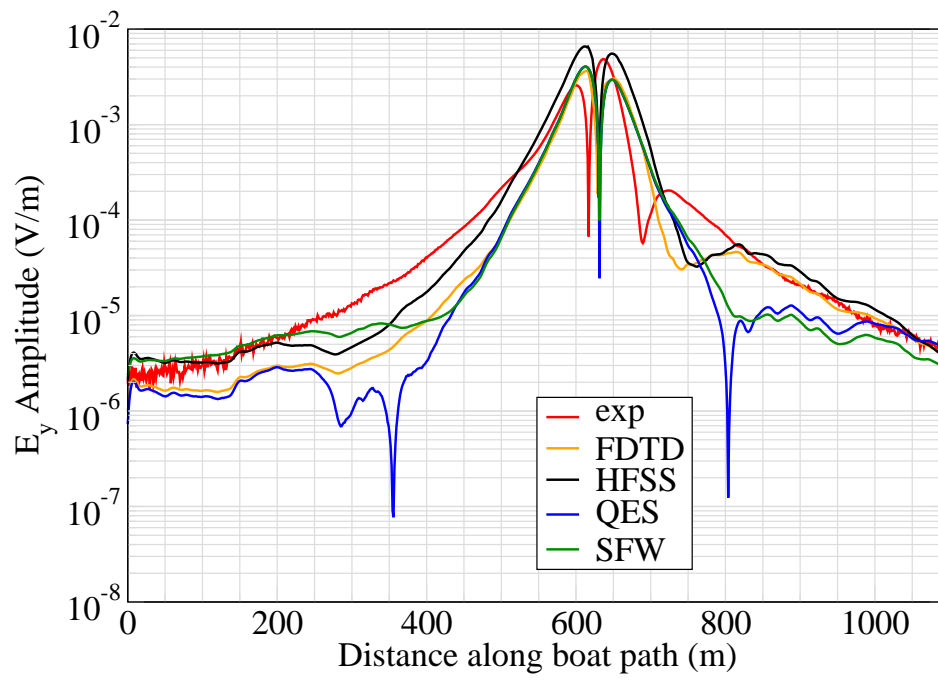


Figure 4: E_y .

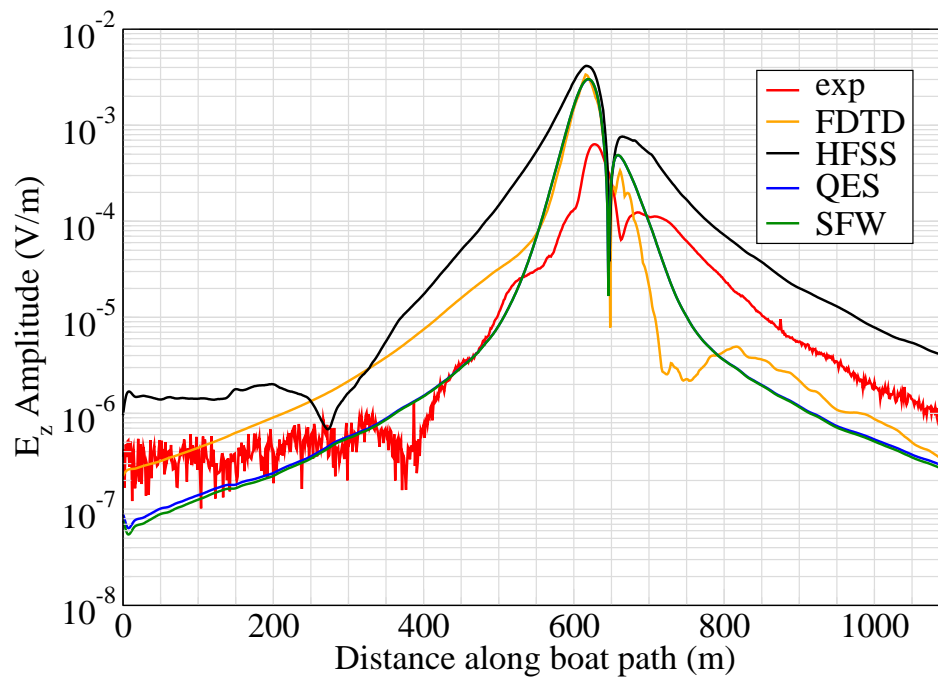


Figure 5: E_z .

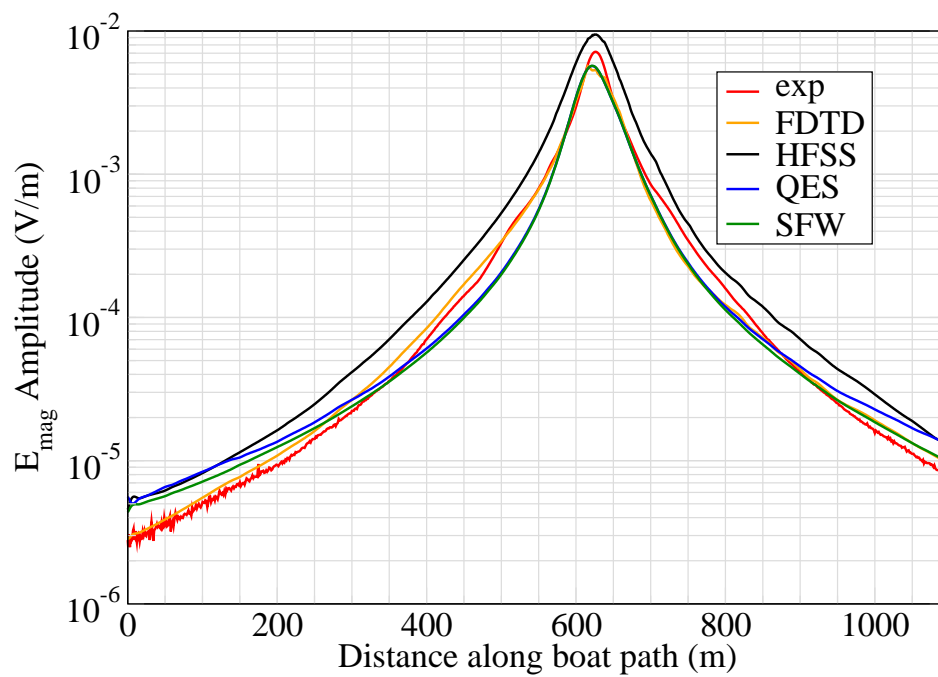


Figure 6: E_{mag} .

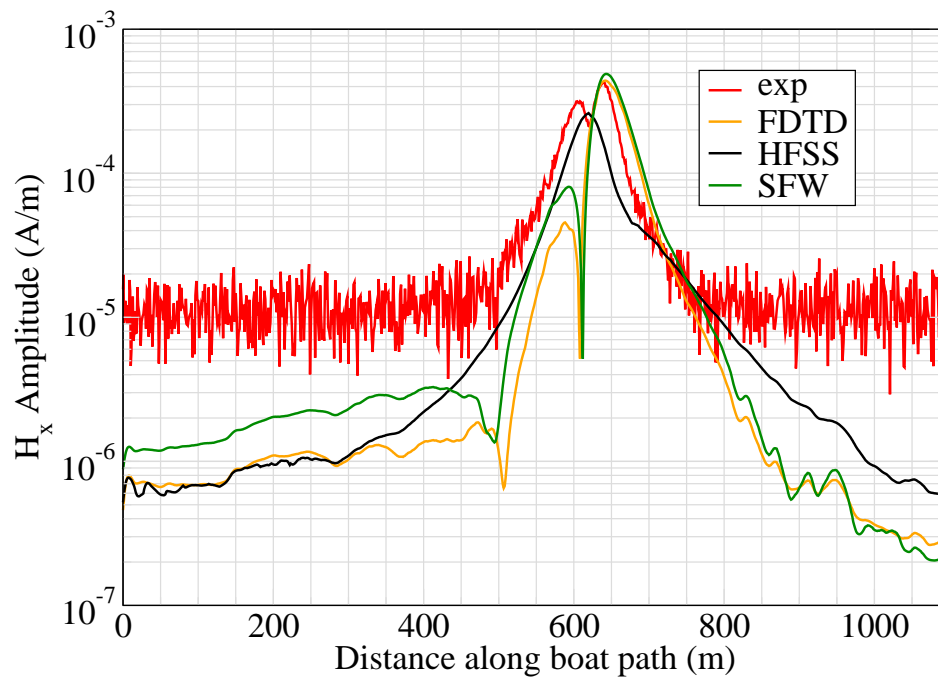


Figure 7: H_x .

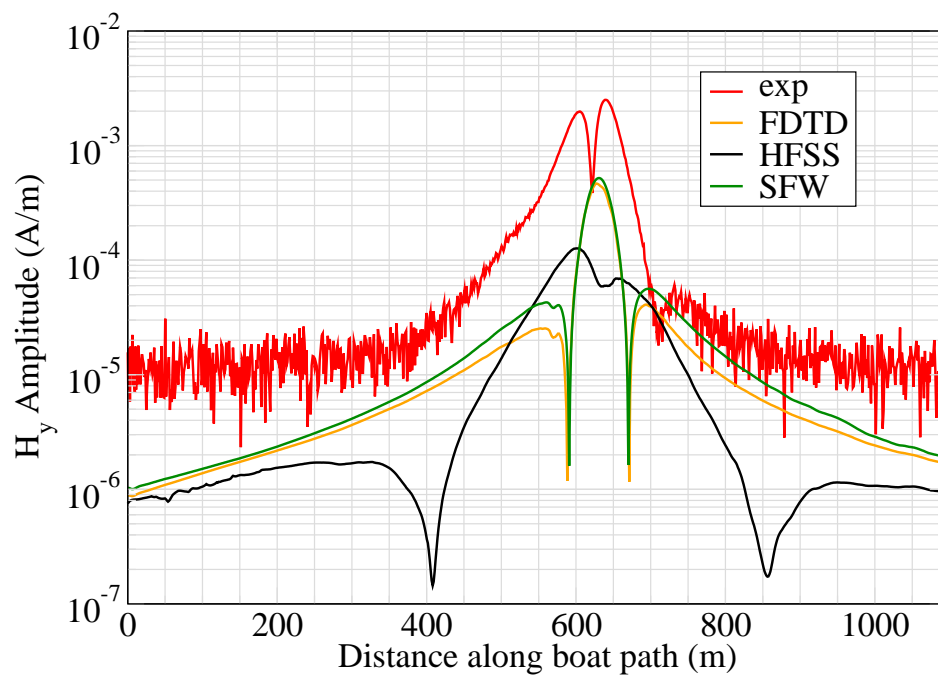


Figure 8: H_y .

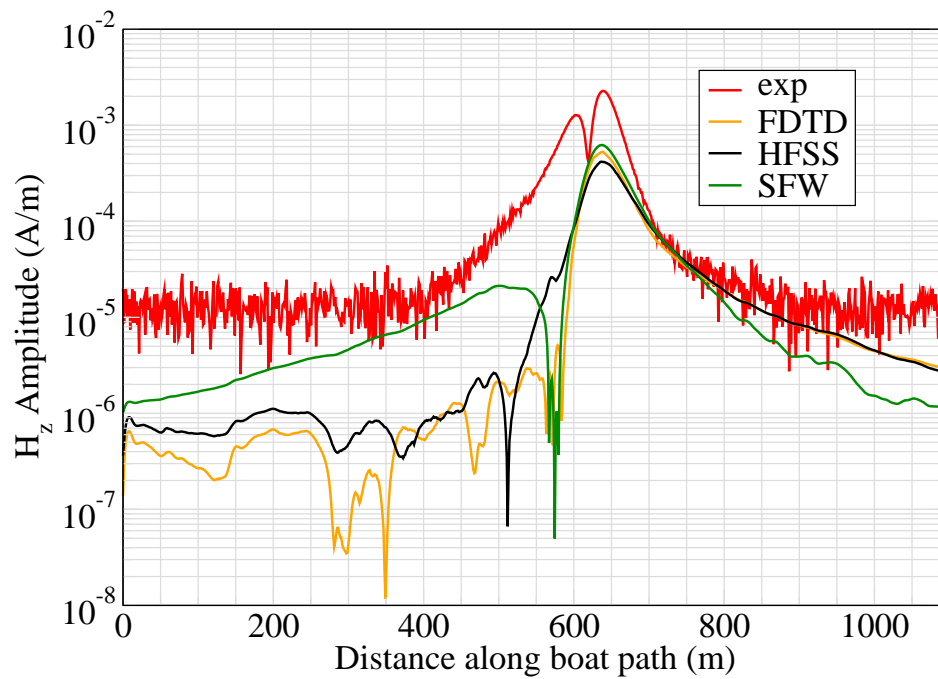


Figure 9: H_z .

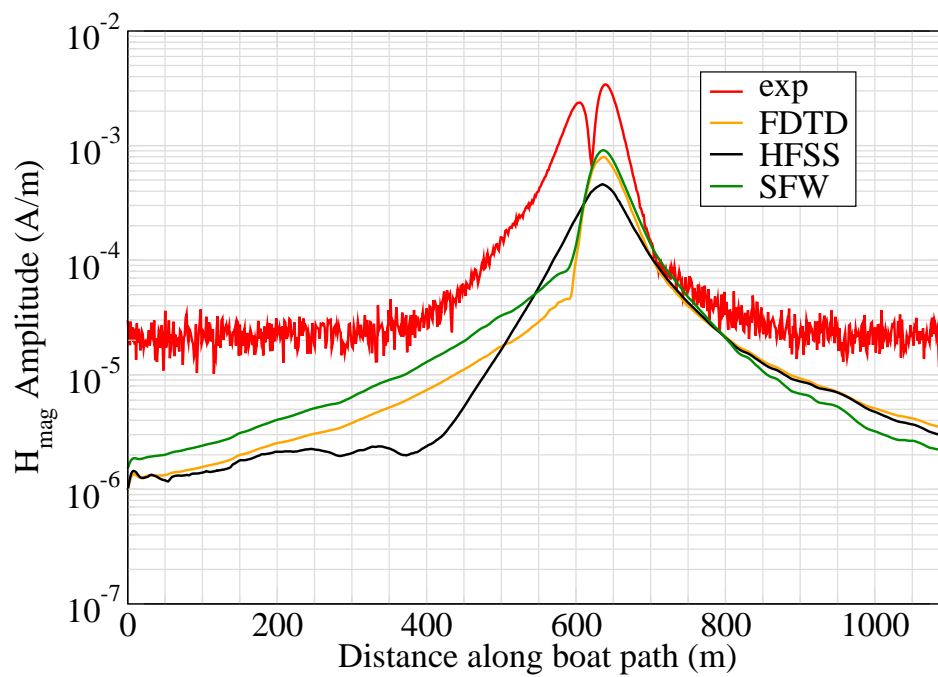


Figure 10: H_{mag} .

Experiment 4

Runs 100.02, 100.04, 100.06, 100.08 and 100.10

Experiment Date: 9/13/2010

1 Discussion

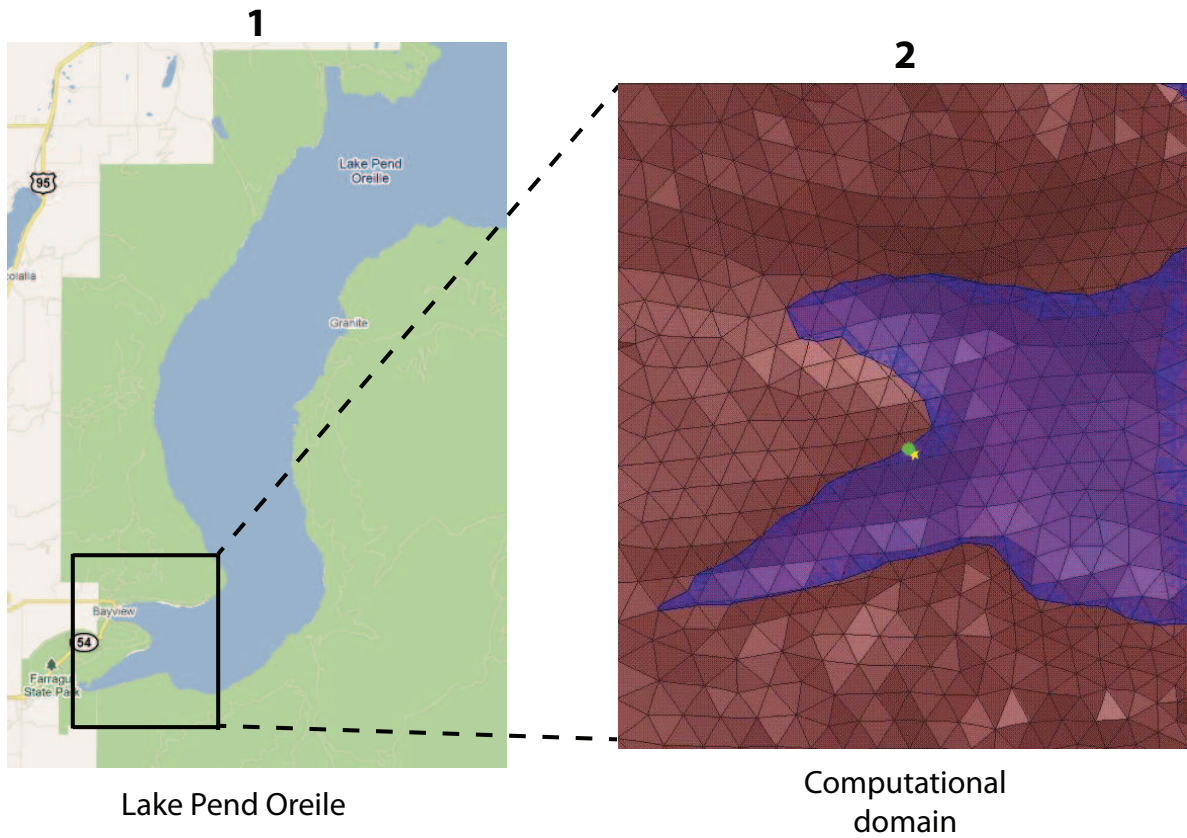


Figure 1: Sensor and source locations; see test report. Sensor is represented by the yellow star; source start and end points represented by green circle and red square.

Source Parameters

- Source Type: VMD (Coil: 3.66 m by 3.66 m with 12 turns).
- Source Strength: 3,886.9 A-m².

- $f = 1000$ Hz.

Environment

- Air: $\sigma = 0$ S/m and $\epsilon_r = 1$
- Water: $\sigma = 0.01$ S/m and $\epsilon_r = 81$
- Mud: $\sigma = 0.0012$ S/m and $\epsilon_r = 1$

Table 1: Simulation Details

	FDTD	HFSS	QES/SFW
Domain Size	200 X 200 X 120 cells	34,361 tets	N/A
Cell Size (m)	10 X 10 X 5	N/A	N/A
Time Step (ns)	13.6	N/A	N/A
Run Time (Hrs)	6.75	0.4	0.01
Water Depth (m)	N/A	N/A	18
Effective Source Area (m)	N/A	$l = 3.66$ $w = 3.66$	$r = 3.66$

Comments

- To implement reciprocity, three simulations per vector field are required for a total of six simulations. Run times correspond to the time required to conduct all six simulations.
- Computational time is based on actual elapsed real time. This number is highly subjective and based on how many other applications might be running at a particular time. However, the reported number is an indication of the amount of time typically needed for a particular simulation. The computer specs are: 16 CPU cores at 2.8 GHz.
- Run times for HFSS are given for a single frequency.
- QES is not applicable for electric or magnetic fields using magnetic source excitation.

2 Simulation Variables

Sensor_P1(x,y,z) [m]	(3226.5215,3497.0578,-3.0846)
Sensor_P2(x,y,z) [m]	(3226.5215,3497.0578,-15.211)
Source_P1(x,y,z) [m]	(3164.9716,3561.9188,0)
Source_P2(x,y,z) [m]	(3164.9716,3561.9188,0)
Source_Plate_Separation [m]	N/A
Source_Size [m X m X #]	[3.658 X 3.658 X 12]
Source_Heading [deg]	NaN
Source_Voltage [V Peak]	12.3218
Source_Current [A Peak]	24.1163
Source_Frequency [Hz]	1000

--- Extra Information ---

Source_Heading_Bounds [deg]	(N/A)
Average_Boat_Speed [m/s]	NaN
Source_Type	Magnetic source (portable)
Sensor_Type	PEMA
Bin_Size [sec]	[335,494,482,483,484]
Number_of_Datapoints	5
Lake_Origin (Easting,Northing)	(737736.502,696691.143)
Analysis_Date	Exp4_ScenSL_28-Jul-2011

3 Source and sensor locations

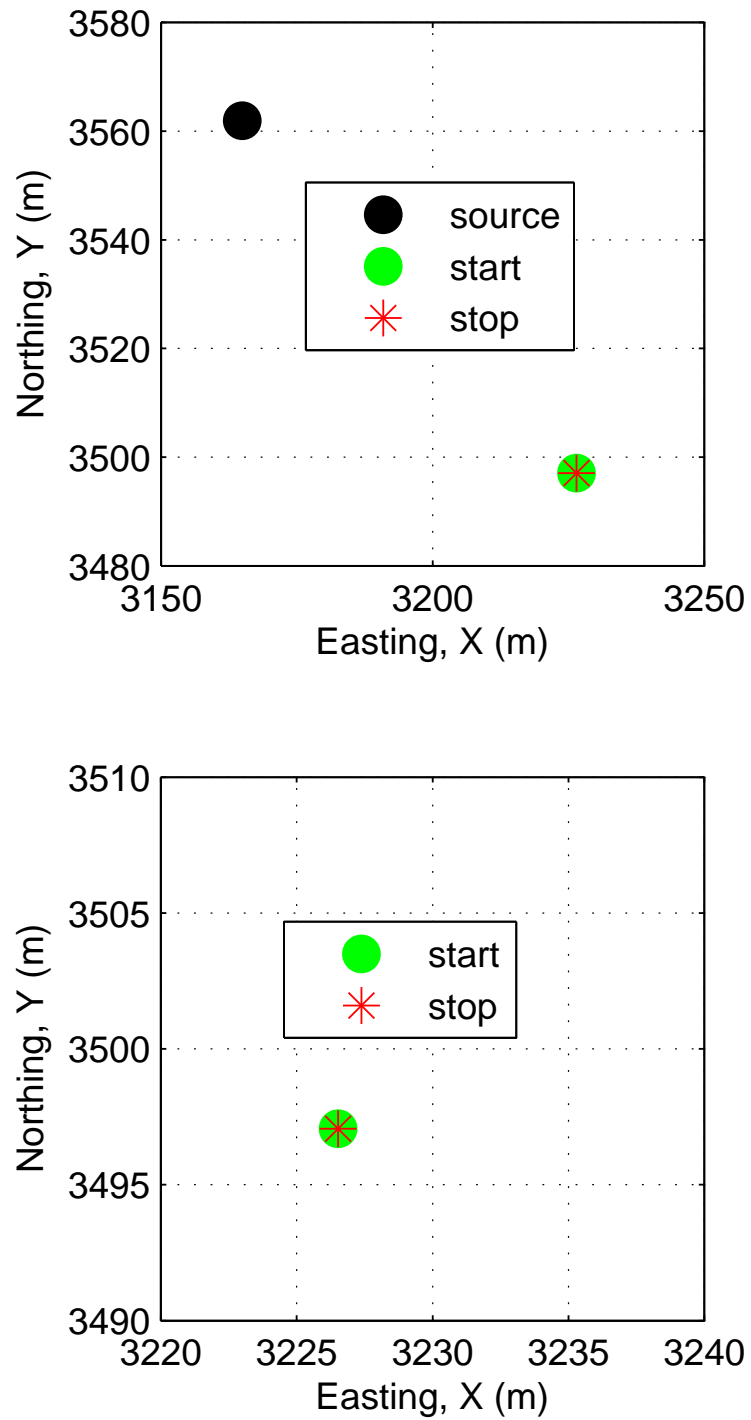


Figure 2: Source and sensor relationship.

4 Plots

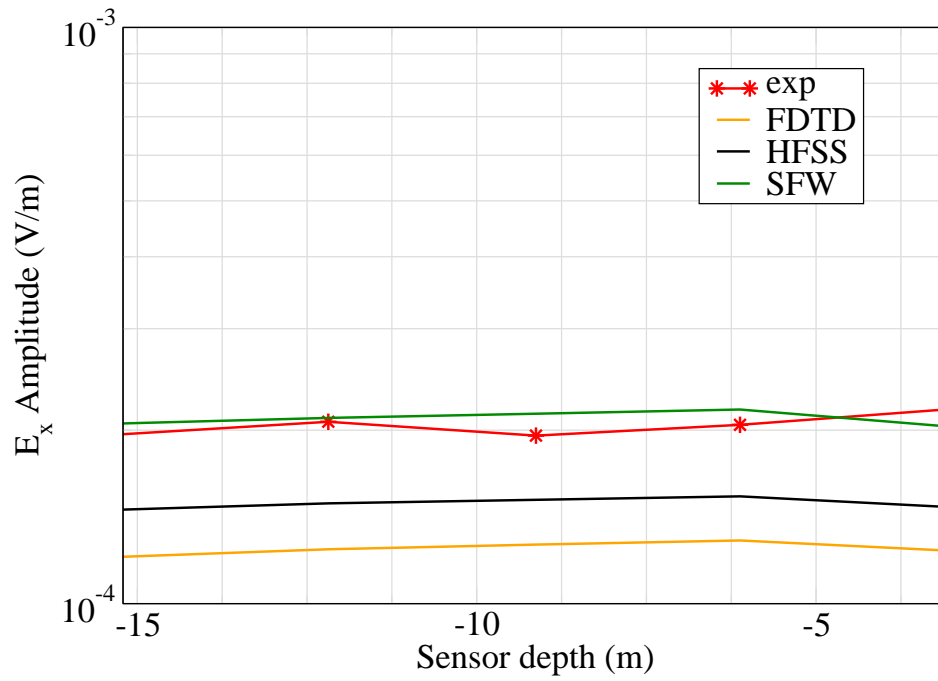


Figure 3: E_x .

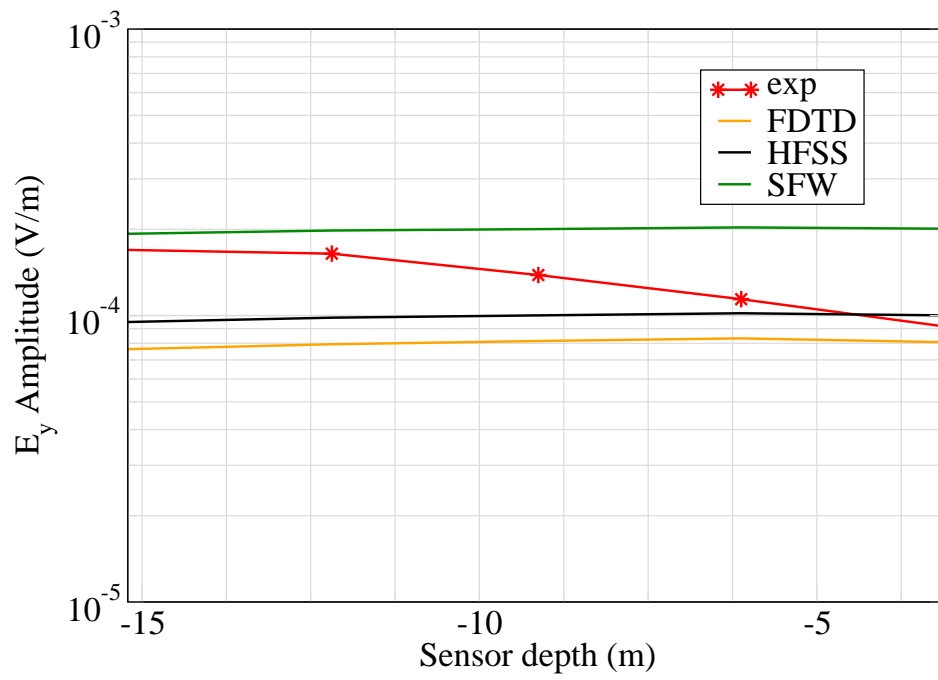


Figure 4: E_y .

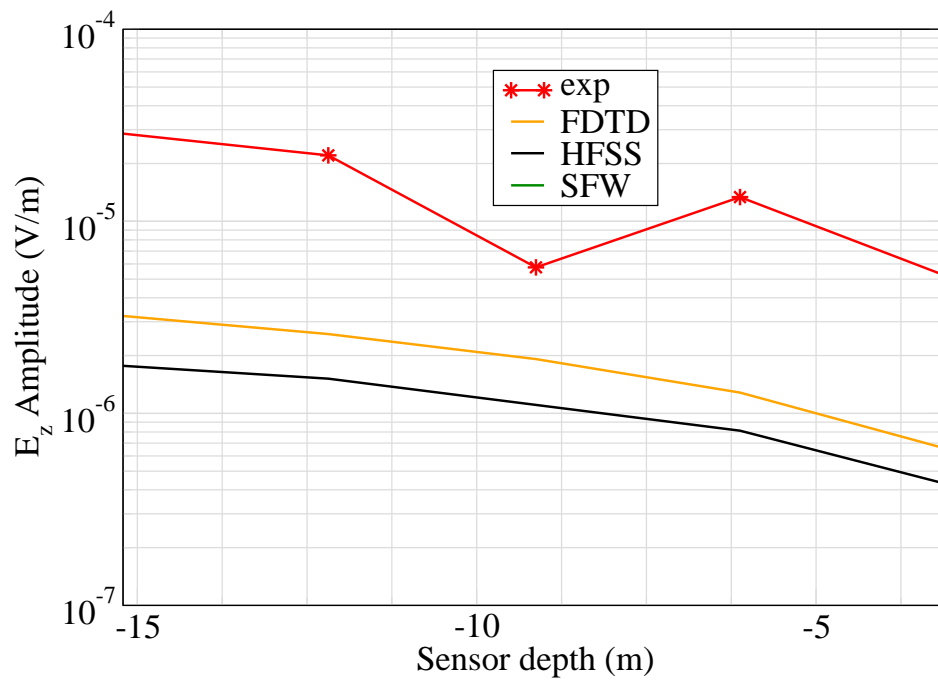


Figure 5: E_z .

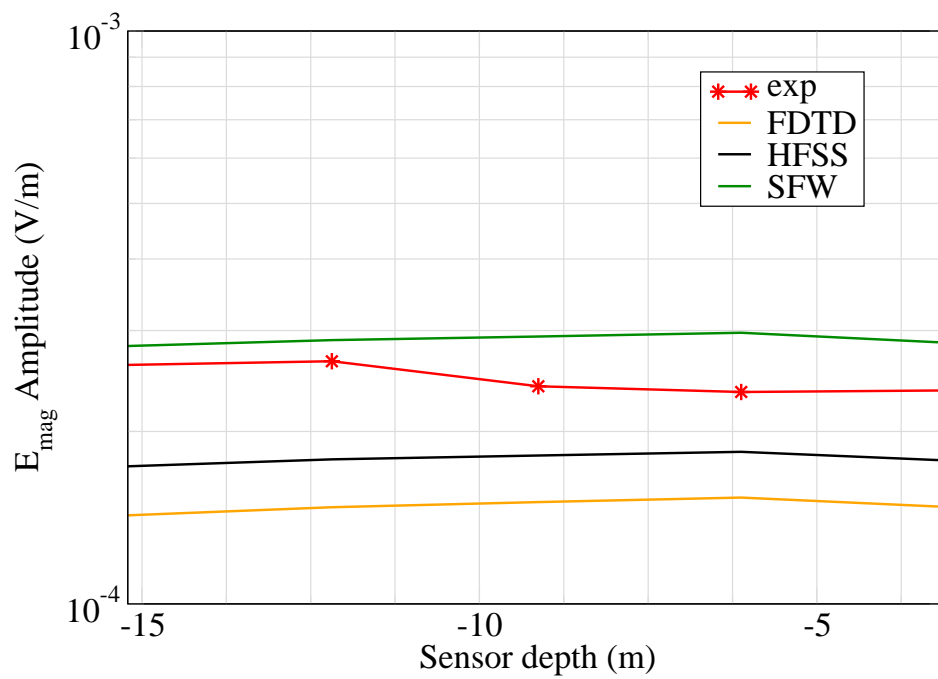


Figure 6: E_{mag} .

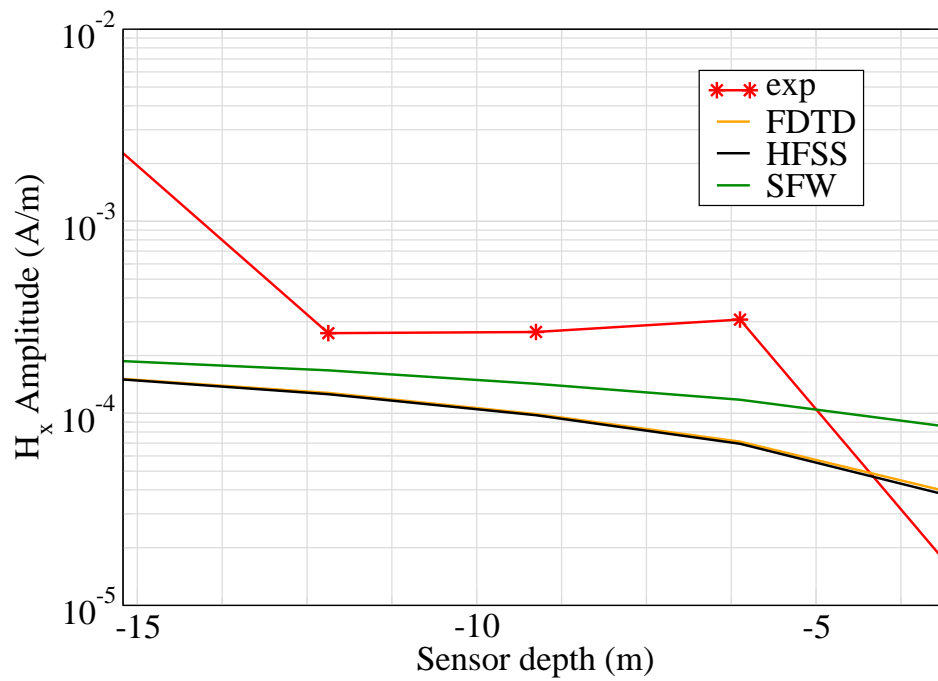


Figure 7: H_x .

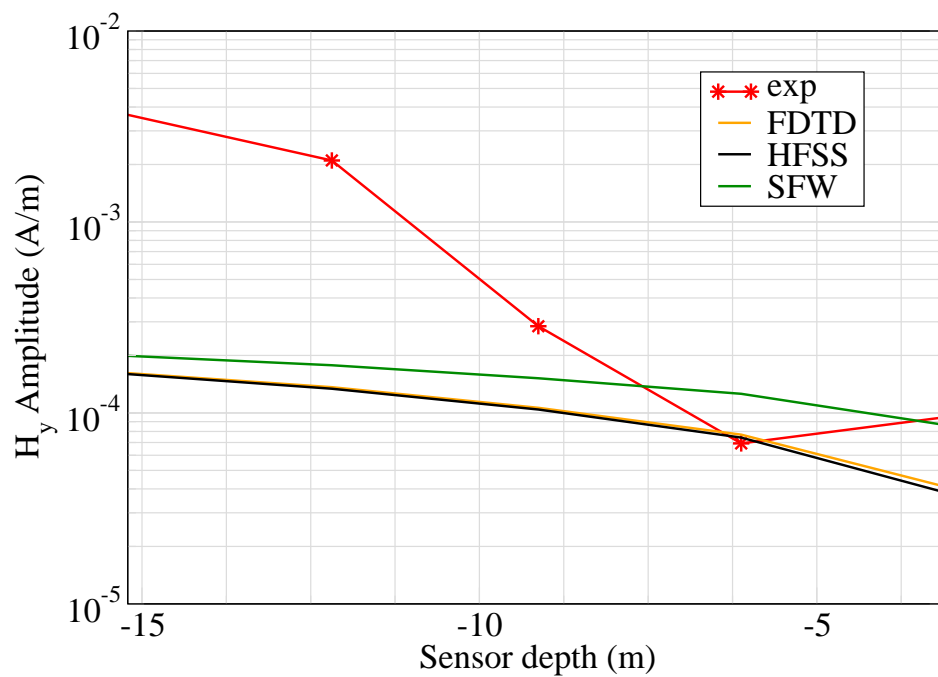


Figure 8: H_y .

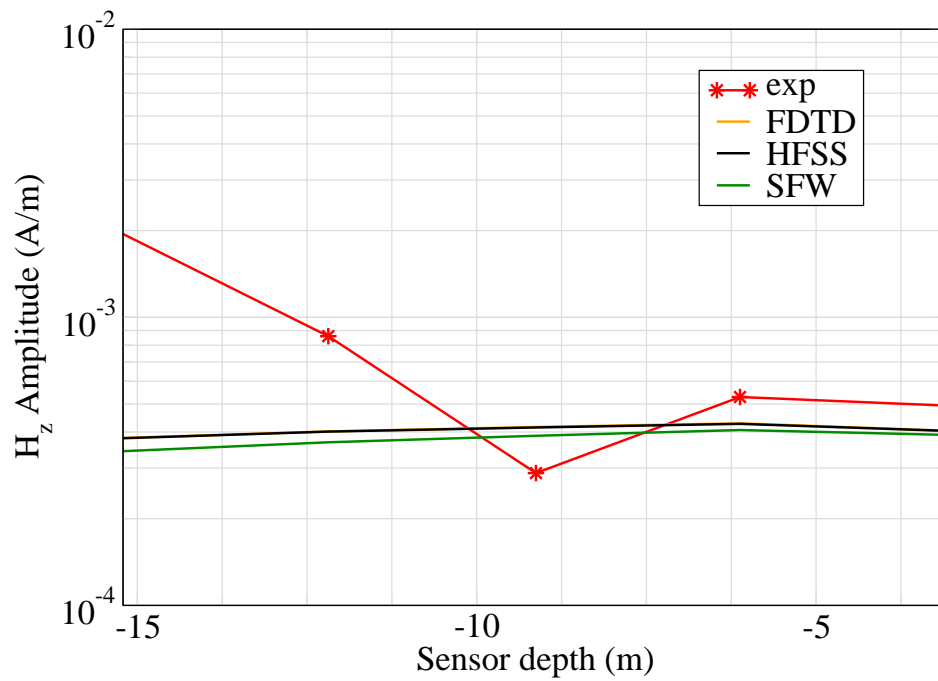


Figure 9: H_z .

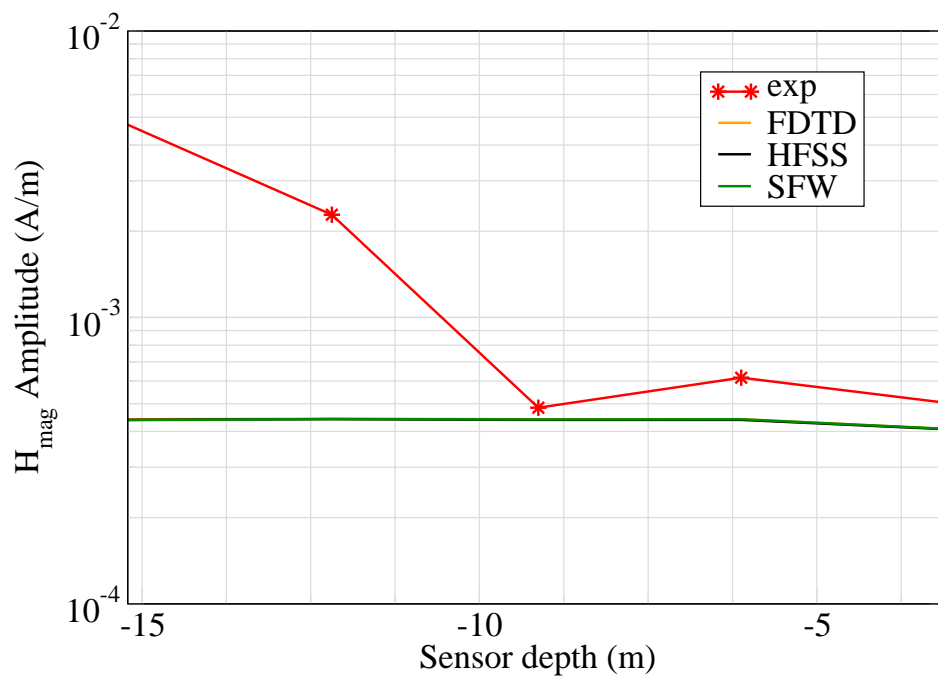


Figure 10: H_{mag} .

Experiment 4

Runs 101.01, 101.03, 101.05, 101.07 and 101.11

Experiment Date: 9/14/2010

1 Discussion

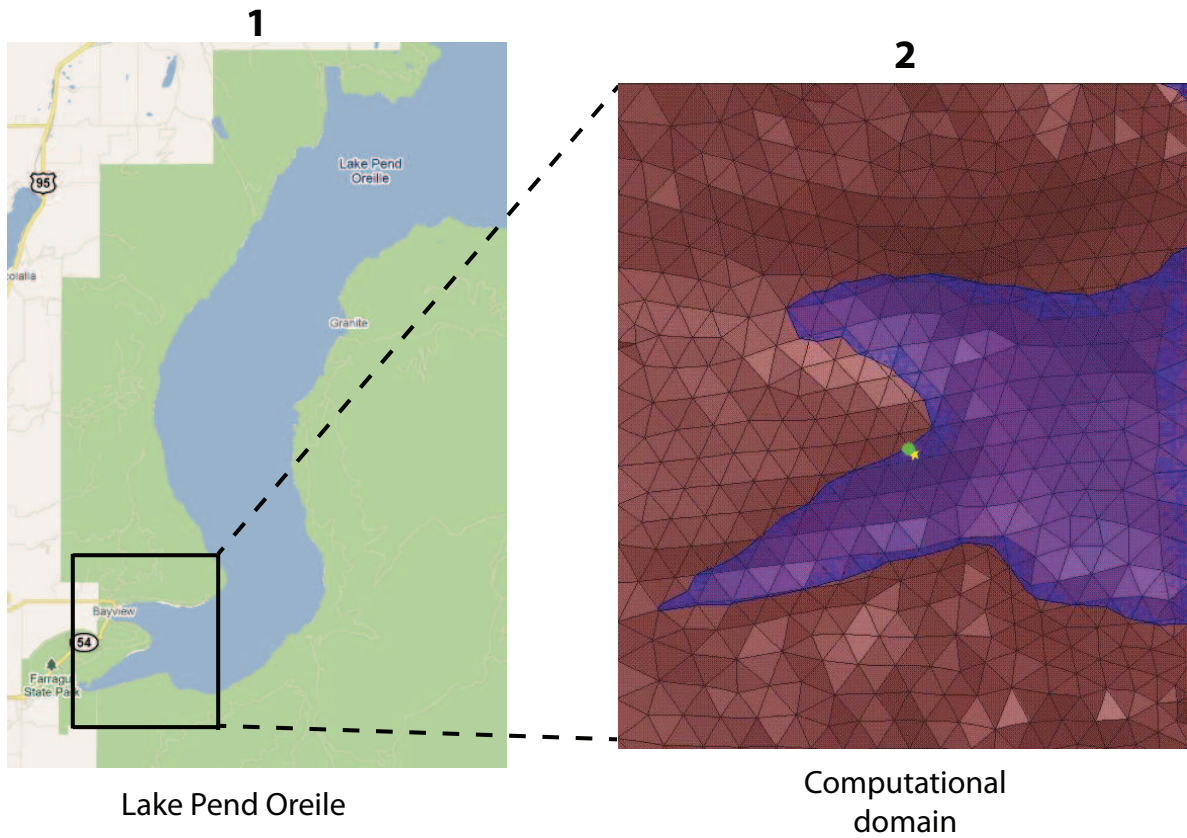


Figure 1: Sensor and source locations; see test report. Sensor is represented by the yellow star; source start and end points represented by green circle and red square.

Source Parameters

- Source Type: HMD (Coil: 3.66 m by 3.66 m with 12 turns).
- Source Strength: 3,290.6 A-m².

- $f = 81$ Hz.

Environment

- Air: $\sigma = 0$ S/m and $\epsilon_r = 1$
- Water: $\sigma = 0.01$ S/m and $\epsilon_r = 81$
- Mud: $\sigma = 0.0012$ S/m and $\epsilon_r = 1$

Table 1: Simulation Details

	FDTD	HFSS	QES/SFW
Domain Size	400 X 400 X 120 cells	40,174 tets	N/A
Cell Size (m)	5 X 5 X 5	N/A	N/A
Time Step (ns)	9.6	N/A	N/A
Run Time (Hrs)	38.6	1.11	0.01
Water Depth (m)	N/A	N/A	18
Effective Source Area (m)	N/A	$l = 3.66$ $w = 3.66$	$r = 3.66$

Comments

- To implement reciprocity, three simulations per vector field are required for a total of six simulations. Run times correspond to the time required to conduct all six simulations.
- Computational time is based on actual elapsed real time. This number is highly subjective and based on how many other applications might be running at a particular time. However, the reported number is an indication of the amount of time typically needed for a particular simulation. The computer specs are: 16 CPU cores at 2.8 GHz.
- Run times for HFSS are given for a single frequency.
- QES is not applicable for electric or magnetic fields using magnetic source excitation.

2 Simulation Variables

Sensor_P1(x,y,z) [m]	(3227.2390,3496.5883,-3.4452)
Sensor_P2(x,y,z) [m]	(3227.2428,3496.5881,-15.0537)
Source_P1(x,y,z) [m]	(3163.7271,3561.9316,0)
Source_P2(x,y,z) [m]	(3163.7271,3561.9316,0)
Source_Plate_Separation [m]	N/A
Source_Size [m X m X #]	[3.658 X 3.658 X 12]
Source_Heading [deg]	0
Source_Voltage [V Peak]	19.7903
Source_Current [A Peak]	20.4933
Source_Frequency [Hz]	81

--- Extra Information ---

Source_Heading_Bounds [deg]	(N/A)
Average_Boat_Speed [m/s]	NaN
Source_Type	Magnetic source (portable)
Sensor_Type	PEMA
Bin_Size [sec]	[269,487,491,484,483]
Number_of_Datapoints	5
Lake_Origin (Easting,Northing)	(737736.502,696691.143)
Analysis_Date	Exp4_ScenSM_28-Jul-2011

3 Source and sensor locations

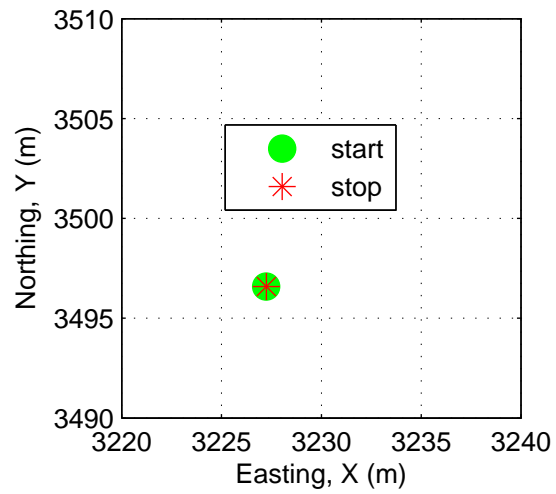
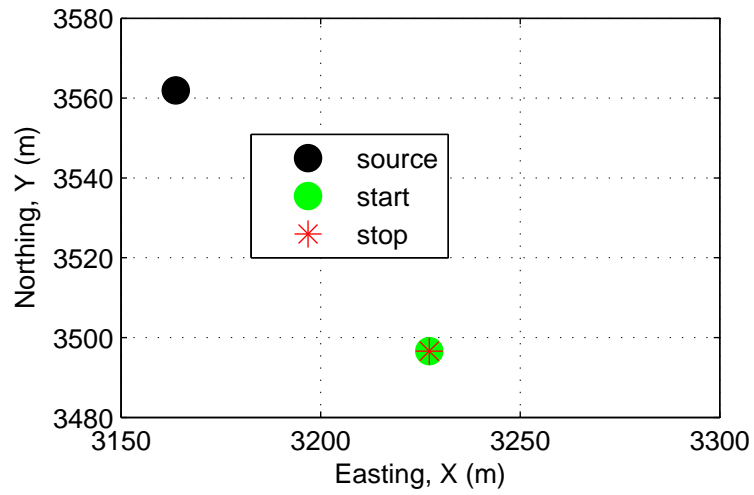


Figure 2: Source and sensor relationship.

4 Plots

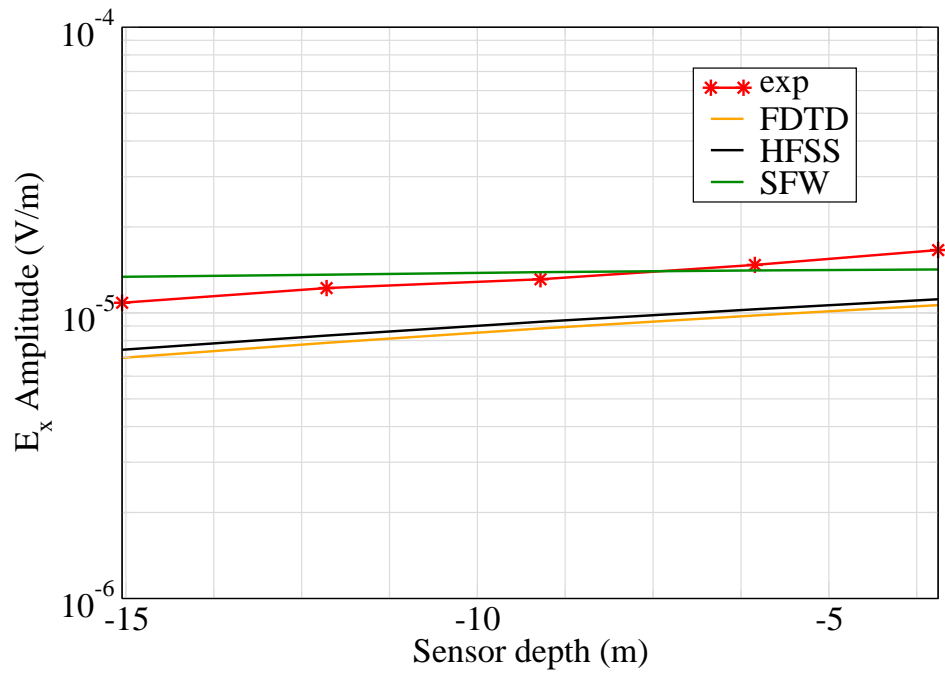


Figure 3: E_x .

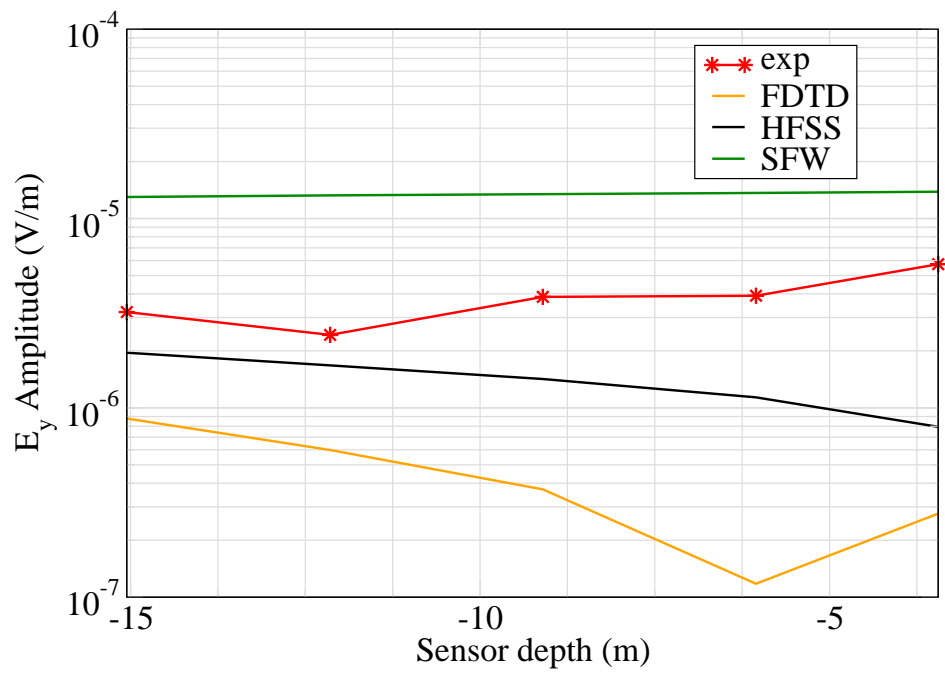


Figure 4: E_y .

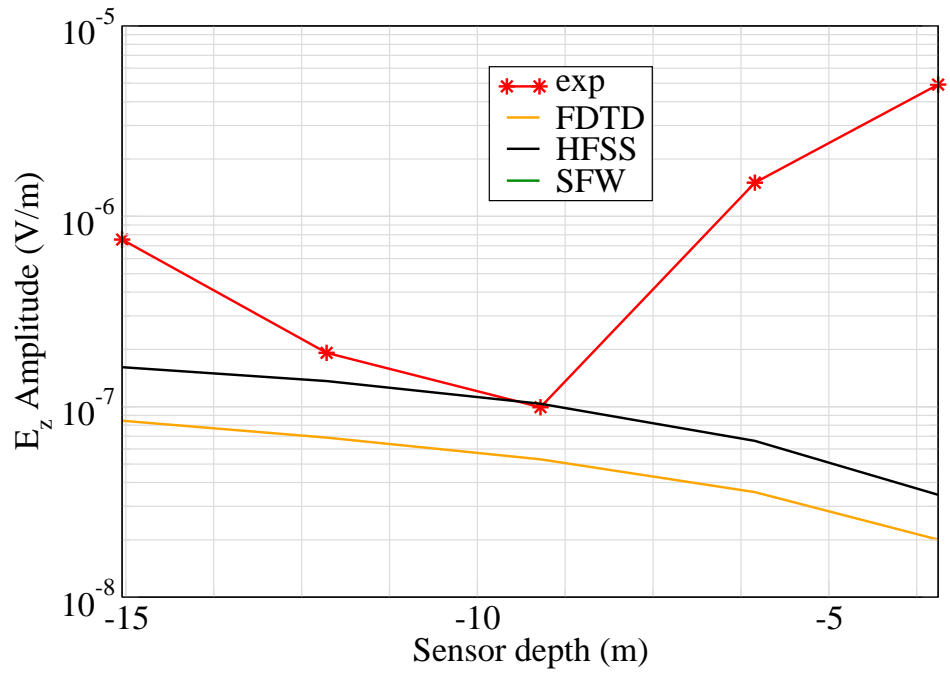


Figure 5: E_z .

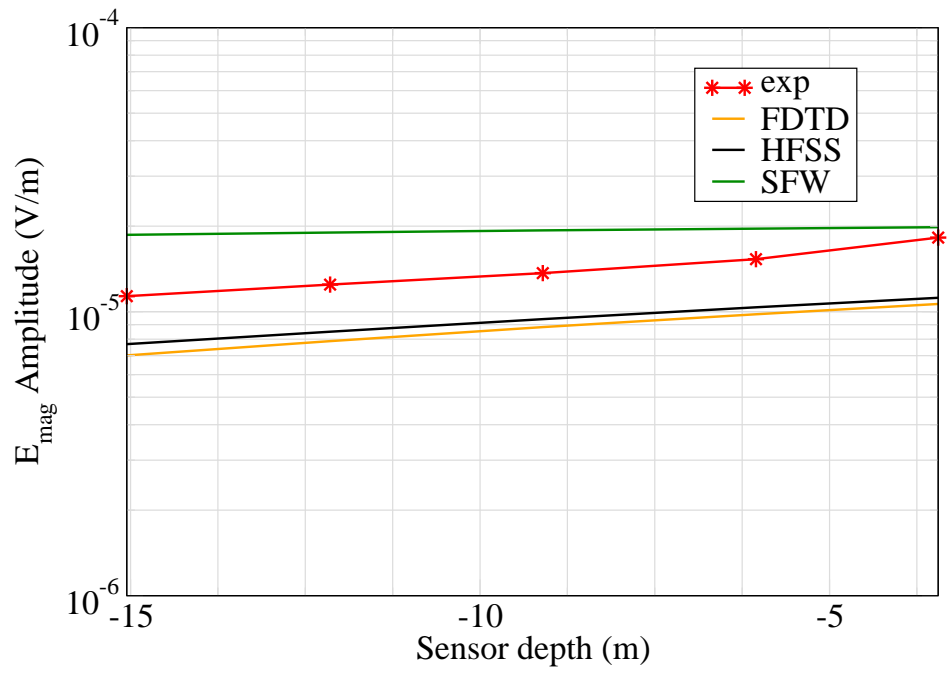


Figure 6: E_{mag} .

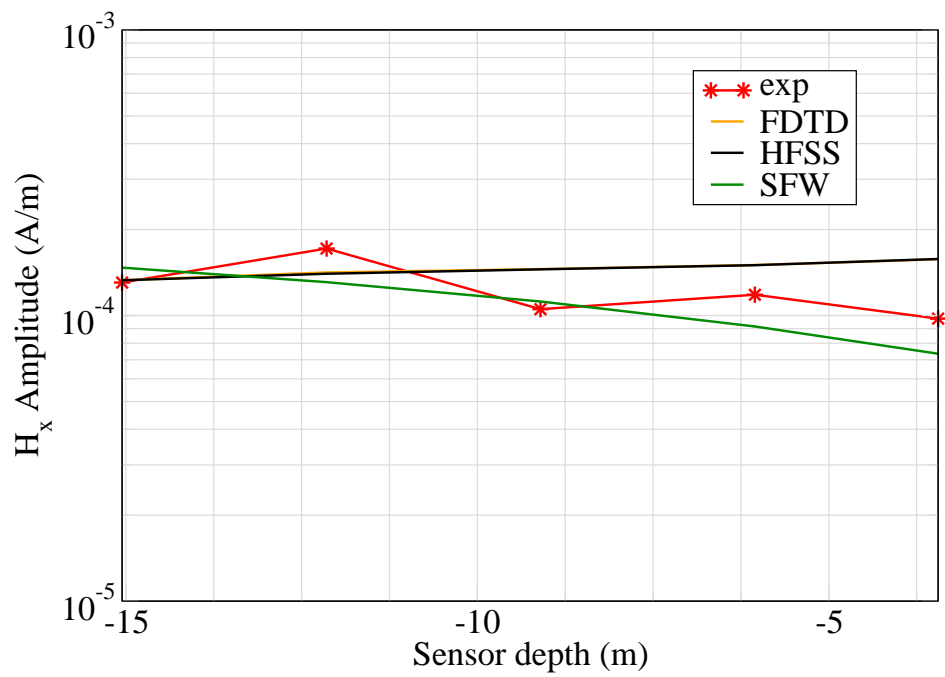


Figure 7: H_x .

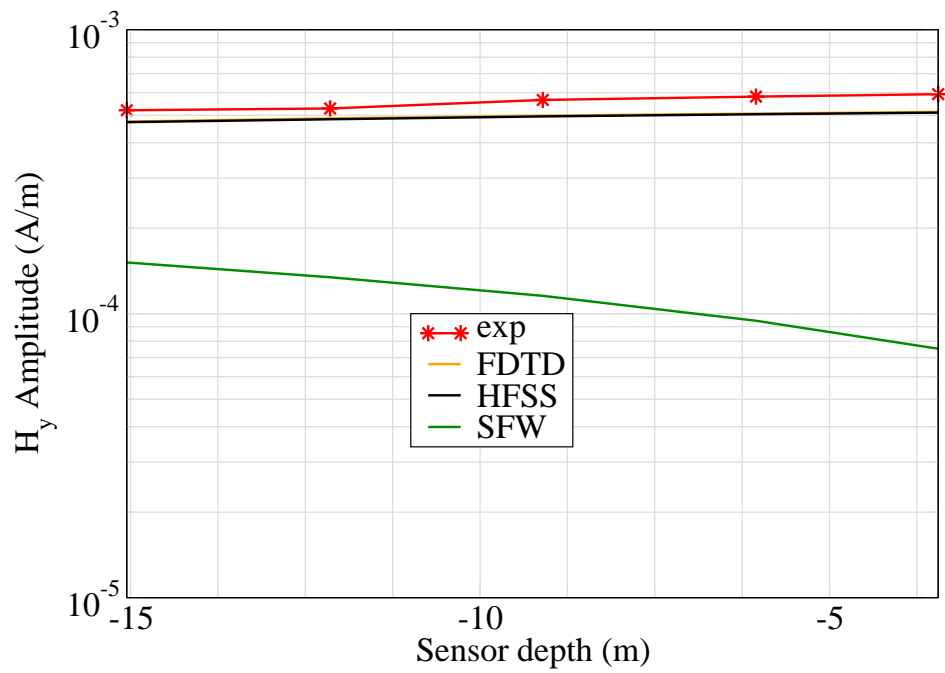


Figure 8: H_y .

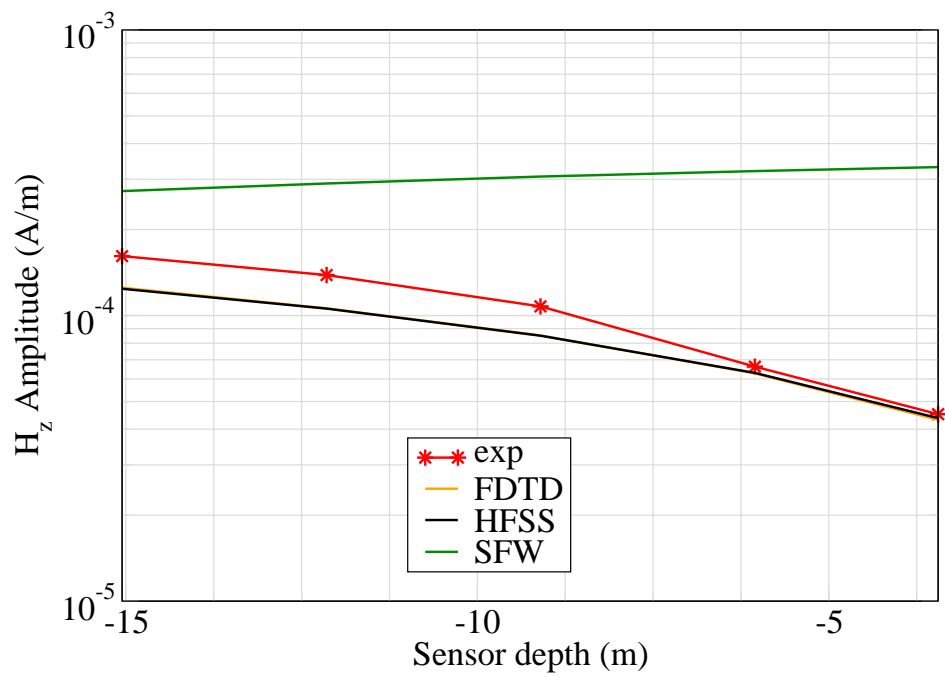


Figure 9: H_z .

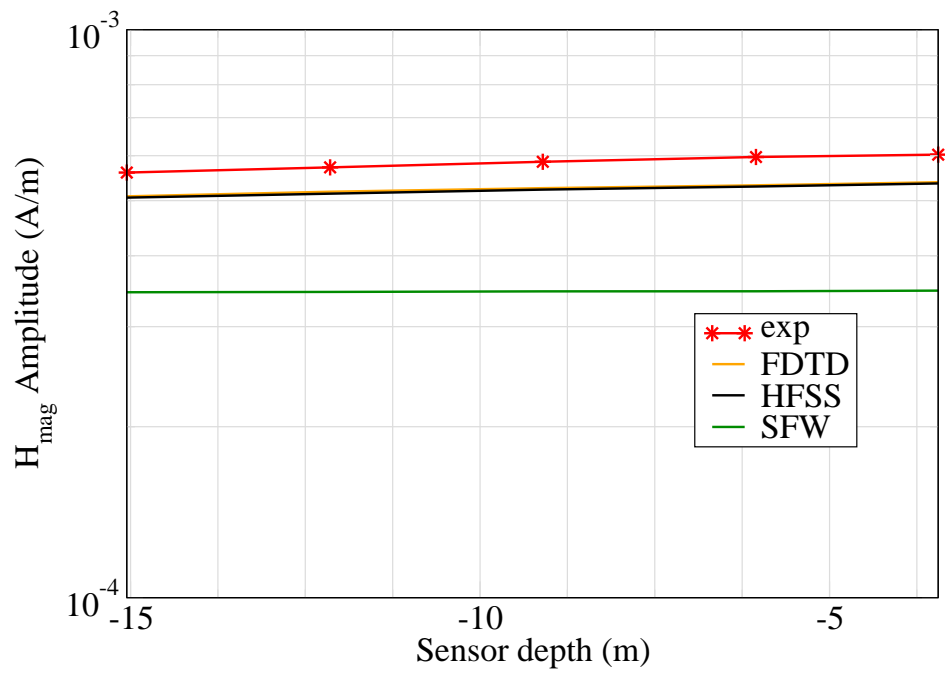


Figure 10: H_{mag} .

Experiment 4

Runs 202.02, 202.05, 202.08, 202.11, 202.14, 202.17, 202.20, 202.23, 202.26

Experiment Date: 9/17/2010

1 Discussion

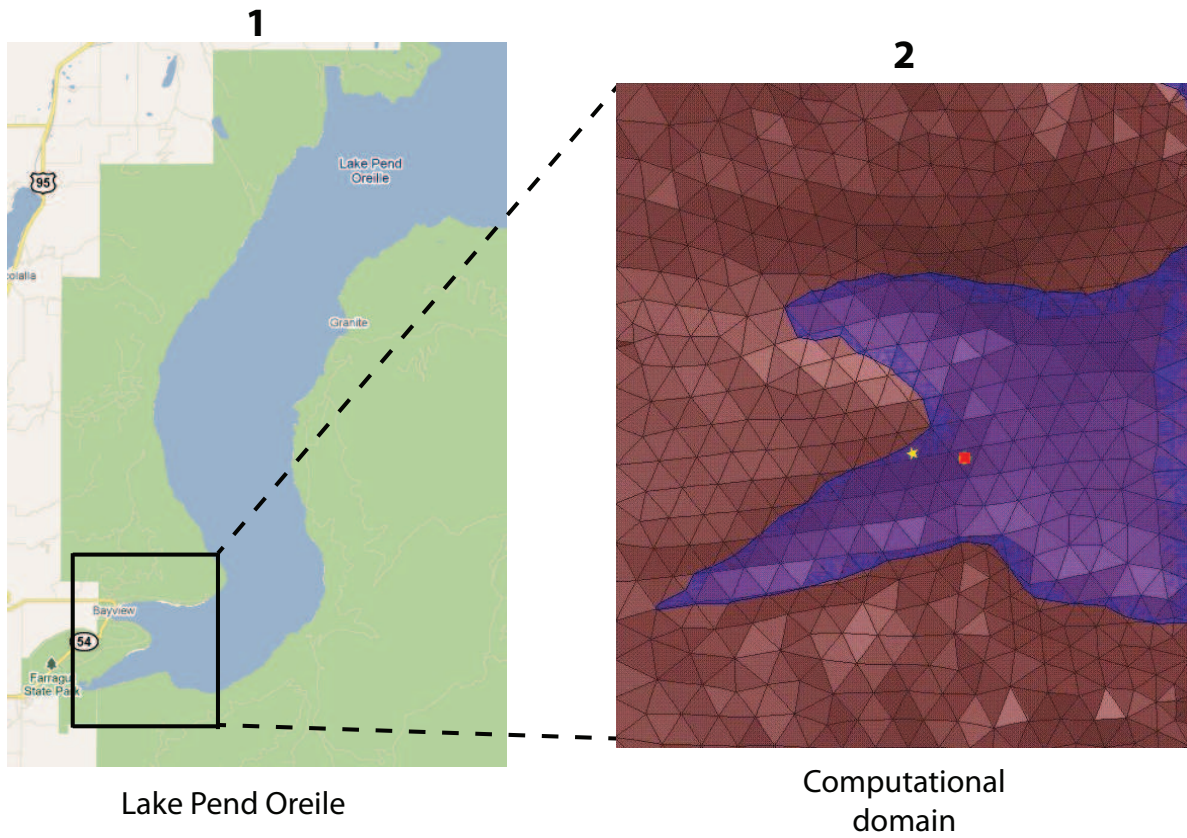


Figure 1: Sensor and source locations; see test report. Sensor is represented by the yellow star; source start and end points represented by green circle and red square.

Source Parameters

- Source Type: HED (Electric Truss: plates 0.61 m by 0.61 m separated by 14.681 m).
- Source Strength: 73.01 A-m.

- $f = 100$ Hz.

Environment

- Air: $\sigma = 0$ S/m and $\epsilon_r = 1$
- Water: $\sigma = 0.01$ S/m and $\epsilon_r = 81$
- Mud: $\sigma = 0.0012$ S/m and $\epsilon_r = 1$

Table 1: Simulation Details

	FDTD	HFSS	QES/SFW
Domain Size	200 X 200 X 120 cells	41,657 tets	N/A
Cell Size (m)	10 X 10 X 5	N/A	N/A
Time Step (ns)	13.6	N/A	N/A
Run Time (Hrs)	42.75	0.35	0.01
Water Depth (m)	N/A	N/A	18
Effective Source Area (m)	N/A	$l = 0.61$ $w = 0.61$	$r = 0.059$

Comments

- To implement reciprocity, three simulations per vector field are required for a total of six simulations. Run times correspond to the time required to conduct all six simulations.
- Computational time is based on actual elapsed real time. This number is highly subjective and based on how many other applications might be running at a particular time. However, the reported number is an indication of the amount of time typically needed for a particular simulation. The computer specs are: 16 CPU cores at 2.8 GHz.
- Run times for HFSS are given for a single frequency.
- QES is not applicable for magnetic fields using electric source excitation.

2 Simulation Variables

Sensor_P1(x,y,z) [m]	(3098.7884,2682.2949,-78.7187)
Sensor_P2(x,y,z) [m]	(3098.7884,2682.2949,-78.8356)
Source_P1(x,y,z) [m]	(3795.3552,3460.4635,-17.3585)
Source_P2(x,y,z) [m]	(3795.3552,3460.4635,-146.8339)
Source_Plate_Separation [m]	14.681
Source_Size [m X m X #]	[0.610 X 0.610 X 2]
Source_Heading [deg]	204.5294
Source_Voltage [V Peak]	312.7811
Source_Current [A Peak]	4.9727
Source_Frequency [Hz]	100

--- Extra Information ---

Source_Heading_Bounds [deg]	(197,212)
Average_Boat_Speed [m/s]	NaN
Source_Type	Electric truss (truss)
Sensor_Type	PEMA
Bin_Size [sec]	[84,83,83,81,81,44,80,80,79]
Number_of_Datapoints	9
Lake_Origin (Easting,Northing)	(737736.502,696691.143)
Analysis_Date	Exp4_ScenSN_28-Jul-2011

3 Boat Path

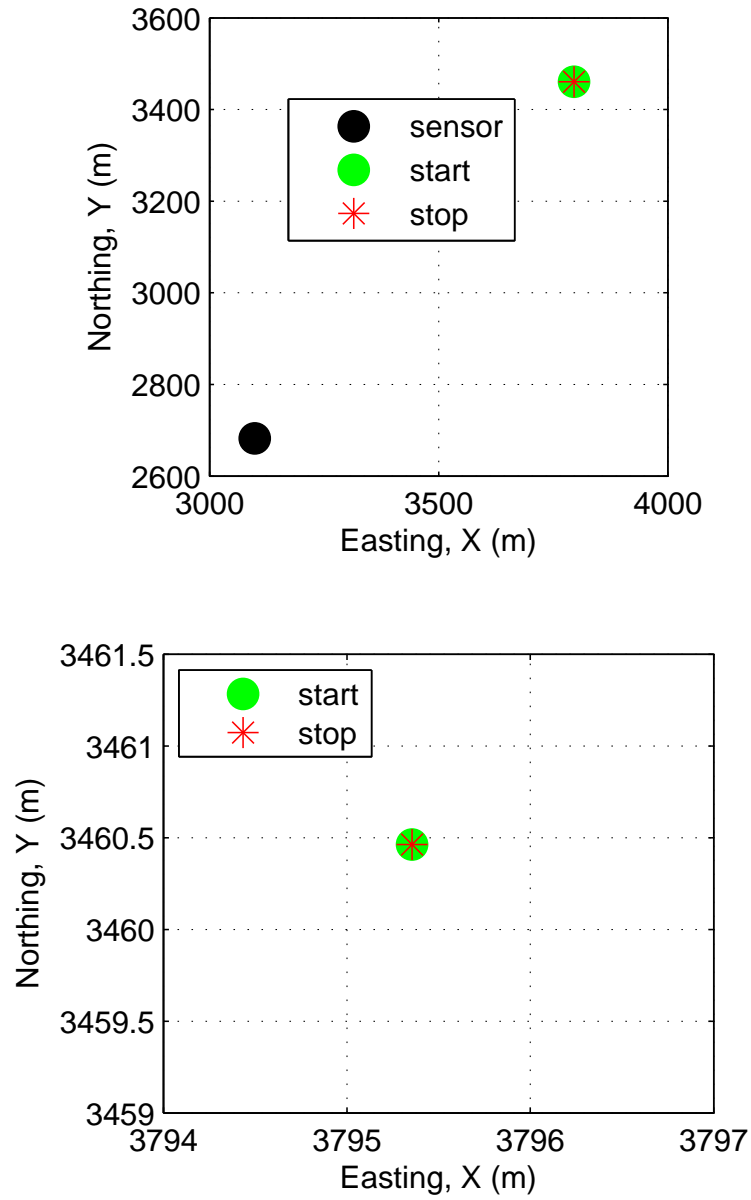


Figure 2: Source and sensor relationship.

4 Plots

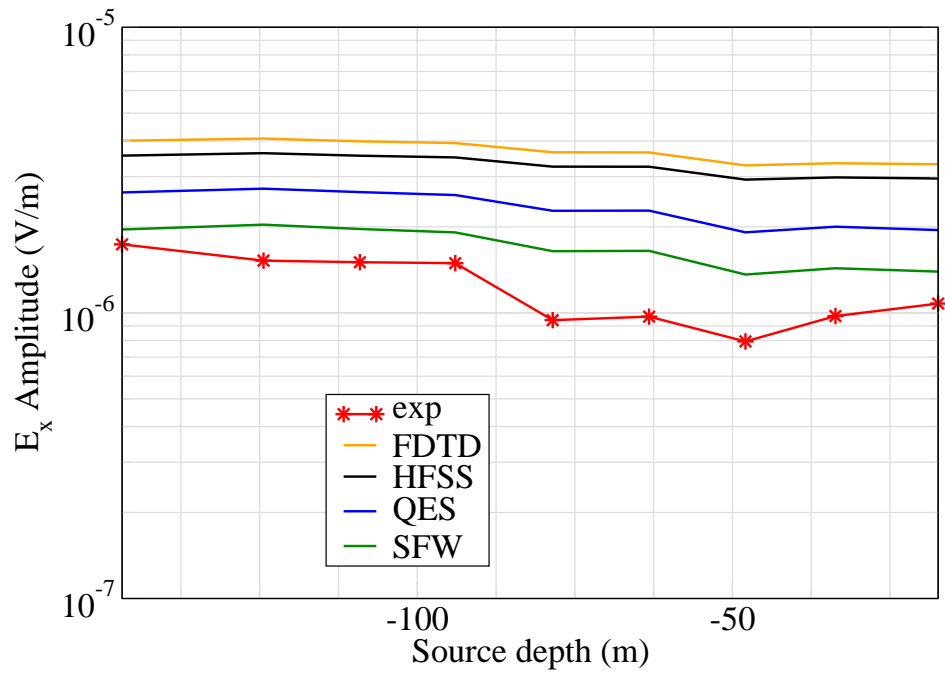


Figure 3: E_x .

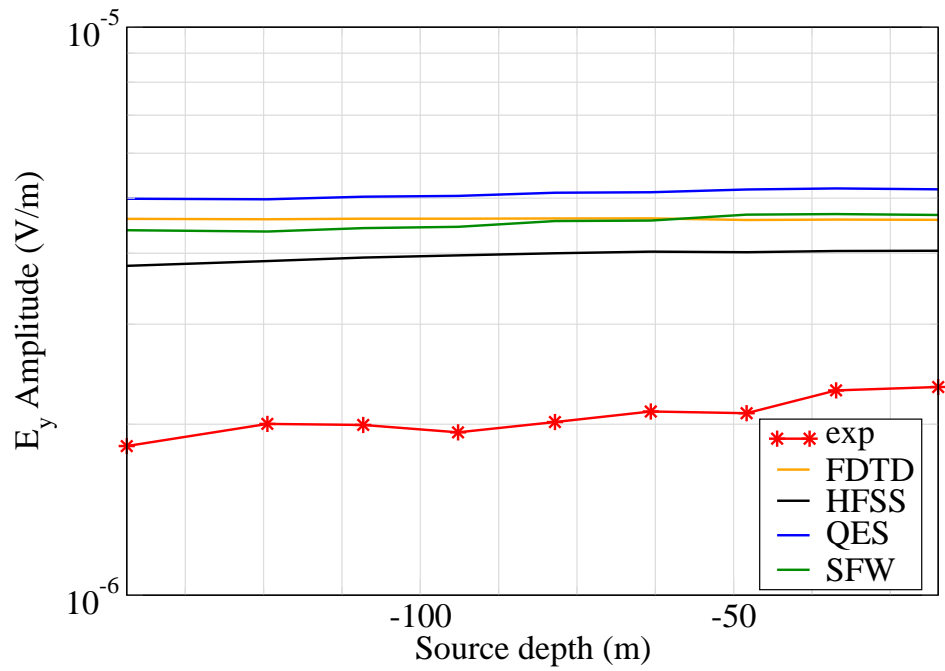


Figure 4: E_y .

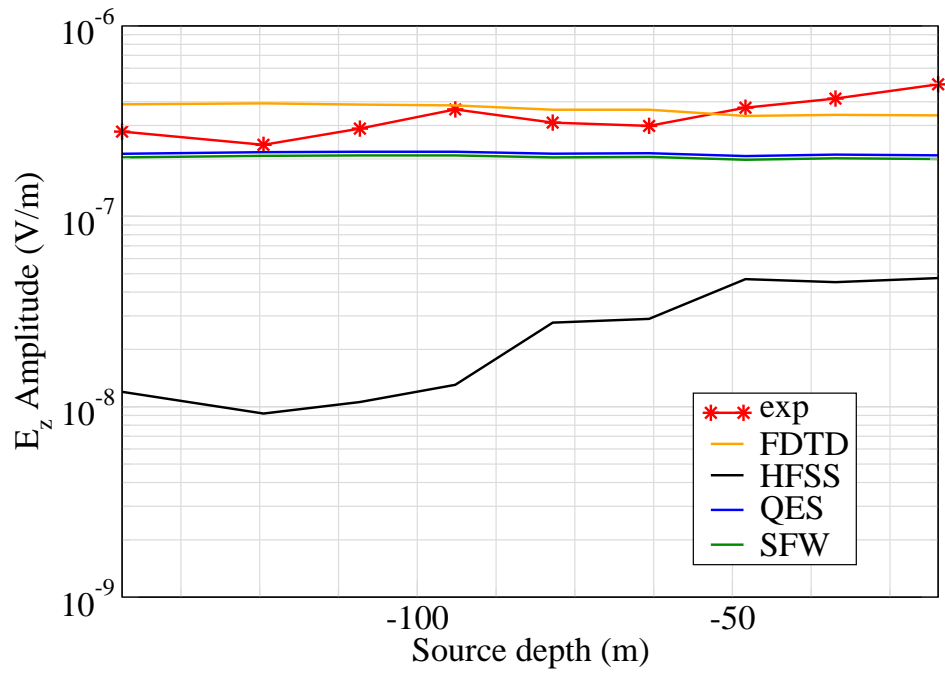


Figure 5: E_z .

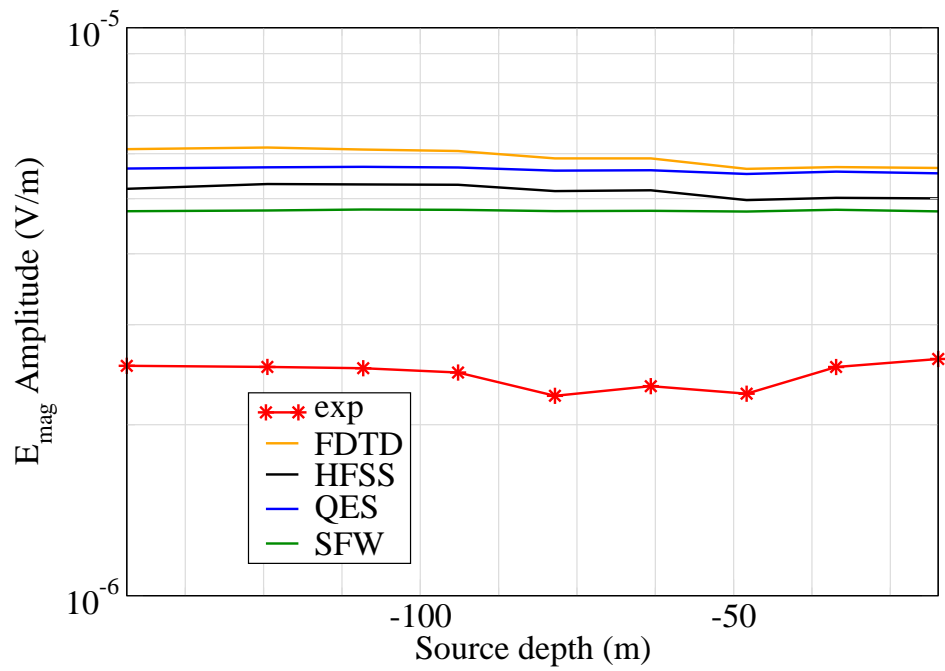


Figure 6: E_{mag} .

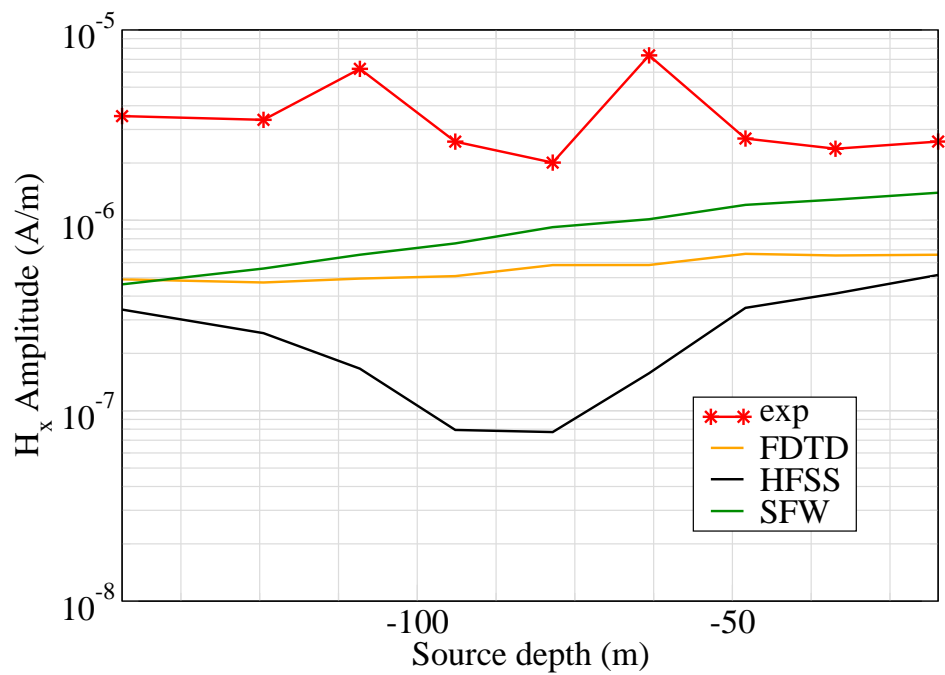


Figure 7: H_x .

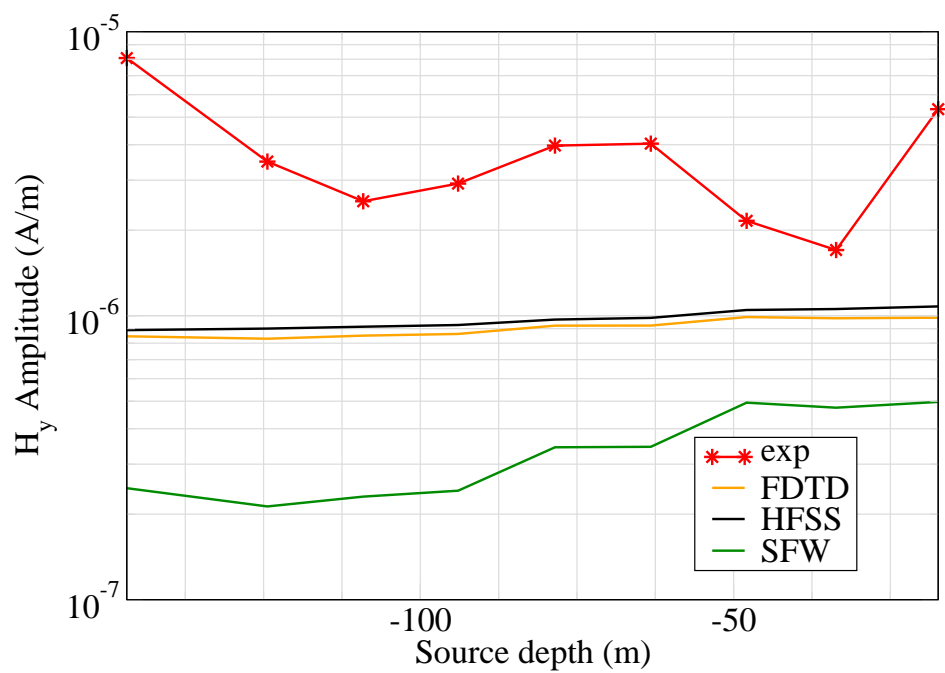


Figure 8: H_y .

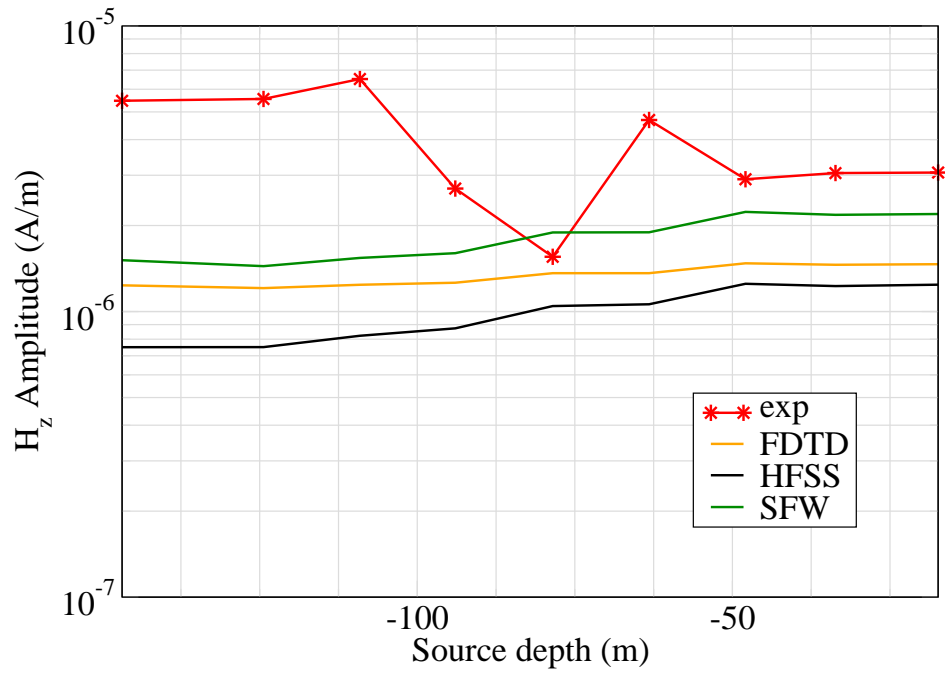


Figure 9: H_z .

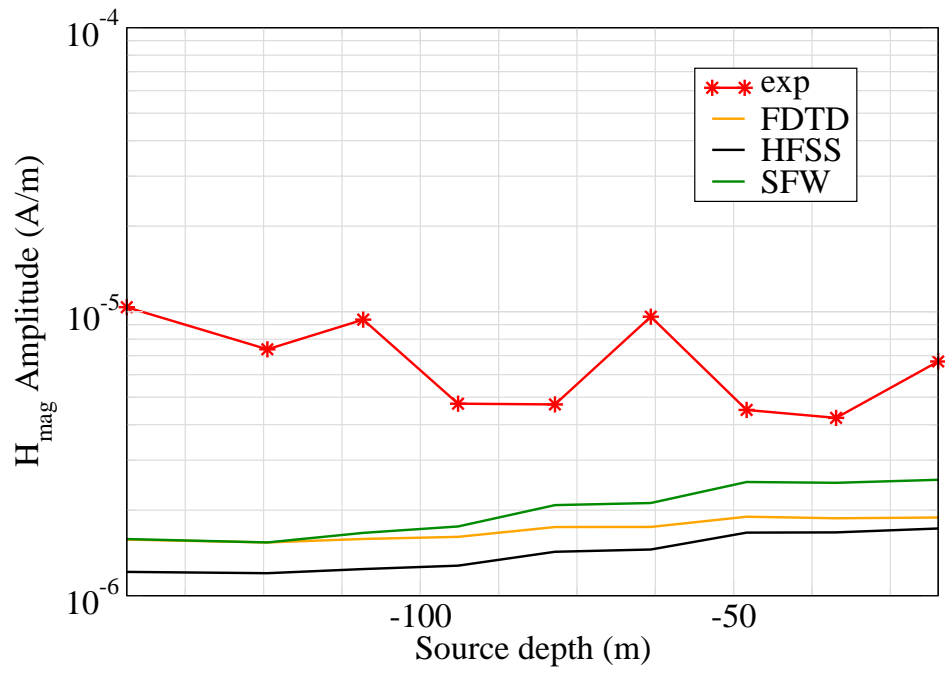


Figure 10: H_{mag} .

Experiment 4

Runs 403.27, 403.39, 403.45, 403.51

Experiment Date: 9/16/2010

1 Discussion

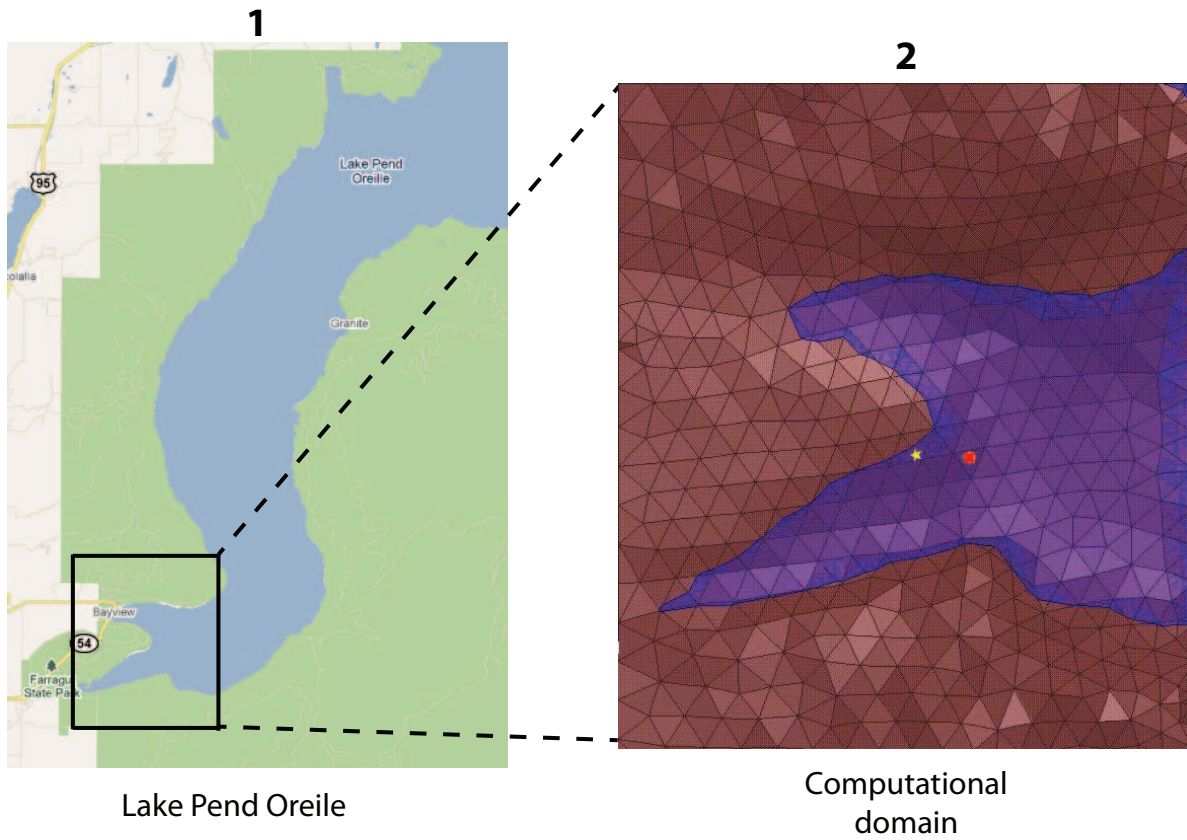


Figure 1: Sensor and source locations; see test report. Sensor is represented by the yellow star; source start and end points represented by green circle and red square.

Source Parameters

- Source Type: HED (Electric Truss: plates 0.61 m by 0.61 m separated by 14.681 m).
- Source Strength: 67.38 A-m.

- $f = 1000$ Hz.

Environment

- Air: $\sigma = 0$ S/m and $\epsilon_r = 1$
- Water: $\sigma = 0.01$ S/m and $\epsilon_r = 81$
- Mud: $\sigma = 0.0012$ S/m and $\epsilon_r = 1$

Table 1: Simulation Details

	FDTD	HFSS	QES/SFW
Domain Size	200 X 200 X 120 cells	42,233 tets	N/A
Cell Size (m)	10 X 10 X 5	N/A	N/A
Time Step (ns)	13.6	N/A	N/A
Run Time (Hrs)	43.25	0.42	0.01
Water Depth (m)	N/A	N/A	18
Effective Source Area (m)	N/A	$l = 0.61$ $w = 0.61$	$r = 0.059$

Comments

- To implement reciprocity, three simulations per vector field are required for a total of six simulations. Run times correspond to the time required to conduct all six simulations.
- Computational time is based on actual elapsed real time. This number is highly subjective and based on how many other applications might be running at a particular time. However, the reported number is an indication of the amount of time typically needed for a particular simulation. The computer specs are: 16 CPU cores at 2.8 GHz.
- Run times for HFSS are given for a single frequency.
- QES is not applicable for magnetic fields using electric source excitation.

2 Simulation Variables

Sensor_P1(x,y,z) [m]	(3651.6965,3517.0424,-16.1685)
Sensor_P2(x,y,z) [m]	(3651.6965,3517.0424,-16.2731)
Source_P1(x,y,z) [m]	(3795.1181,3484.9927,-78.5153)
Source_P2(x,y,z) [m]	(3795.1181,3484.9927,-146.8339)
Source_Plate_Separation [m]	14.681
Source_Size [m X m X #]	[0.610 X 0.610 X 2]
Source_Heading [deg]	338.889
Source_Voltage [V Peak]	301.4797
Source_Current [A Peak]	4.5895
Source_Frequency [Hz]	1000

--- Extra Information ---

Source_Heading_Bounds [deg]	(338,340)
Average_Boat_Speed [m/s]	NaN
Source_Type	Electric truss (truss)
Sensor_Type	PEMA
Bin_Size [sec]	[81,81,81,81]
Number_of_Datapoints	4
Lake_Origin (Easting,Northing)	(737736.502,696691.143)
Analysis_Date	Exp4_ScenS0_28-Jul-2011

3 Boat Path

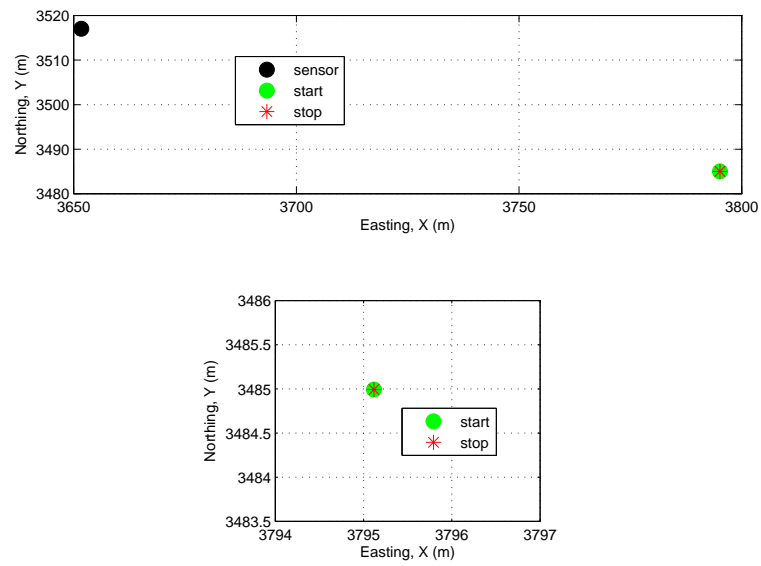


Figure 2: Source and sensor relationship.

4 Plots

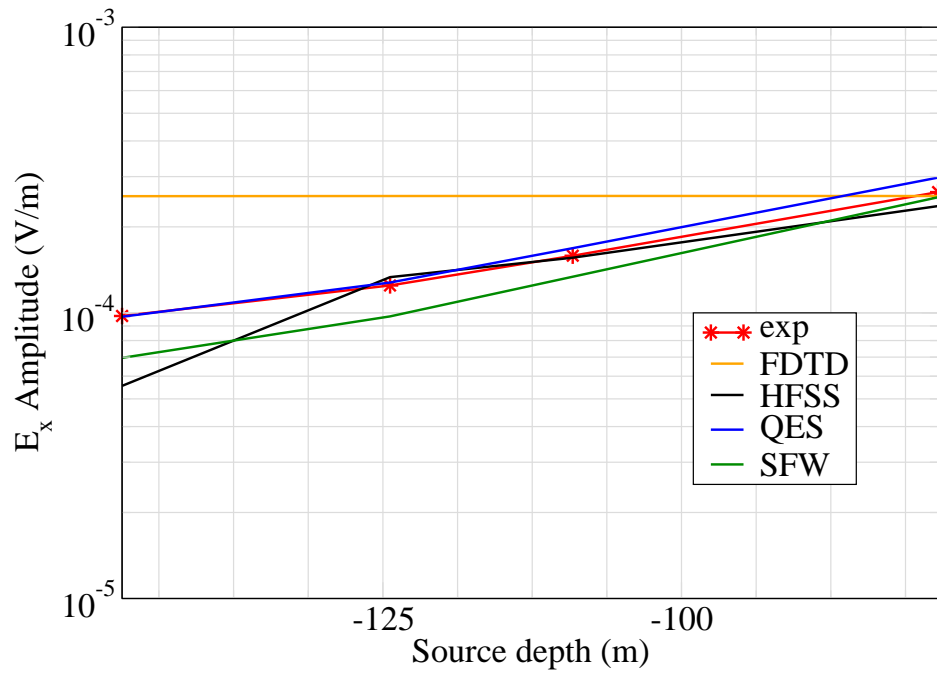


Figure 3: E_x .

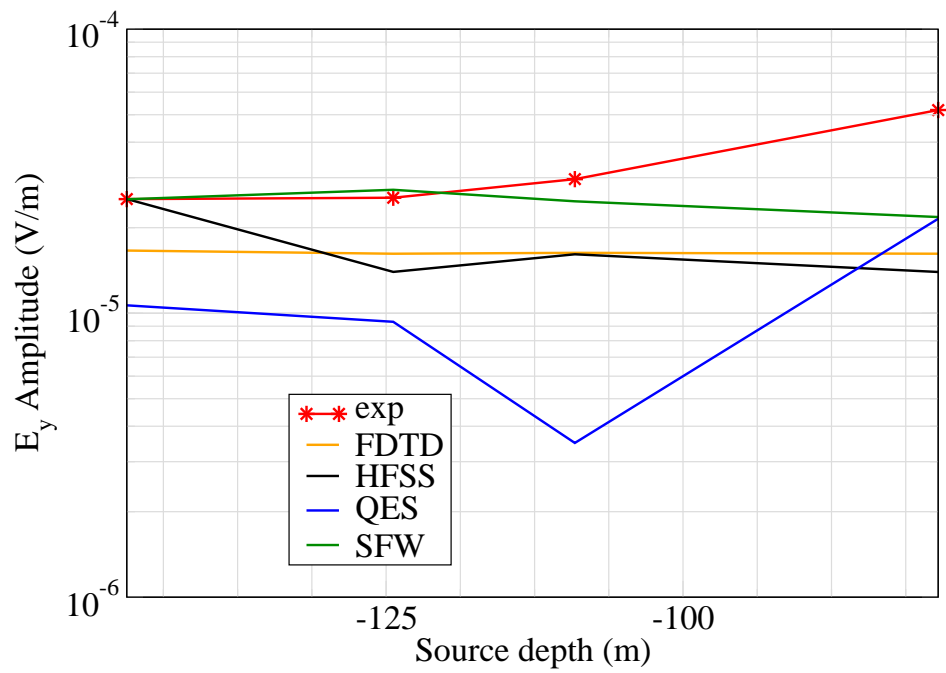


Figure 4: E_y .

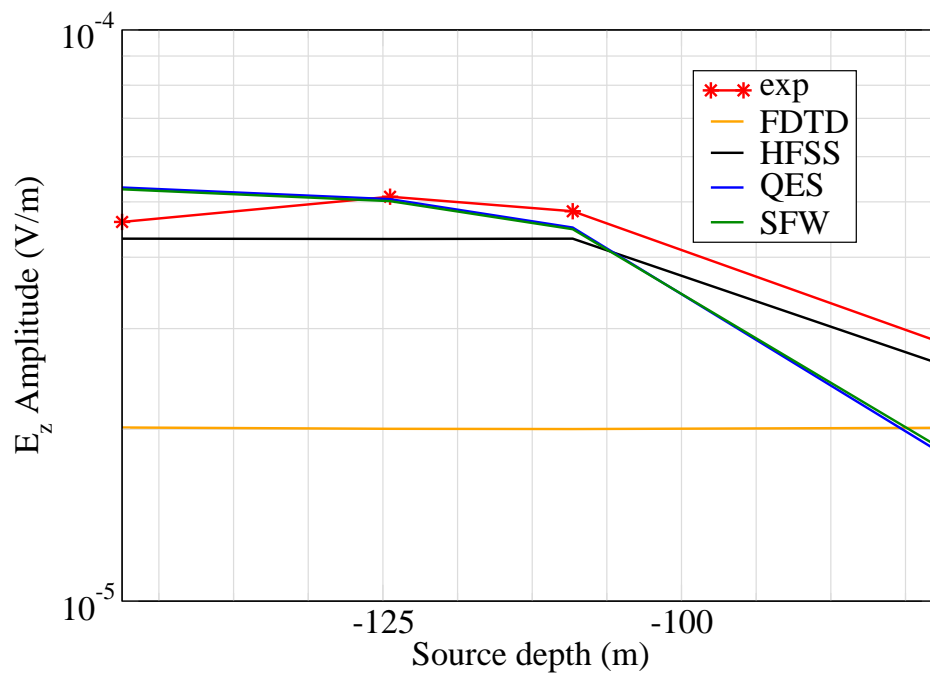


Figure 5: E_z .

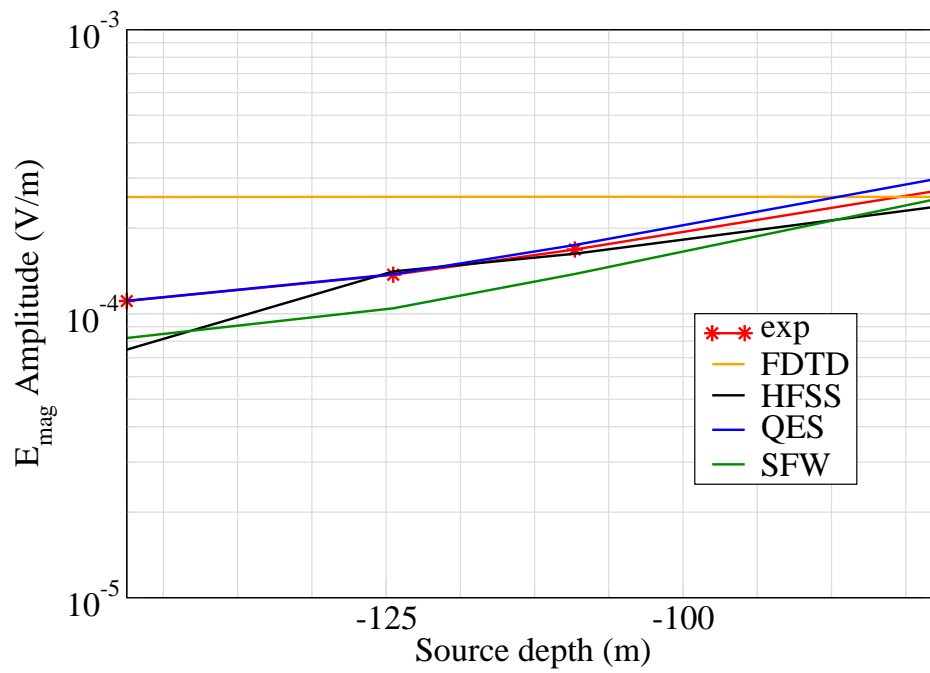


Figure 6: E_{mag} .

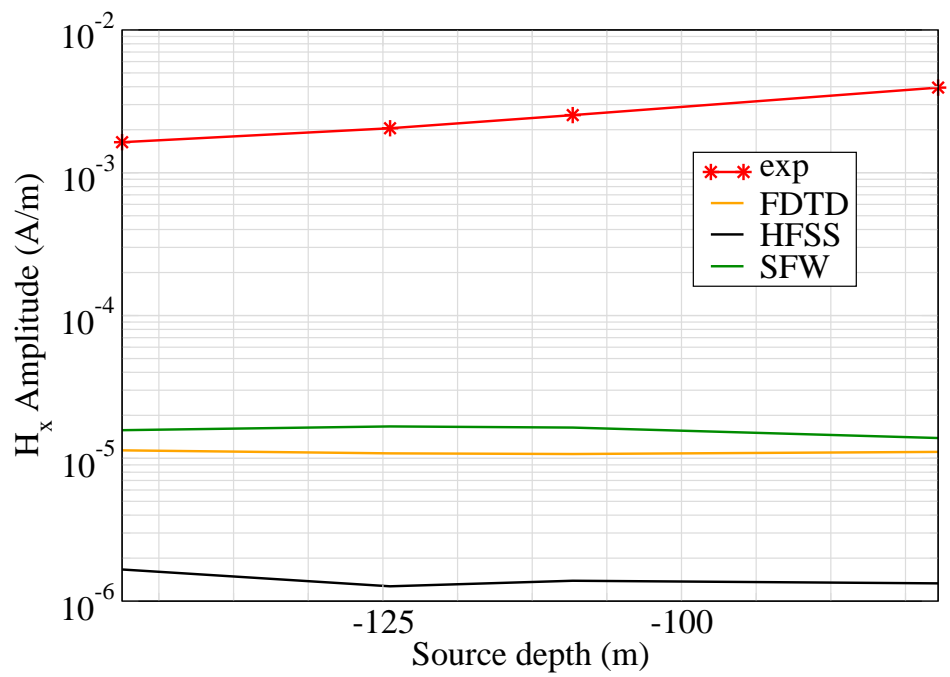


Figure 7: H_x .

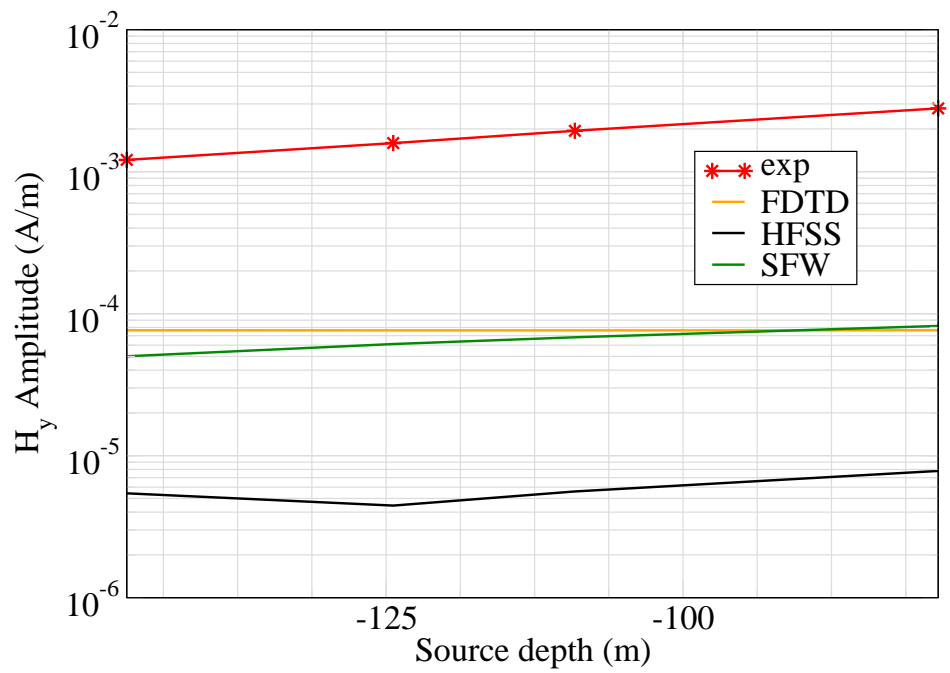


Figure 8: H_y .

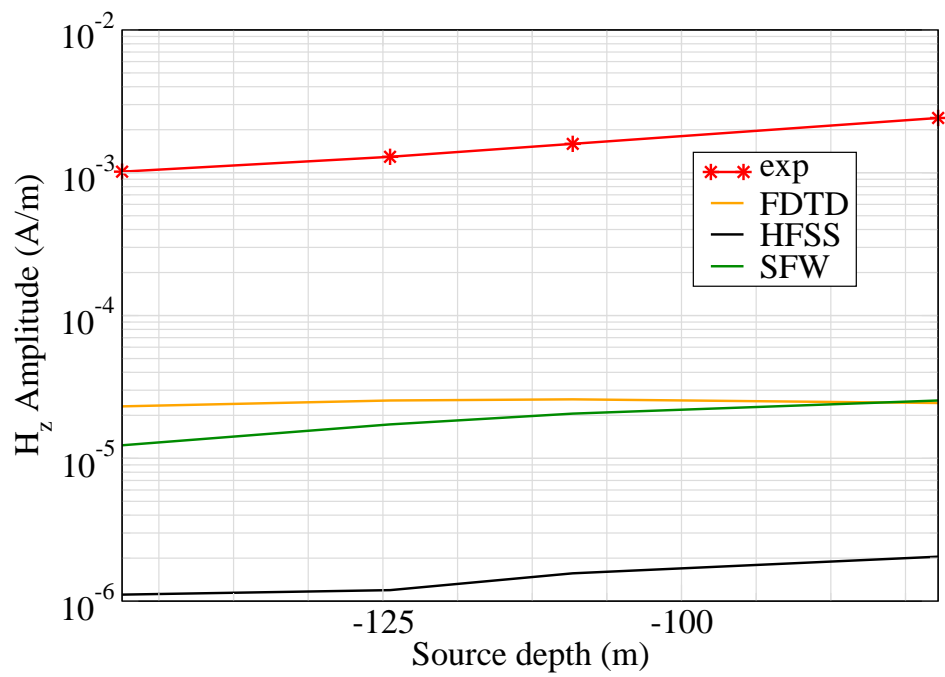


Figure 9: H_z .

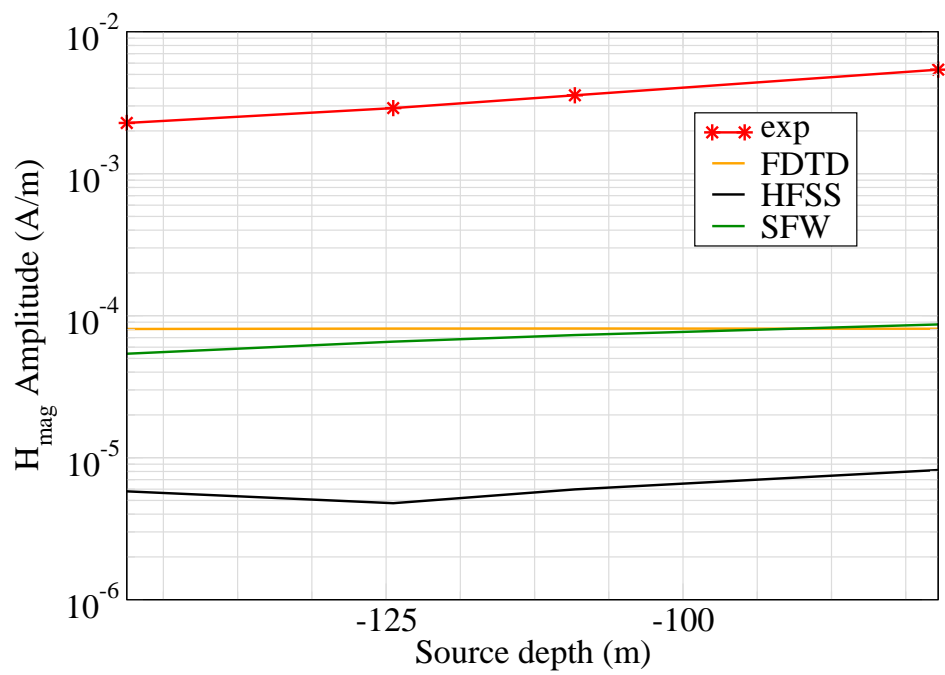


Figure 10: H_{mag} .

Experiment 4

Runs 202.01, 202.04, 202.07, 202.10, 202.13, 202.16, 202.19, 202.22, 202.25

Experiment Date: 9/17/2010

1 Discussion

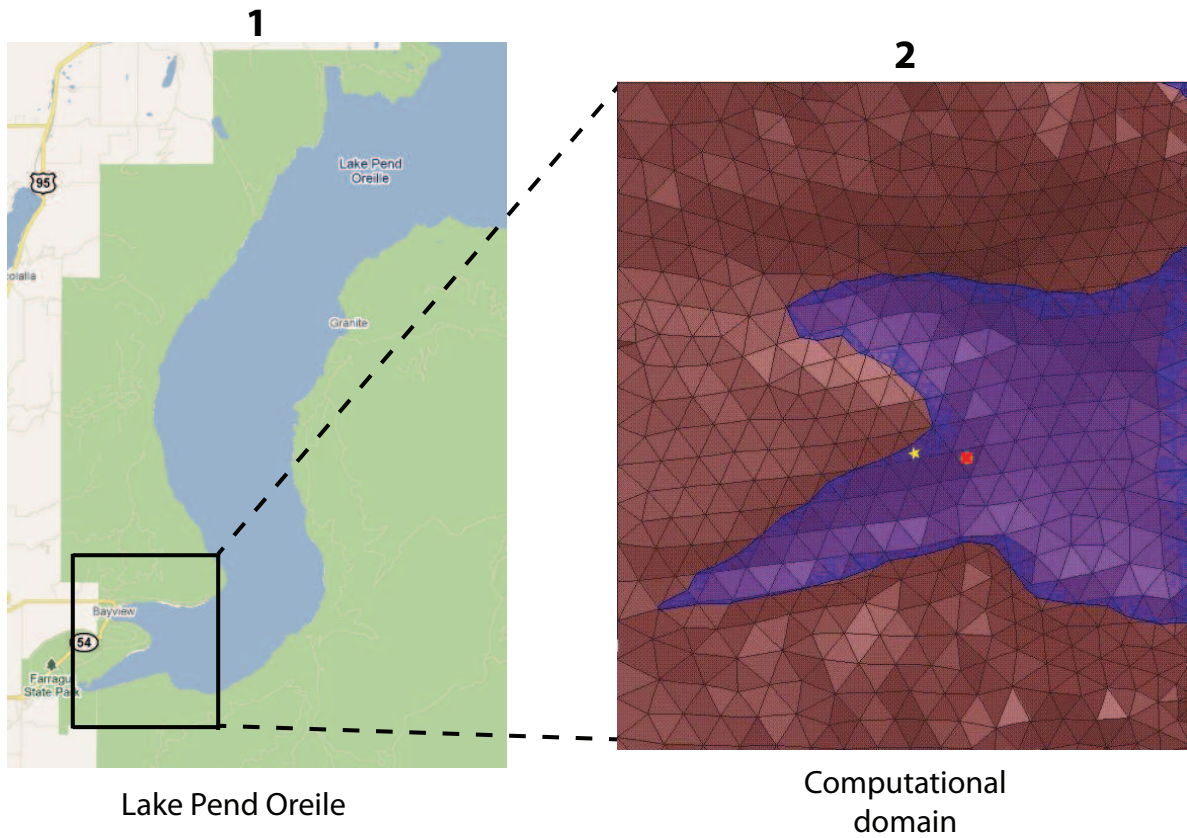


Figure 1: Sensor and source locations; see test report. Sensor is represented by the yellow star; source start and end points represented by green circle and red square.

Source Parameters

- Source Type: HED (Electric Truss: plates 0.61 m by 0.61 m separated by 14.681 m).
- Source Strength: 72.92 A-m.

- $f = 10$ Hz.

Environment

- Air: $\sigma = 0$ S/m and $\epsilon_r = 1$
- Water: $\sigma = 0.01$ S/m and $\epsilon_r = 81$
- Mud: $\sigma = 0.0012$ S/m and $\epsilon_r = 1$

Table 1: Simulation Details

	FDTD	HFSS	QES/SFW
Domain Size	200 X 200 X 120 cells	39,843 tets	N/A
Cell Size (m)	10 X 10 X 5	N/A	N/A
Time Step (ns)	13.6	N/A	N/A
Run Time (Hrs)	41.2	0.5	0.01
Water Depth (m)	N/A	N/A	18
Effective Source Area (m)	N/A	$l = 0.61$ $w = 0.61$	$r = 0.059$

Comments

- To implement reciprocity, three simulations per vector field are required for a total of six simulations. Run times correspond to the time required to conduct all six simulations.
- Computational time is based on actual elapsed real time. This number is highly subjective and based on how many other applications might be running at a particular time. However, the reported number is an indication of the amount of time typically needed for a particular simulation. The computer specs are: 16 CPU cores at 2.8 GHz.
- Run times for HFSS are given for a single frequency.
- QES is not applicable for magnetic fields using electric source excitation.

2 Simulation Variables

Sensor_P1(x,y,z) [m]	(3098.6912,2682.2875,-78.707)
Sensor_P2(x,y,z) [m]	(3098.6912,2682.2875,-78.8333)
Source_P1(x,y,z) [m]	(3795.9552,3459.9500,-17.3467)
Source_P2(x,y,z) [m]	(3795.9552,3459.9500,-146.8339)
Source_Plate_Separation [m]	14.681
Source_Size [m X m X #]	[0.610 X 0.610 X 2]
Source_Heading [deg]	206.4328
Source_Voltage [V Peak]	312.8837
Source_Current [A Peak]	4.9676
Source_Frequency [Hz]	10

--- Extra Information ---

Source_Heading_Bounds [deg]	(197,213)
Average_Boat_Speed [m/s]	NaN
Source_Type	Electric truss (truss)
Sensor_Type	PEMA
Bin_Size [sec]	[83,82,83,80,80,80,80,79,79]
Number_of_Datapoints	9
Lake_Origin (Easting,Northing)	(737736.502,696691.143)
Analysis_Date	Exp4_ScenSQ_28-Jul-2011

3 Boat Path

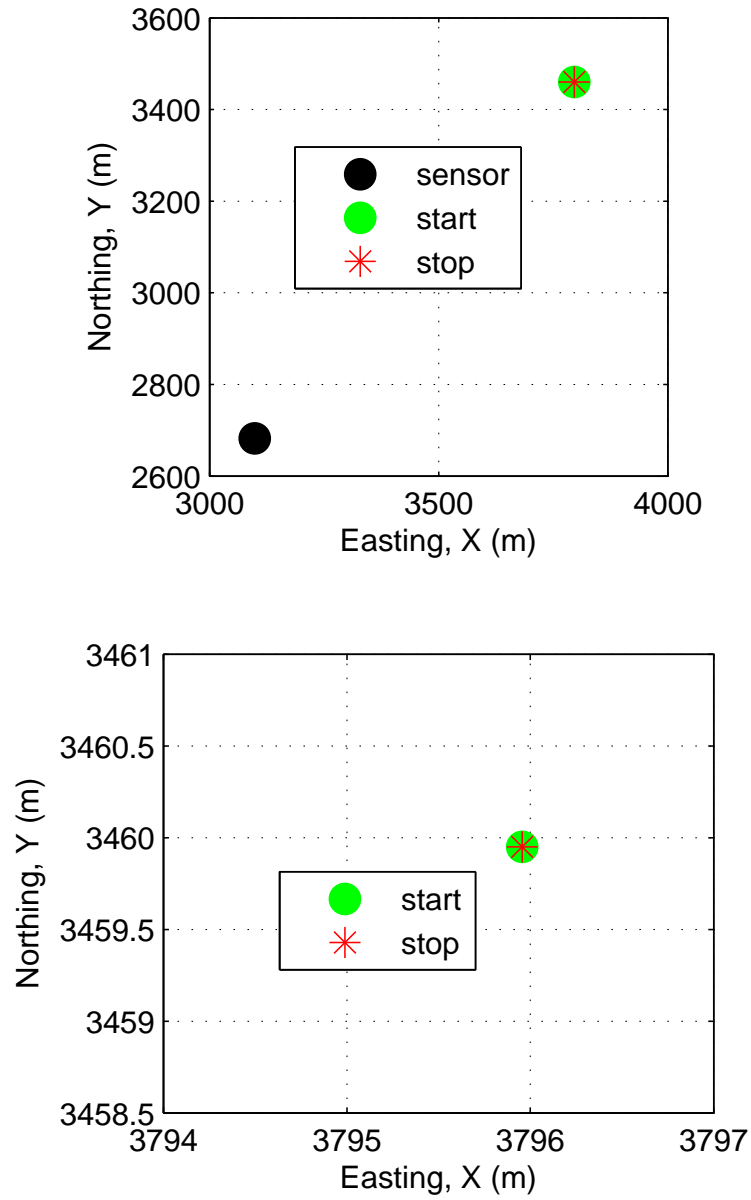


Figure 2: Source and sensor relationship.

4 Plots

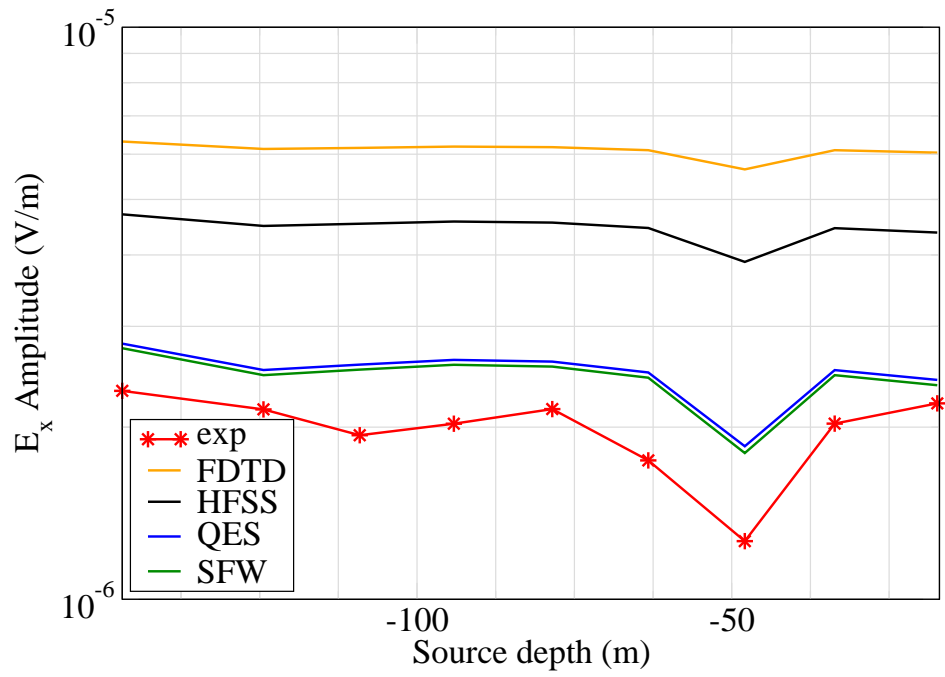


Figure 3: E_x .

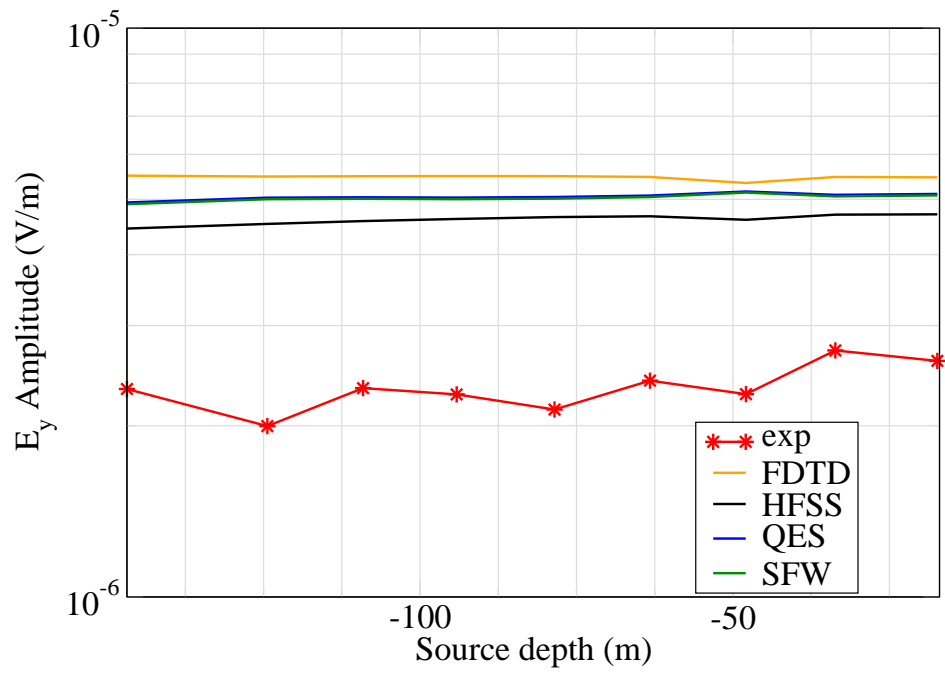


Figure 4: E_y .

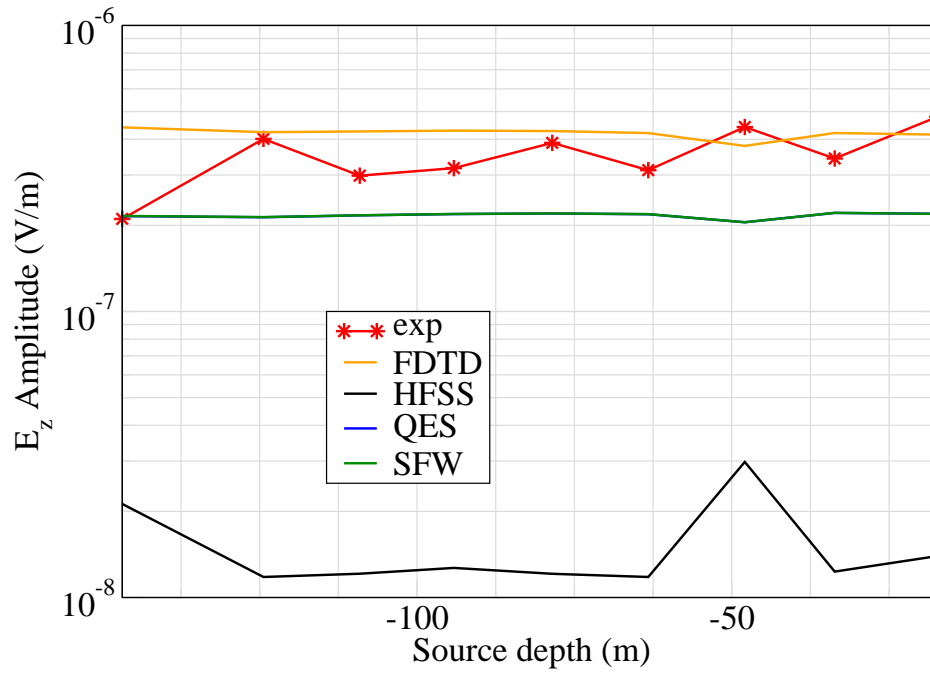


Figure 5: E_z .

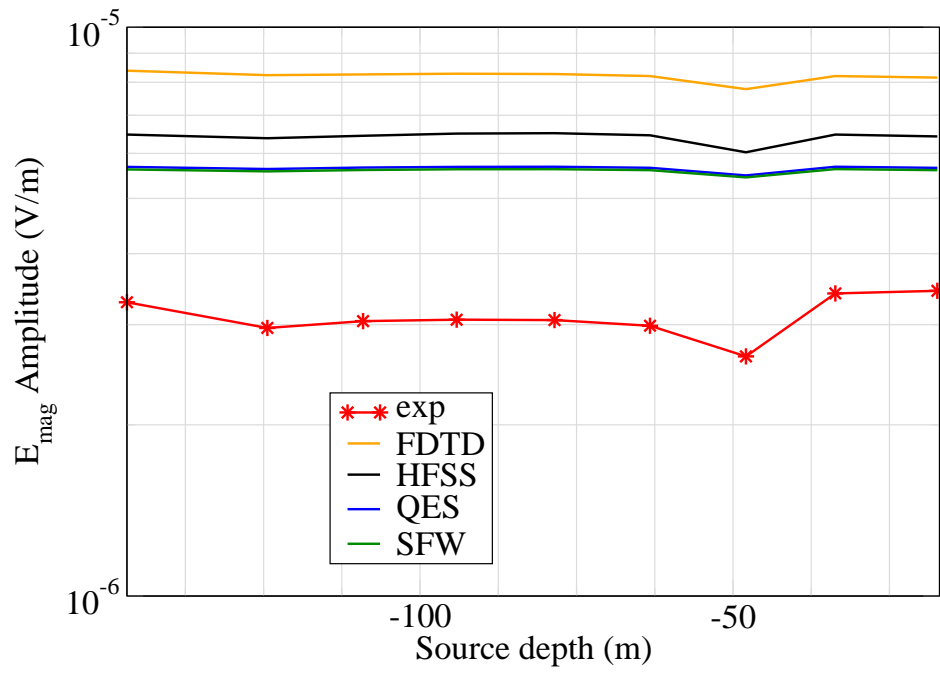


Figure 6: E_{mag} .

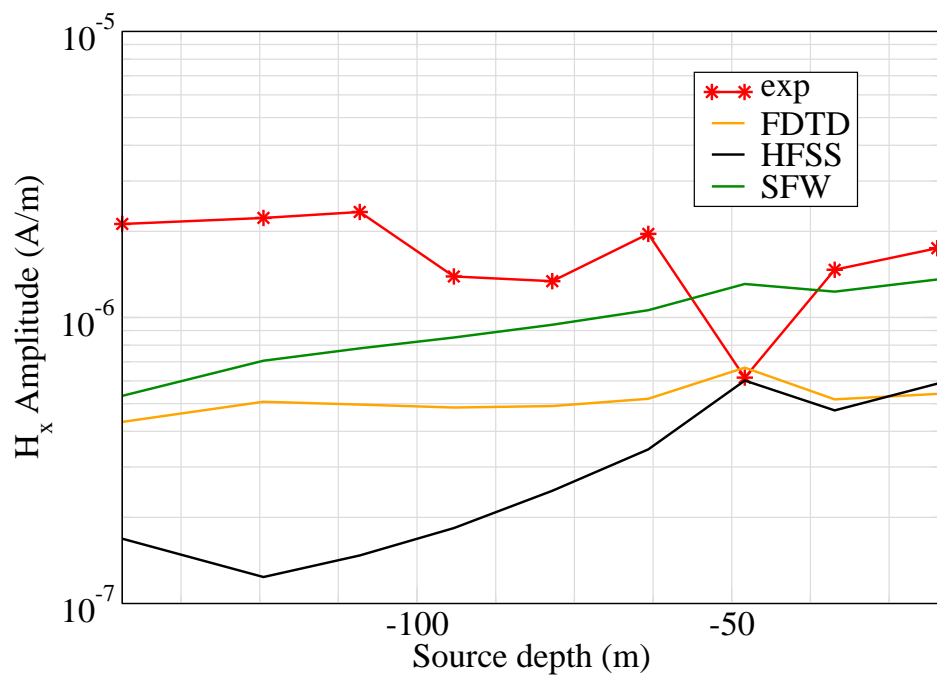


Figure 7: H_x .

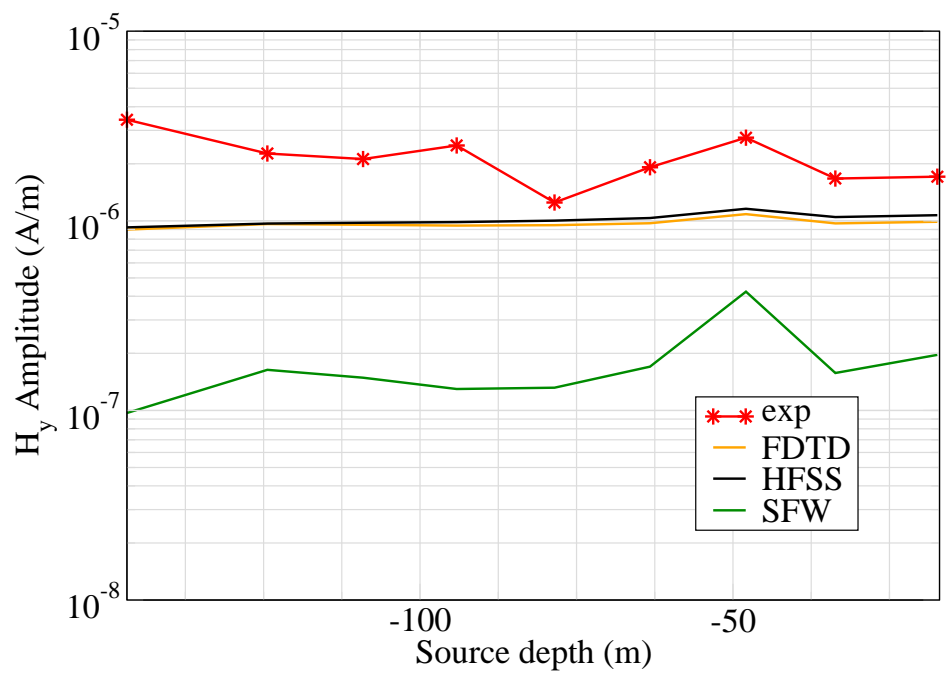


Figure 8: H_y .

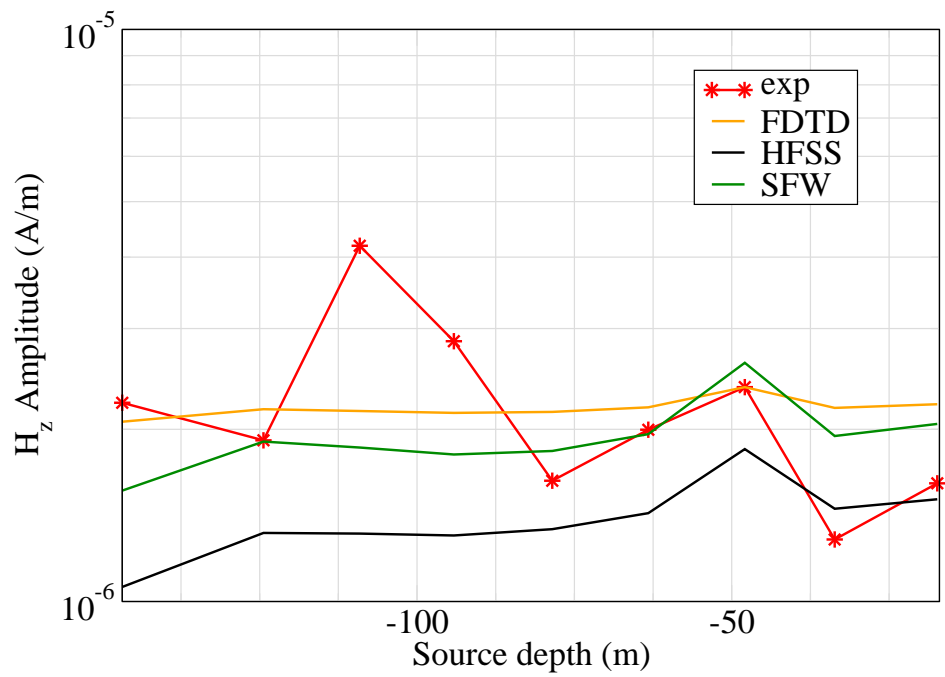


Figure 9: H_z .

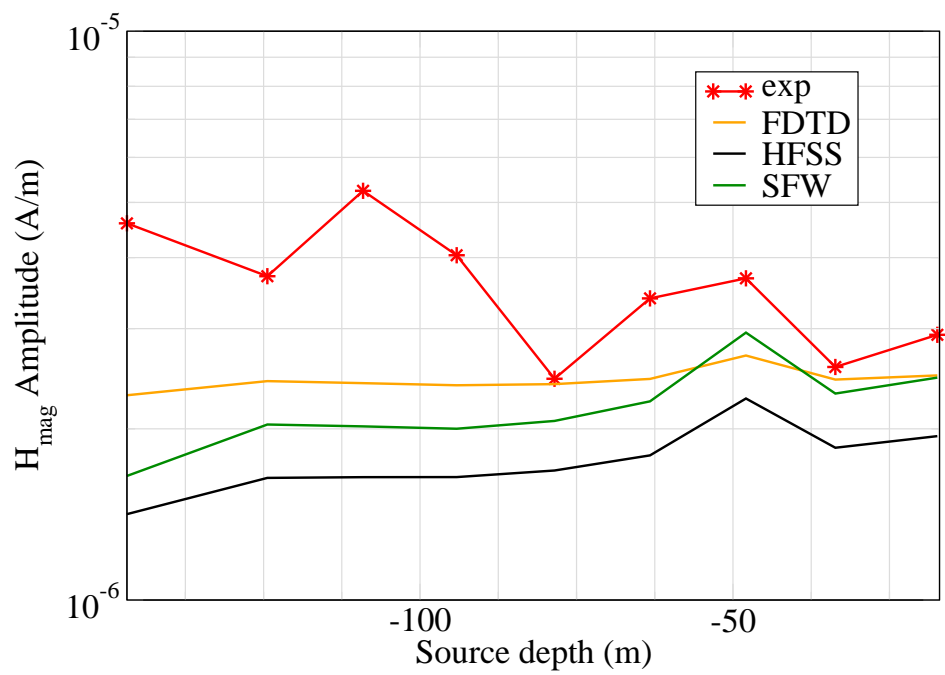


Figure 10: H_{mag} .

Appendix C: Publications

The following publications were funded by this ONR during the Phase One, Two and Three efforts. Reprints of these publications are attached.

Journal Articles:

- Y. Xia and D.M. Sullivan, "Underwater FDTD simulations at extremely low frequencies," *IEEE Antennas and Wireless Propagation Letters*, vol. 7, pp.661-664, 2008.
- Y. Xia and D. M. Sullivan, Z. Li, and R. Olsen "Dual problem space FDTD simulation for underwater ELF applications," *IEEE Antennas and Wireless Propagation Letters*, vol. 8, pp. 498-501, 2009.
- C. L. Wagner and J. L. Young, "FDTD numerical tests of the convolutional-PML at extremely low frequencies," *IEEE Antennas and Wireless Propagation Letters*, vol. 8, pp. 1398-1401, 2009.
- D. M. Sullivan, Y. Xia and D. Butherus, "A perfectly matched layer for lossy media at extremely low frequencies," *IEEE Antennas and Wireless Propagation Letters*, vol. 8, pp. 1080-1083, 2009.

Conference Publications:

- D. M. Sullivan and Y. Xia, "Underwater FDTD simulation at low frequencies," IEEE International Antennas and Propagation Symposium and USNC/URSI Radio Science Meeting, San Diego, CA, June 5-11, 2008.
- Y. Xia and D. M. Sullivan, "Near to far field transformation for underwater ELF simulation," IEEE International Antennas and Propagation Symposium and USNC/URSI Radio Science Meeting, San Diego, CA, June 5-11, 2008.
- Y. Xia, A. Monsoori, D. M. Sullivan and J. Nadobny, "High resolution interpolation for underwater FDTD simulation at ELF frequencies," IEEE International Antennas and Propagation Symposium and USNC/URSI Radio Science Meeting, Charleston, SC, June 1-5, 2009.
- D. M. Sullivan and Y. Xia, "A perfectly matched layer for lossy media at extremely low frequencies," IEEE International Antennas and Propagation Symposium and USNC/URSI Radio Science Meeting, Charleston, SC, June 1-5, 2009.
- C. L. Wagner and J. L. Young, "Characterizing the convolutional perfectly matched layer at extremely low frequencies," 2010 IEEE International Symposium on Antennas and Propagation and CNC/USNC/URSI Radio Science Meeting, Toronto, Ontario, July 2010.
- D. Butherus, Y. Xia, D. M. Sullivan, "Time-domain near-to-far field transformation for underwater FDTD simulations at ELF frequencies," 2010 IEEE International Symposium

on Antennas and Propagation and CNC/USNC/URSI Radio Science Meeting, Toronto, Ontario, July 2010.

- Y. Xia and D. M. Sullivan, “Underwater ELF Simulation using dedicated hardware,” 2010 IEEE International Symposium on Antennas and Propagation and CNC/USNC/URSI Radio Science Meeting, Toronto, Ontario, July 2010.
- D. M. Sullivan, Y. Xia, A. Mansoori, “Large scale underwater FDTD ELF simulations using Acceleware and MPI parallel processing,” URSI International Symposium on Electromagnetic Theory, Berlin, Germany, August 16-19, 2010.
- R. T. Rebich, J. L. Young, C. W. Wagner and R. G. Olsen, “Comparison of the up-over-down approximation with the quasi-electrostatic approximation for ELF fields in layered media,” 2011 IEEE International Symposium on Antennas and Propagation and USNC/URSI Radio Science Meeting, Spokane, WA, July 2011.
- Z. Li and R. G. Olsen, “A simple up-over-and-down model for low frequency horizontal electric dipole propagation near an interface,” 2011 IEEE International Symposium on Antennas and Propagation and USNC/URSI Radio Science Meeting, Spokane, WA, July 2011.
- C. Johnson, C. L. Wagner, R. Rebich, J. L. Young, and D. Butherus, “Propagation of low frequency signals in oceanic environments; theory, simulation and experimentation,” 2011 IEEE International Symposium on Antennas and Propagation and USNC/URSI Radio Science Meeting, Spokane, WA, July 2011.
- J. L. Young and C. L. Wagner, “Moving sources, FDTD and reciprocity,” 2012 IEEE International Symposium on Antennas and Propagation and USNC/URSI Radio Science Meeting, Chicago, Illinois, July 2012

Under Review

- R. G. Olsen and Z. Li, “A simple up-over-and-down model for low frequency horizontal electric dipole propagation near an interface,” *IEEE Transactions on Antennas and Propagation*.
- J. L. Young and C. L. Wagner, “Moving sources, simulation and reciprocity,” *IEEE Transactions on Antennas and Propagation*.

Underwater FDTD Simulation at Extremely Low Frequencies

Yang Xia and Dennis M. Sullivan, *Senior Member, IEEE*

Abstract—This letter describes the application of the finite-difference time-domain (FDTD) method to the simulation of extremely low frequency (ELF) electromagnetic signals under water. This requires substantial modification to the traditional FDTD method, as well as the development of an analytic method needed to verify the accuracy of the FDTD method.

Index Terms—Electromagnetic propagation in absorbing media, extremely low frequencies, finite-difference time-domain (FDTD) methods.

I. INTRODUCTION

MODERN antiship mines can be detonated by the electromagnetic signature of a surface ship [1]. For this reason, it is desirable to have simulation methods to study the propagation of extremely low-frequency (ELF) electromagnetic waves under water. The finite-difference time-domain (FDTD) method [2], [3] is one of the most widely used methods in electromagnetic simulation. However, it has seen limited use for low frequencies in lossy media. In this letter, we describe the use of FDTD for ELF simulation under water. In Section II, we describe the formulation of the FDTD method that has been found to be most appropriate for this application. Section III describes the method of two equations, two unknowns (2E2U) that is used to determine the resulting amplitudes when the FDTD program has reached steady state. Section IV describes an analytic method that was developed to evaluate the accuracy of FDTD at ELF. Section V presents an example of ELF simulation in shallow water, the type of problem that will be of interest for this project. Section VI ends in a discussion, including remarks on future areas of research.

II. METHOD

We begin with the time-domain Maxwell's equations

$$\epsilon_r \epsilon_0 \frac{\partial E}{\partial t} = \nabla \times H - \sigma E \quad (1a)$$

$$\mu_0 \frac{\partial H}{\partial t} = -\nabla \times E. \quad (1b)$$

Manuscript received August 25, 2008; revised October 02, 2008. First published November 21, 2008; current version published January 16, 2009. This work was funded under ONR Grant N00014-17-1-0811 in collaboration with NAVESAE, Carderock Division.

The authors are with the Electrical and Computer Engineering Department, University of Idaho, Moscow, ID 83844 USA (e-mail: dennis@ee.uidaho.edu).

Digital Object Identifier 10.1109/LAWP.2008.2010066

Equation (1) is for three dimensions, but for the purpose of illustration, we limit the discussion to the E_x and H_y fields propagating in the z direction. Equation (1a) can be taken into the sampled time domain using the usual finite-differencing procedures

$$\begin{aligned} \epsilon_r \frac{E_x^{n+1}(k) - E_x^n(k)}{\Delta t} + \left(\frac{\sigma}{\epsilon_0} \right) E_x^{n+1} \\ = \frac{1}{\epsilon_0} \frac{H_y^{n+1/2}(k+1/2) - H_y^{n+1/2}(k-1/2)}{\Delta x}. \end{aligned}$$

We assume the cell size is Δx and the time step is Δt . The E_x^{n+1} can now be calculated from

$$\begin{aligned} E_x^{n+1}(k) = ca(k)E_x^n(k) \\ + cb(k) \left[H_y^{n+1/2}(k+1/2) - H_y^{n+1/2}(k-1/2) \right] \end{aligned} \quad (2a)$$

where

$$ca = \left(1 + \frac{\Delta t \cdot \sigma}{\epsilon_r \epsilon_0} \right)^{-1}, \quad cb = ca \frac{\Delta t}{(\epsilon_r \epsilon_0 \Delta x)}. \quad (2b)$$

There is a crucial choice that was made here. Usually, the E_x term next to the conductivity is averaged across the two time steps

$$\begin{aligned} \epsilon_r \frac{E_x^{n+1}(k) - E_x^n(k)}{\Delta t} + \left(\frac{\sigma}{\epsilon_0} \right) \left(\frac{E_x^{n+1}(k) + E_x^n(k)}{2} \right) \\ = \frac{1}{\epsilon_0} \frac{H_y^{n+1/2}(k+1/2) - H_y^{n+1/2}(k-1/2)}{\Delta x}, \end{aligned}$$

which would lead to the following expression for ca :

$$ca = \left(1 - \frac{\Delta t \cdot \sigma}{2\epsilon_r \epsilon_0} \right) / \left(1 + \frac{\Delta t \cdot \sigma}{2\epsilon_r \epsilon_0} \right). \quad (3)$$

At ELF frequencies in lossy media, the ca of (3) would be negative, leading to a potentially unstable condition. (The implementation of (1b) into FDTD is straight-forward and will not be presented here).

There is another choice that leads to substantially larger time steps, and therefore, substantially faster solutions [4]. Once the cell size Δx is chosen, the time step must be chosen to satisfy the Courant condition, which in three dimensions is

$$\Delta t \leq \frac{\Delta x}{\sqrt{3} \cdot c_{\max}} \quad (4)$$

where c_{\max} is usually the speed of light in a vacuum. The materials that will be of interest for this project are listed in Table I. (An early goal of this project is to study propagation in lakes.

TABLE I
THE PROPERTIES OF THE MATERIALS USED IN THE SIMULATIONS DESCRIBED
IN THIS PAPER [5]

Material	ϵ_r	σ (S/m)
Water	80	0.018
Air	1	0
Lake water	80	0.018
Mud	40	0.002
Metal	1	10^7

That is the reason that lake water is used instead of sea water.) The complex dielectric constant is calculated by

$$\epsilon_r^* = \epsilon_r + \frac{\sigma}{j\omega\epsilon_0}.$$

At ELF frequencies, the imaginary part of the dielectric constant will dominate the magnitude for all the materials except air. Therefore, increasing the dielectric constants of mud or metal to 80 would make very little difference. If we assume every material in Table I has a real dielectric constant of 80, then $c_{\max} = c_0/\sqrt{80}$ and the time step is almost an order of magnitude greater. (c_0 is the speed of light in a vacuum). Even though air is one of the materials listed in Table I, air is a boundary medium in this project. It presents almost perfect reflection to an electromagnetic signal in water, even if the higher dielectric constant is used.

III. THE METHOD OF TWO EQUATIONS, TWO UNKNOWNS

FDTD is a time-domain method. Once the steady state has been reached for a simulation problem, it is desirable to know the resulting amplitude and phase at certain locations in the problem space. For frequencies of about 100 kHz and above, the discrete Fourier transform is the preferred method [6]. We have found that at ELF frequencies, the method of two equations, two unknowns (2E2U) is preferable [7]. In this method, two sample points are taken

$$E_1 = A \sin(\omega_{\text{in}} t_1 + \theta) \quad (5a)$$

$$E_2 = A \sin(\omega_{\text{in}} t_2 + \theta). \quad (5b)$$

Since the input frequency ω_{in} as well as the two sample points t_1 and t_2 are known, the only unknowns are the amplitude A and the phase θ . The concept of solving for two unknowns from the two equations is straight-forward, but the fact that the inverse trigonometric identities must be taken can lead to inconsistencies. It has been found expedient to add an offset time

$$t_{\text{off}} = \frac{1}{2} \left[\frac{\pi}{\omega} - t_1 - t_2 \right] \quad (6)$$

to each of the times t_1 and t_2 . This centers the two sample points symmetrically on the ninety degree axis and avoids problems when taking inverse trigonometric functions.

IV. VERIFICATION OF THE ACCURACY OF THE METHOD

An analytic solution is needed to verify the accuracy of the FDTD method at ELF. One such method that is often used to

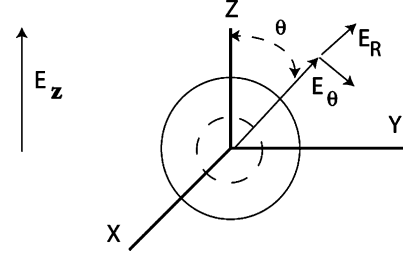


Fig. 1. A layered dielectric sphere in a constant E field.

verify FDTD formulations is a layered dielectric sphere illuminated by a plane wave. A Bessel function expansion is used to calculate the resulting fields [8]. This method is not valid below about 100 kHz.

At low frequencies, the near field can be regarded as a static field. A solution for a layered sphere in a static electric field was developed, as illustrated in Fig. 1. A spherical boundary-value problem has solutions of the form [5]

$$V(R, \theta) = \sum_{n=0}^{\infty} \left[A_n R^n + B_n R^{-(n+1)} \right] P_n(\cos \theta). \quad (7)$$

$P_n(\cos \theta)$ are the Legendre polynomials. In the limit far from the sphere, $V_o(R, \theta)|_{R \rightarrow \infty} \cong -E_0 R \cos \theta$, and inside the sphere $V_1(R, \theta) = A_1 R \cos \theta$. There are two boundary conditions at a dielectric boundary: $E_{1t} = E_{2t}$, $\epsilon_1 E_{1n} = \epsilon_2 E_{2n}$. The two equations resulting from the boundary conditions are

$$B_m + A_m r_m^3 - B_{m+1} - A_{m+1} r_m^3 = 0 \quad (8a)$$

and

$$\begin{aligned} -2 \frac{\epsilon_m}{\epsilon_{m+1}} B_m + \frac{\epsilon_m}{\epsilon_{m+1}} A_m r_m^3 + 2 B_{m+1} \\ - A_{m+1} r_m^3 = 0. \end{aligned} \quad (8b)$$

The constants are determined by Gaussian elimination. Once the potential V is known, the E fields are determined by

$$\mathbf{E} = -\nabla V = -\frac{\partial}{\partial R} V \mathbf{a}_R - \frac{1}{R} \frac{\partial}{\partial \theta} V \mathbf{a}_\theta \quad (9)$$

which can be converted to rectangular coordinates.

In order to compare the FDTD results with the analytic method, we use the three-dimensional problem space illustrated in Fig. 2. A plane wave polarized in the z direction is generated at one end and subtracted out the other end. The cells used in the simulations are five meters cubed and the time steps are 75 ns. A layered sphere with dielectric properties to simulate various materials lies in the center of the total field. The amplitude of the E_z field is determined along the major axes for comparison with the analytic method to evaluate the accuracy of the FDTD simulation. These axes go through the sphere and extend five cells out in each direction. The problem space is 50 cells cubed.

The results of the simulations are shown in Fig. 3. The solid lines are the analytic results and the circles are the FDTD values. Clearly, the comparisons are very good. In Fig. 3(c) there is

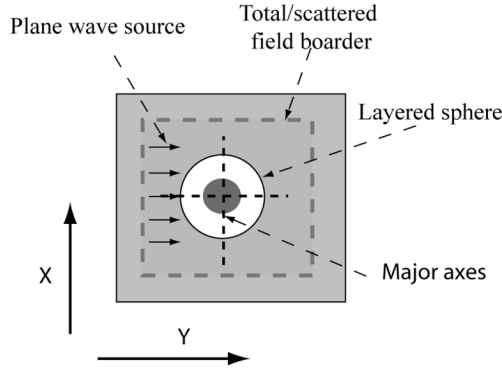


Fig. 2. The configuration of the three-dimensional simulation space used to evaluate the accuracy of the method.

some discrepancy in the air layer in the middle. This is not too worrisome because in our problems of interest, air is a boundary, not a central part of the problem space. Note that this condition was not caused by increasing the dielectric to 80 as discussed above; the same result is obtained using a dielectric of 1 or 80.

V. EXAMPLE

Fig. 4 illustrates the type of simulation of interest for this project. Two dipoles, one used as a transmitter and one as a receiver, are submerged in shallow water. The problem space is $40 \times 60 \times 40$ cells and each cell is 10 m squared. The transmitting current is simulated by the H fields surrounding the middle of the transmitting dipole

$$I_{\text{trans}} = \oint_S \mathbf{H} \cdot d\mathbf{l} \cong 4\Delta x \cdot \begin{pmatrix} H_y(i, j, k) - H_y(i-1, j, k) \\ -H_x(i, j, k) + H_x(i, j-1, k) \end{pmatrix}. \quad (10)$$

The resulting current on the receiver is calculated with a similar equation. Each simulation required 2000 time steps. The results are shown in Fig. 5. The important quantity, H , the transfer function, is the ratio of received current to transmitted current, which is plotted as a function of frequency.

VI. DISCUSSION

A method has been described to simulate electromagnetic waves propagating under water at extremely low frequencies. This approach necessitated substantial modification to the usual FDTD formulations. Furthermore, an analytic method based on the Legendre polynomials was developed to verify the accuracy of the FDTD method.

Those familiar with FDTD methods will notice the lack of discussion on absorbing boundary conditions (ABCs). ABCs are usually required to prevent outgoing signals from being reflected back into the problem space. The very lossy background medium of lake water has prevented this from being a concern for the examples presented in this letter. However, it is likely that an appropriate ABC, probably one based on the perfectly

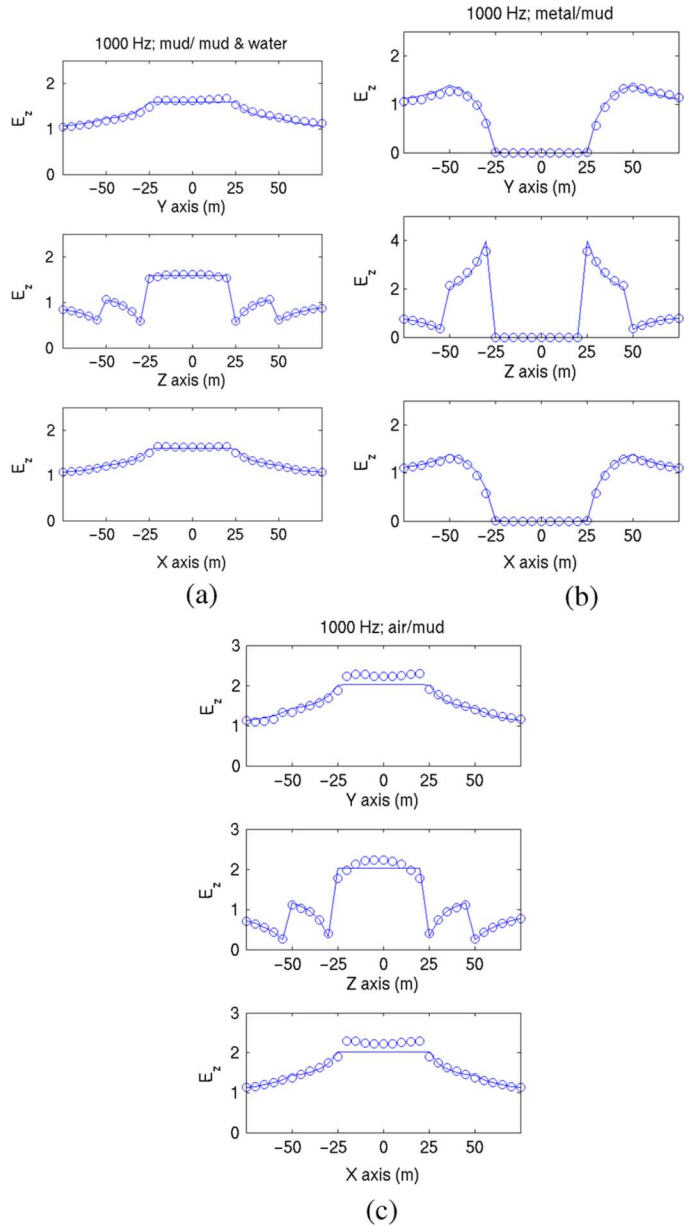


Fig. 3. Comparison of the FDTD values (circles) versus the analytic values (lines) for an incident plane wave at 1 kHz and a layered sphere composed of different media. (a) The inner layer is mud, the outer layer is mud and water. (b) The inner layer is metal, the outer layer is mud. (c) The inner layer is air, the outer layer is mud.

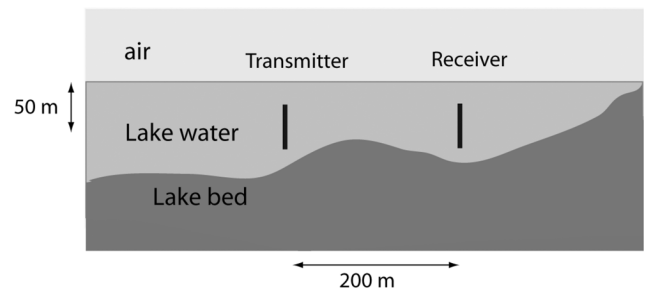


Fig. 4. Two dipoles are submerged in shallow water. One is used as a transmitter and the other as a receiver.

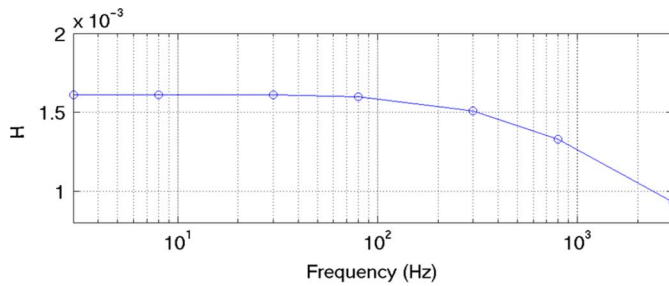


Fig. 5. The transfer function of the two-dipole simulation shown in Fig. 4. The frequency range is 3 Hz to 3 kHz.

matched layer (PML) [9], will be necessary for simulation over long distances.

In this project, it is anticipated that simulation over distances of several kilometers will be required. Some form of near-to-far field transformation will be developed to model the EM sources with relatively high resolution while using lower resolution to model greater distances in the far field.

REFERENCES

- [1] J. J. Holmes, *Exploitation of a Ship's Magnetic Field Signatures*. : Morgan and Claypool Publishers, 2006.
- [2] K. S. Yee, "Numerical solution of initial boundary value problems involving Maxwell's equations in isotropic media," *IEEE Trans. Antennas Propag.*, vol. 17, pp. 585–589, 1966.
- [3] D. M. Sullivan, *Electromagnetic Simulation Using the FDTD Method*. Piscataway, NJ: IEEE Press, 2000.
- [4] D. M. Sullivan, "Exceeding the courant condition with the FDTD method," *IEEE Microw. Guided Wave Lett.*, vol. 6, pp. 289–291, 1996.
- [5] D. K. Chen, *Field and Wave Electromagnetics*, 2nd ed. Reading, PA: Addison-Wesley, 1989.
- [6] C. M. Furse, S. P. Mathur, and O. P. Gandhi, "Improvements to the finite-difference time-domain method for calculating the radar cross section of a perfectly conducting target," *IEEE Trans. Microw. Theory Techn.*, vol. 38, no. 7, pp. 919–927, 1990.
- [7] C. M. Furse, "Faster than Fourier—Ultra-efficient time-to-frequency domain conversions for FDTD simulations," *IEEE Antennas Propag. Mag.*, vol. 42, no. 6, pp. 24–34, 2000.
- [8] R. Harrington, *Time-Harmonic Electromagnetic Fields*. New York: McGraw-Hill, 1961.
- [9] J. P. Berenger, "A perfectly matched layer for the absorption of electromagnetic waves," *J. Comp. Phys.*, vol. 114, pp. 185–200, 1994.

Dual Problem Space FDTD Simulation for Underwater ELF Applications

Yang Xia, Dennis M. Sullivan, Zhi Li, and Robert Olsen

Abstract—The finite-difference time-domain (FDTD) method is being used to simulate extremely low frequencies underwater. In order to expand the potential problem space without reducing the resolution at which the source is modeled, a near-to-far-field transformation method has been developed.

Index Terms—Equivalent sources, finite-difference time-domain (FDTD) methods.

I. INTRODUCTION

UNDERWATER mines pose the greatest threat to surface ships [1]. These mines are no longer restricted to direct contact, but can detect the electromagnetic (EM) signature of a ship and launch a torpedo from hundreds of meters away [2]. The EM radiation of a surface ship tends to be in the extremely low frequency (ELF) range and can propagate underwater over long distances. For this reason, simulation is being used to study underwater EM radiation.

One of the most common methods used in EM simulation is the finite-difference time-domain (FDTD) method [3], [4]. It has recently been shown to be effective at ELF frequencies [5]. However, because it employs a uniform grid, one is always left with the problem of choosing a cell size that is small enough to accurately model the radiating source, but large enough to model an extensive far field. In order to overcome this, a three-dimensional near-to-far-field transformation has been developed. This method involves two separate FDTD simulations. The simulation space in the near-field models the source, whether it is a ship's hull or an antenna, with relatively high resolution; a second simulation space models the far-field with larger cells in order to model propagation hundreds of meters from the source. The transition between near- and far-field is accomplished by applying the equivalence principle [6].

This letter is arranged as follows. The use of the equivalence principle to make the near-to-far-field transition is described in Section II. In Section III, we verify the accuracy of the method by comparison with an analytic method based on Sommerfeld's

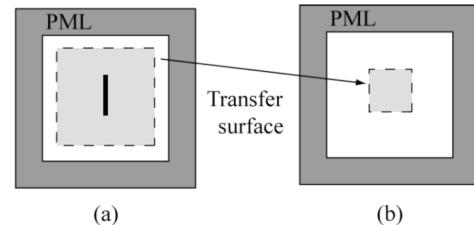


Fig. 1. Two problem spaces are used in the FDTD simulation. (a) The radiating source is modeled in the near-field, and the tangential H-field on the three-dimensional surface are calculated. (b) Using the tangential H-fields, a three-dimensional source is impressed in the far-field. (a) Near-field problem space. (b) Far-field problem space.

half-space method [7]–[9]. In Section IV, a more realistic example of the simulation of a loop antenna in a lake bed is presented. Section V summarizes the letter.

II. THE NEAR-TO-FAR-FIELD TRANSFORMATION

Two three-dimensional FDTD problem spaces are utilized to implement the near-to-far-field transformation (Fig. 1). A problem space with a relatively small cell size (1 m^3) is used to model the source [Fig. 1(a)]. Another problem space with larger cells [13 m^3] is used to model the far-field [Fig. 1(b)]. The ratio of 13 to 1 between far- and near-field cell sizes resulted in near- and far-field problem spaces of about the same size, which seemed to be the optimum case. Each problem space is surrounded by a perfectly matched layer (PML) [10]. (A new PML for ELF frequencies and lossy media has been developed and will be the subject of a future paper.) Each problem space contains a three-dimensional transfer surface where the equivalence principle [6] is implemented. On a surface, the source is uniquely specified by either the tangential E- or H-fields. We use the H-fields. The tangential fields calculated on the transfer surface in the near-field are impressed on the transfer surface in the far-field to form the far-field source. Since the far-field cells are 13 times larger than the near-field cells, only one value out of 13 in the near-field is needed in the far-field. This method is effective even when the medium is inhomogeneous, as will be demonstrated in the next section. There is no coupling from the far-field back to the near-field. This is illustrated in Fig. 2.

III. VERIFICATION OF THE ACCURACY

In this section, the results of the near-to-far-field transformation are compared to analytic results calculated using Sommerfeld's half-space (SHS) problem. SHS problem calculates the resulting fields from an oscillating dipole near a plane interface separating two homogeneous half-space regions, as illustrated in Fig. 3. This method is well described in the literature [7]–[9]

Manuscript received January 23, 2009; revised March 03, 2009. First published March 16, 2009; current version published June 17, 2009. This work was supported by ONR Grant N00014-17-1-0811 in collaboration with NAVESAE, Carderock Division.

Y. Xia and D. M. Sullivan are with the Electrical and Computer Engineering Department, University of Idaho, Moscow, ID 83844 USA (e-mail: dennis@ee.uidaho.edu).

Z. Li and R. Olsen are with the School of Electrical Engineering and Computer Science, Washington State University, Pullman, WA 99164 USA.

Digital Object Identifier 10.1109/LAWP.2009.2017286

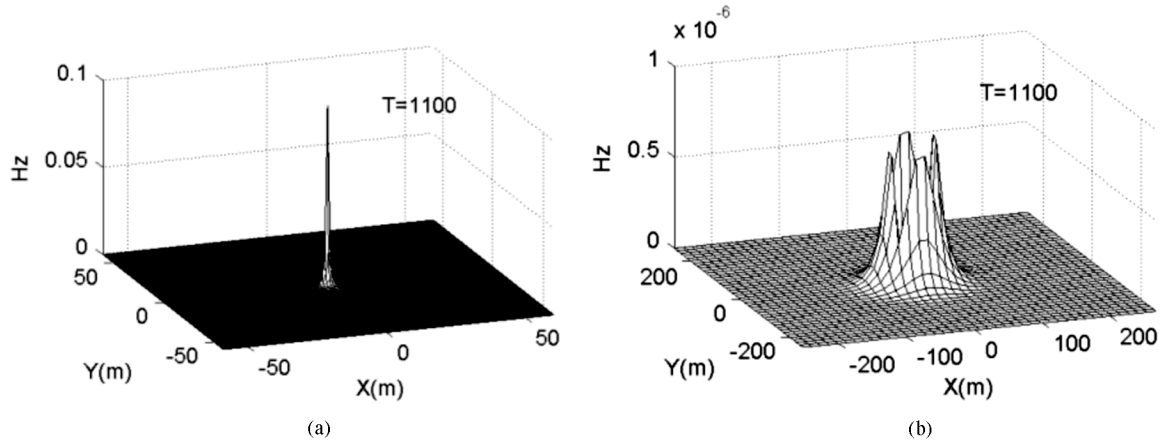


Fig. 2. (a) Near-field mesh plot. (b) Far-field mesh plot.

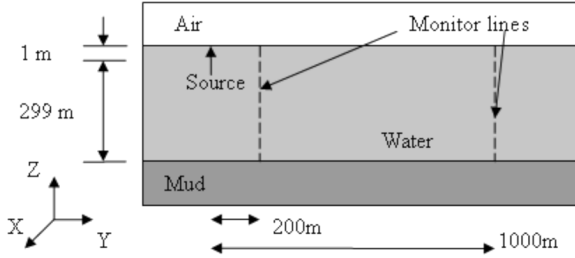
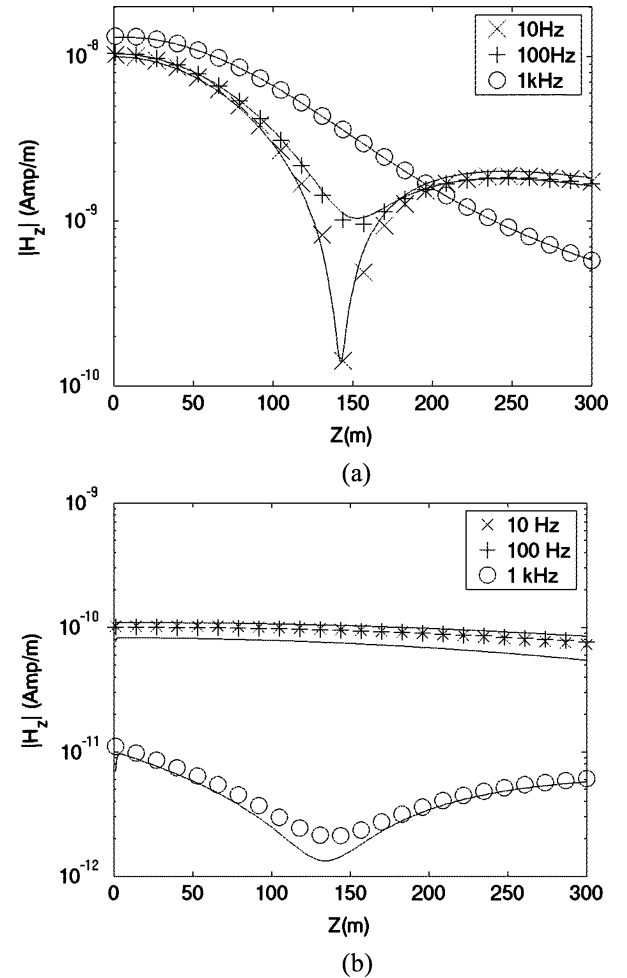
Fig. 3. Diagram of the three-dimensional far-field used in the comparison between the FDTD near-to-far-field transformation and the SHS method. The x -direction (not shown) is 1500 m. The source is a magnetic dipole 1 m below the air-water interface and was generated in the near-field (not shown).

TABLE I
PROPERTIES OF THE MATERIALS USED IN THE SIMULATIONS DESCRIBED
IN THIS LETTER [5]

Material	ϵ_r	σ (S/m)
Air	1	0
Lake water	80	0.018
Mud	40	0.002

and will not be repeated here. In Fig. 3, the upper layer is air, the middle layer is water, and the lower level is mud. The water layer in the middle is 300 m thick. The dielectric properties for water, mud, and air are given in Table I. The dipole is formed by specifying the H_z -field in one 1-m^3 cell in the near-field problem space. The monitor lines represent the places where comparisons between the methods will be made. Note that the FDTD simulations are all three-dimensional.

Comparisons at 200 and 1000 m are shown in Fig. 4(a) and (b), respectively. The simulation required 30 000 time-steps. The amplitudes in each figure are calculated by the method of two equations, two unknowns [11]. The horizontal coordinate is the distance to the air/water surface, and the vertical coordinate is the magnitude of the field. The discrete symbols represent the FDTD calculations, and the solid lines represent the calculations by SHS method. Clearly, the results of the comparisons are very good in all cases.

Fig. 4. Comparisons of the FDTD simulations (the symbols) and the SHS calculations (the lines) for the cell size ratio of 13. The source is near the upper surface of the water layer. The comparisons are made at (a) 200 and (b) 1000 m. Z represents the distance from the surface. (a) Comparison at 200 m. (b) Comparison at 1000 m.

IV. EXAMPLE

This section illustrates the use of FDTD with a near-field, far-field transformation in simulating a more realistic case. One of the goals of the simulation is to verify the accuracy of the

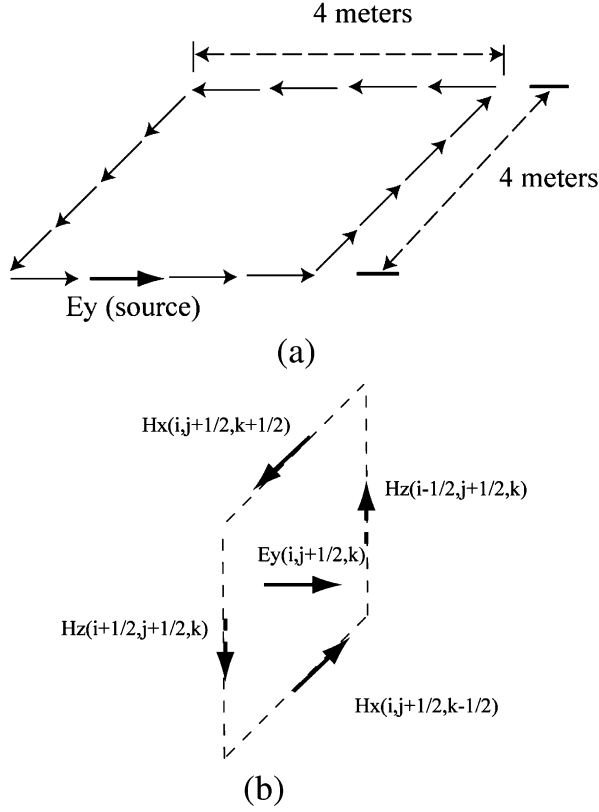


Fig. 5. The simulation of a 4 m × 4 m current loop in FDTD as generated in the near-field. (a) Setting the group of cells at the respective E-field points in the grid simulates a metal loop. (b) Current is simulated by setting an E_y -field to a value. This couples to the surrounding H-fields.

modeling with measured data that can be made in a lake. Because the lake bed is not flat, analytical approaches cannot be used to solve the problem.

The antennas that will be used in the transmission are 4 m × 4 m rectangular current loops. Fig. 5(a) illustrates how this is simulated in the XY-plane in the FDTD space. Metal can be simulated by ensuring that an E-field is zero at a particular point in the space. Therefore, using cells that are 1 m³, the metal loop antenna is simulated at the corresponding E_x or E_y positions, as shown in Fig. 5(a). Since the radius of the wire of the antennas is considerably less than the 1-m cell size, the thin rod approximation [12] is used to model the wire at these positions.

In FDTD, a current cannot be simulated directly, but it can be simulated indirectly by using Ampere's circuit law [13] and specifying the surrounding H-fields

$$I = \oint \frac{1}{\mu_0} \mathbf{H} \cdot d\mathbf{l}. \quad (1)$$

By impressing a hard source on one of the E_y -fields, a value is induced on the surrounding H-fields, as shown in Fig. 5(b). This results in a current via (1).

A model of the lake bed is created for the far-field domain (Fig. 6). The cells are 13 m³. The shape of the lower surface of the water layer shows a complex geometry structure similar to a real lake bed.

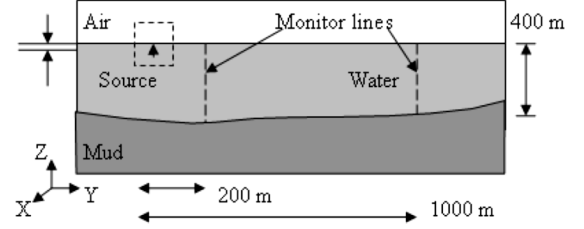


Fig. 6. The lake bed that is simulated in the far-field. The cells in the far-field are 13 m³. The near-field (the enclosed dashed area) contains a current loop located 1 m below the surface of the water.

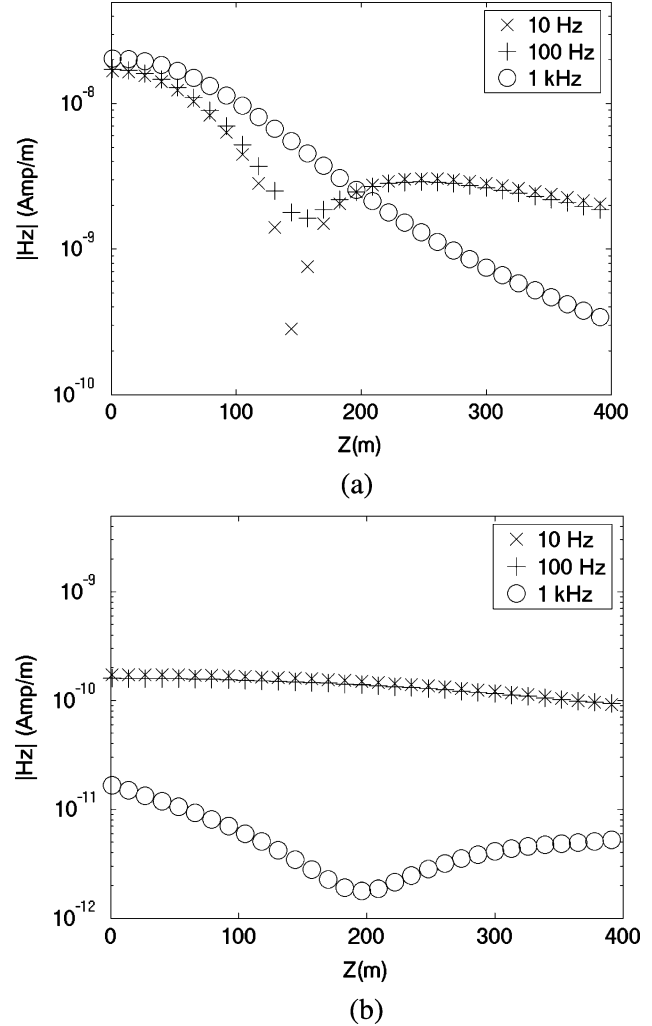


Fig. 7. Results of the simulation illustrated in Fig. 6. Z represents the distance from the surface. (a) The results at 200 m. (b) The results at 1000 m.

Fig. 7(a) and (b) shows the results of the near-to-far-field simulation using the current loop source in the near-field and the lake bed in the far-field at 200 and 1000 m from the source and at three different frequencies, 10, 100, and 1000 Hz. These simulations were done on an HP DL140 GE Quad Core and required about 6 h. Both the near- and far-field problem spaces were 120 cells cubed.

V. SUMMARY

A near-to-far-field transformation utilizing the equivalence principle in conjunction with the FDTD method has been pre-

sented. The accuracy of this method was confirmed by comparisons with analytic results based on Sommerfeld's half-space method. An example illustrating the flexibility of the method in simulating a realistic problem has also been presented.

The method presented in this letter substantially extends the range of FDTD simulations at ELF frequencies for the purpose of determining the vulnerability of surface ships to electromagnetically detonated mines. Accuracy at 1 km has already been confirmed, and it is hoped that the development of a new underwater PML will extend this range to 3 km.

REFERENCES

- [1] R. H. Wilkens and M. D. Richardson, "Mine burial prediction: A short history and introduction," *IEEE J. Ocean. Eng.*, vol. 32, no. 1, pp. 3–9, Jan. 2007.
- [2] J. J. Holmes, *Exploitation of a Ship's Magnetic Field Signatures*. New York: Morgan and Claypool, 2006.
- [3] K. S. Yee, "Numerical solution of initial boundary value problems involving Maxwell's equations in isotropic media," *IEEE Trans. Antennas Propag.*, vol. 14, pp. 302–307, 1966.
- [4] D. M. Sullivan, *Electromagnetic Simulation Using the FDTD Method*. New York: IEEE, 2000.
- [5] Y. Xia and D. M. Sullivan, "Underwater FDTD simulation at extremely low frequencies," *IEEE Antennas Wireless Propag. Lett.*, vol. 7, pp. 661–664, 2008.
- [6] R. Harrington, *Time-Harmonic Electromagnetic Fields*. New York: McGraw-Hill, 1961.
- [7] J. R. Wait, *Electromagnetic Wave Theory*. New York: Harper and Row, 1985.
- [8] W. C. Chew, *Waves and Fields in Inhomogeneous Media*. New York: Van Nostrand Reinhold, 1990.
- [9] L. B. Felsen and N. Marcuvitz, *Radiation and Scattering of Waves*. New York: IEEE, 1994.
- [10] J. P. Berenger, "A perfectly matched layer for the absorption of electromagnetic waves," *J. Comp. Phys.*, vol. 114, pp. 185–200, 1994.
- [11] C. M. Furse, "Faster than Fourier—Ultra-efficient time-to-frequency domain conversions for FDTD simulations," *IEEE Antennas Propag. Mag.*, vol. 42, no. 6, pp. 24–34, 2000.
- [12] J. Nadobny, R. Pontalti, D. M. Sullivan, W. Wladarczk, A. Vaccari, P. Deuflhard, and P. Wust, "A thin-rod approximation for the improved modeling of bare and insulated cylindrical antennas using the FDTD method," *IEEE Trans. Antennas Propag.*, vol. 51, no. 8, pp. 1780–1796, Aug. 2003.
- [13] D. K. Chen, *Field and Wave Electromagnetics*, 2nd ed. New York: Addison-Wesley, 1989.

FDTD Numerical Tests of the Convolutional—PML at Extremely Low Frequencies

Christopher L. Wagner and Jeffrey L. Young, *Fellow, IEEE*

Abstract—Numerical evaluation of the finite-difference time-domain (FDTD) convolutional perfectly matched layer (CPML) at extremely low frequencies (ELF) is conducted herein to arrive at acceptable values for the PML parameters. This is accomplished by conducting numerous simulations of an electric dipole in a $60 \times 60 \times 120$ free-space domain and by benchmarking the simulation data against reference data for strategic observation points within the domain. Results show that PML attenuation on the order of 60 to 70 dB can be obtained for 10 to 1000 Hz signals in the quasi-static region of the dipole.

Index Terms—Absorbing boundary condition, finite-difference time-domain (FDTD) methods, perfectly matched layer (PML).

I. INTRODUCTION

IT IS well known in oceanic environments that only extremely low-frequency (ELF) electromagnetic waves will propagate over long distances due to the high conductivity of saltwater. For this reason, such waves are quite useful in communication links, or can be undesirable emissions, as caused by high-powered electric drives on a ship platform. In either case, the propagation characteristics of these waves can be understood from computer finite-difference time-domain (FDTD) simulation, particularly in the littoral region, where the topological and bathymetry features can be geometrically complex. To accomplish such a simulation, a suitable domain truncation technique is needed for both the water and air regions of the domain. Since the ELF signals are naturally attenuated in the water, the perfectly matched layer (PML) development for the air is the most challenging.

Classical PMLs used in FDTD truncation have poor performance at low frequencies and potentially suffer late-time growth [1]–[3]. The complex frequency stretching scheme introduced by Kuzuoglu and Mittra [4] alleviates these problems. The FDTD CPML implementation of [4] was introduced by Roden and Gedney [5] and is evaluated here for ELF performance. For this work, we consider 10 to 1000 Hz to be the ELF band.

Manuscript received November 12, 2009; accepted December 06, 2009. First published December 31, 2009; current version published January 22, 2010. This work was supported by ONR N0014-08-1170.

The authors are with Department of Electrical and Computer Engineering, University of Idaho, Moscow, ID 83844 USA (e-mail: clwagner@uidaho.edu; jyoung@uidaho.edu).

Color versions of one or more of the figures in this letter are available online at <http://ieeexplore.ieee.org>.

Digital Object Identifier 10.1109/LAWP.2009.2039693

II. FORMULATION

A. The FDTD Problem Statement

The FDTD simulations presented herein used 64-bit double precision calculations. All simulations are performed at the Courant stability limit to minimize dispersion error and to advance time as fast as possible. The FDTD code is a cubic cell implementation, with a cell size of 20 m. The medium is free space. The test domain size is $60 \times 60 \times 120$ cells, including the 10-cell-thick PML. The electromagnetic field is excited by a current source that is at node coordinate (30,20,40). A time-differentiated Gaussian waveform is used as the excitation pulse. This pulse has no dc component, so no persistent charge will be deposited into the grid, which would produce undesirably large dc electric fields [6], [7]. The field is quantified at six observation points located at (30,10,80), (30,20,80), (30,30,80), (30,40,80), (30,50,80), and (50,20,40), respectively. The first set of grid numbers is regarded as observation point 1, the second set as observation point 2, etc. Since the free-space wavelength of a 10-Hz signal is 3000 km, it is clear that the observation points are within the quasi-static region of the dipole. Such near-field observations pose significant challenges to FDTD PML development.

Several test cases are considered that are associated with various PML parameters. The efficacy of each PML is obtained by benchmarking the FDTD data against a reference solution, as described next.

B. Reference Free-Space Problem

To provide a reference solution, a large free-space $200 \times 200 \times 260$ domain with perfect electric conductor (PEC) walls is used. The geometry of the source and receiver points is the same as the PML test cases, but the free-space domain is larger than the test case domains by 140 cells in each direction. This reference domain is large enough that the direct signal is fully resolved from the reflections from the walls, so the reflections can be removed by time-gating. The reference problem only needs to run for a few hundred time-steps to obtain a clean direct signal. This type of reference solution includes all FDTD numerical errors, thus allowing us to isolate the effect of the PML induced errors from all others.

C. Signal Processing

To extract the frequency response data from the time-domain data, fast Fourier transforms (FFT) are used [9]. The simulations are conducted using 200 K time steps, which unfortunately does not give sufficient frequency resolution to observe the ELF response. To circumvent this problem, the time-domain data set is extended with zeros to a length sufficient to obtain the lowest frequency needed. For signals that decay to zero (as is the case

with good PMLs), zero extension is proper. For numerical purposes, we define "zero" as less than 10^{-12} relative to the peak value. The zero extended data sets are then transformed with the FFT. The transformed data sets are then used to compute the frequency-domain performance metric. The time-domain and frequency-domain metrics are described next.

D. The Performance Metrics

To measure the performance of the PMLs, an energy metric is used. The energy includes all the field components in the metric. This eliminates the possibility of choosing an especially strong or weak field component at random. We present both time- and frequency-domain metrics. The time-domain metric is broadband, which contains all spectral information contained in the excitation signal. The frequency-domain metrics are narrow-band, calculated at selected frequencies of interest.

In the time domain, the residual energy error metric is

$$r = \frac{\sum_t (\delta w_e(t) + \delta w_h(t))}{\sum_t (w'_e(t) + w'_h(t))}, \quad (1)$$

where $w'_e(t)$ and $w'_h(t)$ are the electric and magnetic energy densities in the time-gated reference signal, and $\delta w_e(t)$, $\delta w_h(t)$ are the residual energy densities associated with the PML. The summations are over the full simulation time. The reference energy electric and magnetic densities are defined as

$$w'_e(t) = \frac{1}{2} \epsilon \mathbf{e}'(t) \cdot \mathbf{e}'(t) \quad (2)$$

and

$$w'_h(t) = \frac{1}{2} \mu \mathbf{h}'(t) \cdot \mathbf{h}'(t) \quad (3)$$

where $\mathbf{e}'(t)$ is the time-gated reference FDTD electric field vector and $\mathbf{h}'(t)$ is the reference FDTD magnetic field vector. The residual electric energy is given by

$$\delta w_e(t) = \frac{1}{2} \epsilon (\mathbf{e}(t) - \mathbf{e}'(t)) \cdot (\mathbf{e}(t) - \mathbf{e}'(t)) \quad (4)$$

where \mathbf{e} is the PML FDTD electric field vector. Similarly, the residual magnetic energy is

$$\delta w_h(t) = \frac{1}{2} \mu (\mathbf{h}(t) - \mathbf{h}'(t)) \cdot (\mathbf{h}(t) - \mathbf{h}'(t)) \quad (5)$$

where again the primed vector is the reference solution and the unprimed vector is the PML FDTD solution.

In the frequency domain, the residual energy error metric at angular frequency ω is

$$R(\omega) = \frac{\delta W_E(\omega) + \delta W_H(\omega)}{W'_E(\omega) + W'_H(\omega)} \quad (6)$$

where the residual and reference energies are defined in a manner similar to the time-domain case.

E. The PMLs

In the frequency domain, the CPML tensor coefficient as given by Kuzuoglu [4] is

$$s_i = \kappa_i + \sigma_i / (\alpha_i + j\omega\epsilon_o), \quad i = x, y, z. \quad (7)$$

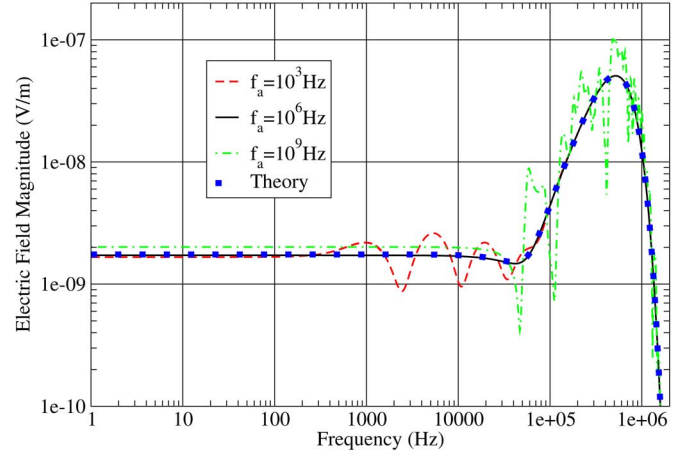


Fig. 1. Hertzian dipole field at observation point 1 for several different PMLs with $\kappa = 1$. The rapid fall-off of amplitude after 1 MHz is due to the limited bandwidth of the source current waveform.

The real coordinate stretch κ , conductivity σ , complex frequency stretch α , and their polynomial scaling characterize the PML.

The test PMLs are 10 cells thick, with the parameters having polynomial scaling. The conductivity σ and coordinate stretch κ use a fourth-order scaling polynomial, while the complex frequency stretch α uses third-order. As is usual with the CPML, the scaling polynomial for the conductivity and real coordinate stretch increases into the PML, while the complex frequency stretch polynomial decreases into the PML. The maximum conductivity is set according to the optimum [8] given by

$$\sigma_{\text{opt}} = \frac{m+1}{150\pi\sqrt{\epsilon_r}\Delta_x} \quad (8)$$

where m is the polynomial order, Δ_x is the space grid size, and ϵ_r is the relative dielectric constant. The maximum complex frequency stretch α is set by

$$\alpha_{\text{max}} = 2\pi\epsilon_0 f_a \quad (9)$$

where f_a is the CPML break frequency.

The problem is to find ranges for the parameters f_a and κ that provide good performance at ELF. This can only be done empirically. Representative test cases are provided next to demonstrate this empirical process.

III. RESULTS

To validate the simulations, the exact Hertzian dipole, frequency-domain solution is compared to the transformed FDTD simulation data in Fig. 1. The field is observed at point 1. When f_a is small, the low-frequency performance of the PML is poor. Likewise, when f_a is excessively large, the PML performs poorly at high frequencies. A PML with a reasonable value of the break frequency provides a simulation that closely matches the theoretical prediction over the full excited frequency band. We have found empirically that $f_a \approx 1$ MHz seems optimum for ELF simulations. This conclusion is also valid when the field is observed at other strategic observation points, i.e. 2, 3, 4, 5, and 6.

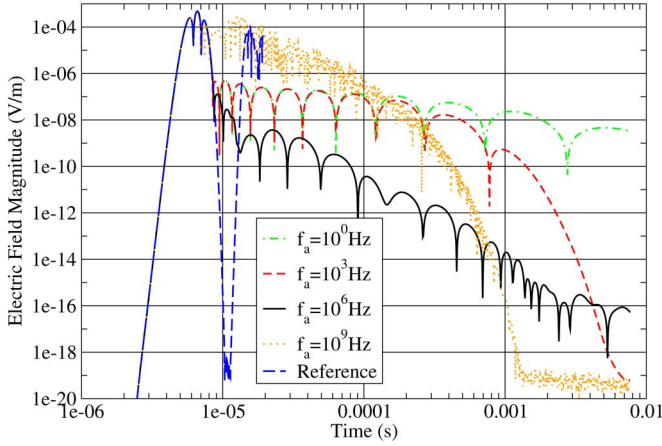


Fig. 2. Time-domain results at observation point 1 for $\kappa = 1$. For times less than about $8e-6$ s, the direct signal is seen. After the direct pulse has passed by the sample point, various levels of residual fields are seen.

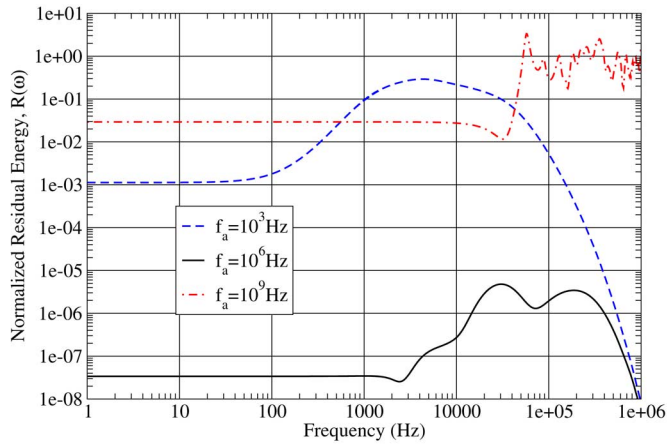


Fig. 3. Normalized PML frequency response at observation point 1 for $\kappa = 1$. Lower amplitudes are better performing PMLs.

See Fig. 2 for the time-domain performance of four test and the reference simulations. The reference simulation shows the direct signal clearly separated from the reflected signals, the latter of which can be removed by time-gating, as noted previously. With $f_a = 1$ Hz, there is slow long-term decay. (In some simulations, when $f_a = 0$, slow growth has even been reported [3].) As f_a is increased to the optimum, the absorption increases relative to the $f_a = 1$ Hz case. As f_a is increased further, the absorption degrades, but still with good late-time fall-off.

In Fig. 3, the frequency-domain residual energy error metric as computed by (6) is shown for observation point 1. In this plot, a better PML will have a lower response. The PML is tested with various break frequencies f_a , each with $\kappa = 1$. With f_a too large or small, there is poor PML absorption. As can be seen in both the time-domain and frequency-domain plots, there is an optimum value for the break frequency for ELF simulations. For the tests performed here, $f_a \approx 1$ MHz provides the best PML absorption at ELF with a relative error on the order of 0.02%.

There is up to a factor of 100 variation in error in PML absorption across the six sample points, as shown in Fig. 4. Surprisingly, sample point 1 has better ELF performance than sample point 5. From a wave perspective, sample point 1 is the grazing incidence case; however, given that the fields are quasi-static,

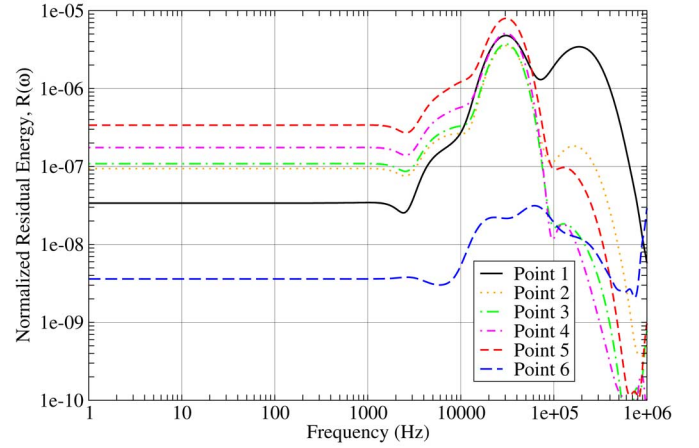


Fig. 4. PML frequency response for $f_a = 10^6$ Hz and $\kappa = 1$ for the six observation points.

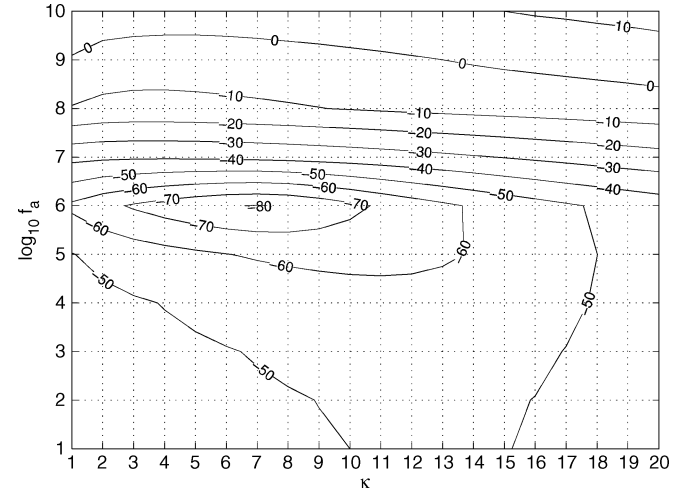


Fig. 5. Time-domain PML residual energy error metric at observation point 1 for various values of the real coordinate stretch κ and the break frequency f_a . FDTD simulations are performed at each grid-line intersection.

grazing incidence has no real meaning. Clearly from Figs. 3 and 4, good choices of parameters provide better than 70 dB of PML absorption over the ELF band at favorable observation locations and more than 60 dB attenuation in unfavorable locations.

A. Time-Domain (Broadband) Performance

Figs. 5 and 6 show the time-domain contours of $10 \log_{10} r$ as κ varies from 1 to 20 and as f_a varies from 1 to 10^{10} Hz for observation points 1 and 5, respectively. There is variation in the location and depth of the global minimum across the six observation points. However, with $f_a \approx 1$ MHz and $3 \lesssim \kappa \lesssim 8$, the PML provides -70 dB or better performance at all six observation locations.

B. Frequency-Domain (Narrowband) Performance

Figs. 7–9 show the frequency-domain PML performance at 100 Hz, 10 kHz, and 1 MHz, respectively. The 1 Hz to 1 kHz optima vary widely with κ , f_a , and observation position. For some specific test locations, frequencies, and PML parameters, there are very deep minima on the order of -120 dB in some cases. Because the location and parameters of these minima do

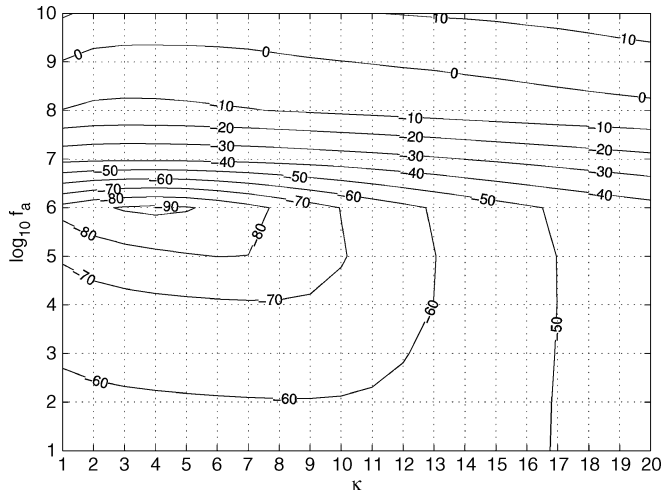


Fig. 6. Time-domain PML residual energy error metric at observation point 5.

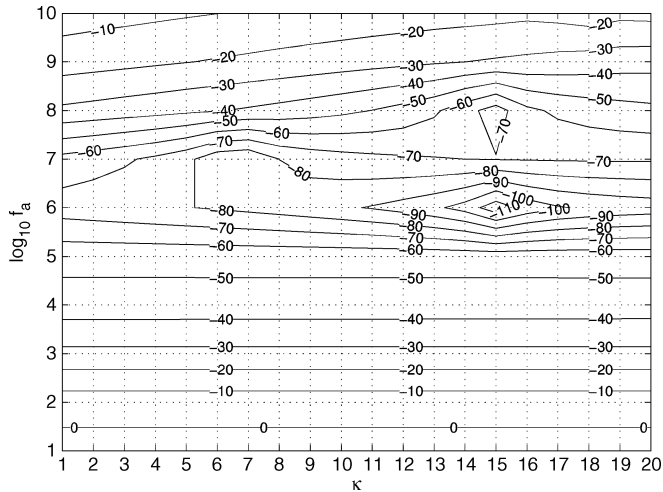


Fig. 7. 100-Hz frequency-domain PML residual energy error metric at observation point 1. At the same observation point, the 1 to 100 Hz results look essentially identical.

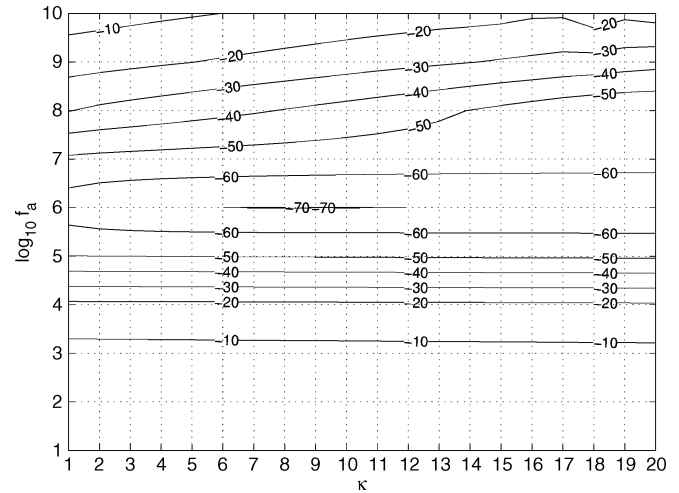


Fig. 8. 10-kHz frequency-domain PML residual energy error metric at observation point 1.

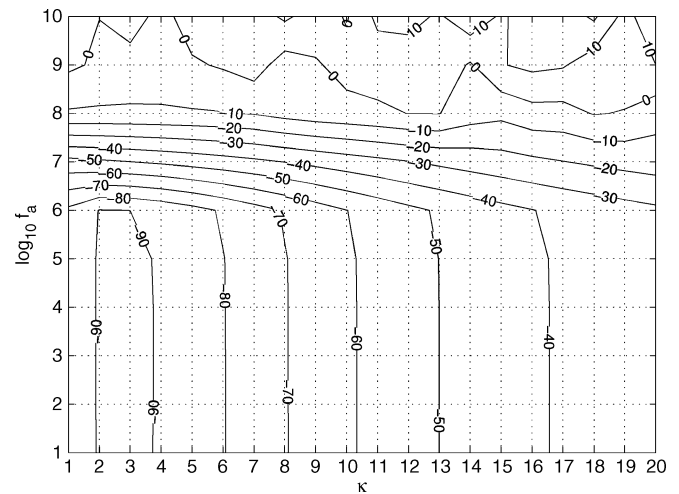


Fig. 9. 1-MHz frequency-domain PML residual energy error metric at observation point 1.

not vary in a regular way, it is important to select operating conditions for the PML based on the performance at several observation locations. For example, at 10 Hz, 100 Hz, and 1 kHz, $f_a \approx 10^6$ Hz with $1 \leq \kappa \leq 20$ provides -60 dB or better PML performance at all six observation points. If $18 \leq \kappa \leq 20$, then the PML provides -70 dB or better performance at all six observation points. Apparently, the narrowband metrics at ELF are improved with larger values of κ as compared to the wideband time-domain metric. Fig. 9 shows that at 1 MHz, smaller values for κ provide the best PML absorption. The optimum PML parameters depend on the metric used and on the frequencies of interest.

IV. CONCLUSION

For ELF PML development, our empirical research shows that when $f_a \approx 1$ MHz, $\kappa \approx 6$, $\sigma = \sigma_{\text{opt}}$, fourth-order polynomials for σ and κ are invoked, and a third-order polynomial for α is invoked, then at least 60 dB of PML attenuation is obtained in the quasi-static region (i.e. very near-field) of the dipole, for both the wideband and ELF narrowband metrics. This is more than adequate for high-quality FDTD simulations in the ELF band.

REFERENCES

- [1] S. Abarbanel and D. Gottlieb, "A mathematical analysis of the PML method," *J. Comput. Phys.*, vol. 134, pp. 357–363, 1997.
- [2] F. L. Teixeira and W. C. Chew, "Perfectly matched layer in cylindrical coordinates," *IEEE Trans. Geosci. Remote Sens.*, vol. 38, no. 4, pp. 1530–1543, Jul. 2000.
- [3] E. Bécache, P. G. Petropoulos, and S. D. Gedney, "On the long-time behavior of unsplit perfectly matched layers," *IEEE Trans. Antennas Propag.*, vol. 52, no. 5, pp. 1335–1342, May 2004.
- [4] M. Kuzuoglu and R. Mittra, "Frequency dependence of the constitutive parameters of causal perfectly matched anisotropic absorbers," *IEEE Microw. Guided Wave Lett.*, vol. 6, no. 12, pp. 447–449, Dec. 1996.
- [5] J. A. Roden and S. D. Gedney, "Convolution PML (CPML): An efficient FDTD implementation of the CFS-PML for arbitrary media," *Microw. Opt. Technol. Lett.*, vol. 27, no. 5, pp. 334–339, Dec. 2000.
- [6] C. L. Wagner and J. B. Schneider, "Divergent fields, charge, and capacitance in FDTD simulations," *IEEE Trans. Microw. Theory Tech.*, vol. 46, no. 12, pp. 2131–2136, Dec. 1998.
- [7] C. M. Furse, D. H. Roper, D. N. Buechler, D. A. Christensen, and C. H. Durney, "The problem and treatment of DC offsets in FDTD simulations," *IEEE Trans. Antennas Propag.*, vol. 48, no. 8, pp. 1198–1201, Aug. 2000.
- [8] A. Taflov and S. Hagness, *Computational Electrodynamics: The Finite-Difference Time-Domain Method*, 3rd ed. Norwood, MA: Artech House, 2005.
- [9] M. Frigo and S. G. Johnson, "The design and implementation of FFTW3," *Proc. IEEE*, vol. 93, no. 2, pp. 216–231, 2005.

A Perfectly Matched Layer for Lossy Media at Extremely Low Frequencies

Dennis M. Sullivan, *Senior Member, IEEE*, Yang Xia, and Das Butherus

Abstract—The perfectly matched layer (PML) has proven to be an effective means of absorbing outgoing waves for finite-difference time-domain (FDTD) simulations. This letter describes the development of a PML specifically for underwater simulations at low frequencies. This is a significant development for this project that involves simulations of electromagnetic signals for long distances under water.

Index Terms—finite-difference time-domain (FDTD) methods, perfectly matched layer (PML).

I. INTRODUCTION

THE single largest threat to surface warships is mines. These mines are often detonated by the electromagnetic signature of a surface ship [1]. For this reason, it is desirable to have simulation methods to study the propagation of extremely low frequency (ELF) electromagnetic waves under water. The finite-difference time-domain (FDTD) method [2], [3] is one of the most widely used methods in electromagnetic simulation and has recently been adapted for ELF's under water [4], [5]. In FDTD simulations, it is necessary to have an absorbing boundary condition (ABC) to truncate the problem space and absorb outgoing waves. One of the most widely used and versatile ABCs is the perfectly matched layer (PML) [6], [7]. There has been some activity in the development of PMLs that are effective in low frequency or dispersive media [8]–[11]. In this letter, we describe the development of a PML that is specifically suited for very lossy media at ELF's.

II. IMPLEMENTATION OF THE PML

A. Berenger's PML in Free Space

Berenger [6] assumed that any plane wave propagating in the direction d near the PML could be broken up into the part traveling perpendicular to the PML d_{\perp} and the part traveling parallel d_{\parallel} (Fig. 1). The two conditions for the PML are the following:

- 1) It must have the same impedance as free space and not present a loss to the wave traveling parallel to the interface.

Manuscript received July 02, 2009; revised August 29, 2009. First published September 29, 2009; current version published October 16, 2009. This work was supported by ONR Grant N00014-17-1-0811 in collaboration with NAVESAE, Carderock Division.

The authors are with the Electrical and Computer Engineering Department, University of Idaho, Moscow, ID 83844-1023 USA. (e-mail: dennis@ee.uidaho.edu).

Color versions of one or more of the figures in this letter are available online at <http://ieeexplore.ieee.org>.

Digital Object Identifier 10.1109/LAWP.2009.2033215

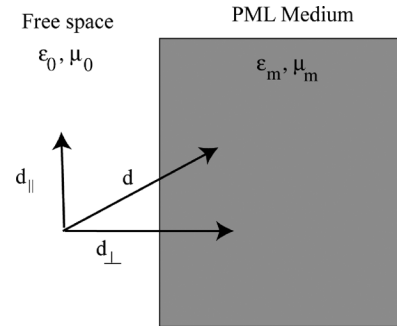


Fig. 1. The PML is implemented by assuming any propagating wave can be broken up into a part that is perpendicular to the PML interface and a part that is parallel to it.

- 2) It must increase the artificial electric and magnetic conductivities such that the impedance still matches that of the free space.

Both of these conditions are met by increasing the electric and magnetic conductivities in the PML such that

$$\eta = \sqrt{\frac{\mu_0}{\epsilon_0}} = \sqrt{\frac{\mu_0 \left(1 + \frac{\sigma_H}{j\omega\mu_0}\right)}{\epsilon_0 \left(1 + \frac{\sigma_E}{j\omega\epsilon_0}\right)}}. \quad (1)$$

Note that this impedance is a real number.

Berenger implemented (1) into the FDTD formulation by a split-step formulation that broke each electric and magnetic field into two components. Most applications assume that the background medium in the main problem space is free space.

B. The PML in a Lossy Medium at ELF's

When the background medium is lake water and the frequencies are in the ELF region, the situation is different. Lake water has a dielectric constant of 80 and a conductivity of 0.018 S/m [12]. For lake water at 1 kHz, the complex dielectric constant is

$$\begin{aligned} \epsilon_w^* &= \epsilon_w + \frac{\sigma_w}{j\omega\epsilon_0} = 80 + \frac{0.018}{j(2\pi \times 10^3)(8.85 \times 10^{-12})} \\ &= 80 - j3.24 \times 10^5 \cong -j3.24 \times 10^5. \end{aligned}$$

Therefore, the impedance is

$$\eta_w = \sqrt{\frac{\mu_0}{\epsilon_w^* \epsilon_0}} \cong \sqrt{\frac{\mu_0}{\epsilon_0 \left(\frac{\sigma_w}{j\omega\epsilon_0}\right)}} = \sqrt{\frac{\mu_0}{\frac{\sigma_w}{j\omega}}}. \quad (2)$$

This impedance can be written in polar coordinates as

$$\eta_w = |\eta_w| \angle 45^\circ.$$

Notice that because the loss term dominates, the impedance is at 45° . The impedance of the PML material must remain at this value, but at the same time increase the loss further as it goes perpendicular into the PML. This can be accomplished by adding a factor s to the conductivity and the permeability

$$\eta_{pml} = \sqrt{\frac{s \cdot \mu_0}{\frac{s \cdot \sigma_w}{j\omega}}} \quad (3)$$

This addition of the s term causes the PML medium to absorb outgoing waves faster than the water medium, but also avoids reflections from the PML medium. The factor s equals one in the background medium, but increases as it goes into the PML.

This implementation may bare a superficial representation to the “stretched coordinates” proposed by Chew and Weedon [13]. However, the s in (3) is a real number as opposed to the complex numbers used in the stretched coordinates. There have been other methods proposed for the PML in lossy media [10], [11] where the conductivity is large enough that it plays a substantial role in the complex dielectric constant. However, the impedance in (3) is for the situation when the imaginary part of the dielectric constant dominates completely.

C. Implementation Into FDTD

We begin with the following formulation of the Maxwell equations for a lossy media:

$$\begin{aligned} \epsilon_w \epsilon_0 \frac{\partial \mathbf{E}}{\partial t} - \sigma \mathbf{E} &= \nabla \times \mathbf{H} \\ \mu_0 \frac{\partial \mathbf{H}}{\partial t} &= -\nabla \times \mathbf{E}. \end{aligned}$$

We will restrict the discussion to the implementation of E_x and H_z propagating in the y -direction perpendicular to the PML

$$\epsilon_w \epsilon_0 \frac{\partial E_x}{\partial t} + \sigma_w E_x = \frac{\partial H_z}{\partial y} - \frac{\partial H_y}{\partial z} \quad (4a)$$

$$\mu_0 \frac{\partial H_z}{\partial t} = \frac{\partial E_x}{\partial y} - \frac{\partial E_y}{\partial x}. \quad (4b)$$

The FDTD formulation leads to the following coupled equations:

$$\begin{aligned} E_x^{n+1}(i, j, k) &= \frac{\epsilon_w \epsilon_0}{(\epsilon_w \epsilon_0 + \sigma_w \cdot \Delta t)} E_x^n(i, j, k) + \frac{(\frac{\Delta t}{\Delta x})}{(\epsilon_w \epsilon_0 + \sigma_w \cdot \Delta t)} \\ &\cdot \left[H_z^{n+1/2}(i, j, k) - H_z^{n+1/2}(i, j-1, k) \right] \\ &\cdot \left[-H_y^{n+1/2}(i, j, k) + H_y^{n+1/2}(i, j, k-1) \right] \end{aligned} \quad (5a)$$

$$\begin{aligned} H_z^{n+1/2}(i, j, k) &= H_z^{n-1/2}(i, j, k) + \frac{\Delta t}{(\mu_0 \Delta x)} \\ &\cdot \left[E_x^{n+1}(i, j+1, k) - E_x^{n+1}(i, j, k) \right] \\ &\cdot \left[E_y^{n+1}(i, j, k) - E_y^{n+1}(i+1, j, k) \right] \end{aligned} \quad (5b)$$

where Δx and Δt are the cell size and time-step, respectively. The implementation of the PML in the H_z field in the y -direction is relatively straightforward. The term s is added only to the y differential

$$\begin{aligned} H_z^{n+1/2}(i, j, k) &= H_z^{n-1/2}(i, j, k) \\ &+ \frac{\Delta t}{(\mu_0 \Delta x)} [E_y^{n+1}(i, j, k) - E_y^{n+1}(i+1, j, k)] \\ &+ \frac{\Delta t}{(s \cdot \mu_0 \Delta x)} [E_x^{n+1}(i, j+1, k) - E_x^{n+1}(i, j, k)]. \end{aligned} \quad (6)$$

Instead of changing the entire term containing s above, we have found it expedient to include a one-dimensional array

$$gy(j) = \frac{1}{s} \quad (7)$$

so (6) becomes

$$\begin{aligned} H_z^{n+1/2}(i, j, k) &= H_z^{n-1/2}(i, j, k) \\ &+ \frac{\Delta t}{(\mu_0 \Delta x)} [E_y^{n+1}(i, j, k) - E_y^{n+1}(i+1, j, k)] \\ &+ gy(j) \frac{\Delta t}{(\mu_0 \Delta x)} \\ &\cdot [E_x^{n+1}(i, j+1, k) - E_x^{n+1}(i, j, k)]. \end{aligned} \quad (8)$$

Adding the PML to the calculation of the E_x field requires that the calculation be split into two equations for propagation in the y and z directions. The s term is only added to the conductivity in the y -direction

$$\begin{aligned} E_{xy}^{n+1}(i, j, k) &= \frac{\epsilon_w \epsilon_0}{(\epsilon_w \epsilon_0 + s \cdot \sigma_w \cdot \Delta t)} E_{xy}^n(i, j, k) + \frac{(\frac{\Delta t}{\Delta x})}{(\epsilon_w \epsilon_0 + s \cdot \sigma_w \cdot \Delta t)} \\ &\cdot [H_z^{n+1/2}(i, j, k) - H_z^{n+1/2}(i, j-1, k)] \end{aligned} \quad (9a)$$

$$\begin{aligned} E_{xz}^{n+1}(i, j, k) &= \frac{\epsilon_w \epsilon_0}{(\epsilon_w \epsilon_0 + \sigma_w \cdot \Delta t)} E_{xz}^n(i, j, k) + \frac{(\frac{\Delta t}{\Delta x})}{(\epsilon_w \epsilon_0 + \sigma_w \cdot \Delta t)} \\ &\cdot [H_y^{n+1/2}(i, j, k-1) - H_y^{n+1/2}(i, j, k)]. \end{aligned} \quad (9b)$$

Once again, it is expedient to implement this by an additional one-dimensional array. Equation (9a) becomes

$$\begin{aligned} E_{xy}^{n+1}(i, j, k) &= fy(j) \cdot ca \cdot E_{xy}^n(i, j, k) \\ &+ fy(j) \cdot cb \cdot [H_z^{n+1/2}(i, j, k) - H_z^{n+1/2}(i, j-1, k)] \end{aligned} \quad (10)$$

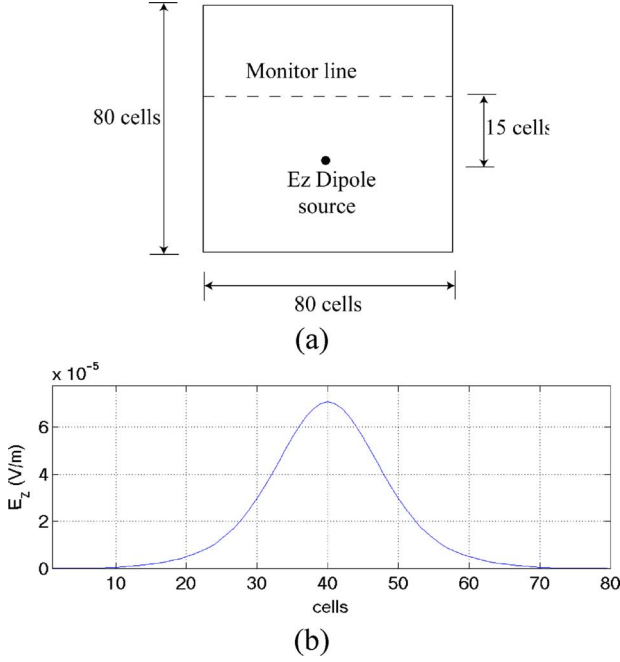


Fig. 2. (a) A dipole source is located in the 80^3 problem space. Once steady state has been reached, the amplitude is determined at a transverse line 15 cells from the source. The cells are 25 m^3 . (b) The amplitude at the monitor line after 4000 time-steps.

where

$$ca = \frac{\varepsilon_w \varepsilon_0}{(\varepsilon_w \varepsilon_0 + \sigma_w \cdot \Delta)} \quad (11a)$$

$$cb = \frac{\left(\frac{\Delta t}{\Delta x}\right)}{(\varepsilon_w \varepsilon_0 + \sigma_w \cdot \Delta t)} \quad (11b)$$

$$fy(j) = \frac{\left(1 + \sigma_w \cdot \frac{\Delta t}{\varepsilon_w \varepsilon_0}\right)}{\left(1 + s \cdot \sigma_w \cdot \frac{\Delta t}{\varepsilon_w \varepsilon_0}\right)}. \quad (11c)$$

In summary, the PML is implemented in the y -direction by the one-dimensional arrays

$$gy(j) = \frac{1}{s} \quad (7^*)$$

$$fy(j) = \frac{\left(1 + \sigma_w \cdot \frac{\Delta t}{\varepsilon_w \varepsilon_0}\right)}{\left(1 + s \cdot \sigma_w \cdot \frac{\Delta t}{\varepsilon_w \varepsilon_0}\right)}. \quad (11c^*)$$

It has been found empirically that an effective formula for the s factor as it goes into the PML is

$$s = 0.2 \cdot (j - j_{\text{edge}})^3 \quad (12)$$

where j_{edge} is the beginning of the PML. This formulation also prevents the largest stretched cells from exceeding the skin depth.

III. RESULTS

In this section, we illustrate the effectiveness of the lossy medium ELF PML. We will start with the problem space illustrated in Fig. 2(a), which is 80 cells cubed. Each cell is 25 m

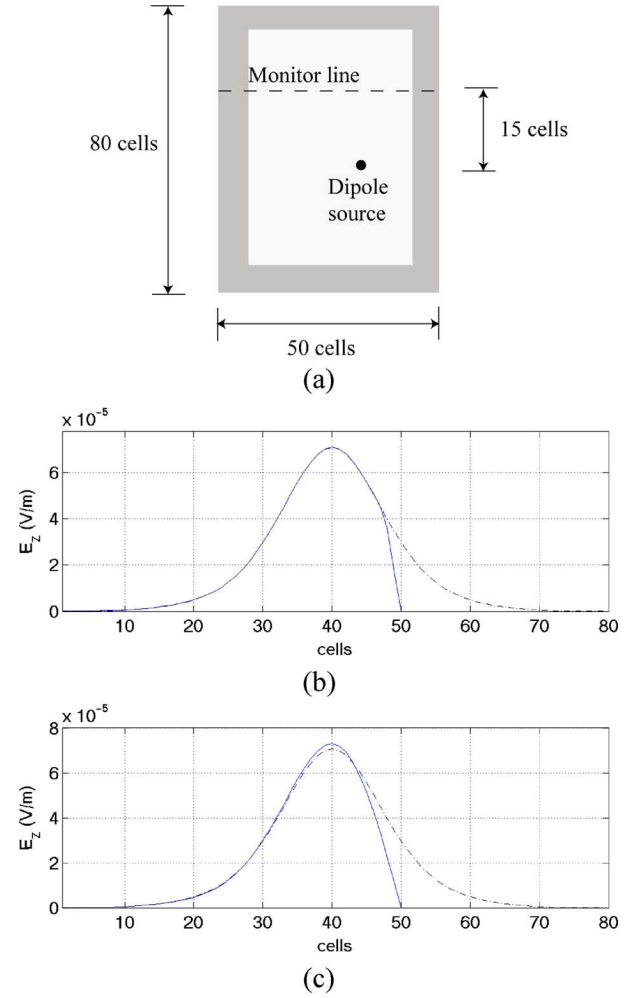


Fig. 3. (a) The problem space is truncated to 10 cells to the right of the source. A four-cell lossy PML has been added to each boundary. (b) The solid line is the amplitude for the simulation in (a), while the dashed line is from the 80 cell monitor line of Fig. 2. (c) The same simulation with no PML.

cubed. The size of 80^3 was needed so that boundary plays no role in the results of the simulation. The source is a single-cell electric dipole. After 4000 time-steps, the amplitude is calculated via the method of two equations, two unknowns (2E2U) [14] at a monitor line 15 cells from the dipole, as shown in Fig. 2(b).

The simulation is then repeated for the truncated problem space shown in Fig. 3(a), where a four-cell PML has been added. In this simulation, the right wall has been moved in to within 10 cells of the source. The results are plotted in Fig. 3(b) (solid line) along with the results of the previous simulation (dashed line). For comparison, Fig. 3(c) is the same simulation with no PML on the truncated wall. Clearly, substantial errors appear when the PML is not present.

In one final simulation, the problem space is reduced to $60 \times 20 \times 20$ cells, as illustrated in Fig. 4(a). The results are shown in Fig. 4(b), where the results of the original simulation of Fig. 2 are presented for comparison. The amplitudes on the monitor line within five cells of the center are identical. Once again, the results without the PML are shown in Fig. 4(c), demonstrating the expected error when no PML is present.

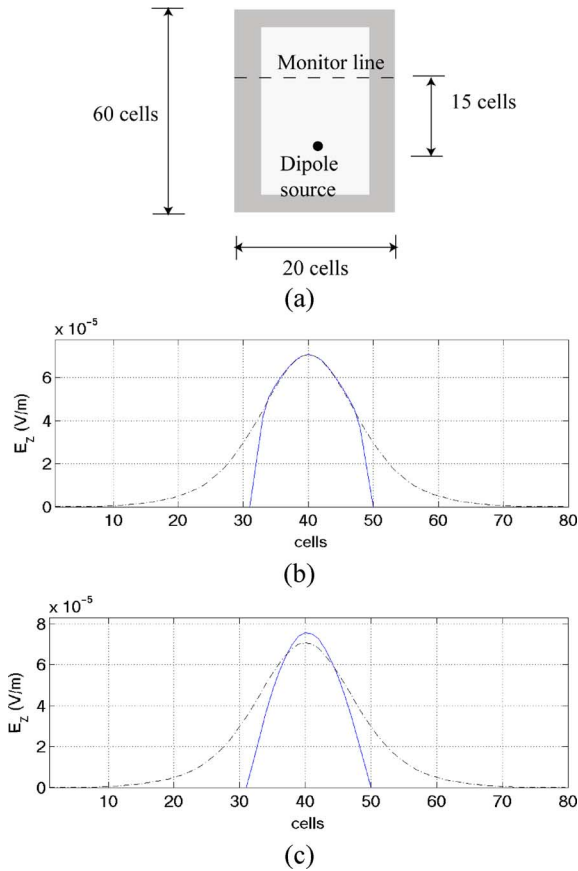


Fig. 4. (a) A simulation similar to Fig. 2 but with the problem space truncated to $60 \times 20 \times 20$ cells. (b) The solid line is the amplitude for the smaller problem space, while the dashed line is the larger problem space of Fig. 2. (c) The same comparison when a $60 \times 20 \times 20$ problem space with no PML is used.

IV. DISCUSSION

A PML has been developed for applications involving ELF's in lossy media. As opposed to the original Berenger PML in free space, this one requires a split E -field, but not a split H -field. Although the use of a PML is not as crucial as it might be in

free space or other lossless media, it substantially decreases the needed computer resources. For instance, in the examples in Section III, it was found that a problem space of 80^3 was necessary to insure that the boundaries were not influencing the results when there was no PML. After the PML was added, the problem space was reduced to $60 \times 20 \times 20$. This represents a reduction in the problems space from 512 000 cells to 24 000 cells.

REFERENCES

- [1] J. J. Holmes, *Exploitation of a Ship's Magnetic Field Signatures*. San Rafael, CA: Morgan & Claypool, 2006.
- [2] K. S. Yee, "Numerical solution of initial boundary value problems involving Maxwell's equations in isotropic media," *IEEE Trans. Antennas Propag.*, vol. AP-14, no. 3, pp. 302–307, May 1966.
- [3] D. M. Sullivan, *Electromagnetic Simulation Using the FDTD Method*. New York: IEEE Press, 2000.
- [4] Y. Xia and D. M. Sullivan, "Underwater FDTD simulation at extremely low frequencies," *IEEE Antennas Wireless Propag. Lett.*, vol. 7, pp. 661–664, 2008.
- [5] Y. Xia and D. M. Sullivan, "Dual problem space FDTD simulation for underwater ELF applications," *IEEE Antennas Wireless Propag. Lett.*, vol. 8, pp. 498–501, 2009.
- [6] J. P. Berenger, "A perfectly matched layer for the absorption of electromagnetic waves," *J. Comput. Phys.*, vol. 114, pp. 185–200, 1994.
- [7] J. P. Berenger, *Perfectly Matched Layer (PML) for Computational Electromagnetics*. San Rafael, CA: Morgan & Claypool, 2007.
- [8] J. De Moerloose and M. A. Stuchly, "Behavior of Berenger's ABC for evanescent waves," *IEEE Microw. Guided Wave Lett.*, vol. 5, no. 10, pp. 344–346, Oct. 1995.
- [9] S. A. Cummer, "A simple, nearly perfectly matched layer for general electromagnetic media," *IEEE Microw. Wireless Comput. Lett.*, vol. 13, no. 3, pp. 128–130, Mar. 2003.
- [10] J. Fang and Z. Wu, "Generalized perfectly matched layer—An extension of Berenger's perfectly matched layer boundary conditions," *IEEE Microw. Guided Waves Lett.*, vol. 5, no. 12, pp. 451–453, Dec. 1995.
- [11] Q. H. Liu, "An FDTD algorithm with perfectly matched layers for conductive media," *Microw. Opt. Technol. Lett.*, vol. 14, pp. 134–137, 1997.
- [12] D. K. Chen, *Field and Wave Electromagnetics*, 2nd ed. New York: Addison-Wesley, 1989.
- [13] W. C. Chew and W. H. Weedon, "A 3D perfectly matched medium from modified Maxwell's equations with stretched coordinates," *Microw. Opt. Technol. Lett.*, vol. 11, pp. 599–604, Jul. 1994.
- [14] C. M. Furse, "Faster than Fourier—Ultra-efficient time-to-frequency domain conversions for FDTD simulations," *IEEE Antennas Propag. Mag.*, vol. 42, no. 6, pp. 24–34, Dec. 2000.

Underwater FDTD Simulation at Low Frequencies

Dennis M. Sullivan* and Yang Xia
Department of Electrical and Computer Engineering
University of Idaho
Moscow, ID 83844-1023

I. Introduction

Modern anti-ship mines can be detonated by the electromagnetic signature of a surface ship [1]. For this reason, it is desirable to have simulation methods to study the propagation of extremely low frequency (ELF) electromagnetic waves under water. The finite-difference time-domain (FDTD) method [2-5] is one of the most widely used methods in electromagnetic simulation. Unfortunately, the discrete Fourier transform method used to quantify the results of the time-domain simulation is not practical at ELF. Furthermore, the Bessel/Legendre expansion method used to verify the FDTD results is also not valid at low frequencies. These two major issues are addressed in this paper. Results comparing the FDTD and an analytic method confirm the accuracy of FDTD at low frequencies.

II. Method

We begin with the normalized time-domain Maxwell's equations

$$\frac{\partial \mathbf{D}}{\partial t} = c_0 \nabla \times \mathbf{H} \quad (1 \text{ a})$$

$$\mathbf{D}(\omega) = \epsilon_r^*(\omega) \mathbf{E}(\omega) \quad (1 \text{ b})$$

$$\frac{\partial \mathbf{H}}{\partial t} = -c_0 \nabla \times \mathbf{E} . \quad (1 \text{ c})$$

The different materials are described through the complex dielectric constant $\epsilon_r^*(\omega) = \epsilon_r + \sigma / j\omega\epsilon_0$. Equations (1 a) and (1 c) are taken to the sampled time domain by the finite-differencing procedure at the heart of the FDTD method. There are several approaches to implement Eq. (1 b) into FDTD [5] and they will not be repeated here.

III. The Method of two equations, two unknowns (2E2U)

After an FDTD simulation has proceeded long enough to reach steady state, a method is needed to determine the amplitude and phase at points within the problem space. The discrete Fourier transform usually used at radio frequencies and higher will not work at ELF. The method of two equations, two unknown (2E2U), which is described in this section, is due to Furse [6].

It is desirable to find the amplitude and phase of a sinusoidal signal from two sample points. The frequency is known, so the two points can be written as:

$$E_1 = A(\sin \omega t_1 + \phi), \quad (2 \text{ a})$$

$$E_2 = A(\sin \omega t_2 + \phi). \quad (2 \text{ b})$$

The values ω , E_1 and E_2 are known, and A and ϕ are to be determined.

It would be advantageous to have the phases of the sample points arranged to be symmetric around the vertical axis, which is accomplished by adding an offset time $t_{\text{off}} = 0.5(\pi / \omega - t_1 - t_2)$. Some mathematical manipulation gives the amplitude and phase:

$$\phi = \tan^{-1} \left\{ \tan \omega(t_1 + t_{\text{off}}) \frac{E_1 - E_2}{E_1 + E_2} \right\}, \quad (3 \text{ a})$$

$$A = \frac{E_1 + E_2}{(2 \sin \omega(t_1 + t_{\text{off}}) \cos \phi)}. \quad (3 \text{ b})$$

IV. Verification of the accuracy of the method

An analytic solution is needed for a layered dielectric sphere in a uniform electric field given by $E_0 \hat{a}_z$, as shown in Fig. 1.

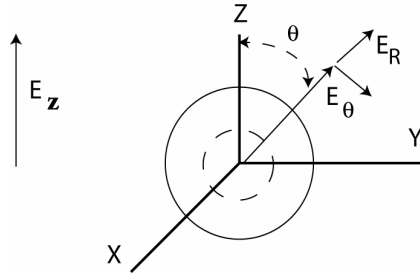


Figure 1. A layered dielectric sphere in a constant E field.

A spherical boundary-value problem has solutions of the form [7]

$$V(R, \theta) = \sum_{n=0}^{\infty} \left[A_n R^n + B_n R^{-(n+1)} \right] P_n(\cos \theta). \quad (4)$$

$P_n(\cos \theta)$ are the Legendre polynomials. In the limit far from the sphere, $V_o(R, \theta)|_{R \rightarrow \infty} \equiv -E_0 R \cos \theta$, and inside the sphere $V_1(R, \theta) = A_1 R \cos \theta$. There are two boundary conditions at a dielectric boundary: $E_{1t} = E_{2t}$, $\epsilon_1 E_{1n} = \epsilon_2 E_{2n}$. The two equations resulting from the boundary conditions are

$$B_m + A_m r_m^3 - B_{m+1} - A_{m+1} r_m^3 = 0$$

and

$$-2 \frac{\epsilon_m}{\epsilon_{m+1}} B_m + \frac{\epsilon_m}{\epsilon_{m+1}} A_m r_m^3 + 2 B_{m+1} - A_{m+1} r_m^3 = 0.$$

The constants are determined by Gaussian elimination. Once the potential V is known, the E fields are determined by:

$$\mathbf{E} = -\nabla V = -\frac{\partial}{\partial R} V \mathbf{a}_R - \frac{1}{R} \frac{\partial}{\partial \theta} V \mathbf{a}_\theta, \quad (5)$$

which can be converted to rectangular coordinates.

In order to verify the accuracy, we use the three-dimensional problem space illustrated in Fig. 2. A plane wave is generated at one end and subtracted out the other end. The cells used in the following simulations are five meters cubed and the time steps are 8.3 nanoseconds. A layered sphere with dielectric properties to simulate various materials lies in the center of the total field. The amplitude of the E field is determined along the major axes for comparison with an analytic method to evaluate the accuracy of the FDTD simulation. These axes go through the sphere and extend five cells out in each direction. The problem space of 50 cubed is surrounded by a perfectly matched layer (PML) of 8 cells [8]. Each cell is 5 meters cubed.

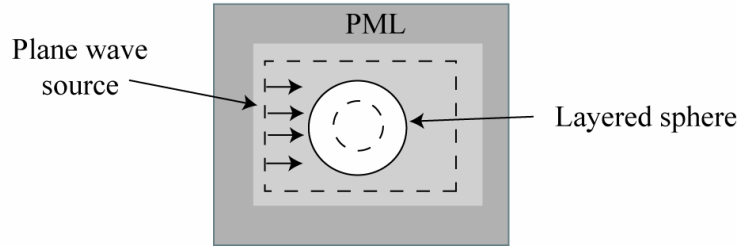


Figure 2. The configuration of the three-dimensional simulation space used to evaluate the accuracy of the method.

Table 1. The properties of the materials

<u>Material</u>	<u>ϵ_r</u>	<u>σ (S/m)</u>
Air	1	0
Water	80	0.018
Mud	40	0.002
Metal	1	10^7

The results of the simulations are shown in Fig. 3. The solid lines are the analytic results and the circles are the FDTD values. Clearly, the comparisons are very good. In Fig. 3.c, there is some discrepancy in the air layer in the middle. This is not too worrisome because in problems of interest, air is a boundary, not a central part of the problem space.

V. Discussion

A method has been described to simulate electromagnetic waves propagating under water at extremely low frequencies. By comparison with an analytic method, it has been shown to be extremely accurate simulating the interaction of ELF plane waves with the materials of interest. Future work will include the modeling of transmitting and receiving antennas.

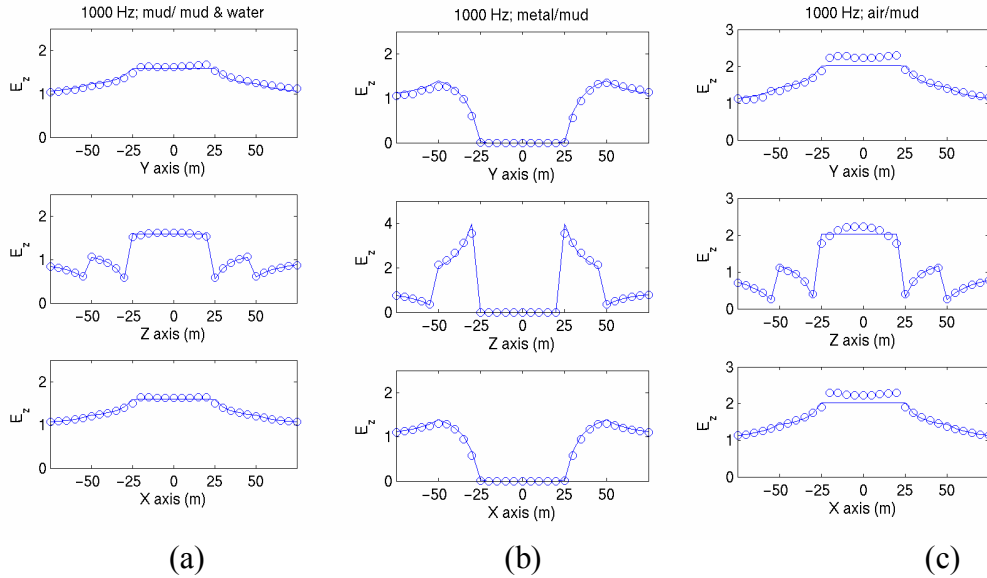


Figure 3. Comparison of the FDTD values (circles) vs. the analytic values for an incident plane wave at 1 kHz and a layered sphere comprised of different media. (a) inner layer is mud, outer layer is mud & water; (b) inner layer is metal, outer layer is mud; (c) inner layer is air, outer layer is mud.

Acknowledgements

This work was funded under ONR grant number N00014-07-1-0811 in collaboration with NAVSEA, Carderock Division, and was supported in part by the National Science Foundation through the San Diego Supercomputer Center under grant ECS9500001 and utilized the STG655 IBM Power4 Supercomputer.

REFERENCES

1. J. J. Holmes, *Exploitation of a ship's magnetic field signatures*, Morgan and Claypool Publishers, 2006.
2. K. S. Yee, "Numerical solution of initial boundary value problems involving Maxwell's equations in isotropic media," *IEEE Trans. Antennas Propagat.*, Vol. 17, pp. 585-589, 1966.
3. A. Taflove, *Computational Electrodynamics: The Finite-Difference Time-Domain Method*. Boston, MA: Artech House, 1995.
4. A. Taflove, *Advances in Computational Electrodynamics: The Finite-Difference Time-Domain Method*. Boston, MA: Artech House, 1998.
5. D. M. Sullivan, *Electromagnetic Simulation Using the FDTD Method*. New York, NY: IEEE Press, 2000.
6. C. M. Furse, "Faster than Fourier—Ultra-efficient time-to-frequency domain conversions for FDTD simulations," *Antennas and Propagation Magazine*, Vol. 42(6), pp. 24-34, 2000.
7. D. K. Chen, *Field and Wave Electromagnetics*, 2nd Ed., New York: Addison-Wesley, 1989.
8. J. P. Berenger, "A perfectly matched layer for the absorption of electromagnetic waves," *J. Comp. Physics*, Vol. 114, pp. 185-200, 1994.

Near to Far Field Transformation for Underwater ELF Simulation

Yang Xia* and Dennis M. Sullivan
Department of Electrical and Computer Engineering
University of Idaho
Moscow, ID 83844-1023

I. Introduction

Anti-ship mines can be detonated by the electromagnetic signature of a surface ship [1]. Electromagnetic (EM) simulation is being developed to assess the propagation of these signals using the finite-difference time-domain (FDTD) method [2-5]. A previous paper has described this and demonstrated the accuracy [6]. A near-field to far-field transformation is being utilized to extend the reach of an FDTD simulation without using extraordinary computer resources.

II. Method Description

Two different problem spaces are used, one for the near field and one for the far field. The near field problem space models the EM source and uses relatively small cells. The far field uses larger cells to model propagation over large distances. The transformation of the propagating wave from the near field to the far field is made by utilizing the equivalence principle [7]. In the near field, the surface currents are calculated over a region containing the source. These surface currents are used to generate surface currents over an area in the far field problem space. The fields within the surface in the far field are held at zero (Fig. 1). Both problem spaces are bordered by a perfectly matched layer (PML) [8]. A time-domain illustration of the process is shown in Fig. 2.

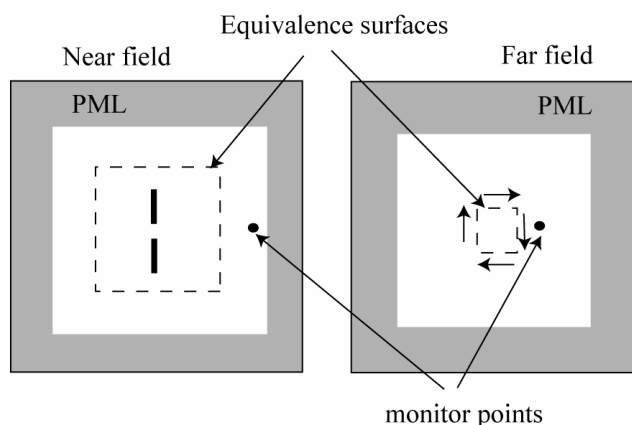


Figure 1. Two problem spaces are utilized in the near field to far field transformation. The near field simulates the source; in this case, a dipole antenna. The cells in the near field are one meter cubed, while those in the far field are thirteen meters cubed.

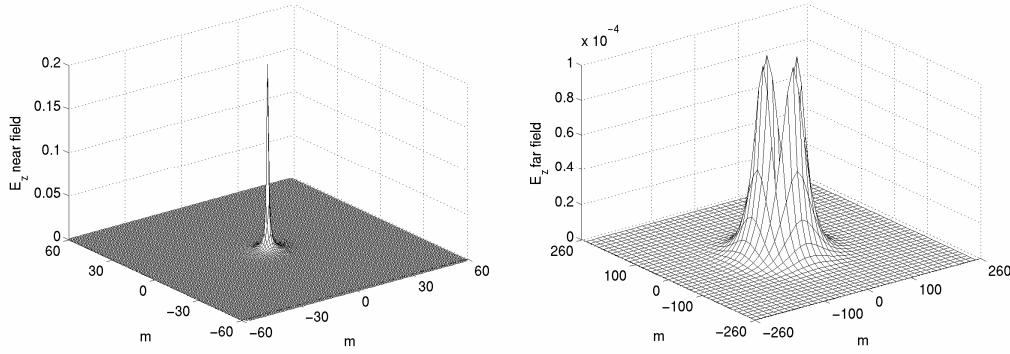


Figure 2. A signal is generated by a dipole in the near field (left). The surface currents from the near field form a rectangular source in the far field (right). The near field uses cells of 1 m^3 ; the far field uses cells of $(13 \text{ m})^3$.

Figure 3 shows a verification of the accuracy in going from the near to the far field. The time-domain data is saved at a monitor point in the near field, as indicated in Fig. 1. The time-domain data is also taken at a corresponding point in the far field. The result in Fig. 3 indicates that an accurate transformation is made.

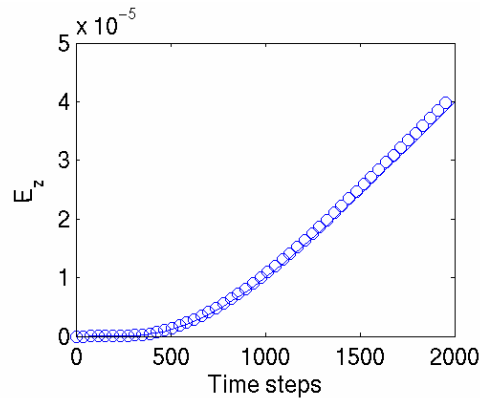


Figure 3. Comparison of the simulated E_z fields at a distance of 52 m from the dipole. The straight line is calculated in the near field while the circles are calculated from the far field.

III. Sample Problem

Figure 4 illustrates the type of simulation of interest in this project. The dielectric properties of the materials are given in Table 1. A near field problem space is used to simulate the dipole antenna using cells of 1 m^3 . It calculates the surface currents to provide a source in the far field problem space, which uses cell of $(13 \text{ m})^3$. This is illustrated in Fig. 5. The frequency of radiation is 1 kHz.

The results collected at the monitor point are shown in Fig. 6. The top part of Fig. 6. shows the time domain data of the E_z field. The bottom part of

Fig. 6 shows the amplitude as calculated by the method of two-equations, two-unknowns [9]. Note that it takes approximately 7000 time steps to reach a steady-state answer.

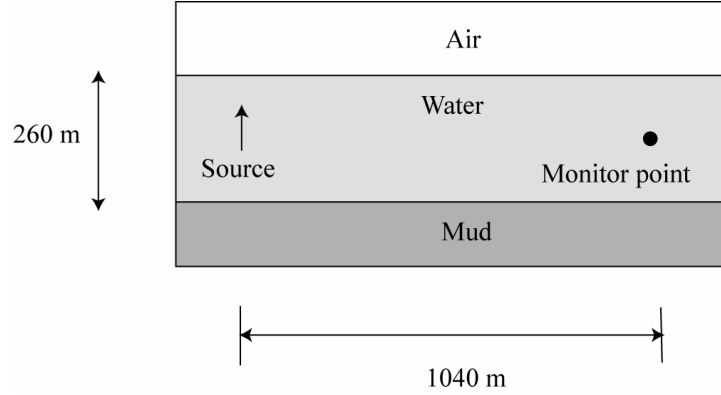


Figure 4. A diagram of an example problem.

Table 1. The dielectric properties of the materials used in this paper

<u>Material</u>	<u>ϵ_r</u>	<u>$\sigma (S/m)$</u>
Air	1	0
Water	80	0.018
Mud	40	0.002
Metal	1	10^7

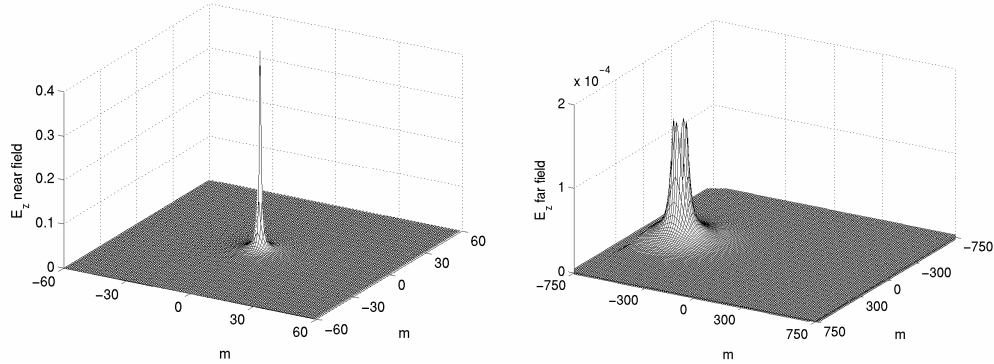


Figure 5. These two pictures show the E_z field after 380 time steps in the near field (left) and the far field (right).

IV. Discussion

We have demonstrated a method to simulate the propagation of ELF waves over long distances in inhomogeneous media utilizing the FDTD method and the equivalence principle. It is believed that this method can play a substantial role in evaluating the EM signatures from surface ships for the purpose of avoiding detection by mines in shallow water.

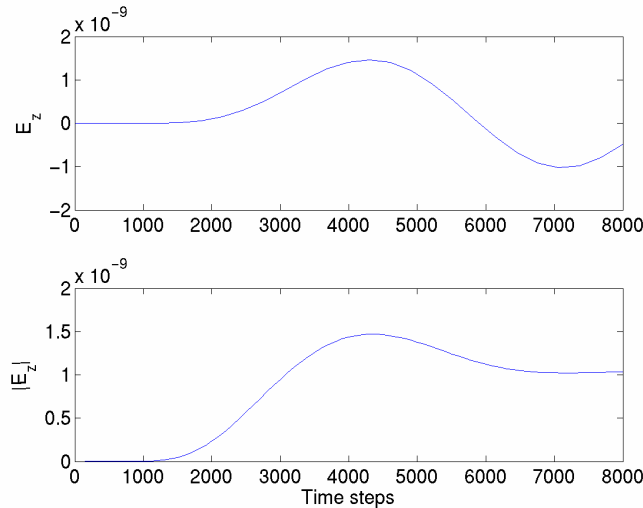


Figure 6. The E_z field at the monitor point illustrated in Fig. 4. The top graph is the time domain data while the bottom graph is the magnitude as calculated by 2E2U.

Acknowledgements

This work was funded under ONR grant number N00014-07-1-0811 in collaboration with NAVESSEA, Carderock Division, and was supported in part by the National Science Foundation through the San Diego Supercomputer Center under grant ECS9500001 and utilized the STG655 IBM Power4 Supercomputer.

REFERENCES

1. J. J. Holmes. *Exploitation of a ship's magnetic field signature*. Morgan and Claypool Publishers, 2006.
2. K. S. Yee, "Numerical solution of initial boundary value problems involving Maxwell's equations in isotropic media," *IEEE Trans. Antennas Propagat.*, Vol. 17, pp. 585-589, 1966.
3. A. Taflove. *Computational Electrodynamics: The Finite-Difference Time-Domain Method*. Boston, MA: Artech House, 1995.
4. A. Taflove. *Advances in Computational Electrodynamics: The Finite-Difference Time-Domain Method*. Boston, MA: Artech House, 1998.
5. D. M. Sullivan. *Electromagnetic Simulation Using the FDTD Method*. New York, NY: IEEE Press, 2000.
6. Y. Xia and D. M. Sullivan, "Underwater ELF simulation using the FDTD method," *IEEE Trans. Antennas Propagat.*, submitted for review.
7. R. F. Harrington. *Time-Harmonic Electromagnetic Fields*. New York, NY: IEEE Press, 2001.
8. J. P. Berenger, "A perfectly matched layer for the absorption of electromagnetic waves," *J. Comp. Physics*, Vol. 114, pp. 185-200, 1994.
9. C. M. Furse, "Faster than Fourier—Ultra-efficient time-to-frequency domain conversions for FDTD simulations," *Antennas and Propagation Magazine*, Vol. 42(6), pp. 24-34, 2000.

High Resolution Interpolation for Underwater FDTD Simulation at ELF Frequencies

Yang Xia^{1*}, Alireza Mansoori¹, Dennis M. Sullivan¹,
and Jacek Nadobny²

1. Department of Electrical and Computer Engineering
University of Idaho
Moscow, ID 83844-1023

2. Clinic for Radiation Oncology
Charité University Clinic
13353 Berlin, Germany

Abstract—A high resolution interpolation scheme for use with the FDTD method at ELF frequencies under water is described. Since the interpolation is applied after the FDTD Simulation, it adds very little to the computation time or resources.

I. Introduction

The single largest threat to surface warships is mines. These mines are often detonated by the electromagnetic signature of a surface ship [1]. For this reason, it is desirable to have simulation methods to study the propagation of extremely low frequency (ELF) electromagnetic waves under water. The finite-difference time-domain (FDTD) method [2, 3] is one of the most widely used methods in electromagnetic simulation and has recently been adapted for ELF frequencies under water [4, 5]. It is desirable to simulate distances on the order of kilometers. For this reason, a near field to far field transformation was developed to allow the source to be simulated with cells on the order of one meter squared, while the far field is simulated with cells of ten meters squared [6]. However, it may be necessary to determine features in the far field with a higher resolution than that of the far field cells (Fig. 1). This paper describes the application of an interpolation scheme that was previously developed for biomedical applications at radio frequencies [7]. It is shown that this method can be used to substantially improve the accuracy of FDTD simulation at ELF frequencies.

II. Method

In the following discussion E will represent the true E field around a boundary, and \tilde{E} represent the averaged FDTD E field value (Fig. 2). At an arbitrary boundary, the electric fields can be represented as the sum of the tangential and normal components

$$\mathbf{E} = \mathbf{E}_t + \mathbf{E}_n \quad (1)$$

$$\tilde{\mathbf{E}} = \tilde{\mathbf{E}}_t + \tilde{\mathbf{E}}_n \quad (2)$$

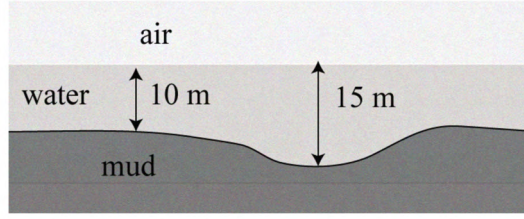


Figure 1. Typical contours in shallow water. Cell sizes on the order of ten meters cubed are used in the far field. This could result in substantial errors when modeling shallow water where mine are often planted.

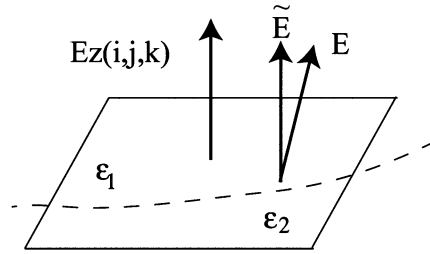


Figure 2. FDTD only calculates values at discrete points, such as $E_z(i,j,k)$. Values at other positions can be approximated by interpolating

Two assumptions are made: The tangential components of the true and the FDTD values are equal

$$\mathbf{E}_t = \tilde{\mathbf{E}}_t, \quad (3)$$

and the normal flux densities are equal

$$\mathbf{D}_n = \tilde{\mathbf{D}}_n. \quad (4)$$

Equation (4) leads to the following relationship between the \mathbf{E} fields:

$$\epsilon \mathbf{E}_n = \tilde{\epsilon} \tilde{\mathbf{E}}_n, \quad (5)$$

where ϵ is the true dielectric constant at that point and $\tilde{\epsilon}$ is the averaged dielectric constant usually used in the FDTD formulation. From Eq. (3) and (5), it can be shown that the true electric field can be calculated by the averaged FDTD \mathbf{E} field with a correction term added. Specifically, in the z direction the \mathbf{E} field is

$$E_z = \tilde{E}_z + \left(\frac{\tilde{\epsilon}_z}{\epsilon_z} - 1 \right) \tilde{E}_{zn} \quad (6)$$

where \tilde{E}_{zn} is calculated by

$$\tilde{E}_{zn} = \hat{n}_z \cdot \left[\left(\hat{n} \cdot \tilde{\mathbf{E}} \right) \hat{n} \right]. \quad (7)$$

In Eq. (7) \hat{n} is the gradient of the dielectric constant and \hat{n}_z is the z component of \hat{n} . The correction is applied after the FDTD simulation is finished. A more detailed explanation is in [7].

III. Verification of the Method

In order to verify the accuracy of the interpolation scheme described in the previous section, we used an analytic method based on Legendre polynomials [5, 6]. This method calculates the values of the E field inside a layered sphere in an electric field. Table one is a list of the materials of interest, along with their dielectric properties. In particular, we will look at the values on an axis at forty-five degrees in the YZ plane because it is at these slanted angles that the largest FDTD error occurs.

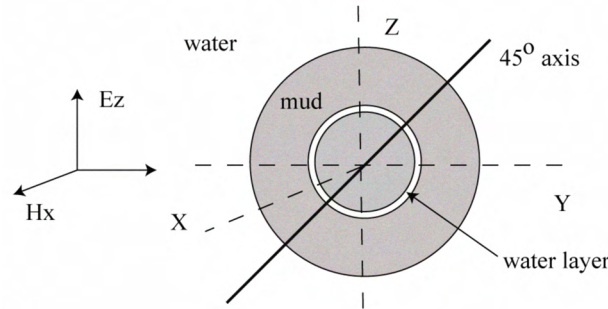


Figure 3. A layered sphere is used to provide an analytic check to the FDTD data. The background medium is water; the sphere is half mud, half water. The narrow layer in the middle is either mud or water.

Table I. The materials used in the simulation

<u>Material</u>	<u>ϵ_r</u>	<u>$\sigma (S/m)$</u>
Water	80	0.018
Mud	40	0.010

We show the results for an FDTD simulation using 10 m cubed cells at 1 kHz in a water medium both before and after the correction is applied. The sphere in Fig. 3 has the characteristics of mud. The thin layer is $\frac{1}{4}$ a cell wide and has the characteristics of water. Figure 4 displays the results. FDTD alone sees the basic features but tends to average the magnitudes out. After the interpolation, a much better agreement is attained, even though the layer is less than one cell.

IV. Discussion

We have described the application of an interpolation scheme that improves the accuracy of FDTD simulation near boundaries. Since the interpolation takes place only after the FDTD simulation, it adds nothing to the

computation time and very little to the needed computer resources. This approach provides more accuracy when large cells on the order of ten meters are used for long range, underwater FDTD simulation.

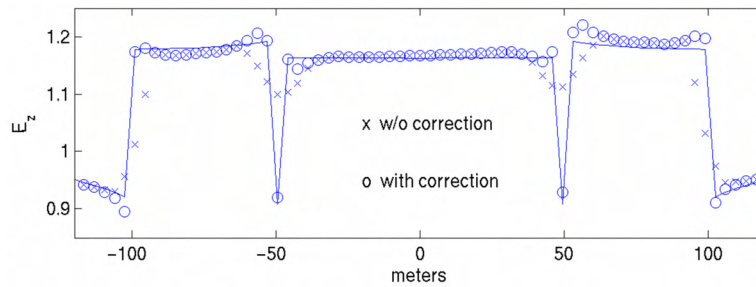


Figure 4. Results for a 1/4 cell (2.5 m) layer of water. The straight line is the analytic values, the x's are from and FDTD simulation before the correction, and the o's are the values after the correction.

Acknowledgements

This work was funded under ONR grant number N00014-07-1-0811 in collaboration with NAVESEA, Carderock Division.

REFERENCES

1. J. J. Holmes, *Exploitation of a ship's magnetic field signatures*, Morgan and Claypool Publishers, 2006.
2. K. S. Yee, "Numerical solution of initial boundary value problems involving Maxwell's equations in isotropic media," *IEEE Trans. Antennas Propagat.*, Vol. 17, pp. 585-589, 1966.
3. D. M. Sullivan, *Electromagnetic Simulation Using the FDTD Method*. New York, NY: IEEE Press, 2000.
4. D. M. Sullivan and Y. Xia, "Underwater FDTD simulation at low frequencies," IEEE International AP-S Symposium, San Diego, July 5-12, 2008.
5. Y. Xia and D. M. Sullivan, "Underwater FDTD simulation at extremely low frequencies," *IEEE Anten. Wireless Prop. Letters*, scheduled for publication.
6. Y. Xia and D. M. Sullivan, "Near to Far Field Transformation for Underwater ELF Simulation," IEEE International AP-S Symposium, San Diego, July 5-12, 2008.
7. J. Nadobny, D. M. Sullivan, P. Wust, M. Seebass, P. Deuflhard, and R. Ferlix, "A high-resolution interpolation at arbitrary interfaces from the FDTD method," *IEEE Trans. Anten. Prop.*, Vol. 46, pp. 1759-1766, Nov. 1998.

A Perfectly Matched Layer for Lossy Media at Extremely Low Frequencies

Dennis M. Sullivan* and Yang Xia
Department of Electrical and Computer Engineering
University of Idaho
Moscow, ID 83844-1023

Abstract—The perfectly matched layer (PML) is an effective means of absorbing outgoing waves for finite-difference time-domain (FDTD) simulations. This letter describes the development of a PML specifically for underwater simulations at low frequencies.

I. Introduction

The single largest threat to surface warships is mines. These mines are often detonated by the electromagnetic signature of a surface ship [1]. For this reason, it is desirable to have simulation methods to study the propagation of extremely low frequency (ELF) electromagnetic waves under water. The finite-difference time-domain (FDTD) method [2, 3] is one of the most widely used methods in electromagnetic simulation and has recently been adapted for ELF frequencies under water [4]. In FDTD simulations, it is necessary to have an absorbing boundary condition (ABC) to truncate the problem space and absorb outgoing waves. One of the most widely used and versatile ABCs is the perfectly matched layer (PML) [5, 6]. There has been some activity in the development of PMLs that are effective in low frequency or dispersive media [7, 8]. In this in this paper we describe the development of a PML that is specifically suited for very lossy media at extremely low frequencies (ELF).

II. Implementation of the PML

Berenger [5] assumed that any plane wave propagating in the direction d near the PML could be broken up into the part traveling perpendicular to the PML, d_{\perp} , and the part traveling parallel, d_{\parallel} (Fig. 1). The two conditions for the PML are:

1. It must have the same impedance as the background and not present a loss to the wave traveling parallel to the interface.
2. It must increase the artificial electric and magnetic conductivities such that the impedance still matches that of the background medium.

Berenger accomplished this by a split-step formulation that broke each electric and magnetic field up into two components. When the background medium is lake water and the frequency is 1 kHz, the complex dielectric constant is

$$\begin{aligned}\varepsilon_w^* &= \varepsilon_w + \frac{\sigma_w}{j\omega\varepsilon_0} = 80 + \frac{0.018}{j(2\pi \times 10^3)(8.85 \times 10^{12})} \\ &= 80 - j3.24 \times 10^5 \cong -j3.24 \times 10^5.\end{aligned}\quad (1)$$

The impedance of the PML material must remain at this value, but at the same time increase the loss further as it goes perpendicular into the PML. This can be accomplished by adding a factor s to the conductivity and the permeability

$$\eta_m = \sqrt{\frac{s \cdot \mu_0}{s \cdot \sigma_w}} \cdot \sqrt{j\omega\varepsilon_0} \quad (2)$$

This causes the PML medium to absorb outgoing waves faster than the water medium, but also avoids reflections.

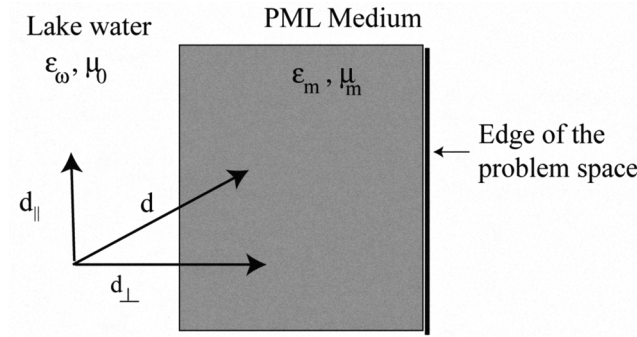


Figure 1. The PML is implemented by assuming any propagating wave can be broken up into a part that is perpendicular to the PML interface and a part that is parallel to it.

The FDTD equations in the split step formulation are:

$$E_{xy}^{n+1} = ca \cdot E_{xy}^n + cb \cdot \text{del_}H, \quad (3 \text{ a})$$

$$ca = \frac{1}{\left(1 + \frac{\Delta t \cdot \sigma_w}{\varepsilon_w \varepsilon_0}\right)} \quad cb = \frac{\Delta t / (\varepsilon_w \varepsilon_0 \Delta x)}{\left(1 + \frac{\Delta t \cdot \sigma_w}{\varepsilon_w \varepsilon_0}\right)} \text{del_}H, \quad (3 \text{ b})$$

$$H_z^{n+1/2} = H_z^{n-1/2} + db \cdot \text{del_}E, \quad (3 \text{ c})$$

$$db = \frac{\Delta t}{\mu_0 \cdot \Delta x}. \quad (3 \text{ d})$$

Recall that to implement the PML we increase the conductivity and the permeability at the same rate by a constant parameter s as shown in Eq. (2).

This is easy to do for the permeability. We add another parameter fy to Eq. (3 c)

$$H_z^{n+1/2} = H_z^{n-1/2} + fy(j) \cdot db \cdot \text{del_}E. \quad (4)$$

Instead of changing db to $\Delta t / (2 \cdot \mu_0 \cdot \Delta x)$, for instance, we simply

set $fy(j) = 0.5$. However, increasing σ_w is not so straight-forward. Notice that it involves both ca and cb . Rather than recalculate the parameters for each increase, we define another parameter

$$gy(j) = \frac{\left(1 + \frac{\Delta t \cdot \sigma_w}{\epsilon_w \epsilon_0}\right)}{\left(1 + \frac{\Delta t \cdot s \cdot \sigma_w}{\epsilon_w \epsilon_0}\right)} \quad (5)$$

The factor is added to Eq. (3 a):

$$E_{xy}^{n+1} = gy(j) \cdot ca \cdot E_{xy}^n + gy(j) \cdot cb \cdot \text{del}_H. \quad (6)$$

In this formulation it is necessary to split the E fields, but not the H fields.

III. Results

In this section we illustrate the effectiveness of the lossy medium PML. We will start with the problem space illustrated in Fig. 2.a, which is 80 cells cubed. Each cell is 25 meters cubed. The source is a single-cell electric dipole. After 4000 time steps, the amplitude is calculated at a monitor line. The simulation is then repeated for the truncated problem space shown in Fig. 2.b where a four-cell PML has been added. In this simulation the left wall has been moved in to within 10 cells of the source. The results are plotted in Fig. 2c along with the results of the previous simulation. The region in the middle is unaffected by the truncated problem space thanks to the absorption of the PML.

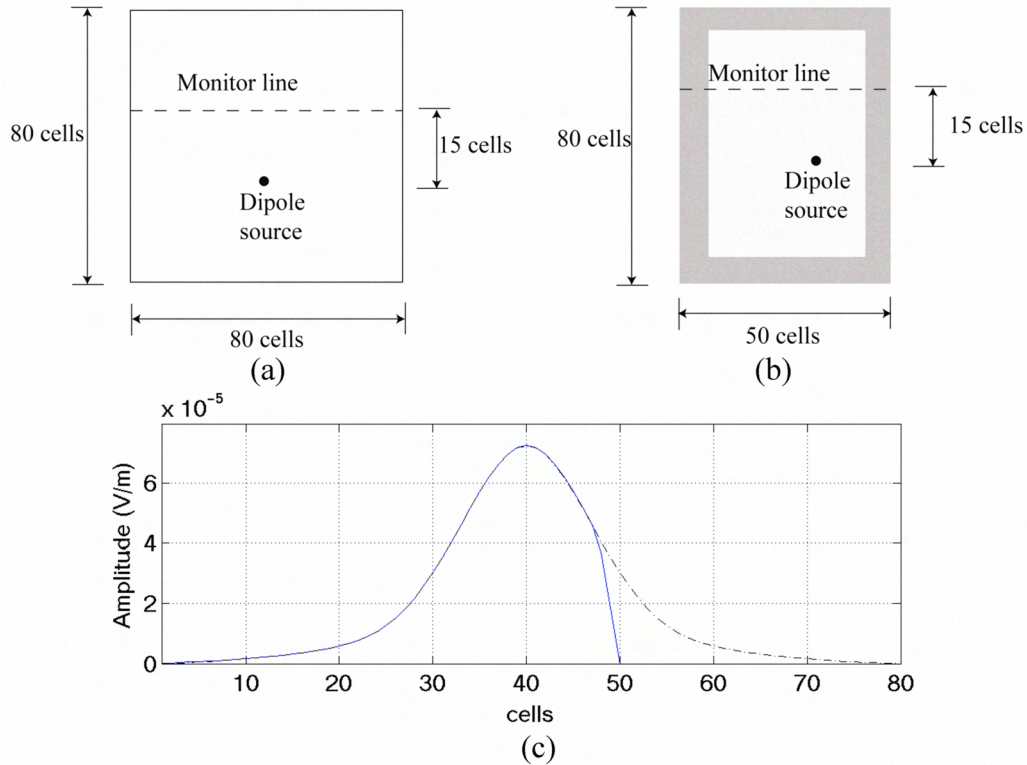


Figure 2. (a) A dipole source is located in the 80 cubed problem space. (b) The problem space is truncated and a four cell PML is added. (c) The amplitude at the monitor line after 4000 time steps for both the original problem space (solid line) and the truncated problem space (dashed line).

IV. Discussion

A perfectly matched layer has been described for applications involving ELF frequencies in lossy media. Although the use of a PML is not as crucial as it might be in free space or other lossless media, its use can result in a substantial decrease in computer resources.

Acknowledgements

This work was funded under ONR grant number N00014-07-1-0811 in collaboration with NAVESSEA, Carderock Division.

REFERENCES

1. J. J. Holmes, *Exploitation of a ship's magnetic field signatures*, Morgan and Claypool Publishers, 2006.
2. K. S. Yee, "Numerical solution of initial boundary value problems involving Maxwell's equations in isotropic media," *IEEE Trans. Antennas Propagat.*, Vol. 17, pp. 585-589, 1966.
3. D. M. Sullivan, *Electromagnetic Simulation Using the FDTD Method*. New York, NY: IEEE Press, 2000.
4. Y. Xia and D. M. Sullivan, "Underwater FDTD simulation at extremely low frequencies," *IEEE Anten. Wireless Prop. Letters*, scheduled for publication.
5. J. P. Berenger, "A perfectly matched layer for the absorption of electromagnetic waves," *J. Comp. Physics*, Vol. 114, pp.185-200, 1994.
6. J. P. Berenger, *Perfectly Matched Layer (PML) for Computational Electromagnetics*, Morgan and Claypool Publishers, 2007.
7. J. De Moerloose, M. A. Stuchly, "Behavior of Berenger's ABC for evanescent waves," *IEEE Micro. Guided Wave Let.*, Vol. 5, pp. 344-346, 1995.
8. S. A. Cummer, "A simple, nearly perfectly matched layer for general electromagnetic media, *IEEE Micro. Wireless Comp. Let.*, Vol 13, pp. 128-130, 2003.

Characterizing the Convolutional Perfectly Matched Layer at Extremely Low Frequencies

Christopher L. Wagner* and Jeffery L. Young

Department of Electrical and Computer Engineering, University of
Idaho, Moscow Idaho, USA

The perfectly matched layer (PML) as a truncation mechanism for the finite-difference, time-domain method has proven its worth in microwave antenna, circuits and scattering applications. However, at extremely low frequencies (ELF) the design of the PML requires special attention due to the quasi-static, rather than wave-like, nature of the electromagnetic field. This paper focuses not only on the design but also on the design method of an ELF-PML by using the convolution-PML (CMPL) of Rodan and Gedney (J. A. Roden and S. D. Gedney, *Microw. Guided Wave Lett.*, vol. 27, no. 5, pp. 334–339, Dec. 2000) as the starting point.

The CMPL has three numerical parameters that impact its absorptive characteristics at ELF. To find these three parameters, we consider a cubic domain that is sufficiently sized to include all important aspects of the problem to be simulated. An electric and magnetic dipole are then placed within that domain to excite all six components of the electromagnetic field. For a given set of ELF-PML parameters, the simulated fields are then recorded and subtracted from a reference solution to form a difference field. This difference field is used to compute a residual energy metric. The process is repeated numerous times until a set of PML parameters is found that minimizes the residual energy metric. When such parameters are found, the ELF-PLM is said to be optimized. Both frequency-domain and time-domain energy metrics can be used and the advantages and disadvantages of each will be presented.

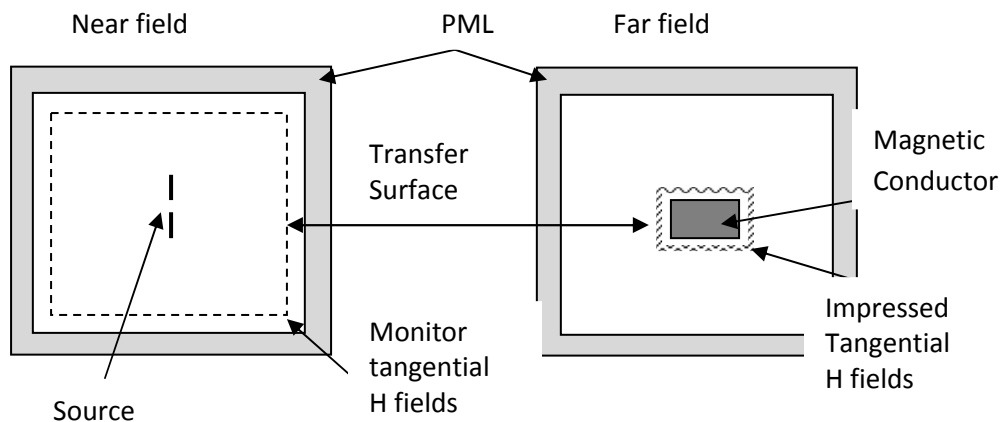
Although the above optimization process can be fully automated, we choose to display the energy metric in terms of contour plots where two of the four PML parameters are fixed and the other two form the ordinate and abscissa of the contour plot. Such plots reveal which parameters strongly impact ELF-PML performance and which ones do not. Moreover, as with all optimization methods, the optimal result depends on the metric chosen. In our case, the time-domain energy metric leads to a different optimal result from the frequency-domain energy metric. This forces the user to make a subjective decision as to what is deemed optimal. Various contour plots are presented to reinforce this claim and FDTD simulations are provided that substantiate the final ELF-PML design.

Time-Domain Near-to-Far Field Transformation for Underwater FDTD Simulations at ELF Frequencies

Das Butherus*, Yang Xia, and Dennis M. Sullivan
Department of Electrical and Computer Engineering
University of Idaho
Moscow, ID 83844-1023

The finite difference time domain method is being used to simulate ELF waves underwater in an attempt to assist the U.S. navy with Anti- ship mine technology. The near to far field transformation method is used in conjunction with FDTD to simulate a source with high resolution in a large domain by exploiting the equivalence principle. This is done by transferring a high resolution problem space associated with the source to a problem space consisting of larger cells. Results have already been obtained using the method for this project (Y. Xia and D.M. Sullivan, 2009). The results were obtained using the method of two equations two unknowns and transferring time domain information from one problem space to another.

Instead of directly transferring the time domain data, this method will illuminate the source with a Gaussian pulse and approximate the fields on the transfer surface as Gaussian pulses. The approximations made at the transfer surface allow a file containing amplitude, offset time, and spread for a particular field to be transferred rather than transferring its entire time evolution. Moreover, using the Gaussian pulse as the input allows information about the systems response for all frequencies to be obtained simultaneously via Fourier analysis.



Underwater FDTD ELF Simulation Using Dedicated Hardware

Yang Xia* ⁽¹⁾ and Dennis M. Sullivan ⁽¹⁾

(1) University of Idaho, Moscow, ID 83844-1023

E-mail: xia2024@vandals.uidaho.edu

Introduction

Mines are the greatest danger to ships [1]. They can be triggered at long distances by tracking the electromagnetic radiation from the ship [2]. Ships generate radiation at extremely low frequencies (ELF). Therefore, simulation methods are being developed to study underwater radiation at ELF frequencies.

The finite-difference time-domain (FDTD) is a powerful method in the EM research area [3, 4]. Previously, we have successfully used FDTD to study the ELF signals in water environments [5]. The results are good. We also have performed the two problem space FDTD simulation for the long distance traveling ELF signal research [6]. Good agreements have been reached when comparing the FDTD approach and analytical method [6]. However, it is often necessary to model relatively small objects but at the same time simulate radiation over long distances. Thus, improving the calculation speed of the FDTD simulation for the ELF project is highly desirable.

In this paper, the ELF FDTD simulations using the Acceleware software development kit (SDK) will be shown [7]. The comparisons of the single core CPU calculation, multi-core parallel CPU calculation and Acceleware calculation will be provided. It can be seen that by using the Acceleware software library great speedup can be achieved for the ELF project. The Acceleware system is faster than the 32-core CPU system whereas at the same time it is much smaller in size and consumes less power than the 32-core CPU system. From the comparison we can also find that the Acceleware system for FDTD is a much more cost-effective computational solution for the ELF project.

Method

The basic programming flow in the Acceleware program is shown in Fig. 1. The first step is accomplished by calling to the Acceleware function `AxOpenSystem()`. This function makes the video card hardware ready to be used after the license file and hardware security check. After the system is opened, `AxCreateSimulation()`

is used to create a FDTD simulation and then a particular simulation space is defined. The `AxCreateSimulation()` function will produce a simulation handle for future uses such as specifying the FDTD simulation properties which are included in Step 3. When the third step is finished, the corresponding Acceleware functions will be applied to make the FDTD simulation ready and the FDTD main loop begins after a simulation is ready. The last step is for system clearance after an Acceleware simulation is over. In the last step, the dynamic allocated arrays are released, the simulation handle is deleted and the connect to the video card hardware is closed by the Acceleware function `AxCloseSystem()`.

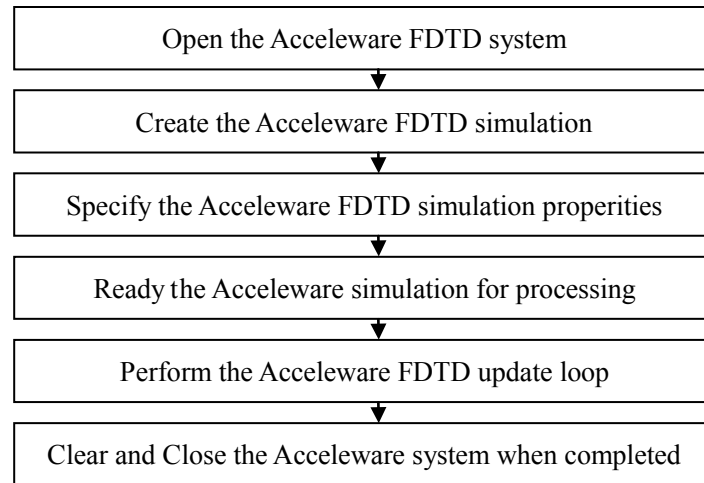


Figure 1. The basic programming flow of the Acceleware program

Example

In this section the comparison of the 1-core CPU calculation, 32-core openmp parallel calculation and Acceleware calculation will be provided. The hardware information is listed in Table I.

Table I. Computer specifications for the comparison

	<u>1-core CPU calculation</u>	<u>32-core CPU calculation</u>	<u>Acceleware calculation</u>
<u>Software</u>	ifort compiler	ifort compiler with parallel option (Openmp)	Acceleware library version 5. 1. 0
<u>Hardware</u>	1 core of a Quad-Core AMD Opteron(tm) Processor 8380	8 Quad-Core AMD Opteron(tm) Processor 8380	NVIDIA Quadro core FX 5600 video card

In the example the problem space is 120 cubed and cell size is 15 meters. The

frequency used in the calculation is 1000 Hz. The source is a vertical magnetic dipole which is 1 meter below the air/water surface. The monitor line is 16 meters deep and in the horizontal direction. The horizontal monitor distance is from 100 meters to 800 meters.

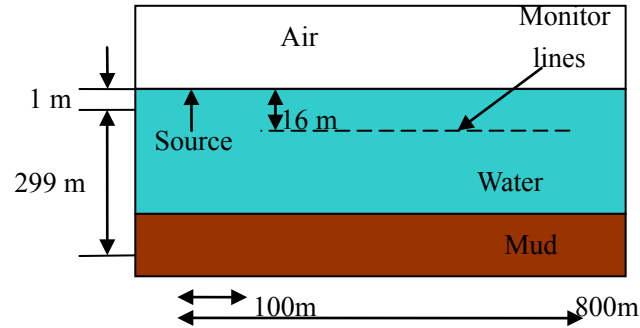


Figure 2. Configuration for the simulation. It is a three layer model in which the monitor line is in the water layer. The monitor line is in the horizontal direction and the magnetic dipole is polarized in the vertical direction.

Figure 3 shows the comparison of the calculations between the normal FDTD and Acceleware FDTD showing that the Acceleware calculation is accurate.

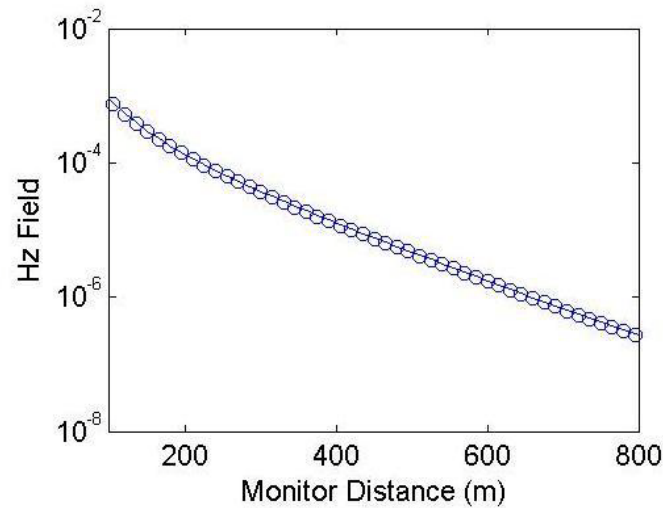


Figure 3. Calculation results of the normal FDTD and Acceleware FDTD method. The line is the normal FDTD calculations and the bubbles are the Acceleware FDTD calculations.

Table II shows the calculation time of the 1-core CPU, 32-core CPU and Acceleware simulations, respectively. It can be seen that the Acceleware

simulation is almost 10 times faster than the 1-core CPU system.

Table II. Calculation time of the three methods

<u>1 core CPU</u>	<u>32 core CPU</u>	<u>Aceleware</u>
63m18s	12m56s	6m26s

Conclusion

The 1-core CPU, 32-core CPU and Aceleware calculations were performed for the comparison. The results show that Aceleware approach is faster than the 1-core CPU calculation and twice as fast as the 32-core CPU calculation.

References

1. Holmes J. J., *Exploitation of a ship's magnetic field signatures*, Morgan and Claypool Publishers, 2006.
2. Hartmann G. K., Truver S. C., *Weapons That Wait*, 2nd Ed, Annapolis, MD: Naval Institute Press, 1991.
3. Yee K. S., "Numerical solution of initial boundary value problems involving Maxwell's equations in isotropic media," *IEEE Trans. Antennas Propagat.*, Vol. 17, pp. 585-589, 1966.
4. Sullivan D. M., *Electromagnetic Simulation Using the FDTD Method*. New York, NY: IEEE Press, 2000.
5. Sullivan D.M., Yang Xia, "Underwater FDTD simulation at extremely low frequencies," *IEEE Ant. and Wireless Prop. Letters*, Vol. 7, pp 661-664, 2008.
6. Xia Y, Sullivan D.M., Li Z, and Olsen R., "Dual Problem Space FDTD Simulation for Underwater ELF Applications," *IEEE Antennas and Wireless Prop. Letters*, Vol. 8, pp. 498-501, 2009.
7. Ong C., Weldon M., Cyca D., Okoniewski M., "Acceleration of large-scale FDTD simulations on high performance GPU clusters," *IEEE APS Intern'l Sym*, June 15, 2009, Charleston, SC.

Large Scale Underwater FDTD ELF Simulations Using Acceleware and MPI Parallel Processing

Dennis M. Sullivan, Yang Xia, and Alireza Mansoori

Department of Electrical and Computer Engineering

University of Idaho

Moscow, ID 83844-1023 USA

dennis@ee.uidaho.edu

xia2024@vandals.uidaho.edu

amansoori@vandals.uidaho.edu

Abstract—Very large FDTD simulations are being developed to determine the underwater propagation of EM signals at ELF frequencies. Two different approaches are being used to handle the large computation spaces, the use of hardware and software by Acceleware, and the use of the Message Passing Interface (MPI) for parallelization.

I. INTRODUCTION

Underwater anti-ship mines are the greatest danger to surface warships. This is of particular interest to the U. S. Navy as it moves towards an “all-electric” fleet [1, 2]. The finite-difference time-domain (FDTD) method [3, 4] is being used to study propagation underwater at extremely low frequencies (ELF) [5]. Comparisons with measured data shows good results over distances up to one kilometre [6].

In anticipating that it will be necessary to pursue simulations over very long distances, more advanced computational methods are being explored to avoid having to wait days to obtain results. The two main methods are: (1) the implementation of an Acceleware software development kit (SDK), and (2) the use of the Message Passing Interface (MPI) software for parallel computation. The two methods will be described in the following two sections. Using a very large problem space of 120^3 cells, a comparison using the two methods against a single processor computer is made to determine the increase in computation time.

II. ACCELEWARE CALCULATIONS

The Acceleware software development kit (SDK) [7] is being used as a means to decrease computation times for large FDTD simulations. A flow chart describing the implementation of the Acceleware is shown in Fig. 1. The first block calls the function `AxOpenSystem()` which makes the video card hardware ready after the license file and hardware security check. In the next block, the call `AxCreateSimulation()` creates an FDTD simulation and

defines a simulation space. In the third step the simulation properties are specified. In the fourth step, the Acceleware functions are applied to make the FDTD simulation ready. Then the main FDTD loop begins. Finally, the function `AxCloseSystem()` releases the dynamically allocated arrays, deletes the simulation handle, and disconnects the video card hardware.

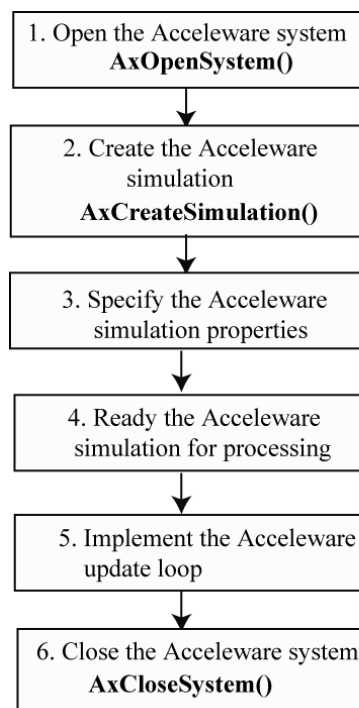


Figure 1. The basic flow diagram for the Acceleware program.

III. PARALLEL FDTD ALGORITHM

There have been several approaches to parallelizing the FDTD algorithm [8-10]. Our parallel FDTD is implemented through the domain decomposition method (DDM), which splits the main problem space into smaller sub-domains [11]. Each sub-domain retains the original qualities of the main space. The non-overlapping DDM requires communication among the sub-domains. This is the role of the message passing interface (MPI) library. Each sub-domain is assigned to an individual core for the FDTD computation in its domain. The balancing of the load among the cores is an important factor in maximizing speed

Figure 2 shows an example of a large problems space that has been divided up into eight equal sub-domains. This configuration is as balanced as possible. A parallel environment has been created so each sub-domain can communicate to the neighboring sub-domains. This minimizes lag which occurs when a core has to wait for data from another sub-domain to continue. Notice that each sub-domain has a position vector containing the X, Y, and Z positions. The position vector is based on the sub-domain positioning axis which is separate from the FDTD axes.

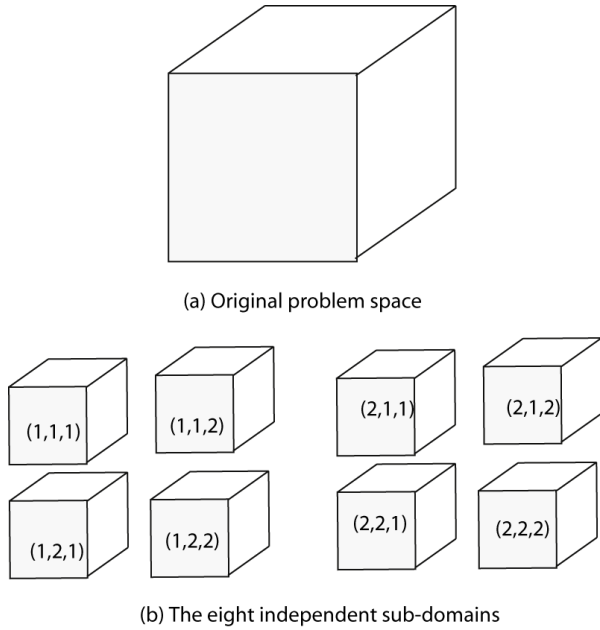


Figure 2. A large computational domain (a) is broken up into eight equal sized subdomains (b).

The sequence illustrated by the flow chart in Fig. 3. Our implementation of the FDTD utilizes the Z transform [12], which must be considered in the process.

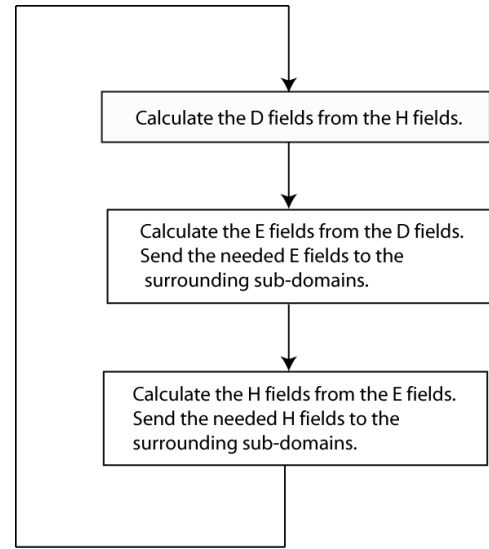


Figure 3. Flow chart for the FDTD simulation using MPI.

IV. COMPARISON

In this section we compare the performance of a single CPU calculation on a workstation with the multiprocessor capability using MPI described in section III, and the Acceleware system described in section II. Figure 4 illustrates the problem space used for the simulations in order to compare relative speed of the different computation systems. The total problem space is 120^3 cells. Each cell represents 15 m^3 . The source is a magnetic dipole in the z direction located one meter below the air/water interface. The resulting H_z field is calculated at a distance 1000 m away. The programs required 30,000 time steps. The results of all FDTD systems were favorable as compared with an analytic method based on Sommerfeld's half-space problem [6], as shown in Fig. 5.

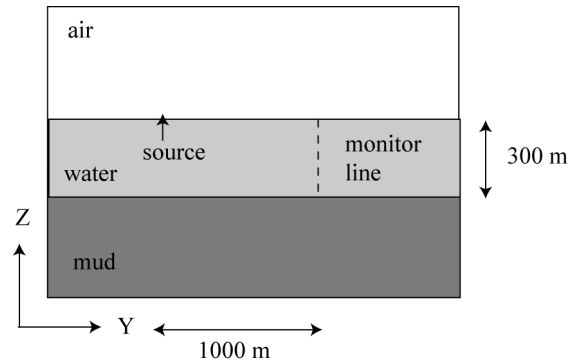


Figure 4. Illustrations of the problem space for the computations to compare the different systems

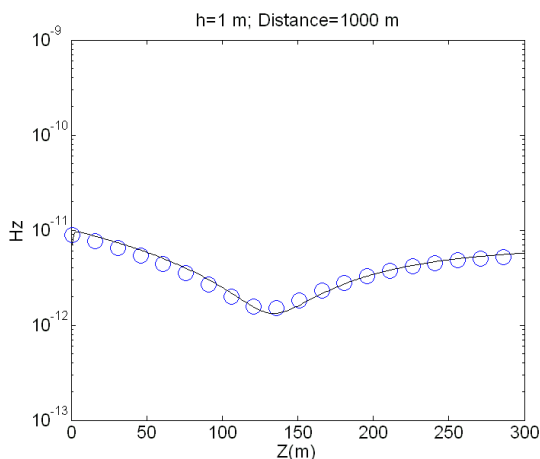


Figure 5. Comparison between the FDTD data (circles) and the analytic data (line) along the monitor line as shown in Figure 3.

Table I summarizes the computation times for three computing approaches. The first uses one core of an HP 785 with 32 cores and 128 gigabytes of main memory. The second approach used 32 cores of the same HP 785 together with the MPI software. The third was done entirely on the

TABLE I. Computational times for the three systems used in the comparison.

One core	62 minutes
32 core w/MPI	9 min 45 sec
Acceleware	6 min 17 sec

V. CONCLUSION

Two approaches have been presented for the underwater ELF simulation of very large domains. The first utilizes the Acceleware system hardware and software. This system has proven to be very fast and efficient. The main advantage is that it is a self-contained system. It does require programming over and above the usual FDTD simulation using a standard program. The second approach utilizing the Message Passing Interface (MPI) to maximize the effectiveness of parallel processing capabilities. It has the advantage of being able to utilize several computer systems to solve one large FDTD simulation. However, it requires substantial programming effort in addition to the FDTD simulation.

ACKNOWLEDGMENT

This work was funded under ONR grant number N00014-07-1-0811 in collaboration with NAVESEA, Carderock Division.

REFERENCES

- [1] J. J. Holmes., *Exploitation of a ship's magnetic field signatures*, Morgan and Claypool Publishers, 2006.

- [2] G. K. Hartmean, S. C. Truver, *Weapons That Wait*, 2nd Ed, Annapolis, MD: Naval Institute Press, 1991.
- [3] K. S. Yee "Numerical solution of initial boundary value problems involving Maxwell's equations in isotropic media," *IEEE Trans. Antennas Propagat.*, Vol. 17, pp. 585-589, 1966
- [4] D. M. Sullivan, *Electromagnetic Simulation Using the FDTD Method*. New York, NY: IEEE Press, 2000.
- [5] Y. Xia, D. M. Sullivan, "Underwater FDTD simulation at extremely low frequencies," *IEEE Ant. and Wireless Prop. Letters*, Vol. 7, pp 661-664, 2008.
- [6] Y. Xia, D.M. Sullivan , Z. Li, and R. Olsen R., "Dual Problem Space FDTD Simulation for Underwater ELF Applications," *IEEE Antennas and Wireless Prop. Letters*, Vol. 8, pp. 498-501, 2009.
- [7] C. Ong, M. eldon, D. Cyca, M. Okoniewski, "Acceleration of large-scale FDTD simulations on high performance GPU clusters, *IEEE APS Intern'l Sym*, June, 2009, Charleston, SC.
- [8] J. J. Simpson, R. P. Heikes, and A. Taflove, "FDTD modeling of a novel ELF radar for a major oil deposits using a three-dimensional geodesic grid of the earth-ionosphere waveguide," *IEEE Trans. Antenna. Propagat.*, Vol. 54, pp. 1734-1741, 2006.
- [9] V. Varadarajan and R. Mittra, "Finite-difference time domain (FDTD), analysis using distributed computing," *IEEE Microwave and Guided Wave Letters*, Vol. 4, No. 5, 144-145, 1994.
- [10] K. C. Chew and V. F. Fusco, "A Parallel Implementation of the Finite Difference Time Domain Algorithm," *International Journal of Numerical Modeling Electronic Networks, Devices and Fields*, 8, 1995, pp. 293-299.
- [11] W. Gropp, E. Lusk, and A. Skjellum, *Using MPI. Portable Parallel Programming with the Message Passing Interface*, Cambridge, Massachusetts, MIT Press, 1994.
- [12] D. M. Sullivan, "Z-transform theory and the FDTD method," *IEEE Trans. Antenna Propagat.*, Vol. 44, pp. 28-34, 1996

Comparison of the Up-Over-Down Approximation with the Quasi-Electrostatic Approximation for ELF Fields in Layered Media

Robert T. Rebich*, Jeffery L. Young and Christopher L. Wagner
University of Idaho
Moscow, Idaho 83844
Email: jyoung@uidaho.edu

Robert G. Olsen
Washington State University
Pullman, Washington 99164
Email: bgolsen@wsu.edu

Abstract—Two approximate methods are presented that quantify low frequency field effects of a horizontal electric dipole in a layered environment. The first is a far-field approximation (relative to water) that is interpreted as the up-over-down effect. In this situation, wave processes are characterized using classical ray optics arguments and equations. The second method focuses on the quasi-static nature of the fields to arrive at an infinite image representation of the field. Both yield good results when compared to the exact solution, albeit the quasi-electrostatic solution does better at extremely low frequencies (e.g. 30 Hz) and the up-over-down solution does better at ultra-low frequencies (e.g. 1,000 Hz).

I. INTRODUCTION

Low frequency wave effects are of considerable importance for applications dealing with deep water communication systems or signal detection from high current sources. To ascertain the strength of these signals, it is common to employ a half-space model that treats the water-air interface as planar and infinitely extended. In open-sea regions, the approximation is unquestionably valid and leads to a closed-form result couched in terms of Fourier-Bessel integrals; i.e. Sommerfeld integrals. These integrals have been studied for many decades, but there appears to be a gap in the literature about the relationship between the quasi-electrostatic solution and the low frequency, up-over-down wave approximation. (In this paper, low frequency is construed to be 30 to 3,000 Hz, which covers the extremely, super and ultra low frequency bands (e.g. ELF, SLF, ULF). We will simply refer to this frequency band as the ELF band in this paper.)

When an ELF source and sensor are placed in water, it is well known that the direct signal from the source to the sensor is highly attenuated due to the conductivity of the water. However, if the source and sensor are just below the surface, it is quite possible that the sensor will record a high signal due to the up-over-down effect. In this case, the signal is weakly attenuated as it travels to the surface, but is unattenuated as it travels across and through the air. Likewise, as the signal penetrates into the water, the signal attenuation is also weak for shallow penetrations. This effect has been recently quantified by Olsen *et al.* [1], who extracted the low-frequency, far-field solution from the full-wave, Sommerfeld solution. The

far-field is understood to be relative to the wavelength of the field in water, which is on the order of hundreds of meters for conductivity values on the order of 0.018 S/m at ELF. In air, the signal wavelengths are in the order of hundreds of kilometers.

It is also possible to extract the low frequency quasi-electrostatic (QES) solution from the Sommerfeld integral and then cast that solution in terms of an infinite summation of equivalent image charges [2]. By doing so, a robust result is also obtained that converges within a few terms. When this result is compared with the the up-over-down (UOD) approximation, the correlation is excellent for certain frequency values. Yet both solutions provide a different perspective about the physics of the problem. A review of the salient equations for the UOD and QES methods, and numerical results from the same are provided in the ensuing sections.

The layered geometry under consideration is that of Figure 1, where a source is placed in region two (i.e. water) at a depth h . The top region is regarded as air and the bottom region is regarded as mud (i.e. ocean or lake floor). The i th region is characterized by the electrical parameters $\sigma_i, \mu_i, \epsilon_i$. Fields are observed at ρ, ϕ, z . Since the up-over-down approximation is primarily an effect at the air-water interface, the mud layer is treated as if it does not exist by making the layer thickness infinite or by making the electrical parameters of region two and three the same. No such approximation is needed for the exact, full-wave solution or for the quasi-electrostatic solution. The exact solution to this problem (i.e. Sommerfeld's result) is well known and is provided in numerous references; see Felsen *et al.* [3] for more information.

A. Up-Over-Down Approximation (UOD)

Consider a y -directed, horizontal dipole of moment Idl as the source of the electromagnetic field. The up-over down approximation is obtained by deforming the integration contour of the Sommerfeld integral about the lower half plane such that it encompasses the branch cuts and poles of the Sommerfeld integrand, as shown in Figure 2. A careful analysis reveals that the integration about the contour associated with k_1 yields a weaker field than that of k_2 ; the integration about the pole

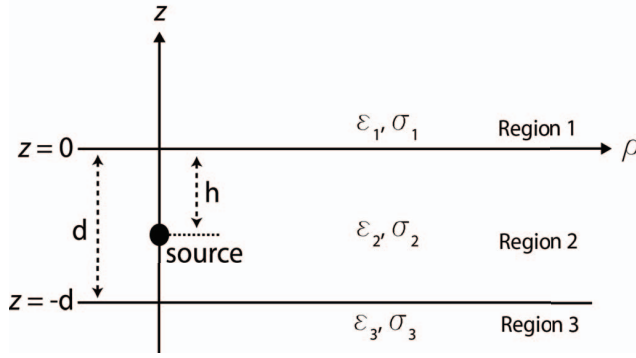


Fig. 1. Three layer geometry.

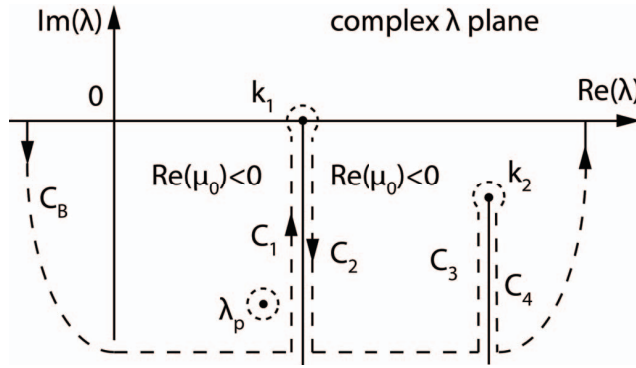


Fig. 2. Contour integration and deformation of the Sommerfeld integrals.

also yields a negligible field. The dominant field component in water is E_x , which is transverse to the dipole and hence is the component to measure or detect in an application problem. For observations in water, Olsen reports that

$$E_x \approx -\frac{3j\eta_2 Idle^{-jk_2 h}}{2\pi k_2} \cdot \frac{e^{-jk_1 \rho}}{\rho^3} \sin \phi \cos \phi \cdot e^{jk_2 z}, \quad (1)$$

where k_1 , k_2 and η_2 are the wavenumber in air, the wavenumber in water and the characteristic impedance of water. The interpretation of this equation is straightforward: The first term is a plane wave traveling in the water up from the source along a path of length h ; the second term is a propagating cylindrical wave function along a path of length ρ with $1/\rho^3$ spreading loss; the third term is a plane wave traveling into the water to the observer at z . The ray-optic depiction of this effect is shown in Figure 3.

Beyond the simplicity of this result and the obvious interpretation, is the $1/\rho^3$ spreading loss term. This is clearly a quasi-static effect associated with the near-field of an antenna. The other terms account for boundary interactions. Olsen provides an interpretation and justification of Eqn. (1) in terms of dipole images. It thus seems reasonable to see if the result can be couched in terms of quasi-electrostatic charge and image concepts without making any appeals to propagation effects.

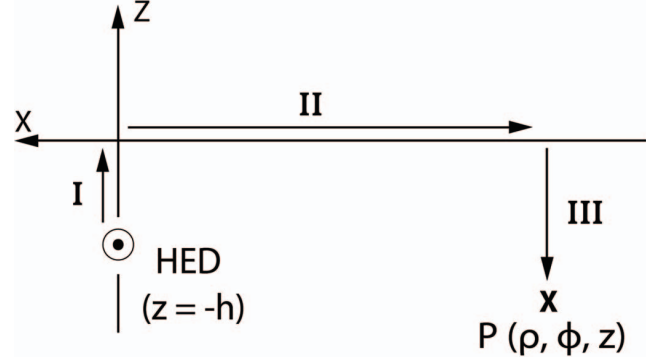


Fig. 3. Ray-optic depiction.

B. Quasi-electrostatic Approximation (QES)

For the quasi-electrostatic method, consider a single charge of strength q placed in the second region at a distance h below the interface. For observations in region 2 the total potential at any given observation point is equal to the superposition of three different potentials. The first is the direct path from the charge to observer and is of unity strength. The second is the upward traveling path caused by the reflection at the $z = -d$ boundary and is of strength A . The last is the downward traveling path caused by the reflection at the $z = 0$ boundary and is of strength B . The total potential is given by,

$$V = \frac{jwq}{4\pi Y_2} \int_0^\infty [e^{-\lambda|z-h|} + Ae^{-\lambda z} + Be^{\lambda z}] J_0(\lambda \rho) d\lambda, \quad (2)$$

where

$$A = \frac{R_{23}(1 + R_{21}e^{2\lambda h})e^{-\lambda(h+2d)}}{1 - R_{23}R_{21}e^{-2\lambda d}} \quad (3)$$

and

$$B = \frac{R_{21}e^{\lambda h} + R_{23}R_{21}e^{-\lambda(h+2d)}}{1 - R_{23}R_{21}e^{-2\lambda d}}. \quad (4)$$

Here R_{21} and R_{23} are reflection-like coefficients, which are determined by enforcing continuity of electric potential and total normal current across each interface. It can be shown that

$$R_{21} = \frac{Y_2 - Y_1}{Y_1 + Y_2} \quad (5)$$

and

$$R_{23} = \frac{Y_2 - Y_3}{Y_2 + Y_3}. \quad (6)$$

Finally, Y_i is the admittance of the i th region, where $Y_i = \sigma_i + j\omega\epsilon_i$. When regions two and three are the same, $R_{23} = 0$.

Since $R_{23}R_{21}e^{-2\lambda d} < 1$, the denominator of Eqns. (3) and (4) can be expanded in an infinite Taylor series in powers of λ , thus allowing for closed-form, term-by-term integration of Eqn. (2). When this is done, we find that

$$V = \frac{K_2}{r} + K_2 \sum_{n=0}^\infty R_{23}^n R_{21}^n \left[\frac{R_{23}}{r_a} + \frac{R_{23}R_{21}}{r_b} + \frac{R_{23}R_{21}}{r_c} + \frac{R_{21}}{r_d} \right], \quad (7)$$

where,

$$K_2 = \frac{j\omega q}{4\pi Y_2} \quad (8)$$

and

$$\begin{aligned} r_a &= \sqrt{\rho^2 + (z + h + 2d(n+1))^2} \\ r_b &= \sqrt{\rho^2 + (z - h + 2d(n+1))^2} \\ r_c &= \sqrt{\rho^2 + (h - z + 2d(n+1))^2} \\ r_d &= \sqrt{\rho^2 + (2nd - z - h)^2}. \end{aligned} \quad (9)$$

It should be clear from the previous equations that the potential can be viewed as a superposition of image charges located at r_a, r_b, r_c and r_d . The strengths for the corresponding images are as follows:

$$\begin{aligned} a_n &= K_2 R_{23}^{n+1} R_{21}^n \\ b_n &= K_2 R_{23}^{n+1} R_{21}^{n+1} \\ c_n &= K_2 R_{23}^{n+1} R_{21}^{n+1} \\ d_n &= K_2 R_{23}^n R_{21}^{n+1}. \end{aligned} \quad (10)$$

The fact that these images are complex suggests that the images are not necessarily in phase with each other or of the same strength. Figure 4 shows the corresponding image locations and strengths represented by Eqn. (7). Finally, since $\mathbf{E} = -\nabla V$,

$$\begin{aligned} E_x &= \frac{K_2}{r^3} x \\ &+ K_2 x \sum_{n=0}^{\infty} R_{23}^n R_{21}^n \left[\frac{R_{23}}{r_a^3} + \frac{R_{23} R_{21}}{r_b^3} + \frac{R_{23} R_{21}}{r_c^3} + \frac{R_{21}}{r_d^3} \right]. \end{aligned} \quad (11)$$

A dipole of extent l is formed via the superposition of a positive charge and a negative charge separated by a distance l . From an implementation point of view, the previous equations can be used for both the positive and negative charges; the placement of the charges is arbitrary. Thus, the horizontal dipole is just one special case of this general formulation. A point-source dipole can be constructed by taking derivatives with respect to the charge position variable in the direction of the line formed by the two charges. These mathematical operations and equations are suppressed in this presentation.

C. Results

The first problem of interest is the two layer, half-space problem in which the upper half space is free space and the lower half space is water, i.e. $\sigma_2 = 0.018$ S/m, $\epsilon_2 = 81\epsilon_0$ and $\mu_2 = \mu_0$ at low frequencies. At ELF, $\sigma_2 \gg \omega\epsilon_2$, thus suggesting that conduction currents dominate displacement currents. First consider Figures 5 and 6, which show the magnitude of E_x as a function of ρ when $h = 30$ m and $z = -20$ m. Figure 5 corresponds to $f = 30$ Hz and Figure 6 to $f = 1,000$ Hz. Both figures show the exact Sommerfeld full-wave (SFW) solution, the up-over-down (UOD) solution and the quasi-electrostatic (QES) solution. Here we see that both approximations predict the exact solution quite well with the correlation slightly degrading as frequency or ρ increase.

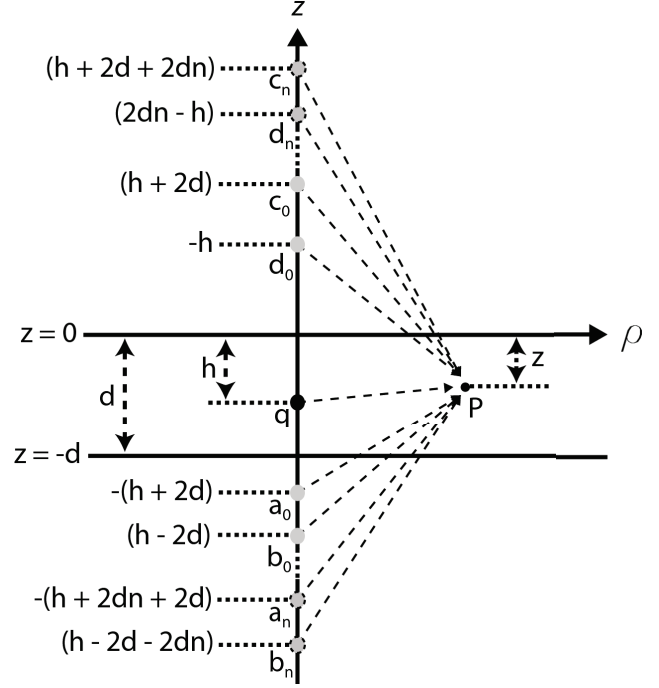


Fig. 4. QES image representation.

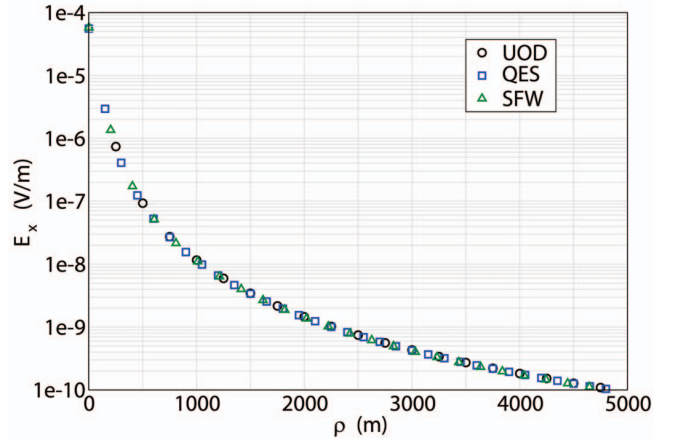


Fig. 5. Comparison data for the UOD, QES and SFW models when $f = 30$ Hz, $h = 30$ m and $z = -20$ m.

The dynamic range of the signal spans between five and seven decades as a result of the dominant $1/\rho^3$ spreading factor that occurs in both the UOD and QES solutions. Moreover, the wave-like effects captured in the UOD solution are clearly equivalent to the image effects of the QES solution.

Consider next Figures 7 and 8. In this case we show E_x as a function of z when $h = 30$ m and $\rho = 300$ m; the frequencies $f = 30$ Hz and $f = 1,000$ Hz are still chosen. These results are more interesting by showing the range of validity of the UOD and the QES approximations. At 30 Hz, the QES solution is superior over the entire range of depths; the UOD solution is inferior by every measure. This is to be

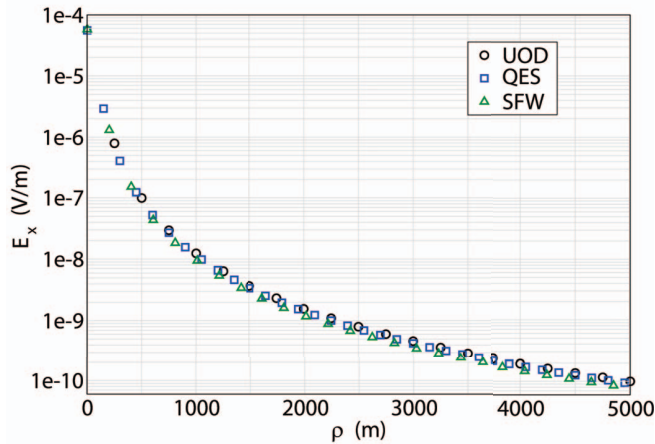


Fig. 6. Comparison data for the UOD, QES and SFW models when $f = 1000$ Hz, $h = 30$ m and $z = -20$ m.

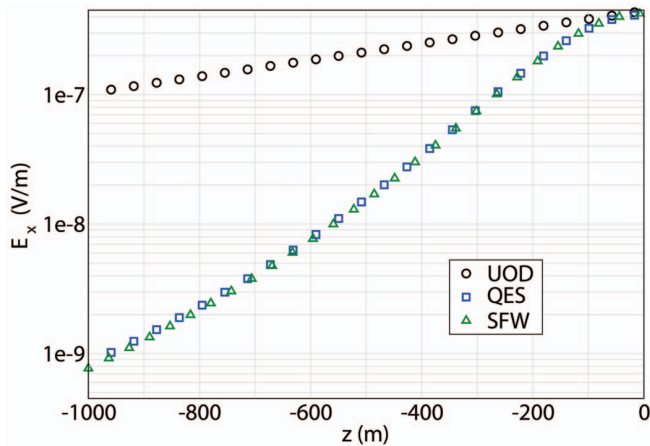


Fig. 7. Comparison data for the UOD, QES and SFW models when $f = 30$ Hz, $h = 30$ m and $\rho = 300$ m.

expected since these distances at 30 Hz correspond to near-field observations (relative to water) associated with quasi-static processes. However, at $f = 1,000$ Hz, the UOD solution predicts the exact solution quite well for depths less than 300 m; the QES solution is in error for all but the shallow depths, since wave processes are present.

For our last comparison, we consider the effect of the lower layer of the three layer geometry of Figure 1 on the UOD and QES approximations. For illustration purposes, let $\sigma_3 = 0.12$ S/m and $d = 25$ m. Figure 9 shows the results for E_x when $f = 1,000$ Hz, $h = 15$ m and $z = -15$ m. As might be expected, the QES data effectively reproduces the exact data, since the third layer is intrinsically accounted for by the infinite image summation. The UOD predicts the correct trend, but is incorrect by an order of magnitude. In other words, the ray-optic paths of up, over and down are incomplete and additional reflection paths from the bottom layer are needed. As the layer thickness increases, with all other parameters being held the same, the need for additional reflection paths lessens as the

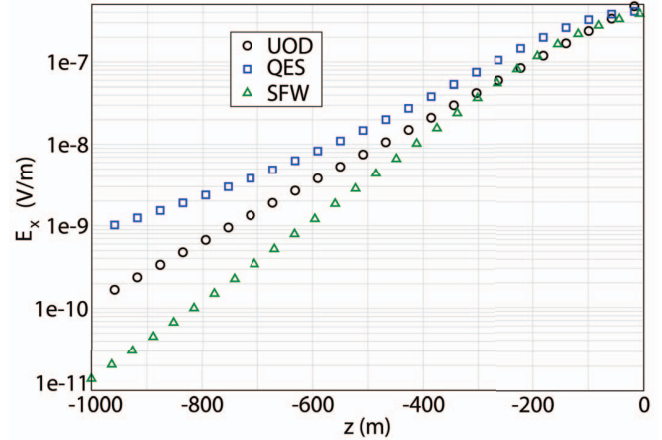


Fig. 8. Comparison data for the UOD, QES and SFW models when $f = 1000$ Hz, $h = 30$ m and $\rho = 300$ m.

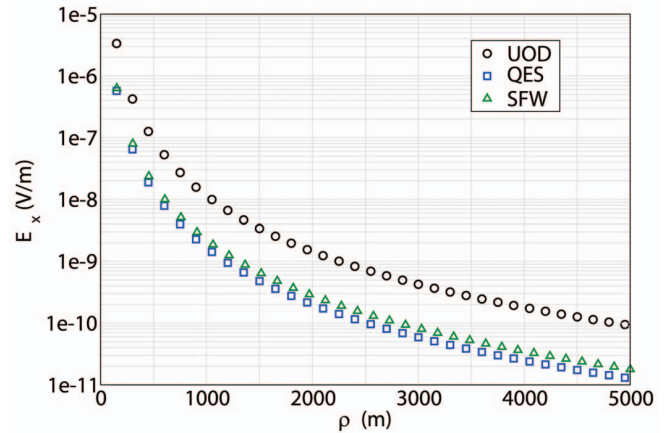


Fig. 9. Comparison data for the UOD, QES and SFW models when $f = 1000$ Hz, $h = 15$ m, $z = -15$ m and $\sigma_3 = 0.12$ S/m.

previous data suggests. However, if the third layer actually represents mud, which is water saturated dirt, the conductivity value is on the order of 0.01 S/m, thus making the mud-water interface more transparent. Data associated with this case indicates that both the QES and the UOD approximations can replicate the exact data quite well even for thin layers.

ACKNOWLEDGMENT

This work was supported by the Office of Naval Research under contract number N00014-09-1-0923.

REFERENCES

- [1] R. G. Olsen and Z. Li, "A simple up-over-and-down model for low frequency horizontal electric dipole propagation near an interface", *IEEE Trans. on Antennas and Propagation*, (submitted, Nov. 2010).
- [2] J. Wait, *Electromagnetic Wave Theory*, Harper & Row, New York, NY, 1985.
- [3] L. B. Felsen and N. Marcuvitz, *Radiation and Scattering of Waves*, IEEE Press, Piscataway, NJ, 1994.

A Simple Up-over-and-down Model for Low Frequency Horizontal Electric Dipole Propagation Near An Interface

Zhi Li^{*(1)} and Robert G. Olsen⁽¹⁾

(1) School of Electrical Engineering and Computer Science
Washington State University, Pullman, WA 99164-2714

The propagation of electromagnetic fields from an electric or magnetic dipole near an interface has been described mathematically for many years using Sommerfeld integrals. In the high frequency case for which the dipole and field point are buried in the lower (and much lossier) medium, simple approximations have been derived that can be interpreted as up-over-and-down propagation (i.e., plane wave from source to the surface – surface wave to a point above the field point – plane wave to the field point). Here the low frequency case is of interest and, for this case, no equivalent simple approximation has been presented. The dipole source is chosen to be a horizontal electric dipole (HED). This was selected because, using achievable dipole moments and commonly available receiving equipment, it can be shown that the HED fields are detectable at larger distances than those of other dipole types (i.e., vertical electric dipole (VED) or vertical (VMD) or horizontal (HMD) magnetic dipoles). One fundamental problem with evaluating the Sommerfeld integrals is that, for electrically large values of horizontal separation in the lossier medium (and significantly smaller vertical dimensions), the rapid oscillations of the Bessel function cause difficulties with the numerical integration. To remedy this problem, the contours of integration are deformed in the complex plane so that the integrand decays exponentially for electrically large values of the horizontal dimension. This transformation will also allow other simplifying approximations that will lead to a simple interpretation of the final result. The final result is a simple expression valid for the low frequency case (i.e., relevant dimensions in the upper medium are electrically small). This result is shown to have an up-over-and-down propagation interpretation described as near field propagation from source to the surface, quasi-static propagation along the interface to above the field point and plane wave propagation to the field point.

Propagation of Low Frequency Signals in Oceanic Environments; Theory, Simulation and Experimentation

Christopher Johnson*, Christopher L. Wagner, Robert Rebich, Jeffery L. Young and Das Butherus
University of Idaho
Moscow, Idaho 83844
Email: jyoung@uidaho.edu

I. INTRODUCTION

The excitation and propagation of extremely, super and ultra low frequency signals (ELF, SLF and ULF) in the range of 30 Hz to 3,000 Hz associated with ocean environments are of particular interest for applications dealing with deep-water communications or sub-surface emissions caused by power generation devices and lines. Due to the relatively long wavelengths on the order of hundreds of meters or so in saltwater and the high-power nature of the sources, it is possible to detect these signals several kilometers from the source. In the current age in which sophisticated electromagnetic modeling tools have been developed for high frequency applications, the question has been asked whether these same tools can be applied to ELF, SLF and ULF applications (referred to as just ELF in subsequent discussions). In particular, we wish to ascertain the usefulness and robustness of the finite-difference, time-domain (FDTD) method, commercial codes (e.g. HFSS and Maxwell), and layered media modeling using Sommerfeld and quasi-electrostatic methods as applied to the ELF propagation problem. Each of these approaches has its strengths and weaknesses, as described in the ensuing sections.

The validation of the aforementioned methods is accomplished in two ways. The first way is to compare the data produced by each method. Since all methods are based on Maxwell's equations, they should all produced the same data, provided that the problem is defined in accordance with the method's underlying assumptions (e.g. flat earth for Sommerfeld modeling). By doing so, we can determine regions of validity, failed assumptions, accuracy, etc. of each modeling approach. The second method compares modeling data with experimental data in which physical sources are used to excite ELF waves in water and air, and low frequency sensors are employed to detect the same as a function of distance. In this case, we deduce whether each approach can adequately capture all the important physics of a real-world problem, provided all necessary information about the problem is known, which it is not, as discussed in the results section.

Two problem spaces are considered in this investigation: 1) layered media consisting of mud, water and air, and 2) actual topological and bathymetric geometric data, and corresponding material data associated with Idlewild Bay, Idaho. Both electric

point sources (i.e. ideal dipole) and magnetic point sources (i.e. electric current loop) are considered; the orientation of these sources may be either horizontal or vertical, relative to the air-water interface. These point sources model actual sources used in the experimental portion of the investigation. Particularly, an electric dipole is fashioned using plate electrodes separated by 4 meters; for the magnetic source, a 3.6 by 3.6 m square loop of 12 turns is utilized.

II. DISCUSSION

A brief outline of the methods and solutions employed in this investigation are provided in the following subsections. Numerical methods include FDTD and frequency-domain, finite-element methods. Analytic methods include Sommerfeld's full-wave solution and the quasi-electrostatic approximation.

A. Finite-Difference Time-Domain Method

The FDTD method easily incorporates complex topological and bathymetric features sampled to cell-sized cubes. Due to the open-domain nature of the problem space and the long wavelengths of ELF signals, the primary challenge in FDTD development is the design of the domain truncation algorithm. Since the ELF signals are naturally attenuated in the water, domain termination for the air is the most important and difficult, since the fields are highly evanescent and quasi-static. Domain termination is implemented using the convolutional PML (CPML) introduced by Roden and Gedney [1].

There are several parameters that must be set in the CPML. The real coordinate stretch, conductivity, complex frequency stretch, and polynomial scaling characterize the CPML. These parameters are set via an optimization procedure similar to that described in [2]. The PML parameter optimization is for domain truncation in air, since there is rapid signal decay in the water.

The FDTD simulations presented herein used 64 bit double precision calculations. All simulations are performed at the Courant stability limit to minimize dispersion error and to advance time as fast as possible. The FDTD simulations use cubic cells, with a cell size of 15 meters. The domain size is $416 \times 501 \times 120$ cells ($6240 \times 7515 \times 1800$ meters), including the 15 cell thick PML. The electromagnetic field

is excited either by a Hertzian current source or current loop depending on the experimental problem being simulated. To extract the frequency response data from the time domain data, fast Fourier transforms (FFT) are used. The simulations are conducted using 200K time steps, which unfortunately does not give sufficient frequency resolution to observe the desired ELF response. To circumvent this problem the time domain data is extended with zeros to a length sufficient to obtain the desired frequency bin size. The zero extended data sets are then transformed with the FFT. The transformed data is normalized with the source signal spectra, and the result is scaled by the experimental current strength. The desired steady-state single frequency data is then extracted and presented in the results section.

In addition to the PML, there are two other primary concerns with FDTD simulations of ELF signals. First, since the problem under consideration deals with waves in highly conductive media, it can be shown that a plane wave of frequency ω will travel a distance l in N_t time steps when

$$N_t = \frac{l}{\delta_x} \sqrt{\frac{3\sigma}{2\epsilon_0\omega}}. \quad (1)$$

This equation simply suggests that for wideband simulations, the number of time steps required is inversely proportional to the square root of frequency. Thus, for a 30 to 3,000 Hz bandwidth, the capturing of the 30 Hz signal will require 10 times more time steps than the 3,000 Hz signal. For even larger bandwidths, the computational time can be prohibitive. Second, the cell size is typically set to resolve geometrical and source features; 5 m to 50 m cells are typical. This results in an over-sampled wave, thus improving dispersion errors at the expense of computational cost.

B. Commercial Solvers: HFSS and Maxwell

As a frequency-domain, finite-element solver, Ansys's High Frequency Structural Simulator (HFSS) [3] is a popular tool to characterize the frequency response of microwave circuits and antennas. It is fairly robust at ELF frequencies provided certain care and precautions are exercised when setting up the problem of interest. To create an electric source in HFSS, three, two-dimensional, rectangular sheets are employed. Two of these sheets form the electrodes and are specified as perfect conductors; the third sheet is used to connect the electrodes with an electric current source impressed upon it. A magnetic source is created by using a flat, two-dimensional, perfectly conducting ring with a local current source impressed in the gap. To truncate the domain, both absorbing boundary conditions (ABC) and PML boundary techniques are considered. The former is easy to implement and is computationally efficient, but the domain boundary needs to be at least a quarter wavelength from sources and scattering objects. The latter can be highly accurate and can be placed nearer to objects, but needs to be redesigned each time geometrical or material parameters are changed. Both PML and ABC techniques have been found effective for ELF signals.

Because the signal frequencies are so low, the fields in the vicinity of the sources are quasi-static, thus suggesting that the strength of the field lines vary with the excitation frequency, but there is little transfer of energy between the electric and magnetic fields to effect propagation. It thus makes sense to consider how well a static solver works in capturing quasi-static fields and to determine the distance in which the field data is no longer quasi-static. Maxwell [4] is a commercial quasi-static solver for both electric and magnetic applications. The construction of sources in Maxwell is accomplished in a different manner than in HFSS. An electric source is designed by assigning voltages to two electrodes; a magnetic source is designed by impressing a current over the cross-section of a perfectly conducting loop. Since there are no wave processes under the quasi-static assumption, the domain is not truncated by the usual absorbing boundary conditions associated with full-wave solvers. Instead, a zero flux condition has proven to be effective in Maxwell whereby normal field components are set to zero on the computational boundary.

C. Sommerfeld Full-Wave Modeling

For the Sommerfeld full-wave (SFW) problem, a flat, three layered space consisting of mud, water and air is considered to approximate a lake or ocean environment. Certainly, such an approximation is valid for the air-water interface and less valid for the water-mud interface. How good or how poor this approximation is, is an important question to be answered.

For a vertical electric dipole oriented along the z -axis, the magnetic vector potential \mathbf{A} is postulated in each region to account for direct, reflected and transmitted paths. For excitations and observations in water, the form of the solution is given by

$$A_z = \frac{Idl}{4\pi} \int_0^\infty [Ae^{-ju_2z} + Be^{ju_2z}] e^{-ju_1h} \frac{J_0(\lambda\rho)}{ju_1} \lambda d\lambda \quad (2)$$

where Idl is the effective dipole moment in A-m. Here A and B are excitation coefficients determined from the boundary conditions and $u_i = \sqrt{k_i^2 - \lambda^2}$. From the Lorentz gauge condition, the corresponding electric scalar potential is

$$V = \frac{Idl}{4\pi Y_2} \int_0^\infty \frac{u_2}{u_1} [Ae^{-ju_2z} - Be^{ju_2z}] e^{-ju_1h} J_0(\lambda\rho) \lambda d\lambda, \quad (3)$$

where Y_2 is the admittance of region two. The electric and magnetic fields in each region are then determined in the usual fashion. By similar methods, the fields associated with a horizontal electric dipole, the vertical magnetic dipole and the horizontal magnetic dipole can equally be determined [5].

Data is available in the literature that quantifies the the Sommerfeld solution. This data has been used to validate our numerical implementation of the solution, which then allows us to use the Sommerfeld solution as a benchmark for the other solutions presented herein, provided that the geometry is layered.

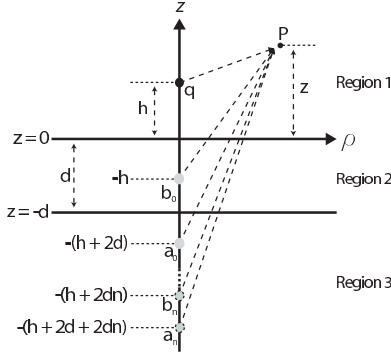


Fig. 1. QES images.

D. Quasi-Electrostatic Half Space Modeling

The quasi-electrostatic (QES) layered media modeling technique is a special case of the more general Sommerfeld, full-wave technique. However, by making use of image theory, we can construct solutions that rapidly converge with just a few terms, making this technique by far the most computationally efficient of all the methods considered herein. The fields within the domain are deemed quasi-electrostatic when the magnetic field has little to no time variation such that $\partial \mathbf{H} / \partial t \approx 0$, which suggests from Faraday's law that the curl of the electric field is zero. The electric field at a given point in space is equal to the negative gradient of the electric scalar potential V at that point. Accounting for interfacial effects associated with reflection and transmission, the scalar potential in region 1 is given by,

$$V = \frac{j\omega q}{4\pi\hat{y}} \int_0^\infty \left[e^{-\lambda|z-h|} + R e^{-\lambda(z+h)} \right] J_0(\lambda\rho) d\lambda, \quad (4)$$

provided that the charge is also in region 1. The complicated reflection and transmission process can easily be accounted for by the use of image charges. The potential can be represented by an infinite number of image charges above or below the original charge at some adjusted height and strength, i.e.,

$$V = \frac{j\omega q}{4\pi\hat{y}} \left[\frac{1}{r} + \sum_{n=0}^{\infty} R_{23}^n R_{21}^n \left[\frac{R_{23}}{r_a} - \frac{R_{21}}{r_b} \right] \right]. \quad (5)$$

The first term represents the original point charge located at $z = h$ with a corresponding unity strength. The second term represents the endless summation of image terms needed to account for all interfacial reflections and transmissions. The height of each image is adjusted by r_a and r_b , which are functions of n . The corresponding strength of each image is adjusted by R_{21} and R_{23} which represents the interfacial reflection-like coefficients. A depiction of the image concept is shown in Figure 1.

The single point charge concept is used to construct an electric dipole by the superposition of two, oppositely charged electrodes. Specifically, this is done by replacing the single charge with a spherical geometry of some radius. Then an additional electrode of opposite charge at some separation distance is added that defines the electric dipole. The image

TABLE I
MATERIAL PROPERTIES

	Region 1, Air	Region 2, Water	Region 3, Mud
ϵ_r	1	81	1
σ	0	0.018	0.012

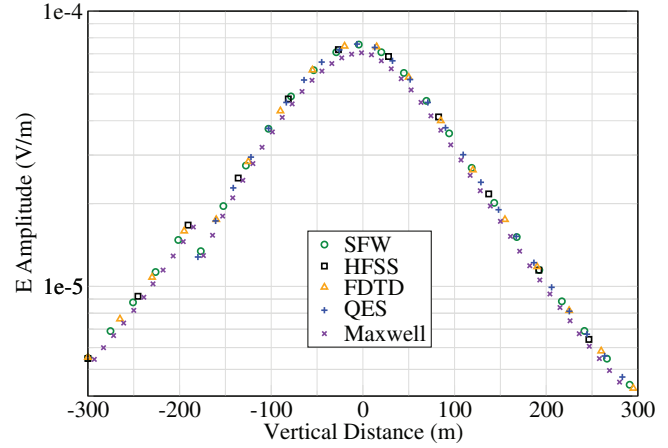


Fig. 2. Calculation results in the three layer geometry at 10 Hz. Source is a horizontal electric dipole.

concept for a single point charge is extended to the electric dipole.

III. NUMERICAL RESULTS

To determine the robustness and limitations of each method, three test cases are considered. The first considers a three layer stratified geometry, as shown in Figure 1. In this case, the Sommerfeld solution is regarded as the benchmark to determine the accuracy of the other methods. The material parameters used in this study are listed in Table I. The thickness of the center region is 180 m. A 10 Hz, 15 A-m horizontal electric dipole is used and is placed at 15 m in the water. The observer is at ρ and z along the end-fire direction of the dipole. Figure 2 shows the amplitude of the electric field as a function of z when $\rho = 150$ m. The correlation between all methods is seen to be very good, thus substantiating each method's validity. As expected from the boundary conditions, a noticeable discontinuity at $z = -180$ m occurs at the water-mud interface. A plot of the amplitude of the magnetic field (not shown) shows equally good correlation.

The second and third cases consider two experimental scenarios that mimic a sea environment by placing sources and sensors in Lake Pend d'Oreille, Idaho. For the second case, a vertical magnetic dipole is located on the shore of the Lake with a dipole moment of 3,271 A-m² at a frequency of 81 Hz. The sensing array is in the water about 95 m away from the source; five separate measurements are recorded at various depths within the water. To obtain accurate simulation data, it is imperative that the simulation codes (e.g. FDTD, HFSS, Maxwell) incorporate all of the geometrical features of the Lake. This was accomplished by reading data from

bathymetry and topological maps, and discretizing that data into height field data. Some smoothing and averaging are necessary to mitigate errors. The height field is input directly into the FDTD code, but additional mesh processing is needed before it can be used in Maxwell or HFSS. This processing step, as accomplished by a software package CUBIT [6], is required to obtain a high quality mesh with the fewest number of tetrahedra. A typical mesh as used in Maxwell or HFSS is shown in Figure 3.

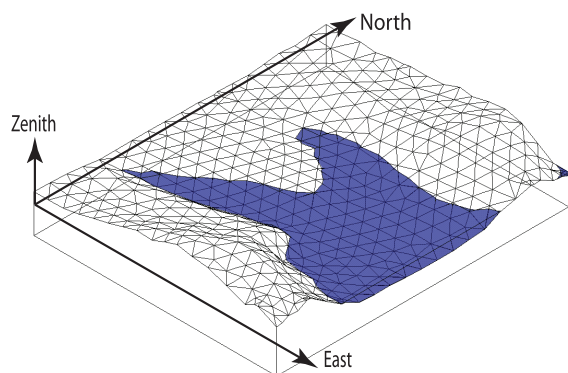


Fig. 3. Geometry of the water and mud layers.

Shown in Figure 4 is experimental electric field data compared with data from FDTD, HFSS and SFW simulations. All data obtained from simulations agree quite well with experimental data, with SFW being the worst with a maximum error of 7%. The one experimental outlier at -3 m is due to effects caused by a barge that hoists the field sensors up and down.

The third case utilized an electric, horizontal dipole with a dipole moment of 8 A-m. The dipole was fixed to the hull of a boat that created a slowly moving source; the sensor array was fixed in the water at a depth of 15.1 m and between the shore and the dipole. The material parameters of Table I

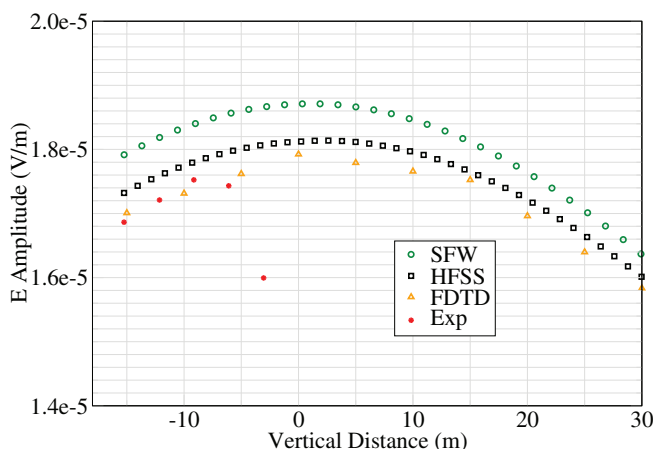


Fig. 4. Comparison of the calculated and experimental electric field magnitude at 81 Hz. Source is a vertical magnetic dipole (a current loop).

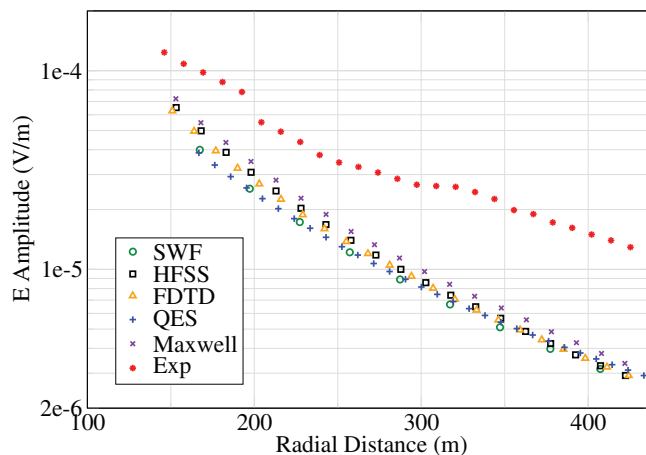


Fig. 5. Comparison of the calculated and experimental electric field for the horizontal electric dipole source at 100 Hz.

still apply. As seen in the plots of Figure 5, the data from SFW, HFSS, FDTD, QES and Maxwell all agree with each other and follow the trend of the experimental data. The error between experiment and simulation, however, is excessive. These two observations suggest that the codes and methods are not invalid, but that the data input into the codes is. Errors between simulation and experimental data are attributed to several factors. First, the Lake bottom and shore were treated as uniformly saturated mud. This is a false assumption since inhomogeneities are present due to rock formations, saturation content, etc. For measurements near the air-water interface and away from the shore, this assumption becomes less significant since the dominant wave mechanisms are associated with the air and water whose materials parameters are known precisely. Second, for observations near a shallow inclining shore, small errors in the discretization geometry can create large ambiguities in the location of the mud-water interface. This problem is a result of using high-resolution height field data that must be sampled to create sufficiently sized FDTD cells or finite-element tetrahedra as a way to reduce the total number of cells or tetrahedra to a manageable number.

ACKNOWLEDGMENT

This work was supported by the Office of Naval Research under contract number N00014-09-1-0923.

REFERENCES

- [1] J. A. Roden and S. D. Gedney, "Convolution PML (CPML): An efficient FDTD implementation of the CFS-PML for arbitrary media," *Microwave and Optical Technology Letters*, vol. 27, no. 5, pp. 334-339, Dec. 2000.
- [2] C. L. Wagner and J. L. Young, "FDTD Numerical Tests of the Convolutional-PML at Extremely Low Frequencies," *IEEE Antennas and Wireless Propagation Letters*, vol. 8, pp. 1398-1401, 2009.
- [3] Ansys Software Corp. *High Frequency Structural Solver* Ver. 12.0.0
- [4] Ibid. *Maxwell* Ver. 12.2.1
- [5] J. Wait, *Electromagnetic Wave Theory*, Harper & Row, New York, NY, 1985.
- [6] The CUBIT Geometry and Mesh Generation Toolkit. Sandia National Laboratories. <http://cubit.sandia.gov/cubit.html>.

Moving Sources, FDTD and Reciprocity

Jeffrey L. Young and Christopher L. Wagner*
 Department of Electrical and Computer Engineering
 University of Idaho
 Moscow, Idaho, USA
 jyoung@uidaho.edu, clwagner@uidaho.edu

Abstract—The use of reciprocity in FDTD simulations is described herein for the case of moving sources. The method is validated against experimental data associated with extremely low frequency EM sources. The correlation between data sets associated with simulation and experiment is excellent.

I. INTRODUCTION

A given electromagnetic problem is typically framed by placing the source at a fixed location and allowing the observer to move to various locations to sample the field. This choice is purely arbitrary when a closed-form solution to the problem is available since both source and observation variables are part of the solution, thus providing knowledge of the field for any source and observation locations. However, for a numerical solution obtained from a finite-difference, time-domain (FDTD) simulation it is almost imperative that the source be regarded as stationary in the grid and the field be sampled throughout the computational domain; otherwise, a new simulation would have to be conducted for each new source location, which is computationally costly.

In certain naval applications in which a moving vessel in an inhomogeneous environment is the source of an electromagnetic emission, the question is raised how to model the fields of this moving source when it transverse thousands of meters in an interval of minutes to hours. Given that a typical FDTD simulation only models electromagnetic phenomena that lasts fractions of a second due to restrictions of the time step imposed by the CFL number, it is clear that a direct simulation of a moving source is not feasible or practical. Clearly an approach is needed that correlates a numerical fixed source, moving observer (FSMO) problem to the experimental fixed observer, moving source (FOMS) problem. (Note: By moving, we strictly mean that the source or observer moves to a particular location and stays at the location while a measurement is taken; it subsequently moves to the next location, an so forth.) This correlation is accomplished via reciprocity.

II. FORMULATION

For purposes of this paper, consider two nonidentical antennas labeled one and two that source or sense the electromagnetic field. These antennas are loaded with impedances Z_1 and Z_2 , respectively, and are arbitrarily located and oriented in some reciprocal, but not necessarily homogeneous domain. We identify the “e” problem of reciprocity in which antenna one is the transmitter and antenna two is the receiver; we identify

the “a” problem of reciprocity in which antenna two is the transmitter and antenna one is the receiver. The corresponding equivalent circuits of these two problems are shown in Figure 1. Here Z_{mn} is an open-circuit impedance parameter of the

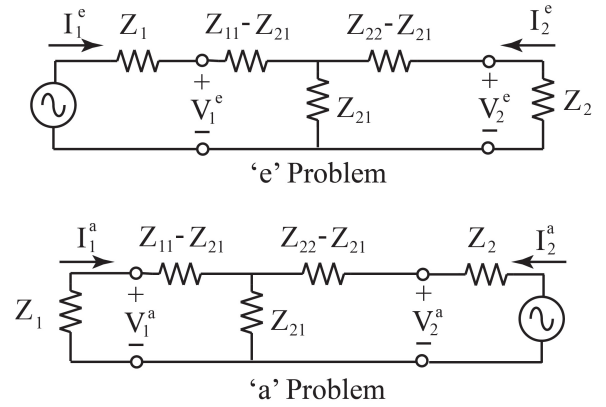


Fig. 1. The equivalent circuits of the two antenna problem.

equivalent network. Assuming that the source currents are known, it follows from these circuits that

$$\begin{aligned} \frac{V_2^e}{I_1^e} &= \frac{Z_{21}Z_2}{Z_{22} + Z_2} \\ \frac{V_1^a}{I_2^a} &= \frac{Z_{21}Z_1}{Z_{11} + Z_1} \end{aligned} \quad (1)$$

and hence,

$$\frac{V_2^e}{I_1^e} = \Lambda \frac{V_1^a}{I_2^a} \quad (2)$$

where

$$\Lambda = \left(\frac{Z_{11} + Z_1}{Z_{22} + Z_2} \right) \left(\frac{Z_2}{Z_1} \right). \quad (3)$$

That is, knowledge of the “a” problem gives direct knowledge of the “e” problem provided the self and load impedances of the network are known.

At any given point in space, we may define a calibration antenna length vector \mathbf{l}_i ($i = 1, 2$) of each antenna that relates the field when the antenna is absent to the port voltage when the antenna is present for a given load impedance, i.e. $V_i = -\mathbf{E}_i \cdot \mathbf{l}_i$ when the ports are loaded with Z_i . We assume that this vector is known. Thus, from Eqn. (2),

$$\mathbf{E}_2^e \cdot \mathbf{l}_2 = \Lambda \frac{\mathbf{E}_1^a \cdot \mathbf{l}_1 I_1^e}{I_2^a}. \quad (4)$$

We now identify the “e” and “a” problems more rigorously. We assume that the “e” problem corresponds to the FOMS scenario associated with the experiment. The “a” problem corresponds to the FSMO scenario associated with a simulation in which \mathbf{l}_2 is directed entirely in x . Letting $\mathbf{l}_2 = l_{2x}\mathbf{a}_x$, we see from the previous equation that

$$E_{2x}^e = \Lambda \frac{\mathbf{E}_1^a \cdot \mathbf{l}_1 I_1^e}{l_{2x} I_2^a}. \quad (5)$$

Likewise, we may construct “b” and “c” problems that corresponds to simulations in which \mathbf{l}_2 is directed entirely in y and z , respectively. Thus, the experimentally measured electric field vector associated with FOMS, i.e. the “e” problem, can be predicted from three simulations associated with FSMO, i.e. the “a”, “b,” and “c” problems, provided the load impedances, open-circuited self impedances, antenna currents and antenna calibration length vectors are known. The first of these is regarded as a given of the experiment. The second can be easily measured at the time of the experiment or predicted *a priori* via simulation. The third is both a given of the experiment and of the simulations. The magnitude of the fourth is regarded as a given from the calibration procedure of the antennas and instrumentation used in the experiment under some assumptions – namely, the field across the antennas is uniform and the antennas are embedded in homogeneous media and away from material discontinuities. Given the size of the sensors and the frequencies involved in the present experiment, these assumptions are not overly restrictive. The direction of the fourth is parallel to the polarization of the antenna. Because the calibration length vector relates the unperturbed field to a measured voltage, the simulation does not need to model antenna one. For if it had to, there would be no advantage in using reciprocity since a new simulation would have to be conducted every time antenna one occupied a new location. Moreover, the simulation does not need to physically model antenna two. Instead, all that is needed is to impress an equivalent current where antenna two resides to create the correct field where antenna one resided. This is advantageous since the modeling of physically small antennas on the orders of meters or less in low frequency simulations that use cell sizes on the order of tens of meters or more and domain sizes on the order of kilometers is computationally problematic.

The determination of the magnetic field vector follows a similar line of thought by making use of experimental electric currents \mathbf{J}^e and numerical magnetic currents \mathbf{M}^a in the context of reciprocity:

$$\int_V \mathbf{H}^e \cdot \mathbf{M}^a dV = - \int_V \mathbf{E}^a \cdot \mathbf{J}^e dV. \quad (6)$$

Thus, a total of six simulations must be conducted to determine all six components of the electromagnetic field for moving source scenarios.

III. EXPERIMENT

The experiment considered in this investigation defines antenna one as a dipole antenna fashioned out of metal

electrodes that are attached to a hull of some non-metallic boat. The electrodes are 0.3 m by 0.6 m and are separated by 4.0 m (on center). The dipole is driven by an extremely low frequency (ELF) source and the boat motors about some lake to represent inhomogeneous domain of water, air and mud. The precise location and direction of the boat is measured at all times using a GPS system. Since the electrodes form electrical contact with the water, a uniform current, which is also measured, flows between them thus achieving an effective calibration length of 4.0 m. The vector orientation is taken to be parallel to the boat path.

As for the sensor (i.e. antenna two), it is submerged in the lake at some fixed location relative to earth longitude and latitude, and at a fixed depth of 14.9 m. The sensor is actually an array of electrically small sensors attached to a plastic truss and arranged in a way to form perpendicular, triaxial vector antenna. Again, the sensor electrodes make direct contact with the water such that the effective length of each axis is roughly equal to the physical size of the array. The orientation of each axis is measured to correlate them to the axis of the fixed coordinate system of the experiment. A data acquisition system is synchronized with the source GPS and is used to sample the field data.

IV. SIMULATIONS AND RESULTS

A simulation of the experiment is conducted using FDTD, where the domain size is 2.0 km by 2.0 km by 0.6 km; the cell size is 10.0 m by 10.0 m by 5.0 m; the time step is 13.6 ns. The domain is truncated with a PML, as described in [1]. A total of 200,000 time steps is needed to achieve convergence. Representative post-processed FDTD field data, as obtained from reciprocity methods, is shown in Figure 2 along with experimental data. The excellent correlation between the two data sets substantiates the methodology outlined in this paper.

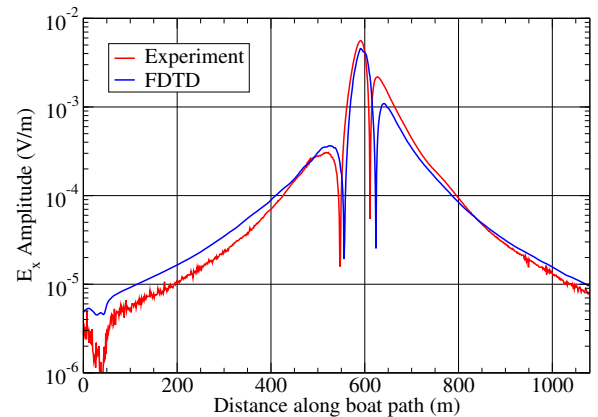


Fig. 2. Representative 10 Hz electric field data.

REFERENCES

- [1] C. L. Wagner and J. L. Young, “FDTD Numerical Tests of the Convolutional PML at Extremely Low Frequencies,” *IEEE Antennas and Wireless Letters*, vol. 8, pp. 1398-1401, 2009.

A Simple Up-over-and-down Model for Low Frequency Horizontal Electric Dipole Propagation Near An Interface

Robert G. Olsen, *Fellow, IEEE*, and Zhi Li, *Student Member, IEEE*

Abstract—The propagation of electromagnetic fields from an electric or magnetic dipole near an interface has been described mathematically for many years using Sommerfeld integrals. In the high frequency case for which the dipole and field point are buried in the lower (and much lossier) medium, simple approximations have been derived that can be interpreted as up-over-and-down propagation (i.e., plane wave from source to the surface – surface wave to a point above the field point – plane wave to the field point). In this paper, a simple expression valid for the low frequency case (i.e., relevant dimensions in the upper medium are electrically small) is derived. In this case the up-over-and-down propagation is described as near field propagation from source to the surface, quasi-static propagation along the interface to above the field point and plane wave propagation to the field point.

Index Terms—Electromagnetic fields, electromagnetic propagation, extremely low frequency.

I. INTRODUCTION

THE electric (E) and magnetic (H) fields due to a dipole (vertical or horizontal, electric or magnetic) buried in a conducting half-space have been well studied for decades and can be written in terms of Sommerfeld integrals [1] – [4]. When the dipole and the observation point are both in the conducting medium close to the interface relative to their horizontal spacing and the frequency is “low”, it is possible to interpret the propagation mechanism as a simple up-over-and-down process. Here, up-over-and-down means that the field propagates vertically up crossing the interface to the free space medium, then propagates horizontally along the interface, and finally propagates vertically down to the observation point. While this behavior is somewhat similar to the high frequency phenomenon observed by previous authors [5], it is also different because the fields in the free space region are quasi-static.

The formulas for the fields given by Sommerfeld integrals are, while exact, very complicated. In this paper, the integrals are simplified by using some reasonable assumptions given the range of parameters of interest. Then a set of simple but very

good approximations to the electric and magnetic fields are obtained. Based on these approximations, the up-over-and-down behavior is observed and discussed. The dipole source here is chosen to be a horizontal electric dipole (HED). The HED was selected because, using achievable dipole moments and commonly available receiving equipment, it can be shown that the HED fields are detectable at larger distances than those of other dipole types (i.e., vertical electric dipole (VED) or vertical (VMD) or horizontal (HMD) magnetic dipoles). To be more specified, it was assumed from this study that the maximum dipole moments for electric and magnetic dipoles are 50 A-m and 2500 A-m² respectively and that the minimum detectable electric and magnetic fields are 1μV/m and 40μA/m respectively. Using these values, the horizontal electric field component that is perpendicular to the HED direction can be detected to a distance of 800 meters to the source. No other field component from any other dipole can be detected beyond about 200 meters.

II. GEOMETRY

The geometry of the model is shown in Fig. 1. A ‘y’ oriented HED, which has a dipole moment of Idl , is on the ‘z’ axis and buried ‘h’ meters below the surface in a conducting half-space ($z < 0$). The upper half space (i.e., $z > 0$) is assumed to be free space.

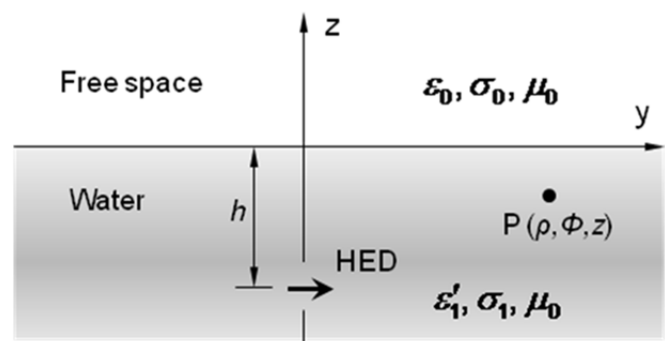


Fig. 1. Geometry of the model

As noted in the figure, ϵ_0 and σ_0 are the permittivity and conductivity of free space and $\sigma_0 = 0$. $\epsilon'_1 = \epsilon_1 - j\sigma_1/\omega$ is the complex permittivity of the lower half space. ϵ_1 and σ_1 are the permittivity and conductivity and $\epsilon_1 = \epsilon_{r1}\epsilon_0$, where ϵ_{r1} is the static relative permittivity. It is assumed that all materials have the permeability of free space μ_0 . The cylindrical coordinate

Manuscript received October 20, 2010. This work was supported in part by the U.S. Office of Naval Research under Grant N00014-08-1-170.

Robert G. Olsen is with Washington State University, Pullman, WA 99163 USA (phone: 509-335-0348; fax: 509-335-9608; e-mail: bgolsen@wsu.edu).

Zhi Li is with Washington State University, Pullman, WA 99163 USA (e-mail: zli@eeecs.wsu.edu).

system (ρ, φ, z) is used in this paper, where $x = \rho \cos \varphi$ and $y = \rho \sin \varphi$.

III. SOMMERFELD INTEGRAL METHOD

The Sommerfeld integral method will be very briefly introduced here. This method uses the integral representations of vector potentials to determine the E and H fields. To find the E and H fields due to the HED, two non-zero components of vector potential are required [6, 7]. Here, the y and z components of the magnetic vector potential, A_y and A_z , are chosen.

$$A_y^0 = K_1 \int_0^\infty f_1(\lambda) e^{-u_0 z} \lambda J_0(\lambda \rho) d\lambda \quad (z \geq 0) \quad (1)$$

$$\begin{aligned} A_y^1 &= K_1 \frac{e^{-jk_1 R}}{R} + K_1 \int_0^\infty f_2(\lambda) e^{u_1 z} \lambda J_0(\lambda \rho) d\lambda \\ &= K_1 \frac{e^{-jk_1 R}}{R} + K_1 I_{y1} \quad (z \leq 0) \end{aligned} \quad (2)$$

$$A_z^0 = K_1 \frac{\partial}{\partial y} \int_0^\infty g_1(\lambda) e^{-u_0 z} \lambda J_0(\lambda \rho) d\lambda \quad (z \geq 0) \quad (3)$$

$$\begin{aligned} A_z^1 &= K_1 \frac{\partial}{\partial y} \int_0^\infty g_2(\lambda) e^{u_1 z} \lambda J_0(\lambda \rho) d\lambda \\ &= K_1 \frac{\partial}{\partial y} I_{z1} \quad (z \leq 0) \end{aligned} \quad (4)$$

where $J_0(\lambda \rho)$ is the Bessel function of the first kind of order zero and

$$\begin{aligned} k_i^2 &= \omega^2 \mu_0 \varepsilon'_i = \omega^2 \mu_0 (\varepsilon_i - j \frac{\sigma_i}{\omega}) \\ u_i &= \sqrt{(\lambda^2 - k_i^2)} \\ K_1 &= \frac{\mu_0 I d l}{4\pi} \end{aligned}$$

ε'_i is the complex permittivity of the i^{th} half space ($i = 0$ or 1 for free space and water, respectively, and $\varepsilon'_0 = \varepsilon_0$). k_i is the wave number where $\text{Re}(k_i) \geq 0$ and $\text{Re}(u_i) \geq 0$ define the proper Riemann sheet of the complex plane. The first term in (2) is the source term and $R = (\rho^2 + z^2)^{1/2}$ is the distance from the dipole to the observation point. I_{y1} and I_{z1} represent the integral terms in (2) and (4), respectively. The source term $K_1 e^{-jk_1 R}/R$ in (2) is the vector potential of the dipole itself in an infinite homogeneous conducting medium. It can be written in integral form as

$$\frac{e^{-jk_1 R}}{R} = \begin{cases} \int_0^\infty u_1^{-1} e^{-u_1(z+h)} \lambda J_0(\lambda \rho) d\lambda & (z+h) \geq 0 \\ \int_0^\infty u_1^{-1} e^{u_1(z+h)} \lambda J_0(\lambda \rho) d\lambda & (z+h) \leq 0 \end{cases} \quad (5)$$

Functions f_1, f_2, g_1 and g_2 are arbitrary coefficient functions of the integration variable λ . They are determined by matching the boundary conditions at $z = 0$. Given the vector potentials A_y and A_z the E and H field can be obtained from:

$$E_x = -\frac{j}{\omega \mu \varepsilon} \cdot \frac{\partial}{\partial x} \left(\frac{\partial A_y}{\partial y} + \frac{\partial A_z}{\partial z} \right) \quad (6)$$

$$E_y = -\frac{j}{\omega \mu \varepsilon} \cdot \left[\frac{\partial}{\partial y} \left(\frac{\partial A_y}{\partial y} + \frac{\partial A_z}{\partial z} \right) + k^2 A_y \right] \quad (7)$$

$$E_z = -\frac{j}{\omega \mu \varepsilon} \cdot \left[\frac{\partial}{\partial z} \left(\frac{\partial A_y}{\partial y} + \frac{\partial A_z}{\partial z} \right) + k^2 A_z \right] \quad (8)$$

$$H_x = \frac{1}{\mu} \left(\frac{\partial A_z}{\partial y} - \frac{\partial A_y}{\partial z} \right) \quad (9)$$

$$H_y = -\frac{1}{\mu} \frac{\partial A_z}{\partial x} \quad (10)$$

$$H_z = \frac{1}{\mu} \frac{\partial A_y}{\partial x} \quad (11)$$

By matching boundary conditions, i.e., the tangential components of E and H fields are continuous cross the $z = 0$ plane, the coefficient functions can be determined as

$$f_1 = \frac{2e^{-u_1 h}}{u_0 + u_1} \quad (12)$$

$$f_2 = \frac{(u_1 - u_0) e^{-u_1 h}}{u_1 \cdot (u_0 + u_1)} \quad (13)$$

$$g_1 = g_2 = \frac{2(\varepsilon'_1 - \varepsilon_0) e^{-u_1 h}}{(u_0 + u_1)(\varepsilon'_1 u_0 + \varepsilon_0 u_1)} \quad (14)$$

The E and H fields in the conducting medium can be formulated by inserting (2), (4), (13) and (14) into (6) ~ (11).

IV. SIMPLIFICATION OF THE INTEGRAL FOR A_z^1

The objective of this paper is to derive simple but acceptable approximations for the fields, which can be interpreted to provide good insight into the physical behavior of the wave propagating from source to receiver. One fundamental problem with evaluating the integrals shown in (1) to (4) is that, for large values of ρ compared to h and z , the rapid oscillations of the Bessel function cause difficulties with the numerical integration. To remedy this problem, the contours of integration will be deformed in the complex plane so that the integrand decays exponentially for large values of ρ . This transformation will also allow other simplifying approximations that will lead to a simple interpretation of the final result.

A. Deformation of The Integral Contour

If (14) is inserted into the integral portion of (4) and the exponential term is removed from $g_2(\lambda)$, this integral becomes

$$I_{z1} = \int_0^\infty g'_2(\lambda) e^{u_1(z-h)} \lambda J_0(\lambda \rho) d\lambda \quad (15)$$

where

$$g'_2(\lambda) = \frac{2(\varepsilon'_1 - \varepsilon_0)}{(u_0 + u_1)(\varepsilon'_1 u_0 + \varepsilon_0 u_1)} \quad (16)$$

Using the identities $J_0(x) = \frac{1}{2} [H_0^{(1)}(x) + H_0^{(2)}(x)]$ and

$$H_0^{(1)}(-x) = -H_0^{(2)}(x)$$

where $H_0^{(1)}(x)$ and $H_0^{(2)}(x)$ are the Hankel functions of the first and second kind of order zero, respectively, the integral range in (15) can be expanded to $(-\infty, +\infty)$. Since u_0 , u_1 , and $g_2'(\lambda)$ are all even functions of λ

$$I_{z1} = \frac{1}{2} \int_{-\infty}^{+\infty} g_2'(\lambda) e^{u_1(z-h)} \lambda H_0^{(2)}(\lambda \rho) d\lambda. \quad (17)$$

For the function $g_2'(\lambda)$, there is one pole, λ_p , and two branch points, k_0 and k_1 , in the complex λ plane. The branch cuts are selected to be vertical lines from the branch points to negative infinity. Then the integral contour in (17) can be deformed into a contour C_B which is illustrated with the dashed line in Fig. 2.

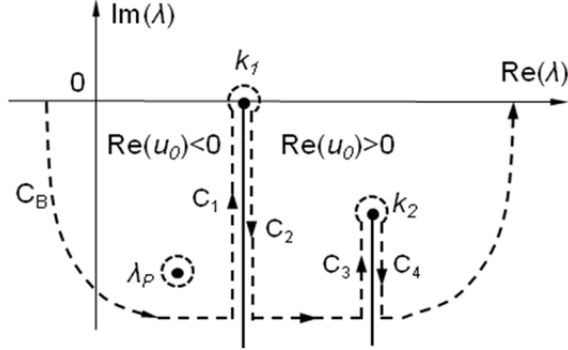


Fig. 2. Deformation of the integral contour for the integration in (4).

With this deformation and the fact that the Hankel function goes to zero exponentially along the infinite semi-circle, the integral along the real axis is converted to the residue of the pole, R_{λ_p} , plus the integrations along $C_1 \rightarrow C_4$, which encompass the two branch cuts. Thus

$$I_{z1} = \frac{1}{2} \int_{C_1+C_2+C_3+C_4} g_2'(\lambda) e^{u_1(z-h)} \lambda H_0^{(2)}(\lambda \rho) d\lambda + R_{\lambda_p}$$

For $|k_1| \gg |k_0|$, the integral along the branch cut of k_1 is much smaller than that of k_0 and can be ignored. Note that, in the complex plane, the sign of u_0 will change when crossing the branch cut associated with k_0 . Given the choice of branch cut, $\text{Re}(u_0) < 0$ and $\text{Re}(u_0) > 0$ on the left and right sides, respectively, as shown in Fig. 2. In addition while the pole is in the proximity of the branch cut integration and is evident in the integrand, its contribution to the integral is negligible for the low frequencies considered here. Thus the pole residue can be ignored. Therefore

$$I_{z1} \approx \frac{1}{2} \int_{C_1+C_2} g_2'(\lambda) e^{u_1(z-h)} \lambda H_0^{(2)}(\lambda \rho) d\lambda. \quad (18)$$

It has been shown that (18) is valid when $h, z \ll \rho$, $|k_1| \gg |k_0|$ and $|k_1 \rho| \gg 1$.

The parameters and their values / value ranges used for the simulations are listed in Table I. The conductivity and permittivity of the lower medium represent typical lake water. They will also be used for all the following simulations in this paper.

B. Simplification of The Integrand

Since $\rho \gg |h|, |z|$, the decay of the integrand along C_1 and C_2 is controlled by the value of $|\lambda \rho|$, the integral can be truncated at $|\lambda \rho| = 10$ and since we assume $|\lambda \rho| \gg 1$

TABLE I LIST OF PARAMETERS AND THEIR VALUES / VALUE RANGES		
	Free space	Conducting medium
Relative permittivity, ϵ_{ri} ($\epsilon_i = \epsilon_{ri} \epsilon_0$)	1	1
Conductivity, σ (S/m)	0	0.018
Permeability, μ (H/m)	$4\pi \times 10^{-7}$	$4\pi \times 10^{-7}$
Dipole depth, h (m)	20	
z (m)	-10	
Horizontal distance, ρ (m)	100 - 10000	
Dipole moment, Idl (A-m)	1	
Frequency, f (Hz)	100 - 3000	

$$u_1 = (\lambda^2 - k_1^2)^{1/2} \approx jk_1 \quad (19)$$

With (19) the exponential term in (18) can be extracted from the integral, which leads to

$$I_{z1} \approx \frac{e^{jk_1(z-h)}}{2} \int_{C_1+C_2} g_2'(\lambda) \lambda H_0^{(2)}(\lambda \rho) d\lambda \quad (20)$$

Further since $|k_0 \rho| \ll 1$ (i.e., quasi-static for $z > 0$), it is reasonable to assume that

$$u_0 = \pm(\lambda^2 - k_0^2)^{1/2} \approx \pm\lambda \quad (21)$$

because $|k_0|$ is very small compared to $|\lambda|$ over the largest portion of the integral. The approximations have been made here can be summarized as

$$\rho \gg |h| \text{ and } |z|, |k_0 \rho| \ll 1, \text{ and } |k_1 \rho| \gg 1$$

Now, if the approximations (19), (21) and $|\epsilon'_1| \gg |\epsilon_0|$ are made in (16) then

$$g_2'(\lambda) \approx \frac{2(\epsilon'_1)}{(\pm\lambda + jk_1)(\pm\epsilon'_1\lambda)} = \frac{2}{\lambda^2 \pm jk_1\lambda}$$

If $g_2^{'+}(\lambda) = \frac{2}{\lambda^2 + jk_1\lambda}$ and $g_2^{'-}(\lambda) = \frac{2}{\lambda^2 - jk_1\lambda}$, represent

$g_2'(\lambda)$ on the right side and left side of the branch cut of k_0 , respectively, then the integral in (20) can be approximated as

$$I'_{z1} \approx \int_{C_1} \frac{2}{\lambda - jk_1} H_0^{(2)}(\lambda \rho) d\lambda + \int_{C_2} \frac{2}{\lambda + jk_1} H_0^{(2)}(\lambda \rho) d\lambda \quad (22)$$

Using the asymptotic approximation $H_0^{(2)}(\lambda \rho) \approx \sqrt{\frac{2j}{\pi\lambda\rho}} \cdot e^{-j\lambda\rho}$

for large $|\lambda \rho|$ (i.e., most of the integral)

$$I'_{z1} \approx 2\sqrt{\frac{2j}{\pi\rho}} \left[\int_{C_1} \frac{e^{-j\lambda\rho} d\lambda}{\sqrt{\lambda}(\lambda - jk_1)} + \int_{C_2} \frac{e^{-j\lambda\rho} d\lambda}{\sqrt{\lambda}(\lambda + jk_1)} \right] \quad (23)$$

Letting $\lambda = k_0 - js$, and changing the integral variable from λ to s , I'_{z1} finally becomes

$$I'_{z1} \approx 2\sqrt{\frac{2j}{\pi\rho}} \cdot e^{-jk_0\rho} \left[\int_0^\infty \frac{je^{-\rho s} ds}{\sqrt{k_0 - js}(k_0 - js - jk_1)} - \int_0^\infty \frac{je^{-\rho s} ds}{\sqrt{k_0 - js}(k_0 - js + jk_1)} \right] \quad (24)$$

Ignoring k_0 in both the denominators of the two integrands, which is reasonable because $|k_0|$ is very small compared to $|s|$ over most of the integral, I'_{z1} reduces to

$$I'_{z1} \approx -2j\sqrt{2/(\pi\rho)} \cdot e^{-jk_0\rho} (I_1 - I_2) \quad (25)$$

where $I_1 = \int_0^\infty \frac{e^{-\rho s} ds}{\sqrt{s}(s+k_1)}$ and $I_2 = \int_0^\infty \frac{e^{-\rho s} ds}{\sqrt{s}(s-k_1)}$. Therefore,

the calculation of the complicated integral in (18) is reduced to the problem of evaluating the two relatively simple integrals in (25). I_1 can be analytically evaluated as [8]

$$I_1 = \sqrt{2\pi/k_1} \cdot D_{-1}(\sqrt{2k_1\rho}) e^{\frac{k_1\rho}{2}}$$

where $D_{-1}(\sqrt{2k_1\rho})$ is the parabolic cylinder function of argument $\sqrt{2k_1\rho}$ with $D_{-1}(\sqrt{2k_1\rho}) = \sqrt{\pi/2} [1 - \Phi(\sqrt{k_1\rho})] e^{\frac{k_1\rho}{2}}$.

The second term in the bracket, $\Phi(\sqrt{k_1\rho})$, is the probability integral, which has the asymptotic approximation for $|k_1\rho| \gg 1$:

$$\Phi(\sqrt{k_1\rho}) \approx 1 - \frac{1}{\sqrt{\pi}} \cdot \frac{e^{-k_1\rho}}{\sqrt{k_1\rho}}$$

Using this result in I_1 , results in

$$I_1 \approx \sqrt{\pi} / (k_1 \sqrt{\rho})$$

Similarly for I_2

$$I_2 \approx -\sqrt{\pi} / (k_1 \sqrt{\rho}).$$

Therefore, the integral in (25) is

$$I'_{z1} \approx -4\sqrt{2}j \frac{e^{-jk_0\rho}}{k_1\rho}$$

The integral I_{z1} then can be approximated as

$$I_{z1} \approx -2\sqrt{2}j e^{jk_1(z-h)} \cdot \frac{e^{-jk_0\rho}}{k_1\rho} \quad (26)$$

It can be shown that (26) is approximately a factor of 1.4 larger than the exact result in (15) and that this difference is relatively stable over a wide range of parameters. Given this and the fact that an attempt to find a missing $\sqrt{2}$ factor did not succeed, a further study of the approximation used to derive (26) was carried out. This study indicated that the dominant part of the error resulted from the replacement of the Hankel function by its asymptotic expansion. Given this, a correction term can be written as

$$I_C \approx 2e^{-jk_0\rho} \int_0^B \left[\frac{1}{s-k_1} - \frac{1}{s+k_1} \right] \times \left[H_0^{(2)}(-j\rho s) e^{jk_0\rho} - \sqrt{\frac{-2}{\pi\rho s}} e^{-\rho s} \right] ds \quad (27)$$

Clearly most of the contribution to this integral comes from small values of ρs . Thus the integral is (somewhat arbitrarily) truncated at $\rho s = B = 0.3$ and the Hankel function is replaced by its small argument expansion. Given this, the correction term is written as

$$I_C \approx 2e^{-jk_0\rho} \int_0^M \left[\frac{1}{s-k_1} - \frac{1}{s+k_1} \right] \times \left[1 - \frac{2j}{\pi} \ln \left(\frac{-j1.781\rho s}{2} \right) - \sqrt{-2/(\pi\rho s)} \right] ds \quad (28)$$

where inside the integral $e^{jk_0\rho} \approx e^{-\rho s} \approx 1$ and $M = B/\rho$. The integral in (28) can be analytically evaluated and the result is

$$I_C \approx I_{C1} + I_{C2} + I_{C3} \quad (29)$$

where

$$\begin{aligned} I_{C1} &= c \cdot \ln \left(\frac{k_1 - B}{k_1 + B} \right) e^{-jk_0\rho} \\ I_{C2} &= -\frac{8jB}{\pi k_1} e^{-jk_0\rho} \\ I_{C3} &= 2je^{-jk_0\rho} \sqrt{\frac{-2}{\pi k_1\rho}} \left[\ln \left(\frac{k_1 - B + 2j\sqrt{k_1 B}}{k_1 + B} \right) \right. \\ &\quad \left. + j \ln \left(\frac{k_1 + B - 2j\sqrt{-k_1 B}}{k_1 - B} \right) \right] \\ c &= 2 \left[1 - \frac{2j}{\pi} \ln \left(\frac{-j1.781B\rho}{2} \right) \right]. \end{aligned}$$

I_{C1} and I_{C3} can be further simplified by expanding the natural logarithm function in Taylor series.

$$I_{C1} \approx -2c \frac{M}{k_1\rho} e^{-jk_0\rho} \quad \text{and} \quad I_{C3} \approx 8\sqrt{\frac{2}{\pi M}} \frac{jM}{k_1\rho} e^{-jk_0\rho}$$

The correction term is then rewritten as

$$I_C \approx \frac{jN}{k_1\rho} e^{-jk_0\rho} \quad (30)$$

where $N = M [-2c - 8/\pi + 8\sqrt{2/(\pi M)}]$ is a constant. It is interesting to note that the functional dependence of (30) is almost identical to that of (26). Hence adding (30) to (26) results in

$$I_{z1} \approx \frac{e^{jk_1(z-h)}}{2} \cdot \frac{je^{-jk_0\rho}}{k_1\rho} [-4\sqrt{2} + N] \quad (31)$$

which is identical to (26) except for the constant and that this constant is approximately 1/1.4 times the constant in (26) when $M = 0.3$ (i.e., $N \approx 1.72$). Then (31) becomes

$$I_{z1} \approx -2je^{jk_1(z-h)} \cdot \frac{e^{-jk_0\rho}}{k_1\rho} \quad (32)$$

When $h, z \ll \rho$, $|k_1| \gg |k_0|$ and $|k_1\rho| \gg 1$, (32) approximates the exact integral very well. These conditions are roughly mapped to the following range of parameters: $h, z < 100\text{m}$, $100\text{Hz} < f < 3000\text{Hz}$, $500\text{m} < \rho < 10000\text{m}$ and $0.001\text{S/m} < \sigma < 100\text{S/m}$. The error of (32) compared to the exact integral of I_{z1} in (15) is less than 10% when $100\text{Hz} < f < 3000\text{Hz}$ and $500\text{m} < \rho < 10000\text{m}$. Fig. 3 shows the comparisons of magnitude and phase angle between the approximation in (32) and the exact integral in (15), with dipole frequency of 1000Hz.

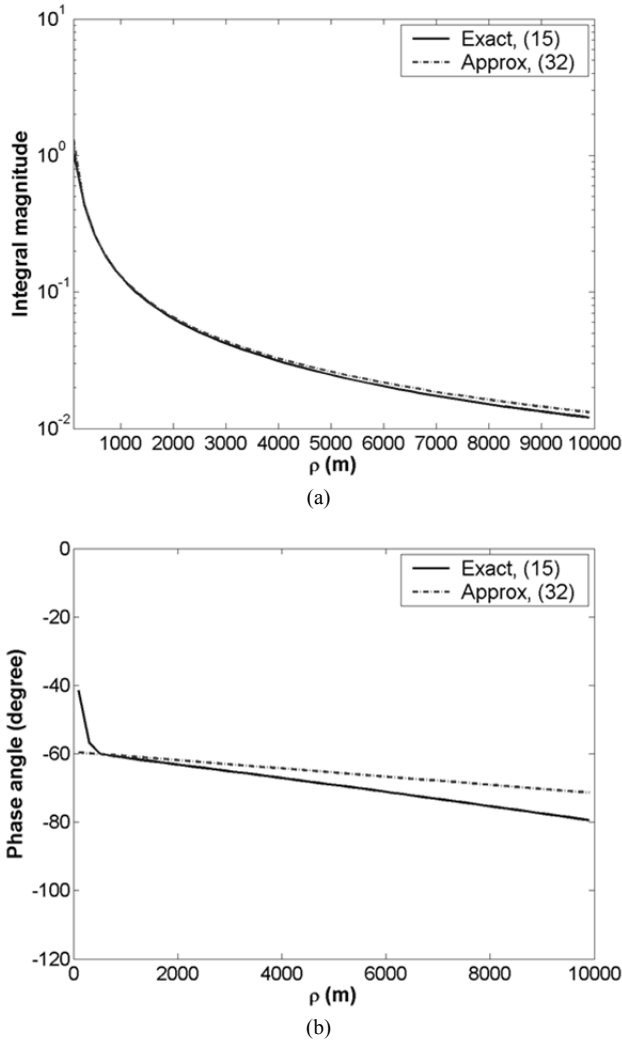


Fig. 3. Exact integral of I_{z1} , (15), vs. approximation, (32), $f = 1000\text{Hz}$: (a) magnitude, (b) phase angle.

This analysis is helpful for understanding the error incurred during the derivation of the approximation for (15). Further, the correction term significantly reduces the error and can be easily calculated. It is shown in (32) and can be used to derive simple results for the E and H fields. Therefore, (32) will be used as the approximation of I_{z1} .

V. SIMPLIFICATION OF THE INTEGRAL FOR A_y^1

If the exponential term is pulled out from $f_2(\lambda)$, I_{y1} of (2) can be rewritten as

$$I_{y1} = \int_0^\infty f_2'(\lambda) e^{u_1(z-h)} \lambda J_0(\lambda \rho) d\lambda \quad (33)$$

where $f_2'(\lambda) = \frac{u_1 - u_0}{u_1 \cdot (u_0 + u_1)}$.

At this point, the strategy for simplifying I_{y1} is the same as that used for I_{z1} . First, the integral contour is expanded and deformed. The deformed contour is the same as that illustrated in Fig. 2 except that there is no pole in this case.

$$I_{y1} = \frac{1}{2} \int_{C_B} f_2'(\lambda) e^{u_1(z-h)} \lambda H_0^{(2)}(\lambda \rho) d\lambda$$

Again, using the argument that the integral along the branch cut of k_0 dominates the total integral, I_{y1} can be approximated as the sum of the integrals along C_1 and C_2

$$I_{y1} \approx \frac{1}{2} \int_{C_1+C_2} f_2'(\lambda) e^{u_1(z-h)} \lambda H_0^{(2)}(\lambda \rho) d\lambda \quad (34)$$

The approximations given in (19) and (21) still work and given these the function reduces to $f_2'(\lambda) \approx \frac{jk_1 \mp \lambda}{jk_1 \cdot (jk_1 \pm \lambda)}$. The

change of signs in it is due to that u_0 takes different signs on the left and right sides of the branch cut of k_0 . The integral in (34) becomes

$$I_{y1} \approx \frac{e^{jk_1(z-h)}}{2jk_1} \left[\int_{C_1} \frac{jk_1 + \lambda}{jk_1 - \lambda} \lambda H_0^{(2)}(\lambda \rho) d\lambda + \int_{C_2} \frac{jk_1 - \lambda}{jk_1 + \lambda} \lambda H_0^{(2)}(\lambda \rho) d\lambda \right]$$

Combining the two integrals on the right hand side results in

$$I_{y1} \approx \frac{e^{jk_1(z-h)}}{2} \int_{C_2} \frac{4\lambda^2}{k_1^2 + \lambda^2} H_0^{(2)}(\lambda \rho) d\lambda.$$

Use the asymptotic approximation of the Hankel function $H_0^{(2)}(\lambda \rho) \approx \sqrt{2j/(\pi\lambda\rho)} \cdot e^{-j\lambda\rho}$, and the variable change $\lambda = k_0 - js$, I_{y1} becomes

$$I_{y1} \approx -2j \sqrt{\frac{2j}{\pi\rho}} e^{jk_1(z-h)} e^{-jk_0\rho} \cdot \int_0^\infty \frac{(k_0 - js)^{3/2}}{k_1^2 + (k_0 - js)^2} e^{-\rho s} ds$$

Since $|s| \gg |k_0|$, all k_0 's in the integrand can be ignored and

$$I_{y1} \approx 2 \sqrt{\frac{2}{\pi\rho}} e^{jk_1(z-h)} e^{-jk_0\rho} \cdot I_3 \quad (35)$$

where $I_3 = \int_0^\infty \frac{s^{3/2}}{s^2 - k_1^2} e^{-\rho s} ds$. From the table of integrals [8], I_3

can be analytically evaluated and further simplified as

$$I_3 \approx -\frac{3\sqrt{\pi}}{4k_1^2} \cdot \frac{1}{\rho^{5/2}}$$

and the integral I_{y1} is

$$I_{y1} \approx -\frac{3\sqrt{2}}{2k_1^2} e^{jk_1(z-h)} \frac{e^{-jk_0\rho}}{\rho^3} \quad (36)$$

Numerical calculations indicate that the approximation, (36), is approximately 6% larger in magnitude than the exact integral, (33). This error is relatively stable over the parameter range $100\text{Hz} < f < 3000\text{Hz}$ and $\rho > 500\text{m}$. Since the error is small for this case, it is not necessary to add a correction term to (36). Rather the factor of $3\sqrt{2}/4 \approx 1.06$ is simply set equal to 1 resulting in:

$$I_{y1} \approx -\frac{2}{k_1^2} e^{jk_1(z-h)} \frac{e^{-jk_0\rho}}{\rho^3} \quad (37)$$

Again, when $h, z \ll \rho$, $|k_1| \gg |k_0|$ and $|k_1\rho| \gg 1$, (37) approximates the exact integral (33) very well. Fig. 4 (a) and (b) give the comparisons of the magnitude and the phase angle between the exact integral of (33) and its approximation (37). For this case, the magnitude error of (37) is even less than 6%

when $\rho > 500\text{m}$.

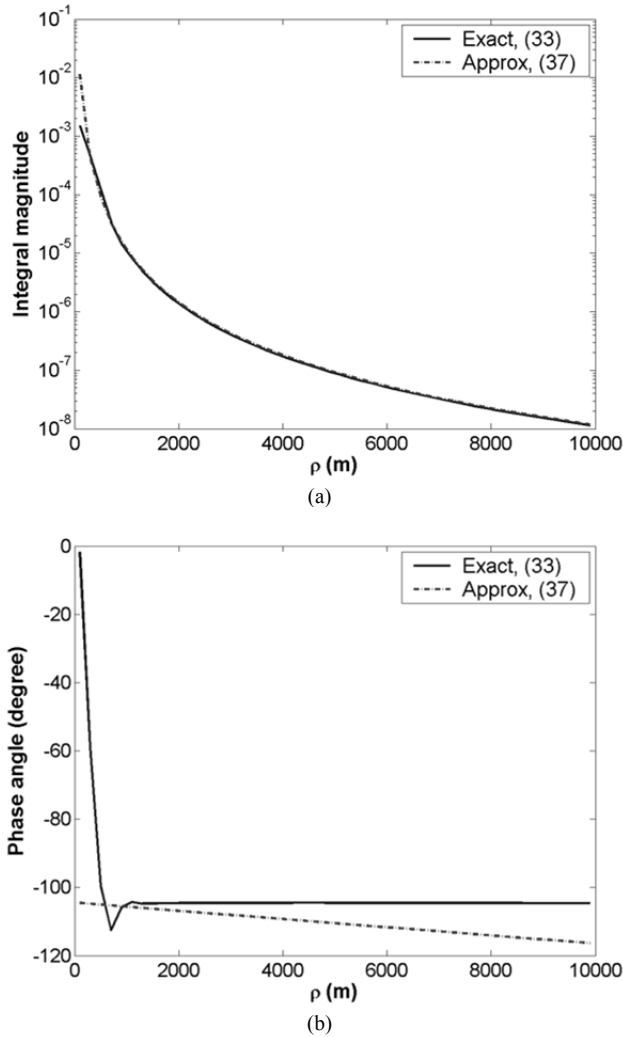


Fig. 4. Exact integral of I_{y1} , (33), vs. approximation, (37), $f=1000\text{Hz}$: (a) magnitude, (b) phase angle.

VI. THE APPROXIMATIONS FOR E & H FIELD

Given the approximations (32) and (37) for the integral portions of the vector potentials A_z^1 and A_y^1 , respectively, the electromagnetic fields can be found. The approximate results for I_{z1} and I_{y1} in (32) and (37), respectively, can be used in (2) and (4) and (6) ~ (11) to find the complete set of E and H fields in water. The components of total E and H fields can be written as the combination of the source terms and the reflected terms.

$$E_x^1 = E_{xs}^1 + E_{xr}^1; \quad E_y^1 = E_{ys}^1 + E_{yr}^1; \quad E_z^1 = E_{zs}^1 + E_{zr}^1;$$

$$H_x^1 = H_{xs}^1 + H_{xr}^1; \quad H_y^1 = H_{ys}^1 + H_{yr}^1; \quad H_z^1 = H_{zs}^1 + H_{zr}^1;$$

where the components with 's' in the subscript refer to the source terms of the fields and those with 'r' in the subscript refer to the reflected fields. The source terms of the fields are

$$E_{xs}^1 = A_1 \cdot \frac{e^{-jk_1 R}}{R^3} (k_1^2 R^2 - 3jk_1 R - 3) \cdot \sin \phi \cos \phi \quad (38a)$$

$$E_{ys}^1 = A_1 \cdot \frac{e^{-jk_1 R}}{R^3} \left[(-k_1^2 R^2 + jk_1 R + 1) + (k_1^2 R^2 - 3jk_1 R - 3) \cdot (\sin \phi)^2 \right] \quad (38b)$$

$$E_{zs}^1 = A_1 \cdot \frac{(z+h)e^{-jk_1 R}}{R^5} (k_1^2 R^2 - 3jk_1 R - 3) \cdot \sin \phi \quad (38c)$$

$$H_{xs}^1 = \frac{Idl}{4\pi} \cdot \frac{(z+h)e^{-jk_1 R}}{R^3} (jk_1 R + 1) \quad (38d)$$

$$H_{ys}^1 = 0 \quad (38e)$$

$$H_{zs}^1 = -\frac{Idl}{4\pi} \cdot \frac{e^{-jk_1 R}}{R^3} (jk_1 R + 1) \cdot \cos \phi \quad (38f)$$

where $A_1 = \frac{jIdl}{4\pi\omega\epsilon_1}$. The simplified reflected fields are

$$E_{xr}^1 \approx 2jA_1 k_0^3 \cdot e^{jk_1(z-h)} \frac{e^{-jk_0 \rho}}{(jk_0 \rho)^3} \left[3 + \frac{15}{(jk_1 \rho)^2} \right] \cdot \sin \phi \cos \phi \quad (39a)$$

$$E_{yr}^1 \approx -2jA_1 k_0^3 \cdot e^{jk_1(z-h)} \frac{e^{-jk_0 \rho}}{(jk_0 \rho)^3} \left[2 + \frac{3-15(\sin \phi)^2}{(jk_1 \rho)^2} \right] \quad (39b)$$

$$E_{zr}^1 \approx -\frac{6jA_1 k_0^4}{k_1} \cdot e^{jk_1(z-h)} \frac{e^{-jk_0 \rho}}{(jk_0 \rho)^4} \cdot \sin \phi \quad (39c)$$

$$H_{xr}^1 \approx \frac{Idl \cdot k_0^3}{2\pi k_1} \cdot e^{jk_1(z-h)} \frac{e^{-jk_0 \rho}}{(jk_0 \rho)^3} [2 - 3(\sin \phi)^2] \quad (39d)$$

$$H_{yr}^1 \approx \frac{Idl \cdot k_0^3}{2\pi k_1} \cdot e^{jk_1(z-h)} \frac{3e^{-jk_0 \rho}}{(jk_0 \rho)^3} \cdot \sin \phi \cos \phi \quad (39e)$$

$$H_{zr}^1 \approx \frac{Idl \cdot k_0^4}{2\pi k_1^2} \cdot e^{jk_1(z-h)} \frac{3e^{-jk_0 \rho}}{(jk_0 \rho)^4} \cdot \cos \phi \quad (39f)$$

The results for E and H fields calculated by (39) are compared to the results from the exact Sommerfeld integral formulas. Fig. 5 shows the comparing result of the reflected field E_{yr}^1 . For the reflected magnetic field, similar result can be obtained.

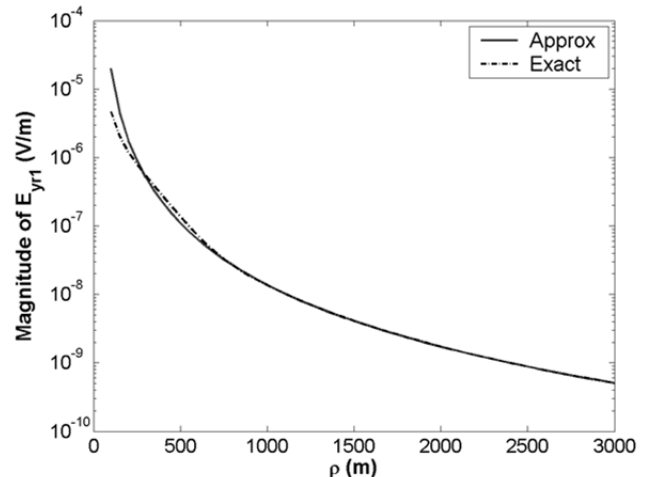


Fig. 5. Exact reflected field E_{yr}^1 vs. its approximation (39b), $\phi = \pi$.

VII. DISCUSSION

At any observation point P, (ρ, ϕ, z) , in the lower conducting medium ($z < 0$), the total field is the combination of the incident field directly from the dipole and the reflected field due to the interface, as shown in (38) and (39), respectively. In the far field of the conducting medium (i.e., $|k_1\rho| \gg 1$, k_1h , k_1z), the incident field is much smaller than the reflected field, which suggests that the propagation mechanism may involve some fields propagating in the low loss free space region and the source term can be ignored.

In fact, the approximations (39a) ~ (39f) can be interpreted to have an up-over-and-down behavior, similar (but not identical) to the mechanism that has been studied in propagation of high frequency radio waves near a boundary [5]. The extremely low frequency (ELF) case is different because the fields in air are quasi-static. Here, some insight into this behavior will be given.

At the observation point P (ρ, ϕ, z) , consider the E_x component, which is perpendicular to the HED's orientation and the easiest component to detect. As discussed, the total field can be approximated by the reflected field component in the far field (i.e., 39a). In the far field of the conducting medium the second term in the bracket is small compared to the constant '3' and can be ignored. Given this, the right hand side of (39a) can be rewritten as

$$E_x^1 \approx -\frac{3j\eta_1 Idl \cdot e^{-jk_1h}}{2\pi k_1} \cdot \frac{e^{-jk_0\rho}}{\rho^3} \sin\phi \cos\phi \cdot e^{jk_1z} \quad (40)$$

where $\eta_1 = (\mu/\epsilon_1)^{1/2}$ is the intrinsic impedance of the conducting medium.

For the up-over-and-down process illustrated in Fig. 6, the field generated by the HED first propagates upward (Part I) and crosses the interface into the free space region. Second, the wave spreads out horizontally (Part II) along the interface. Note that since the upper medium is free space and for the whole range of ρ considered here (i.e., $100 < \rho < 10,000\text{m}$), $|k_0\rho| \ll 1$, the fields in free space are quasi-static. Finally, at the position on the interface right above P, the wave crosses the interface again and propagates vertically down (Part III) to the observation point.

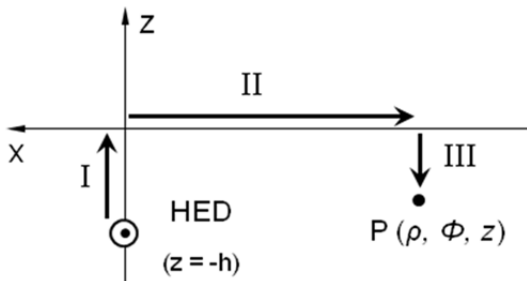


Fig. 6. Illustration of the up-over-and-down path.

To identify (40) as an up-over-and-down process, it is important to show how the different terms have functional dependencies that are characteristic to different portions of the process described above. For example, it will be shown that in the 'up' part of (40) corresponds to propagation in medium #1 and the effect of crossing the interface can be explained by image theory for dielectric-dielectric boundaries. To begin, it is helpful to show how a quasi-static field in the air can be excited by the buried HED. Since it is assumed that $|k_1h| \ll 1$, the

fields near the interface are quasi-static and can be calculated using electrostatic theory with a charge dipole source as shown in Fig. 7a. The dipole moment is qdl (C-m) where q is related to the current, I , of the original HED by

$$I = \frac{dq}{dt} = j\omega q \Rightarrow q = -jI/\omega \quad (41)$$

Image theory for static charges near a dielectric-dielectric interface can be used to find an expression for the electric field in the upper half space (air region). The lower region is replaced by free space and the charges replaced by equivalent charges at the same positions [9], as shown in Fig. 7b.

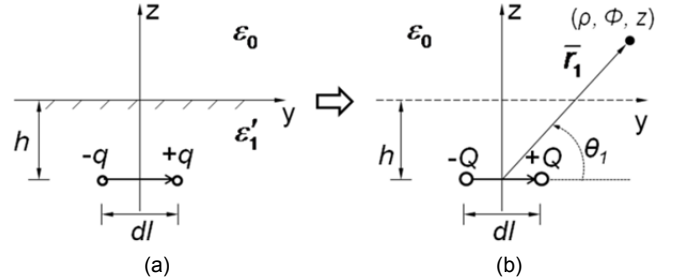


Fig. 7. (a) The static charge dipole replacing the HED and (b) the image of the static dipole.

The equivalent charges are [9]

$$Q = \frac{2\epsilon_0}{\epsilon_0 + \epsilon_1} \cdot q \quad (42)$$

and since $\epsilon_0 \ll \epsilon_1$ (42) can be approximated by

$$Q = 2\epsilon_0 q / \epsilon_1 \quad (43)$$

The image charges form a new equivalent dipole with a moment Qdl , oriented in +y direction that can be used to find the fields in the upper free space region. Using (41) and (43) and known expressions for the fields of static dipoles, the electric field above the interface ($z = 0$) can be found as

$$E_x = \frac{3\omega q dl \eta_1 e^{-jk_1h}}{2\pi k_1} \cdot \frac{\rho^2}{r_1^5} \sin\phi \cos\phi \quad (44a)$$

$$E_y = \frac{\omega q dl \eta_1 e^{-jk_1h}}{2\pi k_1} \cdot \frac{(2\rho^2 \sin^2\phi - \rho^2 \cos^2\phi - h^2)}{r_1^5} \quad (44b)$$

$$E_z = \frac{3\omega q dl \eta_1 e^{-jk_1h}}{2\pi k_1} \cdot \frac{h\rho \sin\phi}{r_1^5} \quad (44c)$$

where $r_1 = (\rho^2 + h^2)^{1/2}$ and θ_1 is defined as shown in Fig. 7. Here, the factor $\exp(-jk_1h)$ has been included to account for the small attenuation between the HED and the surface and to correspond to (40). Equation (44) could be used to calculate the electric field in the upper region, but here, an alternative approach will be taken that leads more directly to an up-over-and-down interpretation for the field expression.

The field in (44) is used to find an equivalent surface charge directly above the source dipole and this will in turn be used to identify an equivalent source on the air-water interface. The surface charge density can be determined from the discontinuity of the normal electric flux density between the two sides of the interface [7], as shown in Fig. 8. The total surface charge on the interface can be found by integrating the normal component of electric flux density, i.e., $\epsilon_0 E_z$, over the whole interface (x-y plane)

$$q_s = \int_0^{2\pi} \int_0^\infty \epsilon_0 E_z \rho d\rho d\phi \quad (45)$$

where E_z is given by (44c) and the much smaller electric field in the water is ignored.

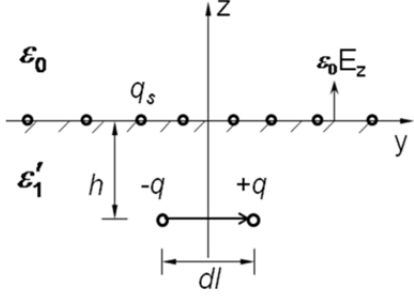


Fig. 8. Equivalent surface charges q_s on the interface ($z = 0$ plane).

Inserting (44c) into (45) results in

$$q_s = \frac{3\omega q dl \epsilon_0 \eta_1 h e^{-jk_1 h}}{2\pi k_1} \int_0^{2\pi} \sin \phi d\phi \int_0^\infty \frac{\rho^2 d\rho}{(\rho^2 + h^2)^{5/2}} \quad (46)$$

Of course, (46) equals zero because the net surface charge over the whole interface is zero. But the equivalent dipole moment of this charge distribution is non-zero and is determined by

$$P_s = \iint_{z=0 \text{ plane}} l_s dq_s \quad (47)$$

where P_s , Fig. 9 (a), is the moment of the equivalent dipole, l_s , as shown in Fig. 9 (b), is the distance between two equal and opposite infinitesimal surface charges at symmetrical positions about the x -axis. By using $l_s = 2\rho \sin \phi$ and (44c), (47) can be rewritten as

$$P_s = \frac{3\omega q dl \epsilon_0 \eta_1 h e^{-jk_1 h}}{2\pi k_1} \int_0^{2\pi} \int_0^\infty \frac{2\rho^3 \sin^2(\phi) d\rho d\phi}{(\rho^2 + h^2)^{5/2}} \quad (48)$$

This can be analytically evaluated [8] and (48) becomes

$$P_s = 2\omega q dl \epsilon_0 \eta_1 / k_1 \quad (49)$$

Inserting (41) into (49) results in

$$P_s = -Idl \cdot (2j\epsilon_0 \eta_1 / k_1) = qdl \cdot (2\epsilon_0 / \epsilon'_1) \quad (50)$$

From (50) it is clear that the moment of the equivalent dipole at the surface is just the moment of the original HED multiplied by a constant coefficient equal to twice the ratio of the free space to water complex dielectric constants. The factor of 2 is due to imaging of the equivalent dipole in the “nearly perfectly conducting” water. Therefore, the ‘up’ (Part I in Fig. 6) part of the propagation process can be understood by noting that the fields from the original HED create an equivalent dipole just above the interface.

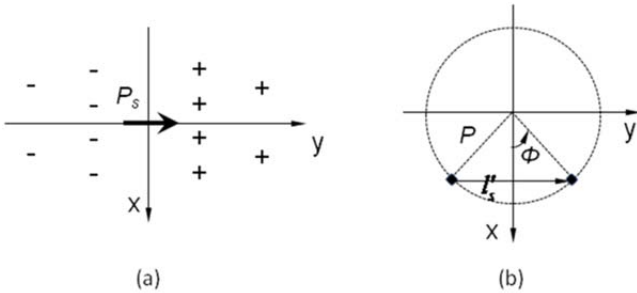


Fig. 9. (a) Nonuniform distribution of the equivalent surface charge on the interface ($z = 0$ plane); (b) geometry to find the moment of the dipole effect due to the surface charge.

The fields in the air region can be calculated by assuming that the equivalent dipole is in free space so that (on the $z = 0$ plane)

$$E_{x,u}^0(\rho, \phi, 0) = -\frac{3j\eta_1 Idl \cdot e^{-jk_1 h} e^{-jk_0 \rho}}{2\pi k_1 \rho^3} \sin \phi \cos \phi. \quad (51)$$

This is the ‘over’ (Part II in Fig. 6) part of the propagation process. Finally, the field in the air passes across the boundary with no attenuation due to the continuity of tangential electric fields. Then, since the field is approximately constant on the interface across a length much larger than the depth of P, the downward propagation must be approximately $e^{jk_1 z}$ (i.e., the ‘down’ or Part III in Fig. 6 part of the propagation. Finally, the expression of electric field component E_x at the observation point P is

$$E_{x,u}^1(\rho, \phi, z) = -\frac{3j\eta_0 Idl e^{-jk_1 h} e^{-jk_0 \rho}}{4\pi k_0} \frac{e^{jk_1 z}}{\rho^3} \sin \phi \cos \phi \cdot e^{jk_1 z} \quad (52)$$

which shows the complete up-over-and-down propagation. Equation (52) is identical to (40).

VIII. CONCLUSIONS

A method to simplify the Sommerfeld integrals for a low frequency HED source buried near an interface between free space and a conducting half space is introduced. Using this method, a simple approximation for its electric fields in the conducting half space is obtained that is valid for distances that are electrically small in free space and electrically large in the conducting medium. The resulting approximation has been shown to be accurate within 10% over a wide range of parameters for which $h, z \ll \rho$, $|k_1| \gg |k_0|$ and $|k_1 \rho| \gg 1$. Finally, the approximation can be interpreted as having up-over-and-down behavior for the propagation path from the conducting medium to free space and vice versa.

ACKNOWLEDGMENT

The author would like to acknowledge Professor Jeff Young at the University of Idaho for his continuous encouragement and numerous ideas.

REFERENCES

- [1] A. Baños, *Dipole radiation in the presence of a conducting half-space*. New York: Pergamon, 1966.
- [2] P. R. Bannister, “Extension of finitely conducting earth-image-theory results to any range”, Naval Underwater Systems Center, New London, CT, Tech. Rep., Jan. 1984.
- [3] J. R. Wait and L. L. Campbell, “The fields of an oscillating magnetic dipole immersed in a semi-infinite conducting medium”, *J. Geophys. Res.*, vol. 58, no. 2, pp. 167-178, 1953.
- [4] A. K. Sinha and P. K. Bhattacharya, “Vertical magnetic dipole buried inside a homogeneous earth”, *Radio Sci.*, vol. 1, no. 3, pp. 379-395, 1966.
- [5] T. Tamir, “Radio wave propagation along mixed paths in forest environments”, *IEEE Trans. Antennas Propagat.*, vol. 25, no. 4, pp. 471-477, Jul. 1977.
- [6] J. R. Wait, “The electromagnetic fields of a horizontal dipole in the presence of a conducting half-space”, *Can. J. Phys.*, vol. 39, no. 7, pp. 1017-1028, 1961.
- [7] C. A. Balanis, *Advanced Engineering Electromagnetics*. NJ: John Wiley & Sons, Inc., 1989.
- [8] I. S. Gradshteyn and I. M. Ryzhik, *Table of integrals series and products*. New York: Academic Press, 1965.
- [9] E. D. Torre and C. V. Longo, *The Electromagnetic Field*. Boston: Allyn and Bacon, Inc., 1969.

Robert G. Olsen (S'66, F'92) is Associate Dean of the College of Engineering and Architecture and the Boeing Distinguished Professor of Electrical Engineering at Washington State University, Pullman, WA, USA. He received the BS degree in electrical engineering from Rutgers University in 1968 and the MS and Ph.D. degrees in electrical engineering from the University of Colorado, Boulder in 1970 and 1974 respectively.

He has been a member of the electrical engineering faculty at Washington State University, Pullman, WA since 1973. During that time he has been a visiting scientist at GTE in Waltham, MA, at ABB Corporate Research in Västerås, Sweden and at EPRI in Palo Alto, CA and a Visiting Professor at the Technical University of Denmark. His research interests include electromagnetic interference from power lines, the electromagnetic environment of power lines, electromagnetic wave propagation, electromagnetic compatibility and electromagnetic scattering. His work in these areas has resulted in approximately 75 publications in refereed journals. His most recent work has been supported by the Electric Power Research Institute, the National Science Foundation and the U.S. Navy.

Prof. Olsen is a Fellow of the IEEE and an Honorary Life Member of the IEEE EMC society. He has served as Technical Editor of the *IEEE Electromagnetic Compatibility Society Newsletter*, as Technical Paper Committee Chair for the 2006 Portland EMC Symposium and Co - Technical Program Chair of the 2007 EMC Zurich in Munich, Germany Symposium. He is the past United States National Committee representative to CIGRE Study Committee 36 (Electromagnetic Compatibility) and past chair of the IEEE Power Engineering Society AC Fields and Corona Effects Working Groups. He is also past Associate Editor of the *IEEE Transactions on Electromagnetic Compatibility* and *Radio Science*.

Zhi Li (S'01) received the B.S. and M.S. degrees in electrical engineering from the Tsinghua University, Beijing, China, in 2000 and 2003, respectively. He is currently working toward the Ph.D. degree in electrical engineering at the Washington State University, Pullman, Washington.

His research interests include electromagnetic compatibility, transmission line analysis, electromagnetic (EM) field measurement, design of EM field sensor for power transmission line, and high voltage and insulation technology.

Roving Sources, Simulation and Reciprocity

Jeffrey L. Young, *Fellow, IEEE*, and Christopher L. Wagner

Abstract—Detailed herein is a post-processing method for modeling the fields of a roving source in an inhomogeneous environment. The method invokes the reciprocity theorem and employs the concept of calibration length and area for the antennas of the problem space. Because the reciprocity theorem is a statement about projections, we show why six simulations are needed to obtain the six components of the electromagnetic field. Detailed FDTD simulations are conducted and validated by measured data, as obtained from several experiments conducted at Lake Pend Orielle, Idaho, USA. Other numerical methods (i.e., finite element, Sommerfeld full-wave, quasi-electrostatic) are also considered to provide additional validation. The problem is germane to naval applications, which justifies the use of extremely low frequencies in the experiment and simulations.

Index Terms—Numerical simulation, moving sources, calibration length, calibration area, reciprocity, extremely low frequencies, ELF.

I. INTRODUCTION

A unique challenge arises when numerical simulation tools are invoked to model a roving antenna relative to an established inertial reference frame to determine the electromagnetic fields at a fixed location. It is common to view the surrounding medium as being stationary, which allows one to construct a numerical grid to model the geometry and materials of the medium. However, the simulation must also model the roving antenna, which suggests that the grid needs to be reconstructed for each new antenna position and orientation. And for each position and orientation a new simulation needs to be conducted. When thousands of source locations are needed, thousands of grid constructions and simulations are overwhelmingly prohibitive even on the fastest of computers. The problem is not alleviated using time-domain solvers like FDTD. A typical FDTD simulation corresponds to a real-time duration of a fraction of a second whereas the time of travel of a moving antenna is minutes to hours. Again it is grossly impractical to simulate this entire duration of time.

In this paper we discuss what is called the fixed observer, moving source (FOMS) scenario in the context of a simulation of a real-world experiment. The simulation is used to predict the experimental outcome (or, the experimental outcome is used to validate the simulation). By moving source we mean an antenna that moves from one location to another; at each source location the observer records the value of the electromagnetic field at one fixed location. Other than being linear and reciprocal, the medium is assumed to be quite general (i.e. inhomogeneous, anisotropic, dispersive). From an experimental point of view the FOMS scenario implicitly assumes three things: 1) that some kind of receiving antenna is

available to measure the fields that coincide with the location of the observer; 2) that the entire receiving assembly has a calibration factor that converts the received voltage or current signal to the actual field as if the receiving antenna were not present; 3) that the receiving antenna is small enough so it can be located arbitrarily near the source antenna without significantly influencing the induced currents and charges of the source antenna. All of these assumptions are practical in the context of modern instrumentation and measurement techniques.

What is not practical, as noted above, is a direct simulation of the FOMS scenario. However, consider the following case in which the receiving antenna at the location of the fixed observer is converted into a transmitting antenna and its fields are recorded at the location of the moving source of the FOMS scenario. We will call this the fixed source, moving observer (FSMO) scenario. The fields of such a scenario are straightforward to simulate. Then by means of the reciprocity theorem it is possible to predict the FOMS outcome from FSMO simulation data. We demonstrate this technique using the FDTD method, but the technique is not dependent on any one numerical method. As for applications, this technique is applied to the naval situation in which a moving boat outfitted with a simple antenna (i.e. electric dipole or electric loop) skims the surface of a lake while emitting a single frequency signal; the fields produced by this antenna are monitored by a submerged, fixed receiving array. The efficacy of this technique is confirmed by comparing experimental data with simulation data.

The principle feature of reciprocity can be demonstrated using impressed current sources even though the currents on the antennas are induced. For impressed electric current sources in an infinitely extended domain it is well known that

$$\int_V \mathbf{J}^a \cdot \mathbf{E}^e dV = \int_V \mathbf{J}^e \cdot \mathbf{E}^a dV, \quad (1)$$

where the superscript “e” corresponds to the experimental FOMS scenario and the superscript “a” to a simulation of the FSMO scenario. More specifically, the previous equation reveals that an x -directed simulation current at the location of the observer in the experiment isolates the x -component of the electric field of the experiment at that location. If we regard the current densities as point sources then the previous equation is conceptually equivalent to

$$E_x^e(\mathbf{r}_2) = \frac{\mathbf{J}^e(\mathbf{r}_1) \cdot \mathbf{E}^a(\mathbf{r}_1)}{J_x^a(\mathbf{r}_2)}, \quad (2)$$

where \mathbf{r}_2 and \mathbf{r}_1 point to P_1 and P_2 , which are the observer and source locations, respectively, of the FOMS scenario. Since \mathbf{J}^e is assumed to be known and since both \mathbf{E}^a and J_x^a are known from the simulation, the experimental field E_x^e

The authors are with the Department of Electrical and Computer Engineering, University of Idaho, Moscow, ID, 83844-1023 USA, e-mail: jyoung@uidaho.edu

Manuscript Submitted July 17, 2012; revised XXX XXX, 20XX.

at P_2 is hence predicted from simulation data. Moreover, the simulation regards the source as being fixed in location at P_2 and the data that it produces for that one simulation includes all points associated with P_1 of the FOMS scenario. Thus, the above equation is invoked at each location of the moving source.

Because the reciprocity theorem is a projection theorem with a scalar result, no information about the y and z electric field components can be obtained from the aforementioned simulation. To obtain that information two additional simulations are required: one that uses a y -directed electric current and one that uses a z -directed electric current. We will call these the “b” and “c” problems, respectively. Following the same line of thinking as above, we obtain

$$\begin{aligned} E_y^e(\mathbf{r}_2) &= \frac{\mathbf{J}^e(\mathbf{r}_1) \cdot \mathbf{E}^b(\mathbf{r}_1)}{J_y^b(\mathbf{r}_2)}, \\ E_z^e(\mathbf{r}_2) &= \frac{\mathbf{J}^e(\mathbf{r}_1) \cdot \mathbf{E}^c(\mathbf{r}_1)}{J_z^c(\mathbf{r}_2)}. \end{aligned} \quad (3)$$

We are also interested in obtaining magnetic field data from electric sources. This can be accomplished using a lesser known form of reciprocity in which the simulation employs magnetic sources, i.e.,

$$\int_V \mathbf{M}^p \cdot \mathbf{H}^e dV = - \int_V \mathbf{J}^e \cdot \mathbf{E}^p dV. \quad (4)$$

From three additional simulations involving magnetic currents in the x , y and z directions at the location of the observer in the FOMS scenario (labeled as “p,” “q,” and “r” problems) and point source idealizations, we obtain

$$\begin{aligned} H_x^e(\mathbf{r}_2) &= - \frac{\mathbf{J}^e(\mathbf{r}_1) \cdot \mathbf{E}^p(\mathbf{r}_1)}{M_x^p(\mathbf{r}_2)}, \\ H_y^e(\mathbf{r}_2) &= - \frac{\mathbf{J}^e(\mathbf{r}_1) \cdot \mathbf{E}^q(\mathbf{r}_1)}{M_y^q(\mathbf{r}_2)}, \\ H_z^e(\mathbf{r}_2) &= - \frac{\mathbf{J}^e(\mathbf{r}_1) \cdot \mathbf{E}^r(\mathbf{r}_1)}{M_z^r(\mathbf{r}_2)}. \end{aligned} \quad (5)$$

That is, a simulated electric field associated with a fixed magnetic source can be used to determine the experiment’s magnetic field of a moving electric source. It follows from the previous two paragraphs that a total of six separate simulations is needed to relate the FSMO scenario to the FOMS scenario.

Although the previous equations conceptually demonstrate the technique of correlating the FOMS scenario to FSMO scenario, they are deficient in application. First, the equations assume that the impressed currents are applied at the terminals of the antenna structure. But doing so with electrically small antennas in large domains creates a modeling challenge in numerical code. That is, we do not want to model the physical antenna structure; rather our focus is on the modeling of the medium between the antennas. Second, the simulations never incorporate a receiving antenna; only field data at the location of the receiving antenna are recorded. It thus follows that these deficiencies must be properly accounted for by appealing to circuit models and the notion of effective length and area, as described next.

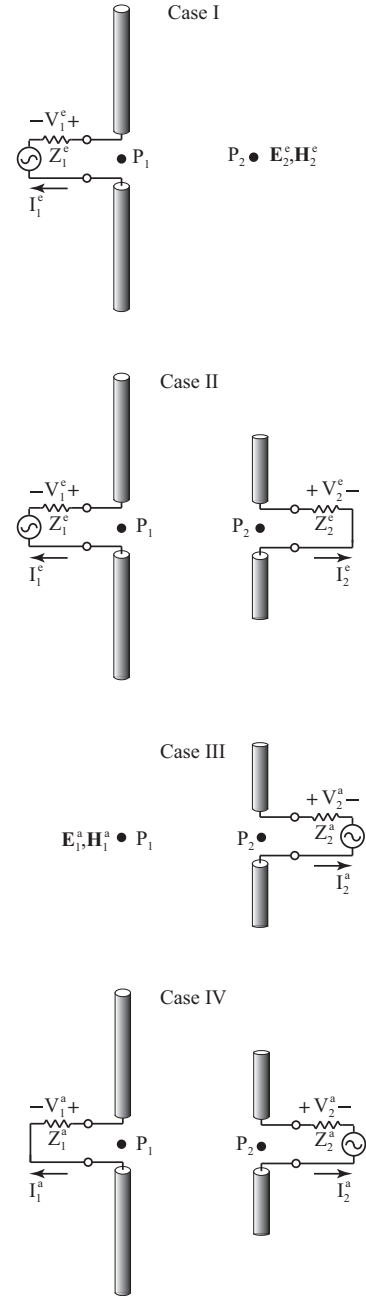


Fig. 1. Four cases used in the application of reciprocity and equivalent calibration length.

II. FORMULATION

The formulation developed herein is based on the comparison of several cases as shown in Figure 1. Case I depicts the original problem in which antenna one is the moving source and the fields are recorded at P_2 ; at one instant in time antenna one is located at P_1 . Case II depicts the actual experiment in which antenna two is used as a receiving antenna to measure the electric field of antenna one. For example, antenna two is a short electric dipole. As for Case III, it represents the reciprocal problem. Here antenna two of the experiment is used as a transmitting antenna and the fields are recorded at P_1 . Finally, Case IV depicts the situation in which antenna two is the source antenna and antenna one is the receiving

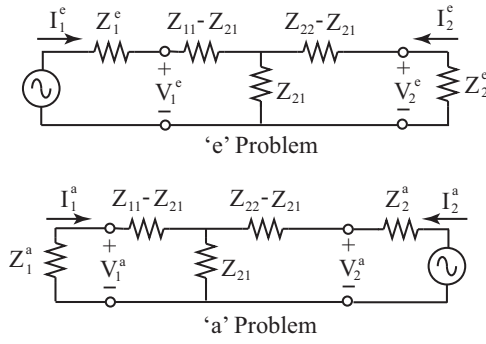


Fig. 2. Equivalent circuits of the two-antenna problem, i.e. Cases II and IV.

antenna. The only differences between each of these scenarios are a) which antennas are acting as sources and receivers, and b) whether an antenna is present or not. Other than those differences, everything else is the same. Antenna one is the same antenna in Cases I, II and IV; antenna two is the same antenna in Cases II, III and IV. Antenna one is always at P_1 ; antenna two is always at P_2 . The point P_1 represents many possible locations, whereas P_2 represents only one location.

Let us first make a comparison between Cases II and IV via reciprocity. From a network point of view electromagnetic field reciprocity reduces to a very simple statement: A network is reciprocal if and only if its impedance matrix is symmetrical. For a two-port network consisting of two antennas, reciprocity says that for a reciprocal network (i.e. medium) $Z_{21} = Z_{12}$, where Z_{21} and Z_{12} are the mutual impedances between ports one and two of the antennas. This simple fact allows us to precisely model the two-antenna configuration of Cases II and IV using the simple T-model circuits of Figure 2. The two circuits of this figure are only different due to the interchange of source and load. The port voltages and currents of these circuits are the port voltages and currents of the antennas. It follows from these circuits that

$$\begin{aligned} \frac{V_2^e}{I_1^e} &= \frac{Z_{21}Z_2^e}{Z_{22} + Z_2^e} \\ \frac{V_1^a}{I_2^a} &= \frac{Z_{21}Z_1^a}{Z_{11} + Z_1^a}, \end{aligned} \quad (6)$$

where Z_1^a is the load impedance at port 1 for the “a” problem and Z_2^e is the load impedance at port 2 for the “e” problem; Z_{ii} is the self impedance of antenna i for $i = 1, 2$. Forming the ratio of these equations, we obtain

$$\frac{V_2^e}{I_1^e} = \Lambda^a \frac{V_1^a}{I_2^a} \quad (7)$$

where

$$\Lambda^a = \left(\frac{Z_{11} + Z_1^a}{Z_{22} + Z_2^e} \right) \left(\frac{Z_2^e}{Z_1^a} \right). \quad (8)$$

That is, knowledge of the “a” problem (i.e., Case IV) gives direct knowledge of the “e” problem (i.e., Case II) provided the self and load impedances of the network are known.

To compare Case I with II and Case III with IV, we invoke the concept of calibration length of the receiving antenna. Specifically, let $V_2^e \equiv -\mathbf{E}_2^e \cdot \mathbf{l}_2$, where V_2^e is the port voltage of antenna two for Case II and \mathbf{E}_2^e is the field at P_2 for Case

I. Likewise, let $V_1^a \equiv -\mathbf{E}_1^a \cdot \mathbf{l}_1$, where V_1^a is the port voltage of antenna one for Case IV and \mathbf{E}_1^a is the field at P_1 for Case III. By definition \mathbf{l}_i is the calibration length factor that characterizes the receiving efficacy of the antenna by relating the incident field of the antenna to the port voltage for a given load impedance. It is the classical effective length vector [1] when the load impedance is an open circuit. The calibration length vector is assumed to be known via some precise calibration procedure or analysis. Using this concept along with Eqn. (7), we obtain the needed relationship between Case I (the original problem) and Case III (the doable simulation problem):

$$\mathbf{E}_2^e \cdot \mathbf{l}_2 = \Lambda^a \frac{\mathbf{E}_1^a \cdot \mathbf{l}_1 I_1^e}{I_2^e}. \quad (9)$$

We now specifically define the “a” problem by assuming that antenna two is polarized in x , which suggests that \mathbf{l}_2 is entirely directed in x . Letting $\mathbf{l}_2 = l_{2x}\mathbf{a}_x$, we see from the previous equation that

$$E_{2x}^e = \Lambda^a \frac{\mathbf{E}_1^a \cdot \mathbf{l}_1 I_1^e}{l_{2x} I_2^e}. \quad (10)$$

Likewise, we may construct “b” and “c” problems that correspond to Case III simulations in which \mathbf{l}_2 is directed entirely in y and z , respectively. Then from Eqn. (9),

$$E_{2y}^e = \Lambda^b \frac{\mathbf{E}_1^b \cdot \mathbf{l}_1 I_1^e}{l_{2y} I_2^e} \quad (11)$$

and

$$E_{2z}^e = \Lambda^c \frac{\mathbf{E}_1^c \cdot \mathbf{l}_1 I_1^e}{l_{2z} I_2^e}, \quad (12)$$

where Λ^b and Λ^c are similar in form to Λ^a . Thus, the experimentally determined electric field vector associated with Case I, i.e. the “e” problem, can be predicted from three simulations associated with Case III, i.e., the “a”, “b”, and “c” problems, provided the load impedances, open-circuited self impedances, antenna currents, and antenna calibration length vectors are known. Equation (10) is equivalent to Eqn. (2), but we see that the Λ^a multiplier is what was missing in the conceptual development of Eqn. (2). Although the load impedances are constants the self-impedances Z_{11} and Z_{22} are not. Strictly speaking when P_1 moves from one location to another both Z_{11} and Z_{22} change. In most cases such changes are negligible. Even when they are not, Z_{ii} is considered to be known from measurement data. That is, Λ^a , Λ^b and Λ^c are known factors for each P_1 and P_2 location.

The determination of \mathbf{H}^e is accomplished in a similar manner, except antenna two of Cases II, III and IV is replaced with an antenna that is optimized for magnetic field sensing (e.g., an electric current loop). The circuit models of Figure 1 are still applicable, but the impedance parameters have different values due to the new choice for antenna two. We will denote the impedance parameters of the present discussion as Z'_{ij} . We will also assume a different load impedance on antenna two and call it Z_2^m . For magnetic field sensing we may thus relate Case II to IV using

$$\frac{V_2^e}{I_1^e} = \Lambda^p \frac{V_1^p}{I_2^p} \quad (13)$$

where

$$\Lambda^p = \left(\frac{Z'_{11} + Z_1^p}{Z'_{22} + Z_2^m} \right) \left(\frac{Z_2^m}{Z_1^p} \right). \quad (14)$$

Case I is compared to Case II and III to IV using the notion of calibration area and length. Specifically, for Z_2^m loading we may let $V_2^e \equiv j\omega\mu A_2 \mathbf{H}_2^e \cdot \mathbf{n}_2$, where A_2 is the calibration loop area of antenna two and \mathbf{n}_2 is the calibration loop normal vector; \mathbf{H}_2^e is the magnetic field at P_2 of Case I. We will assume that $A_2 \mathbf{n}_2$ is known from some calibration procedure. As before let $V_1^p \equiv -\mathbf{E}_1^p \cdot \mathbf{l}_1$ for Z_1^p loading. From Eqn. (13),

$$\mathbf{H}_2^e \cdot \mathbf{n}_2 = - \left(\frac{\Lambda^p}{j\omega\mu A_2} \right) \left(\frac{\mathbf{E}_1^p \cdot \mathbf{l}_1 I_1^e}{I_2^p} \right). \quad (15)$$

We now define the “p” problem by assuming that antenna two’s calibration normal is directed in x and let $\mathbf{n}_2 = \mathbf{a}_x$ and $A_2 = A_{2x}$, in which case

$$H_{2x}^e = - \left(\frac{\Lambda^p}{j\omega\mu A_{2x}} \right) \left(\frac{\mathbf{E}_1^p \cdot \mathbf{l}_1 I_1^e}{I_2^p} \right). \quad (16)$$

Similarly, the “q” and “r” problems are defined for y and z magnetic field sensing, respectively. Then equally so

$$H_{2y}^e = - \left(\frac{\Lambda^q}{j\omega\mu A_{2y}} \right) \left(\frac{\mathbf{E}_1^q \cdot \mathbf{l}_1 I_1^e}{I_2^q} \right) \quad (17)$$

and

$$H_{2z}^e = - \left(\frac{\Lambda^r}{j\omega\mu A_{2z}} \right) \left(\frac{\mathbf{E}_1^r \cdot \mathbf{l}_1 I_1^e}{I_2^r} \right). \quad (18)$$

A potential deficiency of the previous methodology is associated with the effective calibration length and area vectors. These vectors are defined when the medium is unbounded and when the antennas are in the far-field of each other. This latter point is regarded as moot since antenna two is “small”; it can be placed “close” to antenna one. The former point is more critical, since the inhomogeneities of the medium can violate the plane wave assumption inherent to the effective length definition and can change the effective length value for different locations of P_1 . Even so this error is assumed to be minimal for “small” sensing antennas and is also an error mechanism in the experiment.

A second deficiency is more practical. Usually antenna two is either a small triaxial dipole for the measurement of the electric field or a small triaxial electric loop for the measurement of the magnetic field. As the cases of Figure 1 depict the geometrical features of this antenna must be captured in a simulation. Yet its smallness and the fact that P_1 could be arbitrarily close or far from P_2 in a potentially large domain (e.g. dipoles that are meters in size; domains that span kilometers) make the modeling of the dipole or loop challenging in a simulation. Fortunately, the circuit reciprocity relationships require only field information of antenna two, not induced current density information. This means that antenna two can be replaced with an impressed source as long as that source has the same fields as the actual antenna. Instead of simulating an actual electric dipole as antenna two for electric field measurements, one can simulate an impressed dipole of the same electric moment. Likewise, if antenna two is small, is used for magnetic field measurements, and has an calibration loop area of A_2 , then an impressed magnetic

source of moment $K_2 l_2'$ will produce the same field as the loop if $K_2 l_2' = j\omega\mu I_2 A_2$, where I_2 is the current in the loop [2]. Hence, Eqns. (16) – (18) can be replaced with

$$\begin{aligned} H_{2x}^e &= -\Lambda^p \frac{\mathbf{E}_1^p \cdot \mathbf{l}_1 I_1^e}{l_{2x}' K_2^p}, \\ H_{2y}^e &= -\Lambda^q \frac{\mathbf{E}_1^q \cdot \mathbf{l}_1 I_1^e}{l_{2y}' K_2^q}, \\ H_{2z}^e &= -\Lambda^r \frac{\mathbf{E}_1^r \cdot \mathbf{l}_1 I_1^e}{l_{2z}' K_2^r}. \end{aligned} \quad (19)$$

Such a replacement greatly increases the robustness of the simulations. Moreover, the inherent duality between electric field sensing and magnetic field sensing is revealed by comparing the previous equations with Eqns. (10) - (12). A comparison of these same equations with those of (5) shows the correlations between impressed and induced currents.

Finally, there are two other situations worth noting: 1) magnetic source excitation and magnetic field sensing and 2) magnetic source excitation and electric field sensing. The corresponding reciprocity field relationships for impressed currents are

$$\int_V \mathbf{M}^a \cdot \mathbf{H}^e dV = \int_V \mathbf{M}^e \cdot \mathbf{H}^a dV \quad (20)$$

and

$$\int_V \mathbf{J}^p \cdot \mathbf{E}^e dV = - \int_V \mathbf{M}^e \cdot \mathbf{H}^p dV. \quad (21)$$

The development of the circuit relationships follows the exact same logic as presented previously and hence, it is suppressed.

III. RESULTS

The validation of the previously described technique was accomplished by comparing experimental data with processed simulation data. Because the experiment is associated with a naval application, extremely low frequencies (ELF, 10 to 1,000 Hz) were used in conjunction with a large physical domain associated with Lake Pend Oreille, Idaho, USA. The region of the lake used for the experiments reported herein spanned about 8 km on a side and has a depth of greater than 350 meters, with a relatively flat lake floor. The experiments involved exciting electromagnetic fields with some roving source and measuring the resulting electromagnetic field at a fixed location in the lake. The detector array (i.e. antenna two of Case II, Figure 1) was outfitted with triaxial electric and magnetic field sensors; it was about 11×1×2 m long. The approximate position and orientation of the detector array was recorded. The buoyant detector array was anchored to the lake floor using long cables and a complex rigging structure; the cables and the rigging structure were not modeled in simulation. The sources (e.g. antenna one of Case II) were placed on a small non-metallic boat roving in the vicinity of the detector array within a range of meters to kilometers. The source boat was outfitted with two GPS antennas and receivers to allow for precise recording of source position and orientation as a function of time. Neither the boat nor antennas were modeled in simulation. The results presented herein are associated with two fundamental sources: vertical magnetic

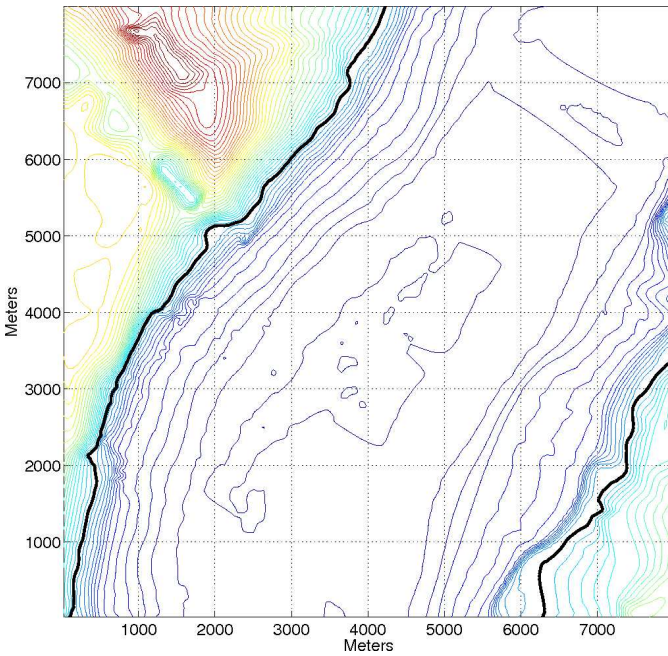


Fig. 3. Contour plot of the simulation space geometry. The contour interval is 25 meters.

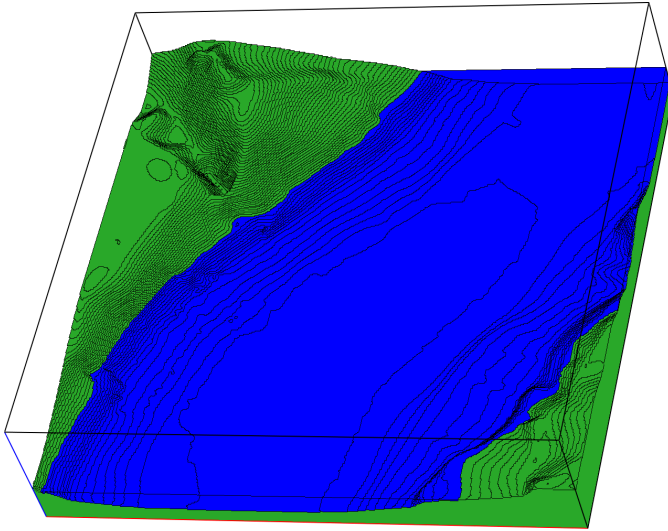


Fig. 4. The full FDTD domain of the Lake spans 8×8 km. Reduced size domains are used for some problems. Contour lines are the top edges of the FDTD cells. For display purposes the cells here are $20 \times 20 \times 20$ meters. In typical calculations $10 \times 10 \times 5$ meters or $5 \times 5 \times 5$ meter cells are used. The sensor array is located near the center of the domain.

dipole (VMD) and horizontal electric dipole (HED). The VMD is a multi-turn 1.3 meter diameter coil excited with a sine wave current; its moment is $184 \text{ A} \cdot \text{m}^2$. The HED consists of submerged copper plates mounted on the boat hull; it was excited by a sine-wave current; the plate separation was 4 m and its moment was $4.8 \text{ A} \cdot \text{m}$. The draft of the boat placed the plates about 0.6 meters below the surface.

With the position and orientation of the source and sensors known, the simulation space can be defined. We set the FDTD domain space to $400 \times 400 \times 100$ cells with each cell being $5 \times 5 \times 5$ meters in size. The simulation space topology is shown

in Figure 3. From this topology averaging techniques are used to construct a height-field that captures the key features of terrain. An example of an FDTD model domain is shown in Figure 4. Material parameters are then assigned to each cell. For water, we used $\epsilon_r = 81$ and $\sigma = 0.01 \text{ S/m}$; for the lake floor we used $\epsilon_r = 1$ and $\sigma = 0.0012 \text{ S/m}$. For ELF frequency signals, however, the conduction currents in the water dominate the displacement currents thus making the permittivity values moot. It follows from these values that at an operating frequency of 100 Hz the water has a skin depth of 503 m and a wavelength of 3.16 km; for air, the wavelength is 3,000 km. The domain thus spans a fraction of a wavelength in air, but about 2.5 wavelengths (or 15.9 skin depths) in water. To maintain stability, we set the time step to the Courant limit and used 200,000 time steps in a typical simulation. Such long simulations are necessary to allow the electromagnetic energy associated with natural diffusion mechanisms to leave the computational domain. A PML optimized for ELF waves is used to truncate the domain [3]. An FFT is performed on the time domain simulation data. For additional validation and checking we also employ other simulation tools – namely, a finite-element, frequency domain method (Ansys HFSS), the Sommerfeld Full Wave method (SFW) [4] and the Quasi Electro-Static (QES) method [5] [6]. An interesting discussion of the up-over-down effect associated with this problem space and the SFW method has been provided by Li and Olsen [7].

Because the experimental source is moving, reciprocity is employed to post-process the data of the six independent simulations of a given experimental scenario. This requires knowledge of Λ^j ($j = a, b, c, p, q, r$). Precise knowledge of the load impedances were not known at the time of the experiment, but they are surmised to be large, thus allowing us to assume that these factors are unity in value. Data provided in the ensuing paragraphs justifies this assumption. Additionally, due to the low frequency nature of the experimental signals, the size of the source antennas, and the size of the receiving array, we assumed the calibration lengths to be the physical length of the antenna structures. Again, the following data corroborates this assertion.

We first examine the HED experiment when $f = 100 \text{ Hz}$. Measured and simulation data associated with the magnitudes of the \mathbf{E} and \mathbf{H} fields are shown in Figures 5 and 6, respectively, when the sensor array was placed at a depth of 8 m. Examining Figure 5, we see that the shape of the calculated electric field matches the experimental data. The amplitude error at larger path distances is attributed to imprecise location and orientation of the sensor array. (Simulations show surprising data sensitivity to translational shifts of several meters and rotational shifts of 5 to 10 degrees.) The assumed unity value of Λ -factors is justified, specifically at the shorter distances. For this experiment the magnitude of the experimental magnetic field in Figure 5 is near the noise floor due to the weak coupling of an electric source to the magnetic field at ELF frequencies. Nonetheless, the simulation data captures the trends in the experimental data. For these HED source plots all of the simulation methods give almost identical results, thus providing additional, independent validation.

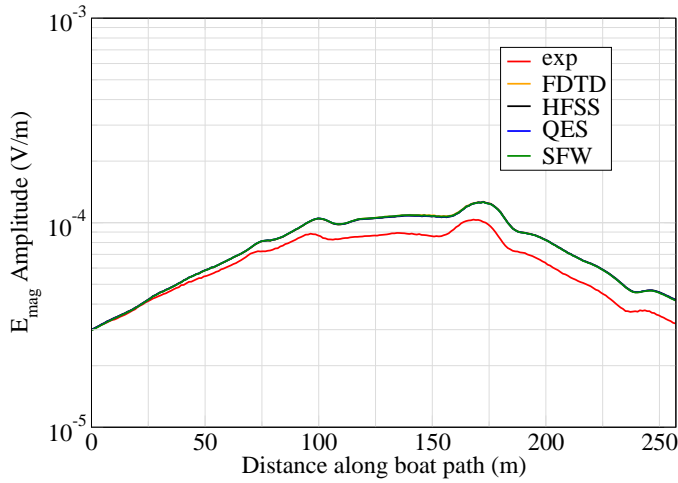


Fig. 5. Magnitude of the \mathbf{E} field as the source boat passes by the sensor array. The sensor array is about 8 meters deep. The signal frequency for this experiment was 100 Hz.

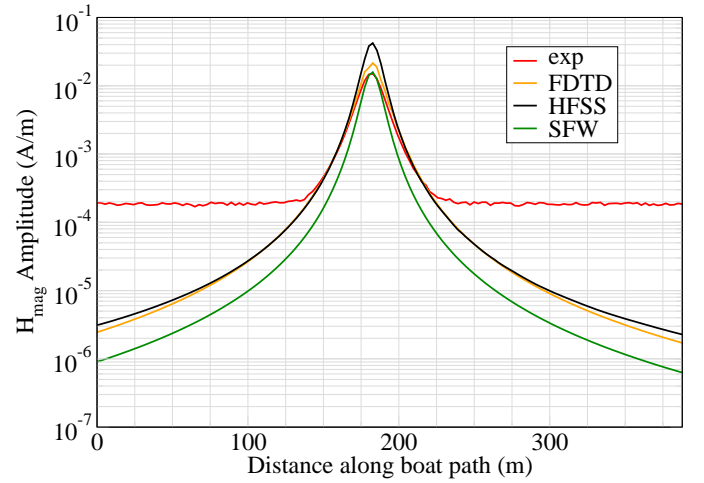


Fig. 8. Magnitude of the \mathbf{H} field. The signal frequency for this experiment was 10 Hz.

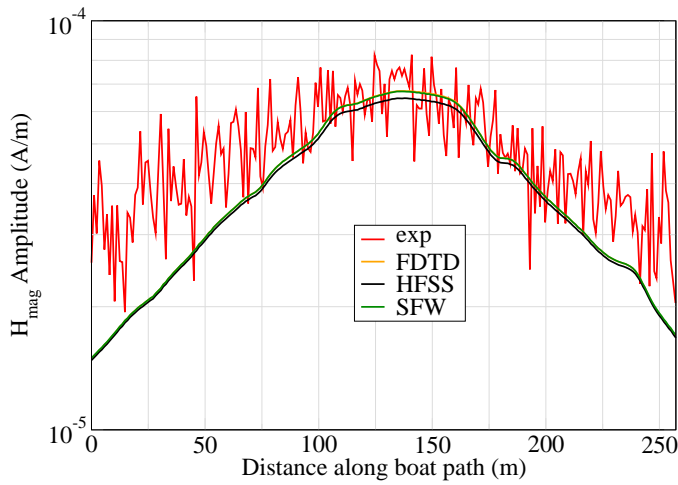


Fig. 6. Magnitude of the \mathbf{H} field. Closest approach of the source boat to sensor array was about 90 meters. The signal frequency for this experiment was 100 Hz.

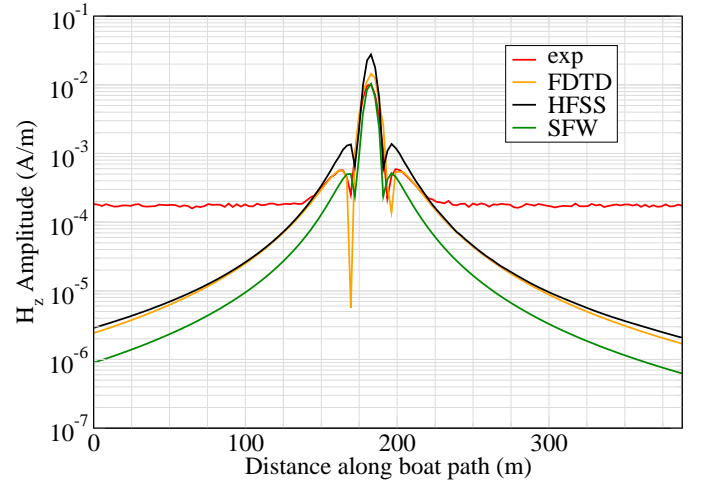


Fig. 9. Magnitude of the z component of \mathbf{H} . Note the small scale structure in the data. The signal frequency for this experiment was 10 Hz.

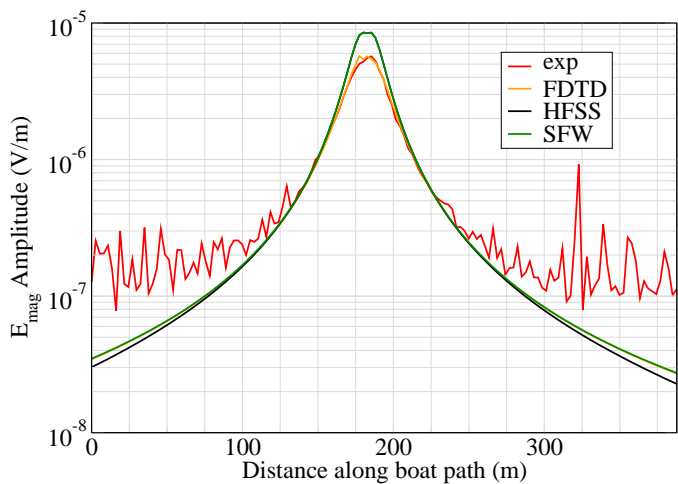


Fig. 7. Magnitude of \mathbf{E} field as the source boat passes by the sensor array. The closest approach of the source boat to sensor array is less than 10 meters. The signal frequency for this experiment was 10 Hz.

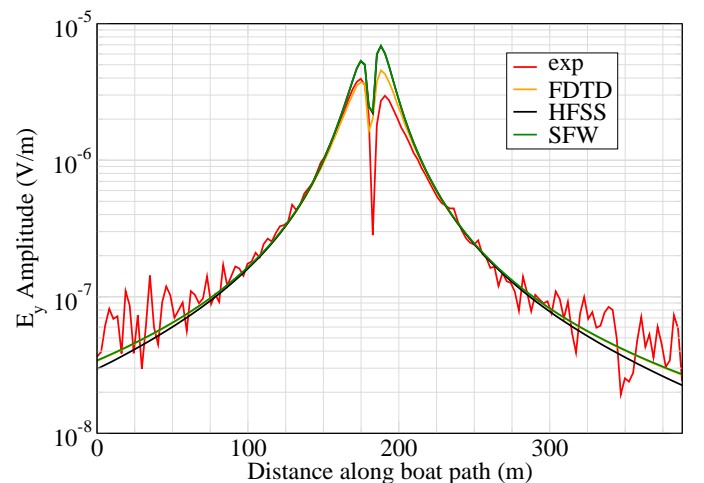


Fig. 10. Magnitude of the y component of \mathbf{E} . The signal frequency for this experiment was 10 Hz.

The VMD results are shown in Figures 7–10 when $f = 10$ Hz and when the sensor array was placed about 8 meters below the water surface. As shown by the field magnitudes in Figures 7 and 8 we can see the fields rise out of the noise floor, peak, and fall back into the noise as the source boat passes the sensor array. The simulations capture the shape and amplitude of the experimental data and predict the below noise floor values. Figure 9 shows the z component of the magnetic field. The data of this component shows some fine structure on a scale much smaller than a wavelength, as manifested by the two minima on each side of the peak. In water the wavelength at 10 Hz is about 10 km; the minima are spaced about 25 meters. This small scale structure places significant demands on the size of the simulations as cells must be small enough to capture such fine details. The ability to capture this fine detail in the simulation data provides further validation of the approach outlined herein. Figure 10 shows the y component of the electric field. In this case there is a null at about 180 m caused by phase reversal as the boat passes by the sensor array. Again, the simulations capture this feature.

IV. CONCLUSION

The measured and simulation data of the previous section provide compelling evidence that supports the use of the reciprocity theorem and the concept of calibration length and area. The reciprocity theorem allows us to interchange source with receiver, but, being a scalar projection theorem, reciprocity also requires six simulations to be conducted to obtain the full six components of the electromagnetic field. Six simulations are indeed a computational burden, but, in comparison to the alternative of thousands of simulations associated with each source location, six simulations are attractive. Moreover, as framed by reciprocity, six is the minimum.

The precision of the method is predicated on the amount of information available from the experiment. We showed herein that Λ -factors are needed to scale the data when source and receiver are interchanged. This means that precise knowledge about the load and self impedances of the experiment are needed at each source location. Less precise is the true calibration length and areas of the antennas. At ELF, good estimates can be obtained from physical size, but these estimates are subject to errors due to placement of the antennas in an inhomogeneous space.

ACKNOWLEDGMENT

This work was supported by the Office of Naval Research under grant number N00014-09-1-0923.

REFERENCES

- [1] C. A. Balanis, *Antenna Theory*, 3rd. Ed., Wiley, New York, NY, 2005.
- [2] R. F. Harrington, *Time-Harmonic Electromagnetic Fields*, McGraw-Hill, New York, NY, 1961.
- [3] C. L. Wagner and J. L. Young, "FDTD numerical tests of the convolutional-PML at extremely low frequencies," *IEEE Antennas and Wireless Propagation Letters*, vol. 8, pp. 1398-1401, 2009.
- [4] L. B. Felsen and N. Marcuvitz, *Radiation and Scattering of Waves*, Prentice-Hall, Englewood Cliffs, NJ, 1973.
- [5] R. T. Rebich, J. L. Young, C. W. Wagner and R. G. Olsen, "Comparison of the up-over-down approximation with the quasi-electrostatic approximation for ELF fields in layered media," *2011 IEEE International Symposium on Antennas and Propagation and USNC/URSI Radio Science Meeting*, Spokane, WA, July 2011.
- [6] J. R. Wait, *Electromagnetic Wave Theory*, Harper and Row, New York, NY, 1985.
- [7] Z. Li and R. G. Olsen, "A simple up-over-and-down model for low frequency horizontal electric dipole propagation near an interface," *2011 IEEE International Symposium on Antennas and Propagation and USNC/URSI Radio Science Meeting*, Spokane, WA, July 2011.



Jeffrey L. Young (F2008) received the BSEE degree from Ohio Northern University in 1981 and the MSEE and PhD degrees from the University of Arizona in 1984 and 1989, respectively. He was formerly a Doctoral Fellow and staff engineer with the Hughes Aircraft Company (1982-1991), Tucson, Arizona. He is currently a Professor of Electrical and Computer Engineering at the University of Idaho (1991-present), Moscow, Idaho and lectures on electromagnetics, antenna theory and design, and microwave circuits. His research interests include

electro-optical modulation, ferrite microwave devices, electromagnetic wave propagation in complex media and modern numerical methods in electromagnetics. He served nine years as an editor of the *IEEE Antennas and Propagation Magazine*, three years as an elected member of the IEEE Antennas and Propagation Society Administrative Committee (2002-2004) and four years as the IEEE Antennas and Propagation Society Chapters Coordinator (2004-2007). He was also the General Chair of the 2011 IEEE Antennas and Propagation Society International Symposium and USNC/URSI National Radio Science Meeting, Spokane, Washington. In addition to these duties, he has served on numerous Technical Program Committees for the IEEE Antennas and Propagation International Symposium and has chaired several technical sessions at the same. Professor Young is a member of URSI (Commission B), an IEEE Fellow and a registered Professional Engineer in the State of Idaho.

Christopher L. Wagner received BSEE and BS in physics degrees from the University of Washington in 1979. He received the MSEE and PhD degrees from Washington State University in 1998 and 2004, respectively. He is currently a Research Engineer and Lecturer at the University of Idaho in Moscow, Idaho. His research interests include transducers, electro-optics, and time domain numerical methods for electromagnetics calculation.

Appendix D: UI MSEE Theses

Three Master of Science in Electrical Engineering theses were concluded during the Phase Three effort. These theses contain important detailed information concerning the theories, simulations and experiments of the effort.

- Robert Rebich, “Multiple-layered quasi-electrostatic model development for extremely low frequencies,” University of Idaho MSEE Thesis, May 2011.
- Das Butherus, “Sensor orientation, reciprocity and software evaluation in the context of extremely low frequency applications,” University of Idaho MSEE Thesis, November 2011.
- Christopher Johnson, “Modeling extremely low frequency electromagnetic signals for naval applications,” University of Idaho MSEE Thesis, November 2011.

MULTIPLE-LAYERED QUASI-ELECTROSTATIC MODEL DEVELOPMENT FOR
EXTREMELY LOW FREQUENCIES

A Thesis

Presented in Partial Fulfillment of the Requirements for the

Degree of Master of Science

with a

Major in Electrical Engineering

in the

College of Graduate Studies

University of Idaho

by

Robert Totorica Rebich

May 2011

Major Professor: Jeffrey L. Young, Ph.D.

AUTHORIZATION TO SUBMIT THESIS

This thesis of Robert Totorica Rebich, submitted for the degree of Master of Science with a major in Electrical Engineering and titled “MULTIPLE-LAYERED QUASI-ELECTROSTATIC MODEL DEVELOPMENT FOR EXTREMELY LOW FREQUENCIES,” has been reviewed in final form. Permission, as indicated by the signatures and dates given below, is now granted to submit final copies to the College of Graduate Studies for approval.

Major Professor _____ Date _____
Jeffrey L. Young

Committee
Members _____ Date _____
Christopher Wagner

_____ Date _____
Ralph S. Budwig

Department
Administrator _____ Date _____
Brian Johnson

Discipline's
College Dean _____ Date _____
Donald M. Blackketter

Final Approval and Acceptance by the College of Graduate Studies

_____ Date _____
Nilsa A. Bosque-Pérez

Abstract

A procedure for modelling extremely low frequency (ELF) signals using a quasi-electrostatic (QES) approximation in a lake environment is the main topic of this thesis. The lake environment is modelled as three parallel layers of air, water and mud, although any non-magnetic materials may be used. The procedure utilizes an image summation technique to capture all boundary reflections and transmissions instead of the usual integral form, which are difficult and complex to integrate numerically. When the integrals are represented by an infinite summation of images, the solution converges with just few image terms for typical source and observation locations and materials. The QES method is validated against the Sommerfeld full-wave (SFW) solution, which itself has been fully validated. The results show that the QES method predicts the potentials and fields very well in the near-field and becomes increasingly inaccurate when distances or frequencies become large. The advantageous feature of the QES method is that the source geometry can be fully modelled in terms of two spherical electrodes separated by some distance. QES simulations execute in the order of seconds, which makes it a favourable and powerful method. The QES solution is also compared against the up-over-down solution [11], which turns out to be equivalent to the QES solution in most cases. The QES and up-over-down solutions describe the same electro-static phenomena from completely different points of view.

Vita

The author received the BSEE degree from the University of Idaho in 2008. He is currently pursuing the MSEE degree from the the University of Idaho were he works as a research assistant in the Department of Electrical and Computer Engineering. His research interests include computational electromagnetics, antennae systems and low frequency wave propagation.

Acknowledgements

I would like to acknowledge the support and guidance of my major professor, Dr. Jeffery L. Young. His knowledge and insight played a major role in the success the research methods presented in the document as well as in the overall success of the research. I would also like the thank the other members of the ELF team, Christopher L. Wagner, Chris Johnson, Das D. Butherus, Chenchen Jimmy Li, Markus Geiger and Neleema Dehal. Their help has been instrumental throughout the project and the creation of this document. Lastly, I would like to thank my committee for their help and guidance throughout the past two years.

This work was supported by the Office of Naval Research under grant number N00014-09-1-0923.

Contents

Abstract	iii
Vita	iv
Acknowledgements	v
1 Introduction	1
1.1 Project Motivation	1
1.2 Background	3
1.3 Scope	3
2 Quasi-Electrostatic (QES) Analytical Development	5
2.1 Point Charge in Region 1	8
2.1.1 Observation in Region 1	12
2.1.2 Observation in Region 2	15
2.2 Point Charge in Region 2	17
2.2.1 Observation in Region 1	20
2.2.2 Observation in Region 2	22
2.3 Dipole in Region 1	23
2.4 Dipole in Region 2	25
3 Results and Validity	28
3.1 QES and Sommerfeld Comparisons	28
3.2 Up-Over-Down Comparisons	33
3.3 Sommerfeld Full-Wave (SFW) Case Study	38
3.3.1 QES vs SFW Scalar Potential Integrals	41

3.3.2	QES vs SFW Potential Summations	45
3.3.3	Quasi-Magnetostatic (QMS) Contribution	50
3.3.4	Summary	56
3.4	Two-layer Reduction	59
3.5	Infinitesimal vs. QES Dipole	60
4	Conclusion	66
A	QES Graphical User Interface Guide	70
A.1	Installing the Solver	70
A.2	Basic Layout	72
A.3	Recommended Simulation Values	80
B	QES Source Code (Matlab)	81

List of Figures

2.1	A depiction showing \mathbf{n} for a two-layered geometry.	7
2.2	Point charge in region 1 for a three-layer configuration.	9
2.3	Superposition of potentials for observations in a) region 1 and b) region 2. . . .	10
2.4	A depiction of the image principle per Eqn. (2.50).	14
2.5	A depiction of the image principle per Eqn. (2.63).	16
2.6	Point charge in region 2 for a three-layer configuration.	18
2.7	Superposition of potentials for observations in a) region 1 and b) region 2. . . .	19
2.8	A depiction of the image principle per Eqn. (2.81).	21
2.9	A depiction of the image principle per Eqn. (2.90).	22
2.10	A depiction of the geometry for the two different dipole types in region 1. . . .	25
2.11	A depiction of the geometry for the two different dipole types in region 2. . . .	27
3.1	Scenario 1.	30
3.2	Scenario 2.	31
3.3	Scenario 3.	32
3.4	Scenario 4.	33
3.5	Contour integration and deformation of the Sommerfeld integrals [11].	35
3.6	Ray-optic depiction.	36
3.7	UOD 2 layer.	37
3.8	UOD 3 layer.	38
3.9	Comparison of Eqns. (2.63), (3.69) and (3.21) for observations in water.	47
3.10	QES region of validity per Eqn. (3.72) where $h = 5$ m, $z = 15$ m.	49
3.11	QES region of validity per Eqn. (3.73) where $h = 5$ m, $z = -5$ m.	50

3.12	Quasi-magnetostatic contribution versus magnitude of electric field in air. . . .	53
3.13	Quasi-magnetostatic contribution versus magnitude of electric field in water. . .	54
3.14	QMS region of validity in air by Eqn. (3.89).	55
3.15	QMS region of validity in air by Eqn. (3.90).	56
3.16	Representation of how a QES dipole is approximated by m infinitesimal dipoles.	61
3.17	Electric field magnitude for $m = 1$ case and QES 40 m dipole with illustration of QES electrodes and infinitesimal dipole locations. Solutions become the same at large distances which is not shown.	62
3.18	Depiction of E_x for $m = 1 - 4$ infinitesimal dipoles and a 40 m QES dipole. . .	64
3.19	Electric field magnitude higher m values. Dots are QES and solid line is SFW. .	65
A.1	A depiction of the directory structure a) before launching executable and b) after launching executable.	71
A.2	Solver directly after launch.	72
A.3	Dipole geometry for the HED. The VED geometry is similar except represented in the yz or xz plane.	74
A.4	Depiction the HED and VED located in region 1 or 2.	75
A.5	Depiction of three sweep options, a) horizontal, b) vertical and c) custom. . . .	76
A.6	Depiction of a) horizontal sweep and b) vertical sweep when <i>sweep angle</i> is zero.	77

List of Tables

3.1	Material Properties	29
3.2	Simulation Details	29
A.1	Recommended simulation values	80

Chapter 1

Introduction

This thesis describes in detail the development, implementation and key findings of how quasi-electrostatic signals at extremely low frequencies (ELF) propagate through material regions, specifically in a lake environment. For the purposes of this thesis, ELF frequencies will be defined as 10 - 1000 Hz. To model a real lake environment, a very complicated topographical model is needed to capture all field interactions with boundary interfaces. To simplify the modelling process the lake model described in this thesis will consist of a parallel three-layered medium of air, water and mud. The middle region is of finite thickness while the top region extends to infinity and the bottom region extends to minus infinity, thus making boundary conditions at region interfaces of importance. Integral expressions for each region are formulated and simplified into infinite image summations for a quick and robust solution. For valid quasi-electrostatic (QES) distances, a numerical solution is obtained within seconds. For this formulation, a domain of validity must be acquired to ascertain the usefulness the quasi-static approximation. This solution will be compared to known full-wave solutions to determine at what distances and frequencies the QES solution is no longer valid.

1.1 Project Motivation

Extremely low frequency (ELF) electromagnetic signals are used by enemy combatants to detect and, subsequently, to incapacitate, by means of surface and subsurface mines, naval vessels. This topic is of high importance to the Navy particularly since ELF signals are one of

the primary signature emissions of the Navys proposed electric ship fleet. In principle, the questions that are being asked in this investigation are: 1) once an ELF signal is generated, how far does it propagate and still be detectable and 2) how can such signals be modelled, excited and measured? To this end, the scenario considered is one in which an ELF source of the electric or magnetic kind is located in or above water, such as a lake or ocean. This source stimulates an ELF signal that is free to propagate in the water and air, and is reflected by various material interfaces, say between the water and air, or between the water and the floor. For purposes of experimental demonstration, the investigation focuses on the scenario of ELF sources and signals in the context of Lake Pend Oreille, where the Acoustic Research Detachment (ARD, Bayview, Idaho) is located and entrusted with the necessary assets to perform validation measurements. The research program associated with this thesis was designed with two major thrusts: Modelling and experimentation. The modelling thrust was coordinated and executed by the University of Idaho (UI), Moscow, Idaho; the experimentation thrust was coordinated and executed by ARD. This thesis focuses primarily on the modelling thrust [1].

The quasi-static solution is of importance for this application due to the focus on low frequency signals. If the near-field region is defined as 0.2λ , the QES region of validity in air is about 6,000 km when frequency is 10 Hz and decreases significantly to 60 km when frequency is increased to 1,000 Hz. For more conductive regions such as lake water, the QES region of validity is much smaller; about 745 m at a frequency of 10 Hz and about 75 m when frequency is increased to 1,000 Hz. Thus we can state that the QES has a large region of validity when frequency and material conductivity are low. As frequency or conductivity are increased, the QES region of validity decreased significantly. When observation locations are outside the QES region of validity, full-wave methods must be implemented to capture all wave-like phenomena.

1.2 Background

A vast amount research has been carried out for electromagnetic wave propagation in multi layered media where a sensor and source are placed in arbitrary regions. The research encompasses many areas which span from high frequency microwave circuit design [2] to low frequency layered earth and geophysical models [3]. Radio wave propagation in the atmosphere also relies heavily on concepts of layered media [4]. Early pioneers such as Sommerfeld and Wait put forth a large effort in developing the mathematical tools to solve such problems [5], [6]. Much of their work involved electric sources radiating above anisotropic half-spaces, where one region was usually a perfect electric conductor [7]. Large amounts of research were also spent in the area of layered-geophysical models of the earth.

In this thesis, an understanding of how quasi-electrostatic waves in a lake environment is developed. Various techniques and methods from the literature were used to solve this problem. For example, Chow found that the solution to a two or three layered micro-strip problem was easily solved using complex images, where solutions were very robust and converged rapidly [2]. For this thesis, similar methods were developed using term-by-term integration of complex integrals. Other researchers, Mosig and Sarkar compare the full-wave solution and the quasi-static solution for a horizontal electric dipole above a multi-layered lossy media and determine the quasi-static region region of validity in a micro-strip transmission line [8]. In terms of applying these methods to a lake environment, the literature shows little information on the subject. The work developed in this thesis extends the understanding of how quasi-static signals behave in a lake environment and also determines its region of validity.

1.3 Scope

This thesis describes in detail the quasi-static solution of a three-layered stratified geometry for this situation where extremely low frequencies are of interest and material properties are similar to that of a lake.

First a mathematical derivation is rigorously developed. The derivation begins with a point charge located in infinite homogeneous space. The quasi-static scalar potential from the point

charge is determined. Three region layers are added by applying boundary conditions at region interfaces. When the boundary conditions are applied, unique scalar potential and field expressions are developed for each of the three layers and are cast in terms of image summations. The problem is completely solved in terms of an infinitesimal point charge. It is beneficial to enlarge the charge to a finite radius, which will form an electrode. A dipole can be formed by taking two electrodes of opposite charge and separate them by a finite distance. The dipole solutions are also cast in terms of image solutions.

Now that the quasi-static three-layer problem has been solved analytically, it is necessary to determine when this solution succeeds and fails. To do this, we will examine how the quasi-static and the exact full-wave solutions relate to determine a corresponding region of validity for the quasi-static solution. During this process, a quasi-magnetostatic solution is revealed which has its own region of validity. A discussion of how an infinitesimal point source and a physically large extensible dipole relate to each other is also described.

This thesis will also discuss the up-over-down (UOD) phenomena as developed by professor Robert Olsen [11]. The UOD phenomena is a complicated wave process involving an upward travelling wave that spreads out cylindrically when it reaches the air-water interface and then travels back down into the water. It turns out that the quasi static solution to the same scenario can predict the UOD phenomena or vice versa. That is, two completely different modelling efforts lead to two completely different results which give identical results.

Chapter 2

Quasi-Electrostatic (QES) Analytical Development

Assume a domain where the media is composed of simple matter, in which case

$$\mathbf{D} = \epsilon \mathbf{E}, \quad (2.1)$$

$$\mathbf{B} = \mu \mathbf{H}, \quad (2.2)$$

and

$$\mathbf{J}^c = \sigma \mathbf{E}. \quad (2.3)$$

Here \mathbf{D} is the electric displacement density, \mathbf{B} is the magnetic flux density, \mathbf{J}^c is the electrical conduction current density, \mathbf{E} is the electric field intensity and \mathbf{H} is the magnetic field intensity. The permittivity ϵ is a product of the relative and free space permittivity so that $\epsilon = \epsilon_r \epsilon_0$, where $\epsilon_0 = 8.854 \times 10^{-12}$ F/m. The domain is absent of magnetic effects so that the permeability is equal to that of free space, $\mu = \mu_0$, where $\mu_0 = 4\pi \times 10^{-7}$ H/m. The electrical conductivity is represented by σ .

The fields within the domain are deemed quasi-electrostatic when the magnetic field has little to no time variation such that

$$\frac{\partial \mathbf{H}}{\partial t} \approx 0. \quad (2.4)$$

As a consequence of Eqn. (2.4), Faraday's law states that the curl of the electric field is then

approximately zero, in which case

$$\nabla \times \mathbf{E} \approx 0. \quad (2.5)$$

From Ampere's law,

$$\nabla \times \mathbf{H} = \frac{\partial \mathbf{D}}{\partial t} + \mathbf{J}, \quad (2.6)$$

where \mathbf{J} represents the combination of conduction and impressed current densities:

$$\mathbf{J} = \mathbf{J}^c + \mathbf{J}^i. \quad (2.7)$$

By taking the divergence of Eqn. (2.6) and knowing that the divergence of a curl is always zero, we find that

$$\nabla \cdot \left(\frac{\partial \mathbf{D}}{\partial t} + \mathbf{J} \right) = \nabla \cdot (\nabla \times \mathbf{H}) = 0. \quad (2.8)$$

Given Eqn. (2.5), the electric field at a given point in space is equal to the negative gradient of the electric scalar potential V at that point;

$$\mathbf{E} = -\nabla V. \quad (2.9)$$

For homogeneous media, it follows from Eqns. (2.8) and (2.9) and from the constitutive relationships of Eqns. (2.1) and (2.2) that

$$\epsilon \frac{\partial}{\partial t} \nabla^2 V + \sigma \nabla^2 V = \nabla \cdot \mathbf{J}^i, \quad (2.10)$$

where ∇^2 is the Laplacian operator. The equation of continuity states that,

$$\nabla \cdot \mathbf{J}^i = -\frac{\partial \rho}{\partial t}, \quad (2.11)$$

where ρ is the impressed charge density, so that

$$\epsilon \frac{\partial}{\partial t} \nabla^2 V + \sigma \nabla^2 V = -\frac{\partial \rho}{\partial t}. \quad (2.12)$$

In the frequency domain, equation Eqn. (2.12) is

$$\nabla^2 V = -\frac{j\omega\rho}{\sigma + j\omega\epsilon}, \quad (2.13)$$

where an $e^{+j\omega t}$ time factor is assumed. A special note is made that V and ρ in Eqn. (2.12) are referenced in the time domain (i.e. $V = V(t)$, $\rho = \rho(t)$) and V and ρ in Eqn. (2.13) are

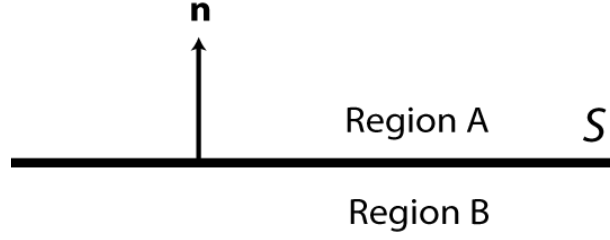


Figure 2.1: A depiction showing \mathbf{n} for a two-layered geometry.

referenced in the frequency domain (i.e. $V = V(\omega)$, $\rho = \rho(\omega)$). Subsequent analysis will be restricted to the frequency domain so that no ensuing confusion should remain.

Suppose we have an interface of two dissimilar media according to Figure 2.1. It then follows from Eqn. (2.5) that on the interface

$$(\mathbf{E}_A - \mathbf{E}_B) \times \mathbf{n} = 0. \quad (2.14)$$

The total induced current within a specific region is given by,

$$\mathbf{J}^t = (\sigma + j\omega\epsilon) \mathbf{E}. \quad (2.15)$$

Given Eqn. (2.15), continuity of normal current states that

$$\mathbf{n} \cdot \mathbf{J}_A^t = \mathbf{n} \cdot \mathbf{J}_B^t \quad (2.16)$$

or,

$$(\sigma_A + j\omega\epsilon_A) \mathbf{n} \cdot \mathbf{E}_A = (\sigma_B + j\omega\epsilon_B) \mathbf{n} \cdot \mathbf{E}_B. \quad (2.17)$$

Once V is determined from solving Eqn. (2.13) in the context of the boundary conditions of Eqns. (2.14) and (2.17) we then use Eqn. (2.9) to determine the electric field \mathbf{E} .

Let us now consider a single point charge of strength q located at the origin in unbounded media. The electric potential is a solution to Eqn. (2.13) such that

$$V = \frac{j\omega q}{4\pi(\sigma + j\omega\epsilon)r} \quad (2.18)$$

where

$$r = \sqrt{x^2 + y^2 + z^2} = \sqrt{\rho^2 + z^2}. \quad (2.19)$$

Eqn. (2.18) is known as the Green's function solution of a point charge at the origin in a lossy homogeneous medium. This solution can be equally expressed in integral form by noting that $\partial/\partial\phi = 0$, in which case Eqn. (2.13) is equivalent to

$$\frac{1}{\rho} \frac{\partial}{\partial \rho} \left(\rho \frac{\partial V}{\partial \rho} \right) + \frac{\partial^2 V}{\partial z^2} = -\frac{j\omega\rho}{\sigma + j\omega\epsilon}. \quad (2.20)$$

When $\rho = q\delta(r)\delta(z)/2\pi$, i.e. a point charge density, the solution to Eqn. (2.20) is a combination of Bessel and exponential functions [9]:

$$V = \frac{j\omega q}{4\pi(\sigma + j\omega\epsilon)} \int_0^\infty J_0(\lambda\rho) e^{-\lambda|z|} d\lambda. \quad (2.21)$$

Now if the charge is located at $z = h$, Eqn. (2.21) may be written as

$$V = \frac{j\omega q}{4\pi(\sigma + j\omega\epsilon)} \int_0^\infty J_0(\lambda\rho) e^{-\lambda|z-h|} d\lambda. \quad (2.22)$$

With the potential determined for a charge in a single homogeneous media, the analysis can be further extended to the three-layered media problem depicted in Figure 2.2. For our purposes, charges and observations will be restricted to regions 1 and 2.

2.1 Point Charge in Region 1

According to Figure 2.2, the charge is placed in region 1 at a height h above the $z = 0$ interface. When the charge is located in region 1, h is regarded as a positive number.

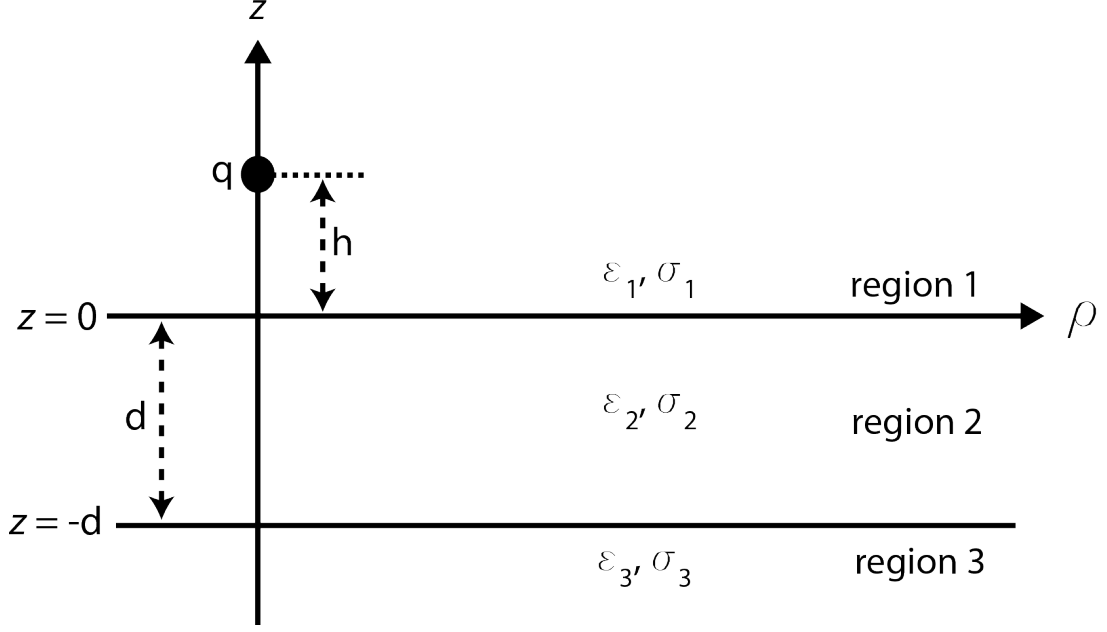


Figure 2.2: Point charge in region 1 for a three-layer configuration.

We construct potential solutions for each region as follows. For observation locations in region 1, where $z > 0$, the total potential at any given point is the superposition of two individual potentials as shown in Figure 2.3a. The first potential represents the direct signal from the charge to observer and is of unity strength. The second potential represents the reflected signal from the $z = 0$ boundary and is of strength R . The total potential at any location in region 1 is given by,

$$V_1 = \frac{j\omega q}{4\pi Y_1} \int_0^\infty [e^{-\lambda|z-h|} + R e^{-\lambda(z+h)}] J_0(\lambda\rho) d\lambda, \quad (2.23)$$

where,

$$Y_1 = \sigma_1 + j\omega\epsilon_1, \quad (2.24)$$

which is the admittivity of region 1.

For observation locations in region 2, where $-d < z < 0$, the total potential at any given point is the superposition of two individual potentials as shown in Figure 2.3b. The first potential represents the downward traveling signal caused by the transmission of the direct signal through the $z = 0$ boundary and is of strength B . The second potential represents the upward traveling signal caused by the reflection at the $z = -d$ boundary and is of strength A .

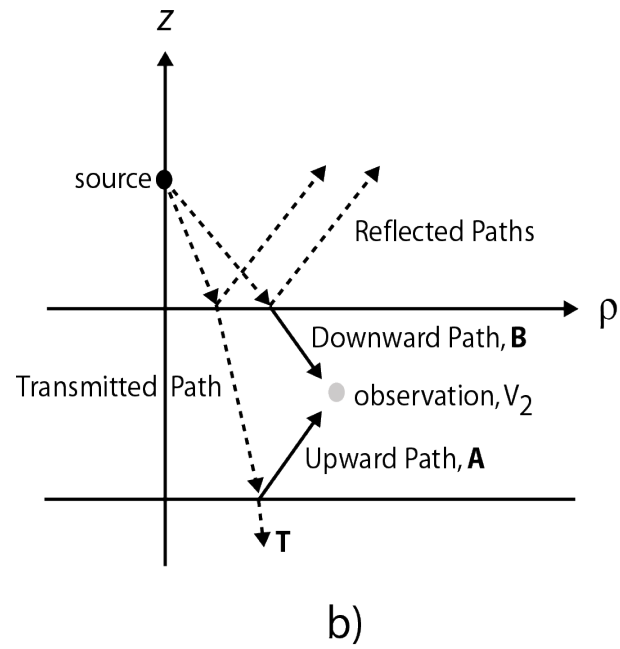
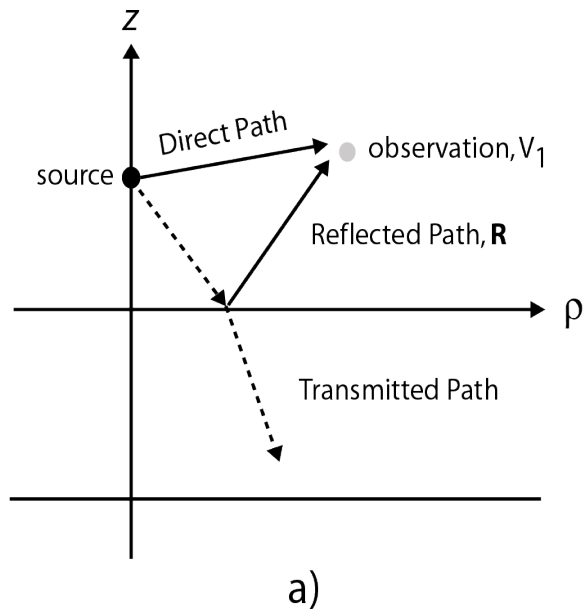


Figure 2.3: Superposition of potentials for observations in a) region 1 and b) region 2.

The total potential at any location in region 2 is given by,

$$V_2 = \frac{j\omega q}{4\pi Y_1} \int_0^\infty [Ae^{-\lambda(z+h)} + Be^{\lambda(z-h)}] J_0(\lambda\rho) d\lambda. \quad (2.25)$$

For observation locations in region 3, where $z < -d$, the potential at any given point represents the transmission of the downward traveling signal in region 2 as it encounters the $z = -d$ boundary and is of strength T . This situation is shown in Figure 2.3b. The total potential at any location in region 3 is given by,

$$V_3 = \frac{j\omega q}{4\pi Y_1} \int_0^\infty T e^{\lambda(z-h)} J_0(\lambda\rho) d\lambda. \quad (2.26)$$

Now that the potential solutions are formulated, the unknowns coefficients R , A , B , T are found by applying the boundary conditions of Eqns. (2.14) and (2.17) in the context of Eqn. (2.9). The boundary conditions must be applied at both region interfaces, i.e. the $z = 0$ and $z = -d$ boundaries. Hence,

$$\begin{aligned} V_1|_{z=0} &= V_2|_{z=0} \\ V_2|_{z=-d} &= V_3|_{z=-d}, \end{aligned} \quad (2.27)$$

and

$$\begin{aligned} Y_1 \frac{dV_1}{dz} \Big|_{z=0} &= Y_2 \frac{dV_2}{dz} \Big|_{z=0} \\ Y_2 \frac{dV_2}{dz} \Big|_{z=-d} &= Y_3 \frac{dV_3}{dz} \Big|_{z=-d}, \end{aligned} \quad (2.28)$$

where, as with Eqn. (2.24), $Y_i = \sigma_i + j\omega\epsilon_i$ for $i = 2, 3$. Applying the above boundary conditions to the potentials of Eqns. (2.23) - (2.26), we obtain a set of four equations with four unknowns given by,

$$1 + R = A + B, \quad (2.29)$$

$$Ae^{\lambda d} + Be^{-\lambda d} = Te^{-\lambda d}, \quad (2.30)$$

$$1 - R = \frac{Y_2}{Y_1}(B - A), \quad (2.31)$$

and

$$Be^{-\lambda d} - Ae^{\lambda d} = \frac{Y_3}{Y_2} Te^{-\lambda d}. \quad (2.32)$$

After many algebraic steps, we find that,

$$R = \frac{R_{23}e^{-2\lambda d} - R_{21}}{1 - R_{23}R_{21}e^{-2\lambda d}}, \quad (2.33)$$

$$A = \frac{R_{23}(1 - R_{21})e^{-2\lambda d}}{1 - R_{23}R_{21}e^{-2\lambda d}}, \quad (2.34)$$

$$B = \frac{(1 - R_{21})}{1 - R_{23}R_{21}e^{-2\lambda d}}, \quad (2.35)$$

and

$$T = \frac{(1 - R_{21})(1 + R_{23})}{1 - R_{23}R_{21}e^{-2\lambda d}}, \quad (2.36)$$

where the interfacial reflection-like coefficients are given by,

$$R_{21} = \frac{Y_2 - Y_1}{Y_1 + Y_2} \quad (2.37)$$

and

$$R_{23} = \frac{Y_2 - Y_3}{Y_2 + Y_3}. \quad (2.38)$$

The potential integrals for charge in region 1 as stated by Eqns. (2.23) - (2.26) are now fully specified and can be integrated numerically or recast in terms of image summations, as described next.

2.1.1 Observation in Region 1

In this section we will take the rather complex potential integral of Eqn. (2.23) and express it as an infinite summation. This is necessary because the integral will eventually be solved in a numerical fashion and the form of Eqn. (2.23) can be difficult to integrate numerically. The following procedure will make the numerical solution quick, efficient and robust.

The potential expression of Eqn. (2.23) is first separated into two parts:

$$V_1 = K_1 \int_0^\infty e^{-\lambda|z-h|} J_0(\lambda\rho) d\lambda + K_1 \int_0^\infty R e^{-\lambda(z+h)} J_0(\lambda\rho) d\lambda, \quad (2.39)$$

where K_1 is the normalized point charge strength in region 1 defined by,

$$K_1 = \frac{j\omega q}{4\pi Y_1}. \quad (2.40)$$

The first term of Eqn. (2.39) can be equally represented in closed-form by comparing Eqns. (2.18) and (2.22), in which case,

$$K_1 \int_0^\infty e^{-\lambda|z-h|} J_0(\lambda\rho) d\lambda = \frac{K_1}{r}. \quad (2.41)$$

In the present and all remaining development, r is defined by,

$$r = \sqrt{\rho^2 + z_s^2} \quad (2.42)$$

with,

$$\rho = \sqrt{x^2 + y^2} \quad (2.43)$$

and

$$z_s = z - h. \quad (2.44)$$

Eqn. (2.41) is commonly referred to as the Weber integral [9]. Equation (2.39) is equally stated as,

$$V_1 = \frac{K_1}{r} + K_1 \int_0^\infty R e^{-\lambda(z+h)} J_0(\lambda\rho) d\lambda. \quad (2.45)$$

We next insert R from Eqn. (2.33) into our expression to obtain,

$$V_1 = \frac{K_1}{r} + K_1 \int_0^\infty \left[\frac{R_{23}e^{-2\lambda d} - R_{21}}{1 - R_{23}R_{21}e^{-2\lambda d}} \right] e^{-\lambda(z+h)} J_0(\lambda\rho) d\lambda. \quad (2.46)$$

When $R_{23}R_{21}e^{-2\lambda d} < 1$ this integral can be expressed as an infinite summation by the following Taylor series expansion,

$$\frac{1}{1-x} = \sum_{n=0}^{\infty} x^n \quad \text{for} \quad |x| < 1. \quad (2.47)$$

This allows us to rewrite Eqn. (2.46) as,

$$V_1 = \frac{K_1}{r} + K_1 \sum_{n=0}^{\infty} R_{23}^n R_{21}^n \int_0^\infty (R_{23}e^{-2\lambda d} - R_{21}) e^{-\lambda(z+h+2nd)} J_0(\lambda\rho) d\lambda. \quad (2.48)$$

A close inspection of the previous integral shows that it has a closed-form solution using Gradshteyn and Ryzhik 6.611.1 [10]:

$$\int_0^\infty e^{-a\lambda} J_0(\lambda\rho) d\lambda = \frac{1}{\sqrt{a^2 + \rho^2}}. \quad (2.49)$$

From this integral identity, it follows that Eqn. (2.48) is equivalent to

$$V_1 = \frac{K_1}{r} + K_1 \sum_{n=0}^{\infty} R_{23}^n R_{21}^n \left[\frac{R_{23}}{r_a} - \frac{R_{21}}{r_b} \right] \quad (2.50)$$

where,

$$r_a = \sqrt{\rho^2 + D_1^2}, \quad (2.51)$$

$$r_b = \sqrt{\rho^2 + D_2^2}, \quad (2.52)$$

$$D_1 = z + h + 2d(n+1), \quad (2.53)$$

and

$$D_2 = z + h + 2dn. \quad (2.54)$$

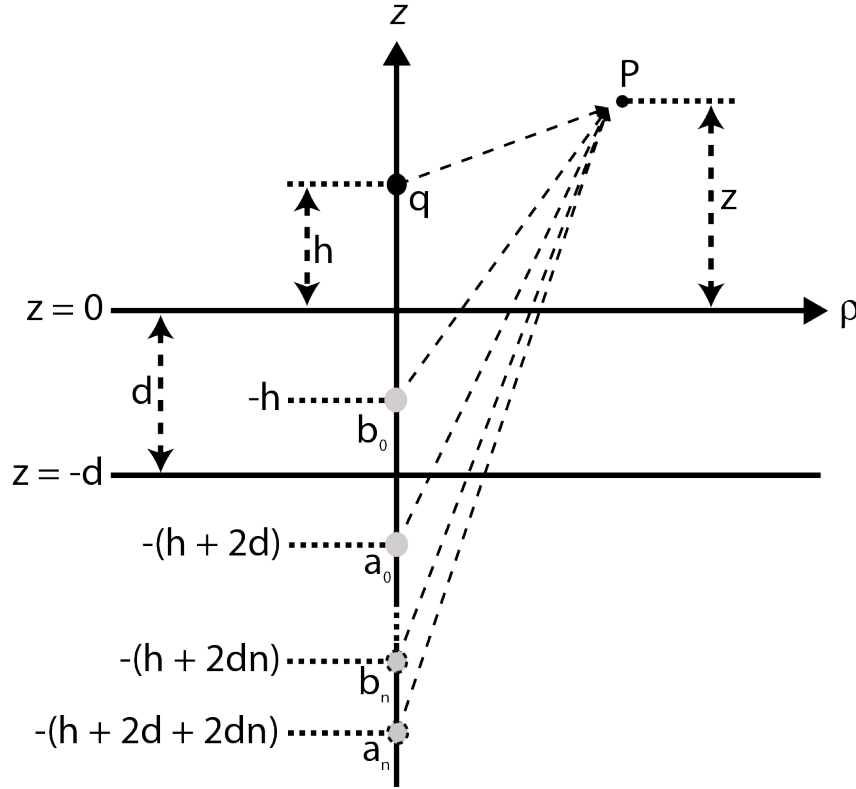


Figure 2.4: A depiction of the image principle per Eqn. (2.50).

The infinite summation in Eqn. (2.50) allows us to view the potential at some observation location as an infinite summation of equivalent charges at different locations with different strengths and phases. Figure 2.4 shows the corresponding image locations and strengths represented by Eqn. (2.50). The fully filled black circle with strength q represents the original

charge and is located at height h . Images a_0 and b_0 represent the first and second terms from the summation of Eqn. (2.50) when $n = 0$ and are presented as gray shaded circles. The image depths are shown relative to the $z = 0$ interface. The remaining image terms, a_n and b_n represent the infinite number of concurring images and are presented as light gray circles with dashed outlines. According to Eqn. (2.50), we see that the strengths for the corresponding weighted images are as follows,

$$a_n = K_1 R_{23}^{n+1} R_{21}^n \quad (2.55)$$

and

$$b_n = K_1 R_{23}^n R_{21}^{n+1}. \quad (2.56)$$

It is insightful to note that the image charges are proportional to the original charge q . For example, when we let $n = 0$ and use K_1 from Eqn. (2.40) we obtain

$$a_0 = \frac{j\omega q R_{23}}{4\pi Y_1} = W_{a_0} q, \quad (2.57)$$

where, W can be defined as a weighting term,

$$W_{a_0} = \frac{j\omega R_{23}}{4\pi Y_1}. \quad (2.58)$$

It is now obvious that each image term is of strength q multiplied by a complex weighting term W . This suggests that the image charges are out of phase with the original charge and scaled appropriately. It is also important to note that as n increases, the weighting terms become increasing small and the distances relative to the observation point become increasingly large. This means that the summation of the images converges very rapidly. Typically, no more than a few terms from the summation are needed for accurate results when dealing with any combination of charge and observation locations.

The electric field vector can be determined by taking the gradient of the potential Eqn. (2.50),

$$\begin{aligned} \mathbf{E} &= -\nabla V \\ &= -\left(\frac{\partial V}{\partial x} \hat{\mathbf{a}}_x + \frac{\partial V}{\partial y} \hat{\mathbf{a}}_y + \frac{\partial V}{\partial z} \hat{\mathbf{a}}_z \right). \end{aligned} \quad (2.59)$$

The electric field components are hence given by,

$$E_x = \frac{K_1}{r^3}x + K_1x \sum_{n=0}^{\infty} R_{23}^n R_{21}^n \left[\frac{R_{23}}{r_a^3} - \frac{R_{21}}{r_b^3} \right], \quad (2.60)$$

$$E_y = \frac{K_1}{r^3}y + K_1y \sum_{n=0}^{\infty} R_{23}^n R_{21}^n \left[\frac{R_{23}}{r_a^3} - \frac{R_{21}}{r_b^3} \right], \quad (2.61)$$

and

$$E_z = \frac{K_1}{r^3}z + K_1 \sum_{n=0}^{\infty} R_{23}^n R_{21}^n \left[\frac{R_{23}D_1}{r_a^3} - \frac{R_{21}D_2}{r_b^3} \right]. \quad (2.62)$$

2.1.2 Observation in Region 2

The aforementioned procedure may also be applied to Eqn. (2.25) to change the complex integral into an infinite summation. The detailed steps will not be shown for this equation due to the similarity with the previous process. The final form of the summation equation is given by,

$$V_2 = K_1(1 - R_{21}) \sum_{n=0}^{\infty} R_{23}^n R_{21}^n \left[\frac{R_{23}}{r_a} + \frac{1}{r_c} \right] \quad (2.63)$$

where,

$$r_c = \sqrt{\rho^2 + D_3^2} \quad (2.64)$$

and

$$D_3 = h - z + 2dn. \quad (2.65)$$

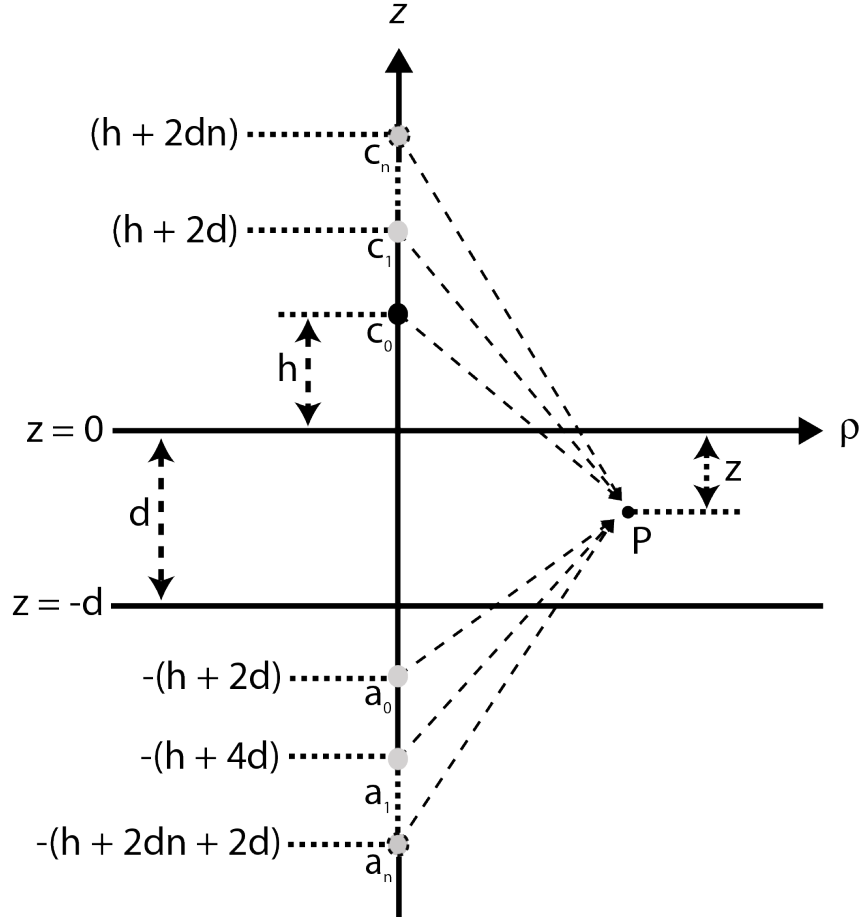


Figure 2.5: A depiction of the image principle per Eqn. (2.63).

Figure 2.5 shows the corresponding image locations and strengths represented by Eqn. (2.63).

The strengths for the corresponding weighted images are as follows,

$$a_n = K_1(1 - R_{21})R_{23}^{n+1}R_{21}^n \quad (2.66)$$

and

$$c_n = K_1(1 - R_{21})R_{23}^nR_{21}^n. \quad (2.67)$$

The electric field components are hence given by,

$$E_x = K_1x(1 - R_{21}) \sum_{n=0}^{\infty} R_{23}^n R_{21}^n \left[\frac{R_{23}}{r_a^3} + \frac{1}{r_c^3} \right], \quad (2.68)$$

$$E_y = K_1y(1 - R_{21}) \sum_{n=0}^{\infty} R_{23}^n R_{21}^n \left[\frac{R_{23}}{r_a^3} + \frac{1}{r_c^3} \right], \quad (2.69)$$

and

$$E_z = K_1(1 - R_{21}) \sum_{n=0}^{\infty} R_{23}^n R_{21}^n \left[\frac{R_{23} D_1}{r_a^3} - \frac{D_3}{r_c^3} \right]. \quad (2.70)$$

2.2 Point Charge in Region 2

In Figure 2.6 the charge is located in region 2 at a depth h below the $z = 0$ interface. When the charge is located in region 2, h is regarded as a negative number.

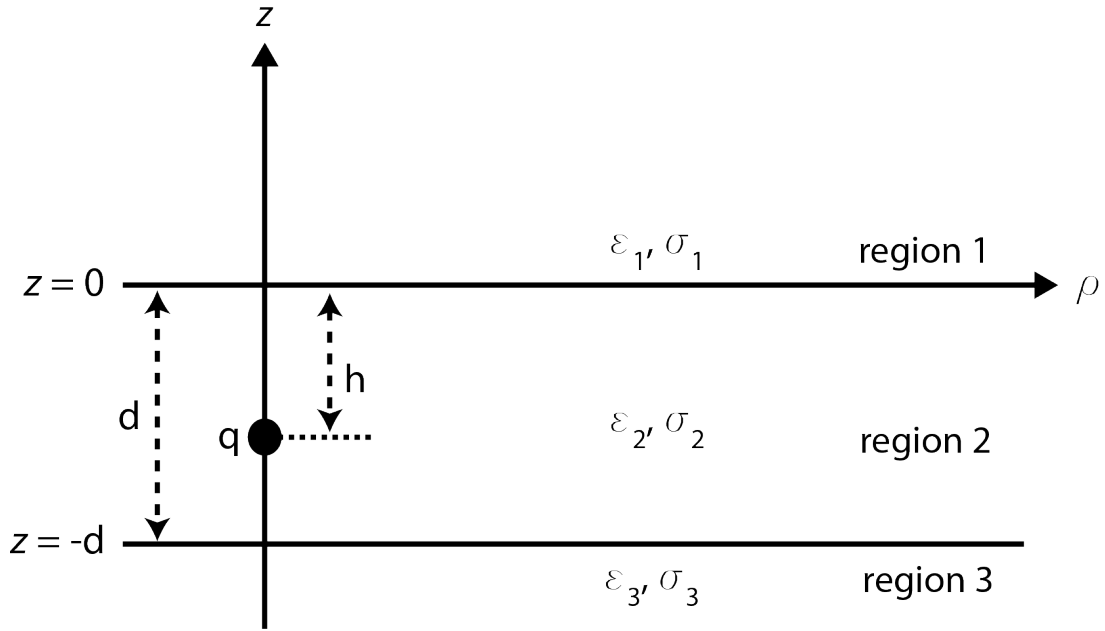


Figure 2.6: Point charge in region 2 for a three-layer configuration.

We construct potential solutions according to Eqn. (2.22) for each region as follows. For observation locations in region 1, where $z > 0$, the total potential at any given observation point is equal to the upward transmitted signal through the $z = 0$ boundary, which is of strength T_1 and is shown in Figure 2.7a. The total potential is given by,

$$V_1 = \frac{j\omega q}{4\pi Y_2} \int_0^{\infty} T_1 e^{-\lambda z} J_0(\lambda \rho) d\lambda. \quad (2.71)$$

For observation locations in region 2, where $-d < z < 0$, the total potential at any given observation point is equal to the superposition of three different potentials and is shown in Figure 2.7b. The first is the direct signal from charge to observer and is of unity strength. The second is the upward traveling signal caused by the reflection from the direct charge from the

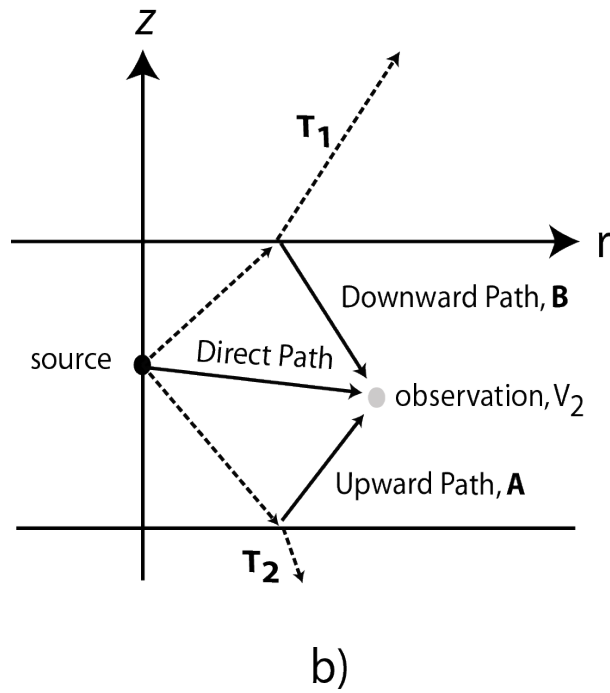
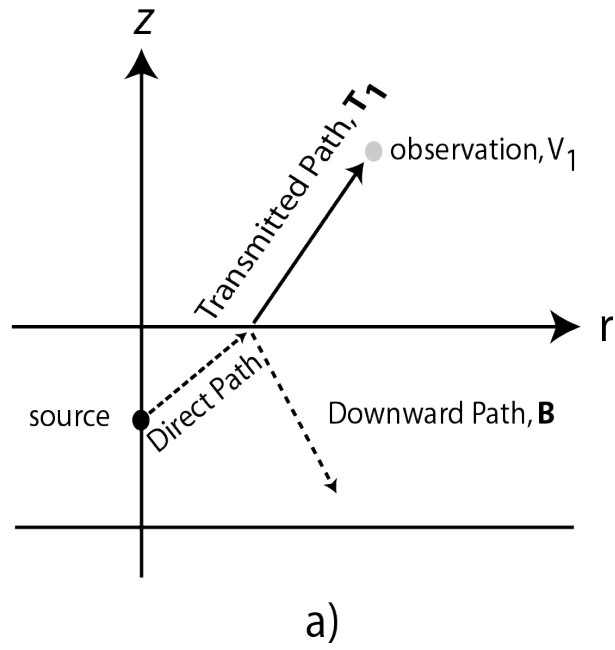


Figure 2.7: Superposition of potentials for observations in a) region 1 and b) region 2.

$z = -d$ boundary and is of strength A . The last is the downward traveling signal caused by the reflection of the direct charge off the $z = 0$ boundary and is of strength B . The total potential is given by,

$$V_2 = \frac{jwq}{4\pi Y_2} \int_0^\infty [e^{-\lambda|z-h|} + Ae^{-\lambda z} + Be^{\lambda z}] J_0(\lambda \rho) d\lambda. \quad (2.72)$$

For observation locations in region 3, where $z < -d$, the total potential is equal to the transmitted signal through the $z = -d$ boundary and is of strength T_2 , and is shown in Figure 2.7b. The total potential is given by,

$$V_3 = \frac{jwq}{4\pi Y_2} \int_0^\infty T_2 e^{\lambda z} J_0(\lambda \rho) d\lambda. \quad (2.73)$$

The same boundary conditions of Eqns. (2.27) and (2.28) still apply. Applying these boundary conditions, we obtain a set of four equations with four unknowns:

$$T_1 = e^{\lambda h} + A + B, \quad (2.74)$$

$$T_2 e^{-\lambda d} = e^{-\lambda(h+d)} + Ae^{\lambda d} + Be^{-\lambda d}, \quad (2.75)$$

$$Y_1 T_1 = Y_2 (e^{\lambda h} + A - B), \quad (2.76)$$

and

$$Y_2 (Ae^{\lambda d} - Be^{-\lambda d} - e^{-\lambda(h+d)}) = -Y_3 T_2 e^{-\lambda d}. \quad (2.77)$$

Solving for the unknown coefficients of interest, we obtain the following equations:

$$T_1 = \frac{(R_{21} + 1)(e^{\lambda h} + R_{23}e^{-\lambda(h+2d)})}{1 - R_{23}R_{21}e^{-2\lambda d}}, \quad (2.78)$$

$$A = \frac{R_{23}(1 + R_{21}e^{2\lambda h})e^{-\lambda(h+2d)}}{1 - R_{23}R_{21}e^{-2\lambda d}}, \quad (2.79)$$

and

$$B = \frac{R_{21}e^{\lambda h} + R_{23}R_{21}e^{-\lambda(h+2d)}}{1 - R_{23}R_{21}e^{-2\lambda d}}. \quad (2.80)$$

2.2.1 Observation in Region 1

The image solution for the configuration of Figure 2.6 with observation in region 1 as stated by Eqn. (2.71) is given as,

$$V_1 = K_2(1 + R_{21}) \sum_{n=0}^{\infty} R_{23}^n R_{21}^n \left[\frac{R_{23}}{r_a} + \frac{1}{r_d} \right], \quad (2.81)$$

where,

$$r_d = \sqrt{\rho^2 + D_4^2} \quad (2.82)$$

and

$$D_4 = z - h + 2dn. \quad (2.83)$$

Here K_2 is the source strength in region 2 defined by,

$$K_2 = \frac{j\omega q}{4\pi Y_2}. \quad (2.84)$$

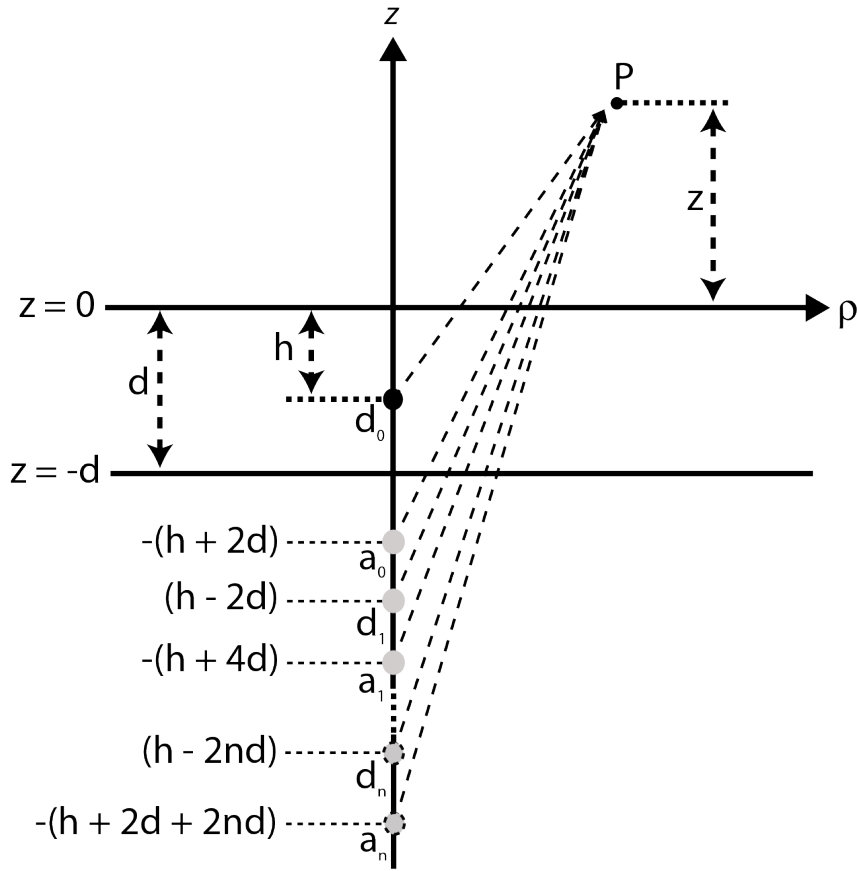


Figure 2.8: A depiction of the image principle per Eqn. (2.81).

Figure 2.8 shows the corresponding image locations and strengths represented by Eqn. (2.81).

The strengths for the corresponding weighted images are as follows,

$$a_n = K_2(1 + R_{21})R_{23}^{n+1}R_{21}^n \quad (2.85)$$

$$d_n = K_2(1 + R_{21})R_{23}^nR_{21}^n. \quad (2.86)$$

The electric field components are hence given by,

$$E_x = K_1 x (1 + R_{21}) \sum_{n=0}^{\infty} R_{23}^n R_{21}^n \left[\frac{R_{23}}{r_a^3} + \frac{1}{r_d^3} \right], \quad (2.87)$$

$$E_y = K_1 y (1 + R_{21}) \sum_{n=0}^{\infty} R_{23}^n R_{21}^n \left[\frac{R_{23}}{r_a^3} + \frac{1}{r_d^3} \right], \quad (2.88)$$

and

$$E_z = K_1 (1 + R_{21}) \sum_{n=0}^{\infty} R_{23}^n R_{21}^n \left[\frac{D_1 R_{23}}{r_a^3} + \frac{D_4}{r_d^3} \right]. \quad (2.89)$$

2.2.2 Observation in Region 2

The image solution for the configuration of Figure 2.6 with observation in region 2 as stated by Eqn. (2.72) is given as,

$$V_2 = \frac{K_2}{r} + K_2 \sum_{n=0}^{\infty} R_{23}^n R_{21}^n \left[\frac{R_{23}}{r_a} + \frac{R_{23} R_{21}}{r_e} + \frac{R_{23} R_{21}}{r_f} + \frac{R_{21}}{r_g} \right], \quad (2.90)$$

where,

$$r_e = \sqrt{\rho^2 + D_5^2}, \quad (2.91)$$

$$r_f = \sqrt{\rho^2 + D_6^2}, \quad (2.92)$$

$$r_g = \sqrt{\rho^2 + D_7^2}, \quad (2.93)$$

$$D_5 = z - h + 2d(n + 1), \quad (2.94)$$

$$D_6 = h - z + 2d(n + 1), \quad (2.95)$$

and

$$D_7 = 2nd - z - h. \quad (2.96)$$

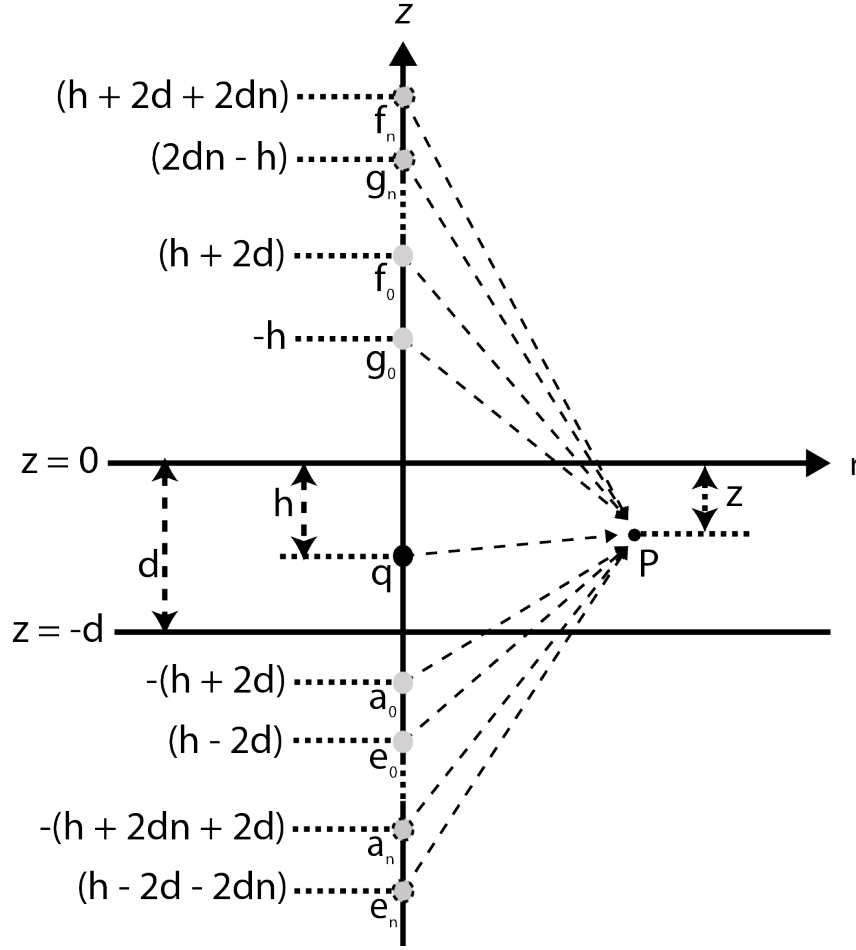


Figure 2.9: A depiction of the image principle per Eqn. (2.90).

Figure 2.9 shows the corresponding image locations and strengths represented by Eqn. (2.90).

The strengths for the corresponding weighted images are as follows,

$$a_n = K_2 R_{23}^{n+1} R_{21}^n, \quad (2.97)$$

$$e_n = K_2 R_{23}^{n+1} R_{21}^{n+1}, \quad (2.98)$$

$$f_n = K_2 R_{23}^{n+1} R_{21}^{n+1}, \quad (2.99)$$

and

$$g_n = K_2 R_{23}^n R_{21}^{n+1}. \quad (2.100)$$

The electric field components are hence given by,

$$E_x = \frac{K_2}{r^3} x + K_2 x \sum_{n=0}^{\infty} R_{23}^n R_{21}^n \left[\frac{R_{23}}{r_a^3} + \frac{R_{23} R_{21}}{r_e^3} + \frac{R_{23} R_{21}}{r_f^3} + \frac{R_{21}}{r_g^3} \right], \quad (2.101)$$

$$E_y = \frac{K_2}{r^3} y + K_2 y \sum_{n=0}^{\infty} R_{23}^n R_{21}^n \left[\frac{R_{23}}{r_a^3} + \frac{R_{23} R_{21}}{r_e^3} + \frac{R_{23} R_{21}}{r_f^3} + \frac{R_{21}}{r_g^3} \right], \quad (2.102)$$

and

$$E_z = \frac{K_2}{r^3} z + K_2 \sum_{n=0}^{\infty} R_{23}^n R_{21}^n \left[\frac{D_1 R_{23}}{r_a^3} + \frac{D_5 R_{23} R_{21}}{r_e^3} - \frac{D_6 R_{23} R_{21}}{r_f^3} - \frac{D_7 R_{21}}{r_g^3} \right]. \quad (2.103)$$

2.3 Dipole in Region 1

Consider the existence of two spherical electrodes of total charge $+q$ and $-q$, of radius a and of separation dl placed in region 1 as shown in Figure 2.10. The electrodes are located at z_1, ρ_1 and z_2, ρ_2 . We will define the configuration of two oppositely charged electrodes as an *electric dipole*. If we assume the charge distribution is uniform across the entire surface of both electrodes then Eqn. (2.50) is valid for the following procedure. Given the charge separation, a potential V_0 is assumed to exist between the electrodes. Let P_1 be any point on the negative charged sphere and P_2 be any point on the positive charged sphere. Then by Eqn. (2.50) and from superposition, we have,

$$V_0 = K_1 \left\{ \frac{1}{r} + \sum_{n=0}^{\infty} R_{23}^n R_{21}^n \left[\frac{R_{23}}{r_a} - \frac{R_{21}}{r_b} \right] \right\}_{P_1}^{P_2} \quad (2.104)$$

where K_1 is given by Eqn. (2.40). We will define the geometrical factor G_1 to be the following:

$$G_1 = \left\{ \frac{1}{r} + \sum_{n=0}^{\infty} R_{23}^n R_{21}^n \left[\frac{R_{23}}{r_a} - \frac{R_{21}}{r_b} \right] \right\}_{P_1}^{P_2}. \quad (2.105)$$

The source strength K_1 is determined by supplying the potential between the two electrodes and calculating the geometrical factor;

$$K_1 = \frac{V_0}{G_1}. \quad (2.106)$$

For a source location in region 1 and observation in region 1 or 2, Eqns. (2.50) and (2.63) are used to construct a two-charge dipole according to Figure 2.10 by superimposing the potentials of the two charges. For observations in region 1,

$$V_1 = K_1 \left\{ \left(\frac{1}{r_2} - \frac{1}{r_1} \right) + \sum_{n=0}^{\infty} R_{23}^n R_{21}^n \left[R_{23} \left(\frac{1}{r_{a2}} - \frac{1}{r_{a1}} \right) - R_{21} \left(\frac{1}{r_{b2}} - \frac{1}{r_{b1}} \right) \right] \right\}. \quad (2.107)$$

For observations in region 2,

$$V_2 = K_1 (1 - R_{21}) \sum_{n=0}^{\infty} R_{23}^n R_{21}^n \left[R_{23} \left(\frac{1}{r_{a2}} - \frac{1}{r_{a1}} \right) + \left(\frac{1}{r_{c2}} - \frac{1}{r_{c1}} \right) \right]. \quad (2.108)$$

The distance terms are given by,

$$r_2 = \sqrt{\rho_2^2 + (z - z_2)^2}, \quad (2.109)$$

$$r_1 = \sqrt{\rho_1^2 + (z - z_1)^2}, \quad (2.110)$$

$$r_{a2} = \sqrt{\rho_2^2 + (z + z_2 + 2dn + 2d)^2}, \quad (2.111)$$

$$r_{a1} = \sqrt{\rho_1^2 + (z + z_1 + 2dn + 2d)^2}, \quad (2.112)$$

$$r_{b2} = \sqrt{\rho_2^2 + (z + z_2 + 2dn)^2}, \quad (2.113)$$

$$r_{b1} = \sqrt{\rho_1^2 + (z + z_1 + 2dn)^2}, \quad (2.114)$$

$$r_{c2} = \sqrt{\rho_2^2 + (z_2 - z + 2dn)^2}, \quad (2.115)$$

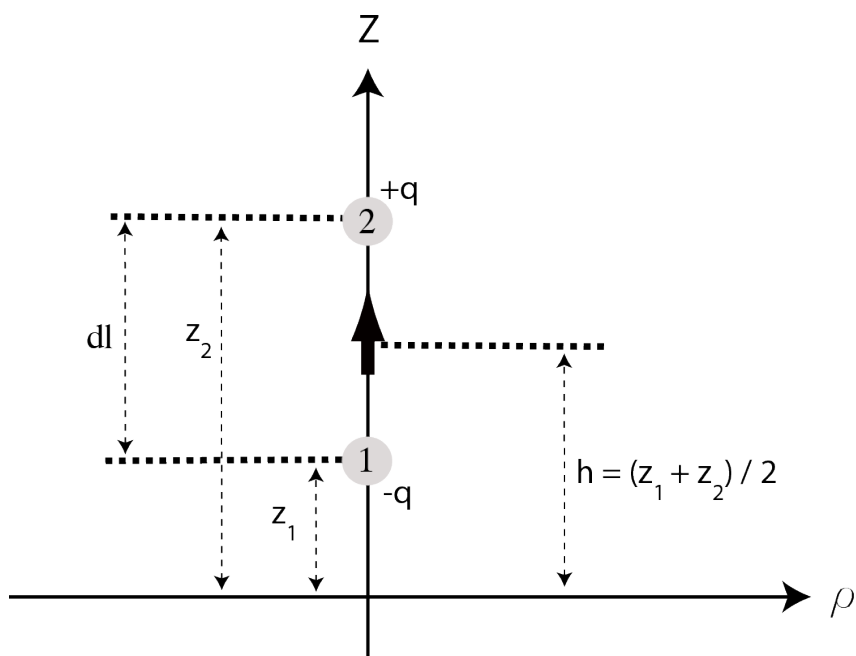
$$r_{c1} = \sqrt{\rho_1^2 + (z_1 - z + 2dn)^2}, \quad (2.116)$$

$$\rho_2 = \sqrt{x_2^2 + y_2^2}, \quad (2.117)$$

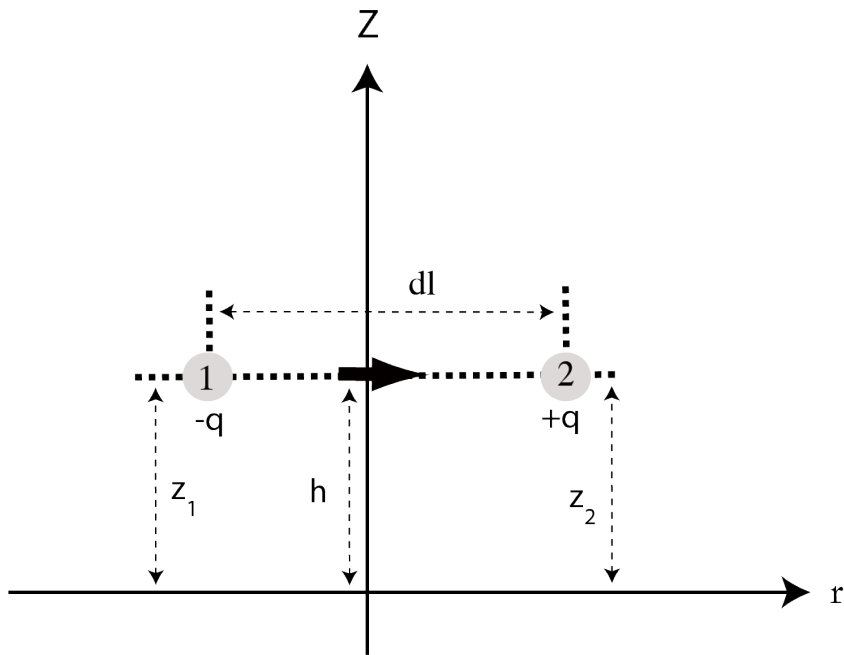
and

$$\rho_1 = \sqrt{x_1^2 + y_1^2}. \quad (2.118)$$

Note that Eqns. (2.107) and (2.108) are valid for any dipole orientation. Two particular dipole cases will be of significant importance: 1) vertical electric dipole (VED), which occurs when two opposite charges share the same ρ location (i.e. $\rho_1 = \rho_2 = \rho$) but do not share the same z location 2) horizontal electric dipole (HED), which occurs when two opposite charges share the same z location (i.e. $z_1 = z_2 = z$) but do not share the same ρ location. This is shown in Figure 2.10.



a) VED



b) HED

Figure 2.10: A depiction of the geometry for the two different dipole types in region 1.

2.4 Dipole in Region 2

For source location in region 2 and by Eqn. (2.90) we have:

$$V_0 = K_2 \left\{ \frac{1}{r} + \sum_{n=0}^{\infty} R_{23}^n R_{21}^n \left[\frac{R_{23}}{r_a} + \frac{R_{23}R_{21}}{r_e} + \frac{R_{23}R_{21}}{r_f} + \frac{R_{21}}{r_g} \right] \right\}_{P_1}^{P_2}. \quad (2.119)$$

We will define the geometrical factor G_2 for this two electrode scenario to be the following:

$$G_2 = \frac{1}{r} + \sum_{n=0}^{\infty} R_{23}^n R_{21}^n \left[\frac{R_{23}}{r_a} + \frac{R_{23}R_{21}}{r_e} + \frac{R_{23}R_{21}}{r_f} + \frac{R_{21}}{r_g} \right]_{P_1}^{P_2}. \quad (2.120)$$

We can determine the source strength by supplying the potential between the two electrodes and calculating the geometrical factor;

$$K_2 = \frac{V_0}{G_2}. \quad (2.121)$$

For a dipole in region 2 and observations in region 1 or 2, a two-charge dipole is constructed using superposition. The result is

$$V_1 = K_2 (1 + R_{21}) \sum_{n=0}^{\infty} R_{23}^n R_{21}^n \left[R_{23} \left(\frac{1}{r_{a2}} - \frac{1}{r_{a1}} \right) + \left(\frac{1}{r_{d2}} - \frac{1}{r_{d1}} \right) \right] \quad (2.122)$$

and

$$V_2 = K_2 \left[\left(\frac{1}{r_2} - \frac{1}{r_1} \right) + \sum_{n=0}^{\infty} R_{23}^n R_{21}^n \left[R_{23} \left(\frac{1}{r_{a2}} - \frac{1}{r_{a1}} \right) + R_{23}R_{21} \left(\frac{1}{r_{e2}} - \frac{1}{r_{e1}} \right) + R_{23}R_{21} \left(\frac{1}{r_{f2}} - \frac{1}{r_{f1}} \right) + R_{21} \left(\frac{1}{r_{g2}} - \frac{1}{r_{g1}} \right) \right] \right], \quad (2.123)$$

where,

$$r_{d2} = \sqrt{\rho_2^2 + (z - z_2 + 2dn)^2}, \quad (2.124)$$

$$r_{d1} = \sqrt{\rho_1^2 + (z - z_1 + 2dn)^2}, \quad (2.125)$$

$$r_{e2} = \sqrt{\rho_2^2 + (z - z_2 + 2dn + 2d)^2}, \quad (2.126)$$

$$r_{e1} = \sqrt{\rho_1^2 + (z - z_1 + 2dn + 2d)^2}, \quad (2.127)$$

$$r_{f2} = \sqrt{\rho_2^2 + (z_2 - z + 2dn + 2d)^2}, \quad (2.128)$$

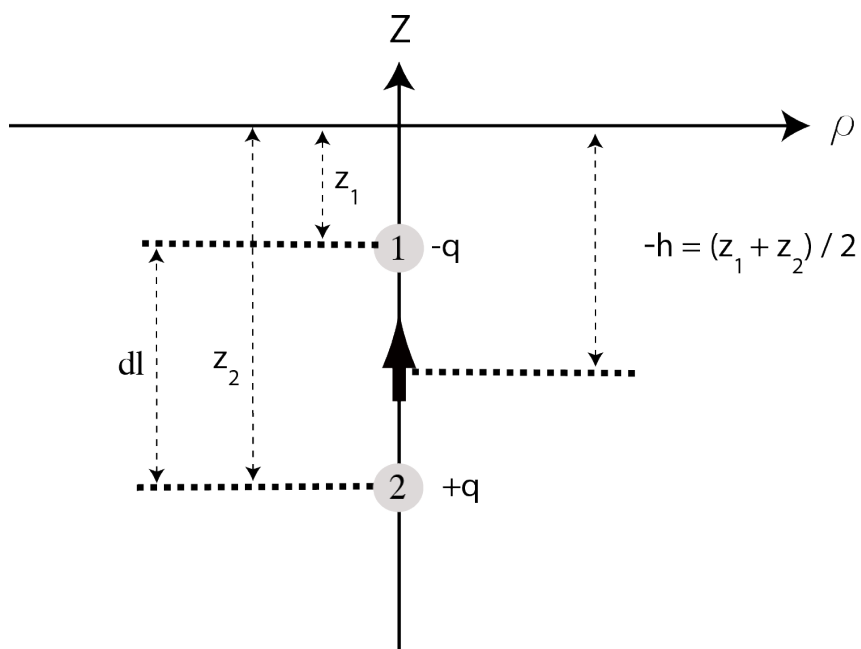
$$r_{f1} = \sqrt{\rho_1^2 + (z_1 - z + 2dn + 2d)^2}, \quad (2.129)$$

$$r_{g2} = \sqrt{\rho_2^2 + (2dn - z - z_2)^2}, \quad (2.130)$$

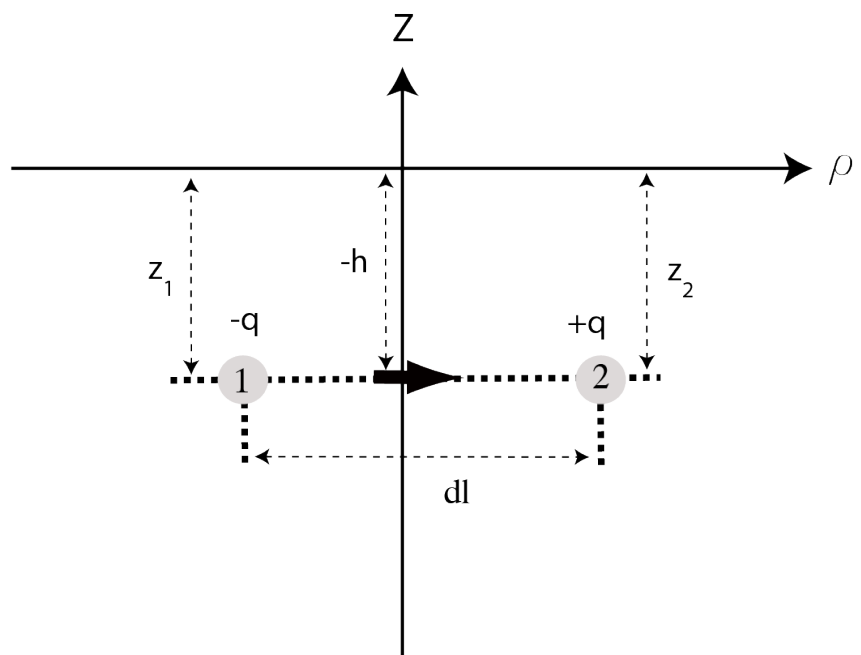
and

$$r_{g1} = \sqrt{\rho_1^2 + (2dn - z - z_1)^2}. \quad (2.131)$$

Note that Eqns. (2.122) and (2.123) are valid for any dipole orientation. The special cases of the HED and VED configuration geometries for region 2 excitations are depicted in Figure 2.11.



a) VED



b) HED

Figure 2.11: A depiction of the geometry for the two different dipole types in region 2.

Chapter 3

Results and Validity

3.1 QES and Sommerfeld Comparisons

In this section the Sommerfeld full-wave solution [9] will be used as a benchmark to compare and validate the QES dipole solution for a parallel 3-layer model. The SFW solution has been fully validated and is regarded as the exact full-wave solution. Note that the SFW solution utilizes an infinitesimal dipole for the source while the QES models a physically large source, this difference is described in full detail in Section 3.5. Lets now discussed some important scenarios for validating the QES solution.

The comparisons will be based upon the geometry of Figure 2.2, where regions material properties are given according to Table 3.1. The depth of region 2, i.e. the depth of the water column, will be set to 180 m. The QES dipole will have an electrode radius of 0.0667 m and an electrode separation of 15 m. Test frequencies of 10, 100 and 1000 Hz will be of interest. The source moment was set to 1 A-m for both the QES and the SFW dipoles. Note that when observations are made in water, the QES solution is frequency independent, i.e.

$\mathbf{J} = (\sigma + j\omega\epsilon) \mathbf{E} \approx \sigma \mathbf{E}$ when $\omega\epsilon \ll \sigma$ so the plot legend will combine all three frequency sweeps.

Four scenarios will be examined and are described according to Table 3.2.

Table 3.1: Material Properties

	region 1	region 2	region 3
ϵ_r	1	81	1
σ	0	0.018	0.012

Table 3.2: Simulation Details

Scenario	Source Type	Source Location	Orientation	Sweep P1, P2
1	HED in water	(0,0,-50)	x -directed	(0,0,-25), (0,3000,-25)
2	VED in water	(0,0,-50)	z -directed	(75,75,-180), (75,75,300)
3	VED in water	(0,0,-50)	z -directed	(150,-1500,-50), (150,1500,-50)
4	HED in air	(0,0,50)	y -directed	(0,0,25), (3000,0,25)

For the first scenario we place a x -directed HED in water at a depth of 50 m. We choose to observe the fields along the y -axis in water at a depth of 25 m, according to $P1$ and $P2$. Figure 3.1 shows the E_{mag} results for the QES and the SFW simulations. We see that the QES predicts the same order of magnitude as the SFW solution for all three frequencies. When the frequency increases from 10 to 1000 Hz, QES shows slight deviations from the SFW prediction for large distances. For this scenario, we conclude with confidence that the QES solution is a valid simulation tool for the parameters specified.

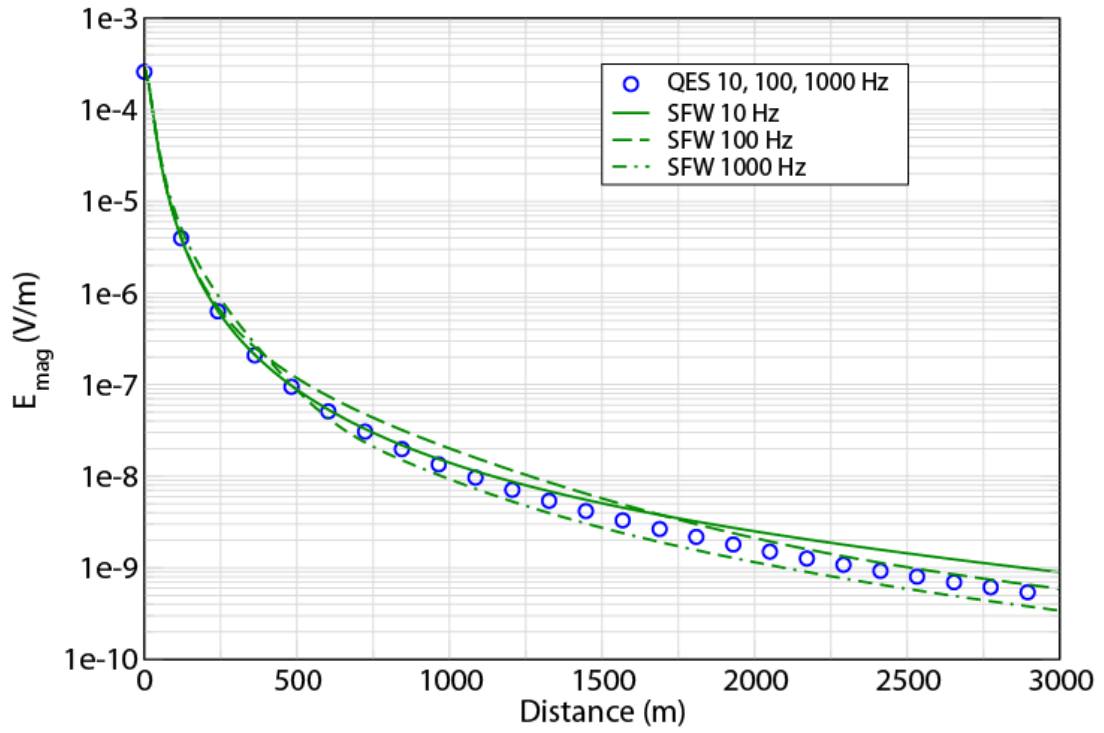


Figure 3.1: Scenario 1.

For the second scenario we will change the orientation of the dipole to be vertical and change the observation path according to Table 3.2. These results are seen in Figure 3.2. Here we see that the QES predicts the SFW solution accurately at all three frequencies and with a slight divergence at 1000 Hz. A similar conclusion to that of scenario one is reached: the QES tool is validated for the specified parameters.

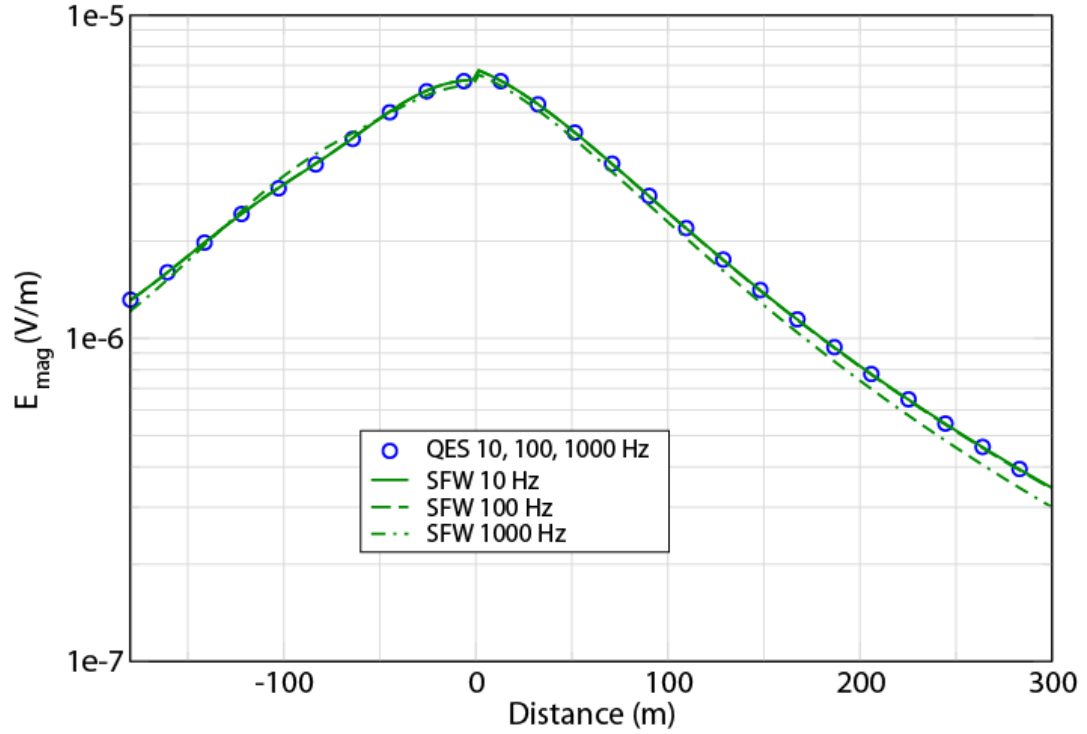


Figure 3.2: Scenario 2.

For the third scenario we will keep the source configuration the same as from the second scenario but change the observation path to be offset and transverse according to $P1$ and $P2$ from Table 3.2. These results are seen in Figure 3.3. We see that the QES predicts the SFW solution very accurately for all distances at 10 Hz. When the frequency is increased to 100 Hz we see slight divergence from the SFW solutions for larger distances. When the frequency is 1000 Hz we see that the QES can only predict accurate fields for very near observations and becomes significantly inaccurate for larger distances. In conclusion, the QES solution can only predict the SFW at low frequencies of 10 Hz and when frequency is increased to 1,000 Hz the QES region of validity is less than 250 m. The QES solution is not a valid simulation tool for the 100 and 1000 Hz frequencies.

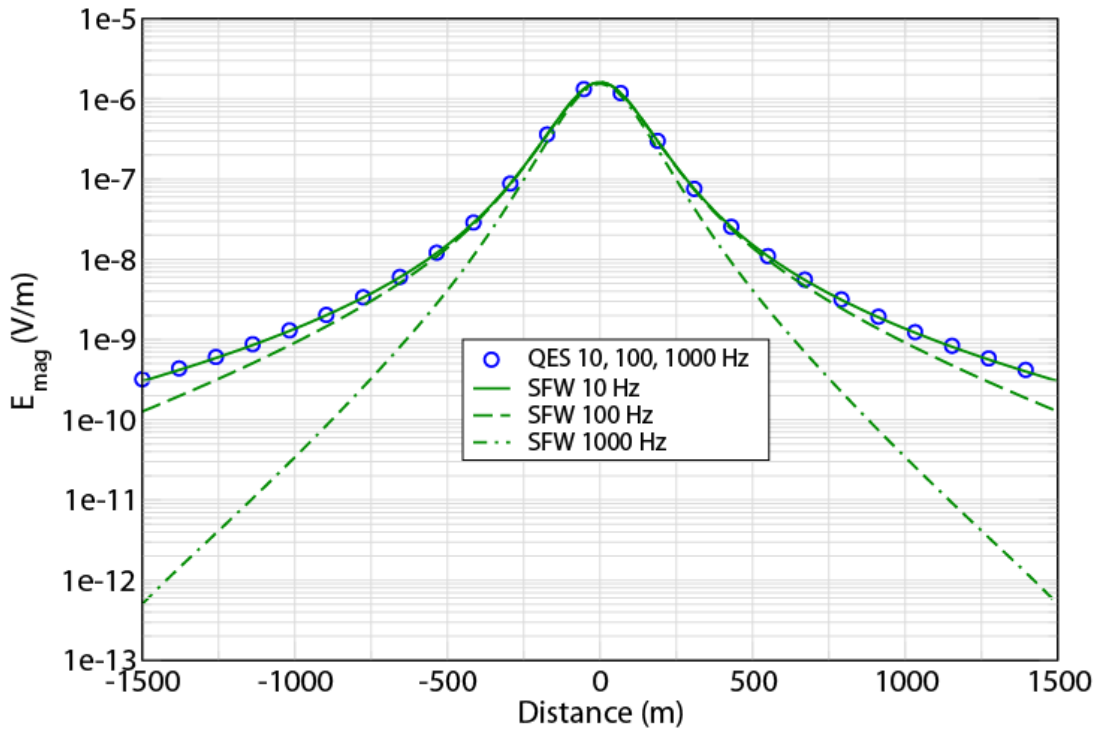


Figure 3.3: Scenario 3.

The final scenario of interest in this section is scenario four. Here we will place the source in air and also observe the fields in air according to Table 3.2. We notice from Figure 3.4 that the QES and the SFW predicts the exact same field for all three frequencies and for all distances shown. The reason we see this effect in air is that the conductivity value for air is zero. This means that the field in air naturally behaves statically and no wave-like phenomena are introduced by the lack of conductivity, unlike sources and observations in water. We see that the QES solution is valid for larger frequencies and distances when observations in air are made.

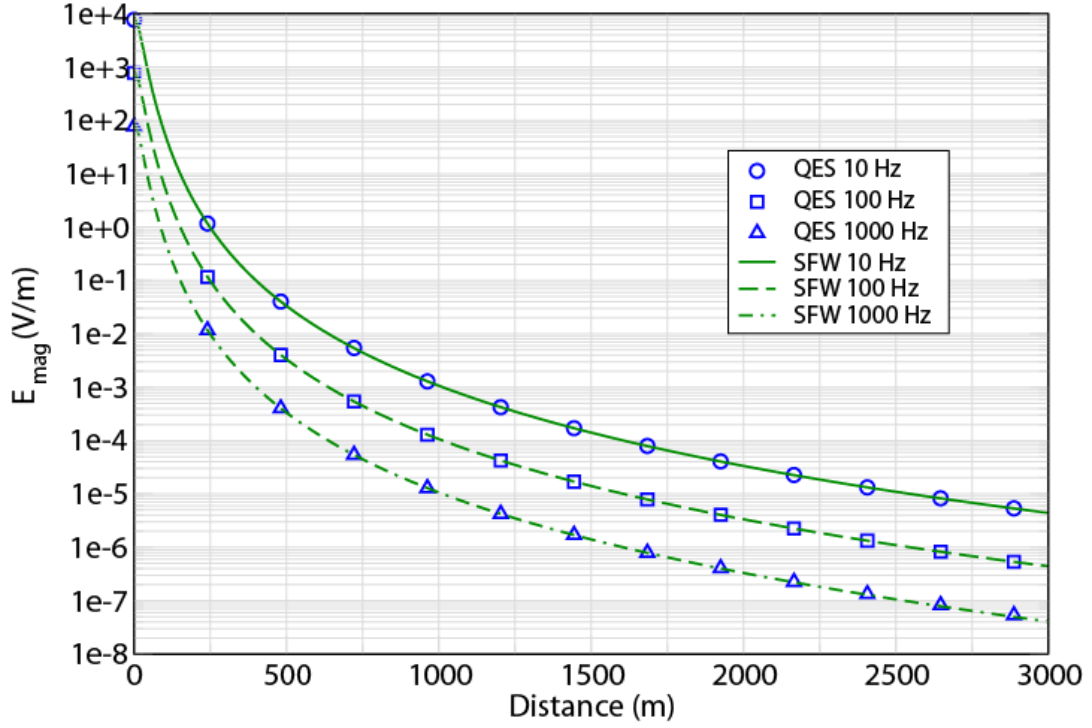


Figure 3.4: Scenario 4.

In conclusion from the above scenarios we see that the QES is a viable solution for the three layered problem when frequencies and observation distances are made small (i.e. 10 Hz for a region of validity of about 745 m in water) or when observations are made in air.

3.2 Up-Over-Down Comparisons

In this section we will examine how the Up-Over-Down (UOD) approximation compares to the QES approximation and the SFW. The UOD approximation is obtained by deforming the integration contour of the Sommerfeld integral about the lower half plane such that it encompasses the branch cuts and poles of the Sommerfeld integrand, as shown in Figure 3.5. A careful analysis reveals that the integration about the contour associated with k_1 yields a weaker field than that of k_2 ; the integration about the pole also yields a negligible field. For a y -directed dipole the dominant field component in water is E_x , which is transverse to the dipole and hence is the component to measure or detect in an application problem. For

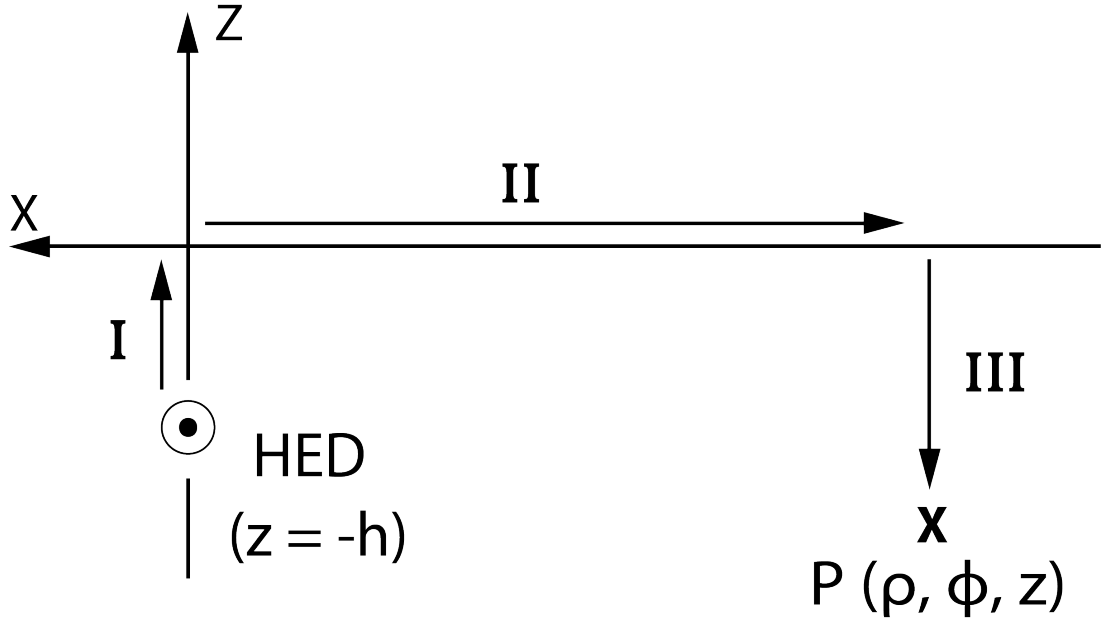


Figure 3.6: Ray-optic depiction.

The QES E_x approximation for the UOD scenario described above is given by Eqn. (2.101) and the SFW is given by Eqn. 3.30. Let us now numerically compare the UOD, QES and the SFW. First we will assume a 2-layer QES and SFW geometry by making region 3 the same material parameters as regions 2 for an equivalent comparison. For this scenario we will let the frequency be 1000 Hz, the depth of the dipole in water be 30 m and the observation line be in water at depth of 20 m. Region properties are given according to Table 3.1, excluding the third layer. The results are shown in Figure 3.7. We can see that the three completely different equations yield identical results for this scenario. It is of interest to add a third layer to the QES and SFW models to see the impact of the third layer. Let the water layer be 25 m deep and region 3 material properties be that of Table 3.1. Also let the dipole be located at a depth of 15 m in water and the observation line be located at a depth of 15 m in water. Figure 3.8 shows the results for this simulation. We see that the QES and the SFW correlate well each other while there is a large inaccuracy associated with the UOD. It is clear from this scenario that the third layer plays a significant role on the field strength.

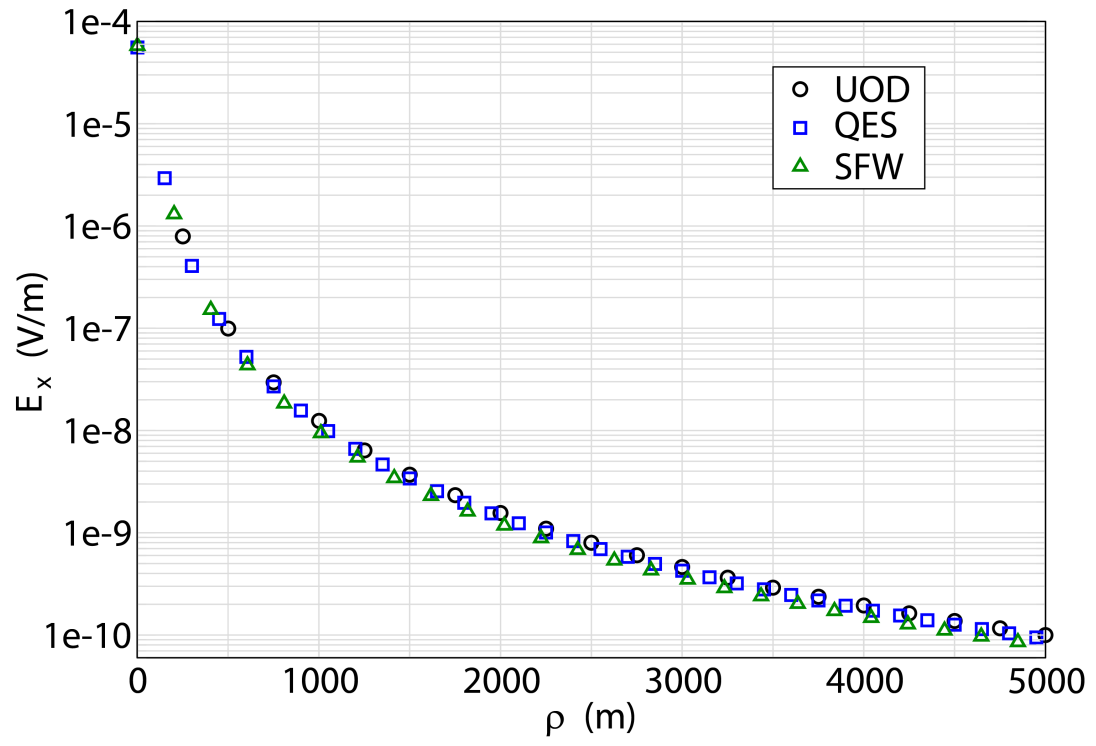


Figure 3.7: UOD 2 layer.

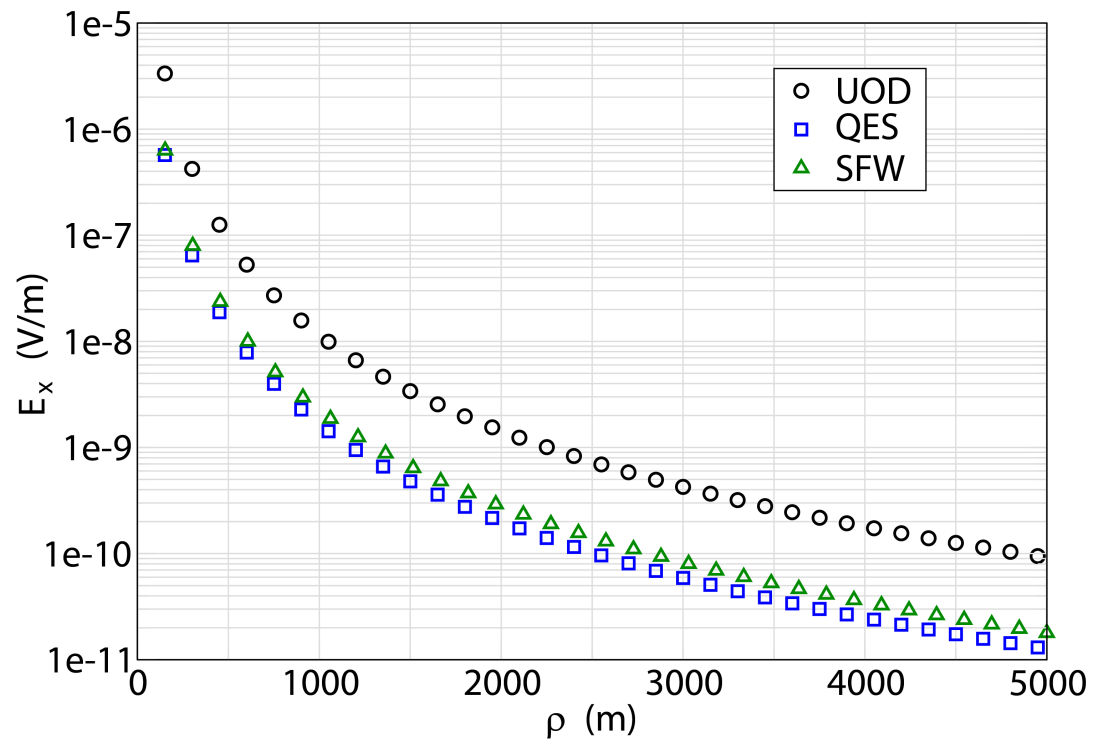


Figure 3.8: UOD 3 layer.

3.3 Sommerfeld Full-Wave (SFW) Case Study

In the following development, the Sommerfeld Full-Wave (SFW) analytical solution for an infinitesimal vertical dipole of moment Idl in region 1 will be considered. Observation locations in regions 1 and 2 are of primary interest. These solutions will be analysed and manipulated to reveal their relationships with a vertical two-charge QES configuration. Note that because of existence of two unique solution types (i.e QES and SFW), all equations specific to this analysis will be marked with a prime (') to ensure no confusion. To begin the analysis we will postulate the magnetic vectors potentials for each region as follows [9],

$$A'_{z1} = \frac{Idl}{4\pi} \int_0^\infty \left[e^{-ju_1|z-h|} + R' e^{-ju_1(z+h)} \right] \frac{J_0(\lambda\rho)}{ju_1} \lambda d\lambda, \quad (3.2)$$

$$A'_{z2} = \frac{Idl}{4\pi} \int_0^\infty \left[A' e^{-ju_2z} + B' e^{ju_2z} \right] e^{-ju_1h} \frac{J_0(\lambda\rho)}{ju_1} \lambda d\lambda, \quad (3.3)$$

and

$$A'_{z3} = \frac{Idl}{4\pi} \int_0^\infty T' e^{ju_3z} e^{-ju_1h} \frac{J_0(\lambda\rho)}{ju_1} \lambda d\lambda \quad (3.4)$$

where,

$$u_i = \sqrt{k_i^2 - \lambda^2} \quad (3.5)$$

and the wave number for a specific region ($i = 1, 2, 3$) is

$$k_i = \sqrt{-j\omega\mu Y_i}. \quad (3.6)$$

The magnetic vector potential is defined by $\mathbf{H} = \nabla \times \mathbf{A}$. A special note is made that the imaginary part in Eqns. (3.5) and (3.6) must be less than zero for decaying waves. The boundary conditions require that E'_ρ and H'_ϕ be continuous across each interface. The components can be calculated using [12],

$$E'_\rho = \frac{1}{Y} \frac{\partial^2 A'_z}{\partial z \partial \rho} \quad (3.7)$$

and

$$H'_\phi = -\frac{\partial A'_z}{\partial \rho}. \quad (3.8)$$

Applying the boundary conditions at $z = 0$ and $z = -d$, we obtain a set of four equations and four unknowns:

$$1 - R' = (B' - A') \frac{Y_1 u_2}{Y_2 u_1}, \quad (3.9)$$

$$B' e^{-ju_2 d} - A' e^{ju_2 d} = T' e^{-ju_3 d} \frac{Y_2 u_3}{Y_3 u_2}, \quad (3.10)$$

$$1 + R' = A' + B', \quad (3.11)$$

and

$$A' e^{ju_2 d} + B' e^{-ju_2 d} = T' e^{-ju_3 d}. \quad (3.12)$$

The four unknowns, A' , B' , R' and T' , are algebraically found to be

$$A' = \frac{-(1 + R'_{21}) R'_{23} e^{-j2u_2 d}}{1 - R'_{21} R'_{23} e^{-j2u_2 d}}, \quad (3.13)$$

$$B' = \frac{1 + R'_{21}}{1 - R'_{21} R'_{23} e^{-j2u_2 d}}, \quad (3.14)$$

$$R' = \frac{R'_{21} - R'_{23} e^{-j2u_2 d}}{1 - R'_{21} R'_{23} e^{-j2u_2 d}}, \quad (3.15)$$

and

$$T' = \frac{(1 + R'_{21})(1 - R'_{23}) e^{-j(u_2 - u_3)d}}{1 - R'_{21} R'_{23} e^{-j2u_2 d}}, \quad (3.16)$$

where the interfacial reflection coefficients are given by

$$R'_{21} = \frac{Y_2 u_1 - Y_1 u_2}{Y_2 u_1 + Y_1 u_2} \quad (3.17)$$

and

$$R'_{23} = \frac{Y_2 u_3 - Y_3 u_2}{Y_3 u_2 + Y_2 u_3}. \quad (3.18)$$

The electric scalar potential in each region is determined using the Lorenz gauge condition, namely

$$V' = -\frac{\nabla \cdot \mathbf{A}'}{Y} = -\frac{1}{Y} \frac{\partial A'_z}{\partial z}. \quad (3.19)$$

Region potentials are thus given as follows,

$$V'_1 = \frac{Idl}{4\pi Y_1} \int_0^\infty \left[e^{-ju_1|z-h|} + R' e^{-ju_1(z+h)} \right] J_0(\lambda \rho) \lambda d\lambda \quad (3.20)$$

and

$$V'_2 = \frac{Idl}{4\pi Y_2} \int_0^\infty \left[A' e^{-ju_2 z} - B' e^{ju_2 z} \right] e^{-ju_1 h} \frac{u_2}{u_1} J_0(\lambda \rho) \lambda d\lambda. \quad (3.21)$$

The electric field in each region can be determined by,

$$\begin{aligned} \mathbf{E}' &= -j\omega\mu\mathbf{A}' - \nabla V' \\ &= j\omega\mu A'_z \hat{\mathbf{a}}_z - \left(\frac{\partial V'}{\partial x} \hat{\mathbf{a}}_x + \frac{\partial V'}{\partial y} \hat{\mathbf{a}}_y + \frac{\partial V'}{\partial z} \hat{\mathbf{a}}_z \right). \end{aligned} \quad (3.22)$$

In terms of field components,

$$E'_x = -\frac{\partial V'}{\partial x}, \quad (3.23)$$

$$E'_y = -\frac{\partial V'}{\partial y}, \quad (3.24)$$

and

$$E'_z = \left(-j\omega\mu A'_z - \frac{\partial V'}{\partial z} \right). \quad (3.25)$$

When we compute Eqns. (3.23) - (3.25) in accordance with Eqns. (3.2) and (3.20) we obtain the following field equations for region 1,

$$E'_x = \frac{Idl}{4\pi Y_1} \frac{x}{\rho} \int_0^\infty \left[\text{sgn}(z-h)e^{-ju_1|z-h|} + R'e^{-ju_1(z+h)} \right] J_1(\lambda\rho)\lambda^2 d\lambda, \quad (3.26)$$

$$E'_y = \frac{Idl}{4\pi Y_1} \frac{y}{\rho} \int_0^\infty \left[\text{sgn}(z-h)e^{-ju_1|z-h|} + R'e^{-ju_1(z+h)} \right] J_1(\lambda\rho)\lambda^2 d\lambda, \quad (3.27)$$

and

$$E'_z = \frac{Idl}{4\pi Y_1} \int_0^\infty \left[e^{-ju_1|z-h|} + R'e^{-ju_1(z+h)} \right] \frac{J_0(\lambda\rho)}{ju_1} \lambda^3 d\lambda. \quad (3.28)$$

where,

$$\text{sgn}(x) = \begin{cases} -1 & \text{if } x < 0, \\ 1 & \text{if } x > 0. \end{cases} \quad (3.29)$$

For region 2, we compute Eqns. (3.23) - (3.25) in accordance with Eqns. (3.3) and (3.21) to get,

$$E'_x = \frac{Idl}{4\pi Y_2} \frac{x}{\rho} \int_0^\infty \left[A'e^{-ju_2z} - B'e^{ju_2z} \right] e^{-ju_1h} \frac{u_2}{u_1} J_1(\lambda\rho)\lambda^2 d\lambda, \quad (3.30)$$

$$E'_y = \frac{Idl}{4\pi Y_2} \frac{y}{\rho} \int_0^\infty \left[A'e^{-ju_2z} - B'e^{ju_2z} \right] e^{-ju_1h} \frac{u_2}{u_1} J_1(\lambda\rho)\lambda^2 d\lambda, \quad (3.31)$$

and

$$E'_z = \frac{Idl}{4\pi Y_2} \int_0^\infty \left[A'e^{-ju_2z} + B'e^{ju_2z} \right] e^{-ju_1h} \frac{J_0(\lambda\rho)}{ju_1} \lambda^3 d\lambda. \quad (3.32)$$

3.3.1 QES vs SFW Scalar Potential Integrals

We now examine how the QES potential integrals relate to the SFW scalar potential integrals for observations in regions 1 or 2. For region 1 observations, we begin with the QES and SFW

potential integrals given by Eqns. (2.23) and (3.20). We will decomposed each potential into two parts for simplicity. For the QES single electric charge solution let

$$V_1 = V_{1a} + V_{1b} \quad (3.33)$$

and for the SFW electric dipole solution let

$$V'_1 = V'_{1a} + V'_{1b}. \quad (3.34)$$

Each specific integral is given by,

$$V_{1a} = \frac{jwq}{4\pi Y_1} \int_0^\infty e^{-\lambda|z-h|} J_0(\lambda\rho) d\lambda, \quad (3.35)$$

$$V_{1b} = \frac{jwq}{4\pi Y_1} \int_0^\infty R e^{-\lambda(z+h)} J_0(\lambda\rho) d\lambda, \quad (3.36)$$

$$V'_{1a} = \frac{Idl}{4\pi Y_1} \int_0^\infty e^{-ju_1|z-h|} J_0(\lambda\rho) \lambda d\lambda, \quad (3.37)$$

and

$$V'_{1b} = \frac{Idl}{4\pi Y_1} \int_0^\infty R' e^{-ju_1(z+h)} J_0(\lambda\rho) \lambda d\lambda. \quad (3.38)$$

Figure 2.10a illustrates the QES charge placement for a vertical QES dipole. The QES charges are separated by a distance dl with its center located at $z = h$. The vertical electric SFW infinitesimal dipole is depicted by an upward pointing arrow and is located at a height $z = h$. To construct the QES, the two opposite charges must be superimposed together. The total potential of the QES dipole is defined as V_{1T} , where $V_{1T} = V_{1A} + V_{1B}$. From Eqns. (3.35) and (3.36),

$$\begin{aligned} V_{1A} &= V_{1a}^+ - V_{1a}^- \\ &= \frac{jwq}{4\pi Y_1} \int_0^\infty e^{-\lambda|z-z_2|} J_0(\lambda\rho) d\lambda - \frac{jwq}{4\pi Y_1} \int_0^\infty e^{-\lambda|z-z_1|} J_0(\lambda\rho) d\lambda \end{aligned} \quad (3.39)$$

and

$$\begin{aligned} V_{1B} &= V_{1b}^+ - V_{1b}^- \\ &= \frac{jwq}{4\pi Y_1} \int_0^\infty R e^{-\lambda(z+z_2)} J_0(\lambda\rho) d\lambda - \frac{jwq}{4\pi Y_1} \int_0^\infty R e^{-\lambda(z+z_1)} J_0(\lambda\rho) d\lambda. \end{aligned} \quad (3.40)$$

Figure 2.10 shows that $z_2 = dl + z_1$. We now substitute z_2 into the previous equations and let $z > z_1, z_2$ and factor to yield

$$V_{1A} = \frac{jwq}{4\pi Y_1} \int_0^\infty e^{-\lambda z} e^{\lambda(\frac{dl}{2} + z_1)} \left(e^{\lambda\frac{dl}{2}} - e^{-\lambda\frac{dl}{2}} \right) J_0(\lambda\rho) d\lambda \quad (3.41)$$

and

$$V_{1B} = \frac{jwq}{4\pi Y_1} \int_0^\infty Re^{-\lambda z} e^{-\lambda(\frac{dl}{2} + z_1)} \left(e^{-\lambda\frac{dl}{2}} - e^{\lambda\frac{dl}{2}} \right) J_0(\lambda\rho) d\lambda. \quad (3.42)$$

To reduce the exponential difference terms, we make use of the following Taylor expansion,

$$e^x = 1 + x + \frac{x^2}{2!} + \frac{x^3}{3!} + \dots \quad \text{for } \forall x. \quad (3.43)$$

Applying this expansion, we obtain

$$e^{\lambda\frac{dl}{2}} - e^{-\lambda\frac{dl}{2}} \approx 1 + \frac{\lambda dl}{2} - \left(1 - \frac{\lambda dl}{2} \right) = \lambda dl. \quad (3.44)$$

We now let physical separation of the charges collapse to zero. Then $dl \rightarrow 0$, $e^{\pm\lambda\frac{dl}{2}} \rightarrow 1$ and $z_1 \rightarrow h$ so that,

$$V_{1A} = \frac{jwqdl}{4\pi Y_1} \int_0^\infty e^{-\lambda z} e^{\lambda h} J_0(\lambda\rho) \lambda d\lambda \quad (3.45)$$

and

$$V_{1B} = -\frac{jwqdl}{4\pi Y_1} \int_0^\infty Re^{-\lambda z} e^{-\lambda h} J_0(\lambda\rho) \lambda d\lambda. \quad (3.46)$$

The electric current in the frequency domain is given as,

$$I = j\omega q, \quad (3.47)$$

in which case

$$V_{1A} = \frac{Idl}{4\pi Y_1} \int_0^\infty e^{-\lambda(z-h)} J_0(\lambda\rho) \lambda d\lambda \quad (3.48)$$

$$V_{1B} = -\frac{Idl}{4\pi Y_1} \int_0^\infty Re^{-\lambda(z+h)} J_0(\lambda\rho) \lambda d\lambda. \quad (3.49)$$

A similar analysis can be provided for $z < z_1, z_2$. Therefore, combining all of our previous subresults, we conclude that the potential of the infinitesimal, vertically oriented, quasi-static electric dipole in region 1, where the total potential is $V_{1T} = V_{1A} + V_{1B}$ is given by

$$V_{1T} = \frac{Idl}{4\pi Y_1} \int_0^\infty [e^{-\lambda|z-h|} - Re^{-\lambda(z+h)}] J_0(\lambda\rho) \lambda d\lambda. \quad (3.50)$$

Here R is given by Eqn. (2.33). By similar analytical steps, it follows that for region 2 observations,

$$V_{2T} = -\frac{Idl}{4\pi Y_1} \int_0^\infty [Ae^{-\lambda(z+h)} + Be^{\lambda(z-h)}] J_0(\lambda\rho) \lambda d\lambda, \quad (3.51)$$

where A and B are given by Eqns. (2.34) and (2.35). These two previous results are consistent with the following relationships:

$$\begin{aligned} V^{dipole} &= -dl \frac{dV^{single}}{dz} && \text{for a direct term} \\ &= +dl \frac{dV^{single}}{dz} && \text{for a reflected term,} \end{aligned} \quad (3.52)$$

where V^{dipole} and V^{single} are the dipole and single charge potentials, and dl is the charge separation. A direct term refers to the charge when there is a direct path between it and the observer, the reflected term refers to the charge when there is a interface between it and the observer.

We are now at the point where we can see the relationship with the SFW solution. We take Eqns. (3.37) and (3.38) and force the condition that $\omega \rightarrow 0$. In this case Eqn. (3.5) for each region is given as,

$$u_1, u_2 \Big|_{\omega \rightarrow 0} \approx -j\lambda. \quad (3.53)$$

When this is applied to Eqns. (3.37) and (3.38), the SFW potential reduces to the QES potential of Eqns. (3.48) and (3.49) repectivley. Specifically,

$$V'_{1a} = \frac{Idl}{4\pi Y_1} \int_0^\infty e^{-\lambda|z-h|} J_0(\lambda\rho) \lambda d\lambda \quad (3.54)$$

and

$$V'_{1b} = \frac{Idl}{4\pi Y_1} \int_0^\infty R'_0 e^{-\lambda(z+h)} J_0(\lambda\rho) \lambda d\lambda \quad (3.55)$$

where,

$$R'_0 = R' \Big|_{\omega \rightarrow 0} = -R. \quad (3.56)$$

Similarly for observations in region 2,

$$V'_{2a} = \frac{Idl}{4\pi Y_2} \int_0^\infty A'_0 e^{-\lambda(z+h)} J_0(\lambda\rho) \lambda d\lambda \quad (3.57)$$

and

$$V'_{2b} = -\frac{Idl}{4\pi Y_2} \int_0^\infty B'_0 e^{\lambda(z-h)} J_0(\lambda\rho) \lambda d\lambda \quad (3.58)$$

where,

$$A'_0 = A' \Big|_{\omega \rightarrow 0} = -\frac{Y_2}{Y_1} A \quad (3.59)$$

and

$$B'_0 = B' \Big|_{\omega \rightarrow 0} = \frac{Y_2}{Y_1} B. \quad (3.60)$$

Therefore, when $\omega \rightarrow 0$, the full-wave scalar potential V'_1 for the vertical electric dipole in region 1 is given by the superposition of Eqns. (3.54) and (3.55):

$$V'_1 = \frac{Idl}{4\pi Y_1} \int_0^\infty \left[e^{-\lambda|z-h|} + R'_0 e^{-\lambda(z+h)} \right] J_0(\lambda\rho) \lambda d\lambda \quad (3.61)$$

and from Eqns. (3.57) and (3.58),

$$V'_2 = \frac{Idl}{4\pi Y_2} \int_0^\infty \left[A'_0 e^{-\lambda(z+h)} - B'_0 e^{\lambda(z-h)} \right] J_0(\lambda\rho) \lambda d\lambda. \quad (3.62)$$

Given R'_0 , A'_0 and B'_0 per Eqns. (3.56), (3.59) and (3.60), we conclude that $V_{1T} = V'_1$ and $V_{2T} = V'_2$ when the QES dipole is of infinitesimal size and when the SFW solution is examined when $\omega \rightarrow 0$; see Eqns. (3.50), (3.51), (3.61), (3.62).

3.3.2 QES vs SFW Potential Summations

In this section we will take the SFW potential solution for the VED in region 1 and examine the potential's integrand in its asymptotic form as $\lambda \rightarrow \infty$, which is equivalent to letting $\omega \rightarrow 0$ per quasi-electrostatic arguments. We begin with Eqn. (3.20). Let I_1 equal the integrand so that,

$$I_1 = e^{-ju_1|z-h|} + R' e^{-ju_1(z+h)}. \quad (3.63)$$

By letting $\lambda \rightarrow \infty$, we see that the limiting form of I_1 is revealed:

$$\begin{aligned} I_{1\infty} = I_1 \Big|_{\lambda \rightarrow \infty} &\approx e^{-\lambda|z-h|} + R'_0 e^{-\lambda(z+h)} \\ &= e^{-\lambda|z-h|} - R e^{-\lambda(z+h)}. \end{aligned} \quad (3.64)$$

Now add and subtract $I_{1\infty}$ to Eqn. (3.20), in which case

$$V'_1 = \frac{Idl}{4\pi Y_1} \int_0^\infty [I_1 - I_{1\infty}] J_0(\lambda\rho) \lambda d\lambda + \frac{Idl}{4\pi Y_1} \int_0^\infty I_{1\infty} J_0(\lambda\rho) \lambda d\lambda. \quad (3.65)$$

Clearly, the second integral represents the quasi-static portion of the full-wave solution; the first integral retains wave-like effects. If we use the expression for R , i.e. Eqn. (2.33), and the Taylor series expansion of Eqn. (2.47), we can again integrate term-by-term. When we do so, we obtain

$$V_1' = \frac{Idl}{4\pi Y_1} \int_0^\infty [I_1 - I_{1\infty}] J_0(\lambda\rho) \lambda d\lambda + V_{1T}. \quad (3.66)$$

Here

$$V_{1T} = \frac{Idl}{4\pi Y_1} \left\{ \frac{z_s}{r^3} + \sum_{n=0}^\infty R_{21}^n R_{23}^n \left[\frac{R_{23} D_1}{r_a^3} + \frac{R_{21} D_2}{r_b^3} \right] \right\} \quad (3.67)$$

where Eqns. (2.42) - (2.44) and (2.51) - (2.54) were used. This V_{1T} is of course the image representation of the integral equation representing the full-wave potential when $\omega \rightarrow 0$ given in Eqn. (3.61).

Likewise for V_2' ,

$$V_2' = \frac{Idl}{4\pi Y_2} \int_0^\infty [I_2 - I_{2\infty}] J_0(\lambda\rho) \lambda d\lambda + V_{2T} \quad (3.68)$$

where

$$V_{2T} = \frac{Idl}{4\pi Y_1} (1 - R_{21}) \sum_{n=0}^\infty R_{21}^n R_{23}^n \left[\frac{R_{23} D_1}{r_a^3} + \frac{D_3}{r_c^3} \right], \quad (3.69)$$

$$I_2 = \left[A' e^{-ju_2 z} - B' e^{ju_2 z} \right] e^{-ju_1 h \frac{u_2}{u_1}}, \quad (3.70)$$

and

$$\begin{aligned} I_{2\infty} = I_2 \Big|_{\lambda \rightarrow \infty} &\approx A_0' e^{-\lambda(z+h)} - B_0' e^{-\lambda(h-z)} \\ &= -A e^{-\lambda(z+h)} - B e^{-\lambda(h-z)}. \end{aligned} \quad (3.71)$$

Again V_{2T} in the above summation is the image representation of the integral given by Eqn. (3.62).

In summary, the full-wave potentials are given by the integrals of Eqns. (3.20) and (3.21). When the low frequency asymptotic form of the integrands of these equations is subtracted from, and then added back to the integrands per Eqns. (3.66) and (3.68), it can be represented in terms of QES dipole images per Eqns. (3.67) and (3.69). The remaining integrands are then rapidly convergent for low frequency analysis. Its thus apparent that the QES solution is valid when

$$\left| \frac{V_1' - V_{1T}}{V_{1T}} \right| \ll 1, \quad (3.72)$$

where V_{1T} is the infinitesimal QES dipole image solution, i.e. Eqn. (3.67) and V_1' is the exact, full-wave scalar potential solution for an electric dipole. For region 2, a similar expression is given

$$\left| \frac{V_2' - V_{2T}}{V_{2T}} \right| \ll 1. \quad (3.73)$$

Simulations were performed using the material characteristics according to Table 3.1. Region 1 is air, region 2 is water and region 3 is mud. For all practical purposes, observations in air, according to Eqns. (2.50), (3.67) and (3.20) are identical for frequencies up to 1000 Hz and for a small dipole separation of 1 m. There is very little wave-like phenomena in the air for these frequency ranges. Figure 3.9 shows results in water. For observations in water, a large divergence is seen between Eqns. (2.63) and (3.69) and Eqn. (3.21), particularly as frequency increases.

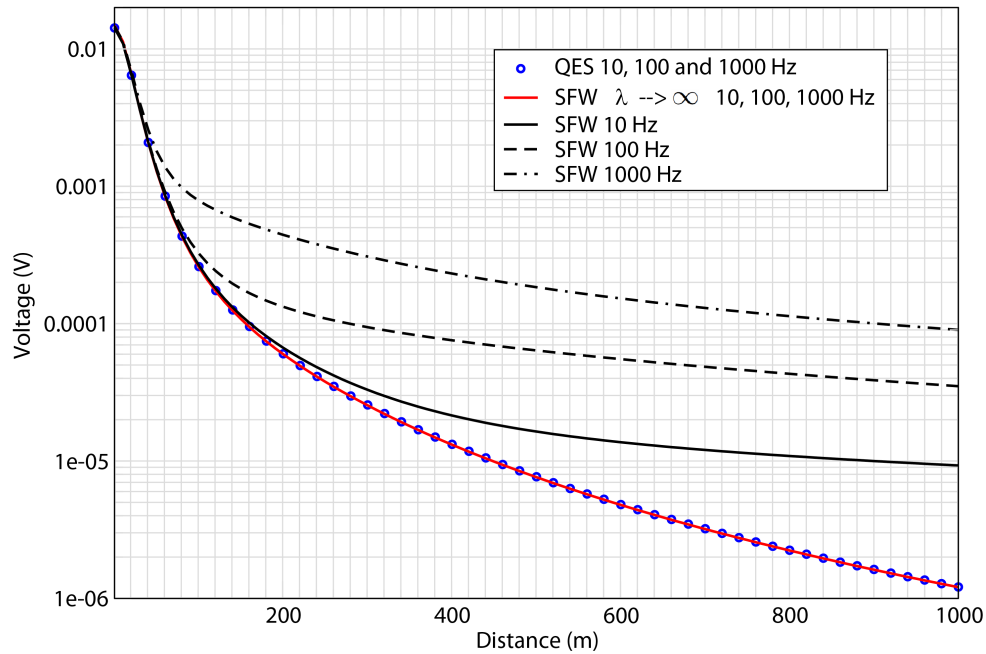


Figure 3.9: Comparison of Eqns. (2.63), (3.69) and (3.21) for observations in water.

Lets now examine the QES range of validity by examining Eqns. (3.72) and (3.73). Assume a vertical electric dipole source located in air at a height of $z = 5$ m with a dipole

moment of 1 A-m. For observations in air, an x -directed horizontal observation line will be placed at a height of $z = 15$ m and for observations in water at a depth of $z = -15$ m. Refer to Figures 3.10 and 3.11 where Eqns. (3.72) and (3.73) are plotted for the above scenarios. It can be seen in Figure 3.10 that the numerical value of Eqn. (3.72) is much smaller than one for all frequencies and for a radial distance between sensor and source of 5 km. We conclude that the QES region of validity can be as large as 5 km for ELF frequencies when observations are made in air. Let's now observe Eqn. (3.73) for the above described scenario. In Figure 3.11, the numerical value of Eqn. (3.73) quickly becomes close to unity or greater when viewed along the horizontal sweep line. It is important to state that the region of validity is a subjective term that is defined by a small number. For purposes of discussion, let 0.1 mark the point when QES is no longer valid. At 10 Hz, the value of Eqn. (3.73) reaches 0.1 at a radial observation distance of about 350 m; at 100 Hz the distance about 100 m and at 1,000 Hz the QES region of validity is less than 50 m. It is concluded that the region of validity is based upon regional conductivity, operational frequency and the absolute observation distance between sensor and source.

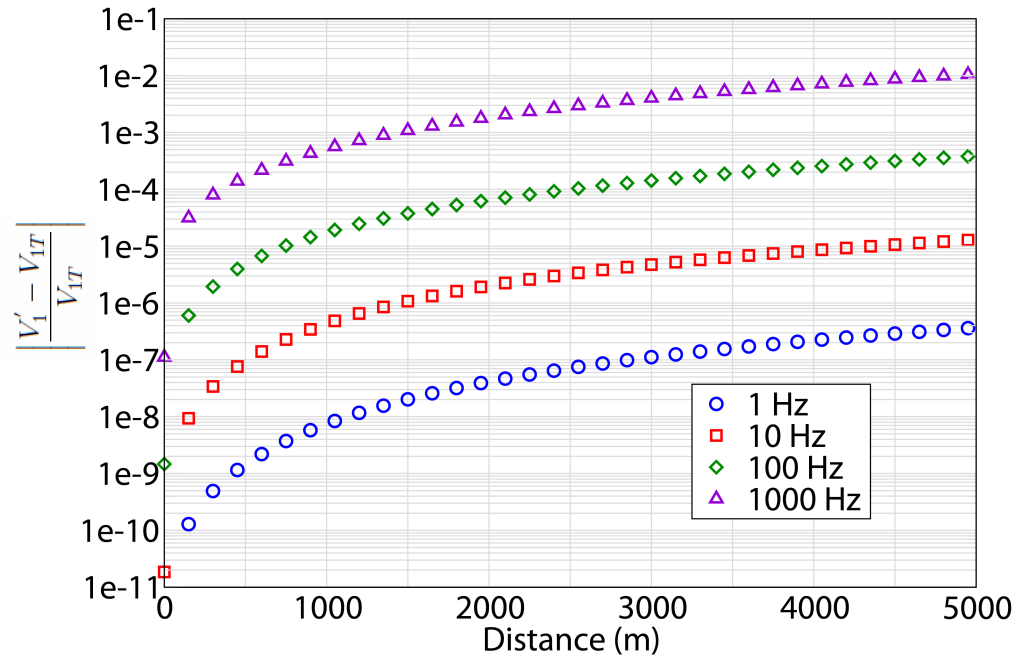


Figure 3.10: QES region of validity per Eqn. (3.72) where $h = 5$ m, $z = 15$ m.

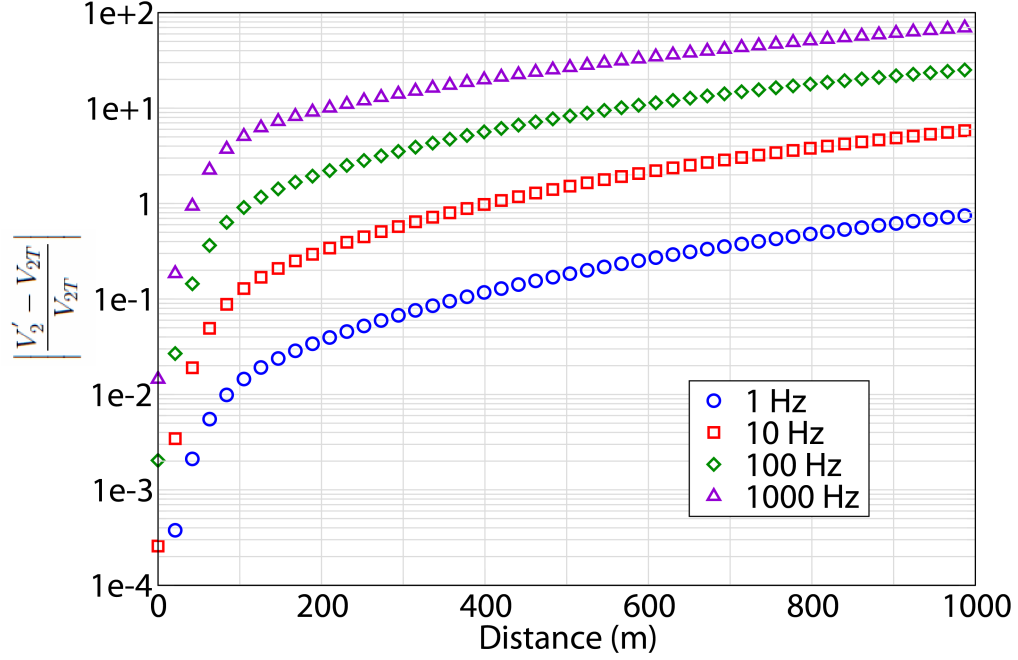


Figure 3.11: QES region of validity per Eqn. (3.73) where $h = 5$ m, $z = -5$ m.

3.3.3 Quasi-Magnetostatic (QMS) Contribution

In this section we reduce the SFW magnetic vector potential to expose the quasi-magnetostatic contribution. To determine the QMS solution we need to examine A'_z when $\lambda \rightarrow \infty$, which is equivalent to $\omega \rightarrow 0$. For observations in region 1, Eqn. (3.2) will be considered first. To do this, we will perform the following addition and subtraction:

$$A'_{z1} = \frac{Idl}{4\pi} \int_0^\infty [L_1 - L_{1\infty}] J_0(\lambda\rho) \lambda d\lambda + \frac{Idl}{4\pi} \int_0^\infty L_{1\infty} J_0(\lambda\rho) \lambda d\lambda \quad (3.74)$$

where,

$$L_1 = \left(e^{-ju_1|z-h|} + R' e^{-ju_1(z+h)} \right) \frac{1}{ju_1} \quad (3.75)$$

and

$$L_{1\infty} = L_1 \Big|_{\lambda \rightarrow \infty} \approx \left(e^{-\lambda|z-h|} + R'_0 e^{-\lambda(z+h)} \right) \frac{1}{\lambda}, \quad (3.76)$$

where R'_0 is given by Eqn. (3.56). The latter integral in Eqn. (3.74) is of most importance and will be defined as

$$A'_{z1\infty} = \frac{Idl}{4\pi} \int_0^\infty L_{1\infty} J_0(\lambda\rho) \lambda d\lambda. \quad (3.77)$$

Inserting Eqn. (3.76) into Eqn. (3.77), applying the Taylor series expansion of Eqn. (2.47) and the integral identity of Eqn. (2.49), we arrive at an image expression given by,

$$A'_{z1\infty} = \frac{Idl}{4\pi} \left\{ \frac{1}{r} + \sum_{n=0}^{\infty} R_{23}^n R_{21}^n \left[\frac{R_{21}}{r_b} - \frac{R_{23}}{r_a} \right] \right\}. \quad (3.78)$$

Now we can see that,

$$A'_{z1} = \frac{Idl}{4\pi} \int_0^\infty [L_1 - L_{1\infty}] J_0(\lambda\rho) \lambda d\lambda + A'_{z1\infty}. \quad (3.79)$$

The total electric field in region 1 according to Eqn. (3.22) is specified by Eqns. (3.66), (3.79) given by

$$\begin{aligned} \mathbf{E}'_1 = & -j\omega\mu A'_{z1\infty} \hat{\mathbf{a}}_z - \nabla V'_{1T} - \frac{Idl}{4\pi Y_1} \nabla \int_0^\infty [I_1 - I_{1\infty}] J_0(\lambda\rho) \lambda d\lambda \\ & - \frac{j\omega\mu Idl}{4\pi} \hat{\mathbf{a}}_z \int_0^\infty [L_1 - L_{1\infty}] J_0(\lambda\rho) \lambda d\lambda. \end{aligned} \quad (3.80)$$

The magnetic field components are given by

$$\mathbf{H} = \nabla \times \mathbf{A} \quad (3.81)$$

and for region 1 observations

$$\mathbf{H}'_1 = \nabla \times (A'_{z1\infty} \hat{\mathbf{a}}_z) + \frac{Idl}{4\pi} \nabla \times \left[\hat{\mathbf{a}}_z \int_0^\infty [L_1 - L_{1\infty}] J_0(\lambda\rho) \lambda d\lambda \right]. \quad (3.82)$$

For observation in region 2 we define the integral terms from Eqn. (3.3) as follows,

$$L_2 = \left(A' e^{-ju_2 z} + B' e^{ju_2 z} \right) \frac{e^{-ju_1 h}}{ju_1} \quad (3.83)$$

and

$$L_{2\infty} = \left(A'_0 e^{-\lambda z} + B'_0 e^{\lambda z} \right) \frac{e^{-\lambda h}}{\lambda}. \quad (3.84)$$

A similar procedure is taken from that of Eqn. (3.78) to get,

$$A'_{z2\infty} = \frac{Idl Y_2}{4\pi Y_1} (1 - R_{21}) \sum_{n=0}^{\infty} R_{23}^n R_{21}^n \left[\frac{R_{23}}{r_a} - \frac{1}{r_c} \right]. \quad (3.85)$$

Now we see that,

$$A'_{z2} = \frac{Idl}{4\pi} \int_0^\infty [L_2 - L_{2\infty}] J_0(\lambda\rho) \lambda d\lambda + A'_{z2\infty}. \quad (3.86)$$

The total electric and magnetic fields in region 2 are

$$\begin{aligned} \mathbf{E}'_2 = & -j\omega\mu A'_{z2\infty} \hat{\mathbf{a}}_z - \nabla V'_{2T} - \frac{Idl}{4\pi Y_1} \nabla \int_0^\infty [I_2 - I_{2\infty}] J_0(\lambda\rho) \lambda d\lambda \\ & - \frac{j\omega\mu Idl}{4\pi} \hat{\mathbf{a}}_z \int_0^\infty [L_2 - L_{2\infty}] J_0(\lambda\rho) \lambda d\lambda \end{aligned} \quad (3.87)$$

and

$$\mathbf{H}'_2 = \nabla \times (A'_{z2\infty} \hat{\mathbf{a}}_z) + \frac{Idl}{4\pi} \nabla \times \left[\hat{\mathbf{a}}_z \int_0^\infty [L_2 - L_{2\infty}] J_0(\lambda\rho) \lambda d\lambda \right]. \quad (3.88)$$

As with the QES region of validity as specified by Eqns. (3.10) and (3.11), we see that the QMS region of validity in region 1 is given by

$$\left| \frac{A'_{z1} - A'_{z1\infty}}{A'_{z1\infty}} \right| \ll 1 \quad (3.89)$$

and for region 2

$$\left| \frac{A'_{z2} - A'_{z2\infty}}{A'_{z2\infty}} \right| \ll 1. \quad (3.90)$$

Here A'_{z1} and A'_{z2} are given by Eqns. (3.79) and (3.86); $A'_{z1\infty}$ and $A'_{z2\infty}$ are given in terms of image contributions per Eqns. (3.78) and (3.85).

Again applying the material characteristics of Table 3.1 we see from Figure 3.12 that the contribution from the QMS term (i.e. $-j\omega\mu A'_{z1\infty}$) is many orders of magnitude below that of the total SFW and QES electric field magnitudes. In air, the QMS terms is of no importance and has almost no contribution to the total field for the distances and frequencies studied. The QMS contribution increases with frequency while the total field magnitude decreases with frequency. This is as we would expect, given that low frequency electric sources weakly excite magnetic fields. For observation in water, where the conductivity is non-zero we see from Figure 3.13 that the contribution from the QMS term is significant. We see that the SFW field magnitude diverges from the QES field magnitude roughly where the QMS becomes dominant, which is around 100 m at 1000 Hz. Also notice now that both the QMS contribution and the total field magnitude increase with frequency. Conductivity significantly changes the characteristics of the field.

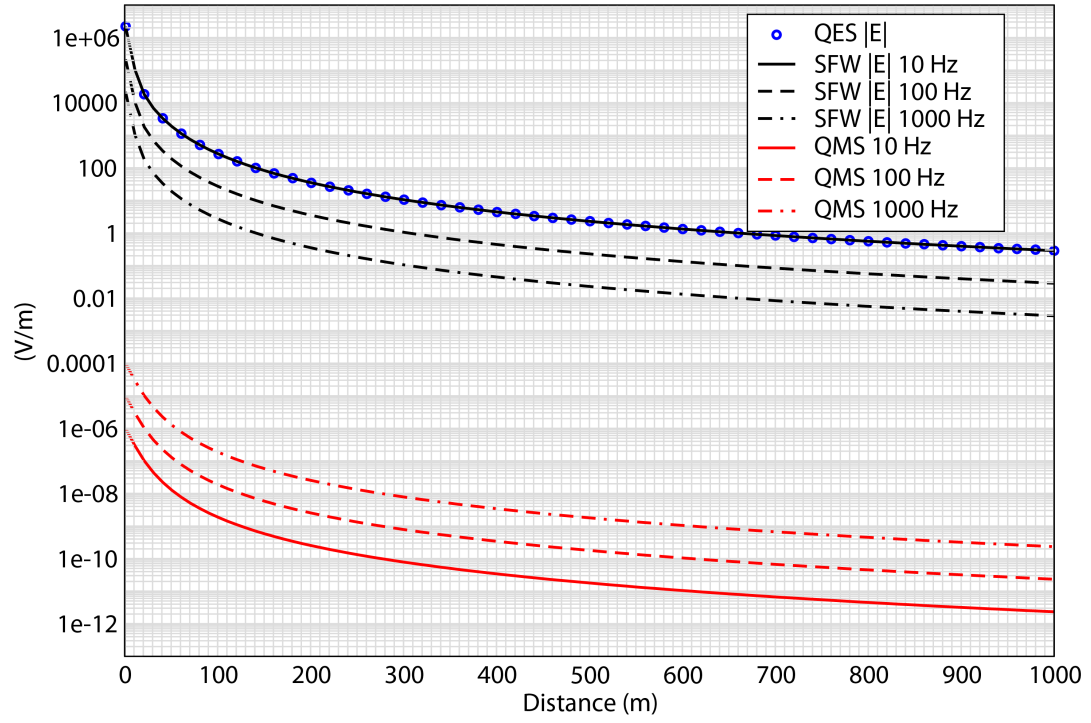


Figure 3.12: Quasi-magnetostatic contribution versus magnitude of electric field in air.

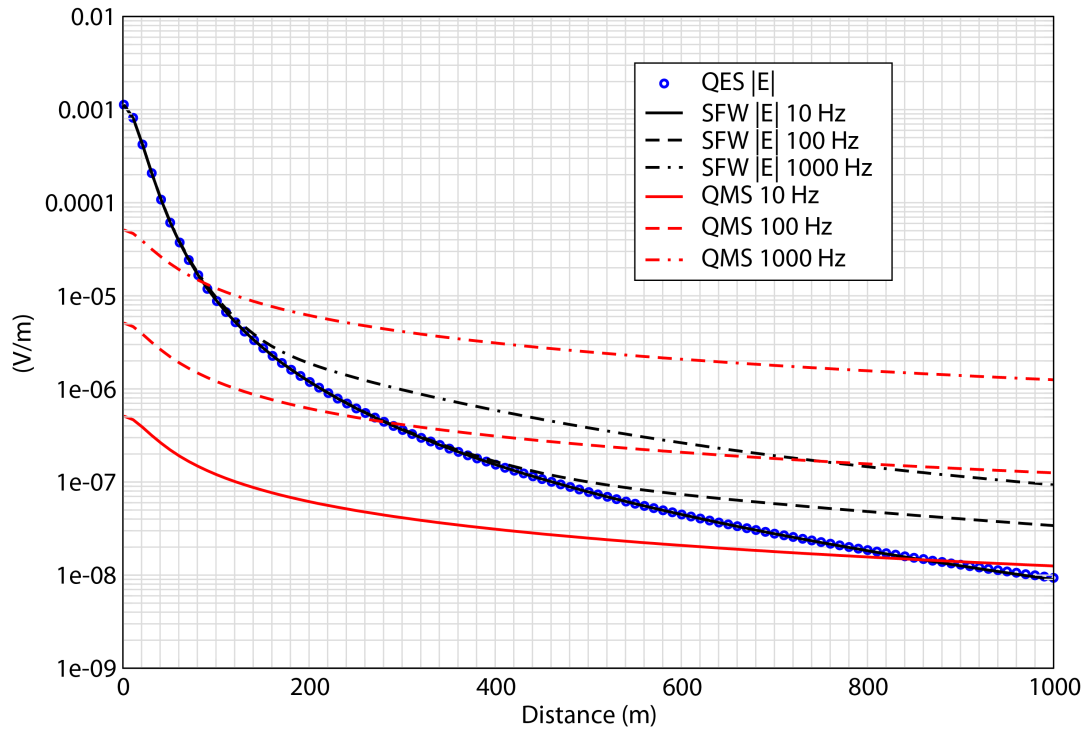


Figure 3.13: Quasi-magnetostatic contribution versus magnitude of electric field in water.

Plots of Eqns. (3.89) and (3.90) are shown in Figures 3.14 and 3.15.

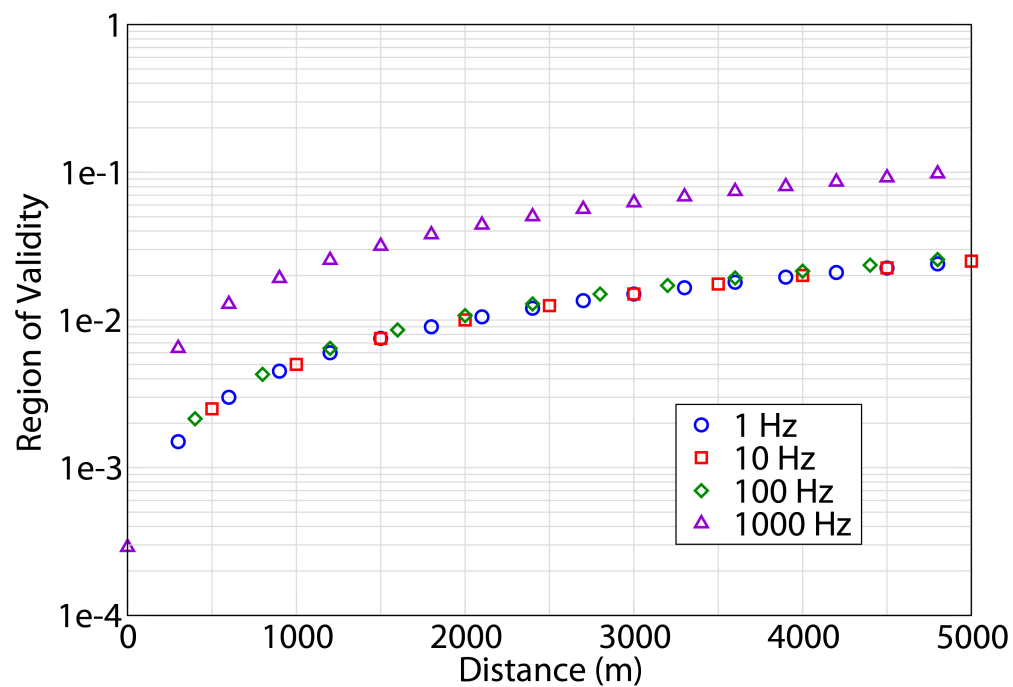


Figure 3.14: QMS region of validity in air by Eqn. (3.89).

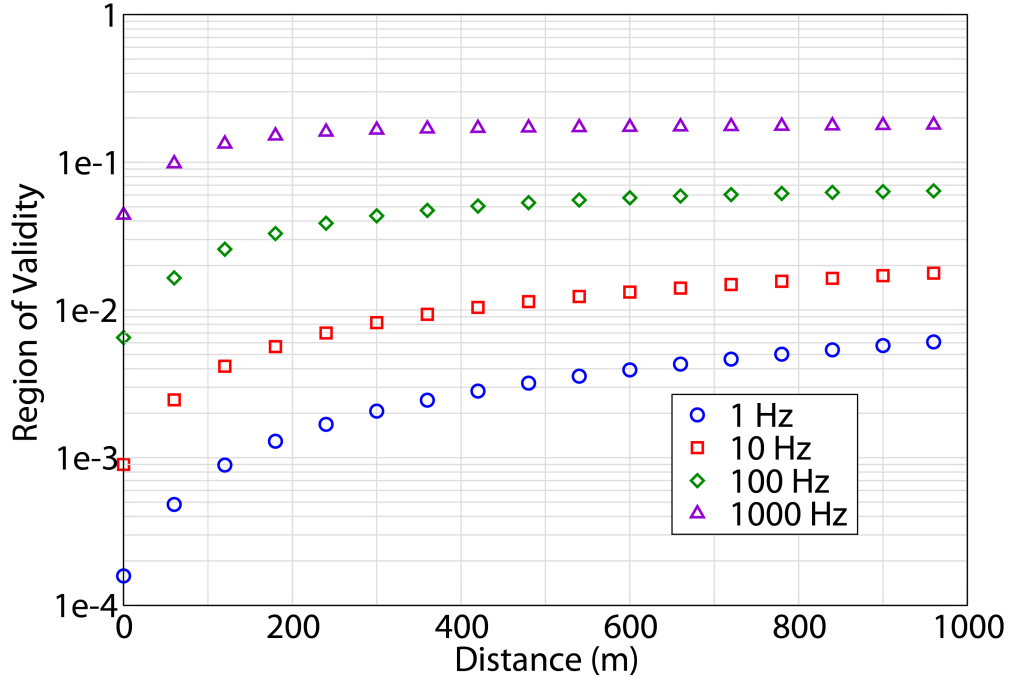


Figure 3.15: QMS region of validity in air by Eqn. (3.90).

3.3.4 Summary

Section 3.3 has revealed some fundamental relationships between the full-wave (FW) and the quasi-electrostatic (QES) solution in the case of the vertical electric dipole. Understanding these relationships is paramount to understanding the limits of the QES solution. Let us summarize the key findings from the previous material.

1. In Section 3.3.1 it was shown that the SFW infinitesimal dipole potential when $\omega \rightarrow 0$ reduces to the QES two-charge dipole potential when $dl \rightarrow 0$. Notationally this can be expressed as,

$$\int \text{FW} \Big|_{\omega \rightarrow 0} = \int \text{QES} \Big|_{dl \rightarrow 0}. \quad (3.91)$$

For example, take the QES dipole potential of Eqns. (3.41) and (3.42) and let $dl \rightarrow 0$ to arrive at Eqns. (3.48) and (3.49), then let $\omega \rightarrow 0$ in the FW potential of Eqns. (3.37) and

(3.38) to arrive at Eqns. (3.54) and (3.55). This procedure verifies the relationship specified by Eqn. (3.91).

2. In Section 3.3.1 it was also demonstrated that the relationship between the potential for a single charge and two charges which form a dipole is simple. When examining Eqns. (2.23) and (2.25) and Eqns. (3.50) and (3.51), we notice that the following relationship is true,

$$\begin{aligned} V^{dipole} &= -dl \frac{dV^{single}}{dz} && \text{for a direct term} \\ &= +dl \frac{dV^{single}}{dz} && \text{for a reflected term.} \end{aligned} \quad (3.92)$$

A direct term refers to the charge when there is a direct path between it and the observer, the reflected term refers to the charge when there is a interface between it and the observer. That is, the scalar potential from a two charge vertical dipole can be found by taking the derivative with respect to z and multiplying by the effective dipole length. Note that this relationship is only valid for an infinitesimal dipole.

3. In 3.3.2 the SFW scalar potential integral was decomposed into two parts: one which contains the time-varying electrodynamic wave effects and one which contains the static, non-wave effects. The static solution was defined when $\lambda \rightarrow \infty$. The dynamic portion represents the total potential minus its static contribution. Eqns. (3.66) and (3.68) expresses this relationship. The term representing the static contribution was expressed by an infinite sum of images, namely Eqns. (3.67) and (3.69) which are the QES dipole summations when $dl \rightarrow 0$. Notationally we may also write,

$$\begin{aligned} V' &= \int \text{SFW} \\ &= \int \text{QES} + \int [\text{SFW} - \text{QES}], \end{aligned} \quad (3.93)$$

where

$$\int \text{QES} = \text{QES} \sum \text{Images.} \quad (3.94)$$

4. In Section 3.3.3 an equivalent quasi-magnetostatic (QMS) term was isolated by allowing $\lambda \rightarrow \infty$ in the magnetic vector potentials of Eqns. (3.2) - (3.3). The procedure to extract

the QMS term is similar Section 3.3.2 and is represented by Eqns. (3.79) and (3.86). The QMS integral equations were cast in terms of infinite image summation represented by Eqns. (3.78) and (3.85). Notationally we can express this as

$$\begin{aligned}\mathbf{A}' &= \int \text{SFW} \\ &= \int \text{QMS} + \int [\text{SFW} - \text{QMS}]\end{aligned}\quad (3.95)$$

where

$$\int \text{QMS} = \text{QMS} \sum \text{Images}. \quad (3.96)$$

5. According to Eqns. (3.22), (3.93) and (3.95) the SFW total electric field is represented by three terms: a term that accounts for the QES contribution, a term that accounts for the QMS contribution and a term that accounts for the time-varying electrodynamic effects. Notationally we can express the total electric field by

$$\begin{aligned}\mathbf{E}' &= \int \text{SFW} \\ &= \int \text{QMS} + \int \text{QES} + \int [\text{SFW} - \text{QMS} - \text{QES}]\end{aligned}\quad (3.97)$$

where Eqns. (3.80) and (3.87) are the explicit equations for the above relationship. From Eqn. (3.81) we see the the components of the magnetic field are given by,

$$\begin{aligned}\mathbf{H}' &= \int \text{SFW} \\ &= \int \text{QMS} + \int [\text{SFW} - \text{QMS}]\end{aligned}\quad (3.98)$$

where these are given by Eqns. (3.82) and (3.88).

6. As a final point, in Section 3.3.2 we determined the region of validity for the scalar potential of the QES infinitesimal dipole. The region of validity in region 1 is determined by,

$$\left| \frac{V_1' - V_{1T}}{V_{1T}} \right| \ll 1 \quad (3.99)$$

and

$$\left| \frac{A_{z1}' - A_{z1\infty}'}{A_{z1\infty}'} \right| \ll 1. \quad (3.100)$$

For region 2,

$$\left| \frac{V'_2 - V_{2T}}{V_{2T}} \right| \ll 1 \quad (3.101)$$

and

$$\left| \frac{A'_{z2} - A'_{z2\infty}}{A'_{z2\infty}} \right| \ll 1. \quad (3.102)$$

It should be noted that the region of validity as specified by the above equations is subjective. There is no precise definition as to how small a small number is. For example, one could say that the QES region of validity is less than 0.1, meaning that the QES and SFW solutions are in error by 10 percent.

3.4 Two-layer Reduction

In this section we will verify the 3-layer solution by some limiting cases and compare it to the 2-layer solution. The solution for a 2-layer QES geometry is already known and will be assumed to be correct. The 2-layered solution consists of a half space configuration with both media extending infinitely in each direction. To validate the 3-layer solution, two observations can be made. First, when the thickness d of the middle layer extends to infinity for the 3-layered solution, it must be equivalent to the 2-layer solution. Second, when the third layer becomes identical to the second layer for the 3-layered problem, the solution will converge to the 2-layered problem. These limiting cases are shown below for source in region 1 and 2.

For region 1, refer to Eqn. (2.33) through Eqn. (2.35) . Let $d \rightarrow \infty$ or let $Y_3 = Y_2$ to acquire the 2-layer configuration,

$$R \longrightarrow -R_{21}e^{-\lambda h} \quad (3.103)$$

$$A \longrightarrow 0 \quad (3.104)$$

$$B \longrightarrow (1 - R_{21})e^{-\lambda h} \quad (3.105)$$

Eqn. (3.103) compares exactly to the reflection coefficient from the 2-layer configuration. Eqn. (3.104) will be non-zero only in the 3-layer configuration because it accounts for the reflections caused by the third region, thus it must be zero for the 2-layer. Also, the transmission coefficient for the 2-layer is identical to Eqn. (3.105).

For region 2, refer to Eqn. (2.78) through Eqn. (2.80) and let $d \rightarrow \infty$ or let $Y_3 = Y_2$,

$$T_1 \longrightarrow (1 + R_{21})e^{\lambda h} \quad (3.106)$$

$$A \longrightarrow 0 \quad (3.107)$$

$$B \longrightarrow R_{21}e^{\lambda h} \quad (3.108)$$

Similar statements can be said about these results. They are equivalent to the 2-layer solution.

3.5 Infinitesimal vs. QES Dipole

In this section we investigate how the electric field produced by an infinitesimal dipole compares to the physically large QES dipole. The solution for an infinitesimal dipole will be that of the SFW Sommerfeld model, see Appendix B. Recall the geometrical structure of the QES dipole, two electrodes with a finite radius separated by a distance dl . If an infinitesimal dipole and a physically large source are to be compared, it is necessary place the infinitesimal dipole at the geometric center of the QES dipole. In this case, the near field characteristics of the electric field between the two dipoles will differ, see Figure 3.17. For more accurate near field comparisons we divide dl into m equal elements each of length δ , given by

$$\delta = \frac{dl}{m}. \quad (3.109)$$

At the center of each element, an infinitesimal dipole is placed according to Figure 3.16. If $m = 1$, a single infinitesimal dipole is centered between the two electrodes, and for increasing value of m , the length of the QES dipole is subdivided even further. For simplicity, assume the dipoles are orientated along the positive x -axis, symmetric about the x and y axes and located at some height. The y and z locations for each m^{th} infinitesimal dipole will be the same while only the x location will change. Each occupies its own spacial location along the x -axis is given by,

$$x_n = dl \left(\frac{1}{2m} + \frac{n-1}{m} - \frac{1}{2} \right) \quad (3.110)$$

where n represents a single dipole and is given by

$$n = 1, 2, 3, \dots m. \quad (3.111)$$

If the total current between the QES electrodes is I then the total QES dipole moment is given by $I dl$. Each infinitesimal dipole is then of equal current amplitude given by

$$I_m = \frac{I}{m} \quad (3.112)$$

where the infinitesimal dipole moment is δI_m .

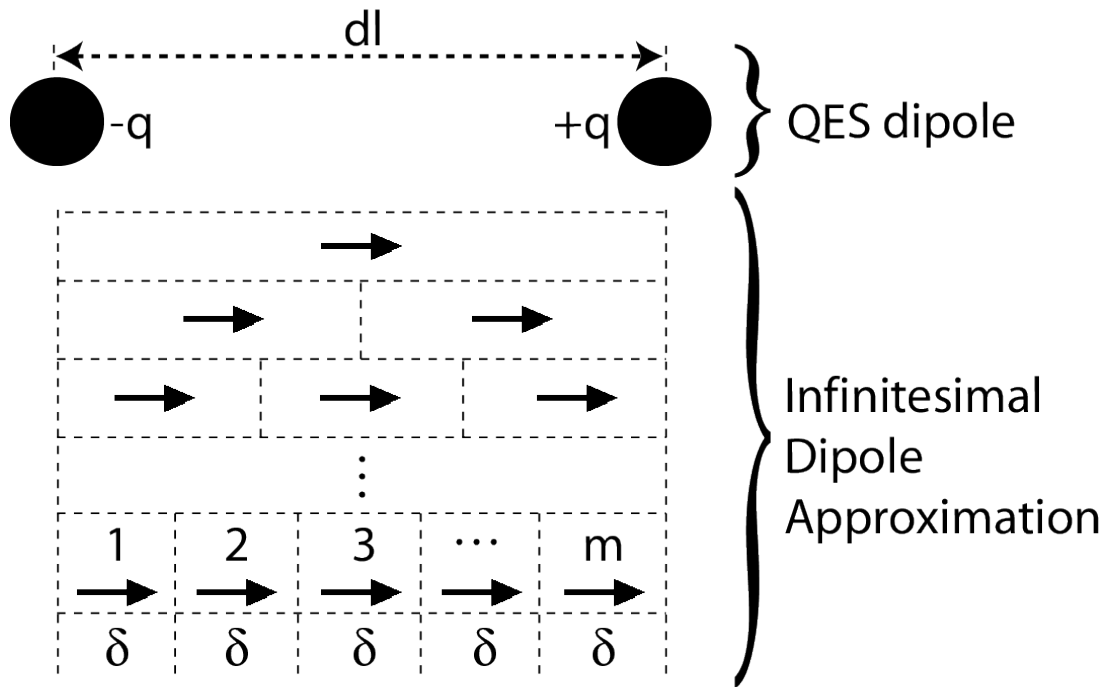


Figure 3.16: Representation of how a QES dipole is approximated by m infinitesimal dipoles.

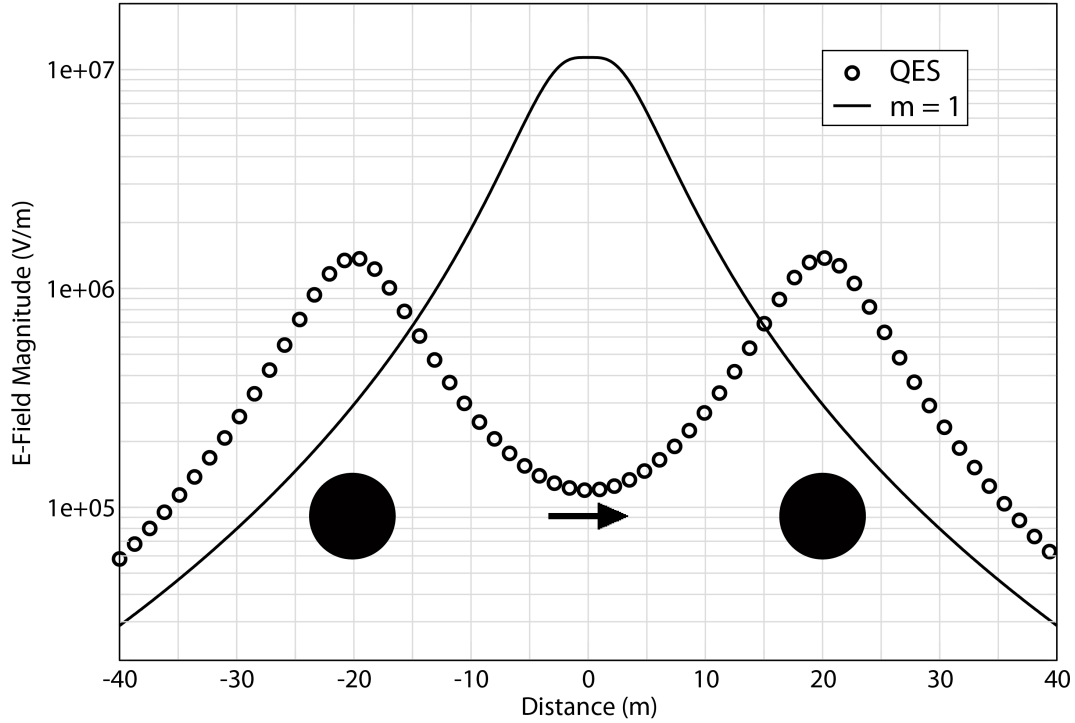


Figure 3.17: Electric field magnitude for $m = 1$ case and QES 40 m dipole with illustration of QES electrodes and infinitesimal dipole locations. Solutions become the same at large distances which is not shown.

In Figure 3.17 we set the separation of the QES electrodes to 40 m, and align it along the $+x$ -axis, where the two electrodes evenly spaced about the y -axis. This QES horizontal dipole has a current of 1 A and is placed in the air. An observation line is slightly above the dipole and sweeps radially out along the $+x$ -axis. We see that the QES electric field magnitude behaves as we expected, increasing to a maximum precisely where it passes over each electrode and then decays as normal. This is illustrated in the figure by overlaying the QES dipole on the plot. When $m = 1$ we see a fundamental difference between the two dipoles, the field magnitude for the infinitesimal dipole starts at a maximum value where it is directly over itself then decays as normal. It seems reasonable to say that the approximation accuracy can be increased by placing more infinitesimal dipoles at strategic locations. In Figure 3.18 we see the

case where $m > 1$ and the result is impressive. When we subdivide the QES dipole into smaller and smaller elements we see that the infinitesimal dipoles predict the exact same field magnitude as a physically large QES dipole would. It is interesting to note the oscillations as m increases, this is partially caused by the field component is the same direction as the sweep, in this case E_x inverts as it passes over multiple dipole. In Figure 3.18 we see the cases for $m = 1 - 4$. Arrows are placed to show the corresponding x locations for the infinitesimal dipoles. It is interesting to note how the dips in the field are spatially related each dipole.

It is also of interest to show how the infinitesimal dipole solution for higher values of m converges to the QES dipole field magnitude as shown in Figure 3.19.

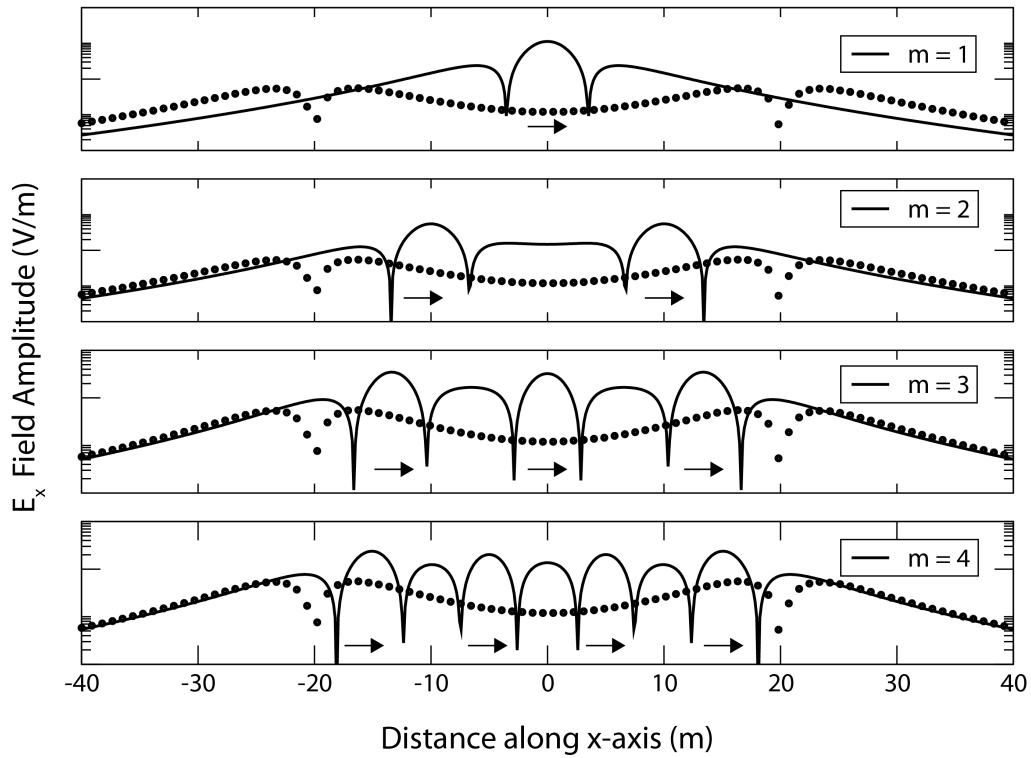


Figure 3.18: Depiction of E_x for $m = 1 - 4$ infinitesimal dipoles and a 40 m QES dipole.

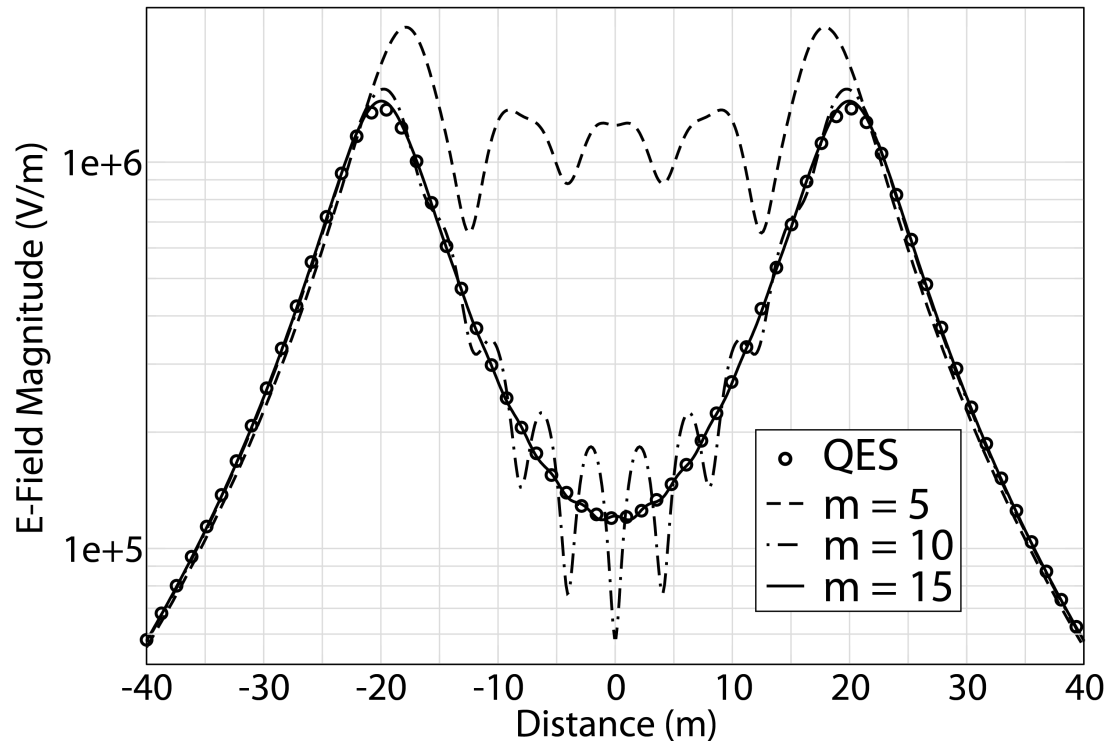


Figure 3.19: Electric field magnitude higher m values. Dots are QES and solid line is SFW.

Chapter 4

Conclusion

In conclusion, the method described in this thesis for modelling a three layered geometry has been shown to be successful. The QES method has shown it can accurately replicate the full-wave method in most configurations where sensor and source locations fall within a defined QES region of validity. When outside the region of validity, the QES method will fail because it cannot account for wave-like processes, unlike the full-wave solution. The QES region of validity is dependent on wavelength of the signal in a particular material. The wavelength at ELF frequencies is dominated by the material conductivity of the medium. This is because the conduction current is orders of magnitude larger than the displacement current. Thus it can be said that increasing conductivity results in decreasing the wavelength, which results in a decreasing region of validity. For the applications of this thesis where materials were that of air, water and mud, the region of validity changed greatly when moving from air to water. In air, where the conductivity is almost zero and frequencies are ELF, the region of validity is as large as 5 km in most cases. When changing to water, where the conductivity is much larger, the region of validity decreased to 75 m for 1000 Hz in some cases. For the bottom mud layer, which was given a conductivity similar to that of water, similar statements can be made about its region of validity. It should be noted that even when observations outside of the QES region of validity are made, the QES can still provide an accurate approximation to the correct order of magnitude of the field. In other words, the QES method can be used for a rough approximation of the field strength even when wave processes are present.

The QES method was implemented into code, and the simulation times are on the order of seconds. The simulations are significantly faster than other methods used to simulated the same lake environment. When the lake bathymetry and topography are included in simulation models such as the finite difference time domain (FDTD) and the Ansoft High Frequency Structural Solver (HFSS), simulation times can be on the order of hours to days. Lake bathymetry and topography are only important when sources or sensors are near material interfaces. If sources and sensors are located where lake geometry is flat and nearly planar, the QES solution is ideal. In an open lake environment where the water is about 300 m deep and the geometry is close to three flat layers, modelling detailed features of the lake walls and bed do not yield much gain in field accuracy. When it comes to an extremely fast and robust static solution to lake or ocean modelling the QES method is ideal. Experimentally, the QES method is advantageous to the SFW method because of its ability to model an extensible source. When electrode separation is large and near-field observations are made, its is favourable to use QES so that the effects of the extensible source are captured.

It has also been demonstrated that the up-over-down (UOD) phenomena and the QES processes are one of the same processes. In most cases where a horizontal electric dipole is radiating in water, the UOD or the QES solution can be used to approximate the correct electric field magnitude. Each method was developed from completely different points of view, but each gives almost identical results.

There are several opportunities for future work. The QES electrodes only have the ability to be spherical, which could be a disadvantage if extremely near field observations are made. The ability to model flat plates or electrodes of arbitrary shape could be advantageous. A similar approach to this thesis could involve a quasi-magnetostatic solver where sources are magnetic and modelled with physically large current loops. This thesis only describes in detail how to place sources and sensors in regions one and two; it may be beneficial to follow the approach in this thesis to solve for the scalar potential and fields in region three. Finally, a detailed study of the convergence of the summation may be useful. There was no detailed convergence criterion presented in this thesis.

Bibliography

- [1] J. L. Young, D. M. Sullivan, R. G. Olsen and Christopher L. Wagner, "Investigation of ELF Signals Associated with Mine Warfare: A University of Idaho and Acoustic Research Detachment Collaboration, Phase Two", Proposal to the Office of Naval Research, pp. 2, 2010. *IEEE Trans. on Microwave Theory and Techniques*, vol. 39, No. 7, pp. 1120-1125, 1991.
- [2] Y. L. Chow, "Complex images for electromagnetic field computation in multilayered media",
- [3] J. A. Kong, "Electromagnetic fields due to dipole antennas over stratified anisotropic media", *Geophysics*, vol. 37, no. 6, pp. 985-996, 1972.
- [4] K. A. Norton, "The propagation of radio waves over the surface of the earth in the upper atmosphere", *Proceedings of the Institute of Radio Engineers*, vol. 24, no. 10, pp. 1203-1236, 1936.
- [5] A. Sommerfeld, *Partial differential equations in physics*, Academic Press Inc., New York, 1949.
- [6] J. R. Wait, *Electromagnetic Waves in Stratified Media*, Institute of Electrical and Electronics Engineers, New York, 1995.
- [7] J. R. Wait, "Fields of a horizontal dipole over a stratified anisotropic half-space", *IEEE Transactions on Antennas and Propagation*, vol. 14, no. 6, pp. 790-792, 1966.
- [8] J. R. Mosig and T. K. Sarkar, "Comparison of quasi-static and exact electromagnetic fields from a horizontal electric dipole above a lossy dielectric backed by an imperfect

ground plane”, *IEEE Trans. on Microwave Theory and Techniques*, vol. 34, no. 4, pp. 379-387, 1986.

- [9] J. R. Wait, *Electromagnetic Wave Theory*, Harper and Row, New York, pp. 19, 1985.
- [10] I. S. Gradshteyn and I.M. Ryzhik, *Table of Integrals, Series and, Products*, Corrected and Enlarged, Academic Press, Florida, 1980.
- [11] R. G. Olsen, ”A simple up-over-down model for low frequency horizontal electric dipole propagation near an interface”, *IEEE Trans. on Antennas and Propagation* (submitted, Nov. 2010).
- [12] R. F. Harrington, *Time-Harmonic Electromagnetic Fields*, Wiley, New York, pp. 202, 2001.

Appendix A

QES Graphical User Interface Guide

This appendix will act as a guide to introduce and instruct the user to how the QES software code is used. The solver has been programmed with a Matlab GUI front-end. The software is accompanied by an m-file that can be used for modification of the code. The solver has been packaged into a stand-alone application and can be installed on a PC without the need of a Matlab license. The code was developed using a Windows XP professional PC running MatLab 7.8.0(R2009a). This guide will only focus on the GUI frontend and will not describe details of the main m-file code.

A.1 Installing the Solver

The GUI frontend is very straight forward and simple to use. To start the application, find and launch the executable file named `QES_V4_final.exe` as depicted by Figure A.1a. Figure A.2 shows the frontend immediately after launching the executable. When the GUI launches for the first time, it creates two directories: 1) *QES data* - location where the GUI stores temporary files and where data file are outputted by default and 2) *QES projects* - location to save and load QES projects. These directories are shown in Figure A.1b.

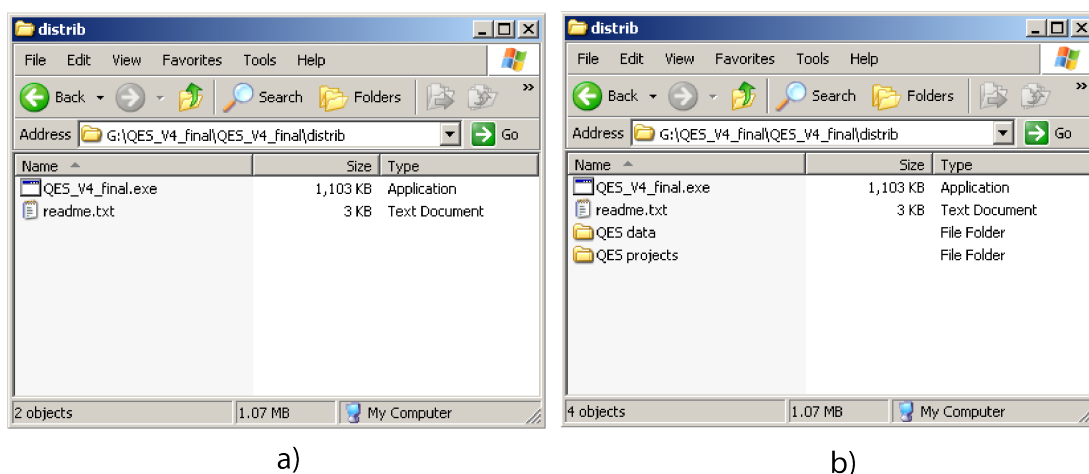


Figure A.1: A depiction of the directory structure a) before launching executable and b) after launching executable.

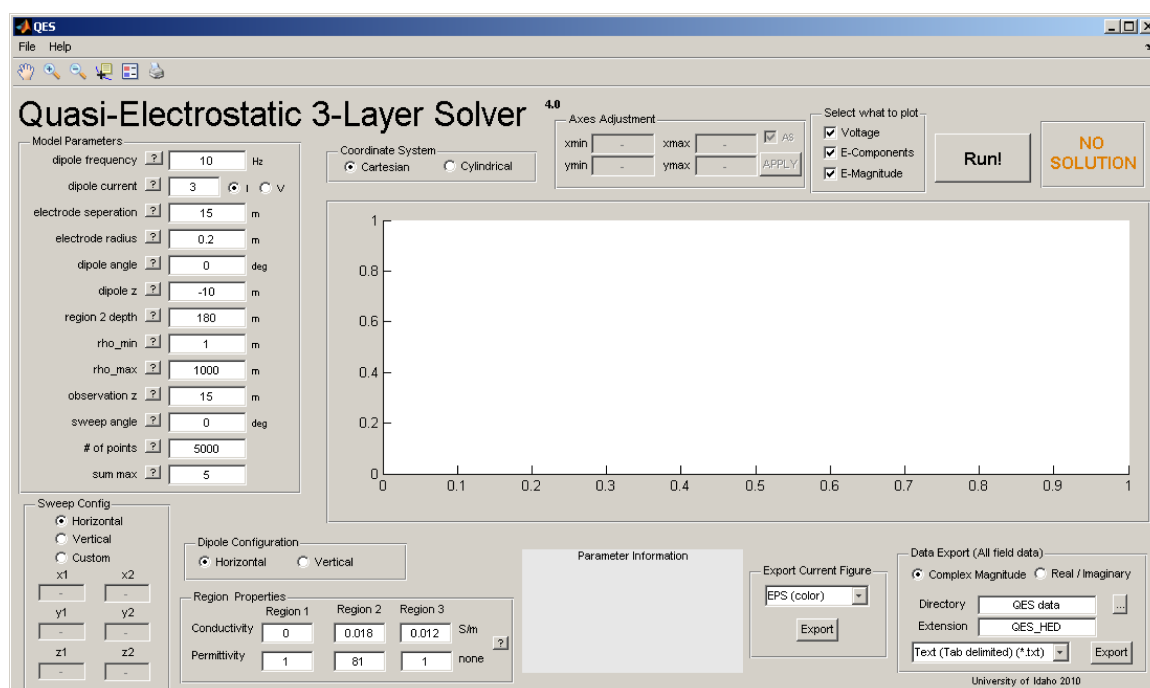


Figure A.2: Solver directly after launch.

A.2 Basic Layout

The GUI is broken up into eight main sections: 1) Model Parameters 2) Sweep Configuration 3) Dipole Configuration 4) Coordinate System 5) Axis Adjustment 6) Plot Selection 7) Export

Current Figure and 8) Data Export. Each section is described in detail next.

Model Parameters

- **dipole frequency** - operating frequency of the dipole in units of Hertz.
- **dipole current/voltage** - current or voltage between the two opposing electrodes that form the dipole in units of Amps rms or Volts rms.
- **dipole frequency** - operating frequency of the dipole in units of Hertz.
- **dipole current/voltage** - current or voltage between the two opposing electrodes that form the dipole in units of Amps rms or Volts rms.
- **electrode separation** - absolute distance separating the two electrodes according to dl in Figure A.3 in units of meters. Note that the figure shows the separation for a HED, but is the same for VED.
- **electrode radius** - radius of the electrode according to a in Figure A.3 in units of meters. Note that the figure shows the radius for a HED, but is the same for VED.
- **dipole angle** - refers to the orientation of the dipole in the xy plane according to β in Figure A.3 and is in units of degrees measured anti-clockwise from the x -axis. Note that this angle is only of importance when dealing with the HED, this angle is meaningless when dealing with the VED and is disabled out when selected.
- **dipole z** - refers to the height of the dipole center above or below the region 1-2 boundary according to Figure A.4 and is in units of meters. For dipole location in region 1, this is a positive number and for dipole locations in region 2, this is a negative number.
- **region 2 depth** - refers to the absolute depth of region 2 according to d in Figure A.4 and is in units of meters and is a positive number.
- **rho_min, rho_max** and **observation z** - These parameters will change when a vertical or custom sweep is selected. Sweep types will be described next. Initially a horizontal sweep is assumed and is specified by these parameters.

- **# of points** - refers to the number of sampling points for the current sweep.
- **sum max** - refers to the number of image terms to sum. The images summation are rapidly converging so no more than 5-10 terms are needed for most simulation cases.

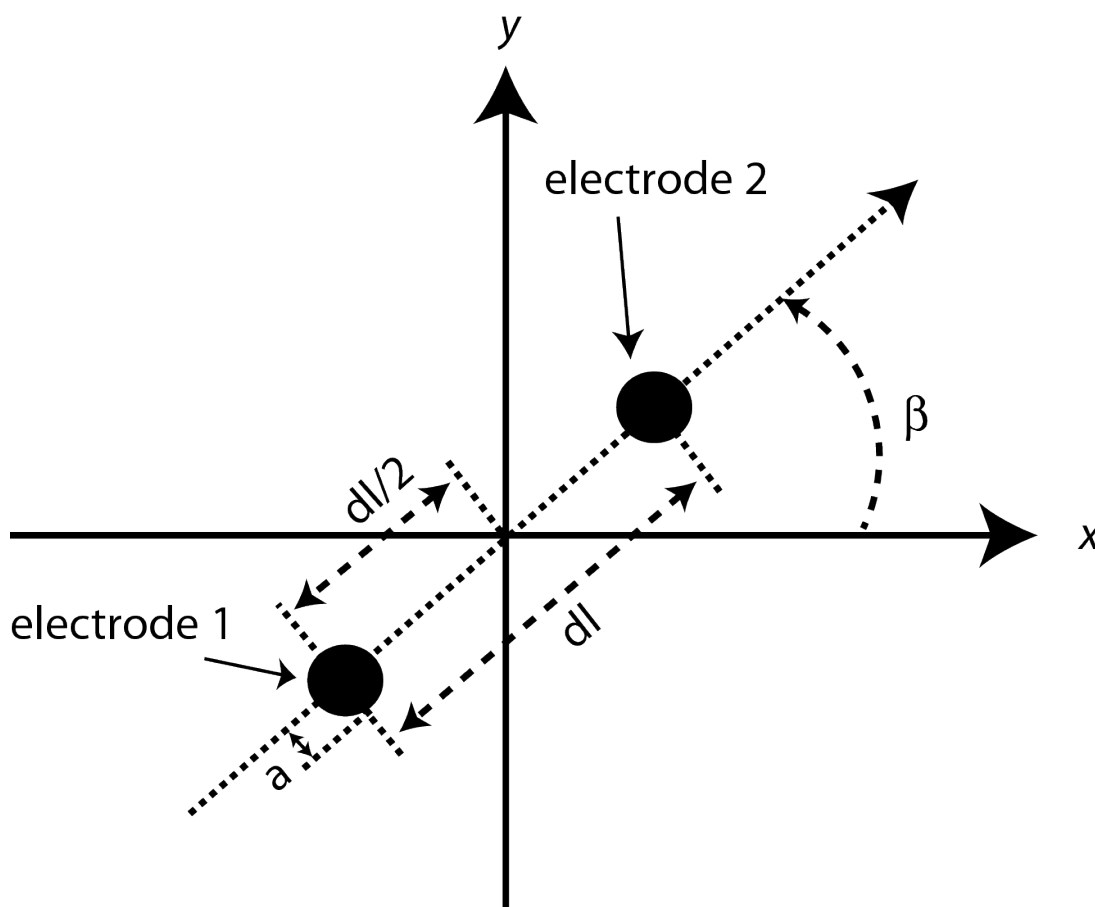


Figure A.3: Dipole geometry for the HED. The VED geometry is similar except represented in the yz or xz plane.

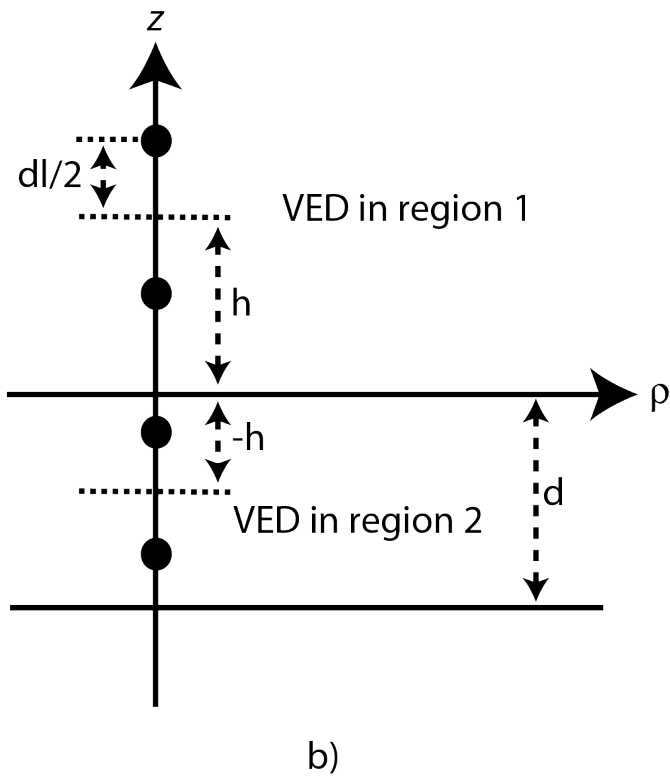
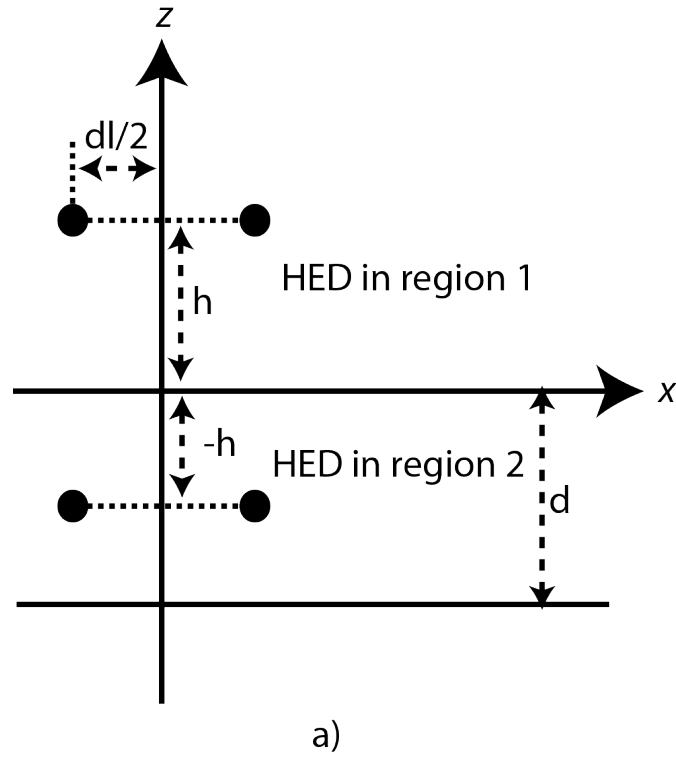


Figure A.4: Depiction the HED and VED located in region 1 or 2.

Sweep Configuration

There are three different sweep options: 1) horizontal, 2) vertical and 3) custom. Figure A.5 illustrates the GUI layout for each type of sweep.

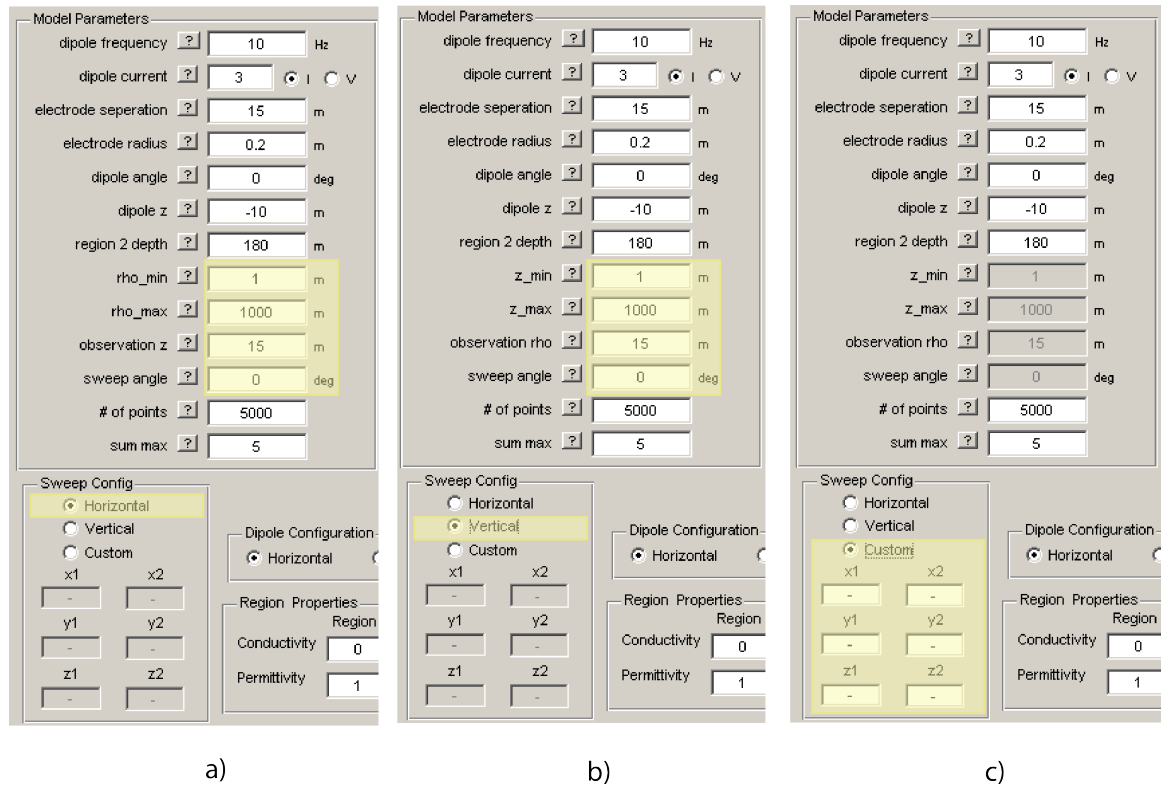


Figure A.5: Depiction of three sweep options, a) horizontal, b) vertical and c) custom.

Horizontal Sweep

To perform a horizontal sweep, select the *horizontal* radio button located in the *sweep config* box of the GUI. A horizontal sweep is depicted by Figure A.6a. The figure shows an observation line starting at ρ_{min} and ending at ρ_{max} . The elevation of the observation line is at height $observation\ z$ and is a positive number according to the figure and will be negative when located in region 2. The *sweep angle* is the angle to which the observation line is directed and is measured counter-clockwise from the x -axis. For example, a horizontal sweep down the positive x -axis corresponds to a sweep angle of zero.

Vertical Sweep

To perform a vertical sweep, select the *vertical* radio button located in the *sweep config* box of the GUI. A vertical sweep is depicted by Figure A.6b. The figure shows an observation line

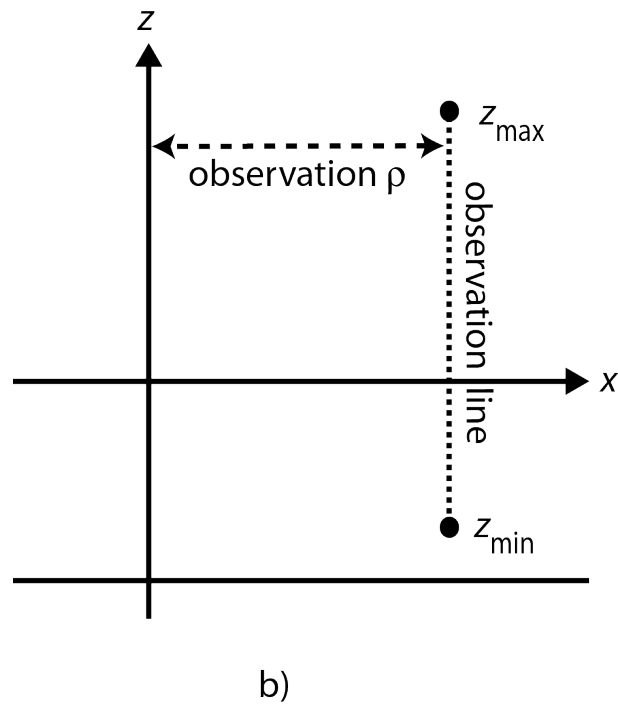
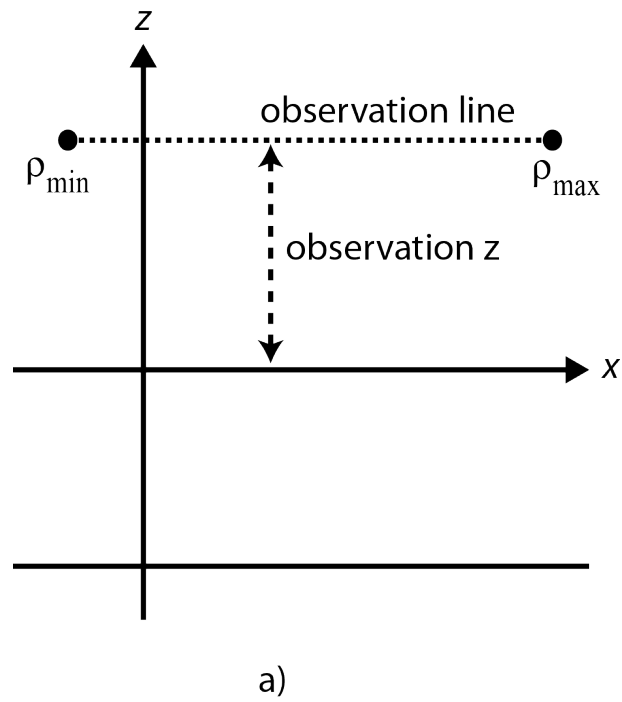


Figure A.6: Depiction of a) horizontal sweep and b) vertical sweep when *sweep angle* is zero.

starting at z_{min} and ending at z_{max} . The observation line is located at a radial distance of $observation\ rho$. The *sweep angle* is measured the same as for the horizontal sweep.

Custom Sweep

If the desired sweep does not fall under the horizontal or vertical sweep category an arbitrary sweep line can be made. For a custom sweep line, select the *custom* radio button located in the *sweep config* box. The custom sweep is defined by a start point and an end point, specifically described by x_1, y_1, z_1 and x_2, y_2, z_2 .

Dipole Configuration

Horizontal electric dipole - HED

By default the HED is selected. The HED is naturally orientated along the positive x -axis. Its geometrical dimensions and strength are specified in the *Model Parameters* section of the GUI.

Vertical electric dipole - VED

The VED can be chosen by selecting the *vertical* radio button. Now the dipole is orientated along the positive z -axis. Its geometrical dimensions and strength are specified in the *Model Parameters* section of the GUI.

region Properties

In this box, the relative permittivity (ϵ_r) and the conductivity (σ) in units for each region are specified.

Coordinate System

Either *cartesian* coordinates given by x, y and z or *cylindrical* coordinates given by in ρ, ϕ and z can be used for plotting. By default the natural coordinate system is chosen to be cartesian.

Axes Adjustment

In this box, the minimum and maximum limits for the x and y axes can be set after a simulation is run. If no simulation data is available then this box is disabled. To enable it, run a valid simulation and uncheck the *AS* checkbox, set the desired limits and click *apply*. The plot will resize to the desired limits. To auto scale back to the original axes, uncheck the *AS* checkbox and click *apply*.

Plot Selection

Here the user will decide what is to be displayed on the plot. There are three checkbox options

to choose from: *Voltage*, *E-Components* and *E-Magnitude*. To view all data on the same plot, select all three checkboxes. To view an individual quantity, select the appropriate checkbox.

Run!

When all parameters are specified, click the *Run!* button to start the simulation. A progress bar will appear and the length will depend on the number of plotting points selected. Once this is done, data will appear on the plot.

Valid, Invalid or No Solution

Here the user will see the validity of the simulation data. If the box displays in green, *VALID SOLUTION* then the data on the plot is valid and the data can be exported. If the box displays in red, *INVALID SOLUTION* then the plot data is not valid and no data can be exported. Note that the GUI is set up to render a valid solution invalid if any parameter is changed. If the box displays in orange, *NO SOLUTION* then no solution is available and no data can be exported.

Parameter Information

This box will display useful information about a specific input box when the question mark box is click.

Export Current Figure

This box will export the current figure in a variety of formats for display purposes. The pull down menu will show the valid output formats.

Data Export

The simulation data can only be exported once a valid simulation exists and the indicator says *VALID SOLUTION*. If the indicator says anything else, the data will not be available to export. The data will be exported into three separate files: 1) field components and their distance 2) field magnitude and its distance and 3) voltage and its distance. The data can be exported by its complex magnitude or by its real and imaginary parts by selecting the appropriate radio button. Also, the data file format can be changed by the pull down menu. Once the data is ready to export, choose a directory and click on the *Export* button.

Save and Load simulation data

Under the *File* menu, a simulation state can be saved for later use. If a simulation data file is already present, it can be loaded into the GUI by selecting load.

A.3 Recommended Simulation Values

Table A.1: Recommended simulation values

Parameter	Value	Units
dipole frequency	1 – 3000	Hertz
dipole voltage	> 0	V_{RMS}
dipole current	> 0	A_{RMS}
electrode separation	$> 2a$	meters
electrode radius	> 0	meters
dipole angle	0 – 360	degrees
dipole z	$a < z < -(d - a)$	meters
region 2 depth	$> 2a$	meters
ρ_{min} / z_{min}	$-3000 / > -d$	meters
ρ_{max} / z_{max}	$< 3000 / < 3000$	meters
observation z / ρ	$0 < z < -d / -3000 < \rho < 3000$	meters
sweep angle	0 – 360	meters
# of points	> 1	degrees
sum max	2-10	no units

Appendix B

QES Source Code (Matlab)

This appendix shows the source code for the QES.

```

1  %%%%%%%%%%%%%%%%%%%%%%%%%%%%%%%%%%%%%%%%%%%%%%%%%%%%%%%%%%%%%%%%%%%%%%%%%
2  % Quasi-electrostatic Solver QES
3  % Robert T. Rebich
4  % University of Idaho 2010
5  % Department of Electrical and Computer Engineering
6  %
7  % This code will compute the potential (V) and electric
8  % field (E) components for a quasi-electrostatic (QES)
9  % dipole located in either region 1 or region 2. The
10 % dipole can be horizontally directed for a HED or
11 % vertically directed for a VED. If the dipole is located
12 % in region 1, h will be a positive number and locations
13 % in region 2 will be regarded as negative. The thickness
14 % of region 2 is entered as a positive number.
15 %
16 %
17 %                               z
18 %

```

```

19  %
20  %
21  %
22  %
23  %
24  %
25  %
26  %   z=0
27  % -----|-----> rho
28  %
29  %
30  %
31  %
32  %
33  %   z=-d
34  % -----|-----
35  %
36  %
37  %
38  %
39  %
40  %
41  %
42  %%%%%%%%%%%%%%%%%%%%%%%%%%%%%%%%%%%%%%%%%%%%%%%%%%%%%%%%%%%%%%%%%%%%%%%%%
43
44  %DIPOLE PARAMETERS
45  freq = 10;           %dipole frequency. (hertz)
46  sep = 15;            %electrode separation. (meters)
47  rad = 0.2;          %electrode radius. (meters)
48  h = 10;              %vertical location of dipole +/- . (meters)
49  theta2 = 0;          %dipole angle wrt x-axis measured

```

```

50                                     %counterclockwise. (degrees)
51 src_typ = 'HED';                   %HED or VED.
52 vi_typ = 'I';                      %for voltage use 'V'. for current use 'I'.
53 ST = 100;                          %voltage or current strength. (volts, amps)
54
55 %SWEEP PARAMETERS
56 swp_typ = 'H';                     %'H' horizontal, 'V' vertical, 'C' custom.
57 swp_line = 15;                     %for 'H' elevation of line. (meters)
58                                     %for 'V' radial distance of line. (meters)
59 swp_min = -100;                    %for 'H' rho min, for 'V' z min. (meters)
60 swp_max = 100;                     %for 'H' rho max, for 'V' z max. (meters)
61 xx1 = 0;                           %x1 for 'C'. (meters)
62 yy1 = 0;                           %y1 for 'C'. (meters)
63 zz1 = 0;                           %z1 for 'C'. (meters)
64 xx2 = 0;                           %x2 for 'C'. (meters)
65 yy2 = 0;                           %y2 for 'C'. (meters)
66 zz2 = 0;                           %z2 for 'C'. (meters)
67 theta1 = 0;                        %sweep angle wrt to x-axis
68                                     %measured counterclockwise. (degrees)
69
70 %REGION PARAMETERS
71 d = 100;                            %thickness of middle layer. (meters)
72 sig1 = 0;                           %conductivity region 1. (s/m)
73 sig2 = 0.018;                       %conductivity region 2. (s/m)
74 sig3 = 0.012;                       %conductivity region 3. (s/m)
75 eps1 = 1;                           %permittivity of region 1.
76 eps2 = 81;                           %permittivity of region 2.
77 eps3 = 1;                           %permittivity of region 3.
78 eps0 = 8.85418e-12; %free space permittivity.
79
80 %OTHER PARAMETERS

```

```

81 npts = 1000;           %number of points to plot.
82 sum_max = 10;          %number of image terms to sum.
83 plot_typ = 0;          %0 for cartesian, 1 for cylindrical.
84
85 %%%%%%%%%%%%%%%%%%%%%%%%%%%%%%%%%%%%%%%%%%%%%%%%%%%%%%%%%%%%%%%%%%%%%%%%%
86 %%%%%%%%%%%%%%%%%%%%%%%%%%%%%%%%%%%%%%%%%%%%%%%%%%%%%%%%%%%%%%%%%%%%%%%%%
87
88 %START OF MAIN CODE
89
90 %CUSTOM SWEEP CONFIGURATION
91 if(strcmp(swp_typ, 'C'))
92     %decimate x, y and z by the number of points selected
93     x_space = linspace(xx1,xx2,npts+1);
94     y_space = linspace(yy1,yy2,npts+1);
95     z_space = linspace(zz1,zz2,npts+1);
96
97     %determine all the rho's, phi's and z's to sweep
98     rho_cust = sqrt(x_space.^2+y_space.^2);
99     phi_cust = atan(y_space./x_space)*180/pi;
100    z_cust = z_space;
101
102    %calculate the absolute length of sweep
103    dist = sqrt((xx1-xx2)^2+(yy1-yy2)^2+(zz1-zz2)^2);
104
105    %decimate length of sweep into npts for plotting
106    dist_cust = linspace(0,dist,npts+1);
107
108    %length of main loop for custom sweep
109    length_main = npts;
110 else
111    %length of main loop for natural sweep (horz and vert)

```

```

112     length_main = npts;
113 end
114
115 %SET INITIAL COORDINATES FOR ELECTRODES
116 if(strcmp(src_typ,'HED'))
117     y1 = 0;          y2 = 0;
118     x1 = -sep/2;     x2 = sep/2;
119     z1 = h;          z2 = h;
120     rad1 = rad;      rad2 = rad;
121 end
122
123 if(strcmp(src_typ,'VED'))
124     y1 = 0;          y2 = 0;
125     x1 = 0;          x2 = 0;
126     rad1 = rad;      rad2 = rad;
127     if h > 0
128         z1 = h-sep/2;      z2 = h+sep/2;
129     else
130         z1 = h+sep/2;      z2 = h-sep/2;
131     end
132 end
133
134 %REGION ADMITTANCES
135 Y1 = sig1 + 1i*2*pi*freq*eps1*eps0;
136 Y2 = sig2 + 1i*2*pi*freq*eps2*eps0;
137 Y3 = sig3 + 1i*2*pi*freq*eps3*eps0;
138
139 %REFLECTION COEFFICIENTS
140 R21 = (Y2-Y1)/(Y1+Y2);
141 R23 = (Y2-Y3)/(Y2+Y3);
142

```



```

143 %DETERMINE THE GEOMETRICAL FACTOR
144 if h > 0
145     x = x1 + rad1;
146     y = y1;
147     z = z1;
148     rho1 = sqrt((x-x1)^2 + (y-y1)^2);
149     rho2 = sqrt((x-x2)^2 + (y-y2)^2);
150     r1 = sqrt(rho1^2 + (z-z1)^2);
151     r2 = sqrt(rho2^2 + (z-z2)^2);
152     for n = 1:1:sum_max
153         cnst = (R23^n)*(R21^n);
154         D11 = z+z1+2*d*n+2*d;
155         D12 = z+z2+2*d*n+2*d;
156         D21 = z+z1+2*d*n;
157         D22 = z+z2+2*d*n;
158         ra1 = sqrt(rho1^2 + D11^2);
159         ra2 = sqrt(rho2^2 + D12^2);
160         rb1 = sqrt(rho1^2 + D21^2);
161         rb2 = sqrt(rho2^2 + D22^2);
162         R1(n) = cnst*(R23/ra1 - R21/rb1);
163         R2(n) = cnst*(R23/ra2 - R21/rb2);
164     end
165     G2 = (1/r2 + sum(R2)) - (1/r1 + sum(R1));
166
167     x = x2 - rad2;
168     y = y2;
169     z = z2;
170     rho1 = sqrt((x-x1)^2 + (y-y1)^2);
171     rho2 = sqrt((x-x2)^2 + (y-y2)^2);
172     r1 = sqrt(rho1^2 + (z-z1)^2);
173     r2 = sqrt(rho2^2 + (z-z2)^2);

```

```

174     for n = 1:1:sum_max
175         cnst = (R23^n)*(R21^n);
176         D11 = z+z1+2*d*n+2*d;
177         D12 = z+z2+2*d*n+2*d;
178         D21 = z+z1+2*d*n;
179         D22 = z+z2+2*d*n;
180         ra1 = sqrt(rho1^2 + D11^2);
181         ra2 = sqrt(rho2^2 + D12^2);
182         rb1 = sqrt(rho1^2 + D21^2);
183         rb2 = sqrt(rho2^2 + D22^2);
184         R1(n) = cnst*(R23/ra1 - R21/rb1);
185         R2(n) = cnst*(R23/ra2 - R21/rb2);
186     end
187     G1 = (1/r2 + sum(R2)) - (1/r1 + sum(R1));
188
189     Geo = G2-G1;
190
191     if(strcmp(vi_typ,'V'))
192         K1 = ST/Geo;
193     else
194         imped = Geo/(4*pi*Y1);
195         V0 = ST*imped;
196         K1 = V0/Geo;
197     end
198
199 else
200     x = x1 + rad1;
201     y = y1;
202     z = z1;
203     rho1 = sqrt((x-x1)^2 + (y-y1)^2);
204     rho2 = sqrt((x-x2)^2 + (y-y2)^2);

```

```

205     r1 = sqrt(rho1^2 + (z-z1)^2);
206     r2 = sqrt(rho2^2 + (z-z2)^2);
207     for n = 1:1:sum_max
208         cnst = (R23^n)*(R21^n);
209         D11 = z+z1+2*d*n+2*d;
210         D12 = z+z2+2*d*n+2*d;
211         D51 = z-z1+2*d*n+2*d;
212         D52 = z-z2+2*d*n+2*d;
213         D61 = z1-z+2*d*n+2*d;
214         D62 = z2-z+2*d*n+2*d;
215         D71 = 2*d*n-z-z1;
216         D72 = 2*d*n-z-z2;
217         ra1 = sqrt(rho1^2 + D11^2);
218         ra2 = sqrt(rho2^2 + D12^2);
219         re1 = sqrt(rho1^2 + D51^2);
220         re2 = sqrt(rho2^2 + D52^2);
221         rf1 = sqrt(rho1^2 + D61^2);
222         rf2 = sqrt(rho2^2 + D62^2);
223         rg1 = sqrt(rho1^2 + D71^2);
224         rg2 = sqrt(rho2^2 + D72^2);
225
226         R1(n) = cnst*(R23/ra1 + R23*R21/re1 + ...
227                 R23*R21/rf1 + R21/rg1);
228         R2(n) = cnst*(R23/ra2 + R23*R21/re2 + ...
229                 R23*R21/rf2 + R21/rg2);
230     end
231     G2 = 1/r1 - 1/r2 + sum(R1) - sum(R2);
232
233     x = x2 - rad2;
234     y = y2;
235     z = z2;

```

```

236     rho1 = sqrt((x-x1)^2+(y-y1)^2);
237     rho2 = sqrt((x-x2)^2+(y-y2)^2);
238     r1 = sqrt(rho1^2 + (z-z1)^2);
239     r2 = sqrt(rho2^2 + (z-z2)^2);
240     for n = 1:1:sum_max
241         cnst = (R23^n)*(R21^n);
242         D11 = z+z1+2*d*n+2*d;
243         D12 = z+z2+2*d*n+2*d;
244         D51 = z-z1+2*d*n+2*d;
245         D52 = z-z2+2*d*n+2*d;
246         D61 = z1-z+2*d*n+2*d;
247         D62 = z2-z+2*d*n+2*d;
248         D71 = 2*d*n-z-z1;
249         D72 = 2*d*n-z-z2;
250         ra1 = sqrt(rho1^2 + D11^2);
251         ra2 = sqrt(rho2^2 + D12^2);
252         re1 = sqrt(rho1^2 + D51^2);
253         re2 = sqrt(rho2^2 + D52^2);
254         rf1 = sqrt(rho1^2 + D61^2);
255         rf2 = sqrt(rho2^2 + D62^2);
256         rg1 = sqrt(rho1^2 + D71^2);
257         rg2 = sqrt(rho2^2 + D72^2);
258
259         R1(n) = cnst*(R23/ra1 + R23*R21/re1 + ...
260                 R23*R21/rf1 + R21/rg1);
261         R2(n) = cnst*(R23/ra2 + R23*R21/re2 + ...
262                 R23*R21/rf2 + R21/rg2);
263     end
264     G1 = 1/r1 - 1/r2 + sum(R1) - sum(R2);
265
266     Geo = G2-G1;

```

```

267
268     if(strcmp(vi_typ, 'V'))
269         K2 = ST/Geo;
270     else
271         imped = Geo/(4*pi*Y2);
272         V0 = abs(ST*imped);
273         K2 = V0/Geo;
274     end
275 end
276
277 %DECIMATE SWEEP LINE
278 if(strcmp(swp_typ, 'C'))
279     stepp = linspace(min(dist_cust), ...
280         max(dist_cust), npts+1);
281 else
282     stepp = linspace(swp_min, ...
283         swp_max, npts+1);
284 end
285
286 %ADJUST ELECTRODE ORIENTATION IN THE X-Y PLANE
287 x1 = (-sep/2)*cosd(theta2);
288 y1 = (-sep/2)*sind(theta2);
289 x2 = (sep/2)*cosd(theta2);
290 y2 = (sep/2)*sind(theta2);
291
292 %RESET SENSOR COORDINATES
293 x = 0;
294 y = 0;
295 z = 0;
296
297 %MAIN LOOP

```

```

298 for j=0:1:length_main
299
300     %PERCENTAGE INDICATOR
301     percent_done = j/(length(step)) * 100
302
303     %SET SENSOR COORDINATES
304     if(strcmp(swp_typ, 'H'))
305         x = stepp(j+1)*cosd(theta1);
306         y = stepp(j+1)*sind(theta1);
307         z = swp_line;
308     elseif(strcmp(swp_typ, 'V'))
309         x = swp_line*cosd(theta1);
310         y = swp_line*sind(theta1);
311         z = stepp(j+1);
312     elseif(strcmp(swp_typ, 'C'))
313         x = x_space(j+1);
314         y = y_space(j+1);
315         z = z_space(j+1);
316     end
317
318     %CALCULATE DISTANCES
319     rho1 = sqrt((x-x1)^2+(y-y1)^2);
320     rho2 = sqrt((x-x2)^2+(y-y2)^2);
321     r1 = sqrt(rho1^2 + (z-z1)^2);
322     r2 = sqrt(rho2^2 + (z-z2)^2);
323
324     %DIPOLE LOCATION IN REGION 1
325     if h > 0
326
327         %OBSERVATION IN REGION 1, DIPOLE IN REGION 1
328         if (z > 0)

```

```

329      %COMPUTE VOLTAGE AND E-FIELD
330      for n = 0:1:sum_max
331          cnst = (R23^n)*(R21^n);
332          D11 = z+z1+2*d*n+2*d;
333          D12 = z+z2+2*d*n+2*d;
334          D21 = z+z1+2*d*n;
335          D22 = z+z2+2*d*n;
336          ra1 = sqrt(rho1^2 + D11^2);
337          ra2 = sqrt(rho2^2 + D12^2);
338          rb1 = sqrt(rho1^2 + D21^2);
339          rb2 = sqrt(rho2^2 + D22^2);
340
341          Ex1img(n+1) = cnst*(x-x1)*(R23/ra1^3 - ...
342                                R21/rb1^3);
343          Ex2img(n+1) = cnst*(x-x2)*(R23/ra2^3 - ...
344                                R21/rb2^3);
345          Ey1img(n+1) = cnst*(y-y1)*(R23/ra1^3 - ...
346                                R21/rb1^3);
347          Ey2img(n+1) = cnst*(y-y2)*(R23/ra2^3 - ...
348                                R21/rb2^3);
349          Ez1img(n+1) = cnst*(D11*R23/ra1^3 - ...
350                                D21*R21/rb1^3);
351          Ez2img(n+1) = cnst*(D12*R23/ra2^3 - ...
352                                D22*R21/rb2^3);
353          V_sum(n+1) = cnst*(R23*(1/ra2-1/ra1) + ...
354                                (1/rb2-1/rb1));
355      end
356
357      Ex1_img = K1*((x-x1)/r1^3 + sum(Ex1img));
358      Ex2_img = K1*((x-x2)/r2^3 + sum(Ex2img));
359      Ex_img(j+1) = Ex2_img - Ex1_img;

```

```

360     Ey1_img = K1*((y-y1)/r1^3 + sum(Ey1img));
361     Ey2_img = K1*((y-y2)/r2^3 + sum(Ey2img));
362     Ey_img(j+1) = Ey2_img - Ey1_img;
363     Ez1_img = K1*((z-z1)/r1^3 + sum(Ez1img));
364     Ez2_img = K1*((z-z2)/r2^3 + sum(Ez2img));
365     Ez_img(j+1) = Ez2_img - Ez1_img;
366     E_mag(j+1) = sqrt(Ex_img(j+1).^2 + ...
367                       Ey_img(j+1).^2 + Ez_img(j+1).^2);
368     V(j+1) = K1*((1/r2-1/r1) + sum(V_sum));
369
370     end
371
372     %OBSERVATION IN REGION 2, DIPOLE IN REGION 1
373     if (z < 0)&&(z > -d)
374         %COMPUTE VOLTAGE AND E-FIELD
375         for n = 0:1:sum_max
376             cnst = (R23^n)*(R21^n);
377             D11 = z+z1+2*d*n+2*d;
378             D12 = z+z2+2*d*n+2*d;
379             D31 = z1-z+2*d*n;
380             D32 = z2-z+2*d*n;
381             ra1 = sqrt(rho1^2 + D11^2);
382             ra2 = sqrt(rho2^2 + D12^2);
383             rc1 = sqrt(rho1^2 + D31^2);
384             rc2 = sqrt(rho2^2 + D32^2);
385
386             Ex1img(n+1) = cnst*(x-x1)*(R23/ra1^3 + ...
387                                   1/rc1^3);
388             Ex2img(n+1) = cnst*(x-x2)*(R23/ra2^3 + ...
389                                   1/rc2^3);
390             Ey1img(n+1) = cnst*(y-y1)*(R23/ra1^3 + ...

```



```

391                                     1/rc1^3);
392     Ey2img(n+1) = cnst*(y-y2)*(R23/ra2^3 + ...
393                                     1/rc2^3);
394     Ez1img(n+1) = cnst*(R23*D11/ra1^3 - ...
395                                     D31/rc1^3);
396     Ez2img(n+1) = cnst*(R23*D12/ra2^3 - ...
397                                     D32/rc2^3);
398     V_sum(n+1) = cnst*(R23*(1/ra2-1/ra1) + ...
399                                     (1/rc2-1/rc1));
400     end
401
402     Ex_img(j+1) = K1*(1-R21)*(sum(Ex2img) - ...
403                                     sum(Ex1img));
404     Ey_img(j+1) = K1*(1-R21)*(sum(Ey2img) - ...
405                                     sum(Ey1img));
406     Ez_img(j+1) = K1*(1-R21)*(sum(Ez2img) - ...
407                                     sum(Ez1img));
408     E_mag(j+1) = sqrt(Ex_img(j+1).^2 + ...
409                                     Ey_img(j+1).^2 + Ez_img(j+1).^2);
410     V(j+1) = K1*(1-R21)*sum(V_sum);
411     end
412
413     %DIPOLE LOCATION IN REGION 2
414     else
415
416         %OBSERVATION IN REGION 1, DIPOLE IN REGION 2
417         if (z > 0)
418             %COMPUTE VOLTAGE AND E-FIELD
419             for n = 0:1:sum_max
420                 cnst = (R23^n)*(R21^n);
421                 D11 = z+z1+2*d*n+2*d;

```

```

422         D12 = z+z2+2*d*n+2*d;
423         D41 = z-z1+2*d*n;
424         D42 = z-z2+2*d*n;
425         ra1 = sqrt(rho1^2 + D11^2);
426         ra2 = sqrt(rho2^2 + D12^2);
427         rd1 = sqrt(rho1^2 + D41^2);
428         rd2 = sqrt(rho2^2 + D42^2);
429
430         Ex1img(n+1) = cnst*(x-x1)*(R23/ra1^3 + ...
431                                1/rd1^3);
432         Ex2img(n+1) = cnst*(x-x2)*(R23/ra2^3 + ...
433                                1/rd2^3);
434         Ey1img(n+1) = cnst*(y-y1)*(R23/ra1^3 + ...
435                                1/rd1^3);
436         Ey2img(n+1) = cnst*(y-y2)*(R23/ra2^3 + ...
437                                1/rd2^3);
438         Ez1img(n+1) = cnst*(R23*D11/ra1^3 + ...
439                                D41/rd1^3);
440         Ez2img(n+1) = cnst*(R23*D12/ra2^3 + ...
441                                D42/rd2^3);
442         V_sum(n+1) = cnst*(R23*(1/ra2-1/ra1) + ...
443                                (1/rd2-1/rd1));
444
445     end
446     Ex_img(j+1) = K2*(1+R21)*(sum(Ex2img) - ...
447                                sum(Ex1img));
448     Ey_img(j+1) = K2*(1+R21)*(sum(Ey2img) - ...
449                                sum(Ey1img));
450     Ez_img(j+1) = K2*(1+R21)*(sum(Ez2img) - ...
451                                sum(Ez1img));
452     E_mag(j+1) = sqrt(Ex_img(j+1).^2 + ...

```

```

453             Ey_img(j+1).^2 + Ez_img(j+1).^2);
454     V(j+1) = K2*(1+R21)*sum(V_sum);
455     end
456
457     %OBSERVATION IN REGION 2, DIPOLE IN REGION 2
458     if (z < 0)&&(z > -d)
459         %COMPUTE VOLTAGE AND E-FIELD
460         for n = 0:1:sum_max
461             cnst = (R23^n)*(R21^n);
462             D11 = z+z1+2*d*n+2*d;
463             D12 = z+z2+2*d*n+2*d;
464             D51 = z-z1+2*d*n+2*d;
465             D52 = z-z2+2*d*n+2*d;
466             D61 = z1-z+2*d*n+2*d;
467             D62 = z2-z+2*d*n+2*d;
468             D71 = 2*d*n-z-z1;
469             D72 = 2*d*n-z-z2;
470             ra1 = sqrt(rho1^2 + D11^2);
471             ra2 = sqrt(rho2^2 + D12^2);
472             re1 = sqrt(rho1^2 + D51^2);
473             re2 = sqrt(rho2^2 + D52^2);
474             rf1 = sqrt(rho1^2 + D61^2);
475             rf2 = sqrt(rho2^2 + D62^2);
476             rg1 = sqrt(rho1^2 + D71^2);
477             rg2 = sqrt(rho2^2 + D72^2);
478
479             Ex1img(n+1) = cnst*(x-x1)*(R23/ra1^3 + ...
480                                     R23*R21/re1^3 + ...
481                                     R23*R21/rf1^3 + ...
482                                     R21/rg1^3);
483             Ex2img(n+1) = cnst*(x-x2)*(R23/ra2^3 + ...

```

```

484             R23*R21/re2^3 + ...
485             R23*R21/rf2^3 + ...
486             R21/rg2^3);
487     Ey1img(n+1) = cnst*(y-y1)*(R23/ra1^3 + ...
488             R23*R21/re1^3 + ...
489             R23*R21/rf1^3 + ...
490             R21/rg1^3);
491     Ey2img(n+1) = cnst*(y-y2)*(R23/ra2^3 + ...
492             R23*R21/re2^3 + ...
493             R23*R21/rf2^3 + ...
494             R21/rg2^3);
495     Ez1img(n+1) = cnst*(R23*D11/ra1^3 + ...
496             R23*R21*D51/re1^3 - ...
497             R23*R21*D61/rf1^3 - ...
498             R21*D71/rg1^3);
499     Ez2img(n+1) = cnst*(R23*D12/ra2^3 + ...
500             R23*R21*D52/re2^3 - ...
501             R23*R21*D62/rf2^3 - ...
502             R21*D72/rg2^3);
503     V_sum(n+1) = cnst*(R23*(1/ra2-1/ra1) + ...
504             R23*R21*(1/re2-1/re1) + ...
505             R23*R21*(1/rf2-1/rf1) + ...
506             R21*(1/rg2-1/rg1));
507
508     end
509     Ex_img1 = K2*((x-x1)/r1^3 + sum(Ex1img));
510     Ex_img2 = K2*((x-x2)/r2^3 + sum(Ex2img));
511     Ey_img1 = K2*((y-y1)/r1^3 + sum(Ey1img));
512     Ey_img2 = K2*((y-y2)/r2^3 + sum(Ey2img));
513     Ez_img1 = K2*((z-z1)/r1^3 + sum(Ez1img));
514     Ez_img2 = K2*((z-z2)/r2^3 + sum(Ez2img));

```

```

515         Ex_img(j+1) = Ex_img2 - Ex_img1;
516         Ey_img(j+1) = Ey_img2 - Ey_img1;
517         Ez_img(j+1) = Ez_img2 - Ez_img1;
518         E_mag(j+1) = sqrt(Ex_img(j+1).^2 + ...
519                             Ey_img(j+1).^2 + ...
520                             Ez_img(j+1).^2);
521         V(j+1) = K2*((1/r2-1/r1) + sum(V_sum));
522     end
523 end
524 end
525
526 %SAVE VOLTAGE AND E-FIELD DATA
527 DATA = [stepp.',V.',Ex_img.',Ey_img.',Ez_img.',E_mag.'];
528 save 'tmp' DATA
529
530 %COORDINATE TRANSFORMATIONS
531 if(~plot_typ)
532     E1 = abs(Ex_img);
533     E2 = abs(Ey_img);
534     E3 = abs(Ez_img);
535 else
536     E1 = abs(cosd(thetal)*Ex_img - sind(thetal)*Ey_img);
537     E2 = abs(-sind(thetal)*Ex_img + cosd(thetal)*Ey_img);
538     E3 = abs(Ez_img);
539 end
540
541 %PLOTTING
542 Voltage = abs(V);
543 E_magnitude = abs(E_mag);
544
545 figure(1)

```

```

546 semilogy (stepp,E1,'r',stepp,E2,'b',stepp,E3,'g','LineWidth',2)
547 hold on
548 semilogy (stepp,Voltage,'m','LineWidth',2)
549 hold on
550 semilogy (stepp,E_magnitude,'k','LineWidth',2)
551 hold off
552 if (~plot_typ)
553     legend('Ex','Ey','Ez','Voltage','Magnitude')
554 else
555     legend('E_\rho','E_\phi','Ez','Voltage','Magnitude')
556 end
557
558 if(strcmp(swp_typ,'H'))
559     xlabel('Horizontal Distance (m)')
560 else
561     xlabel('Vertical Distance (m)')
562 end
563 ylabel('E-Field (V/m), Voltage (V), Magnitude (V/m)')
564 xlim([min(stepp) max(stepp)]);
565 grid on;

```

SENSOR ORIENTATION, RECIPROCITY AND SOFTWARE EVALUATION IN THE
CONTEXT OF EXTREMELY LOW FREQUENCY APPLICATIONS

A Thesis

Presented in Partial Fulfillment of the Requirements for the

Degree of Master of Science

with a

Major in Electrical Engineering

in the

College of Graduate Studies

University of Idaho

by

Das deLeon Kuhnhausen Butherus

November 2011

Major Professor: Jeffrey L. Young, Ph.D.

AUTHORIZATION TO SUBMIT THESIS

This thesis of Das Butherus, submitted for the degree of Master of Science with a major in Electrical Engineering and titled “SENSOR ORIENTATION, RECIPROCITY AND SOFTWARE EVALUATION IN THE CONTEXT OF EXTREMELY LOW FREQUENCY APPLICATIONS,” has been reviewed in final form. Permission, as indicated by the signatures and dates given below, is now granted to submit final copies to the College of Graduate Studies for approval.

Major Professor _____ Date _____
Jeffrey L. Young

Committee

Members _____ Date _____
Christopher L. Wagner

_____ Date _____
Dean Edwards

Department

Administrator _____ Date _____
Brian Johnson

Discipline's

College Dean _____ Date _____
Larry Stauffer

Final Approval and Acceptance by the College of Graduate Studies

_____ Date _____
Jie Chen

Abstract

The U.S. Navy is interested in the propagation of low frequency electromagnetic waves in marine environments for the purpose of mine detection. As a result, a large theoretical and experimental effort was undertaken to understand this phenomenon, where the University of Idaho was employed on the theoretical side of the project. The details associated with this portion of the project alone are incredibly vast. The main focus of this thesis is to describe three topics of concern within these details. The first of these topics is concerned with a field transformation from a coordinate sytem associated with a sensor into a coordinate system defined in terms of geographic North, where it is assumed that coordinate system associated with the sensor can experience some rotation. The next topic is associated with the reciprocity theorem as applied to the project. Finally, there is a discussion about the commercial software program Maxwell, which is being investigated as a candidate for a viable simulation tool.

Vita

The author received his BSEE degree from Montana Tech of the University of Montana in 2008. He is currently pursuing his MSEE degree from the the University of Idaho and working as a research assistant in the Department of Electrical and Computer Engineering. His research interests include electromagnetic theory,computational electromagnetics, and antenna design.

Acknowledgements

I would like to thank Dr. Jeffery L. Young for mentoring and guiding me throughout my graduate education. I would also like to thank Dr. Christopher L. Wagner, Chris Johnson, Robert Rebich, Chenchen Jimmy Li, Markus Geiger, Neelima Dahal and my committee for working with me throughout the project; without whom, this thesis would not have been possible.

This work was supported by the Office of Naval Research under grant number N00014-09-1-0923.

Table of Contents

Abstract	iii
Vita	iv
Acknowledgements	v
Table of Contents	vi
1 Introduction	1
1.1 Project Motivation	1
1.2 Background	1
1.3 Scope	2
2 Coordinate System Standardization for a Sensor under Rotation	5
2.1 Theory	6
2.1.1 Horizontal Plane Rotation	6
2.1.2 Azimuthal Rotation	9
2.2 Experiment	12
2.2.1 Experimental Setup	12
2.2.2 Building the Helmholtz Coil	13
2.2.3 Experimental Procedure	15
2.3 Error and Results	16
2.3.1 Results	16
2.3.2 Error	20
3 Reciprocity Applied To ELF Simulations	27
3.1 Reciprocity Theorem	27

3.2	Reciprocity Applied To ELF Simulations	31
3.3	Method Validation	34
4	ELF Simulations Using Ansys Maxwell	37
4.1	Solution Types	38
4.1.1	“Eddy Current” Solution Type	38
4.1.2	“DC-conduction” Solution Type	38
4.2	Source Modeling	39
4.2.1	Electric Source Modeling	39
4.2.2	Impedance Matching	40
4.2.3	Magnetic Source Modelling	40
4.2.4	Relative Coordinate Systems	41
4.2.5	Reciprocity and Source Modeling	41
4.3	Modeling a Lake Environment	42
4.3.1	Importing a Model of the Lake Bed	42
4.3.2	Creation of Air and Water Regions	43
4.3.3	Material Properties	44
4.4	Meshing	46
4.5	Domain Truncation	48
4.5.1	“DC-conduction” Boundaries	48
4.5.2	“Eddy Current” Boundaries	50
4.6	Extracting Field Data	52
4.7	Method Validation	53
4.8	Experimental Comparisons	55
5	Conclusion	61
	Bibliography	64
A	Rotation Compensation Code	66
B	Reciprocity Processing Code	74

List of Figures

2.1	Tilt angle definitions.	6
2.2	Azimuthal angle definitions.	9
2.3	Experimental setup.	12
2.4	Helmholtz coil design.	13
2.5	20 Hz signal collected in rotating coordinate system s	17
2.6	20 Hz signal after transformation into coordinate system m	17
2.7	20 Hz signal collected in stationary coordinate system m	18
2.8	FFT of 20 Hz signal after transformation into coordinate system m	19
2.9	FFT of 20 Hz signal in stationary coordinate system m	19
2.10	The effect of magnetic materials on the magnitude of the magnetic field collected in coordinate system m	21
2.11	The effect of magnetic materials on the magnitude of the magnetic field collected in coordinate system s	22
2.12	Magnitude of the magnetic field collected in m for the small signal, 20 Hz experiment.	23
2.13	Magnitude of the magnetic field collected in s for the small signal, 20 Hz experiment.	23
2.14	Unfiltered ϕ_x	25
2.15	Filtered ϕ_x	25
2.16	Data created from inconsistent sampling rates.	26
3.1	Comparisons of electric field components.	35
3.2	Comparisons of magnetic field components.	36

4.1	Simulation model of Idlewild Bay.	44
4.2	Material ambiguity effects.	45
4.3	Flow diagram of adaptive meshing process.	46
4.4	Comparison of good and bad meshing schemes.	48
4.5	“DC-conduction” boundary effects on fields.	49
4.6	“Eddy current” boundary effects on fields for 1000 Hz.	51
4.7	“Eddy current” boundary effects on fields for 10 Hz.	52
4.8	Illustration of three layer scenario.	53
4.9	Electric field results obtained for a three layer comparison.	54
4.10	Magnetic field results obtained for a three layer comparison.	54
4.11	Electric field comparisons for scenario 304.01.	56
4.12	Magnetic field comparisons for scenario 304.01.	57
4.13	Electric field comparisons for scenarios 100.02, 100.04, 100.06, 100.08 and 100.10.	58
4.14	Magnetic field comparisons for scenarios 100.02, 100.04, 100.06, 100.08 and 100.10.	58
4.15	Electric field comparisons for scenario 1016.	59
4.16	Magnetic field comparisons for scenario 1016.	60

List of Tables

2.1	Error percentages between signals collected in coordinate system m and signals transformed into coordinate system m	20
4.1	Material Properties	45

Chapter 1

Introduction

1.1 Project Motivation

The Navy is changing their fleet to incorporate electric drive propulsion systems. These new systems are expected to create large electromagnetic fields in the extremely low frequency (ELF) range. These fields may then be detected and used to detonate mines, which may threaten naval vessels. It is therefore of considerable interest to the Navy to be able to understand ELF field and wave phenomenon. The primary interest is the range detection of ELF signals generated by sources similar to the new electric drive systems. It is desirable to model phenomenon associated with these ELF frequencies using numerical simulation and validate the simulations using experimental methods. The experimentation and research associated with these interests were conducted at Lake Pend Orielle in Bayview, ID, where experiments were conducted by the ARD (Acoustic Research Detachment). The modeling and simulations portion of this effort was then conducted by the University of Idaho (UI) [1].

1.2 Background

The sensors used in the ELF experiments are able to detect components of electric and magnetic fields along three orthogonal axes. This allows for a representation of experimental electric and magnetic fields in a coordinate system defined by the sensor's axes. Simulations

are carried out in a coordinate system relative to true north. The use of two different coordinate systems introduces a problem for comparisons between experimental and simulation results. This problem is addressed by considering a coordinate system transformation.

The idea of coordinate system transformation has existed for over two centuries. Euler proved that three angles could sufficiently describe a three dimensional rotation about a fixed point in the eighteenth century [2]. A more modern document written by Berner encompasses many of the methods currently used for rotations [3]. Euler angles are still commonly used for some applications, but this thesis demonstrates that they would not be a practical option for this project.

In the ELF experiment, the majority of the experiments were conducted with the sensor stationary and the source either in motion or situated in many locations. Simulation tools on the other hand, are able to obtain fields in many locations for one source location within a simulation. It is therefore convenient to be able to excite the experimental sensor and monitor the fields in the locations of the experimental source in ELF simulations. This is expected to be achieved through the use of the reciprocity theorem.

The reciprocity theorem is a very important and widely known theorem in electromagnetics. Lorentz clearly stated the reciprocity theorem as applied to electromagnetics in 1895 [4], which is why it is most commonly referred to as the Lorentz reciprocity theorem. Since then the reciprocity theorem has evolved through many works to be consistent with more modern notation and has been used in various applications. In this thesis a discussion of the reciprocity theorem is extended to its application in the ELF project.

1.3 Scope

To transform a vector from a sensor's coordinate system into a coordinate system defined by true north, relationships need to be established between the two coordinate systems. The sensor is expected to provide information including tilt angles and magnetic fields. The assumption is made that the sensor can have rotational motion about its origin. This creates additional complexity, specifically in the context of Fourier analysis.

The method used in this thesis performs this transformation with the use of two matrices. The first matrix transforms the vector into a coordinate system in the horizontal plane using the tilt angles from the sensor. The second matrix then uses the direction of Earth's magnetic field to transform the vector into a coordinate system relative to true north. This transformation is expected to transform field's representations from the sensor's coordinate system into the coordinate system defined by true north for every instant in time.

Reciprocity is applied to use a stationary source within simulations to obtain fields for an experimental scenario that has a moving source, but a stationary sensor. Applying reciprocity to this scenario is not as simple as interchanging the source and sensor.

To apply reciprocity correctly to this scenario, the experimental sensor is first excited as the source within simulations to obtain the fields reactions onto the experimental source. Reciprocity is then used to obtain the reaction of the fields created by the experimental source onto the sensor. Employing some assumptions, we utilize these relationships to obtain experimental fields using the fields produced from simulations.

Simulation tools used in the ELF project are challenged with the task of being able to solve complicated geometries associated with the Lake at low frequencies. Some simulation tools used in this project are custom and some are commercial solvers. Some of the simulation tools make assumptions associated with frequency or geometry, which may or may not make them unsuitable for ELF applications.

The commercial solver Maxwell (a product of the Ansys corporation) is investigated in this thesis. Maxwell is able to model fairly complicated geometries. It is also able to model fairly complicated sources. However, assumptions about frequency are inherently made, which makes Maxwell either a static or quasi-static solver, depending on the media and source type being modeled. There are many nuances associated with Maxwell. The challenge is then tailoring Maxwell to the specific needs of the ELF project. It is expected that Maxwell is capable of modeling some of the complicated geometries associated with the ELF project; how well Maxwell is able to do this is a key question of this thesis.

This thesis contributed to the project by creating matrices capable of transforming a field representation from the sensor's coordinate system into a coordinate system defined by true

north. It shows how relationships are established between these coordinate systems and how these relationships are then used to transform fields. It then shows how these matrices perform in an experiment. Contributions were also made to the project associated with the use of reciprocity. This thesis illustrates correct and incorrect interpretations of the reciprocity theorem. It then shows how reciprocity is applied to the ELF project, where only a single component of the electric or magnetic field can be found from a particular simulation using reciprocity. Lastly, this thesis contributed to the project by showing how the commercial software program Maxwell is tailored to the needs of the ELF project. Maxwell's strengths and weaknesses are discussed and comparisons of its fields are shown, both against experimental results and against results obtained by other simulation tools used on the project.

Chapter 2

Coordinate System Standardization for a Sensor under Rotation

The purpose of this effort is to transform electric and magnetic field data recorded from a sensor into a standardized coordinate system relative to magnetic north. The strategy uses tilt angles from a sensor and the magnetic field of the Earth to rotate the electric and magnetic field components from the sensor's coordinate system into a coordinate system defined by magnetic north. The problem with this approach is that rotations in three dimensions do not commute, so the method of using Euler angles to analytically perform three rotations is not applicable. The method discussed here uses vectors, in the context of two rotational operations. The first rotation puts the components in terms of a coordinate system that is defined on the horizontal plane. This coordinate system's position is azimuthally defined in terms of the position of the sensor's x -axis. The second rotation then azimuthally rotates the components to define them in terms of a new coordinate system with a y -axis that is aligned with magnetic north. An experiment was conducted to prove that the rotations were correctly transforming components from the sensor's coordinate system into a coordinate system defined by magnetic north. This experiment was designed to make comparisons between fields observed with a sensor in a stationary coordinate system and fields transformed into that coordinate system after being observed by a sensor under rotation.

2.1 Theory

2.1.1 Horizontal Plane Rotation

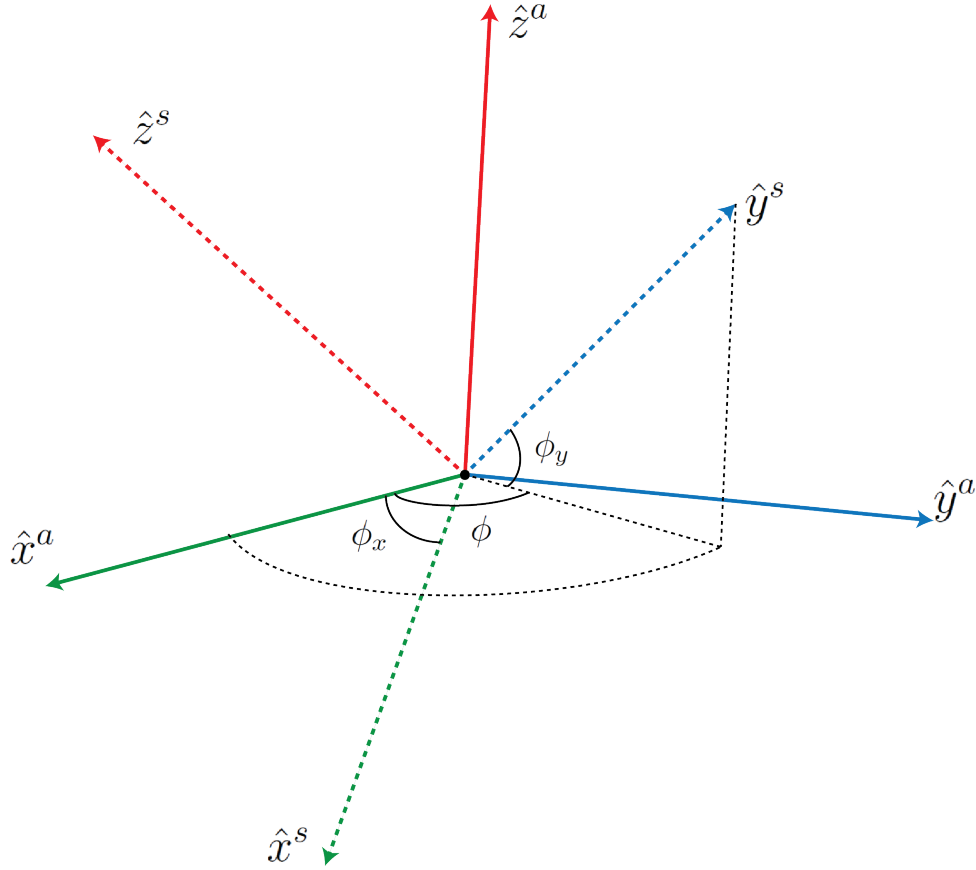


Figure 2.1: Tilt angle definitions.

Two tilt angles are defined as shown in Figure 2.1 in terms of two coordinate systems. The s coordinate system is defined in terms of the sensor's axes and the arbitrary coordinate system a is defined on the horizontal plane, arbitrarily situated in an azimuthal sense. Here ϕ_x and ϕ_y are defined as the angles between the horizontal plane and the x and y axes of the sensor, respectively. The signs associated with ϕ_x and ϕ_y are dictated by the right hand rule when considering x^s -axis rotations about the y^s -axis and y^s -axis rotations about the x^s -axis. Coordinate system a is defined by forcing the x^s -axis to lie in the x^a - z^a plane. The unit vector \hat{x}^s is then represented in terms of the a coordinate system as,

$$\hat{x}^s = \cos \phi_x \hat{x}^a - \sin \phi_x \hat{z}^a. \quad (2.1)$$

An angle ϕ is defined from the x -axis of the a coordinate system to the projection of the sensor's y -axis onto the horizontal plane. The y -axis of the sensor is then represented in terms of the a coordinate system as,

$$\hat{y}^s = \cos \phi \cos \phi_y \hat{x}^a + \sin \phi \cos \phi_y \hat{y}^a + \sin \phi_y \hat{z}^a. \quad (2.2)$$

The angle ϕ can be found by exploiting orthogonality of the sensor's coordinate system such that,

$$\hat{x}^s \cdot \hat{y}^s = \cos \phi \cos \phi_x \cos \phi_y - \sin \phi_x \sin \phi_y = 0, \quad (2.3)$$

in which case,

$$\phi = \cos^{-1}(\tan \phi_x \tan \phi_y). \quad (2.4)$$

It should be noted that the principle value of the arccosine function restricts the angle ϕ to a maximum of 180° . However, a ϕ larger than 180° corresponds to a situation where the z -axis of the sensor is larger than 90° from the vertical axis. The two tilt angles ϕ_x and ϕ_y alone do not provide enough information to identify if the sensor is upside down, so this restriction on ϕ is unavoidable without having addition information.

The z -axis of the sensor can be represented in terms of the horizontal coordinate system by performing the cross product:

$$\begin{aligned} \hat{z}^s &= \hat{x}^s \times \hat{y}^s \\ &= \sin \phi_x \sin \phi \cos \phi_y \hat{x}^a - (\cos \phi_x \sin \phi_y + \sin \phi_x \cos \phi \cos \phi_y) \hat{y}^a + \cos \phi_x \sin \phi \cos \phi_y \hat{z}^a. \end{aligned} \quad (2.5)$$

From Eqns. (2.1), (2.2) and (2.5), the sensor axes are completely defined in terms of the horizontal coordinate systems as,

$$\begin{bmatrix} \hat{x}^s \\ \hat{y}^s \\ \hat{z}^s \end{bmatrix} = R \begin{bmatrix} \hat{x}^a \\ \hat{y}^a \\ \hat{z}^a \end{bmatrix}, \quad (2.6)$$

where,

$$R = \begin{bmatrix} \cos \phi_x & 0 & -\sin \phi_x \\ \cos \phi \cos \phi_y & \sin \phi \cos \phi_y & \sin \phi_y \\ \sin \phi_x \sin \phi \cos \phi_y & -\cos \phi_x \sin \phi_y - \sin \phi_x \cos \phi \cos \phi_y & \cos \phi_x \sin \phi \cos \phi_y \end{bmatrix}. \quad (2.7)$$

The matrix R is an orthogonal matrix, so its inverse is equal to its transpose [5]. Moreover, it can be considered a transformation from the a coordinate system into the s coordinate system. The matrix R^{-1} is then used to transform field components from coordinate system s into coordinate system a for a vector field \vec{B} , where,

$$\begin{aligned} \vec{B} &= B_x^a \hat{x}^a + B_y^a \hat{y}^a + B_z^a \hat{z}^a \\ &= B_x^s \hat{x}^s + B_y^s \hat{y}^s + B_z^s \hat{z}^s. \end{aligned} \quad (2.8)$$

It follows from Eqn (2.6) that

$$\begin{bmatrix} B_x^a \\ B_y^a \\ B_z^a \end{bmatrix} = R^{-1} \begin{bmatrix} B_x^s \\ B_y^s \\ B_z^s \end{bmatrix} \quad (2.9)$$

where,

$$R^{-1} = \begin{bmatrix} \cos \phi_x & \cos \phi \cos \phi_y & \sin \phi_x \sin \phi \cos \phi_y \\ 0 & \sin \phi \cos \phi_y & -\cos \phi_x \sin \phi_y - \sin \phi_x \cos \phi \cos \phi_y \\ -\sin \phi_x & \sin \phi_y & \cos \phi_x \sin \phi \cos \phi_y \end{bmatrix}. \quad (2.10)$$

This procedure transforms \vec{B} from the sensor's coordinate system into an arbitrary coordinate system in the horizontal plane using the angles ϕ_x and ϕ_y . A limitation associated with using these angles is that they provide no information about whether or not the sensor is upside-down. It is then necessary to make the assumption that the sensor's z -axis is not tilted more than 90° from vertical in an experiment. After the rotation is performed the fields are in terms of a horizontal coordinate system that is azimuthally situated relative to the position of the x -axis of the sensor. An additional rotation about the z -axis is then needed to transform field components into a particular horizontal coordinate system.

2.1.2 Azimuthal Rotation

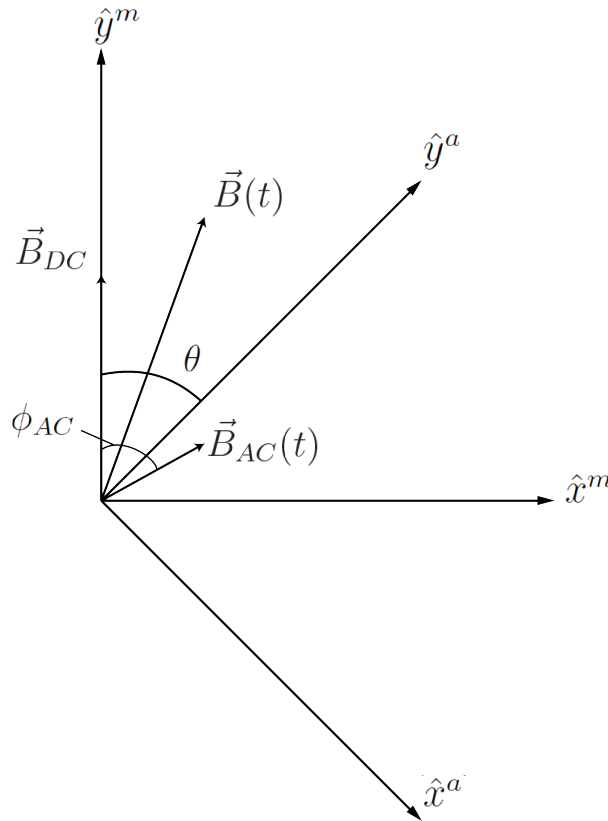


Figure 2.2: Azimuthal angle definitions.

The transformation of a vector from the arbitrary horizontal coordinate system a into a coordinate system m defined in terms of magnetic north is achieved by multiplying that vector by a rotation matrix. The coordinate system m is defined with its y -axis parallel to magnetic

north and angles are defined according to Figure 2.2. The vector \vec{B} can then be transformed from the a coordinate system into the m coordinate system via,

$$\begin{bmatrix} B_x^m \\ B_y^m \\ B_z^m \end{bmatrix} = \begin{bmatrix} \cos \theta & \sin \theta & 0 \\ -\sin \theta & \cos \theta & 0 \\ 0 & 0 & 1 \end{bmatrix} \begin{bmatrix} B_x^a \\ B_y^a \\ B_z^a \end{bmatrix}, \quad (2.11)$$

where θ is a function of time, i.e. $\theta = \theta(t)$. To find the angle $\theta(t)$ the vector $\vec{B}(t)$ is first decomposed into a static and a dynamic component. That is, let

$$\vec{B}(t) = \vec{B}_{DC} + \vec{B}_{AC}(t). \quad (2.12)$$

The ensuing development assumes that the static component is the Earth's magnetic field. The dynamic component then includes ambient noise, noise induced by rotation, and the measured ELF signals. Figure 2.2 shows the vectors in terms of both the a and m coordinate systems. Components of the vector \vec{B} are represented in terms of coordinate system a as,

$$\begin{aligned} B_x^a(t) &= \vec{B}(t) \cdot \hat{x}^a \\ &= \vec{B}_{DC} \cdot \hat{x}^a + \vec{B}_{AC}(t) \cdot \hat{x}^a \\ &= B_{DC} \cos(90^\circ + \theta(t)) + B_{AC}(t) \cos[90^\circ - (\phi_{AC}(t) - \theta(t))] \\ &= -B_{DC} \sin \theta(t) - B_{AC}(t) \sin[\theta(t) - \phi_{AC}(t)] \end{aligned} \quad (2.13)$$

and

$$\begin{aligned} B_y^a(t) &= \vec{B}(t) \cdot \hat{y}^a \\ &= \vec{B}_{DC} \cdot \hat{y}^a + \vec{B}_{AC}(t) \cdot \hat{y}^a \\ &= B_{DC} \cos \theta(t) + B_{AC}(t) \cos[\theta(t) - \phi_{AC}(t)]. \end{aligned} \quad (2.14)$$

The time series data for $B_x^a(t)$ and $B_y^a(t)$ are processed with a low pass filter after being

obtained from the first rotation. The assumption that $\theta(t)$ is comprised of frequencies lower than some cut-off frequency f_c associated with a low pass filter is made. The angle $\phi_{AC}(t)$ is also assumed to be associated with lower frequencies, but $B_{AC}(t)$ is assumed to be mainly associated with frequencies much higher than f_c . It is also assumed that B_{DC} is much much larger in magnitude than $B_{AC}(t)$ for all frequencies lower than f_c . With these assumptions in place, the following statements can be made about the filtered fields:

$$[B_x^a(t)]_{LPF} \approx -B_{DC} \sin \theta(t) \quad (2.15)$$

and

$$[B_y^a(t)]_{LPF} \approx B_{DC} \cos \theta(t). \quad (2.16)$$

The angle $\theta(t)$ can then be found by dividing Eqn. (2.15) by Eqn. (2.16), to obtain:

$$\theta(t) \approx \tan^{-1} \left(\frac{-[B_x^a(t)]_{LPF}}{[B_y^a(t)]_{LPF}} \right). \quad (2.17)$$

This result is inserted back into the rotation matrix of Eqn. (2.11) to obtain fields transformed into a coordinate system relative to magnetic north for every instant in time.

In summary, tilt angles ϕ_x and ϕ_y are collected from a sensor along with field data. Eqn. (2.4) then uses ϕ_x and ϕ_y to calculate ϕ . These three angles are then used in Eqs. (2.9) and (2.10) to transform the fields from the sensor's coordinate system into a coordinate system in the horizontal plane. The fields $B_x^a(t)$ and $B_y^a(t)$ are then filtered and used to find the angle $\theta(t)$ from Eqn. (2.17). The rotation matrix in Eqn. (2.11) then uses $\theta(t)$ to transform the fields into a coordinate system relative to magnetic north.

2.2 Experiment

2.2.1 Experimental Setup



Figure 2.3: Experimental setup.

An experiment was performed to prove that the rotations developed in the previous section were correctly transforming components from a magnetic sensor into a standardized coordinate system relative to magnetic north. The details of the experiment are provided next.

The experiment took place in an open field to avoid error associated with the presence of hard and soft iron. Here, magnetic materials with permanent magnetization are referred to as hard iron and magnetic materials without permanent magnetization are referred to as soft iron. Magnetic materials or permanent magnets in the vicinity of the sensor cause disturbances in the magnetic fields that may be unaccounted for in any analysis. A Helmholtz coil was used to create a small dynamic signal to produce a uniform field in the vicinity of the sensor. The sensor itself was a STEVAL-MKI063V1 demonstration board with a triaxial accelerometer and magnetometer. A Tektronix CFG250 function generator was used to excite the Helmholtz coil. A picture of the experimental setup is shown in Figure 2.3. The data was collected by a laptop computer using a USB connection to the sensor and a GUI from the sensor's manufacturer.

2.2.2 Building the Helmholtz Coil

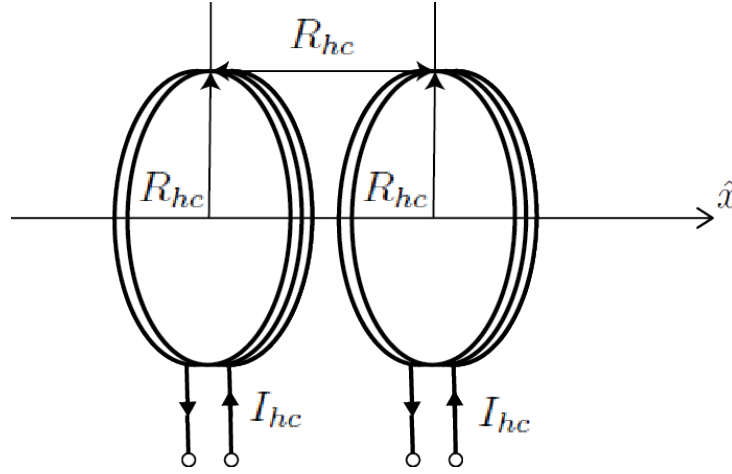


Figure 2.4: Helmholtz coil design.

A small coil was excited with the frequency generator to gauge how well the sensor could detect a signal in the presence of a large field produced by the Helmholtz coil. The small coil was wound with 34 gauge wire, had a radius of $R_{sc} = 2.5$ inches and had 80.5Ω of total resistance, which corresponds to 236 turns (i.e. $n_{sc} = 236$). The frequency generator was able to output a current of $I_{sc} = 57$ mA at 10 Hz using the small coil as its load. At this frequency, the coil is extremely electrically small, so static equations are sufficient to characterize it. From Cheng [6] the axial magnetic field is given by

$$B_x = \frac{\mu_0 n I R^2}{2 (x^2 + R^2)^{3/2}}, \quad (2.18)$$

where R is the radius of the coil. The field was measured with the sensor located at the center of the small coil, so this result is evaluated at $x = 0$ to obtain an equation that is used to estimate the axial component B_{sc} of the small coil:

$$B_{sc} = \frac{\mu_0 n_{sc} I_s}{2 R_{sc}}. \quad (2.19)$$

Next consider the Helmholtz coil design. Figure 2.4 illustrates a typical Helmholtz coil design, where two identical coils are separated by a distance equal to their radii. This Helmholtz coil will produce an approximately uniform magnetic field component B_{hc} at its

center. The first and second derivatives of B_{hc} with respect to distance in the direction of B_{hc} are equal to zero (i.e. $dB_{hc}/dx = d^2B_{hc}/dx^2 = 0$) [6]. An equation for the field component B_{hc} at the center of a Helmholtz coil of radius R_{hc} is obtained by superimposing the solution of a second coil with Eqn. (2.18) that is displaced axially from the original by a distance equal to the radius R_{hc} and evaluating the total solution at the midpoint between the two. Namely [6],

$$B_{hc} = \left(\frac{4}{5}\right)^{\frac{3}{2}} \frac{\mu_0 n_{hc} I_{hc}}{R_{hc}}, \quad (2.20)$$

where n_{hc} is the number of turns on each coil and I_{hc} is the current passing through the coils. An estimate for the field strength B_{hc} relative to the B_{sc} from the small coil read by the sensor is obtained by dividing Eqn. (2.20) by Eqn. (2.19). Letting $R_{hc} = 7.25$ inches, we obtain

$$\frac{B_{hc}}{B_{sc}} = (0.49) \frac{n_{hc} I_{hc}}{n_{sc} I_{sc}}. \quad (2.21)$$

If it is assumed that the frequency generator has zero internal impedance, we find that Eqn. (2.21) can be used to estimate B_{hc} for a given number of turns relative to the strength of B_{sc} measured by the sensor. A desired B_{hc} was chosen from the assumption that the sensor would easily be able to detect roughly half of the magnitude of signal detected from exciting the small coil (i.e. $B_{hc} = 0.49 B_{sc}$). This assumption is used in Eqn. (2.21) to produce the design equation:

$$n_{hc} I_{hc} = n_{sc} I_{sc}. \quad (2.22)$$

At this point the wire gauge and the number of turns are the only two design parameters that need to be chosen. However, design Eqn. (2.22) is dependant on I_{hc} , which is also unknown. These three parameters are all dependant on one another, so there is actually three dependant variables associated with the design. This is due to the total resistance of the coil being directly proportional to the number of turns n_{hc} and the gauge of wire chosen. If it can be assumed that the voltage of the frequency generator will not change when the Helmholtz coil is used as its load, the current I_{hc} is then also directly proportional to n_{hc} and the gauge of wire. Twenty five gauge wire was chosen to maximize cross-section area, but still be malleable

enough to wind. A thicker wire is desirable because it has less resistance, so more current I_{hc} can be produced for a smaller number of turns n_{hc} . An n_{hc} of 65 was then decided upon to produce a field roughly two thirds of B_{sc} observed by the sensor. The Helmholtz coil was wound by hand and all length measurements were made using a standard measuring tape.

2.2.3 Experimental Procedure

Four successful experiments were conducted using the experimental procedure described herein. These four experiments are referred to as either small signal experiments or large signal experiments. Large signal experiments were conducted with the amplitude set to maximum on the frequency generator and small signal experiments were associated with half of maximum. Experiments were done at 10 and 20 Hz for both the large and small signal experiments.

The sensor was placed on a cardboard box roughly in the center of the Helmholtz coil where the gradient of the dynamic field is ideally zero. The Helmholtz coil was placed with its axis roughly pointing in the northeast direction. The choice for this orientation was arbitrary other than the desire to have the dynamic signal distributed along both the x^m and y^m axes. The sensor was connected to a laptop and appropriate settings were adjusted in the GUI (i.e. sampling rates and desired outputs).

The position of the sensor was adjusted while monitoring the GUI to get the axes of the sensor into the horizontal coordinate system m with all of the ambient, horizontal magnetic field contained in the positive y -direction. This was achieved by monitoring the GUI to simultaneously set the two tilt angles and the x -component of the magnetic field to zero while keeping the y -component of the magnetic field positive.

The frequency generator was turned on to excite the Helmholtz coil with a small 20 Hz signal at about 0.5 A. After sampling rates and output formats were changed in the GUI, 40 s of tilt angle and magnetic field data were collected from the sensor while it remained stationary in the coordinate system m . The sampling interval of 40 s was chosen to have enough time to perform rotations and to have a sufficiently long sample time for the purpose of Fourier analysis.

Another 40 s of data was then collected while the sensor was arbitrarily rotated in all directions. The sensor was rotated by physically lifting it from its resting place and rotating it by hand. Care was taken to rotate the sensor at a slow speed as close to the center of the Helmholtz coil as possible with the z -axis less than ninety degrees from the vertical direction. Here, it is noted that the sensor must be in the center of the Helmholtz coil to be able to assume a uniform field, so any movement off center will result in error. The frequency generator was then turned off and the procedure was repeated for the other experiments.

2.3 Error and Results

2.3.1 Results

The data collected with the sensor being rotated were processed with Matlab using the aforementioned rotation matrices in Eqns. (2.9) and (2.11). The Matlab script can be found in Appendix A. The operation of these matrices on the time array data will in theory transform the field component data collected from the rotating sensor's coordinate system s into coordinate system m for every instant in time. The processed data are then compared to the data collected with the sensor sitting stationary in the m coordinate system.

The operation of the matrices on the data sets is illustrated by comparing the time domain data associated with the small signal, 20 Hz experiment before and after being transformed; see Figures 2.5 and 2.6, respectively.

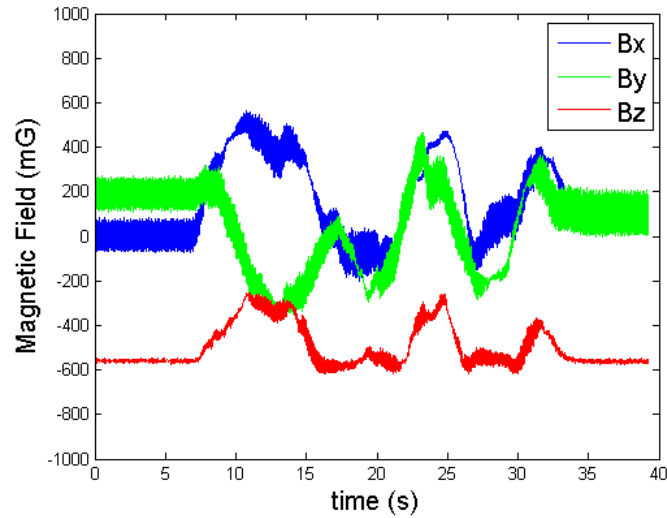


Figure 2.5: 20 Hz signal collected in rotating coordinate system s .

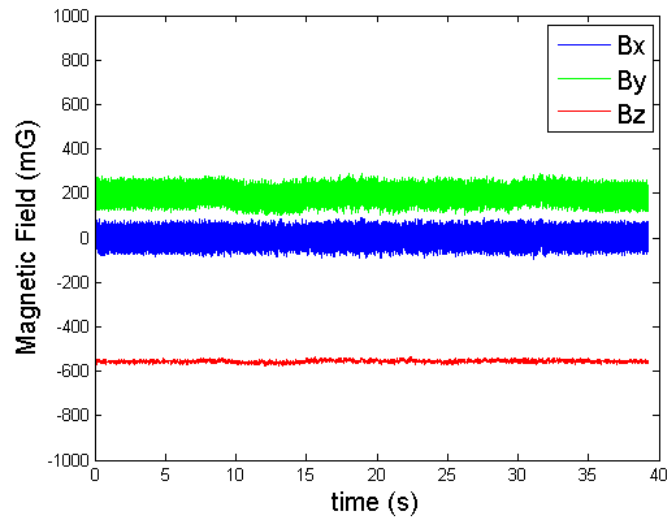


Figure 2.6: 20 Hz signal after transformation into coordinate system m .

Ideally, any perturbations associated with rotation should be removed through this transformation process. The processed data set in Figure 2.6 can then be compared to Figure 2.7, which is the data set collected in the small signal, 20 Hz experiment with the sensor sitting stationary in coordinate system m .

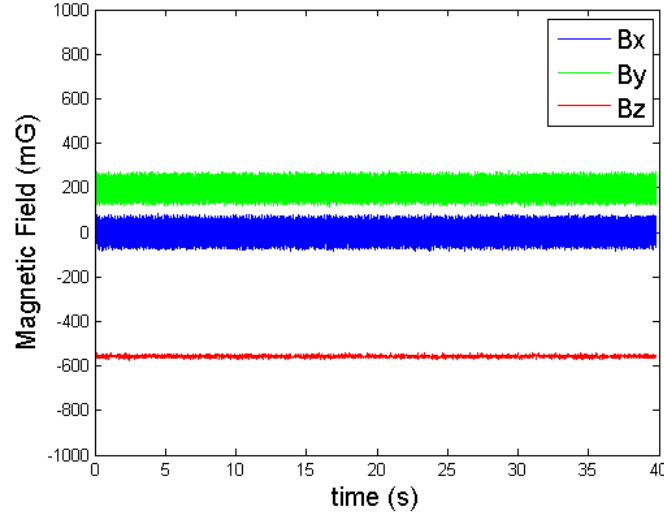


Figure 2.7: 20 Hz signal collected in stationary coordinate system m .

Two major assumptions need to be made to gauge how well the matrices are transforming the data. One assumption is that the sensor experienced the same signal in both cases and the other being that the signal collected in the stationary case was in fact collected in coordinate system m . Figures 2.6 and 2.7 are not identical, but their similarities allude to correct transformations on the part of the matrices. Error between these two data sets could be calculated to get a better understanding of how well the entire data set is being transformed. However, the primary purpose of this procedure is to transform the components of the dynamic signal created by the Helmholtz coil into coordinate system m . It is therefore appropriate to compare the magnitude of the Fourier transform between these data sets at the frequency of the dynamic signal.

Fast Fourier Transforms (FFT's) of the processed data and the data collected while the sensor was stationary are shown for the x -component of the small signal, 20 Hz experiment in Figures 2.8 and 2.9, respectively. Hanning windowing was used in conjunction with these FFT's.

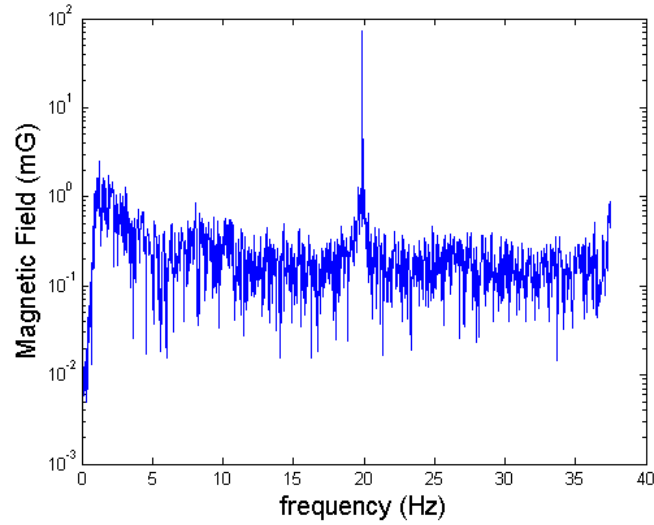


Figure 2.8: FFT of 20 Hz signal after transformation into coordinate system m .

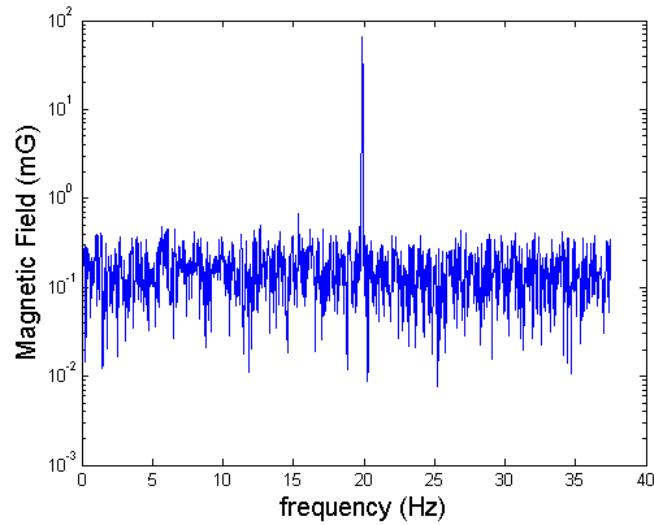


Figure 2.9: FFT of 20 Hz signal in stationary coordinate system m .

It is interesting to note that the processed data of Figure 2.8 show that the magnitude of the DC component tends to zero. This is indicative of the data being correctly rotated into a coordinate system relative to magnetic north. Any residual dc magnetic field found in the x -component of coordinate system m is associated with an error in the rotation process.

The percent error between the magnitude of the processed data transformed into m and the magnitude of the data collected with the sensor sitting stationary in m was calculated for all

three components for both the 10 Hz and the 20 Hz experiments. These magnitudes were taken at the experimental frequency. The percentages are shown in Table 2.3.1.

Experiment	Error B_x	Error B_y	Error B_z
small 20 Hz	6.42	12.36	16.30
large 20 Hz	11.18	6.63	6.28
small 10 Hz	1.72	1.17	22.10
large 10 Hz	6.82	9.58	63.71

Table 2.1: Error percentages between signals collected in coordinate system m and signals transformed into coordinate system m

2.3.2 Error

There are many sources for the error in Table 2.3.1. One of the largest sources of error is associated with the placement of the sensor into coordinate system m . This error would particularly affect percentages associated with comparisons of the z -components, making it a good candidate for causing the large error on the z -components in the large 10 Hz experiment. The magnitude of the field's z -component is much smaller than that of the x or y components, so a slight interchange of components will result in a relatively large change in the magnitude of the z -component.

Another source of error is assumed to be from the non-uniformity of the dynamic field in the Helmholtz coil. Care was taken to keep the sensor near the center of the Helmholtz coil, but the sensor was slightly elevated from its resting place so it could be rotated. The gradient of the field should be close to zero near the center of the Helmholtz coil, but some error was assumed to be associated with this process. Moreover, the Helmholtz coil was non-ideal, which could further contribute to non-uniformity of the dynamic field in the vicinity of the sensor.

Error was also assumed to be introduced from the presence of hard and soft iron. This problem caused earlier experiments to produce completely erroneous results. The sensor has a built in “hard iron calibration” process to mitigate this error, but the process was not able to

compensate for the presence of magnetic materials when the sensor was taken out of its resting position and rotated. Even the steel connector on the USB cable connecting to the sensor was found to produce unacceptable amounts of error.

Error caused by magnetic materials was noticeable in the magnitudes of the magnetic flux density vector measurements recorded from the sensor. Errors introduced by rotations cannot affect vector magnitudes and error affiliated with the dynamic signal produced by the Helmholtz coil will show up exclusively in the dynamic signal; large changes in the DC offset of the magnitude of the signal is an indication that magnetic materials are present. An illustration of the effect of magnetic materials on the magnitudes of an earlier experiment is shown in Figures 2.3.2 and 2.3.2, where Figure 2.3.2 is the magnitude of a signal recorded with the sensor sitting stationary in coordinate system m and Figure 2.3.2 is the magnitude of a signal recorded while the sensor was being rotated.

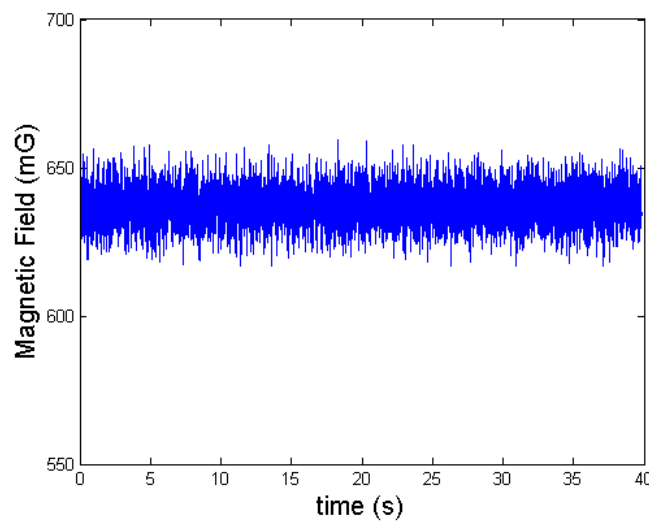


Figure 2.10: The effect of magnetic materials on the magnitude of the magnetic field collected in coordinate system m .

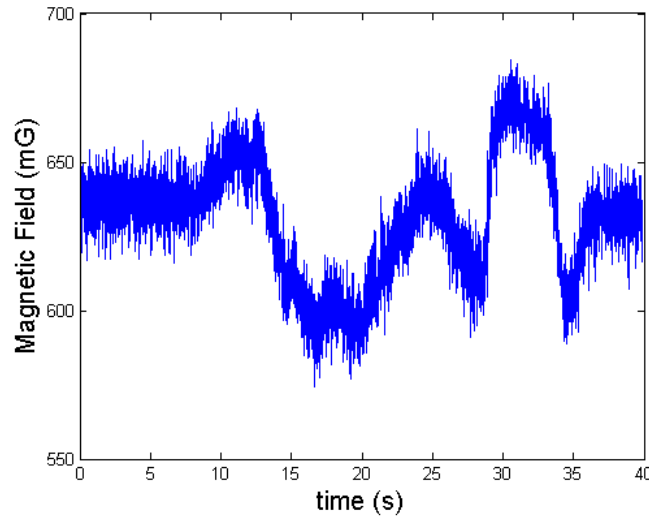


Figure 2.11: The effect of magnetic materials on the magnitude of the magnetic field collected in coordinate system s .

We removed the connector and the USB cord was soldered directly to the sensor before conducting the later experiments. The experiments were then conducted as far away from any magnetic materials as was manageable. A gazebo in a local park was selected as a suitable test location, where power was readily available. Any nails or other magnetic materials in the vicinity of the experiment could still potentially cause problems. A comparison of the magnitudes of the magnetic fields recorded in the small signal, 20 Hz experiment can be seen in Figures 2.12 and 2.3.2. Here, the signal in Figure 2.12 was taken with the sensor sitting stationary in coordinate system m and Figure 2.3.2 was taken while the sensor was being rotated.

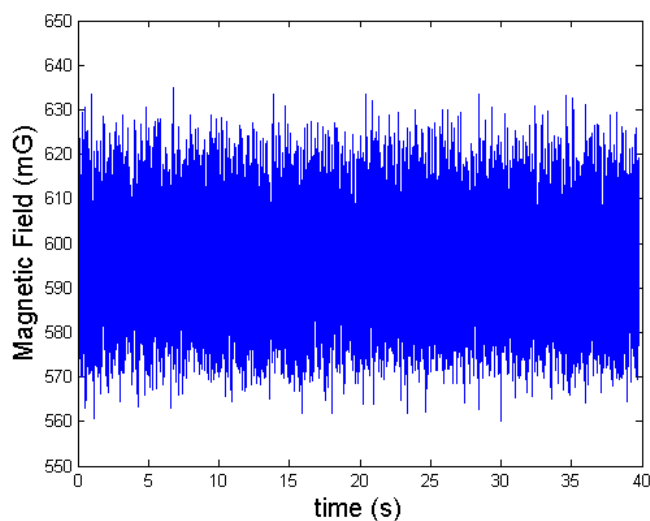


Figure 2.12: Magnitude of the magnetic field collected in m for the small signal, 20 Hz experiment.

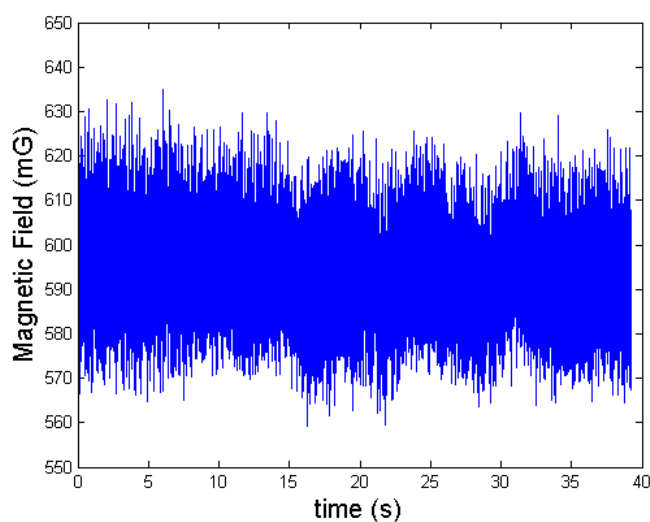
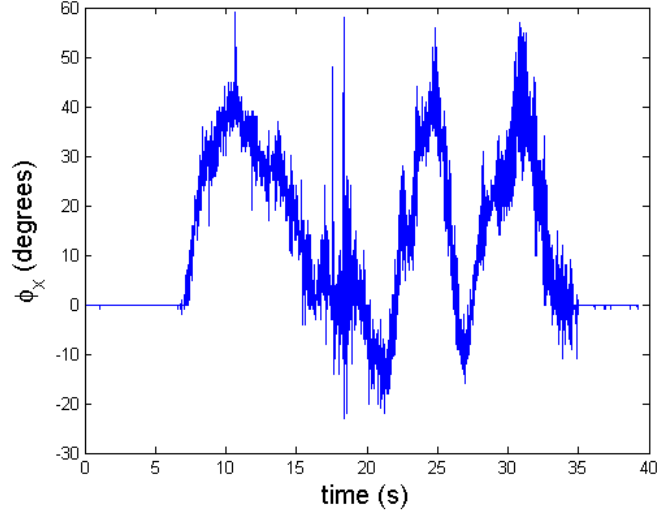
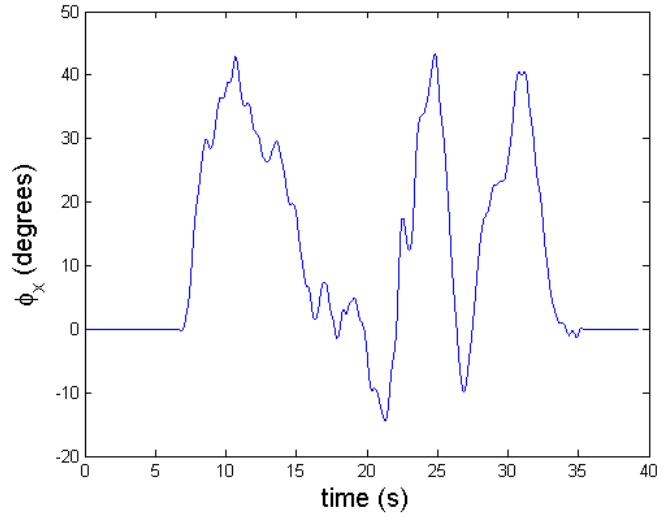


Figure 2.13: Magnitude of the magnetic field collected in s for the small signal, 20 Hz experiment.

A comparison of the magnitudes in this more recent and successful experiment demonstrates a large improvement by the removal of magnetic materials. However, disagreement between Figures 2.12 and 2.3.2 give an illustration of errors still present. This error could arguably be attributed to magnetic materials still present, but it could also be caused by changes in the position of the sensor in a non-uniform dynamic field while being rotated.

Filtering processes are another place where error may have occurred. Both the tilt angles and the fields associated with the azimuthal rotation were filtered using a fourth-order low-pass Butterworth filter. A Butterworth is a maximally flat filter, which is its primary reason for being used. The filter was used in conjunction with a built in function in Matlab called “filtfilt”, which runs the data through the filter in both the forward and reverse directions. This function has the property of creating zero phase distortion on a signal, which is its primary purpose for being used [7]. One thing to note about this filter is that the integrity of a time array is compromised at both its beginning and its end after being filtered. This problem was assumed to be mitigated by the use of a Hanning window in the case where magnitudes from FFT’s are used for comparisons.

A cut-off frequency of 2 Hz was used to filter the tilt angles. This implies that the frequencies associated with changes in the angles corresponding to tilting the sensor out of the horizontal plane during rotation were assumed to be lower than 2 Hz. Changes in angles composed of higher frequencies are then assumed to correspond to artificial noise induced from the sensor. Hence, if this cut-off frequency is chosen to be too high, artificial rotations will be performed according to noise from the sensor. However, if the cut-off frequency is chosen to be too low, motion of the sensor may not be captured. This frequency was chosen to be low because error associated with motion of the sensor is assumed to be more acceptable in actual ELF applications. An illustration of the effects of the filter on ϕ_x of the small signal, 20 Hz experiment is shown in Figures 2.15 and 2.14. Here, Figure 2.15 is filtered and Figure 2.14 is unfiltered.

Figure 2.14: Unfiltered ϕ_x .Figure 2.15: Filtered ϕ_x .

A cut-off frequency of 1 Hz was used to filter the $B_x^a(t)$ and $B_y^a(t)$ that are used to find the angle ϕ used for azimuthal rotation. This frequency was chosen to capture the majority of the low frequency components of the signal. However, FFT data showed that magnitudes of components at the frequency of the dynamic signal in the coordinate system relative to true north were completely unaffected by changes to this cut-off frequency up to 10 Hz. This observation strengthened the argument that B_{DC} can be assumed to be much larger than $B_{AC}(t)$ in Eqns. (2.15) and (2.16).

The last thing to note about error in this experiment is the process of sampling. There is always some small error associated with sampling, but the sampling error in this experiment can be attributed to separate sampling frequencies for the magnetometer and accelerometer readings from the sensor. The sensor sampled at a rate of 75 Hz for the accelerometer readings and 100 Hz for magnetometer readings. The data file outputted by the sensor included redundant values for the accelerometer to make the accelerometer and magnetometer arrays the same length. This operation introduced error and harmonics into the FFT's that are seen in the data of Figure 2.16.

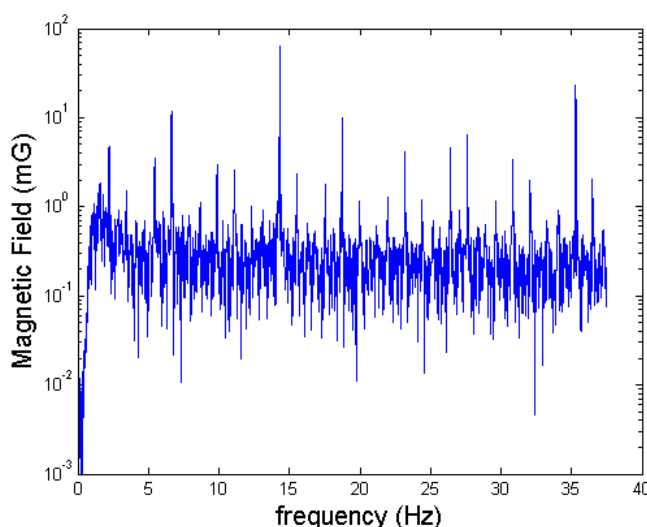


Figure 2.16: Data created from inconsistent sampling rates.

This problem was resolved by deleting both the accelerometer and magnetometer data when redundant values were seen simultaneously in all three components of the accelerometer. The probability of all three components naturally producing redundant values at the same instant is extremely small after consideration of the random noise induced on each component by the sensor. We effectively set the sampling rate for both the magnetometer and accelerometer data sets to be 75 Hz by performing this operation. Fourier transforms then produced results like those seen in Figure 2.8.

Chapter 3

Reciprocity Applied To ELF Simulations

It is convenient from a simulation point of view for experiments to be conducted with stationary sources and moving sensors. This scenario is easily simulated by exciting a model of the experimental source and obtaining field solutions at the sensor locations taken from the experiment. However, the majority of the experiments conducted in the ELF project had a stationary sensor and either a source that was placed in several locations or a source that moved throughout an experiment (i.e. source was placed on the hull of a moving boat). A simulation then needs to model a moving source or several simulations need to be conducted for different source locations. It is much easier from a simulation point of view to consider the source as stationary while observing the fields in many locations. Fortunately, the correlation between a moving source experiment to a moving sensor experiment can be achieved by exploiting the reciprocity theorem.

3.1 Reciprocity Theorem

The ensuing development follows the work done by Young [8]. First, a volume V enclosed by the surface S is considered. The medium contained within the volume V is assumed to be linear, but no other restrictions are initially made on material properties. The electrical properties of the materials associated with V are then expressed in terms of the material tensors $\bar{\bar{\epsilon}}$, $\bar{\bar{\sigma}}$ and $\bar{\bar{\mu}}$. The unit vector \hat{n} is defined as being normal to the surface S and directed into V . Next, two sets of fields are considered for two separate scenarios. Both of these

scenarios occur within V and will be referred to as the a problem and the b problem.

The fields in the a problem are due to impressed currents \vec{J}^a and \vec{M}^a . A relationship between the fields and sources for the a problem is given by Maxwell's equations as,

$$\begin{aligned}\nabla \times \vec{E}^a &= -j\omega\bar{\bar{\mu}} \cdot \vec{H}^a - \vec{M}^a \\ \nabla \times \vec{H}^a &= j\omega\bar{\bar{\epsilon}} \cdot \vec{E}^a + \bar{\bar{\sigma}} \cdot \vec{E}^a + \vec{J}^a.\end{aligned}\quad (3.1)$$

Similarly, the fields for the b problem are due to \vec{J}^b and \vec{M}^b and their relationships are stated as,

$$\begin{aligned}\nabla \times \vec{E}^b &= -j\omega\bar{\bar{\mu}} \cdot \vec{H}^b - \vec{M}^b \\ \nabla \times \vec{H}^b &= j\omega\bar{\bar{\epsilon}} \cdot \vec{E}^b + \bar{\bar{\sigma}} \cdot \vec{E}^b + \vec{J}^b.\end{aligned}\quad (3.2)$$

It is emphasized that the fields and current distributions of the a and b problems are not the same, in general, but that they reside within the same volume V composed of the same electrical parameters $\bar{\bar{\epsilon}}$, $\bar{\bar{\sigma}}$ and $\bar{\bar{\mu}}$.

A relationship between the fields of the a and b problems is desired in this analysis. To do this, the following scalar products are first performed on Eqns. (3.1) and (3.2):

$$\begin{aligned}\vec{H}^b \cdot \nabla \times \vec{E}^a &= -j\omega\vec{H}^b \cdot \bar{\bar{\mu}} \cdot \vec{H}^a - \vec{H}^b \cdot \vec{M}^a \\ \vec{E}^a \cdot \nabla \times \vec{H}^b &= j\omega\vec{E}^a \cdot \bar{\bar{\epsilon}} \cdot \vec{E}^b + \vec{E}^a \cdot \bar{\bar{\sigma}} \cdot \vec{E}^b + \vec{E}^a \cdot \vec{J}^b.\end{aligned}\quad (3.3)$$

One of these equations is then subtracted from the other and the vector identity,

$$\nabla \cdot (\vec{E}^a \times \vec{H}^b) = \vec{H}^b \cdot \nabla \times \vec{E}^a - \vec{E}^a \cdot \nabla \times \vec{H}^b, \quad (3.4)$$

is used to give the result:

$$-\nabla \cdot (\vec{E}^a \times \vec{H}^b) = j\omega \vec{H}^b \cdot \bar{\bar{\mu}} \cdot \vec{H}^a + j\omega \vec{E}^a \cdot \bar{\bar{\epsilon}} \cdot \vec{E}^b + \vec{E}^a \cdot \bar{\bar{\sigma}} \cdot \vec{E}^b + \vec{H}^b \cdot \vec{M}^a + \vec{E}^a \cdot \vec{J}^b. \quad (3.5)$$

After operating on the remaining curl equations, we find that

$$\begin{aligned} \vec{H}^a \cdot \nabla \times \vec{E}^b &= -j\omega \vec{H}^a \cdot \bar{\bar{\mu}} \cdot \vec{H}^b - \vec{H}^a \cdot \vec{M}^b \\ \vec{E}^b \cdot \nabla \times \vec{H}^a &= j\omega \vec{E}^b \cdot \bar{\bar{\epsilon}} \cdot \vec{E}^a + \vec{E}^b \cdot \bar{\bar{\sigma}} \cdot \vec{E}^a + \vec{E}^b \cdot \vec{J}^a, \end{aligned} \quad (3.6)$$

in which case the difference of the two equations yields

$$-\nabla \cdot (\vec{E}^b \times \vec{H}^a) = j\omega \vec{H}^a \cdot \bar{\bar{\mu}} \cdot \vec{H}^b + j\omega \vec{E}^b \cdot \bar{\bar{\epsilon}} \cdot \vec{E}^a + \vec{E}^b \cdot \bar{\bar{\sigma}} \cdot \vec{E}^a + \vec{H}^a \cdot \vec{M}^b + \vec{E}^b \cdot \vec{J}^a. \quad (3.7)$$

The following definitions are then assumed to be valid:

$$\begin{aligned} \vec{E}^a \cdot \bar{\bar{\epsilon}} \cdot \vec{E}^b &\equiv \vec{E}^b \cdot \bar{\bar{\epsilon}} \cdot \vec{E}^a \\ \vec{H}^a \cdot \bar{\bar{\mu}} \cdot \vec{H}^b &\equiv \vec{H}^b \cdot \bar{\bar{\mu}} \cdot \vec{H}^a \\ \vec{E}^a \cdot \bar{\bar{\sigma}} \cdot \vec{E}^b &\equiv \vec{E}^b \cdot \bar{\bar{\sigma}} \cdot \vec{E}^a, \end{aligned} \quad (3.8)$$

These equations are valid when the material tensors are symmetric (i.e. $\bar{\bar{\epsilon}} = \bar{\bar{\epsilon}}^T$, $\bar{\bar{\sigma}} = \bar{\bar{\sigma}}^T$ and $\bar{\bar{\mu}} = \bar{\bar{\mu}}^T$). When this is true, a material is said to be reciprocal. Materials considered in the ELF project are treated as simple media, which easily satisfies these definitions.

Eqn. (3.7) is now subtracted from Eqn (3.5) to obtain,

$$-\nabla \cdot (\vec{E}^a \times \vec{H}^b - \vec{E}^b \times \vec{H}^a) = \vec{E}^a \cdot \vec{J}^b - \vec{E}^b \cdot \vec{J}^a - \vec{H}^a \cdot \vec{M}^b + \vec{H}^b \cdot \vec{M}^a, \quad (3.9)$$

which is the reciprocity theorem in point-form. This result is then integrated over the volume V and the divergence theorem is applied to obtain the global form of the reciprocity theorem.

If we note that \hat{n} points into V , we conclude that

$$\oint_S \left(\vec{E}^a \times \vec{H}^b - \vec{E}^b \times \vec{H}^a \right) \cdot \hat{n} dS = \int_V \vec{E}^a \cdot \vec{J}^b - \vec{E}^b \cdot \vec{J}^a - \vec{H}^a \cdot \vec{M}^b + \vec{H}^b \cdot \vec{M}^a dV. \quad (3.10)$$

A useful way to think of Eqn. (3.10), is to consider the situation where no impressed currents exist within the volume V . Eqn. (3.10) then reduces to,

$$\oint_S \left(\vec{E}^a \times \vec{H}^b \right) \cdot \hat{n} dS = \oint_S \left(\vec{E}^b \times \vec{H}^a \right) \cdot \hat{n} dS \quad (3.11)$$

This result is called the Lorentz reciprocity theorem for source free regions [9]. Eqn. (3.11) gives a relationship between fields in the a and b problems on the surface S .

Another result is obtained by considering a case in which the surface integral on the left side of Eqn. (3.10) vanishes. For this case, the surface S is assumed to extend out to infinity, which is the assumption made in ELF applications. The fields on the surface S decay to zero because the surface is infinitely far away from any sources. Another way to make this argument is by considering a homogeneous medium and assuming far-field conditions $E_\theta = \eta H_\phi$ and $E_\phi = -\eta H_\theta$ with $\hat{n} = \hat{a}_r$. The integrand on the left side of Eqn. (3.10) then becomes,

$$\begin{aligned} \left(\vec{E}^a \times \vec{H}^b - \vec{E}^b \times \vec{H}^a \right) \cdot \hat{a}_r &= E_\theta^a H_\phi^b - E_\phi^a H_\theta^b - E_\theta^b H_\phi^a + E_\phi^b H_\theta^a \\ &= \eta \left(H_\phi^a H_\phi^b + H_\theta^a H_\theta^b - H_\phi^a H_\phi^b - H_\theta^a H_\theta^b \right) = 0. \end{aligned} \quad (3.12)$$

Equation (3.10) thus reduces to

$$\int_V \vec{E}^a \cdot \vec{J}^b - \vec{H}^a \cdot \vec{M}^b dV = \int_V \vec{E}^b \cdot \vec{J}^a - \vec{H}^b \cdot \vec{M}^a dV. \quad (3.13)$$

This is the result used in ELF simulations. Harrington uses the notation of reactions such that

$$\langle a, b \rangle = \langle b, a \rangle \quad (3.14)$$

where,

$$\begin{aligned}\langle a, b \rangle &= \int_V \vec{E}^a \cdot \vec{J}^b - \vec{H}^a \cdot \vec{M}^b dV \\ \langle b, a \rangle &= \int_V \vec{E}^b \cdot \vec{J}^a - \vec{H}^b \cdot \vec{M}^a dV.\end{aligned}\tag{3.15}$$

An interpretation of Eqn. (3.13) can then be given as the reaction of field a on source b is equal to the reaction of field b on source a [9].

3.2 Reciprocity Applied To ELF Simulations

ELF simulations that use reciprocity are conducted by modeling the experimental sensor as the source and then obtaining a field component in the direction of the polarization of the experimental source at the location of the experimental source. In the experiment electric dipoles and current loops are used for transmitting antennas and electromagnetic sensor arrays are employed as receiving antennas.

The problem with modeling the experimental sensor is that it needs to be modeled as six separate antennas (i.e. one electric and magnetic dipole impressed on each principle axis) instead of just one. If the reciprocity theorem is applied to this scenario directly, it will yield one scalar equation with too many unknowns. However, reciprocity can be applied analytically, where each one of the six antennas is excited in a separate ELF simulation. A field component in the direction of the experimental source is then obtained at the location of the experimental source for each simulation. Reciprocity is then applied to obtain a relationship for one component of the total electric or magnetic field measured in the experimental case. Electric field components are obtained by modeling the sensor with electric currents and magnetic field components are obtained by modeling the sensor with magnetic currents.

In this development the electric dipole source is modeled as an electric current element and the electric current loop is modeled as a magnetic current element. The source currents are assumed to be delta functions to bring about a simplified integration. That is, let

$$\begin{aligned}\vec{J}^e &= I^e \ell^e \delta(x - x_e) \delta(y - y_e) \delta(z - z_e) \hat{a}_e \\ \vec{M}^e &= k^e \ell^e \delta(x - x_e) \delta(y - y_e) \delta(z - z_e) \hat{a}_e.\end{aligned}\quad (3.16)$$

Where x_e , y_e and z_e correspond to the location of the experimental source, ℓ^e is the length of the experimental source and I^e and k^e are the electric and equivalent magnetic current amplitudes of the experimental source, respectively. The unit vector \hat{a}_e is associated with the orientation of the experimental source. In Cartesian coordinates,

$$\hat{a}_e = \cos \phi \sin \theta \hat{a}_x + \sin \phi \sin \theta \hat{a}_y + \cos \theta \hat{a}_z. \quad (3.17)$$

Here, θ is defined from the z -axis as the elevation angle to the experimental source and ϕ is defined from the x -axis as the azimuthal angle to the experimental source.

The sensor is modeled as an electric or magnetic current that is oriented on one principle axis to obtain one component of either the electric or magnetic field in the experimental case. These sources are then expressed as,

$$\begin{aligned}\vec{J}^{si} &= I^{si} \ell^{si} \delta(x - x_s) \delta(y - y_s) \delta(z - z_s) \hat{a}_i \\ \vec{M}^{si} &= k^{si} \ell^{si} \delta(x - x_s) \delta(y - y_s) \delta(z - z_s) \hat{a}_i,\end{aligned}\quad (3.18)$$

where $i = x, y, z$. Here, x_s , y_s and z_s correspond to the location of the source within the simulations, so they also correspond to the location of the sensor in the experiment. The superscript e is associated with the experiment and the superscript si is representative of a simulation with an i directed source. The length of the source in a simulation is represented by ℓ^{si} , and I^{si} and k^{si} are the electric and magnetic current amplitudes of the source used in a simulation, respectively.

A specific case is considered in which the experimental source is an electric dipole and electric fields are of interest. This implies that $\vec{M}^{si} = \vec{M}^e = 0$. Eqn. (3.13) then reduces to,

$$\int_V \vec{E}^e \cdot \vec{J}^{si} dV = \int_V \vec{E}^{si} \cdot \vec{J}^e dV. \quad (3.19)$$

Eqns. (3.16), (3.17) and (3.18) are then substituted into Eqn. (3.19) to obtain a relationship between the i component of the experimental electric field and the electric fields obtained from a simulation using an i directed current density as its source. Doing this, we obtain

$$E_i^e = \frac{I^e \ell^e [\cos \phi \sin \theta E_x^{si} + \sin \phi \sin \theta E_y^{si} + \cos \theta E_z^{si}]}{I^{si} \ell^{si}}. \quad (3.20)$$

It is important to note that it is over simplistic to define the current densities in Eqns. (3.16) and (3.18) as having zero length. The current densities may be described with currents that are considered constant along a path in the direction of their respective orientations. The necessary assumptions in this development are that the source currents and fields are considered constants along the paths of the impressed current densities when applying reciprocity. We obtain an identical result to that of Eqn. (3.20) using these more general assumptions.

A similar result is obtained for the magnetic field components associated with an electric dipole. In this case, the sensor must be modeled as a magnetic current within simulations, which implies $\vec{J}^{si} = \vec{M}^e = 0$. Eqn. (3.13) then reduces to,

$$\int_V \vec{H}^e \cdot \vec{M}^{si} dV = - \int_V \vec{E}^{si} \cdot \vec{J}^e dV. \quad (3.21)$$

Here it is noted that magnetic current elements are used to model current loops in the experiment and current loops are used to model the sensor in simulation tools that do not allow for magnetic current excitation. It is then appropriate to make use of the fact that an electric current loop creates the same fields as a magnetic current element when [9],

$$k\ell = j\omega\mu IS. \quad (3.22)$$

An expression for the magnetic field components associated with an electric source is then obtained by substituting Eqns. (3.16), (3.17), (3.18), and (3.22) into Eqn. (3.21) to obtain,

$$H_i^e = -\frac{I^e \ell^e [\cos \phi \sin \theta E_x^{si} + \sin \phi \sin \theta E_y^{si} + \cos \theta E_z^{si}]}{j\omega \mu I^{si} S^{si}}. \quad (3.23)$$

Thus, six simulations are conducted to obtain all of the magnetic and electric field components for a single experiment (i.e one simulation for every magnetic or electric component excitation) involving moving sources and inhomogeneous media.

This same procedure is used to obtain fields for experiments that use electric current loops as their sources. For this case, $\vec{J}^e = 0$ and the sensor is modeled with \vec{J}^{si} or \vec{M}^{si} depending on whether electric or magnetic field components are of interest. These assumptions are then used in Eqn. (3.13) to obtain the electric and magnetic field components for an experimental magnetic source as,

$$E_i^e = -\frac{j\omega \mu I^e S^e [\cos \phi \sin \theta H_x^{si} + \sin \phi \sin \theta H_y^{si} + \cos \theta H_z^{si}]}{I^{si} \ell^{si}} \quad (3.24)$$

and

$$H_i^e = \frac{I^e S^e [\cos \phi \sin \theta H_x^{si} + \sin \phi \sin \theta H_y^{si} + \cos \theta H_z^{si}]}{I^{si} S^{si}}. \quad (3.25)$$

It is interesting to note that the moment and the orientation of the experimental source are specified in post-processing associated with reciprocity and not within ELF simulations. This can be seen from Eqns. (3.20), (3.23), (3.24) and (3.25).

3.3 Method Validation

The method of applying reciprocity to ELF simulations was validated using a code developed by Washington State University (WSU) that implements the Sommerfeld Full-Wave (SFW) solution [10]. This code is valid for a three layer geometry (i.e. air, water and mud) and uses electric or magnetic current elements for excitations. A validation process was conducted for Experimental scenario 2021 [11]. This experimental scenario used a 4 m electric dipole that was placed on the hull of a moving boat and a stationary sensor. The SFW code was used to simulate this experiment for both the moving source case and the six cases needed to obtain the

electric and magnetic field components using reciprocity. The fields from the non-reciprocal simulations were then used as the benchmarks for these comparisons.

Experimental scenario 2021 used an electric source excitation, so electric field components at the location of the experimental source were of interest for the SFW simulations associated with the reciprocal case. To obtain the electric field components, three SFW simulations were performed using three electric current element excitations located at the position of the experimental sensor and polarized in the direction of each principle axes. The electric field components obtained from these simulations at the location of the experimental source were then post-processed with Matlab using Eqn. (3.20) to obtain the electric field components associated with the non-reciprocal case. The comparison between these electric field components and the electric field components obtained from the non-reciprocal simulation are shown in Figure 3.1.

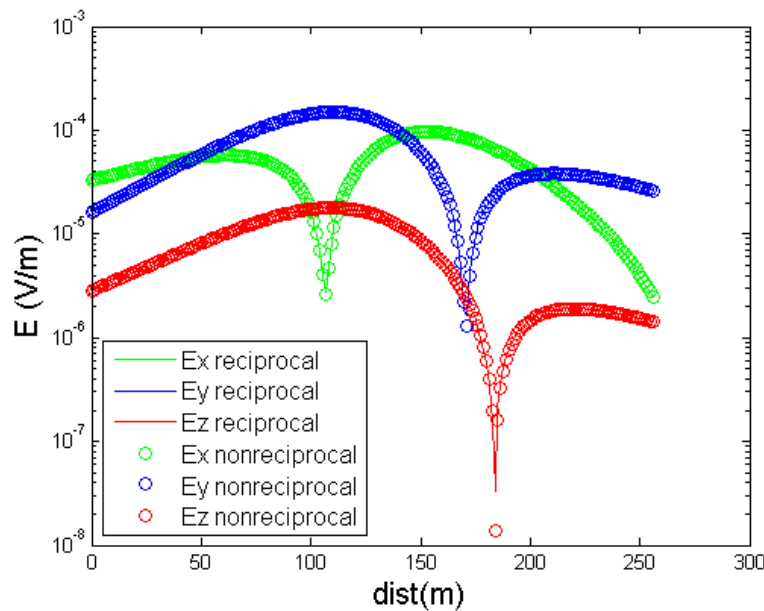


Figure 3.1: Comparisons of electric field components.

The remaining three SFW simulations were conducted to obtain magnetic field components and used three magnetic current element excitations located at the position of the experimental sensor and polarized in the direction of each principle axes. Electric field components associated with these simulations were obtained at the location of the

experimental source and processed with Matlab using Eqn. (3.23) to obtain magnetic field components for the non-reciprocal case. The comparison between these magnetic field components and the magnetic field components obtained from the non-reciprocal simulation are shown in Figure 3.2.

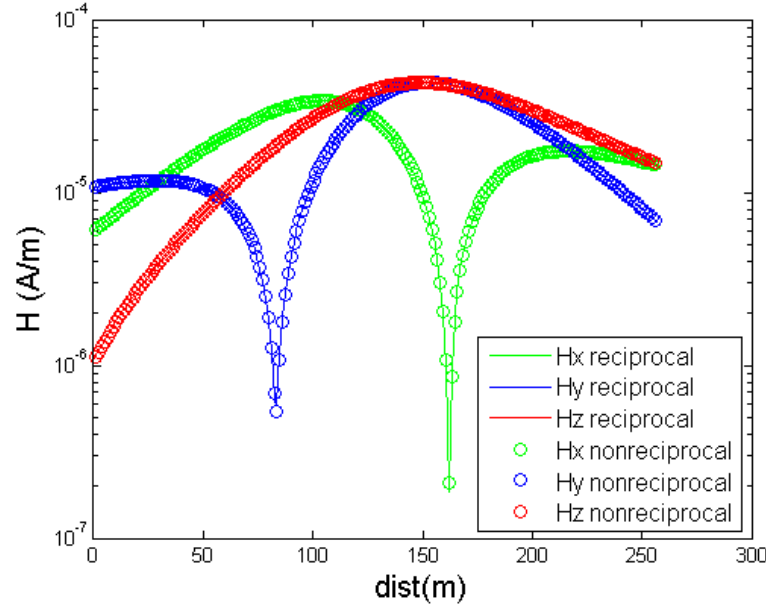


Figure 3.2: Comparisons of magnetic field components.

The comparisons in Figures 3.1 and 3.2 show excellent correlation between the non-reciprocal case and the case where reciprocity was applied for both the electric and magnetic fields. One thing to note about this validation is that the assumptions made in Eqns. (3.20) and (3.23) associated with the excitations being point sources are perfectly satisfied because the SFW simulations use electric or magnetic current point sources for field excitation.

Chapter 4

ELF Simulations Using Ansys Maxwell

Experiments were conducted at two locations on Lake Pend Orielle. One of the locations was a large expanse of the Lake that was chosen for its incredible depth and lack of topological variance. These properties make modeling this portion of the Lake easy and also allows for the use of analytic methods that are not capable of modeling topological variances. Moreover, material properties of the Lake bed have little effect on fields because of the depth of the Lake in this region. The second location used for experimentation was at the southern tip of the Lake in Idlewild Bay. This location was chosen to see how well simulation tools could model an area with significant topological variance and shallow depths of water. One of the simulation tools capable of handling these more complicated models is Maxwell.

Maxwell is a commercial software program created by Ansys. Its interface is very similar to Ansys's High Frequency Structural Solver (HFSS). Like HFSS, Maxwell is a finite element method (FEM) solver that is able to model complicated geometries. However, Maxwell is not designed for high frequency applications. It has many solution types available to a user, all of which give quasi-static or completely static solutions.

There are many nuances associated with tailoring Maxwell and its various solution types to the needs of the ELF project. These nuances will be discussed in this chapter along with the processes of modeling the Lake and sources. Domain truncation and meshing are also discussed because of their importance to FEM solvers. Lastly, the process of extracting data will be discussed in the context of reciprocity and its use in Maxwell.

4.1 Solution Types

The first step in setting up an experimental simulation in Maxwell is to establish a solution type. Each solution type utilizes a different kind of solver within Maxwell that has different limitations associated with types of sources and materials that can be simulated. Some of these solvers can only retrieve magnetic or electric fields due to their static nature. The solution types that are available in Maxwell are: Electrostatic, DC-conduction, Transient, Magnetostatic and Eddy Current.

4.1.1 “Eddy Current” Solution Type

The Eddy Current solution type is selected to simulate the magnetic sources (i.e. electric current loops) used in the experiments. The Eddy Current solution type is able to take into account eddy currents and displacement currents in regions where the conductivity is finite and above the insulator/conductor threshold. The insulator/conductor threshold is a design setting in Maxwell that dictates whether or not material conductance will be considered in a simulation. Hence, the Eddy Current solver is not a static solver in these regions. In other regions, the Eddy Current solver uses a magnetostatic potential to obtain fields. As a consequence the Eddy Current solver is unable to obtain electric field data in these regions. This means that electric fields cannot be obtained in air because air is defined as an insulator. Another limitation of the Eddy Current solution type is that it is unable to simulate a current source where the divergence of the current density is unequal to zero [13]. This excludes the Eddy Current solution type from being able to simulate experiments that use an electric dipole as the source.

4.1.2 “DC-conduction” Solution Type

Experiments that use an electric dipole for the source are simulated using the DC-conduction solution type. The DC-conduction solution type is a static solver, but it incorporates current density into its electric potential where materials have finite conductances above the insulator/conductor threshold [13]. One thing to note about selecting the DC-conduction

solution type is that the “include insulator” box must be checked to obtain fields inside insulators. The DC-conduction solution type is a purely electrostatic solver in regions where the materials are defined as insulators (i.e. conductances are below the insulator/conductor threshold). Because the DC-conduction solution type is a static solver, magnetic field data cannot be obtained from a simulation. Another limitation of the DC-conduction solver is that it cannot impress currents to form an electric dipole. This restricts its use to simulating an electric dipole by specifying voltages on two separate electrodes.

Because of their static nature, the magnetostatic and electrostatic solution types are unable to incorporate finite conductances into their solutions. This restriction makes these solution types nonapplicable for the ELF applications considered herein.

4.2 Source Modeling

4.2.1 Electric Source Modeling

Electric sources in the ELF experiments are electric dipoles created by separating two electrodes (i.e. copper plates) from each other by some distance and then exciting the electrodes with a voltage. These electric dipoles were placed under water on either a truss or on the hull of a moving boat. The sensor was also placed under the water.

In Maxwell these electric dipoles are modeled by separating two sheets from each other and then assigning half of the terminal voltage to each sheet. The separation distance between the electrodes is equal to the length of the dipole of the experiment. The problem with this approach is that the fields obtained from these solvers are strongly dependant on current distributions. The plate sizes have almost no effect on the fields away from the plates as long as the current in the simulation matches that of the experiment. The plate size can be arbitrary, since the plates are extremely electrically small at ELF frequencies. To obtain current distributions comparable to that of the experiment, the impedance of the modeled source has to be the same as that of the experimental source, which it is not, in general. A user is unable to specify currents in Maxwell, but currents can be calculated using the fields calculator contained within the program. This allows the user to solve the problem of obtaining currents

by matching the impedance of the source in Maxwell to that of the source of the experiment. However, almost all of the experiments in this project use reciprocity, in which case impedance matching is unnecessary.

4.2.2 Impedance Matching

Impedance matching in Maxwell is achieved using a utility called Optimetrics. Optimetrics utilizes outputs from the fields calculator to calculate the total current flowing from one electrode to the other and then adjusts the electrode sizes until this current is equal to the experimental current. To obtain currents from the fields calculator, a box must be created around one of the electrodes. Any object will do, but the object cannot be classified as a non-model object in Maxwell. The material assigned to the box must be the same as the material that surrounds the electrode (e.g. water, when the electrode is in water). Once a simulation is completed the fields calculator obtains the total current flowing into the electrode by integrating the normal component of the electric current density over the surface of the box. Optimetrics is then configured using this expression for current to adjust the size of the electrodes until the impedance of the modeled source is equal to that of the experiment.

Parametric sweeps are another feature of Maxwell that can be used for impedance matching. A parametric sweep essentially runs several simulations over a range of variables assigned to a parameter in Maxwell. Impedance matching is achieved by running sweeps using plate size as a variable with the experimental voltage impressed between the plates. Fields are then extracted when the current obtained from the fields calculator best matches the current measured in the experiment.

4.2.3 Magnetic Source Modelling

Magnetic sources in the experiment are electric coils. One of these coils is wound on a circular structure and placed on the bow of a boat with its moment pointing in the vertical direction (i.e. along the z -axis). The other coil is wound on a rectangular structure that was oriented in either the vertical or horizontal directions. Magnetic sources in the experiments are located above the water's surface, while the sensors are positioned beneath the surface of the water.

A magnetic source is modeled in Maxwell by a single loop of wire; the wire is assumed to be a perfect electric conductor (PEC). The area of the loop is made the same as the area of the antenna used in the experiment being considered. Currents in the loop of a simulation are the product of an experimental current and the number of turns of the experimental coil. A coil is excited with a current by inserting a two dimensional sheet in the cross section of a loop and then exciting it with a current. The coils themselves are modeled by subtracting PEC cylinders or rectangular PEC boxes from each other, depending on whether the circular or rectangular magnetic source is being modeled. There is no need for impedance matching when using a magnetic source because currents are directly impressed.

4.2.4 Relative Coordinate Systems

One matter of convenience to note about source creation in Maxwell is the creation of relative coordinates systems. It is very convenient to create a source in a relative coordinate system and then change the location and orientation of the relative coordinate system instead of directly changing the location and orientation of the source itself. Locations and orientations of sources can then be changed using parametric sweeps, which are very convenient for production runs and simulations that use reciprocity.

4.2.5 Reciprocity and Source Modeling

Simulation tools utilize reciprocity by obtaining field components from separate simulations that orient the source along each principle axis and then post-processing the simulation data using Eqns. (3.20), (3.23), (3.24) and (3.25). This implementation is achieved by aligning the source with the x -axis of a relative coordinate system and then reorienting the x -axis of that relative coordinate system to point the source in the direction of each principle axis in the domain's global coordinate system. This process is much easier than directly reorienting the source because the orientation of the relative coordinate system is expressed in terms of variables, which can then be changed during a parametric sweep within Maxwell.

It is interesting to note that impedance matching is unnecessary when reciprocity is implemented. The currents in each of the three simulations can be arbitrary, as long as their

values are available to the user for the post-processing associated with reciprocity. Maxwell obtains these currents using the fields calculator and the aforementioned method.

The last thing to note about reciprocity and source modeling in Maxwell is that the experimental source is not excited in scenarios that use reciprocity. Following the argument from the previous chapter, the sensor is excited as the source when using reciprocity. Hence, it is more appropriate to model the sensor in Maxwell simulations that use reciprocity. However, this is unnecessary, due to the electrically small nature of both the sensor and the source in ELF experiments. It is necessary to ensure that the modeled source in Maxwell is made electrically small and that the moment of the source is known for post-processing purposes.

4.3 Modeling a Lake Environment

4.3.1 Importing a Model of the Lake Bed

Faceted models of the Lake bed are imported into Maxwell to model topography. These models are created using Matlab, AutoCAD, and Cubit. The following process is a summary of work done by Mr. Chenchen Li [11].

Three data sources are inputted into Matlab: 1) Points are imported from an Idaho Geological Survey bathymetry AutoCAD drawing; 2) A 10 m elevation data file from InsideIdaho.org is used, which originates from a United States Geological Survey (U.S.G.S.) national elevation dataset; 3) points are read directly from a U.S.G.S map. Matlab then combines these three data sets using criteria associated with redundant or inconsistent points and common references. The resulting data set is an irregularly spaced height field with points referenced to the U.S.G.S map. Matlab interpolates these points to make the height field regularly spaced at intervals dictated by the user and then normalizes the points to an origin defined by the user. This height field is imported into AutoCAD to create a three dimensional mesh. The mesh is then turned into a solid using AutoCAD.

The solid is imported into the meshing program Cubit where the surfaces of the model are combined into a composite surface and re-meshed using Cubit's meshing scheme and a user defined interval that dictates the minimum meshing length allowed. This new surface is then

converted into several ACIS surfaces, which are then stitched together to form a solid. The solid is then imported into Maxwell. In the creation of this model, the coordinate system is defined with its origin at the air-water interface. The positive z -axis is defined as up; the positive y -axis is defined as north; the positive x -axis is defined as east.

Several of these models with different restrictions on the maximum lengths of facets were made available. Models created with smaller facets are able to model the topography of the Lake with better resolution, but simulation times increase considerably due to a larger demand for computational resources.

Two types of errors can occur while importing a model. These errors are classified as either geometrical errors or topological errors. Geometrical errors are associated with the underlying geometry and topological errors are associated with how faces, edges, etc. are connected. Hence, any faces that are disjointed from topological errors need to be aligned and the healing process within Maxwell needs to be performed on the imported object.

4.3.2 Creation of Air and Water Regions

The air and water regions can then be added by creating two boxes around the imported model and then subtracting them from the model. The box associated with the water starts at the bottom of the model and extends up to the origin. The box associated with the air starts at the origin and extends up to create the top of the simulation domain. An example of a simulation domain after subtracting these boxes from the imported model is shown in Figure 4.1.

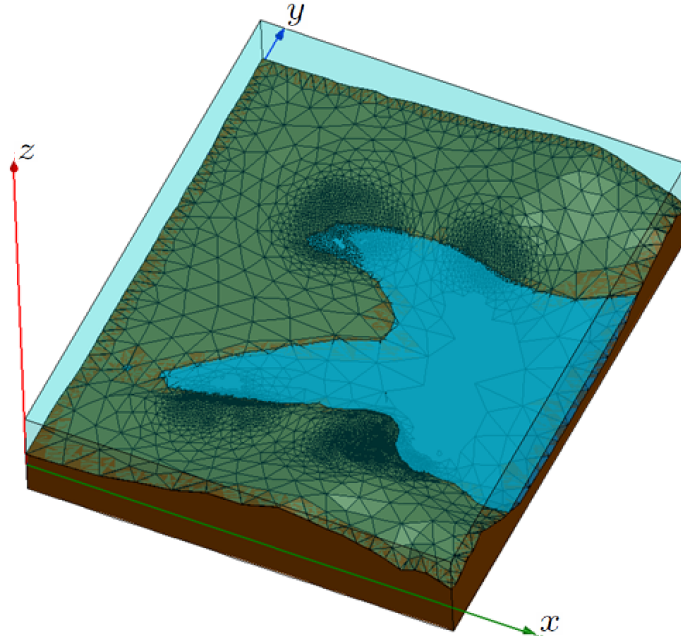


Figure 4.1: Simulation model of Idlewild Bay.

4.3.3 Material Properties

Once objects are created in a simulation domain material properties need to be specified. There is significant ambiguity associated with this process because material properties and distribution of materials are unknown in actual experiments. In a Maxwell simulation environment we assume that everything is composed of homogeneous regions of either mud, water or air.

These material ambiguities are assumed to be responsible for many errors associated with the simulations. An illustration of how conductivity ambiguities affect fields is shown in Figure 4.2, where the dominant electric component E_y is monitored along the x -axis for a y directed electric dipole situated on the origin of a simulation domain while changing the conductivities σ_m and σ_w . Here, σ_m and σ_w are the conductivities associated with the mud and water, respectively. For this comparison, the source was located underwater.

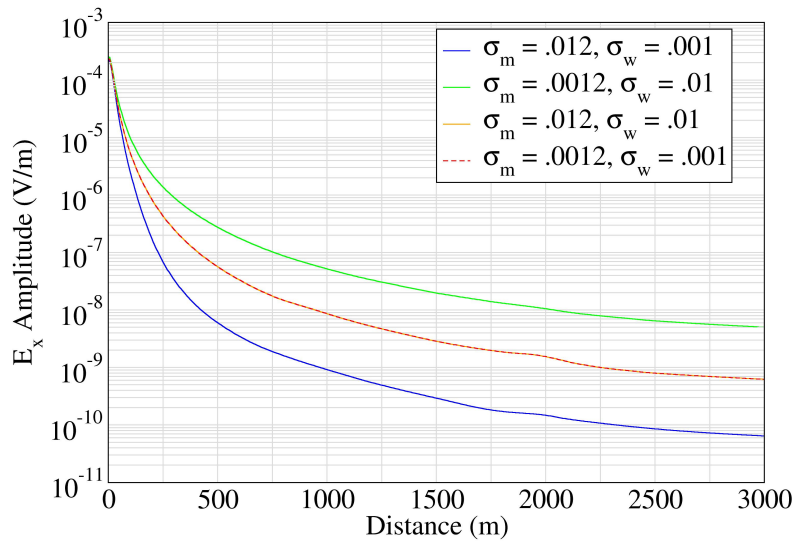


Figure 4.2: Material ambiguity effects.

de It can be seen in Figure 4.2 that the values chosen for conductivity significantly affects the strengths of fields obtained within simulations. In fact a quasi-static analysis reveals that $E_x \sim 1/\sigma_w$ [12], thus explaining the large variations in the data of Figure 4.2

Material properties assigned to these three materials are assumed to be frequency independent for ELF simulations. The material properties used in ELF simulations are listed in Table 4.1. However, since $\sigma \gg \omega\epsilon$ at ELF frequencies the actual value of ϵ_r is moot.

Table 4.1: Material Properties

	air	water	mud
ϵ_r	1	81	1
σ	0	0.01	0.0012
μ_r	1	1	1

In Maxwell, special attention needs to be given to the insulator/conductor threshold in the Design Settings window. The insulator/conductor threshold setting needs to have a lower value than that of any conductivity assigned to a material in a simulation domain in Maxwell. Any

material with a conductivity lower than the insulator/conductor threshold will be treated as an insulator (i.e. $\sigma = 0$).

4.4 Meshing

Proper meshing is essential in Maxwell to obtain good simulation results. There is an adaptive meshing process in Maxwell that attempts to construct the best mesh. The user is also able to customize the mesh inside or on the surface of objects. An illustration of Maxwell's adaptive meshing process is shown in a flow diagram in Figure 4.3.

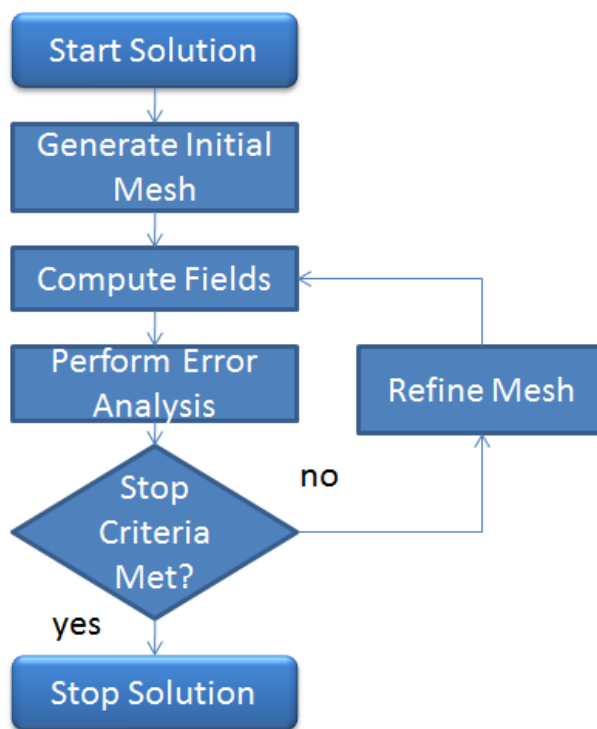


Figure 4.3: Flow diagram of adaptive meshing process.

The adaptive meshing process will automatically create more refined mesh around sources and object interfaces. The stopping criteria for the adaptive meshing process in Maxwell is set to a percent energy error by default. If a user is not satisfied with the amount of error that is allowed by this process in a region where fields are of interest, the user can manually restrict the lengths of mesh elements in that area.

For this project we found it to be more effective to restrict the size of elements inside of

objects rather than on the surface of objects. Objects are created near areas where fields are expected to be extracted and the lengths of mesh elements are restricted inside of those objects. These areas of extraction are in locations where the sensor or the source is moving or has many locations in an experiment. The areas where the fields are extracted are referred to as sweep lines and correspond to areas where the sensor or source is located in an experiment, depending on whether or not reciprocity is being used to simulate a particular experiment.

For vertical sweeps the objects used for meshing are simple boxes that can be assigned as non-model objects. For horizontal sweeps, where the sweep line is not on a principle axis, boxes are created by making a two dimensional sheet and then extending it along a line using the sweep option located in the draw menu in Maxwell. This is done because a box must be created on a principle axis and because meshing on a box created in a relative coordinate system applies mesh operations in arbitrary locations. One thing to note about creating a mesh box this way in Maxwell is that the object created is not technically a box, so the object must be created as a model object. A consequence of this is that these mesh boxes are unable to cross any material boundaries. Another thing to note is that extracting data on the surface of these kinds of objects can have an adverse effect on the fields. For this reason meshing boxes for horizontal sweeps are generally offset by a few meters from their respective sweep lines.

An illustration of how poor meshing affects extracted fields can be shown in Figure 4.4. This figure depicts a scenario where fields are extracted along a line that starts at the location of a y -directed electric dipole and sweeps outward along the y -axis. For this scenario, a mesh box is inserted along this extraction line and the mesh inside the box is both loosely restricted and finely restricted for comparisons. In the finely restricted case, mesh elements inside the mesh box are restricted to one meter in length. The lengths of elements were not manually restricted in the loosely restricted case, but adding the mesh box effectively causes the adaptive meshing process to mesh loosely along the extraction line. If smoothness is any guide, it is clear from this figure that the finely restricted case yields superior results.

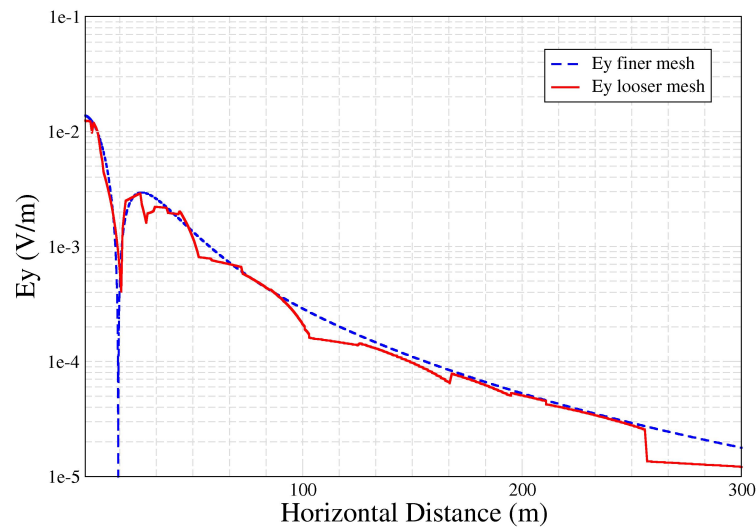


Figure 4.4: Comparison of good and bad meshing schemes.

4.5 Domain Truncation

Domain truncation is another simulation concern that a user needs to be aware of in Maxwell. This is important because reflections occur from the boundaries associated with simulation domains that are not physical. These reflections adversely affect the fields within simulations. A measure of the effectiveness of a domain truncation scheme is then how well it is able to emulate an open domain that extends to infinity.

4.5.1 “DC-conduction” Boundaries

The DC-conduction solution type uses a zero flux boundary condition as the default for domain truncation, where flux cannot cross boundaries and the vector \vec{E} is defined as being tangential to the boundary. There is also an option for a boundary condition where the tangential fields are forced to zero, but this condition is used as the default boundary condition at the interfaces between objects in Maxwell and performs poorly as a domain truncation scheme [13].

An illustration of how well the zero flux boundary condition performs as the boundary is

displaced from the source and sweep line by different distances is shown in Figure 4.5. Figure 4.5 shows several scenarios, where the dominant component E_y is monitored along a line that sweeps outward in the x -direction from a y directed electric dipole. This figure shows the case where the source and monitor line are located in the water, which is most representative of the majority of ELF experiments employing electric sources. The difference between the scenarios depicted in Figure 4.5 is that a boundary in the x - z plane is moved towards the source and monitor line by different distances in the y direction. The legend in Figure 4.5 refers to the distances that the boundary is displaced from the source and sweep line for each of the scenarios.

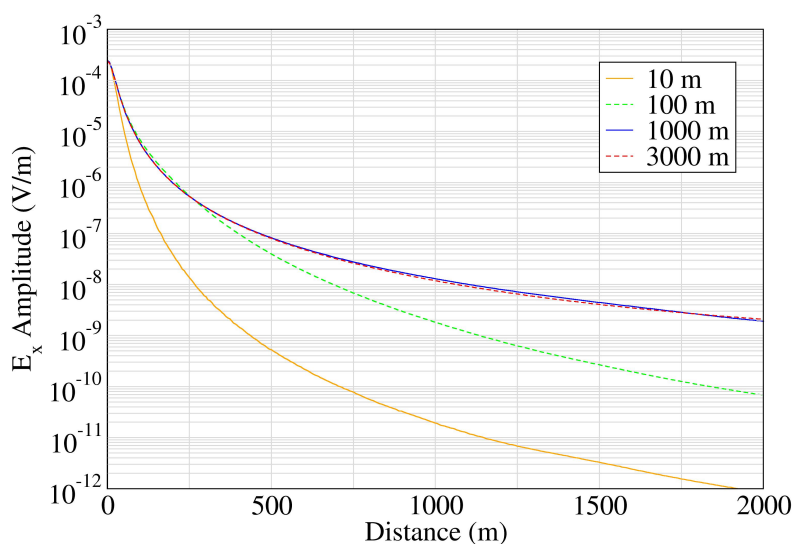


Figure 4.5: “DC-conduction” boundary effects on fields.

In Figure 4.5 the field component E_y is seen to be unchanged by the displacement of the boundary from 1000 m away from the source and monitor line, and 3000 m away from the source and monitor line. This indicates that good results will be obtained from a simulation when the source and monitor line are kept 1000 m or more from the boundaries of an ELF simulation.

4.5.2 “Eddy Current” Boundaries

The Eddy Current solution type in Maxwell also uses a zero flux boundary condition as its default domain truncation scheme. However, this zero flux boundary condition defines the field vector \vec{H} as being exclusively tangential at the boundary. The Eddy Current solver has the additional option of assigning a radiation boundary for domain truncation. This is due to the fact that the Eddy Current solution type is a full-wave solver in regions where the conductivity is finite. The radiation boundary is based on the assumption that waves become spherical as they propagate away from their sources. This boundary condition is used in Maxwell to simulate unbounded Eddy currents, where the simulation domain consists of finite conductivities above the insulator/conductor threshold. This domain truncation scheme is then not applicable to ELF applications in which an insulator (air) is a large part of the simulation domain. Moreover, the Eddy current solution type obtains magnetostatic solutions in insulator regions, so the use of a radiation boundary in air would be inappropriate [13].

An illustration of how well the zero flux boundary condition in the Eddy Current solver performs is shown in Figure 4.6. Again the fields in this figure were obtained for several scenarios where a boundary in the x - z plane was moved towards the source and monitor line by different distances. The difference between the scenarios depicted in Figure 4.6 and the scenarios depicted in Figure 4.5 is that the source is a y directed magnetic loop located just above the waters surface, which best represents ELF experiments that employ magnetic sources. Figure 4.6 then shows H_y as the dominant component being monitored along the x -axis.

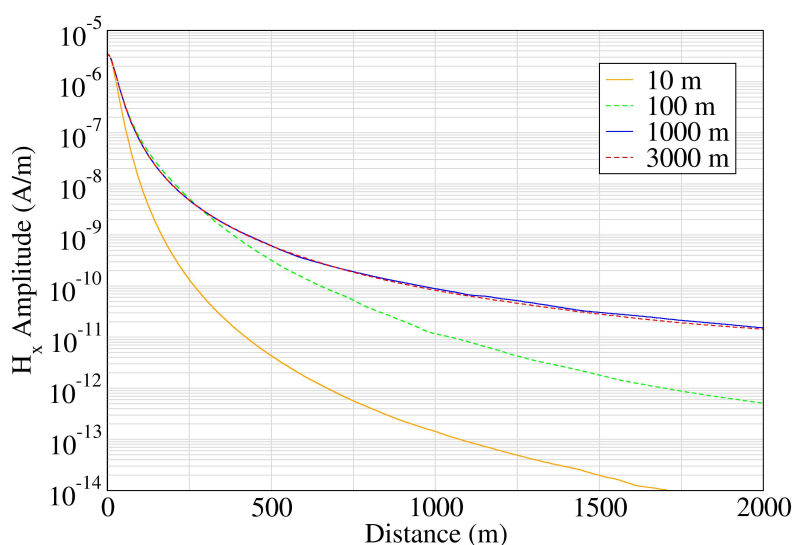


Figure 4.6: “Eddy current” boundary effects on fields for 1000 Hz.

In this Figure the field component H_y is seen to be unchanged by the displacement of the boundary from 1000 m away from the source and monitor line to 3000 m away from the source and monitor line. Good results are obtained from the Eddy current solver using magnetic sources as long as the source and monitor line are kept at least 1000 m from boundaries in ELF simulations. We note that frequency needs to be specified for simulations that use the Eddy-current solution type. The zero flux boundary conditions are most useful for static types of fields, so the scenarios depicted in Figure 4.6 were all conducted at the highest frequency used in ELF experiments (i.e. 1000 Hz). A depiction of this scenario at the lowest frequency used in ELF experiments (i.e. 10 Hz) is shown in Figure 4.7.

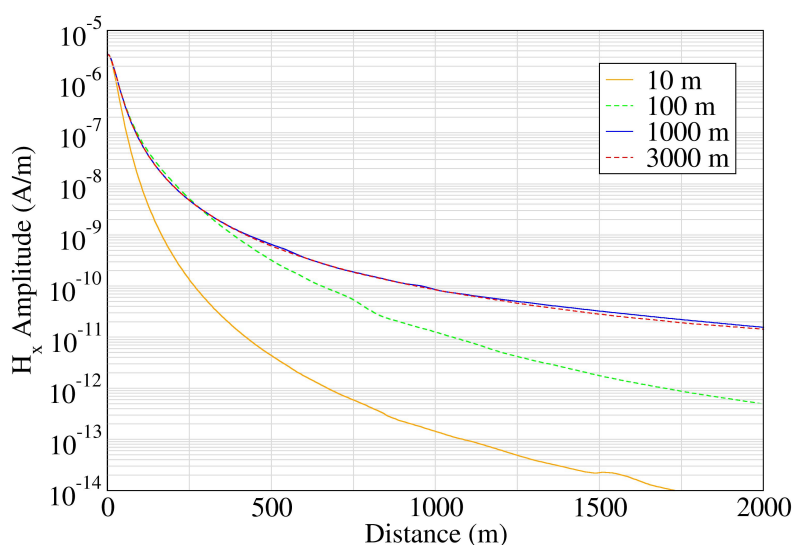


Figure 4.7: “Eddy current” boundary effects on fields for 10 Hz.

Figure 4.7 demonstrates that the source and sensor must be kept at least 1000 m from boundaries in simulations conducted at 10 Hz.

4.6 Extracting Field Data

Data in Maxwell is extracted using the Fields Calculator. A points file is created in Matlab that corresponds to the location of the sweep line or the location of points where the user is interested in extracting data. This points file is generated using data associated with source or sensor locations from an experiment or from points along a line created using the location of two points. The Fields Calculator in Maxwell then uses this points file to extract field components and export them to a file that is inputted into Matlab. This file contains the x , y and z locations and components of the complex electric or magnetic fields for all of the points exported from the Fields Calculator.

For non-reciprocal cases, the field information in the output file is written to a text file using Matlab. For non-reciprocal cases Matlab is used to post-process the fields using Eqns. (3.20), (3.23), (3.24) and (3.25). For this case the heading and source strength is accounted for

in the post-processing and not in the simulations themselves. This gives simulations using reciprocity the advantage of being able to change the source orientation and strength for every point that is extracted from Matlab. The data for source strength and orientation is provided by the same file that contains the location of the points to be extracted. The source strength is relatively constant throughout these experiments, but the polarization of the source has to be accounted for in ELF applications. Examples of the Matlab scripts used for post-processing can be found in Appendix B for both The Eddy Current and DC-conduction solution types.

4.7 Method Validation

Several simulation tools used in the ELF project were validated against each other using a three layer geometry like the one shown in Figure 4.8.

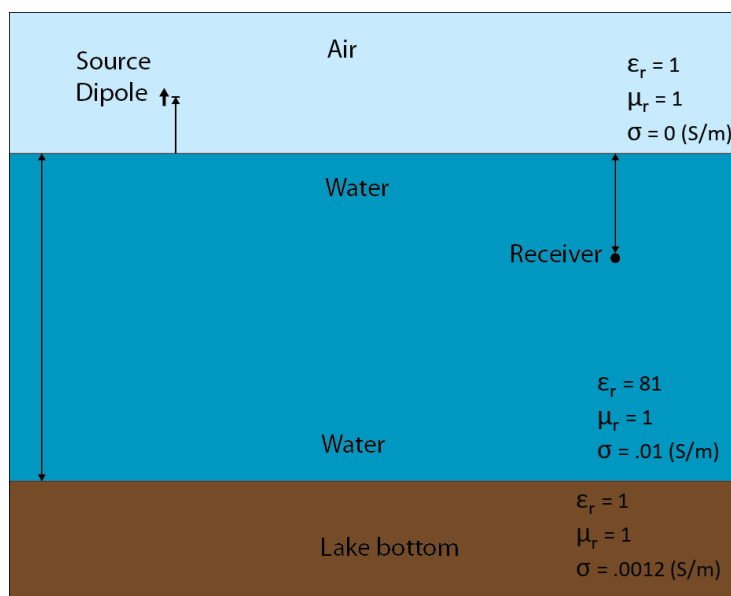


Figure 4.8: Illustration of three layer scenario.

This geometry was selected for its simplicity and the availability to construct closed-form solutions using quasi-static and full wave methods. Results for the magnitude of the electric field obtained from one of these comparisons can be seen in Figure 4.9, where the proven SFW method is used as the benchmark for comparisons.

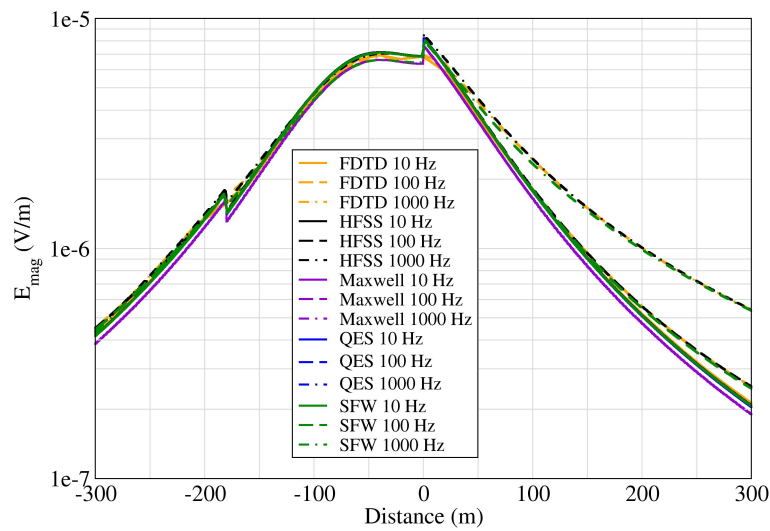


Figure 4.9: Electric field results obtained for a three layer comparison.

Results for the magnitude of the magnetic fields obtained for this comparison are shown in Figure 4.10.

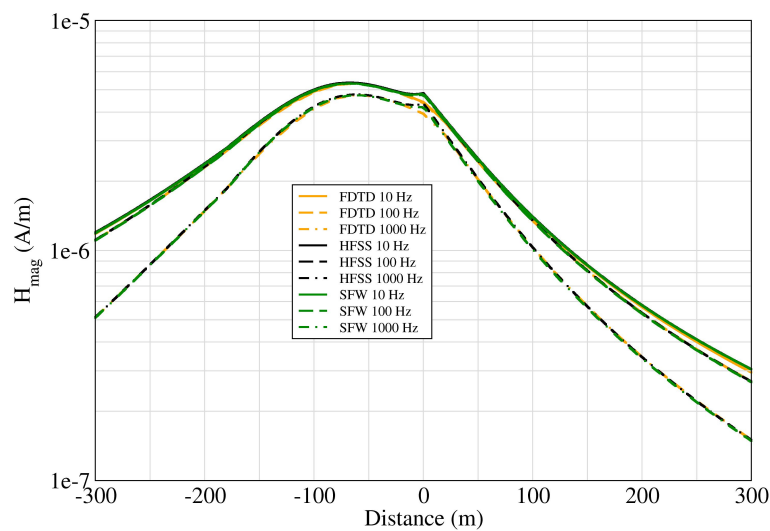


Figure 4.10: Magnetic field results obtained for a three layer comparison.

These fields were obtained along a sweep line underneath the water for an electric source

situated just beneath the water's surface. The correlation between all of the simulation methods is excellent, which can be seen from Figures 4.9 and 4.10. Similar results were obtained for many other comparisons using both electric and magnetic sources in a three-layer geometry.

4.8 Experimental Comparisons

Significant experimental data exists to validate the data from Maxwell and other methods. Some of the comparisons between experimental and simulation results are more favourable than others.

Experimental scenario 304.01 [11] is considered as an example of one of the more favourable experiments conducted. This scenario was conducted in Idlewild Bay, so Figure 4.1 is an illustration of the model that is used by Maxwell to simulate this experiment. This model has much more topological variation than the model of the northern part of Lake Pend Orielle, so this example utilizes Maxwell's strength to be able to model topological variations. The source in this example is a 4 m electric dipole placed on the hull of a boat that is moving north-east along the western shore line of the Bay. The dipole was operating at a frequency of 10 Hz. Reciprocity is then used to process the simulations to account for the source being in motion using the previously discussed methods of Chapter 3. The sensor was a portable electromagnetic array (PEMA) that was located on the shore, roughly in the middle of the sweep line associated with the boat path.

Comparisons between the magnitudes of the electric fields obtained from simulation tools and the magnitude of the electric field obtained from the experiment are shown in Figure 4.11.

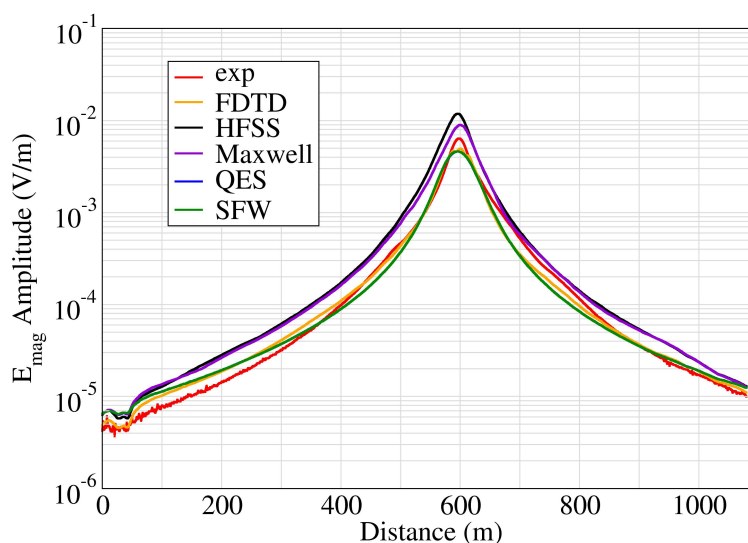


Figure 4.11: Electric field comparisons for scenario 304.01.

Figure 4.11 shows that the correlation between the magnitudes of the electric fields obtained from simulations and the magnitudes of the electric field obtained from the experiment are excellent. Likewise, comparisons between the magnitudes of the magnetic fields are shown in Figure 4.12. This figure shows that there is also excellent correlation between the magnitudes of the magnetic fields obtained from the experiment and the magnitudes of the magnetic fields obtained from simulations. Here, comparisons can only be made where the experimental fields have a higher amplitude than the noise floor associated with the sensor.

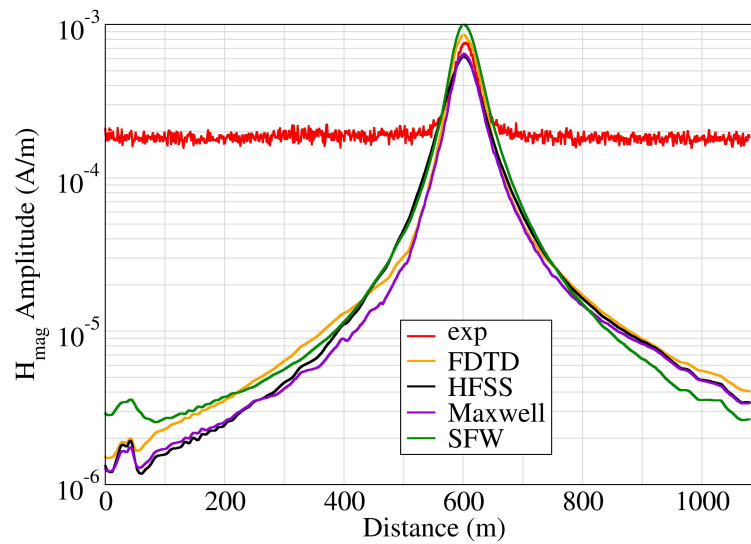


Figure 4.12: Magnetic field comparisons for scenario 304.01.

Experimental scenarios 100.02, 100.04, 100.06, 100.08 and 100.10 [11] had different sensor locations, but all shared the same source at the same location, operating at the same frequency (i.e. 1000 Hz). They could then all be solved together in one simulation without the use of reciprocity. The source was an electric current loop with its moment vertically oriented. The source was placed on the shore in Idlewild Bay. The PEMA was used as the sensor, which was placed off-shore submerged underneath the water. Comparisons for electric and magnetic fields obtained from simulation tools and the experiment are shown for these scenarios in Figures 4.8 and 4.8.

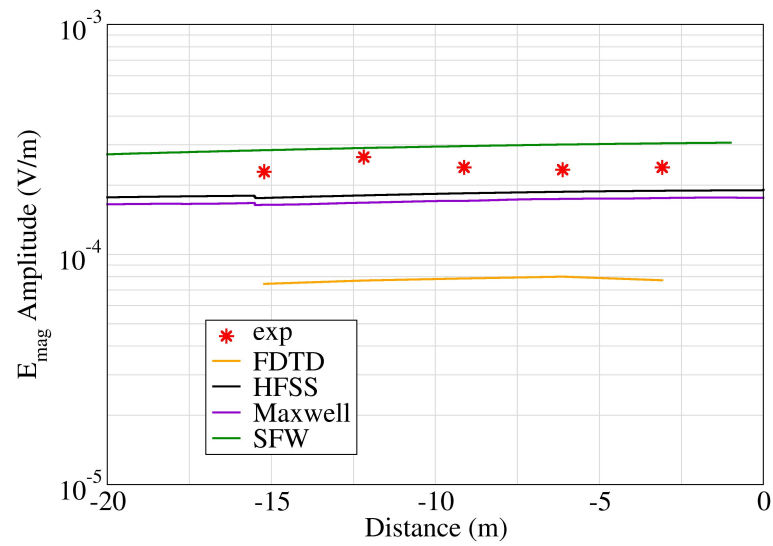


Figure 4.13: Electric field comparisons for scenarios 100.02, 100.04, 100.06, 100.08 and 100.10.

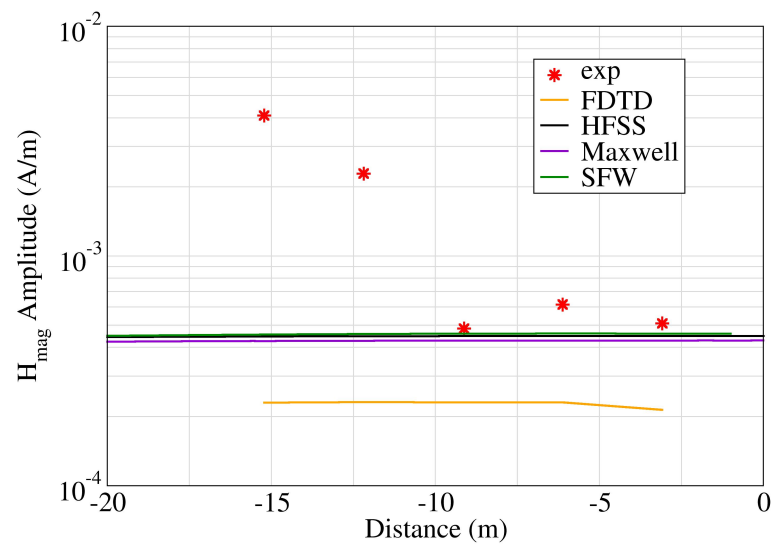


Figure 4.14: Magnetic field comparisons for scenarios 100.02, 100.04, 100.06, 100.08 and 100.10.

The correlation between fields obtained from simulations and experiments is not so good in Figures 4.8 and 4.8. This data is therefore considered unfavourable from the point of view of

the ELF project. The most likely source of error for this disagreement between experimental and simulation data is conjectured to be the inability to properly model material properties associated with the Bay.

Experimental scenario 1016 [11] was conducted in the northern part of Lake Pend Orielle, where there is less topological variation than the Bay. This scenario used a vertically oriented electric current loop as its source, which was placed on the bow of a moving boat. Reciprocity was then used to process simulations associated with this experiment to account for the source moving. The source was excited at a frequency of 10 Hz. The electromagnetic array (EMA) was used as the sensor in this scenario. Comparisons for electric and magnetic fields obtained from simulation tools and the experiment are shown in Figures 4.15 and 4.16.

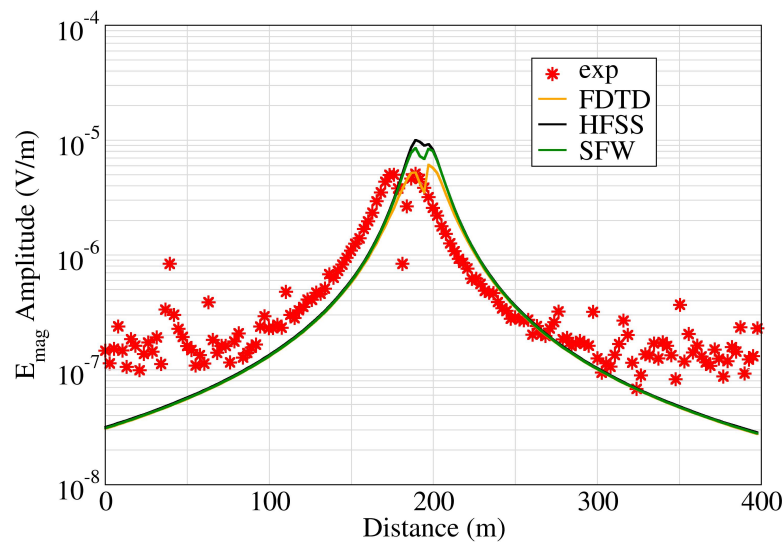


Figure 4.15: Electric field comparisons for scenario 1016.

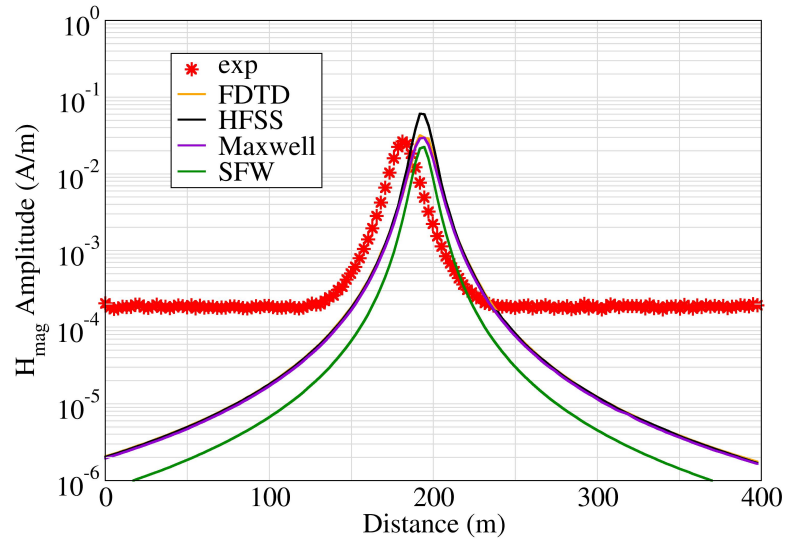


Figure 4.16: Magnetic field comparisons for scenario 1016.

The correlation between fields obtained from simulations and experiments is favourable in Figures 4.15 and 4.16. This part of the Lake has very little topological variation and very deep water, so material ambiguities are not assumed to be a major issue. However, there is a discrepancy between the location of this source in simulations and the experimental case for this scenario, which is assumed to be the reason for the experimental data appearing to be shifted from the simulation data.

Chapter 5

Conclusion

This thesis described solutions to three problems that addressed sensor orientation, reciprocity, and the tailoring of Maxwell to the needs of the ELF project. The outcomes of these solutions are summarized below.

The first topic of this thesis addresses the transformation of a field from the coordinate system of a sensor's axes to a coordinate system relative to true north for the purpose of experimental comparisons. To do this two matrices were created to transform field components from the sensor's coordinate system into a coordinate system defined in terms of magnetic north. It is then trivial to perform an additional two-dimensional rotation to get the components into a coordinate system relative to true north. The first of these matrices used tilt angles from the sensor to transform field components from the sensor's coordinate system into a coordinates system defined on the horizontal plane. This transformation is invalid if the sensor's z -axis is tilted more than 90 degrees from vertical. The performance of this rotation is strongly dependant on the accuracy of the tilt angles outputted by the sensor for each instant of time. The second matrix azimuthally rotates components from this horizontal coordinate system into a coordinate system relative to magnetic north. The accuracy of this rotation is dependant on how well a filtering process can differentiate noise and impressed signals from the Earth's magnetic field. The presence of magnetic materials can also affect this rotation adversely. A sensor generally has a calibration process to mitigate the error from the presence of magnetic materials, but this process cannot account for sensor rotation in the vicinity of

these materials. An experiment was performed to prove that these matrices were correctly transforming field components into a coordinates system relative to magnetic north. This experiment showed some success. Errors were assumed to be associated with both the aforementioned problems and problems with manually placing and rotating the sensor.

Another topic of this thesis is the implementation of the reciprocity theorem. Most of the experiments conducted in the project had a source that was either moving or placed in many locations; in both cases the sensor was stationary. The use of the reciprocity theorem allows a user to excite the sensor and obtain fields at the location of the experimental source within a simulation. One impediment encountered in this application of reciprocity is the triaxial sensor used in ELF experiments needs to be modeled as six antennas instead of just one (i.e. one antenna for each magnetic or electric field component detected). Six simulations are then conducted using electric or magnetic dipole current sources polarized in the direction of the desired field component. Electric dipole sources are used to obtain electric field components and magnetic dipole sources are used to obtain magnetic field components.

There were many assumptions made for this implementation of reciprocity. These assumptions are either weakly or strongly related to the assumption that the source and sensor used in the ELF project are extremely electrically small. Technically, simulations that use reciprocity model a complicated sensor and a source that is simultaneously in several locations. However, isolated, extremely electrically small objects do not strongly perturb fields. As a consequence, source and sensor materials are either not modeled or incorrectly modeled in ELF simulations that use reciprocity. Impressed currents are assumed to be constant along the path between the terminals of the transmitting antennas and induced fields are assumed to be constant along the path between the terminals of the receiving antennas for both the simulation and experimental scenarios. Electrical size has an effect on this last assumption because a spatial change of phase across the terminals of a given antenna is related to the frequency of operation and therefore the electrical length of separation between the antenna's terminals. Lastly, electric loop sources used in ELF simulations and experiments are assumed to be point sources for scenarios that use reciprocity. This assumption becomes more valid as the source gets increasingly small.

This implementation of reciprocity was validated by using the SFW method to simulate a particular experiment for both the reciprocal and nonreciprocal cases. The correlation between the fields obtained from these to cases was excellent. The SFW method uses point sources, so this validation of reciprocity may not be representative of an actual experiment as one would like. However, the SFW method compares very well with other simulation tools that use a more complicated source model.

The last point of discussion in this thesis describes the process of tailoring Ansys Maxwell to fit the needs of the ELF project. Maxwell was found to be able to obtain good results for ELF simulations that were comparable to those obtained by other simulation tools used in the project. However, Maxwell has many nuances associated with its many solution types. A user needs to be able to choose an appropriate solution type for the particular type of scenario being simulated. Moreover, all of these solution types give either static or quasi-static types of solutions. For ELF simulations, Maxwell's DC conduction solution type was appropriate for simulations that use electric sources and the Eddy current solution type for simulations that use magnetic sources. Impedance matching is necessary for nonreciprocal simulations that use electric sources and the DC conduction solution type. For reciprocal cases currents must be calculated for electric sources using the fields calculator contained within Maxwell. A user also needs to be aware of domain truncation, meshing and the insulator/conductor threshold, regardless of the solution type being used. An important consequence of domain truncation is that the source and sweep lines should be kept 1000 m or more away from boundaries within a Maxwell simulation domain. Proper meshing and domain truncation schemes are very important in Maxwell for obtaining good results and short simulation times.

Bibliography

- [1] J. L. Young, D. M. Sullivan, R. G. Olsen and Christopher L. Wagner, “Investigation of ELF Signals Associated with Mine Warfare: A University of Idaho and Acoustic Research Detachment Collaboration, Phase Two”, Proposal to the Office of Naval Research, pp. 2, 2010.
- [2] Florian Cajori, *A History of Mathematics*, Macmillan and Co., New York, p. 253., 1894.
- [3] Paul Berner, *Technical Concepts Orientation, Rotation, Velocity and Acceleration, and the SRM*, Version 2.0, SEDRIS, 2008.
- [4] Tapan K. Sarkar, *History of Wireless*, John Wiley and Sons, New Jersey, p. 19, 2006.
- [5] Mary L. Boas, *Mathematical Methods in the Physical Sciences*, Wiley, New Jersey, p. 138, 2006.
- [6] David K. Cheng, *Field and Wave Electromagnetics*, Addison-Wesley, Massachusetts, pp. 238-298, 1989.
- [7] *MATLAB and Simulink Release Notes for R2009a*, The MathWorks, Inc., 2009.
- [8] J.L. Young, ECE 539, Advanced Topics in Electromagnetics, Course Notes, University of Idaho, 2010.
- [9] R. F. Harrington, *Time-Harmonic Electromagnetic Fields*, Wiley, New York, pp. 117-118, 2001.
- [10] J. R. Wait, *Electromagnetic Wave Theory*, Harper and Row, New York, p. 19, 1985.

- [11] J.L. Young and C.L. Wagner, “Investigation of ELF Signals Associated with Mine Warfare: A University of Idaho and Acoustic Research Detachment Collaboration, Phase III,” Final Report, Office of Naval Research, 2012.
- [12] Robert T. Rebich, *Multiple-Layered Quasi-Electrostatic Model Development for Extremely Low Frequencies*, M.S. Thesis, University of Idaho, 2011
- [13] Maxwell V12, Internet resource document, Ansys, 2009.

Appendix A

Rotation Compensation Code

This appendix shows the Matlab code used to transform fields from the s coordinate system into the m coordinate system for the rotation experiments. It also includes the code used for the FFT comparisons associated with these experiments.

```
% Rotation compensation experiment

%%

clear all
close all
clc

%load fields and distances from file
fils= importdata('dyn20q.dat');
%put into a matrix
dsts = fils.data;

%separate matrix into vectors
x = dsts(:,1); % x-comp of magnetic field
y = dsts(:,2); % y-comp of magnetic field
z = -dsts(:,3); % z-comp of magnetic field
```

```

txzi = dsts(:,4)*pi/180; %tiltx
tyzi = -dsts(:,5)*pi/180; %tilty

dt = 1/75; % time step
NN = length(x); %length of array

%%
% sampling rate standardization

m = 0;
for n = 2:NN
    %leave out redundant values
    if z(n) == z(n-1) & y(n) == y(n-1) & x(n) == x(n-1)
        dt;
    else

m = m+1;

%redefine vectors for new sampling rate
hxu(m) = x(n-1); %x-comp of magnetic field
hyu(m) = y(n-1); %y-comp of magnetic field
hzu(m) = z(n-1); %z-comp of magnetic field
txz(m) = txzi(n-1); %phix unfiltered
tyz(m) = tyzi(n-1); %phiy unfiltered

    end
end

l = length(hxu); %new array length
t = (1:l)*dt; %time

```

```

%%

%filter tilt angle data

fc = 2; % tilt angle cutoff freq
perct = 2*dt*fc;%sample percent cutoff
[nn,dd] = butter(4,perct,'low');%create butterworth filter

phix = filtfilt(nn,dd,txz); %filtered phix
phiy = filtfilt(nn,dd,tyz); %filtered phiy

%plot phix filtered
figure(8)
plot(t,phix*180/pi)
ylabel('\phi_x (degrees)','fontsize', 15)
xlabel('time (s)','fontsize', 15)
%title('full rotation')

%plot phix unfiltered
figure(9)
plot(t,txz*180/pi)
ylabel('\phi_x (degrees)','fontsize', 15)
xlabel('time (s)','fontsize', 15)
%title('full rotation')

%%

% Rotation into the horizontal plane

phi = acos(tan(phiy).*tan(phix));

```

```

hxr = cos(phix).*hxr + cos(phi).*cos(phiy).*hyr + ...
      sin(phix).*sin(phi).*cos(phiy).*hzu;

hyr = sin(phi).*cos(phiy).*hyr - (cos(phix).*sin(phiy) + ...
      sin(phix).*cos(phi).*cos(phiy)).*hzu;

hxr = -sin(phix).*hxr + sin(phiy).*hyr + ...
      cos(phix).*sin(phi).*cos(phiy).*hzu;

%%
% define full tilt rotation

% fields in horizontal plane representation
hxr = hxr;
hyr = hyr;
hzu = hzu;

%%
% filter fields to obtain theta

fc = 1; %filter cutoff frequency for theta
perc = 2*dt*fc;%sample percent cutoff
[n,d] = butter(4,perc,'low');%create butterworth filter

hxf = filtfilt(n,d,hxr);%filter field component
hyf = filtfilt(n,d,hyr);%filter field component

hres = sqrt(hxf.^2+hyf.^2);%resultant

%%

```

```

% get rotation angle in radians

theta = atan2(-hxf,hyf);%rotation angle
%%
%rotate to magnetic north

hxp = cos(theta).*hxt + sin(theta).*hyt;
hyp = -sin(theta).*hxt + cos(theta).*hyt;
hzp = hzt;
%%
%Rotate to true north

theta = 15.1;

hxd = cosd(theta).*hxp + sind(theta).*hyp;
hyd = -sind(theta).*hxp + cosd(theta).*hyp;
hzd = hzp;
%%
%plot magnetic components

figure(1)
plot(t,hxt,'b')
hold on
plot(t,hyt,'g')
plot(t,hzt,'r')
hold off
ylabel('A/m')
xlabel('time(s)')
title('tilted data')
legend('hx','hy','hz')

```

```
%ylim([-20 20]);
```

```
figure(2)
plot(t,hxf,'b')
hold on
plot(t,hyf,'g')
%plot(t,hres,'r')
hold off
legend('hx','hy','resultant')
ylabel('A/m')
xlabel('time(s)')
title('filtered data')
%ylim([-20 20]);
```

```
figure(3)
plot(t,hxu,'b')
hold on
plot(t,hyu,'g')
plot(t,hzu,'r')
hold off
ylabel('Magnetic Field (mG)','fontsize', 15)
xlabel('time (s)','fontsize', 15)
%title('raw data')
h = legend('Bx','By','Bz');
set(h, 'fontsize', 15);
ylim([-1000 1000])
```

```
figure(5)
```

```

plot(t,hxp,'b')
hold on
plot(t,hyp,'g')
plot(t,hzp,'r')
hold off
ylabel('Magnetic Field (mG)', 'fontsize', 15)
xlabel('time (s)', 'fontsize', 15)
%title('full rotation')
h = legend('Bx', 'By', 'Bz');
set(h, 'fontsize', 15);
ylim([-1000 1000])

%FFT comparison code for rotations

close all
%%

% clip index for deleting beginning and end points
clip = 1;
cn = ceil(clip/dt);

%define signal to FFT
res =hxp(cn:l-cn);

%new array length
N = length(res);

%%

%niquest freq.

```



```

fn = .5/dt;

t = dt:dt:N*dt;%time array
df = 1/(N*dt);%freq step
freq = 0:df:fn-df; %freq. array

sig = res;%redefine signal

%establish window
win = (hanning(N)).';%hanning window

foyo = 4/N*fft(win.*sig);%perform FFT and normalize

fp = abs(foyo(1:length(freq)));%take abs value of FFT

%plot signal in time
figure(1)
plot(t,sig);
xlabel('time(s)')
ylabel('B(mgauss)')
%title('B vs. time')

%plot signal in frequency
figure(2)
semilogy(freq,abs(fp));
%title('fft magnitude By')
ylabel('Magnetic Field (mG)','fontsize', 15)
xlabel('frequency (Hz)','fontsize', 15)
ylim([1e-3 1e2])

```

Appendix B

Reciprocity Processing Code

This appendix shows the Matlab code used to get experimental fields from the fields obtained by Maxwell. There are three sets of code included: electric fields from an electric source, magnetic fields from an electric source and magnetic fields from a magnetic source.

```
% Electric fields from an electric source using reciprocity
%%
clear all
close all
clc
%%
%get files from Maxwell
data = importdata('rh4qEx.fld', ' ');
exf(:, :) = data.data;

data = importdata('rh4qEy.fld', ' ');
eyf(:, :) = data.data;

data = importdata('rh4qEz.fld', ' ');
ezf(:, :) = data.data;
%%
```

```

 file for headings and points locations

[FileName,PathName] = uigetfile('Z:\scenarios in progress\*.');
FullPath = fullfile(PathName, FileName);

load(FullPath)

%%

pts = exp_data(:,9:11);%extract points array from file
sphi = exp_data(:,15);%%extract heading array from file

lx = cosd(sphi);%heading
ly = sind(sphi);%heading
lz = 0;%costheta

iexp = 4.9669; %experimental current
momexp = iexp*14.681; %experimental moment

dlsim = 4; %dipole length in Maxwell

ix = 0.666479550400576; %currents for an x-directed dipole in Maxwell
iy = 0.666237691803378; %currents for an y-directed dipole in Maxwell
iz = 0.665187364349678; %currents for an z-directed dipole in Maxwell

%get experimental fields
Ex = momexp*(lx.*exf(:,4)+ly.*exf(:,5)+lz.*exf(:,6))/(ix*dlsim);
Ey = momexp*(lx.*eyf(:,4)+ly.*eyf(:,5)+lz.*eyf(:,6))/(iy*dlsim);
Ez = momexp*(lx.*ezf(:,4)+ly.*ezf(:,5)+lz.*ezf(:,6))/(iz*dlsim);

%get sweep vector
d = zeros(length(pts),1);

%create array to sweep along source
for i=2:length(pts)

```

```

    d(i) = d(i-1) +sqrt(dot((pts(i,:)-pts(i-1,:)),(pts(i,:)-pts(i-1,:))));
end

%experimental electric fields
E(:,1) = d;
E(:,2) = abs(Ex);
E(:,3) = abs(Ey);
E(:,4) = abs(Ez);
E(:,5) = sqrt(Ex.^2+Ey.^2+Ez.^2);

%plot electric fields
semilogy(d,E(:,2),'r')
hold on
semilogy(d,E(:,3),'b')
semilogy(d,E(:,4),'g')
hold off

%output file
dlmwrite('exprh4qE.txt',E,'delimiter','\t','newline','pc');

% Magnetic fields from an electric source using reciprocity

%%
clear all
close all
clc
%%

%get files from Maxwell
data = importdata('rh4qHx.fld',' ');
exf(:, :) = data.data;

```

```

data = importdata('rh4qHy.fld', ' ');
eyf(:, :) = data.data;

data = importdata('rh4qHz.fld', ' ');
ezf(:, :) = data.data;
%%
    %input file for headings and points locations
[FileName, PathName] = uigetfile('Z:\scenarios in progress\*. *');
FullPath = fullfile(PathName, FileName);

load(FullPath)
%%
%extract points array from file
pts = exp_data(:, 9:11);
sphi = exp_data(:, 15); %heading angle

lx = cosd(sphi);
ly = sind(sphi);
lz = 0; %costheta

fexp = 10; %experimental frequency
iexp = 4.9669; %experimental current
expmom = 14.681*iexp; %experimental moment

ix = 9.495; %area of loop in Maxwell
iy = 9.495; %area of loop in Maxwell
iz = 9.495; %area of loop in Maxwell

mu = 4*pi*1e-7;

```

```

w = 2*pi*fexp;

%get experimental fields
Hx = -expmom*(lx.*(exf(:,4)+1i*exf(:,5))+ly.*(exf(:,6)+1i*exf(:,7))+lz.*...
    (exf(:,8)+1i*exf(:,9)))/(ix*1i*w*mu);
Hy = -expmom*(lx.*(eyf(:,4)+1i*eyf(:,5))+ly.*(eyf(:,6)+1i*eyf(:,7))+lz.*...
    (eyf(:,8)+1i*eyf(:,9)))/(iy*1i*w*mu);
Hz = -expmom*(lx.*(ezf(:,4)+1i*ezf(:,5))+ly.*(ezf(:,6)+1i*ezf(:,7))+lz.*...
    (ezf(:,8)+1i*ezf(:,9)))/(iz*1i*w*mu);

%make path vector
d = zeros(length(pts),1);
%create array to sweep along source
for i=2:length(pts)
    d(i) = d(i-1) +sqrt(dot((pts(i,:)-pts(i-1,:)),(pts(i,:)-pts(i-1,:))));
end

%d = exf(:,3);

H(:,1) = d;
H(:,2) = abs(Hx);
H(:,3) = abs(Hy);
H(:,4) = abs(Hz);
H(:,5) = sqrt(Hx.^2+Hy.^2+Hz.^2);

semilogy(d,H(:,2),'r')
hold on
semilogy(d,H(:,3),'b')
semilogy(d,H(:,4),'g')
hold off

```

```

%output file
dlmwrite('exprh4qH.txt',H,'delimiter','\t','newline','pc');

% Magnetic fields from a magnetic source using reciprocity

clear all
close all
clc

%get files from Maxwell
data = importdata('rh2hHx.fld',' ');
exf(:, :) = data.data;

data = importdata('rh2hHy.fld',' ');
eyf(:, :) = data.data;

data = importdata('rh2hHz.fld',' ');
ezf(:, :) = data.data;

%%
%input file for headings and points locations
[FileName,PathName] = uigetfile('Z:\scenarios in progress\*.');
FullPath = fullfile(PathName, FileName);

load(FullPath)

%%
%extract points array from file
pts = exp_data(:,9:11);

```

```

sphi = 0;%heading angle

lx = 0;%sintheta*cosphi
ly = 0;%sintheta*sinphi
lz = 1;%costheta

iexp = 19.4327; %experimental current
in = iexp*7*1.36; % #loops x area in experiment

ix = 9.495; %area of loop in maxwell
iy = 9.495;
iz = 9.495;

%get experimental fields
Hx = in*(lx*(exf(:,4)+1i*exf(:,5))+ly*(exf(:,6)+1i*exf(:,7))+lz*...
    (exf(:,8)+1i*exf(:,9)))/ix;
Hy = in*(lx*(eyf(:,4)+1i*eyf(:,5))+ly*(eyf(:,6)+1i*eyf(:,7))+lz*...
    (eyf(:,8)+1i*eyf(:,9)))/iy;
Hz = in*(lx*(ezf(:,4)+1i*ezf(:,5))+ly*(ezf(:,6)+1i*ezf(:,7))+lz*...
    (ezf(:,8)+1i*ezf(:,9)))/iz;

%get sweep vector
d = zeros(length(pts),1);

%create array to sweep along source
for i=2:length(pts)
    d(i) = d(i-1) +sqrt(dot((pts(i,:)-pts(i-1,:)),(pts(i,:)-pts(i-1,:))));
end

%get experimental H fields
H(:,1) = d;
H(:,2) = abs(Hx);
H(:,3) = abs(Hy);

```



```

H(:,4) = abs(Hz);
H(:,5) = sqrt(abs(Hx).^2+abs(Hy).^2+abs(Hz).^2);

%plot fields
semilogy(d,H(:,2),'r')
hold on
semilogy(d,H(:,3),'b')
semilogy(d,H(:,4),'g')
hold off

%output files
dlmwrite('rh2hrealH.txt',Hr,'delimiter','\t','newline','pc');
dlmwrite('rh2himagH.txt',Hi,'delimiter','\t','newline','pc');

```

Modelling Extremely Low Frequency Electromagnetic Signals for Naval Applications

A Thesis

Presented in Partial Fulfilment of the Requirements for the

Degree of Master of Science

with a

Major in Electrical Engineering

in the

College of Graduate Studies

University of Idaho

by

Christopher Donald Johnson

November 2011

Major Professor: Jeffrey L. Young, Ph.D.

AUTHORIZATION TO SUBMIT THESIS

This thesis of Christopher Donald Johnson, submitted for the degree of Master of Science with a major in Electrical Engineering and titled “Modelling Extremely Low Frequency Electromagnetic Signals for Naval Applications,” has been reviewed in final form. Permission, as indicated by the signatures and dates given below, is now granted to submit final copies to the College of Graduate Studies for approval.

Major Professor _____ Date _____
Jeffrey L. Young

Committee

Members _____ Date _____
Christopher L. Wagner

_____ Date _____
Wudneh Admassu

Department

Administrator _____ Date _____
Brian Johnson

Discipline's

College Dean _____ Date _____
Larry Stauffer

Final Approval and Acceptance by the College of Graduate Studies

_____ Date _____
Jie Chen

Abstract

Modelling and simulation of extremely low frequency (ELF) signals using a commercial electromagnetic solver using and several custom analytical tools is the main focus of this thesis. The thesis outlines the steps to model a set of experiments conducted at Lake Pend Orielle. The development of domain models to represent the real world experimental and the demonstration Ansys' High Frequency Structural Solver (HFSS) can be used to solve this class of problem is an important contribution of this thesis. The results of HFSS are compared against several other simulation tools. The results show that HFSS is able to solve these types of problems, but has some limitations. Likewise analytical methods are developed to help understand the limitations and benefits of using simplifying assumptions such as single material domain approximations and source geometry simplification. This thesis also discusses a data management strategy for making comparisons between experimental data sets and data sets generated by simulations. Finally, information is provided in here on how to devise an automated data collection scheme for the source of the experiment and how to create a mesh from topological and symmetrical data, as obtained from geological surveys.

Vita

The author received the BSEE degree from the University of Idaho in 2008. He is currently pursuing the MSEE degree from the the University of Idaho were he works as a research assistant in the Department of Electrical and Computer Engineering. His research interests include computational electromagnetics, antennae systems and low frequency wave propagation.

Acknowledgements

I would like to acknowledge the support and guidance of my major professor, Dr. Jeffery L. Young. His knowledge and insight played a major role in the success the research methods presented in the document as well as in the overall success of the research. I would also like the thank the other members of the ELF team, Christopher L. Wagner, Robert Rebich, Das D. Butherus, Chenchen Jimmy Li, Markus Geiger and Neleema Dehal. Their help has been instrumental throughout the project and the creation of this document. Lastly, I would like to thank my committee for their help and guidance throughout the past two years.

This work was supported by the Office of Naval Research under grant number N00014-09-1-0923.

Contents

Abstract	iii
Vita	iv
Acknowledgements	v
1 Introduction	1
1.1 Project Motivation	2
1.2 Background	2
1.3 Scope	3
2 Experimental Work	5
2.1 Data Acquisition(DAQ)	6
3 Using HFSS (High Frequency Structural Solver) for ELF Simulations	11
3.1 Building Models in HFSS	11
3.1.1 Mud	12
3.1.2 Air and Water	12
3.1.3 The Source	14
3.2 Domain Truncation	22
3.3 Mesh and Mesh Operations	29
3.4 Excitation	31
3.5 Analysis Setup	33
3.6 Optimetrics	36
3.7 Reciprocity	36
3.8 Validation	37

3.9	Multi-CPU and Multi-Core Platforms	66
4	Electric Current Loop	68
4.1	Square Loop: Numerical Integration and Finite-Difference Derivatives	68
4.2	Square Loop: Analytical Derivatives and Numerical Integration	74
4.3	Circular Loop: Closed Form Series Solution	76
4.4	Square Loop: Far Field Approximation	81
4.5	Current Loop Comparisons	84
4.5.1	Homogeneous Comparisons	84
4.5.2	Three Layer Comparisons	97
5	Experimental Data Management and Processing	103
5.1	Data Matrix Format	103
5.2	MatLab Preprocessing Scripts	104
5.3	Main Analysis Script	104
6	Model Building	106
6.1	Map Data	106
6.1.1	Matlab Compilation and Interpolation	107
6.2	AutoCAD	107
6.3	Cubit	109
6.4	HFSS VB Scripts	110
7	Conclusion	113

List of Figures

2.1	Flow diagram for ELF Source DAQ.	8
2.2	Flow diagram of main DAQ read and signal save loop.	8
2.3	Flow diagram of GPS read loop.	9
2.4	Flow diagram of orientation read loop.	9
2.5	Flow diagram of GPS and orientation save loop.	10
2.6	Flow diagram of signal generator configuration loop.	10
3.1	Example of completed model.	13
3.2	Example of completed model.	13
3.3	Example of electric dipole implementation.	14
3.4	Example of magnetic dipole implementation.	15
3.5	Impedance Matching.	22
3.6	Illustration of three layer problem space.	24
3.7	Electric fields in air using a radiation boundary condition.	25
3.8	Magnetic fields in air using a radiation boundary condition.	26
3.9	Electric fields in air for the PML boundary condition.	27
3.10	Magnetic fields in air for the PML boundary condition.	27
3.11	Electric fields in water for the radiation boundary condition.	28
3.12	Electric fields in water for the PML condition.	29
3.13	Example of how mesh can effect the solution.	31
3.14	Example of how solution order can affect a solution.	34
3.15	HFSS analysis set-up menu.	35
3.16	Scenario 3L1, Sweep 3, Magnitued E field.	39

3.17 Scenario 3L1, Sweep 3, Magnitued H field.	39
3.18 Scenario 3L4, Sweep 4, Magnitued E field.	40
3.19 Scenario 3L4, Sweep 4, Magnitued H field.	40
3.20 Scenario 3L5, Sweep 5, Magnitued E field.	41
3.21 Scenario 1, magnitude E_x field.	42
3.22 Scenario 1, magnitude E_y field.	43
3.23 Scenario 1, magnitude E_z field.	43
3.24 Scenario 1, magnitude E field.	44
3.25 Scenario 1, magnitude H_x field.	44
3.26 Scenario 1, magnitude H_y field.	45
3.27 Scenario 1, magnitude H_z field.	45
3.28 Scenario 1, magnitude H field.	46
3.29 Scenario 2, magnitude E_x field.	47
3.30 Scenario 2, magnitude E_y field.	47
3.31 Scenario 2, magnitude E_z field.	48
3.32 Scenario 2, magnitude E field.	48
3.33 Scenario 2, magnitude H_x field.	49
3.34 Scenario 2, magnitude H_y field.	49
3.35 Scenario 2, magnitude H_z field.	50
3.36 Scenario 2, magnitude H field.	50
3.37 Scenario 3, magnitude E_x field.	52
3.38 Scenario 3, magnitude E_y field.	53
3.39 Scenario 3, magnitude E_z field.	53
3.40 Scenario 3, magnitude E field.	54
3.41 Scenario 3, magnitude H_x field.	54
3.42 Scenario 3, magnitude H_y field.	55
3.43 Scenario 3, magnitude H_z field.	55
3.44 Scenario 3, magnitude H field.	56
3.45 Scenario 4, magnitude E_x field.	57

3.46	Scenario 4, magnitude E_y field.	57
3.47	Scenario 4, magnitude E_z field.	58
3.48	Scenario 4, magnitude E field.	58
3.49	Scenario 4, magnitude H_x field.	59
3.50	Scenario 4, magnitude H_y field.	59
3.51	Scenario 4, magnitude H_z field.	60
3.52	Scenario 4, magnitude H field.	60
3.53	Scenario 5, magnitude E_x field.	61
3.54	Scenario 5, magnitude E_y field.	62
3.55	Scenario 5, magnitude E_z field.	62
3.56	Scenario 5, magnitude E field.	63
3.57	Scenario 5, magnitude H_x field.	63
3.58	Scenario 5, magnitude H_y field.	64
3.59	Scenario 5, magnitude H_z field.	64
3.60	Scenario 5, magnitude H field.	65
3.61	Time vs. N Cores.	67
4.1	Single length of current.	69
4.2	Square loop	70
4.3	Geometry for evaluating the radiation field.	82
4.4	Line 1, magnitude of E_x field. General, SFW and FDTD are hidden by the other traces.	85
4.5	Line 1, magnitude of E_y field. General, SFW and FDTD are hidden by the other traces.	85
4.6	Line 1, magnitude of E_z field. General, SFW and Harrington calculate zero for this component.	86
4.7	Line 1, magnitude of H_x field. General and FDTD are hidden by the other traces.	86
4.8	Line 1, magnitude of H_y field. General and FDTD are hidden by the other traces.	87
4.9	Line 1, magnitude of H_z field. General and FDTD are hidden by the other traces.	87

4.10	Line 2, magnitude of E_x field. General, HFSS and FDTD are hidden by the other traces.	88
4.11	Line 2, magnitude of E_y field. General, SFW and FDTD are hidden by the other traces.	88
4.12	Line 2, magnitude of E_z field. SFW and Harrington calculate zero for this component.	89
4.13	Line 2, magnitude of H_x field. General and FDTD are hidden by the other traces.	89
4.14	Line 2, magnitude of H_y field. General and FDTD are hidden by the other traces.	90
4.15	Line 2, magnitude of H_z field. General, FDTD and HFSS are hidden by the other traces.	90
4.16	Line 3, magnitude of E_x field. General, FDTD and SFW are hidden by the other traces.	91
4.17	Line 3, magnitude of E_y field. FDTD is hidden by the other traces.	91
4.18	Line 3, magnitude of E_z field. SFW and Harrington calculate zero for this component.	92
4.19	Line 3, magnitude of H_x field. General and FDTD are hidden by the other traces.	92
4.20	Line 3, magnitude of H_y field. General, FDTD and SFW are hidden by the other traces.	93
4.21	Line 3, magnitude of H_z field. General and FDTD are hidden by the other traces.	93
4.22	Line 4, magnitude of E_x field. General and FDTD are hidden by the other traces.	94
4.23	Line 4, magnitude of E_y field. General and FDTD are hidden by the other traces.	94
4.24	Line 4, magnitude of E_z field. SFW and Harrington calculate zero for this component.	95
4.25	Line 4, magnitude of H_x field. General and FDTD are hidden by the other traces.	95
4.26	Line 4, magnitude of H_y field. General, FDTD and HFSS are hidden by the other traces.	96
4.27	Line 4, magnitude of H_z field. General, FDTD and HFSS are hidden by the other traces.	96
4.28	Magnitude of the electric field components.	98

4.29	Magnitude of the magnetic field components.	98
4.30	Magnitude of the electric field components.	99
4.31	Magnitude of the magnetic field components.	100
4.32	Magnitude of the electric field components.	101
4.33	Magnitude of the magnetic field components.	101
5.1	Flow diagram for Main Analysis Script.	105
6.1	Example of an AutoCAD model.	108
6.2	Example of an AutoCAD model.	109
6.3	Example of Cubit faceted model.	110
6.4	Example of Cubit faceted model (Idlewilde Bay).	110
6.5	Partial topology build with VB scripting.	111
6.6	Completed Idlewilde Bay topology model with VB scripting.	112
6.7	Completed deep water topology model with VB scripting.	112

List of Tables

3.1	Simulation Details	38
3.2	Observer location along line from P1 to P2	38
4.1	Sweep Lines	84

Chapter 1

Introduction

The steady progress of the Navy towards an all electric fleet has created many challenges and scientific questions that need to be answered. Of paramount concern to the Navy is vulnerabilities created from this change in technology, particularly those vulnerabilities associated with electromagnetic emissions. Hence, it is necessary to understand the signals that will be produced by electric ships and how they propagate in environments where ships are deployed. The signals expected to be most strongly excited and to propagate the furthest are extremely low frequency signals (ELF). ELF will be considered as the band of frequencies from 10 Hz to 1000 Hz in this thesis. With the signals so understood they can be anticipated and appropriate countermeasures can be designed. To that end it is desirable to have electromagnetic models that can predict the emitted signals within multitude of environments.

Developed in tandem with this project are several other methods that attempt to model the aforementioned scenario. One is a custom Finite-Difference Time-Domain (FDTD) solver developed primarily by Dr. Christopher L. Wagner of the University of Idaho (UI). His code is a standard FDTD implementation, but with several key custom features that are needed for ELF signal simulation - namely, PML and source implementation. A second approach developed by Dr. Robert G. Olsen of Washington State University (WSU) is the three-layer, Sommerfield Full-wave (SFW) methodology. This approach assumes idealized sources and stratified medium to find a closed-form analytic solution that is then numerically evaluated. A third approach, as developed by Robert T. Rebich, considered a quasi-electrostatic (QES)

source simplification in a stratified medium to find a closed-form analytical solution. That analytical solution is numerically evaluated to predict electric fields.

This thesis will describe in detail the steps and methods used in modelling extremely low frequency signals in maritime environments. The thesis will provide an overview of some experimental considerations and then discuss the development of methods used to model these experiments. With each method a set of validations will be presented. Additional challenges that had to be resolved were the management of large amounts of simulation and experimental data; the solution to these challenges is also discussed herein.

1.1 Project Motivation

As the Navy of tomorrow takes shape, there is concern about its vulnerabilities. Because the new ships that are being designed for the Navy may to be completely electric, they could produce large electromagnetic signals, which could lead to detection by enemy mines. Clearly, a scientific study of these signals is needed. Being able to characterize them, model them and predict them will help design engineers anticipate ship vulnerabilities. By understanding the vulnerabilities of the ships, the design engineers may be able to mitigate the risk or even eliminate the risk altogether. To accomplish this, experiments were designed with the focus of producing similar situations to what would be encountered by these ships. To this end the experiments were conducted at Lake Pend Oreille by the Acoustic Research Detachment (ARD, Bayview, Idaho) with support from the University of Idaho (UI, Moscow, Idaho). The research on the modelling and simulation of ELF signals was performed by UI. With this partnership in place the major tasks of experimentation and modelling could be accomplished. This thesis will span both the experimental and modelling efforts, but will be primarily concerned with the modelling effort.

1.2 Background

The modelling of electromagnetic signals in or near an inhomogeneous earth using electromagnetic simulation tools has always been a challenge. The myriad of materials present

(e.g. trees, rocks, buildings, etc.) and the near infinite number of combinations and arrangements of these materials make it all but impossible to simulate the environment as it is. Typically, simplifications are needed to make a simulation feasible, such as considering the universe as a single homogeneous material such as air or water. A more reasonable simplification is to consider parallel, homogeneous layers. These simplifications can be valid in some cases—for example, short range flat terrains and open ocean environments. An example of the latter case would be what is used to model the upper atmosphere of a planet or the air-water interface far away from the shore. However, near a littoral region, these simplifications are less valid. It is a goal of this thesis to determine methods that can accurately model complex terrain and to determine the effects of terrain on the electromagnetic fields.

1.3 Scope

The ability to predict and measure electromagnetic fields is of utmost concern to this project. Several chapters in this thesis will deal directly with the support that was given to the experimental effort and with the analysis of the data that came from the experiments. Another chapter will discuss modelling the terrain and challenges associated with the building a computational mesh of that terrain.

The final two chapters consider the question of modelling the scenario of electromagnetic sources in maritime environments in the context of the experiments conducted at Lake Pend Oreille. These two chapters will address two methods of simulating the fields of some experiment; one will consider a commercial solver marketed by Ansys called High Frequency Structural Solver (HFSS). HFSS is a finite-element, frequency-domain solver that is able to handle complex terrains and sources. Because of its origins as a high frequency solver it was not known *a priori* if this tool would be able to handle ELF class of problems. Part of the focus of this thesis is to determine if it could in fact be effectively used and the challenges that would result in using it. The second method considers a greatly simplified problem and then attempts to find closed-form expressions that can be solved analytically and numerically. For this purpose a single loop of current is considered in a homogeneous medium. The results of this

method are compared with the results associated with current loops in non-homogeneous media to ascertain the effects, if any, on ELF signals.

Chapter 2

Experimental Work

Starting in 2009, the Acoustic Research Detachment(ARD) conducted a series of four experiments at Bayview, Idaho on Lake Pend Oreille. The experiments concluded in September 2011. These experiments were designed to collect ELF electromagnetic field data that would be used to validate simulation and modelling tools. These experiments used three types of electric dipole sources, two electric current loop sources and two sensor arrays, which were comprised of both electric and magnetic field sensors.

The first of these experiments was designed as a proof-of-concept experiment and was used to test methods of deploying the sensor and sources. This experiment was also used to make sure the experimentalist had all the measurement equipment, computers and storage devices ready to record experimental data in a way that would assure a positive outcome for more comprehensive experiments in the future.

The second experiment was designed with the purpose of recording data in as near an ideal environment as possible. The experiment was conducted in a deep part of the Lake – over a 1000 ft deep and far away from shore. The experiment approximated a three layered problem space of air, water and mud, with the third layer representing mud, which has little effect on the measured data. This elimination of potential boundary complications helped provide a starting point for comparisons between simulation and experimental results. However, it was not possible to remove all of none ideal influences. Most notable are the deployment equipment and platforms. The experiment consisted of a short, 4 m electric dipole, a long 40 m

electric dipole, and the boat mounted electric current loop of radius 3.5 m. All three sources were mounted on a boat and moved just below the water surface for the case of electric sources and just above the water surface for the case of the magnetic source. All of these signals were recorded from a stationary, submerged sensor array that was placed in the center of the experimental range and at two depths. One depth was approximately 8 meters and the second depth was approximately 300 meters.

The third experiment was moved into a much shallower region of the Lake called Idlewilde Bay with the purpose of introducing terrain influences. This region is much more difficult to model, due to the proximity of the boundaries relative to the source and sensors. It was chosen to test the robustness of the modelling tools. In addition to the terrain influences, two new sources were deployed. The first was a 40 ft electric dipole mounted on a truss such that it could be suspended from a barge to any depth desired. It had a horizontal dipole orientation but could be rotated azimuthally to any angle by rotating the deployment barge. For the other source, a large electric current loop was deployed on a small plastic barge that was anchored to shore. This source could be deployed in a vertical or horizontal orientation at any azimuthal angle. The small boat mounted current loop was not used in this experiment nor was the 40 m electric dipole.

The fourth experiment was again done in Idlewilde Bay with the purpose of redoing several of the experiments of Experiment Three so that data at more depths could be recorded to give more data points for comparison. In addition to the rerunning of Experiment Three, it was desired to get near field data and magnetic field data from a stationary source. The magnetic source data from experiment three was unusable.

2.1 Data Acquisition(DAQ)

Besides providing consulting for the experiments, the University of Idaho (i.e. the author of this thesis) also developed a data acquisition system (DAQ) for use with the 40 ft electric truss source. This system was used to record voltages, currents, positional, orientation and timing data that would provide information about the source state for simulations. The system would

also control the signal for the source as well as saving all the data files.

Hardware

The hardware used was procured from National Instruments:

- NI PXI-1042: Chassis
- NI PXI-8105: Controller
- NI PXI-4472: A2D
- NI PXI-8430: RS232 Serial
- NI PXI-8431: RS485 Serial

Software

The controlling software was written exclusively in National Instruments LabView, V8.2.

LabView is a graphical programming language that is designed for use in laboratory environments where small, customized control programs are needed. The digital acquisition (DAQ) control code is divided into five different sections or functions. Each of these sections are in their own while loop and are meant to function independently from each other. There is some sharing of data between them but, it is very limited. An overview of these sections of code is shown in Fig. 2.1. A detail listing is not provided since LabView is written using a graphical use interface (GUI); the command line text is too large to be instructive.

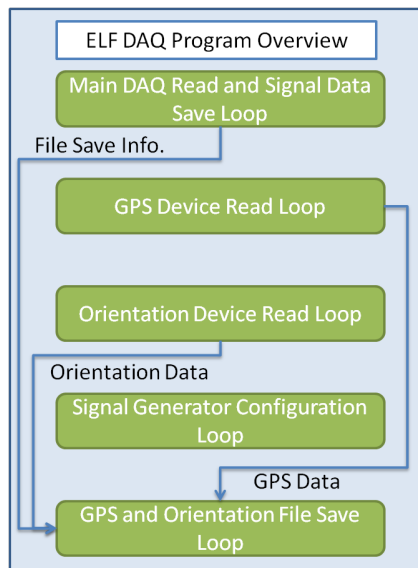


Figure 2.1: Flow diagram for ELF Source DAQ.

The first section controls the analog to digital converter (ADC) sampling card and writes a binary file that will record the signal information. The binary file is a proprietary series binary file type created by National Instruments call “TDMS” and is used for easy appending of binary files in a real-time manner. The signals read and recorded by this card are: system voltages, currents from a clamp-on current meter and shunt resister, pulse per second from the global positioning satellite (GPS) acquisition system, and waveform signal recorded directly from the function generator. A flow diagram of this while loop is shown in Fig. 2.2.

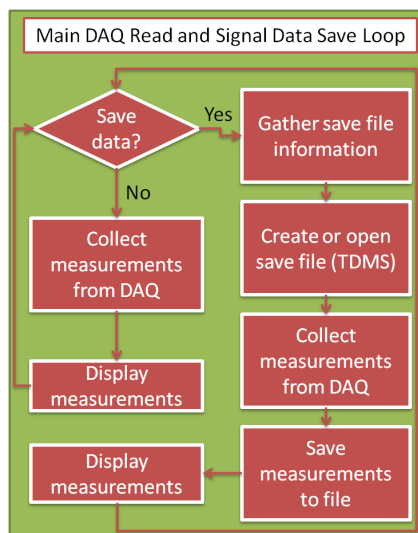


Figure 2.2: Flow diagram of main DAQ read and signal save loop.

The second section, a flow diagram of which is shown in Fig. 2.3, reads the GPS strings that come from the Trimble GPS receivers. These text strings are parsed and displayed to the user GUI. These strings are provided from the GPS receiver at a once-per-second rate.

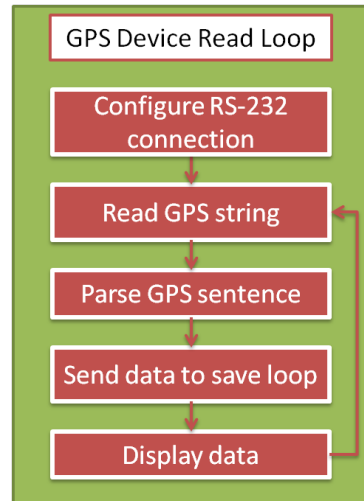


Figure 2.3: Flow diagram of GPS read loop.

The third function, a flow diagram of which is shown in Fig. 2.4, reads a sensor package that is submerged with the source. The package includes a temperature meter, pressure gauge, three-axis accelerometer and a two-axis magnetometer used for compass heading. This data is transmitted back to the DAQ via RS-485 and is parsed, displayed to the user and recorded to a text file that included timing information from the GPS.

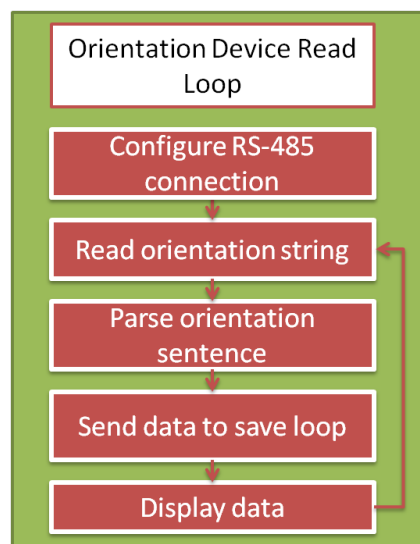


Figure 2.4: Flow diagram of orientation read loop.

The forth function receives the data from the GPS device read loop and the orientation sensor read loop, and records the data to text files. It takes the last date/time stamp from the GPS and labels the files. These files are created one per second. A flow diagram of this function is shown in Fig. 2.5.

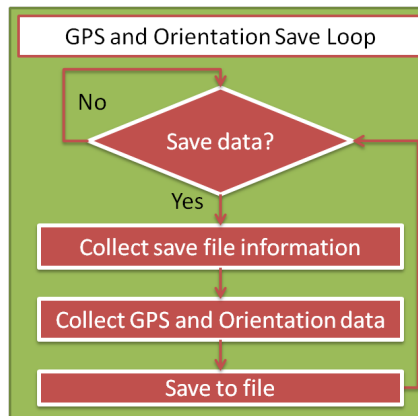


Figure 2.5: Flow diagram of GPS and orientation save loop.

The fifth and final section is the control interface for the function generator. It allows the user to change the signal to the power amplifier and see the current settings all on one screen. A flow diagram detailing this function is shown in Fig. 2.6.

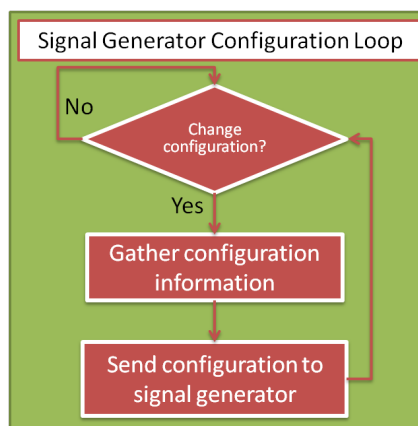


Figure 2.6: Flow diagram of signal generator configuration loop.

Chapter 3

Using HFSS (High Frequency Structural Solver) for ELF Simulations

HFSS is a finite-element, frequency-domain Maxwellian solver that has been used for over two decades in fields such as microwave circuit and antenna design. This commercial solver has been well tested in that community. The single, biggest advantage of this solver is that it has the ability to model complex geometry, such as a lake environment including shorelines. And being a commercial code, it has a track record of being a reliable software tool. Obversely, being a commercial code, it cannot be modified to handle custom applications. It is a purpose of this thesis to see if HFSS is well suited for ELF electromagnetic field modelling.

3.1 Building Models in HFSS

The first step in simulating an ELF scenario is to create a model in HFSS. The scenario of interest has four sub-components of interest: air, water, mud, and source. The two sub-components of most interest in this work are mud and source, since they are outside the standard model making steps for HFSS or they have specific requirements to obtain valid simulations.

3.1.1 Mud

Although the sub-environment in the simulation is called “mud,” it is not representing only mud in the real world domain. Integrated into this single material descriptor are things like rock, trees, bushes and anything else that forms the “land”. This is not strictly necessary, but for practical reasons it is assumed that “mud” is a homogeneous material. HFSS has the ability to model thousands of different materials in a single simulation but this requires increasing amounts of computational resources. In addition to the extra computational resources, considerable expense and undertaking would be required to get all of the material parameters and to create an accurate map of the objects associated with these parameters. It is not clear at this time that by doing so a significant increase in accuracy from a single homogeneous value estimate would be achieved.

Even though the exact material parameters were not used because of the aforementioned reasons, the topology and bathymetry of the region are straightforward to determine. The first step is to collect and compile geometric data for the region of interest. The second step is to create a 3D model of a solid object. Once that object is created it is imported into HFSS and assigned material parameters. Note that each object in HFSS is only allowed one set of material parameters. (This is the reason why it becomes impractical to create an inhomogeneous representation of the earth in HFSS.) After the object for mud is imported and parameters are assigned then air, water and the source are included in the HFSS model.

3.1.2 Air and Water

Given the flat nature of the air and water interface, the air and water regions are easy to model in HFSS using standard HFSS functions. This is done by first creating two boxes, one for the air and one for the water. The air-water interface is set to a height consistent with the model for the mud. The “subtract” command is then used to remove the the area of air and water that overlap with the mud. After the air and water were added to the model, the last step is to create the source. Examples of what a complete model may look like are shown in Figure 3.1 and Figure 3.2.

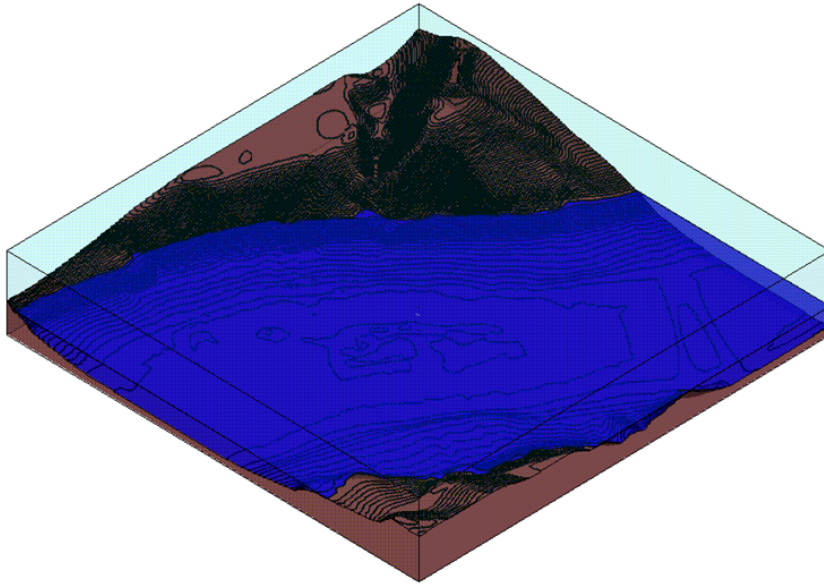


Figure 3.1: Example of completed model.

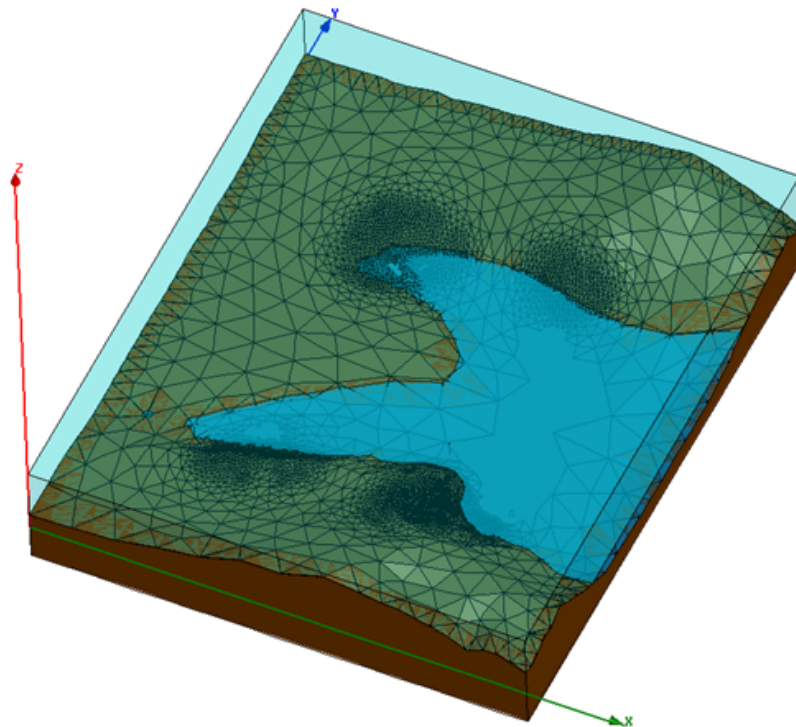


Figure 3.2: Example of completed model.

3.1.3 The Source

There is a need to replicate several sources of the experiment, each of which has a different implementation. The sources considered herein are of two fundamental radiating types: an electric dipole and a magnetic dipole. The electric dipole is created by exciting a potential difference between two conducting plates. This potential difference produces a current that flows between the two conducting plates. An example of this source is shown in Fig. 3.3.

Three versions of this electric dipole were considered: A short, 4 m dipole attached to the hull of a boat, a long, 40 m dipole attached to the hull of two boats (one pulled behind the other), and a 40 ft truss. The magnetic dipole is created by wrapping a conductor on a supporting core and impressing a current between the ends of the conductor such that the current flows along the conductor. An example of this source is shown in Fig. 3.4. Two versions of this current loop were used. One was a small 3 ft radius, 7 turn loop attached to the bow of a boat and the second was a 12 ft by 12 ft, 12 turn loop set on a plastic dock.

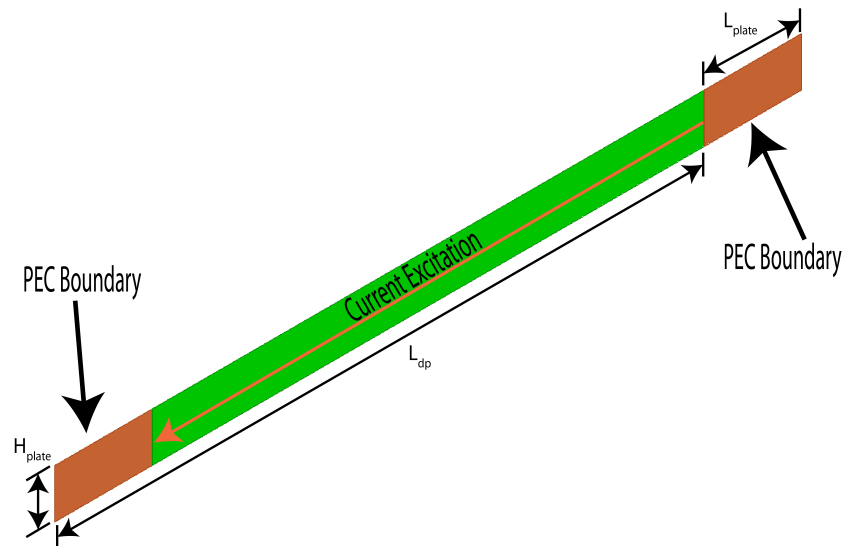


Figure 3.3: Example of electric dipole implementation.

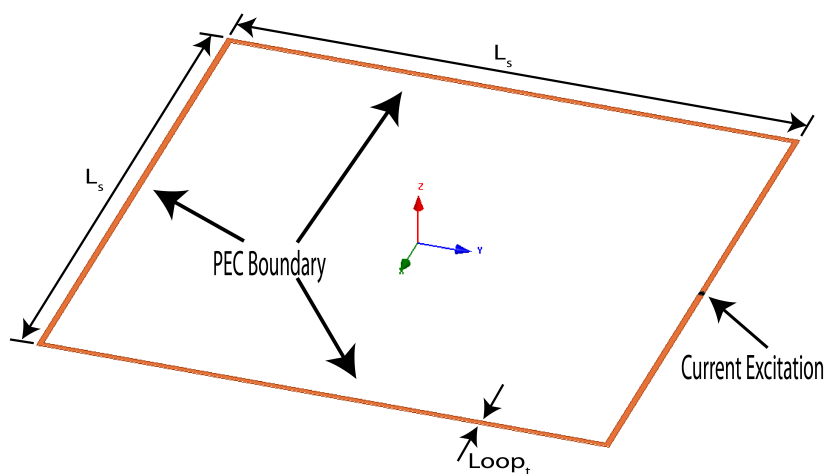


Figure 3.4: Example of magnetic dipole implementation.

3.1.3.1 Electric Source

There are only three electric sources used in the experiments. They are similar to each other, but depending on if the source is moving or not the implementations are different. For moving sources, the additional step of applying the reciprocity theorem is needed. The three sources are all electric dipoles and differ only in size and how they are moved and positioned. The first dipole has two, 1 ft by 2 ft copper plates attached to the bottom of a fiberglass boat hull. The second has three, 1 ft copper plates with two attached to a fiberglass boat hull and the third attached to a separate fiberglass boat hull that is towed behind the first with a 40 meter lead. The last two sources have 2 ft copper plates separated by a 40 ft truss that is suspended by ropes below a floating deployment barge.

The first case is the simplest. A non-moving electric source is modelled by placing two conducting plates (i.e. electrodes) in the domain and then impressing a sheet of current between them. The conducting plates are in actuality two dimensional sheets with a perfect electrical conductor boundary condition assigned them. The current sheet is also a two dimensional sheet on the same plane as the electrodes and stretched between them. The current will be discussed in more detail in Section 3.4.

In the case of a moving source there are two options. One is to do a simulation for each of the source/sensor positions. That could result in hundreds of simulations and is not considered

practical, as it takes approximately 30 minutes for each simulation. The other is to apply reciprocity so that the source can be moved to the sensor location and the fields can be taken from the path of the source. Reciprocity will be discussed in further detail in Section 3.7. With the application of reciprocity it is possible to reduce the number of simulations for a moving source down to six, i.e. one simulation for each component of the fields.

Detailed Source Build

The following procedure gives details on how the electric sources were constructed for this project. The symbols S_θ and S_ϕ reference the source dipole moment orientation in spherical coordinates with the x,y,z axis in the direction of east, north, and vertical.

1. Define a relative coordinate system with the following parameters:

- Origin: SourceX, SourceY, SourceZ

- Orientation:

- * X Axis:

- ◇ $x = \sin(S_\theta) \cos(S_\phi)$

- ◇ $y = \sin(S_\theta) \sin(S_\phi)$

- ◇ $z = \cos(S_\theta)$

- * Y Point:

- ◇ $x = -\sin(S_\phi)$

- ◇ $y = \cos(S_\phi)$

- ◇ $z = 0$

2. Create Positive Electrode

Create a 2D sheet and define it as follows:

- Position:

- * $x = \frac{L_{dp} - L_{plate}}{2}$

- * $y = 0$

$$* z = \frac{-H_{plate}}{2}$$

- Axis: Y
- X Size: L_{plate}
- Z Size : H_{plate}

Apply a PEC boundary condition to the finished sheet.

3. Create Negative Electrode

Create a 2D sheet and define it as follows:

- Position:

$$* x = \frac{-L_{dp} - L_{plate}}{2}$$

$$* y = 0$$

$$* z = \frac{-H_{plate}}{2}$$

- Axis: Y
- X Size: L_{plate}
- Z Size: H_{plate}

Apply a PEC boundary condition to the finished sheet.

4. Create Current Gap Sheet

Create a 2D sheet and define it as follows:

- Position:

$$* x = \frac{-L_{dp} + L_{plate}}{2}$$

$$* y = 0$$

$$* z = \frac{-H_{plate}}{2}$$

- Axis: Y
- X Size: $L_{dp} - L_{plate}$

- Z Size: H_{plate}

Apply a current source excitation to this sheet such that it extends from the negative to the positive electrodes.

3.1.3.2 Magnetic Source

There were two magnetic sources used in the set of experiments. We find that depending on whether or not the source is moving the source will require different treatment. The two types of magnetic sources are as follows. The first one considers a 7 turn electric current loop of wire placed in a horizontal plane on the bow of a fiberglass boat. This places the dipole moment of the source in a purely vertical orientation. The source provides an effective area of 9.5 m with the turns factored in. With a source current of 1 A the dipole moment of the source is $9.5A * m^2$. The second one considers a magnetic source that is 12 ft by 12 ft by 12 turn current loop supported on a wooden frame and floating on a 20 ft by 20 ft plastic dock. This source could be placed with the current moment pointing towards zenith or it could be placed with the moment pointing horizontally at any azimuthal angle. The first magnetic source was the only one to move and was never used as a stationary source.

The stationary source is simulated with a single electric current loop by implementing the following steps:

- Start with two circular two dimensional sheets.
- Place both on the same plane and centered on the same point.
- Make one slightly smaller than the other and subtract it from the larger such that a thin ring is left.
- Assign a perfect electric conductor boundary condition to the surface.
- Remove a small gap from the ring and place another two dimensional sheet in that gap.
- Apply a current excitation to that sheet such that the current will circulate along the ring.
- Orientate the source in the direction specified by the experiment.

The moving magnetic source will be modelled the same way as the electric sources with an implementation of reciprocity. This makes it only necessary to do six simulations to model the fields. As with the electric source the particulars of this reciprocal implementation will be discussed in Section 3.7.

Detailed Source Build

The following gives details on how the magnetic sources were constructed for this project. The symbols S_θ and S_ϕ reference the source dipole moment orientation in spherical coordinates.

1. Define a relative coordinate system with the following parameters:

- Origin: SourceX, SourceY, SourceZ
- Orientation:

* X Axis:

$$\diamond x = \sin(S_\theta) \cos(S_\phi)$$

$$\diamond y = \sin(S_\theta) \sin(S_\phi)$$

$$\diamond z = \cos(S_\theta)$$

* Y Point:

$$\diamond x = -\sin(S_\phi)$$

$$\diamond y = \cos(S_\phi)$$

$$\diamond z = 0$$

2. Create outer edge:

Create a 2D sheet and define it as follows:

- Position:

$$* x = 0$$

$$* y = \frac{-(L_s + Loop_t)}{2}$$

$$* z = \frac{-(L_s + Loop_t)}{2}$$

- Axis: X

- Y Size: $L_s + Loop_t$
- Z Size: $L_s + Loop_t$

3. Create inner edge:

Create a 2D sheet and define it as follows:

- Position:

$$* x = 0$$

$$* y = \frac{-L_s + Loop_t}{2}$$

$$* z = \frac{-L_s + Loop_t}{2}$$

- Axis: X
- Y Size: $L_s - Loop_t$
- Z Size: $L_s - Loop_t$

4. Subtract inner edge from outer edge to create a ring.

5. Create current gap:

Create a 2D sheet and define it as follows:

- Position:

$$* x = 0$$

$$* y = \frac{L_s - Loop_t}{2}$$

$$* z = \frac{-Loop_t}{2}$$

- Axis: X
- Y Size: $Loop_t$
- Z Size: $Loop_t$

6. Subtract current gap from the ring.

7. Assign PEC boundary to the ring.

8. Assign excitation to current gap.

3.1.3.3 Source Impedance Matching

Because the sources used in the experiments were not ideal, modelling them exactly is very difficult. In an actual experiment, the source is a composition of wires, barges, generators, crane and instruments, none of which are easily modelled in HFSS. Fortunately, we do not need to simulate the sources on that level of detail. However, modeling the source strength properly is very important. To do this, the concept of source impedance matching was employed. In HFSS, a voltage can be applied across the gap of two conducting plates and produce a current between them as shown in Figure 3.5. The adjustment of the plate size makes it possible to adjust the current between the conductors without altering the voltage between them. This is done until the voltage and current between the plates match some experimental result that is being simulated. This results in an impedance match and will produce a signal of equal magnitude to that of the experiment. This will not necessarily produce the correct fields of the experiment in the near field.

Because the voltage and the current of the experiment are both known, also known is the impedance of the experiment by the relationship $Z_{exp} = V_{exp}/I_{exp}$. If the impedance of the experiment is matched to the impedance of the simulation, $Z_{sim} = V_{sim}/I_{sim}$ and we set $Z_{exp} = Z_{sim}$, then $V_{exp}/I_{exp} = V_{sim}/I_{sim}$. Since the voltage is the impressed value in the simulation we set it to match the experiment, $V_{exp} = V_{sim}$. Thus, for the impedances to be match as desired we obtain the condition $I_{exp} = I_{sim}$. Because all the factors that contribute to the impedance of the experiment are not taken into consideration in the simulation, making the plates of the simulation the same size as the experiment will not result in the same current as the experiment. To match the currents the plate size of the simulation is adjusted until the simulation current is the same as that in the experiment. The plate size in the experiment is not likely to match the simulation experiment because of the aforementioned reason.

If the source is modeled with an impressed current instead of an impressed voltage, the previous method is not needed. The impressed current was the method used for this project and the impressed voltage method was only used as a validation of concept. It is a valid method, but requires considerations that the current method did not.

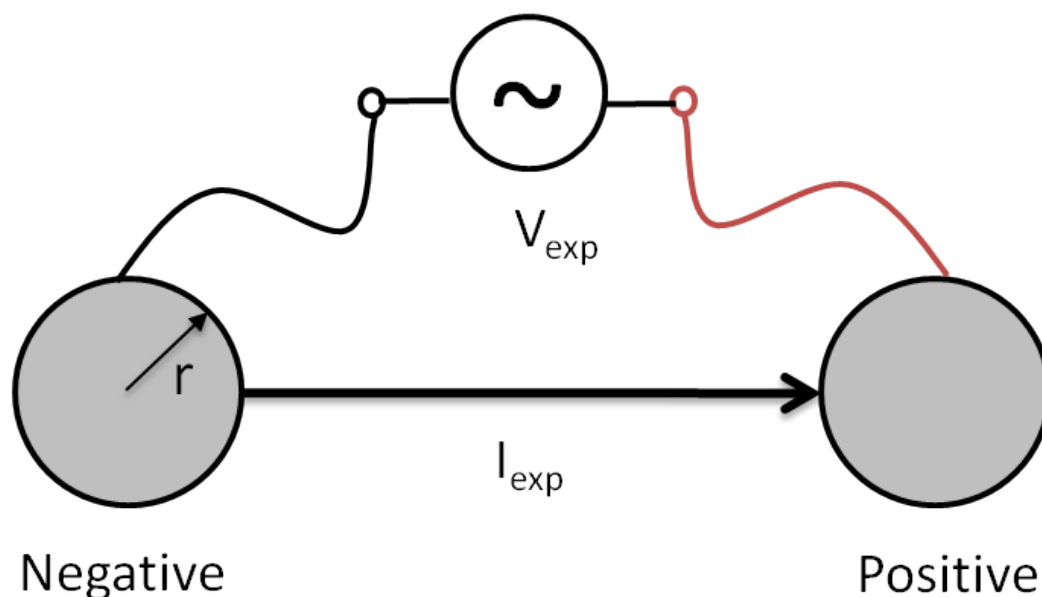


Figure 3.5: Impedance Matching.

3.2 Domain Truncation

As with all numerical electromagnetic solvers, domain truncation is of paramount importance. In some solvers the domain truncation is built into the very equations that are to be solved, e.g. method of moments. In the cases of finite element solvers or FDTD solvers this is not the case and a truncation scheme must be employed. For HFSS there are several methods to choose from, but for this project only two were used. The two are “Radiation” and “Perfectly Match Layer (PML).” Of these two, the radiation boundary condition was most commonly used.

The PML is a truncation method that attempts to surround the domain with a layer of artificial material that matches the impedance of the bordering material, but introduces high loss terms so that the propagating signal is absorbed. When the signal has passed through the PML and reaches the actual computational boundary it is so small that any reflections are insignificant. In terms of HFSS, the software has a wizard that will set up a PML with the user specifying a few parameters to help influence the PML effectiveness. The user also has the option to construct a PML from scratch, but this is not straightforward. It does, however, give the user complete control over the PML design. The reasons for using a PML is that it can be

extremely effective and can be placed very close to the source. Unfortunately, the PML method increases the domain volume, which requires more computational resources. Such resources can be significant. Also, a PML will have to be redefined for every new model and does not lend itself to rapid simulation reproduction.

The radiation boundary condition of HFSS assumes that the fields outside the domain are outwardly travelling spherical waves. This allows HFSS to get the needed field information at the edge of the domain. The reasons for using the radiation boundary are that it is simple to define, it does not need to be redesigned with each new model, and it is computationally cheap. It does, however, require that the boundary with the radiation be “far enough” from the source. HFSS documentation defines “far” as being greater than 1/4th wavelength. The guideline given by the HFSS documentation can be conservative and is greatly influenced by material properties and frequency of interest. For this project it has been found that the radiation boundary can be as close as 1/100th wavelength or 3000 meters at a 1000 Hz without causing significant errors to be introduced. This is because of the high loss materials of the water and mud.

3.2.0.4 Radiation vs. PML

To understand how these two boundary truncations methods work for ELF signals, several studies were conducted on simple domain geometries. One is a simple homogeneous domain with air and water. Second is a three layer model with air, water and mud as shown in Fig. 3.6.

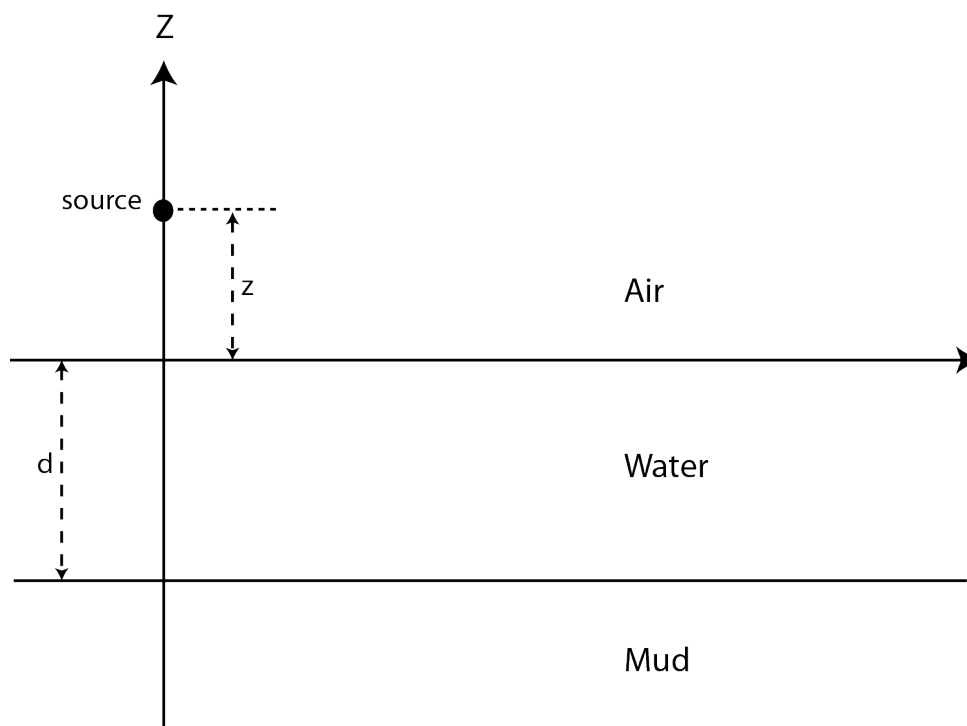


Figure 3.6: Illustration of three layer problem space.

The first study is the homogeneous domain in which the PML is compared with the radiation boundary condition. Although both air and water were modeled, the loss terms in water and wavelengths in air make air the more relevant example for this discussion. The wavelength of a 1000 Hz signal in air is approximately 300 km. It is impractical to simulate this large of a domain; all simulation domains will be of sub-wavelength size. The question is how small can the domain be made before domain truncation errors become a problem. To see how well the truncation methods worked in HFSS, a homogeneous domain was shrunk from 10 km by 10 km by 10 km down to 2 km by 2 km by 2 km. At each reduction the fields were measured radially from the origin along the x -axis to the domain edge. These fields were then compared to each other. Ideally, if the truncation method was perfect the lines would lay on top of each other all the way to their respective domain edges. As seen in Fig. 3.7 through Fig. 3.10 this is not always the case.

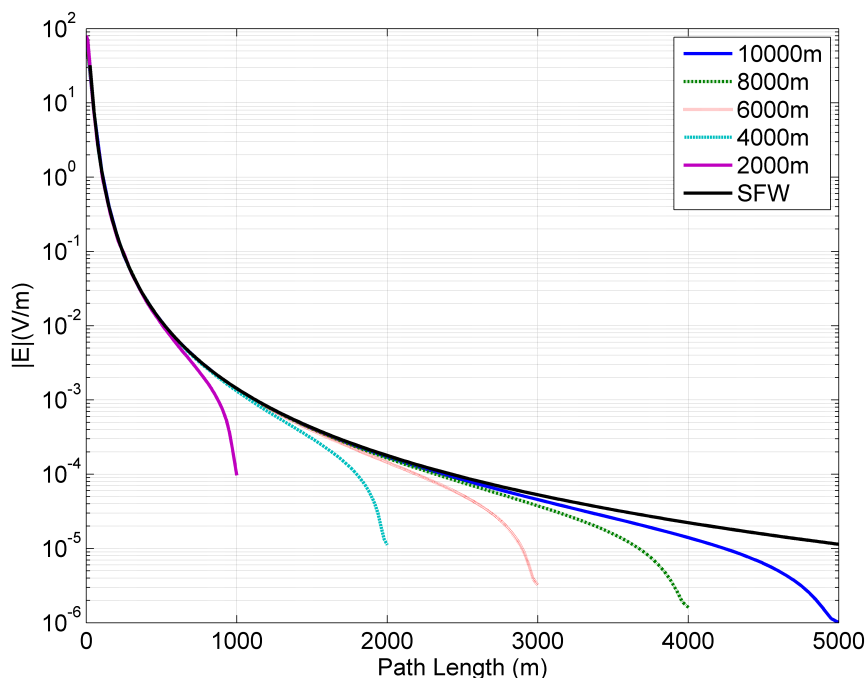


Figure 3.7: Electric fields in air using a radiation boundary condition.

Fig. 3.7 and Fig. 3.8 show data for the radiation boundary condition. The plots of the electric fields in Fig. 3.7 show that the fields consistently and dramatically diverge from the analytical solution near the domain. The analytical solution is the Sommerfield Full-wave Solution (SFW). The SFW method is very robust and has the domain truncation condition embedded into the fundamental equations. The divergence from the analytical solution happens at a range of 400 meters for the 2000 meter domain and for the 10000 meter domain size it starts to diverge about 3500 meters from the domain edge. This says that although the fields can be accurate near the source, care must be given when measuring near the boundary of the domain. Also of interest is the fact that the magnetic fields are weakly affected by the boundary condition as shown in Fig. 3.8. It is not clear at this time why the magnetic fields seem to be largely unaffected by the radiation boundary but the electric fields are.

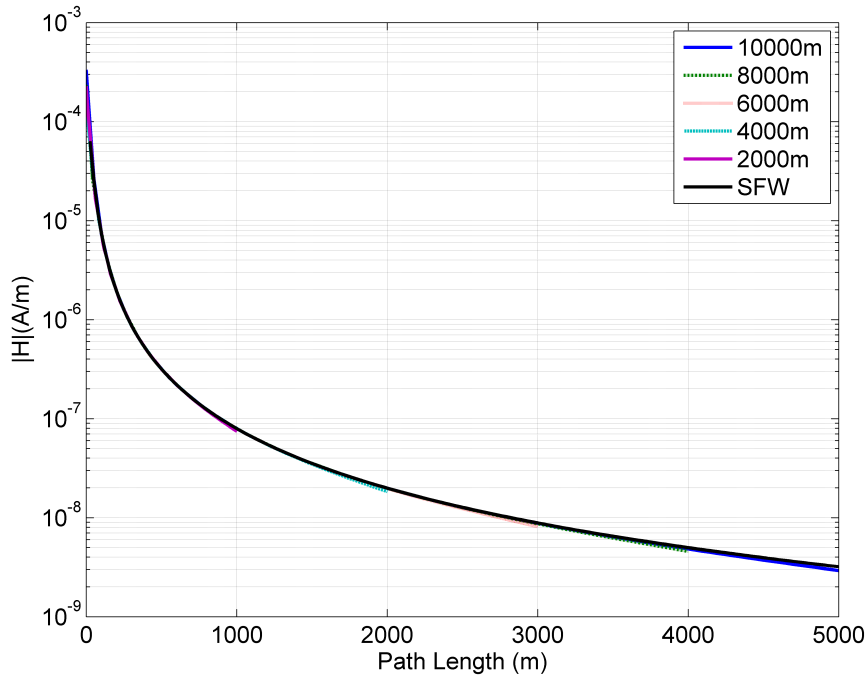


Figure 3.8: Magnetic fields in air using a radiation boundary condition.

In the case of the PML boundary truncation the results are more accurate. Shown in Fig. 3.9 and Fig. 3.10 are the fields for the same case as discussed previously. Fig. 3.9 makes it apparent that the solver using a PML is much better at producing accurate fields closer to the boundary than a solver using a radiation condition. However, for both methods the magnetic fields are highly accurate near the domain edge.

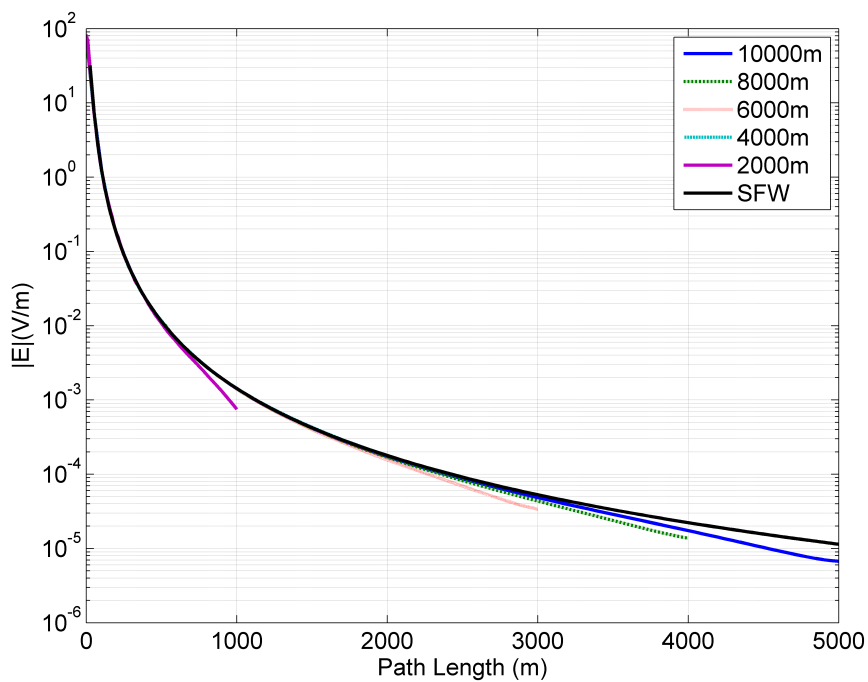


Figure 3.9: Electric fields in air for the PML boundary condition.

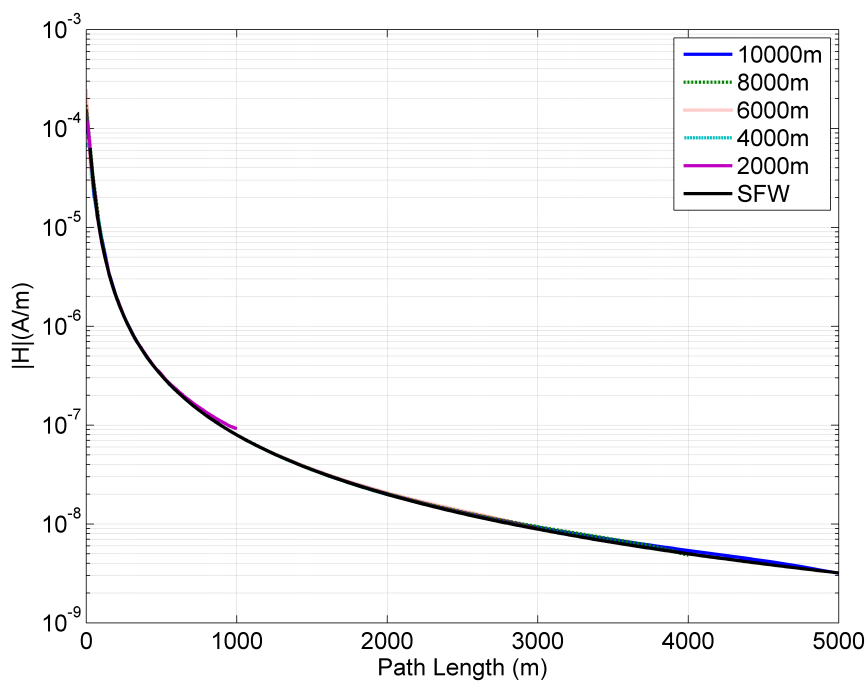


Figure 3.10: Magnetic fields in air for the PML boundary condition.

Also of interest is the performance of the boundary conditions in a lossy media. Since lossy media naturally attenuates the EM field, the field at the domain edge is significantly weak so as to make truncation condition almost moot. Figures 3.11 and 3.12 show this case. HFSS does a much better job matching the analytical case until it reaches a computational limit or the numerical noise floor. This makes determining if the boundary conditions are working in the larger domains difficult. In the case of the smaller domains, the results suggest that the boundary truncations are in fact working well. This would tend to suggest that it would be the same case with larger domains but the water itself does most of the attenuation.

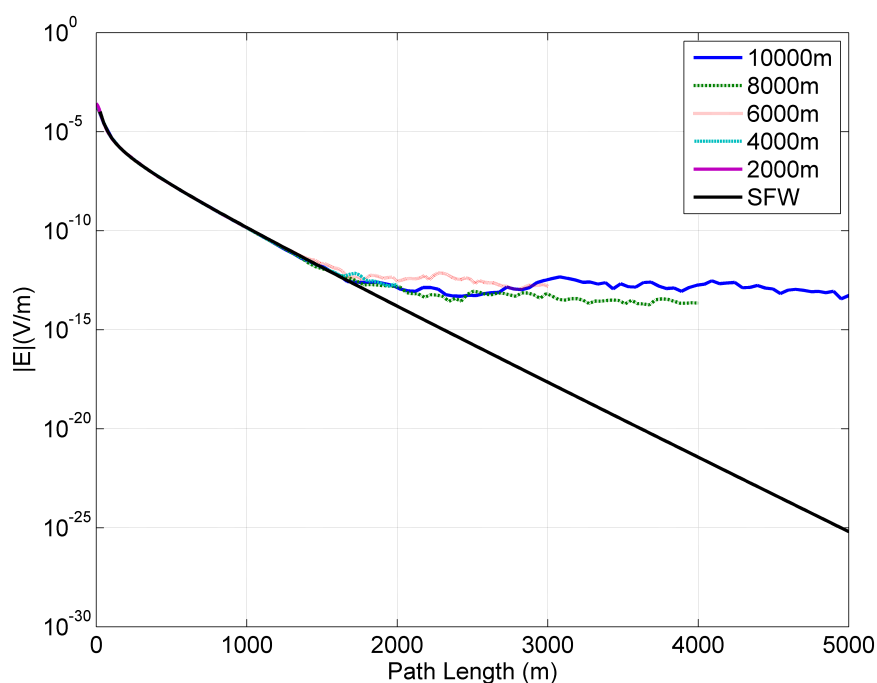


Figure 3.11: Electric fields in water for the radiation boundary condition.

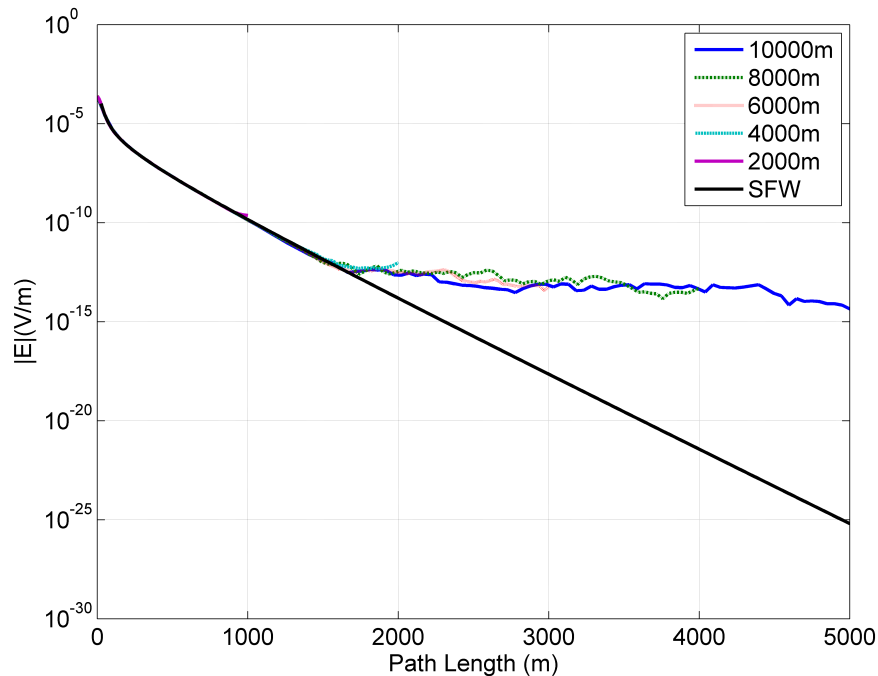


Figure 3.12: Electric fields in water for the PML condition.

We also desire to know how effective the two truncation methods would be in a situation where both a lossy and lossless medium were present. This was tested using a simulation of a three-layer domain. The analytical solution and several other simulation tools were used as benchmarks. The results of these simulations are discussed at length in Section 3.8, as is the set-up for the simulation. Figures 3.16 through 3.18 show that the boundary truncations are able to provide accurate results for three layer models. Fig. 3.20 suggests that is not the case when there are electric sources in air and the domain is too small.

3.3 Mesh and Mesh Operations

Because HFSS is a finite element solver, the computational mesh plays an important role in the accuracy of the results and the speed of the simulation. HFSS will primarily do most of the meshing automatically but it can be influenced by the user in a few ways.

HFSS has what is called an adaptive meshing scheme that attempts to redefine the mesh after a solution is first found. This process is done by first defining an initial mesh. It places

mesh edges along the edges of objects and mesh faces along object faces. It makes choices of edge lengths for each of these elements based on user set criteria and model geometry until it has the minimum number of elements needed to meet that particular criteria. This results in more mesh elements near small, geometrically complicated objects. After this initial mesh is set, the solver then builds the finite element matrix and attempts to solve the corresponding system of linear equations. If a solution is found, it will then calculate a residual energy. It will then refine the mesh, again to criteria set by the user, and attempt to find a solution for the new mesh. If it finds a solution then it again calculates a residual energy and compares this to the residual energy from the previous mesh. The difference of energies is compared to the convergence criteria set by the user and if this convergence criteria is met then the solution is considered to have converged. This is not to say that the solver will stop. The user can require that the solver have N number of consecutive converged passes before it is allowed to stop. HFSS defaults to one converged pass. More details about convergence criteria will be given in Section 3.5.

Mesh operations allows the user to restrict meshing elements within objects or on faces and edges. This helps the user to focus computational resources on areas of interest. For our purposes, directed mesh operations allow for the simulation to focus on the locations of the sensor and frees the solver to use very large elements in other areas where the fields and geometry do not significantly vary. To direct the meshing a rectangular box is inserted such that it encloses the path the sensor or source will sweep along and then places a restriction on mesh element edge length inside that box. For this project, a 10 meter by 10 meter by X meter box is used, where X is the length of the sweep path. Our experience suggests a maximum of 10 meter for edge length works well. This box does not need to be a model object. A non-model object in HFSS is not considered present in the simulation space and has no material properties but can influence the mesh creation. A non-model object is generally preferable, but that is not always possible. If it is a model object, then simply treating it as the same material that surrounds it has shown to be effective and has no influence on the results of the simulation.

The effects of poor meshing on simulation results is not always easy to distinguish from that of complicated fields or computational noise. Fig. 3.13 shows an example of how the

mesh can affect the results of a simulation. Figure 3.13 shows field data for the two different simulations. Both simulations are identical but for one, the dash blue line, had mesh operations applied to the area of interest. This produce a much smother trend than the simulation that was unrestricted in its meshing. The sudden jumps in the fields in the course mesh are at edges of meshing elements.

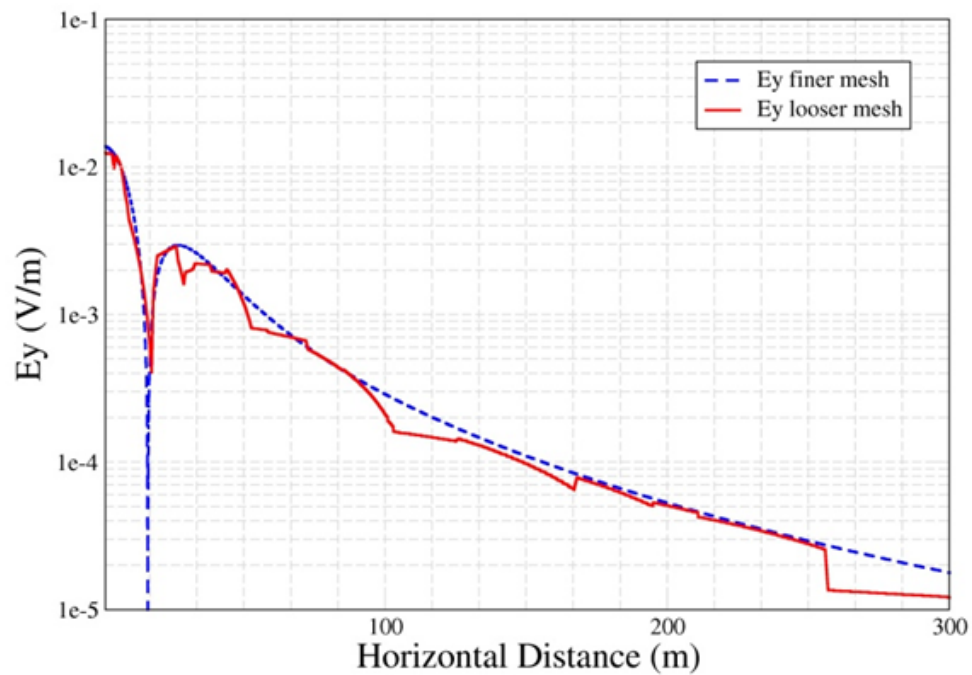


Figure 3.13: Example of how mesh can effect the solution.

3.4 Excitation

HFSS has many different ways to simulate energy sources, but for this thesis only one is of particular interest; three others will be mentioned for completeness of discussion. The excitation types that will be considered are the two Hertzian sources, Voltage Source and the Current Source.

3.4.0.5 Hertzian Sources

The Hertzian excitations are ideal dipoles sources and are implemented as equivalent sources. The user defines a sphere of some radius and HFSS determines the currents that would be present on that sphere if an ideal dipole was present at the center and then impresses those currents on that sphere for the simulation. These excitations do not require any structure modelling but as of version 12.1 they did not work well in any medium other than air or vacuum. For this reason they are not applicable for this project.

3.4.0.6 Voltage Source

The voltage excitation is a good method for simulating the electric source for this project and provides accurate results. The only reason it was not used regularly was because of the extra requirement to match the impedance of the experiment by adjusting the plate size of the source. This step can be a time consuming process as it required the running of a simulation, calculating the current, adjusting the plate size, re-running the simulation with new plate size and repeating until the simulation current matched the experiment. The method of Impedance Matching was covered in detail in Section 3.1.3.3.

3.4.0.7 Current Source

The current source excitation turned out to be the most useful for this project. By simply impressing a current on a two dimensional sheet and providing a conduction path, we found that any source used in the experiment could be simulated. The current source excitation impresses a uniform surface current on the selected sheet in the direction of the integration line. The magnitude is specified by the user in total Amperes and not Amperes per meter. This is because HFSS will calculate the current density needed for a cross section of the sheet to attain the total specified current. Because this is an impressed current, material parameters have no effect on the current impressed on the sheet.

3.5 Analysis Setup

The “Analysis Setup” of the simulation is a very important part of the simulation’s accuracy and performance. Poor choices in this section can result in poor or inaccurate solutions and can greatly impact the amount of time and computational resources required to run the simulation.

One of the first options in the “Analysis Setup” is the solution criteria. This is the setting that tells HFSS when its solution has converged sufficiently. HFSS will assign some default values what will change based on the type of simulation. The criteria is related to a change in total energy in the fields from one solution to the next. HFSS calculates the total energy in a particular iteration and makes a direct comparison to the previous iteration. HFSS uses this comparison for a single figure of merit called, “delta energy.” Delta energy is the parameter that the user sets as a target for convergence. When the delta energy from one iteration to the next is less than the user’s target goal, the solution is considered to be converged by HFSS. HFSS will stop or continue to run more iterations depending on the setting of minimum number of passes and minimum number of convergent passes set by the user.

The solution frequency is an important value that is also specified by the user. The solution frequency can have added importance if the simulation will be used in a “frequency sweep.” The solution frequency is used for frequency dependent materials and for refining the mesh. Because the solution frequency is used for mesh refinement it is the driving consideration when choosing which frequency to use as the solution frequency associated with frequency sweeps. After the simulation has determined a solution for the first time at the solution frequency the mesh will not be redefined for the frequency sweep and HFSS will compute a solution at each frequency using the final mesh. Because the mesh is not optimized for each frequencies in the frequency sweep it may cause a reduction in accuracy if the solution frequency is poorly chosen.

The order of the bases function is very valuable for controlling the accuracy, speed and memory requirements of a simulation. The basis function option window is shown in Fig. 3.15. There are four options for the user to select from: Zero Order, First Order, Second Order and Mixed Order. The first three specify the order of accuracy and are the orders of the bases functions used in the simulation. These three will cause the simulation to vary greatly in speed.

The higher the order, the slower the solutions, more RAM required to determine the fields and the smoother the data will be. Mixed order attempts to make use of all the orders in the same simulation. By using lower order in areas where the field is not changing rapidly and higher order in areas near boundaries, sources and interfaces, the solver may be able to reduce the computation requirements without sacrificing accuracy. Using this had varying degrees of success in this project; for this reason, it was not used in favour of the second order basis functions. Shown in Fig. 3.14 is an example of how the order of the basis function can effect the results of a simulation. The zeroth order determines the solution much quicker then the second, on the order of a 1/10 of the time it takes for the same simulation using second order. However, Fig. 3.14 gives some field variation relative to the higher-order bases functions.

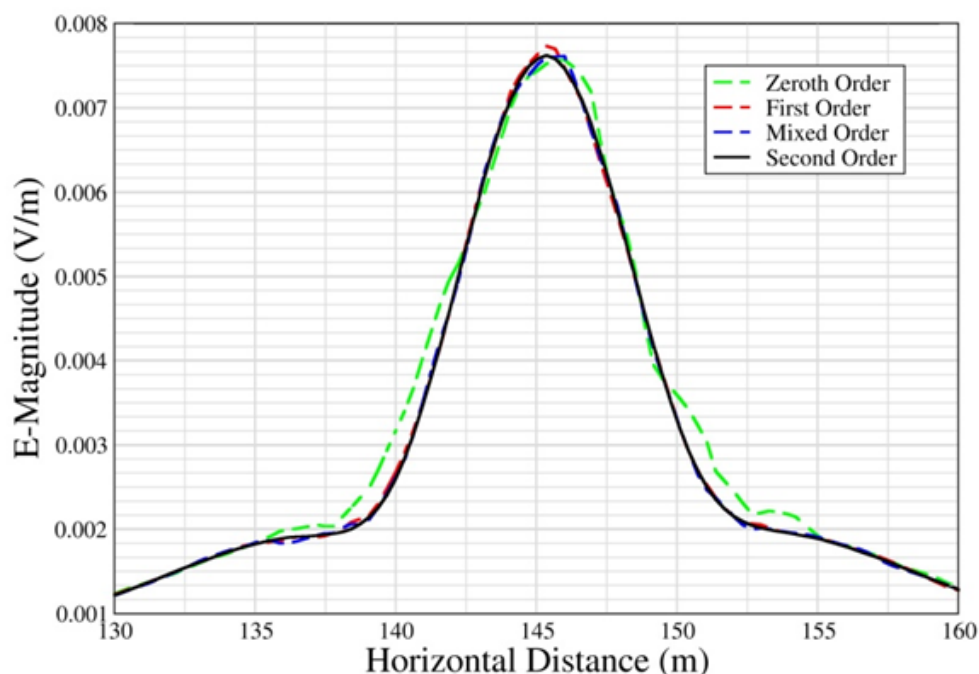


Figure 3.14: Example of how solution order can affect a solution.

In version 12, HFSS introduced a second solver option called “iterative solver.” Previously, the matrix was always inverted using direct matrix methods. This could result in very computationally expensive simulations for large matrices or matrices that were poorly

conditioned. The iterative solver on the other hand attempts to find a solution for the matrix by iteration. Starting with an initial guess for a solution, the solver goes through an iterative process where it will stop when the solution change from one iteration to the next is small. The parameter that sets the iterative convergence criterion is called the “Relative Residual” value, as shown in Fig. 3.15.

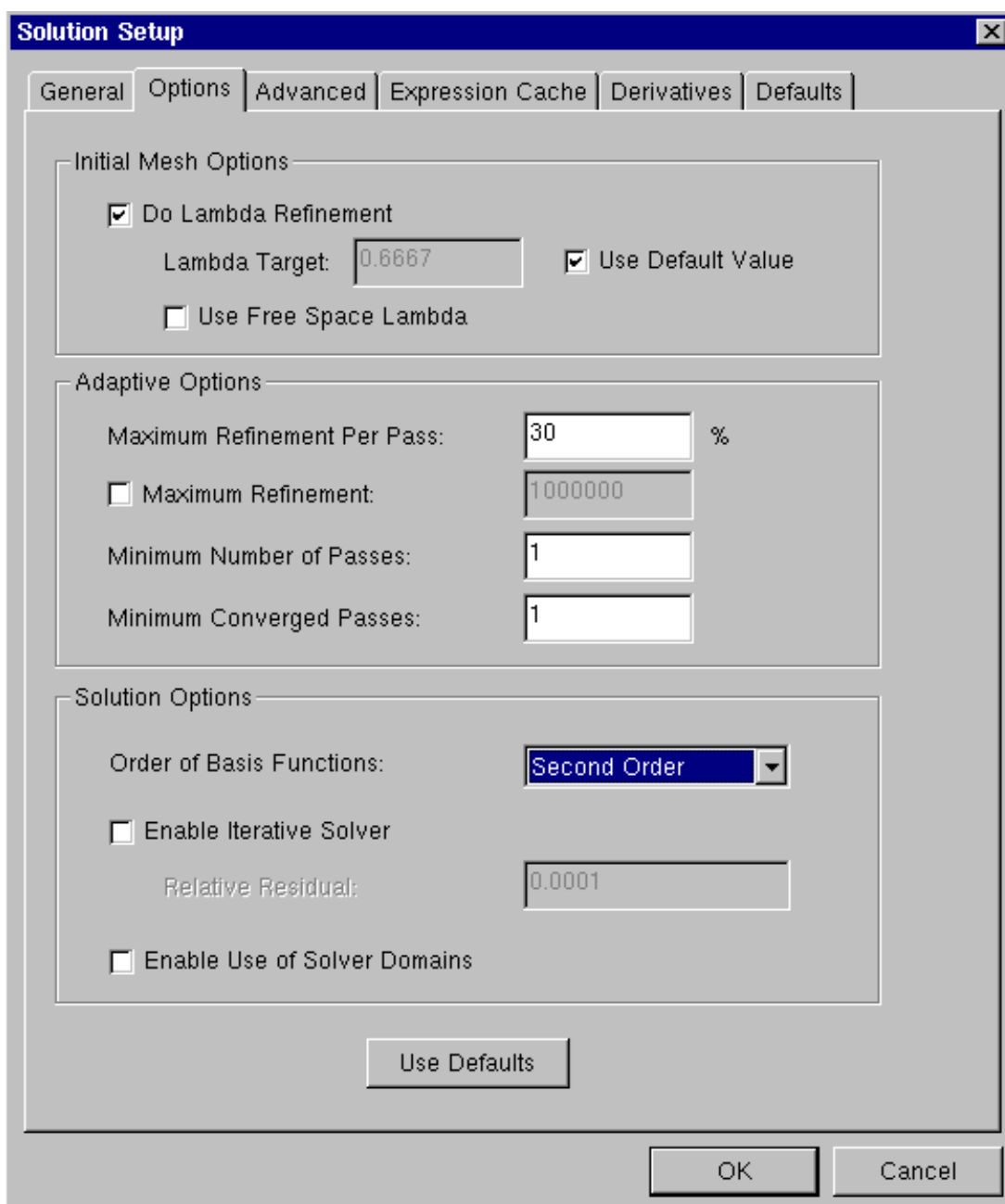


Figure 3.15: HFSS analysis set-up menu.

3.6 Optimetrics

The Optimetrics option in HFSS is used to conduct parameter sweeps and optimizations. It is not strictly needed to complete a simulation in this project, but it eliminates the need to build many models when only one thing changes. In the case of this project, it is used to change the orientation of the source among the three cardinal coordinates of the domain when reciprocity is applied. This is very easy to do with a “parametric sweep.” The parametric sweep is an option under the optimetrics section of a design. It allows the user to set a series of values for a design variable that the tool will solve for one at a time. So if the orientation of the dipole moment is set as variables, optimetrics can easily change that orientation. HFSS will then save the results for each simulation within the same design. The data are easily accessed without having to open up three different designs. For this reason parametric sweeps were used extensively during this project.

3.7 Reciprocity

More often than not during an experiment conducted during this project the source was moved along a path rather than the sensor. This was done for many logistical reasons and will not be discussed here. This did, however, create a difficult problem for the solvers of the project, since such solvers consider fixed sources and moving observation points, i.e. sensor. Because of this, the concept of reciprocity is employed. Reciprocity allows for the swapping of source and sensor within a domain. Reciprocity states that the mutual impedance response between two antennas is the same when the source and receiver are interchanged for open circuit conditions. This suggests that the moving source, fixed receiver experiments can be modelled using a moving receiver and a fixed source. For impressed currents, the invocation of reciprocity is straightforward. For induced currents on actual antennas, consideration must be given to the various antenna impedances of the system. Unfortunately, these various impedances are not completely known which leads to ambiguities. It is for this reason that we assume that the system of induced currents is approximately equivalent to a system of impressed currents. Clearly, errors are introduced into the data as a result of this approximation, but it is made out

of necessity. A detail explanation of how reciprocity is to be invoked is provided by Butherus [5].

3.8 Validation

The validation of HFSS is accomplished using two different methods. The first validation will be compared with other methods such as Finite Difference TimeDomain (FDTD), Sommerfield Full-wave (SFW), Quasi-electrostatic (QES) and Ansys Maxwell. SFW is considered the benchmark method as it has been extensively tested and is very robust for three layer modelling. FDTD and Maxwell are also extremely useful for validation because they are able to model complex geometries like HFSS. The second method that HFSS will be validated by, is to compare simulation data against experimental data.

Consider the case where the geometry was defined by a canonical problem. The conical problem is a three layer stratified domain, as shown in Fig. 3.6. The parameters are defined as follows.

Problem Statement:

- Water depth: $d = 180$ m.
- Water surface: $z = 0$.
- E-source: 2 ft x 2 ft plates at 15 m separation.
- H-source: 12 ft by 12 ft loop.
- Frequency = 10 Hz, 100 Hz and 1000 Hz.

Material Parameters:

- Region 1: $\sigma = 0$ S/m and $\epsilon_r = 1$
- Region 2: $\sigma = 0.018$ S/m and $\epsilon_r = 81$
- Region 3: $\sigma = 0.012$ S/m and $\epsilon_r = 1$

Outlined in Table 3.1 and Table 3.2 are further parameters for the canonical problem defined previously. The tables include information about source position, orientation and strength as well as observation sweeps beginning and ending points.

Table 3.1: Simulation Details

Scenario	Source Type	Source Location	Orientation	Dipole Moment
3L1	HED in water	(0,0,-50)	x -directed	1 A-m
3L2	VED in water	(0,0,-50)	z -directed	1 A-m
3L3	HMD in water	(0,0,-50)	x -directed	1 A-m ²
3L4	VMD in water	(0,0,-50)	z -directed	1 A-m ²
3L5	HED in air	(0,0,50)	y -directed	1 A-m
3L6	VED in air	(0,0,50)	z -directed	1 A-m
3L7	HMD in air	(0,0,50)	y -directed	1 A-m ²
3L8	VMD in air	(0,0,50)	z -directed	1 A-m ²

Table 3.2: Observer location along line from P1 to P2

Points	Sweep 1	Sweep 2	Sweep 3	Sweep 4
P1	(0,0,-25)	(0,0,25)	(75,75,-300)	(150,-1500,-50)
P2	(0,3000,-25)	(3000,0,25)	(75,75,300)	(150,1500,-50)

The results of several of these simulations are shown in Fig. 3.16 through 3.20. HFSS was able to provide results that were very consistent with the result provided by the other simulation tools. The caption of each figure will list which scenario the figure is related to in Table 3.1 as well as the sweep from Table 3.2 and the field components represented. In each of these figures, except for Fig. 3.20, the correlation between the various method is excellent, thus substantiating HFSS as a viable tool for ELF field studies and simulations. The cause for the poor data in Fig. 3.20 is unclear, but fortunately the scenario has no counterpart in any experiments conducted in conjunction with the project.

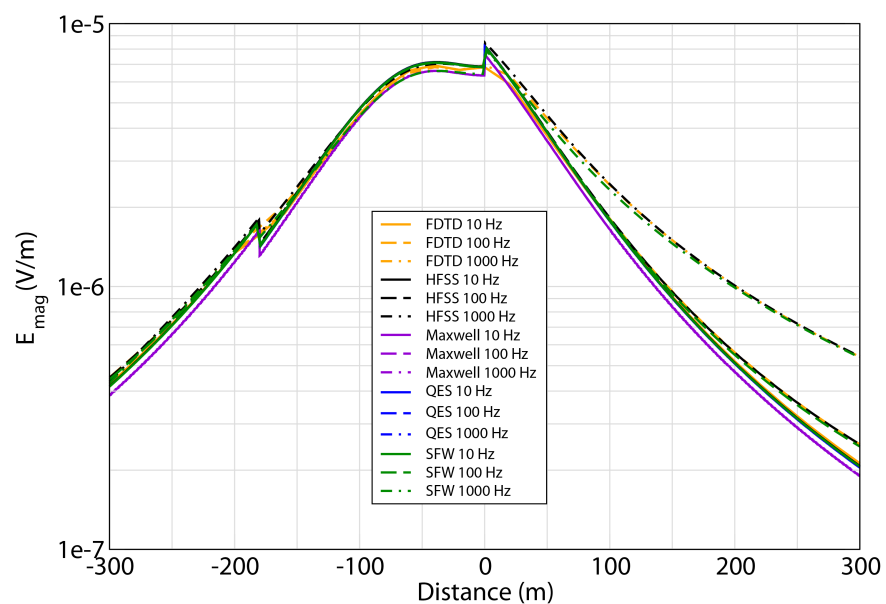


Figure 3.16: Scenario 3L1, Sweep 3, Magnitued E field.

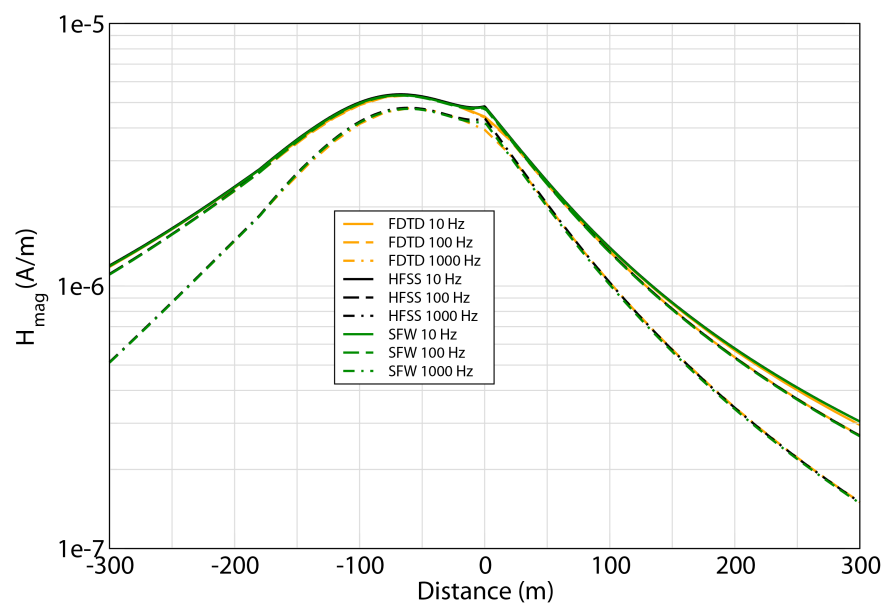


Figure 3.17: Scenario 3L1, Sweep 3, Magnitued H field.

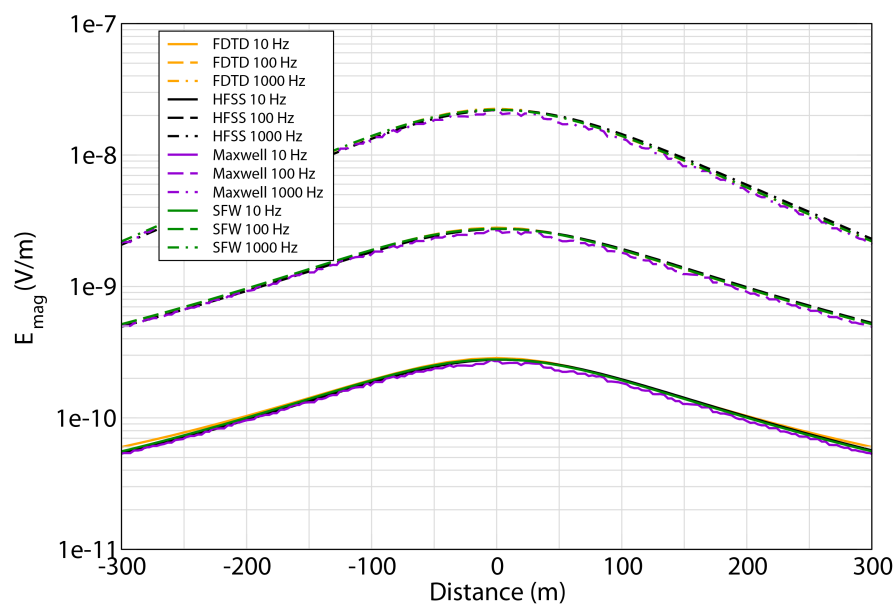


Figure 3.18: Scenario 3L4, Sweep 4, Magnitued E field.

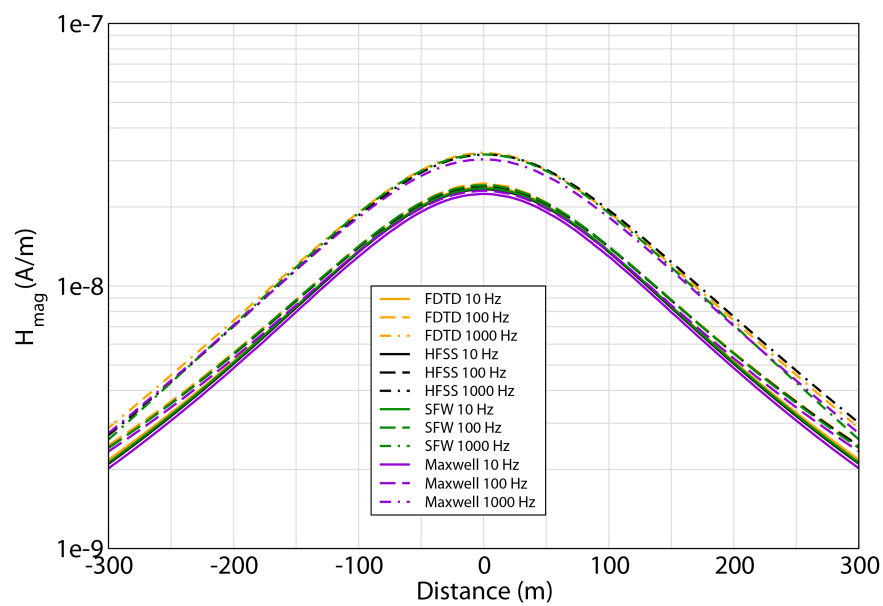


Figure 3.19: Scenario 3L4, Sweep 4, Magnitued H field.

It is believed that this poor performance with respects to the 10 Hz simulation was due to several factors such as domain size and proximity of the boundary to the source.

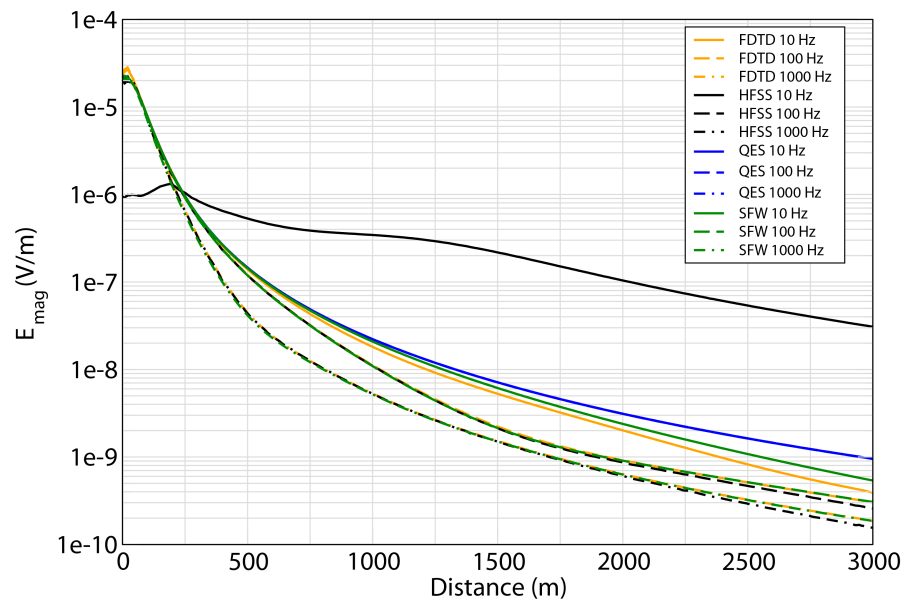


Figure 3.20: Scenario 3L5, Sweep 5, Magnitued E field.

The second validation method relied on experimental data. This is a more complex task in that it requires a better understanding of the experiment and how the simulation should be configured. Things like a moving source are not easy to implement in HFSS and require a great deal more time. It is necessary to simplify the simulation by using reciprocity. The application of reciprocity is discussed in more detail in Section 3.8. Through the course of this project twenty-three experimental scenarios were considered that validated or invalidated the data from simulations. Several of these scenarios are presented next for discussion.

Scenario 1

Scenario 1 is a vertical magnetic dipole (VMD) mounted on the bow of a boat and moved along a straight path passing over the sensor, which is submerged below the waters surface.

Source Parameters

- Source Type: VMD (Mag Boat: $r = 0.657$ m with 7 turns).
- Source Strength: 184.31 A-m².
- $f = 10$ Hz.

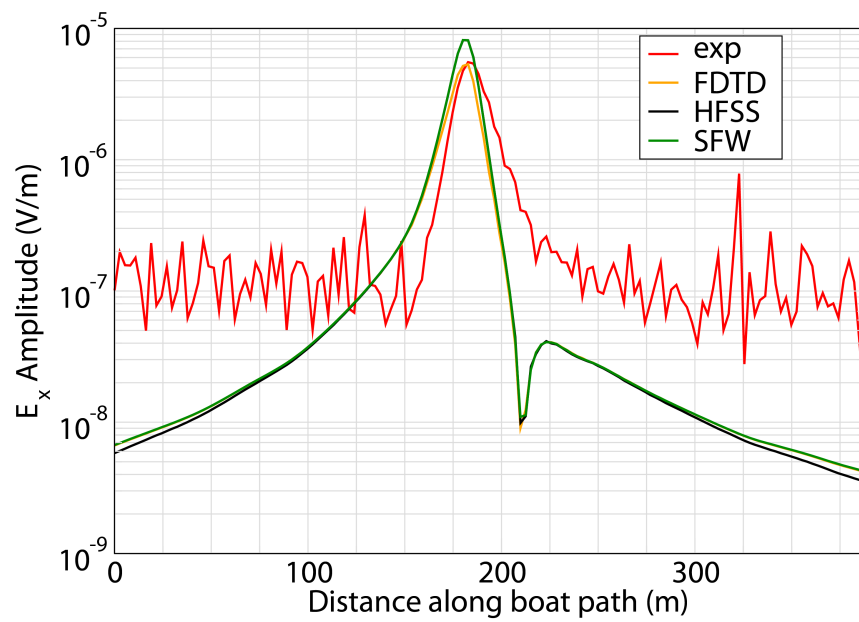


Figure 3.21: Scenario 1, magnitude E_x field.

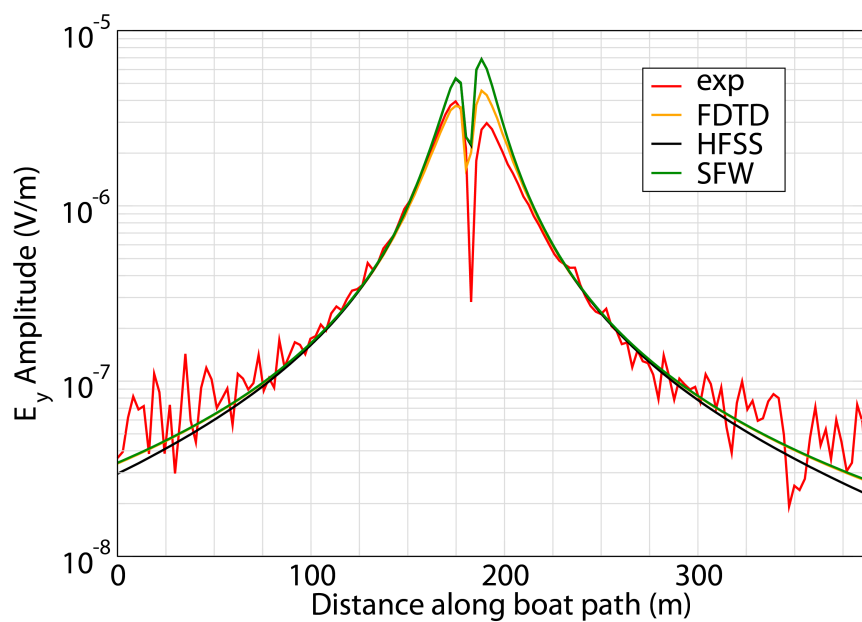


Figure 3.22: Scenario 1, magnitude E_y field.

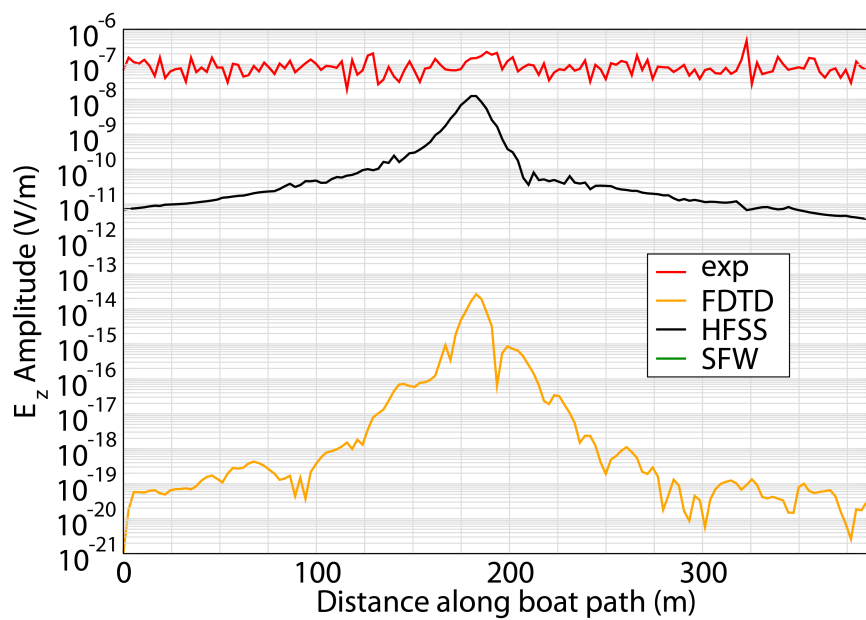


Figure 3.23: Scenario 1, magnitude E_z field.

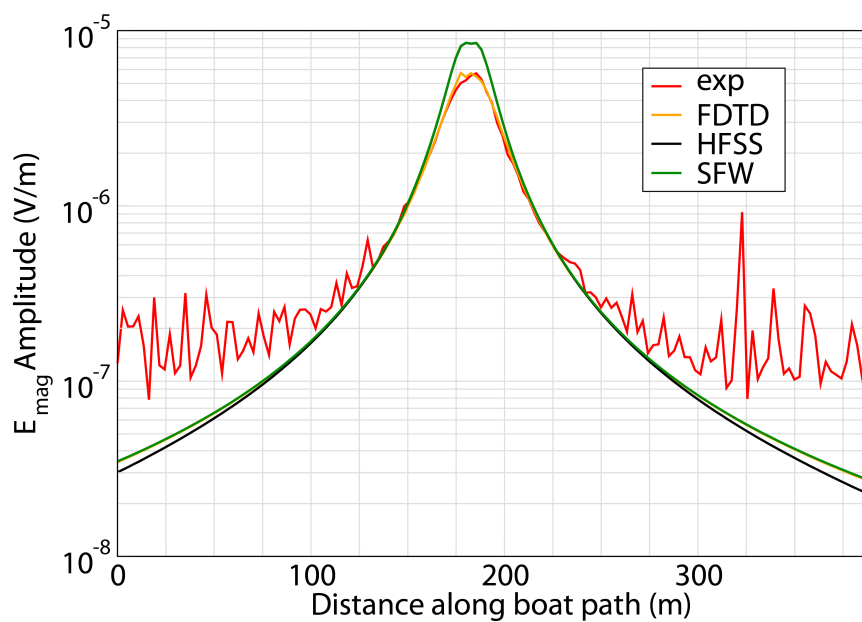


Figure 3.24: Scenario 1, magnitude E field.

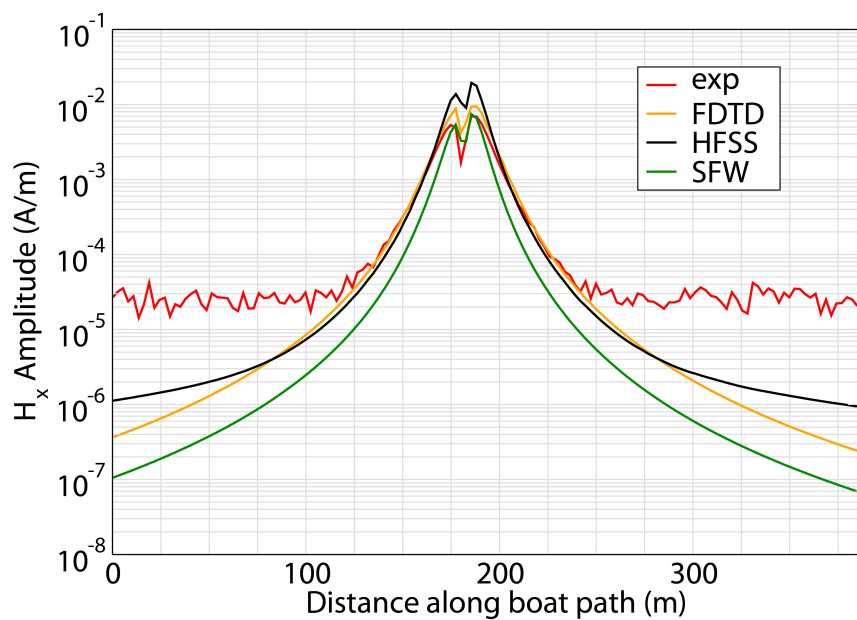


Figure 3.25: Scenario 1, magnitude H_x field.

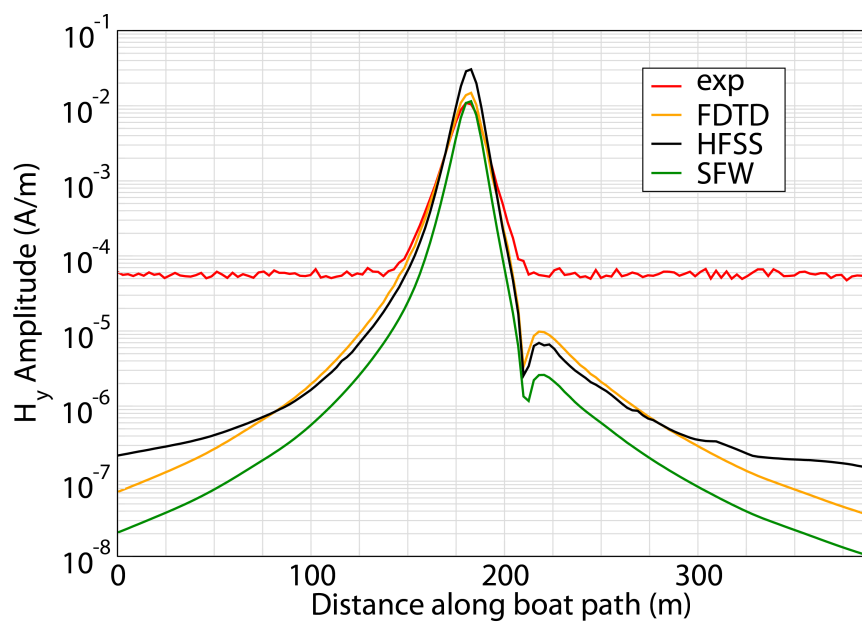


Figure 3.26: Scenario 1, magnitude H_y field.

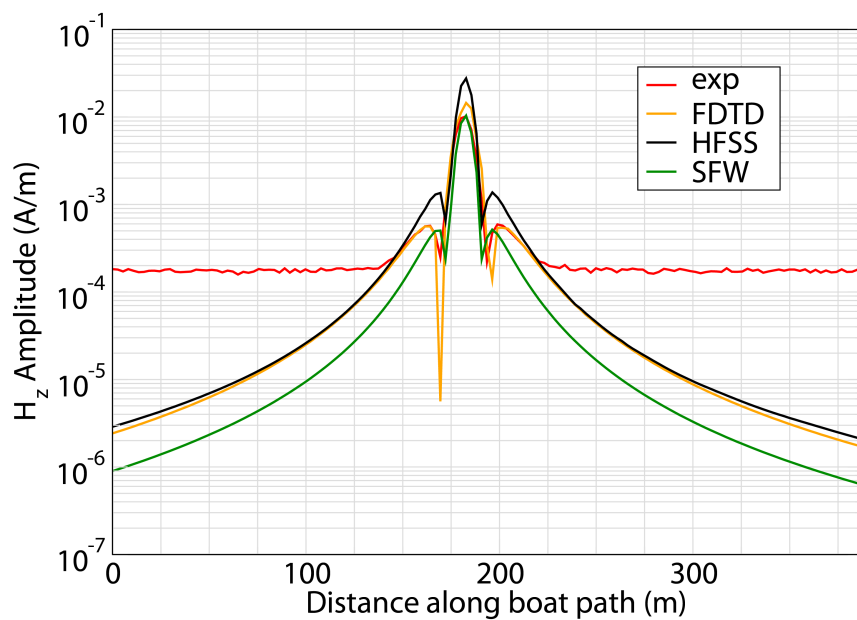


Figure 3.27: Scenario 1, magnitude H_z field.

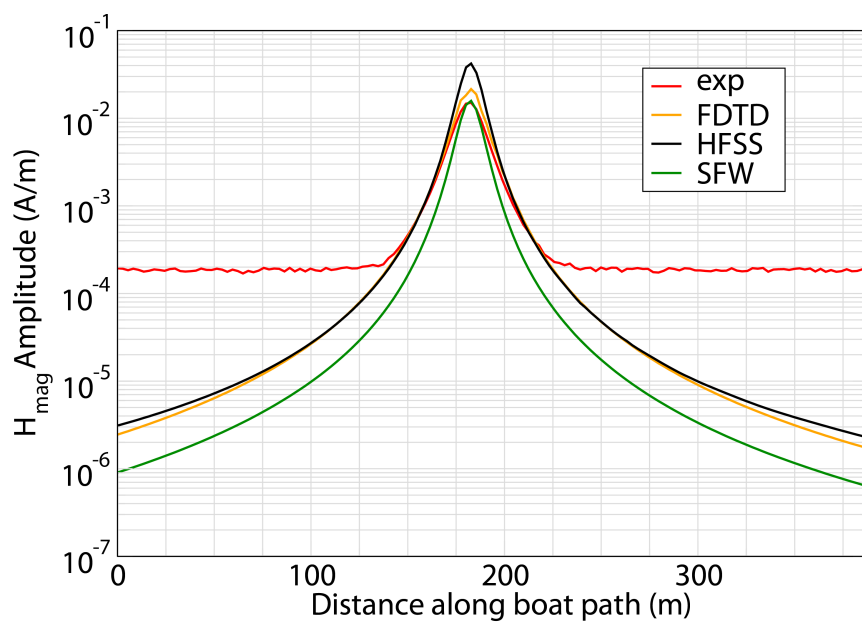


Figure 3.28: Scenario 1, magnitude H field.

Scenario 2

Scenario 2 is a horizontal electric dipole (HED). It consists of two copper plates mounted to the keel of a boat separated by 4 meters. It is piloted along a straight line passing over a sensor submerged below the water surface.

Source Parameters

- Source Type: HED (Boat Hull: plates 0.61 m by 0.305 m separated by 4 m).
- Source Strength: 4.78 A-m.
- $f = 100$ Hz.

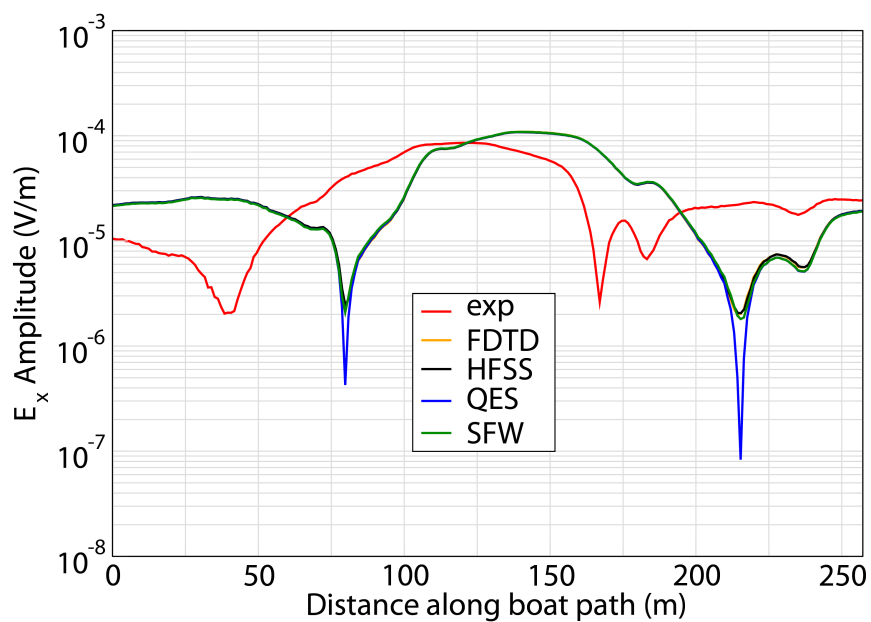


Figure 3.29: Scenario 2, magnitude E_x field.

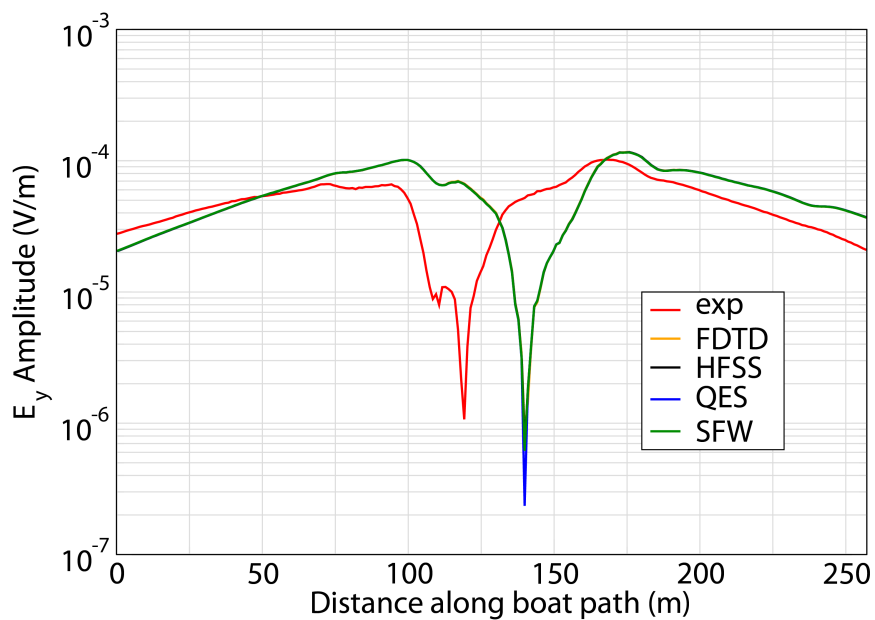


Figure 3.30: Scenario 2, magnitude E_y field.

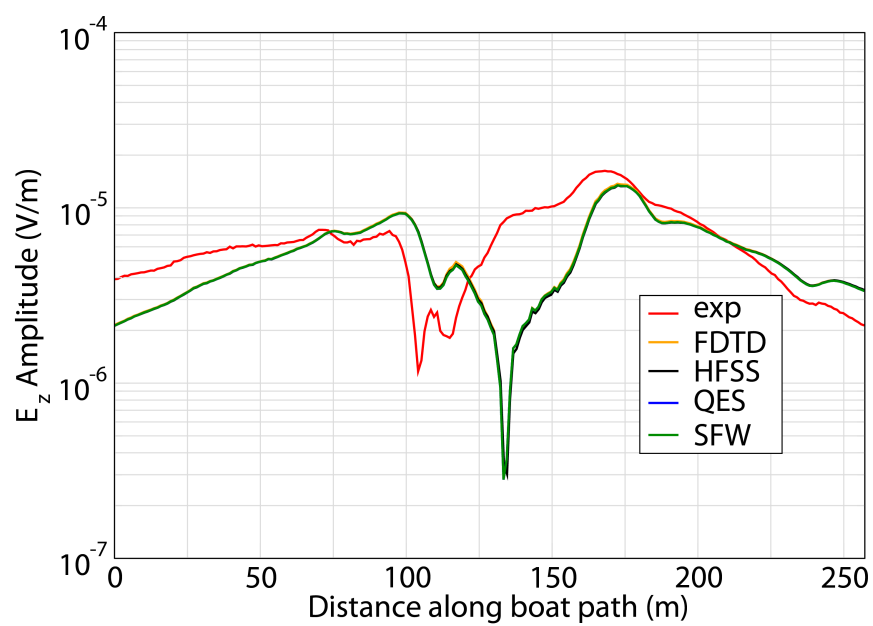


Figure 3.31: Scenario 2, magnitude E_z field.

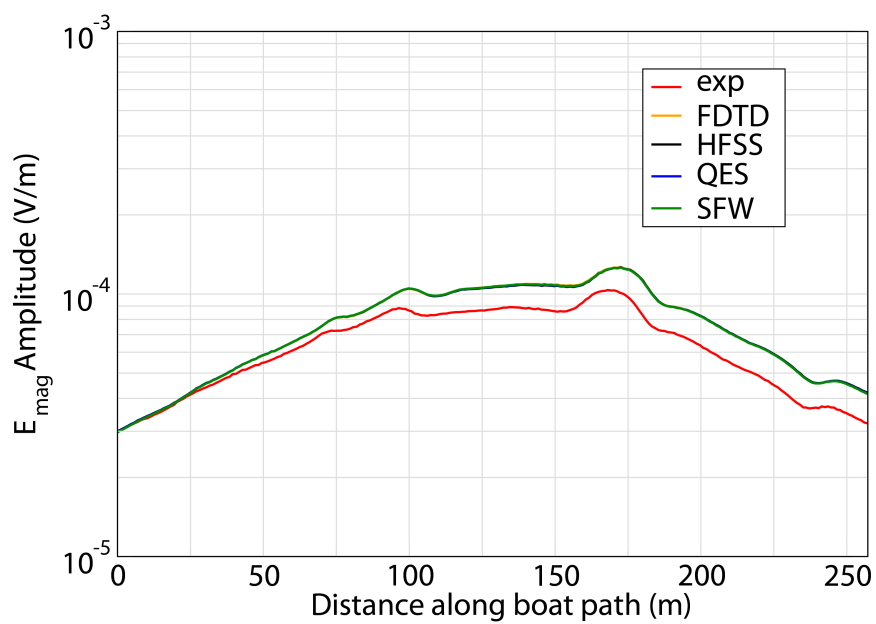


Figure 3.32: Scenario 2, magnitude E field.

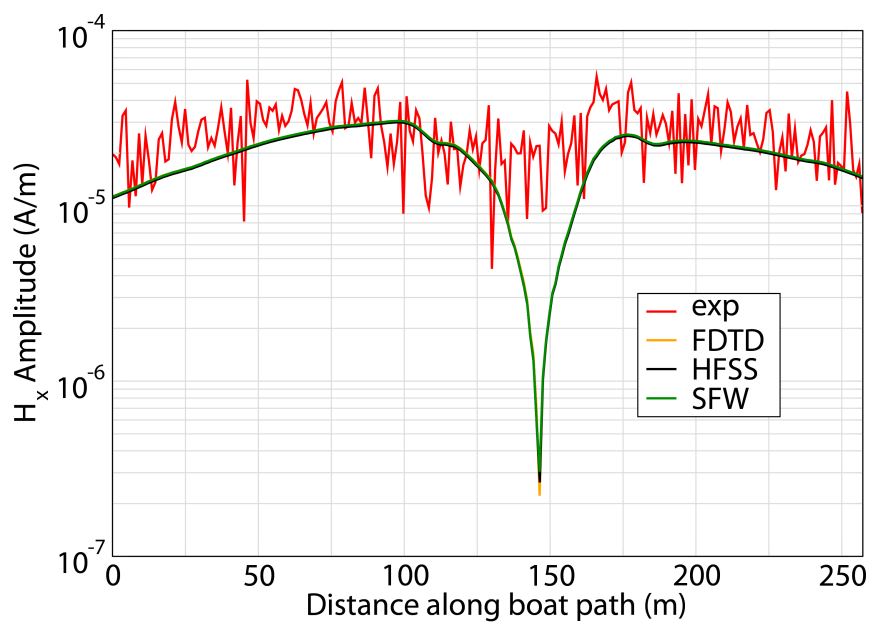


Figure 3.33: Scenario 2, magnitude H_x field.

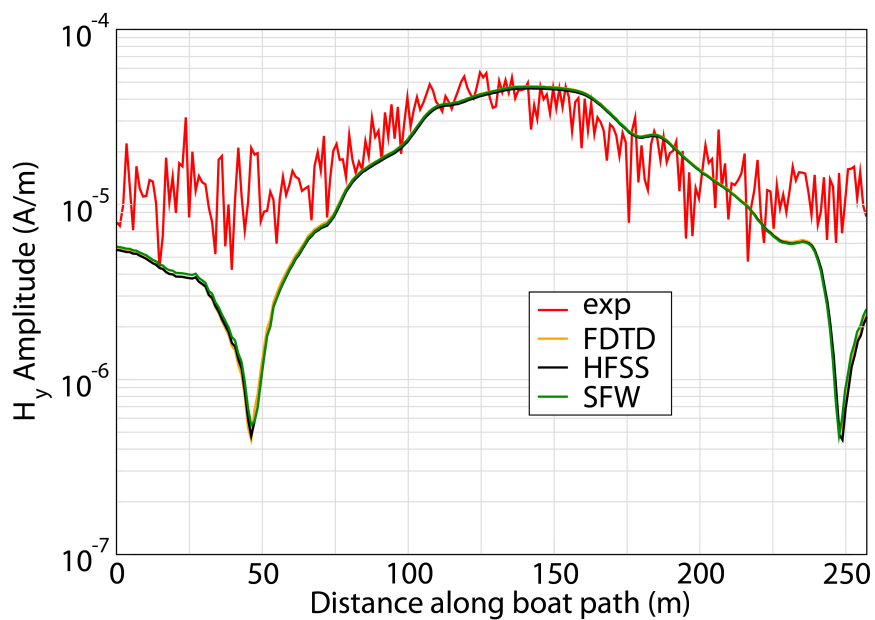


Figure 3.34: Scenario 2, magnitude H_y field.

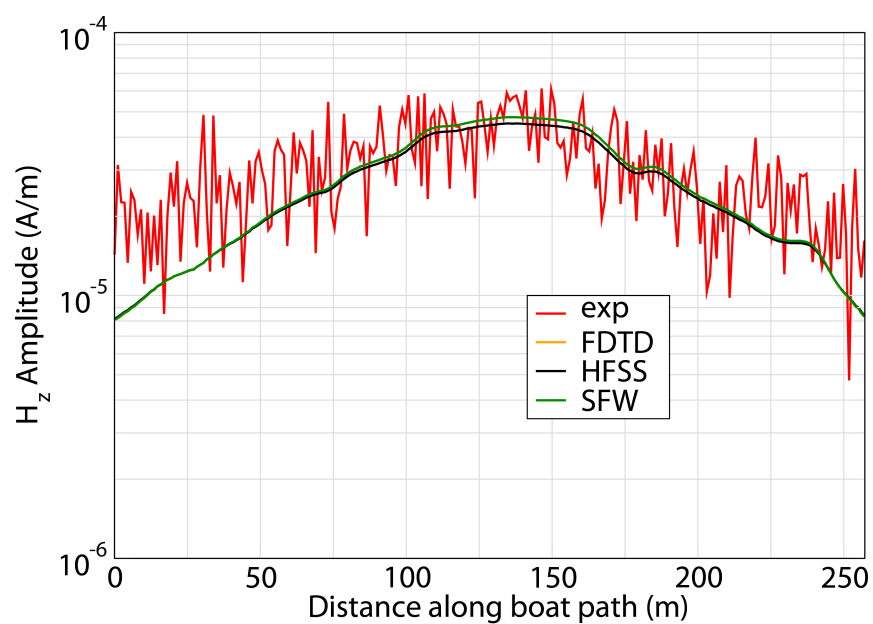


Figure 3.35: Scenario 2, magnitude H_z field.

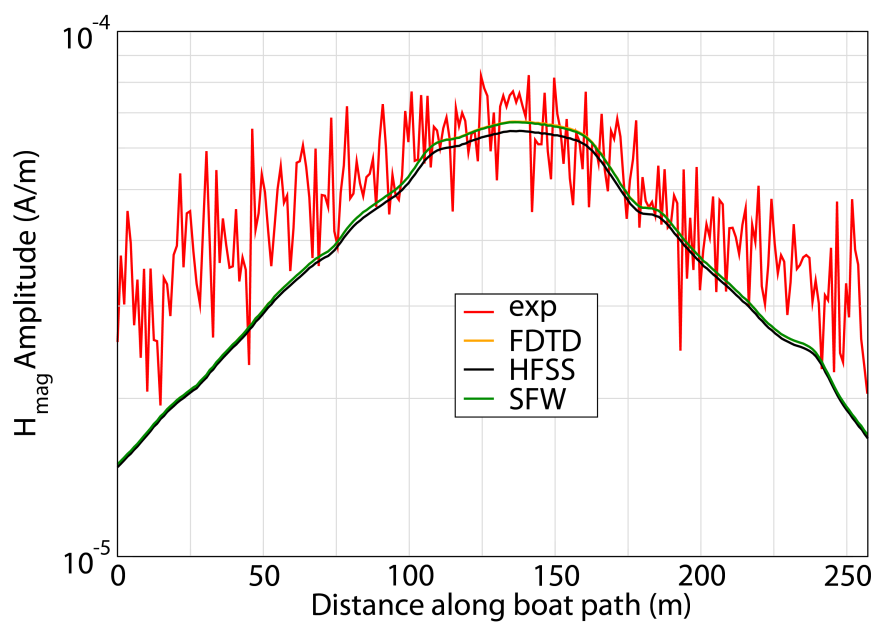


Figure 3.36: Scenario 2, magnitude H field.

Both Scenario 1 and Scenario 2 were conducted in a deep part of the lake with very little geometrical variation. Fig. 6.7 is a model of the region where this portion of the experiment was conducted. This lack of variation made modelling much more simple and resulted in very consistent results. Scenario 1 is perhaps the best example of the results. Simulations were clearly able to predict complex behavior such as nulls and peaks in both the electric and magnetic fields. Magnitudes were not perfect, but were consistent within 50 percent of the experimental data. Scenario 2 shows more interesting comparisons between experimental and simulation data. Again the simulations were able to predict very similar trends and magnitudes. It is clear, however, there is some kind of shift in the comparison. After extensive investigation, we believe that this shift and the small shift in Scenario 2 are due to a lack of precise knowledge of the location of the sensor. It was initially believed that shifts in the source or sensor locations were on the order of meters and such shifts would not really effect the results much because of the large signal wavelengths. It has since been found that shifts on the order of 5 meters can easily produce shifts in the fields on the order seen in Scenario 1 and 2. Unfortunately, the location of the sensor could not be determined any more accurately than was already done for these simulations.

The following three scenarios were conducted in a different region of the lake than the first two scenarios and with several different pieces of equipment. The region was in an area called Idlewilde Bay and Fig. 6.6 is a model of that area. The area has significant variance in geometry and many shallow areas that had to be modelled in the various simulations. These two characteristic are the very reasons why this area was chosen for these experiments. We expected that this area would prove much more challenging than the deeper area of the Lake.

Scenario 3

Scenario 3 is a large magnetic coil mounted on a portable plastic dock. The coil is mounted such that the dipole moment is normal to the air-water interface. A sensor is then moved vertically in the water column some distance away.

Source Parameters

- Source Type: VMD (Coil: 3.66 m by 3.66 m with 12 turns).
- Source Strength: 3,273.94 A-m².
- $f = 81$ Hz.

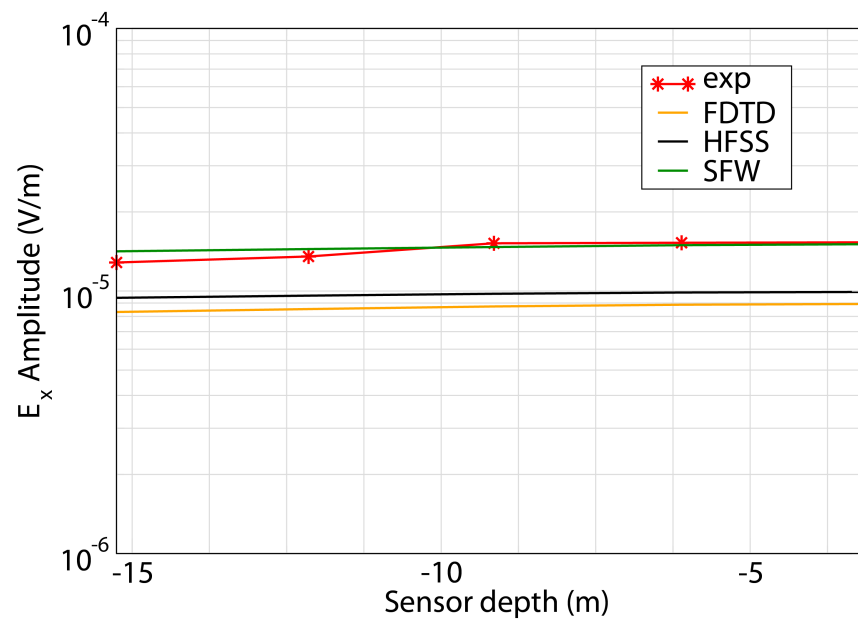


Figure 3.37: Scenario 3, magnitude E_x field.

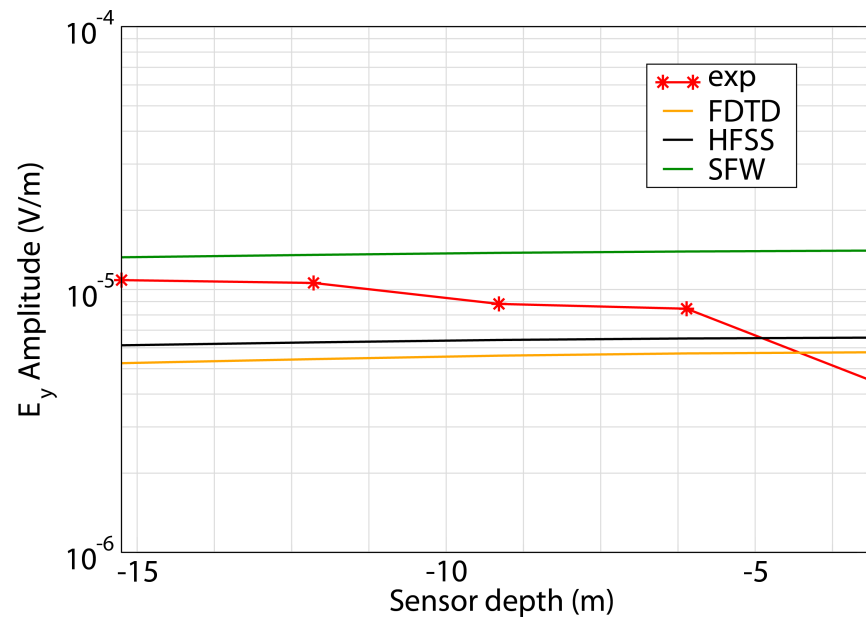


Figure 3.38: Scenario 3, magnitude E_y field.

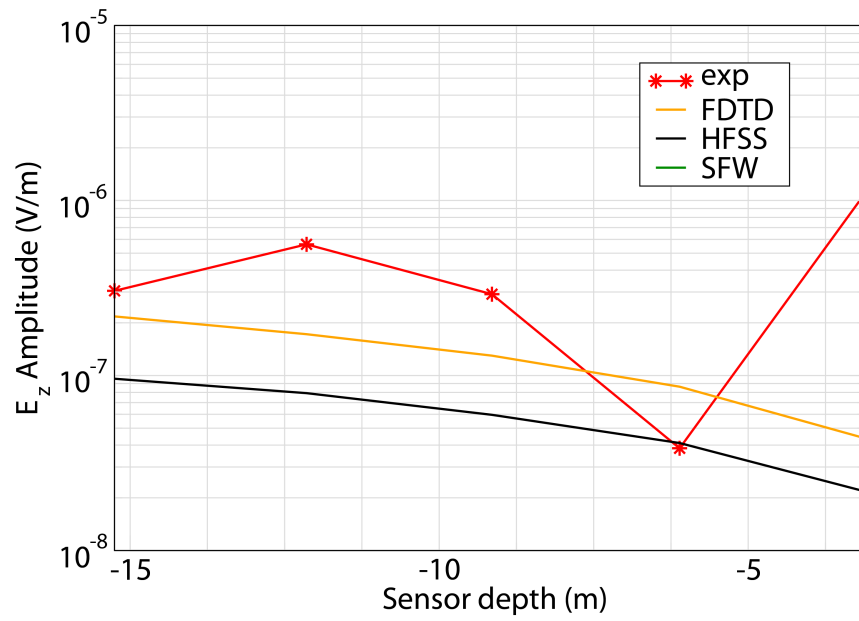


Figure 3.39: Scenario 3, magnitude E_z field.

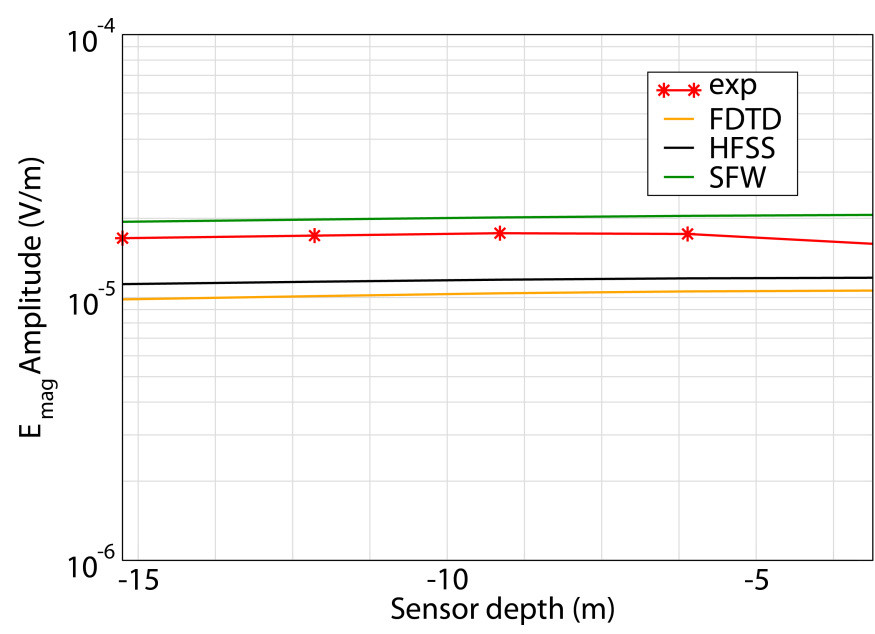


Figure 3.40: Scenario 3, magnitude E field.

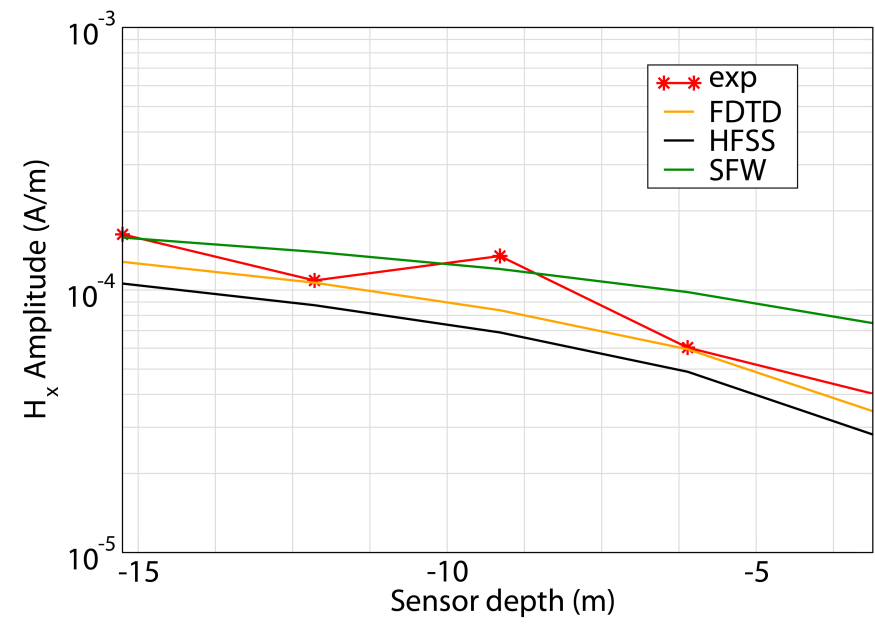


Figure 3.41: Scenario 3, magnitude H_x field.

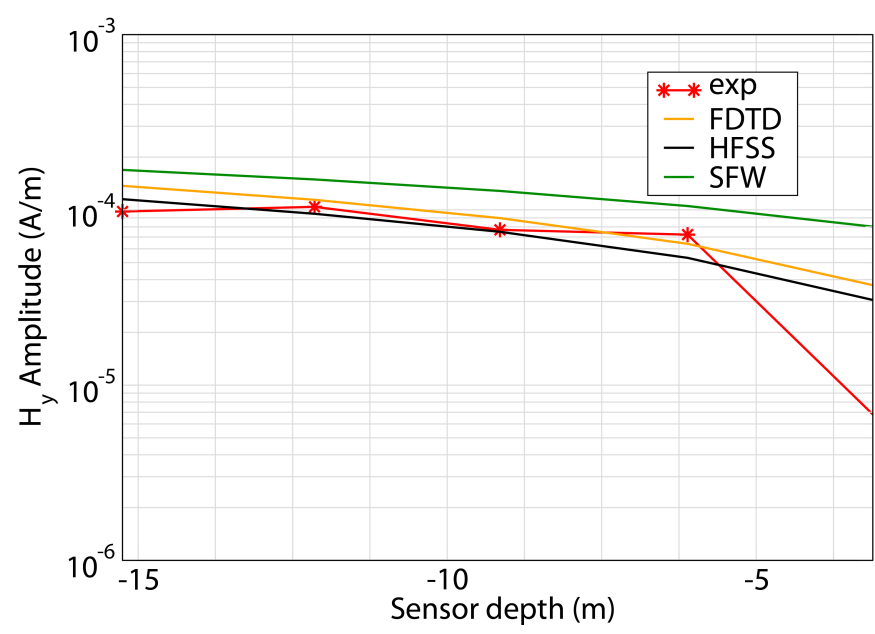


Figure 3.42: Scenario 3, magnitude H_y field.

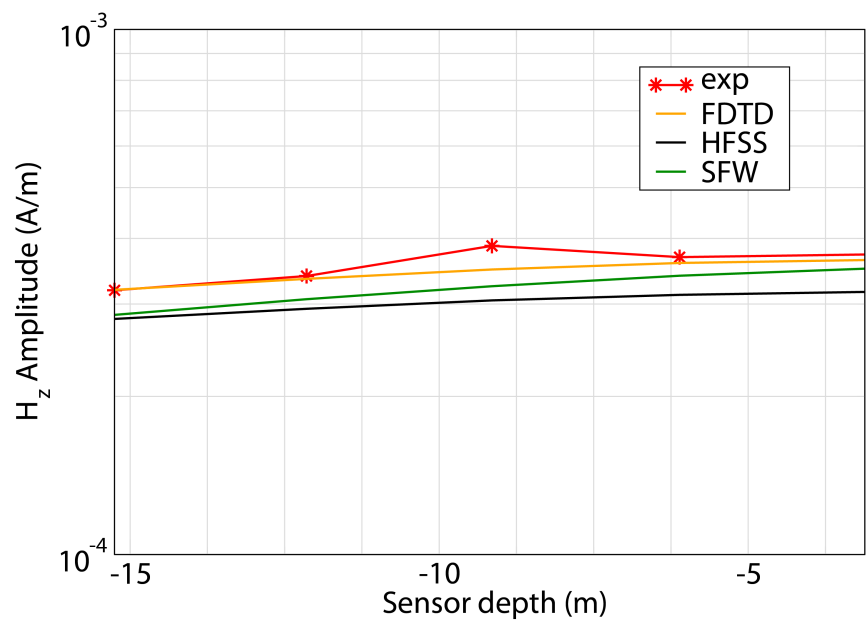


Figure 3.43: Scenario 3, magnitude H_z field.

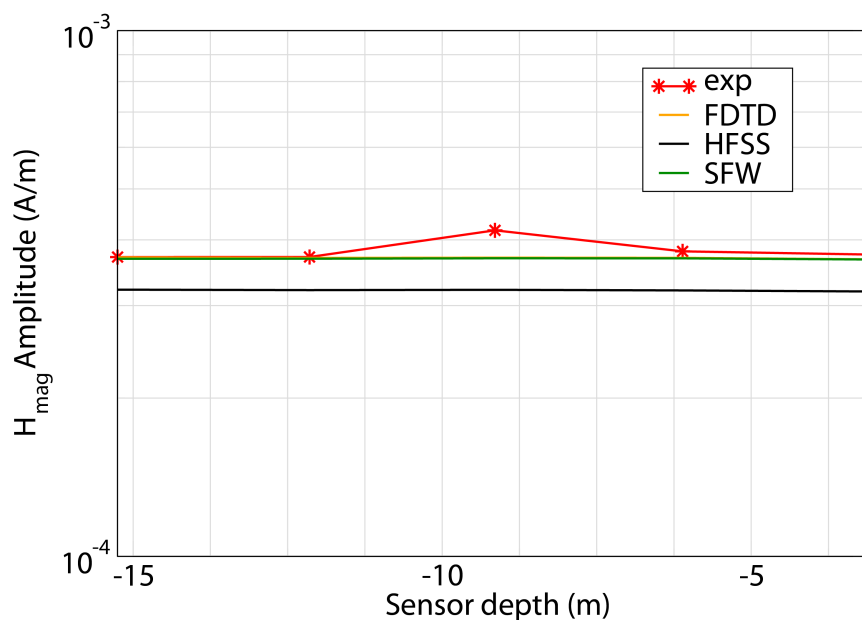


Figure 3.44: Scenario 3, magnitude H field.

Scenario 4

Scenario 4 is a large magnetic coil mounted on a portable plastic dock. The coil is mounted such that the dipole moment is parallel to the air-water interface and in the east direction. A sensor is then moved vertically in the water column some distance away.

Source Parameters

- Source Type: HMD (Coil: 3.66 m by 3.66 m with 12 turns).
- Source Strength: 3,290.6 A-m².
- $f = 81$ Hz.

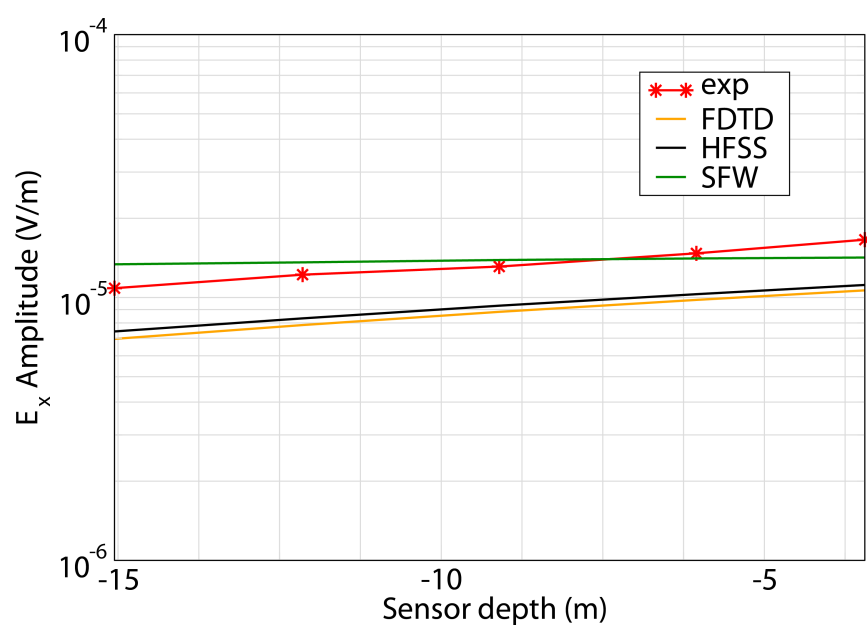


Figure 3.45: Scenario 4, magnitude E_x field.

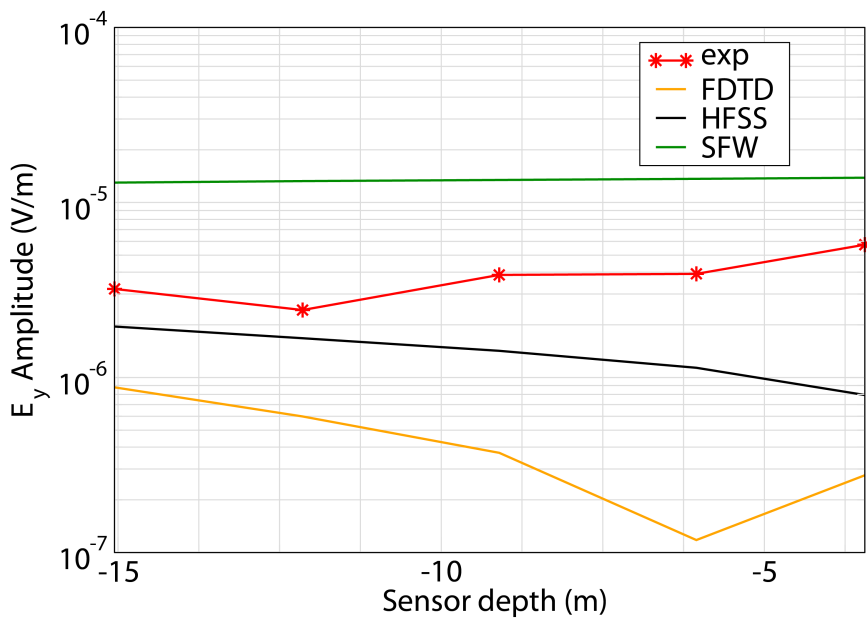


Figure 3.46: Scenario 4, magnitude E_y field.

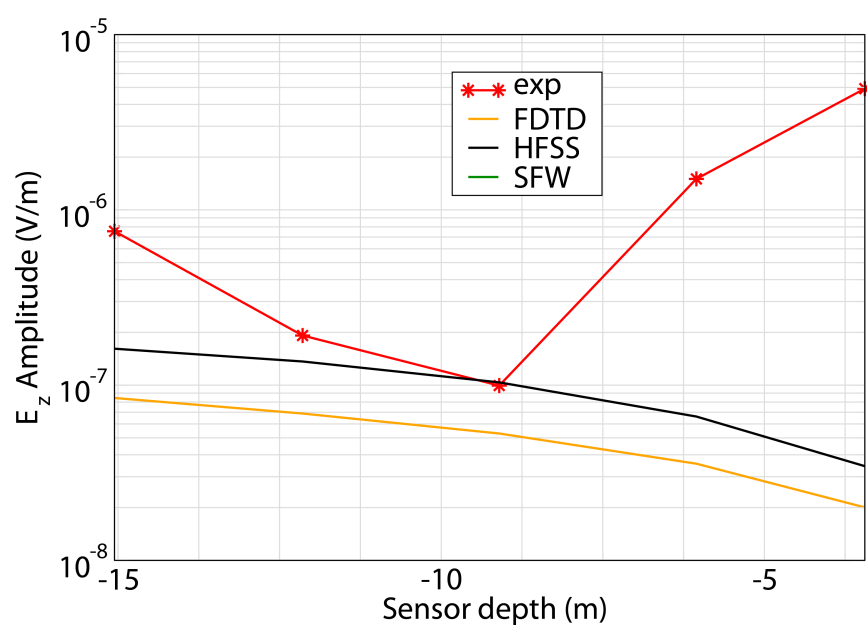


Figure 3.47: Scenario 4, magnitude E_z field.

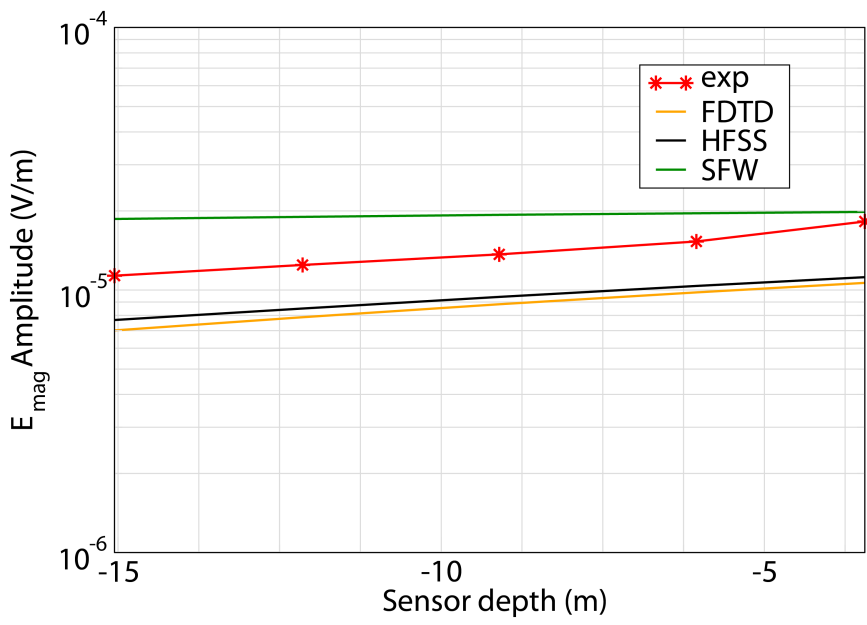


Figure 3.48: Scenario 4, magnitude E field.

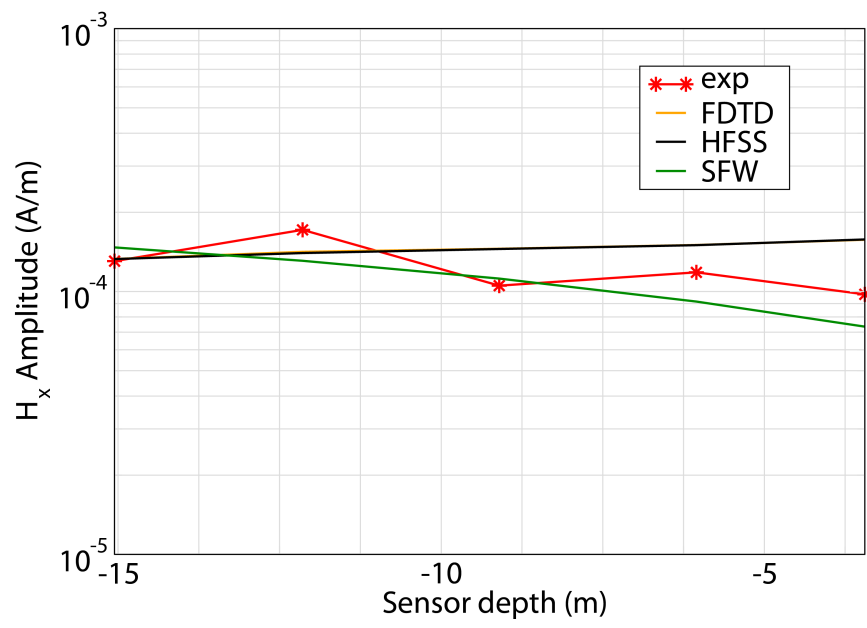


Figure 3.49: Scenario 4, magnitude H_x field.

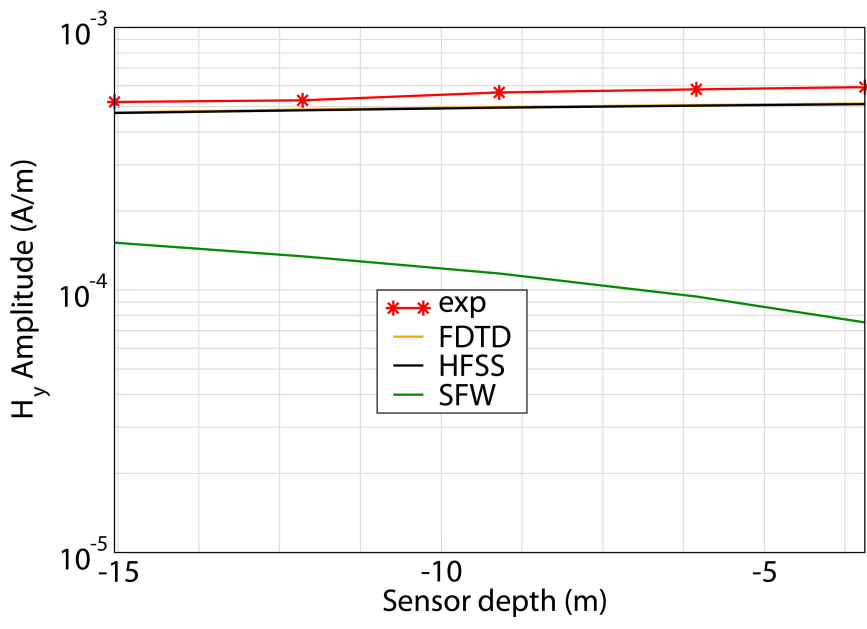


Figure 3.50: Scenario 4, magnitude H_y field.

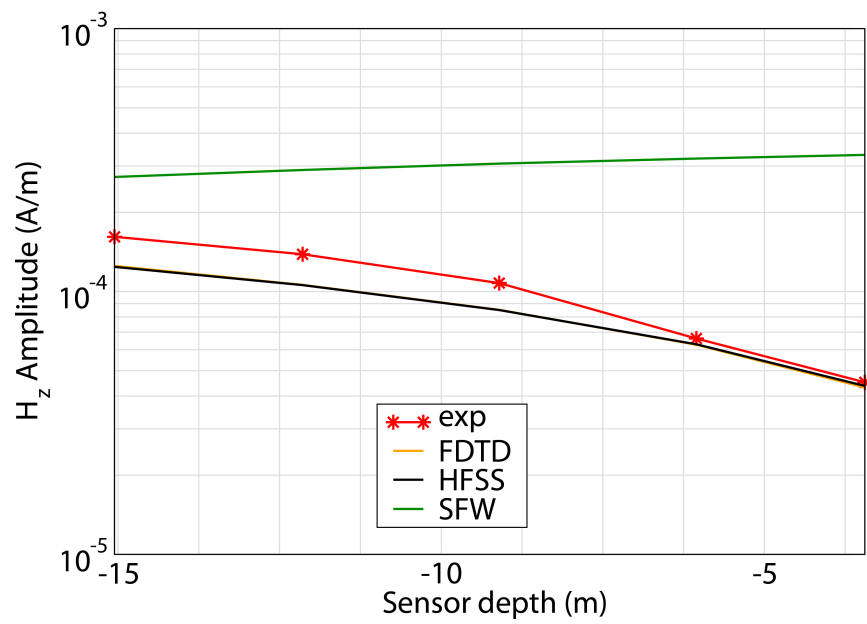


Figure 3.51: Scenario 4, magnitude H_z field.

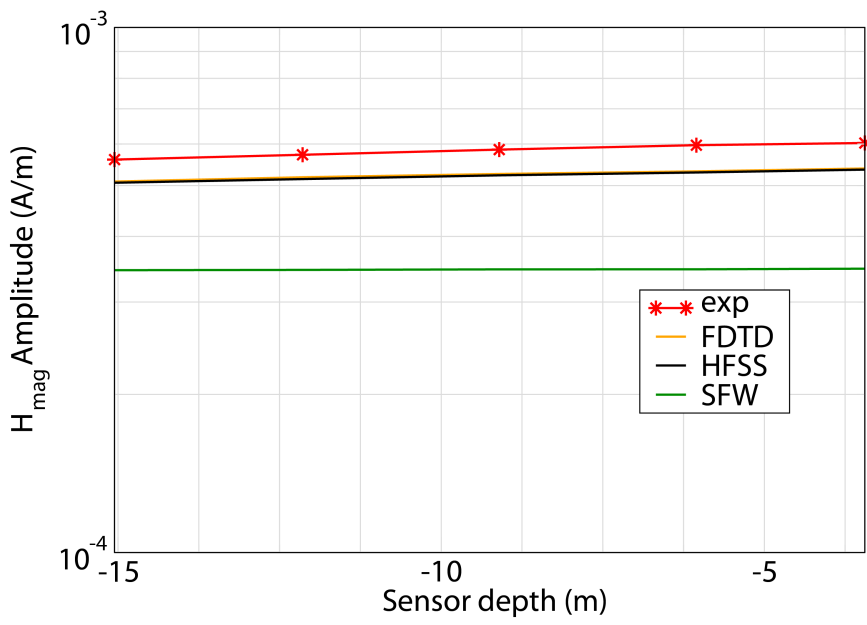


Figure 3.52: Scenario 4, magnitude H field.

Scenario 5

Scenario 5 is an HED mounted on the hull of a boat. That boat is piloted along a straight line parallel to a section of shoreline and passing between the shoreline and the sensor. The sensor is held at a fixed depth below the water surface.

Source Parameters

- Source Type: HED (Boat Hull: plates 0.61 m by 0.305 m separated by 4 m).
- Source Strength: 11.33 A-m.
- $f = 100$ Hz.

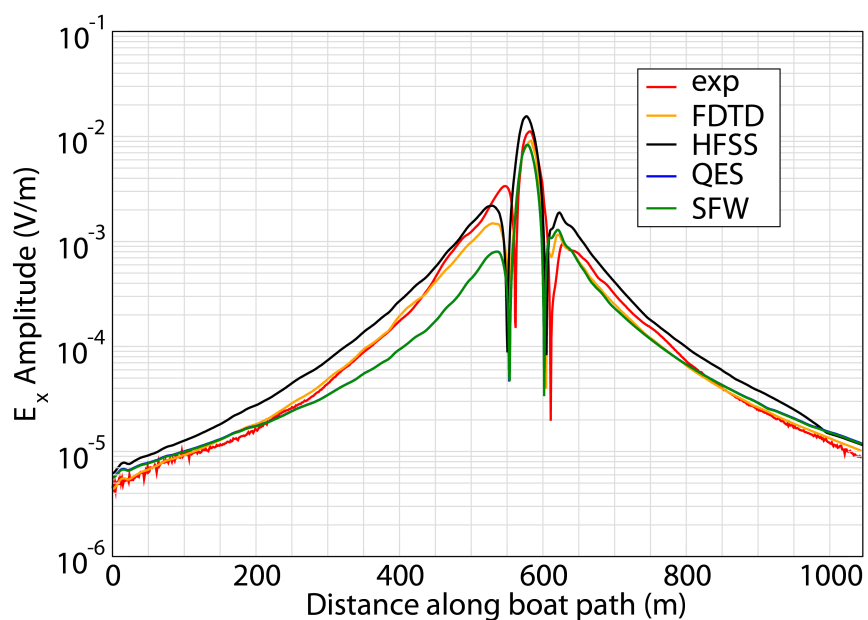


Figure 3.53: Scenario 5, magnitude E_x field.

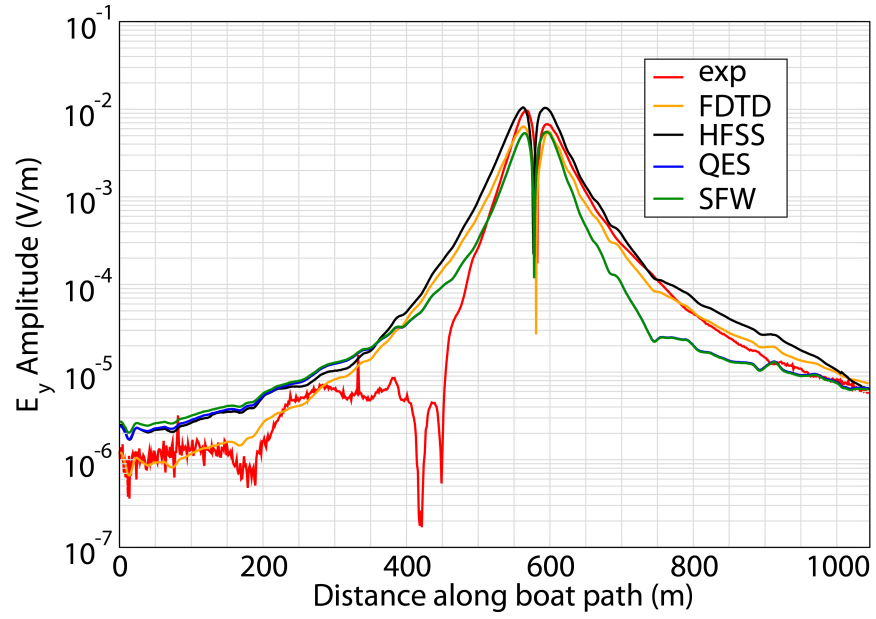


Figure 3.54: Scenario 5, magnitude E_y field.

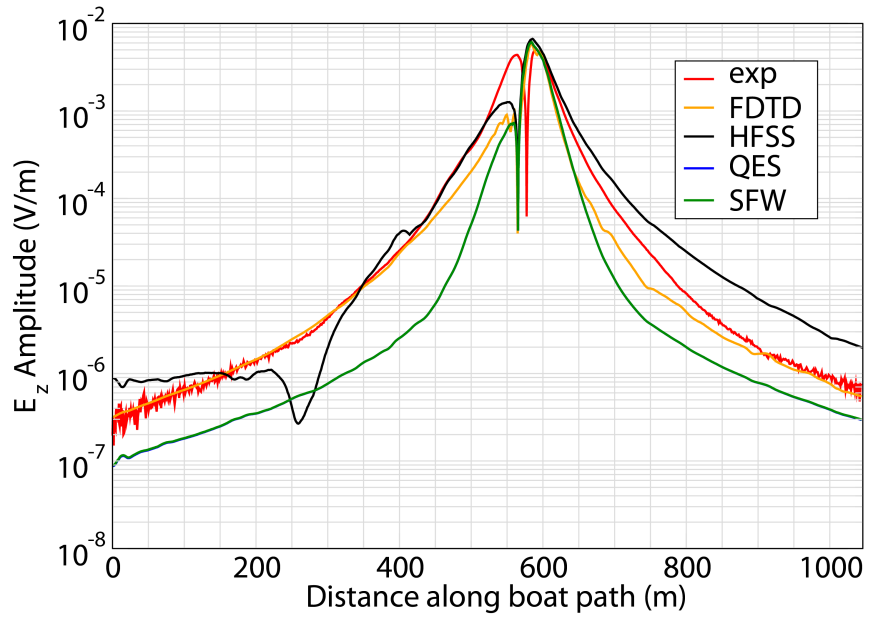


Figure 3.55: Scenario 5, magnitude E_z field.

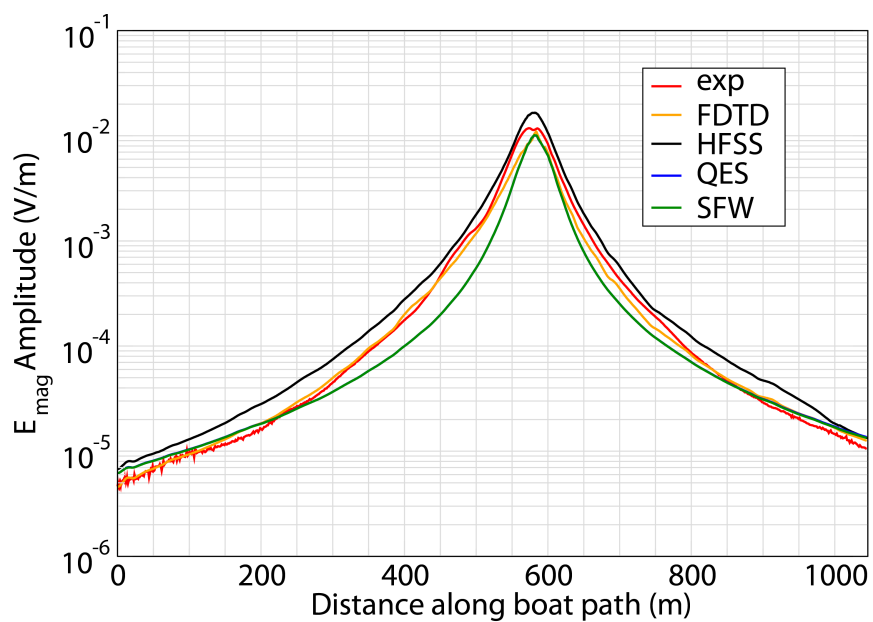


Figure 3.56: Scenario 5, magnitude E field.

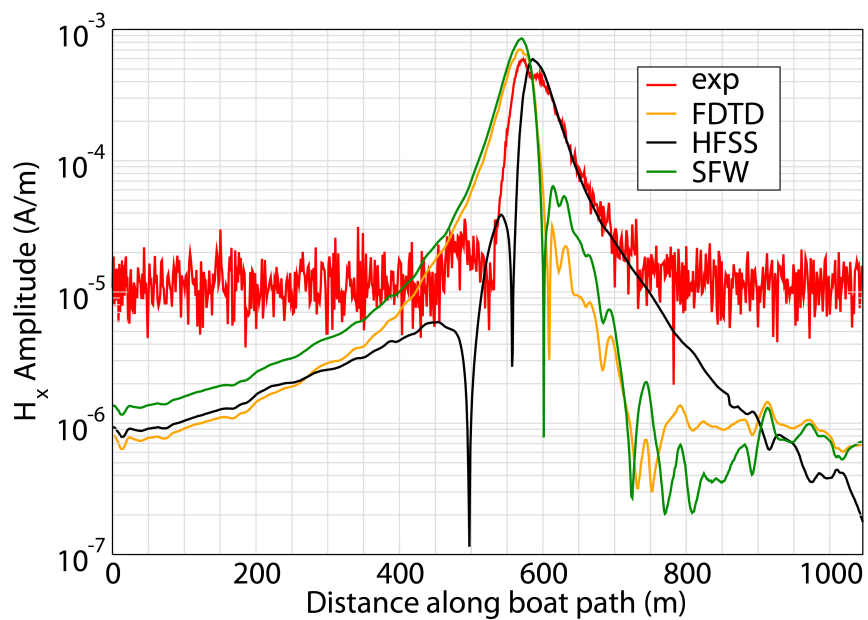


Figure 3.57: Scenario 5, magnitude H_x field.

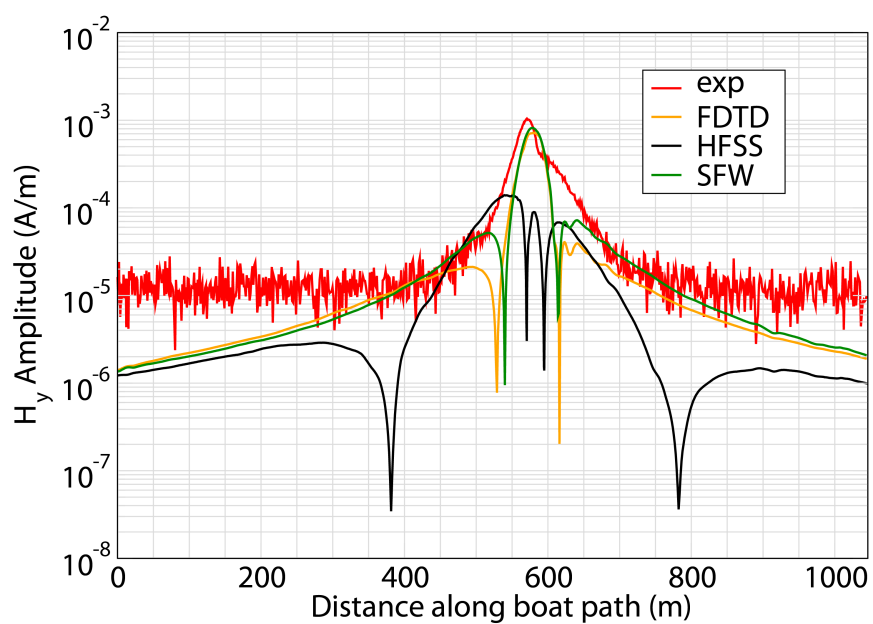


Figure 3.58: Scenario 5, magnitude H_y field.

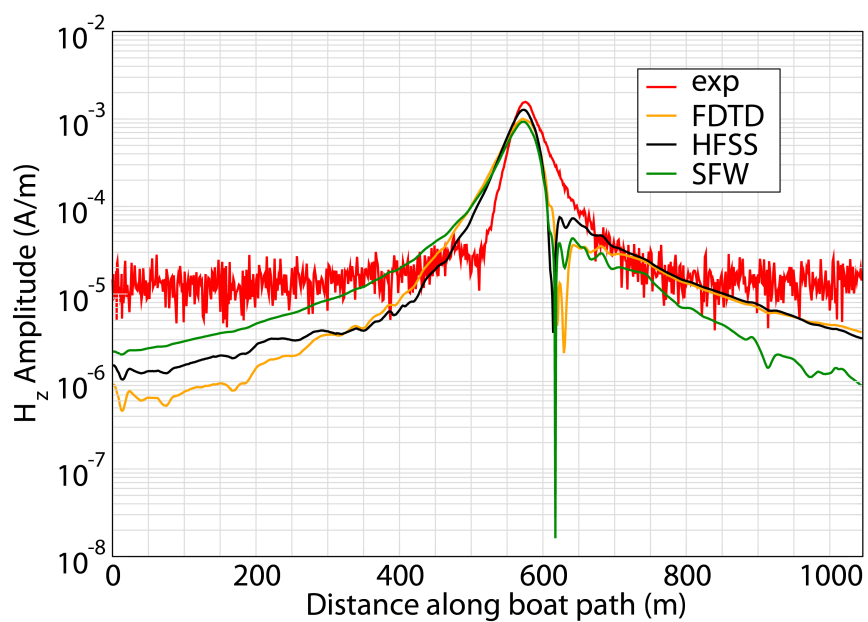


Figure 3.59: Scenario 5, magnitude H_z field.

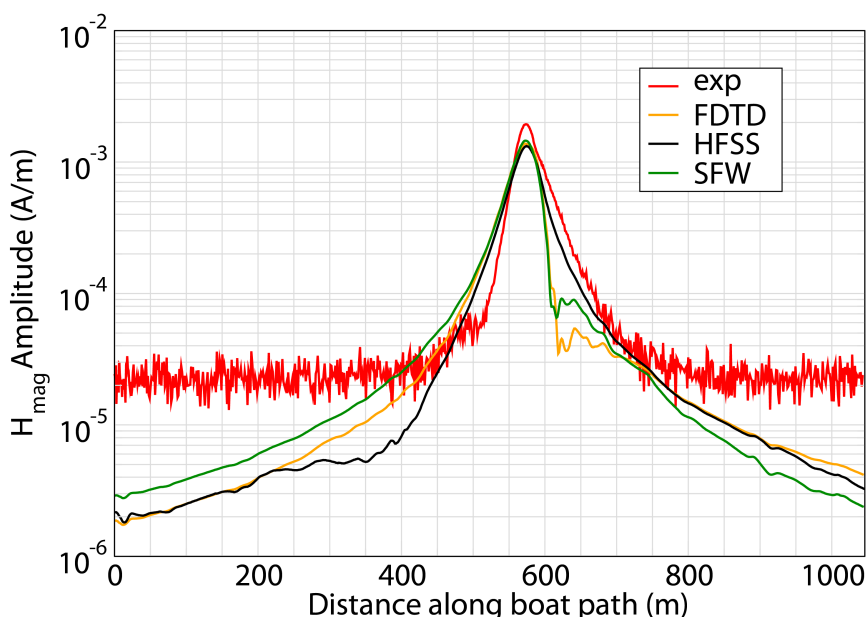


Figure 3.60: Scenario 5, magnitude H field.

The experiments conducted in Idlewild Bay proved to be much more challenging, as was expected. In fact, the predictions from each simulation tool produced different results from each other. The differences between the simulation tools and experiments were much more clear in these sets of experiments. All these differences are believed to be a culmination of several factors. Differences in simulations come partly because of differences in how the different tools model the geometry of the land and lake bottom. In the first area this had very little importance. SFW and QES are both three layer models, are unable to predict any topology variations, and must assume some average depth. FDTD uses a stair stepped approximation of the topology, where HFSS uses a triangle faceted approximation. This reason alone can produce significant differences. Differences between the simulations and experiments are believed to come from several areas. First, is the deployment equipment. Large barges with significant amounts of metal are not simulated, but have some influences on the field. Second, is inaccuracies in the map and model creations that do not truly reflect the real world geometries. Finally, the material parameters for inhomogeneous regions of the Lake floor and shore have to be represented as a single value which is a gross over simplification.

The results of the comparisons are still in many ways very good. The electric field magnitude is consistently close to the experimental results; HFSS can predict strong components of the electromagnetic field very well. It is not known at this time why HFSS had inconsistent results in computing magnetic fields for this case.

3.9 Multi-CPU and Multi-Core Platforms

The size of the simulations considered in this project made it impractical to use a standard desktop PC. As a result of this size factor several high-powered computing platforms were used to run these simulations. These platforms had anywhere from 8 to 32 cores and anywhere from 32 to 128 GB of RAM. An initial impulse might be to use all the computing resources of each platform to solve a single problem. This would be a good approach if there was a linear relationship between performance and resources, i.e. each additional core and each additional GB of RAM would produce a linear increase in computational speed. This turned out not be the case and that the benefits quickly dwindled after only four cores of CPU usage, as seen in Fig.3.61. One computer that was used extensively, named Einstein, has 32 cores with 2.5 GHz CPUs and 128 GBs of RAM. Another platform named Biot has 8 cores with 2.6 GHz CPUs and 32 GBs RAM. Finally a third machine named Uda is the most modern platform, it has 16 cores with 2.8 GHz CPUs and has 32 GBs of RAM. Even though Einstein has more resources, it does not perform as well as either of the other platforms. This is because of two reasons. First is the processor speeds. Second is the computer architecture, which determines the efficiency in passing data between cores and memory. However, Einstein can run much bigger simulation spaces than the other two platforms. Fig. 3.61 shows the results of a series of simulations that were conducted to demonstrate this diminishing return. A moderate sized model was created and solved on each platform while limiting the number of processors that HFSS had access to.

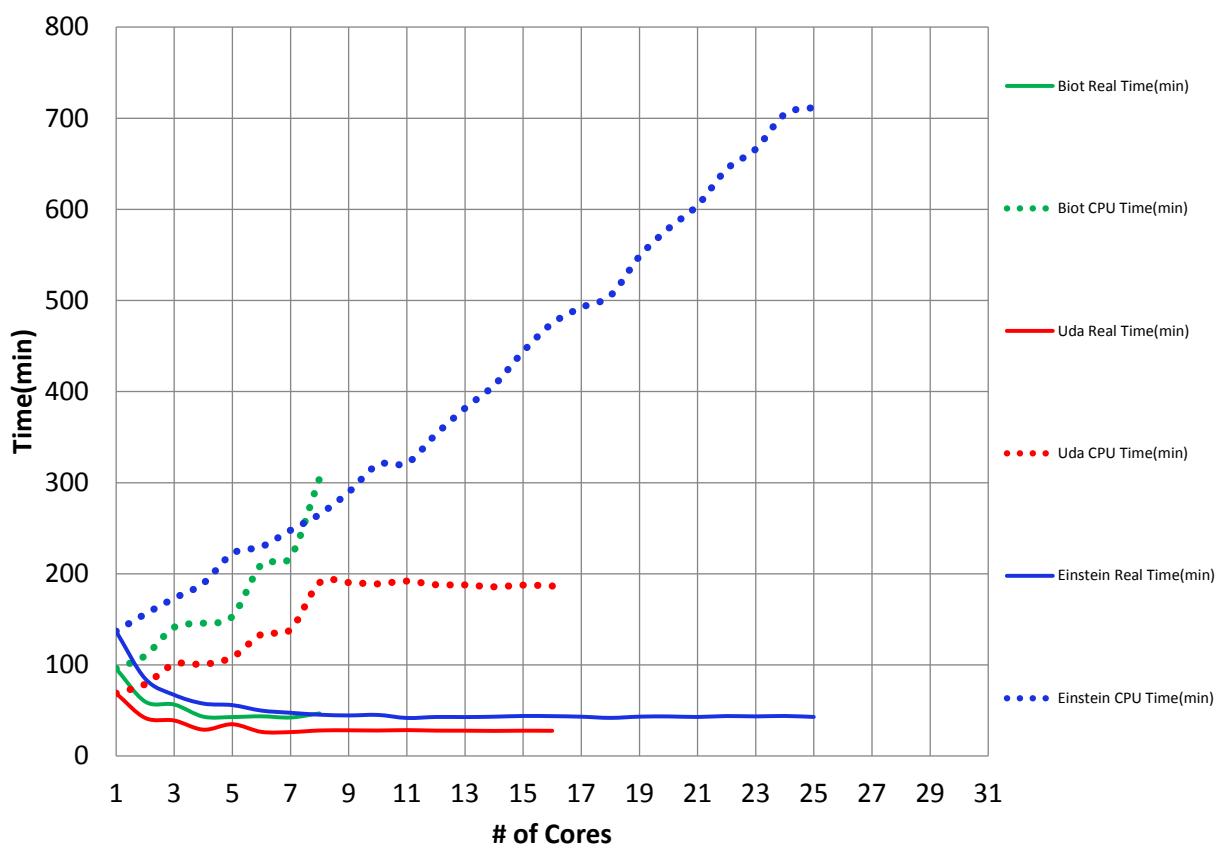


Figure 3.61: Time vs. N Cores.

RAM on the other hand had much different considerations involved. First the amount of RAM needed is directly related to the size of the matrix that is going to be inverted and directly related to the number of meshing elements needed for the model. It is possible to limit the amount of memory that HFSS can use, but this will only mean that if the simulation reaches this limit then it will stop and return a “no solution.” The more RAM used does slow the simulation, however, in that it means larger and larger amounts of data must be moved through the bus of the computer. If that pipeline is narrow, it will quickly increase the simulation time. The bus speed and size is where consideration of the computers architecture must be given. Computer architecture with more RAM bandwidth is desirable. There is a similar limitation for hard drive access but it is not as significant as that of the RAM. In short, the amount of RAM will influence the size of the simulations that can be solved where the bandwidth of the RAM bus and number of processors will influence the speed of the simulation.

Chapter 4

Electric Current Loop

One of the two electromagnetic source types used in the series of experiments was an electric current loop. To better understand how things like shape, material parameters, and the air-water interface may affect the accuracy of these simulations it was desired to have an analytical solution for a loop of physical size and shape that more closely matched the experiment. The following chapter will outline the effort made towards this goal. A similar analysis was conducted by Rebich [4] with regards to the electric sources of the experiment.

4.1 Square Loop: Numerical Integration and Finite-Difference Derivatives

Consider a single line current orientated on the xy -plane and parallel to the y -axis but offset by a distance of $L/2$ distance. The element is of length L and of uniform current I_m as shown in Fig. 4.1. The current density is assumed to be of the following form:

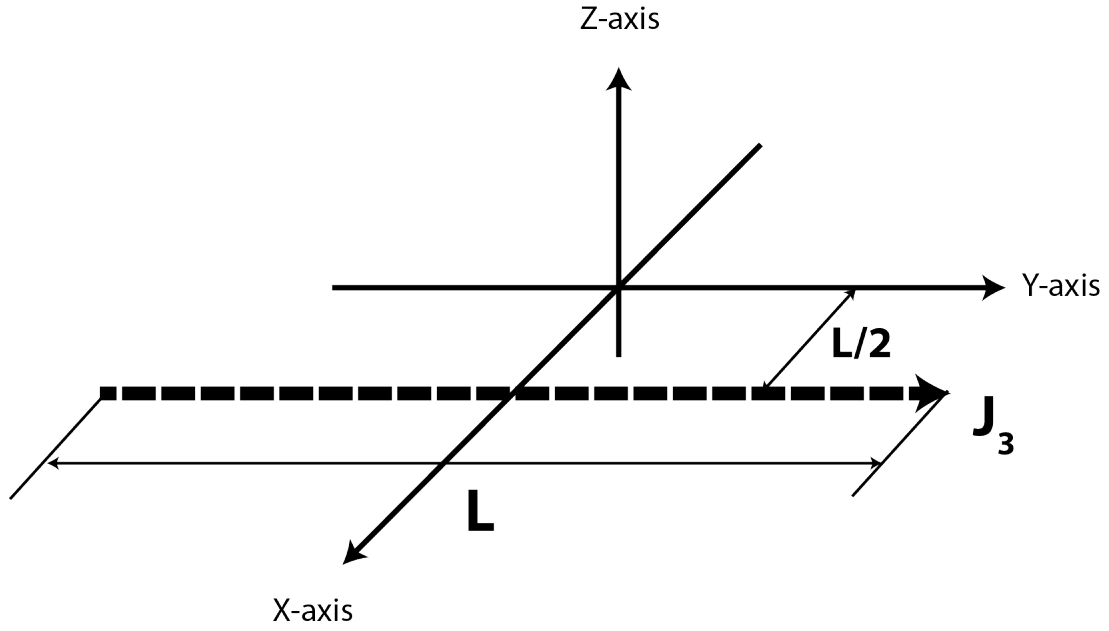


Figure 4.1: Single length of current.

$$\vec{J}_3 = I_m \hat{a}_y \delta(z) \delta\left(x - \frac{L}{2}\right) \left[u\left(y + \frac{L}{2}\right) - u\left(y - \frac{L}{2}\right) \right], \quad (4.1)$$

where $u(y)$ is the step function such that $u(y) = 1$ for $y > 0$ and $u(y) = 0$ for $y \leq 0$. For a homogeneous medium with a current \vec{J} , the magnetic vector potential \vec{A} is given by [3]

$$\vec{A} = \frac{1}{4\pi} \int \int \int \vec{J}(\vec{r}') g(\vec{r}, \vec{r}') dV' \quad (4.2)$$

where

$$g(\vec{r}, \vec{r}') = \frac{e^{-jk|\vec{r}-\vec{r}'|}}{|\vec{r}-\vec{r}'|}. \quad (4.3)$$

This formulation of magnetic vector potential is based on the Lorenz gauge condition. Here \vec{r} is the position vector of the observer and \vec{r}' is the position vector of the source; $k = \omega\sqrt{\mu\epsilon}$ and is the wavenumber. If the current shown in Fig. 4.1 and quantified by Eqn. (4.1) is inserted into Eqn. (4.2) then

$$A_y = \frac{I_m}{4\pi} \int_{-\frac{L}{2}}^{\frac{L}{2}} \frac{e^{-jk\sqrt{(x-\frac{L}{2})^2+(y-y')^2+z^2}}}{\sqrt{(x-\frac{L}{2})^2+(y-y')^2+z^2}} dy'. \quad (4.4)$$

Likewise, a current element orientated parallel to the x -axis is given by

$$\vec{J}_1 = I_m \hat{a}_x \delta(z) \delta\left(y + \frac{L}{2}\right) \left[u\left(x + \frac{L}{2}\right) - u\left(x - \frac{L}{2}\right) \right], \quad (4.5)$$

and can be shown to have a vector potential of

$$A_x = \frac{I_m}{4\pi} \int_{-\frac{L}{2}}^{\frac{L}{2}} \frac{e^{-jk\sqrt{(x-x')^2 + (y+\frac{L}{2})^2 + z^2}}}{\sqrt{(x-x')^2 + (y+\frac{L}{2})^2 + z^2}} dx'. \quad (4.6)$$

For the currents reflected about their respective axis and reversed in direction, we have

$$\begin{aligned} \vec{J}_2 &= -I_m \hat{a}_x \delta(z) \delta\left(y - \frac{L}{2}\right) \left[u\left(x + \frac{L}{2}\right) - u\left(x - \frac{L}{2}\right) \right] \\ \vec{J}_4 &= -I_m \hat{a}_y \delta(z) \delta\left(x + \frac{L}{2}\right) \left[u\left(y + \frac{L}{2}\right) - u\left(y - \frac{L}{2}\right) \right], \end{aligned} \quad (4.7)$$

in which case

$$A_y = \frac{-I_m}{4\pi} \int_{-\frac{L}{2}}^{\frac{L}{2}} \frac{e^{-jk\sqrt{(x+\frac{L}{2})^2 + (y-y')^2 + z^2}}}{\sqrt{(x+\frac{L}{2})^2 + (y-y')^2 + z^2}} dy' \quad (4.8)$$

$$A_x = \frac{-I_m}{4\pi} \int_{-\frac{L}{2}}^{\frac{L}{2}} \frac{e^{-jk\sqrt{(x-x')^2 + (y-\frac{L}{2})^2 + z^2}}}{\sqrt{(x-x')^2 + (y-\frac{L}{2})^2 + z^2}} dx'. \quad (4.9)$$

If all four current elements are then placed in the same domain end to end such that it forms a square loop as shown in Fig. 4.2, the total vector potential would be the superposition of all four vector potentials. That is, $\vec{A} = A_x \hat{a}_x + A_y \hat{a}_y$, where,

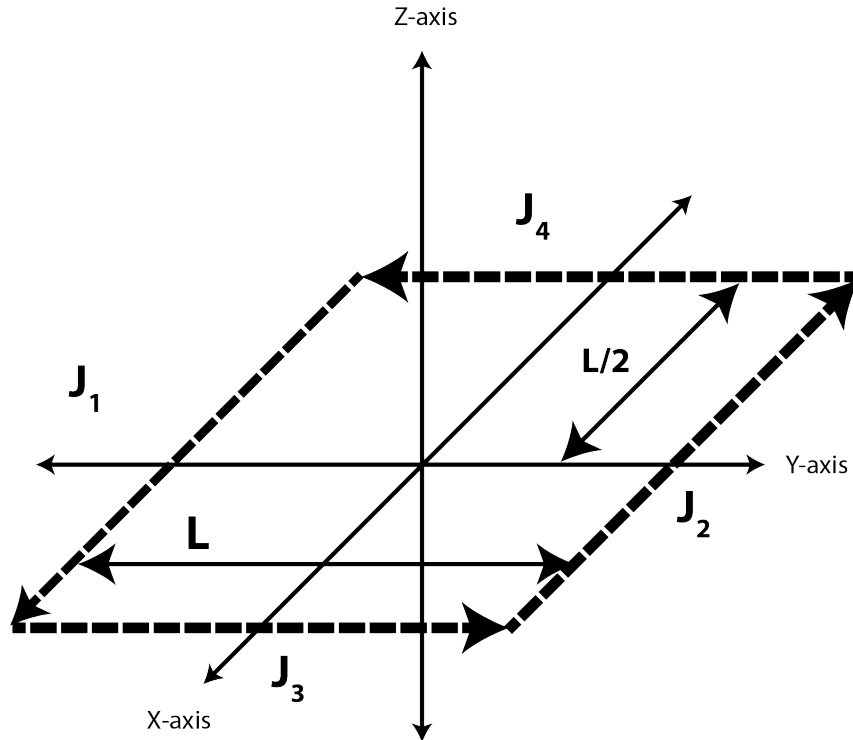


Figure 4.2: Square loop

$$A_x = \frac{I_m}{4\pi} \int_{-\frac{L}{2}}^{\frac{L}{2}} \frac{e^{-jk\sqrt{(x-x')^2 + (y+\frac{L}{2})^2 + z^2}}}{\sqrt{(x-x')^2 + (y+\frac{L}{2})^2 + z^2}} dx' - \frac{I_m}{4\pi} \int_{-\frac{L}{2}}^{\frac{L}{2}} \frac{e^{-jk\sqrt{(x-x')^2 + (y-\frac{L}{2})^2 + z^2}}}{\sqrt{(x-x')^2 + (y-\frac{L}{2})^2 + z^2}} dx' \quad (4.10)$$

$$A_y = \frac{I_m}{4\pi} \int_{-\frac{L}{2}}^{\frac{L}{2}} \frac{e^{-jk\sqrt{(x-\frac{L}{2})^2 + (y-y')^2 + z^2}}}{\sqrt{(x-\frac{L}{2})^2 + (y-y')^2 + z^2}} dy' - \frac{I_m}{4\pi} \int_{-\frac{L}{2}}^{\frac{L}{2}} \frac{e^{-jk\sqrt{(x+\frac{L}{2})^2 + (y-y')^2 + z^2}}}{\sqrt{(x+\frac{L}{2})^2 + (y-y')^2 + z^2}} dy' \quad (4.11)$$

From the vector potential \vec{A} , we can find the \vec{H} field from

$$\vec{H} = \nabla \times \vec{A} \quad (4.12)$$

which is equivalent to

$$\vec{H} = \left(\frac{\partial A_z}{\partial y} - \frac{\partial A_y}{\partial z} \right) \hat{a}_x - \left(\frac{\partial A_z}{\partial x} - \frac{\partial A_x}{\partial z} \right) \hat{a}_y + \left(\frac{\partial A_y}{\partial x} - \frac{\partial A_x}{\partial y} \right) \hat{a}_z. \quad (4.13)$$

Equations (4.10), (4.11) and (4.13) can be evaluated in several ways. First and perhaps most desirable would be to find a closed form analytical expression for the magnetic fields. This proved very difficult because of the integrations. Although a closed form expression was found using techniques similar to those of Werner [2], the expressions proved to be even more difficult to evaluate numerically. This conclusion led to a second method, as described next. The integral is first evaluated numerically and the curl is then evaluated numerically by using a finite difference approximation. The magnetic field at any point in space can be found approximately by discretizing Eqn. (4.13) to yield

$$H_x(x, y, z) = \left[\frac{A_z(x, y + \frac{\Delta y}{2}, z) - A_z(x, y - \frac{\Delta y}{2}, z)}{\Delta y} \right] - \left[\frac{A_y(x, y, z + \frac{\Delta z}{2}) - A_y(x, y, z - \frac{\Delta z}{2})}{\Delta z} \right] \quad (4.14)$$

$$H_y(x, y, z) = \left[\frac{A_x\left(x, y, z + \frac{\Delta z}{2}\right) - A_x\left(x, y, z - \frac{\Delta z}{2}\right)}{\Delta z} \right] - \left[\frac{A_z\left(x + \frac{\Delta x}{2}, y, z\right) - A_z\left(x - \frac{\Delta x}{2}, y, z\right)}{\Delta x} \right] \quad (4.15)$$

$$H_z(x, y, z) = \left[\frac{A_y\left(x + \frac{\Delta x}{2}, y, z\right) - A_y\left(x - \frac{\Delta x}{2}, y, z\right)}{\Delta x} \right] - \left[\frac{A_x\left(x, y + \frac{\Delta y}{2}, z\right) - A_x\left(x, y - \frac{\Delta y}{2}, z\right)}{\Delta y} \right]. \quad (4.16)$$

where $\Delta x, \Delta y, \Delta z$ are finite difference cell dimensions. These equations will converge to the exact value as $\Delta x, \Delta y, \Delta z \rightarrow 0$. Likewise the electric fields can be found from the following expression.

$$\vec{E} = -j\omega\mu\vec{A} + \frac{\nabla(\nabla \cdot \vec{A})}{j\omega\epsilon} \quad (4.17)$$

$$\vec{E} = -j\omega\mu\vec{A} + \frac{1}{j\omega\epsilon} \nabla \left(\frac{\partial A_x}{\partial x} + \frac{\partial A_y}{\partial y} + \frac{\partial A_z}{\partial z} \right) \quad (4.18)$$

$$E_x = -j\omega\mu A_x + \frac{1}{j\omega\epsilon} \frac{\partial}{\partial x} \left(\frac{\partial A_x}{\partial x} + \frac{\partial A_y}{\partial y} + \frac{\partial A_z}{\partial z} \right) \quad (4.19)$$

$$E_y = -j\omega\mu A_y + \frac{1}{j\omega\epsilon} \frac{\partial}{\partial y} \left(\frac{\partial A_x}{\partial x} + \frac{\partial A_y}{\partial y} + \frac{\partial A_z}{\partial z} \right) \quad (4.20)$$

$$E_z = -j\omega\mu A_z + \frac{1}{j\omega\epsilon} \frac{\partial}{\partial z} \left(\frac{\partial A_x}{\partial x} + \frac{\partial A_y}{\partial y} + \frac{\partial A_z}{\partial z} \right). \quad (4.21)$$

If the same finite difference method is applied to the electric fields, we find that

$$\begin{aligned}
 E_x(x, y, z) = & -j\omega\mu A_x(x, y, z) \\
 & + \frac{1}{j\omega\epsilon} \left[\left(\frac{A_x(x + \Delta x, y, z) - A_x(x, y, z)}{\Delta x \Delta x} \right) \right. \\
 & + \left(\frac{A_y(x + \frac{\Delta x}{2}, y + \frac{\Delta y}{2}, z) - A_y(x - \frac{\Delta x}{2}, y - \frac{\Delta y}{2}, z)}{\Delta x \Delta y} \right) \\
 & + \left. \left(\frac{A_z(x + \frac{\Delta x}{2}, y, z + \frac{\Delta z}{2}) - A_z(x - \frac{\Delta x}{2}, y, z + \frac{\Delta z}{2})}{\Delta x \Delta z} \right) \right] \\
 & - \frac{1}{j\omega\epsilon} \left[\left(\frac{A_x(x, y, z) - A_x(x - \Delta x, y, z)}{\Delta x \Delta x} \right) \right. \\
 & + \left(\frac{A_y(x - \frac{\Delta x}{2}, y + \frac{\Delta y}{2}, z) - A_y(x - \frac{\Delta x}{2}, y - \frac{\Delta y}{2}, z)}{\Delta x \Delta y} \right) \\
 & + \left. \left(\frac{A_z(x - \frac{\Delta x}{2}, y, z + \frac{\Delta z}{2}) - A_z(x - \frac{\Delta x}{2}, y, z + \frac{\Delta z}{2})}{\Delta x \Delta z} \right) \right] \quad (4.22)
 \end{aligned}$$

$$\begin{aligned}
 E_y(x, y, z) = & -j\omega\mu A_y(x, y, z) \\
 & + \frac{1}{j\omega\epsilon} \left[\left(\frac{A_x(x + \frac{\Delta x}{2}, y + \frac{\Delta y}{2}, z) - A_x(x - \frac{\Delta x}{2}, y + \frac{\Delta y}{2}, z)}{\Delta y \Delta x} \right) \right. \\
 & + \left(\frac{A_y(x, y + \Delta y, z) - A_y(x, y, z)}{\Delta y \Delta y} \right) \\
 & + \left. \left(\frac{A_z(x, y + \frac{\Delta y}{2}, z + \frac{\Delta z}{2}) - A_z(x, y + \frac{\Delta y}{2}, z + \frac{\Delta z}{2})}{\Delta y \Delta z} \right) \right] \\
 & - \frac{1}{j\omega\epsilon} \left[\left(\frac{A_x(x + \frac{\Delta x}{2}, y - \frac{\Delta y}{2}, z) - A_x(x - \frac{\Delta x}{2}, y - \frac{\Delta y}{2}, z)}{\Delta y \Delta x} \right) \right. \\
 & + \left(\frac{A_y(x, y, z) - A_y(x, y - \Delta y, z)}{\Delta y \Delta y} \right) \\
 & + \left. \left(\frac{A_z(x, y - \frac{\Delta y}{2}, z + \frac{\Delta z}{2}) - A_z(x, y - \frac{\Delta y}{2}, z + \frac{\Delta z}{2})}{\Delta y \Delta z} \right) \right] \quad (4.23)
 \end{aligned}$$

$$\begin{aligned}
E_z(x, y, z) = & -j\omega\mu A_z(x, y, z) \\
& + \frac{1}{j\omega\epsilon} \left[\left(\frac{A_x(x + \frac{\Delta x}{2}, y, z + \frac{\Delta z}{2}) - A_x(x - \frac{\Delta x}{2}, y, z + \frac{\Delta z}{2})}{\Delta z \Delta x} \right) \right. \\
& + \left(\frac{A_y(x, y + \frac{\Delta y}{2}, z + \frac{\Delta z}{2}) - A_y(x, y - \frac{\Delta y}{2}, z + \frac{\Delta z}{2})}{\Delta z \Delta y} \right) \\
& + \left. \left(\frac{A_z(x, y, z + \Delta z) - A_z(x, y, z)}{\Delta z \Delta z} \right) \right] \\
& - \frac{1}{j\omega\epsilon} \left[\left(\frac{A_x(x + \frac{\Delta x}{2}, y, z - \frac{\Delta z}{2}) - A_x(x - \frac{\Delta x}{2}, y, z - \frac{\Delta z}{2})}{\Delta z \Delta x} \right) \right. \\
& + \left(\frac{A_y(x, y + \frac{\Delta y}{2}, z - \frac{\Delta z}{2}) - A_y(x, y - \frac{\Delta y}{2}, z - \frac{\Delta z}{2})}{\Delta z \Delta y} \right) \\
& + \left. \left(\frac{A_z(x, y, z) - A_z(x, y, z - \Delta z)}{\Delta z \Delta z} \right) \right]. \tag{4.24}
\end{aligned}$$

This method like the closed form analytical solution proved difficult to evaluate numerically, although for a very different reason. The integrals could be evaluated using several numerical methods, but the numerical derivatives of the these integrands were found to be susceptible to numerical noise resulting from the difference in the arguments of the magnetic vector potentials. This difficulty led us to consider yet another approach, as described next.

4.2 Square Loop: Analytical Derivatives and Numerical Integration

The difference between the approach outlined in this section and Section 4.1 is that in this section the derivatives were evaluated before integration. This resulted in a single integration that is evaluated numerically to find the values for the fields without the challenge of the derivatives amplifying numerical noise. This approach does increase the chance that the original integrand could become even more peaked near a singularity and, as a result, more difficult to compute numerically. This concern is only important, fortunately, when field

observations are made very close to the loop.

Consider again the problem shown in Fig. 4.2 with magnetic vector potentials given by Eqns. (4.10) and (4.11). The electromagnetic fields are still found from Eqns. (4.12) and (4.17.) If the derivatives are moved inside the integration and if the derivatives of the integrand are taken, we find that the fields are expressed in the following forms:

$$H_x = \frac{zI_m}{4\pi} \int_{-\frac{L}{2}}^{\frac{L}{2}} \left[\frac{e^{-jkR_4}}{R_4^2} \left(jk + \frac{1}{R_4} \right) - \frac{e^{-jkR_3}}{R_3^2} \left(jk + \frac{1}{R_3} \right) \right] dy' \quad (4.25)$$

$$H_y = \frac{zI_m}{4\pi} \int_{-\frac{L}{2}}^{\frac{L}{2}} \left[\frac{e^{-jkR_2}}{R_2^2} \left(jk + \frac{1}{R_2} \right) - \frac{e^{-jkR_1}}{R_1^2} \left(jk + \frac{1}{R_1} \right) \right] dx' \quad (4.26)$$

$$H_z = \frac{I_m}{4\pi} \left[\int_{-\frac{L}{2}}^{\frac{L}{2}} \left[\frac{(x + \frac{L}{2}) e^{-jkR_4}}{R_4^2} \left(jk + \frac{1}{R_4} \right) - \frac{(x - \frac{L}{2}) e^{-jkR_3}}{R_3^2} \left(jk + \frac{1}{R_3} \right) \right] dy' \right. \\ \left. - \int_{-\frac{L}{2}}^{\frac{L}{2}} \left[\frac{(y - \frac{L}{2}) e^{-jkR_2}}{R_2^2} \left(jk + \frac{1}{R_2} \right) - \frac{(y + \frac{L}{2}) e^{-jkR_1}}{R_1^2} \left(jk + \frac{1}{R_1} \right) \right] dx' \right] \quad (4.27)$$

$$E_x = \frac{-j\omega I_m \mu}{4\pi} \int_{-\frac{L}{2}}^{\frac{L}{2}} \left[\frac{e^{-jkR_1}}{R_1} - \frac{e^{-jkR_2}}{R_2} \right] dx' \\ + \frac{I_m}{j4\omega\epsilon\pi} \int_{-\frac{L}{2}}^{\frac{L}{2}} \left[\frac{(x - x')^2 e^{-jkR_2}}{R_2^2} \left(\frac{1}{R_2} \left(\frac{1}{(x - x')^2} - \frac{3}{R_2^2} \right) + jk \left(\frac{1}{(x - x')^2} - \frac{jk}{R_2} - \frac{3}{R_2^2} \right) \right) \right. \\ \left. - \frac{(x - x')^2 e^{-jkR_1}}{R_1^2} \left(\frac{1}{R_1} \left(\frac{1}{(x - x')^2} - \frac{3}{R_1^2} \right) + jk \left(\frac{1}{(x - x')^2} - \frac{jk}{R_1} - \frac{3}{R_1^2} \right) \right) \right] dx' \\ + \frac{I_m}{j4\omega\epsilon\pi} \int_{-\frac{L}{2}}^{\frac{L}{2}} \left[\frac{(y - y') (x - \frac{L}{2}) e^{-jkR_3}}{R_3^3} \left((jk)^2 + \frac{3jk}{R_3} + \frac{3}{R_3^2} \right) \right. \\ \left. - \frac{(y - y') (x + \frac{L}{2}) e^{-jkR_4}}{R_4^3} \left((jk)^2 + \frac{3jk}{R_4} + \frac{3}{R_4^2} \right) \right] dy' \quad (4.28)$$

$$E_y = \frac{-j\omega I_m \mu}{4\pi} \int_{-\frac{L}{2}}^{\frac{L}{2}} \left[\frac{e^{-jkR_3}}{R_3} - \frac{e^{-jkR_4}}{R_4} \right] dy' \\ + \frac{I_m}{j4\omega\epsilon\pi} \int_{-\frac{L}{2}}^{\frac{L}{2}} \left[\frac{(y - y')^2 e^{-jkR_4}}{R_4^2} \left(\frac{1}{R_4} \left(\frac{1}{(y - y')^2} - \frac{3}{R_4^2} \right) + jk \left(\frac{1}{(y - y')^2} - \frac{jk}{R_4} - \frac{3}{R_4^2} \right) \right) \right. \\ \left. - \frac{(y - y')^2 e^{-jkR_3}}{R_3^2} \left(\frac{1}{R_3} \left(\frac{1}{(y - y')^2} - \frac{3}{R_3^2} \right) + jk \left(\frac{1}{(y - y')^2} - \frac{jk}{R_3} - \frac{3}{R_3^2} \right) \right) \right] dy' \\ + \frac{I_m}{j4\omega\epsilon\pi} \int_{-\frac{L}{2}}^{\frac{L}{2}} \left[\frac{(x - x') (y + \frac{L}{2}) e^{-jkR_1}}{R_1^3} \left((jk)^2 + \frac{3jk}{R_1} + \frac{3}{R_1^2} \right) \right. \\ \left. - \frac{(x - x') (y - \frac{L}{2}) e^{-jkR_2}}{R_2^3} \left((jk)^2 + \frac{3jk}{R_2} + \frac{3}{R_2^2} \right) \right] dx' \quad (4.29)$$

$$\begin{aligned}
E_z = & \frac{zI_m}{j\omega\epsilon 4\pi} \int_{-\frac{L}{2}}^{\frac{L}{2}} \left[\frac{(x-x')e^{-jkR_1}}{R_1^3} \left((jk)^2 + \frac{3jk}{R_1} + \frac{3}{R_1^2} \right) \right. \\
& \left. - \frac{(x-x')e^{-jkR_2}}{R_2^3} \left((jk)^2 + \frac{3jk}{R_2} + \frac{3}{R_2^2} \right) \right] dx' \\
& + \frac{zI_m}{j\omega\epsilon 4\pi} \int_{-\frac{L}{2}}^{\frac{L}{2}} \left[\frac{(y-y')e^{-jkR_3}}{R_3^3} \left((jk)^2 + \frac{3jk}{R_3} + \frac{3}{R_3^2} \right) \right. \\
& \left. - \frac{(y-y')e^{-jkR_4}}{R_4^3} \left((jk)^2 + \frac{3jk}{R_4} + \frac{3}{R_4^2} \right) \right] dy'
\end{aligned} \tag{4.30}$$

where

$$R_1 = \sqrt{(x-x')^2 + \left(y + \frac{L}{2}\right)^2 + z^2} \tag{4.31}$$

$$R_2 = \sqrt{(x-x')^2 + \left(y - \frac{L}{2}\right)^2 + z^2} \tag{4.32}$$

$$R_3 = \sqrt{\left(x - \frac{L}{2}\right)^2 + (y-y')^2 + z^2} \tag{4.33}$$

$$R_4 = \sqrt{\left(x + \frac{L}{2}\right)^2 + (y-y')^2 + z^2}. \tag{4.34}$$

This formulation for the electromagnetic fields of a square current loop when integrated numerically produced highly accurate results. Comparisons will be shown in Section 4.5.

4.3 Circular Loop: Closed Form Series Solution

A fourth method considers the closed-form solution of a circular loop of current, in which it is assumed that a square loop and circular loop will generate virtually the same field. Consider a loop of current circulating about the z -axis and parallel to the xy -plane. The current is uniform at all points along the circle and the circle has a radius of a . The electric and magnetic vector potentials will take the form of [3]

$$A_r = H_\nu^{(2)}(kr) \left[B_1 P_\nu^m(\cos \theta) + B_2 Q_\nu^m(\cos \theta) \right] e^{-jm\phi} \tag{4.35}$$

$$F_r = \hat{H}_\nu^{(2)}(kr) \left[B'_1 P_\nu^m(\cos \theta) + B'_2 Q_\nu^m(\cos \theta) \right] e^{-jm\phi}, \tag{4.36}$$

where $\hat{J}_\nu(kr)$ is the Bessel function of the first kind, $\hat{H}_\nu^{(2)}(kr)$ is the modified spherical Hankel function of the second kind and where $P_\nu^m(\cos \theta)$ and $Q_\nu^m(\cos \theta)$ are associated Legendre functions. From the following equations the electromagnetic fields are found:

$$E_r = \frac{1}{\hat{y}} \left(\frac{\partial^2}{\partial r^2} + k^2 \right) A_r \quad (4.37)$$

$$E_\theta = \frac{-1}{r \sin \theta} \frac{\partial F_r}{\partial \phi} + \frac{1}{\hat{y}r} \frac{\partial^2 A_r}{\partial r \partial \theta} \quad (4.38)$$

$$E_\phi = \frac{1}{r} \frac{\partial F_r}{\partial \theta} + \frac{1}{\hat{y}r \sin \theta} \frac{\partial^2 A_r}{\partial r \partial \phi} \quad (4.39)$$

$$H_r = \frac{1}{\hat{z}} \left(\frac{\partial^2}{\partial r^2} + k^2 \right) F_r \quad (4.40)$$

$$H_\theta = \frac{1}{r \sin \theta} \frac{\partial A_r}{\partial \phi} + \frac{1}{\hat{z}r} \frac{\partial^2 F_r}{\partial r \partial \theta} \quad (4.41)$$

$$H_\phi = \frac{-1}{r} \frac{\partial A_r}{\partial \theta} + \frac{1}{\hat{z}r \sin \theta} \frac{\partial^2 F_r}{\partial r \partial \phi}. \quad (4.42)$$

Consider for the moment only the fields that are in the range of $r < a$. Consider also the following geometric arguments and simplifications:

1. Standing wave.
2. Finite fields at $r = 0$.
3. Finite fields at $\theta = 0$ and $\theta = \pi$.
4. Fields independent of ϕ (i.e. $\partial/\partial\phi = 0$).
5. TE_r fields (i.e. $A_r = 0$).

This results in F_r taking the form of

$$F_r = \sum_{n=0}^{\infty} a_n \hat{J}_n(kr) P_n(\cos \theta) \quad \text{for } r < a. \quad (4.43)$$

Apply similar geometric arguments and simplifications to the fields for $r > a$ by assuming the following:

1. Outward travelling wave.

2. Finite fields at $\theta = 0$ and $\theta = \pi$.
3. Fields independent of ϕ (i.e. $\partial/\partial\phi = 0$).
4. TE_r fields (i.e. $A_r = 0$).

These arguments result in F_r taking the following form:

$$F_r = \sum_{n=0}^{\infty} b_n \hat{H}_n^{(2)}(kr) P_n(\cos \theta) \quad \text{for } r > a. \quad (4.44)$$

The same arguments used to simplify F_r can be used to further simplify the field components.

From TE_r fields and $\partial/\partial\phi = 0$ the field components reduce to

$$E_\phi = \frac{1}{r} \frac{\partial F_r}{\partial \theta} \quad (4.45)$$

$$H_r = \frac{1}{\hat{z}} \left(\frac{\partial^2}{\partial r^2} + k^2 \right) F_r \quad (4.46)$$

$$H_\theta = \frac{1}{\hat{z}r} \frac{\partial^2 F_r}{\partial r \partial \theta}, \quad (4.47)$$

where $E_r = E_\theta = H_\phi = 0$. The boundary conditions at $r = a$ require the tangential electric field to be continuous at $r = a$. This is equivalent to

$$E_\phi \Big|_{r=a^+} = E_\phi \Big|_{r=a^-}. \quad (4.48)$$

After simplification of Eq. (4.45) we find that

$$F_r \Big|_{r=a^+} = F_r \Big|_{r=a^-} \quad (4.49)$$

and

$$\sum_{n=0}^{\infty} a_n \hat{J}_n(kr) P_n(\cos \theta) \Big|_{r=a^+} = \sum_{n=0}^{\infty} b_n \hat{H}_n^{(2)}(kr) P_n(\cos \theta) \Big|_{r=a^-} \quad (4.50)$$

where

$$b_n = a_n \frac{\hat{J}_n(ka)}{\hat{H}_n^{(2)}(ka)}. \quad (4.51)$$

At $r = a$, $\hat{n} \times (\vec{H}^+ - \vec{H}^-) = \vec{J}_s$, where $\hat{n} = \hat{a}_r$ and $\vec{H} = H_r \hat{a}_r + H_\theta \hat{a}_\theta$. Hence

$$H^+ \hat{a}_\phi - H^- \hat{a}_\phi = \vec{J}_s \quad (4.52)$$

and

$$\frac{1}{\hat{z}r} \frac{\partial^2 F_r}{\partial r \partial \theta} \Big|_{r=a^+} - \frac{1}{\hat{z}r} \frac{\partial^2 F_r}{\partial r \partial \theta} \Big|_{r=a^-} = J_\phi \quad (4.53)$$

so that

$$\frac{\partial}{\partial \theta} \sum_{n=0}^{\infty} b_n \hat{H}_n^{(2)'}(ka) P_n(\cos \theta) - \frac{\partial}{\partial \theta} \sum_{n=0}^{\infty} a_n \hat{J}_n'(ka) P_n(\cos \theta) = \frac{\hat{z}a}{k} J_\phi. \quad (4.54)$$

If Eq. (4.51) is substituted into Eq. (4.54), we obtain

$$\frac{\partial}{\partial \theta} \sum_{n=0}^{\infty} P_n(\cos \theta) \frac{a_n}{\hat{H}_n^{(2)}(ka)} \left[\hat{J}_n(ka) \hat{H}_n^{(2)'}(ka) - \hat{J}_n'(ka) \hat{H}_n^{(2)}(ka) \right] = \frac{\hat{z}a}{k} J_\phi. \quad (4.55)$$

From the Wronskian of Bessel's equation,

$$\hat{J}_n(ka) \hat{H}_n^{(2)'}(ka) - \hat{J}_n'(ka) \hat{H}_n^{(2)}(ka) = j \quad (4.56)$$

in which case

$$\frac{\partial}{\partial \theta} \sum_{n=0}^{\infty} P_n(\cos \theta) \frac{a_n}{\hat{H}_n^{(2)}(ka)} (-j) = \frac{\hat{z}a}{k} J_\phi, \quad (4.57)$$

where

$$J_\phi = -\frac{1}{a\eta} \frac{\partial}{\partial \theta} \sum_{n=0}^{\infty} P_n(\cos \theta) \frac{a_n}{\hat{H}_n^{(2)}(ka)}. \quad (4.58)$$

Now from E-16 in [3]

$$\frac{\partial}{\partial \theta} P_n(\cos \theta) = P_n'(\cos \theta) \quad (4.59)$$

so that

$$J_\phi = -\frac{1}{a\eta} \sum_{n=0}^{\infty} a_n \frac{P_n'(\cos \theta)}{\hat{H}_n^{(2)}(ka)}. \quad (4.60)$$

From orthogonality,

$$\int_0^\pi P_n'(\cos \theta) P_l'(\cos \theta) \sin \theta d\theta = \begin{cases} \frac{2n(n+1)}{2n+1} & \text{for } n = l, \\ 0 & \text{for } n \neq l \end{cases} \quad (4.61)$$

and

$$\int_0^\pi J_\phi P_l'(\cos \theta) \sin \theta d\theta = \int_0^\pi -\frac{1}{\eta a} \sum_{n=0}^{\infty} P_n'(\cos \theta) P_l'(\cos \theta) \sin \theta \frac{a_n}{\hat{H}_n^{(2)}(ka)} d\theta, \quad (4.62)$$

in which case

$$\int_0^\pi J_\phi P_n'(\cos \theta) \sin \theta d\theta = -\frac{1}{\eta a} \sum_{n=0}^{\infty} \frac{a_n}{\hat{H}_n^{(2)}(ka)} \frac{2n(n+1)}{2n+1} \quad (4.63)$$

and

$$a_n = \eta a \frac{-(2n+1)}{2n(n+1)} \hat{H}_n^{(2)}(ka) \int_0^\pi J_\phi P_n'(\cos \theta) \sin \theta d\theta. \quad (4.64)$$

For a loop current on the xy -plane with radius a , the current I_m can be defined as follows.

$$I_m = \int_0^\pi J_\phi a d\theta \quad (4.65)$$

where

$$J_\phi = \frac{I_m}{a} \delta\left(\theta - \frac{\pi}{2}\right) \quad (4.66)$$

If Eqn. (4.66) is substituted into the integration term of Eqn. (4.64), we find that

$$\int_0^\pi J_\phi P'_l(\cos \theta) \sin \theta d\theta = \int_0^\pi \frac{I_m}{a} \delta\left(\theta - \frac{\pi}{2}\right) P'_n(\cos \theta) \sin \theta d\theta \quad (4.67)$$

or

$$\int_0^\pi J_\phi P'_n(\cos \theta) \sin \theta d\theta = \frac{I_m}{a} P'_n(0). \quad (4.68)$$

If a_n simplified further, we obtain the following expression:

$$a_n = \eta I_m \frac{-(2n+1)}{2n(n+1)} \hat{H}_n^{(2)}(ka) P'_n(0). \quad (4.69)$$

Next, by substituting Eqn. (4.51) and Eqn. (4.69) into Eqns. (4.43) and (4.44), we conclude that

$$F_r = \begin{cases} \eta I_m \sum_{n=1}^{\infty} \frac{-(2n+1)}{2n(n+1)} \hat{H}_n^{(2)}(ka) P'_n(0) \hat{J}_n(kr) P_n(\cos \theta) & \text{for } r < a, \\ \eta I_m \sum_{n=1}^{\infty} \frac{-(2n+1)}{2n(n+1)} \hat{H}_n^{(2)}(kr) P'_n(0) \hat{J}_n(ka) P_n(\cos \theta) & \text{for } r > a. \end{cases} \quad (4.70)$$

Since

$$E_\phi = \frac{1}{r} \frac{\partial F_r}{\partial \theta}$$

then

$$E_\phi = \begin{cases} \frac{\eta I_m}{r} \sum_{n=1}^{\infty} \frac{-(2n+1)}{2n(n+1)} \hat{H}_n^{(2)}(ka) P'_n(0) \hat{J}_n(kr) P'_n(\cos \theta) & \text{for } r < a, \\ \frac{\eta I_m}{r} \sum_{n=1}^{\infty} \frac{-(2n+1)}{2n(n+1)} \hat{H}_n^{(2)}(kr) P'_n(0) \hat{J}_n(ka) P'_n(\cos \theta) & \text{for } r > a. \end{cases} \quad (4.71)$$

Moreover,

$$H_r = \frac{1}{\hat{z}} \left(\frac{\partial^2}{\partial r^2} + k^2 \right) F_r$$

so that

$$H_r = \begin{cases} \frac{I_m}{jk} \sum_{n=1}^{\infty} \frac{-(2n+1)}{2n(n+1)} \hat{H}_n^{(2)}(ka) P'_n(0) P_n(\cos \theta) \left[\hat{J}_n''(kr) + k^2 \hat{J}_n(kr) \right] & \text{for } r < a, \\ \frac{I_m}{jk} \sum_{n=1}^{\infty} \frac{-(2n+1)}{2n(n+1)} \hat{J}_n(ka) P'_n(0) P_n(\cos \theta) \left[\hat{H}_n^{(2)''}(kr) + k^2 \hat{H}_n^{(2)}(kr) \right] & \text{for } r > a. \end{cases} \quad (4.72)$$

Finally,

$$H_\theta = \frac{1}{\hat{z}r} \frac{\partial^2 F_r}{\partial r \partial \theta}$$

in which case

$$H_\theta = \begin{cases} \frac{I_m}{jkr} \sum_{n=1}^{\infty} \frac{-(2n+1)}{2n(n+1)} \hat{H}_n^{(2)}(ka) P'_n(0) \hat{J}'_n(kr) P'_n(\cos \theta) & \text{for } r < a, \\ \frac{I_m}{jkr} \sum_{n=1}^{\infty} \frac{-(2n+1)}{2n(n+1)} \hat{H}_n^{(2)'}(kr) P'_n(0) \hat{J}_n(ka) P'_n(\cos \theta) & \text{for } r > a. \end{cases} \quad (4.73)$$

This formulation turned out to be very robust and converges very quickly. It does not model the shape of one of the sources used in the experiment, but it does model the magnetic source that was mounted to the bow of a boat. This formulation also allows for a convenient change in loop size for different size sources.

4.4 Square Loop: Far Field Approximation

This final formulation of the current loop problem is for far-field observations. This simplification allows for a completely different development and a direct comparison to other methods, where all are considered to be in the far field.

Consider again the square loop described in Figure 4.2. If we consider only the fields such that $r \gg r'_{max}$, as suggested in Fig. 3-22 of [3], then

$$\left| r - r' \right| \rightarrow r - r' \cos(\xi). \quad (4.74)$$

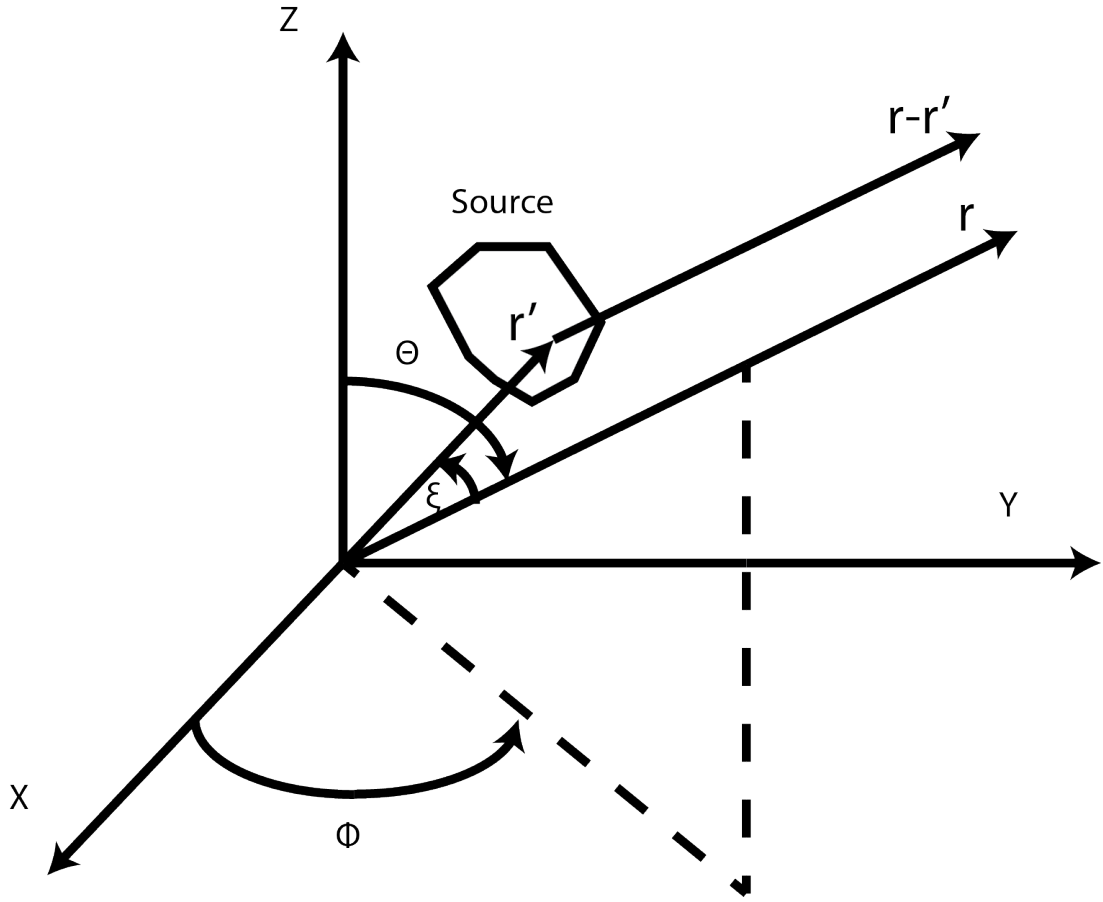


Figure 4.3: Geometry for evaluating the radiation field.

The second term of Eqn. (4.74) can be neglected in the magnitude factors but it cannot be neglected in the phase factors unless $r'_{max} \ll \lambda$. If this approximation is applied to the vector potentials then

$$\vec{A} = \frac{e^{-jkr}}{4\pi r} \iiint \vec{J}(r') e^{jkr' \cos(\xi)} d\tau'. \quad (4.75)$$

By using conventional transformations between Cartesian and spherical coordinates, we obtain

$$r' \cos(\xi) = \left(x' \cos \phi + y' \sin \phi \right) \sin \theta + z' \cos \theta. \quad (4.76)$$

By substituting Eqn. (4.76) and the current \vec{J}_1 , as given by Eqn. 4.5, into Eqn. (4.75) we obtain for one leg of the loop,

$$\begin{aligned} \vec{A}_1 = \frac{e^{-jkr}}{4\pi r} \iiint I_m \hat{a}_x \delta\left(y' + \frac{L}{2}\right) \delta(z') \left[u\left(x' + \frac{L}{2}\right) - u\left(x' - \frac{L}{2}\right) \right] \\ \times e^{jk\left(x' \cos \phi + y' \sin \phi\right) \sin \theta} dx' dy' dz'. \end{aligned} \quad (4.77)$$

This previous equation reduces to

$$\vec{A}_1 = \frac{e^{-jkr}}{4\pi r} \int_{-\frac{L}{2}}^{\frac{L}{2}} I_m \hat{a}_x e^{jk(x' \cos \phi - \frac{L}{2} \sin \phi) \sin \theta} dx'. \quad (4.78)$$

Repeating this process for the current \vec{J}_2 , as given by Eqn. 4.7, we obtain,

$$\vec{A}_2 = -\frac{e^{-jkr}}{4\pi r} \int_{-\frac{L}{2}}^{\frac{L}{2}} I_m \hat{a}_x e^{jk(x' \cos \phi + \frac{L}{2} \sin \phi) \sin \theta} dx'. \quad (4.79)$$

Superposition of \vec{A}_1 and \vec{A}_2 yields an expression for A_x

$$A_x = \frac{I_m}{4\pi} \frac{e^{-jkr}}{r} \int_{-\frac{L}{2}}^{\frac{L}{2}} e^{jk(x' \cos \phi - \frac{L}{2} \sin \phi) \sin \theta} - e^{jk(x' \cos \phi + \frac{L}{2} \sin \phi) \sin \theta} dx', \quad (4.80)$$

which is equivalent to

$$A_x = \frac{I_m L}{j2\pi} \frac{e^{-jkr}}{r} \sin \left(\frac{kL}{2} \sin \phi \sin \theta \right) \text{sinc} \left[k \frac{L}{2} \cos \phi \sin \theta \right], \quad (4.81)$$

where $\text{sinc}(x) = \sin x/x$. If the same procedure is followed for \vec{J}_3 and \vec{J}_4 , then

$$A_y = \frac{-I_m L}{j2\pi} \frac{e^{-jkr}}{r} \sin \left(\frac{kL}{2} \cos \phi \sin \theta \right) \text{sinc} \left[k \frac{L}{2} \sin \phi \sin \theta \right]. \quad (4.82)$$

Within the radiation zone of some homogeneous medium the electric and magnetic fields are characterized by

$$E_\theta = \eta H_\phi \quad (4.83)$$

$$E_\phi = -\eta H_\theta \quad (4.84)$$

where

$$E_\theta = -j\omega\mu A_\theta \quad (4.85)$$

$$E_\phi = -j\omega\mu A_\phi. \quad (4.86)$$

Again, by making use standard transformations of the coordinate components from Cartesian to spherical, we see that

$$A_\phi = -A_x \sin \phi + A_y \cos \phi \quad (4.87)$$

$$A_\theta = A_x \cos \theta \sin \phi + A_y \cos \theta \cos \phi. \quad (4.88)$$

The comparisons between the different formulations are provided in Section 4.5.

4.5 Current Loop Comparisons

The following show results and comparisons between the different formulations of the loop antenna. Table 4.1 lists the four different observation sweep lines that were used for comparison. Although there are only four sweeps listed other comparisons were made and the results were all very favorable, but data are not provided. In the following comparisons, “General” refers to the fields as derived in Section 4.2 and “Harrington” refers to the fields as derived in Section 4.3.

Problem Statement:

- H-source strength: 1 Am^2
- Frequency = 10 Hz, 100 Hz and 1000 Hz
- Material parameters: $\sigma = 0 \text{ S/m}$ and $\epsilon_r = 1$

4.5.1 Homogeneous Comparisons

Table 4.1: Sweep Lines

Sweep	X1	Y1	Z1	X2	Y2	Z2
Line 1	-10	-10	0	-130	-130	130
Line 2	-100	100	-130	-100	100	130
Line 3	-130	5	10	130	5	10
Line 4	-130	-100	-50	100	130	-50

4.5.1.1 Line 1 at 1000 Hz

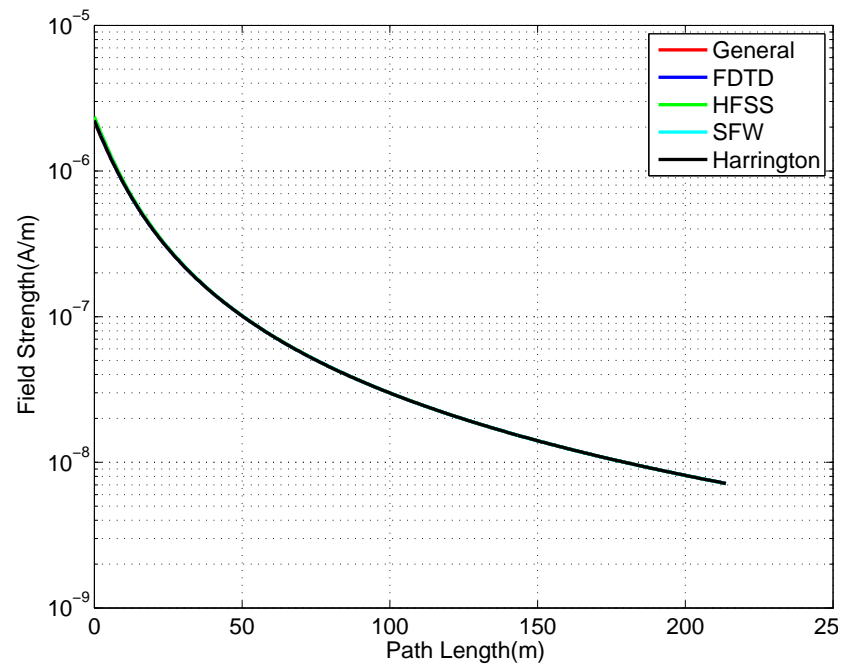


Figure 4.4: Line 1, magnitude of E_x field. General, SFW and FDTD are hidden by the other traces.

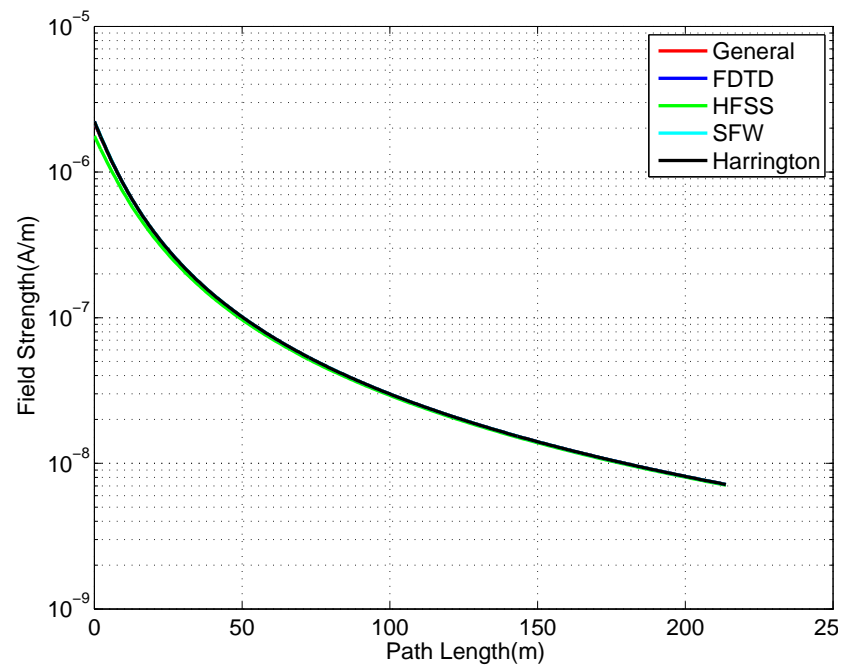


Figure 4.5: Line 1, magnitude of E_y field. General, SFW and FDTD are hidden by the other traces.

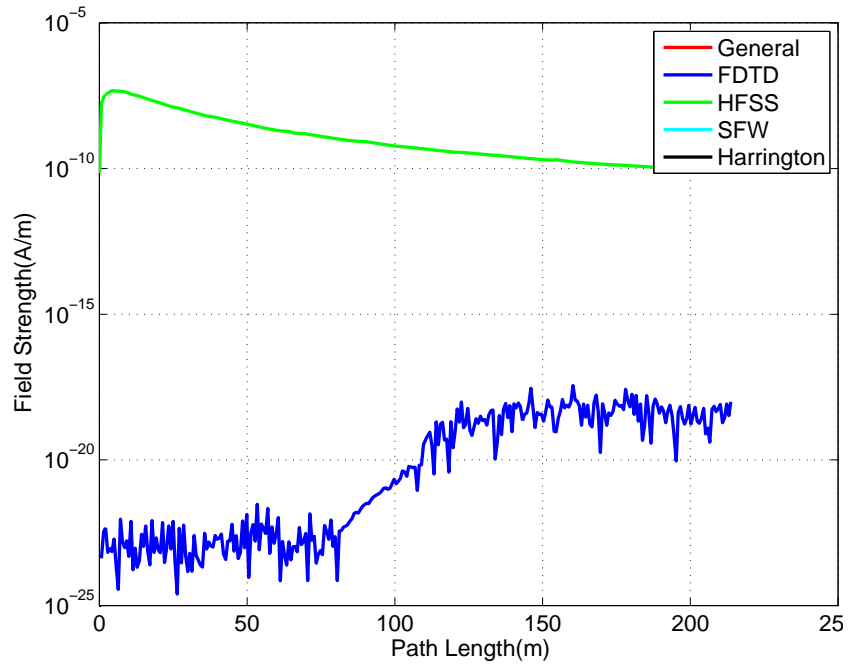


Figure 4.6: Line 1, magnitude of E_z field. General, SFW and Harrington calculate zero for this component.

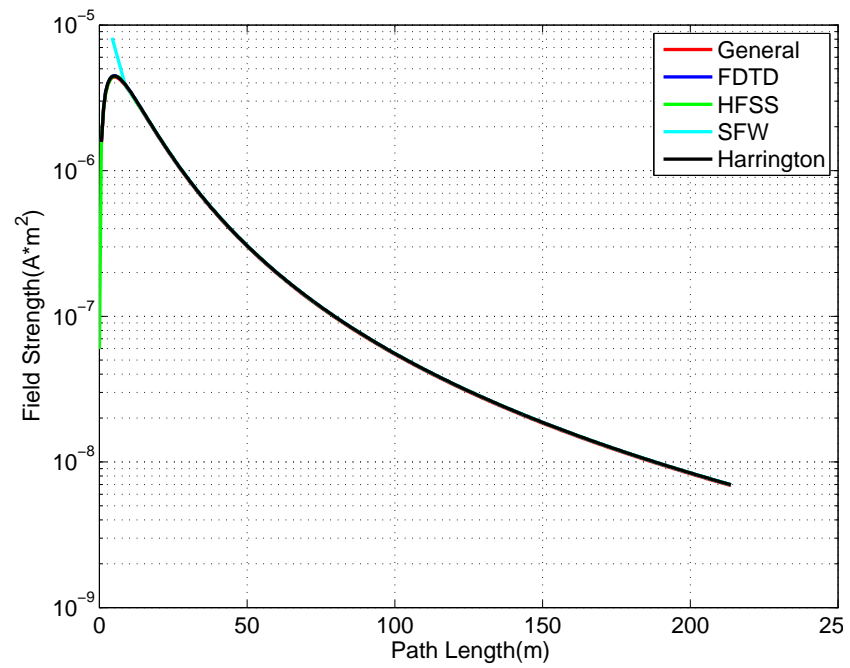


Figure 4.7: Line 1, magnitude of H_x field. General and FDTD are hidden by the other traces.

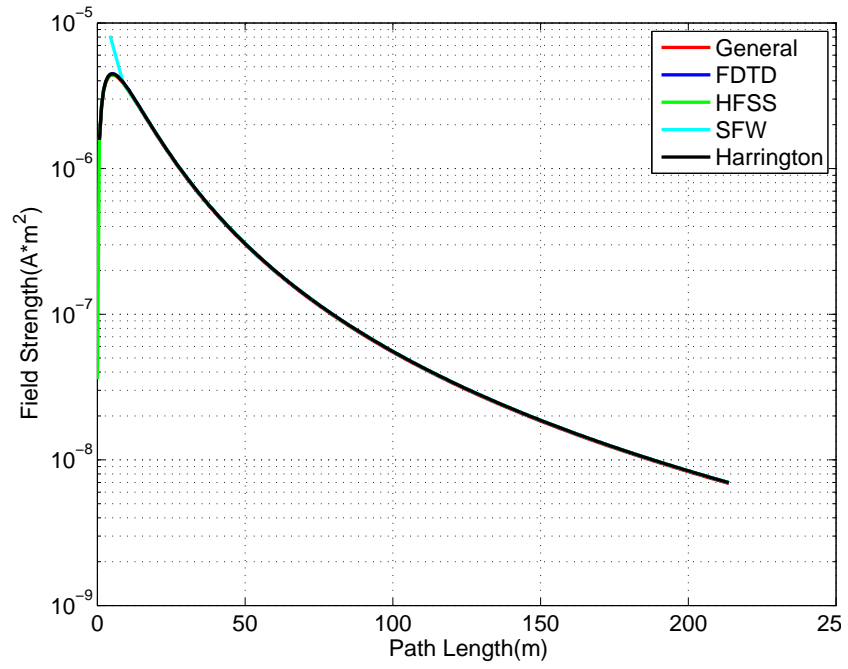


Figure 4.8: Line 1, magnitude of H_y field. General and FDTD are hidden by the other traces.

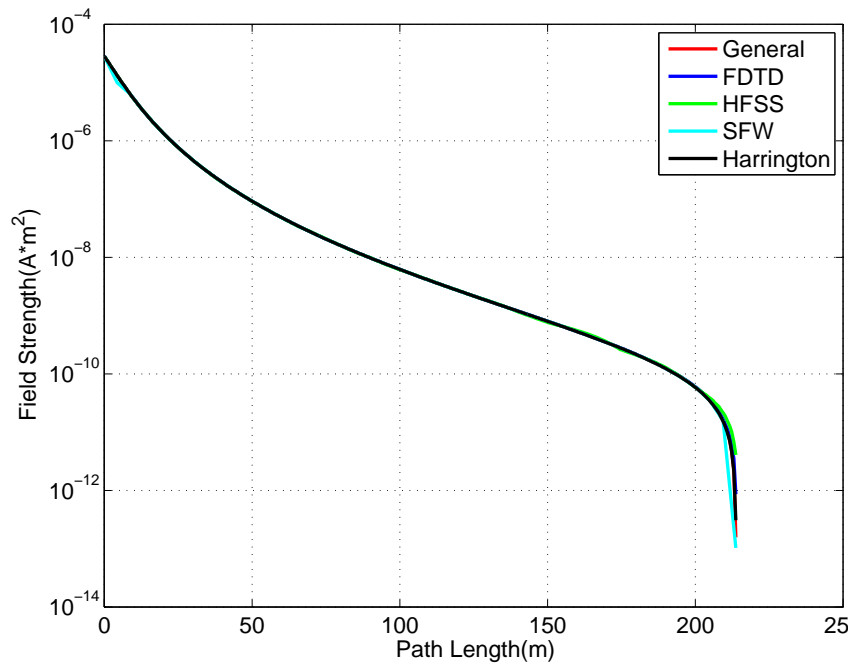


Figure 4.9: Line 1, magnitude of H_z field. General and FDTD are hidden by the other traces.

4.5.1.2 Line 2 at 10 Hz

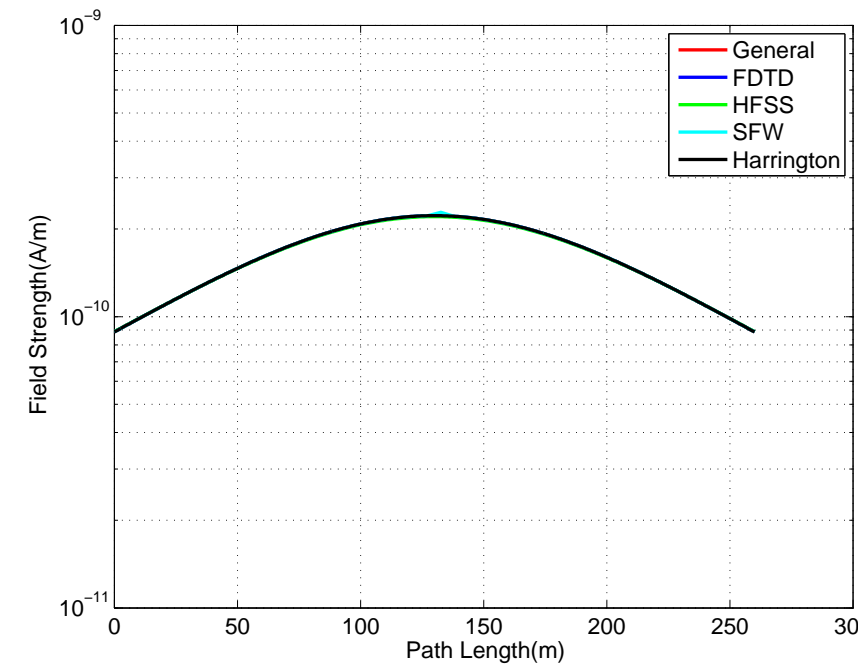


Figure 4.10: Line 2, magnitude of E_x field. General, HFSS and FDTD are hidden by the other traces.

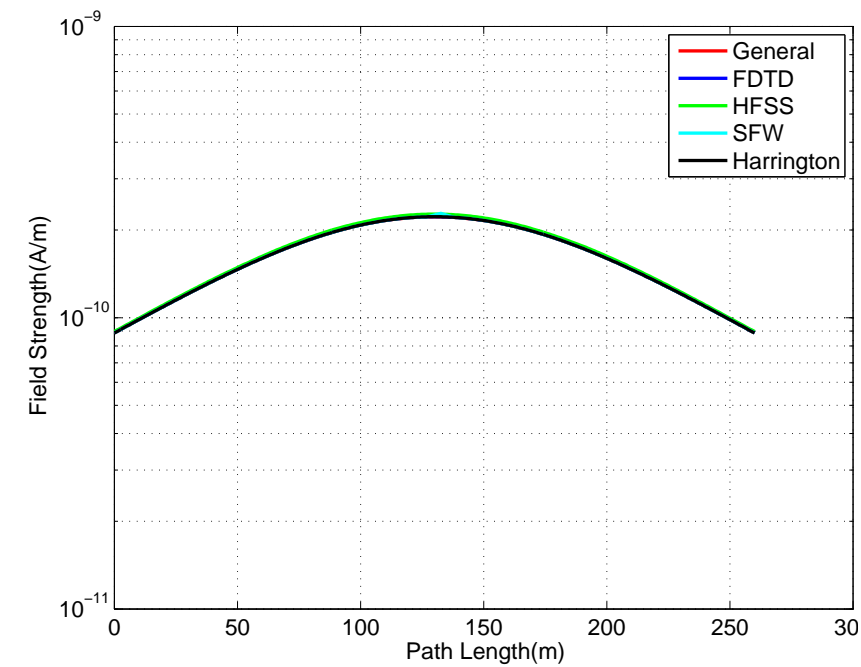


Figure 4.11: Line 2, magnitude of E_y field. General, SFW and FDTD are hidden by the other traces.

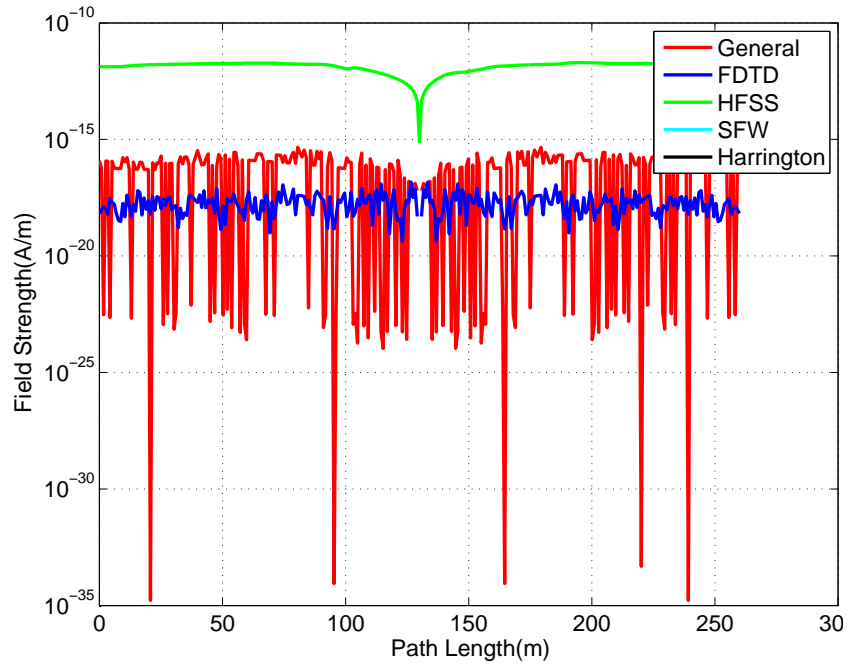


Figure 4.12: Line 2, magnitude of E_z field. SFW and Harrington calculate zero for this component.

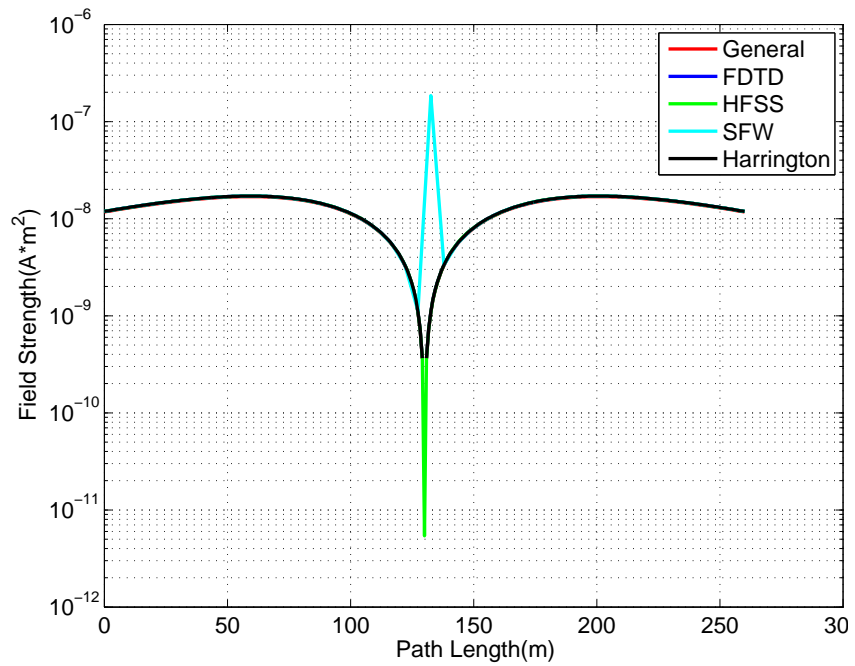


Figure 4.13: Line 2, magnitude of H_x field. General and FDTD are hidden by the other traces.

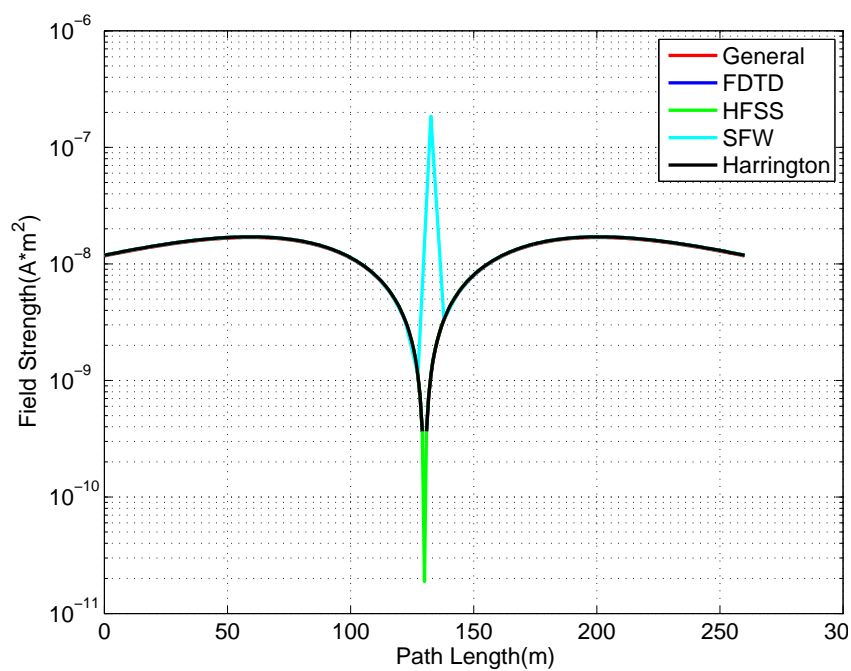


Figure 4.14: Line 2, magnitude of H_y field. General and FDTD are hidden by the other traces.

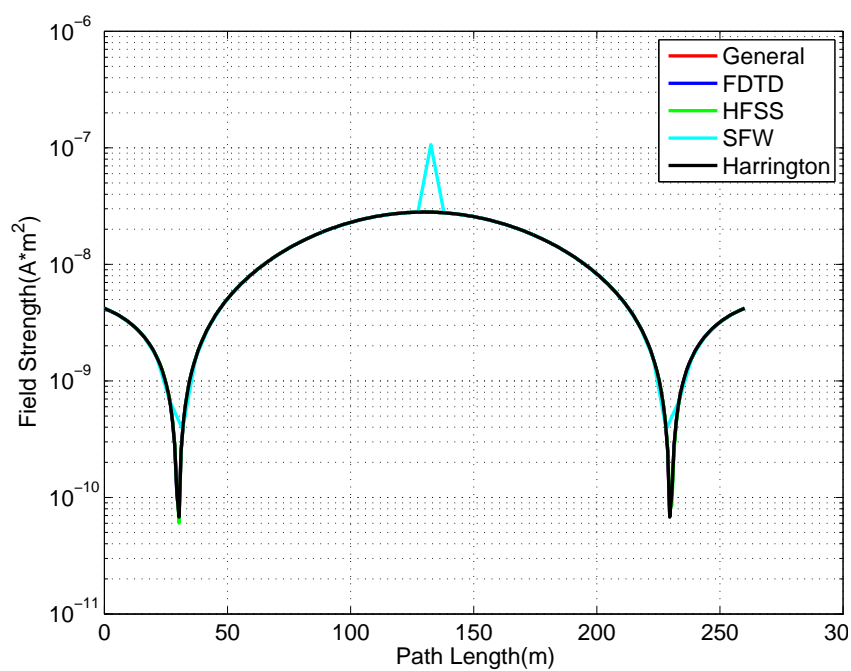


Figure 4.15: Line 2, magnitude of H_z field. General, FDTD and HFSS are hidden by the other traces.

4.5.1.3 Line 3 at 1000Hz

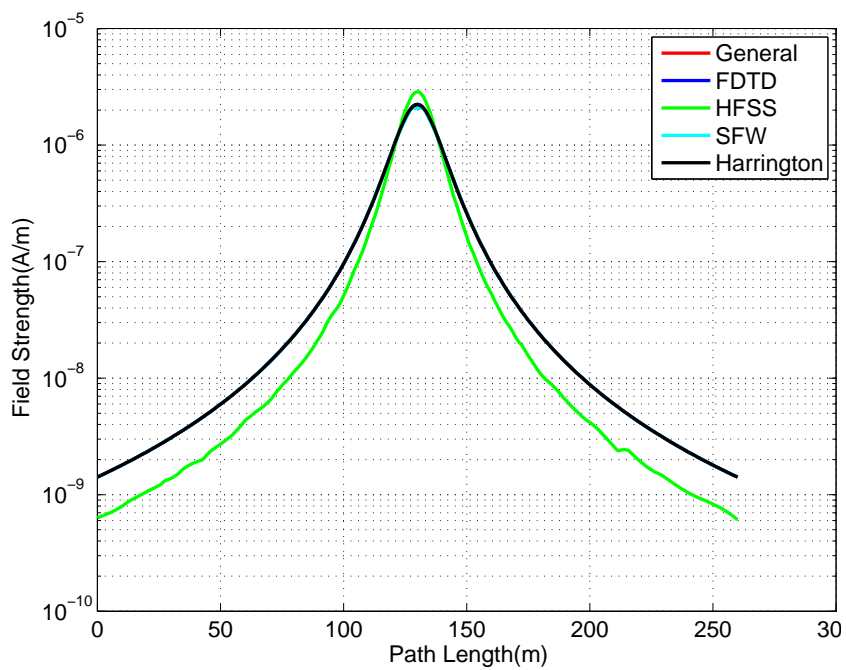


Figure 4.16: Line 3, magnitude of E_x field. General, FDTD and SFW are hidden by the other traces.

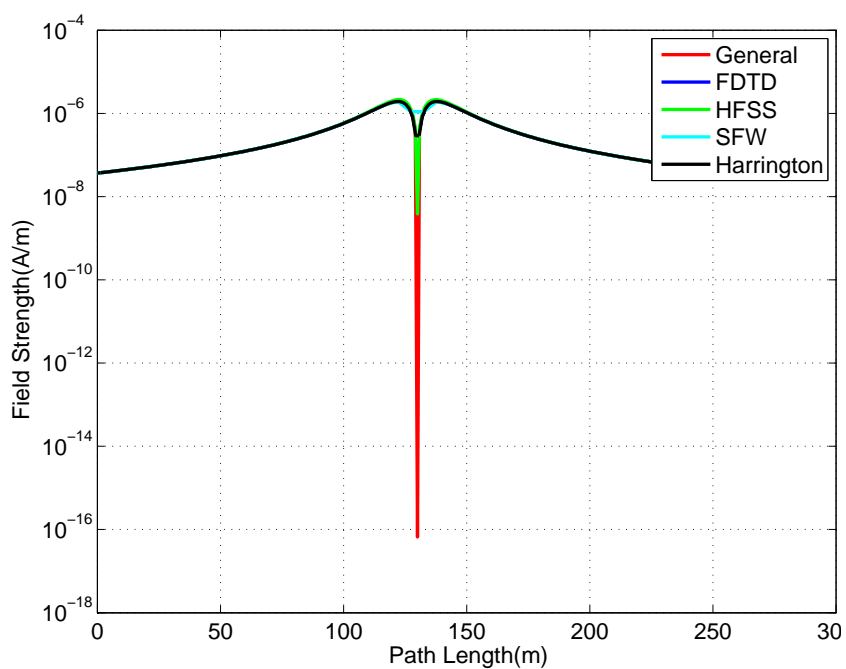


Figure 4.17: Line 3, magnitude of E_y field. FDTD is hidden by the other traces.

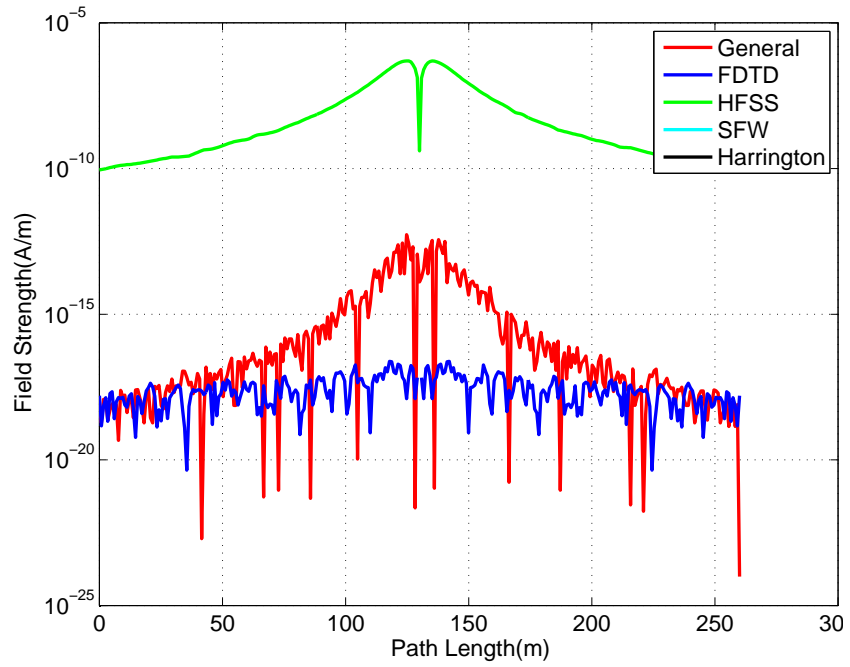


Figure 4.18: Line 3, magnitude of E_z field. SFW and Harrington calculate zero for this component.

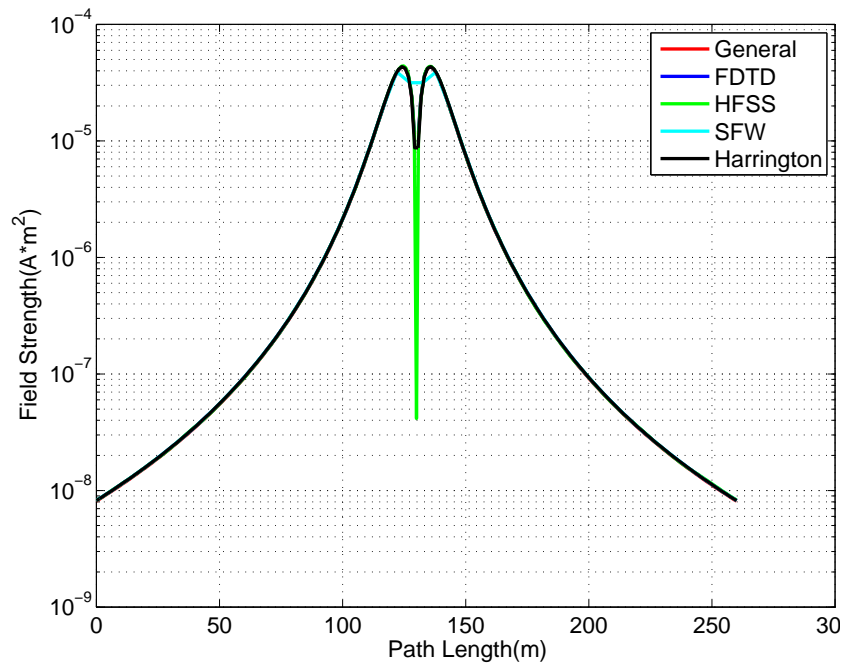


Figure 4.19: Line 3, magnitude of H_x field. General and FDTD are hidden by the other traces.

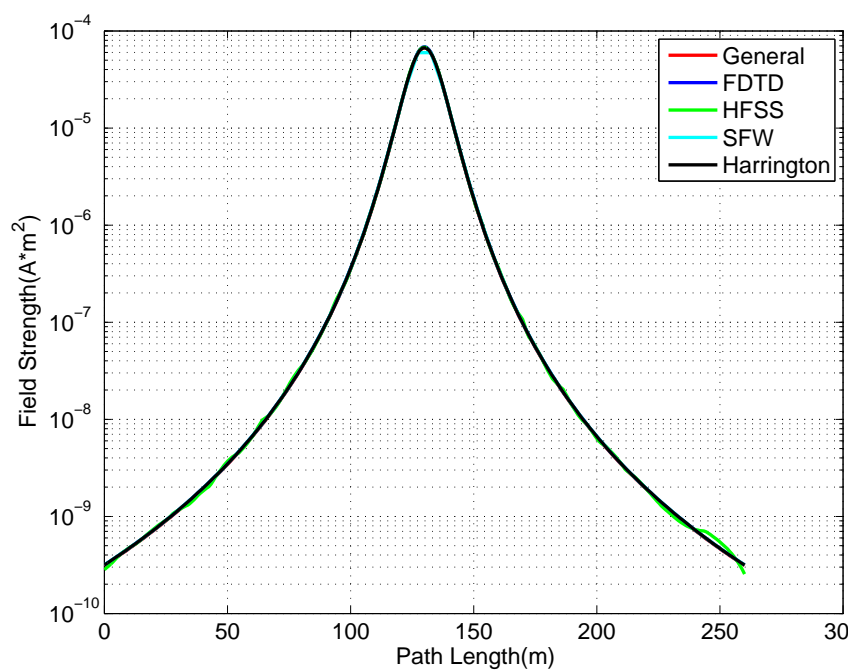


Figure 4.20: Line 3, magnitude of H_y field. General, FDTD and SFW are hidden by the other traces.

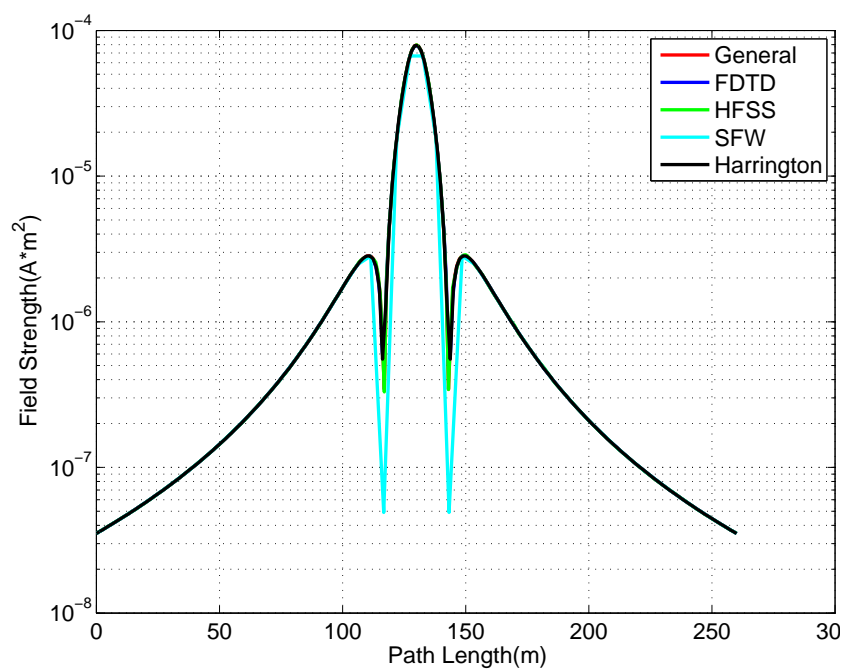


Figure 4.21: Line 3, magnitude of H_z field. General and FDTD are hidden by the other traces.

4.5.1.4 Line 4 at 100Hz

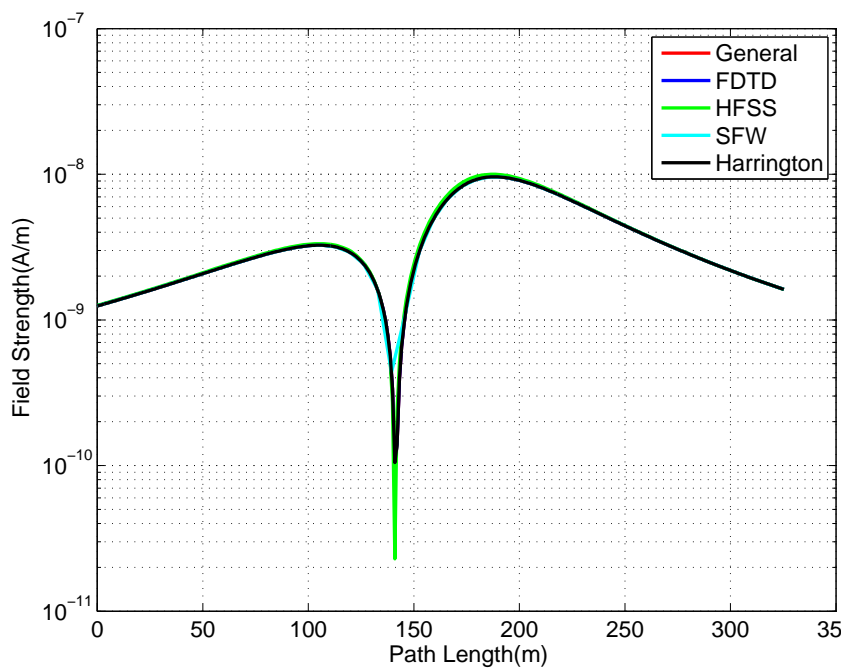


Figure 4.22: Line 4, magnitude of E_x field. General and FDTD are hidden by the other traces.

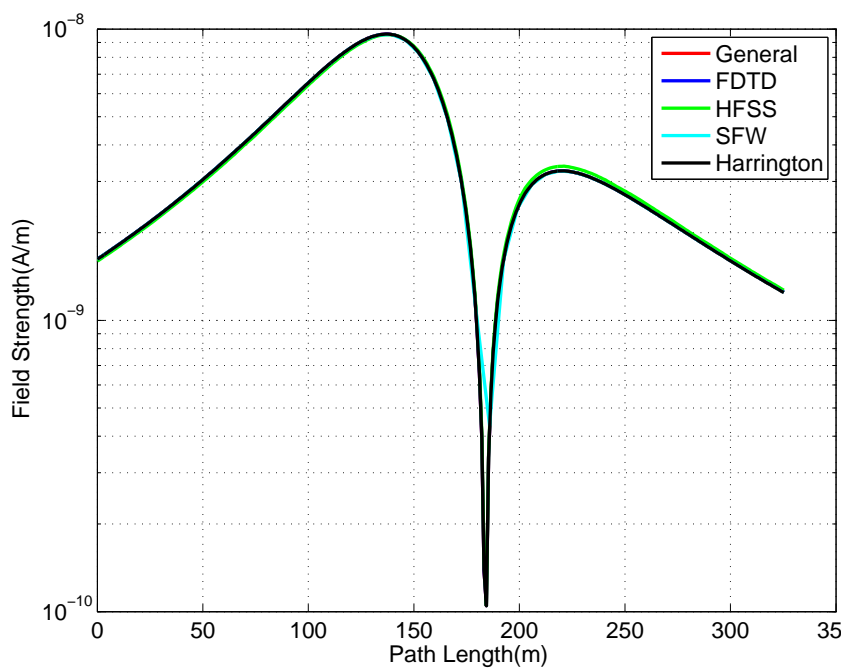


Figure 4.23: Line 4, magnitude of E_y field. General and FDTD are hidden by the other traces.

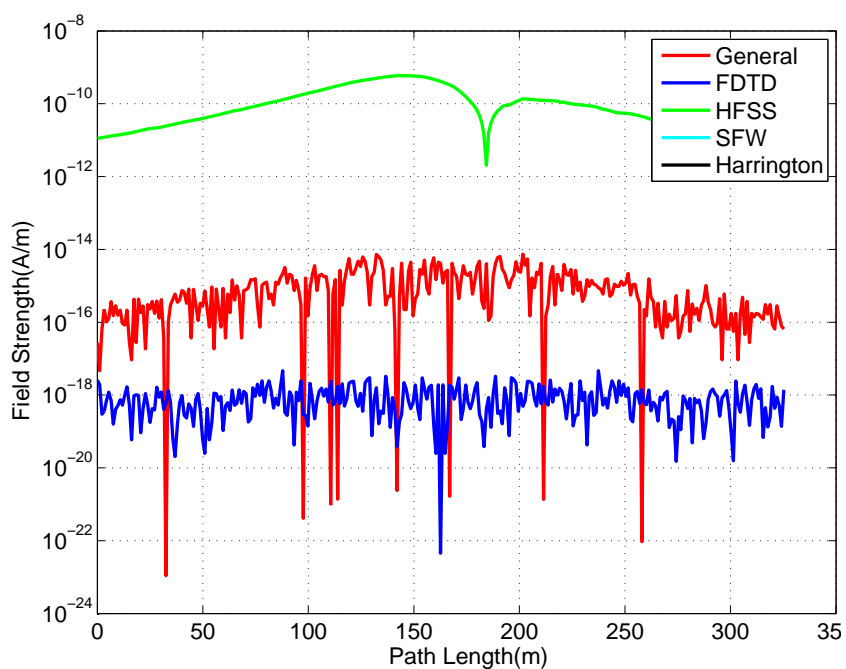


Figure 4.24: Line 4, magnitude of E_z field. SFW and Harrington calculate zero for this component.

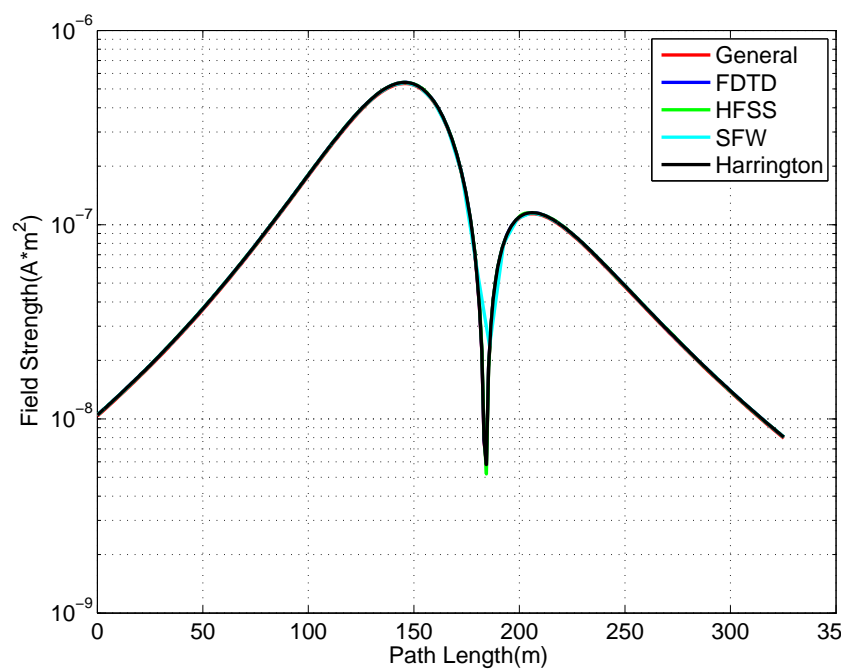


Figure 4.25: Line 4, magnitude of H_x field. General and FDTD are hidden by the other traces.

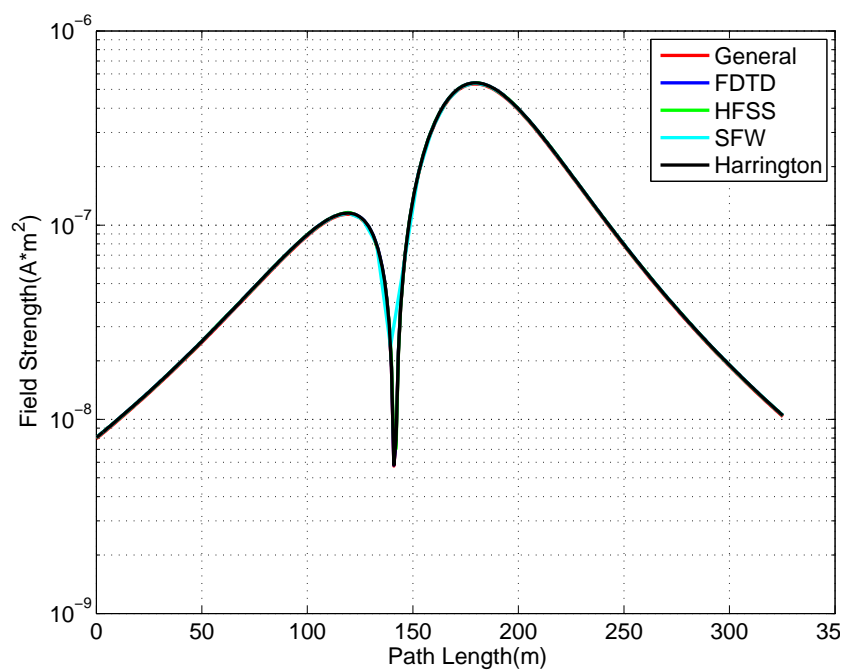


Figure 4.26: Line 4, magnitude of H_y field. General, FDTD and HFSS are hidden by the other traces.

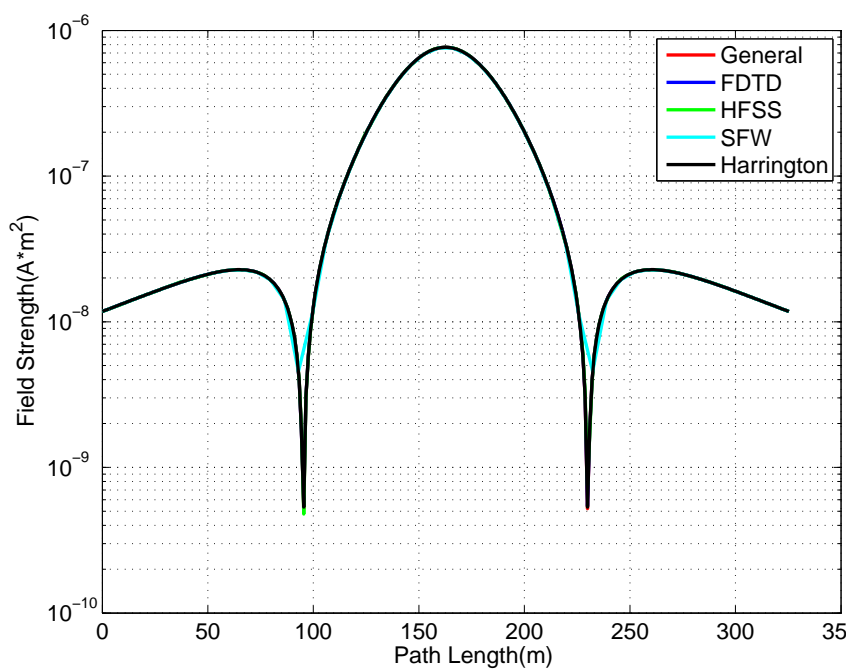


Figure 4.27: Line 4, magnitude of H_z field. General, FDTD and HFSS are hidden by the other traces.

The four comparisons shown illustrate the excellent correlation between the different methods. The general form formulation does well in most cases but in some situations it is susceptible to a numerical noise floor. This might be helped with better integration methods.

4.5.2 Three Layer Comparisons

Consider again the three layer stratified domain in Fig. 3.6. It was desired to know if the air-water interface would have any effect on the signal of a magnetic source. In order to answer that question a set of comparisons were made in which a homogeneous model was compared to the three layer model of Fig. 3.6. In this comparison of problems, the sources of both cases occupy the same point in space as does the observation point. The only difference between the two is that one has a domain filled with air and the other with layered material.

Source in Air

Problem Statement:

- Water depth: $d = 300$ m
- Water surface: $z = 0$
- Source height: $z = 10$
- H-source: 1 m by 1 m loop
- Frequency = 100 Hz

Material Parameters:

- Region 1: $\sigma = 0$ S/m and $\epsilon_r = 1$
- Region 2: $\sigma = 0.018$ S/m and $\epsilon_r = 81$
- Region 3: $\sigma = 0.012$ S/m and $\epsilon_r = 1$

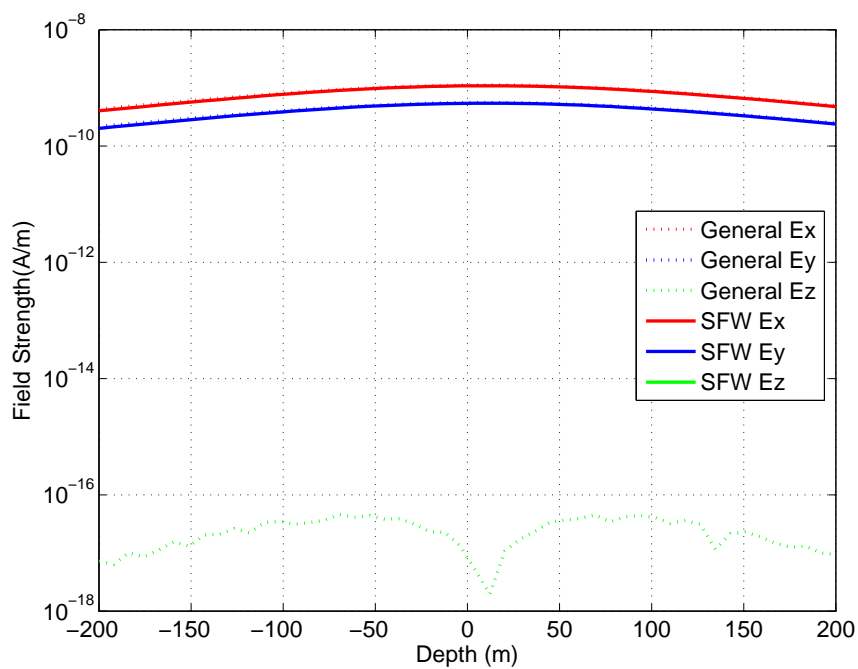


Figure 4.28: Magnitude of the electric field components.

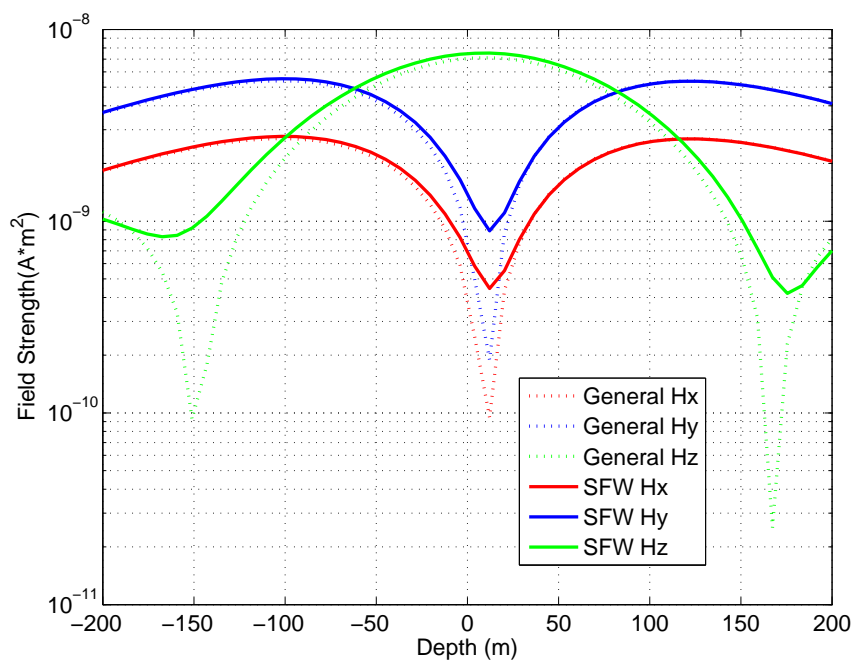


Figure 4.29: Magnitude of the magnetic field components.

Source in Water

Problem Statement:

- Water depth: $d = 300$ m
- Water surface: $z = 0$
- Source depth: $z = -10$
- H-source: 1 m by 1 m loop
- Frequency = 10 Hz

Material Parameters:

- Region 1: $\sigma = 0$ S/m and $\epsilon_r = 1$
- Region 2: $\sigma = 0.018$ S/m and $\epsilon_r = 81$
- Region 3: $\sigma = 0.012$ S/m and $\epsilon_r = 1$

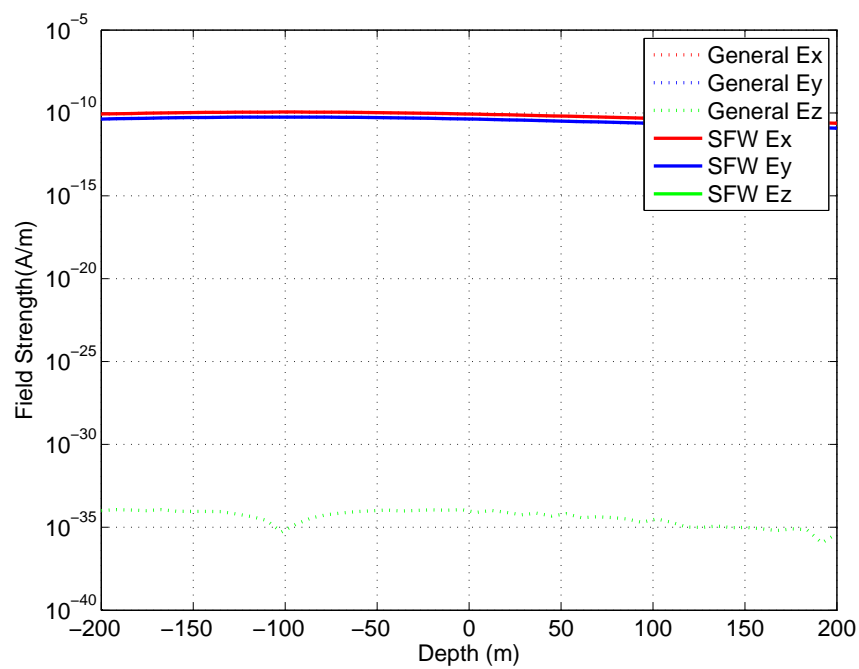


Figure 4.30: Magnitude of the electric field components.

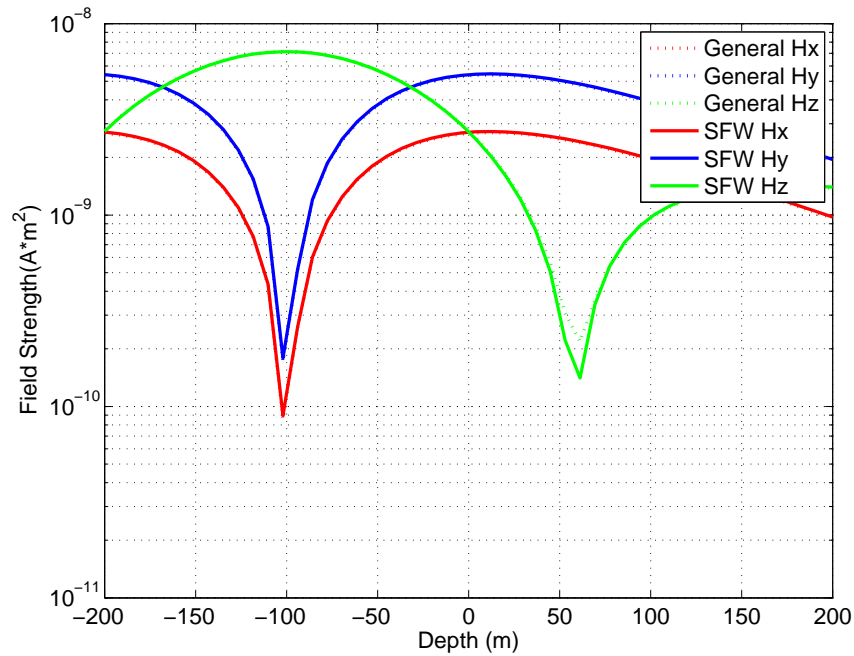


Figure 4.31: Magnitude of the magnetic field components.

Source in Deep Water

Problem Statement:

- Water depth: $d = 300$ m
- Water surface: $z = 0$
- Source depth: $z = -100$
- H-source: 1 m by 1 m loop
- Frequency = 1000 Hz

Material Parameters:

- Region 1: $\sigma = 0$ S/m and $\epsilon_r = 1$
- Region 2: $\sigma = 0.018$ S/m and $\epsilon_r = 81$
- Region 3: $\sigma = 0.012$ S/m and $\epsilon_r = 1$

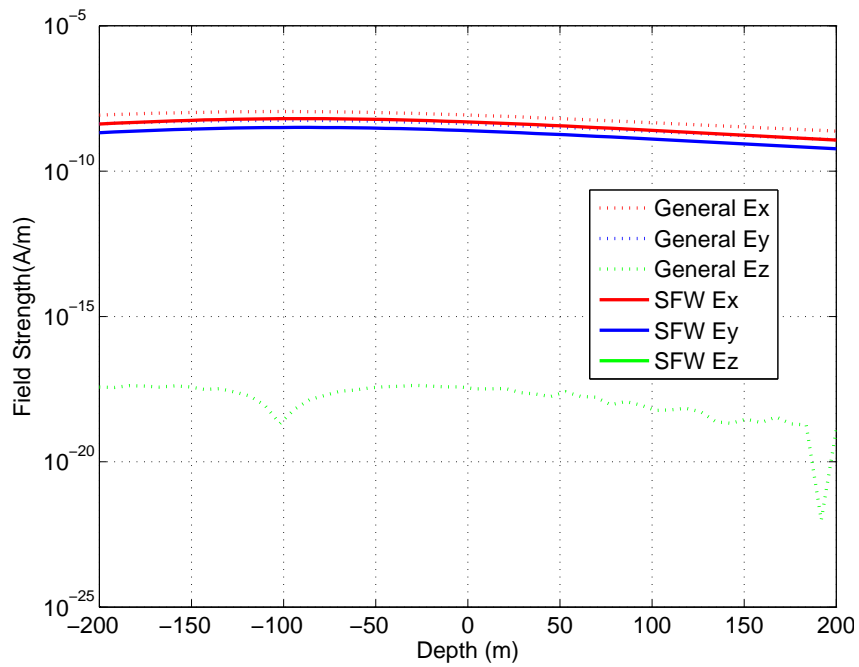


Figure 4.32: Magnitude of the electric field components.

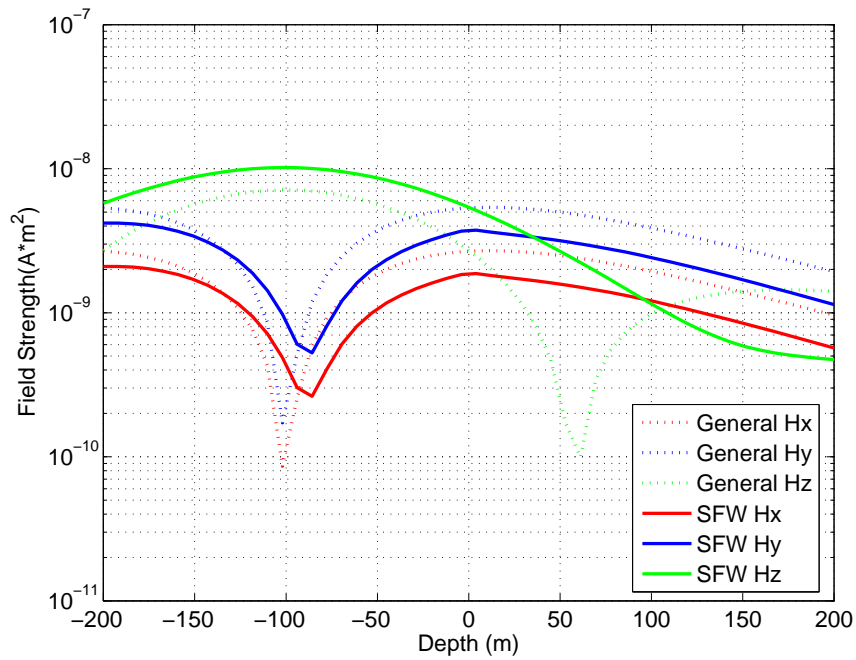


Figure 4.33: Magnitude of the magnetic field components.

The three previous scenarios are part of a set of 9 comparisons that were made. The set of comparisons that were made consist of 3 different source locations and 3 different frequencies each. These comparisons have made it clear that the presence of the air-water interface does in

fact influence the fields. The comparisons also reveal that the influence is related to frequency. The higher the frequency, the stronger the effects of the interface are seen on the fields. Section 4.5.2 shows excellent correlation between the two different simulation tools. Both electric fields and magnetic fields show very little differences. The only difference is the E_z component. This is not a problem however. That component evaluates identically to zero for SFW and is essentially zero for the general solution as well. Next is the scenario in Section 4.5.2. This simulation was conducted at 100 Hz instead of at the 10 Hz of the previous example. The electric fields again correlate very well with E_z being the only outlier and for the same reason as stated previously. The magnetic fields, however, start to show some differences. Nulls associated with the three layer model (i.e. SFW) no longer go as deep as for the homogeneous (i.e. General) model. There is also a slight separation in the H_z components. Overall the magnetic fields still correlate very well. The final scenario, for which the results are shown in section 4.5.2, show even more divergence from the homogeneous solution. This comparison is at 1000 Hz. The electric fields now begin to show a slight deviations from each other but overall they are very well correlated. The E_z component still is an outlier for the aforementioned reasons. The magnetic fields of this scenario are clearly different. The H_x and H_y components are now starting to diverge and have different null locations. The H_z of the three layer model is now calculating a different trend and missing a null location all together. In comparisons to the results at 10 Hz this is clearly different and the interface does have an strong effect on the magnetic field while a having a very weak effect on the electric field. This conclusion meets our expectations. The electric field will be influenced by charge on the air-water interface and the magnetic field will be influenced by induced eddy currents. The former is weakly induced by a loop of current and is frequency independent at low frequencies. The latter effect is strongly dependent on frequency. In comparison to the scenarios from Chapter 3 the results are still very good.

Chapter 5

Experimental Data Management and Processing

Given the amount of experimental data collected in any given experiment, the management and processing of that data is an important component of the ELF project. With each experiment creating tens of gigabytes of data, the processing of that data created hundreds of gigabytes of more data. The simulations created even more data. And with the dozens of documents and hundreds of plots and graphs, it quickly became apparent that a system or strategy for management of all this data was needed. Not only was the shear volume of data difficult to deal with, but the non-uniformity of the data formats that came out of the experiments and simulation tools made it difficult to determine sources of errors and to make sure all data was being used properly. With these challenges in mind a strategy was devised to coordinate data management. This is described next.

5.1 Data Matrix Format

The first challenge in the management of the experimental data was to take the various forms of the data produced by the experiments and convert them into a standard format that did not require the processing tools to be able to interpret the dozens of possible variations in format. To accomplish this the data are converted into a “standard” form that is called the Data Matrix

Format. To convert all this data, dozens of MatLab scripts were written to automate this process as much as possible.

The experimental data was organized into experimental numbers one through four. Next it was organized into days of the each experiment, typically five days per experiment. Then under each experimental day are the individual experimental runs. Under each individual run are all the source and sensor files for that particular run. Depending on the experiment, source, day, and run time there could be hundreds to thousands of data files.

There are also five sets of files for each second of experimental data collected: a sensor signal file, source signal file, a source orientation file, and a GPS file for both source and sensor. These files are all standardized so that the main analysis script has a consistent input from each experiment and anything that had to be uniquely dealt with would be taken care of in the preprocessing MatLab scripts.

5.2 MatLab Preprocessing Scripts

The need to standardize the data from the experiments meant that an automated process needed to be devised. Many software tools could have done this job but MatLab was chosen because of its simplicity in implementing the scripts, its universal availability and its relative speed in processing data. Five different MatLab scripts were created for each day of each experiment. Each script processes the appropriate experimental data for a particular output file. The scripts transform, modify, calculate or create place holders for this file and in general do whatever is necessary to format the files into standard form.

5.3 Main Analysis Script

The main analysis script is the MatLab code that is responsible for analysing a selected set of experimental data. The code is written with the expectation that all data is in Data Matrix Format. After analysing the desired set of data, the main analysis script outputs various parameters that are needed to replicate the experiment in simulation and format the analysed data for comparison. Fig. 5.1 is a flow diagram that illustrates the process that the main

analysis script takes in analysing experimental data. The code starts by having the user input information about the type of data to be examined. Next the script checks the data to make sure that all needed parts of the data are present and what sets of data to allow. After collecting all the appropriate data it is rotated into a common coordinate system and the time domain signal data is transformed using Fast Fourier Transforms (FFT). This data is then compiled and exported so that it can be used to set up simulations and to establish an experimental benchmark.

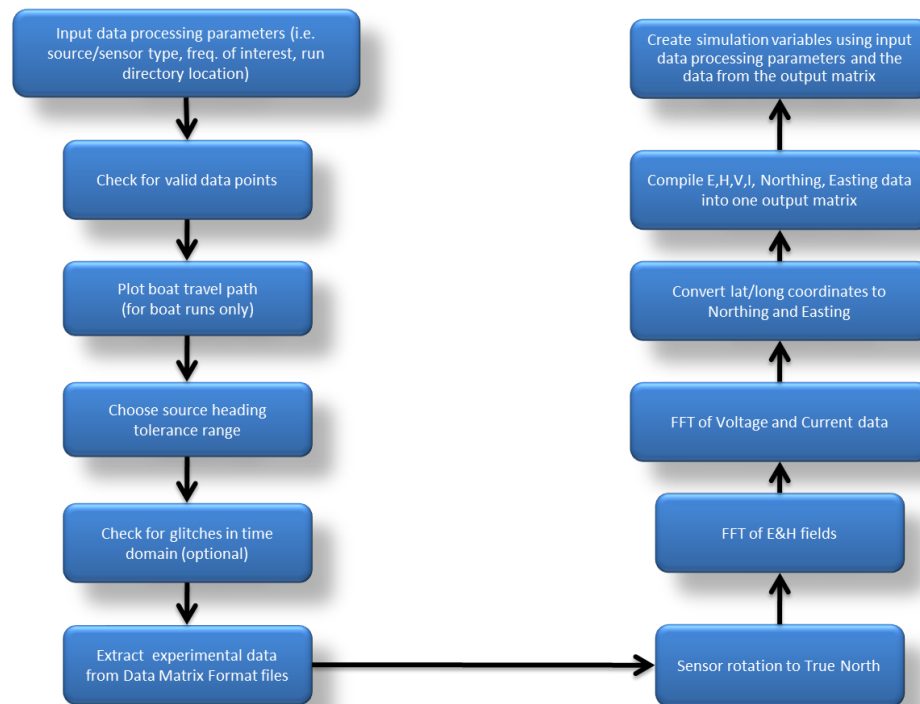


Figure 5.1: Flow diagram for Main Analysis Script.

Chapter 6

Model Building

To simulate the environment of an experiment it is necessary to create a model of that environment. The experiments of this project were conducted in a lake and therefore it was necessary to recreate that lake environment for simulation. This recreation of the lake is not a simple endeavour. It takes considerable time and effort to make a reasonable model. By reasonable, we mean that it is impossible to recreate the environment in infinite detail. It is also impractical to recreate it in even great detail. Inevitably, the model must make a compromise between accuracy and resolution for time and effort of the person doing the modelling. This chapter will discuss the many challenges involved in the creation of a simulation model of the type used in the ELF project and about the compromises needed in order to make it usable.

6.1 Map Data

The map data used in the construction of the Lake model has several important considerations. One consideration is how old the available data is. It may be correct to assume that the earth does not vary over spans of time on the order of decades, but depending on the external forces such as rivers and the influence of man, the terrain can change considerably and have a significant impact. This is not to say that a year old map will not be of use, but that some judgement is needed by the person that will be using it. The next consideration is relevant data. This is somewhat of an obvious statement but it is meant to illustrate that the map must have enough resolution in the area of interest so that significant interpolation is not needed. Next is

accuracy. Again this is a very obvious statement, but it is necessary to understand what kind of accuracy the map data has and this may not always be given or known. If the mistake of assuming that the topological data or bathymetric data is more accurate than it is in reality is made, then it may not show any obvious problems, but can result in missing significant structure that affected the experiment and are left out of models. The final consideration is the understanding the convention that the data is conforming to. There are many formats that topological data can be given in and there exists the possibility that non-standard conventions will be used that require reformatting. This is a significant challenge when obtaining data from multiple sources. Making all of the data sets in this project agree to the same standard took significant time to understand how each was defined and thus how each were related to each other. The map data used for the construction of the simulation models came from three sources: U.S.G.S map (1st ed. Sept. 1950), Idaho Geologic Survey Bathymetry AutoCAD Drawing and 10 m elevation data from InsideIdaho.org (Originates from U.S.G.S. EROS Data Center, 1999.)

6.1.1 Matlab Compilation and Interpolation

After the map data sets are chosen, data needs to be transformed into a single set, which can be accomplished using MatLab. Once the three data sets are made into a single matrix of irregular data points, we next use interpolation methods to create data at regular intervals in terms of a height field. This was decided because several of the tools that are used to create the models for the simulation worked better with regularly defined geometries. To get this regular height field MatLab is used to perform a linear interpolation on the data to create a new height field at points defined by the user at regular spacing. The spacing choice is arbitrary from the viewpoint of the interpolation, but will be relevant for many of the following tools.

6.2 AutoCAD

AutoCAD is a drafting software created by Autodesk. This project uses it to take the regular spaced height field that is created in MatLab and change it into a three dimensional solid

object. This object is constructed of regular surface triangles. Fig. 6.1 and Fig. 6.2 are examples of two regions of the experimental domain that have been processed and made into 3D models. This solid object can be imported into many of the simulation tools, such as HFSS. However, due to the high number of surface elements, the corresponding mesh in HFSS is too resolved to be practical for simulations. Hence, the mesh needs to be processed to lower the total number of tetrahedra used in HFSS. This can be done by creating a less resolved height field from MatLab and by interpolating with larger spacing, but this could lead to omission of topological details that are needed in the simulation and leave more surface elements in areas where not much, if any, changes in the surface are occurring. To address this need, we acquired a mesh processing tool called Cubit. Note that AutoCAD has its own limitations on computing and will not be able to handle extremely large mesh files. It has at present a limitation of 255 by 255 height points in the matrix that is imported from MatLab and this does not seem to be influenced by the amount of memory, computer architecture or operating system. This constraint appears to be a limitation hard-coded into AutoCAD. The size of this matrix does not influence the size of the domain, but rather it creates a dependency between the size of the domain and the resolution. The larger the desired domain, the less resolved the domain will be.

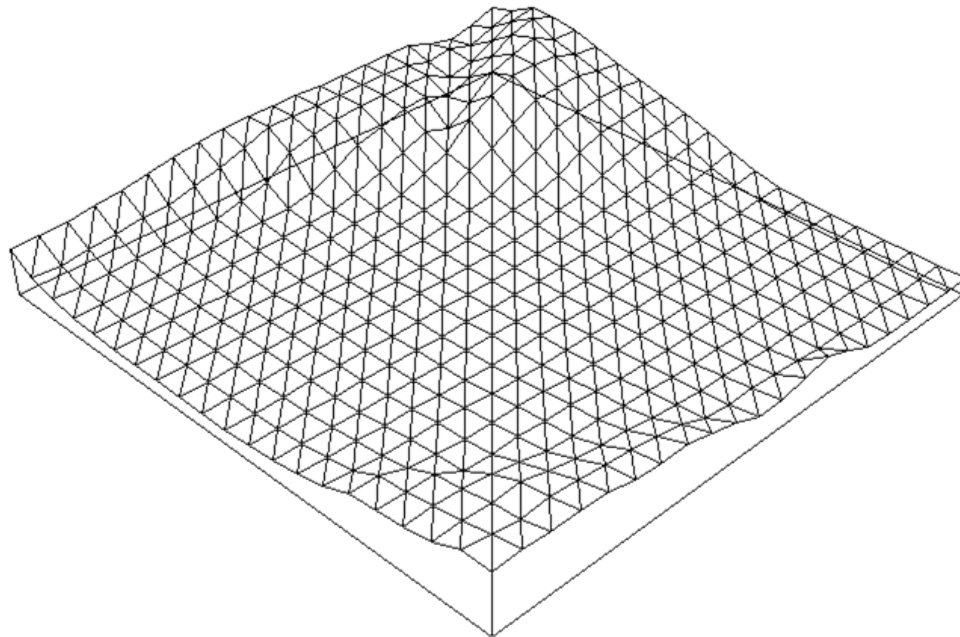


Figure 6.1: Example of an AutoCAD model.

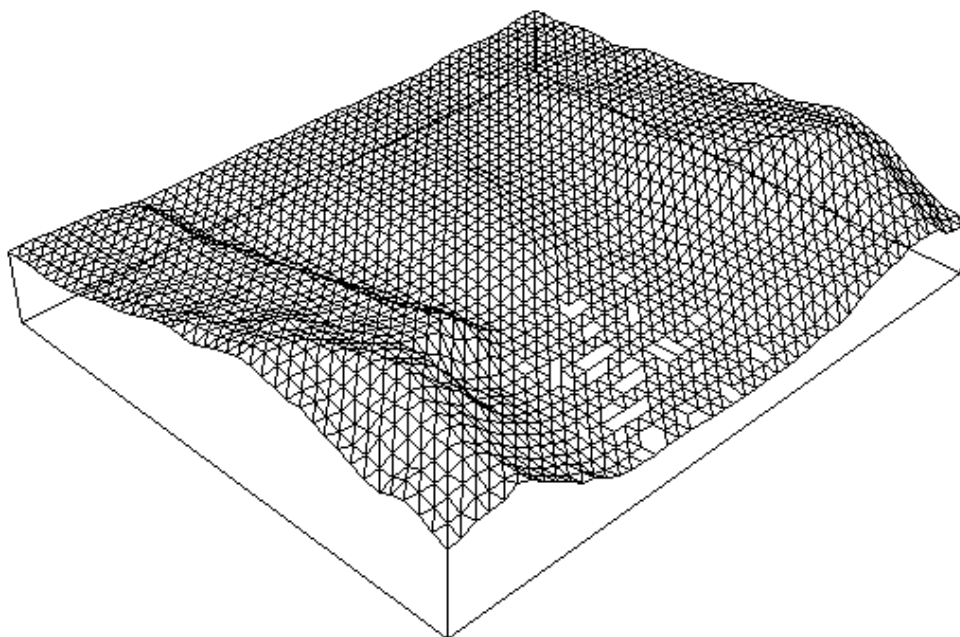


Figure 6.2: Example of an AutoCAD model.

6.3 Cubit

Cubit is a meshing program created by Sandia National Laboratories. Cubit is used in this project to redefine the surface mesh of the three dimensional objects created in AutoCAD. Cubit attempts to take areas of the topological surface that show little change and combine them into fewer, larger mesh elements; it takes areas of rapid change and converts them into smaller and higher concentrations of surface elements. By redefining the surface mesh in this manner, Cubit is able to reduce the computational burden of the model without necessarily sacrificing detail or accuracy. Like AutoCAD this tool does have a limitation on the size and resolution of the model being created. Cubit, however, is not limited in the same way that AutoCAD is. It is only limited by the resources of the computing platform. More memory, bigger bandwidth and faster processors all allow for bigger and more resolved models. Fig. 6.3 and Fig. 6.4 are examples of models that have undergone mesh processing by Cubit. These models are the finished models from Fig. 6.1 and Fig. 6.2, respectively. Note the change in size and number of surface elements and the concentration of elements in areas of varying terrain.

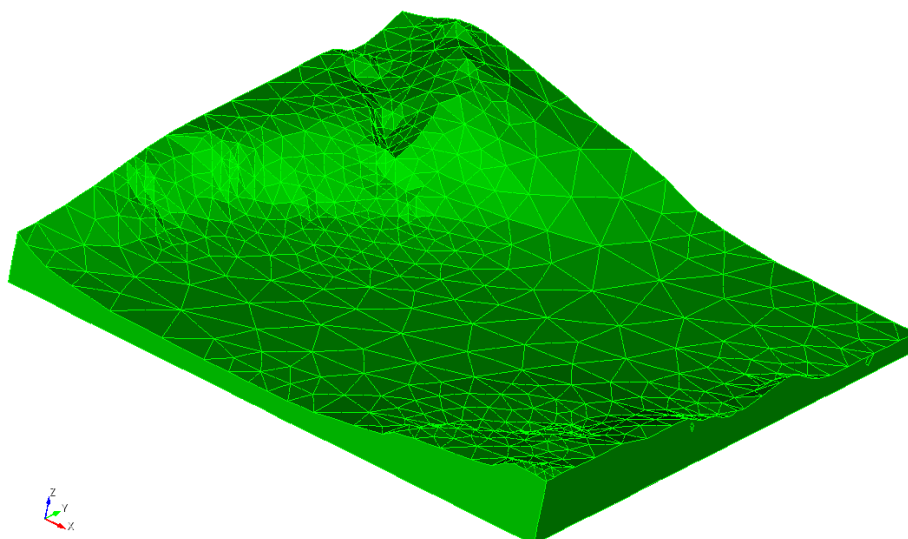


Figure 6.3: Example of Cubit faceted model.

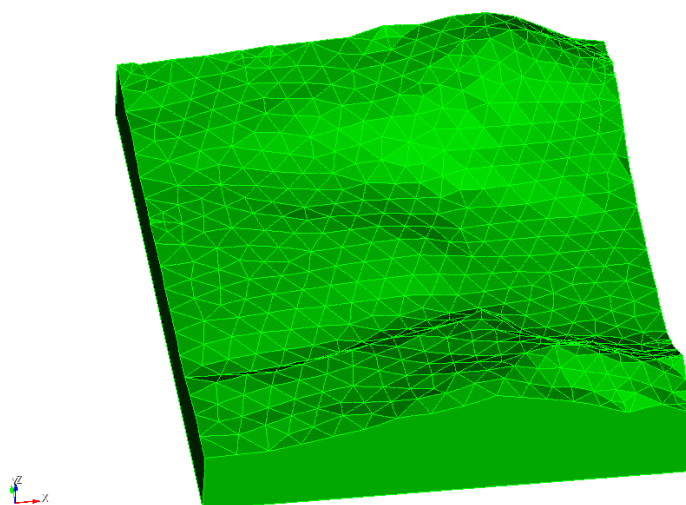


Figure 6.4: Example of Cubit faceted model (Idlewilde Bay).

6.4 HFSS VB Scripts

An alternative method for creating a model for use in HFSS is to use the Visual Basic (VB) functionality in the program. It is possible, for example, to have HFSS create a series of varying height rectangles such that when they are all combined they create a “stair-step” approximation of the desired model. This functionality is typically used to create rapidly new

models with predictable changes and to run simulations using these models after they are created. It also allows for outside programs to control and interface with HFSS easily. This project used the VB scrips and MatLab to create tens or hundreds of thousands of rectangles needed to create the solid. First, the height field created by Matlab is interpolated or decimated to the desired resolution. MatLab then reads this data point-by-point, creating a command line for each point and saving it to a text file. The resulting text file will be a series of VBS commands with a line for each rectangle and some overhead commands that are needed by HFSS to create the model. This means the text file could be hundreds of thousands of lines long and may need to be broken into a series of smaller files. After this file, or the files, are created, they are then read by HFSS, at which time the tool will rapidly start to create the rectangles for the model. At regular intervals the rectangles are combined into a single object. The more objects that HFSS must deal with, the slower the process well progress. Fig. 6.5 is a partially complete model. A full model will be comprised of many of these slices.

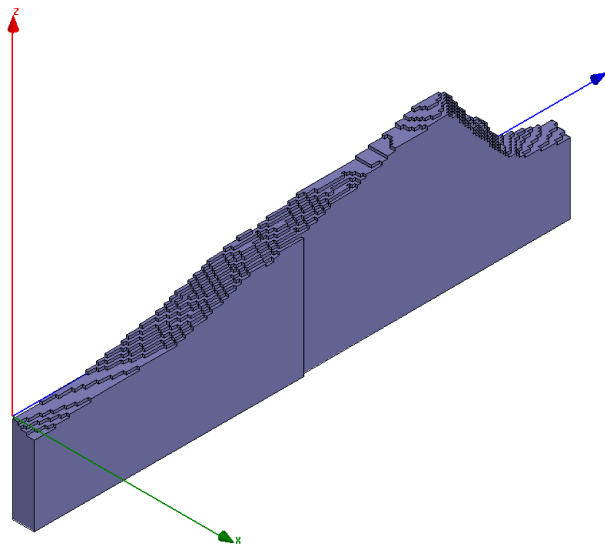


Figure 6.5: Partial topology build with VB scripting.

After the final rectangle is created and combined into the growing single object that is the terrain of the model, the VB script ends. The resulting model is now ready to be used in a simulation or be exported and used in other simulations. This stair-step approximation can provide a more detailed model in some regards and does not require the additional tools of AutoCAD and Cubit to create a usable model. This type of model does tend to require more

computer resources to work with than a faceted model and consideration for the resolution verses speed trade-off must be addressed by the user. Fig. 6.6 and Fig. 6.7 are examples of two models used in this project.

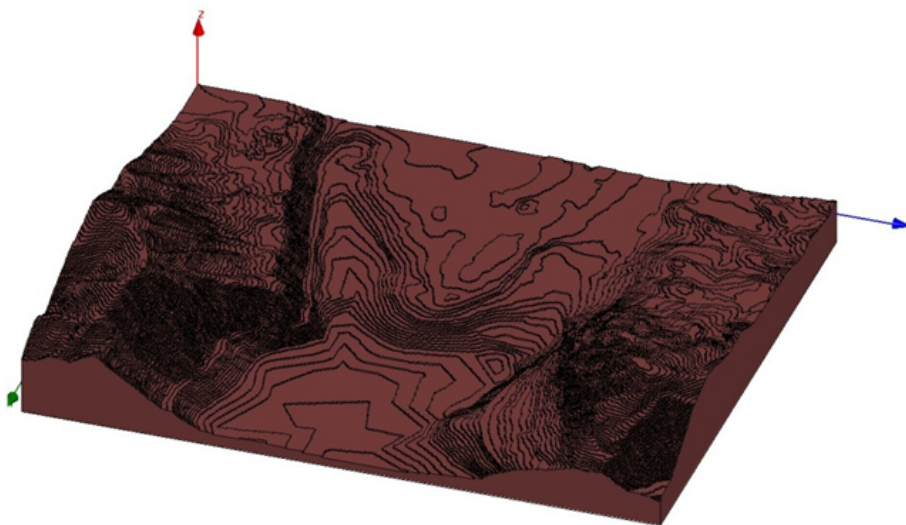


Figure 6.6: Completed Idlewild Bay topology model with VB scripting.

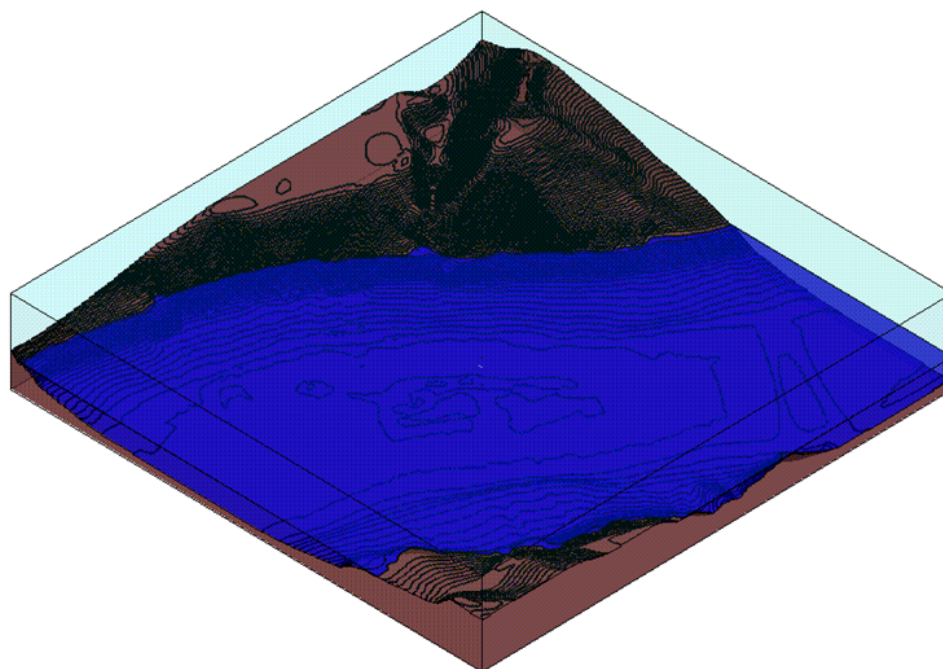


Figure 6.7: Completed deep water topology model with VB scripting.

Chapter 7

Conclusion

In conclusion, this project provided some interesting and important research challenges. The magnitude and the complexity of the experiments that were needed just to provide the validation data was significant. With that information we were able to make many favourable comparisons between the data from the experiment and modelling tools. Although much of the experimental data collected was of use we also discovered that the data set was incomplete. Data that was not collected and perhaps should have been was: water conductivity in the vicinity of the source and sensor, material parameters in multiple sections of the Lake, and precise knowledge of the locations of all the sensors and sources. Although we were able to obtain good enough data to make valid comparisons, it could have been better and would have allowed for better validation.

The limitations on domain modelling, for example, make it impossible to model an actual lake with a high degree of accuracy, so a compromise had to be made in order to conduct that simulation. This leads to errors that have to be understood by the user. Incomplete knowledge of the material parameters is an example of this kind limitation. Domain truncations schemes, source modelling, and hardware are also examples of limitations that make modelling a lake in perfect fidelity impossible.

The complexity of coordinating all the experimental source data using the DAQ was a major undertaking. The coordination of all the inputs and timing data was an important part of a successful outcome for the experiments. The DAQ system performed as expected and was

able to record the source configuration and state.

One of the big questions at the start of this project and thesis was the viability of HFSS as a tool for the simulation of ELF signals. After some initial challenges HFSS has been found to be usable for that purpose, but as with any commercial tool there are limitations and nuances in its use for ELF signal modelling. Because HFSS is a commercial solver it is widely available, used by many people, and has regular updates and improvements. This wide acceptance makes HFSS a good option with respect to the expense of developing an in-house simulation tool. The computing platform that this tool will be placed on will greatly effect its ultimate usability. For large simulations high powered workstations are needed. If sufficient care is given to the limitations and compromises outlined in this thesis then HFSS can provide good results in a wide range of applications.

A second question of this thesis was to determine how big of an impact the air-water interface had on fields created by a magnetic source. Several analytical formulations of a square loop and a circular loop were derived for this purpose and compared to that of an ideal source three layer model. Also another question to be answered was how did the shape of the source in the models compare with the actual experimental source. It was found that a circular loop formulation provided very good agreement with the square loop formulation for field observations greater than a few meters. The question of the air-water interface was also answered by a series of comparisons in which it was discovered that at frequencies lower than 10 Hz the air-water interface was all but transparent. This was not true as the frequency increased. At 100 Hz it was clear that some differences start to show. The differences are more pronounced in the z component of the magnetic fields. But, as the frequency is increased to 1000 Hz, the differences in all the magnetic field components are dramatic. It should be noted that although there are some differences in the electric fields caused by the air-water interface, it is not significant with ELF signals excited by current loops.

Challenging parts of this project that were not initially anticipated were that of data management and model construction. Early on in the project before any simulations could be conducted for experimental comparison purposes, an accurate model of the lake topology was needed. Difficulties such as accurate, up-to-date maps and making the different sets of map

data mesh well were all things that had to be resolved. It was also found that many compromises of resolution had to be made due to hardware limitations. The data management of this project quickly became difficult as well. A great deal of time was spent to devise a system and strategy to make the large amount of data manageable.

Finally, the goals outlined for this thesis research have been fully met. A system for measuring and recording source information was developed and used successfully. HFSS was determined to be viable option for modelling ELF signals in maritime environments. It was determined that shape of the magnetic source only affected results within a few meters and that the air-water interface has an impact as frequency is increased. Lastly, methods used for model creation and data management were examined and utilized.

Bibliography

- [1] J. L. Young, D. M. Sullivan, R. G. Olsen and Christopher L. Wagner, "Investigation of ELF Signals Associated with Mine Warfare: A University of Idaho and Acoustic Research Detachment Collaboration, Phase Two", Proposal to the Office of Naval Research, pp. 2, 2010. *IEEE Trans. on Microwave Theory and Techniques*, vol. 39, no. 7, pp. 1120-1125, 1991.
- [2] D. H. Werner, "An Exact Formulation for the Vector Potential of a Cylindrical Antenna with Uniformly Distributed Current and Arbitrary Radius", *IEEE Transactions on Antennas and Propagation*, vol. 41, no. 8, pp. 1009-1018, 1993.
- [3] R. F. Harrington, *Time-Harmonic Electromagnetic Fields*, Wiley, New York, pp. 269, 2001.
- [4] R. T. Rebich (2011), *Multiple-Layered Quasi-Electrostatic Model Development for Extremely Low Frequencies*, Master of Science Thesis, University of Idaho, Moscow, Idaho.
- [5] D. K. Butherus (2011), *Sensor Employment, Reciprocity and Ansys Maxwell in the Context of Extremely Low Frequency Applications*, Master of Science Thesis, University of Idaho, Moscow, Idaho.

Appendix E: Auxiliary Documents

The following documents and reference materials were used during the course of the Phase One, Two and Three efforts. Reprints of these documents are attached.

- Sea-Bird Electronics, “Application Note 30: Fresh Water Conductivity Measurements Using the SBE-19 SEACAT Profiler,” March 2001. (Company proprietary document; available upon request.)
- Ed Fitzgerald, “Memorandum: Engineering Performance of HRA/EMA Configuration (ISMS 2008-0007),” April 11, 2008.
- Patrick M. Molvik and Jeanne Hom, “Lake Pend Oreille Bottom Sediment Resistance Measurement,” August 1, 2008.

MEMORANDUM

To: Duane Nightingale, Sam Taylor (ARD), Brad Ross, Matt Conti (Alion)
From: Ed Fitzgerald
Date: 11 April 2008
Subj: Engineering Performance of HRA/EMA Configuration (ISMS 2008-0007)
Ref: [1] "Analysis of High Resolution Array Performance," by Ed Fitzgerald, Memo ISMS 2006-004 dated 26 June 2006

1. Summary

The engineering performance of the High Resolution Array (HRA) /Electro-Magnetic Array (EMA) configuration was analyzed in terms of the following areas:

- Acoustic template measurements,
- Acoustic Tracking extensions,
- Acoustic calibration repeatability,
- Stability of the array in withstanding wake-induced motion, and
- Good beamforming performance with low side lobe levels.

Engineering tests in these areas were conducted at the start of the RimJet propulsor testing program. The results indicate that the HRA/EMA has adequate performance in all of the above areas.

2. Modifications to Original HRA Configuration

Previous measurements [1] had documented that the floats were significant sources of acoustic scattering. To alleviate these effects, two new truss sections were added (one on each end) and the floats were relocated to the truss ends. This moved the floats outboard of the active part of the HRA aperture, so that the effects of acoustic scattering into the array hydrophones could be minimized.

The EMA was then added to the basic structure as shown in Figure 1. The EMA sensor electronics were housed in a pressure vessel (EMPV) located outboard of and underneath one of the floats. This geometry was selected so that acoustic scattering from the pressure vessel would be shadowed by the float for the hydrophones closest to that end of the array.

3. HRA Acoustic Survey Measurements

Several acoustic survey measurements were taken. The repeatability of the measured positions was less than ± 1 mm. Figure 2 shows the change in position from the ideal design value for each axis in the array body frame, where the x-axis runs along the array axis, the y-axis is horizontally transverse, and the z-axis is positive downwards. The maximum departure from the ideal position was 8.5 mm in the x direction, 3.5 mm in the y direction, and 76.5 mm in the z direction. The departure in the z

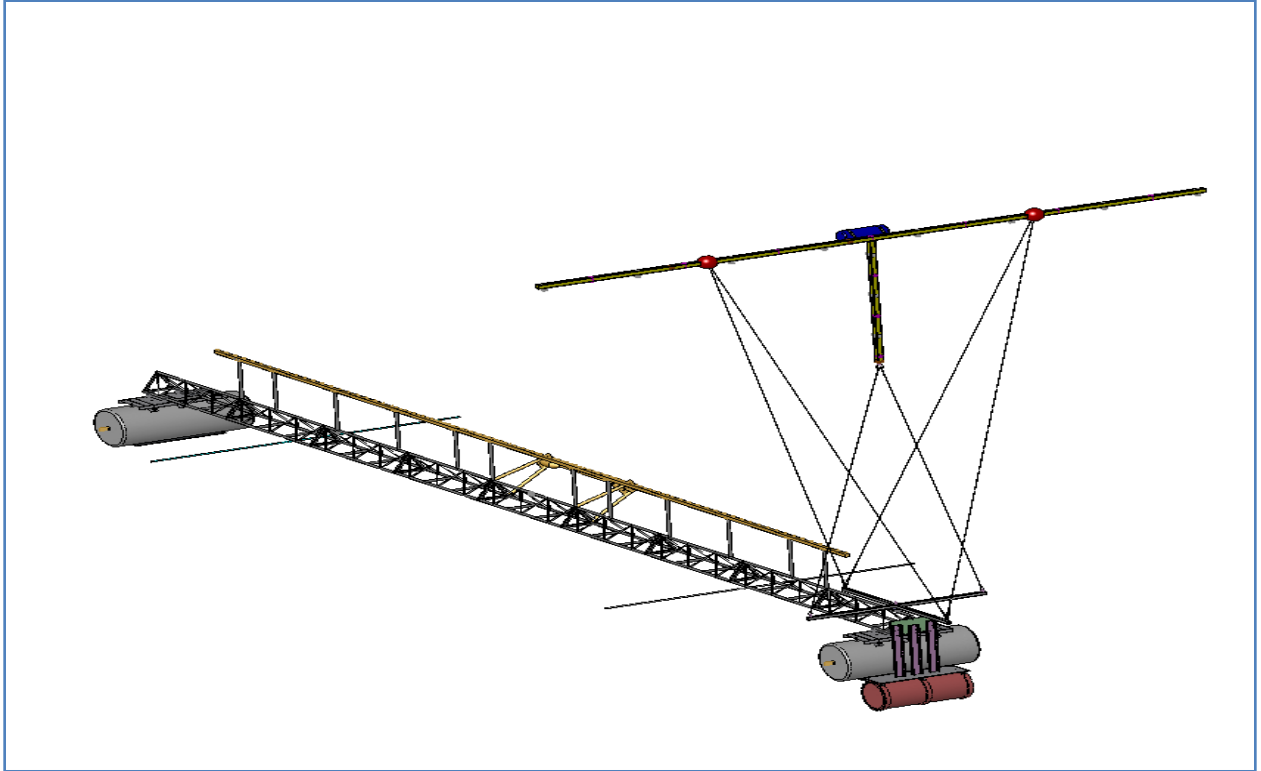


Figure 1. Reconfigured HRA with Attached EMA.

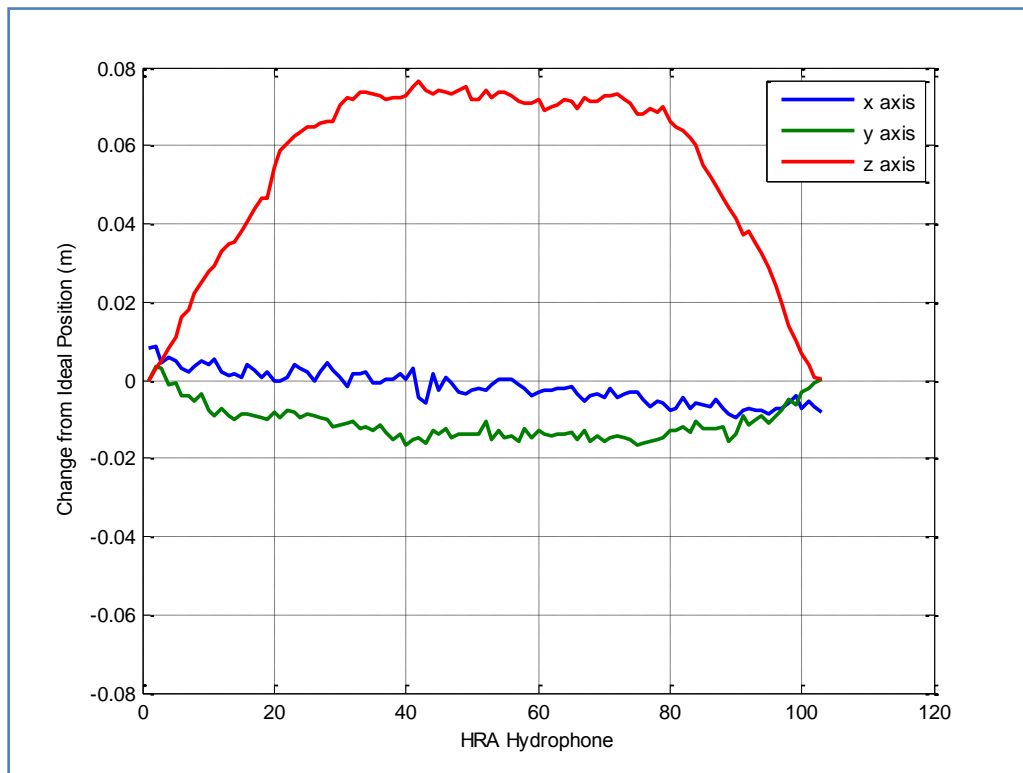


Figure 2. Deviations in Hydrophone Positions from Ideal Locations.

direction amounts to a downward sag of about 3 inches (over 60 feet of linear aperture). These values are all well within the acceptable range.

4. Acoustic Tracking Extensions

The acoustic tracking software previously developed for the HRA was modified to add tracking for two additional hydrophones, one on each end of the EMA horizontal arm. Typical outputs from this program are shown in Figures 3-8. The locations of the two tracking hydrophones on the EMA horizontal

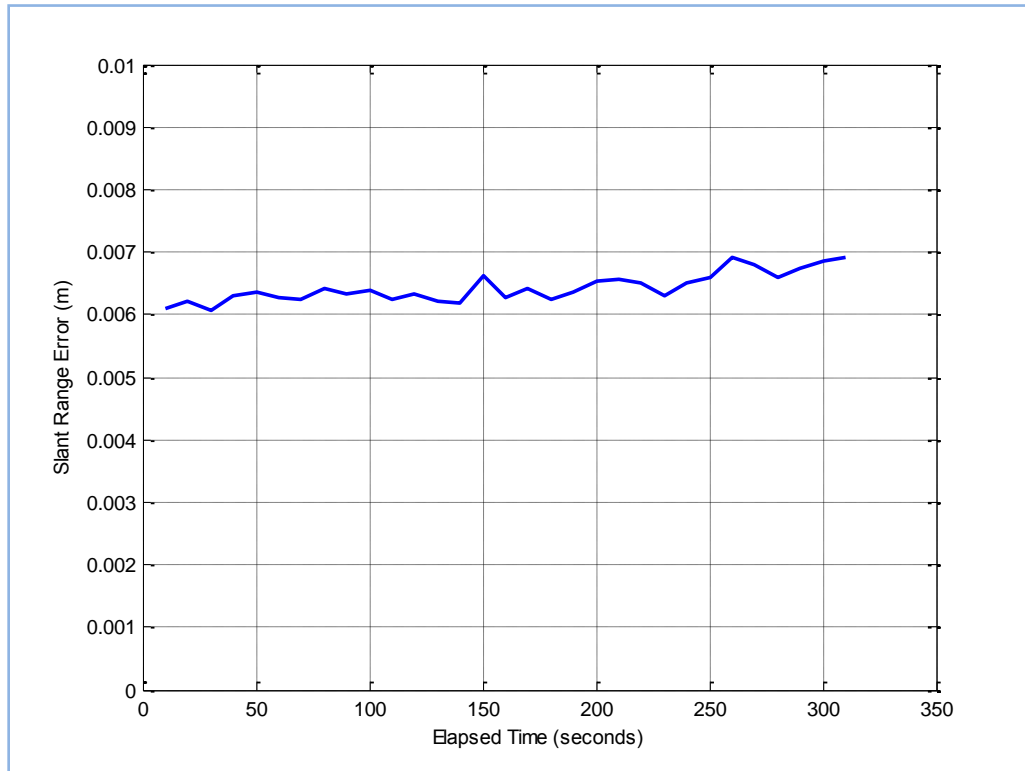


Figure 3. Typical Slant Range Errors.

arm are given in HRA Array Body Frame (ABF) coordinates in Table 1. In this frame, the x-axis coincides with a line from HRA-1 to HRA-103 where the origin is at the midpoint between these two phones. The z-axis points downward and the y-axis is horizontal in a right-handed system.

Coordinate	HLM-5	HLM-6
X	10.9714 m	11.9261 m
Y	7.2626 m	-5.9152 m
Z	-9.4843 m	-10.1559 m

Table 1. Coordinates of EMA Tracking Phones.

The average height of the EMA above the HRA is 9.82 m (32.2 feet).

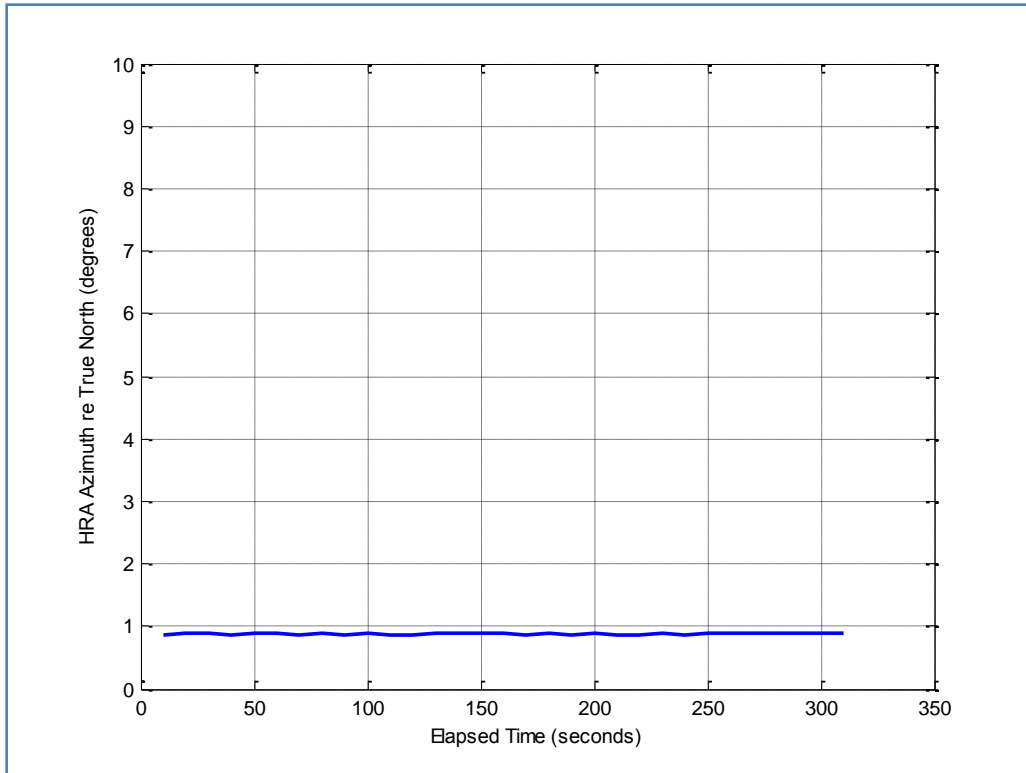


Figure 4. HRA Azimuth.

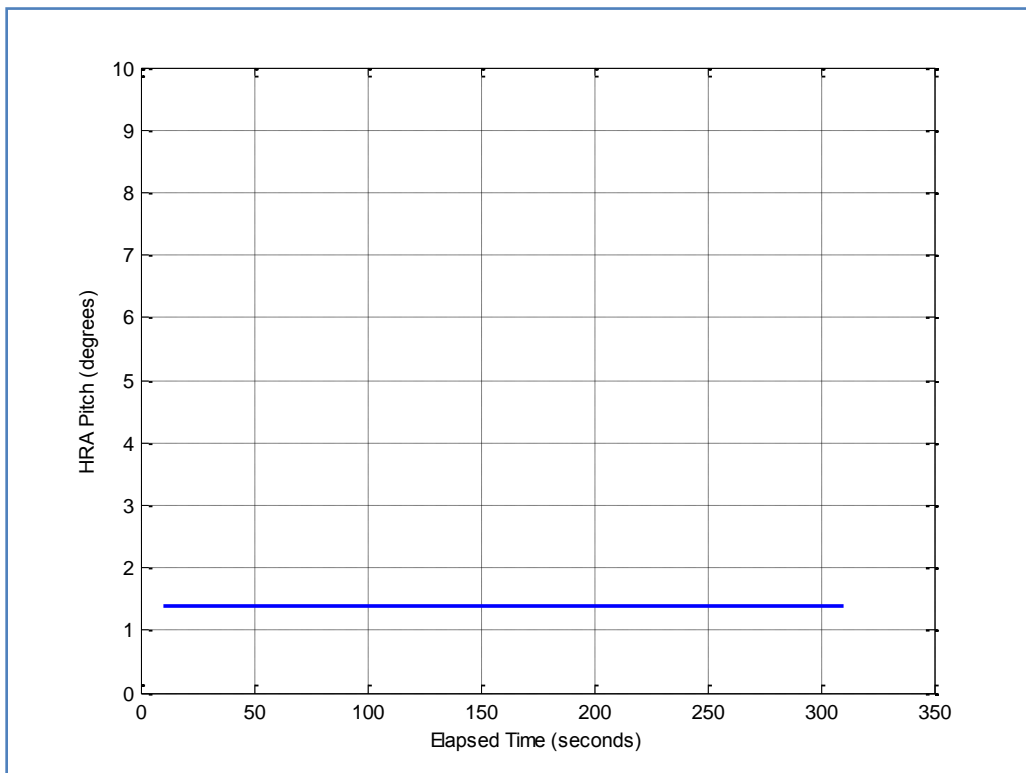


Figure 5. HRA Pitch.

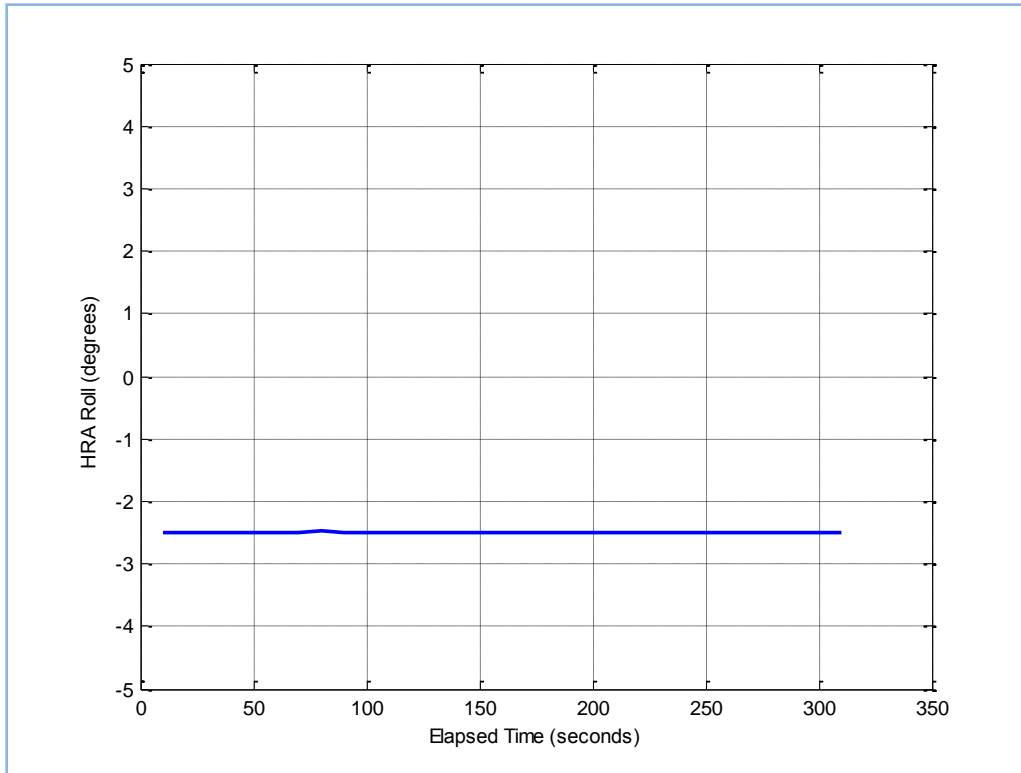


Figure 6. HRA Roll.

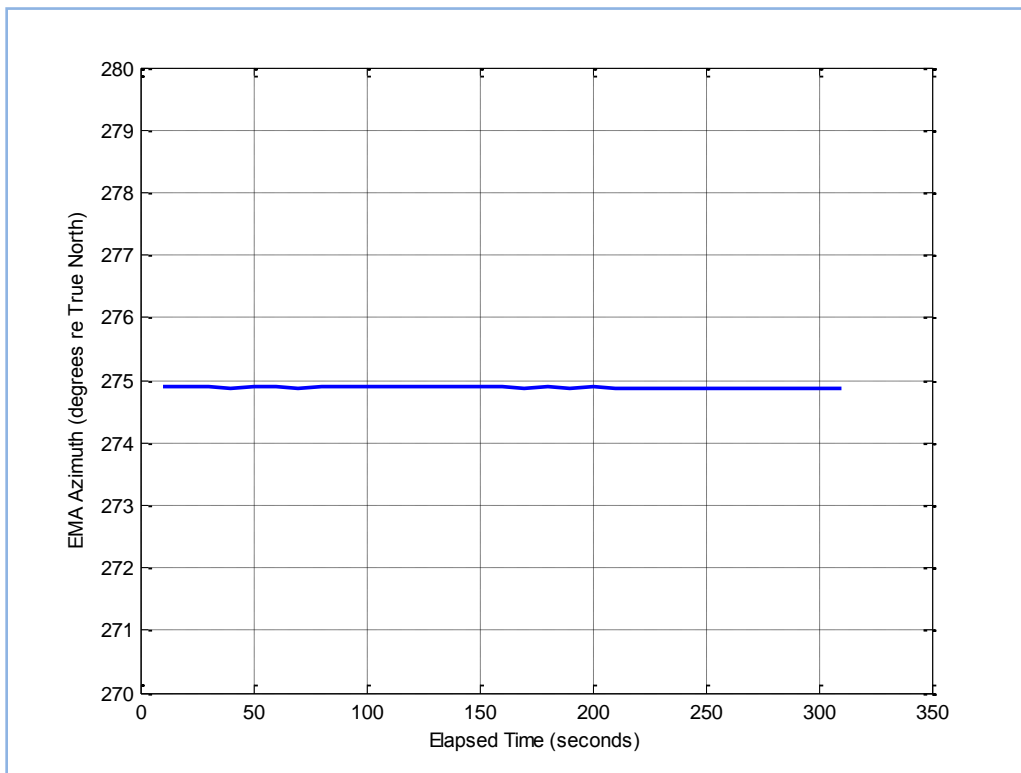


Figure 7. EMA Azimuth.

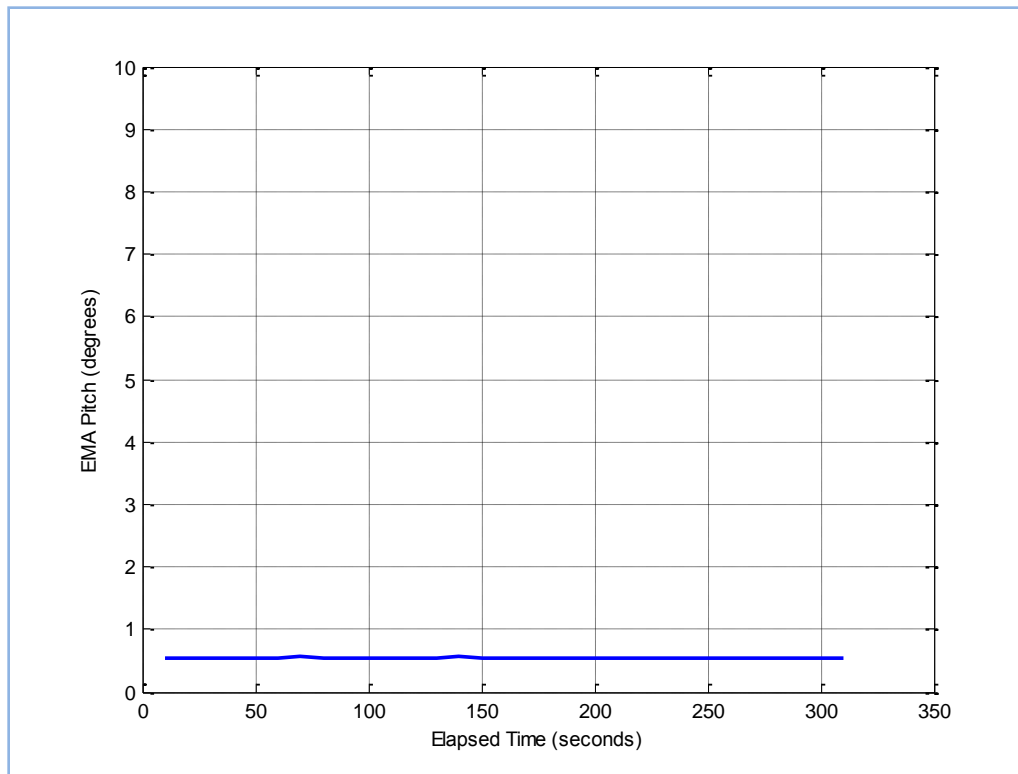


Figure 8. EMA Pitch.

5. HRA Acoustic Calibration Results

The HRA was hauled down to a depth of about 62 meters below the NFRA depth for its acoustic calibration, using ensonification from the ST2-6 projector on the NFTA. The calibration data were analyzed to determine the variability due to scattering off the HRA floats, as well as the basic repeatability of the calibration. The variability of the raw sensitivities across a 350-700 Hz band was calculated for each hydrophone in terms of the standard deviations of the dB sensitivities across the band. The results are shown in Figure 9, which can be compared to Figure 8 of [1]. It can be seen that the configuration change of moving the floats outboard of their previous positions was successful in reducing scattering in the middle of the HRA active aperture. The significant scattering levels are in the 10 hydrophones at each end of the HRA, where the beamformer shading weights are small.

The repeatability of the HRA acoustic calibration was examined by comparing two calibrations taken before and after the repair of OBE-20 in the array. The sensors associated with this OBE (HRA-85 to HRA-91) were excluded from the comparison. The average difference between the calibration values (performed about 25 hours apart) was only 0.02 dB – a very small value. Hence the HRA acoustic calibration showed excellent repeatability. Since the orientation of the array with respect to the NFTA projector didn't change over this period, it is very possible that there are biases in the calibration due to the presence of scattering from the HRA floats, the HRA structure, and the EMA structure and imbedded floatation materials. The differences between calibrations are shown in Figure 10. The differences are

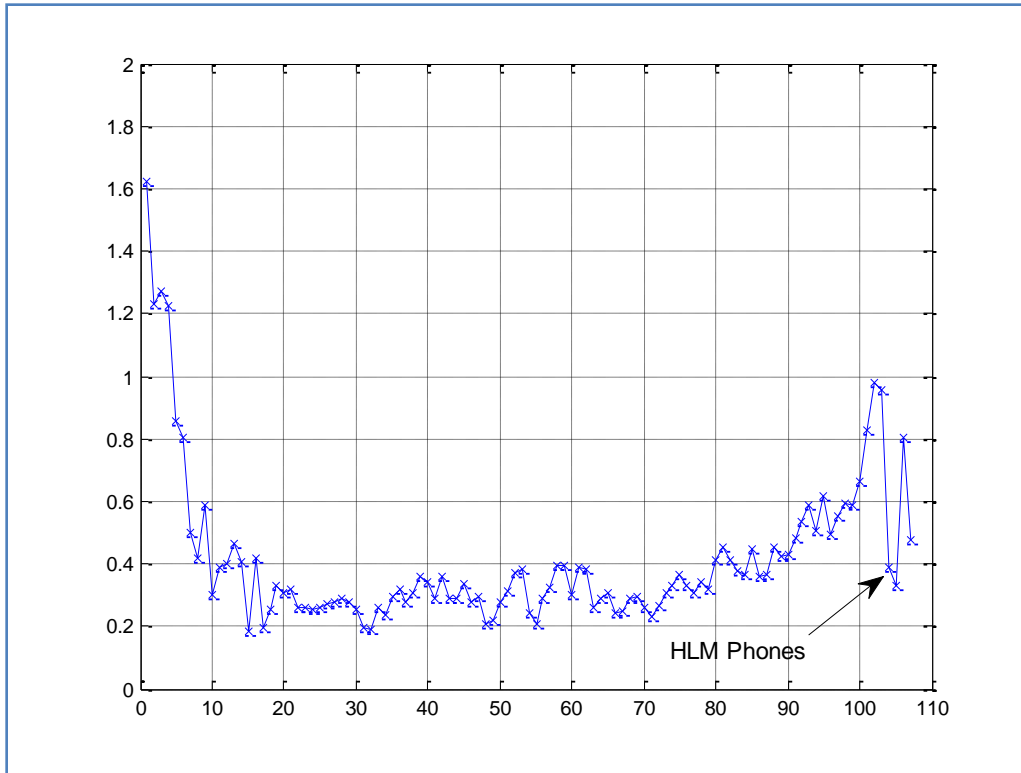


Figure 9. Variability in Sensitivities versus Hydrophone Position.

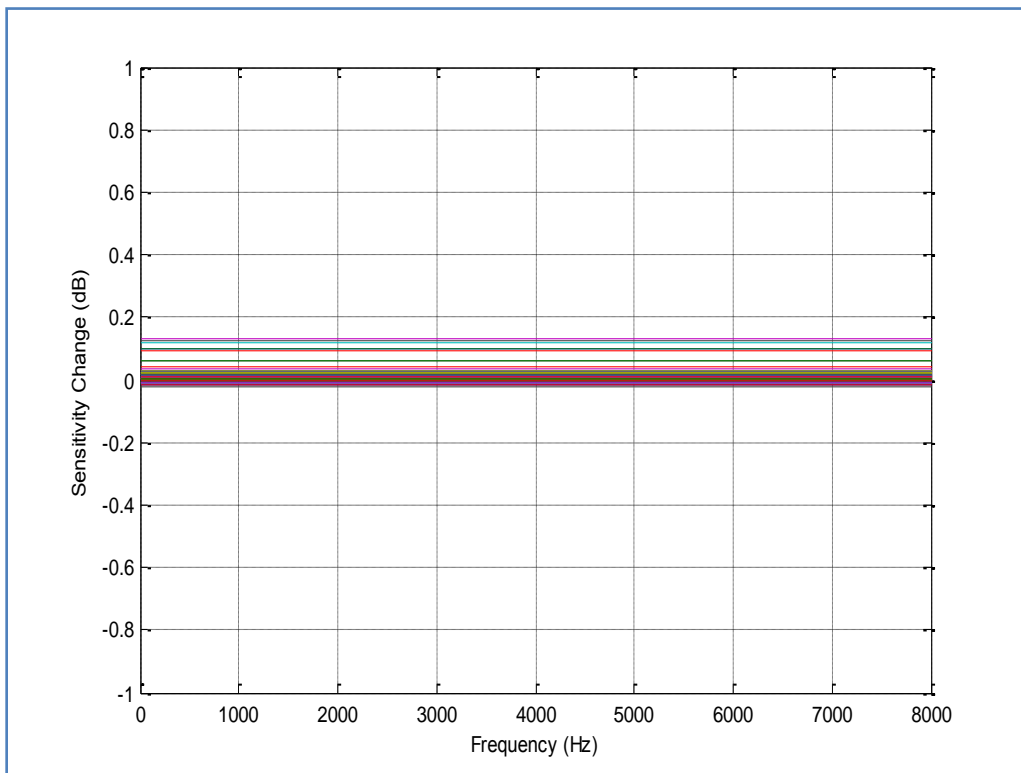


Figure 10. Change in Measured HRA Acoustic calibrations.

constant as a function of frequency because the sensitivity for each hydrophone is taken as an average of the raw sensitivities (measured every 2 Hz) across the 500-1000 Hz band.

6. Stability in Withstanding Wake-Induced Motion

The sensitivity of the HRA/EMA to wake-induced motion was studied by using a special experiment script that emitted tracking pings every second using a minimal number of paths (5 NFRA pingers to 6 HLM phones). The SEA JET made passes over the array at different speeds while the positions of the HLM tracking hydrophones were tracked. A particular high speed run (Run 55801) at 124 RPM was used in the subsequent analyses. None of the runs passed directly over the HRA.

Figure 11 shows the RMS slant range error between the calculated HLM phone positions and those measured using the raw travel times. There was an 8-second gap around CPA where the radiated

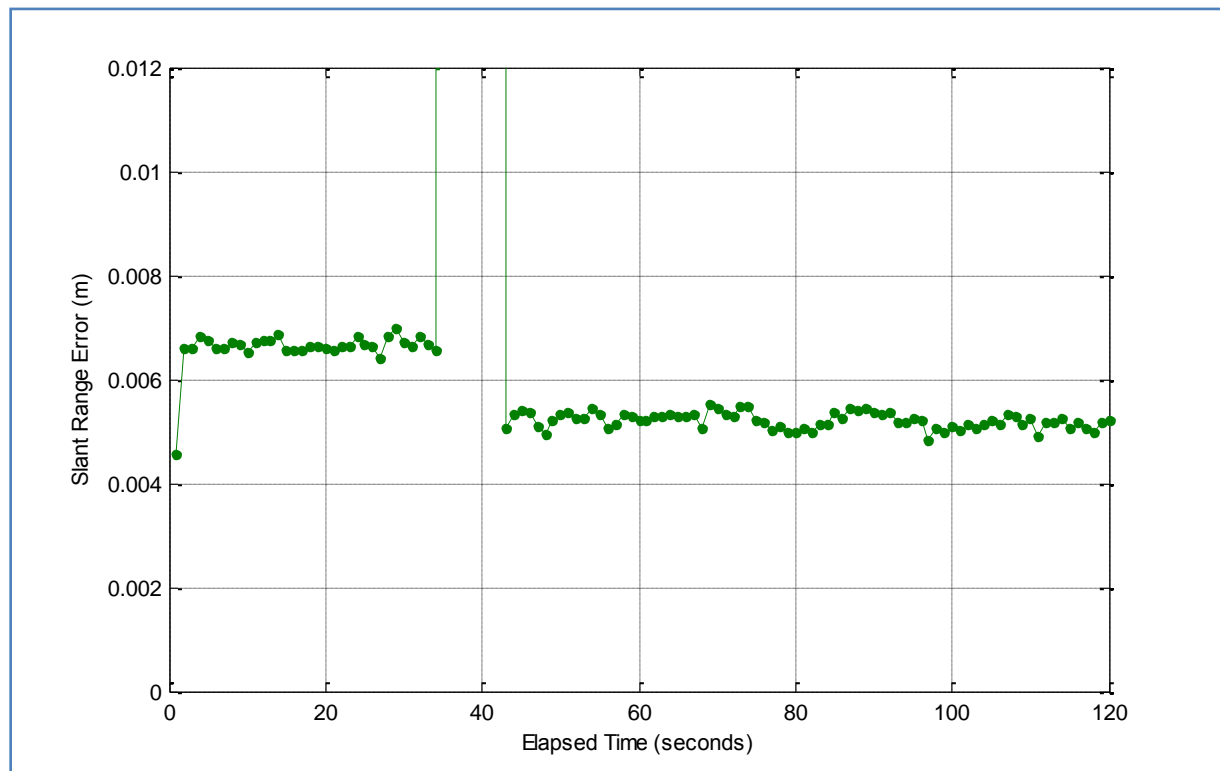


Figure 11. Slant Range Error versus Elapsed Time.

noise of the vessel caused a dropout of the tracking. Otherwise, the RMS tracking errors were 5-7 mm.

Figures 12-14 show the HRA azimuth, pitch, and roll versus elapsed time. The X and Y offsets of the HRA midpoint (in NTIF coordinates) are shown versus time in Figures 15-16. The EMA azimuth and pitch are shown in Figures 17-18. The EMA X, Y, and Z offsets are shown in Figures 19-21.

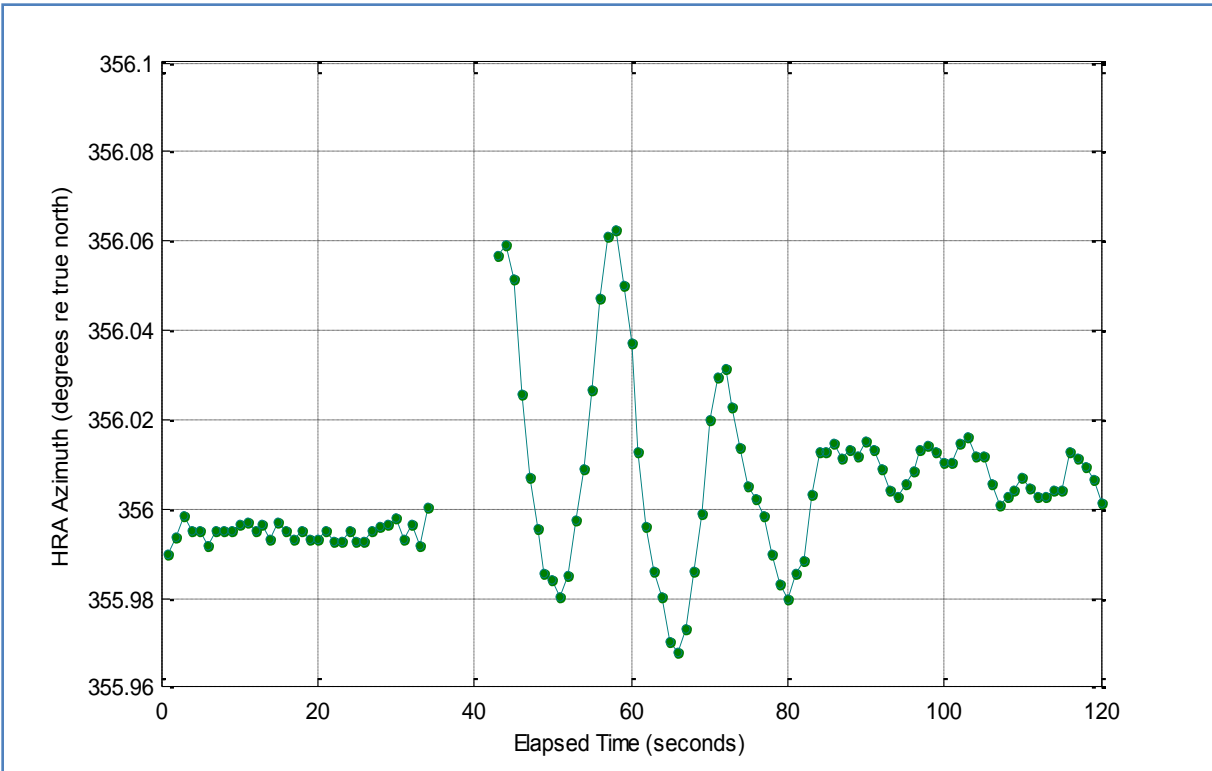


Figure 12. HRA Azimuth versus Elapsed Time.

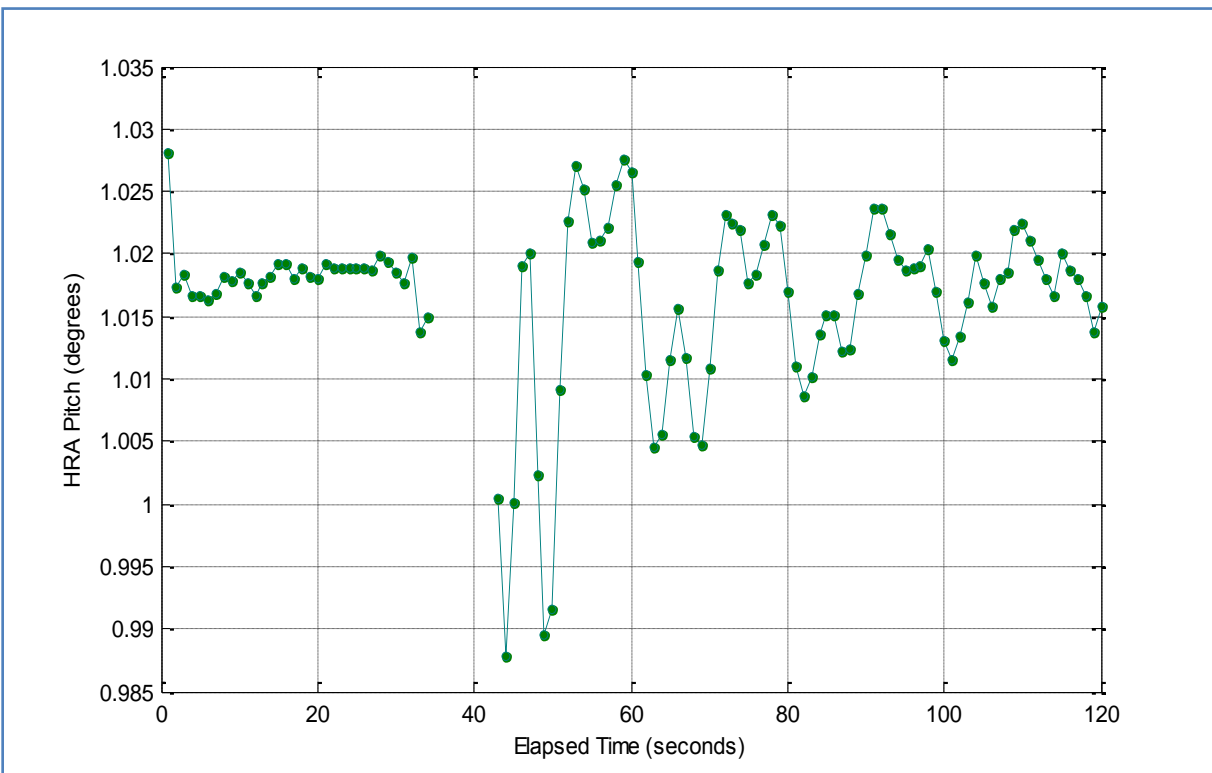


Figure 13. HRA Pitch versus Elapsed Time.

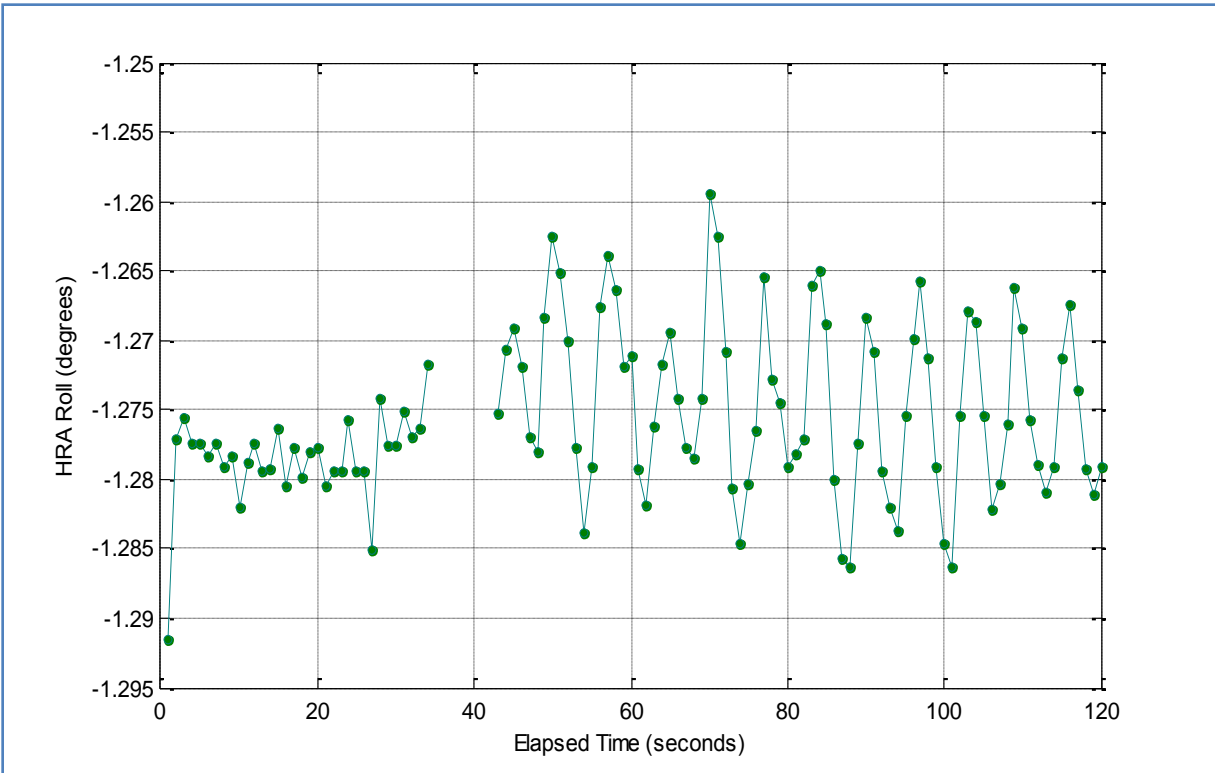


Figure 14. HRA Roll versus Elapsed Time.

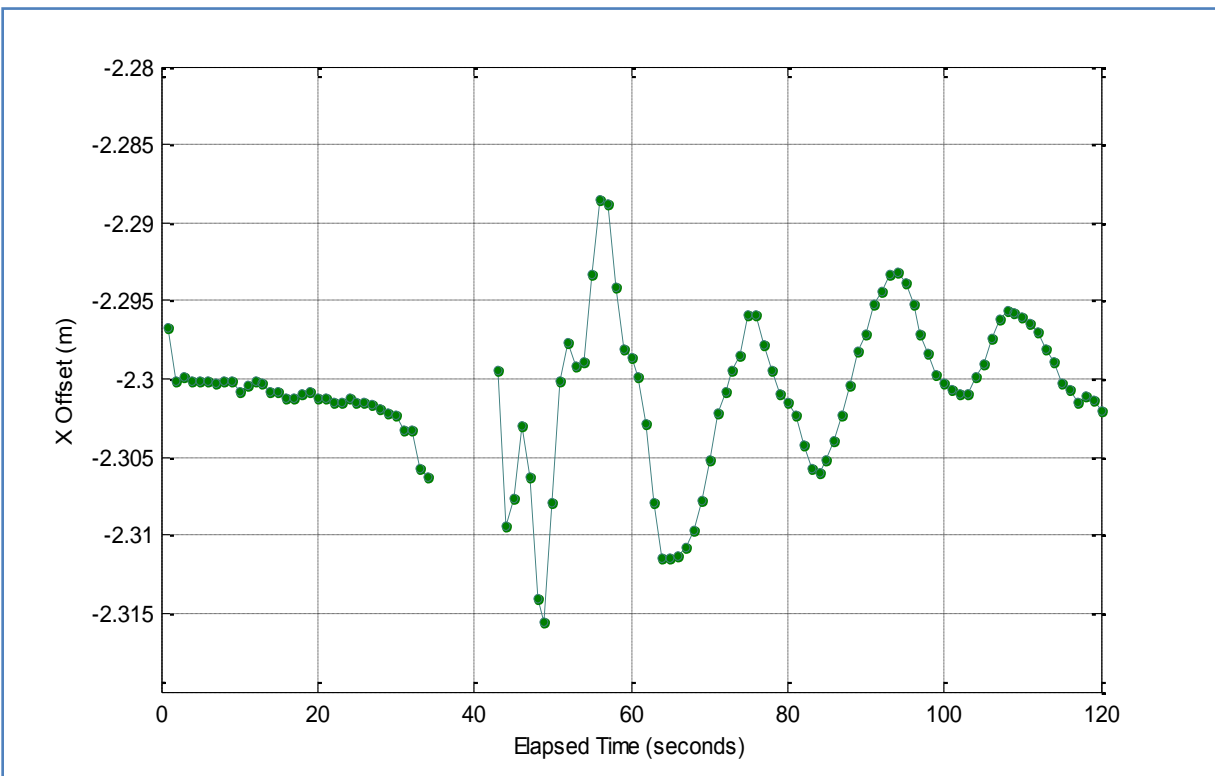


Figure 15. HRA Midpoint X-Offset (re NTIF) versus Elapsed Time.

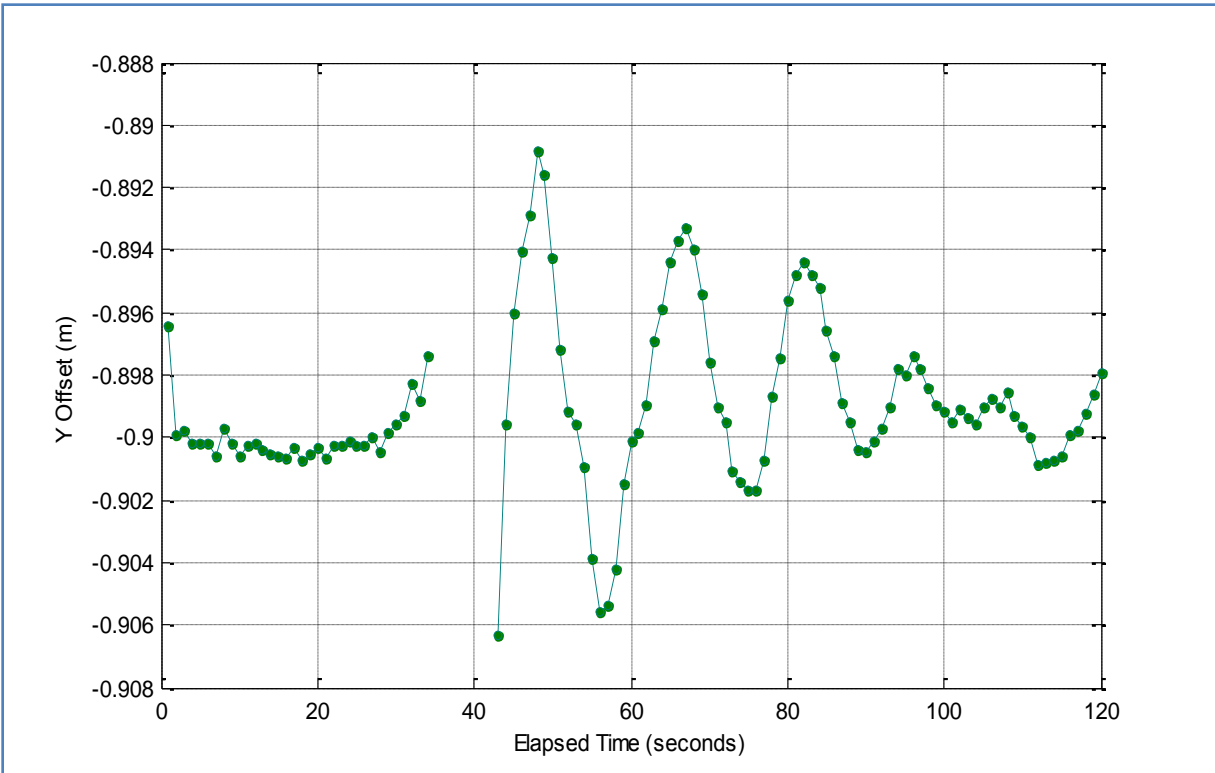


Figure 16. HRA Midpoint Y-Offset (re NTIF) versus Elapsed Time.

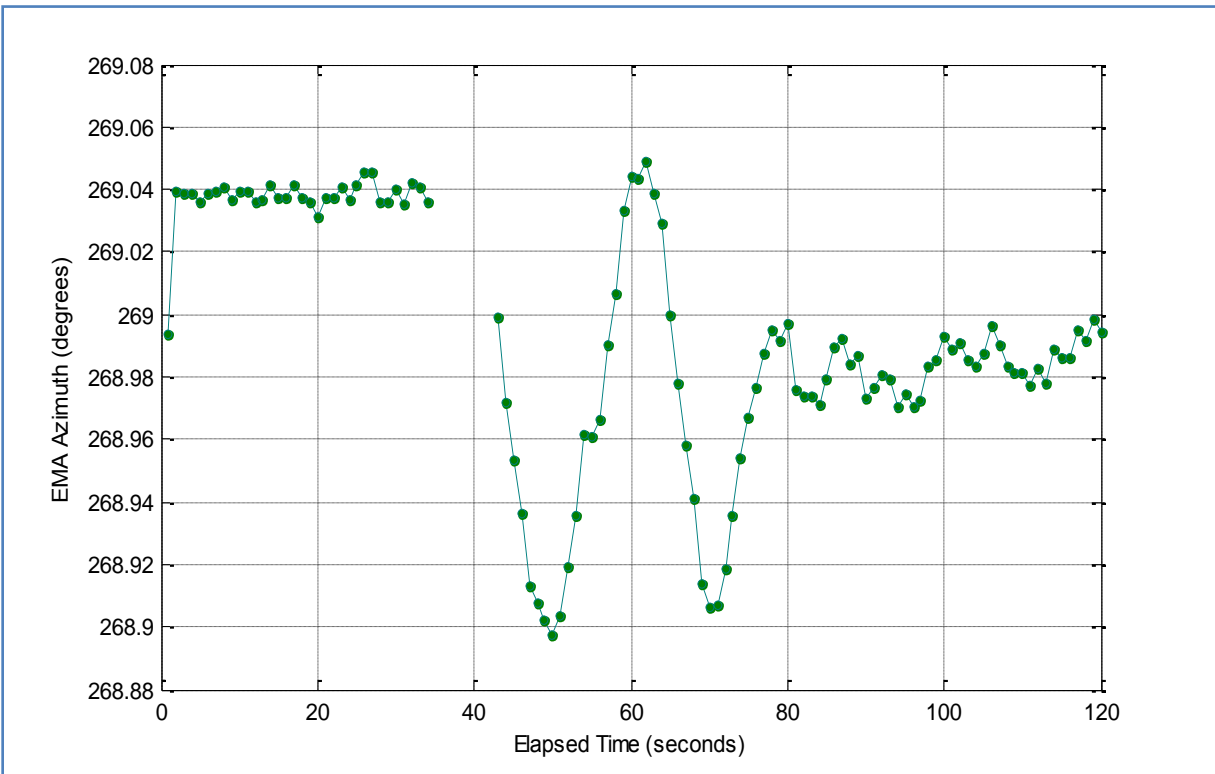


Figure 17. EMA Azimuth versus Time.

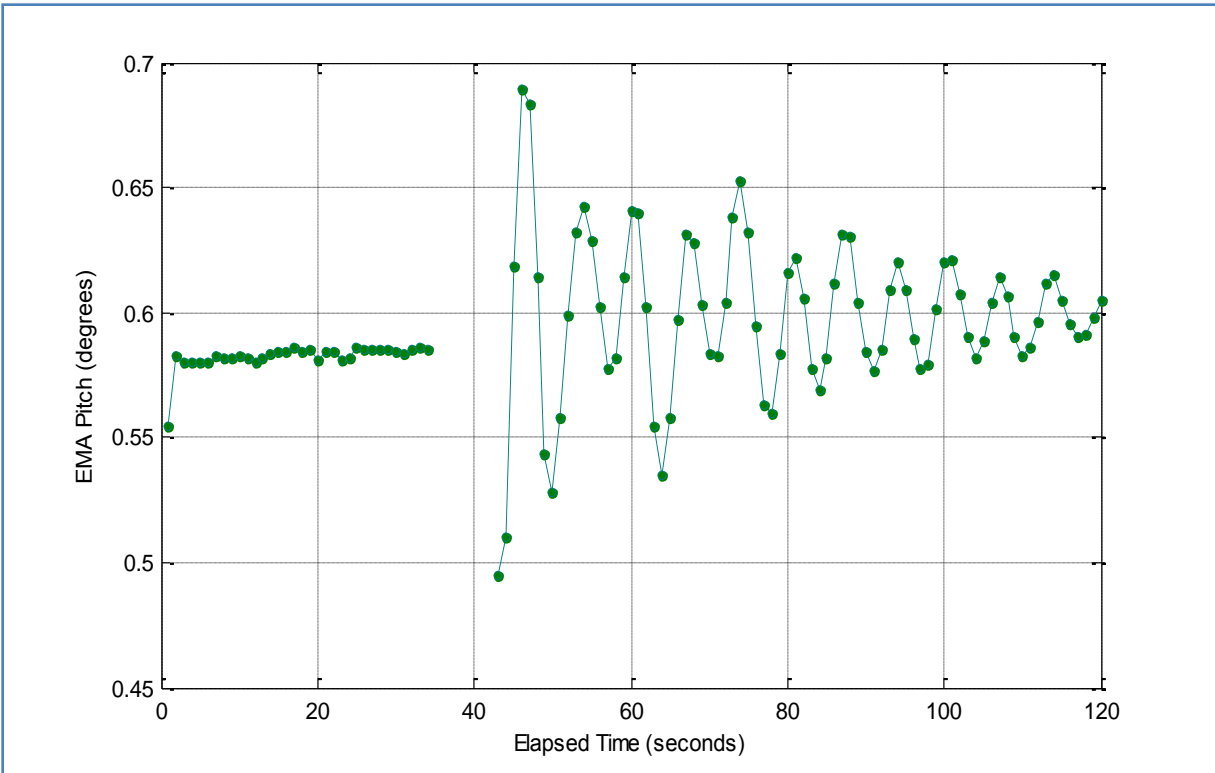


Figure 18. EMA Pitch versus Time.

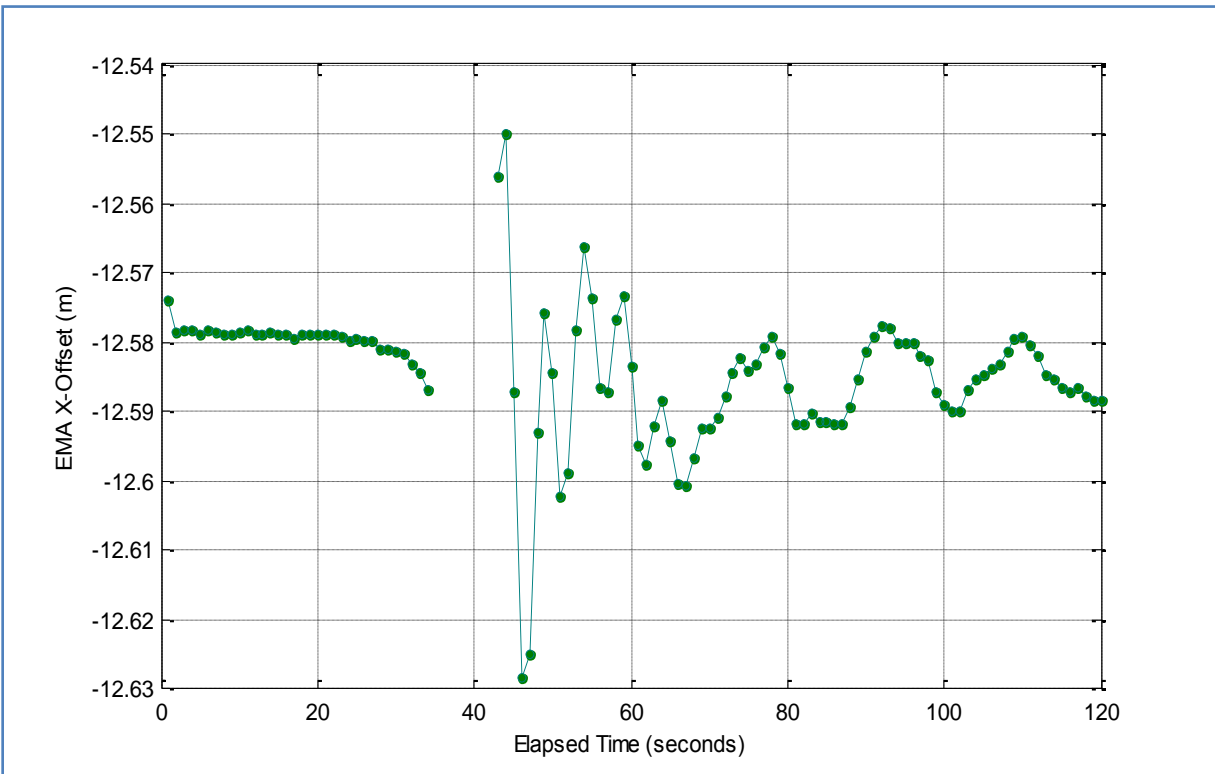


Figure 19. EMA X-Offset (re NTIF) versus Time.

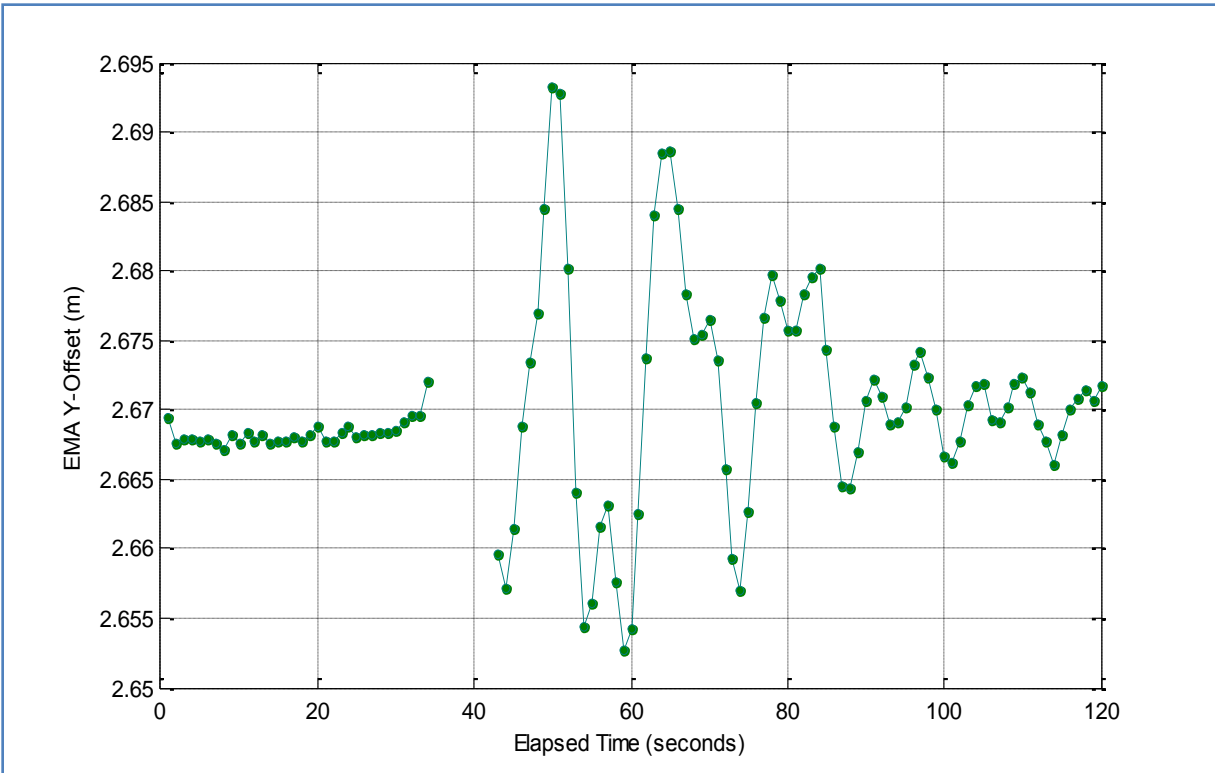


Figure 20. EMA Y-Offset (re NTIF) versus Time.

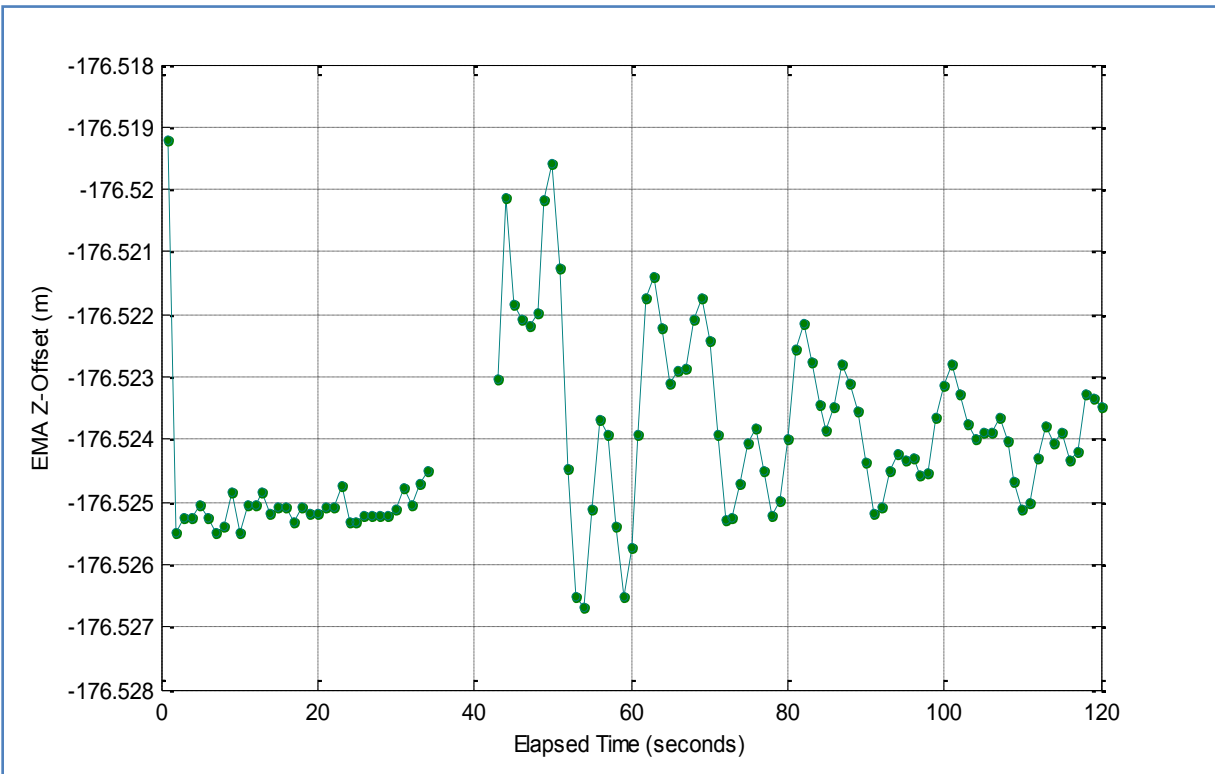


Figure 21. EMA Z-Offset (re NTIF) versus Time.

Although no data is available in the 8-second dropout period, the data that follows this dropout strongly suggests that no un-measured extreme excursions in wake-induced motion have occurred. The peak observed wake-induced angular rotations are summarized in Table 2. The peak displacements are given in Table 3. The displacements in Table 3 are relative to the NTIF coordinate system. It can be seen

Rotation	Peak Excursion
HRA azimuth	+0.06°
HRA pitch	-0.03°
HRA roll	+0.02°
EMA azimuth	-0.14°
EMA pitch	+0.11°

Table 2. Peak Angular Excursions due to Wake-Induced Motion.

Displacement	Peak Excursion
HRA x-offset	-1.5 cm
HRA y-offset	+0.9 cm
EMA x-offset	-5.0 cm
EMA y-offset	+2.5 cm
EMA z-offset	+0.6 cm

Table 3. Peak Displacements due to Wake-Induced Motion.

that the angular rotations of both the HRA and EMA are very small. The peak displacements of the HRA look reasonably small. The worst-case EMA displacement is 5 cm (~ 2 inches).

7. Beamforming Performance

It was expected that moving the support floats and adding the EMA (with its own floatation) would affect the beam patterns of the HRA due to changes in the scattering off the floatation and other mechanical structure. The beamforming performance was checked using a small work boat to run across the array. The propeller acoustic signal approximates an omnidirectional noise source. The GPS position of the boat was tracked during the run. Of the three available experiments, only one run - #1002 - was available for downloading in uncorrupted form. The boat speed was about 17.5 knots, and the CPA slant range from the propulsor to the HRA midpoint was 31.9 meters. A total of 52 seconds of CAMS data were collected during this run. This was processed using the time domain beamformer (HTS) program and then converted to running power spectra with a bin spacing of 32 Hz and 50% overlap. These spectra were averaged across time using a running 7-point filter. The GPS data was also processed to estimate the bearing of the propulsor as a function of time. The ideal beam pattern as a function of time was calculated from this bearing. This was scaled to match the peak of the measured beam response.

Comparisons of the measured versus ideal beam patterns at different frequencies are shown in Figures 22-25. It can be seen that the side lobe response of the measured beam patterns shows an indication of being degraded to a level of -20 db to -25 dB, versus the ideal level of -30 dB or more.

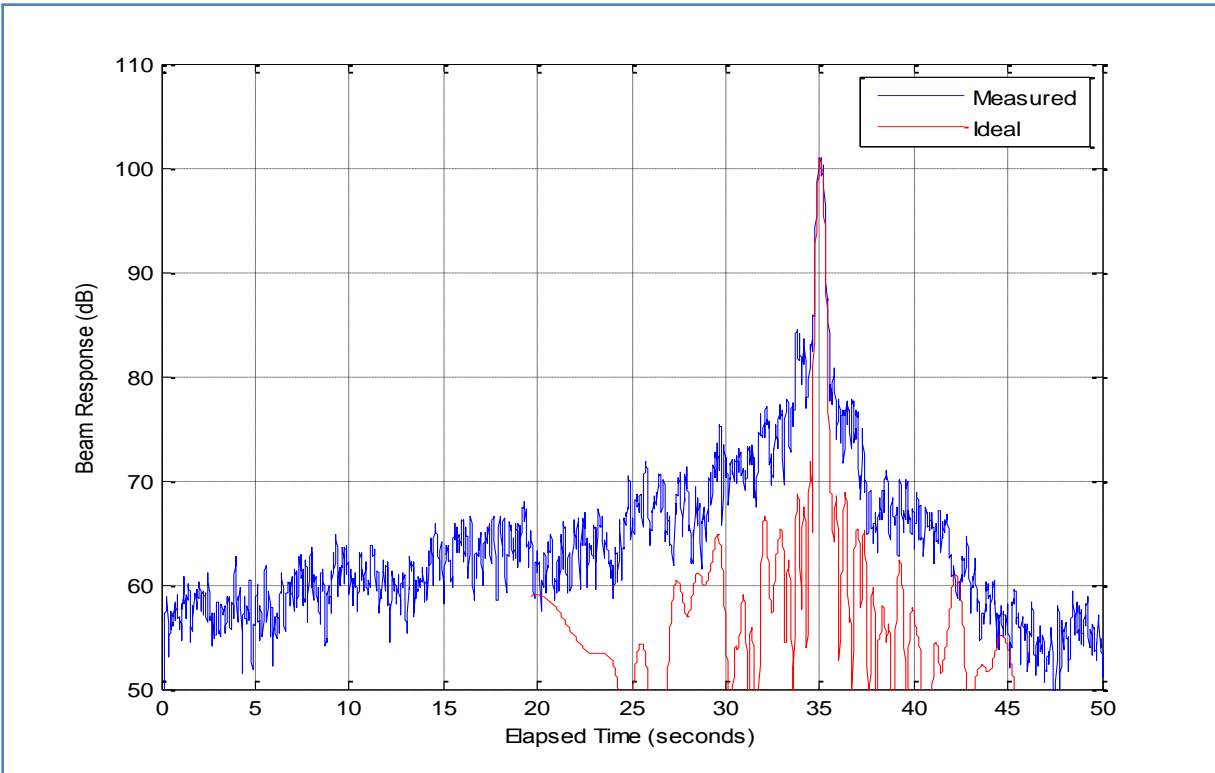


Figure 22. Beam Response at 5,600 Hz.

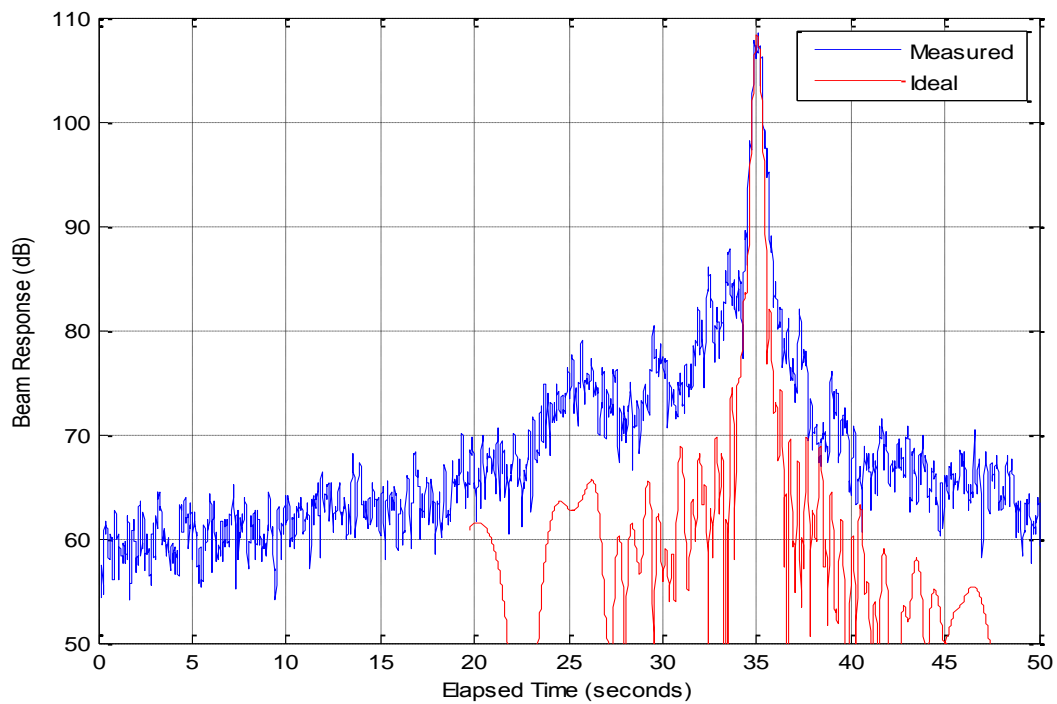


Figure 23. Beam Response at 2,560 Hz.

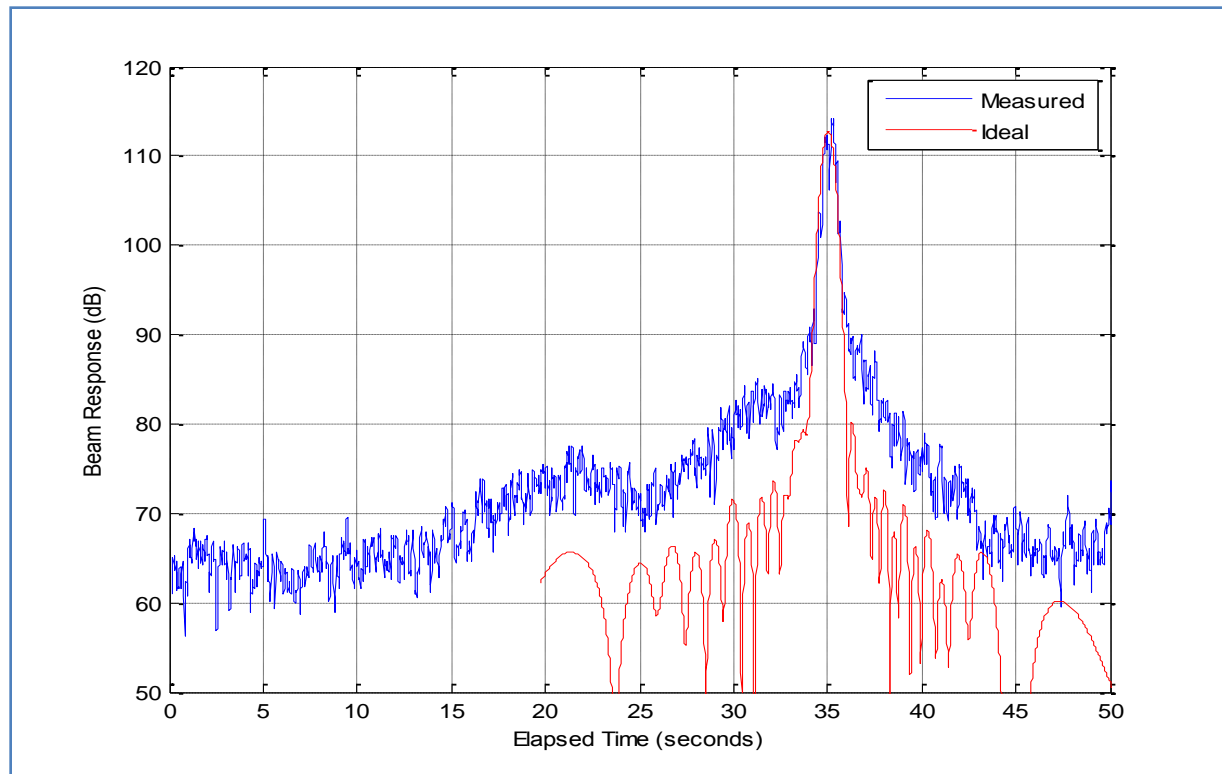


Figure 24. Beam Response at 1,280 Hz.

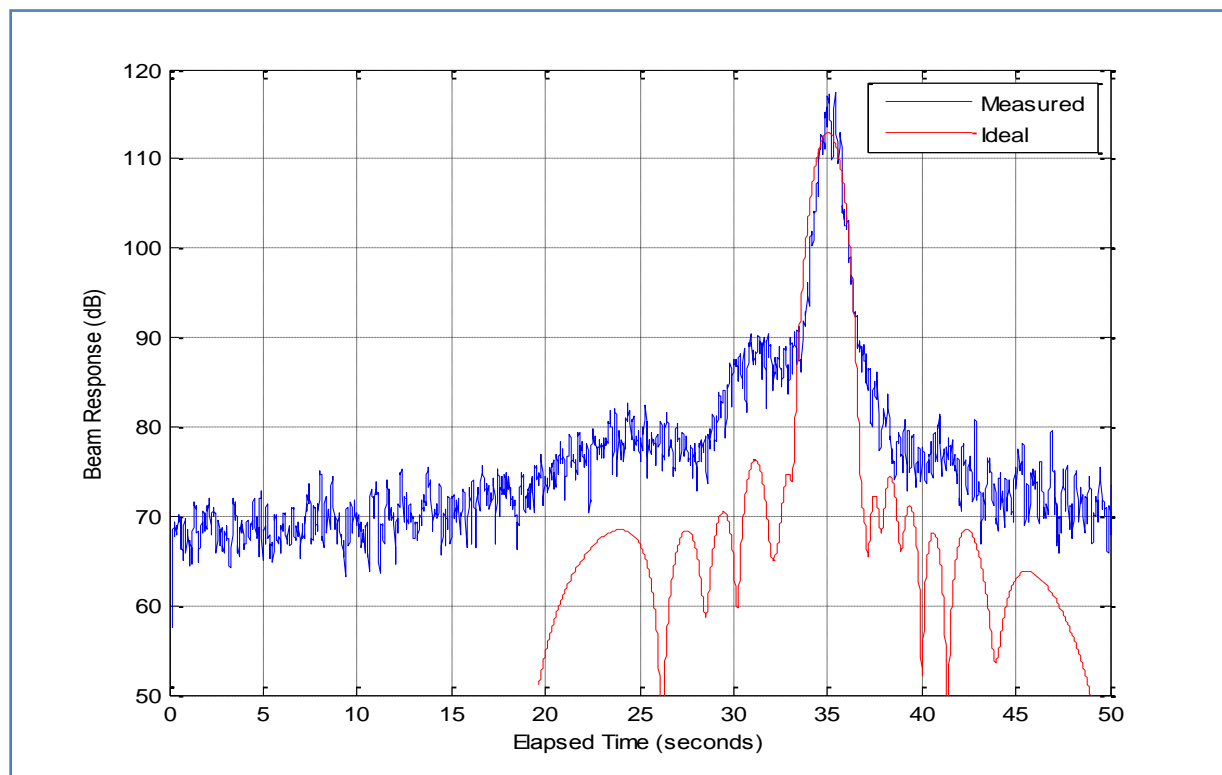


Figure 25. Beam Response at 640 Hz.

This is an indication that acoustic scattering from the floatation and other hardware (e.g., pressure vessels) is affecting the beamforming performance. A pseudo-color plot of the run is shown in Figure 26.

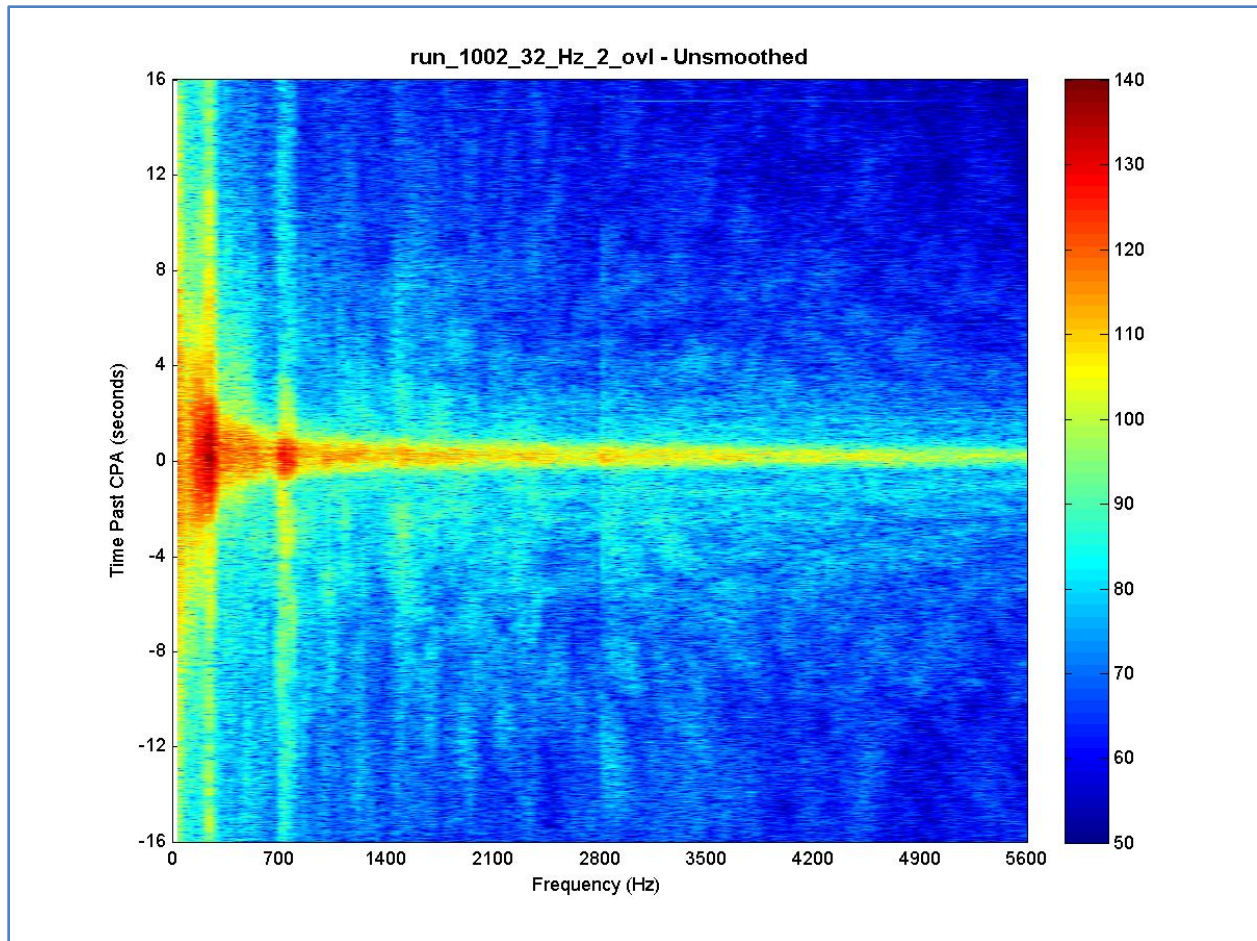


Figure 26. Pseudo-color Plot of Beam Response.

It can be seen that the beam has higher side lobes than would be expected in the ideal case. Previous measurements without the EMA (and its pressure vessels) showed typical side lobe levels of around -30 dB as documented in [1]. Hence, this data indicates that the HRA performance has been degraded to some extent by the addition of the EMA and its associated floatation and electronics pressure vessels.

8. Conclusions

The results of this engineering assessment can be summarized as follows. The HRA, with the addition of the EMA, performs nominally with respect to tracking, acoustic survey measurements, acoustic calibration, and acceptably small responses to wake-induced motion. There appears to be some degradation in the HRA beam side lobe levels; however, the array is still very usable in mapping hot spots in the vessel signature.

August 1, 2008

Prepared by Patrick M. Molvik & Jeanne Hom

Lake Pend Oreille Bottom Sediment Resistance Measurement

Task: Measure the resistance of collected lake bottom sediment.

Experiment: A clean copper plate was affixed to one end of a length of PVC pipe with rubber putty. The pipe was then filled with a sample of mud to slightly over-brimming. A second copper plate was then compressed over the open end of the pipe such that the copper plate came in even contact with the pipe and mud. A resistance measurement was then made by applying the electrodes of a multi-tester to the copper plates. Initially readings were on the order of 1.5 kOhms rapidly increasing to 2.0 kOhms leveling off to the recorded readings. It should be noted that as the water/mud slurry continued to separate, the resistance continued to slowly increase.



Data:

$$\text{Pipe Length: } h := \begin{pmatrix} 152.19 \\ 151.94 \\ 152.24 \\ 152.38 \\ 152.23 \\ 151.91 \\ 152.10 \\ 152.25 \end{pmatrix} \text{ mm}$$

$$\text{Pipe Diameter: } d := \begin{pmatrix} 77.25 \\ 77.12 \\ 77.30 \\ 77.23 \\ 77.30 \\ 77.32 \\ 77.26 \\ 77.34 \end{pmatrix} \text{ mm}$$

$$\text{Resistance: } R := \begin{pmatrix} 2200 \\ 2900 \\ 3000 \end{pmatrix} \Omega$$

Results:

$$h_{\text{avg}} := \text{mean}(h) \quad h_{\text{avg}} = 152.15 \text{ mm} \quad d_{\text{avg}} := \text{mean}(d) \quad d_{\text{avg}} = 77.27 \text{ mm}$$

$$R_{\text{avg}} := \text{mean}(R) \quad R_{\text{avg}} = 2.7 \times 10^3 \Omega \quad A := \frac{\pi d_{\text{avg}}^2}{4} \quad A = 4.689 \times 10^{-3} \text{ m}^2$$

$$\sigma := \frac{h_{\text{avg}}}{A \cdot R_{\text{avg}}} \quad \sigma = 12.019 \frac{\text{mm}}{\text{m}^2 \cdot \Omega}$$

Appendix F

Finite-Difference Time-Domain User's Manual

Christopher L. Wagner

July 17, 2012

Contents

1	Getting Started	4
1.1	Building the Software	4
1.2	Using the Software	5
1.2.1	A Simple Simulation	5
1.2.2	Three Layer Simulation	5
1.2.3	Lake Simulation	9
1.3	Listings	10
1.3.1	Example Configuration: simple.cfg	13
1.3.2	Example Configuration: layer.cfg	14
1.3.3	Example Configuration: lake4A.cfg	15
2	FDTD Description	16
2.1	Unit Cells and Domain Boundary	16
2.1.1	Cell Size and Convergence	16
2.2	Sources	17
2.2.1	Normalization	18
2.3	Material Modeling	18
2.4	Perfectly Matched Layer	18
2.5	Configuration Commands	18
3	Postprocessing	23
3.1	Postprocessing Theory	23
3.2	Reciprocity Theory	23
4	Data File Formats	26
4.1	FDTD sample Output Files	26
4.2	Heightfield Input Files	26

List of Figures

1.1	Live display window	9
1.2	Model Geometry of lake Pend Oreille	10
1.3	Fields on lake Pend Oreille	11
1.4	Transparent Water	12
2.1	Unit cell of the FDTD grid.	17

List of Tables

1.1	Live Field Display Control	6
1.2	Materials Display Control	7
1.3	Fields Display Control	8
1.4	Mouse Control of Display View	8
2.1	Miscellaneous Configuration Commands	19
2.2	Domain Configuration Commands	20
2.3	OpenGL Fields Display Commands	20
2.4	Perfectly Matched Layer Configuration Commands	20
2.5	Material Configuration Commands	21
2.6	PEC Object Commands	21
2.7	Source Configuration Command	21
2.8	Function specification	21
2.9	Source Functions	22
2.10	Field Sampling Configuration Commands	22
4.1	Sample Data File Format	26

Chapter 1. Getting Started

This document is not a tutorial on the Finite-Difference Time-Domain (FDTD) method or electromagnetics simulation. Rather, it will focus on using the University of Idaho FDTD software. A limited technical discussion of this FDTD implementation and usage issues is given in Chapter 2. The FDTD simulation is controlled with configuration files that are passed to the program at run time. Multiple configuration files may be passed to the program. The software does not need to be recompiled to perform a new simulation, the analyst only needs to create a new configuration file.

Direct any inquiries to:

Dr. Christopher Wagner

clwagner@uidaho.edu

208-885-6035 office

1.1 Building the Software

The first thing to do is build the software. In order to build, you will need a modern Linux system with development tools installed. Such tools include a C compiler and library development headers. Copy the distribution file to a working directory of your choice. Build the software by typing the following at the command prompt:

```
$ tar xzf ftdt-deliver.2011-03-24-1657.tgz
$ make
```

There should be no errors or warnings in the build of the FDTD code. If the build does not complete, debug it, or contact your IT staff, or the author. The distribution filename (ftdt-deliver.2011-03-24-1657.tgz in the above example) will vary depending on the software version. Simply substitute the name of the file you received in the above example. The executable created in the build can be installed into the user's bin directory (which can be added to the user's path) with `make install`. No administrator privileges are required to build, install, or use the software. Administrator privileges would be required to install the executable in a system owned directory such as `/usr/local/bin`. All that is required to "install" the programs is to copy the executable to whatever location is desired, and the set the permissions as needed.

Many modern compilers use automatic vectorization and parallelization. The automatic vectorization will substantially increase the update speed of the compiled code, use it. The free AMD and GNU compilers (open64 and gcc), as well as the commercial Intel compiler will all perform auto vectorization. See your compiler documentation for instructions on enabling features. The auto parallelization feature may or may not improve performance, testing will be required.

1.2 Using the Software

The primary scientific output of the software is time-domain electromagnetic vector field values written to disk files. To assist with verifying the simulation model configuration, a graphical display is provided. The graphics uses “OpenGL,” a standard graphical control language. The magnitude of the fields on a 2-dimensional slice can be graphically displayed as the simulation progresses – a “live” display. This can help the analyst verify the location and behavior of the source(s), as well as the field behavior. The 2D slice of the fields will be displayed in a 3D view of the domain. The 3D view allows visualization of the model geometry (water, shore, etc). The user control of the graphical display is crude, via keystrokes and mouse movements.

1.2.1 A Simple Simulation

As a first example a simulation of a Hertzian source in a small empty domain with natural boundaries (PEC walls) will be demonstrated. The included configuration file is “simple.cfg,” shown in Section 1.3.1. Because it is a small domain (100^3 cells), it should run quickly on any modern workstation. To run this simulation enter the following from the build directory

```
./fdtd-viewer simple.cfg
```

a graphics window should open. The window might look similar to that shown in Figure 1.1. The display is controlled with keystrokes typed while the “FDTD Fields Viewer” window has focus (is active). Some of the commands are given in Table 1.1. The graphical display should be disabled for production runs due to the computational costs. You should have hardware accelerated OpenGL for best performance. Typically NVIDIA graphics hardware, with proper driver software, provides good results.

1.2.2 Three Layer Simulation

A more useful simulation is now presented. The three layer problem has exact solutions available (e.g., Sommerfeld), so the FDTD solutions can be compared with exact values. A three layer simulation can accurately predict the fields in water with a flat, uniform floor; especially in deep water so the floor has minimal effect. To perform this simulation materials will need to be added to the empty box, and the domain will need to be terminated with a perfectly matched layer (PML). The layers will be created in the x-y plane, with interface surfaces at planes of constant z. It is a trivial extension to make any number of layers. Additionally the vector field values will need to be exported, either at a point or along a sample line.

Material extents, source locations, and sensor locations can be specified with either cell based or physical meters coordinates. Cells coordinates are specified in cell units from the domain origin, increasing to the domain size in cells. Cell coordinates are therefore greater than or equal to zero ($0 \leq \text{cell coordinate} < \text{domain size in cells}$). Meters coordinates are specified with respect to a logical origin. For example the air-water interface can be the z axis

Live On-Screen Graphics Control Commands	
Key	Function
q	Stop update loop and complete normal exit. Waits until not paused.
space	Pause / resume the simulation, or step in single step mode.
t	Toggle single step mode. Space to step.
i	Initialize (restart) the simulation. Must be paused to take effect.
v	Toggle display of fields inside PML region. (for scaling issues)
H	Home the view. Restore to initial view. (find lost domain)
y or Y	Decrease or increase point size. Used in display of point objects.
u or U	Decrease or increase of line size. Used in display of lines.
B	Toggle background white/black.
O	Toggle domain boundary outline.
k or l	Reduce or increase display update rate wrt time steps.
m	Toggle “movie” – writing of ppm graphics files for animations.
;	Write ppm image file to /path/Geometry-xxx.ppm, xxx is image number. Path is set in configuration file.
Up/Down Arrows	Rotate display window about X.
Right/Left Arrows	Rotate display window about Y.
Home/End	Rotate display window about Z.
A	Toggle annotation display on/off.
F	state dump (debug feature).
D	state dump (debug feature).

Table 1.1: Some of the commands for “FDTD Fields Viewer” window. The window size can also be changed by dragging the corner or using the window expand button in the title bar. Details depend on the window manager used. The graphics window must have focus for the commands to have effect.

Materials Display Control	
Key	Function
d	Toggle display (on/off) of 3D objects.
T	Toggle top contour. Displays top contour or layer-cake lines.
C	Toggle contours on/off.
L	Cycle through contour colors.
w	Toggle display of cell outlines (wireframe).
X	Lighting toggle on/off.
1	Toggle Light 1 on/off.
!	Toggle light 1 direction $\pm z$.
2	Toggle Light 2 on/off.
@	Toggle light 2 direction $\pm x$.
3	Toggle Light 3 on/off.
#	Toggle light 3 direction $\pm y$.
4	Toggle Light 4 on/off.
\$	Toggle light 4 direction $\pm z$.
5	Toggle Light 5 on/off.
%	Toggle light 5 direction $\pm z$.
6	Toggle Light 6 on/off.
^	Toggle light 6 direction $\pm x$.
7	Toggle Light 7 on/off.
&	Toggle light 7 direction $\pm y$.
8	Toggle Light 8 on/off.
*	Toggle light 8 direction $\pm z$.
G or g	Toggle display on/off of points, lines and planes.
S	Cycle active material.
V	Toggle visibility of active material.
J	Toggle active material transparency on/off.
K	Cycle active material colors.
W	Cycle transparent color alpha 0.0, 0.5, 1.0
N	Cycle blend function.

Table 1.2: Commands to control the display of materials, such as the heightfields and layers used to build lake models. Lights 1–5 are fixed in world coordinates, lights 6–8 are fixed in the material objects local coordinate system. Points are used to display source or sensor locations, lines are used to display sensor lines or PEC lines, and planes are used for PEC planes.

Fields Display Control	
Key	Function
f	Toggle display of field slice planes.
[No graphical smoothing of field slices.
]	Graphical (texture) smoothing of all field slices.
e or E	Decrease or increase (cycle) display planes to active.
a	Cycle through the slice axis of the active field display.
s	Global/local frame scaling of active plane. Local scaling is frame by frame scaling.
r	Reset the global scale of active plane.
p or o	Increase/decrease the the view plane coordinate of active plane.
n	Toggle between node or cell data display of active plane. No charge in cell display.
pageup	Increase dynamic range of active plane. (logarithmic compression)
pagedown	Decrease dynamic range of active plane. (0=linear)
z	Field select. Cycles through E,H,Q,EHQ for active plane.
Z	Component select. Cycles through x, y, z components and vector magnitude of active plane.
M	Cycle texture mode.

Table 1.3: Control of the display of field sample slices. All fields, or individual fields (components or magnitudes) can be displayed. Charge is only available in node display mode. Local scaling is per frame, so it will not correctly represent the change between frames. To see the change between frames it is necessary to use global scaling. The global scale usually needs to be reset if changing field or component display when using global scaling.

Mouse Control of Display View	
Button	Function
right	rotate about z
left	pan
scroll-up	Zoom Out (Increase FOV)
scroll-down	Zoom In (Decrease FOV)
center	rotate about x, rotate about y

Table 1.4: The orientation and position of the simulation domain can be controlled with the mouse. The mouse can also change the size of the display window, using whatever method the display manager supports.

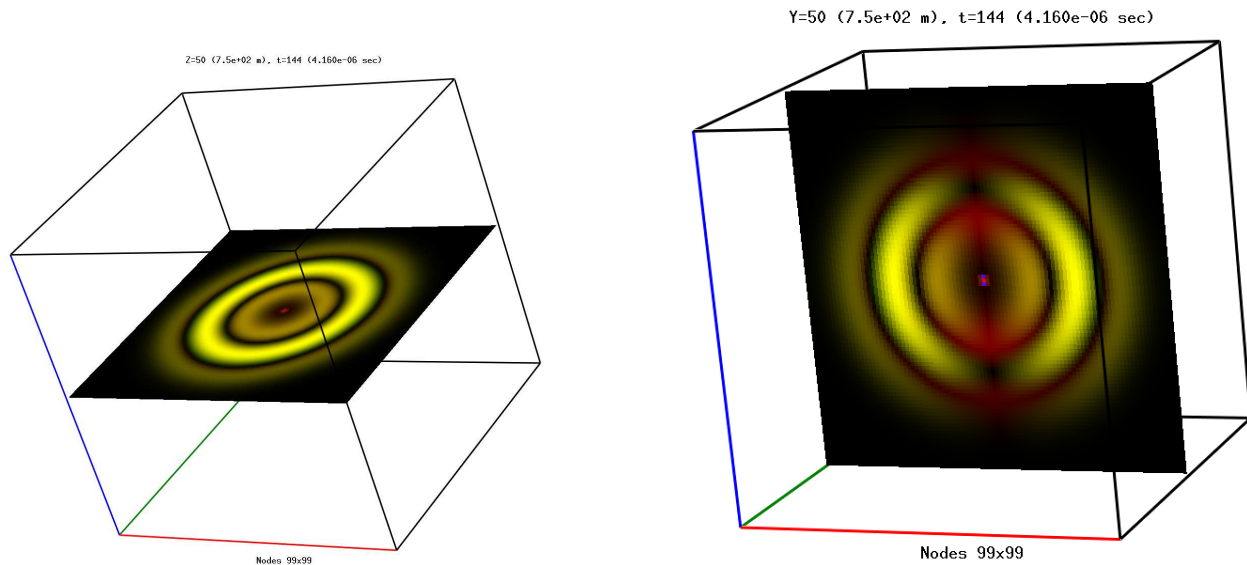


Figure 1.1: Example of the contents of the display window. The window decorations (title bar, etc.) are not shown. The red color is the magnitude of the \mathbf{E} field, green is the magnitude of \mathbf{H} , and blue is the magnitude of the charge. The colors blend, so if \mathbf{E} and \mathbf{H} are both strong the display color will be yellow. These snapshots are taken before the wavefront has reflected from the walls of the domain. The color figures do not display well on-screen, printed copies should preserve the image quality.

origin. In this layer example locations in the air have a positive z value, and locations in the water have negative z values. A configuration file for the three layer problem is “layer.cfg,” which is listed in Section 1.3.2. The PML, materials, and sample locations are defined as shown in the listing. To run this simulation enter the following from the build directory

```
./fdtd-viewer layer.cfg
```

1.2.3 Lake Simulation

The third example uses the UI’s topological data for the south-west region of lake Pend Oreille. This is the region of the lake used in Phase 3 experiments. This topological data has a registration error compared to GPS coordinates used in the Phase 3 experiments. This error is compensated using the FDTD configuration “domain_origin” to shift the x,y coordinates to match GPS coordinates placing the magnetic source at the shoreline. The simulation configuration is similar to runs 100.01, 100.03, 100.05, 100.07 and 100.09. These experiments were performed on 9/13/2010. To run the simulation enter at the command prompt

```
./fdtd-viewer lake4A.cfg
```

The configuration file currently specifies the /tmp directory for writing of data. The lake geometry can be examined with the display window. The displayed geometry will be similar

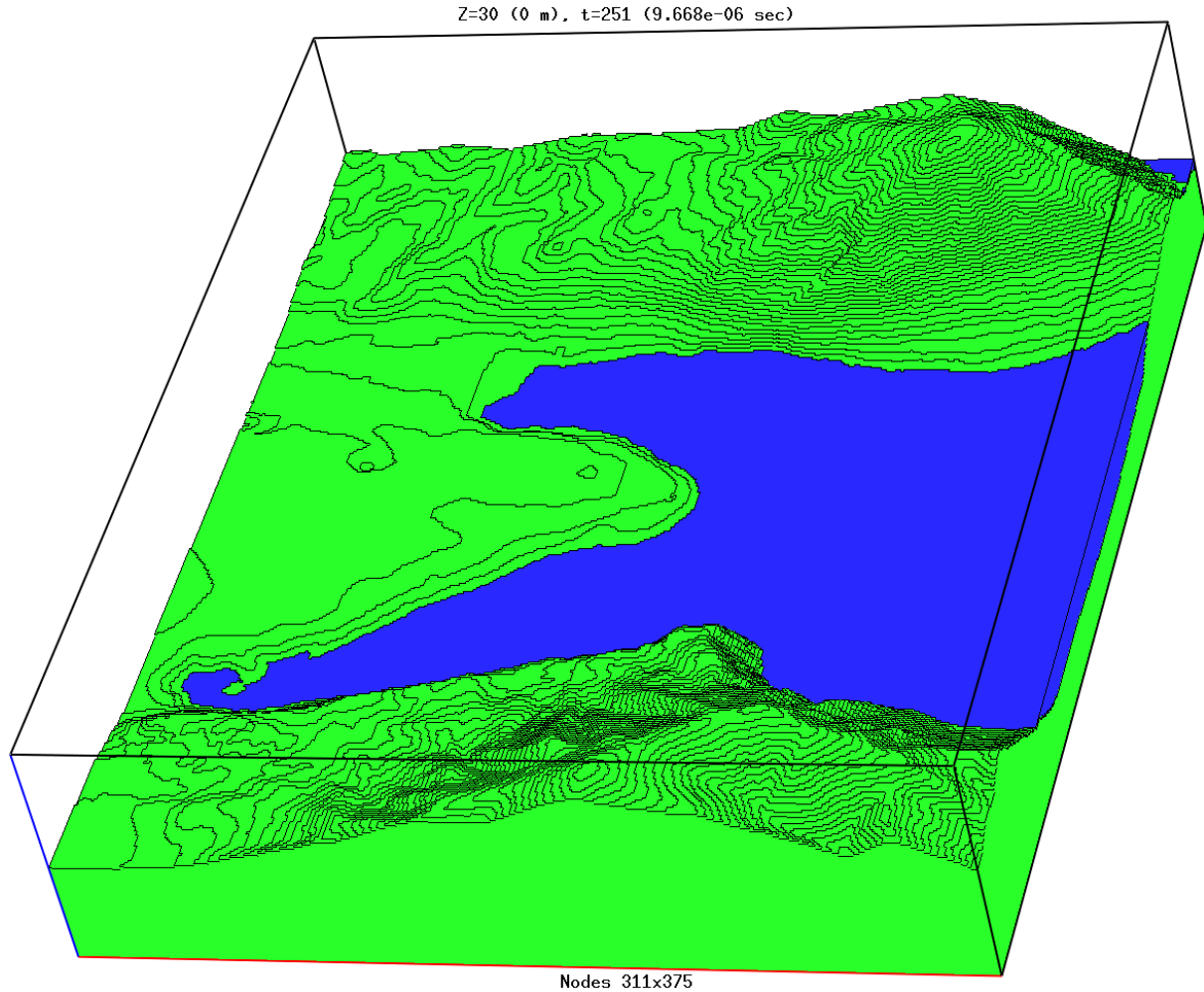


Figure 1.2: Model Geometry of lake Pend Oreille near Bayview. Contour lines are the outlines of the top of the FDTD cells.

to that shown in Figure 1.2. The view can be rotated with the arrow keys or by using the mouse, see Tables 1.1 and 1.4. Depending on the graphics performance of your machine, you may need to turn the geometry off (with 'd') in order to rotate the scene in a responsive manner.

The field slice display can be used with the geometry display. The fields on the water surface can be seen as shown in Figure 1.3. The model geometry can be turned off, so the fields under water can be visualized.

1.3 Listings

These listings are the example configurations and scripts mentioned previously. Details of the configuration commands are given in Section 2.5.

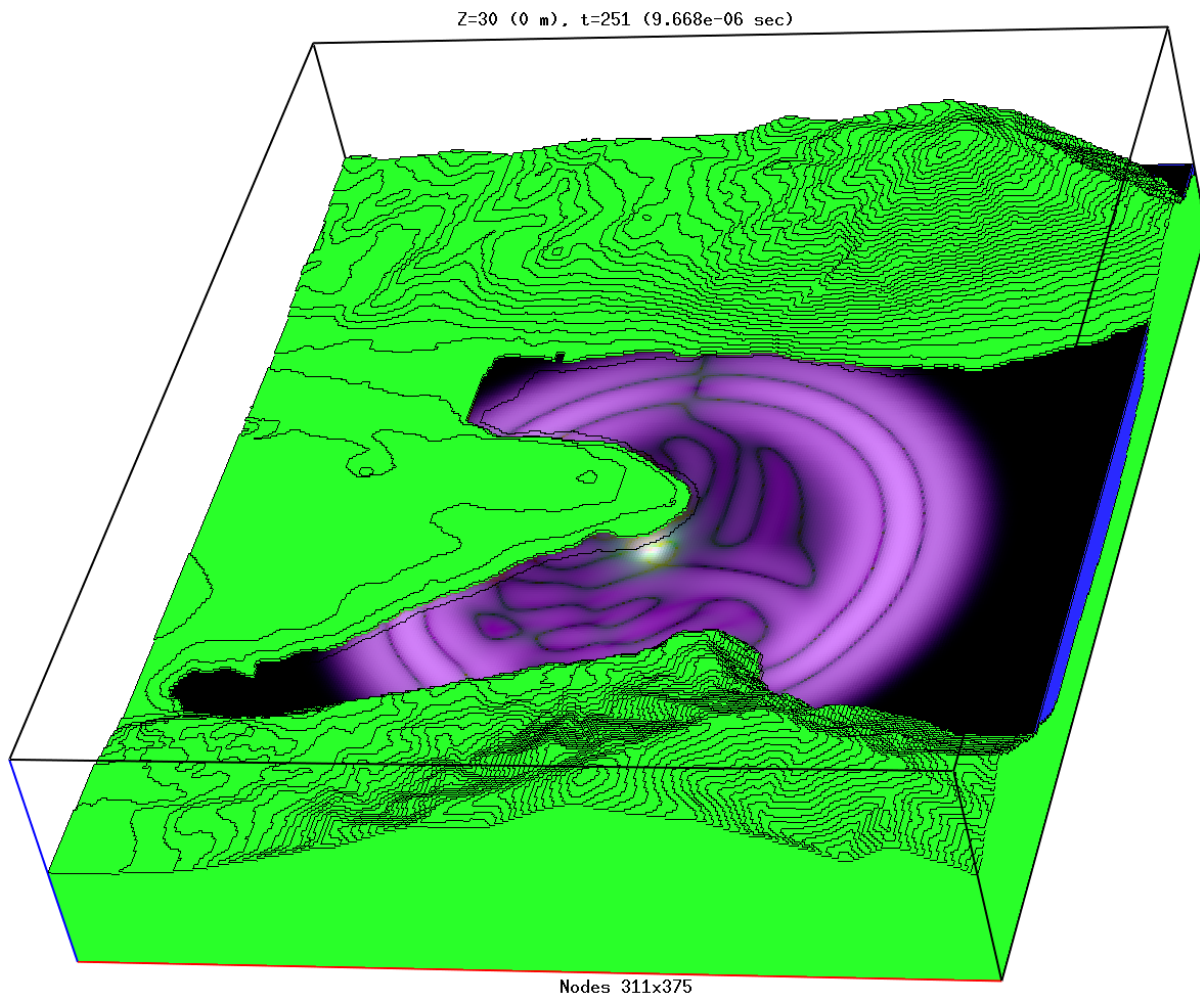


Figure 1.3: Fields on the surface of lake Pend Oreille near Bayview. For this plot, the fields are shown as: Red is magnitude of \mathbf{E} , Green is Magnitude of \mathbf{H} , and Blue is Magnitude of Q .

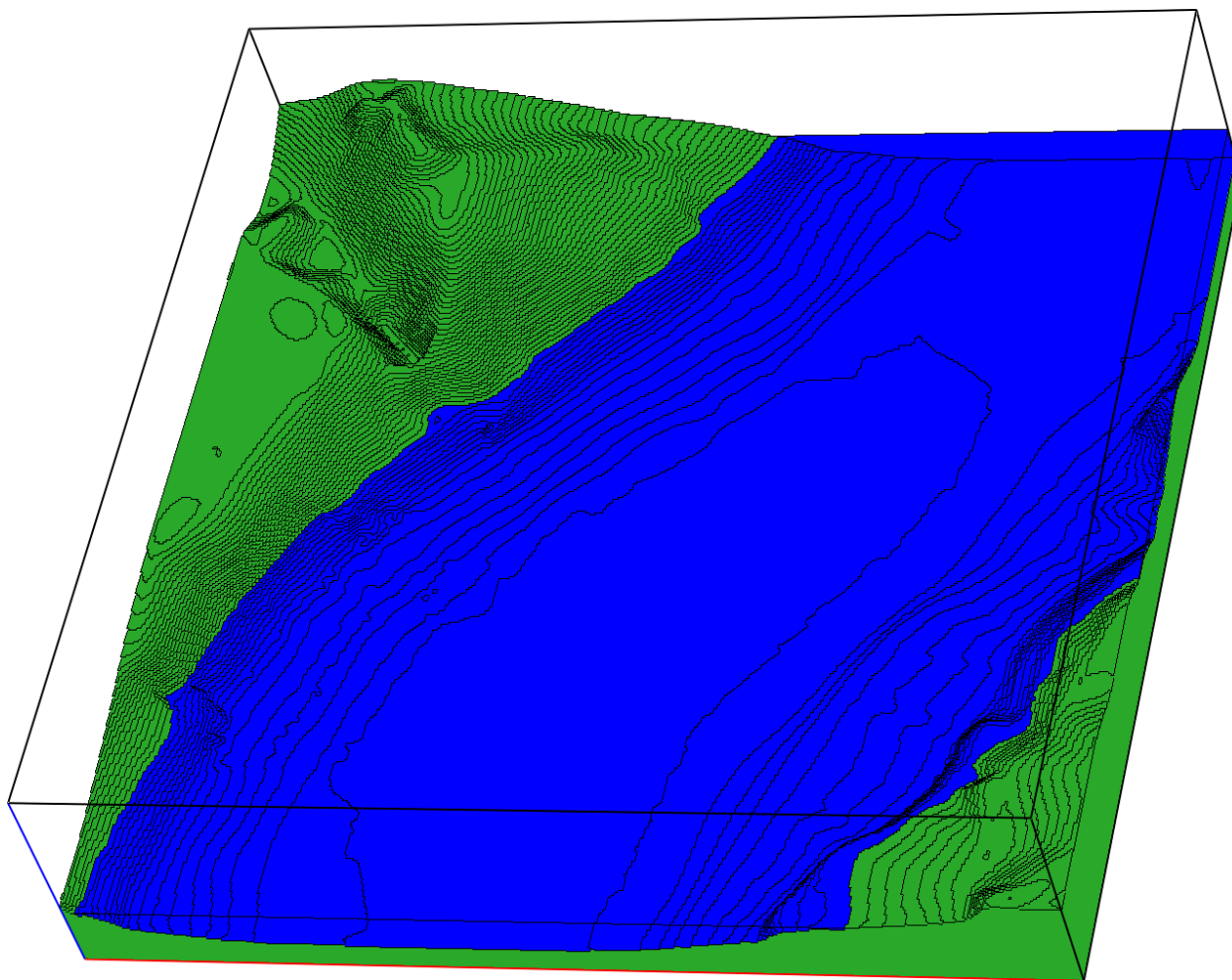


Figure 1.4: Geometry display with transparent water. The transparency implementation is not a general arbitrary transparent materials display. The case of a single transparent material, like the lake water shown, is implemented.

1.3.1 Example Configuration: simple.cfg

```
# EM 3D FDTD ELF configuration file.
# Control options
verbose          4          verbosity level
PML              0          no PML
message          100        message rate divisor
magnetic         0          no magnetic materials

# Domain Specification
domain_size      100,100,100    domain size, in cells
domain_time      200000         run time, steps
domain_delta     15             cubic grid cell size, meters
time_factor      1.0           Courant factor, 0<value<=1.0

# Material parameters of the background space. These values are used to
# calculate the time step. It is the analyst's responsibility to ensure
# that the background material has the highest propagation speed of all
# the materials in the domain.

#Background_Conductivity      0.0
#Background_Dielectric 1.0
#Background_Permeability 1.0

# on-screen openGL display
live          1          activate display
live_plane    Z,50
live_rate     1          rate of display updates

# Setup the source
# source {loop|hertz} {cells|meters} theta phi x y z {function spec}
source hertz cells 0,0 50,50,50 dgauss, 16.0, 100.0, 0.0, 1.0

# sample path sets the directory for output files
sample_path    /tmp
# point_sample {E|H} {cells|meters} {X,Y,Z}
#point_sample E cells 60,50,60
```

1.3.2 Example Configuration: layer.cfg

```
# EM 3D FDTD ELF configuration file.
# Control options
verbose          5          be more verbose
PML              1          use CPML Absorbing boundary
message         100         message rate divisor
magnetic        0          Do not use magnetic materials

# Domain Specification
domain_size      200,200,100      domain size, in cells
domain_origin    2000.,2000.,1000. logical origin, meters
domain_time      200000          run time, steps
domain_delta     20              cubic grid cell size, meters
time_factor      1.0             courant factor, 0<value<=1.0

# Material parameters of the background space.
# these values are used to calculate the time step
Background_Conductivity 0.000001
Background_Dielectric   1.0
#Background_Permeability 1.0

# PML spec
pml_order         3.5             grading exponent for conductivity
pml_alpha_order   3.5             grading exponent for cfs
pml_plane         1,1,1,1,1       active planes lower x,y,z upper x,y,z
pml_thickness     15             thickness in cells
pml_kappa         3              max real coord stretch
pml_freq          1e6             max cfs frequency
pml_autosigma     1              auto config sigma max (Gedney opt)
pml_autoalpha     1              auto config alpha max (from pml_freq)

# on-screen OpenGL display
live              1              activate display
live_plane        Z,50           initial view plane
live_rate         1              rate of display updates

# Materials. Order maters, later entries overwrite earlier entries.
# Block {cells|meters} Lower corner, upper corner, dielectric, conductivity [, permeability]
# layer {cells|meters} z height, dielectric, conductivity [, permeability]
layer meters      0 81 0.01 Water layer
layer meters -300 1 0.001 Bottom Material

# Excitation source
# source {loop|hertz} {cells|meters} theta phi x y z {function spec}
source hertz meters 90,90 0.0,0.0,-10.0 gauss, 16.0, 100.0, 0.0, 1.0

# sample path sets the directory for output files
sample_path       /tmp
# line_sample {E|H} {cells|meters} {startX,Y,Z} {finishX,Y,Z} {num intervals}
# point_sample {E|H} {cells|meters} {X,Y,Z}
```

1.3.3 Example Configuration: lake4A.cfg

```
# EM 3D FDTD ELF configuration file.
verbose      5          be more verbose
PML          1          use CPML Absorbing boundary
message      100        message rate divisor

# Domain Specification
domain_size   312,376,90    domain size, in cells 20m map
domain_time   200000        run time, steps
domain_delta   20          cubic grid cell size
domain_origin 50.,-80.,600. Logical Origin (registration offset, water level )
time_factor    1.0         courant factor, 0<value<=1.0
Background_Conductivity 0.0
Background_Dielectric  1.0

# PML configuration
pml_order      3.5          grading exponent for conductivity
pml_alpha_order 3.5        grading exponent for cfs
pml_plane      1,1,1,1,1    active planes lower x,y,z upper x,y,z
pml_thickness  15          thickness in cells
pml_kappa      3           max real coord stretch
pml_freq       1e6         max cfs frequency
pml_autosigma  1           auto config sigma max (Gedney opt)
pml_autoalpha  1           auto config alpha max (from pml_freq)

# on-screen OpenGL display
live          1           activate display
live_plane    Z,30        initial view plane
live_rate     1           rate of display updates

# Materials. Order matters, the materials use Constructive Solid Geometry
# later entries overwrite earlier entries.
# sphere {cells|meters} center x,y,z, radius, dielectric, conductivity [,rel_perm]
# Block {cells|meters} Lower corner, upper corner, dielectric, conductivity [,rel_perm]
# layer {cells|meters} interface layer z coord, dielectric, conductivity [,rel_perm]
# Heightfield {cells|meters} filename {zero level} ,dielectric, conductivity [,rel_perm]

# Water layer
layer meters 0.0 81.0, 0.010
# Lake bathymetry
Heightfield meters Topo-Bayview-20m.dat 0.0 1. 0.0012

#source {loop|hertz} {cells|meters} theta phi x y z {function spec}
source loop meters 0,0 3163.8,3561.7,-10 dgauss, 16.0, 100.0, 0.0, 1.0

# Data sampling setup
# path to where data files go
sample_path    /tmp
# line_sample {E|H} {cells|meters} {startX,Y,Z} {finishX,Y,Z} {num intervals}
#line_sample   E meters      3225.6,3498.1,20.0 3225.6,3498.1,-20.0 10
#line_sample   H meters      3225.6,3498.1,20.0 3225.6,3498.1,-20.0 10
```

Chapter 2. FDTD Description

There are several possible choices of implementation details for FDTD code. Such details include the definition of the unit cell, and field components tangent to domain boundaries.

2.1 Unit Cells and Domain Boundary

This FDTD code uses the unit cell shown in Figure 2.1. The domain walls have tangent \mathbf{E} elements, so the natural boundary condition is PEC. The cells do not need to be cubic. When fields are displayed in the “live” window, either cells or nodes may be specified. For the live display, ‘cells’ refers to field values interpolated to the center of the unit cells, and ‘nodes’ refers to field values interpolated to the corners of the unit cell.

2.1.1 Cell Size and Convergence

The cell size must be chosen to balance the simulation time with the need for geometric and field fidelity. Also when measuring near an interface (e.g., air-water) the cells must be fine enough to avoid sampling problems at the interface. The cells need not be cubic, so the analyst can have finer cells size in the direction perpendicular to the interface. For example if the air-water interface is in the $z = 0$, plane the cells can have a small z axis size. If the fields 1 meter below the air-water interface are required, 2 meter cells in the z direction could be used. Because of staggering this will allow sampling of the fields 1 meter deep without any fields above the interface entering into the interpolated exported data. With cells larger then $2m$ in the z direction, the z component of the \mathbf{E} field sampled at a depth of $1m$ will have some above the surface contribution to the interpolated data, and so may not be accurate. The x and y components would not suffer the same problem due to the staggering of the fields in the grid. However, cubic cells have better dispersion-error performance, so if possible use small cubic cells.

A major question is whether the simulation is producing valid results. FDTD, with small enough cells, will produce accurate results. In the limit as the cell size goes to zero, FDTD becomes an exact electromagnetic solver. It is impractical to always run with tiny cells, simulations need to be run with cells large enough to get good results without prohibitive simulation times. There are two issues: does the simulation have sufficient spatial resolution to accurately capture spatial variations of the fields, and has the simulation been run long enough for the diffusion processes of low frequencies to occur in conductive media (water). Two convergence tests are needed:

1. Increase the simulation time by a factor of two (without changing cell size). If the low frequency results change the simulation time is not provably sufficient for diffusion processes to complete at the sample locations.

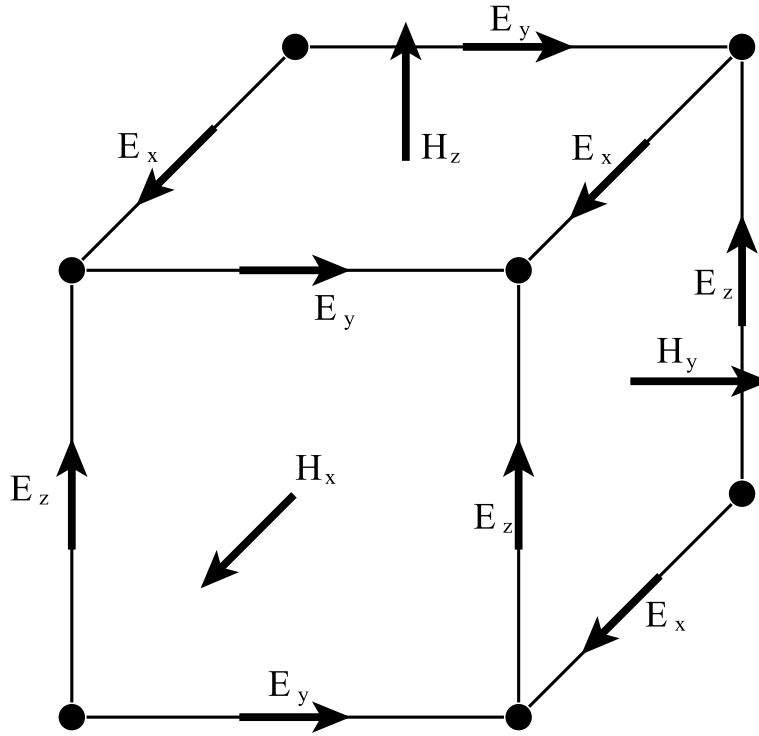


Figure 2.1: Unit cell of the FDTD grid.

2. Reduce the cell size by a factor of two in all 3 dimensions. To cover the same space-time range the computation cost will increase 16 fold. Twice as many time steps will be needed. If the resulting field spatial variations change in the new simulation the grid size is not provably sufficiently fine to resolve the spatial variation.

The diffusion issue is range dependent. Sample locations close to the source will require less time to complete the diffusion compared to sample locations distant from the source. The spatial variation issue has range and geometry dependence. Distant from the source (and scattering objects) the fields do not have rapid spatial variation. Near the source or scattering objects the fields may have rapid variation. For example it is common for fields to change sign as the sensor passes near a source. If this behavior is important, fine cells will be required.

2.2 Sources

Electric and magnetic Hertzian and electric current loops may be specified. In order to allow the source to be at arbitrary positions and orientation a superposition of elemental currents is used. While this does allow for positioning flexibility, it can increase the size of the source to several cells. This is only problematic for observation close to the source. If field behavior close to the source is desired, the analyst may need to use small cells and physically model

the elements of the source. For the ELF project physical modeling of the source was not usually performed due to computation costs.

Loop sources will not produce the desired fields for non-cubic cells, when the loop direction is such that the cell edges are not equal length. For example if the cells are $10 \times 10 \times 5$ meters, a loop with moment purely in z will work as desired. However, if the loop moment has an x or y component, then the loop would not be square and would not radiate the desired fields. Either make sure the cells are square perpendicular to the moment components, or use the magnetic Hertzian source. Caution is required with a magnetic Hertzian to ensure the simulations remain physical.

2.2.1 Normalization

Maxwell's equations require the current density, \mathbf{J} . Typical experiments specify the current, the code divides the current by the transverse area to get current density. Theoretical source strengths are specified with moments, so the code also normalizes to the cell longitudinal size or loop area. Since cells can be non-cubic, these two normalizations are geometrically desirable. Additionally these normalizations remove cell size issues from postprocessing, only the current spectral density and source moment are required. See Chapter 3 for details.

2.3 Material Modeling

All material geometry is sampled to cells. There is no subdivision of the cells. A cell has a conductivity, dielectric constant, and optionally a relative permeability. There is no limit to the number of different types of materials that can be specified. Currently the shapes available are spheres, blocks, layers, cylinders and height-fields. Height-fields are read from data files produced from topographic and bathymetric data. Cells under the height-field are assigned the specified material properties.

Blocks or layers are used to specify grid-aligned rectangular regions, such as lake water. A height-field could then specify the shape for the bottom and mountains, as in the lake example.

2.4 Perfectly Matched Layer

Most simulations will require the use of PML to terminate the domain. The PML has several parameters to specify to configure the PML. PML performance testing is described in two papers included with the document pack provided by the UI ELF team.

2.5 Configuration Commands

The simulation is controlled with directives placed into configuration files. The command syntax is a simple keyword,value,... structure. If there are multiple commands for a single

Miscellaneous Commands		
Keyword	Values	Function
verbose	1 – n	Startup messages detail level (expected to change)
message	1 – n	rate messages printed during update loop
#	anything	Comment

Table 2.1: Miscellaneous commands and comments.

valued feature, the last instance will control the feature. Sources, materials, and sample points or lines can have multiple instances. All will have effect. Options and keywords may be separated with whitespace or a comma (with or without whitespace). Whitespace consists of spaces and/or tabs. A single command should not have embedded newlines. After a syntactically complete command, all characters to the newline are comments. Commands and options are not case sensitive.

The command parsing has limited error recovery. If an error is detected, the job will usually stop. Some cases generate warnings. It is possible to write commands that will crash the program during command parsing. For example splitting a correct command with a newline will usually cause a segment fault (crash) during reading of the commands. The run listing should show the command just before the segfault. The error is typically in the line or two before the crash. Commands that reference locations outside the simulations space will either terminate the program with an error, or the coordinates will be limited to the simulation space. Commands with syntax errors that are not detected may lead to unpredictable behavior. For example if numerical values are missing in a command, comment text at the end of the command will be read as the missing values. Since the text will not produce valid numerical values, the simulation will run with bad configuration data. This might lead to a crash, or unpredictable behavior.

Because the program will accept multiple configuration files, and due to the simple syntax, automatic generation of configurations options is possible. Automatic configuration has been used to run tens of thousands of FDTD simulations with multiple parameter variations when testing PML configurations.

Domain Configuration Commands		
Keyword	Values	Function
domain_size	x,y,z	domain size in integer cells.
domain_time	n	Number of time steps
domain_deltas	dx,dy,dz	size of cell in meters
domain_delta	dx	size of cubic cell in meters
domain_origin	x_0, y_0, z_0	logical origin in meters from 0,0,0 cell
time_factor	0.0–1.0	Time-step fraction of Courant limit
magnetic	0/1	Use (1) or do not use (0) magnetic materials
Background_Conductivity	σ	Conductivity of “empty” space
Background_Dielectric	ϵ_r	Dielectric constant of “empty” space
Background_Permability	μ_r	relative permeability of “empty” space

Table 2.2: Commands to set the domain configuration. The domain size can only be specified in cells.

Live on-screen OpenGL display		
Keyword	Values	Function
live	0/1	Activate display
live_plane	axis,n	Initial plane, axis is one of x, y, z
live_rate	1–n	rate of display updates

Table 2.3: Commands to configure the live on-screen display of fields.

Perfectly Matched Layer		
Keyword	Values	Function
pml	0/1	1=enable PML domain termination
pml_order	0–x	Grading exponent for conductivity
pml_alpha_order	0–x	Grading exponent for cfs
pml_plane	1,1,1,1,1,1	Active planes – xlower,xupper,y1,yu,zl,zu
pml_thickness	n	Thickness in cells
pml_kappa	1–x	Max real coord stretch
pml_freq	x	Max cfs frequency
pml_autosigma	0/1	Auto config sigma max (Gedney opt)
pml_autoalpha	0/1	Auto config alpha max (from pml_freq)

Table 2.4: PML configuration commands.

Material Configuration Commands			
Keyword and Options			
Block	$\left\{ \begin{array}{c} \text{Cells} \\ \text{Meters} \end{array} \right\}$	$\{\text{Lower corner x,y,z}\} \{\text{Upper corner x,y,z}\} \{\text{material properties}\}$	
Layer	$\left\{ \begin{array}{c} \text{Cells} \\ \text{Meters} \end{array} \right\}$	$\{\text{z height}\} \{\text{material properties}\}$	
Sphere	$\left\{ \begin{array}{c} \text{Cells} \\ \text{Meters} \end{array} \right\}$	$\{\text{Origin x,y,z}\} \text{radius}, \{\text{material properties}\}$	
Heightfield	$\left\{ \begin{array}{c} \text{Cells} \\ \text{Meters} \end{array} \right\}$	$\{\text{filename}\}, \{\text{z axis zero level}\} \{\text{material properties}\}$	
Cylinder, $\{\text{Origin x,y,z}\}, \text{radius}, \{\text{axis: 'x','y','z'}\}, \{\text{material properties}\}$			

Table 2.5: Commands to set material geometries. Any number of materials and objects may be specified. The sphere will be spherical for meters specifications, even with non-cubic cells. For cells specification the sphere command will produce an ellipsoid when cells are not cubic. Cylinders are currently only specified in cells. Material properties are currently `dielectric.constant`, `conductivity` and optionally `relative.permeability`.

PEC Object Configuration Commands	
Keyword and Options	
pec_wire	$\{\text{axis: 'x','y','z'}\}, \{\text{Origin x,y,z}\} \text{length}$
pec_sheet	$\{\text{plane: 'x','y','z'}\} \text{elevation } \{u_0, v_0\}, \{u_m, v_m\}$

Table 2.6: One and two dimensional grid-aligned PEC objects. 3D PEC objects can be made with the materials commands using a very high conductivity.

Source Configuration Command		
Keyword and Options		
source	$\left\{ \begin{array}{c} \text{Hertz} \\ \text{loop} \\ \text{magnetic} \end{array} \right\}$	$\left\{ \begin{array}{c} \text{Cells} \\ \text{Meters} \end{array} \right\} \{\theta, \phi\} \{\text{Origin x,y,z}\} \{\text{Function specification}\}$

Table 2.7: Command to set Hertzian, electric loop or Magnetic Hertzian sources. Any number of sources may be specified. The angle θ is the polar angle from the $+z$ axis in degrees. The angle ϕ is the azimuthal angle counter-clockwise (towards $+y$ axis) from the $+x$ axis in degrees. The **Function specification** part is described in Table 2.8 below.

Function Specification	
Function, width, delay, period, amplitude	The function names are given in table 2.9 below. The width, delay, and period are in time steps at 100% of the Courant limit.

Table 2.8: Source function specification. Not all functions use all specifications, but all must always be specified. For example the Gaussian function does not use the period specification; the value is ignored.

Time-Dependent Source Functions Names		
Keyword	Description	Variables
gaussian or gauss	Gaussian pulse	W,D,A
dgaussian or dgauss	Derivative of Gaussian	W,D,A
d2gaussian or d2gauss	Second derivative of Gaussian	W,D,A
d3gaussian or d3gauss	Third derivative of Gaussian	W,D,A
d4gaussian or d4gauss	Fourth derivative of Gaussian	W,D,A
burst	Gaussian envelope sin function	W,D,P,A
sin	Sine function	D,P,A
cos	Cosine function	D,P,A
smooth_sin	Smooth start sine function	W,D,P,A
delayedsin	Delayed start sine function	D,P,A
delayedcos	Delayed start cosine function	D,P,A
pulsesin	Sine gated by rectangular pulse	W,D,P,A
pulsecos	Cosine gated by rectangular pulse	W,D,P,A
raisedcos	Raised cosine	D,P,A
delta	Pulse one time-step long	D,A
step	Step function	D,A
pulse	Square pulse	W,D,A
doublet	Single time-step positive, followed by single time-step negative	D,A
dpulse	Doublet with specified pulse width	W,D,A
spaced_doublet	Doublet with zero between peaks	D,A
ricker	Ricker wavelet. Essentially equivalent to the second derivative of a Gaussian.	W,D,A

Table 2.9: Source functions currently available. Harmonic functions like sine and cosine are not truly harmonic due to turn-on transients. Functions like the step, delta, pulse, etc. are poor choices due to the large high-frequency components in the signal. Many of these source functions were used for experimental purposes, and may be removed. The “W,D,P,A” specifiers are the width, delay, period, and amplitude values as shown in Table 2.8. When the W,D,A specifiers do not apply to a function, some value for each must still be specified.

Field Sampling Configuration Commands		
Keyword and Options		
point_sample	$\begin{Bmatrix} \mathbf{E} \\ \mathbf{H} \end{Bmatrix}$	$\begin{Bmatrix} \text{Cells} \\ \text{Meters} \end{Bmatrix} \{ \text{Coordinate } x,y,z \}$
line_sample	$\begin{Bmatrix} \mathbf{E} \\ \mathbf{H} \end{Bmatrix}$	$\begin{Bmatrix} \text{Cells} \\ \text{Meters} \end{Bmatrix} \{ \text{Start } x,y,z \} \{ \text{Finish } x,y,z \} \{ \text{Number of sample intervals} \}$
sample_path	/path/to/output/data	

Table 2.10: Commands to setup field sampling. Samples may be taken at any point or along any line in the simulation space. Interpolation is used to calculate the fields at arbitrary positions. Each sample point will produce a file of vector components over time. Files will have four columns: ‘time Xcomp Ycomp Zcomp’. The **E** and **H** samples are staggered in time by 1/2 time step.

Chapter 3. Postprocessing

It is expected that Carderock's post processing will be done in Matlab, or other similar program (IDL, ...). The primary post processing step is to FFT the data sets. Once the data is transformed, data is extracted from FFT files to produce plots.

3.1 Postprocessing Theory

The time domain (wideband) data needs to be converted to the steady-state harmonic result. This is done by passing the FDTD data through an FFT. It is then normalized to the transformed current, and scaled by the moment. The single frequency of interest is then extracted from the data for each sample location to produce a data file of harmonic data vs. distance along the sample path. The calculation at a single sample point, using the Fourier transformed data, is

$$\mathbf{E}_{\text{norm}}(\omega) = m \frac{\mathbf{E}(\omega)}{J(\omega)} \quad (3.1)$$

where m is the moment (A·m for dipoles, A·m² for current loops), $\mathbf{E}(\omega)$ is the complex Fourier transform of the FDTD time-domain data, and $J(\omega)$ is the complex Fourier transform of the current waveform of the FDTD source. The complex division in (3.1) is performed at each frequency. Typically the magnitude of the components of $\mathbf{E}_{\text{norm}}(\omega)$ are then compared with the experiment of other simulation results. Simply substitute \mathbf{H} for \mathbf{E} in (3.1) for the magnetic field processing.

3.2 Reciprocity Theory

Lorentz reciprocity with electric and magnetic current sources is expressed as

$$-\nabla \cdot (\mathbf{E}^s \times \mathbf{H}^e - \mathbf{E}^e \times \mathbf{H}^s) = \mathbf{E}^s \cdot \mathbf{J}^e + \mathbf{H}^e \cdot \mathbf{M}^s - \mathbf{E}^e \cdot \mathbf{J}^s - \mathbf{H}^s \cdot \mathbf{M}^e. \quad (3.2)$$

If we assume the electric (or magnetic, as required) current sources are localized and can be written with Dirac delta functions

$$\mathbf{J}^s = \mathbf{J}_0^s \delta(\mathbf{r}) \quad \mathbf{J}^e = \mathbf{J}_0^e \delta(\mathbf{r}) \quad (3.3)$$

and volume integrate (3.2) over all space with only electric current sources, we obtain

$$\mathbf{E}^e \cdot \mathbf{J}_0^s = \mathbf{E}^s \cdot \mathbf{J}_0^e. \quad (3.4)$$

This relation provides information about projections of fields onto the currents. If we do not have additional information (such as that the currents and fields are parallel) then we

cannot use (3.4) to find the predicted vector field from a single simulation with source and sensor exchanged. We need to perform the exchange when the source is moving, as the simulations do not have moving source capabilities. Since reciprocity provides information about projections, we can perform three simulations with the current in each coordinate direction. Then the three results can be combined to obtain the resulting prediction.

Now given the experimental current is

$$\mathbf{J}^e = J_x^e \mathbf{x} + J_y^e \mathbf{y} + J_z^e \mathbf{z} \quad (3.5)$$

and the three simulation currents are

$$\mathbf{J}^1 = J_0 \mathbf{x}, \quad (3.6)$$

$$\mathbf{J}^2 = J_0 \mathbf{y}, \quad (3.7)$$

$$\mathbf{J}^3 = J_0 \mathbf{z}, \quad (3.8)$$

then the three reciprocity relations will be

$$E_x^e = \frac{1}{J_0} (E_x^1 J_x^e + E_y^1 J_y^e + E_z^1 J_z^e), \quad (3.9)$$

$$E_y^e = \frac{1}{J_0} (E_x^2 J_x^e + E_y^2 J_y^e + E_z^2 J_z^e), \quad (3.10)$$

$$E_z^e = \frac{1}{J_0} (E_x^3 J_x^e + E_y^3 J_y^e + E_z^3 J_z^e). \quad (3.11)$$

In summary the reciprocity relations for the electric field with an experimental electric current source are

$$\mathbf{E}^e \cdot \mathbf{J}^s = \mathbf{E}^s \cdot \mathbf{J}^e. \quad (3.12)$$

$$\mathbf{E}_{\text{predict}}^e = \frac{1}{J_0} \begin{bmatrix} E_x^1 & E_y^1 & E_z^1 \\ E_x^2 & E_y^2 & E_z^2 \\ E_x^3 & E_y^3 & E_z^3 \end{bmatrix} \begin{bmatrix} J_x^e \\ J_y^e \\ J_z^e \end{bmatrix} \quad (3.13)$$

In order to calculate the expected magnetic field we assume a simulation point magnetic current and the same experimental electric current as before

$$\mathbf{H}^e \cdot \mathbf{M}^s = -\mathbf{E}^s \cdot \mathbf{J}^e \quad (3.14)$$

$$\mathbf{H}_{\text{predict}}^e = -\frac{1}{M_0} \begin{bmatrix} E_x^4 & E_y^4 & E_z^4 \\ E_x^5 & E_y^5 & E_z^5 \\ E_x^6 & E_y^6 & E_z^6 \end{bmatrix} \begin{bmatrix} J_x^e \\ J_y^e \\ J_z^e \end{bmatrix} \quad (3.15)$$

We also have similar relations for the experimental magnetic dipole case.

$$\mathbf{H}^e \cdot \mathbf{M}^s = \mathbf{H}^s \cdot \mathbf{M}^e \quad (3.16)$$

$$\mathbf{H}_{\text{predict}}^e = \frac{1}{M_0} \begin{bmatrix} H_x^1 & H_y^1 & H_z^1 \\ H_x^2 & H_y^2 & H_z^2 \\ H_x^3 & H_y^3 & H_z^3 \end{bmatrix} \begin{bmatrix} M_x^e \\ M_y^e \\ M_z^e \end{bmatrix} \quad (3.17)$$

$$\mathbf{E}^e \cdot \mathbf{J}^s = -\mathbf{H}^s \cdot \mathbf{M}^e \quad (3.18)$$

$$\mathbf{E}_{\text{predict}}^e = -\frac{1}{J_0} \begin{bmatrix} H_x^4 & H_y^4 & H_z^4 \\ H_x^5 & H_y^5 & H_z^5 \\ H_x^6 & H_y^6 & H_z^6 \end{bmatrix} \begin{bmatrix} M_x^e \\ M_y^e \\ M_z^e \end{bmatrix} \quad (3.19)$$

There is an equivalence between electric current loops (strength IS) and magnetic Hertzian dipoles (strength Kl). When the two source strengths are related by

$$Kl = j\omega\mu IS \quad (3.20)$$

then the sources will radiate the same fields. The scaling implied by (3.20) will be required if the M sources are loops. The magnetic sources in the experiment are always loops, simulations can use either loops or magnetic Hertzian dipoles. When there are different types of magnetic sources, such as experimental current loop and simulation magnetic dipole, the scaling of (3.20) will be required.

See the paper “Roving Sources, Simulation and Reciprocity” by J. L. Young and C. L. Wagner included in the final report for further details of the reciprocity processing.

Chapter 4. Data File Formats

4.1 FDTD sample Output Files

The ASCII coded point sample files have four data columns separated by spaces as shown in Table 4.1.

time ₀	x-component	y-component	z-component
time ₁	x-component	y-component	z-component
⋮	⋮	⋮	⋮

Table 4.1: Sample Data Format for both the **E** and **H** files.

The line-sample files have the same individual format as the point sample files, with filenames having an increasing suffix along the linear path of the sample. For example if there are two intervals along the line (see Table 2.10) there will be three point sample files named: `LineVecE-Line001-000.dat`, `LineVecE-Line001-001.dat` and `LineVecE-Line001-002.dat`, or similarly for magnetic field sampling. The distance between the sample points along the line is given by output from the FDTD code. The number in the “-Line001-” part of the filename will increment for additional line **E** samples.

The filename formats are compile-time options. For example, line sample filenames can be changed so that “-Line001-” would be replaced with coordinates of the sample line. The coordinate would be in cells or meters, depending on how the line was specified. While coordinates are useful meta-data, the filenames do become somewhat lengthy and cumbersome. As provided here, the “-Line001-” format is used.

4.2 Heightfield Input Files

The heightfield files are ASCII coded files containing heights in meters. The first line of heightfield data files consists of two integers, x_{size} and y_{size} ; these values are the size of the heightfield in cells. Each subsequent line has x_{size} floating point height values. There will be y_{size} data lines, or $y_{\text{size}} + 1$ total lines in the file.

Using the interpretation that the FDTD $+x$ axis is east, and the FDTD $+y$ axis is north, the first height value is the south-west corner of the heightfield. Subsequent values in each data line moves to the east. And subsequent lines are further north. It is not complicated to make file readers for other heightfield file formats.